Advance Materials Development and Applied Mechanics

Edited by
Keishi Matsuda, P.S. Pa and Wiseroad Yun

TRANS TECH PUBLICATIONS

Advance Materials Development and Applied Mechanics

Edited by
Keishi Matsuda
P.S. Pa
Wiseroad Yun

Advance Materials Development and Applied Mechanics

Selected, peer reviewed papers from the
3rd International Conference on
Advanced Materials Design and Mechanics
(ICAMDM2014),
May 23-24, 2014, Singapore

Edited by

Keishi Matsuda, P.S. Pa and Wiseroad Yun



Copyright © 2014 Trans Tech Publications Ltd, Switzerland

All rights reserved. No part of the contents of this publication may be reproduced or transmitted in any form or by any means without the written permission of the publisher.

Trans Tech Publications Ltd
Churerstrasse 20
CH-8808 Pfaffikon
Switzerland
http://www.ttp.net

Volume 597 of
Applied Mechanics and Materials
ISSN print 1660-9336
ISSN cd 1660-9336
ISSN web 1662-7482

Full text available online at *http://www.scientific.net*

***Distributed** worldwide by*

Trans Tech Publications Ltd
Churerstrasse 20
CH-8808 Pfaffikon
Switzerland

Fax: +41 (44) 922 10 33
e-mail: sales@ttp.net

and in the Americas by

Trans Tech Publications Inc.
PO Box 699, May Street
Enfield, NH 03748
USA

Phone: +1 (603) 632-7377
Fax: +1 (603) 632-5611
e-mail: sales-usa@ttp.net

Preface

Dear Distinguished Authors and Guests,

The Organizing Committee warmly welcomes you to 2014 the 3rd International Conference on Advanced Materials Design and Mechanics (ICAMDM2014) (TTP Conference ID: 1039), held on 23-24 May, 2014 in Singapore.

The aim of 3rd ICAMDM2014 is to present the latest research and results of scientists (professors, students, PhD Students, engineers, and post-doc scientist) related to Advanced Materials Design and Mechanics topics. This conference provides opportunities for the different areas delegates to exchange new ideas and application experiences face to face, to establish business or research relations and to find global partners for future collaboration.

After the peer-review process, the submitted papers were selected on the basis of originality, significance, and clarity for the purpose of the conference. The selected papers and additional late-breaking contributions to be presented as lectures will make an exciting technical program. The conference program is extremely rich, featuring high-impact presentation. We hope that the conference results constituted significant contribution to the knowledge in these up to date scientific field.

The proceeding records the fully refereed papers presented at the conference. The main conference themes and tracks are Advanced Materials Design and Mechanics: Nanomaterials and Technologies, Advanced Material, Composite Materials and it's Applications and Technologies, Films, Coating and Surface Engineering and Other topics. Hopefully, all participants and other interested readers benefit scientifically from the proceedings and also find it stimulating in the process.

On behalf of the organizing committee, I would like to especially thank Dorthe, Sandra, Anne, Tanja and all the editors from Trans Tech Publications for their great support to 3rd ICAMDM2014. Without their excellent editorial work, 3rd ICAMDM2014 will not be published so timely and successfully.

Finally we wish all the authors and attendees of 3rd ICAMDM2014 a unique, rewarding and enjoyable memory at 3rd ICAMDM2014 in Singapore. We look forward to your participation in the 4th ICAMDM2015 in 2015.

With our warmest regards,

Keishi Matsuda, P. S. Pa, Wiseroad Yun
Conference Organizing Chair

June 10, 2014

Committees and Sponsors

Committees

Conference Chair
Jing Guo, Harbin (Dalian) Section CIS Chapter, China

Workshop Chairs
Wen-Fang Yen, Hwa Hsia Institute of Technology, Taiwan
Jing Guo, Harbin (Dalian)Section CIS Chapter, China
Ching-Kuo Wang, Taiwan Society of Android Robotics, Taiwan
Technical Program Committee Chairs
Ching-Chih Kuo, Hwa Hsia Institute of Technology, Taiwan
Wen-Jieh Wang, Hwa Hsia Institute of Technology, Taiwan

Technical Program Committee Chairs
XinSheng Peng, Zhejiang University, China
BaiDa Zhang, National University of Defense Technology, China
Hanchen Huang, University of Connecticut, USA
George Baciu,The Hong Kong Polytechnic University, HongKong
Daoheng Sun, Xiamen University, China
Xie Xiaohui, Shenzhen institutes of advanced technology, Chinese academy of sciences, China
Qing He, North China Electric Power University, China
Miaolei Zhou, Jilin University, China
Desheng Li, Anhui Science and Technology University, China
Zhixin Yang, University of Macau, Macau
International Program Committee Chair (UK)
James B.P.Lim, Queen's University Belfast, UK

International Program Committee Chair (Canada)
Quan Wang, University fo Manitoba, Canada

International Program Committee Chair (South Africa)
Ratnam Paskaramoorthy, University of the Witwatersrand, South Africa

International Program Committee Chair (Japan)
Keishi Matsuda, Matsuyama University, Japan (Guest Editor)
Tao Liu, Kochi University of Technology, Japan
Yasushiro Nishioka, Nihon University, Japan
Ikuo IHARA, Nagaoka University of Technology, Japan

International Program Committee Chair (Korea)
Kyoungjin Kim, Kumoh National Institute of Technology, Korea
Hwa-Young Jeong, Kyung Hee University, Korea
Hyun-Do YUN, Chungnam National University, Korea
Park Wan-Shin, Chungmam National University, Korea
Wiseroad Yun, Chungnam National University, Korea （Guest Editor）

International Program Committee Chair (Taiwan)
Chiung-Hui Chen, Department of Digital Media Design, Asia University, Taiwan
JiaShiun Chen, National Taipei University of Technology, Taiwan
Hao-En Chueh, Yuanpei University, Taiwan
Wen-Tsai Sung, National Chin-Yi University of Technology, Taiwan
Yung-Tse,Tsai,National Chiayi University,Taiwan

International Program Committee Chair (Malayisa)
CheeFai Tan,Universiti Teknikal Malaysia Melaka,Malaysia
Mohd Sapuan Salit, Universiti Putra Malaysia, Malaysia

International Program Committee Chair (India)
C.N.Ashok Kumar, VIT University, India
Sreenivasan M, GKM College of Engineering & Technology, India
Sukumar Puhan, GKM College of Engineering & Technology, India
M. Sreenivasan, GKM College of Engineering & Technology, India

International Program Committee Chair (Thailand)
Komson Jirapattarasilp, King Mongkut's University of Technology Thonburi, Thailand
Anuchit Uchaipichat, Vongchavalitkul University, Thailand

Table of Contents

Preface, Committees and Sponsors

Chapter 1: Nanomaterials and Technologies

The Study of High Efficiency Photovoltaic Devices with Metal Nanoparticles
L.Z. Hsieh, M.H. Lin and X.M. Duan 3

Thermal Bubble Nucleation in a Nanochannel: An Experiment Investigation
M. Chen, K.P. Jiang, D.W. Jiang, D.D. Chen and Y.F. Zhao 7

Effect of Cosurfactants on Pore Sizes of Continuous Highly Ordered Mesoporous Silica Nanofibers
Y. Zhou, W.P. Zhang, G. Wang, Y.Q. Zhang, J.H. Cao and D.Y. Wu 13

Influence of Uniaxial Stress on the Stress-Strain Curve Measured by Nanoindentation
I. Ihara, K. Ohtsuki and I. Matsuya 17

The Preparation and Characterization of ZnO/Graphene Nanocomposites
Z.P. Wang, G.L. Wu and Y. He 21

Study of Nano Coating Micron Calcite Reaction Process and Influence Factors
N.B. Huo, S. Liu and X.J. Jia 28

Resistances of Nano-Titanium Dioxide on the Ultraviolet Aging of Poly(butylene succinate)
L. Liu, Y.R. Wang, Y.P. Zuo, D. Liu and B.H. Guo 32

Advances of Study on the Developments and Applications of Carbon Nanotubes
A.Y. Zhang 36

Monte Carlo Simulation of the Dispersion of Carbon Nanotubes in Cement Matrix
B.M. Wang, Y. Zhang, M.L. Yu and Y. Han 40

Preparation and Antibacterial Activity of Silver Doping Nano Zinc Oxide
Q. Li, X.H. Zhao, X.W. Li, L.P. Wang, Q.Q. Liu and C. Zhang 45

Preparation of Amorphous Silicon Carbide Nanostructures via Solvothermal Method
H.X. Li, G.Y. Li, T.J. Hu, X.D. Li and Y.Q. Yang 49

Doped TiO_2 Nanotube for Lithium Ion Battery
X.X. Hu, J.X. Liu, Z.Y. Wu, X.R. Zheng and M. Ma 53

Chapter 2: Advanced Material, Composite Materials and its Applications and Technologies

Information Systems for Composite Materials: Requirements and Challenges
W. Dangelmaier, T. Sommer-Dittrich, J. Streichhan and M. Monhof 59

Mechanical Properties of DGEBA/Amidoamine Blend at Non-Stoichiometric Ratios
B. Satheesh, N. Warrior and K.Y. Tshai 63

Research on Adsorption Kinetics Models' Fitting Values of H_2O_2 Oxidated Loofah Sponge on Methylene Blue
Y.H. Dou, Y.W. Wang, X.H. Zhao, Y. Wang, X.W. Li, M. Wang, Q. Li and Q. Li 72

Thermal Tuning of Vibration Band Gaps in Thin Phononic Crystal Plates with Nitinol
H.J. Zhao, R.Q. Liu and H.W. Guo 78

Synthesis of $Cu_2ZnSnSe_4$ Compounds Using Solvo-Thermal Method
C.S. Chou, J.W. Jhang, P. Wu and W.H. Lu 84

The Effect of Guide Sleeves on Shear Behavior of 3D Weaving Composites
X.C. Wu, Z.D. Shan, F. Liu and Y. Wang 89

The Microstructure and Mechanical Properties Research of FeCrWMoV-Series High Temperature Self-Compensation Lubricating Composite Materials
Y. Han, Y.J. Wang, S.R. Wang and G.J. Xue 95

Continuously Large-Scale Preparation of Multi-Layer Graphene Grown on Polycrystalline SiC Microspheres
J. Ma, G.Y. Li, Z.Y. Chu, T.J. Hu, Y.H. Li and X.D. Li 99

Effects of Mechanical Alloying on Microstructure and Properties of Powder Injection Moulded SiC_p-Reinforced Aluminium Composite
T. Patcharawit, S. Klahan, P. Rupkrathok and N. Chuankrerkkul 103

Hydrothermal Synthesis and Upconversion Properties of Yb^{3+}, Tm^{3+} Co-Doped Gd_6MoO_{12} Phosphor with Regular Morphologies
J.Y. Sun, B. Xue, Q.M. Di, Q.G. Xu and L. Han 109

A First-Principles Study of Electron-Phonon Coupling of OsB_2
Y.Q. Wang, J. Gao and S.P. Yan 113

Photoluminescence and Energy Transfer from Sm^{3+} to Eu^{3+} in $Na_3YSi_2O_7$ Phosphor for Light-Emitting Diodes
J.Y. Sun, D.P. Cui, Q.M. Di, Q.G. Xu and L. Han 117

Compressive Properties of Corevo® Foam under Uni-Axial Loading Based on Experimental and Numerical Analysis
M.A. Sulong, V. Mathier, T. Fiedler, I.V. Belova and G.E. Murch 121

Fine Spin Filtering Effect in Co-Phthalocyanine Molecule Induced by the Spin Polarization of Co Atom
Y.H. Zhou, X.H. Qiu, L.L. Zhou and Y.L. Peng 127

Recent Developments in Molecularly Imprinted Solid Phase Extraction Technology
G.J. Shen and H.Y. Pei 131

Effect of Cooling Rate on the Microstructures and Mechanical Properties of Mg-Y Alloys
G.C. Sim, K.S. Tun, X.H. Tan, C.K.J. Weng, K.W.R. Onn, M. Gupta and T.K. Lee 135

Observation of Corrosion Resistance of 13Cr-2Ni-2Mo Stainless Steel Quenched by Induction Heating
K. Kida, K. Okamoto, M. Ishida, K. Mizobe and T. Shibukawa 140

Study on the Use of Fleshings-Derived Collagen in Post Tanning Operations
M. Puccini and D. Castiello 144

Chapter 3: Films, Coating and Surface Engineering

Ionic Distribution in Plasma for the Process of Electron-Beam Physical Vapor Deposition
C.Y. Ho and W.C. Wu 153

Flaking Initiation Life under Rolling Contact Fatigue of Ceramic Coated Steels Quenched after Coating Process
H. Tanabe, K. Ogawa, M. Nishizawa, Y. Izumi and T. Takamatsu 157

Preparation, Characterization and Dielectric Property of Novel Poly(cyanate ester) Thin Films
X.Y. Zhao, Z.Y. Sun and M.Z. Wang 161

The Influencing Factors for the Thickness of Silica Sol-Gel Film by the Dip Coating Process
J.H. Lei and R.D. Zhang 165

Preparation and Properties of Pyrolytic Carbon Coating on Carbon Materials Used in Czochraski Single Crystal Silicon Furnace
W. Zhao, B. Zhu and W.W. Cao 170

Effects of Laser Parameters on the Formation of Al_2O_3-TiC Coating by Laser-Assisted Combustion
C.X. Lu, H.P. Li, P. Chen, L.H. Xue and Y.W. Yan 175

A Study on the Resistive Switching of $La_{0.7}Sr_{0.3}MnO_3$ Film Using Spectromicroscopy
H.S. Lee, K.M. Kang, W.J. Han, T.W. Lee, C.S. Park, Y.J. Choi and H.H. Park 184

The Production of ITO Transparent Conductive Materials and the Development Prospect in the Field of Biological Information
J.J. Liu, H. Men, Q.T. Zheng, W.K. Jiang, H.H. Gao and X. Zhao 188

Chapter 4: Machining and Forming Materials Technologies, other Manufacturing Technologies

A Method to Select Optimal Cutting Force Model Using the Measured Process Transfer Function
M. Zhu, X.X. Yu, W.W. Xiao and K.M. Mao 195

A Pre-Processing Method of ProCAST Based on Pro/E and HyperMesh
W. Huang, H.M. Shen, M.J. Hu, S. Li and X. Chen 203

Assessment of the Influence of Welding Parameters on Distortion
F.R. Locatelli, W.J.P. Casas and R.F.L. Filho 208

Design and Optimization of Honeycomb Corrugated Chaff Forming Roller
X.P. Yang, B. Zhong and C.J. Luo 213

Effect of Backplate Thermal Diffusivity on Mechanical Properties of Double Sided Friction Stir Welded Aluminum for Ship Structure
A. Zubaydi, N. Muhayat, Sulistijono, M.Z. Yuliadi, B. Santosa, D. Setyawan and S. Haqi 219

Study on External Grind-Hardening Experiments and the Analysis of Hardening Effects for 40Cr Steel
G. Yang, Z.T. Han and C.L. Du 223

Study of Spatial Ellipsoid Helix Interpolation Algorithm Based on Multi-Axis Lathe
X.P. Yang, Z.M. Zhou, Y.J. Gu and L.X. Wang 228

Research on Flange State during Spinning of AZ31 Magnesium Alloy Rotators
L.L. Li, Z.Y. Cai, H.Q. Xu, M. Wang, R. Zhang, D.L. Wang, Y.L. Zhang and X.F. Gao 233

Numerical Simulation and Analysis for Blow-Off Flow Field of a Wet Skin Pass Mill
H.J. Qiao and D.R. Gao 238

Molecular Dynamics Simulation of Two-Phase Structures of Copper Formed by Laser Grooving
P. Wen, G. Tao and P.J. Zhou 242

Study on Optimal Spacing and the Residual Height Parameter of Blade Part in MASTERCAM
S.H. Xiao and W.C. Zhou 249

Effect of Preheat Temperature on Friction Stir Welded Aluminum Alloy 5052 Joints
N. Muhayat, Triyono, B. Kusharjanta and R.T. Handika 253

FE Modelling of Residual Stresses and Validation Using Chip-Mechanism and Microstructural Analysis of Ultrasonic Vibration Assisted Turning of Ti Alloy Ti-6Al-4V
S. Patil, D. Sheed and R. Singh 257

Research on Performance of Foundry Sand under the Effect of Chemical Binder
Q.Z. Sun, J.G. Yan, P.Q. Zhang, Z.K. Zhao and H. Du 262

The Effect of the Initial Temperature of Ring Blank on Conical Ring Rolling Process
W. Meng, G.Q. Zhao and Y.J. Guan 266

Effects of External Magnetic Field on Intensity of Plasma Flow
C.Y. Ho, Y.H. Tsai and C. Ma 272

Formation and Distribution Mechanism of Intermetallic Compounds of Al/Mg Joint with Zn Transition Metal
Q. Gao, K.H. Wang, H. Ma and W.G. Feng 276

Chapter 5: Applied Mechanics and Construction Engineering

Concrete Strength Variability in Italian RC Buildings: Analysis of a Large DataBase of Core Tests
A. Masi, A. Digrisolo and G. Santarsiero 283

Buckling Behavior of Catheter Reinforced with Braids under Axial Compression after Torsion: Effect of Deformation Speed on Buckling Region
Y. Kato 291

Effect of Fiber Volume Fraction on Compressive and Flexural Properties of High-Strength Steel Fiber Reinforced Concrete
K.L. Ahn, S.J. Jang, Y.J. Yun, D.G. Yu and H.D. Yun 296

Analysis of Guyed Transmission Tower Dynamic Characteristic
F.L. Gan and X.B. Jia 300

Analysis of the Forms of Attachment Frame and Stress Characteristics
B. Li, J. Liu and K.W. Wang 304

Damping Analysis of Laminated Plates Using Complex Stiffness Method
Q.Q. Wu and M.Q. Wang 308

Influence of Axial Compression Ratio on Seismic Behavior of Reactive Powder Concrete (RPC) Beam-Column Joints
Y.Z. Ju, C.Y. Li and D.H. Wang 312

Influence of Curing Temperature on the Compressive Strength of High Performance Concrete
S.W. Kim, W.S. Park, N.Y. Eom, Y.I. Jang, H.D. Yun and D.G. Kim 316

Mechanical Properties of Reactive Powder Concrete Containing Fly Ash under Different Curing Regimes
D.H. Wang, Y.Z. Ju and W.Z. Zheng 320

Static Stress Changes and Triggering Imposed by Wenchuan Earthquake on Lushan M7 Earthquake
D.N. Lei, Y.J. Cai and H. Li 324

Structural Behaviors of Non-Ductile Reinforced Concrete Frames with Engineered Cement Composite (ECC) Wing Wall Elements
D.H. Kang, W.G. Lim, H.R. Kim, M.H. Lee and H.D. Yun 328

The Influence of Base Pre-Tilting on the Dynamic Properties of Angle Towers
Y.P. Li, L. Li and X.Y. Yang 332

Stress Analysis and Structure Improvement on Arm of Ladle Turret
X.Y. Zhang and L.K. Guan 336

Cathodic Prevention and Cathodic Protection of Concrete Slab with Zinc Sacrificial Anode
J.A. Jeong 341

Engineering Properties of Controlled Low-Strength Material Made with Residual Soil and Class F Fly Ash
Y.N. Sheen, L.J. Huang and D.H. Le 345

On the Multiple Linear Regression and Artificial Neural Networks for Strength Prediction of Soil-Based Controlled Low-Strength Material
L.J. Huang, Y.N. Sheen and D.H. Le 349

Measurement of Sliding Wear of Shot-Peened Partially Stabilized Zirconia Plate
H. Koike, K. Iwanaka and K. Takahashi 353

Chapter 6: Robotics, Control System and Measurement Technologies

Application of Fuzzy Control Theory in Obstacle Avoidance Simulation of Intelligent Wheelchair
F. Li 361

Research on Flexible Centroid Measurement Method for Segments of Large-Thrust Carrier Rocket
X.L. Zhang, L.S. Zhang, W.Y. Tang, C. Wang and W.C. Liu 365

Simulation Research on the Compound Control System of Internal Model Add Feed-Forward Compensator
S.B. Zhang 372

Wind-Induced Vibration Control for Transmission System Using Steel-Lead Viscoelastic Damper
F.L. Gan and H.L. Jiang 376

Fuzzy PID Control of ABS Based on Real-Time Road Surface Identification
B. Wang, P.P. Lu, H. Guan and J. Jing 380

The Application Research of Non-Nuclear Density Gauge Electromagnetic Technology in the Road Engineering
J.L. Chai and Y. Wang 384

Lie Algebraic Structure and Poisson Conservation Law for One Class of Multi-Dimensional Coupled Oscillators
Y. Sun, B.Y. Chen and J.L. Fu 388

Three-Level SVPWM Inverter with Li-Ion Battery Driven for Robot Motor
S. Chen and C.C. Chen 393

Development of Practical Wrist Rehabilitation Robot by Mirror Effect
I. Yamamoto, M. Matsui, N. Inagawa, T. Tsuji, K. Hachisuka, F. Wada and A. Hachisuka 397

K-MORE: Design of a Kinect Motion Oriented iRobotics Environment
H.H. Ku, T.S. Kao and C.H. Chi 401

Dynamic Control of Gait and Posture Training on Robot
C.C. Chen, S.H. Ciou, Y.S. Hwang, Y.L. Chen and S. Chen 407

Novel Strengthened Structure of Stair-Climbing Robots on Campus
C.K. Wang, Y.H. Wu and Y.S. Cheng 411

Chapter 7: Electrical Devices and Embedded Systems, Machine Elements, Systems and Mechanisms

Computer Aided Design of a New Universal Clamping Mechanism
J.Z. Li 417

Experimental Study of Corrosion Sensors for the Design Technology of Bridge Longevity
J.A. Jeong 421

A Theoretical Study of the Phase Angle for the β Type Pulse-Steam Stirling Expander
G.J. Lai, C.K. Lin, Y. Kobayashi, M. Matsuo and M.C. Chiu 425

Damage Identification of the Blade Based on Distributed Fiber Bragg Grating Sensors
Y.H. Zhang and W.Y. Yang 431

Design of Electrochemical Biosensor on Naphthalene Content Detection in Water Based on SCM
Y. Liu, Y.P. Yu, H.Y. Wu and R.K. Chang 435

Design of Reflective/Diffractive Objective Optical System for Handed Low-Light Night Vision Google
N. Li and R.L. Zhang 439

Fault Diagnosis of Mechanized Bridge's Electrical System Based on I^2C-bus and Virtual Instrument Technology
Y.S. Sun, X.Q. Yang, L. Pei and S. Yan 444

Meshing Efficiency of Involute Helical Gears Based on Elastohydrodynamic Lubrication
B. Wang and X.B. Chen 450

Research about Deformations Identification for Globoidal Cam Machine Based on Multi-Body System Theory
L.P. Zhao, H.R. Chen, Y.Y. Yao, H. Zhao and P. Yan 454

Selective Tension Apparatus Development of Vibration Membrane for Stereo Speaker Production
U.S. Kim, Y.J. Jung, B.W. Jeong, M.S. Kim, G.S. Yang and J.W. Park 458

The Establishment and Weight Calculation Method of Evaluation Indexes for the Float Board Propulsion System
Y.Q. Cai, F.M. Zeng and J.L. Liu 464

The Simulation Studies of PWM Voltage Source Rectifier under Unbalanced Grid Voltage
J.L. Zhang and Y.R. Li 468

The Skimmer Selection Based on Fuzzy Decision in Response to Oil Spill
Y.D. Zhang and Y. Liu 472

Research on Manufacturing of Blade Screw in Solid-Liquid Separator
J.J. Wang, K. Wang and Q. Wu 476

VLC-LED Receiver Condenser with Optimized CPC
Z.X. Wu, Y.J. Nie, W. Jin, Z.X. Zhang, Q. Qiao and E.D. Gu 480

300 MW Coal Tangential Boiler Furnace Numerical Simulation
H.X. Liu and B.X. Li 484

Optimization Design Analysis on Electrical Performance of ITER Axial Composite Insulation Break
C.C. Yang 488

Research on Overloading Protection of Permanent Magnetic Coupler in Coal Mine
W.Q. Yuan, Y. Liu, D. Li and G.Y. Meng 492

The Research of Drive Roll's Dynamics Characteristics
S.H. Li 498

Analysis and Research on the Picking Roller of the Half-Feed Peanut Combine Harvester
X.L. Lü, Z.C. Hu and B.L. Peng 502

Statics and Grasp Stiffness Analysis of an Underactuated Cable-Truss Mechanism
N. Wu, R.Q. Liu and H.W. Guo 507

An All-Digital, Cyclic and Synthesizable TDC in the ADPLL-Based Clocking Digital Systems for Multidomain Power Management
S.H. Chen and M.B. Lin 515

Chapter 8: Vehicles, Transport and Navigation Development

A Novel Adaptive UKF and its Application in the SINS/GPS Integrated Navigation
Y. Li, S.S. Gao and Y. Yang 521

A Variable Proportional Valve Braking Force Distribution Strategy Including SOC Constraints of Electric Vehicles
H.X. Yu and Z.Y. Lin 525

Finite Element Analysis of Key Component on Two Wheels Scooter
Z.D. Huang, Y.P. Du, B.Q. Liu, G. Yang, Y.F. Liu and X.G. Zhao 531

Multi-Objective Optimization for the Section Structure of Sandwich Plate Applied in the High-Speed Train Compartments
Y.Q. Wang, X. Chen, B. Wang, X.B. Kuang and X.G. Tian 535

Secondary Developments of ANSYS for Temperature and Stress Field Simulation of Brake Disc Based on VB
M.L. Wu, X.Y. Zhu and J.Y. Zuo 540

Simplified Dynamics Modeling of Seat-Passenger in Vehicle Frontal Crash
Y.Y. Wang, Z.Y. Lyu, L.L. Wang and Z.H. Yan 544

Study on the Stress Variation Mechanism for the Rails under the Wheels Repeated Rolling Effects
H. Song, L.B. Song, J.K. Yao, F.B. Lian and W. Li 551

SINS Transfer Alignment Based on Robust SDRE Filter
D.Y. Wang, P. Sun, J.Y. Peng and X.H.G. Xu 557

CHAPTER 1:

Nanomaterials and Technologies

Applied Mechanics and Materials Vol. 597 (2014) pp 3-6
© (2014) Trans Tech Publications, Switzerland
doi:10.4028/www.scientific.net/AMM.597.3

The Study of High Efficiency Photovoltaic Devices with Metal Nonoparticles

Li-Zen Hsieh[1*], Mo-Hua Lin[2], and Xi-Ming Duan[2]

[1] Department of Electrical Engineering, Hwa Hsia Institute of Technology, Taiwan (R.O.C.)

[2] Department of Electrical and Electronic Engineering, CCIT, National Defense University, Taiwan (R.O.C.)

E-mail: lzhsieh@cc.hwh.edu.tw

Keywords: surface plasmon resonance(SPR), metal nanoparticles(MNPs) , solar cell.

Abstract. The photovoltaic devices with free electrons of nano metal were studied by nano metal scattering and near-field surface plasmon resonance (SPR) enhancing. The results revealed that devices with metal nonoparticles can improve the photoelectric conversion efficiency of solar cells. The metal nanoparticles roughness also reduced the incident light reflection and increased the electrical conductivity of metal characteristics.

Introduction

Silicon solar cell had been discussed for several decade years, due to its abundant and plentiful sources on earth. Device fabricated cost was also much cheaper than organic solar cell and has higher efficiency. Because of above mentioned advantages, silicon solar cell became more popular issues. In this paper, we have successfully achieved to raise solar cell's efficiency by surface nanoparticles with variety manufacturing parameters such as particle size, deposition thickness and annealing temperature[1-3].

According to the Mie scattering theory, the extinction coefficient of metal balls in above 100-nanometer particles mainly was dominated over the scattering of balls, then major extinction coefficients of tiny nanoparticles for absorption behaves were very different. The nano metal scattering, surface-plasmon-resonance (SPR) enhancement[4] and ionized free electron of nano-metal[5] can increase the efficiency of solar cells. For optical properties, the first two mechanisms related nano metal characteristics with their kind of metal, size, and metal surroundings. The efficiency was increased by the scattering of nano-particles, which caused to increase path in the absorption layer for the long-wavelength light. For electrical properties, the surface resistivity of devices can be reduced by ionized electrons which were stimulated by absorption light.

Experiments, results and discussion

A metal silver film deposited on silicon substrate by thermal evaporator and following high-temperature annealing to form metal nanoparticles (MNPs). By annealing process, the different thickness of silver film can form silver nanorods or nanocone structures with different angle and aspect ratio in the process of the annealing heating with different annealing temperatures.

The photoelectric measurement was analyzed by UV/visible spectrum. The nanoparticles surface-plasmon properties were also explored by metal nanoparticles on a silicon solar cell with Ni/Au interdigitated pattern and the measurements are achieved by a xenon-arc-lamp solar simulator which simulate solar light with filtered chip to provide a stable solar light source (AM1.5G; 1000W/m^2).

The silver film were deposited on silicon substrate by thermal evaporator at constant vacuum level of 5×10^{-7} torr and stable flux, but different time. There were three deposited periods of time for 10, 15 and 20sec and they formed film thicknesses of 15.2 nm, 25.6 nm and 40.7 nm, respectively. The longer deposition time is proceeded, the thicker film thickness we have.

Table 1 experimental results of reflectance for the cases of different thickness of silver film at different annealing temperatures (i.e., 300 ^{0}C, 400 ^{0}C and 500 ^{0}C, respectively). For the incident light wavelength of 450 nm, the reflectivity of the original silicon wafer from 44.8% increased to 50.6%, 52.3% and 62.2% with different thickness silver thin film of 15.2 nm, 25.6 nm and 40.7 nm, respectively. All of the three Ag coating thin film samples have higher reflectance, because of high mirror-like surface. But the MNPs were formed after appropriate annealing temperature and the reflectivities can be reduced. For 400℃-annealing samples, the reflectivity of the original silicon wafer from 44.8% decreased to 28.7%, 19.1% and 18.8% respectively, shown in Table 1.

Table 1 Experimental results of reflectance for the cases of different thickness of silver film at 300 ^{0}C-, 400 ^{0}C- and 500 ^{0}C-annealing temperatures, respectively.

Thickness	reflectivity	300℃-reflectivity	400℃-reflectivity	500℃-reflectivity
Original	44.8 %	-	-	-
15.2 nm	50.6 %	42.7 %	28.7 %	34.6 %
25.6 nm	52.3 %	38.2 %	19.1 %	22.7 %
40.7 nm	62.2 %	32.1 %	18.8 %	20.1 %

Initially, silver film will first crack, stress-released and thus nucleate elliptical particles by sufficient heat effect. The different silver nanoparticles sizes were form by different thickness of silver film, i.e., (a) raging in 60-70 nm for the case of silver thickness with 15.2 nm, (b) raging in 80-90 nm for the case of silver thickness with 25.6 nm and (c)raging in 120-180 nm for the case of silver thickness with 40.7 nm, respectively. Figure 1 showed the reflectance of different ranged diameters of Ag nanoparticles formed from silver film [i.e., 60-70 nm (solid square black line), 80-90 nm (red circular line) and 120-200 nm (blue up-triangle line), respectively] as a function of wavelength in the range of 300-1100 nm. Data also supplied for Table 1 at incident light wavelength of 450nm. For photoelectric characteristics measurements, samples were fabricated by photolithography steps with interdigitated electrodes of 6-μm-width 8-μm-spacing and the following plating method of silver nano-particles was fabricated on the surface.

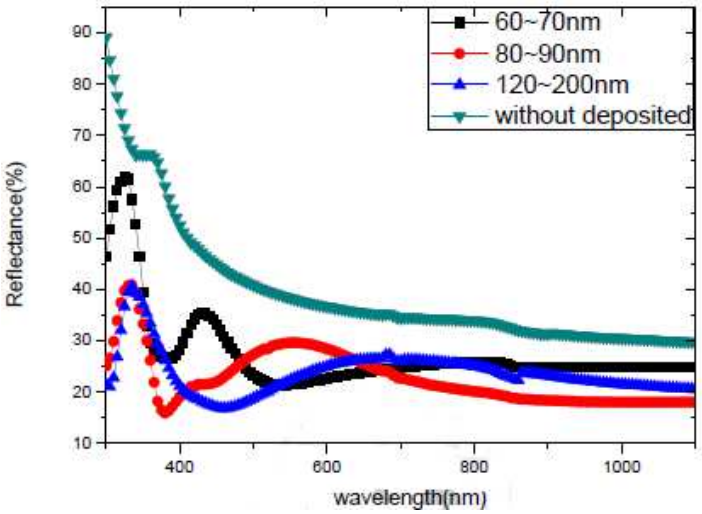


Fig.1 Reflectance with different size of Ag nanoparticles.

The photocurrent and the dark current without significantly increased which has no nanoparticles in Fig.2(a). Figures 2(b), (c), (d) were separately prepared for silver nanoparticles size 60-70 nm, and 80-90 nm and 180-200 nm and the photocurrent/darkcurrent (P/D) ratio be raised to 1.913, 1.78 and 1.114 times respectively. Because of silver nanoparticles localized surface and the effect of plasmon resonance, the incident photons can be effectively absorbed.

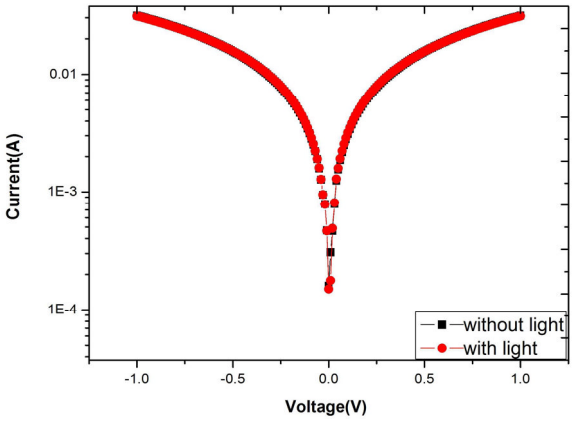


Fig. 2(a). I-V curve with no nanoparticles.

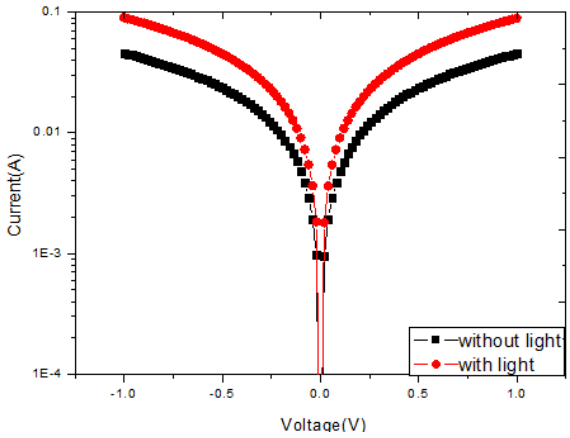
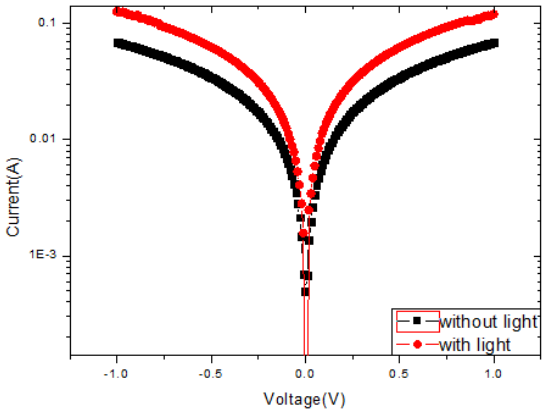


Fig.2(b) I-V curve with particles size 60~70nm.



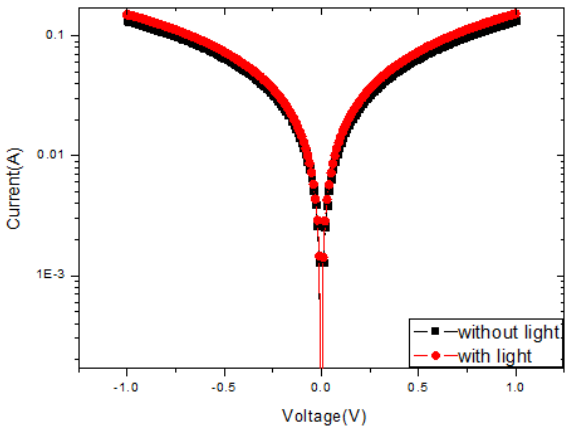


Fig. 2(c) I-V curve with particles size 80~90nm. Fig. 2(d) I-V curve with particles size 180~200nm.

Figure 3 showed I-V curves of solar cells without and with different size of nanoparticles, that detected by solar simulator. The conversion efficiency (η) of solar cell with silver nanoparticles of

60-70 nm was raised from the 12.7% to 17.1% and has the most advancement in this three samples. For the samples coating silver nanoparticles of 80-90 nm, the η was changed from 12.7% to 14.8%, when the samples with silver nanoparticles (120 to 200-nm diameter), the η was up to 13.3%. The better η was existent with smaller nanoparticle size coating on surface, the improvement inferred with both of nano-metal scattering effect and surface-plasmon-resonance (SPR) enhancement.

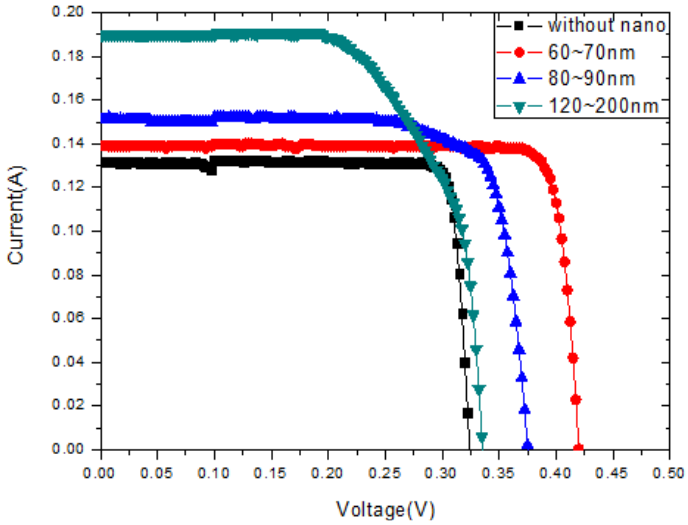


Fig. 3 I-V curves for solar cells without and with different size of nanoparticles.

Conclusion

In this study, the photoelectric conversion efficiency of solar cells with metal nanoparticles was obviously more promotive than the one without metal nanoparticles. However, we found that the solar cell was prepared silver nano particles of 60 to70-nm dimension have the high conversion efficiency, over 4.4% raise. The η was improved efficiently and simply by MNPs coating on surface.

Reference

[1] L. J. Sherr, S.-H Chang, G. C. Schatz, R. P. V. Duyne, B. J. Wiley, and Y. Xia, "Localized Surface Plasmon Resmon Resonance Spectroscopy of Single Silver Nanocubes " , Nan Lett.5, pp.2034-2038, 2005.

[2] E.-S. kwak, J. Henzie, S.-H. Chang, S. K. Gray, and G. C. Schatz, "Surface Plasmon Standing Waves in Large-Area Sub wavelength Hole Arrays", 78 Nano Lett.5, pp.1963, 2005.

[3] L. Yin, V. K. Vlasko -Vlasov, A. Rydh, J. Pearson, U. Welpl, S-H. Chang, S. K. Gray, G. C. Schatz ,D. E. Brown, and C. W. Kimball, "Surface Plasmons at Single Nanohles in Au-fims", Appl. Phys. Lett. 85, pp.467-469, 2004.

[4] Chen, F.; Johnston, R. L. Plasmonic Properties of Silver Nanoparticles on Two Substrates. Springer Science: Plasmonics 2009, 147–148.

[5] H. Raether, "Surface plasmons on smooth and rough surface and on gratings", Springer, New York, 1988.

Applied Mechanics and Materials Vol. 597 (2014) pp 7-12
© (2014) Trans Tech Publications, Switzerland
doi:10.4028/www.scientific.net/AMM.597.7

Thermal bubble nucleation in a nanochannel: an experiment investigation

Min Chen[a]*, Kunpeng Jiang[b], Dawei Jiang[c], Dongdong Chen[d]

and Yanfang Zhao[e]

School of Mechanical Engineering, Jiangsu University, Zhenjiang 212013, China

[a]email: chenmin@mail.ujs.edu.cn, [b]email: 993817062@qq.com, [c]email: 313075443@qq.com, [d]email: 925759573@qq.com, [e]email: yanfang45@163.com

* corresponding author

Keywords: Nanochannel; thermal bubble; Coulter counter; Micro-nanofabrication

Abstract. We investigated the Nano-scale thermal bubble nucleation based on the principle of Coulter counter. With micro-nanofabrication technologies, a device was designed and fabricated, and a detection platform was set up which was used to investigate the thermal bubble nucleation of aqueous solution confined in a nanochannel with a cross size of about 100 nm×100 nm. Results show that with the temperature of the solution confined in the nanochannel increasing, the current through the channel increases first and then decreases, and vanishes after a fluctuating period. It can be found that the generating thermal bubbles can hinder the current flowing through the nanochannel. In addition, the shrinking and expanding of thermal bubbles' volume correspond to the increase and decrease of the current. Finally, the thermal bubbles block the nanochannel entirely. Through the experiment results, our device can be applied to investigate the complex behaviors of thermal bubble produced in aqueous solution confined in nanochannels, effectively.

Introduction

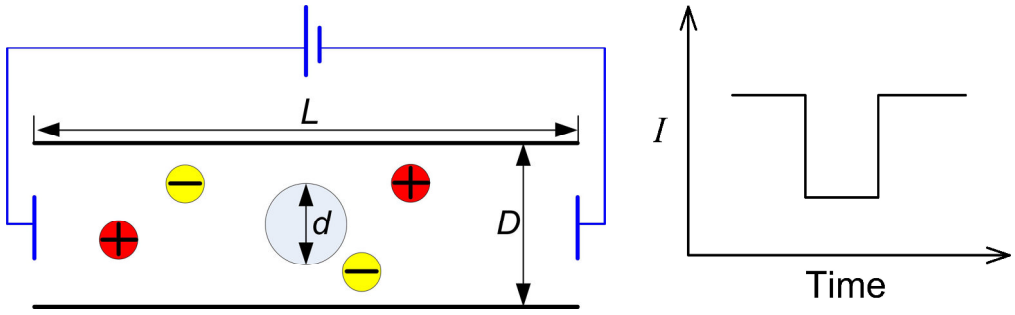
Thermal bubble nucleation in confined spaces has both fundamental interests and important applications, including micro-pumps, inkjet printers, heat exchangers, various actuators and so on [1-4]. Lin *et al.* [5, 6] firstly experimentally studied thermal bubble nucleation in micro-fabricated channels. They found the important result that thermal bubbles formed at nearly the critical temperature. Peng *et al.* [7-11] also performed a series of experimental and theoretical studies to understand thermal bubble nucleation in microchannels, based on which they developed some criteria for thermal bubble nucleation in microchannels. However, the mechanism for requiring high superheat to initiate thermal bubble in microchannels is still unclear. Meanwhile, the classical theory of thermal bubble nucleation mainly considers the behavior of thermal bubble embryos of sizes larger than the critical size and therefore, associated with meaningful classical thermodynamic properties [12]. However, in nano-confined spaces, where the bubble embryos are so small and occur in a very short timescale, the application of the classical thermal bubble nucleation theory is questionable. Considering the fundamental theory the extensive application, it is important to study the complex behaviors of nano-scale thermal bubble.

In this paper, a strategy to investigate thermal bubble nucleation confined in a nanochannel based on the principle of Coulter counter was proposed. With micro-nanofabrication technologies, a device containing a nanochannel with a cross size of about 100 nm×100 nm was fabricated and a detection platform was set up. Then the platform was used to investigate the thermal bubble

nucleation of aqueous solution confined in a nanochannel. Other equipments such as data acquisition card and high-precision galvanometer were also utilized. Our experimental results indicate that the designed device can be used to investigate the complex behaviors of thermal bubble produced in aqueous solution confined in a nanochannel effectively.

Experiment principle

In this paper, the thermal bubble behaviors in a nanochannel are investigated indirectly, through the Coulter counter principle. Coulter counter was firstly invited by Coulter in 1948, which could be used to detect the number and size of biological cells and other partials dispersed in solution [13, 14]. The principle of Coulter counter is sketched in Fig. 1, in which the battery, wire and solution constitute a conductive loop. When a particle appears in the channel, the electrical resistance of the channel will rise due to the insulation of the particle; while the initial resistance value can be measured in the solution contains no particles. Then, the electric current will drop until the particles flow through the channel. The pulse characteristic between the electric current and time can be obtained, as shown in Fig. 1b. Furthermore, the particle size by taking into account the proportional relationship between the particle size and pulse amplitude can be computed. The Coulter counter has been wisely applied in production and research domains because of its simple principle and convenient operation [15-19].



(a) (b)

Fig. 1 The principle of Coulter counter. (a) The Schematic diagram of the measurement system. (b) The corresponding current drop when the channel is blocked

Where, d is the diameter of the particles in the solution and D is the diameter of the nanopore. When a channel is in a micron scale, the nucleation of thermal bubbles in it can be observed clearly through modern equipments [20]. However, if the channel size drop to tens or several nanometers, it is difficult to observe the thermal bubble nucleation directly with recent experimental techniques. However, using the Coulter counter principle, the bubble in the nanochannel like a particle can be observed. The emergence of bubble will enhance the resistance of the channel, which will results in an electric current drop, and the current drop value corresponds to the bubble size. The bubble behaviors can also be investigated through the variation of current along with time, and the bubble size can be computed by the current reduce. In this paper, the thermal bubble behaviors in nanochannel are investigated indirectly, through the principle stated above.

The design and fabrication of device

The specific design of the device, which is used to research the thermal bubble nucleation in aqueous solution confined in a nanochannel, is stated as following. Firstly, electrolyte of certain concentration is injected into the sink on one side of the device. In our experiment NaCl and KCl solution are used. Then, the solution flows into the nanochannel region through microchannel and

enters the microchannel on the other side of the device. When the micro and nano channels are filled with solution, a certain voltage is applied across the heating electrodes and the solution is heated by the current thermal effect of the heating circle. Simultaneously, the variation of the current across the nanochannel is measured to investigate the behavior of the thermal bubble generated in the nanochannel.

To achieve the target of experiment, the device should contain micro and nano channels and the heating circle which is used to heat the solution in nanochannel. The micro and nano channels should be bonded with a cover because the solution will evaporate fast if it is exposed in the air. Based on the above considerations, a cover should be fabricated to protect the solution in the channels. Therefore, the designed device should contain two components i.e. the main part and the cover.

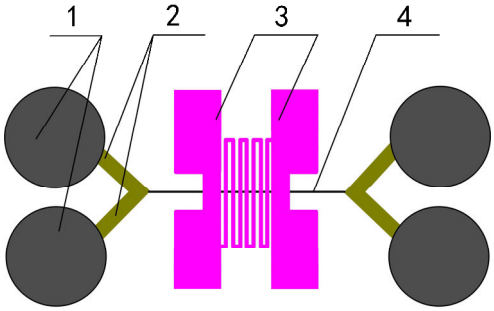


Fig. 2 The main part of the device

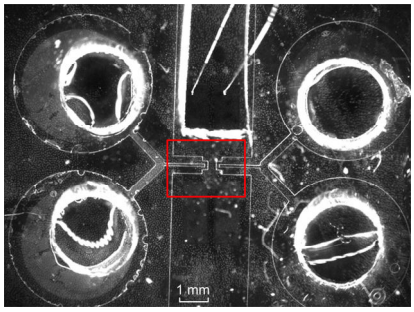


Fig. 3 A realistic photo of the experiment device

Fig. 2 shows the design of the main part of the device. As shown in Fig. 2, the main part of the device includes four components: (1) four sinks, (2) micro-channels, (3) heating electrode and circle and (4) nano-channel. As shown in Fig. 2, the heating electrode and circle are above the nanochannel and the design width of the heating circle, in the center of the electrode, is 2 μm which has an electric resistance of 600 Ω. There are four terminals in the heating electrode shown in Fig. 2, with which the electric resistance of the heating circle can be accurately measured through four-probe method [21]. The temperature with TCR (temperature coefficient of resistance), furthermore can be obtained. When a certain voltage is applied across the electrodes, the heating circle will produce Joule heating to heat the solution confined in the nanochannel.

The design size of the nanochannel is 100nm in width and 60~100 nm in height. Due to the tininess of the nanochannel, it will be easily blocked, if bonded to the cover directly. The nanochannel is under the surface for the purpose of maintaining the cleanness and smoothness of the nanochannel when the main part bonds to the cover.

Polydimethylsiloxane (PDMS) is the most popular material used in micro-fluid chips. The cover of the device is made of PDMS. The main part was obtained undergoing some usual micro-nano fabrication techniques, mainly including deposition, spinning coating photoresist, electron beam lithography, removing photoresist, dissolving, washing and airing. After the respective fabrication of the main part and the cover, the whole device is assembled with forceps under microscopy. Fig. 3 gives a realistic photo of the whole device used to investigate the thermal bubble nucleation confined in nanochannel. The center of red part is the heating circle shown in Fig. 2. The PDMS above the sinks is removed and certain amount of solution is injected in the sink by micro syringe. In addition, the PDMS in device shown in Fig.3 is removed. The two wires are extracted from two terminals of the heating electrode through specific tool.

Results and discussion

The dependence of current in nanochannel on the variation of voltage applied on heating circle. The computed theoretical electrical resistance is about 1.75×109 Ω, while the measurement value is 1.0×109 Ω which is within the error range considering the processing error and measuring error. This shows that in experiment electrolyte can enter and fill the nanochannel. After the nanochannel is confirmed to be unimpeded, a certain heating voltage is applied on the heating electrodes and the voltage between both sides of nanochannel is ensured to be 1.0 V. Then the variation of the current along with heating voltage is measured. Because the relationship between current across the nanochannel and heating voltage was not known and the mode of the controllable output voltage in data acquisition card was unable to chosen, an external power supply (CSI12001X) is connected to the electrodes and the heating voltage is modulated manually. At the start, the applied voltage is set as 0.1 V and increased 0.2 V per minute. The dependence of the current in the nanochannel on the variation of the heating voltage is plotted in Fig. 4.

As shown in Fig. 4, when the heating voltage increases from 0.1 V to 1.5 V i.e. from 0 to 500 seconds in the time axis, the current in the nanochannel increases gradually. This is attributed to the reason that the conductivity of electrolyte increases as the temperature rises. Simultaneously, there is a short rise in the current profile corresponding to every sudden increase of heating voltage, which is caused by the impact of voltage to the measured current signal. Next, when the voltage from 1.5 V to 2.7 V i.e. from 500 to 1000 seconds, there is a decreasing trend in the current curve. Maintain the voltage at 2.7 V for about 8 minutes, corresponding to the time axis from 1000 to 1500 seconds, the investigated current declines continuously. We think in the period thermal bubbles maybe develop to hinder the current by increasing the resistance. The velocity of the voltage increment reduces to 0.1 V per minute after 2.7 V and the measured current exhibits complex variation of increase and decrease which corresponds to the shrinking and expanding of the thermal bubbles in the nanochannel. Finally the current drops to zero suddenly when the voltage reaches 8 V, namely at 4200 seconds. In the nanochannel, thermal bubbles are large enough to block the current.

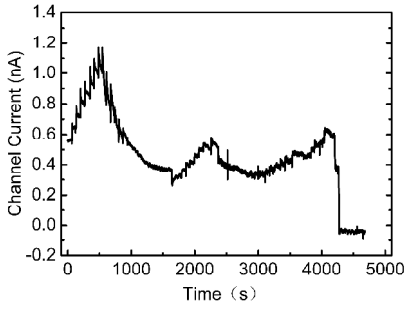


Fig. 4 The current across the nanochannel

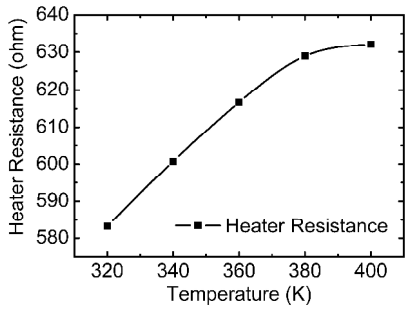


Fig. 5 The variation of heater resistance to temperature

Through the experiment, it is obviously that the current in the nanochannel strongly depends on the applied voltage. At the beginning, as the voltage rises, the solution temperature becomes higher, the conductivity grows and the current enhances. When the voltage approaches to certain value, the thermal bubbles appear and have a large effect on the current by the variation of their volumes. The result plotted in Fig. 5 is very preliminary because we cannot confirm the appearance of thermal bubbles. Furthermore, the most importance parameter i.e. the temperature of the nanochannel should be measured to investigate the influence of the voltage on the current and the appearance of thermal bubbles.

The testing of TCR. Following the measurement principle shown in Fig. 1, the resistance of heating circle was measured with Ohm's Law in the experiment. The temperature was calculated through TCR. In order to get accurate temperature, we should obtain TCR firstly.

The resistance was measured when the temperature of the nanochannel reached equilibrium in a sealed vacuum chamber using 3ω thermal conductivity measurement test rig [21]. In order to acquire reliable results, measurement was conducted 30 min after the system achieved set value. Fig. 5 displays the variation of heater resistance relative to temperature. With the temperature rising from 320 K to 380 K, the dependence of resistance on temperature is linear. However, the TCR became unstable when the temperature is higher than 400 K. As shown in Fig. 5, the resistance of electrodes is not constant and monotonously decreases with time.

From the results, the resistance of heating circle is unstable in high temperature region and it is not proportional to temperature. We think this appearance maybe attributed to the lack of annealing in sputtering process of heating circle region, which can make the metal structure inside reach equilibrium. Without annealing, the effect of temperature on the resistance can be ignored when it is low, while more obvious with the temperature increasing due to the inside unstable organization.

In Ref. 22, it was found that the resistance performance of sputtered layer would be improved by annealing. Nevertheless, the device in our experiment didn't undergo annealing process owing to the production cost and cycle. While, we attempted to measure the real-time temperature of heating circle by micro thermocouple, but we failed when stick micro thermocouple to the circle.

Summary

In order to investigate the thermal bubble behaviors in a nanochannel using the principle of Coulter counter, an experiment device with 100nm-wide and 60~100nm-high nanochannel was designed and fabricated. During the experiments, the solution could enter and fill the nanochannel, and the channel was smooth exhibited by the obtained ionic current. When heating voltage applied on the electrodes, a series results were gained to describe the relationship between the current and heating voltage. It was found that the current showed complexity of increase and decrease along variation of voltage. Based on this, we speculated that thermal bubbles appeared in the nanochannel and the increase and decrease of current corresponded to the swell and reduction of bubble volume. In addition, TCR was determined by observing the relationship between circle resistance and temperature, which was used to acquire the dependence of heating temperature on voltage. As shown by results, under 380K, heating circle has a stable TCR, while higher than 380K, doesn't. This may be attributed to the lack of annealing process in device fabrication.

Acknowledgements

M. Chen acknowledges the financial support from the Natural Science Foundation of China (Grant No.51206064), the University Natural Science Funds of Jiangsu Province (Grant No. 12KJB470003) and the Initial Research funds for the faculty of Jiangsu University (Grant No. 12JDG051)

References

[1] J.H. Tsai, L.W. Lin, A thermal-bubble-actuated micronozzle-diffuser pump, J. Microelectromech. S. 11(2002) 665-71.
[2] S. Mitsuhiro, I. Tsubasa, U. Shinji, M. Takaaki, S. Kazuo, Fabrication of a bubble-driven arrayed actuator for a tactile display, J. Micromech. Microeng.18(2008) 065012.
[3] D. Broek, M. Elwenspoek, Bubble nucleation in an explosive micro-bubble actuator, J. Micromech. Microeng.18(2008) 064003.
[4] R. Furberg, B. Palm, S.H. Li, M. Toprak, M. Muhammed, The Use of a Nano- and Microporous Surface Layer to Enhance Boiling in a Plate Heat Exchanger, J. Heat Trans-T. ASME. 131(2009) 101010.
[5] L.W. Lin, Microscale thermal bubble formation: Thermophysical phenomena and applications, Microscale Therm. Eng. 2(1998) 71-85.
[6] L. Lin, K. Udell, A. Pisano, Liquid-vapor phase transition and bubble formation in micro structures, Therm. Sci. Eng.2(1994) 52-9.
[7] X. Peng, H. Hu, B. Wang, Bubble formation of liquid boiling in microchannels, Sci. China Ser E: Technol Sci. 41(1998) 404-10.
[8] X.F. Peng, H.Y. Hu, B.X.Wang, Boiling nucleation during liquid flow in microchannels, Int J Heat Mass Transfer.41(1998) 101-6.
[9] X.F. Peng, D. Liu, D.J. Lee, Y. Yan, B.X. Wang, Cluster dynamics and fictitious boiling in microchannels, Int J Heat Mass Transfer. 43(2000) 4259-65.
[10] J.T. Zhang, X.F. Peng, G.P. Peterson, Analysis of phase-change mechanisms in microchannels using cluster nucleation theory, Microscale Thermophys Eng. 4(2000) 177-87.
[11] X.D. Wang, X.F. Peng, Y. Tian, B.X. Wang, Formation, structure, and evolution of boiling nucleus and interfacial tension between bulk liquid phase and nucleus, Heat Mass Transfer. 41(2005) 651-8.
[12] T. Kinjo, K. Ohguchi, K. Yasuoka, M. Matsumoto, Computer simulation of fluid phase change: vapor nucleation and bubble formation dynamics, Comput Mater Sci. 14(1999) 138-41.
[13] W.B.Coulter, Means for counting particles suspended in a fluid, 1953.
[14] W.H. Coulter, High speed automatic blood cell counter and cell size analyzer, Proc Natl Electron Conf. 1956.
[15] O.A. Saleh, L.L. Sohn, Quantitative sensing of nanoscale colloids using a microchip Coulter counter, Rev Sci Instrum. 72(2001) 4449-51.
[16] O.A. Saleh, L.L. Sohn, An Artificial Nanopore for Molecular Sensing, Nano Lett. 3(2002) 37-8.
[17] A. Carbonaro, L.L. Sohn, A resistive-pulse sensor chip for multianalyte immunoassays, Lab on a Chip. 5(2005) 1155-60.
[18] V.J. Ashish, Z. Jiang, H. Jun, C. Joan, Detection and counting of micro-scale particles and pollen using a multi-aperture Coulter counter, Meas Sci Technol. 17(2006) 1706.
[19] R. Rodriguez-Trujillo, C.A. Mills, J. Samitier, G. Gomila, Low cost micro-Coulter counter with hydrodynamic focusing, Microfluid Nanofluid. 3(2007) 171-6.
[20] X.F. Peng, Y. Tien, D.J. Lee, Bubble nucleation in microchannels: statistical mechanics approach, Int J Heat Mass Transfer. 44(2001) 2957-64.
[21] J. Yang, S. Waltermire, Y. Chen, A.A. Zinn, T.T. Xu, D. Li, Contact thermal resistance between individual multiwall carbon nanotubes, Appl Phys Lett. 96 (2010).
[22] M.M. Nayak, S. Srinivasulu, K. Rajanna, S. Mohan, A.E. Muthunayagam, Electrical and strain-sensitive behaviour of sputtered gold films, J Mater Sci Lett. 12(1993) 119-21.

Applied Mechanics and Materials Vol. 597 (2014) pp 13-16
© (2014) Trans Tech Publications, Switzerland
doi:10.4028/www.scientific.net/AMM.597.13

Effect of Cosurfactants on Pore Sizes of Continuous Highly Ordered Mesoporous Silica Nanofibers

Yan Zhou[1, 2, a], Wenpeng Zhang[1, 2], Gang Wang[1, 2], Yanqing Zhang[1, 2], Jianhua Cao[1, b] and Dayong Wu[1, c *]

[1]Technical Institute of Physics and Chemistry, Chinese Academy of Sciences, 29 Zhongguancun East Road, Beijing 100190, China

[2]University of Chinese Academy of Sciences, Beijing 100049, China

[a]syzhouyan@mail.ipc.ac.cn, [b]caojh@mail.ipc.ac.cn, [c]dayongwu@mail.ipc.ac.cn

Keywords: mesoporous materials, silica, nanofiber, cosurfactant, coaxial electrospinning

Abstract. Highly ordered mesoporous silica nanofibers with no core/sheath structure were prepared by coaxial electrospinning combined with the solvent evaporation induced surfactant assembly (EISA) process. The mesoporous structures have been proved and the effect of different cosurfactants on pore sizes of mesoporous silica nanofibers has been investigated.

Introduction

Much interest has been attracted by the mesoporous silica materials due to their promising properties in many fields, such as separation, catalyst and drug delivery [1]. Among various morphologies such as mesoporous spheres, tubes and nanofibers, highly ordered mesoporous nanofibers are very important for special applications such as medical materials [2]. General methods such as applying the porous anodic alumina membrane as template, self-assembly at oil–water interface or spinning have already been used to prepare ordered mesoporous fibers [3,4]. However, those methods cannot prepare the nanofibers with highly ordered mesoporous structures and uniform diameters in large scale or the length of the nanofibers was limited by the templates. In order to solve the problem, some interest has been focused on electrospinning method.

Previously, our team has reported the fabrication of continuous highly ordered mesoporous silica nanofibers with core/sheath structure through a coaxial electrospinning strategy combined with the EISA concept of the surfactant [5]. As we know, pore size is always playing a very important role in the functional performance of mesoporous materials. Many studies on controlling pore sizes of silica block materials have been reported . Fore example, Pingyun Feng et al has a report on control of pore sizes in mesoporous silica [6]. However, few studies on pore sizes of highly ordered mesoporous silica nanofibers have been reported up to now.

Herein, we use the similar method to prepare highly ordered mesoporous silica nanofibers. Considering the cosurfactant can increase the capacity of micelles, we investigate the effect of different cosurfactants on pore sizes of highly ordered mesoporous silica nanofibers.

Experimental Section

Materials and instruments

All chemicals were of analytical grade and were used as received. Polymethylmethacrylate (PMMA, M_w=996000) and Pluronic F127 (PEO_{106}-PPO_{70}-PEO_{106}) were obtained from Sigma-Aldrich. Tetraethoxysilane (TEOS) was obtained from Alfa Aesar. A coaxial electrospinning device was used. Calcination was carried out in a muffle furnace. Transmission electron microscopic (TEM) images were obtained using a JEOL-2100 microscope and scanning electron microscopic (SEM) images were obtained using a Hitachi S-4300 instrument. Small-angle X-ray diffraction (XRD) tests were

measured on Rigaku D/max-2000 wide angle goniometer (Cu-K_α radiation, λ=0.15418 nm). Nitrogen adsorption isotherms were determined using QUADRASORB SI.

Preparation of highly ordered mesoporous silica nanofibers

The preparation was completed as follows: Pluronic F127 (0.8 g) was dissolved in ethanol (1.15 g) followed by adding nitric acid (0.32 g, 0.3 M) into the mixture, then TEOS (1.6 g) was added to the mixture with stirring, resulting in a clear solution. Keeping the solution stirred for 2 h at room temperature formed a sol, which was subsequently injected to the inner capillary of the coaxial electrospinning device. Driven by a syringe pump, another solution consisting of PMMA (0.78 g) and chloroform (10 mL) was injected to the outer capillary. These two liquids were fed at rates of 0.2 mL/h, 1.5mL/h respectively. The spinneret that was made of stainless steel, the inner capillary and the outer capillary were connected to a DC high-voltage supply. Usually, the output voltage was tuned in the range of 7.5 kV~9.5 kV to form steady electrospinning jets of starting materials. The ground collection plate of aluminium foil was located at a fixed distance of 10 cm from the needle tip. After 5 h, the as-electrospun fibers were collected and then kept at 60 °C for 12 h. Subsequently, the result nanofiber membrane was aged at 90 °C for 1 h to perfect liquid crystalline structure. This proper aging process was essential to stabilize and to control the mesoporous structures before removal of the structure-directing agent. Thereafter, the nanofiber membrane was calcined at 550 °C in air for 6 h to remove the structure-directing agent and PMMA completely. Finally the high-quality ordered mesoporous silica nanofibers were obtained.

Replacing ethanol with butanol, hexanol and octanol respectively and keeping the same to other conditions, repeat the experiments according to the above mentioned procedures.

Results and Discussion

In the four experiments, silica precursor composed of TEOS, alcohol, water and F127 with the same mass ratio at pH = 1–2 was used as the inner fluid, and PMMA solution (5 wt% in chloroform) was used as the outer spinning liquid. The SEM images of the as-spun silica nanofibers using ethanol as cosurfactant before and after being calcined were shown in Fig. 1. As shown in Fig. 2a, b, c and d, PMMA/silica composite fibers with diameters between 850 nm and 1060 nm are randomly arranged in a nonwoven network. After calcination, mesoporous silica fibers with diameters reducing to 700 nm are obtained (Fig. 2e, f, g and h). The shrinkage in diameter can be attributed to the loss of PMMA and F127.

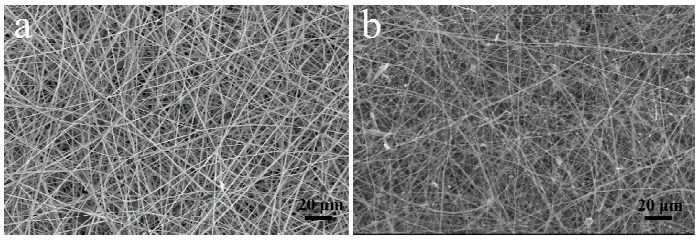


Fig. 1 SEM images of (a) the as-spun PMMA/silica nanofibers before and (b) after being calcined at 550 °C for 6 h.

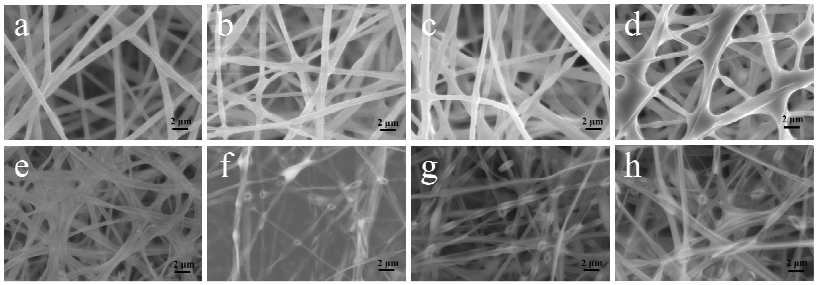


Fig. 2 SEM images of (a, b, c, d) the as-spun PMMA/silica nanofibers before and (e, f, g, h) after being calcined at 550 °C for 6 h, using (a, e) ethanol, (b, f) butanol, (c, g) hexanol and (d, h) octanol as cosurfactant respectively.

In order to observe the detailed mesoporous structures of electrospinning silica nanofibers, after the removal of PMMA and F127 by calcination, silica nanofibers were observed under a JEOL-2100 transmission electron microscope. The TEM images of Fig. 3 clearly show a highly ordered mesoporous silica nanofiber with paralleled channels. The channel width in average is about 5 nm.

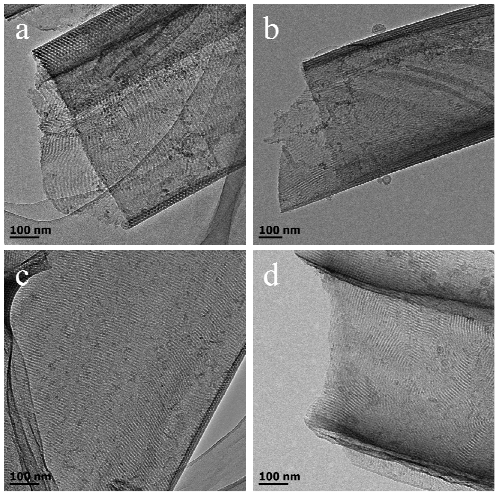


Fig. 3 TEM images of the calcined silica nanofibers using (a) ethanol, (b) butanol, (c) hexanol and (d) octanol as cosurfactant respectively.

The small-angle XRD patterns (Fig. 4) display four well-resolved diffraction peaks at 2θ angles of about 0.94°, 1.35°, 1.72° and 2.34°, which can be indexed as the (100), (110), (200) and (210) reflections of typical hexagonally packed mesoporous respectively [7]. The cell parameter (a^0) can be calculated from the position of the (100) reflection according to the Bragg's Equation. It is obvious that the mesoporous structural cell parameter decreases gradually as the cosurfactant changes from ethanol to octanol. It indicates that the pore size also decreases as the cosurfactant changs. The rule is very distinct. On the contrary, the cell parameter increases when the cosurfactant changes from butanol to hexanol in preparing mesoporous silica block materials [6].

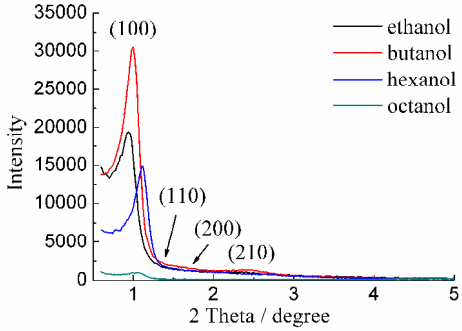


Fig. 4 Small-angle XRD patterns of the calcined silica nanofibers using different alcohols.

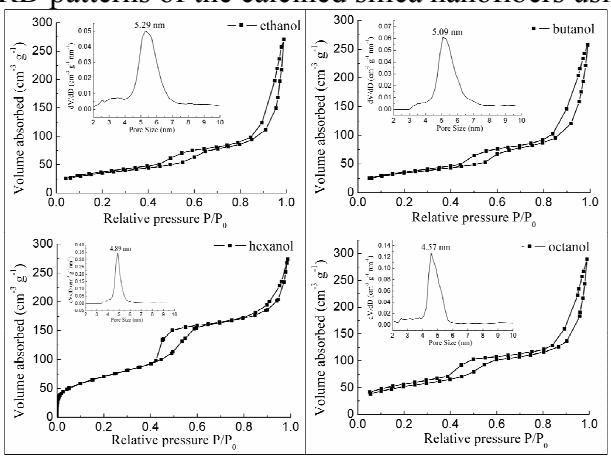


Fig. 5 Nitrogen absorption isotherms (insert: NLDFT pore size distribution from absorption) of the calcined silica nanofibers using different alcohols.

The nitrogen adsorption isotherms (Fig. 5) reveal four typical IV-type curves with H1-type hysteresis loop, which are characteristics of mesoporous materials with cylindrical channels. The pore sizes can be calculated from the absorption data using the NLDFT model. The pore sizes in average are about 5 nm. They are essentially consistent with those evaluated from TEM images. The pore sizes in average decrease gradually from 5.29 nm to 4.57 nm when the cosurfactant changes from ethanol to octanol. The results are also consistent with those from small-angle XRD. The existence of the differences may be due to the distinct manufacturing processes.

Summary

We have successfully prepared highly ordered mesoporous silica nanofibers with no core/sheath structure by coaxial electrospinning with the EISA concept, and have investigated the effect of different cosurfactants on pore sizes of mesoporous silica nanofibers. The characterization has given evidence for the highly ordered mesoporous structures. The analytical results from the small-angle XRD tests and the nitrogen adsorption isotherms both show that pore sizes in average decrease gradually when the cosurfactant changes from ethanol to octanol. The rule is very distinct from that in mesoporous silica block materials, which may be due to the distinct manufacturing processes.

Acknowledgements

This work was financially supported by the National Natural Science Foundation of China (21272243) and the Strategic Priority Research Program of the Chinese Academy of Sciences (XDA090100105). We are grateful to Dr. Hui Wang (TIPC, CAS) and Dr. Yang Li (Tsinghua University) for give some experimental help.

References

[1] Z. Teng, G. Zheng, Y. Dou, et al, Highly ordered mesoporous silica films with perpendicular mesochannels by a simple Stober-solution growth approach, Angew. Chem. Int. Ed. 51 (2012) 2173-2177.

[2] Z. Ma, H. Ji, Y. Teng, et al, Engineering and optimisation of medically multi-functional mesoporous SiO2 fibers as effective wound dressing material, J. Mater. Chem. 21 (2011) 9595-9602.

[3] J. Wang, C.-K. Tsung, W. Hong, et al, Synthesis of Mesoporous Silica Nanofibers with Controlled Pore Architectures, Chem. Mater. 16 (2004) 5169-5181.

[4] Z. Yang, Z. Niu, X. Cao, et al, Template synthesis of uniform 1D mesostructured silica materials and their arrays in anodic alumina membranes, Angew. Chem. Int. Ed. 42 (2003) 4201-4203.

[5] H. Wang, D. Wu, D. Li, et al, Fabrication of continuous highly ordered mesoporous silica nanofibre with core/sheath structure and its application as catalyst carrier, Nanoscale 3 (2011) 3601-3604.

[6] P. Feng, X. Bu and D. J. Pine, Control of Pore Sizes in Mesoporous Silica Templated by Liquid Crystals in Block Copolymer-Cosurfactant-Water Systems, Langmuir 16 (2000) 5304-5310.

[7] W. Dong, Y. Sun, C. W. Lee, et al, Controllable and Repeatable Synthesis of Thermally Stable Anatase Nanocrystal-Silica Composites with Highly Ordered Hexagonal Mesostructures, J. Am. Chem. Soc. 129 (2007) 13894-13904.

Applied Mechanics and Materials Vol. 597 (2014) pp 17-20
© (2014) Trans Tech Publications, Switzerland
doi:10.4028/www.scientific.net/AMM.597.17

Influence of Uniaxial Stress on the Stress-Strain Curve Measured by Nanoindentation

Ikuo Ihara[1, a *], Kohei Ohtsuki[2,b] and Iwao Matsuya[1,c]

[1] Department of Mechanical Engineering, Nagaoka University of Technology, Nagaoka, Niigata 940-2188, Japan

[2] Graduate Student, Graduate School of Nagaoka University of Technology, Nagaoka, Niigata 940-2188, Japan

[a] ihara@mech.nagaokaut.ac.jp, [b] s103020@stn.nagaokaut.ac.jp, [c]matsuya@mech.nagaokaut.ac.jp

Keywords: Nanoindentation, Stress-strain curve, Stress dependence, Compressive stress

Abstract. A nanoindentation technique with a spherical indenter of tip radius 10 μm is applied to the evaluation of stress-strain curve at a local area of a pure iron under the uniaxial compressive stress exerted through the iron, and the influence of the compressive stress on the estimated stress-strain curve has been examined. A continuous multiple loading method is employed to determine the stress-strain curve. In the method, a set of 21 times of loading/unloading sequences with increasing terminal load are made and load-displacement curves with the different terminal loads from 0.1 mN to 100 mN are then continuously obtained and converted to a stress-strain curve. To examine the stress dependence of the stress-strain curve, the estimation by the nanoindentetion is performed under different uniaxial compressive stresses up to 250 MPa. It has been found that the stress-strain curve determined by the nanoindentation shifts upward as the compressive stress increases and the quantity of the shift is almost equal to the uniaxial stress acting on the iron specimen. It is also noted that the yield stress (0.2 % proof stress) estimated from the stress-strain curve increases almost proportionally to the uniaxial stress and the increase ratio tends to decrease as the stress reaches around 200 MPa.

Introduction

There are growing demands for measuring materials properties of small-sized materials and thin films used for Micro-Electro-Mechanical-Systems (MEMS) as well as any other industrial materials. In particular, mechanical properties which are directly related to the elastic and plastic behaviours are strongly required to be measured because accurate values of such properties are indispensable for better machine design and CAE applications. Unfortunately, there is little knowledge about such microscopic mechanical properties even for widely used industrial materials such as steel, aluminium, and other metals. This is basically because of difficulty in measuring them in submicron or submilimeter volumes. Nanoindentation is known as a sophisticated technique providing measurements for both hardness and elastic modulus at a small volume on a material surface [1][2]. In fact, the hardness and Young's modulus obtained by nanoindentation can be used as representative values for plastic and elastic properties, respectively. However, those values are not always good enough for practical applications. It is strongly required to know a stress-strain curve which is directly related to material deformation behaviour in both elastic and plastic regions.

Because of the importance of determining tensile materials properties from the experimentally measured indentation load-depth curve, in the past decade, numerous researches on the application of nanoindentation have extensively been made to the estimations of mechanical properties [1]-[13]. In these investigations, spherical indenters are often used and attempts have been made to determine stress-strain curves. Also, continuous multiple indentation method is applied to determine stress-strain curves of industrial materials [3][4][7][9]. The method called "multiple partial unloading" or "continuous multiple loading" seems to be one of the promising candidates to determine the strass-strain curves that is closely relating to tensile or compressive properties of materials. The optimum values for experimental parameters used in the method were examined to

determine the indentation stress-strain properties quantitatively [9]. Recently, the continuous multiple loading method was applied to stress-strain curve estimation of a steel and the influences of measurement condition on the obtained stress-strain are examined [14]-[16]. Although the method is attractive and has the potential for the mechanical properties determination at local areas, there remain some unclear issues for practical uses of the method. In this work, the influence of the compressive stress on the stress-strain curve estimated by nanindentation has been examined experimentally.

Determining Stress and Strain Curve from Nanoindentation

When a spherical indenter penetrates into a material as shown in Fig. 1, the deformation is classified into three stages of elastic, elastic plastic, and fully plastic. When the stress field due to indentation satisfies the yield condition, local plastic deformation starts to occur beneath the spherical indenter and expands to the free surface. The mean contact pressure gradually increases in the fully plastic zone. This deformation behavior in indentation is similar to uniaxial tensile test. When the indenter proceeds to penetrate, the so called "pile-up" or "sink in" occurs at the edge of the indenter which leads to change in contact area for a given depth. Figure 1 represents a "pile-up" situation where R is the radius of spherical tip, a is contact radius and h_c is contact depth with consideration to piling-up.

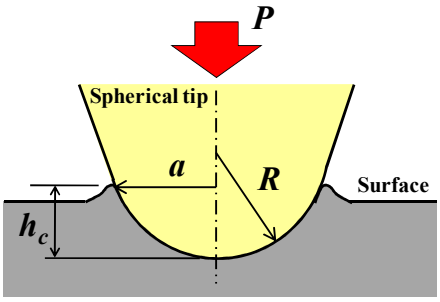


Fig. 1 Schematic of spherical-tip nanoindentation.

Since the stress and strain fields beneath the indenter during loading are not homogeneous, it is reasonable to use an averaged value beneath the indenter rather than a certain value at a specific position, as suggested by Ahn and Kwon [7]. The terms of representative stress σ_R and representative strain ε_R are used as an averaged stress and strain beneath the indenter, respectively. Representative stress σ_R can be expressed using mean contact pressure P_m as follows [5][14],

$$\sigma_R = \frac{P_m}{c} = \frac{P}{c\,\pi a^2} \quad , \tag{1}$$

where P is maximum terminal load at each unloading step, c is constraint factor depending on deformation regime. For simplicity, we use c = 2.8, which corresponds to fully plastic regime. Representative strain ε_R is defined as the average plastic strain depth in direction by analyzing the area change during indentation as follows [15][17],

$$\varepsilon_R = \ln\frac{2}{1+\cos\gamma} = \frac{2}{1+\sqrt{1-(a/R)^2}} \quad , \tag{2}$$

where, γ is the contact angle of the indenter and specimen. The details of determining σ_R and ε_R are shown in [5][14]-[16].

Experiment and Result

Specimens used were a pure iron. The dimension was about 7 × 7 × 4 mm. The specimen surface was ground and polished with 1 μm Al_2O_3 powders. A load-controlled nano-indenter ENT-2100 from

Elionix Inc., is employed. This tester provides continuous multiple loading/partial-unloading indentations with load and displacement resolutions of 4.0 nN and 0.06 nm, respectively. The relationship between indentation load and penetration depth were measured continuously by using diamond spherical-tip indenters with radius of 10 μm. Indentation was repeated at 7 different locations.

Nanoindentation tests are perfumed under different compressive stresses up to 250 MPa using a loading device as shown in Fig. 2. Fig. 3 shows a typical measurements result of continuous multiple indentations load versus indentation depth. The specimen is indented with a series of 21 loading/unloading sequences with increasing terminal load from 0.1 mN to 100 mN as shown in Fig. 3. It is clearly seen that the penetration depth degreases with the compressive stress. Stress-strain relations are determined from the load-displacement curves using Eqs. (1) and (2). Fig. 4 shows the stress-strain curves estimated under different compressive stresses. As expected from the result of Fig. 3, a stress dependence of the stress-strain curve is clearly observed. It has been found that the stress-strain curve shifts upward as the compressive stress increases and the quantity of the shift is almost equal to the stress acting on the iron. It is also been found that the yield stress (0.2 % proof stress) roughly estimated from the stress-strain curve increases almost proportionally to the stress and the increase ratio tends to decrease as the stress reaches around 200 MPa. It seems reasonable that this phenomenon may be related to the stress state on yielding of the iron.

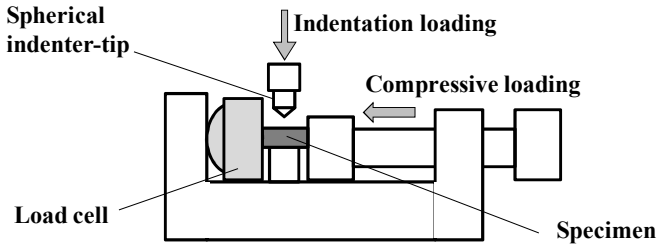


Fig. 2 Schematic of a loading device for applying compressive stress to specimen.

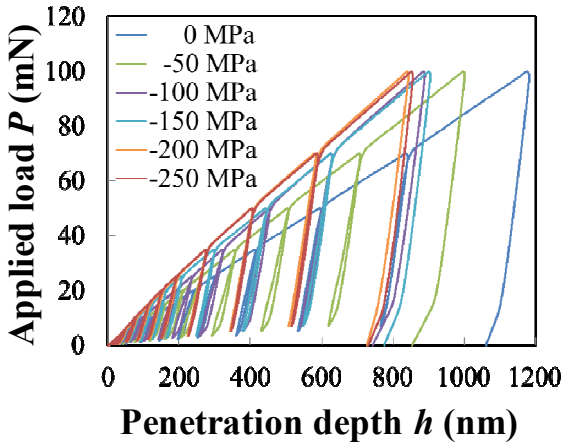


Fig. 3 Measured load-displacement curves by continuous multiple loading method under different compressive stresses.

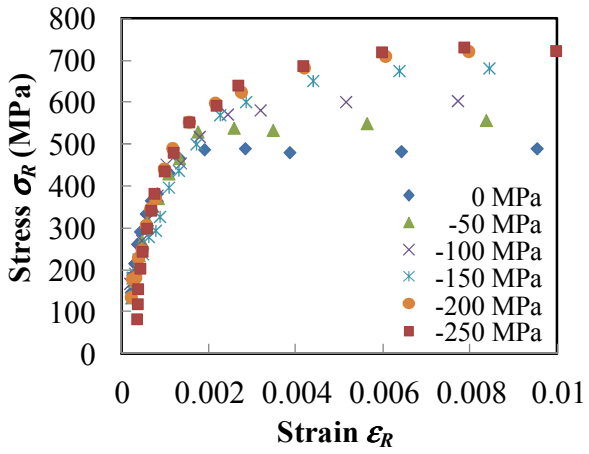


Fig. 4 Estimated stress-strain curves under different compressive stresses.

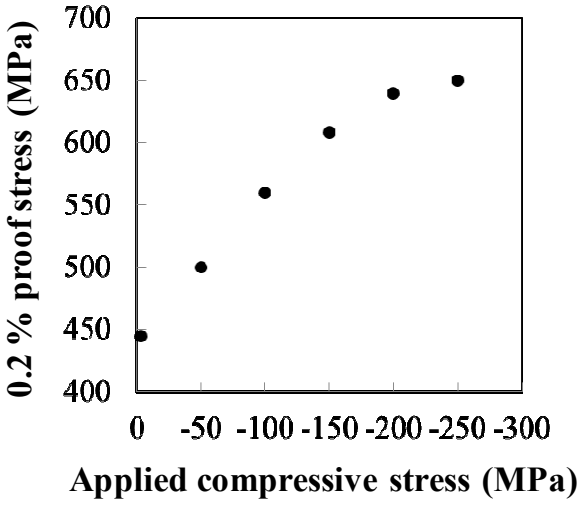


Fig. 5 Variation in the 0.2% proof stress roughly estimated by the nanoindentation with the compressive stress.

Conclusions

The influence of the compressive stress on the stress-strain curve estimated by nanindentation has been examined and a stress dependence of the curve has clearly been found. Although further studies are necessary to understand the stress dependence, the result obtained here could be helpful in understanding the influence of macroscopic stress or residual stresses that often exist in material surface on nanoindentation tests.

References

[1] W. C. Oliver, and G. M. Pharr, An improved technique for determining hardness and elastic modulus using load and displacement sensing indentation experiments, J. Mater. Res., 7(1992) 1564-1583.
[2] W. C. Oliver, and G. M. Pharr, Measurement of hardness and elastic modulus by instrumented indentation: Advances in understanding and refinements to methodology, J. Mater. Res., 19(2004) 3-20.
[3] J. S. Field, and M. V. Swain, A simple predictive model for spherical indentation, J. Mater. Res., 8(1993) 297-306.
[4] J. S. Field, and M. V. Swain, Determining the mechanical properties of small volumes of material from submicrometer spherical indentations, J. Mater. Res., 10(1994) 101-111.
[5] Y.-T. Cheng, and C.-M. Cheng, Can stress-strain relationships be obtained from indentation curves using conical and pyramidal indenters?, J. Mater. Res., 14(1999) 3493-3496.
[6] R. Nowak, M. Pessa, et al., Elastic and plastic properties of GaN determined by nano-indentation of bulk crystal, Applied Physics Letters, 75(1999) 14(1999) 2070-2072.
[7] J.-H. Ahn, and D. Kwon, Derivation of plastic stress-strain relationship frm ball indentation: Examination of strain definition and pileup effect, J. Mater. Res., 16(2001) 3170-3178.
[8] S. Stauss, P. Schwaller, et al., Determining the stress-strain behaviour of small devices by nanoindentation in combination with inverse methds, Microelectronic Engineering, 67(2003) 818-825.
[9] E.-C. Jeon, J.-S. Park, and D. Kwon, Statistical analysis of experimental parameters in continuous indentation tests using taguchi method, Transactions of ASME, 125(2003) 406-411.
[10] A. C. Fischer-Cripps, Critical review of analysis and interpretation of nanoindentation test data, Surface & Coatings Technology, 200(2006) 4153-4165.
[11] S. Basu, A. Moseson, and M. W. Barsoum, On the determination of spherical nanoindentation stress-strain curves, J. Mater. Res., 21(2006) 2628-2637.
[12] T. F. Juliano, et al., Extracting stress-strain and compressive yield stress information form spherical indentation, Army Research Laboratory Report, ART-TR-4299(2007) 1-15.
[13] Y. I. Golovin, Nanoindentation and mechanical properties of solids in submicrovolumes, thin near-surface layers, and films: a review, Physics of the Solid State, 50(2008) 2205-2236.
[14] I. Ihara, T. Matsumoto, Y. Yajima, J. Uegaki, and Y. Shima, Application of Continuous Multiple Loading with Spherical-tip Nanoindentation to Mechanical Property Evaluations of Industrial Materials, Proc. 11th HARDMEKO Conference, Pattaya, Chonburi, Thailand, 2011, pp.201-204.
[15] R. G.-G. Fatt, I. Ihara, T. Yudate, M. Ichimura, J. Uegaki, and Y. Shima, Microscopic Determination of Stress-strain Relationship by Continuous Multiple Nano-indentation Technique, Proc. of the 3rd JSME/ASME International Conference on Materials and Processing, Corvallis, Oregon, USA, 2011, ICMP2011-51147.
[16] I.Matsuya, G.-G. Fatt, and I. Ihara, Quantitative Evaluation of Stress-Strain Curves by Spherical-Tip Nanoindentation with Variable Radius Method, Journal of Solid Mechanics and Materials Engineering, 7(2012) 155-162.
[17] Y. V. Milman, B. A. Galanov, and S. I. Chugunova, Plasticity characteristic obtained through hardness measurement, Acta Metallurgica et Materialia, 41(1993) 2523-2532.

Applied Mechanics and Materials Vol. 597 (2014) pp 21-27
© (2014) Trans Tech Publications, Switzerland
doi:10.4028/www.scientific.net/AMM.597.21

The Preparation and Characterization of Zno/Graphene Nanocomposites

Zepeng Wang[1, a *], Guilong Wu[1, b], Yan He[1, c]

[1]School of Electromechanical Engineering, Qingdao University of Science and Technology,No.99 Songling Road, Qingdao,Shandong Province, 266061, P.R.China

[a]wzp_ww1@126.com, [b]wuguilong001@163.com , [c]heyan_sd@163.com

Keywords: graphene, $Zn(OH)_2$/graphene nanocomposites, ZnO/graphene nanocomposites

Abstract. Graphene-based composites now has been payed more and more attention to because it can make up many shortcomings of the pure single-layer graphene.In many papers ,there are one same phenomenon said that graphene can not be well dispersed in matrix since it's high specific surface area and high surface energy.In this work,we reported the preparation of ZnO/graphene nanocomposites through the way of situ-reaction in the surface of graphite oxide.Then,the nanocomposites were characterized by X-ray diffraction(XRD), Fourier Transform-Infared spectroscopy(FTIR),transmission electron microscopy(TEM), and thermogravimetry(TG). The results indicated that the graphene oxide had been reduced by hydrazine hydrate and the ZnO crystal attached to the surface of graphene well.The ZnO/graphene nanocomposites can be expected to be dispersed in some kinds of rubber to improve their electric and thermal conductivities in the following experiments.

Introduction

Since two scientists from University of Manchester received the dingle-layer graphene in 2004,it has got more and more attention by the scientists from all over the world and lots of industries[1,2]. Graphene,as the two-dimensional structure material,has showed many advantages such as high modulus, high light transmittance, high electric conductivity, and the best thermal conductivity in all the now-known material[3-5]. D.L.Nika and A.Alexander got the thermal conductivities from the theoretical and experimental way respectively, and the results from different researchers are of big discrete[6,7].However ,all the results showed the same view that the thermal conductivity of graphene is very high.Based on the above ,we expected that the graphene can resolve the thermal problem in rubber.However,the high surface energy become the biggest difficult in the process of the mixing between graphene and matrix.SHENG kai-xuan and Yu Li solved this problem by exchanging the graphene to graphene oxide in the matrix[8,9],but in this work a new method was proposed.

Zinc oxide(ZnO) is one kind of important constituent in almost all rubber system.Recently, ZnO-based composition was also reported in many papers .R.KAUR used zinc acetate[$Zn(CH_3CO_2)_2 \cdot 2H_2O$,purity 99.5%] to get ZnO film in order to load yttrium to it's surface[10]. Using the situ synthesis, nanoscale ZnO particles can be easily synthesized. In this paper,we got the ZnO particles from $ZnCl_2$ and $NH_3 \cdot H_2O$.GO(graphite oxide) had many oxide-containing groups on it's surface ,so it could be contacted to the some metal hydroxides such as $Zn(OH)_2$ nanoscale particles[11].Then ,we heated $Zn(OH)_2$ to get the nanoscale ZnO particles.When the temperature becomes higher than 125℃, $Zn(OH)_2$ can be easily thermal decomposed to ZnO and H_2O[12].MA has tested the DTA and TG of the pure Zn（OH）$_2$, here we got the same conclusion[13,14].

Experimental

Materials and measurements. The chemicals we used in this experiments were all reagent grade.200 mesh of graphite was bought from Qing Dao Huateng graphite Technology Company Limited.The structure of the samples was observed by X-ray diffraction(XRD，RINT2000 vertical goniometer) with Cu K α radiation and the morphology was observed by transmission electron microscopy(TEM, JEM--2100) .The samples for TEM were prepared by dropping the products on a carbon-coated copper grid after ultrasonic(KQ-DE100) dispersing in pure alcohol.Fourier transform-Infrared (FT-IR) spectra were recorded on a VERTEX 70 spectrometer with KBr pellets in the 4000-400 cm^{-1} region. The themogravimetry(TG) was carried out with a NETZSCH STA 449C thermal analyzer to get the decomposition temperature.

Synthesis of graphite oxide. Graphene oxide was synthesized by a analogous Hummers method from 200 mesh 99.99% natural flake graphite powder[15]. In the beginning,250ml of concentrated sulfuric acid(H_2SO_4) was putted in a 1000ml round-bottomed flask which was immersed in ice bath to lowered the temperature to below 5℃.After stirring for 30 minutes,8g of flake graphite powder and 10g anhydrous sodium nitrate($NaNO_3$) were dumped into the cold H_2SO_4. The temperature must be controlled under 15℃, then 30g of potassium permanganate was putted in the system in 30 minutes in this process.After this, the whole reaction apparatus was moved into oil bath and the temperature was controlled at 35℃ with the stirring continued.3 hours later,poured 460ml of deionized (DI) water into the flask slowly and at this time the color of the solution became golden from blue black.Successively regulated temperature to 98℃ and reacted 2 hours, then reduced temperature to 60℃ and added 50ml of 30% H_2O_2 to reduce the residual $KMnO_4$. At this time the solution released a lot of bubbles. Another 2 hours later, the reaction was stopped and the mixture was poured into a big beaker, the mixture would stratify if it was allowed to stand for more than half an hour.Finally,the mixture was filtered and washed with 3% H_2O_2 and DI water 4 times respectively.After that ,3% HCl was used to wash the remaining product and barium chloride($BaCl_2$) to detect the $(SO4)^{2-}$ followed by much DI water to remove the acid.The resulting solid was dried at 50℃ for 48 hours and dried in vacuo for 24 hours. For further experiments,the final product was sealed into a big sealed bag.

Synthesis of graphene/ZnO nanocomposites. In the process of preparing the ZnO/graphene nanocomposites,400mg of graphite oxide was dispersed in 800ml of DI water by ultra-sonication.Ammonia(28wt%) was dropped into the solution to adjust the PH to around 10 and 0.24ml of hydrazine hydrate(85%) was dropped into.At the same time, 5.44g $ZnCl_2$(0.4mol) was dissolved into 200ml of DI water.After mixing the two kinds of solution together,the mixture was put into a 1L flake to react for 5 hours in 100℃ in oil bath.The final solid getting after filtering was washed by DI water and pure alcohol.Finally,the product was dried in 45℃ for 48 hours to get the $Zn(OH)_2$/graphene nanocomposites. The composites was annealed at 300℃ for 2h in a tube furnace with nitrogen atmosphere. After cooling, ZnO/graphene nanocomposites was obtained.

Results and discussion

X-ray diffraction(XRD) results were showed in the Figure.1 to determine the phase and structure of the synthesized samples.As showed in the picture,a very sharp peak appeared at $2\theta = 11.74^{o}$ in the XRD line of the synthesized graphene oxide(Fig.1a), corresponding to the (001)reflection of graphite oxide[16].After calculated by Prague equation($2d\sin\theta=\lambda$), the layer spacing was 1.54nm, wider than original graphite.From the lines of nanocomposites(Fig.1b and 1c), it can be clearly seen that the peak at $2\theta = 11.74^{o}$disappeared, and no characteristic peak of graphite appeared, suggesting that the layers of graphite oxide was stripped well. The location of the peaks here were unanimous

with the results in other articles[17], confirming the truth of the two kinds of crystal were $Zn(OH)_2$(Fig.1b) and ZnO(Fig.1c) [18]. Except that, the peaks of ZnO/graphene composite were sharper than that of $Zn(OH)_2$/graphene composites, although they emerged at very similar angles in the two lines, this can be considered that the crystallinity of ZnO was higher than $Zn(OH)_2$ crystal we made.

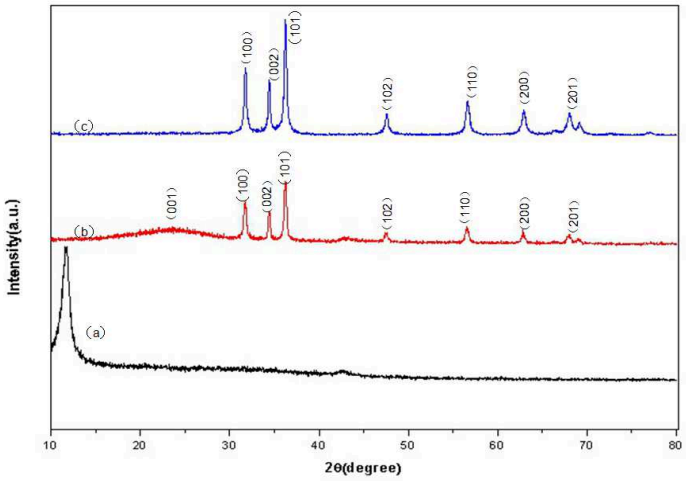


Fig.1 XRD patterns of (a) graphite oxide (b) $Zn(OH)_2$/graphene nanocomposites (c)ZnO/graphene nanocomposites.

The FT-IR spectra of the samples were showed in Fig.2. As it showed in the picture,the oxygen-containing groups of graphite oxide were illustrated by the bonds at 1058,1226,1380,and 1724cm^{-1}(Fig.2a),which separately represented the C-O stretching vibrations,C-OH stretching peak,carboxyl C-O,and carboxyl C=O groups.The peak at 1626cm^{-1} could owe to the stretching vibration of the C=C skeleton,that might be because that the six-membered ring structure of the graphene had been broken partically.As well,the strong peak at 3413cm^{-1} could be interpreted as the transmittance of the absorb of the O-H stretching vibration.Figure 2b showed the FT-IR spectra of pure $Zn(OH)_2$,which was synthesized in the way that putting Zinc chloride to the alkaline water.As showed in the Fig.2b,the peak at 3412cm^{-1} illustrated that in $Zn(OH)_2$ there were a lot of –OH groups.The other absorption peaks at 899,1390,1492,and 1638$cm^{-1}$from the pure $Zn(OH)_2$ sample could also indicate the element oxygen was existed in the crystal $Zn(OH)_2$.Fig.2d is the infrared spectroscopy of $Zn(OH)_2$/graphene nanocomposites.

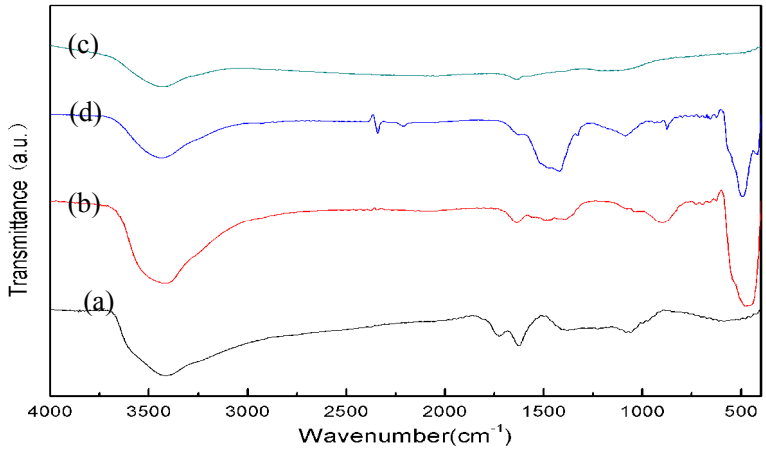


Fig.2 FT-IR spectra of (a)graphite oxide,(b)pure $Zn(OH)_2$,(c) ZnO / graphene nanocomposites,and (d) $Zn(OH)_2$ / graphene nanocomposites.

From the lines it could be seen clearly that the peaks we got here were smaller than the Fig.2b because of the interaction between $Zn(OH)_2$ and graphene.the peak at 3426cm^{-1} also the –OH group stretching vibration but the strength became weaker.Except the peaks around 3400cm^{-1},both of fig.2d and 2c ($Zn(OH)_2$/graphene and ZnO/graphene) lines were substantially same with the results of $Zn(OH)_2$ and ZnO FTIR spectra reported in other article[19].In fig.2c, the peak at 2341cm^{-1} could be owed to the interaction between oxygen in ZnO and graphene,and the peak at 1419cm^{-1} could be attributed to skeletal vibration of the graphene sheet and stretching vibretion of Zn-O,respectively.

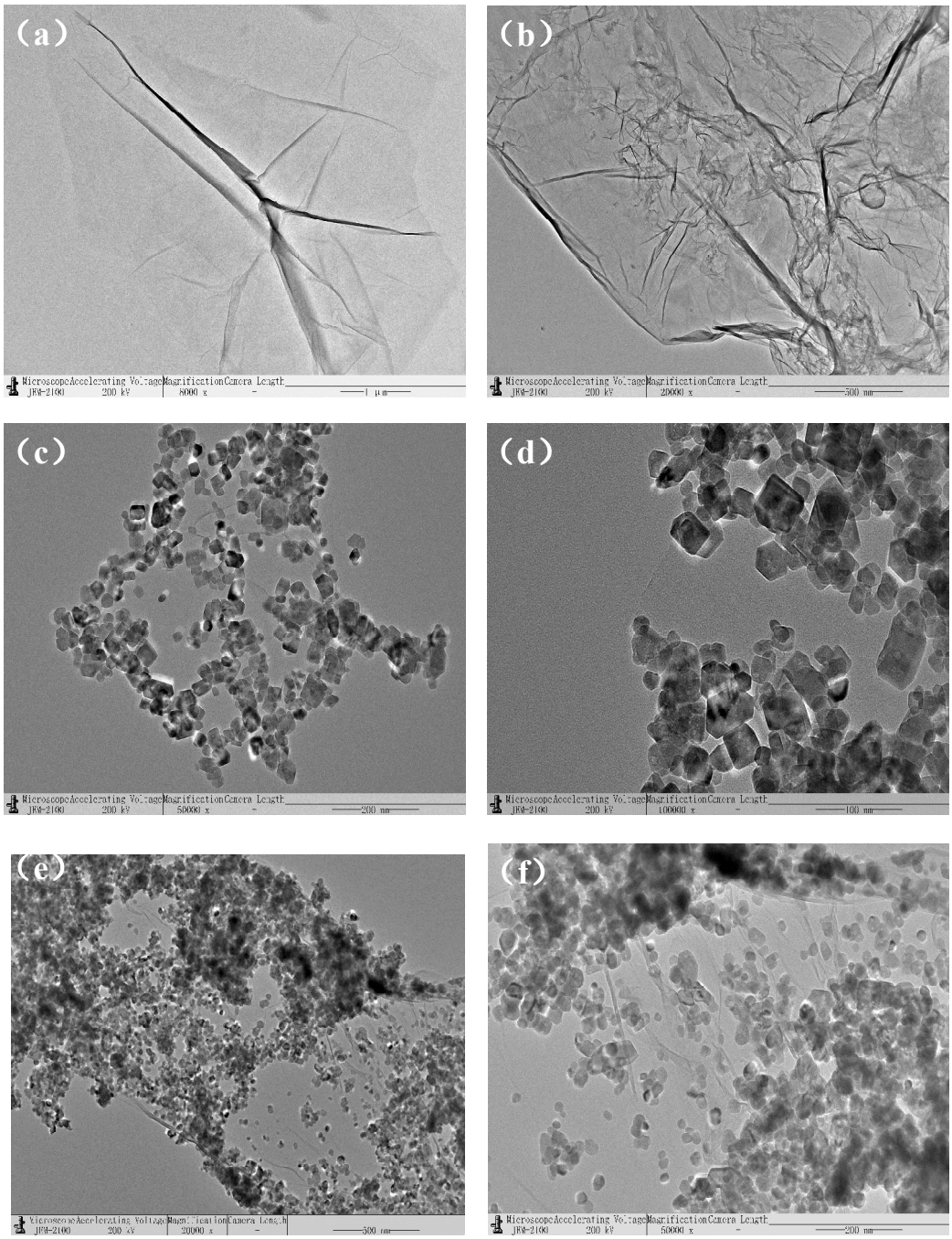


Fig.3 (a) and (b) TEM patterns of graphite oxide and graphene getting from chemical reduction; (c) and (d) TEM patterns of $Zn(OH)_2$/graphene nanocomposites;(e) and (f) TEM patterns of ZnO/graphene nanocomposites.

Fig.3 showed TEM images of the samples from which the shape of the samples and the size of the nanoscale particles could be obtained accurately.Fig.3a was the graphene ,from this picture we considered the graphene oxide we made in this way was one-layer film and it's size was about 5 μm .Since the high specific surface area,some fold formed.Fig.2b was the graphene getting form GO reduced by hydrazine hydrate.Because most of the oxygen-containing groups were excepted,the surface energy rose and more folds toke shape.Fig.3c and 3d are the TEM images of $Zn(OH)_2$/graphene, it could be seen clearly that many particles attached to the surface and edge of the film.The edge of the graphene film was illustrates by the numbers of particles whose size were about 30nm and the XRD above had prove them $Zn(OH)_2$ particles.in the fig.3e and 3f, the particles changed from $Zn(OH)_2$ to ZnO. What's more, to the particles, the shape changed greatly but the size did not.

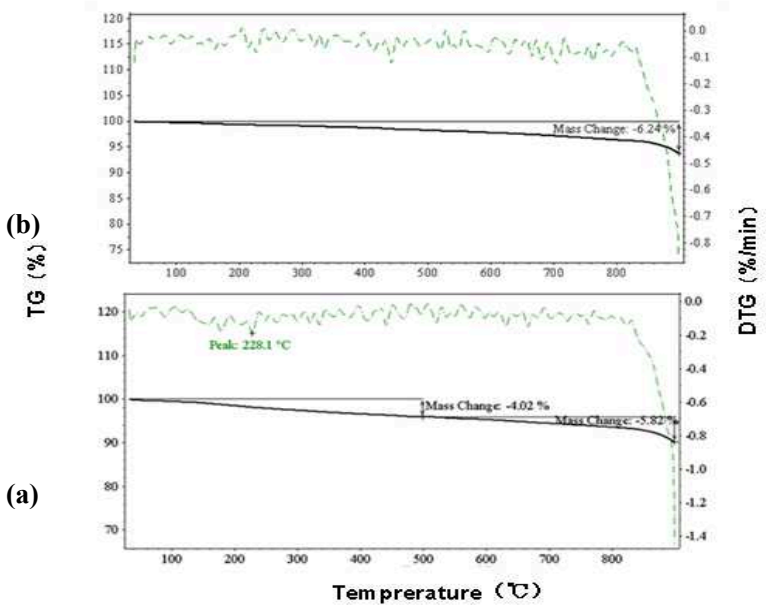


Fig.4 The TG and DTG of the ZnO /Graphene and $Zn(OH)_2$/Graphene nanocomposites

TG and DTG of $Zn(OH)_2$/graphene and ZnO/graphene nanocomposites sample were showed in the Fig.4.Fig.4a was the curves to describe the mass change of $Zn(OH)_2$/graphene composites with the temperature increasing and Fig.4b represented ZnO/graphene.in Fig.4a,two stages of losing mass were showed. From room temperature to 500℃,the mass changed for -4.02%,and from 500 to 1000 ℃,the mass changed -5.82% once more., so the mass lost by -9.84 totally. One peak at 228.1℃ was got in the DTG curve,this means that at that tempreture the speed of mass losing got a fastest point. In fig.4b, the mass losing was decreased to -6.24% because the sample b had been heated at 300℃ to make the $Zn(OH)_2$ decomposed into ZnO.The speed of mass losing became slowly and the peak could not be found. Overall, $Zn(OH)_2$/graphene nanocomposites became ZnO/Graphene nanocomposites when the temperature increased above 125℃, the margin of mass losing was not very large.

Conclusions

The 30nm $Zn(OH)_2$ nanoparticles were successfully prepared out on the surface of the graphene using the method of in-situ synthesis. After heating the sample, ZnO/graphene nanocomposites was easily obtained.It was shown that one-layer graphene was decorated by ZnO nanoparticles to form a kind of film-like material.What's more, the low-temperature heating of 300 did not break the structure of graphene film. When the temperature returned at 1000℃,the mass losing could get

about 10%. What is more, It could be expected that the method here can be extended to other compound of metal oxide/group-containing sheet material composites and the ZnO/graphene could be expected to improve the dispersion of graphene in matrix such as rubber or resin.

Acknowledgements

Authors are thankful for the support in part by Department of Science and Technology of Shandong province, P.R.China for this project (The scientific research foundation of Outstanding Young Scientist Award of Shandong province, BS2012CL014).

Reference

[1] Ji Won Suk, Alexander Kitt, *et al*, Transfer of CVD-Grown monolayer graphene onto arbitrary substrates, ACSnano.56(2011)916-6924.

[2] Jing-xiang Zhao, Hong-xia wang, Bo Gao, *et al*, Chemical functionalization of graphene via aryne cycloaddition: a theoretical study, Springer-Verlag. 2011,10.1007/s00894-011-1309-8.

[3] Zhou Wang, Xiu-zhi Tang, Zhong-Zhen Yu, *et al*. Dispersion of graphene oxide and its flame retardancy effect on epoxy nanocomposites, Chinese Journal of Polymer Science. 2 (2011) 368-376.

[4] Haiqing Hu, Yin Liu, Qingnian Wang, *et al*, A study on the preparation of highly conductive grapheme, Materials Letters.65(2011) 2582-2584.

[5] K.S. Novoselov, A.K. Geim, S.V., *et al*, Science. 306(2004)666–73.

[6] D. L. Nika, E.P.Pokatilov, A.S.Askerov, *et a1*, Phonon thermal conduction in grapheme: Role of Umklapp and edge roughness scattering, Phys.Rev.B. 79(2009)155413.

[7] Alexander A, Balandin, Suchismita Ghosh, *et a1*. Superior thermal conductivity of single-layer grapheme, Nano Lett. 8(2008):902-907.

[8] Sheng Kai-Xuan, Xu Yu-Xi, Li Chun, *et al*. High-performance self-assembled graphene hydrogels prepared by chemical reduction of graphene oxide, New Carbon Materials. 26(2011)102-106.

[9] Yu Li, Qihua Wang, Tingmei Wang, *et al*, Preparation and tribological properties of graphene oxide/nitrile rubber nanocomposites, J Mater Sci .47 (2012)730–738.

[10] R. Kaur, A .V. Singh, *et al*, Physical properties of natively textured yttrium doped zinc oxide films by sol-gel,Journal of Materials Science: Materials In Electronics.16 (2005) 649– 655.

[11] Zhengyuan Ji, Jili Wu,Xiaoping Shen, *et al*, Preparation and characterization of graphene/NiO nanocomposites,J Mater Sci .(2011) 46:1190–1195.

[12]Zumdahl, S.Steven, Chemical Principles, 6th Ed., Houghton Mifflin Company, Boston, 2009.

[13] Ma Ru yan, Gao yuan-feng,Pang Xian-yong,The preparation of nanometer zinc hydroxide and the phase transition research, J Shanxi Agric Univ (Natural Science Edition).31 (2011) :105~108.

[14] Dapeng Wu, Yi Jiang, Junli Liu, *et al*,Template route to chemically engineering cavities at nanoscale: a case study of $Zn(OH)_2$ template, Nanoscale Res Lett . 5 (2010)1779–1787

[15] Wang Lina, Chen Chengmeng, Yang Yonggang, *et al*, The preparation and properties of graphene oxide sheets/phenolic resin composites, Materials Review. 24(2010) :85-59.

[16] Guo Peng,Preparation, assembly and application of graphene, Beijing University of Chemical Technology.2010

[17] Olga Khvostikova, Helmut Hermann, Horst Wendrock, *et al*, Effect of the microstructure on the intercalation and exfoliation behaviour of graphite, J Mater Sci. 46 (2011):2422–2430.

[18] Han Dong, Ren Xiang-ling, Chen Dong, *et al*, Preparation and photocatalytic property of ZnO nanoparticles, Photographic Science and Photochemistry.23(2005):52-55.

[19] S.C.Singh, Effect of oxygen injection on the size and compositional evolution of ZnO/$Zn(OH)_2$ nanocomposite synthesized by pulsed laser ablation in distilled water, Springer,J Nanopart Res.13 (2011)4143–4152.

Applied Mechanics and Materials Vol. 597 (2014) pp 28-31
© (2014) Trans Tech Publications, Switzerland
doi:10.4028/www.scientific.net/AMM.597.28

Study of nano coating micron calcite reaction process and influence factors

Huo Ning Bo[1, a *], Liu Sheng[1,b] and Jia Xiao Jing[2,c]

[1] Institute of Chemical Engineering and Textile, Binzhou Vocational College, China

[2] Boxing People's Hospital, China

[a]huoningbo@126.com, [b]liusheng@163.com, [c]jiaxiaojing1980@126.com

Keywords: composite particles; Nano-$CaCO_3$; coating process

Abstract. Adjusting the proportion of gases and stirring rate and other parameters, the value of pH, electrical conductivity, electrode potential, temperature of the system were tested online under different parameters. According to the results of scanning electron microscopy , the coating effect of different reaction stages and the influence of different coating processes were analyzed.

Introduction

White mineral fillers are widely used in rubber, paint and other polymer materials. However, there are problems in use such as weak combination with the polymer matrix and local stress concentration , thus its application was limitted[1]. Coating nanometer $CaCO_3$ particles on the mineral particles,changing the surface properties of micron powder,the smooth cleavage surface becomes rough, its sharp edges will be passivated, the binding force between the filler and polymer materials will be effectively increased, the problem of composite local stress concentration will be solved,so the advantages of nanoparticles will be effectively used and high performance composite materials will be obtained while reducing the cost of production. It has been reported the use of $Ca(OH)_2$-H_2O-CO_2 system to coat dolomite powder. By adjusting the type and amount of additives to produce nano-$CaCO_3$ with chain structure coating layer on surface of dolomite particle, good effects have been achieved[2-4]. However, the reaction process and influencing factors about the preparation of nanocomposite particles in $Ca(OH)_2$-H_2O-CO_2 reaction system yet will be explored.

Experiment

The calcium hydroxide solution is added into the reactor, After stirring and dispersing a certain time, the ultrafine calcite powder was added into the system to form a concentration of $Ca(OH)_2$ solution according to 20% of the total mass. The stirring speed is stabilized at a certain value. Mixture gas of CO_2 and air is introduced into the reactor with a volumetric flow rate.Stirring constantly to control the reaction process, so that the gas, liquid and solid will be mixed uniformly. pH, electrical conductivity, electrode potential, temperature of the system will be recorded every 2min during the reaction.The reaction will be stopped after a certain time, the supernatant will be discarded, the precipitate will be dried and weighed and samples will be taken do SEM analysis.

Results and discussion

Analysis of the coating effect at different reaction time. Stirring speed is maintained on 400rpm, six groups of reaction were stopped at 5,10,15,20,25,30 min, and six sets of samples were obtained. PH, electrical conductivity, electrode potential and temperature were measured every 2min during the reaction. The data would be measured every 1min when parameter values suddenlly changed to improve the accuracy of the test. Measured variation of PH, electrical conductivity, electrode potential and temperature was shown in Figure 1,2,3,4.

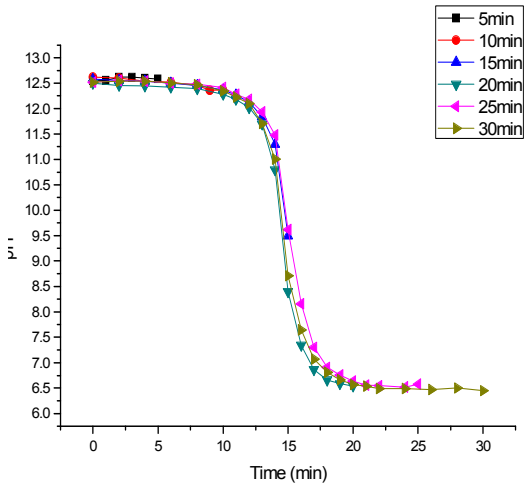


Figure 1 pH trend chart of the system during the reaction

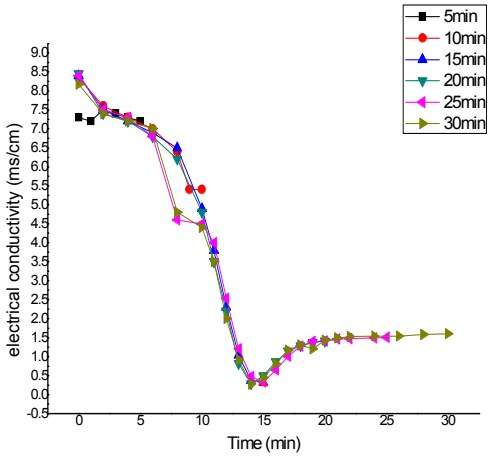


Figure 2 Electrical conductivity trend chart of the system during the reaction

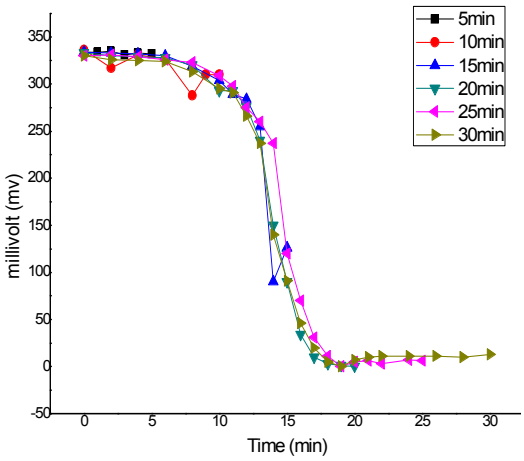


Figure 3 Electrode potential trend chart of the system during the reaction

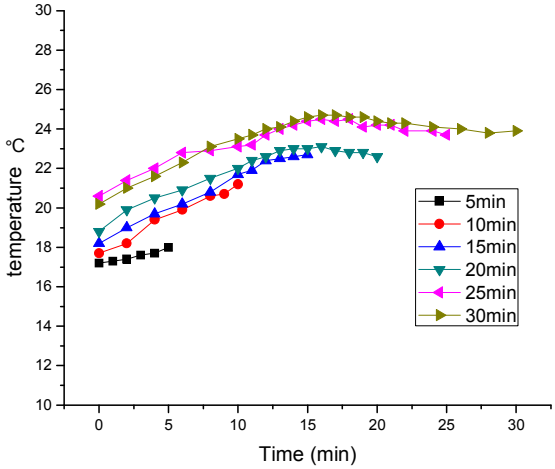


Figure 4 Temperature trend chart of the system during the reaction

Seen from Figures 1 and 2, PH, electrical conductivity and electrode potential of six groups reaction had good reproducibility.The change of parameter values was little in the reaction beganning period of 10min which demonstrated $Ca(OH)_2$ solution was supersaturated. At this time, the partial surface of the calcite had formed $CaCO_3$ nuclei ,as SEM shown in Figure 5(a). Within 10~14min, parameter values changed abruptly, the degree of supersaturation of the solution $CaCO_3$ increased continuously as the reaction progresses. Strong homogeneous nucleation occured at 14min, which explained the system reached a critical concentration at this time. As seen from Figure 5(b), a large number of $CaCO_3$ nucleation formed and developped or became mutual agglomeration, which were adsorbed in the surface of the mineral powder particles and connected to the powder particles of the mineral matrix as a whole. PH, electrical conductivity and electrode potential parameter data reflected consistently that $Ca(OH)_2$ reaction was complete at 14min. After 14min of the reaction, the system concentration of $Ca(OH)_2$ decreased significantly,and the values stabilized after 23min,which was due to HCO_3^- generated in the system. From Figure 5 (c) ,the surface of calcite formed good coated $CaCO_3$ nuclei, so the mineral powder particles with sharp edges and flat cleavage surface were changed.

System temperature chang was shown in Figure 4, which indicatted that the reaction was exothermic.The reaction was stopped at the time about 14min, the reaction temperature was the

highest at this time point, which was consistent with the trends exhibited in Figure 1 to Figure 3. Six groups of the reaction temperature in the system did not show a good reproducibility,which may be caused by the difference of the ambient temperature.

Effect of different coated stirring speed on reaction time. The stirring speed was controlled in 200, 400, 600 and 800 rpm, simultaneously,electrical conductivity was determinated. Conductivity minimum value appearing time was 200rpm in 8.5min, 400rpm in 11.5min, 600rpm in 14min, 800rpm in 18.5min.So the faster the stirring speed, the shorter the time of electrical conductivity reaching the minimum value, the shorter the reaction time. From Figure 5(d), the obtained coating layer of nano-$CaCO_3$ is not uniform when the rotating speed is 200rpm. This is because the solution can not be distributed evenly, and the generated nano-$CaCO_3$ can easily get together rather than attach to surface of the mineral powder particle. Also, mass transfer resistance between liquid film and main liquid in the reaction system is large,so the rate of diffusion of CO_2 gas phase to liquid phase is small, then the reaction will take a longer time and produanction efficiency is lower. With increasing intensity stirring, the reaction system achieved uniform mixing, mass transfer and diffusion resistance was greatly reduced, which significantly speeded up the reaction rate. Seen from Figure 5 (c) ,nano-$CaCO_3$ achieved orderly growth at mineral particle surface at a stirring speed of 400rpm, and better coating results were gotten. SEM image in Figure 5(e) showed that the coating in mineral particle surface had a less effective in the speed of 600 and 800rpm. This is because the crystal ion in the surface of mineral particles is destroyed with the stirring speed further accelerated, the mineral particles in the ordered nano $CaCO_3$ growth on the surface is broken, orderly growth of nano-$CaCO_3$ on the surface is broken. While accelerating the generation of $CaCO_3$, there are not enough time to grow on the particle surface, the nano-$CaCO_3$ attached to the particle surface even is washed off.

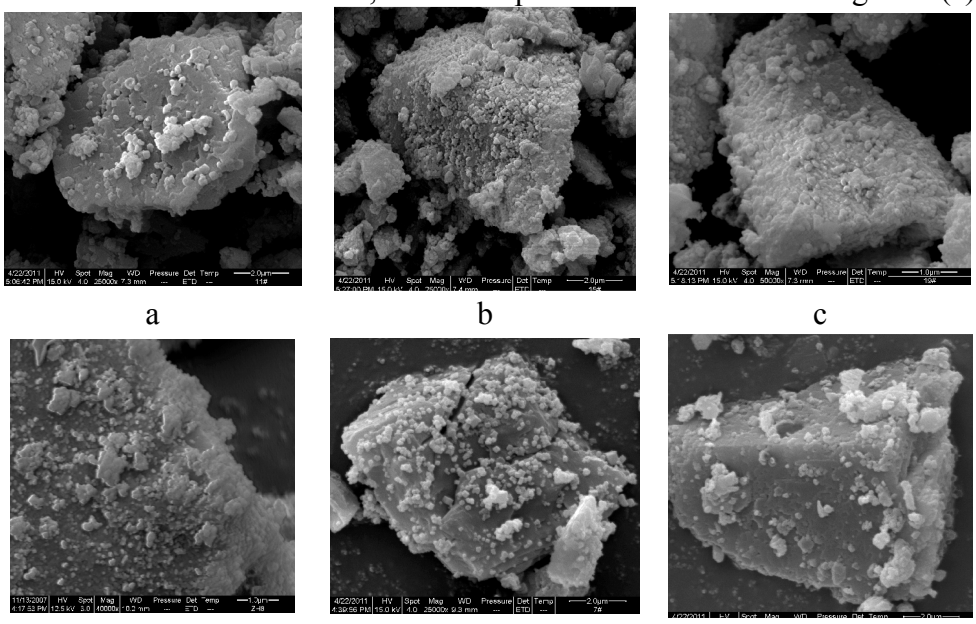
Analysis of coated product weight increment ratio at different reaction time. The solution of 0.3mol / L concentration was prepared. The reaction solution volume in the reactor was 1.5L, so the desired quality of solid $Ca(OH)_2$ was 33.3g. Mineral powder of 1000 mesh number was added according to an amount of 20% of the total mass of the system,so the required mineral powder particles quality was 306.7g. Fixed stirring speed 400rpm, introducing flow rate of CO_2 0.5m^3 / h and air 0.25m^3/h, the reaction time of six groups reaction was 5,10,15,20,25,30 min,respectively. After drying the entire sample, the six samples were weighed, we could calculate the actual weight values. The theoretical weight could be calculated according to the assumed condition that all $Ca(OH)_2$ had changed into coating nano-$CaCO_3$.According to the following formula to calculate the ratio:

$$\text{ratio of weight increment (\%)}=\frac{\text{actual weight gain}}{\text{Theoretical weight gain}}\times 100\%$$

The measured values were 28.3% in 5min, 50.3% in 10min, 76.1% in 15min, 79.0% in 20min, 78.9% in 25min and 78.9% in 30min.The initial reaction product weight increment ratio was increasing. At this point,the reaction was in the stage of generation and growth of nano-$CaCO_3$ on the surface of the mineral, and the reaction has not been completed. About 15min from the start of the reaction, the ratio gradually stabilized, which showed that the reaction is substantially complete at 15min or earlier. This is consistent with the test result previously described. It was found that there is a gap between the actual and theoretical weight increment, and the actual data was only about 80% theoretical data. This may be because part of the $Ca(OH)_2$ was coated on the mineral particle surface without reacting with CO_2, or because of any other loss of material.

Effect of the proportion of gas on the reaction process. Under the stirring action, $Ca(OH)_2$ and water are uniformly mixed for preparation of suspension. Then the mixed gas of CO_2 and air was introduced into the suspension,and occured carbonation reaction with $Ca(OH)_2$. CO_2 is a gas-phase reaction medium, the concentration and flow rate of which can significantly affect the reaction progress and the degree of coating powder particles. Fixed the reaction solution volume 1.5L, the system concentration of $Ca(OH)_2$ 0.3mol / L, stirring speed was 400rpm. When all of the gas was CO_2, the nano-$CaCO_3$ was easy to agglomerate, completely covering the surface of the particle can not be achieved, as shown in Figure 5 (f). This is because in the local area, driving force of CO_2 dissolution and diffusion was large, the carbonation reaction occured, but the reaction was not spread

evenly in solution, which resulted in the irregular growth or agglomeration of nano-$CaCO_3$ in the powder surface. Maintain introducing flow rate of CO_2 0.5m^3 / h, the ratio of CO_2 in the gas mixture was gradually reduced. When the ratio of CO_2 to air is 2:1, nano-$CaCO_3$ nuclei in the system was adsorbed on the calcite particles surface, and continued to grow or reunion, eventually connected with mineral particles as a whole. In this case ,the coated particles were shown in Figure 7 (c) .



a b c

d(200rpm) f(600rpm) g(100%CO_2)

Figure 5 SEM photographs of coated reaction product at different conditions

Conclusion

This paper analyzed the variation of pH, electrical conductivity, electrode potential and system temperature in the process of reaction, and carried out analysis of morphologies of different reaction product. Online monitoring data changes in different stages of the reaction were consistent.

Surface morphology of nano-coated powder was observed By SEM, the best value of the gas ratio, stirring intensity and other parameters in the experiment was explored. Better coating effect could be achieved under the experimental condition.

This paper studied the coated product weight increment ratio,the trend of which reflected the reaction process. It was also found that the coated product weight increment ratio had not reached a higher level under the present experimental conditions. This aspect needs to be further studied.

Note: This article is the research results of Binzhou Vocational College Science and Technology Development Program (No. 2013XYKT06) and Binzhou Municipal Science and Technology Development Program (No. 2013ZC0705)

References

[1] G.S. GAI, Micro-Nanometer Particle Composition and Functional Design,Beijing. 2008, 147.

[2] G.S. GAI,Y.F. YANG,S.M. FAN, Preparation and properties of composite mineral powders, J. Powder Technology.153(2005)153-158.

[3] Y.F. YANG, G.S. GAI, S.M. FAN, Nanostructured modification of mineral particle surfaces in $Ca(OH)_2$-H_2O-CO_2 system, J. Journal of Materials Processing Technology. 170(2005)58-63.

[4] K. Damir,V. Neda,The influence of some Naturally Occurring Minerals on The Precipitation of Calcium Carbonate Polymorphs, J. WaterRes. 34(2000)179-184.

Applied Mechanics and Materials Vol. 597 (2014) pp 32-35
© (2014) Trans Tech Publications, Switzerland
doi:10.4028/www.scientific.net/AMM.597.32

Resistances of Nano-Titanium Dioxide on the Ultraviolet Aging of Poly(butylene succinate)

Li Liu[1,2,a], Yongren Wang[1,b*],Yuping zuo[1,c], Dan Liu[2,d], Baohua Guo[2,e*]

[1]Mechatronics Engineering Department, Lanzhou Vocational Technical College, Lanzhou, 730070, China

[2]Institute of Polymer Science & Engineering, Department of Chemical Engineering, Tsinghua University, Beijing, 100084, China

*Corresponding author, email: [a]liziyun2@sina.com, [e]bhguo@mail.tsinghua.edu.cn

Keywords: poly(butylene succinate), titanium dioxide, ultraviolet aging, nano-composites

Abstract. Poly(butylene succinate)/titanium dioxide nano-composite was prepared by melt blending in a HAAKE mixer. The degradation was studied under ultraviolet aging conditions. The SEM results showed that there were not any visible pores in the nano-composite surface, which indicated that the addition of TiO_2 could resist the ultraviolet degradation in some degree. The FT-IR results presented that the neat PBS and 1 wt% PBS/TiO_2 nano-composite had an overall increased peak intensities, especially for the carbonyl group. The intensities of neat PBS after 72h ultraviolet aging were increased significant than that of the 1 wt% PBS/TiO_2 nano-composite. FT-IR results further confirmed the SEM results and revealed the mechanism of the PBS degradation under ultraviolet aging conditions.

Introduction

As a biodegradable polymers, poly(butylene succinate) (PBS) have received much attention both in fundamental research and in industry technology for their potential in environmental protection. PBS shows several interesting properties[1], including good biodegradability, melt processibility, thermal properties, and chemical resistance. Unfortunately, insufficient stiffness, low melt viscosity, slow crystallization rates, and high price have limited PBS processing and potential applications as compared with those of commodity plastics [2, 3]. Therefore, many research groups have tried different methods to improve the properties of PBS. Clay-containing polymer composite is one of the promoted methods to improve the properties of polymer matrix, because the low volume additions of clay particles into the polymer matrix will provide remarkable improvement compared to the neat polymer[4]. TiO_2 is one of the most studied compounds in materials science. Due to some significant properties, it is used in many fields, such as photocatalysis, dye-sensitized solar cells, and biomedical devices[5]. In order to improve the resistance properties on the ultraviolet aging of PBS matrix, the TiO_2 nano-particles were introduced in this research to reveal the mechanism of resistance on the ultraviolet aging of PBS.

Experimental

Material. PBS was kindly supplied by Blue Ridge Tunhe Chemical Industry Joint Stock Co., Ltd. (Xinjiang, China). Titanium dioxide (TiO_2) was purchased from Hangzhou Wanjing new material Co., Ltd. (Zhejiang, China).

Preparation. The PBS/TiO_2 nano-composite was processed by melt blending with a RS600 HAAKE mixer (Germany). The mixing was carried out at 140 °C and the rotary speed was 60 rpm. Briefly, the fabrication of the PBS/TiO_2 nanocomposite containing 1 wt% TiO_2 was processed as follows: 49.5 g PBS was first added into HAAKE mixer at 140 °C for 2 minutes for premelting. Then, 0.5 g TiO_2 was added into the melt and mixed for another 10 minutes. The neat PBS was processed in the same procedures as a reference.

Characterization. The morphologies of TiO_2 and PBS/TiO_2 nanocomposites were examined by scanning electron microscopy on the JEOL JSM-7401 (Japan) at an accelerating voltage of 3 kV. Nano-composite sample was prepared by thermoforming the sheet at 160 °C, and then it was put in liquid nitrogen for 10 min before fracture. The fracture surface was coated with platinum prior to examination.

Fourier transformed infrared spectrum (FT-IR) of all samples were recorded on a Nicolet-6700 spectrometer (USA) in a wavenumber range from 400 to 4000 cm^{-1}. The resolution and scanning time were 4 cm^{-1} and 32 times, respectively.

Results and discussion

SEM analysis. The TiO_2 morphology and its dispersion states in polymer matrix were investigated by SEM analysis. The representative results were presented in Fig.1 (a)-(b).

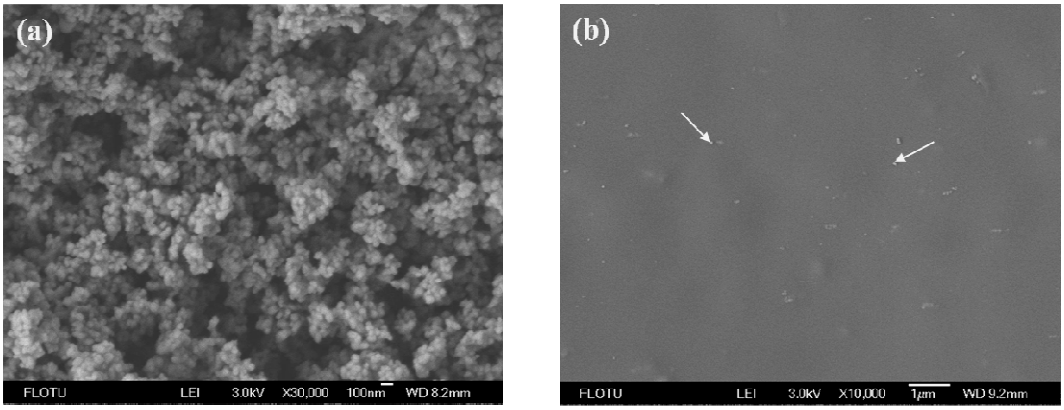


Fig. 1 SEM images of (a) TiO_2 and (b) the fractured surface of 1 wt% PBS/TiO_2 nano-composite

Fig.1 (a) showed the images of TiO_2, which presented a spherical morphology and forms aggregate. The diameter of TiO_2 was about 40 nm. Fig.1 (b) showed the SEM image of the fracture surfaces of nano-composite. The white arrows in Fig.1 (b) indicated that TiO_2 can be well separated from aggregate in PBS matrix. The reason, as reported by Qi et. al.[6], was that the strong interactions between the particle surface and polymer matrix.

Fig.2(a)-2(b) showed the surface morphologies of neat PBS and the 1 wt% PBS/TiO_2 nano-composite after 72h ultraviolet aging.

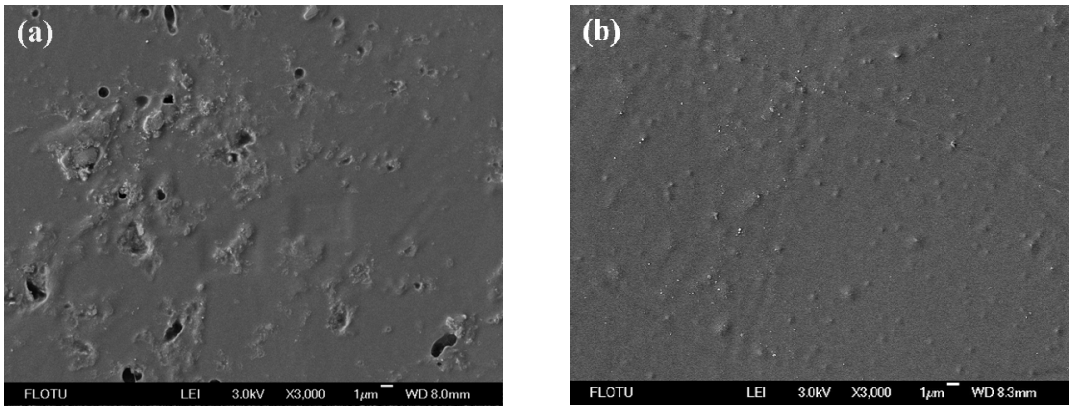


Fig. 2 SEM images of ultraviolet degradation 72h of (a) neat PBS and (b) 1 wt% PBS/TiO_2 nano-composite

Obviously, the surface of neat PBS had many visible microcracks and pores, which indicated that the neat PBS was easy to degrade under ultraviolet conditions. On the contrary, the surface of 1 wt% PBS/TiO_2 nano-composite was still remained unaltered. Therefore, there were not any visible pores in the nano-composite surface, which means that the addition of TiO_2 could resist the ultraviolet degradation in some degree. The above results indicated that 1 wt% PBS/TiO_2 nano-composite had a relatively lower degradation rate compared to neat PBS.

Although surface cracks and pores were the direct evidence, the content of the cracks need to be further confirmed. Therefore, FT-IR was employed to reveal the mechanism of the degradation under ultraviolet aging.

FT-IR analysis. FT-IR spectra of the neat PBS and 1 wt% PBS/TiO_2 nano-composite were presented in Fig.3 (a)-3(b).

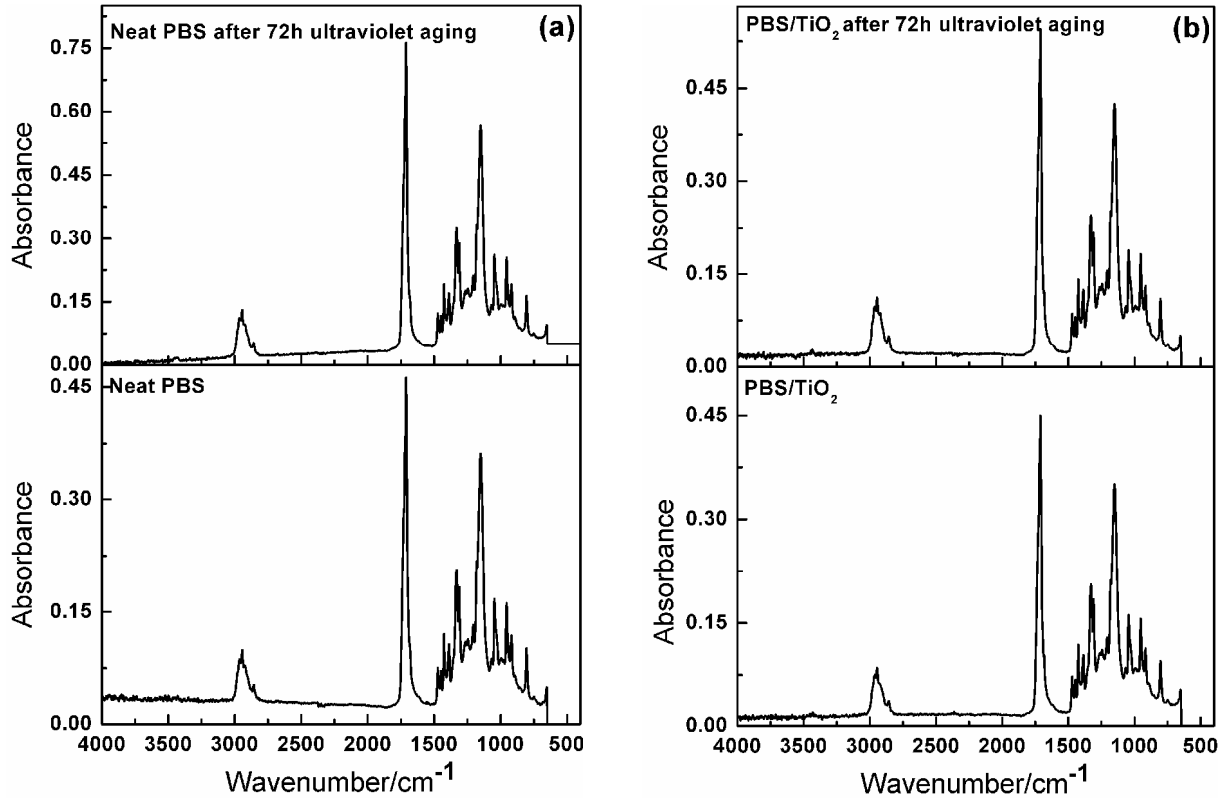


Fig.3 FT-IR Spectra of (a) neat PBS and (b) 1 wt% PBS/TiO_2 nano-composite

According to the previous work[7, 8] , the peak at 3430 cm^{-1} was ascribed to the hydroxyl stretching. The peak at 2946 cm^{-1} was due to the C–H stretching. The carbonyl stretching band appeared at about 1737 and 1715 cm^{-1}, the higher wavenumber to the amorphous region and the lower wavenumber corresponded to the crystalline region. The peak at 1426 cm^{-1} was attributed to the C–H bending. The peak at 1157 cm^{-1} may have resulted from C–O–C stretching for the functional groups in the ester linkage of PBS. The peak at 1046 cm^{-1} was assigned to the C–O stretching vibrations of PBS.

Compared to the samples before and after 72h ultraviolet aging, the neat PBS and 1 wt% PBS/TiO_2 nano-composite showed an overall increased peak intensities, especially for the carbonyl group. The similar result was once reported by Phua et al. [9] in PBS/organo-montmorillonite nanocomposites system. After 72h ultraviolet aging, the intensity of the carbonyl group increased, which indicated that the occurrence of chain scission after ultraviolet aging. In addition, the intensities of neat PBS after 72h ultraviolet aging were increased significant than that of the 1 wt% PBS/TiO_2 nano-composite, which suggested that the addition of TiO_2 could resist ultraviolet degradation. Therefore, the carbonyl group intensity was lower than that of the neat PBS. FT-IR results further confirmed the SEM results, and revealed the mechanism of the PBS degradation under ultraviolet aging conditions.

Summary

The PBS/TiO_2 nano-composite was successlly processed by melt blending with a RS600 HAAKE mixer. The degradation was studied under ultraviolet aging conditions. The SEM results showed that there were not any visible pores in the nano-composite surface, which indicated that the addition of TiO_2 could resist the ultraviolet degradation in some degree. Therefore, 1 wt% PBS/TiO_2

nano-composite had a relatively lower degradation rate compared to the neat PBS. The FT-IR results presented that the neat PBS and 1 wt% PBS/TiO_2 nano-composite showed an overall increased peak intensities, especially for the carbonyl group. The intensities of neat PBS after 72h ultraviolet aging increased significant than that of the 1 wt% PBS/TiO_2 nano-composite, which suggested that the addition of TiO_2 could resist ultraviolet degradation. Therefore, the carbonyl group intensity of was lower than that of the neat PBS, which consistented with the SEM results. FT-IR results further confirmed the SEM results and revealed the mechanism of the PBS degradation under ultraviolet aging conditions.

Acknowledgements

This work was supported by the National 863 Program of China (Grant No. 2011AA02A203) and the National Natural Science Foundation of China (Grant No. 20974060).

References

[1] J. Xu, B.H. Guo. Poly (butylene succinate) and its copolymers: research, development and industrialization,Biotechnology journal, 5 (2010), 1149-1163.

[2] V. Tserki, P. Matzinos, E. Pavlidou, et. al. Biodegradable aliphatic polyesters. Part I. Properties and biodegradation of poly (butylene succinate-co-butylene adipate),Polymer degradation and stability, 91 (2006), 367-376.

[3] A. Vassiliou, K. Chrissafis, D. Bikiaris, In situ prepared PBSu/SiO_2 nanocomposites. Study of thermal degradation mechanism,Thermochimica Acta, 495 (2009), 120-128.

[4] S.S. Ray, Visualisation of Nanoclay Dispersion in Polymer Matrix by High-Resolution Electron Microscopy Combined with Electron Tomography,Macromolecular Materials and Engineering, 294 (2009), 281-286.

[5] P. Roy, S. Berger, P. Schmuki, TiO_2 nanotubes: synthesis and applications, Angewandte Chemie International Edition, 50 (2011), 2904-2939.

[6] Z. Qi, H. Ye, J. Xu, J. Chen, B. Guo, Improved the thermal and mechanical properties of poly (butylene succinate-co-butylene adipate) by forming nanocomposites with attapulgite, Colloids and Surfaces A: Physicochemical and Engineering Aspects, 421 (2013), 109-117.

[7] Z. Qi, H. Ye, J. Xu, J. Peng, J. Chen, B. Guo, Synthesis and characterizations of attapulgite reinforced branched poly (butylene succinate) nanocomposites, Colloids and Surfaces A: Physicochemical and Engineering Aspects, 436 (2013), 26-33.

[8] T. Dong, Y. He, K.m. Shin, Y. Inoue, Formation and Characterization of Inclusion Complexes of Poly (butylene succinate) with α-and γ-Cyclodextrins, Macromolecular bioscience, 4 (2004), 1084-1091.

[9] Y.J. Phua, N.S. Lau, K. Sudesh, W.S. Chow, Z.M. Ishak, A study on the effects of organoclay content and compatibilizer addition on the properties of biodegradable poly (butylene succinate) nanocomposites under natural weathering, Journal of Composite Materials, (2014), 1-12.

Applied Mechanics and Materials Vol. 597 (2014) pp 36-39
© (2014) Trans Tech Publications, Switzerland
doi:10.4028/www.scientific.net/AMM.597.36

Advances of Study on the Developments and Applications of Carbon Nanotubes

Aying Zhang[*1,2]

[1]Harbin University, Harbin 150086, People's Republic of China

[2]Harbin Institute of Technology, Harbin 150001, People's Republic of China

[*]zaying@sina.com

Keywords: Carbon nanotubes; Developments; Applications

Abstract. Many electronic applications of carbon nanotubes crucially rely on techniques of selectively producing either semiconducting or metallic CNTs, preferably of certain chirality. Several methods of separating semiconducting and metallic CNTs are known, but most of them are not yet suitable for large-scale technological processes. The most efficient method relies on density-gradient ultracentrifugation, which separates surfactant-wrapped nanotubes by the minute difference in their density. This density difference often translates into difference in the nanotube diameter and (semi)conducting properties. Another method of separation uses a sequence of freezing, thawing, and compression of SWNTs embedded in agarose gel.

Introduction

A 2006 editorial written by Marc Monthioux and Vladimir Kuznetsov in the journal Carbon described the interesting and often-misstated origin of the carbon nanotube. A large percentage of academic and popular literature attributes the discovery of hollow, nanometer-size tubes composed of graphitic carbon to Sumio Iijima of NEC in 1991 [1].

In 1952 L. V. Radushkevich and V. M. Lukyanovich published clear images of 50 nanometer diameter tubes made of carbon in the Soviet Journal of Physical Chemistry. This discovery was largely unnoticed, as the article was published in the Russian language, and Western scientists' access to Soviet press was limited during the Cold War. It is likely that carbon nanotubes were produced before this date, but the invention of the transmission electron microscope (TEM) allowed direct visualization of these structures.

Carbon nanotubes have been produced and observed under a variety of conditions prior to 1991. A paper by Oberlin, Endo, and Koyama published in 1976 clearly showed hollow carbon fibers with nanometer-scale diameters using a vapor-growth technique. Additionally, the authors show a TEM image of a nanotube consisting of a single wall of graphene. Later, Endo has referred to this image as a single-walled nanotube [2].

In 1979, John Abrahamson presented evidence of carbon nanotubes at the 14th Biennial Conference of Carbon at Pennsylvania State University. The conference paper described carbon nanotubes as carbon fibers that were produced on carbon anodes during arc discharge. A characterization of these fibers was given as well as hypotheses for their growth in a nitrogen atmosphere at low pressures.

In 1981, a group of Soviet scientists published the results of chemical and structural characterization of carbon nanoparticles produced by a thermocatalytical disproportionation of carbon monoxide. Using TEM images and XRD patterns, the authors suggested that their “carbon multi-layer tubular crystals” were formed by rolling graphene layers into cylinders. They speculated that by rolling graphene layers into a cylinder, many different arrangements of graphene hexagonal nets are possible. They suggested two possibilities of such arrangements: circular arrangement and a spiral, helical arrangement [3].

In 1987, Howard G. Tennett of Hyperion Catalysis was issued a U.S. patent for the production of “cylindrical discrete carbon fibrils” with a “constant diameter between about 3.5 and about

70 nanometers..., length 102 times the diameter, and an outer region of multiple essentially continuous layers of ordered carbon atoms and a distinct inner core....” [4].

Iijima’s discovery of multi-walled carbon nanotubes in the insoluble material of arc-burned graphite rods in 1991 and Mintmire, Dunlap, and White’s independent prediction that if single-walled carbon nanotubes could be made, then they would exhibit remarkable conducting properties helped create the initial buzz that is now associated with carbon nanotubes. Nanotube research accelerated greatly following the independent discoveries by Bethune at IBM and Iijima at NEC of single-walled carbon nanotubes and methods to specifically produce them by adding transition-metal catalysts to the carbon in an arc discharge. The arc discharge technique was well-known to produce the famed Buckminster fullerene on a preparative scale, and these results appeared to extend the run of accidental discoveries relating to fullerenes. The original observation of fullerenes in mass spectrometry was not anticipated, and the first mass-production technique by Krätschmer and Huffman was used for several years before realizing that it produced fullerenes. The discovery of nanotubes remains a contentious issue. Many believe that Iijima’s report in 1991 is of particular importance because it brought carbon nanotubes into the awareness of the scientific community as a whole [5].

Potential Applications

Structural

Because of the carbon nanotube’s superior mechanical properties, many structures have been proposed ranging from everyday items like clothes and sports gear to combat jackets and space elevators. However, the space elevator will require further efforts in refining carbon nanotube technology, as the practical tensile strength of carbon nanotubes can still be greatly improved.

For perspective, outstanding breakthroughs have already been made. Pioneering work led by Ray H. Baughman at the NanoTech Institute has shown that single and multi-walled nanotubes can produce materials with toughness unmatched in the man-made and natural worlds [6].

Carbon nanotubes are also a promising material as building blocks in bio-mimetic hierarchical composite materials given their exceptional mechanical properties (~1 TPa in modulus, and ~100 GPa in strength). Initial attempts to incorporate CNTs into hierarchical structures led to mechanical properties that were significantly lower than these achievable limits. Windle et al. have used an in situ chemical vapor deposition (CVD) spinning method to produce continuous CNT yarns from CVD grown CNT aerogels. With this technology, they fabricated CNT yarns with strengths as high as ~9 GPa at small gage lengths of ~1 mm, however, defects resulted in a reduction of specific strength to ~1 GPa at 20 mm gage length. Espinosa et al. developed high performance DWNT-polymer composite yarns by twisting and stretching ribbons of randomly oriented bundles of DWNTs thinly coated with polymeric organic compounds. These DWNT-polymer yarns exhibited unusually high energy to failure of ~100 $J \cdot g^{-1}$, and strength as high as ~1.4 GPa. Effort is ongoing to produce CNT composites that incorporate tougher matrix materials, such as Kevlar, to further improve on the mechanical properties toward those of individual CNTs.

Because of the high mechanical strength of carbon nanotubes, research is being made into weaving them into clothes to create stab-proof and bulletproof clothing. The nanotubes would effectively stop the bullet from penetrating the body, although the bullet's kinetic energy would likely cause broken bones and internal bleeding [7].

Electrical Circuits

Nanotube-based transistors, also known as carbon nanotube field-effect transistors (CNTFETs), have been made that operate at room temperature and that are capable of digital switching using a single electron. However, one major obstacle to realization of nanotubes has been the lack of technology for mass production. In 2001 IBM researchers demonstrated how metallic nanotubes can be destroyed, leaving semiconducting ones behind for use as transistors. Their process is called

"constructive destruction," which includes the automatic destruction of defective nanotubes on the wafer. This process, however, only gives control over the electrical properties on a statistical scale.

The potential of carbon nanotubes was demonstrated in 2003 when room-temperature ballistic transistors with ohmic metal contacts and high-k gate dielectric were reported, showing 20–30x higher ON current than state-of-the-art Si MOSFETs. This presented an important advance in the field as CNT was shown to potentially outperform Si. At the time, a major challenge was ohmic metal contact formation. In this regard, palladium, which is a high-work function metal was shown to exhibit Schottky barrier-free contacts to semiconducting nanotubes with diameters >1.7 nm [8].

The first nanotube integrated memory circuit was made in 2004. One of the main challenges has been regulating the conductivity of nanotubes. Depending on subtle surface features a nanotube may act as a plain conductor or as a semiconductor. A fully automated method has however been developed to remove non-semiconductor tubes [9].

Another way to make carbon nanotube transistors has been to use random networks of them. By doing so one averages all of their electrical differences and one can produce devices in large scale at the wafer level. This approach was first patented by Nanomix Inc. It was first published in the academic literature by the United States Naval Research Laboratory in 2003 through independent research work. This approach also enabled Nanomix to make the first transistor on a flexible and transparent substrate.

Large structures of carbon nanotubes can be used for thermal management of electronic circuits. An approximately 1 mm–thick carbon nanotube layer was used as a special material to fabricate coolers, this material has very low density, ~20 times lower weight than a similar copper structure, while the cooling properties are similar for the two materials.

In 2013, researchers demonstrated a Turing-complete prototype micrometer-scale computer. Carbon nanotube transistors as logic-gate circuits with densities comparable to modern CMOS technology have not yet been demonstrated [10].

Electrical Cables and Wires

Wires for carrying electrical current may be fabricated from pure nanotubes and nanotube-polymer composites. Recently small wires have been fabricated with specific conductivity exceeding copper and aluminum; these cables are the highest conductivity carbon nanotube and also highest conductivity non-metal cables. Recently, composite of carbon nanotube and copper have been shown to exhibit nearly one hundred times higher current-carrying-capacity than pure copper or gold. Significantly, the electrical conductivity of such a composite is similar to pure Cu. Thus, this Carbon nanotube-copper (CNT-Cu) composite possesses the highest observed current-carrying capacity among electrical conductors. Thus for a given cross-section of electrical conductor, the CNT-Cu composite can withstand and transport one hundred times higher current compared to metals such as copper and gold [11].

Actuator

The exceptional electrical and mechanical properties of carbon nanotubes have made them alternatives to the traditional electrical actuators for both microscopic and macroscopic applications. Carbon nanotubes are very good conductors of both electricity and heat, and they are also very strong and elastic molecules in certain directions [12].

Paper Batteries

A paper battery is a battery engineered to use a paper-thin sheet of cellulose (which is the major constituent of regular paper, among other things) infused with aligned carbon nanotubes. The nanotubes act as electrodes; allowing the storage devices to conduct electricity. The battery, which functions as both a lithium-ion battery and a supercapacitor, can provide a long, steady power output comparable to a conventional battery, as well as a supercapacitor's quick burst of high power

and while a conventional battery contains a number of separate components, the paper battery integrates all of the battery components in a single structure, making it more energy efficient [13].

Solar Cells

One of the promising applications of single-walled carbon nanotubes (SWNTs) is their use in solar panels, due to their strong UV/Vis-NIR absorption characteristics. Research has shown that they can provide a sizeable increase in efficiency, even at their current unoptimized state. Solar cells developed at the New Jersey Institute of Technology use a carbon nanotube complex, formed by a mixture of carbon nanotubes and carbon buckyballs (known as fullerenes) to form snake-like structures. Buckyballs trap electrons, but they can't make electrons flow. Add sunlight to excite the polymers, and the buckyballs will grab the electrons. Nanotubes, behaving like copper wires, will then be able to make the electrons or current flow.

Additional research has been conducted on creating SWNT hybrid solar panels to increase the efficiency further. These hybrids are created by combining SWNT's with photexcitable electron donors to increase the number of electrons generated. It has been found that the interaction between the photoexcited porphyrin and SWNT generates electro-hole pairs at the SWNT surfaces. This phenomenon has been observed experimentally, and contributes practically to an increase in efficiency up to 8.5% [14].

Medical

In the Kanzius cancer therapy, single-walled carbon nanotubes are inserted around cancerous cells, and then excited with radio waves, which causes them to heat up and kill the surrounding cells.

Researchers at Rice University, Radboud University Nijmegen Medical Centre and University of California, Riverside have shown that carbon nanotubes and their polymer nanocomposites are suitable scaffold materials for bone cell proliferation and bone formation [15].

Acknowledgements

This work was financially supported by the Special Research Foundation of Harbin Science and Technology Innovation Talents (Grant No. RC2013QN017021).

References

[1] X. Wang, Q.Q. Li, J. Xie and et al: Nano Lett. Vol. 9 (2009), p. 3137

[2] S. Gullapalli, M.S. Wong: Chem Eng Prog. Vol. 107 (2011), p. 28

[3] J.W. Mintmire, B.I. Dunlap and et al: Phys. Rev. Lett. Vol. 68 (1992), p. 631

[4] R. Martel, V. Derycke and et al: Phys. Rev. Lett. Vol. 87 (2001), p. 256805

[5] J. Cumings, A. Zettl: Sci. Vol. 289 (2000), p. 602

[6] R.B. Pipes, S.J.V. Frank and et al: Compos Sci Technol. Vol. 63 (2003), p. 1349

[7] C.Y. Li, E.T. Thostenson and T. W. Chou: Compos Sci Technol. Vol. 68 (2008), p. 1445

[8] J.S. Leng, H.B. Lu and et al: MRS Bull. Vol. 34 (2009), p. 848

[9] H.B. Lu, Y.J. Liu and et al: Appl Phys Lett. Vol. 96 (2010), p. 084102

[10] M.J. Biercuk, M.C. Llaguno and et al: Appl Phys Lett. Vol. 80 (2002), p. 2767

[11] Z. Wang, Z.Y. Liang and et al: Compos Part A-Appl Sci Manuf. Vol. 35 (2004), p. 1225

[12] H.B. Lu, Y.J. Liu and et al: Smart Mater. Vol. 19 (2010), p. 75021

[13] H.B. Lu, K. Yu and et al: Polym Int, Vol. 59 (2010), p. 766

[14] B.R. Stoner, S.R. Akshay and et al: Appl Phys Lett. Vol. 99 (2011), p. 183104

[15] C.B. Parker, S.R Akshay and et al: J. Mater. Res, Vol. 27 (2012), p. 1046

Applied Mechanics and Materials Vol. 597 (2014) pp 40-44
© (2014) Trans Tech Publications, Switzerland
doi:10.4028/www.scientific.net/AMM.597.40

Monte Carlo Simulation of the Dispersion of Carbon Nanotubes in Cement Matrix

Bao Min Wang[1, a], Yuan Zhang[2, b *], Ming Li Yu[3, c] and Yu Han[4]

[1]Institute of Building Materials, School of Civil Engineering, Dalian University of Technology Dalian 116024 China

[2]Institute of Building Materials, School of Civil Engineering, Dalian University of Technology Dalian 116024 China

[3]School of Control Science and Engineering, Dalian University of Technology Dalian 116024 China

[4]Institute of Building Materials, School of Civil Engineering, Dalian University of Technology Dalian 116024 China

[a]wangbm@dlut.edu.cn, [b]zhangyuan89@mail.dlut.edu.cn, [c]303178405@qq.com

Keywords: Monte Carlo Simulation; carbon nanotubes (CNTs); cement matrix

Abstract. In this paper, the dispersion of carbon nanotubes (CNTs) in cement matrix was analyzed by Three-dimensional Monte Carlo Simulation. A Hard core model was employed which was not allow the intersection among CNTs in a simulated three-dimensional representative volume element (3-D RVE). The position and the orientation of CNTs were assumed to follow the uniformly random distribution. The results showed that CNTs were dispersed randomly and it was helpful for the further simulation calculation about mechanical, conductivity and piezoresistivity properties.

Introduction

Since they were discovered by Iijima S. in 1991 [1], carbon nanotubes (CNTs) have been considered as a promising candidate for the next generation high performance and multi-functional composites materials for their high stiffness, high specific strength and high conductivity, such as biomedical science [2, 3], field emission [4, 5], super-capacitors [6, 7], molecular sensors [8, 9] and reinforced composites [10, 12].

As a newly reinforced functional material, CNTs were used in cement mortar and concrete to improve the mechanical performance and functional properties. Li [13] reported that a 25% reinforcement in flexural strength was obtained, with a 19% increasing rate in compressive strength by addition of 0.5% (by weight of cement) CNTs. Musso [14] found that a higher concentration of CNTs can increase the compressive strength by nearly 20%. The results obtained by Wang [15] showed that the optimum concentration of CNTs in cement was 0.08%, which presented the maximum enhancement in flexural and compressive strength.

Though the mechanical properties of CNTs/cement composites were analyzed, little work about the simulation of dispersion of CNTs in matrix have been done, including polymer and solvent. Grujicic [16] carried out a 3-D Monte Carlo computational analysis of bundling effects in single-wall carbon nanotubes (SWCNTs) in terms of the percolation behavior of nanocomposite materials. Li [17] studied the transport properties of nanocomposites by using polygons 2-D analysis to simulate the filler curvature. Sun [18, 19] made a 3-D Monte Carlo simulation composed of conducting nanofillers and insulating polymer matrix to investigate the electrical conductivity of nanocomposites.

In most existing composites simulations, a soft core model is employed to allow the intersection among CNTs [20, 22]. However, this model apparently goes against the physical principle that CNTs can never penetrate through each other partially or completely. In this study, a hard core model was used to solve this problem. The position and the orientation of CNTs were assumed to follow the uniformly random distribution by using the Matlab software. The results showed that CNTs were

dispersed randomly, which was helpful for the further simulation calculation about mechanical, conductivity and piezoresistivity properties.

Simulation and Calculation Procedure

Simulation Procedure. (I) First, a 3-D cubic RVE was defined and the periodic boundary condition was applied. All the CNTs should be defined in this cubic RVE and the outside boundaries of the RVE should be cut.

(II) A single CNT that was assigned in the RVE completely was defined. The parameters (i.e. starting point, length, diameter, ending point and generated angle) should also be determined. The defined single CNT was shown in Fig.1.

(III) The shortest distance between any two CNTs should be defined for quantifying individual resistors. We defined two single CNTs AB and CD, and the line MN is the distance between AB and CD. This shortest distance should not be less than the diameter of CNTs. The two single CNTs simulation sketch was shown in Fig.2.

(IV) Define the parameters of cement matrix.

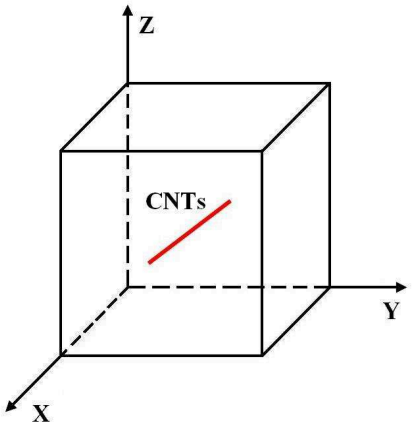


Fig.1 The defined single CNT in 3-D cubic RVE

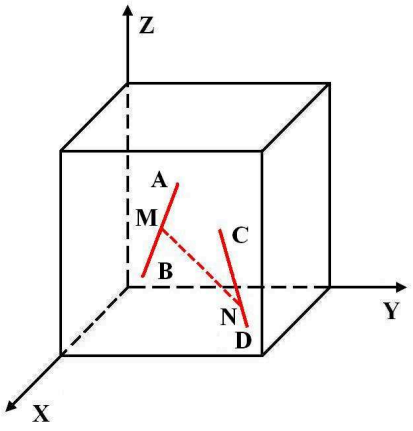


Fig.2 The designed two CNTs simulation sketch

Calculation Procedure. As mentioned in Section 2.1, we defined two single CNTs AB and CD. The coordinates of each point A, B, C, D were A(a_i, c_i, e_i), B(b_i, d_i, f_i), B(a_j, c_j, e_j)and D(b_j, d_j, f_j), respectively. The length and diameter of a single CNT were defined as L and D, respectively. Then, we take two arbitrary points (point M and point N) in AB and CD and the length of line MN should be the distance of AB and CD. Two variables t and s were introduced, where t and s were both stayed in the range of 0~L. Finally, the coordinates of arbitrary points M and N were calculated.

$M\ [a_i+t/L(b_i-a_i),\ c_i+t/L(d_i-c_i),\ e_i+t/L(f_i-e_i)]$, $N\ [a_j+s/L(b_j-a_j),\ c_j+s/L(d_j-c_j),\ e_j+s/L(f_j-e_j)]$

We calculated the length of MN, and defined the f(t, s) as the square of the length.

$$f(t,s)=\{[a_i+t/L(b_i-a_i)-a_j-s/L(b_j-a_j)]^2+[c_i+t/L(d_i-c_i)-c_j.s/L(d_j-c_j)]^2+[e_i+t/L(f_i-e_i)-e_j-s/L(f_j-e_j)]^2\} \quad (1)$$

If we defined $\Delta a=a_i-a_j$, $\Delta c=c_i-c_j$, $\Delta e=e_i-e_j$,

$$C_1=2[\Delta a*(b_i-a_i)/L+\Delta c*(d_i-c_i)/L+\Delta e*(f_i-e_i)/L] \quad (2)$$

$$C_2=-2[(b_i-a_i)(b_j-a_j)/L^2+(d_i-c_i)(d_j-c_j)/L^2+(f_i-e_i)(f_j-e_j)/L^2] \quad (3)$$

$$C_3=-2[\Delta a*(b_j-a_j)/L+\Delta c*(d_j-c_j)/L+\Delta e*(f_j-e_j)/L] \quad (4)$$

$$C_4=\Delta a^2+\Delta c^2+\Delta e^2 \quad (5)$$

The eq.(2)~(5) were substituted into eq.(1), and finally we obtained a new equation.

$$f(t,s)=t^2+C_1t+C_2ts+s^2+C_3s+C_4 \quad (6)$$

We calculated the partial differential of eq.(8) about s and t, and a new limitation condition was obtained, which was shown in eq.(7)~(10).

$$\frac{\partial f(t,s)}{\partial t}=2t+C_1+C_2s=0 \quad (7)$$

$$\frac{\partial f(t,s)}{\partial s}=2s+C_3+C_2t=0 \quad (8)$$

$$\frac{\partial^2 f}{\partial t^2}=2\geq 0 \quad (9)$$

$$\left(\frac{\partial^2 f}{\partial t^2}\right)\left(\frac{\partial^2 f}{\partial s^2}\right)-\left(\frac{\partial^2 f}{\partial t\partial s}\right)^2=4-C_2^{\ 2}\geq 0 \quad (10)$$

The eq.(7) and (8) were substituted into eq.(1), and the minimum value of t, s and the shortest distance were calculated and the results were showed in eq. (11)~(13).

$$t=\frac{2C_1-C_2C_3}{C_2^{\ 2}-4} \quad (11)$$

$$s=\frac{2C_3-C_1C_2}{C_2^{\ 2}-4} \quad (12)$$

$$d_{\min}=\sqrt{\frac{C_2^{\ 2}C_4+C_1^{\ 2}+C_3^{\ 2}-C_1C_2C_3-4C_4}{C_2^{\ 2}-4}}\geq D \quad (13)$$

Simulation Program Procedure. Not using the simulation software (ANSYS 12.0 software et al) that other studies employed, we used the Matlab 7.0 software to accomplish this simulation work. The entire simulation program and the simulated result were shown below. The result showed that the CNTs dispersed well in cement matrix.

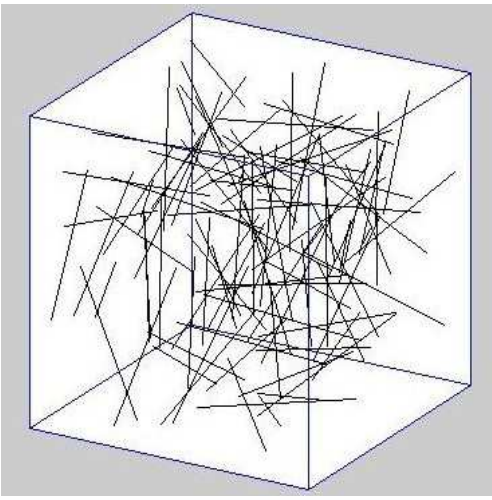


Fig.3 The simulated dispersed effect of CNTs in cement matrix

Conclusions

Three-dimensional Monte Carlo Simulation was applied in this simulation for evaluating the dispersion of carbon nanotubes in cement matrix. A three-dimensional representative volume element (3-D RVE) was simulated firstly, and a hard core model was employed which did not allow the CNTs to penetrate through each other partially or completely, which was follow the physical principle. The position and orientation of CNTs were assumed to follow the rule of uniformly random distribution. The results showed that the CNTs were homo-dispersed in cement matrix and this may have a further understanding for the enhancement of CNTs in matrix in computational and simulation analysis, including the further simulation calculation of mechanical, conductivity and piezoresistivity properties.

Acknowledgements

The authors would like to express appreciation for the financial support by the National Natural Science Foundation of China (51278086), the Program for New Century Excellent Talents in University by Ministry of Education of the People's Republic of China (NCET-12-0084), Liaoning BaiQianWan Talents Program (2012921073), Dalian Plan Projects of Science and Technology (2012A13GX024 and 2013A16GX113) and the Construction Safety and Environment State Key Laboratory Open Fund (201202).

References

[1] S. Iijima. Helical microtubules of graphitic carbon, Nature, 354 (1991) 56-58.

[2] Z. Liu, S. Tabakman, K. Welsher, et al. Carbon nanotubes in biology and medicine: in vitro and in vivo detection, imaging and drug delivery, Nano Res., 2 (2009) 85-120.

[3] W. Yang, P. Thordarson, J.J. Gooding, et al. Carbon nanotubes for biological and biomedical applications, Nanotechnology, 41 (2007) 412001-1-8.

[4] A.A. Kuznetzov, S.B. Lee, M. Zhang, et al. Electron field emission from transparent multiwalled carbon nanotube sheets for inverted field emission displays, Carbon, 48 (2010) 41-46.

[5] I. Lahiri, R. Seelaboyina, J.Y. Hwang, et al. Enhanced field emission from multi-walled carbon nanotubes grown on pure copper substrate, Carbon, 48, (2010) 1531-1538.

[6] M. Kaempgen, C.K. Chan, J. Ma, et al. Printable thin film supercapacitors using single-walled carbon nanotubes, Nano Lett., 9, (2009) 1872-1876.

[7] J. Yan, J. Liu, Z. Fan, et al. High-performance supercapacitor electrodes based on highly corrugated grapheme sheets, Carbon, 50 (2012) 2179-2188.

[8] H. Jin, D.A. Heller, M. Kalbacova, et al. Detection of single-molecule H_2O_2 signalling from epidermal growth factor receptor using fluorescent single-walled carbon nanotubes, Nature Nanotechnology, 5, (2010) 302-309.

[9] D.R. Kauffman, D.C. Sorescu, D.P. Schofield, et al. Understanding the sensor response of metal-decorated carbon nanotubes, Nano lett., 10, (2010) 958-963.

[10] M. Mazaheri, D. Mari, Z.R. Hesabi, et al. Multi-walled carbon nanotube/nanostructured zirconia composites: Outstanding mechanical properties in a wide range of temperature, Compos. Sci. Technol., 71, (2011) 939-945.

[11] M.K. Yeh, N.H. Tai and J.H. Liu. Mechanical behavior of phenolic-based composites reinforced with multi-walled carbon nanotubes, Carbon, 44 (2006) 1-9.

[12] B.M. Wang, Y. Han and S. Liu. Effect of highly dispersed carbon nanotubes on the flexural toughness of cement-based composites, Constr. Build. Mater., 46 (2013) 8-12.

[13] G.Y. Li, P.M. Wang and X. Zhao. Mechanical behavior and microstructure of cement composites incorporating surface-treated multi-walled carbon nanotubes, Carbon, 43 (2005) 1239-1245.

[14] S. Musso, J.M. Tulliani, G. Ferro, et al. Influence of carbon nanotubes structure on the mechanical behavior of cement composites, Compos Sci Technol, 69 (2009) 1985-1990.

[15] B. Wang, Y. Han and T. Zhang. Morphological properties of surface-treated carbon nanotubes in cement-based composites, J. Nanosci. Nanotech., 12 (2012) 8415-8419.

[16] M Grujicic, G Cao and R Singh. A computational analysis of the percolation threshold and the electrical conductivity of carbon nanotubes filled polymeric materials, J. Mater. Sci., 39 (2004) 4441-4449.

[17] C. Li, E.T. Thostenson, T.W. Chou. Sensors and actuators based on carbon nanotubes and their composites: A review, Compos., Sci., Technol., 68 (2008) 1227-1249.

[18] Y. Yu, G. Song and L. Sun. Determinant role of tunneling resistance in electrical conductivity of polymer composites reinforced by well dispersed carbon nanotubes, J. Appl. Phys., 108 (2010) 084319-1-5.

[19] Y. Yu, S. Song, Z. Bu, et al. Influence of filler waviness and aspect ratio on the percolation threshold of carbon nanomaterials reinforced polymer nanocomposites, J. Mater. Sci., 48 (2013) 5727-5732.

[20] F. Dalmas, R. Dendievel, L. Chazeau, et al. Carbon nanotube-filled polymer composites. Numerical simulation of electrical conductivity in three-dimensional entangled fibrous networks, Acta Mater., 54 (2006) 2923-2931.

[21] J. P. Vassal, L. Orgeas, and D. Favier. Modelling microstructure effects on the conduction in fibrous materials with fibre-fibre interface barriers, Modell. Simul, Mater. Sci. Eng., 3 (2008) 035007-1-19.

[22] M. Foygel, R. D. Morris, D. Anez, et al. Theoretical and computational studies of carbon nanotube composites and suspensions: Electrical and thermal conductivity, Phys. Rev. B., 71 (2005) 104201-1-8.

Applied Mechanics and Materials Vol. 597 (2014) pp 45-48
© (2014) Trans Tech Publications, Switzerland
doi:10.4028/www.scientific.net/AMM.597.45

Preparation and antibacterial activity of silver doping nano zinc oxide

Qun Li[1,a], Xi-Hui Zhao[1,b], Xiao-Wen Li[1,c], Li-Ping Wang[2,d], Qian-Qian Liu[1,e], Chao Zhang[1,f]

[1]Collaborative Innovation Center for Marine Biomass Fibers, Materials and Textiles of Shandong Province, Qingdao University, Qingdao 266071, P.R. China
[2]Hospital of Ocean University of China, Song Ling Road, Qingdao, 266100, P.R. China
[a]qunli501@163.com, [b]gaozxh@163.com, [c]lixiaowen5456@163.com, [d]maomiping@126.com, [e]qianerfighting@163.com, [f]xiaoyuccapricorn@163.com

Keywords: Silver doping nano Zinc oxide, Antibacterial activity, Antibacterial mechanism, Preparation

Abstract

Zinc oxalate dihydrate as the precursor of anometer zinc oxide (nano-ZnO) was prepared by direct precipitation method. The zinc oxalate dihydrate was dispersed in a silver nitrate solution, and then the resulting solution was filtered and dried under 120℃. The silver doping nano-Zinc oxide (nano-SDZO) was obtained by decrepitating the zinc oxalate dihydrate cake under 500℃. The microstructure of nano-ZnO and nano-SDZO were characterized by TEM, and the chemical reaction in the heat burst process was described. The nano-ZnO particles were 50-60 nm in diameter, and the particle size of nano-SDZO in the range of 20-100 nm. Antibacterial activity of the nano-ZnO and nano-SDZO were compared. The results show that all of the ZnO samples inhibited the growth of *S. aureus* and *E. coli*, and nano-SDZO showed a relatively higher inhibition rate than other samples. Two possible mechanisms were proposed to explain the inhibition of bacteria.

Introduction

There is intense research interest in the preparation and applications of nanomaterials. Interest in this area is an essential requirement, not only for the fundamental researchers in this field, but also for the development of biomedical and engineering applications. As a new type of green antibacterial agent, nano-ZnO has been a successful paradigm in the developing of antibacterial and deodorant synthetic fibers [1]. However, the report on enhancing the antibacterial activity by doping silver was relatively fewer [2-5].

Taking into account the above facts and in order to enhance the antibacterial activity of nano-ZnO, in this paper, silver doping nano zinc oxide were prepared and characterized by SEM. The antibacterial activity and the antibacterial mechanism were studied.

Experimental

Materials and physical measurements. All chemicals used were of reagent grade. The nano Zinc oxide was prepared on an automatic temperature control furnace made by ourselves. Transmission electron micrograph (TEM) was obtained on a JEM-1200EX electron microscope.

Preparation of nano-SDZO. The preparation of nano-SDZO consists of three steps. The first step was the synthesis of Zinc(II) oxalate. A 60 g portion of oxalate saturated aqueous solution was added dropwise into a Zinc(II) chloride (70 g) saturated aqueous solution. After stiring for 1 h, the mixture was filtered, washed until no chloride ion was tested (Ag^+ detection method) and then dried under vacuum. The filter cake (A) was divided into two parts (A1, A2). The second step was the preparation of the precursor of silver doping nano zinc oxide (nano-SDZO). To a stirred silver nitrate solution was added the A1 part. The mixture was stirred quickly at for 3 min, the resulting solution was filtered and the zinc oxalate cake surface deposition with silver nitrate (B) was obtained. The third step was the preparation of nano-SDZO and nano-ZnO. B part and A2 part were dried under 120℃. The nano-SDZO and nano-ZnO were obtained by decrepitating the zinc oxalate dihydrate cake under 500℃ for 1 h. TEM was used to characterize the sample.

Identification and content determination of silver in nano-SDZO. (1) In order to identify the silver in nano-SDZO, 10% thin hydrochloric acid solution 20 mL was added into a test tube containing a

small amount of nano-SDZO, heated. Then the mixture of nitric acid and sulphuric acid were added into the test tube.

(2) To determine the content of silver in nano-SDZO, 10% thin hydrochloric acid solution 20 mL was added into a test tube containing 2.000g nano-SDZO, and was heated. After cooling the mixture was filtered, washed with water and then dried 120℃for 3h. The content of silver in nano-SDZO was obtained using the following equation:

$$X = \frac{M_1}{M_2} \times 100\% \tag{1}$$

where M_1 and M_2 correspond to the weight for the testing compounds and for the testing compounds in remnant form.

Antibacterial activities. Antibacterial activities of the nano-SDZO and nano-ZnO together with ordinary zinc oxide were evaluated against two bacteria strains including Staphylococcus aureus (ATCC6538) and Escherichia coli (8099) by using the bacteriostatic circle method.

Results and discussion

Identification and doping quantity determination of silver in nano-SDZO. (1) After the nano-SDZO dissolved by acid, there are black residues in the test tube. The residue completely dissolved in hot high concentrations of nitrate and sulfate mixed solution. White powder was precipitated as the NaCl solution was added dropwise into the diluted mixed solution. The results proved the existence of silver, which can be explained by the following equations:

$$(ZnO)_x(Ag)_y(s) + HCl(aq) \rightarrow ZnCl_2(aq) + Ag(s)\ \text{black} \tag{2}$$

$$Ag\ (s) + HNO_3(\text{concentrated}) + H_2SO_4(\text{concentrated}) \rightarrow AgNO_3(aq) \tag{3}$$

$$Ag^+(aq) + Cl^-(aq) \rightarrow AgCl(s)\ \text{white} \tag{4}$$

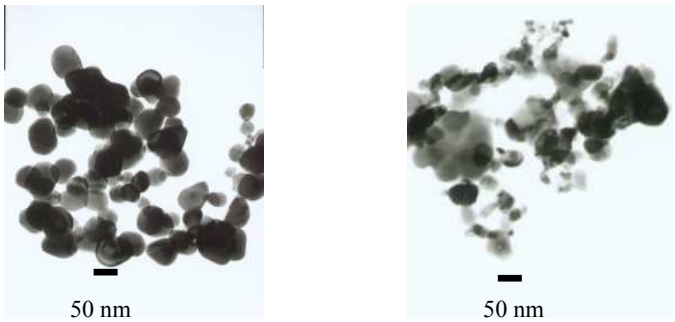
(2) The content of silver doping in nano-SDZO was calculated as follows:

M_1=0.0413g, M_2=2.0000g:

$$X = \frac{M_1}{M_2} \times 100\%;\ X = \frac{0.0413}{2} \times 100\% = 2.065\% \tag{5}$$

There, the content of silver doping in nano-SDZO was 2.065%.

TEM analyze. Figure 1 show the TEM image of nano-ZnO and nano-SDZO.



(a) nano-ZnO (b) nano-SDZO

Fig. 1. TEM images of nano-ZnO and nano-SDZO.

It can be seen clearly that: nano-ZnO and nano-SDZO were irregular sphere, the particle size of the former is 50-60 nm, and the latter is in a wider range of 20-100nm. The results suggest that silver doping affect the process of thermal explosion and the tendency of the particle aggregation.

The distribution of pure silver on the surface of nano-ZnO particles can not be observed in the TEM image. From the preparation process, it can be inferred that silver nitrate was adsorbed on the surface of zinc oxalate dihydrate the precursor of nano-ZnO. When being heated burst, silver nitrate molecular crumble with the precursor crystal, and Ag^+ was reduced by CO.

$$Zn(C_2O_4)\cdot 2H_2O\,(s) \xrightarrow{\Delta} ZnO\,(s) + CO_2\,(g) + CO(g) + H_2O(g) \tag{6}$$

$$Ag^+\,(s) + CO(g) \rightarrow Ag(s) + CO_2(g) \tag{7}$$

or

$$AgNO_3(s) \rightarrow Ag(s) + NO_2(g) + O_2(g) \tag{8}$$

Visibly, a large amount of gas generated from the thermal decomposition play the role of molecular mill, and "thermal crack" is the main factor in obtaining nano-SDZO. Doping with silver, the sizes of nano-SDZO particles become smaller as more gas was generated.

The silver doping nano-ZnO should be incomplete silver wrapping nano powder, and silver "ornament" on nano-ZnO surface may be the main features of nano-SDZO. After doped by silver, the aggregate of the nano particles increase, and there are cluster aggregations.

Antibacterial activities. Antibacterial circle experiments results of ZnO, nano-ZnO and nano-SDZO were shown in table 1 and figure 2.

Table 1 Antibacterial circle experiments results

Samples	Particle size	Antibacterial circle radius against E. coli (mm)		Antibacterial circle radius against S. aureus (mm)	
		light	dark	light	dark
ZnO	≥1μm	4	3	6	5
nano-ZnO	50~60nm	10	8	13	11
nano-SDZO	20~100nm	14	10	16	12

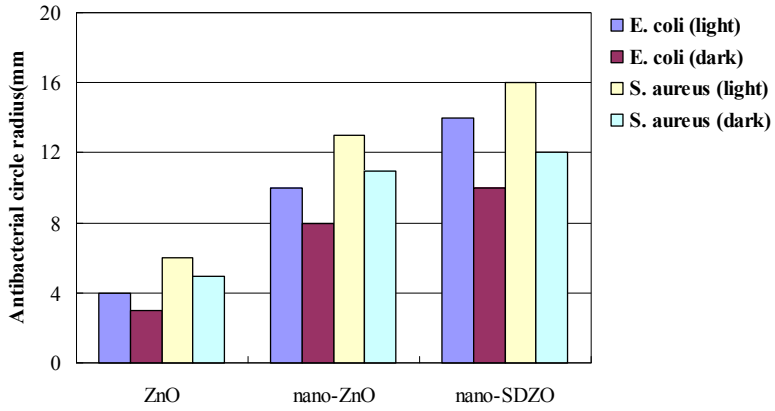


Fig. 2. Antibacterial circle radius against E. coli and S. aureus with or without light, by ZnO, nano-ZnO and nano-SDZO, respectively.

As shown in table 1 and figure 2, ZnO also has antibacterial activities, but the antibacterial circle radius of nano-ZnO is two times higher. The three samples all have better antibacterial activities with light than those of without light. Nano-SDZO has better antibacterial activities than those of nano-ZnO. All of the three samples have better antibacterial activities against S. aureus than E. coli.

The antibacterial property of nano-ZnO or nano-SDZO is closely related with the antibacterial mechanism. There are two kinds of antibacterial mechanism of nano-ZnO or nano-SDZO. The first is the photocatalytic oxidation antibacterial mechanism. In the sunlight, especially under ultraviolet irradiation, ZnO (Ag) particles absorb light energy (hv), and the electron on the valence band was excited onto the conduction band, forming the high-energy electron (e^-), and resulting in the positively charged hole (h^+) on the valence band. The surrounding water and oxygen could obtain energy from these energetic electrons and holes to produce free radicals:

$$ZnO\ (Ag) + hv \rightarrow h^+ + e^- \quad (9)$$

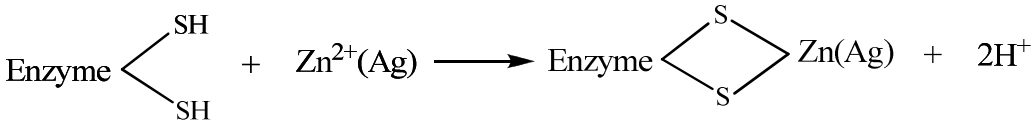
$$H_2O + h^+ \rightarrow \cdot OH + H\cdot \quad (10)$$

$$O_2 + e^- \rightarrow O_2^- \quad (11)$$

$$O_2^- + H\cdot \rightarrow \cdot OH + \cdot O \quad (12)$$

The hydroxyl free radical (·OH) and atomic oxygen (·O) has strong oxidation ability, which could kill the bacteria.

The second is the dissolved metal ions antibacterial mechanism. Zinc (Ag) ions will gradually free. When entering bacterial cell, the metal ions will bind with the protease make the protein inactive and thus kill the bacteria.



The antibacterial activities are the consequence of the two mechanisms, which can be proved by the results that nano-ZnO also has antibacterial activities and the samples all have better antibacterial activities with light.

The observation that all of the three samples have better antibacterial activities against S. aureus than E. coli can be rationalized by the following reason:

S. aureus is a gram positive bacteria (pI 2~3), while E. coli belongs to gram negative bacteria (pI 4~5). In the near neutral or weak alkaline environment, bacteria are negatively charged, and gram positive bacteria load more. The hole on the surface of nano-ZnO or nano-SDZO is positive charge, so the nano particles can be adsorbed by the bacteria, and killed the bacteria, and the gram positive bacteria can be killed easier than the gram negative bacteria.

The antibacterial activity of nano-SDZO is better than that of nano-ZnO, especially in the absence of light. So Nano-SDZO could have more applications.

Conclusions

(1) The filter cake of the zinc oxalate dihydrate doped with silver nitrate was dried under 120℃. The nano-SDZO irregular spherical powder in the size of 20-100 nm was obtained by decrepitating the filter cake under 500℃ for 1 h. A large amount of gas generated from the thermal decomposition play the role of molecular mill, and "thermal crack" is the main factor in obtaining nano-SDZO.

(2) Nano-SDZO with silver doping amount of 2% has better antibacterial activities than those of nano-ZnO. Nano-SDZO could have more applications as it has better antibacterial activity than that of nano-ZnO, especially in the absence of light.

References

[1] Q. Li, S.L. Chen, W.C. Jiang, Preparation of Zinc oxide nano-particle and the development of nano functional textiles, Textile Dyeing and Finishing J. 25(4) (2003) 5-8.

[2] S.M. Zhou, X.H. Zhang, X.M. Meng, K. Zou, X. Fan, S.K. Wu, S.T. Lee, The fabrication and optical properties of highly crystalline ultra-long Cu-doped ZnO nanowires, Nanotechnology 9(15) (2004) 1152- 1155.

[3] T. Tani, L. Madler, S.E. Pratsinis, Synthesis of zinc oxide/silica composite nanoparticles by flame spray pyrolysis. J. Mater. Sci. 21(37) (2002) 4627-4632.

[4] P.M. Sabura Begum, K.K. Mohammed Yusuff, R. Joseph, Preparation and use of nano zinc oxide in neoprene rubber, Int. J. Polymer. Mater. 57(12) (2008) 1083-1094.

[5] L.C. Ann, S. Mahmud, S.K.M. Bakhori, A. Sirelkhatim, D. Mohamad, H. Hasan, A. Seeni, R.A. Rahman. Antibacterial responses of zinc oxide structures against *Staphylococcus aureus*, *Pseudomonas aeruginosa* and *Streptococcus pyogenes*, Ceramics Int. 40 (2014) 2993-3001.

Applied Mechanics and Materials Vol. 597 (2014) pp 49-52
© (2014) Trans Tech Publications, Switzerland
doi:10.4028/www.scientific.net/AMM.597.49

Preparation of amorphous silicon carbide nanostructures via solvothermal method

Huan-xiang Li[1,2] , Gong-yi Li[1*] Tian-jiao Hu[1], Xiao-dong Li[1], Yun-quan Yang[2]

[1] College of Science, National University of Defense Technology, Changsha 410073, China.

[2] School of Chemical Engineering, Xiangtan University, Xiangtan, 411105, China.

[*]nudtlgy@gmail.com

Keywords: Silicon carbide, solvothermal method, nanostructures, polymethylsilane (PMS).

Abstract: A solvothermal method was developed to synthesize silicon carbide nanoflakes and nanowires through pyrolysis of polymethylsilane (PMS) at 550 °C in solution. Evidences from HRTEM, SAED, FTIR and XPS indicated that the products were amorphous nanostructures which mainly consisted of Si, C elements and trace amount O element. Owing to concrete quantum confinement effects, the unique nanostructures have strong photoluminescence centered at 410-430 nm under excitation wavelength of 350 nm.

Introduction

With outstanding physical and mechanical properties, such as high mechanical strength, high hardness, low density, high thermal conductivity, low thermal expansion coefficient, large band gap, and excellent oxidation and corrosion resistances, silicon carbide (SiC) has long been considered as the best candidate applied in harsh environment (high temperature, oxidation condition). Due to the small dimensional effect, some properties of SiC nanostructures are largely improved compared with bulk SiC material [1]. Recently, 2H-SiC nanoflakes have been synthesized through low-temperature solvothermal route by Qian's group [2]. And 6H-SiC nanowires [3] and cone-shaped 6H-SiC nanorods [4] can be prepared by microwave method and arc-discharge process. Based on the chemical vapor deposition (CVD) route, Li [5] successfully fabricated centimeters-long 3C-SiC nanowires at 1300 °C. Although many papers have studied on the preparation of SiC crystal nanostructures, there are still no significant breakthrough on the synthesis of amorphous SiC nanostructures. Therefore, the development of reliable and efficient route to prepare amorphous SiC nanostructure will be meaningful on some level. In this paper, we report a solvothermal route to synthesize amorphous SiC nanoflakes and nanowires at relative lower temperature (550 °C) for the first time.

Experiment detail

In a typical process, 59 g toluene (analytical grade), 2 g polymethylsilane (PMS) (gift from National University of Defense Technology), 0.1 g ferrocene and (analytical grade) and 0.2 g polyvinylpyrrolidine (PVP, analytical grade) were loaded into a stainless steel autoclave with a capacity of about 170 ml. The autoclave was sealed and maintained 1.5 h at 550 °C, 8Mpa, then cooled to room temperature naturally. The raw products was firstly filtrated to discard toluene, and then was dried in desiccator at 70 °C for 5 h to remove remnant toluene, a yellow-black sample was finally obtained.

The microstructure and morphology were examined by a high-resolution transmission electron microscope (HRTEM, TECNAI-F20) and scanning electron microscopy (SEM, S-4800). The FTIR spectra were measured with a TENSOR 27 IR spectrophotometer. The chemical bonding state of Si and C in the nanowires was characterized with X-ray photoelectron spectroscopy (XPS, K-Alpha 1063). The steady-state photoluminescence spectra were measured on a JYTAU-3 spectrofluorometer. All measurements were performed at room temperature.

Results and Discussion

Fig. 1 shows the typical SEM images of the as-synthesized SiC nanostructures. The SEM images, as shown in Fig. 1a-b, reveal the general morphology of nanostructures. It can be clearly seen that both nanoflakes and nanowires are randomly aligned, and product were mainly nanoflakes. As shown in Fig. 1c, the nanoflakes surface was very clean and the thickness was about several tens of nanometers. Fig. 1d shows the nanowires with smooth surface was twist and randomly oriented. The length of the nanowires was up to several tens of microns. The nanowires have nearly uniform diameters within the range between 100 and 200 nm. The obtained nanowires were much different with the SiC nanowires synthesized by other group [6, 7].

The morphology of the as-obtained nanostructures was further observed by TEM, SAED and HRTEM. Fig. 1e shows a typical TEM image of the SiC nanoflakes, the almost half transparent state of the nanoflakes indicate their thickness is very small. The lattice fringes cannot be seen in HRTEM of nanoflakes (Fig.1f) that suggests the nanoflakes is amorphous. And the SAED pattern of the nanoflakes (Fig.1g) agrees with the above result. The Fig. 1h is TEM image of the SiC nanowires, which is very similar to the shape of nanostructures in Fig. 1d. Moreover, results from SAED patterns (Fig. 1g and 1j) of nanowires and nanoflakes also indicate their amorphous nature because no signals can be detected by SAED (Fig. 1g and 1j).

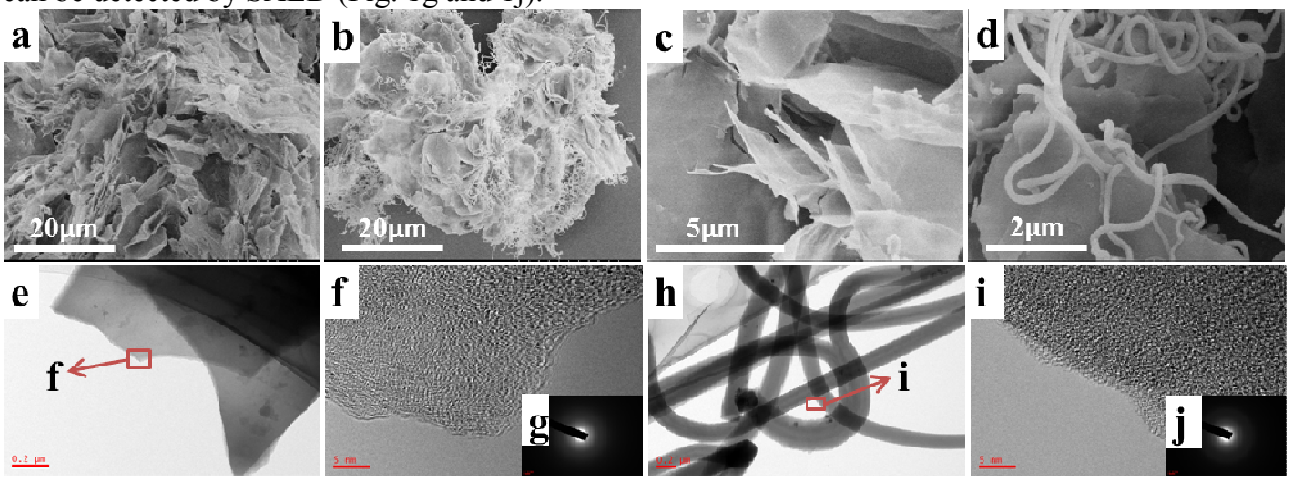


Fig 1. SEM images (a, b, c and d) of obtained SiC nanoflakes and nanowires, HRTEM images (e and f) and SAED pattern (g) of obtained SiC nanoflakes. HRTEM images (h and i) and SAED pattern (j) of obtained SiC nanowires.

The FTIR spectrum of the as-synthesized sample was shown in Fig. 2. The absorption peak at 803 cm^{-1} is associated with the transverse optical (TO) photon vibration mode of the Si–C bond [2], which reveals that SiC exists in the products. The absorbance peaks between 1000 cm^{-1} and 1100 cm^{-1} may be assigned to the Si-O-Si stretching modes, which are common in SiC materials [8]. The oxygen element might have come from the raw materials or the residue air in the autoclave. The absorbance peaks at around 2860-2960 cm^{-1} and 1385-1460 cm^{-1} are attributed to C-H bond vibration, and the peak at 1272 cm^{-1} is associated with Si–CH_3 vibration. These absorbance peaks indicate that the PMS do not fully pyrolyzed and thus the obtained product is amorphous.

The XPS spectrum of the as-prepared SiC nanostructures is shown in Fig. 3a, which indicates that the product is consisted of Si, C and O element. The broad and asymmetrical Si2p peak (Fig. 3b) indicates that the chemical state of the Si element do not contain Si^0. It can be divided to three peaks at 100.6 eV, 102.3 eV and 103.3 eV by peak fitting calculation. We assigned the Si2p peak at 100.6 eV to Si–C covalent bonds, the peak at 102.3 eV to Si–CH_3 covalent bonds which was observed in Fig. 2 and the peak at 103.2 eV to Si–O covalent bonds, respectively [9]. High-resolution spectrum of the C1s indicated that it also has a broad and asymmetrical peak (Fig. 3(b)). After peak fitting, we found that the C1s peak was superimposed by two peaks, which were located at 283.2 eV and 284.2 eV, respectively. They should correspond to the C1s peaks in SiC and hydrocarbon. All of results were coincident with the data from FTIR (Fig. 2).

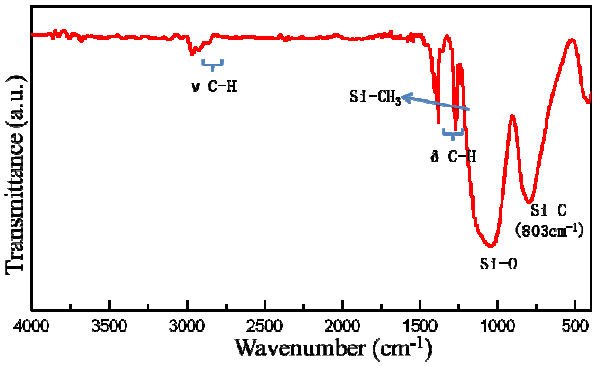


Fig 2. FTIR spectra of obtained SiC nanostructure. The absorbance peaks at around 2860-2960 cm^{-1} and 1385-1460 cm^{-1} are attributed to C-H stretching vibration and C-H scissoring vibration; the peak at 1272 cm^{-1} is owed to Si–CH_3 vibration; the peak at 803 cm^{-1} is Si–C stretching vibration; the absorbance peaks between 1000 cm^{-1} and 1100 cm^{-1} may be assigned to the feature Si-O-Si stretching vibration.

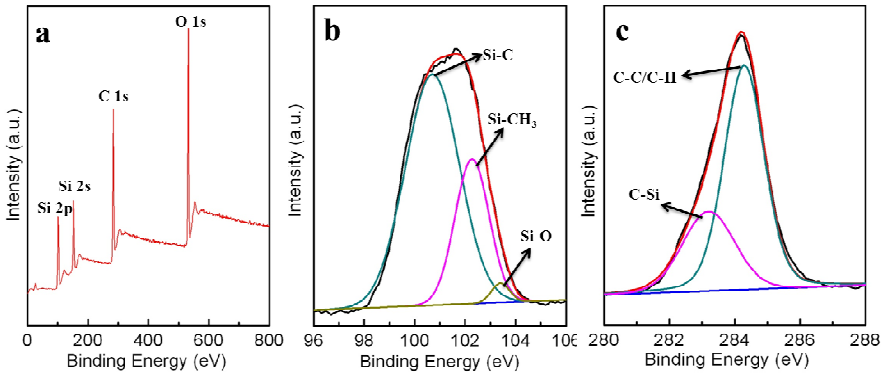


Fig .3 XPS spectrum (a) high-resolution spectrum of the Si 2p region (b) and high-resolution spectrum of the C 1s region(c) of SiC nanostructures.

The room-temperature photoluminescence (PL) spectrum of the obtained SiC nanostructure are shown in Fig 4. The three PL peaks with strong intensity are clearly observed at 410 nm, 430 nm and 475 nm, respectively, which should be induced by quantum confinement effects since the emission peaks of bulk SiC are usually at longer wavelength. It was different with previously reported PL spectra of SiC nanostructure [10]. Recently, various emission bands of SiC nanostructures have been reported [7, 11], indicating that the luminescence characteristics strongly depend on the microstructure of SiC nanomaterials. Therefore, the unique optical performances might be attributed to the as-prepared sample of amorphous nanoflakes and nanowires, since amorphous nanostructures might have more defects than crystals. However, the emission mechanism is still not clear, further study is needed to clarify the phenomenon.

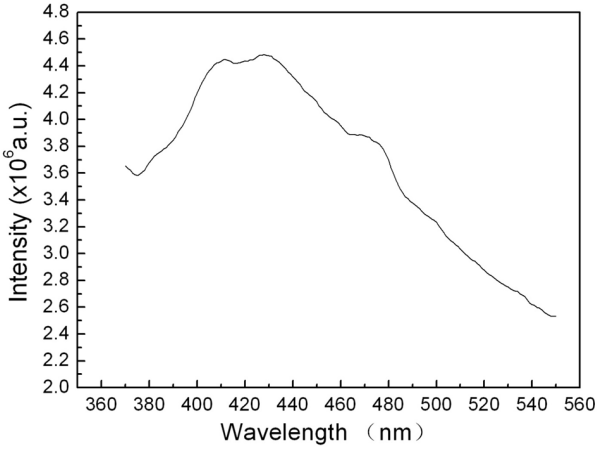


Fig 4. Photoluminescence spectrum of the amorphous SiC nanostructures

Summary

In summary, the SiC nanoflakes with thickness of several tens of nanometers and nanowires with diameters of 100~200 nm have been prepared by pyrolysis of polymethylsilane in toluene at 550°C. The HRTEM and SAED analysis of the as-synthesized sample indicate that the nature of SiC nanostructures is amorphous. The unique nanostructures have strong photoluminescence centered at 410-430 nm under excitation wavelength of 350 nm due to concrete quantum confinement effects.

Acknowledgements

The authors are thankful for the help from Mr. Yong Yang, as well as the financial support from the National Natural Science Foundation of China (Granted No.51102281) and Research Project of National University of Defense Technology (Granted No.JC13-02-11).

References

[1] Xia Y, Yang P, Sun Y, One-dimensional nanostructures: Synthesis, characterization, and applications, Adv.Mater. 15(5) (2003) 353-389.

[2] Zou G, Dong C, Xiong K, Low-temperature solvothermal route to 2H-SiC nanoflakes, Appl. Phys. Lett. 88 (2006) 71913.

[3] Wei G, Qin W, Wang G, The synthesis and ultraviolet photoluminescence of 6H-SiC nanowires by microwave method, J. Phys. D: Appl. Phys. 41 (2008) 235102.

[4] Li Y, Xie S, Zhou W, Cone-shaped hexagonal 6H-SiC nanorods, Chem Phys Lett. 356 (2002) 325-330.

[5] Li G, Li X, Chen Z, Large Areas of Centimeters-Long SiC Nanowires Synthesized by Pyrolysis of a Polymer Precursor by a CVD Route, J. Phys. Chem. C. 113 (2009) 17655-17660.

[6] Zhou W, Yan L, Wang Y, SiC nanowires:A photocatalytic nanomaterial, Appl. Phys. Lett.89 (2006) 13105.

[7] Zhang E, Tang Y, Zhang Y, Synthesis and photoluminescence property of silicon carbon nanowires synthesized by the thermal evaporation method, Physica E. 41 (2009) 655-659.

[8] Fan J, Li H, Jiang J, 3C-SiC Nanocrystals as Fluorescent Biological Labels, Small. 4(8) (2008) 1058-1062.

[9] Henderson E J, Veinot J G C, From Phenylsiloxane Polymer Composition to Size-Controlled Silicon Carbide Nanocrystals, J. Am. Chem. Soc. 131 (2009) 809-815.

[10] Ju Z, Xing Z, Guo C, Sulfur-assisted approach for the low-temperature synthesis of β-SiC nanowires, Eur. J. Inorg. Chem. (2008) 3883-3888.

[11] Ting Li L X, Liancheng Wang, Lishan Yang, Synthesis and characterization of 3C and 2H-SiC nanocrystals starting from SiO2,C2H5OH and metallic Mg, J. Alloy. Compd, 484 (2009) 341-346.

Applied Mechanics and Materials Vol. 597 (2014) pp 53-56
© (2014) Trans Tech Publications, Switzerland
doi:10.4028/www.scientific.net/AMM.597.53

Doped TiO_2 nanotube for lithium ion battery

Xiaoxiao Hu[1,a], Jianxiong Liu[1,b*], Zhengyu Wu[2,b], Xinrui Zheng[1,c], Miao Ma[1,d],

[1]Faculty of Materials Science and Engineering, [2]Faculty of science

Kunming University of Science and Technology, Kunming 650093, China

[a]hbyshxx@163.com, [b]ljx5192665@163.com, [b]WUZY501@163.com, [c]zxr6684119@126.com, [d]mamiaokunming@163.com

Keywords: TiO_2 nanotube, lithium ion battery, dope

Abstract. Doped TiO_2 nanotubes for lithium ion batteries have attracted extensive attentions over the recent years, owing to their better electrochemical performances than bare TiO_2 nanotubes. The forms of doping are various, depending on different dopants and preparation methods. In this paper, the preparation methods of doped TiO_2 nanotubes, the forms of doping and the impacts on electrochemical performances for LIBs are reviewed. Meanwhile, the mechanism of doping is described briefly. The new directions of research on this field are proposed.

Introduction

On account of the excessive consumption of non-renewable resources and the irresistible trend of shifting to the renewable energy resources, rechargeable Li-ion batteries (LIBs) have provided the possibility because of their high specific energy and power storage capacity [1]. Recently, studies exploring new electrode materials for LIBs have focused on reducing the size of materials to nanoscale. And when nanomaterials are used as electrode materials, LIBs exhibit low polarization under high current charge/discharge, short diffusion depth of Li^+, high reversible performance and good cycling stability, due to their large surface-to-volume ratios and interfaces between the electrode and electrolyte [2].

TiO_2 nanotubes (TNTs) are considered as a promising solid-electrolyte interface (SEI)-free material for LIBs when they are compared with traditional carbon-based electrodes. Without the formation of this SEI layer, LIBs can show better kinetic properties and structure stability during lithiation/delithiation [3]. However, TiO_2 is a kind of semiconductor materials and it has a wide band gap (Anatase: 3.2eV, Rutile: 3.0eV), resulting in poor electrical conductivity. And this shortage leads to the capacity of TiO_2 greatly reducing from its theoretical capacity (335mAh/g) to the actual electrochemical capacity (168mAh/g), which limits the performance of TiO_2 nanotubes for LIBs.

According to the band theory, reducing the width of band gap by introducing in new conduction band between the conduction band and valence band can significantly improve the conductivity of semiconductor. And based on this theory, the electrochemical performance of TiO_2 nanotubes can be improved via doping, which has attracted considerable attention in recent decades. In this paper, metal doping, nonmetal doping and oxide doping TiO_2 nanotubes for modifying the electrochemical property of LIBs are reviewed in detail.

1 metal doped TiO_2 nanotubes for LIBs

It is said that conductive metals are added frequently to LIBs to construct conductive network. And this network is essential to compensate for the low electronic conductivity as well as increase the battery power and fast charge/discharge performance [4,5].

Several groups have reported their studies on Ag doped TNTs for LIBs because of its excellent electrical conductivity. He et al. [4] firstly prepared TNTs using a sol-gel method and then obtained Ag nanoparticles coated TNTs by traditional silver mirror reaction. They demonstrated that the capacity degradation of TNTs was 16.57% at 600mA/g after 40 cycles while it decreased to 6.99% for Ag-TNTs composties. It was obvious that Ag nanoparticles, which disperses on the surface of

TNTs, were responsible for the improvements of reversible capacity and cycling stability at high current density. Besides, the cell polarization also decreased marvelously as a result of the addition of Ag. Fang et al. [5] prepared the doped TNTs via thermal decomposition on the basis of self-organized TiO_2 nanotube arrays by anodizing. They illustrated the conductive Ag at the surface of TNTs was beneficial for the diffusion of lithium ion, leading to the increasing of the reversible capacity and cycling stability. Moreover, the charge/discharge capacity and charge transfer resistance have been improved at the same time. Guan et al. [6] have studied the lithium-ion intercalation performance of Ag nanoparticles onto bamboo-type TiO_2 nanotube arrays, prepared via anodic oxidation and pulsed electrochemical deposition. Compared with bare TNTs, they achieved some improvements on areal Li-ion intercalation capacities as well as cycleability. Furthermore, higher discharge capacity, better high-rate cycling durability and superior electrochemical kinetics for silver coated TiO_2 nanoribbons/nanotubes were confirmed by Rahman et al. [7].These TNTs were synthesised by the reflux method, and Ag particles were deposited on the surface of the TNTs using the silver mirror reaction. The electrochemical investigations showed that the Ag/TNTs electrode presented a discharge capacity of 132.73 mAh/g at 60 mA/g and 102.39 mAh/g at 120 mA/g even after 50 cycles. However, the discharge capacity respectively were 121.05 and 83.66 mAh /g under the same condition. And it can be found the coulombic efficiency of Ag/TNTs were 99.55% at 60 mA/g and 99.11% at 120 mA/g, which were higher than TNTs' 99.24% at 60 mA/g and 99.00% at 120 mA/g.

Kyerematen et al. [8,9] have reported that Sn-doped TiO_2 nanotube arrays exhibited improved discharge capacity while the irreversible capacity was too large in comparison with TNTs. They fabricated the Sn-doped TNTs by anodization of co-sputtered Ti and Si thin films for the first time. And according to their research, Sn was in the form of substitution for Titanium which had no influences on the morphology of the tubes.

2 nonmetal doped TiO_2 nanotubes for LIBs

Recently, graphene/TNTs composites for LIBs have aroused great interest, due to the superior electrical conductivity, high surface-to-volume ratio, ultrathin thickness, structural flexibility and chemical stability of graphene. Wang et al. [10] have successfully synthesized uniform TiO_2 nanotubes directly grown on curved graphene sheets by a one-step hydrothermal method, forming a cross-linked and interpenetrated nanotube/nanosheet structure. And this unique structure provided facile transports of Li^+ and electrons, thus improving the specific capacity and rate capability.

Xu et al. [11] have synthesized carbon-doped TNTs through a sol-gel and subsequent hydrothermal process. Their research showed that the initial discharge/charge capacity reached 291.7 mAh/g and 267.4 mAh/g, and even after 30 cycles, the reversible capacity still remained 211 mAh/g with a coulombic efficiency larger than 99.7%, revealing an excellent reversibility and cycling stability. They considered that the band gap of TiO_2 narrowed for the reason of C doping. The 2p pathways of O and C overlapped, leading to the redshift of the absorption bands. Kang et al. [12] have presented a hydrothermal reaction of rutile particles combined with a sol-gel method using poly(vinyl pyrrolidone) and following heat treatment at 300, 400 and 500°C to fabricate carbon-coated TNTs. And they proved that this composite annealed at a high temperature (400 and 500°C) allowing better cycle performance and high-rate capacity than coated and uncoated TNTs annealed at a low temperature (300°C). However, the initial discharge capacity of all the coated materials suffered some loss in contrast to the uncoated TNTs. Park et al. [13,14] have prepared carbon-coated TNTs by hydrothermal method with an addition of glucose in the starting powders. And in terms of their opinion, the coated carbon on the nanotube, which acts as a dispersant, have effectively suppressed the agglomeration of TNTs, allowing easy access of Li-ions and electrons to the whole surface of nanotubes, and thus leading to the better lithiation performance.

3 oxide doped TiO_2 nanotubes for LIBs

For designing the composites, SnO_2 can be a good choice because of its theoretical capacity of 781 mAh/g. The SnO_2 can promote the capacity of bare TNTs greatly, while the TNTs can accommodate the volume changes of SnO_2 during Li^+ charge/discharge processes. And there is no doubt, this synergistic effect can create excellent electrochemical performances for LIBs. Du et al. [15] have reported SnO_2 nanocrystals on self-organized TiO_2 nanotube arrays via a facile solvothermal method. It was found that the capacity can be controlled by varying the TiO_2 length as well as SnO_2 loading. And the areal capacity of SnO_2/TNTs sample proved to be more than twice that of the TNTs at multiple current density of 10 $\mu A/cm^2$, 20 $\mu A/cm^2$, 40 $\mu A/cm^2$, 80 $\mu A/cm^2$, 100 $\mu A/cm^2$ and 150 $\mu A/cm^2$.

Transition metal oxides, such as Fe_3O_4, Nb_2O_5, Ta_2O_5, ZnO, Cr_2O_3, MnO, NiO, Co_3O_4 and Cu_2O, have been regarded as promising anode materials for LIBs [16]. According to this, a small number of Co_3O_4 and NiO particles have been doped into TiO_2 nanotube arrays by Kyerematen et al. [17]. These doped TNTs were prepared via anodization, electrodeposition and thermal treatments. On the same deposition conditions, Co particles turned out to be sparse with large size, while Ni exhibited a higher density of small particles, due to their discrepant nucleation and growth mechanisms. And after annealing at 500°C, submicron Co_3O_4 and NiO particles on the surface of TNTs were acquired. In both cases, the addition of transition metal oxides into the TNTs increased the capacity values by a factor of ~4. An et al. [18] have made some efforts on NiO/TNTs composites, too. However, one of the most basic differences is that the TNTs they prepared were a mixing of TiO_2(B) and anatase phases. It was demonstrated that nanotubes of anatase and TiO_2(B) had different advantages with respect to electrochemical lithium storage. The lithium ion diffusion is mainly related to the anatase phase, while the electrochemical reaction activity is attributed to the TiO_2(B) phase. Besides, Rajaa et al. [19] have demonstrated that ordered arrays of vertically oriented Ti-Mn oxide nanotubes,which were synthesized by a simple electrochemical anodization technique on a Ti-Mn alloy foil, revealed improved electrochemical properties. For example, the nominal capacity was about 474 mAh/g and remained constant even after 30 cycles at 1 C discharge rate. In addition, TiO_2 nanotube arrays which were decorated by Fe_2O_3 hollow nanorods have fabricated successfully by Yu et al. [20]. The novel heterostructure was prepared by growing FeOOH nanospindles onto the well-aligned TiO_2 nanotube arrays and subsequent thermal conversion to Fe_2O_3 hollow nanorods. This combination of active metal oxide and TNTs delivered almost twice the discharge capacity that of TNTs at a current density of 100 $\mu A/cm^2$.

$Li_4Ti_5O_{12}$ (LTO), which has been studied intensively for use as an anode material in lithium secondary batteries, have some advantages of lower volume change during charge/discharge to provide superior cycle performance, chemical and electrochemical stability and excellent thermal characteristics to improve battery safety. To make full use of TNT's higher capacity and LTO's excellent plateau property, various compositions have been prepared by Kim.et al. [21]. And as a result, the samples of TNT: LTO= 2: 8 and 4: 6 showed superior cycle performance and high-rate capability, due to their higher electrode densities and small interfacial resistance.

Conclusions

In order to meet the requirements of improving the performances of LIBs and expanding their applications to more fields,such as Hybrid Electrical Vehicle (HEV), plug-in hybrid electric vehicle (PHEV),and Smart grid [22], doped TNTs have been studied for many years. However, the doping elements and methods are limited. It is generally known that wider researches have been carried out on doped TNTs for photocatalysis. And probably, their doping methods may help with the fabrication of doped TNTs with more promising elements. More recently, the researches on a new type of core- shell-structured materials called coaxial nanotubes and preparing TNTs composites by anodization of Ti alloys may provide more references for doped TNTs.

Acknowledgements

We gratefully acknowledge financial support from the National Natural Science Foundation of China (NSFC51062009,NSFC51164020).

References

[1] B.G. Lee, S.C. Nam, J. Choi: Current Applied Physics 12 (2012) 1580-1585

[2] B. Cao, J.W. Xu, L.H. Ding, W.F. Zhang: ELECTROCHEM ISTRY Vol. 12No. 4 Nov. 2006

[3] W.H. Ryu, D.H. Nam, Y.S. Ko, R.H. Kim, H.S. Kwon: Electrochimica. Acta. 61. (2012) 19–24

[4] B.L. He, B. Dong, H.L. Li: Electrochemistry Communications 9 (2007) 425–430

[5] D.Fang, K.L. Huang, Sh.Q. Liu, Zh.J. Li: Journal of Alloys and Compounds 464 (2008) L5–L9

[6] D.Sh. Guan, Y. Wang: Ionics (2013) 19:879–885

[7] M.M. Rahman, J.Zh. Wang, D. Wexler, Y.Y. Zhang, X.J. Li, Sh.L. Chou, H.K. Liu: J Solid State Electrochem. (2010) 14:571–578

[8] N.A. Kyerematen, V. Hornebecq, P. Knauthb, T. Djeniziana: Electrochimica. Acta. 62 (2012) 192–198

[9] N.A. Kyerematen, F. Vacandio, M.T. Sougrati, H. Martinez, J.C. Jumas, P. Knauth, T. Djenizian: Journal of Power Sources 224 (2013) 269e277

[10] J. Wanga, Y. Zhou, B. Xiong, Y.Y. Zhao, X.J. Huang, Z.P. Shao: Electrochimica. Acta. 88 (2013) 847–857

[11] J.W. Xu, Y.F. Wang, Z.H. Li, W.F. Zhang: Journal of Power Sources 175 (2008) 903–908

[12] K.Y. Kang, Y.G. Lee, S. Kim, S.R. Seo, J.C. Kim, K.M. Kim: Materials Chemistry and Physics 137 (2012) 169e176

[13] S.J. Parka, H. Kimb, Y.J. Kimc, H. Leea: Electrochimica. Acta. 56 (2011) 5355–5362

[14] S.J. Parka, Y.J. Kimb, H. Leea: Journal of Power Sources 196 (2011) 5133–5137

[15] G.D. Du, Z.P. Guo, P. Zhang, Y. Li, M.B. Chen, D. Wexlerb, H. Liua: J. Mater. Chem., 2010, 20, 5689–5694 | 5689

[16] W.J. Li, Zh.W. Fu: Applied Surface Science 256(2010)2447-2452

[17] N. A. Kyerematen, Ch. Lebouin, P. Knauth, T. Djenizian: Electrochimica. Acta. 88 (2013) 814–820

[18] L.P. An, X.P. Gao, G.R. Li, T.Y. Yan, H.Y. Zhu, P.W. Shen: Electrochimica. Acta. 53 (2008) 4573–4579

[19] K.S. Rajaa, M. Misrab: ECS Trans. 2011 volume 33, issue 29, 31-44

[20] L.Yu, Zh.Y. Wang, L. Zhang, H.B. Wu, X. Wen, D. Lou: J. Mater. Chem. A., 2013,1, 122-127

[21] K.M. Kim , K.Y. Kang, S. Kim, Y.G. Lee: Current Applied Physics 12 (2012) 1199e1206H. Han

[22] H. Han, T. Song, E.K. Lee, A. Devadoss, Y. Jeon, J. Ha,Y.C. Chung, Y.M. Choi,Y.G. Jung, U. Paik: ACS Nano, 2012, 6 (9), pp 8308–8315

CHAPTER 2:

Advanced Material, Composite Materials and its Applications and Technologies

Applied Mechanics and Materials Vol. 597 (2014) pp 59-62
© (2014) Trans Tech Publications, Switzerland
doi:10.4028/www.scientific.net/AMM.597.59

Information systems for composite materials: requirements and challenges

Wilhelm Dangelmaier[1,a] , Thomas Sommer-Dittrich[2,b], Jenny Streichhan[1,c*], Markus Monhof[1,d]

[1]Heinz Nixdorf Institute, Fuerstenallee 11, 33102 Paderborn, Germany

[2]Daimler AG, 70546 Stuttgart, Germany

[a]whd@hni.uni-paderborn.de

[b]thomas.sommer-dittrich@daimler.com

[c]jenny.streichhan@hni.uni-paderborn.de

[d]monhof@live.uni-paderborn.de

Keywords: fiber-reinforced composite, material data management, information system, database, lightweight construction, composite material, material database, project management, data model, data storage

Abstract. Using fiber-reinforced composites (FRC) in automotive lightweight construction currently is too expensive to achieve a wide distribution. To assist the engineers' material selection process suitable information systems are needed. Development of those are a hard task due to the complex structure of FRC. In this paper we give an insight to the problem domain and introduce requirements which should be met by an information system for composite data storage.

Introduction

The selection of adequate materials is a crucial point in automotive lightweight construction. Especially for the FRC this is a difficult task, due to diversified parameters which are used to describe the material. The selection is typically based on specific values of the material, e.g. tensile strength or stiffness. Those specific values are determined by material tests. Since the required samples and the exploration of the materials are rather expensive there is a need for a good test result management. This avoids duplicate tests of the same material and allows reuse of former results, inside an organization.

In the following we will provide a description of the problem domain material tests to develop an information system for material test data. We will focus on fiber-reinforced composites esp. continuous strand-reinforced since there are fewer than there are for other material classes like metals. We will describe the requirements for a composite material information system. Afterwards we have a look at existing approaches to see which requirements they met.

Problem domain

Foreign Influences. Rising environmental concerns and law restrictions lead to a demand on lighter automobiles to reduce fuel consumption and pollutant emission. One way to save mass is to replace currently used materials with lighter ones. Besides aluminum, fiber reinforced composites "provide a wide range of potential […] applications" [1]. The direct impact of the mass reduction is not the only part where fuel is saved. Since the reduction changes the handling characteristics "adjustments of the gear ratio or engine displacement" [2] are possible without lowering the driving performance [3]. Those are called *secondary effects* [2].

Currently FRC are not that common in automotive lightweight construction. There are several problems which inhibit them from broader distribution. The main reason for not using FRCs are the higher costs compared to traditional materials [1]. For automotive construction the limit of

additional costs per saved kilogram lays around five euros [4]. In 2001 [1] stated, that the costs for carbon fibers “have to drop by 50% […] to be economically viable”. So presently FRC are mainly used for nonstructural parts like “hoods and decklids” [5].

Internal Influences. In order to select adequate materials and to start component simulation the engineers need comprehensive information about the material. Mostly those facts are not available and have to be determined by material tests. Since those tests are rather expensive a good data management can help to reduce costs by speeding up the selection process by providing clear representations and search capabilities and by giving an overview of the available materials and their capabilities to prohibit duplicate tests of the same material.

Since the descriptions of composite materials are complex, there are special requirements on the database, in which the actual data are stored, and information systems, which are used to access and visualize the data in a proper way.

Information System requirements

The overall goal of the information system is to provide the exact data the user needs. In this paper we will mainly focus on the material selection process by engineers. So information about the material composition and the corresponding characteristics are needed. Since the properties of FRCs depends on “environmental properties, and process history” [6] those data have to be provided, too.

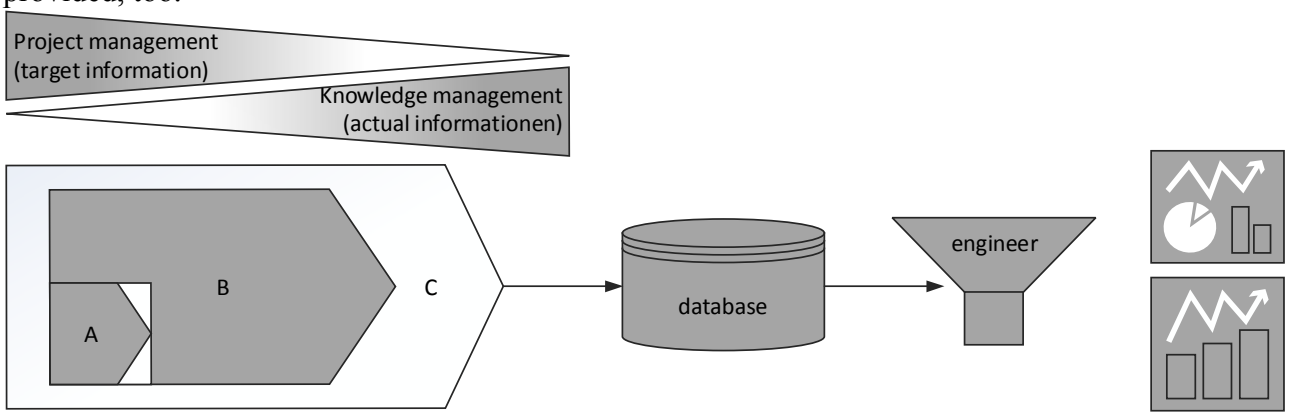


Fig. 1: Requirements on information systems for composite materials.

Fig. 1 shows different requirements on information systems for composite materials. The first of those - on the right side of the figure - was already mentioned: the needed data must be accessible in the needed way. The user (i.e. the engineer) must have the possibility to filter the materials and display the corresponding data in a clear fashion. This is not different from other information systems. The exception covers the needed data for FRCs. On the left side the needed information are summarized with C, but it splits up in process information (B) and material information (A)

Overall Data (C). The big arrow labeled with C are all the data which occur over time. These data are stored inside a database to provide a single data source for the users. There are four different kinds of data which should be stored*: material data, process data, machine data* and *processed data*. The machine data are simply the raw results which are created during a test. The processed data are calculated or statistical values for one or more tests of the same material with the same test parameters. So machine and processed data describe the test results. Material and process data have to be looked at more in detail since they are providing two other requirements on the information system. These are needed to provide a clear description of the material including all process steps needed to build the object which is tested and to assure traceability.

Material Data (A). The material definition - and therefore the material data - consists of two types of data. First structural data which is the chemical composition and second the physical format (like geometry) of the concrete construction elements. Since specific values for composite materials are depending on the shape of the tested element, both of these data are required to describe the material. So the structural data give information about the material itself and the

physical format about a concrete occurrence of the material (i.e. material which is used in a process).

Process Data (B). The process mapping describes what steps should be and are actually done with a construction element. For example a plate of a material is cut in smaller parts - called samples - which are the test objects. Both the data of the plate and samples must reference to real existing elements.

Project & Knowledge Management. This description of the process mapping lead to another aspect of the data, which is visualized in the top of the figure: the data can be categorized in the two classes 'project management' and 'knowledge management'. Where the first term is used for target data which describe what should be done and the second for the actual data. Typically the amount of 'project management' will decrease in time while the 'knowledge management' data will increase. For example at the beginning the material data is needed to allow the production of a certain element. Therefore these data, which are target data since they provide the specification what to produce, has to be gathered. When the produced elements and samples actually exist, the amount of new target data is reducing while the actual data is rising. The same is true for data about the tests. At first the specification of the test parameters and conditions is needed and after the tests started the machine data are stored.

As mentioned before traceability should be achieved by the information system. For example for a calculated specific value (which would be processed data). It must be possible to get the corresponding raw results from which they are calculated, as well as the tested element with information about the components the composite is made of and about the process in which it was produced. This goal can be achieved by additionally storing references between the data records. Therefore it's possible to exactly reproduce where certain data comes from.

The separation of the process data from the corresponding objects provide the benefit that additional information can be stored for each process. Therefore for example management data like shipping or billing information can be included. This allows building an integrated information system which makes sense since at least some of the data are needed in business processes apart from the mere tests. For example for ordering material samples the exact specification of the material and samples are needed.

Another requirement is that the origin of the data has to be clear, because data from different sources are stored inside one database. Firstly there might be reference data from the manufacturer, which is rare for composites, but occasionally occur for components (e.g. fibers or adhesive), or other publically available sources. Secondly - which typically will be the bigger part - there is the data which is gathered in material tests inside the company. The reliability of these sources is often not known and may vary for different materials due to qualification of the tester or institute. Because of the different sources the data exists in different formats and have to be imported into the central database to provide a single source of information. Since the data will have different unit of measurements the database must be capable of handling those or offer some sort of normalization step in the import process.

Existing databases and information systems for composite materials

Over the last 20 years there have been a few different approaches to provide reliable sources for composite material information. But, with Granta MI, there is only one commercially successful software meeting most requirements mentioned above. In the remainder we will focus on the description of Granta MI that is given in [6], which is based on the so called "AGATE" data-set. A big difference between Granta MI and the described requirements model is that no management data are stored. Therefore these have to be handled in another system which then has to reference to Granta MI for the specification data. Depending on the software which is used that might not be possible and lead to more work for the user. Since part of the management data (for example the production date of an element) is later also stored in Granta MI this might lead to duplicate data in different databases. Besides Granta MI there are other approaches meeting some of the introduced requirements. In the following we will address some of them.

The aforementioned “AGATE” was a project initiated in 1995 by NASA [7] to develop “a composite material property shared database process” [7]. As a result an online available collection [8] of documents containing material properties is available. In 2005 NASA started the National Center for Advanced Materials Performance (NCAMP) to refine and enhance the AGATE processes [7]. Despite there are no information systems, AGATE and NCAMP provide templates for material and process specification documents for structural descriptions. This is related to the data storage of the requirements given in this paper. Another approach is “MatWeb”[9], an online database containing material properties, in which most materials are not FRCs. Since the database does not contain material or process specifications the material properties are referenced by name. MatWeb provides searching capabilities to find materials with certain properties. Also the comparison of two materials is possible. So MatWeb only meets some of the introduced requirements. The “SNL/MSU/DUE composite material fatigue database” [10] is a public available spreadsheet from the Montana State University. It contains parts of the material, process and machine data as introduced before. Whether the material data are rather in detail -but only on the level of the composite; the matrix and fibers are only referenced by name – the process data are reduced to a process type name and conditioning. The test results are given for each test for which an identifier and a code of the used sample are supplied. Since the database is a spreadsheet document the search and filter capabilities of the software in which it is opened can be used, but there are also disadvantages like heavily redundant data.

Conclusion and outlook

In this paper we described the problem of managing composite material data and presented requirements on information systems. We briefly introduced approaches of material databases and information systems which address some of the stated requirements. For the future we plan to publish our results from implementing an information System which meets the requirements introduced in this paper, for a german car manufacturing company.

References

[1] S. Das, The cost of automotive polymer composites: a review and assessment of DOE's lightweight materials composites research, Oak Ridge, TN: Oak Ridge National Lab., 2001, p.3-11

[2] T. Gaensicke and M. Goede, "Die Technische Motivation," in Leichtbau in der Fahrzeugtechnik, Wiesbaden, Springer Vieweg, 2013, pp. 31-42. p.3

[3] G. Ellenrieder, T. Gaensicke, M. Goede and H. G. Herrmann, "Die Leichtbaustrategien," in Leichtbau in der Fahrzeugtechnik, Wiesbaden, Springer Vieweg, 2013, pp. 43-118

[4] C. Koffler and K. Rohde-Brandenburger, "On the calculation of fuel savings through lightweight design in automotive life cycle assessments", The International Journal of Life Cycle Assessment, vol. 15, no. 1, 2010, pp. 128-135.

[5] E. Fuchs, F. Field, R. Roth and R. Kirchain, "Strategic materials selection in the automobile body: Economic opportunities for polymer composite design," Composites Science and Technology, vol. 68, no. 9, 2008. pp. 1989

[6] W. Marsden and S. Warde, Data Management for Composite Materials, Cambridge, 2010, p. 3

[7] Y. Ng and J. Tomblin, "NCAMP Standard Operating Procedures (SOP)," 2010, pp. 5-7

[8] For more Information see: http://www.niar.wichita.edu/agate/

[9] For more Information see: http://www.matweb.com

[10] For more Information see: http://www.coe.montana.edu/composites/

Applied Mechanics and Materials Vol. 597 (2014) pp 63-71
© (2014) Trans Tech Publications, Switzerland
doi:10.4028/www.scientific.net/AMM.597.63

Mechanical Properties of DGEBA/Amidoamine Blend at non-Stoichiometric Ratios

Britto Satheesh [*1], Nick Warrior [2], K.Y. Tshai [3]

Department of Mechanical, Materials & Manufacturing Engineerng, University of Nottingham

([1,3] Malaysia, [2] United Kingdom)

[*1] brittosatheesh@gmail.com, [2] nick.warrior@nottingham.ac.uk,

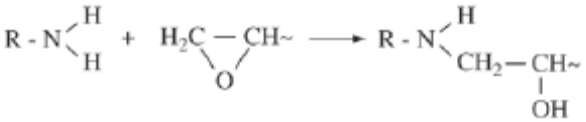
[3] kim-yeow.tshai@nottingham.edu.my

Keywords: Epoxy, hardener, homopolymerization, mechanical properties, mixing ratio.

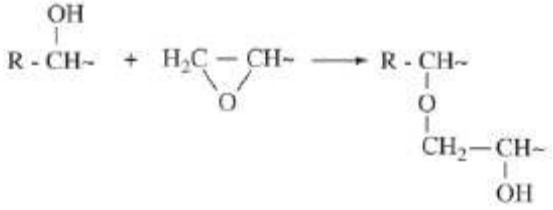
Abstract. In this paper, the effect of varying mixing ratio of Diglycidyl ether of bisphenol A (DGEBA)/aliphatic amidoamine hardener on the behavior of dynamic cure profile and mechanical properties of the resulting thermoset was investigated. Epoxy/hardener sample with a stoichiometric mixing ratio of 2:1 are tested against non-stoichiometric ratios of 3:1 and 4:1. The tensile, flexural, and hardness properties of the specimens were measured while SEM is employed to investigate the fracture surface and analyze the failure. Results showed that epoxy enriched samples (non-stoichiometric) has a much brittle behavior and the DGEBA/hardener samples tend to fail under relatively small strain.

Introduction

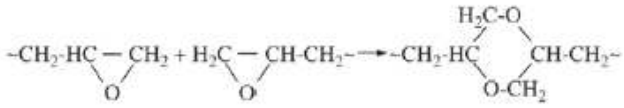
Stoichiometric composition of epoxy/hardener is often essential in determining an optimum yield of the cured thermoset. Varying degree of mixing ratios may be referred as an internal variable capable of influencing the mechanical properties through changes in the chemical and physical structure of the constituents. The epoxy-hardener system involved in this study falls into the category of epoxy-amidomine reaction where the cure reaction are initially led by the amino addition reaction, occurring between the Primary Amines (-NH) and the epoxide group. During the initial stage, one of the active hydrogen from primary amines reacts with the active sites of an epoxy group and results in the formation of Hydroxyl Group (-OH) and a secondary amine [1].



The above reaction leads to the formation of strong hydrophilic hydroxyl groups. In the case of non-stoichiometry formulations with excess of epoxy monomer, the epoxy resin has an increased probability to react with hydroxyl groups in the mixture, leading to the formation of ether groups,



This stage of reaction tends to increase viscosity and reduces molecular mobility thereby restricting movement of unreacted secondary amines. In this phase, the reaction is also temperature sensitive where linear growth and branching takes place to form a glossy, thermoplastic solid. Finally homopolymerization reactions can be catalyzed by steric hindered tertirary amines, leading to the formation of the p-dioxane ring structure [1].



Increasing epoxy parts in a sample helps in the formation of epoxides that has an oxygen atom in a three memobored ring. Therefore increasing epoxy parts in a sample can improve mechanical properties because of the higher reactive regions present in the epoxide ring. These changes affect the macromolecular structure due to excess addition of DGEBA. Industries use a certain recommended ratio to develop epoxy resins for optimal use. In this paper, the physical and mehcnical characteristics of resin are investigated when non-stoichiometric ratios are used. The problem of working with off-stoichiometric mixtures is that latent reaction sites could remain on the macromolecular structure developed and under the proper conditions the structure can evolve, resulting in changes on the mechanical performance of the material. Temperature is clearly one external parameter that could cause changes to the system. Therefore non-stoichiometric ratios and its effect on mechanical properties and physical changes in the developed epoxy/hardener system are studied.

Materials & Methodology

Materials. Curing agent used in this study is a highly reactive amidoamine hardener which contains an average of 2 amine hydrogen per molecule [2]. The CP210DF Part A resin (DGEBA) and CP210DF Part B hardener (Amidoamine) were supplied by 'Camel Polymers' Malaysia. Table 1 showed the properties of the resin and hardener used in this study.

Table 1 : Properties of the epoxy resin and amidoamine hardener.

	Epoxy	Hardener
Code	**CP210DF Part A**	**CP210DF Part B**
Viscosity[Pa.s]/ at 25^{o}C	1.5-2.1	0.15-0.30
Molar mass [g]	189-200	90
Color	Clear	Brown
Gel time [min]	180	-
Shore D Hardness	-	80-85

Methodology. The epoxy resin CP210DF Part A (DGEBA) and the aliphatic amidoamine hardener CP210DF Part B were prepared in both the stoichiometric and non-stoichiometric in accordance to the following three mixing ratios.

i. Ratio 2:1 (two part of epoxy with one part hardener, stoichiometric ratio)

ii. Ratio 3:1 (non-stoichiometric ratio)

iii. Ratio 4:1 (non-stoichiometric ratio)

In industrial applications, the stoichiometric ratio is strictly followed without much investigation. In the current study, weights of the contents are measured using OHAUS weighing scales prior to mixing and care was taken to avoid any errors that may occur due to excess content. Three specimens were prepared for each of the mixing ratio.

Specimen Preparation. Epoxy resin (CP210DF part A) and hardener (CP210DF part B) are continuously stirred within a magnetic stirrer to achieve a homogenous mixture and any induced bubble is eliminated through the use of vacuum desiccators for 30 mins. The mixture is then heated for 4 hours and maintained at a temperature 70°C until a cured final product is obtained. Fig. 1

showed the cured thermoset at stoichiometric ratio of 2:1. Non-stoichiometric mixing ratios, 3:1 and 4:1 epoxy/hardener produced similar moulded specimen. However the non-stoichiometric ratios required a significant longer cure period of 5 and 6 hours respectively for ratios 3:1 and 4:1. In appearance, the final specimen for ratio 2:1 turned out hard and smooth whereas for non-stoichiometric ratios there was uneven curing and rough surfaces.



Fig. 1. Moulded epoxy/hardener sample for stoichiometric ratio of 2:1.

Analytical Tests. Various empirical measurements were carried out to investigate the resulting variation between specimen with non-stoichiometric and stoichiometric ratios. Three samples were made for each mixing ratio. Sanning Electrong Microscopy (SEM) images were used for analysing the fracture surfaces of epoxy/hardener samples with different mixing ratios. Tensile, hardness and bending tests were performed to investigate the mechanical properties such as yield stregth, Ultimate Tensile Stress (UTS),strain at failure, the hardness of the material, the flexural properties and failure mechanism. The Vickers hardness test measures the hardness and it uses a diamond pyramid with a square base for indendation. Once test position is confirmed, indenter applies a force of 1 Kg for 10-15 s. The tensile properties were determined ondumbbell samples using a Universal Testing Machine (UTM-Shiamdz AG-I) with a load cell of 50 kN capacity. The tensile test sample for all analysis are prepared using a standard cutting die of 16.5×2.0×0.5 cm and the measurements were carried out at a cross head speed of 50 mm/min according to ASTM-D-638. Flexural test also known as bending test are performed to evaluate tensile strengths of brittle materials as such materials are difficult to test in simple uniaxial tension due to cracking in the grips [3]. The specimen samples for flexural testing have a rectangular cross section (80 mm x 10 mm x 2 mm) and is loaded under 3-point bending.

Results

Tensile Test Results. The chemical reaction in a thermosetting resin forms a three-dimensional (3D) structure with high rigidity. The structural rigidity increases with degree of cross-linking. Because of the high degree of cross-linking and the rigid 3D network structure, these materials have low flexibility and can be brittle Fig. 2 shows the tensile stress/strain response of epoxy/hardener samples with different mixing ratios.

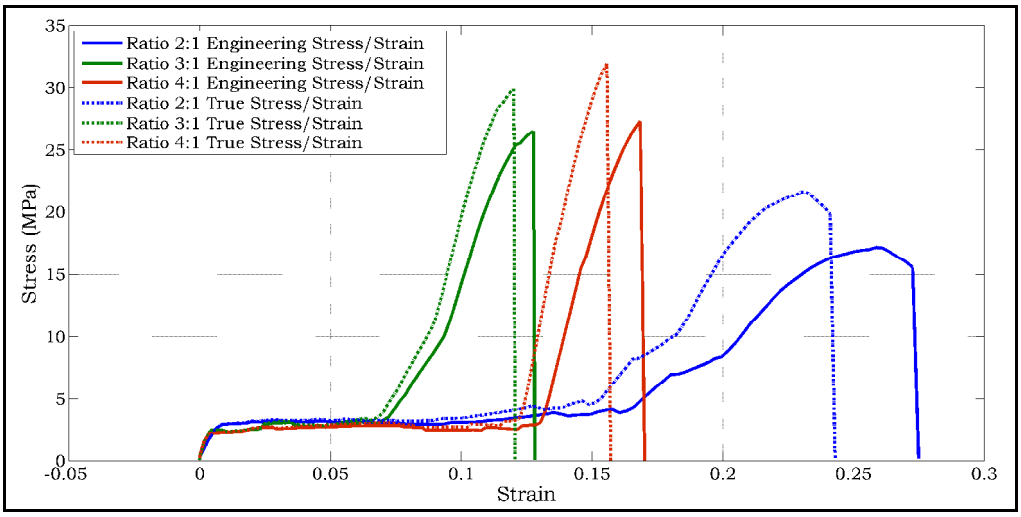


Fig. 2. Stress-strain response of different epoxy-hardener mix ratios..

The stress-strain response demonstrated 4 regions of deformation behaviors [3] (plastic region, strain hardening, necking and fracture) during tensile test of the stoichiometric ratio of 2:1. When the quantity of epoxy is increased by 3 parts and 4 parts to 1 part of hardener, the sample still shows 4 regions but without necking, and the load drops quickly after fracture. The plastic region for stoichiometric ratio is comparatively higher than that of non-stoichiometric ratios of 3:1 and 4:1, signifying a more ductile behavior with large elongation strain prior to failure. The strain hardening region is less obvious in stoichiometric ratio and almost shows a decreasing in strain hardening rate immediately before UTS. The overall strain region from yield point to UTS is significantly higher in ratio 2:1 compared to other mixing ratios. A larger strain as observed in ratio 2:1 arise due to the higher degree of cross linking in the 3D network formed within the sample [4, 5]. For non-stoichiometric ratio, the strain hardening occurred at a much lower strain indicated a lower degree of curing when excessive epoxy resins are added, thus imitating brittle behavior.

Effect on Young's Modulus. Rigidity depends on a firm cohesion between neighboring chains and it is obvious that specific groups which establish strong intermolecular bonds between such chains will affect the mechanical properties. Material rigidity could be established with inter-chain hydrogen bonding [6]. DGEBA resin consist a high level of –OH group at every carbon atom and increasing the number of epoxy part in hardener can affect the elastic modulus of an epoxy/hardener sample. The higher the modulus the stiffer the material [7] and the value of elastic modulus was derived from the initial slope of the stress-strain curve.

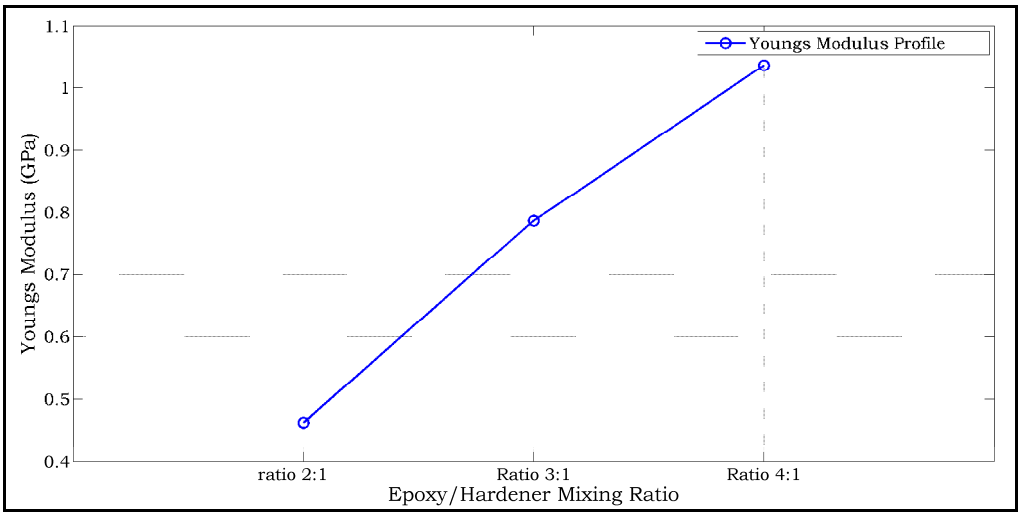


Fig. 3. Young's modulus of different epoxy-hardener mix ratios.

Fig. 3 shows the effect of increasing epoxy/hardener ratio on elastic modulus of epoxy/amidoamine system. An epoxy system with amine class hardener can initiate the homopolymerization of a polymer due to the cationic nature of the hardener. Fig. 3 demonstrated that elastic modulus increases almost linearly with the amount of epoxy parts in the mixture system. Homopolymerization and epoxy ring opening by hydroxyl groups leading to the formation of ethers can reduce the ability of the material to stretch and therefore the material becomes tight and imitates brittle behavior with higher plasticity. High reactivity nature of amines for stoichiometric ratio can improve the mechanical properties but increasing epoxy content can lead to more homopolymerization and hence an increase in Young's modulus.

Effect on Ultimate Tensile Strength (UTS). The UTS is the maximum stress that a material withstands when subjected an applied load [8]. The UTS for all three samples at each mixing ratio were considered for estimation of mean UTS and strain at UTS. The error bars for each mixing ratio show the Standard Deviation (SD).

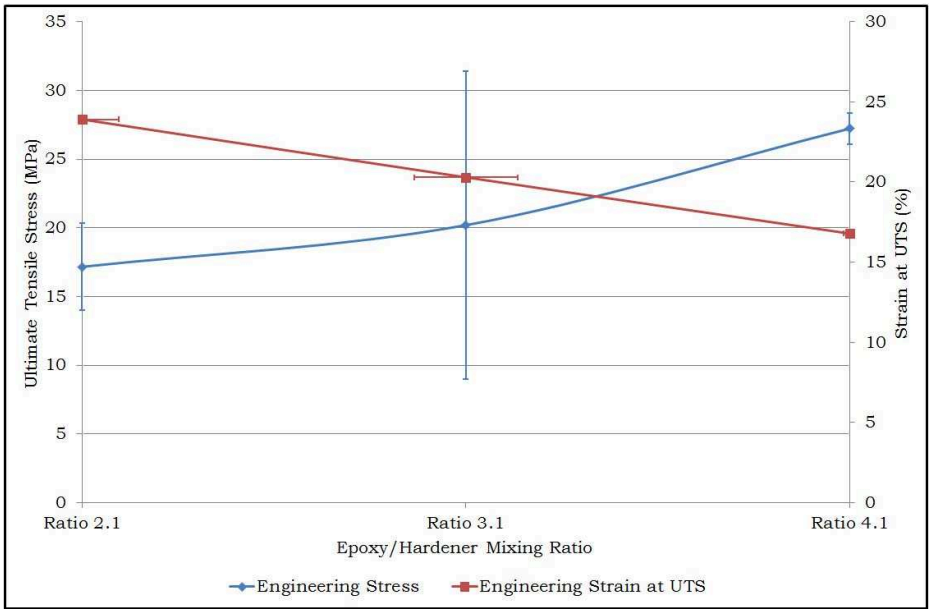


Fig. 4. Ultimate tensile strength and failure strain for different mixing ratios.

For DGEBA/amidoamine system, UTS increased with increasing epoxy content where the epoxy rich formulation exhibits the higher stress at break. The degree of cross-linking is optimum with adequate structural rigidity thereby making the material ductile when stoichiometric ratios of 2:1 are used. For non-stoichiometric ratio there is a significant change to the material behavior because the UTS recorded is much higher compared to that of 2:1 (Fig. 4). The ductility of the material is also shown from the strain chart, where the strain at UTS decreased when mixing ratio is increased. Average strains at non-stoichiometric ratios of 3:1 and 4:1 are found to be 12 and 16% respectively and this change is relatively small compared to that of ratio 2:1 which exhibited a strain value greater than 23%. This higher value of strain at ratio 2:1 suggested that a stoichiometric mixing ratio provides better cross-linking and improves ductility. The error bars for ratios 2:1 and 4:1 are relatively small but high SD for 3:1 suggest that the experimental repeatability might be compromised during mixing and moulding samples. UTS increases when the composition of epoxy in the mixture increased. The decrease in strain value related to the material's rigidity and suggested that the molecules are tightly packed with shorter chain between cross-linkage, thereby increasing the strength of the material and hence the material behaves more in a brittle fashion. Brittle nature with increase epoxy parts is due to the formation of ether groups and homopolymerization that takes place during an epoxy reaction.

Effect on Fracture Surfaces. Increasing mixing ratio capable of impart changes to the mechanical properties and it can either fall into a category of ductile materials where the material

shows increased stretching and bending or they can fall under category of brittle materials where the materials fail without exhibiting any plasticity under loads. Fig. 5 shows the SEM fracture surfaces of different epoxy/hardener ratio deformed to failure under tensile loading. For the stoichiometric ratio of 2:1, the tensile stress/strain chart showed all 5 regions exhibited by a ductile material. For non-stoichiometric ratios, necking could not be observed and the material exhibit brittle characteristics under tensile loading. Ductile properties for ratio 2:1 are again evident from the SEM images of fracture surfaces where the presence of parabolic dimples confirms the cup and cone form of fracture. This form of fracture in ductile materials is due to necking of the fracture surface along with the formation of voids. Ratio 2:1 exhibits a clear region of necking before cracking and this characteristic induces cracking in the material. Voids also play an integral role in crack formation in ductile materials. Therefore for ratio 2:1, crack propagates from necking and void formation during tensile loading. The presence of parabolic dimples symbolic fibrous pull out due to the shear fracture that happens after the initial crack propagation. For non-stoichiometric ratios 3:1 and 4:1, the sample shows a brittle fracture surface as is evident from the SEM mircograph. Grishchuk, S. *et al*. [9] observed the formation of similar fracture surfaces when epoxy samples undergo brittle fracture. In mixing ratio 4:1, the crack runs perpendicular to the stress, with lines and ridges originated from the crack and spreading out across the surface. This form of fracture is a representation of epoxy materials failed in a brittle manner. The fracture surface for 3:1 and 4:1 showed that fracture occurred though the grain boundary hence confirming that that fracture is intergranular fracture. In intergranular fracture, the crack travels through the grain boundaries. With all this observations we can confirm that there is ductile fracture in ratio 2:1 and brittle fracture in non-stoichiometric ratios of 3:1 and 4:1.

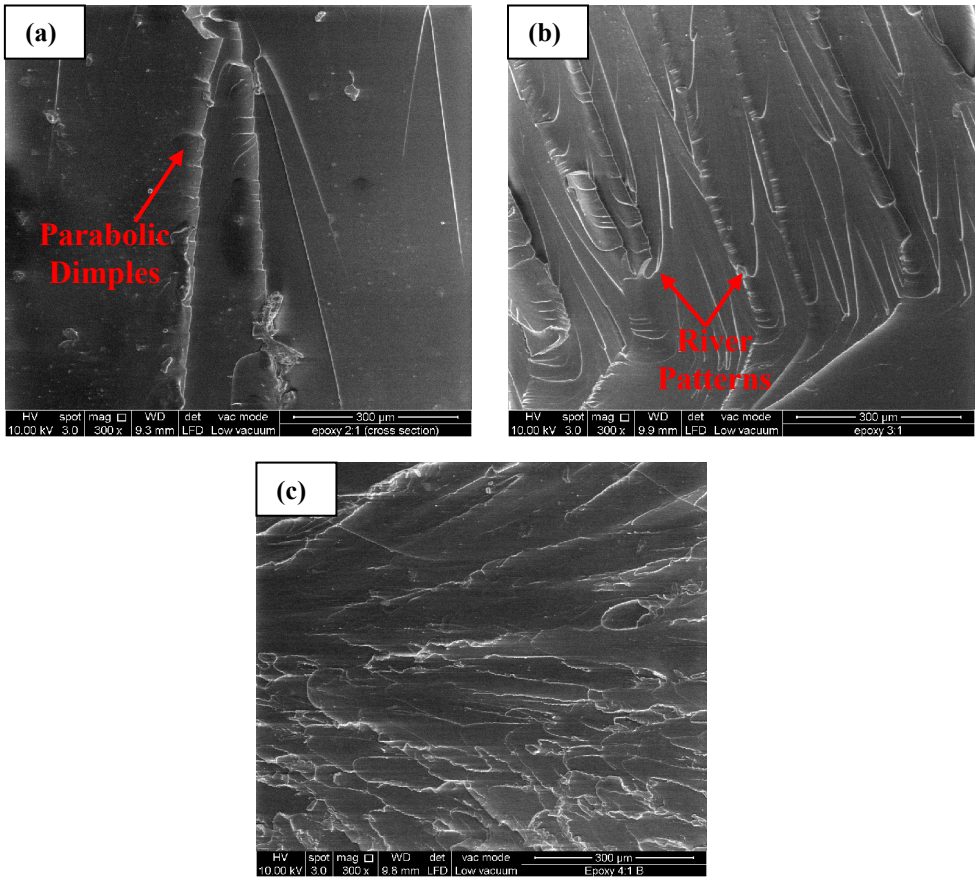


Fig. 5. Tensile fracture surface for different epoxy/hardener mixing ratio. (a) Stoichiometric (b) Non-stoichiometric ratio 3:1 and (c) Non-stoichiometric ratio 4:1.

Hardness Test Results. Hardness is a property of penetration strength, deformation strength, etc., but in most, hardness test depends on the penetration strength of the material surface [10].

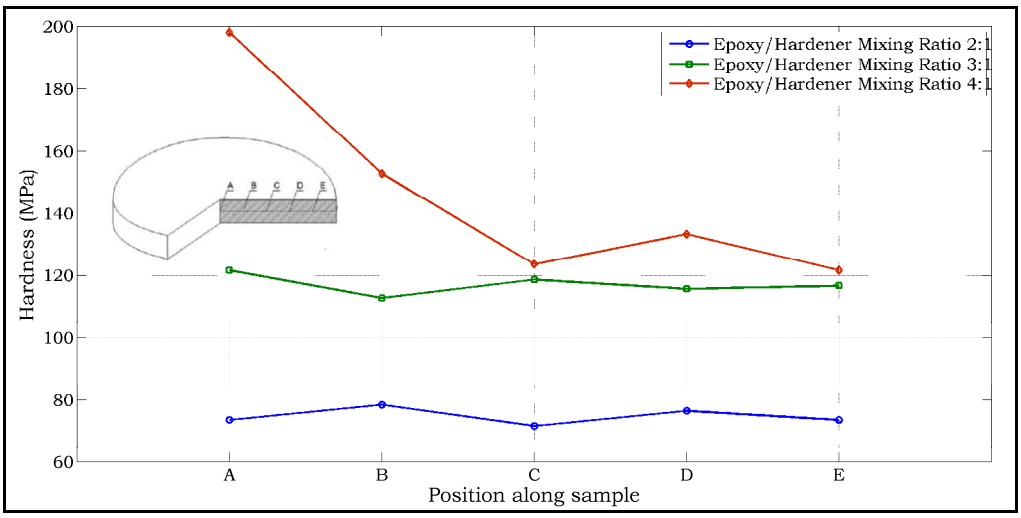


Fig. 6. Hardness results for epoxy/hardener sample at different positions. 'A', 'B', 'C', 'D' and 'E' represents the section of the sample as shown in the chart.

Fig. 6 show the hardness test results taken at 5 positions along the radius of the specimen. The results represent the ability of the material's resistance to elastic distortions, scratching, abrasion, or penetration on its surface. It can be observed that the specimen with stoichiometric ratio has a much lower hardness reading, signifying a greater degree of crosslinking and formation of 3D network as the material tends to be more flexible. On the other hand, as the ratio of epoxy content increases, this flexibility decreases and the specimen becomes stiffer thereby producing higher hardness values. Another noticeable effect seen on increasing epoxy parts is that, for ratios 2:1 and 3:1 the hardness value at all 5 positions seem to follow a certain profile but for the epoxy rich formulation of 4:1, point A shows a significantly higher hardness value prior to a drop at point B. This confirms that, as the epoxy ratio increases, there are excessive unreacted molecules and uneven cross-linking being established within the sample. Excessive use of epoxy potentially result in incomplete homopolymerization [4] and causes uneven surface finish, primarily due to incomplete cross-linking pattern across the sample which may form multiple crack propagation sites.

Flexural Strength Results. The flexural performance of the epoxy rich formulation was evaluated through 3 point bending. SEM images of fracture surfaces after tensile loading proved that, epoxy rich sample of ratio 4:1 failed under brittle conditions and such failure happened due to intragranular fracture mode. The flexural stress/strain chart confirmed that, 4:1 ratio sample broke at a stress of 75 MPa whereas samples 2:1 and 3:1 continued to show greater ductility.

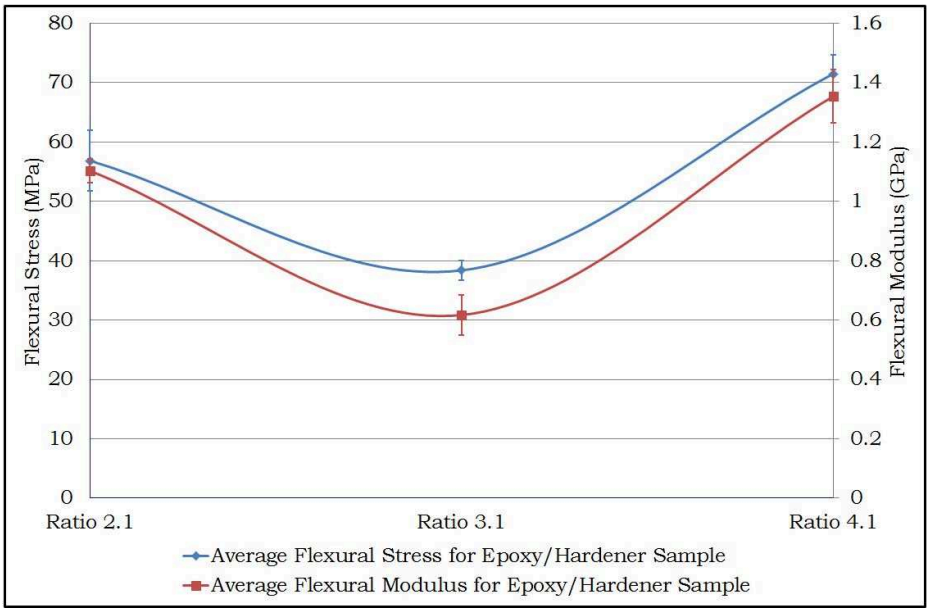


Fig. 7. Flexural stress and modulus for varying mixing ratio of epoxy/hardener.

Fig. 7 depicts the average flexural stress and modulus of specimen subjected to 3-point bending. It can be seen that as the epoxy content increases, the average flexural stress shows a decrease but subsequently increase pattern. Increasing DGEBA epoxy content in epoxy/hardener sample open up more of the epoxy rings and henceforth making the sample brittle. The evidence of this brittleness was well listed in Fig. 2, where the necking region slowly disappeared above stoichiometric ratio. Epoxy rich formulations of 3:1 and 4:1 failed showing brittle behavior. Large amount of epoxy groups leads to brittleness of the materials through the reaction with -OH group or with each other through homopolymerization [11]. In order to achieve better flexural respond, it is important for the reaction to have higher amine content to induce more ring opening mechanism [4]. Although at stoichiometric ratio of 2:1, the flexural stress recorded is lower than 4:1 due to higher cross linking causes the material to be more ductile and hence lower bending moment. The flexural stress also increases because of the amidoamine hardener present in the system. Amidoamine hardener consists of tertiary amines and amides and their properties are inferior to either amine or polyamides. Therefore weak linkages between the hardener and the resin can be another reason on why the sample for 2:1 is broken with a small load.

Conclusions

Epoxy resins usage in composite industry is ever increasing with versatile compositions and formulations. Resins play an integral role in holding fibers within the composites and therefore modified compositions are used for enhancing material properties. In the present work, DGEBA resins with three different epoxy to hardener mixing ratios are tested to evaluate the effect of increasing resin content on mechanical properties. The tensile stress/strain data shown in Fig. 2 revealed that a much brittle thermoset was produced when the quantity of epoxy resin is increased by 3 or 4 parts, and the deformation response did not show any necking thus the plasticity in non-stoichiometric ratios is lost. This was evident from a sample mixed with mixing ratio 4:1. Curing becomes increasingly difficult as epoxy content increases, potentially due to fewer activation of hardener to bond with epoxy molecules. This may be the main reason why mechanical properties can be compromised if non-stoichiometric ratios are used. Homopolymerization of a polymer due to the cationic nature of the hardener plays an important role in dynamic cure chemistry of epoxy. Increase in epoxy content records higher value of Young's modulus hence suggesting that, the material packing is much denser. In a densely packed specimen, the brittle behavior tends to dominate. High reactivity nature of amines for stoichiometric ratio can improve the mechanical properties but increasing epoxy content can lead to more homopolymerization and hence an increase

in Young's modulus. Brittle nature with increase in epoxy content may also arise due to the formation of ether groups and homopolymerization that takes place during the reaction. Fractures surfaces of the tensile samples produced using SEM shows that for ratios 4:1, the crack is perpendicular to applied stress. The ductile fracture is less obvious at 3:1. The flexural test showed that sample of 2:1 and 3:1 are more ductile than 4:1. Mechanical properties showed highest values for non-stoichiometric ratios and this shows that increasing epoxy content increased the hardness and tensile properties.

References

[1]. D'Almeida. M. R. J., De Menezes. W. G., and Monteiro. N. S., *"Ageing of the DGEBA/TETA Epoxy System with Off-Stoichiometric Compositions"*, Materials Research, Vol.6 (3), pp.415-420 (2003).

[2]. Tanaka, Y. and Bauer, R. S., *"Curing Reactions. in Epoxy Resins Chemistry and Technology"*, May, C. A., 2nd Ed., Marcel Dekker, Inc., New York, 285 (1988).

[3]. Norman E.Dowling, *"Mechanical behaviour of materials, Engineering Methods for Deformation, Fracture, and Fatigue. "*, Ed.4th, pp.100-234.

[4]. Mariam, E.A. (2010), *"A Study on the Effect of Hardener on the Mechanical Properties of Epoxy Resin"*, MSc Thesis., University of Technology: Republic of Iraq.

[5]. Odegard, G.M. and Bandyopadhyay. A., "Physical Aging of Epoxy Polymers and Their Composites", Journal of Polymer Science Part B: Polymer Physics, Vol.49 (24, pp.1695-1716 (2011).

[6]. Shaorong. L., Ban. J., Yu. C., and Deng.W., *"Properties of Epoxy Resins Modified with Liquid Crystalline Polyurethane"*, Irnanian Polymer Journal, Vol.19(9), pp.669-678 (2010).

[7]. Ferreira.J.A.M., Costa.J.D.M., Reis. P.N.B., and Capela.C., *"A Study on the Stiffness and Toughness of Enhanced Nanofilled Epoxy composites"*, Anales de Mecanica de la Fractura, Vol.1(28), pp.291-296 (2011).

[8]. Jean-Marie. B*, "Composite Materials. Mechanical Behavior and Structural Analysis."*, pp.15-23.

[9]. S. Grishchuk1, Z. Mbhele2, S. Schmitt1, J. Karger-Kocsis, *"Structure, Thermal and Fracture Mechanical Properties of Benzoxazine-Modified Amine-cured DGEBA Epoxy Resins"*, Express Polymer Letters, Vol.5 (3), pp.273-282(2011).

[10]. Sherman, D. and Brandon, D., *"Mechanical Properties of Hard Materials and Their Relation to* Microstructure*"*, Advance Engineering of Material, Vol. 1, no. 3-4, pp.161-181 (1999).

[11]. Cuddihy, E., Moacanin, *"Superposition of Dynamic Mechanical Properties in the Glassy State"*, Journal of Polymer Science Part A-2(Polymer Physics), Vol.(9), pp.1627-1634(1970).

Applied Mechanics and Materials Vol. 597 (2014) pp 72-77
© (2014) Trans Tech Publications, Switzerland
doi:10.4028/www.scientific.net/AMM.597.72

Research on adsorption kinetics models' fitting values of H_2O_2 oxidated loofah sponge on methylene blue

Dou Yanhan[a], Wang Yanwei[b], Zhao Xihui[c], Wang Yue[d], Li Xiaowen[e], Wang Min[f], Li Qiong[g], Li Qun[h*]

Qingdao University marine biomass fiber materials and Textiles Collaborative Innovation Center in Qingdao, Shandong, China

[a]douyh89@gmail.com, [h]qunli501@163.com

Keywords: H_2O_2 oxidized loofah sponge; MB adsorption kinetics; model fit; adsorption mechanism

Abstract. Oxidized alkaline loofah sponge (OAL) was given by treating alkaline loofah sponge (AL) with H_2O_2, four classic adsorption kinetics models which were Lagergren's pseudo-first-order, Pseudo-second-order equation, the Elovich equation and Intraparticle diffusion were applied to study how the different oxidation degrees of loofah sponge impacted on the values of fitting goodness of the above models and to determine which kind of model was the best fit of the adsorption process and adsorption mechanism. The results showed that Pseudo-second-order equation's fitting degree was proposed to be best and adsorption mechanism was chemical adsorption by ionic bonding, at the same time, as hydrogen bonds increased, water molecules formed a barrier to impede MB diffusing into the micro-structure.

1 Introduction

Loofah sponge which is mainly composed of cellulose (60%), hemicellulose (30%) and lignin (10%) [1], is the vascular bundles of towel gourd fruit. Cellulose is a linear macromolecule which is composed of monomeric unit of a β-D-glucopyranose linking through 1,4-glucosidic linkage, then the long-chains are combined into bundles of cellulose through intermolecular hydrogen bonds and Van der Waals forces. One glucose unit has three free hydroxyl groups (-OH) on the C atoms, two secondary carbon hydroxyls in 2, 3-position, one primary carbon hydroxyl in 6-position, so oxidation reaction can be happened. In this paper, a portion of the hydroxyl groups were oxidized to aldehydes or carboxyls, which, in fact, increased the polarity of cellulose, the same as adsorbent's electrostatic attraction, and further enhanced the adsorption capacity. H_2O_2 molecules generated random oxidation on carbon atoms which had hydroxyl groups[2]. The degree of oxidation could not be controlled completely. The possible oxidation process were Fig.1.

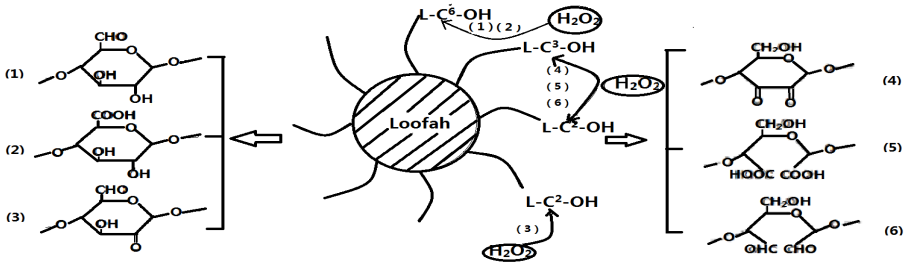


Fig. 1 H_2O_2 oxidized loofah cellulose process

Loofah sponge's vascular bundles have continuous hollow porous structure and multi-channel layering pore system[3]. Due to the unique space physics structure large surface areas are formed, which benefits the adsorption capacity. Thus, lots of researches have been conducted on the adsorption properties of loofah sponge [4-9]. However, there is a lack of kinetic adsorption equation

of oxidized loofah sponge because the analysis of solid-liquid adsorption theories and deduce of a suitable adsorption kinetic equation have always been difficult [10]. In this paper, we chose methylene blue (MB) as adsorbate and used oxidized alkali loofah sponge (OAL) which treated with three different concentrations of H_2O_2 (5%, 10%, 15%) as adsorbents. After adsorption spectrophotometry was utilized to detect the MB's concentration to evaluate the adsorption ability of different adsorbents. By means of data arrangement, we could verify that if oxidized degree of OAL had an effect on adsorption capacity and how much they changed. Four classic adsorption kinetics models which were Lagergren's pseudo-first-order equation (L-F), Pseudo-second-order equation (P-S), the Elovich equation (E) and Intraparticle diffusion equation (I-D) were applied to study how the different oxidation degrees of loofah sponge impacted on the values of fitting goodness of the above models and to determine which kind of models was the best fit for the adsorption process. The conclusion could be applied as a theoretical support to the analysis of OAL adsorption model, meanwhile by comparing loofah sponge's adsorption values before and after oxidation, electrostatic adsorption theory could be validated [11].

2 Experiments

2.1 Materials loofah sponge (Jiangsu Province) were chopped into 2-3mm pieces, NaOH (AR), H_2O_2 (30% wt, AR), methylene blue(Tianjin Institute of Fine Chemicals retrocession, AR), distilled water, visible spectrophotometer (720S, China), centrifuge (Feige TDL80-2B), magnetic thermostatic mixer (ZNCL), air-blowing heater (101-0 Tianjin Taisite Instrument Co.), electronic balance (FA2004N Shanghai precision instrument Co., Ltd.)

2.2 Alkali pretreatment The loofah sponges were rinsed with distilled water. Then pretreated them with 4% (wt) NaOH at 373K for 3h in the reflux unit to strip the majority of pectin, hemicellulose and lignin, leading to more multi-gap structures of cellulose exposed, which meant there were larger specific surface area to be adsorbed. However, cellulose's polar groups enhanced hydration capacity, thus more water molecules got close to them and formed a layer of water, the distance between the fibers were deprived more farther. Then washed them with distilled water until the pH of solution was 7 and dried them in oven at 373K for 6h. By means of alkalization, the space between the cellulose molecules became larger and more beneficial attachment [12].

2.3 Oxidative modification H_2O_2 solutions (200ml) at concentrations of 5%, 10%, 15% (wt) were taken into 3 beakers, 10g AL was immersed in the above solutions respectively, then heated and stirred them (323K, 3h). Samples of oxidation loofah sponges were obtained after drying (343K, 6h), labeled with OAL-1, OAL-2, OAL-3.

2.4 MB standard curve plotted The MB concentrations of 0.1mg/L, 0.2 mg/L, 0.3mg/L, 0.4mg/L, 0.5mg/L, 0.6mg/L were measured at λ_{max}=664nm.According to Lambert-Beer law, the absorbance A (y-axis) was proportional to the concentration (x-axis), so we could obtain a straight linear equation.

$$y=-0.0017x+0.19019\ (R^2=0.99964) \quad (1)$$

2.5 Adsorption kinetics experiments Added 80mg AL into 100mL 10mg/L MB solution, stirred it in the water bath (293K, 200rpm), measured the absorbance at intervals until the absorbance did not change significantly. Then the same experiments were repeated except that the adsorbent AL was replaced with OAL-1, OAL-2, OAL-3. All the adsorption quantity changes with the time were recorded. Adsorption amounts q_t (mg/g) at some point can be calculated by the Eq.2.

$$q_t=(C_0-C_t)V/m \quad (2)$$

Wherein, C_0 (mg/L) and C_t (mg/L) are MB initial concentration values and MB concentration values at some point, respectively.

3. Results and discussion

In this paper, four simplified models, L-F (4), P-S (5), E (6) and I-D (7), were applied to detect kinetics of MB adsorption for AL, OAL-1, OAL-2, OAL-3, respectively. Four models' formulas are as follows.

$$\ln (q_e-q_t) =\ln q_e-k_1 t \quad (3)$$

$$t/q_t=1/k_2\, q_e^2+t/q_e \quad (4)$$

$$q_t=1/\beta \ln (\alpha\beta) +1/\beta \ln t \quad (5)$$

$$q_t=k_i t^{1/2} \quad (6)$$

Wherein, q_e (mg/g) and q_t (mg/g) are the adsorption equilibrium values and adsorption amount at some point, respectively. k_1 (/min) is the proposed as adsorption rate constant of L-F. k_2 (g/mg/min) is the P-S adsorption rate constant. β (g/mg) is connected with the degree of surface coverage and chemical activation energy. α (mg/g/min) is the initial adsorption rate. k_i (mg/g/min$^{1/2}$) refers diffusion rate constant.

The fitting values of the matching between the experimental data and four kinds of kinetic adsorption models were shown in Table 1. For L-F, the adsorption process of AL fitted best, but the fitting intercept q_e (2.53840 mg/g) which was calculated differed with the experimental data q_e (11.19406 mg/g) greatly. Moreover OAL-1, OAL-2, OAL-3 had poor fit. Therefore, AL, OAL-1, OAL-2, OAL-3 adsorption processes didn't match L-F. This may be due to MB^+ and H^+ in the solution competing with each other in the limited adsorption positions.

For P-S, all of the correlation coefficients R^2 were above 0.99, which were higher than L-F model. Moreover the calculated q_e (11.10741, 9.75895, 11.59017, 10.31459 mg/g) inosculated well with experimental data q_e (11.19406, 9.55410, 11.58184, 10.02376 mg/g). The results revealed that P-S model was more consistent to experimental values compared with L-F model. The fact was in accord with H. Demir's conclusion[13]. Fitting curves were shown in Fig. 2.

Table 1 showed that both of the E and I-D matched poorer than L-F and P-S. Through fitting curves (not shown) of I-D, all of four fitting lines did not pass through the origin, which meant the particles diffusion were not the unique rate controlling step [14].

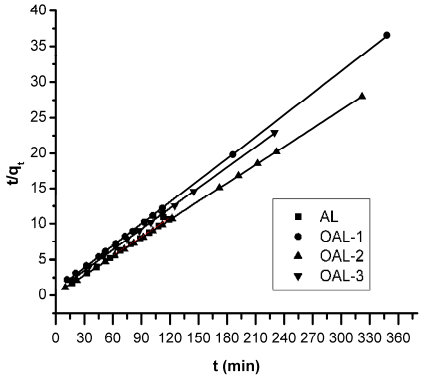


Fig. 2 Changes of MB adsorption varied with time on AL, OAL-1, OAL-2, OAL-3

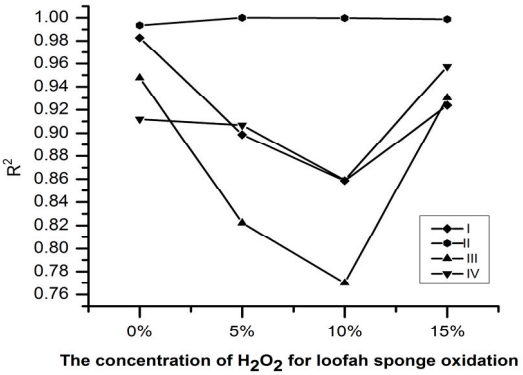


Fig. 3 Four kinds of adsorption kinetic models fitting degrees for MB adsorption on AL，OAL-1，OAL-2，OAL-3 (I. L-F, II. P-S, III. E, IV. I-D)

Table 1 Kinetic parameters of adsorbing MB on AL, OAL-1, OAL-2, OAL-3

AL	Lagergren's pseudo-first-order				Pseudo-second-order equation			
	k_1[/min]	q_e[mg/g]	R^2	P[%]	k_2[g/mg/min]	q_e[mg/g]	R^2	P[%]
AL	0.04077	2.53840	0.98269	77.32372	0.06892	11.10741	0.99355	0.77414
OAL-1	0.01252	2.01049	0.89874	78.87156	0.01322	9.75895	0.99987	2.55764
OAL-2	0.00894	0.96392	0.85862	91.67734	0.03233	11.59017	0.99999	0.07196
OAL-3	0.03204	5.00451	0.92387	50.07352	0.01689	10.31459	0.99978	2.90142

AL	The Elovich equation			Intraparticle diffusion equation	
	α[mg/g/min]	β[g/mg]	R^2	K_i[mg/g/min$^{1/2}$]	R^2
AL	820409.37	1.67474	0.94762	0.22497	0.91182
OAL-1	19.813113	0.82825	0.82234	0.61415	0.90671
OAL-2	3267539.9	1.81222	0.76999	0.42242	0.85937
OAL-3	734.196	1.17785	0.93036	0.28155	0.95732

Fig.3 showed that fitted values of L-F, P-S, E, I-D varied with the oxidation degrees of loofah sponge. After oxidation the fitted values of the L-F, E, I-D models decreased, while P-S just the reverse. Moreover, P-S also had highest fitting degree on the whole, which meant that it was the most consistent of the four kinetic models with the realistic data. Since the P-S is based on the assumption that adsorption rate is controlled by the chemical adsorption mechanism[15], which involves electron sharing or electron transferring between the adsorbent and adsorbate. Thus the process of oxidized loofah sponge adsorbing MB was mainly chemical adsorption by ionic bonds. The adsorbate MB was a small polar molecule which could ionize a positive charge (MB^+) which was chromogenic group in solution, at the same time, the adsorbent oxidized loofah sponge had more negative ions (e.g. -COOH) which were active adsorption points. According to electrostatic adsorption theory[11] ($-COO^- + A^+ \rightarrow -COOA$) electrostatic adsorption force were enhanced. However, equilibrium adsorption values (q_e) of P-S did not change in a uniform way as the oxidation degree of loofah sponge deepened. It might because after oxidation the hydrogen bonds between water molecules and oxygen-containing functional groups (-OH, -CHO, etc.) increased and formed a barrier wall of water molecules which hindered MB^+ diffusing into micropores[16-18] (Fig.4). The fact of irregular changes of the adsorption values before and after oxidation just verified the adsorption mechanism.

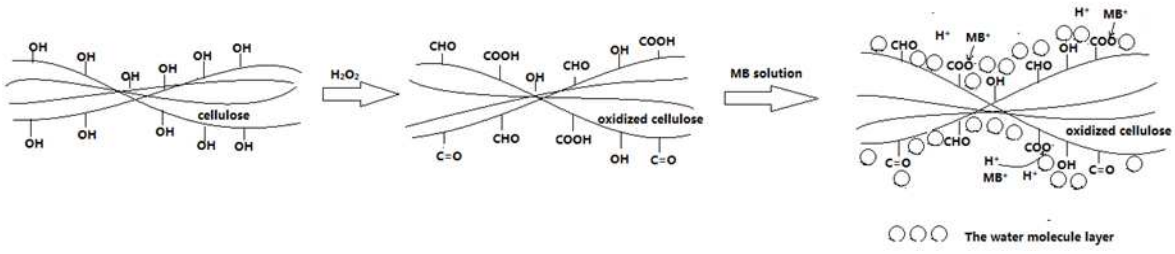


Fig.4 Adsorption mechanism schematic

4 Conclusions

For modified loofah, the adsorption of MB mainly depended on electrostatic attraction. However equilibrium adsorption values (q_e) did not change in a uniform way as the oxidation degree of loofah sponge deepened. It might because after oxidation the hydrogen bonds between water molecules and oxygen-containing functional groups (-OH, -CHO, etc.) increased and formed a barrier wall of water molecules which hindered MB^+ diffusing into micropores.

For the four adsorption kinetics models, P-S was the best fit. And oxidized loofah sponge fitted better than the unoxidized one. Therefore, in regard to researches on the adsorption kinetic models of loofah sponge or loofah sponge oxidation, P-S could be considered first.

Acknowledgments

We are thankful for the financial support from Key Laboratory of Green Processing and Functional Textile of New Textile Materials, Ministry of Education (Nos. GTKL2009013).

References

[1] Ghali[a], S. Msahli[a], M. Zidi[b], F. Sakli[a], Effect of pre-treatment of Luffa fibres on the structural properties, Materials Letters 63 (2009) 61–63

[2] Xu Yunhui, Chen Yuyue, Lin Hong, Research on progress and development trend of oxidized cellulose, Suzhou University Journal (Engineering Science Edition) 2006, 26-2

[3] Alessandro Zampieri[a], Godwin T.P. Mabande[a], Thangaraj Selvam[a], Wilhelm Schwieger[a*], Alexander Rudolph[a], Ralph Hermann[a], Heino Sieber[b], Peter Greil[b], Biotemplating of Luffa cylindrica sponges to self-supporting hierarchical zeolite macrostructures for bio-inspired structured catalytic reactors, Materials Science and Engineering C 26 (2006) 130 – 135

[4] Mohd. Rafatullaha, Othman Sulaimana, Rokiah Hashima, Anees Ahmadb, Adsorption of methylene blue on low-cost adsorbents: A review. Journal of Hazardous Materials 177 (2010) 70–80

[5] G. HENINI[a*], Y. Laidani[a], F. Souathi[b], S. Hanin[c], Study of static adsorption system phenol/Luffa cylindrical fiber for industrial treatment of wastewater, Energy Procedia 18 (2012) 395 – 403

[6] V. K. Guptaa, S. Agarwala, P. Singha, D. Pathaniac, Acrylic acid grafted cellulosic Luffa cylindrical fiber for the removal of dye and metal ions, Carbohydrate Polymers 98 (2013) 1214–1221

[7] N. Akhtar[a], A. Saeed[b], M. Iqbal[b*], Chlorella sorokiniana immobilized on the biomatrix of vegetable sponge of Luffa cylindrica: a new system to remove cadmium from contaminated aqueous medium, Bioresource Technology 88 (2003) 163–165

[8] Hao feng et al., The sorption of active red dye onto chitosan/cellulose hybrid particles, Adanced Materials Rearch, 115 (2011) 183-185.

[9] Min-Yun Chang[a], Ruey-Shin Juang[b], Equilibrium and kinetic studies on the adsorption of surfactant, organic acids and dyes from water onto natural biopolymers, Colloids and Surfaces A: Physicochem. Eng. Aspects 269 (2005) 35–46.

[10] R.C. Bansal, M. Goyal, Activated Carbon Adsorption, CRC Press Taylor & Francis Group 6000, Suite 300 Boca Raton, FL, 2005.

[11] U.J. Rivera, P.M.Sanchez, Adsorption of Cr (III) on ozonised activated carbon, Importance of Cπ—cation interactions, J.Water Research, 37.14 (2003) 3335~3340.

[12] L. Ghali, S. Msahli, M. Zidi, F. Sakli, Effect of pre-treatment of Luffa fibres on the structural properties, J.Materials Letters 63 (2009) 61–63

[13] H. Demir, A. Top, D.Balköse, S.ülkü., Dye adsorption behavior of Luffa cylindrica fiber , Journal of Hazardous Materials 153 (2008) 389–394

[14] C.L. Ye*, N. Hu, Z.K. Wang, Experimental investigation of Luffa cylindrica as a natural sorbent material for the removal of a cationic surfactant, Journal of the Taiwan Institute of Chemical Engineers 44 (2013) 74–80

[15] Y.S. Peat Ho and G. Mckay*, The kinetics of sorption of divalent metal ions onto sphagnum moss, Wat. Res. Vol. 34, No. 3 (2000) pp. 735±742
[16] C.C. Leng, N.G. Pinto, J. Carbon, 35.9 (1997) 1375~1385.
[17] C.O. Ania, J. B. Parra, Pis J. J., J. Fuel Processing Technology, 79.3 (2002) 265-271.
[18] T. Garcia, R. Murillo, J.Cazorla Amoros D. Carbon, 42 (8-9) (2004) 1683-1689.

Applied Mechanics and Materials Vol. 597 (2014) pp 78-83
© (2014) Trans Tech Publications, Switzerland
doi:10.4028/www.scientific.net/AMM.597.78

Thermal Tuning of Vibration Band Gaps in Thin Phononic Crystal Plates with Nitinol

Haojiang Zhao[a *], Rongqiang Liu[b] and Hongwei Guo[c]

School of Mechatronics Engineering, Harbin Institute of Technology, Harbin, 150080, China

[a *]email:123476186@qq.com, [b]email: liurq@hit.edu.cn, [c]email: ghwhit@163.com

Keywords: Phononic Crystal; Thin Plate; Vibration Band Gap; Thermal Tuning

Abstract. Vibration band structures of thin phononic crystal plates (PCPs) with square array and graphite array of nitinol inserts are calculated by the plane wave expansion (PWE) method. The influences of filling fraction are considered when investigating the effects of the varying temperature on the band gaps. Vibration band gaps of these PCPs can be tuned by changing temperature. This study will be useful in designing PCPs with tunable gaps.

Introduction

The propagation of elastic waves or vibration in periodic composites called phononic crystals (PCs) has been extensively studied for the past two decades. The most important characteristic of PCs is the elastic band gaps, where elastic waves or vibration are prohibited. However, traditional PCs can't adjust their band gaps when the needed gaps change, because the frequency range of gaps will be limited once the PCs are manufactured.

Thus, many researchers have devoted to design PCs with tunable band gaps. The present methods to tune the gaps can be divided into two types: mechanical adjustment by changing the shape and orientation of the lattice or the inserts [1-4], and external-fields adjustment by changing materials property through a varied external field [5-11]. Smart materials were used as components of PCs, such as piezoelectric materials [5], electro-rheological fluid [6], magnetostrictive materials [7], magneto-rheological fluid [8], ferroelectric ceramic materials [9] and shape memory alloys (SMAs) [10-11]. Band gaps of PCs with smart materials can be tuned through a varied external field. Especially, SMAs possess a wide range of the elasticity modulus during the process of phase transition from martensite to austenite. With this feature, the band gaps of PCs with SMAs can be tuned by changing the temperature. Yeh and Chen [10] investigated the longitudinal wave propagation in beam composed of SMAs and constrained layer damping which covered with a constrained layer. Ruzzene and Baz [11] found that when the SMAs inserts act as sources of impedance mismatch with tunable characteristics, the longitudinal wave propagation in rods can be reduced. Although the PCPs are just one of the most practical structures of PCs, aforementioned previous investigations do not involve PCPs with SMAs yet.

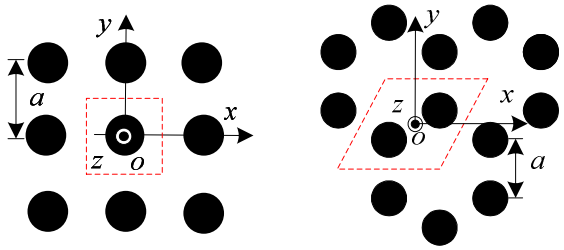
Nitinol is one of the most widely used SMAs, with triple of the elasticity modulus in the austenite phase than in the martensite phase. In this paper, we study thin PCPs containing nitinol inserts. Band structures are calculated by the PWE method. The effects of the temperature, filling fraction of nitinol inserts and the lattice shapes on band gaps are considered.

Model and method

PCPs composed of square array and graphite array of nitinol cylinders in epoxy substrate are investigated in this paper, as shown in Fig.1. The plate thickness direction is assumed to be parallel to the z axis of the Cartesian coordinates system (O, x, y, z). The centre distance of neighboring inserts in both square array and graphite array is a, and the radius of the rods is R.

When the plate thickness is far smaller than a, the conditions of thin plate are satisfied. According to Kirchhoff's hypothesis, the vibration of the PCPs can be described by the displacements of the

middle surface of the plates. The longitudinal vibration band gaps of the studied PCPs are calculated by the PWE method. A detailed discussion on the method is referred in Ref.[13]. Totally 441 plane waves are used, and good convergence can be obtained. Reduced frequency $\overline{\omega} = \omega a / 2\pi c_t$ is used, where c_t is the velocity of shear wave in the epoxy.



(a) (b)

Fig. 1. Transverse cross section of (a) the square and (b) graphite array. The dotted lines represent the unit cell of the lattice. The black cylinders denote the nitinol inserts.

To investigate the effects of the temperature on the band gaps, the relationship of nitinol's elasticity modulus D and temperature T must be obtained. According to Brinson's constitutive model of SMAs, the elasticity modulus D can be reduced as [12]

$$D = D_A + \xi (D_M - D_A) \tag{1}$$

where ξ denote the martensite volume fraction, respectively; superscripts "M" and "A" denote martensite and austenite respectively. For simplicity, effects of the stress and the strain on D are ignored, which means only temperature is considerd. According to Ref. [12], the relationship of ξ and T during the transformation from martensite to austenite can be written as

$$\xi = \frac{\xi_0}{2}\{\cos[\alpha_A (T - A_s)] + 1\}, \ \alpha_A = \frac{\pi}{A_f - A_s} \tag{2}$$

where A_s and A_f are the start temperature and finish temperature of the transformation. Thus, D can be written as a function of T:

$$D = D_A + \frac{\xi_0}{2}(D_M - D_A)\left\{\cos\left[\frac{\pi(T - A_s)}{A_f - A_s}\right] + 1\right\}, A_s \le T \le A_f \tag{3}$$

The values of A_s and A_f for the nitinol used in this paper are 34.5 °C and 49 °C, respectively. The curve of nitinol's elasticity modulus versus the temperature is shown in Fig. 3.

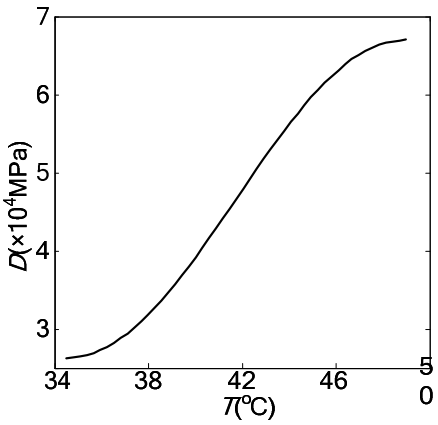


Fig. 2. Elasticity modulus D of nitinol vs. temperature T

The other material parameters are shown in Table 1. All materials used in this paper are assumed to be elastically isotropic.

Table 1. Mass density ρ, Young's modulus E and Poisson's ratio v of the component materials

Materials	ρ[kg m^{-3}]	E[Pa]	v
Epoxy	1180	4.5×10^{9}	0.38
Nitinol as martensite	6421	2.63×10^{10}	0.38
Nitinol as austenite		6.70×10^{10}	

Numerical results and discussion

First, the longitudinal vibration band structures of PCPs with square array of nitinol cylinders are calculated by the PWE method. For square array, the maximum filling fraction f of the cylinders without overlap is about 0.78. The first ten vibration bands obtained by calculating along the high symmetric edges ΓXM of the PCPs with f=0.45 are shown in Fig. 3, for (a)T=34.5 °C (martensite only), (b) T=42 °C (martensite partly) and (c) T=49 °C (austenite only). It can be found that under all the three temperatures, the gap between 3-4 bands exists. And the width and boundaries of this gap increase with the temperature. In addition, gaps between 7-8, 9-10 bands open when T=34.5 °C, as well as gap between 5-6 bands when T=49 °C. Thus, the gap width, location and quantity in the PCPs with square array of nitinol cylinders can be tuned by changing the temperature.

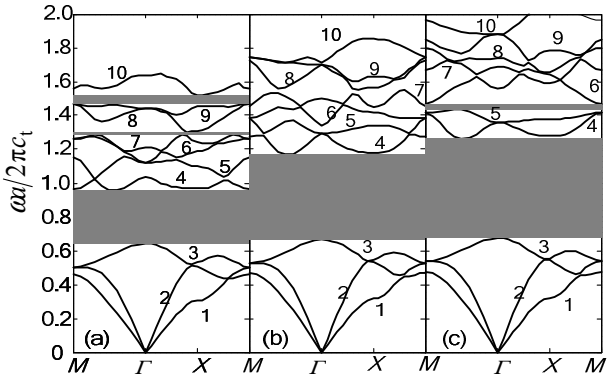


Fig. 3. Longitudinal vibration band structures of PCPs with a square array of nitinol cylinders when f=0.45, (a) T=34.5°C, (b) T=42 °C and (c) T=49 °C.

Now, let us analyze the effects of the filling fraction f and temperature T on the width and location of the gap between 4-5 bands in the square-array PCPs, as shown in Fig. 4. Each vertical bar in Fig. 4a

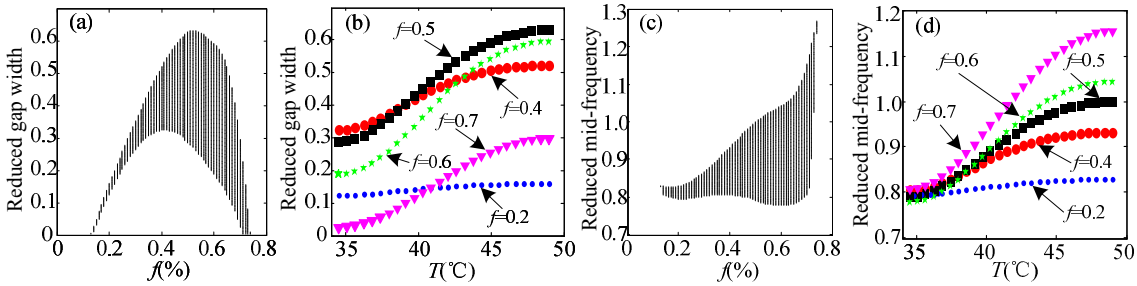


Fig. 4. Variations of the gap between 3-4 bands in the PCPs with square array of nitinol cylinders vs. the filling fraction f and temperature T. (a) Gap widths during the phase transition as a function of f. (b) Gap widths for several given f as a function of T. (c) Gap mid-frequency during the phase transition as a function of f. (d) Gap mid-frequency for several given f as a function of T.

indicates the change range of reduced gap width during the phase transition of the nitinol cylinders. The gap exists during a range of f from 0.13 to 0.74. The gap width first increases with f, then decreases. The peak of the minimum width during the phase transition appears at f=0.4, and the peak of the maximum widths appears at f=0.5. With f increasing, the change range of the gap width caused

by the phase transition firstly increases and then decreases, turning at f=0.6. Details of the variations of gap width for several given f as a function of T are shown in Fig. 4b. It can be found that gap width for each f increases with temperature. The location of the gaps can be indicated by there mid-frequencies. Variations of mid-frequency of this gap during the phase transition for each filling fraction are shown in Fig. 4c. With f increasing, the change range of mid-frequency caused by the phase transition firstly rises and reaches its maximum at f=0.7, then declines with the gap's attenuation. Details of the variations of the mid-frequency for several given f as a function of T are shown in Fig. 4d. It can be found that the mid-frequency for each f rises with the temperature. And mid-frequencies for each f are close to each other at the beginning of the phase transition.

Then, the longitudinal vibration band structures of PCPs with a graphite array of nitinol cylinders are investigated. For a graphite array, the maximum filling fraction f of the cylinders without overlap is about 0.60. The first ten vibration bands of the PCPs when f=0.40 are shown in Fig. 5, for (a) T=34.5 °C (martensite only), (b) T=42 °C (martensite partly) and (c) T=49 °C (austenite only). It is found that under all the three temperatures, the gaps between 6-7, 8-9 bands exist. The gap widths and boundaries of this gap increase with the temperature. In addition, gaps between 9-10 bands open when T=34.5 °C and T=49 °C, as well as gaps between 4-5, 5-6 bands when T=49 °C. Thus, the gap width, location and quantity in the PCPs with graphite array of nitinol cylinders can also be tuned by changing the temperature.

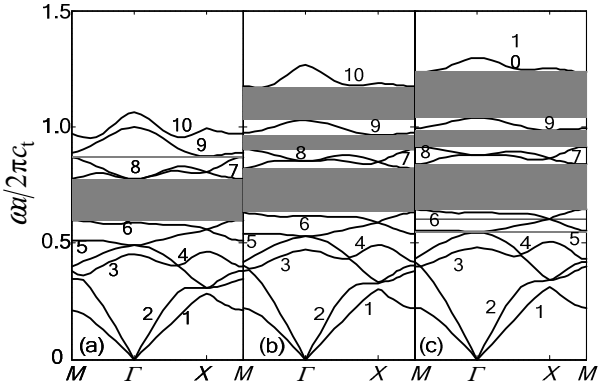


Fig. 5. Longitudinal vibration band structures of PCPs with a graphite array of nitinol cylinders when f=0.40, (a) T=34.5 °C, (b) T=42 °C and (c) T=49 °C.

Finally, The effects of f and T on the widths and locations of the gap between 6-7 bands in the graphite-array PCPs as investigated, as shown in Fig. 6. The gap exists during a range of f from 0.12 to 0.58. The gap width first increases with f, then decreases. The peak of the minimum widths during

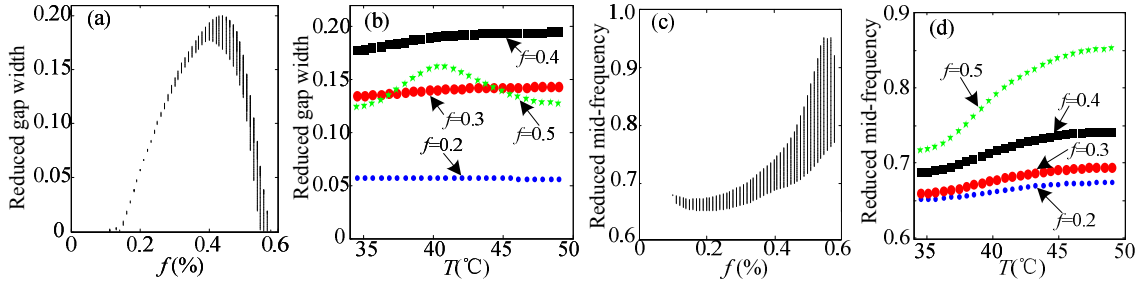


Fig. 6. Variations of the gap between 6-7 bands in the PCPs with graphite array of nitinol cylinders versus f and T. (a) The gap widths during the phase transition as a function of f. (b) The gap widths for several given f as a function of T. (c) The gap mid-frequency during the phase transition as a function of f. (d) The gap mid-frequency for several given f as a function of T.

the phase transition appears at f=0.4, and the peak of the maximum widths appears at f=0.44. With f increasing, the change range of the gap width caused by the phase transition firstly increases, and then decreases, turning at f=0.54. Details of the variations of the gap widths for several given f as a function of T are presented in Fig. 6b. When f=0.2, 0.3 and 0.4， the gap width slowly decreases with T. When f=0.5, the gap width firstly increases with T and reaches its maximum at T=41°C,then decreases. In

other words, when f=0.5, the gap width reaches its maximum with the nitinol in partial martensite. Variations of the gap mid-frequency during the phase transition for each f are shown in Fig. 6c. With f increasing, the change range of mid-frequency caused by the phase transition firstly increases and reaches its maximum at f=0.55, then declines with the gap's attenuation. Details of the variations of the mid-frequency for several given f as a function of T are shown in Fig. 6d. The mid-frequency for each f increases with T.

Summary

The effects of the temperature on longitudinal vibration band gaps of square-lattice and graphite-lattice PCPs with nitinol as inserts are investigated. Numerical results show that the width, location and quantity of band gaps can be tuned by changing temperature in the temperature range of the phase transition of the nitinol inserts. Furthermore, the tunable range of band gap in PCPs with square array is larger than that in PCPs with square array. The largest tunable ranges of the widths and locations of gaps can be obtained by a suitable filling fraction of the nitinol inserts. The findings in this paper can be used to guide the design of much more practical phononic devices with tunable gaps.

Acknowledgements

Funding for this work is provided by the "111 Project" (Grand NO. B07018).

References

[1] L. Feng, X.P. Liu, M.H. Lu, et al., Refraction control of acoustic waves in a square-rod-constructed tunable sonic crystal, Phys. Rev. B 73(2006) 193101.

[2] F. Liu, F. Cai, Y. Ding and Z. Liu, Tunable transmission spectra of acoustic waves through double phononic crystal slabs, Appl. Phys. Lett. 92(2008) 103504.

[3] F. Li, D. Ngo, J. Yang and C. Daraio, Tunable phononic crystals based on cylindrical Hertzian contact, Appl. Phys. Lett. 101(2012) 171903.

[4] J.H. Jang, C.K. Ullal, T. Gorishnyy, et al., Mechanically tunable three-dimensional elastomeric network/air structures via interference lithography, Nano Lett. 6(2006) 740-743.

[5] F. Casadei, M. Ruzzene, L. Dozio and K.A. Cunefare, Broadband vibration control through periodic arrays of resonant shunts: experimental investigation on plates, Smart Mater. Struct. 19(2010) 015002.

[6] J.Y. Yeh, Control analysis of the tunable phononic crystal with electrorheological material, Physica B: Condensed Matter 400(2007) 137-144.

[7] O.B. Matar, J.F. Robillard, J.O. Vasseur, et al., Band gap tunability of magneto-elastic phononic crystal, J. Appl. Phys. 111(2012) 054901.

[8] Z. Xu, F. Wu and Z. Guo, Shear-wave band gaps tuned in two-dimensional phononic crystals with magnetorheological material, Solid State Communications 154(2013) 43-45.

[9] K.L. Jim, C.W. Leung, S.T. Lau, S.H. Choy and H.L.W Chan, Thermal tuning of phononic bandstructure in ferroelectric ceramic/epoxy phononic crystal, Appl. Phys. Lett. 94(2009) 193501.

[10] J.Y. Yeh, L.W. Chen, Wave propagations of a periodic sandwich beam by FEM and the transfer matrix method, Composite structures 73(2006) 53-60.

[11] M. Ruzzene, A.M. Baz, Attenuation and localization of wave propagation in periodic rods using shape memory inserts, SPIE's 7th Annual Int. Symp. on Smart Structures and Materials 2000: 389-407.

[12] K. Tanaka, A thermomechanical sketch of shape memory effect: one-dimensional tensile behavior, Res Mechanica 18(1986) 251-263.

[13] D. Yu, Y. Liu, G. Wang, J. Wen and J. Qiu, Vibration property of two dimensional phononic crystal thin plate, Chinese Journal of Mechanical Engineering 42(2006) 150-154.

Applied Mechanics and Materials Vol. 597 (2014) pp 84-88
© (2014) Trans Tech Publications, Switzerland
doi:10.4028/www.scientific.net/AMM.597.84

Synthesis of $Cu_2ZnSnSe_4$ Compounds Using Solvo-thermal Method

Chuen-Shii Chou [1, a *], Jhih-Wei Jhang[1,b], Ping Wu [2,c], Wei-Hua Lu[1,d]

[1] National Pingtung University of Science and Technology

Pingtung 912, Taiwan

[2] Singapore University of Technology and Design

20 Dover Drive, Singapore 138682

[a]cschou@amil.npust.edu.tw, [b]sstroed@gmail.com, [c]wuping@sutd.edu.sg, [d]whl@mail.npust.edu.tw

Keywords: Solvo-thermal Process, $Cu_2ZnSnSe_4$ Compounds, Band gap.

Abstract. We reported a fabrication of $Cu_2ZnSnSe_4$ (CZTSe) via an elemental solvo-thermal method. To suppress the sublimation of Se, we made use of binary compounds of high vaporization temperature by first converting solid Se into a liquid-like alloy. Single-phase CZTSe compounds with the band gap of 1.32 eV were successfully synthesized and characterized. The effect of synthesizing temperature on the formation of CZTSe was also investigated.

1. Introduction

Among renewable energy resources, solar energy is the most readily available. Copper zinc stannum sulfer (CZTS) [1] and copper zinc stannum selenide (CZTSe) are most recent alternatives. Sophisticated methods (such as thermal co-evaporation [2], pulsed-laser deposition [3], thermal evaporation [4], and RF magnetron sputtering [5]) have been used to fabricate a CZTSe absorber for a PV cell. Aside from these costly vacuum methods, co-electrodeposition [6] and co-electroplating [7] for Cu–Zn–Sn as well as solid state reaction [8] and solvo-thermal route [9] for $Cu_2ZnSnSe_4$ have also been reported.

For any solvo-thermal method, suppressing the loss of Se, which is governed by chemical thermodynamics, is a major challenge. By referring to the solvo-thermal method [10], a new synthesis process was formed and carried out to successfully fabricate CZTSe composite particles. Interestingly, our approach enabled a shorter synthesis time and lower temperature than the recent report [9], in which CZTSe particles were prepared in ethylene glycol or ethylenediamine with a surfactant of Polyvinylpyrrolidone. Aside from this, the results presented herein are the partial works of our paper [11].

2. Experiment Detail

2.1. *Synthesis of CZTSe composite particles*

The starting materials used to synthesize $Cu_2ZnSnSe_4$ composite particles include: (1) copper (Cu) powder with a size of ≦ 75 μm and a purity of 99%; (2) zinc (Zn) powder with a size of ≦ 50 nm and a purity of 99.99%; (3) stannum (Sn) powder with a size of 150 nm and a purity of 99.70%; and (4) selenium (Se) powder with a size of ≦ 150 μm and a purity of ≧ 99.50%. These materials were purchased from Aldrich, USA. A solvent of Triethylenetetramine ($C_6H_{18}N_4$, TETA), which has a boiling point of 266 – 267℃, a pH value of 14, and a density of 0.9818 gcm^{-3}, was purchased from Acros, Belgium, and it was used to dissolve the starting materials.

The procedure for the preparation of 0.005 mole $Cu_2ZnSnSe_4$ composite particles is as follows. (1) A high precision balance (Dener Instrument, TP-214) was used to scale the required starting materials [Cu (0.6350 g), Zn (0.3270 g), Sn (0.5935 g), and Se (1.5792 g)]; (2) Sn powder and 50 ml TETA were loaded in a flask and agitated on a stirrer/hot plate at 80℃ for 1 h, Se powder was added in the flask and mixed with Sn at 80℃ for 2 h, and Cu and Zn powders were then added in the flask and

mixed with the mixture of Sn and Se at 80℃ for 2 h; (3) the inlet of the flask was sealed up first and the contents were heated at a preset temperature for 20 h; (4) after cooling to the ambient temperature, the ethanol was added to the flask to part the precipitates from the bottom of flask; and (5) the precipitates were separated from the ethanol using a centrifuge (CF-15CR), and they were then dehydrated in a forced convection oven (DV-603) at 60℃. Table 1 lists the synthesis conditions for each preparation.

Table 1 Test conditions of preparing CZTSe composite particles

	Mixing		Synthesizing	
	Temperature ( )	Method	Temperature ( )	Time (h)
Test 1	80	Multi-Stage	150	20
Test 2			180	

2.2. ***Characterization of CZTSe composite particles***

A powder X-ray diffractometer (D8 Advance, BRUKER AXS) was used to obtain the phase and crystallographic structure of prepared composite particles. A scanning electron microscope (HITACHI, S-3000N) was used to obtain the morphology of the prepared particles. The chemical composition of prepared composite particles was analyzed using an energy dispersive spectrometer (HORIBA, EX-200).

An UV-VIS-NIR spectrophotometer (Jasco, V-600) with an integrating sphere was used to investigate the absorbance and the transmission (T) of a layer of the prepared composite particles. The absorption coefficient (α) of a layer of the prepared composite particles with a thickness (d) of 10 μm was obtained using $\alpha = \ln(1/T)/d$ [12]. The absorption coefficient was then used to calculate the band gap of the prepared composite particles according to the method described in our previous works [12].

3. Results and Discussion

3.1 XRD patterns

It is important to note that the synthesizing temperature substantially affects the formation of the single-phase CZTSe composite particles. For example, at a fixed synthesizing time of 20 h, as the synthesizing temperature increased from 150℃ (Test 1) to 180℃ (Test 2), the single-phase CZTSe composite particles were successfully obtained, and their three major peaks at $2\theta = 27.22^\circ$, $2\theta = 45.22^\circ$, and $2\theta = 53.62^\circ$, which corresponded to the diffraction from (112), (204), and (312) planes, respectively, were observed in the XRD patterns of the single-phase CZTSe composite particles in Test 2, as shown in Fig. 1.

This result can be attributed to the fact that the synthesizing temperature at 180℃, which is above the glass transition temperature of Sn, results in a faster self-diffusion of Sn, compared with the synthesizing temperature of 150℃. It can be further explained by the following: (1) the glass transition temperature of Sn is about two-thirds of its melting point (232℃), and it is about 155℃; (2) the synthesizing temperature in Test 1 (150℃) is lower than the glass transition temperature of Sn, so at the synthesizing temperature of 150℃, the element of Sn has a higher diffusion activation energy (or slower diffusion) than that of Sn synthesized at 180℃ (Test 2); and (3) the slower diffusion of Sn makes this synthesis route difficult for forming the single-phase CZTSe composite particles.

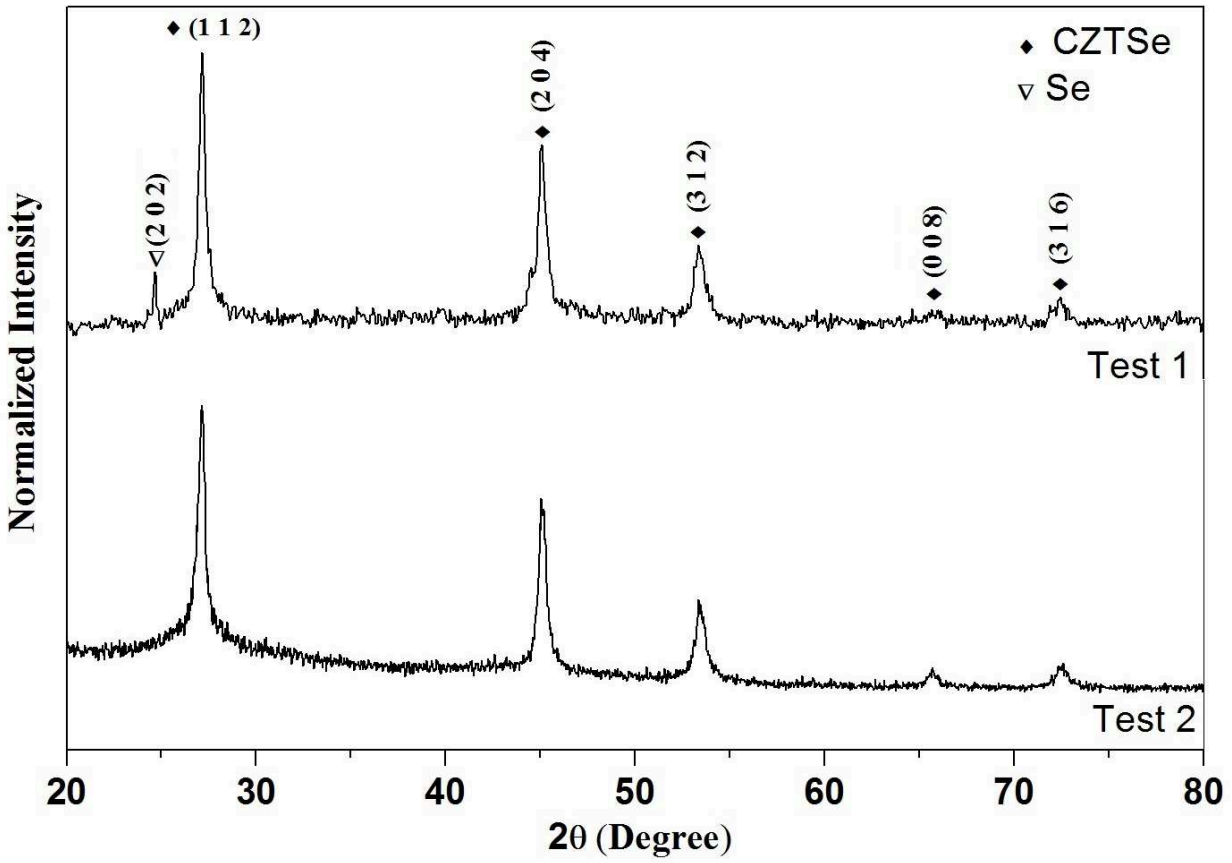


Figure 1 XRD patterns of the composite particles in Tests 1 and 2

3.2 SEM and EDS of CZTSe composite particles

Figure 2 shows the SEM micrographs (15.0 k) and EDS analysis of the single-phase CZTSe composite particles in Test 2. The atomic percentages of Cu, Zn, Sn, and Se in the single-phase CZTSe composite particles in Test 2 were 23.65%, 13.55%, 13.83%, and 48.97%, respectively, and the chemical formula for this CZTSe compound was $Cu_{1.93}Zn_{1.1}1Sn_{1.23}Se_4$, which was closer to the chemical formula of the stoichiometric CZTSe ($Cu_2ZnSnSe_4$).

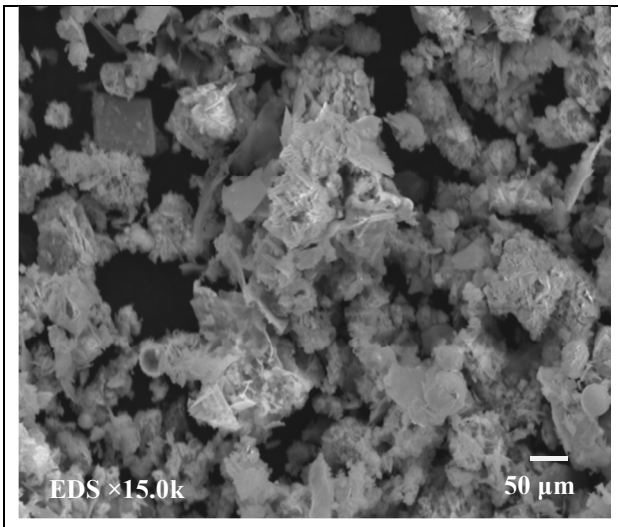
Du et al. observed that the CZTSe composite particles were mainly composed of hexagonal sheet-like microstructures with sizes of 1–2 μm , and the individual hexagon sheet was composed of lots of tiny interconnected particles with a diameter of about 20 nm [9]. Besides the solvo-thermal route, Wibowo et al. observed that using a solid state reaction method, the $Cu_2ZnSnSe_4$ powder crystallized into the stannite phase with a high degree of crystallinity after elemental Cu, Zn, Sn, and Se powders near stoichiometric molar ratios reacted at 500℃ for 6 h [13].

3.3 Band gap of CZTSe composite particles

Figure 3 shows the variations in $(\alpha h\nu)^2$ of the single-phase CZTSe composite particles synthesized at 180℃ with the band gap ($h\nu$) in Test 2. The value of band gap in Test 2 was 1.32 eV. The value of the band gap of CZTSe compound prepared by Du et al. [9] was in the range of 1.0–1.5 eV.

Conclusions

In this research, the sequence of mixing starting materials was investigated. Sn powder and TETA were mixed first, Se powder was then added in the solution, and Cu and Zn powders were finally mixed with the mixture of Sn. Under synthesizing temperature of 180℃ for 20 h, single-phase CZTSe compounds with the band gap of 1.32 eV were successfully synthesized.



Test 2		
Element	Weight (%)	Atomic (%)
Cu L	19.03	23.65
Zn L	11.22	13.55
Se L	48.96	48.97
Sn L	20.79	13.83
Total	100.00	100.00

Figure 2 SEM micrographs (15.0 k) and EDS analysis of CZTSe composite particles in Test 2

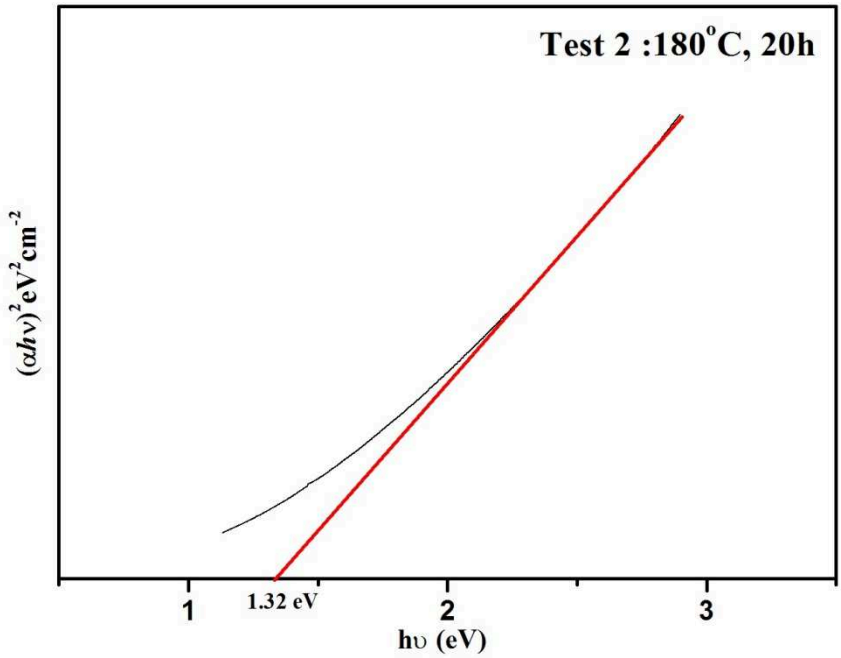


Figure 3 Variations in $(\alpha h\nu)^2$ of the single-phase CZTSe composite with the band gap ($h\nu$).

Acknowledgements

The authors would like to thank National Science Council, Taiwan for financially supporting this research under Contract No. NSC 102-2221-E-020-025 and to thank National Pingtung University of Science and Technology, Taiwan for financially supporting this research under Contract No. NPUST 102009.

References

[1] A.V. Moholkar, S.S. Shinde, A.R. Babar, K.U. Sim, Y.B. Kwon, K.Y. Rajpure, P.S. Patil, C.H. Bhosale, J.H. Kim, Development of CZTS thin films solar cells by pulsed laser deposition: Influence of pulse repetition rate, Sol. Energy. 85 (2011) 1354-1363.

[2] D. Park, D. Nam, S. Jung, S.J. An, J. Gwak, K. Yoon, J.H. Yun, H. Cheong, Optical characterization of $Cu_2ZnSnSe_4$ grown by thermal co-evaporation, Thin. Solid. Films. 519 (2011) 7386-7389.

[3] J. He, L. Suna, N. Ding, H. Kong, S. Zuo, S. Chen, Y. Chen, P. Yang, J. Chu, Single-step preparation and characterization of $Cu_2ZnSn(SxSe_{1-x})_4$ thin films deposited by pulsed laser deposition method, J. Alloys. Compd. (2012) 34-37.

[4] C. Shi, G. Shi, Z. Chen, P. Yang, M. Yao, Deposition of Cu_2ZnSnS_4 thin films by vacuum thermal evaporation from single quaternary compound source, Mater. Lett. 73 (2012) 89-91.

[5] R.A. Wibowo, W.S. Kim, E.S. Lee, B. Munir, K.H. Kim, Single step preparation of quaternary $Cu_2ZnSnSe_4$ thin films by RF magnetron sputtering from binary chalcogenide targets, J. Phys. Chem. Solids. 68 (2007) 1908-1913.

[6] J. Li, T. Ma, M. Wei, W. Liu, G. Jiang, C. Zhu, The $Cu_2ZnSnSe_4$ thin films solar cells synthesized by electrodeposition route, Appl. Surf. Sci. 258 (2012) 6261-6265.

[7] Z. Chen, L. Han, L. Wan, C. Zhang, H. Niu, J. Xu, Jinzhang Xu, $Cu_2ZnSnSe_4$ thin films prepared by selenization of co-electroplated Cu–Zn–Sn Precursors, Appl. Surf. Sci. 257 (2011) 8490-8492.

[8] R.A. Wibowo, W.H. Jung, K.H. Kim, Synthesis of $Cu_2ZnSnSe_4$ compound powders by solid state reaction using elemental powders, J. Phys. Chem. Solids. 71 (2010) 1702-1706.

[9] Y.F. Du, W.H. Zhou, Y.L. Zhou, P.W. Li, J.Q. Fan, J.J. He, S.X. Wu, Solvothermal synthesis and characterization of quaternary $Cu_2ZnSnSe_4$ particles, Mater. Sci. Semicond. Process. 15 (2012) 214-217.

[10] E. Yassitepe, Z. Khalifa, G.H. Jaffari, C.S. Chou, S. Zulfiqar, M.I. Sarwar, S.I. Shah, A new route for the synthesis of $CuIn_{0.5}Ga_{0.5}Se_2$ powder for solar cell applications, Powder Technol. 201 (2010) 27-31.

[11] C.S. Chou, F.C. Su, K. Chen, P. Wu, C.S. Tseng, Thermo-chemistry guided synthesis of $Cu_2ZnSnSe_4$ compounds using solvo-thermal method, Advanced Powder Technology (In Press).

[12] C.S. Chou, Y.J. Lin, R.Y. Yang, K.H. Liu, Preparation of TiO_2/NiO composite particles and their applications in dye-sensitized solar cells, Adv. Powder Technol. 22 (2011) 31-42.

[13] R.A. Wibowo, W.H. Jung, K.H. Kim, Synthesis of $Cu_2ZnSnSe_4$ compound powders by solid state reaction using elemental powders, J. Phys. Chem. Solids. 71 (2010) 1702-1706.

Applied Mechanics and Materials Vol. 597 (2014) pp 89-94
© (2014) Trans Tech Publications, Switzerland
doi:10.4028/www.scientific.net/AMM.597.89

The effect of guide sleeves on shear behavior of 3D weaving composites

XiaochuanWu[1,2,a], ZhongdeShan[1,b*], FengLiu[1], YuanWang[1]

[1]State Key Lab of Advanced Forming Technology & Equipment of China, China

[2] Engineering Research Institute of University Science and Technology Beijing, China

[a]themailofzoeps@163.com, [b]shanzd@cam.com.cn

Keywords: 3D weaving composite, Guide sleeve, Short-beam shear strength, Delamination, 3-point bending test

Abstract. In this study, guide sleeves are brought into 3D weaving composite preforms. The process vacuum assisted resin infusion (VARI) was used to fabricate the 3D weaving composite with guide sleeves. The load-deflection curves and shear behaviors of the 3D weaving composites with guide sleeves were obtained by means of the 3-point bending test. The fracture micrographs of the materials were studied by SEM. The effects of guide sleeves' diameter and interval on the shear behavior and fracture mechanisms of the 3D weaving composites were analyzed. The results showed that the guide sleeves could prevent delamination effectively by bridging fiber layer and pinning crack extending along the fiber layer. Fracture toughness of the composite parts increase because of deformation, fracture of guide sleeves and debonding of interface. The diameter and interval of guide sleeves is smaller, which means the volume fraction of guide sleeves is higher, the interlaminar shear strength higher for the bridging is stronger.

Introduction

Composite materials are extensively used in a number of industries such as aerospace, navigation, engineering machinery, automobile construction, because of their high specific strength, specific stiffness, decay resistance and outstanding designability characteristic[1-2]. Two-dimensional structure composites were used widely before the 1930s for its simple forming process. The Z-yarns was brought into two- dimensional structure composites in 1960s, obtained three-dimensional structure composites. Z-yarns are able to bridge delaminated cracks to avoid delamintation and increase impact resistance. It means composites could be used as the principle force bearing component to realize lightweight of large-scale machinery and equipment[3]. But the existing weaving process is complex and time-consuming. Furthermore the scale of composite is limited by existing weaving process and equipments[4-5]. For all the above reasons, three-dimensional structure composites are yet to realize a wide range of applications.

China academy of machinery science & technology invented a flexible oriented 3D composite woven process, which improve the automaticity of woven process effectively by bringing guide template and guide sleeves into 3D weaving process. The innovative woven process can realize rapid manufacturing of large-scale 3D composite preforms, even solid bars and columns[6].

State key lab of advanced forming technology & equipment of china[7-8] have studied the effect of guide sleeve materials on interface bonding, but no data has been published on the effect of guide sleeves on the mechanical properties of 3D composites. For this reason, this paper experimentally examines the effect of different diameter and interval of guide sleeves on the interlaminar shear strength(ILSS) of 3D composites by short-beam shear test and observation of failure mode.

2 Experimental

2.1Materials

The preforms with carbon fiber as reinforcement and carbon/vinyl bars as guide sleeves were prepared by the flexible oriented 3D composite woven process. The matrix choose epoxy resin (viscosity is 300 cp at 25 ℃, final strength is 62-68 MPa and density is 0.94-0.95 g/cm3) made by State key laboratory of advanced forming technology and equipment.

To avoid disturbing by bending stress, the sample size is recommended[9]:

Specimen length = thickness × 6.0 （1）

Specimen width = thickness × 2.0 （2）

Span length = thickness × 4.0-5.0 （3）

The preforms were impregnated using VARI process as follows: ①40 ℃ for 1h to remove air bubbles used DZF-6050 vacuum drying oven, ②impregnate epoxy resin, ③80 ℃for 2h and 120 ℃ for 3h to cure used CS101-2A drying oven.

Samples are numbered by different diameter and interval of guide sleeves (see in Table 1).Take S4-6 for example, the first figure “4” stands for the diameter of guide sleeve is 4mm, the last figure “6” stands for the interval of guide sleeves is 6mm.

Table1
Parameters design of samples

Sample number		Interval l mm）		
		6	4.5	2
Diameter d(mm)	6	S6-6	S6-4.5	S6-2
	4	S4-6	S4-4.5	S4-2
	2	S2-6	S2-4.5	S2-2
	1.5	S1.5-6	S1.5-4.5	S1.5-2

2.2 Short-beam shear test

Short-beam shear test is the most common method to measure ILSS, which use three-point bending test with small span ratio(see in Figure1[9]). Because in this test method, shear is the dominant applied loading. The interlaminar shear failure will be clearly observed[10-11].

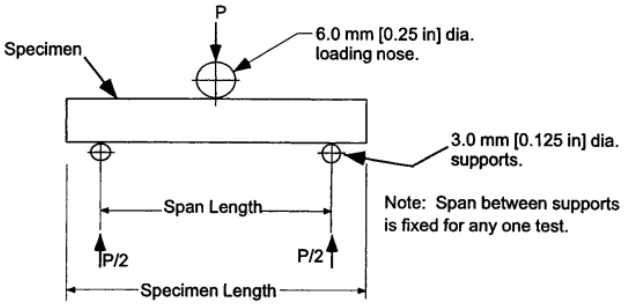


Fig1 Load diagram of short-beam shear test

Short-beam shear tests are made used in universal material testing machine. Set the speed of testing at 1mm/min, span ratio at 5.

Calculate the short-beam shear strength using equation(4)[9] as follows:

$$\sigma = \frac{3P_{max}}{4bh} \quad (4)$$

Where:

σ = short-beam shear strength, MPa;

P_{max} = maximum load observed during the test, N;

b = measured specimen width, mm;

h = measured specimen thickness, mm.

2.3 Short-beam shear failure mode observation

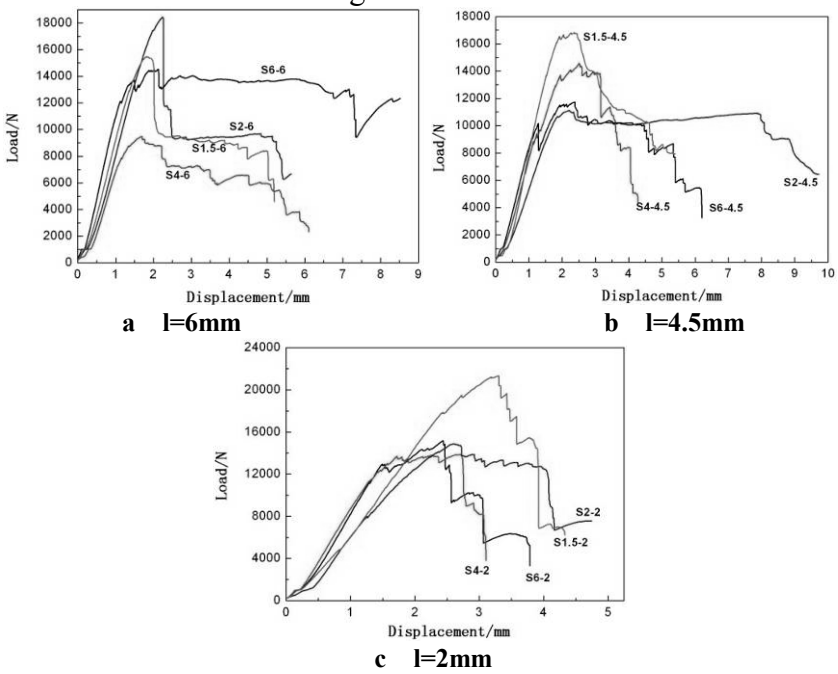
The shear failure mode of samples is observed with optical camera and ZEISS ULTRA 55 Field-Emission Scanning Electron Microscope.

3 Result and discussion

3.1 Interlaminar shear property

3.1.1Behavior of interlaminar shear

Load-displacement curves are shown in figure 2.



a l=6mm **b l=4.5mm**

c l=2mm

Fig.2 Load-displacement curves of short-beam samples

When the interval of guide sleeves is 6mm(see in figure2a), there are four stage in the load-displacement curves: deformation zone, the first phase of destruction, yield phase and fracture. That is typical fracture character of pseudoplastic[12]. During the same stage, the peak loads of samples with different diameter are quite different. The maximum peak is more than 14KN(S6-6), while the minimum is about 7KN(S4-6). When the interval is 4.5mm(see in figure2b), there are only two samples (S6-4.5 and S2-4.5) show yield behavior during test. When the interval is 2mm(see in figure2c), the samples all show typical brittle failure with no yield behavior.

During the test, cracks first show in resin, then extend along interface of fiber and resin. The cracks suffocate due to guide sleeves. Then guide sleeves deform and the interface of guide sleeve and resin debond. That can improve toughness of samples for absorbing a large number of deformation energy.

3.1.2 Interlaminar shear strength(ILSS)

The comparison of ILSS with different parameters of guise sleeves is showed in figure 3.

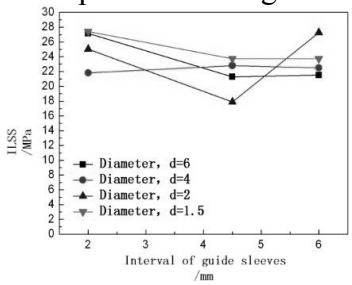


Fig.3 Comparison of ILSS with different parameters of guise sleeves

Figure3 shows that when the diameter of guide sleeve is 1.5mm, ILSS decrease with increasing interval of guide sleeves, as well as that with diameter is 6mm. Meanwhile, ILSS of samples with 1.5mm diameter guide sleeves is higher than others. When the diameter is 4mm, ILSS is not susceptible to interval, the difference between the maximum strength and minimum is less than 1MPa. Whereas, ILSS of samples with 2mm diameter guide sleeves are susceptible to interval, with amplitude increasing up to 56%.

Guide sleeves can bridge and pinning cracks with posting to preforms along thickness direction. The effect of bridge and pinning is remarkable with the volume fraction of guide sleeves increasing. Therefore, the smaller the diameter and interval are, the higher the ILSS.

3.2 Failure mode

Failure mode is also important for finding out the influence of guide sleeves on ILSS of 3D woven composites, except load-displacement curves. Figure 4, 6 and 7 respectively show post-rift samples with 6mm, 4.5mm, 2mm interval.

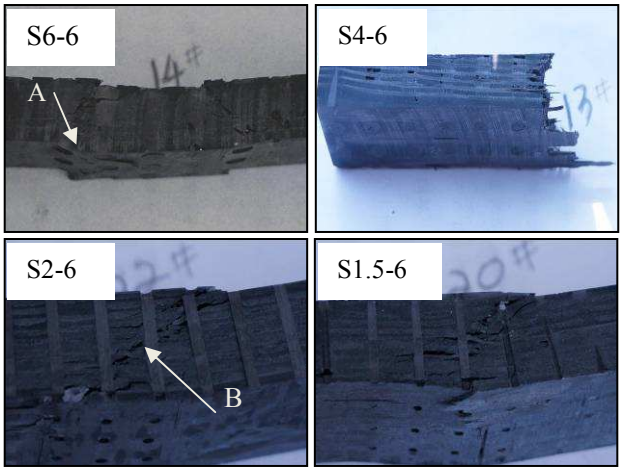


Fig.4 Failure mode of samples with 6mm interval

As show in figure4, cracks in S6-6 extend along length direction, then hampered by guide sleeves. Therefore, there is no obvious interlaminar shear behavior in samples. Furthermore, pits on bottom of sample show that the interface of guide sleeves and resin matrix debond, which result in increasing toughness. The failure of S4-6 is the same as S6-6. As show in figure4, the appearance of fracture becomes out-of –flatness with fiber pulling-out. For that reason, the failure mode of S4-6 is flexible. Figure5 shows that there is resin attached to the fibers pulling-out. That shows strong bonding between fibers and resin matrix. Meanwhile, the interface of guide sleeves and resin debond during test. That will absorb a large amount of deformation energy. Hence, the toughness increase. Guide sleeves can also impede extending of cracks when the diameter is small. However there is limit on impeding for the limit energy absorption of guide sleeves with small diameter. But the extending of cracks will change direction.

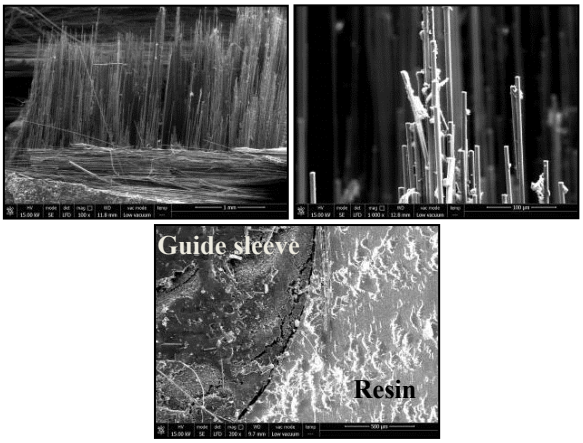


Fig.5 Fracture morphology of S4-6

Failure modes of samples with 4.5mm interval are shown in figure6. Guide sleeves can defend the extending of cracks effectively, as well as the samples with 6mm diameter. The guide sleeves are rarely out of shape when the diameter is 6mm or 4mm, while hardly distort when diameter is 2mm or 1.5mm (see point A in figure6).

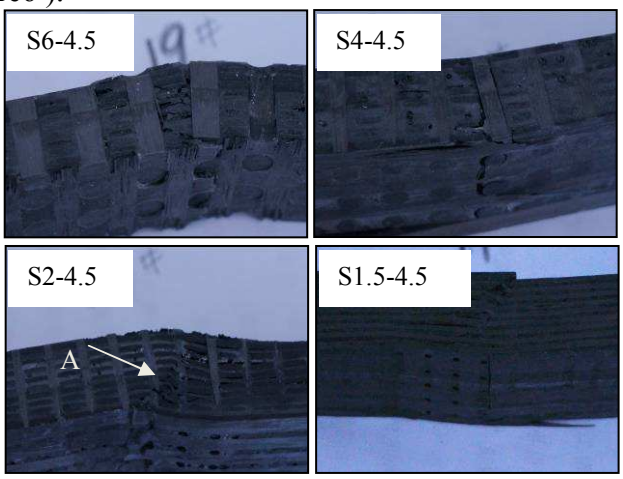


Fig.6 Failure mode of samples with 4.5mm interval

It is worth to notice that there is mixture failure mode in samples with 4.5mm interval: tensile failure of a little fiber and interlaminar shear. Under the same condition of diameter the interval is smaller, the bridging is stronger for increasing of volume fraction of guide sleeves. Then the shear stress increase. Fibers on the bottom of S4-4.5 and S1.5-4.5 are fractured obviously. That match failure behavior of S4-4.5 and S1.5-4.5 showed in Figure2b, which showed that stress in the first stage of S4-4.5 and S1.5-4.5 is higher than others.

The failure modes are quite different when the interval is 2mm compared with other intervals. The main failure mode of sample with 2mm interval is tensile fracture on the bottom.

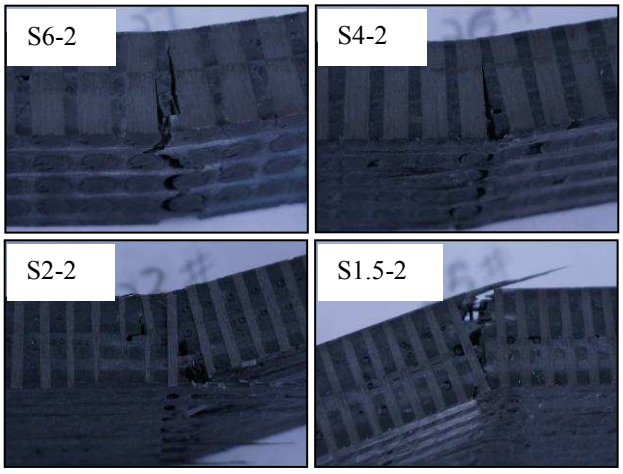


Fig.7 Failure mode of samples with 2mm interval

During the short-beam shear test, compressive stress is on the upper surface and tensile stress is on the bottom of sample. The interlaminar shear damage occurs when the stress inside is equal to interlaminar stress. When the interval of guide sleeves is 2mm, the failure mode is tensile fracture on the bottom. In other words, the ILSS of samples with 2mm interval is higher than others. Because when the stress inside equals to tensile stress results in tensile fracture on the bottom, there is not interlaminar shear damage occurs. Figure7 show the failure mode of samples with 2mm interval. Cracks extend along interface of fiber and resin, and turn to debonding the interface of guide sleeve and resin along the length direction of guide sleeves.

4 Conclusion

1. Fracture toughness of the composite parts increase because of debonding of interface of guide sleeves and resin matrix, deformation and fracture of guide sleeves.

2. The guide sleeves which can prevent delamination effectively by bridging fiber layer and pinning cracks extending along the fiber layer.

3. The diameter and interval of guide sleeves are smaller, which means the volume fraction of guide sleeves is higher, the interlaminar shear strength higher for the bridging is stronger.

Acknowledgement

The study is supported by National Nature Science Foundation of China, keyproject, Grant No: 51035003.

References

[1] L.Tong, A.P.M., M.K.Bannister, 3D Fiber Reinforced polymer Composites, 2008.

[2] Ansar M., W. Xinwei, Z. Chouwei, Modeling strategies of 3D woven composites: A review, Composite Structures, 93(2011)1947-1963.

[3] Du Shanyi, Advanded composite materials and aerospace engineering, Acta Material Composites Sinica, 24(2007)1-12.

[4] O.A. Golra, J. Tariq, N. Ehsan, et al, Strategy for introducing 3D fiber reinforced composites weaving technology, Procedia Technology, 2012:211-216.

[5] A.P. Mouritz, M.K.B., P.J. Falzon, et al, Review of applications for advanced three-dimensional fibre textile composites, Composites Part A: Applied Science and Manufacturing, 30(1999) 1445–1461.

[6] Zhongde Shan, Feng Liu, Juanjuan Qiao, et al, 3D weaving forming technology and equipment for composites, Proceedings of the International Conference on Advanced Technology of Design and Manufacture, 3-5 Nov.2011.Changzhou:2011.

[7] Qiao Juanjuan, Shan Zhongde, Liu Feng, et al, Study on choice of guide sleeve material based on 3D hybrid woven forming of composites, Proceedings of the International Conference on Advanced Technology of Design and Manufacture, 3-5 Nov.2011.Changzhou:2011.

[8] Xiaochuan Wu, Zhongde Shan, Feng Liu, et al, Fundamental research of guide sleeves in 3D weaving composites, Advanced Materials and Engineering Materials Ⅲ, 2014:213-220.

[9] ASTM D2344-2000, Standard Test Method for Short-Beam Strength of Polymer Matrix Composite Materials and Their Laminates.

[10] Yi xiaosu, Du shanyi, Zhang litong, Composite materials handbook, 2009, Beijing: Chemical Industry Press.

[11] T.R. Walter, G. Subhash, B.V. Sankar, et al, Monotonic and cyclic short beam shear response of 3D woven composites, Composites Science and Technology, 70(2010)2190-2197.

[12] Han Li-jun, Li Tie-hu, Liu Jian-jun, et al, Interlaminar fracture behavior of 3D C/C composites using z-pins as through-thickness reinforcement, New Carbon Materials, 19(2004)97-101.

[13] Sun Le-min, Li He-jun, Zhang Shou-yang, Fracture characteristics of pitch-based carbon-carbon composites, New Carbon Materials, 16(2001)28-31.

Applied Mechanics and Materials Vol. 597 (2014) pp 95-98
© (2014) Trans Tech Publications, Switzerland
doi:10.4028/www.scientific.net/AMM.597.95

The Microstructure and Mechanical Properties Research of FeCrWMoV-Series High Temperature Self- Compensation Lubricating Composite Materials

Ying Han[1,a], Yan Jun Wang[1,b*], Shou Ren Wang[1,c],Guang JI Xue[1,d]

[1] School of Mechanical Engineering, University of Jinan, Jinan, 250022, China

[a]abchanying@126.com, [b]me_wangyj@ujn.edu.cn, [c]sherman0158@tom.com, [d]xuegj.1990@163.com

Keywords: sinter; matrix material; microstructure; properties

Abstract：High temperature self-compensation lubricating composite materials were fabricated by vacuum sintering method in this work. The FeCrWMoV alloy powder was used as the basic material, the TiC and Co ceramic powder was used as reinforcing material and TiH_2 and $CaCO_3$ was used as pore-forming material. The changes of the crushing strength, micro-hardness and porosity were analyzed with the temperature. The pore structure and surface morphology of the preforms were analyzed using scanning electron microscope (SEM). The conclusion is that the most appropriate sintering temperature is 1250^{o}C in the process of sintering, and the formation of secondary organization has significant influence on the properties of composite materials.

Introduction

In the modern industry, high temperature self-lubricating composite materials are widely used in aerospace, biology, medicine and other industries, due to its superior mechanical performances [1]. It is added solid lubricant to the matrix materials in the composite. In the process of working, the solid lubricant can reduce the surface friction coefficient and wear. However, the way of adding solid lubricants into the metal ceramic matrix powder before sintering has undesirable side effects [2]. Such as the solid lubricants may be oxidized at high sintering temperature, which will damage its lubricating properties [3].

In order to overcome the negative aspect, a novel kind of high temperature self-lubricating composite materials has been developed. First of all, preform with orderly micro-pores was prepared by using high temperature vacuum hot pressing sintering process. Then, melting solid lubricant is infiltrated into the orderly micro-pores of preform by impregnation technology [4, 5]. The lubrication mechanism is that solid lubricant infiltrated to the friction surface to provide lubrication. These micro-pores function in a way similar to sweat glands of human beings [6]. The composite materials with high strength and toughness and has good self-lubrication property. The physical and mechanical properties of the composite material mainly depend on the preform with micro-pores. In this paper, based on TiC/FeCrWMoV metal ceramic matrix material and TiH_2/$CaCO_3$ pore-forming additives, the structure and mechanical properties of preform were analyzed.

Experiments

Test materials. The main function of the matrix in composite materials is to sustain load. To make the matrix has high strength and toughness is to ensure the composition design of matrix material. FeCrWMoV alloy powder was used as matrix material, TiC/Co ceramic powder as reinforcing material and TiH_2/$CaCO_3$ as pore-forming material. These powders were sintered under the vacuum degree at 10^{-1}-10^{-2} Pa. When the temperature rose to 400^{o}C, H_2 was resolved by TiH_2 and the micro-pores were formed in the process. While at 800^{o}C, CO_2 was resolved by $CaCO_3$. The release of the CO_2 and H_2 left orderly micro-pores in the preform, the strength of which was enhanced by the Ti.

Table1 shows the compositions and its volume fraction of the matrix material. And the chemical component of FeCrWMoV alloy powder was shown in table2.

Table1 The compositions and its volume fraction of the matrix material

Alloy powder	Ceramic powder	Pore-forming material	Lubrication	Additives
FeCrWMoV 79%	TiC+Co 7.5+2.5%	TiH_2+$CaCO_3$ +$C_{36}H_{70}O_4Zn$ 4.5%	graphite 0.5%	Cu_3P 6%

Table2 The chemical component of FeCrWMoV alloy powder

The chemical component (vol.%)							Average grading	Density	Compressib-ility factor	Mobility
C	Cr	Mo	W	V	Si	[O]	μm	g/cm^3	g/cm^3	s/50g
0.8-0.9	3.8-4.4	4.5-5.5	5.5-6.75	1.75-2.2	0.18-2.1	< 0.35	25/50	3.11	>5.0	<25

Material preparation. FeCrWMoV alloy powder was used as matrix material and TiH_2/$CaCO_3$ as pore-forming material. These powders were sintered under the vacuum degree at 10^{-1}-10^{-2} Pa. When the temperature rose to 400°C, H_2 was resolved by TiH_2 and the micro-pores were formed in the process. While at 800°C, CO_2 was resolved by $CaCO_3$. The micro-pores were come into cut-through in the surface during the process. The strength and toughness of preform were influenced significantly by the pore structure characteristics (such as porosity, pore shape, size and distribution).

Therefore, the factors (such as powder material, the ratio of components, the forming pressure and sintering temperature) of influence pore structure were considered at the process of preparing materials [7]. In this work, sintering temperature was selected as the main factors to analyze its impact on materials. The specific process of sintering metal ceramic material is as follows：

(1) Mixed material: every material powder was weighted respectively by electronic scales according to the ratio of composition. And then mixed powder was putted into the stainless steel tube of ball mill. In order to avoid the oxidation of powder in the process of ball mill, the stainless steel tube was filled with a certain amount of argon gas for protecting.

(2) The mold stress forming: the mixed powder was putted into the mold after ball mill. The size of the sample is Ø10×8mm by using press machine, forming pressure is 200-400MPa and the holding time is 5min.

(3) Sintering: the forming sample was putted into the vacuum sintering furnace for sintering. The sintering temperature is 1210-1260°C and the holding time is 60min. The pressure is 30MPa and the holding time is 30min. The sample was taken out at room temperature from the furnace.

Experimental method. The liquid static equilibrium method is used to test the density and the porosity of the preform. The crushing strength and micro-hardness of preform were tested using HVS-type micro-hardness tester and hydraulic testing machine respectively. Friction and wear properties of the composites were investigated using a high temperature XP-5 pin-on-disk wear tester. The samples microstructures and worn surface morphology were characterized using scanning electron microscope (SEM) equipped with an energy dispersive spectroscope.

Results and Discussion

Microstructure. Fig.1 shows the pore structure of metal ceramic preform. It can be seen that holes are homogeneously distributed and interpenetrated through the matrix. The release of the CO_2 and H_2 left orderly micro-pores in the preform, the strength of which was enhanced by the Ti. In the process, the liquid organization of the preform has been formed, so micro-pores can be formed. According to the theory of surface tension and surface energy, the shape of the pores is round in the process in order to maintain the lowest energy state [8]. Meanwhile, the formation of secondary organization in the process of sintering influenced the performance of matrix material. The wear degree of composite

materials is mainly depended on the performance of secondary organization in the process of material preparation [9].

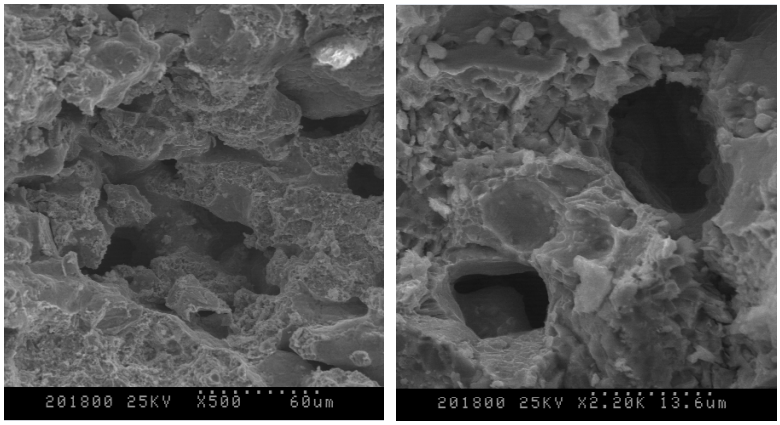


Fig.1 The pore structure of metal ceramic preform

Mechanical property. It can be seen that the porosity was decreased slowly with the rising of sintering temperature in Fig.2. In the process of sintering, in order to guarantee the preform with good strength and toughness, the porosity should controlled in the range of 15-30% [10]. With the rising of sintering temperature, every component in the preform was mutual diffusion. The forming of sintering neck leads to the decrease of porosity [11].

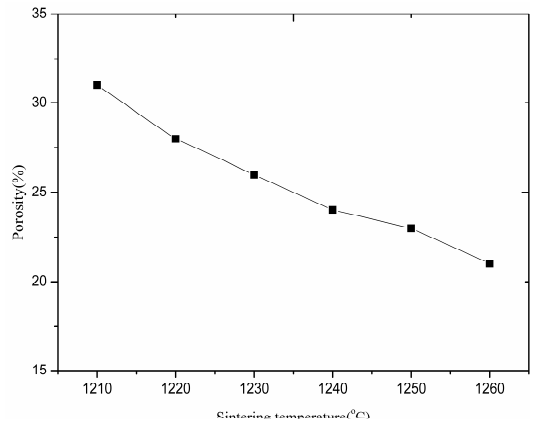


Fig.2 The influence of porosity with the changing of sintering temperature

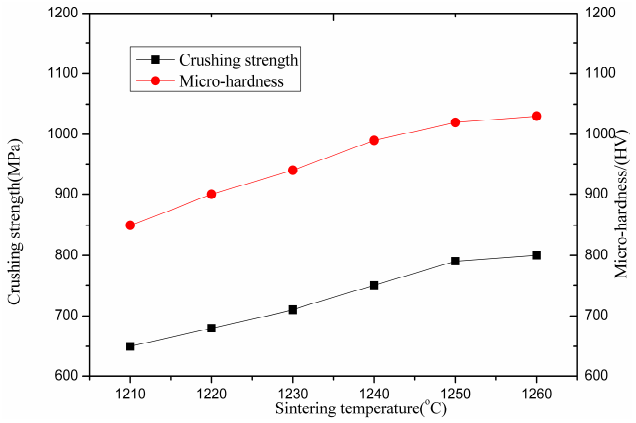


Fig.3 The influence of the crushing strength and micro-hardness with the changing of sintering temperature

The curve of crushing strength and micro-hardness with the changing of sintering temperature is shown in Fig.3. It can be observed that the crushing strength and micro-hardness were improved as the rising of sintering temperature. When the temperature reached to 1250°C, the curve began to change gently. When the range of porosity is 0-30%, the relationship between strength and porosity is as follows [12]:

$$\sigma = \sigma_0 \exp^{-B\varepsilon} \tag{1}$$

Where σ_0 is the strength of dense material (MPa), σ is the strength of porous material (MPa), ε is the porosity(%) and B is the scale factor.

It is evident that with the increasing of porosity, the strength of the material is reduced. Therefore, the porosity of preform is influenced by sintering temperature. With the increasing of sintering temperature, the strength of the material is improved and the porosity is reduced. Also, the crushing strength and micro-hardness were improved with the decreased of cut-through holes.

Conclusions

$TiH_2/CaCO_3$ was used as pore-forming material. The micro-pores were uniformly distributed and interpenetrated in the preform. Meanwhile, the formation of secondary organization in the process of sintering influenced the performance of matrix material. In the process of preparing FeCrWMoV-series high temperature self-compensation lubricating composite materials, as the sintering temperature rising, the crushing strength and micro-hardness were improved, while the porosity of preform was decreased slowly. So the most appropriate sintering temperature is at 1250^{o}C.

Acknowledgement

The authors would like to thank the National Natural Science Foundation of P.R. China for the financial support (ID: 51275208) and Science Foundation of Shandong Province of P.R. China for the financial support (ID: 2011GGX10321).

References

[1] Z.M.Liu, Elevated temperature diffusion self-lubricating mechanisms of a novel cermet sinter with orderly micro-pores, Wear. 262 (2007) 600-606.

[2] L.Y.Yang, Z.M.Liu, Microstructure and tribological properties of Ti-Al self-lubricating materials, Journal of Wuhan University of technology. 30 (2008) 118-120.

[3] X.L.Kong, Y.B.Liu, Y.Lu, P/M metal-matrix high-temperature solid self-lubricating materials, Powder metallurgy technology. 19 (2001) 86-92.

[4] Y.J.Wang, Z.M.Liu, Tribological properties of high temperature self-lubrication metal ceramics with an interpenetrating network, Wear. 265 (2008) 1720-1726.

[5] Y.B.Zhang, D.Z.Xing, Z.M.Liu, The study of high-temperature self-lubricating materials pore structure and lubricants driven, Lubrication engineering. 34 (2009) 5-8.

[6] F.Xie, Study on contact stability of high temperature sweating and lubricating cellular solids, Wuhan: Wuhan University of Technology, 2011.

[7] J.S.Han, W.M.Liu, J.J.Lv, Tribological properties of Fe-Mo-(MoS_2/PbO) high temperature self-lubricating material, Journal of material science and engineering. 26 (2008) 117-120.

[8] R.Zhang, Porosity and strength of SiC porous ceramics, Diamond and Abrasives Engineering. 4 (2000) 38-40.

[9] J.L.Li, D.S.Xiong, M.F.Huo, Friction and wear properties of Ni-Cr-W-Al-Ti-MoS_2 at elevated temperatures and self-consumption phenomena, Wear. 265 (2008) 566-575.

[10] F.L.Han, The brief introduction of criterion of MPIF(America) “the criterion of self-lubricating metallurgical materials” in 1998, Powder metallurgy industry. 10 (2000) 36-46.

[11] H.D.Ding, Sintering model about expansion and shrinkage, The Transactions of Nonferrous Metals Society of China. 11 (2001) 45-50.

[12] W.Duckworth, Discussion of ryshkewitch paper by winston duckworth, Journal of the American Ceramic Society. 36 (1953) 68-70.

Applied Mechanics and Materials Vol. 597 (2014) pp 99-102
© (2014) Trans Tech Publications, Switzerland
doi:10.4028/www.scientific.net/AMM.597.99

Continuously large-scale preparation of multi-layer graphene grown on polycrystalline SiC microspheres

Jun Ma, Gong-yi Li*, Zeng-yong Chu, Tian-jiao Hu, Yi-he Li and Xiao-dong Li

College of Science, National University of Defense Technology, Changsha, People's Republic of China, 410073

*nudtlgy@gmail.com

Keywords: multi-layer graphene; silicon carbide; large scale; chemical vapor deposition

Abstract: Gram scale multi-layer graphene grown on polycrystalline SiC microspheres were prepared by continuously preparation method in argon through chemical vapor deposition process using liquid polysilacarbosilane as raw material. The observation of products obtained at different temperature confirmed the growth is temperature dependent process. The method could be developed to synthesis hybrid nanostructures based on multi-layer graphene grown on polycrystalline SiC microspheres.

Introduction

As a novel carbon based nanomaterials, graphene was first discovered by Geim at 2004 [1]. The exceptional two-dimensional (2D) crystals appear in a flat monolayer or multi-layer (less than 10 layers) of covalently bonded carbon atoms which are tightly packed into benzene-ring structure. Owing to the 2D electron gas fantastic physical and chemical properties, graphene is expected to be applied in high performance electronics. Moreover, with unique properties as transparency, conductivity and elasticity electronic properties, graphene have attracted much attention in transparent protective coatings and barrier films.

Until now, several methods, including mechanical cleavage of graphite [1], exfoliation of graphite by a solution-based process, epitaxial growth graphene through chemical vapor deposition on special metals [2-4] and by thermal decomposition of silicon carbide (SiC) in ultrahigh vacuum [5, 6], and thermal splitting of SiC granules [7], have been developed to serve applications such as graphene-based composite [8], high-frequency transistor[9], stretchable transparent electrodes [10] and sensors [11, 12]. Recently, we have reported that multi-layer graphene standing on SiC microsphere can be acquired *via* one-pot chemical vapor deposition on silicon wafer [13]. The unique morphology may find potential applications in high performance metal-free catalysts. However, the yield is hard to be increased because the final products are numerous stacked SiC microspheres on the area-limited Si wafer substrate. The vapor-solid phase transfer process could continuously produce multi-layer graphene grown on polycrystalline SiC microspheres if we can continuously provide raw materials. Thus, a continuously large-scale low-cost preparation method is developed in this paper to prepare multi-layer graphene grown on polycrystalline SiC microspheres at large-scale.

Experiment section

Continuously large scale prepare multi-layer graphene grown on polycrystalline SiC microspheres was performed in argon by pyrolysis of liquid polysilacarbosilane (*l*-PS, gift from National University of Defense Technology, Changsha, China) in N_2 (purity≥99.999%) which is continuously injected into the horizontal furnace by a syringe pump (Figure 1).

In the typical preparation process, five ceramic boats were placed in the center of the horizontal furnace. After the atmosphere was replaced by argon, the furnace is heated up to certain temperature at the rate of 10°C/min. Then *l*-PS was injecting into the furnace by syringe pump at the rate of 0.1 mL/min. During the injection, the temperature of high temperature zone is kept at certain

temperature. The furnace was allowed to cool down to room temperature after the pyrolysis of *l*-PS had been finished. Three samples obtain at 1300°C, 1100°C and 900°C is named as S1300, S1100 and S900.

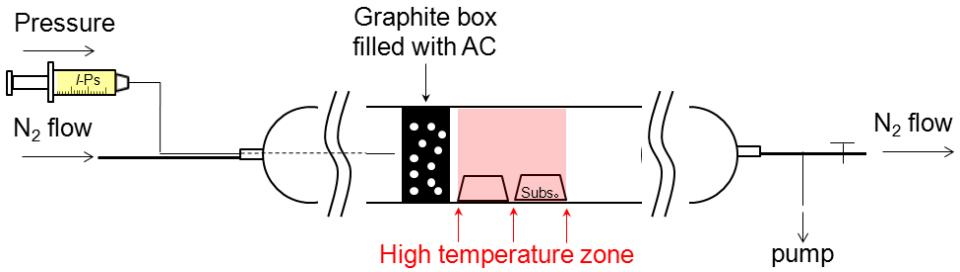


Figure 1 The continuously preparation system of multi-layer graphene grown on polycrystalline SiC microspheres

Products were characterized with X-ray diffractometer (XRD, Siemens D500, λ=0.1541 nm), Scanning Electron Microscopy (SEM, Hitachi S-4800 FE), Transmission Electron Microscopy (TEM, TECNAI-F20) with Energy Dispersive X-ray spectroscopy (EDX) apparatus, Infrared Spectroscopy (IR, TENSOR27).

Result and discussion

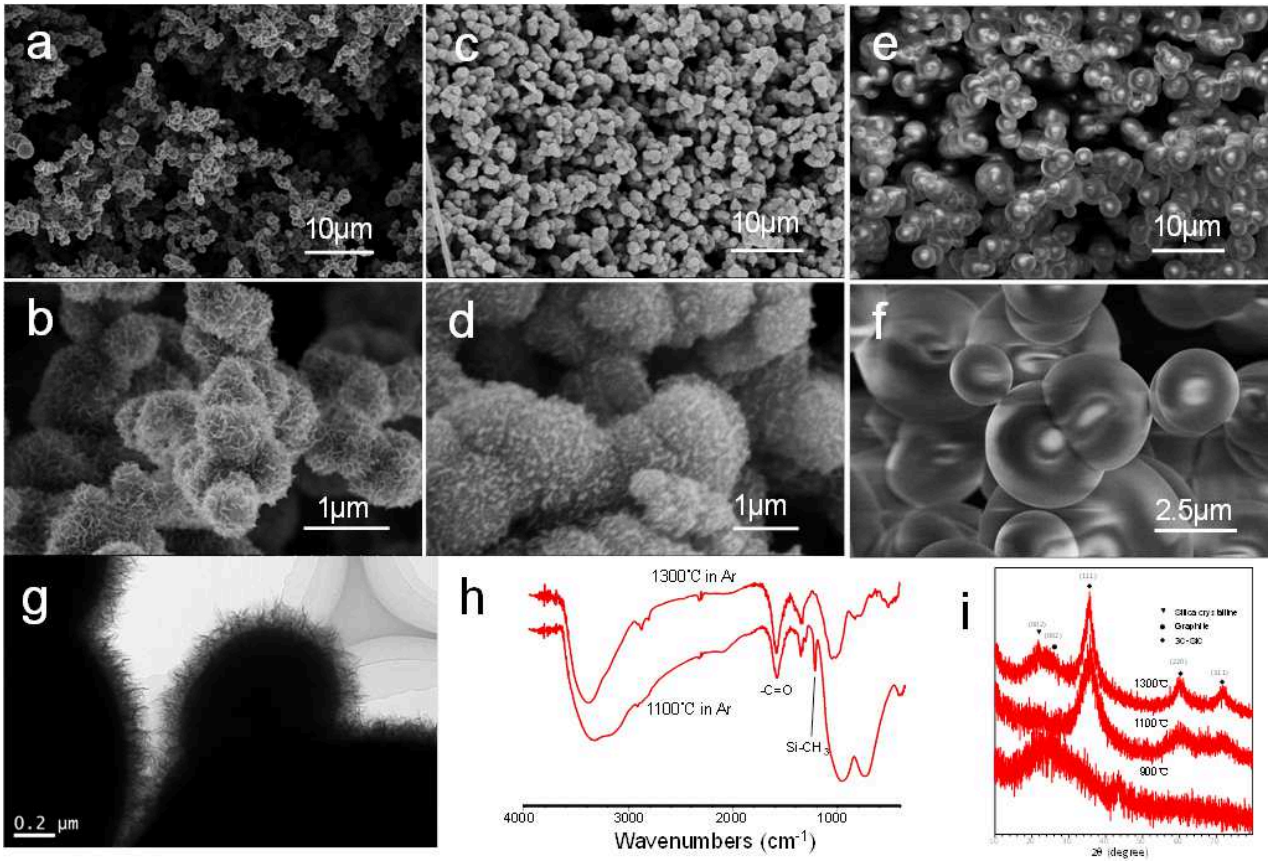


Figure 2 SiC microsphere obtained at 1300°C (a, b), 1100°C (c, d) and 900°C (e, f); TEM images of SiC microspheres obtained at 1300°C (g); IR spectra of *l*-PS and SiC microspheres obtained at 1300°C and 900°C(h); XRD pattern of SiC microsphere obtained at 1300°C, 1100°C and 900°C (i)

Compared with the former one-pot method (the yield is milligram scale), the continuously preparation method could largely promote the yield to gram scale. The as-prepared products at different temperature (1300°C, 1100°C and 900°C) was investigated by SEM (Figure 2a-f). With approximately the same magnification, the average diameter of the three samples (S1300, S1100 and S900) is gradually reduced with increasing temperature. A software (Nano Measure) is utilized to

measure the diameters of microspheres in SEM picture and gave an average diameter finally. The average diameters of S1300 (Figure 2a-b), S1100 (Figure 2c-d) and S900 (Figure 2e-f) are ~0.9 μm, ~1.2 μm and ~3.3 μm, respectively. It should be noted that S900 have a perfect globose shape, which probably derived from surface tension of liquid. But S1100's surface is just obviously wrinkled compared with S1300's fluffy surface, means the microstructure is significantly changed. The morphology change could be confirmed by XRD (Figure 2i). S900 were not well crystallized and even not fully pyrolyzed, because no peaks of SiC crystal could be found in the XRD pattern (Figure 2i, S900) and the IR absorption peak of Si-CH_3 group vibration (~1210 cm^{-1}) was still obviously existed (Figure 2h). Results from XRD analysis also indicate a preliminary crystallization of S1100 compared with S1300. To sum up, the dimension of microspheres derived from *l*-PS is reduced with increasing temperature because the microspheres would gradually pyrolyze and crystallize to multi-layer graphene standing on SiC microspheres and thus shrink at the same time. During the pyrolysis process (the *l*-PS was directly injecting into the furnace at 1300°C, 1100°C and 900°C), there should be a fast and coherent volatilization, solidification and crystallization procedure responsible for the formation of finally nanostructure.

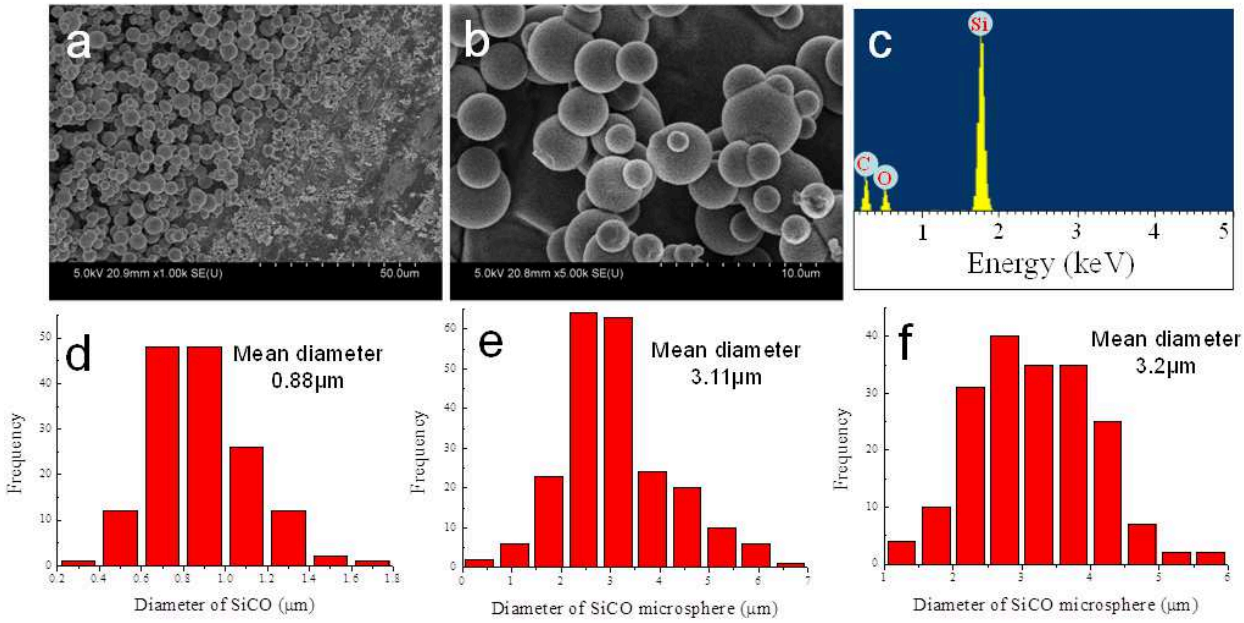


Figure 3 The SEM images (a, b) and EDS spectrum (c) of SiC microspheres obtained at 1300°C; the average diameter histogram of S900 (f) and top layer (d), under layer (e) SiC microsphere of S1300

A scratch was made on S1300 by a tweezer. The SEM images (Figure 3a, 3b) shows that the down layer SiC microspheres is little different compared with the top layer. The graphene on the surface of under layer SiC microspheres is shorter and the average diameter is much bigger than that of top layer SiC microspheres. The average diameter histograms of S900 (f) and top layer (d), under layer (e) SiC microsphere of S1300 are shown in Figure 3d, 3e, 3f. Obviously, the average diameter of SiC microspheres on top layer is only 28.3% of that on under layer, and 27.5% of that in M900. However, the SiC microspheres on top layer and down layer have the same element species including silicon, carbon and oxygen. The results suggest that the shrink rate of SiC microspheres on top layer is faster than that on under layer during the pyrolysis process. This might because the pyrolysis gas is easier to release on the top layer which will facilitate the pyrolysis reaction equilibrium.

Summary

As an alternative method of preparing multi-layer graphene, *l*-PS was pyrolysis *via* CVD route to continuously produce gram-scale multi-layer graphene grown on polycrystalline SiC microspheres. The method provides a continuously preparation strategy to large-scale fabricate multi-layer graphene grown on polycrystalline SiC microspheres. The pyrolysis reaction is a temperature

dependent process, which also might be hindered by pyrolysis atmosphere in furnace. The newly developed continuously preparation system could be applied to fabricate some interesting hybrid nanostructures by just changing the raw materials or gas.

Acknowledgement

The authors are thankful for the help from Ren-bin Wei and Yang-jie Chen from Changsha University, as well as the financial support from the National Natural Science Foundation of China (Granted No. 51102281) and Research Project of National University of Defense Technology (Granted No. JC13-02-11).

References

[1] K S Novoselov, A K Geim, S V Morozov, D Jiang, Y Zhang, S V Dubonos, I V Grigorieva, A A Firsov. Electric field effect in atomically thin carbon films, Science. 306 (2004) 666-669.

[2] Y Pan, H Zhang, D Shi, J Sun, S Du, F Liu, H Gao. Highly Ordered, Millimeter-Scale, Continuous, Single-Crystalline Graphene Monolayer Formed on Ru (0001), Adv. Mater. 20 (2008) 1-4.

[3] A Nageshima, K Nuka, H Itoh, T Ichinokawa, C Oshima, S Otani. Electronic states of monolayer graphite formed on TiC(111) surface, Surf. Sci. 291 (1993) 93-98.

[4] T A Land, T Michely, R J Behm, J C Hemminger, G Comsa. STM investigation of single layer graphite structures produced on Pt(111) by hydrocarbon decomposition, Surf. Sci. 264 (1992) 261-270.

[5] C Berger, Z Song, T Li, X Li, A Y Ogbazghi, R Feng, Z Dai, A N Marchenkov, E H Conrad, P N First, W A de Heer. Ultrathin Epitaxial Graphite: 2D Electron Gas Properties and a Route toward Graphene-based Nanoelectronics, J. Phys. Chem. B. 108 (2004) 19912-19916.

[6] W A de Heer, C Berger, X Wu, P N First, E H Conrad, X Li, T Li, M Sprinkle, J Hass, M L Sadowski, M Potemski, G Martinez. Epitaxial graphene, Solid State Commun. 143 (2007) 92-100.

[7] D Deng, X Pan, H Zhang, Q Fu, D Tan, X Bao. Freestanding Graphene by Thermal Splitting of Silicon Carbide Granules, Adv. Mater. 22 (2010) 2168-2171.

[8] S Stankovich, D A Dikin, G H B Dommett, K M Kohlhaas, E J Zimney, E A Stach, R D Piner, S T Nguyen, R S Ruoff. Graphene-based composite materials, Nature. 442 (2006) 282-286.

[9] Y M Lin, C Dimitrakopoulos, K A Jenkins, D B Farmer, H Y Chiu, A Grill, P Avouris. 100-GHz Transistors from Wafer-Scale Epitaxial Graphene, Science. 327 (2010) 662.

[10] K S Kim, Y Zhao, H Jang, S Y Lee, J M Kim, K S Kim, J Ahn, P Kim, J Choi, B H Hong. Large-scale pattern growth of graphene films for stretchable transparent electrodes, Nature. (2009).

[11] T S Sreeprasad, A A Rodriguez, J Colston, A Graham, E Shishkin, V Pallem, V Berry. Electron-Tunneling Modulation in Percolating Network of Graphene quantum Dots: Fabrication, Phenomenological Understanding, and Humidity/Pressure Sensing Applications, Nano Lett. 13 (2013) 1757-1763.

[12] F Schedin, A K Geim, S V Morozov, E W Hill, P Blake, M I Katsnelson, K S Novoselov. Detection of individual gas molecules adsorbed on graphene, Nat. Commun. 6 (2007) 652-655.

Applied Mechanics and Materials Vol. 597 (2014) pp 103-108
© (2014) Trans Tech Publications, Switzerland
doi:10.4028/www.scientific.net/AMM.597.103

Effects of Mechanical Alloying on Microstructure and Properties of Powder Injection Moulded SiC_p-Reinforced Aluminium Composite

Tapany Patcharawit[1, a*], Suthin Klahan[1], Patcharee Rupkrathok[1] and Nutthita Chuankrerkkul[2, b]

[1]School of Metallurgical Engineering, Suranaree University of Technology, Thailand

[2]The Metallurgy and Materials Science Research Institute, Thailand

[a] tapany@sut.ac.th (corresponding author), [b] nutthita.C@chula.ac.th

Keywords: Mechanical-alloying, Powder, Injection, Aluminum, Composite, Microstructure, Hardness

Abstract. This research investigated effects of mechanical alloying on microstructure and hardness of 30 vol.% SiC_p - reinforced aluminium composites produced by powder injection moulding. Mechanical alloying was performed via an attrition mill prior to feedstock preparation at 52% and 55% solid loadings. Powder injection molding was operated at 170 ^oC followed by debinding and sintering at 680-740 ^oC. Experimental results showed that mechanical alloying aided better mixing of aluminium powder and SiC_p such that certain amounts of SiC_p was observed to be engulfed into deformable aluminium powder matrix. This in turn increased the interfaces between the two phases, thus facilitating sintering of the composite. By employing mechanical alloying, the effective sintering temperature has significantly reduced from 740 ^oC down to 700 ^oC. Improved sintered density and hardness were obtained by increasing % solid loading and sintering temperature.

Introduction

Aluminium composites possess relatively good hardness, light weight and reasonable wear resistance and are of interest for automotive and aerospace applications. A range of researches on conventional (compaction) powder metallurgy production have widely been studied and reported to produce the composites with uniform microstructure and good mechanical properties [1, 2]. Investigations on the composite production via Powder Injection Moulding (PIM) are quite however limited. The PIM process has been increasingly recognized for the fabrication of high-performance materials according to its low cost for mass production and near-net shape fabrication [3]. The PIM involves 1) powder and binder mixing to prepare feedstocks, 2) injection moulding to produce green parts, 3) debinding and 4) sintering to give finished parts. The process is therefore promising for composite production such as SiC_p-reinforced aluminium composites. In comparison to the liquid route productions for instance semi-solid casting, stir-mixing and liquid infiltration, the PIM with its lower operating (sintering) temperature could suppress the brittle Al_4C_3 formation and reduces wettability problems [4-6]. Previous works on PIMed SiC_p-reinforced aluminium composites have been reported to give uniform microstructure of well-distributed 10 vol.% SiC_p in the aluminium matrix whereas a further increase in SiC_p contents for example 20-40 vol.% has unfortunately resulted in deleterious properties due to large porosity observed along clusters of SiC_p [7, 8]. Moreover, the sintering temperature has to be raised up to 740-780 ^oC, which are excessively high and could provide undesirable phase formation. This research therefore aimed to study mechanical alloying employed in the stage of powder mixing prior to injection moulding and to investigate its effects on sintering of SiC_p-reinforced aluminium composite.

Experimental

Aluiminium (Al-4.5Cu alloy) powder and 30 vol.% SiC_p with average diameters of 86.7 μm and 21.0 μm respectively were ball milled for two hours prior to mechanical alloying using an attrition mill. Mechanical alloying was carried out at 800 rpm for 2, 4, 6, 8, 10 and 12 hrs. The selected mechanical alloying condition was then used for the preparation of feedstocks by mixing with a

multi-component binder at 52% and 55% solid loadings. Powder injection moulding was operated at 170 ^{o}C and 45 MPa injection pressure using a laboratory-scaled, plunger-typed machine. The green samples of 5x5x50 mm^3 dimensions were debound and sintered over 680-740 ^{o}C in a nitrogen atmosphere. Microstructures investigation of green and sintered samples were carried out using OM and SEM coupled with EDX analysis. Green and sintered bulk densities along with macro Vickers hardness were measured. Figure 1 demonstates mechanical alloying and powder injection molding utilized in this research.

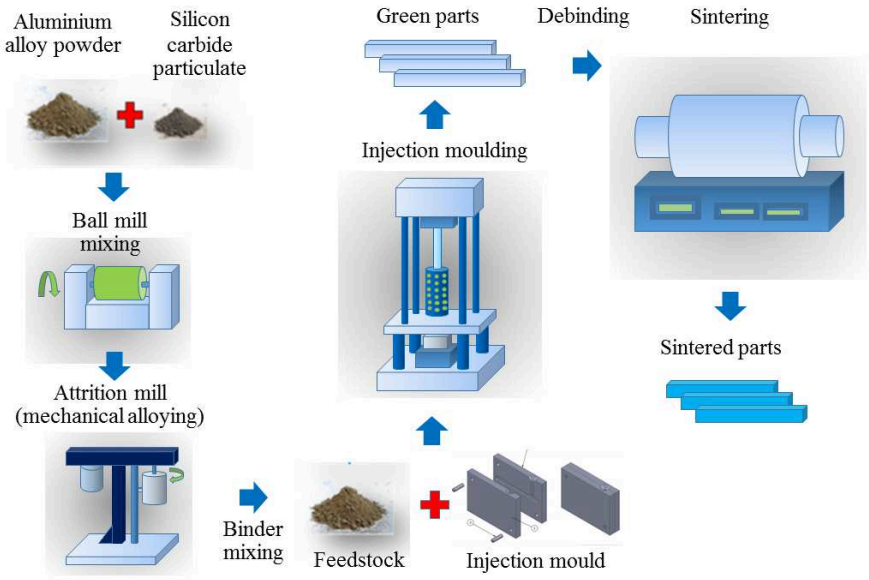
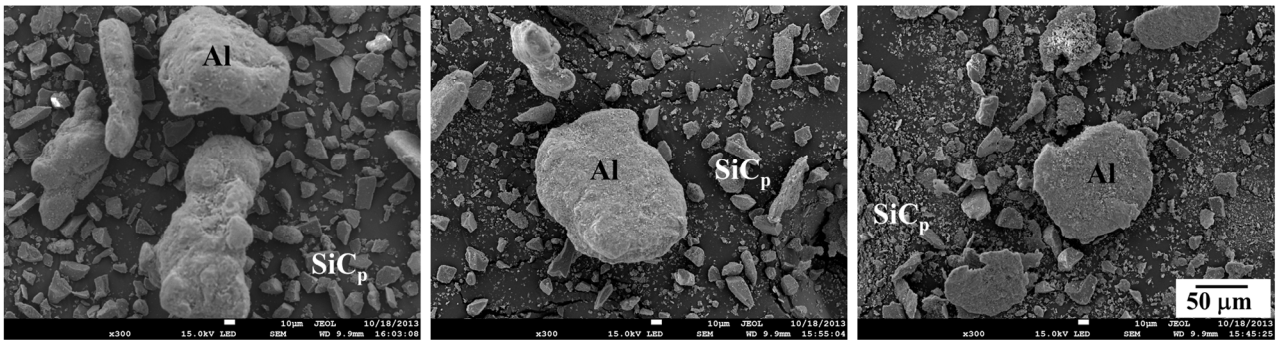


Fig. 1 Mechanical alloying and injection moulding

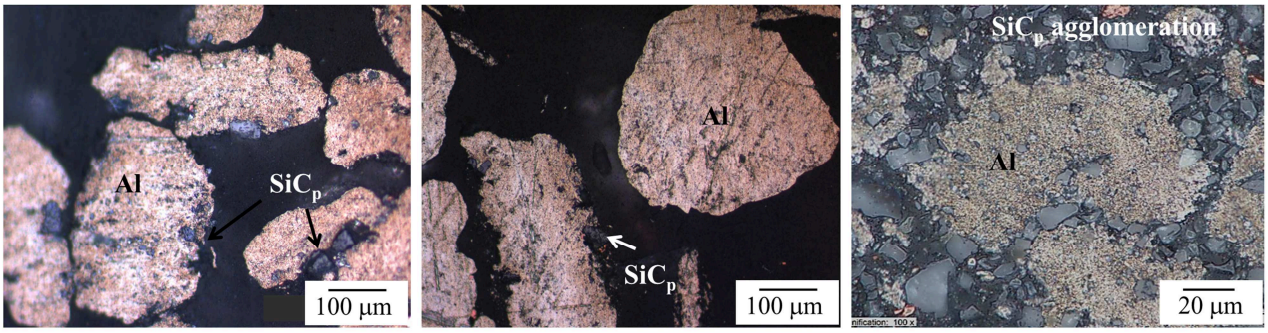
Results

Microstructures. SEM micrographs of aluminium powder and SiC_p after mechanical alloying for 2, 6 and 12 hours are illustrated in Figs. 2 a) – c). Mechanical alloying for 2 hours exhibited no significant change in morphology of aluminium powder in comparison to that of pre-mechanical alloying powders. Only small amounts of SiC_p fragmentation was noticed at this stage. As the mechanical alloying time increased to 6 hours, some of aluminium powder became flatten while SiC_p fragmentation took place at a higher degree. Higher amount of SiC_p was observed both on aluminium powder surface and within the powder interior as depicted in Fig. 3 a). However after mechanical alloying for 8 to 12 hours, SiC_p became very dusty, as confirmed by Fig. 2 c), and only fine SiC_p were observed to be embedded on aluminium powder surface, as demonstrated in Fig. 3 b) respectively. It might be that excessive periods of mechanical alloying might cause breakage of SiC_p into larger amounts of very fine particulate which was separated from larger ones. Therefore mechanical alloying of aluminum powder and SiC_p for 6 hours was preferably selected for the next step of feedstock preparation (binder mixing).



a) 2 hours **b) 6 hours** **c) 12 hours**

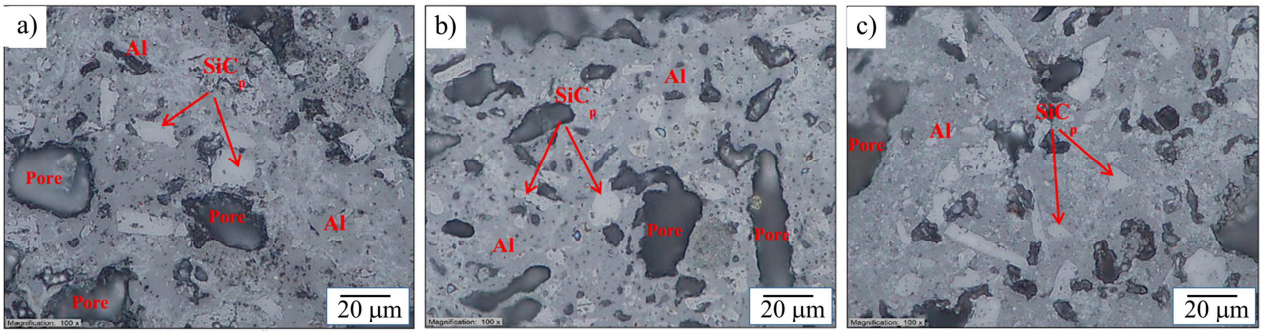
Fig. 2 SEM micrographs showing aluminium powder and SiC_p after mechanical alloying.



a) Mechanical alloying for 6 hours **b) Mechanical alloying for 12 hours** **c) Green microstructure of 55% solid loading**

Fig. 3 Microstructures of mixed powders after mechanical alloying a) for 6 hours and b) 12 hours, and c) green microstructure.

Microstructures of the green samples (after injection moulding) are shown in Fig 3 c), showing smaller sized SiC_p surrounding the larger aluminium powder both embedded in multi-component polymeric binder (dark). Portion of SiC_p was observed within the aluminium powder as a result of mechanical alloying. Porosity was occasionally observed scattering throughout. Moreover, the green microstructure of 55% solid loading comprised greater amounts of solid (aluminium powder and SiC_p) in comparison to that of 52% solid loading.



a) 52% Solid loading, sintered at 700°C

b) 55% Solid loading, sintered at 700°C

c) 55% Solid loading, sintered at 740°C

Fig. 4 Microstructures of sintered parts prepared at 52 and 55% solid loading.

It is noted that samples sintered at 680 °C have failed to remain their shapes and have become into a powder form, while sintering at 700 °C and at higher degrees was feasible. In comparison to previous work [8], it has been reported that sintering of 30 vol. %SiC_p-reinforced aluminium composite without mechanical alloying could start at 740 °C. The sintered microstructures of SiC_p-reinforced aluminium composite with mechanical alloying prepared at 52% and 55% solid loadings are demonstrated in Figs. 4 a) – c). It can be seen that the composite prepared at lower %solid loading provided relatively higher porous microstructure. As the sintering temperature increased from 700°C to 740 °C, densification of the composite was observed at a certain degree, as shown in Figs. 5 b) and c). The sintered microstructure showed large and smaller-sized SiC_p distributed throughout the aluminium matrix.

SEM examination on sintered microstructure revealed some SiC_p embedded in the aluminium matrix and some SiC_p located along micro-porosity scattering throughout, as illustrated in Fig. 5 a). (Noted that gold sputtering was carried out on SEM samples to improve image quality) EDX analysis showed peaks of Al and Cu as the matrix together with Si and C as the reinforcement. Oxygen was present as SiO_2 surface film on SiC_p due to a pre-surface treatment at 1000 °C for 4 hours to increase wettability between SiC_p and aluminium and to suppress brittle Al_4C_3 formation [4-6]. The existence of nitrogen is related to the N_2 sintering atmosphere employed in this research, giving the formation of AlN, which involved in the densification process [9].

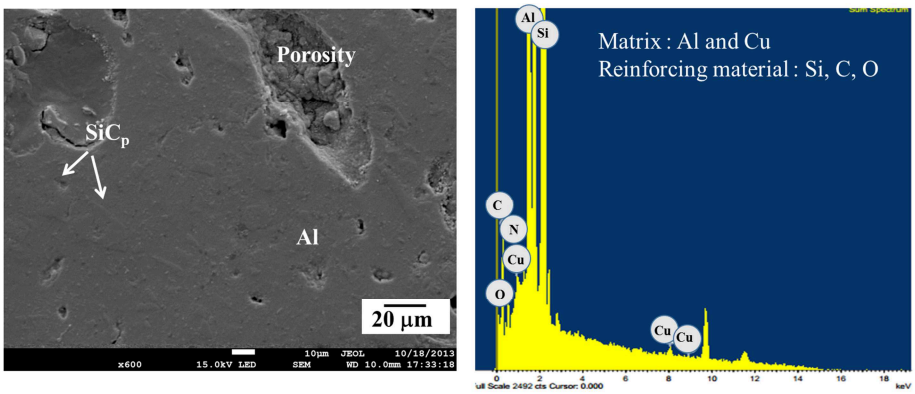


Fig. 5 EDX analysis of SiC_p-reinforced aluminium composite sintered at 740°C.

Table 1: Green properties of green parts prepared at 52 and 55% solid loadings

Properties	52% Solid Loading	55% Solid Loading
Bulk green density ($g.cm^{-3}$)	1.60	1.70
Theorectical bulk green density ($g.cm^{-3}$)	1.94	2.00
Shore D hardness	38.0	46.9
Flexural strength (MPa)	17.5	36.2

Green properties. The green bulk density was found to increase with %solid loading and was noticably lower than the theorectical density determined by considering the rule of mixture as follows;

$$\rho_{c,th} = \rho_{Al}V_{Al} + \rho_{SiC}V_{SiC} + \rho_{Binder}V_{Binder} \quad \text{Eq. 1}$$

where densities of aluminum powder is 2.78 $g.cm^{-3}$[10], SiC_p is 3.20 $g.cm^{-3}$ and polymeric binder is 0.90 $g.cm^{-3}$. V_{Al}, V_{SiC} and V_{Binder} are volume fractions of aluminium powder, silicon carbide and polymeric binder respectively. The results are summarised in Table 1. Shore D hardness and flexural strength also increased with increasing %solid loading, thus indicating better strength and handling.

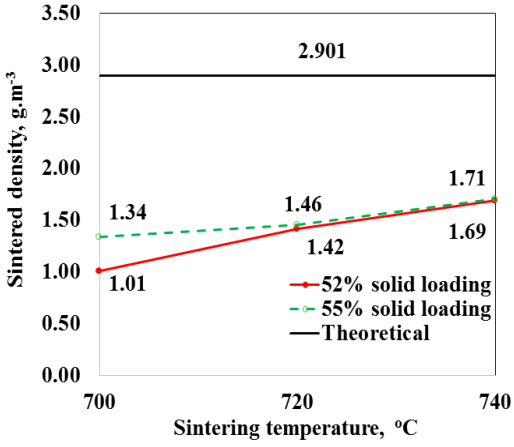


Fig. 6 Sintered bulk density of 30 vol.% SiC_p-reinforced aluminium composite prepared by mechanical alloying.

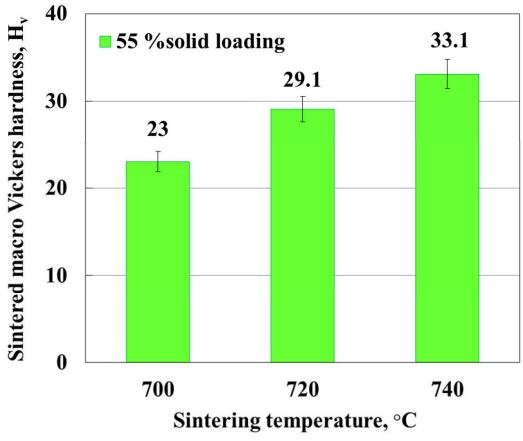


Fig. 7 Macro Vickers hardness of 30 vol.% SiC_p-reinforced aluminium composite prepared by mechanical alloying.

Sintered properties. After sintering, the sintered bulk density tended to increase with increasing sintering temperatures, as shown in Fig. 6. Composites prepared at higher solid loading (55%) again provided the higher sintered bulk density values than those obtained from the composites preparted at 52% solid loading. However these measured values are much lower than the theoretical sintered density of 2.901 $g.cm^{-3}$, obtained by the rule of mixture from Eq. 1, without $\rho_{Binder}V_{Binder}$ term.

Macro Vickers hardness values also provided a similar trend to that of sintered density, as demonstrated in Fig. 7. The highest hardness value of 33.1 H_v was achieved when sintering was operated at the highest sintering temperature at 740 ^oC obtained from composite prepared at 55% solid loading. It was noted that the composite prepared at 52% solid loading became broken after hardness testing. This might be due solely to large amount of porosity observed in the sintered microstructure where the structure could not sustain the deformation load. It is noted that large porosity observed from sintered microstructures of both 52% and 55% solid loadings is associated with SiC_p agglomeration along periphery of aluminium powder, as seen in Fig. 3 c), which made sintering more difficult. Falling out of SiC_p was noticed during metallographic preparation.

Discussion

According to previous works on powder injection moulding of SiC_p-reinforced aluminium composite [7, 8], it was shown that increasing SiC_p contents from 10 vol.% to 40 vol.% led to increasing the onsets of sintering temperatures from 660 ^oC to 780 ^oC respectively. This might be related chiefly to higher amounts of SiC_p contents in playing a key role as a heat sink effect due to its high melting point of ~2730 ^oC in comparison to aluminium alloy used in this research, where its sintering temperature was suggested at only 550 ^oC. Increasing SiC_p contents therefore required higher sintering temperature to facilitate liquid phase sintering along boundaries of aluminium-aluminium and aluminium-SiC_p in this case. Higher viscous flow allowed certain amount of the aluminium melt to fill along such boundaries to give a significant degree of sintering shrinkage. Although the SiC_p-reinforced aluminium composites could be sintered via the aforementioned PIM technique, porosity was routinely observed across the microstructures, especially at higher SiC_p additions. Although higher sintering temperature helped to support liquid phase sintering, however too high temperature might led to excessive shrinkage, warping and undesirable phase formation, which subsequently resulted in chemical and mechanical degradation of the composites.

Mechanical alloying employed in this research imparted SiC_p engulfment into deformable aluminum matrix as shown in Figs. 2) and 3). Plastic deformation rendered flattening of aluminium powder whereas fragmentation seemed to dominate for SiC_p during mechanical alloying. Though successful mechanical alloying involved deformation/cold-welding/fracture mechanisms to give homogeneously mixed globules of reinforcement and aluminium matrix [11], SiC_p-fragmentation has been quite severely dusty by using the attrition milling employed in this research when milling time was higher than 6 hours. It might be that, for the selected mechanical alloying speed at 800 rpm and high amounts of reinforcement, SiC_p fragmentation was possibly much faster than deformation of softer aluminium powder and then became a dominant mechanism over longer period of mechanical alloying. To certain degree of mechanical alloying, cold-welding of smaller sized SiC_p into deformable aluminium powder subsequently took place and thus partly increased interfaces between aluminium and SiC_p. Mechanical alloy time was then selected at 6 hours to give partly mixed powders at this stage for injection moulding. With mechanical alloying, sintering of PIMed 30 vol.% SiC_p-reinforced aluminium composite could therefore be feasible at 700 ^oC. This onset of the sintering temperature is significantly lower than sintering temperature at 740 ^oC of non-mechanical alloying PIMed 30 vol.% SiC_p-reinforced aluminium composite, where sintered density and hardness are comparable [8]. It can be explained that mechanical alloying increased the internal energy of the particles [12], plausibly by means of increasing SiC_p-aluminium interfaces. Changes in particle sizes (both in aluminium powder and SiC_p) as well as modified surface characteristics also affected chemical behaviour of the powders [13], which substantiated liquid-phase sintering.

Moreover, increasing sintering temperature from 700 ^oC up to 740 ^oC in this research increased sintering kinetics by increasing the liquid amount to fill into microvoids among aluminium powder and SiC_p. Shrinkage has been measured to be approximately 15-20% over 700 ^oC to 740 ^oC sintering temperatures. Furthermore, increasing in %solid loading from 52% to 55% again increased more solid contacts between aluminium powder and SiC_p. Thus, increasing both sintering temperature and % solid loading offered enhanced sintered density and hardness.

Conclusions

For 30 vol.% SiC_p-reinforced aluminium composite, mechanical alloying via attrition milling for 6 hours at 800 rpm could offer good distribution of SiC_p within aluminium matrix. Mechanical alloying facilitated the sintering of the composite by increasing interfaces between aluminium powder and SiC_p, resulting in lowered effective sintering temperature in comparison to non-mechanical alloying composite. Improved density and hardness were obtained by increasing sintering temperature from 700 ^oC to 740 ^oC and increasing %solid loading from 52% to 55%.

Acknowledgements

Thanks are due to the School of Metallurgical Engineering, Suranaree University of Technology and the Metallurgy and Materials Science Research Institute, Thailand, for facility and technical supports. The National Research Council of Thailand (NRCT) is accredited for research funding.

References

[1] A.H. Tavakoli, A. Simchi, S.M. Seyed Reihani, Study of the compaction behavior of composite powders under monotonic and cyclic loading, Composites Sci. and Tech. 65 (2005) 2094-2104.

[2] K.Yamaguchi, N. Takakura, S. Imatani, Compaction and sintering characteristics of composite metal powders, J. of Mater. Proc. Tech. 63 (1997) 364-369.

[3] Loh, N.H., S.B. Tor, K.A. Khor, Production of metal matrix composite part by powder injection molding, J. of Mater. Proc. Tech.108 (2001) 398-407.

[4] J.-C. Lee, J.-P. Ahn, J.-H. Shim, Z. Shi, H.-I. Lee, Control of the interface in SiC/Al composites. Scrip.Mater. 41 (1999) 895-900.

[5] L. Zhang, X.-H. Qu, B.-H. Duan, X.-B. He, M.-L. Qin, S.-B. Ren, Wettability and pressureless infiltration mechanism in SiC-Cu systems, Inter. J. of Min., Metal. and Mater.16 (2009) 327-333.

[6] M. Boonma, P. Subarporn, R. Bobuangern, T. Patthanakitdamrong, T. Thuanwong, T. Patcharawit, Process parameter-microstructure-mechanical property relations of SiC_p-reinforced aluminum composites produced by powder-injection casting, J. of Met., Mater. and Min. 21 (2011) 85-93.

[7] T. Patcharawit, B. Inpanya, N. Chuankrerkkul, Silicon carbide-reinforced aluminum matrix composite fabricated by powder injection molding. in The 2nd International Conference on Process Engineering and Advanced Materials (ICPEAM2012). June 2012. Kualar Lumpur, Malaysia.

[8] T. Patcharawit, P. Tongkhon, A. Wiangsamut, P. Auisungnoen, N. Chuankrekkuk, Powder Injection Molding of 20-40 Vol.% Silicon Carbide Particulate-Reinforced Aluminum Composites, App. Mech. and Mater. 376 (2013) 17-22.

[9] T. Pieczonka, T. Schubert, S. Baunack, B. Kieback, Dimensional behaviour of aluminium sintered in different atmospheres, Mater. Sci. and Eng. A, 478 (2008) 251-256.

[10] J.M. Martín, F. Castro, Liquid phase sintering of P/M aluminium alloys: effect of processing conditions, J. of Mater. Proc. Tech. 143-144 (2003) 814-821.

[11] J.B. Fogagnolo, F. Velasco, M.H. Robert, J.M. Torralba, Effect of mechanical alloying on the morphology, microstructure and properties of aluminium matrix composite powders, Mater. Sci.and Eng. A, 342 (2003) 131-143.

[12] H. Arik, Effect of mechanical alloying process on mechanical properties of α-Si_3N_4 reinforced aluminum-based composite materials, Mater. & Design, 29 (2008) 1856-1861.

[13] S.A. Barseghyan, Y. Sakka, Mechanochemical activation of aluminum powder and synthesis of alumina based ceramic composites, Ceramics Inter. 39 (2013) 8141-8146.

Applied Mechanics and Materials Vol. 597 (2014) pp 109-112
© (2014) Trans Tech Publications, Switzerland
doi:10.4028/www.scientific.net/AMM.597.109

Hydrothermal synthesis and upconversion properties of Yb^{3+}, Tm^{3+} co-doped Gd_6MoO_{12} phosphor with regular morphologies

Jiayue Sun* ,Bing Xue, Qiumei Di, Qiguang Xu, Liu Han

School of Science, Beijing Technology and Business University, Beijing, 100048, China

*Email: jiayue_sun@126.com

Keywords: Hydrothermal synthesis; morphologies; upconversion luminescence

Abstract. Yb^{3+}, Tm^{3+} co-doped Gd_6MoO_{12} phosphors were prepared by the hydrothermal method. After tuning the PH value and EDTA, phosphors present different morphologies including hexagonal prisms, spindles, and spheres. Under 980nm excitation, the upconversion luminescence properties of the as-prepared phosphors are studied based on changing the synthesis condition. It is found that usage of EDTA and pH changing both play crucial key in the formation of morphology. Pumping power on the UC luminescence properties and level diagram mechanism of Gd_6MoO_{12}:Yb^{3+}/Tm^{3+}phosphor have also been discussed.

Introduction

In recent years, lots of attentions have been paid to infrared to visible up-converted luminescence (UCL) in rare earth ions doped phosphors, due to their potential applications [1]. However, such applications are highly dependent on size, morphology and other fundamental factors [2], not only their chemical composition. Many reports on rare earth doped tungstate and molybdate matrix have been studied [3]. These materials usually been synthesized through high temperature solid method, sol–gel method and hydrothermal reaction method. By comparison, hydrothermal treatment has advantages in preparing various inorganic materials with less pollution, high purity, and controllable morphology [4]. In the synthesis process, the varying of the conditions has a significant effect on the morphology of the final samples, further influencing luminescence properties.

Experimental

The $Gd_{5.74}MoO_{12}$:$0.25Yb^{3+}$, $0.01Tm^{3+}$ samples were prepared by hydrothermal method. Starting materials are $(NH_4)_6Mo_7O_{24}\cdot 4H_2O$ (99.0%), Tm_2O_3 (99.99%), Gd_2O_3 (99.99%), Yb_2O_3 (99.99%) HNO_3 (65%-68%) and $C_{10}H_4N_2O_8Na_2\cdot 2H_2O$ (EDTA) (A.R.).Stoichiometric Tm_2O_3, Gd_2O_3 and Yb_2O_3were separately dissolved in dilute HNO_3. EDTA and $Mo^{6+}$are prepared by the stoichiometric $C_{10}H_4N_2O_8Na_2\cdot 2H_2O$ and $(NH_4)_6Mo_7O_{24}\cdot 4H_2O$ separately dissolved in the deionized water (EDTA/Ln^{3+} =1). Then, the transparent three rare earth nitric acid solution and the Mo^{6+} were mixed. Finally, the mixed solution was transferred into a 50 ml Teflon bottle and maintained at the temperature of 200°C for20h.As cooled to room temperature, the precipitates were separated, washed and dried at 80°C for 12h.The structures were analyzed by Shimadzu model XRD-6000 X-ray powder diffraction. The upconversion emission was recorded by using FluoroLog-3 spectrophotometer equipped with an external power-controllable 980nm semiconductor laser. The morphologies were recorded by scanning electron microscope.

Results and discussion

Figure.1 (I) shows the typical XRD patterns of the prepared products synthesized at the pH of 3(a), pH=9 (b) and the addition of EDTA (c). From figure, we can observe that the peaks are well agreed with the literature of JCPDS Card (No. 24-1085) of Gd_6MoO_{12}, which indicates the crystal lattice of the Gd_6MoO_{12} host can be obtained.

Figure.1 (II-IV) shows the SEM images of the $Gd_{5.74}MoO_{12}$:0.25Yb^{3+}, 0.01Tm^{3+}samples under different synthesis conditions. Figure.1 (II) presents the morphology of long hexagonal prism. The average length size of them is about 500μm. When pH increased up to 9, the spindle like shape was obtained (figure.1 (III)). The above information indicates that pH is responsible for the uniform morphology.

The crystal growth process has already been extensively studied in the past decade [5]. As pH increases up to alkalinity condition, the spindles appeared indicates the growth of length facets and the side facets had been prevented. From figure.1 (IV), the sphere morphology was obtained in pH=3/EDTA condition, which indicates that sequestering effects of EDTA on all directions are uniform.

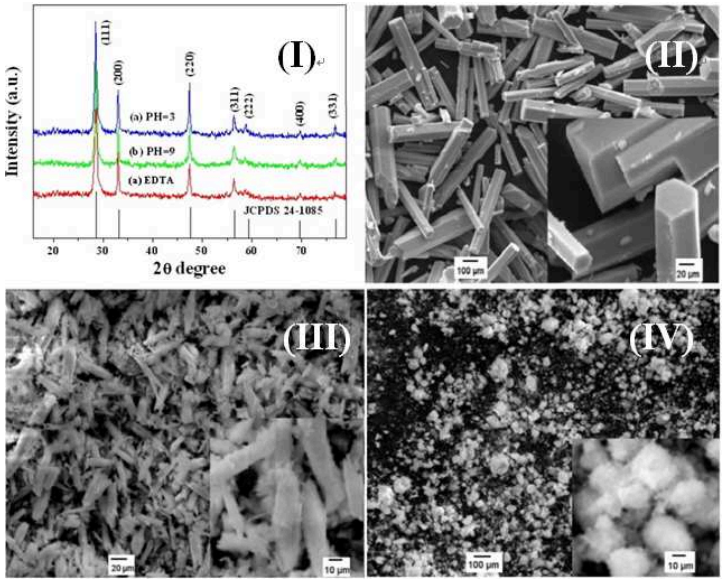


Figure.1 (I) X-ray diffraction patterns of Gd_6MoO_{12}:Yb^{3+}/Tm^{3+}obtained at different conditions: (a) pH=3, (b) pH=9, (c) pH=3/EDTA and their corresponding SEM images.

Figure.2 (sample a-c) shows the UCL spectra of different morphology crystals. Under the excitation of 980nm, figure.2 (a) presents the relatively stronger red and blue emission compared with the figure.2 (b, c), this is due to the prisms have higher crystallinity than spheres and spindles and lower defect concentrations. In this paper, the defects of samples (b and c) can be observed from their tough surface. This indicates that hexagonal prism is better than other morphologies to produce high visible emission in this paper.

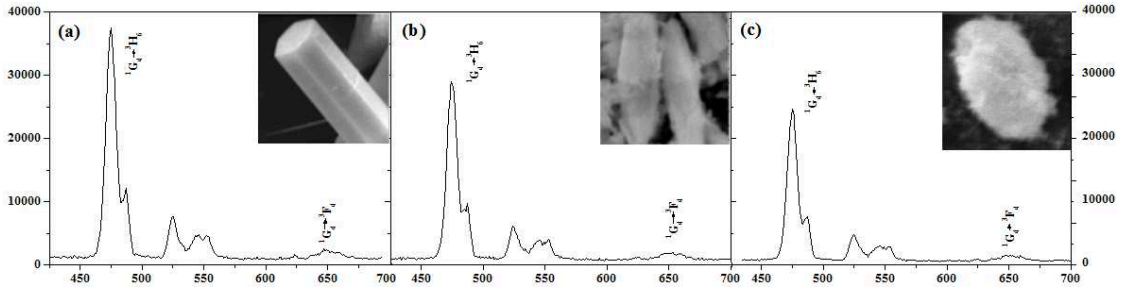


Figure.2 UCL spectra pumped by a 980 nm laser diode for three synthesize conditions: (a) pH=3; (b) pH=9; (c) pH=3/EDTA

To understand the pump power density on the luminescence properties, the pump power dependent UC curve had been given. In figure.3, the two photons process corresponds to the red emission [6]. The calculated blue emission is a two photons process, which is deviating from the typical three photons process; this can be due to the competition between the linear decay and up conversion of the excited states.

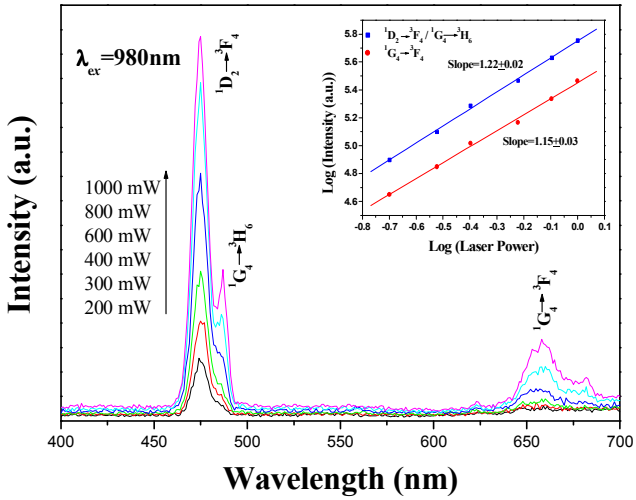


Figure.3 Power dependence of UCL intensities of $^1G_4 \rightarrow {}^3H_6$, $^1D_2 \rightarrow {}^3F_4$ and $^1G_4 \rightarrow {}^3F_4$ emissions of sample (a) under 980 nm laser diode pump.

The mechanism of Yb^{3+} as sensitizer and Tm^{3+} activator UC luminescence system had been researched widely [7].The relative diagram can be seen from figure.4.

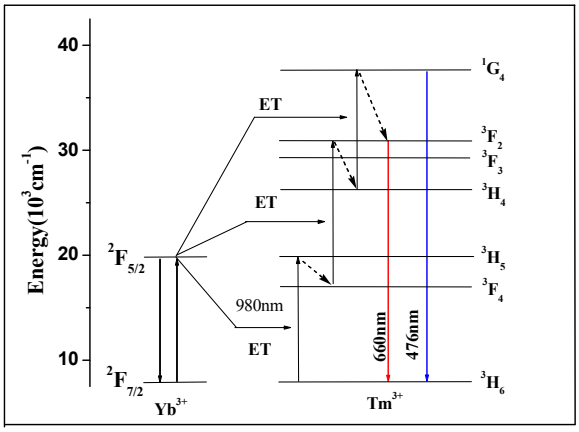


Figure.4 Schematic energy levels of Yb^{3+} and Tm^{3+} ions in the as-prepared $Gd_6MoO_{12}:Yb^{3+}/Tm^{3+}$ sample.

The three photons process of blue emission produced by Tm^{3+} can be explained by the three successive energy transfer from Yb^{3+} to Tm^{3+} and the two photons process of red emission by the two successive energy transfer from Yb^{3+} to Tm^{3+}. According to the Pollnauetal's report [8], the value of n deviate the typical data is due to thecompetition between the linear decay and up conversion of the excited states.

Conclusion

In summary, the crystal ofYb^{3+}/Tm^{3+} co-doped Gd_6MoO_{12} had been synthesized by the hydrothermal method. According to changing the reaction condition (pH, EDTA), the various morphologies and different luminescence properties had been researched. The different morphologies illustrated that pH and EDTA have played a different role on the crystal growth. The final results demonstrated that the hexagonal prisms morphology has the strongest luminescence emission due to its higher crystallinity. Further, the mechanism of the UC luminescence had been given also.

Acknowledgements

This work was financially supported by the National Natural Science Foundation of China (No. 20976002), the Beijing Natural Science Foundation (No. 2122012), Key Projects for Science and Technology of Beijing Education Commission (KZ201310011013), Project of Transformation and Industrialization of College Scientific & Technological Achievements, and Projects of the combination of Manufacture, Education & Research of Guangdong Province (No.2011B090400100), Graduate Student Scientific Research and Academic Innovation Project Funding of Beijing Technology and Business University.

References

[1] J. Li, Z.D. Hao, X. Zhang, Y.S. Luo, J.H. Zhao, S.Z. Lü, J. Cao, J.H. Zhang, Hydrothermal synthesis and upconversion luminescence properties of β-$NaGdF_4:Yb^{3+}/Tm^{3+}$ andβ-NaGdF4:Yb^{3+}/Ho^{3+}, J. Colloid Interface Sci.,392 (2012)206-212.

[2]J.Y. Sun, J.B. Xian, H.Y. Du, Hydrothermal synthesis of BaYF5:Yb3+/Er3+ upconversion luminescence submicrospheres by a surfactant-free aqueous solution route, J. Phys. Chem. Solids, 72 (2011) 207-213.

[3]Z.G. Xia, W. Zhou, H.Y. Du, J.Y. Sun, Synthesis and spectral analysis of Yb3+/Tm3+/Ho3+-doped Na0.5Gd0.5WO4 phosphor to achieve white upconversion luminescence, Mater. Res. Bull., 45 (2010) 1199-1202

[4] H.Y. Du, J.F. Sun, Z.G. Xia, J.Y. Sun,Luminescence Properties of $Ba_2Mg(BO_3)_2:Eu^{2+}$Red Phosphors Synthesized by a Microwave-Assisted Sol-Gel Route,J. Electrochem. Soc.156 (2009) 361-366

[5]C.X. Li, Z.W. Quan, J. Yang, P.P. Yang, J. Lin, Highly uniform and monodisperse β-$NaYF4:Ln^{3+}$ (Ln = Eu, Tb, Yb/Er, and Yb/Tm) hexagonal microprism crystals: hydrothermal synthesis and luminescent properties,Inorganic Chemistry, 46 (2007) 6329-6337.

[6]L.J. Gong,M. Ma, C.F. Xu, X.J. Li, S.P. Wang, J.G. Lin, Q.B. Yang, Multicolor upconversion emission of dispersed ultrasmall cubic Sr_2LuF_7 nanocrystals synthesized by a solvothermal process, J.Lumin., 134 (2013) 718-723.

[7]T. Jiang, W.Y. Song, S.S. Liu, W.P. Qin,Synthesis and upconversion luminescence properties study of NaYbF4:Tm3+ crystals with different dopant concentration,J. Fluorine Chem.,140 (2012) 70-75.

[8] M. Pollnau, D.R. Gamelin, S.R. Lüthi, H.U. Güdel, M.P. Hehlen, Power dependence of upconversion luminescence in lanthanide and transition-metal-ion systems, Phys. Rev. B: Condens. Matter Mater. Phys., 61(2000) 3337-3346.

Applied Mechanics and Materials Vol. 597 (2014) pp 113-116
© (2014) Trans Tech Publications, Switzerland
doi:10.4028/www.scientific.net/AMM.597.113

A First-Principles Study of electron-phonon coupling of OsB_2

Yueqin Wang[a*], Juan Gao[b], Shaoping Yan[c]

School of Mathematics and Physics, Anhui University of Science and Technology, Huainan 232001, China

[a]yueqin@mail.ustc.edu.cn, [b]gaojuan800@sina.com, [c]spyan581@163.com

Keywords: OsB_2, first-principles, electron-phonon coupling, superconductivity

Abstrct: We investigated the lattice dynamics and electron-phonon coupling (EPC) of superhard material OsB_2 by first-principles linear response calculations. The calculated EPC parameters for the optical phonon modes at Γ indicate that the heavy Os atoms play the most important role in deciding the superconducting behavior, and there are sizeable contributions from lighter B atoms to EPC. Our calculated EPC constant is 0.42, and the estimated superconducting transition temperature T_c is 2.1 K using the Coulomb pseudopotential μ^*=0.125, in excellent agreement with the experimental ones.

Introduction

Hard materials are of great interest due to their important industrial applications ranging from abrasives and cutting tools to scratch-resistant coatings. Some potential hard materials such as C_3N_4, BC_2N, and B_6O have been synthesized, but they must be synthesized under extreme high pressure and high temperature, making them expensive as like *c*-BN. Since the successful synthesis of the ultra-incompressible hard material OsB_2 under ambient pressure,[1] there has been a renewed interest in the study of metal diborides. The discovery of superconductivity in boron-doped diamond has stimulated intensive research on the superconductivity of superhard materials.[2] Experiments show that OsB_2 becomes superconducting below 2.1 K.[3] Yogesh *et al*. have been reported that OsB_2 is moderate-coupling superconductors with electron-phonon constants $\lambda \approx 0.4$-0.5[4]. Although the mechanical and electronic properties of OsB_2 have been investigated theoretically in recent years,[4-7] there is no theoretical work on its lattice dynamics and superconductivity. In this Letter, we present a first-principles study on its lattice dynamics and superconductivity, and our calculated EPC and estimated superconducting transition temperature are in excellent agreemnt with the experimental ones.[3]

Calculation Methods

We performed our calculations within the plane-wave implementation of the generalized gradient approximation (GGA) to density-functional theory (DFT) in the PWscf package.[8] We used Vanderbilt ultrasoft potential with Perdew-Wang 91 exchange correction. For the determination of the self-consistent potential, conjugate-gradient algorithm is used. The kinetic energy cutoff of the plane wave basis is 50 hartree. The *k*-point integration for construction of the induced charge density, geometrical optimization, and calculation of the dynamical matrix is performed over 6×12×8 Monkhorst-Pack grid, and a finer 12×20×16 grid is used in the phonon linewidth calculation. The dynamical matrices and phonon linewidth are computed on a 2×4×2 *q*-point mesh, and real-space force constants are then found by Fourier transform of the dynamical matrices.

The phonon and EPC calculations are carried out using density-functional perturbation theory in the linear response. The electron-phonon spectral distribution function (Eliashberg function) is defined as,

$$\alpha^2 F(\omega) = \frac{1}{2\pi N(E_F)} \sum_{\mathbf{q}\nu} \frac{\gamma_{\mathbf{q}\nu}}{\omega_{\mathbf{q}\nu}} \delta(\omega - \omega_{\mathbf{q}\nu}) \tag{1}$$

Where $\gamma_{\mathbf{q}\nu}$ and $\omega_{\mathbf{q}\nu}$ stand for the phonon linewidth and frequency of a phonon mode ν with momentum **q**. Within the phonon mediated theory of superconductivity, T_c can be estimated using Allen-Dynes modification on McMillan's solution[9] of the Eliashberg equation,

$$T = \frac{\omega_{ln}^{ph}}{1.20} \exp\left[-\frac{1.04(1+\lambda)}{\lambda - \mu^*(1+0.62\lambda)} \right] \tag{2}$$

Where μ^* describes the effective electron-electron repulsion.

Calculation Results Analysis

OsB_2 has an orthorhombic lattice (space group *Pmmn*, No. 59) (in Fig. 1) with the experimental lattice parameters *a*=4.683 Å, *b*=2.872Å, and *c*=4.076 Å.[10] We first optimize the lattice constant and internal coordinates to get a relaxed structure for OsB_2. Our calculated equilibrium lattice parameters are *a* =4.695 Å, *b* =2.874 Å, and *c* =4.082 Å, in good accordance with experimental data.

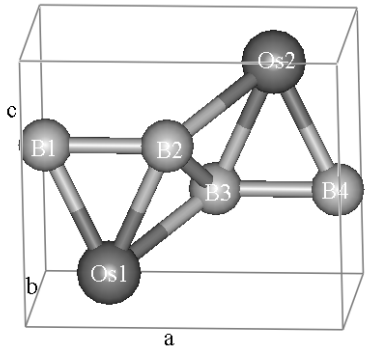


Fig. 1 The crystal structure for OsB_2.

The zone-center phonon modes are of special importance. They play a crucial role in the EPC for some metal compounds and some doped semiconductor systems. The unit cell of OsB_2 contains six atoms, which give rise to a total of 18 phonon branches. We list the vibration modes, symmetries and frequencies of the 15 zone-center optical phonons in Table 1. The three groups are Raman-active (mode 1-9), infrared-active (mode 10-14) and silent modes(mode 15), respectively. All these optical phonon modes within the atoms vibrate along the *c* axis, easily yield vacancies in B-B sheets. The highest frequency at Γ is a onefold B_{1u} mode, contributed by the vibration of B atom along the *c* axis. The three lowest frequency optical modes (<300 cm^{-1}) are dominated by the motion of heavy Os atoms, while the high frequency optical modes (>400 cm^{-1}) are dominated by the motion of lighter B atoms. The EPC constant for each optical phonon mode at Γ is listed in the last row in Table 1. We see that the largest couplings are contributed by the vibrations of Os atom along the *c* axis. Although the coupling in each optical phonon mode of B atom vibration is small, the summation of these couplings has a sizeable contribution to EPC.

The calculated phonon dispersion curve and phonon density of states for OsB_2 are shown in Fig. 2. We notice that the phonon modes are separated to two groups in frequency throughout the whole BZ. Namely, the soft group with frequencies below 300 cm^{-1} and the hard group with frequencies between 400 cm^{-1} and 900 cm^{-1}. We can see that the phonon band structure is doubly-degenerated along the N-K direction, indicating a *p* character throughout the Brillouin Zone. The phonon density of states shows that OsB_2 has a sizable phonon hardening effect, because of the strong B-B covalent bonding. The Eliashberg function $\alpha^2F(\omega)$ plot is shown in Fig. 3. The large peaks in the low-frequency part and the high-frequency part of the total $\alpha^2F(\omega)$ indicate a strong EPC interaction. Detailed analysis shows that the EPC derived from Os-vibrations-related modes is stronger than those of B-vibrations-related, consistent with the results of EPC parameters analysis at Γ.

Table 1 Zone-center optical phonon modes of OsB_2. The involved atoms in each mode and their vibration directions ($\perp$ for out-of-plane, || for in-plane) are listed. f and λ represent the frequency and EPC constant, respectively.

Mode	Symmetry	Vibrations	f [cm^{-1}]	λ
1	B_{3g}	Os$_\perp$	103.1	0.086
2	B_{2g}	Os$_\perp$	170.3	0.080
3	A_g	Os$_\perp$	209.8	0.084
4	B_{2g}	B$_\perp$	577.5	0.004
5	B_{1g}	B$_\perp$	634.0	0.022
6	B_{3g}	B$_\perp$	671.9	0.000
7	A_g	B$_\perp$	687.3	0.066
8	B_{2g}	B$_\perp$	730.2	0.008
9	A_g	B$_\perp$	747.1	0.038
10	B_{2u}	B$_\perp$	409.5	0.000
11	B_{3u}	B$_\perp$	419.3	0.000
12	B_{1u}	B$_\perp$	573.4	0.024
13	B_{3u}	B$_\perp$	691.2	0.000
14	B_{1u}	B$_\perp$	863.6	0.006
15	A_u	B$_\perp$	467.2	0.000

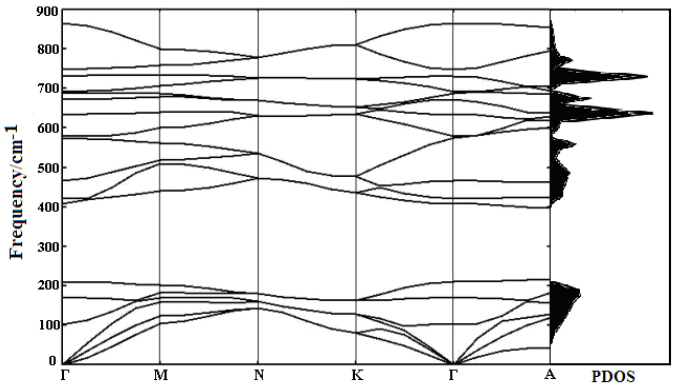


Fig. 2 Phonon band structure and phonon density of states for OsB_2. Γ=(0,0,0), M=(0,0.5,0), N=(0.5,0.5,0), K=(0.5,0,0), and A=(0,0,0.5).

The total electronic density of states (DOS) for OsB_2 are plotted in Fig. 4. Our calculated total electronic DOS at the Fermi level for OsB_2 is $N(E_F)$=0.62 states/(eV·f.u.) (f.u.=formula unit), well compared with the values estimated by previously band structure calculation $N(E_F)$=0.59 states/(eV·f.u.).[11] We can see that the Fermi levels of OsB_2 is locate nearly at the valley in DOS profile. This feature may explain the small T_c in OsB_2. The calculated average frequency ω_{ln}^{ph} is 462.2 cm^{-1}. Our calculated EPC constant is 0.42, and the estimated T_c is 3.8(1.6) K for μ^*=0.1(0.15). We obtain exactly the Coulomb pseudopotential μ^*=0.125 when T_c=2.1 K.

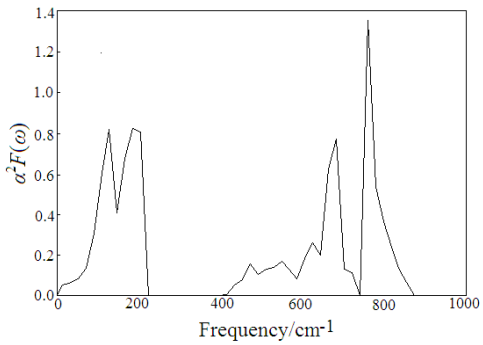


Fig. 3 The Eliashberg function $\alpha^2F(\omega)$ of OsB_2.

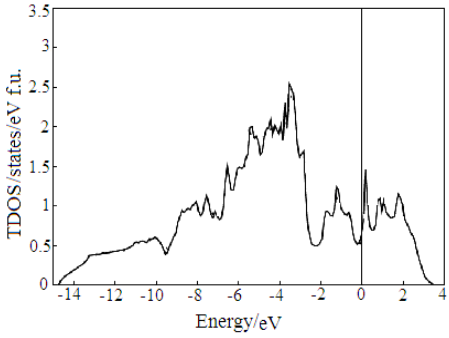


Fig. 4 The total electronic density of states of OsB_2.

Summary

We have calculated the lattice dynamics and superconductivity of OsB_2 using density-functional perturbation theory in the linear response. The superconductivity in OsB_2 is found to be mediated by the EPC, consistent with experimental result. The Os-vibrations-related phonon modes contribute most part to EPC, and the B-vibrations-related phonon modes give sizable contributions. The calculated EPC constant and T_c are in excellent agreement with the experimental ones. To entirety clarify the origin of superconductivity and phonon contribution requires much futher experimental work on the lattice dynamics and electron-phonon interaction of the superconductor itself.

References

[1] R. W. Cumberland et al., Osmium Diboride, An Ultra-Incompressible, Hard Material, J. Am. Chem. Society, 127 (2005) 7264-7265.

[2] X. J. Chen, V. V. Struzhkin, Z. G. Wu, M. Somayazulu, J. Qian, S. Kung, A. N. Christensen, Y. S. Zhao, R. E. Cohen, H. Mao and R. J. Hemley, Hard superconducting nitrides, Proc. Natl. Acad. Sci., 102 (2005) 3198–3201.

[3] J. M. Vandenberg, B. T. Matthias, E. Corenzwit and H. Barz, Superconductivity of some binary and ternary transition-metal borides, Mat. Res. Bull. 10 (1975) 889-894.

[4] Y. Singh, A. Niazi, M. D. Vannette, R. Prozorov and D. C. Johnston, Superconducting and normal-state properties of the layered boride OsB2, Phys. Rev. B 76 (2007) 214510.

[5] M. M. Zhong, X. Y. Kuang, Z. H. Wang, P. Shao, L. P. Ding, X. F. Huang, Phase stability, mechanical properties, hardness, and possible reactive routing of chromium triboride from first-principle investigations, J. Chem. Phys. 117 (2013) 10643-10652.

[6] E. Deligoz, K. Colakoglu, Y. O. Ciftci, Lattice dynamical and thermodynamical properties of ReB2, RuB2, and OsB2 compounds in the ReB2 structure, Chin. Phys. B, 21 (2012) 106301.

[7] J. Wang, Y. J. Wang, Mechanical and Electronic Properties of 5d Transition Metal Diborides MB2 (M=Re, W, Os, Ru), J. Appl. Phys. 105 (2009) 083539(6).

[8] Information on http://www.pwscf.org/.

[9] W. L. McMillan, Transition temperature of strong-coupled superconductors, Phys. Rev. 167 (1968) 331-344.

[10] R. B. Roof Jr., and C. P. Kempter, New orthorhombic phase in the Ru-B and Os-B systems, J. Chem. Phys. 37 (1962) 1473-1476.

[11] Z. Y. Chen, H. J. Xiang, J. L. Yang, J. G. Hou and Q. S. Zhu, Structural and electronic properties of OsB_2: A hard metallic materials, Phys. Rev. B 74 (2006) 012102(4).

Applied Mechanics and Materials Vol. 597 (2014) pp 117-120
© (2014) Trans Tech Publications, Switzerland
doi:10.4028/www.scientific.net/AMM.597.117

Photoluminescence and energy transfer from Sm^{3+} to Eu^{3+} in $Na_3YSi_2O_7$ phosphor for light-emitting diodes

Jiayue Sun*, Dianpeng Cui, Qiumei Di, Qiguang Xu, Liu Han

School of Science, Beijing Technology and Business University, Beijing, 100048, China

*Email: jiayue_sun@126.com

Keywords: Rare earth, Energy transfer, Luminescence materials, Light emitting diode

Abstract. A series of $Na_3YSi_2O_7$: Eu^{3+}, Sm^{3+} samples have been synthesized via solid-state reaction technique. The phase structure and luminescence properties are characterized using powder X-ray diffraction, photoluminescence excitation and emission spectra. Effective energy transfer occurs from Sm^{3+} to Eu^{3+} and Sm^{3+}/Eu^{3+}-codoped $Na_3YSi_2O_7$ shows more intense red light compared to that of Eu^{3+}-doped sample under UV light excitation.

Introduction

Sakamoto et al. discussed the potential application for $Na_3YSi_2O_7$:Eu^{3+} phosphor in fluorescent lamps and white LED [1]. However, the luminescence efficiency remains relatively low due to the weak absorption probability of f → f transitions of Eu^{3+} [2]. One of the popular ways to overcome such difficulty is to co-dope trivalent rare-earth ions, which can absorb the excitation energy and transfer the absorbed energy to Eu^{3+}. Because the energy gap between the $^4G_{5/2}$ level of Sm^{3+} and the $^5D_0$ level of Eu^{3+} is small (approximately 600 cm^{-1}), it makes possible the phonon-assisted energy transfer from the $^4G_{5/2}$ level of Sm^{3+} to the $^5D_0$ level of Eu^{3+} [3,4]. In this work, Sm^{3+}/Eu^{3+} co-doped $Na_3YSi_2O_7$ samples have been synthesized and characterized by virtue of corresponding instruments. Luminescence properties and energy transfer behavior have been discussed in detail.

Experimental

A series of $Na_3(Y_{1-x}Eu_x)Si_2O_7$ (x = 0.04, 0.08, 0.12, 0.16, 0.20), $Na_3(Y_{1-y}Sm_y)Si_2O_7$ (y = 0.01, 0.03, 0.05, 0.07, 0.09) and $Na_3(Y_{0.84-y}Eu_{0.16}Sm_y)Si_2O_7$ (y = 0.01, 0.03, 0.05, 0.07, 0.09) were prepared via solid-state reaction technique. The starting materials, Na_2CO_3 (AR), SiO_2 (AR), Y_2O_3 (99.99%), Eu_2O_3 (99.99%) and Sm_2O_3 (99.99%) were weighed stoichiometrically and ground evenly in an agate mortar. Subsequently the powder mixture was transferred into muffle furnace and was calcined at 1300°C for 3h in ambient air. After calcining, the samples were cooled to room temperature naturally in the furnace, and ground again into powder for phase structure and properties characterization.

X-ray powder diffraction (XRD) patterns were performed on a Bruker D2 Phaser diffractometer at a scanning rate of 12°/min in the 2θ range from 10 to 80° (Cu Kα radiation, 40kV, 30mA, λ = 1.5418 Å). Photoluminescence excitation (PLE) and photoluminescence (PL) spectra were recorded using a Hitachi F-7000 fluorescence spectrophotometer, and a 150 W xenon lamp was used as the excitation source. All the measurements were performed at room temperature.

Results and discussion

The compound $Na_3YSi_2O_7$ crystallizes in a hexagonal system ($P6_3/m$, Z = 6) with lattice parameters a = b = 9.422(1) Å, c = 13.790(2) Å, c/a = 1.4636 and V = 1060.18 (27) $Å^3$. The unit cells along the *c*-axis and *a*-axis are depicted in Fig. 1. It is mainly composed of [SiO_4] tetrahedral framework and [SiO_4] tetrahedra in pairs share a O2 atom as the point. There are two non-equivalent Y lattice sites, a total of 6 Y atoms, a Si site 12 atoms, four Na sites 20 atoms and four O sites 42 atoms, namely, a cell consisting of 80 atoms.

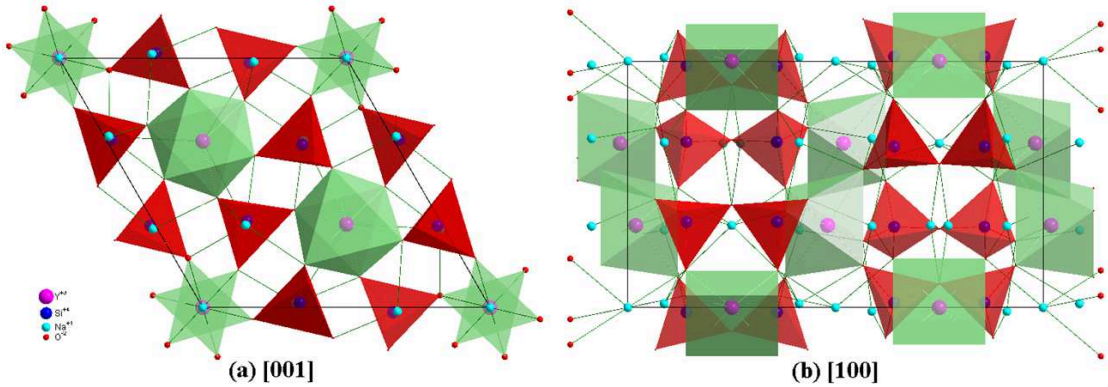


Fig. 1 Unit cell representation of $Na_3YSi_2O_7$ along the *c*-axis and *a*-axis. Pink, blue, cyan, and red spheres stand for Y, Si, Na and O ions, respectively.

The powder X-ray diffraction patterns of (a) $Na_3(Y_{0.84}Eu_{0.16})Si_2O_7$, (b) $Na_3(Y_{0.91}Sm_{0.09})Si_2O_7$, (c) $Na_3(Y_{0.81}Eu_{0.16}Sm_{0.03})Si_2O_7$ phosphors and reference standard card are shown in Fig. 2. It exhibits that all the diffraction peaks of samples can be exactly assigned to the pure hexagonal phase of $Na_3YSi_2O_7$ judging by JCPDS file 72-2011 and no impurities or secondary phases can be detected in the limitation of the XRD resolution, indicating that the doped rare earth ions have not caused significant change in the crystal structure. According to Bragg's theory, the enlarged strongest diffraction plane (114) shift to the lower 2θ values from (a) to (c), as illustrated in the inset, which can prove that larger Sm^{3+} (CN = 6, r =0.958Å) and Eu^{3+} (CN = 6, r =0.947Å) have substituted Y^{3+} (r = 0.900Å when CN = 6). Therefore, the obtained samples are single phase.

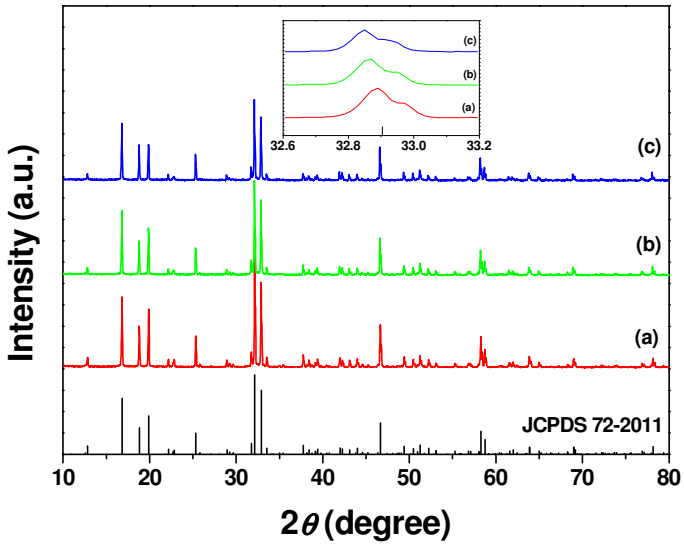


Fig. 2 XRD patterns of (a) $Na_3(Y_{0.84}Eu_{0.16})Si_2O_7$, (b) $Na_3(Y_{0.91}Sm_{0.09})Si_2O_7$, (c) $Na_3(Y_{0.81}Eu_{0.16}$-$Sm_{0.03})Si_2O_7$ and JCPDS card no. 72-2011 as a reference. The inset shows the enlarged plane (114).

To explore photoluminescence performance of Sm^{3+}/Eu^{3+} co-doped phosphor materials, the excitation (PLE) and emission (PL) spectra for 4 mol% Eu^{3+} and 1 mol% Sm^{3+} doped sample are shown in Fig. 3. As can be seen from Fig. 3(a), the PL spectrum of $Na_3(Y_{0.96}Eu_{0.04})Si_2O_7$ consists of several narrow emission bands which are attributed to the transition from the $^5D_{0,1}$ excited states to the ^7F_J ground states of Eu^{3+}, such as $^5D_1 \rightarrow {}^7F_1$ (534 nm), $^5D_1 \rightarrow {}^7F_2$ (555 nm), $^5D_0 \rightarrow {}^7F_1$ (590 nm), $^5D_0 \rightarrow {}^7F_2$ (614 nm) and $^5D_0 \rightarrow {}^7F_3$ (653 nm). The strongest emission peak is located at 614 nm, suggesting that the ligand field deviates from inversion symmetry, and monitored at 614 nm, the optimal PLE peak lies at 393 nm which can be assigned to $^7F_0 \rightarrow {}^5L_6$ transition of Eu^{3+}. For $Na_3(Y_{0.99}Sm_{0.01})Si_2O_7$, the PLE spectrum is composed of several excitation bands due to the characteristic f → f transitions of Sm^{3+} and the 403 nm strongest excitation peak originates from $^6H_{5/2} \rightarrow {}^4K_{11/2}$ transition, as shown in Fig. 3(b). The PL spectrum consists of several emission bands which correspond to the transitions from the $^4G_{5/2}$ excited state to the $^6H_{J/2\ (J = 5, 7, 9)}$ ground states of Sm^{3+}. The 608 nm strongest emission peak stems from $^4G_{5/2} \rightarrow {}^6H_{7/2}$ typical transition and the other emission peaks locate at 564 nm and 650 nm which are ascribed to $^4G_{5/2} \rightarrow {}^6H_{5/2}$ and $^4G_{5/2} \rightarrow {}^6H_{9/2}$ transitions, respectively. Furthermore, the emission bands are split because of the Stark effect of the $^4G_{5/2}$ state [5].

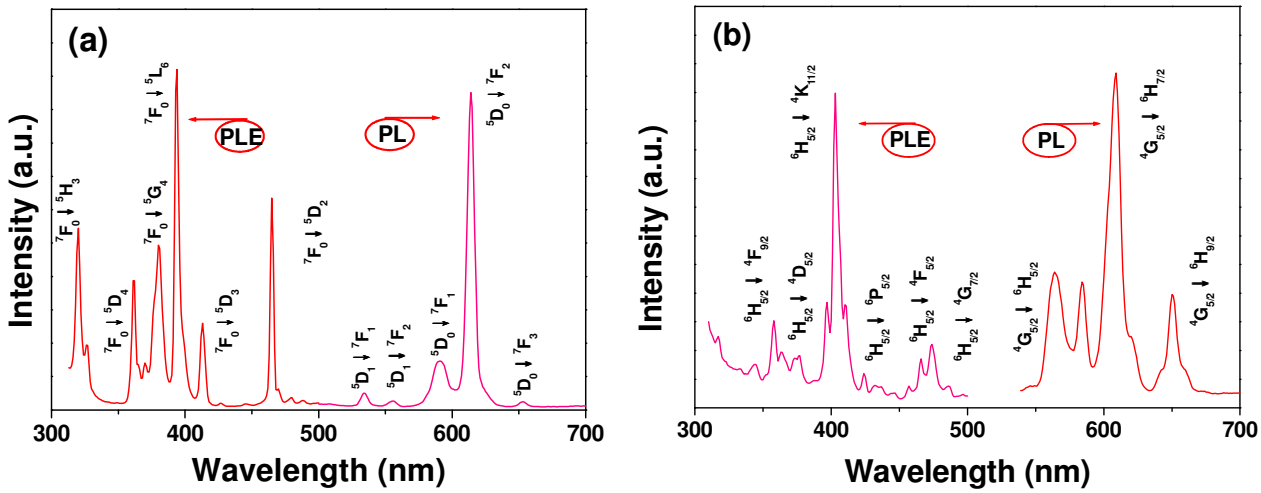


Fig. 3 PLE and PL spectra of (a) $Na_3(Y_{0.96}Eu_{0.04})Si_2O_7$, (b) $Na_3(Y_{0.99}Sm_{0.01})Si_2O_7$ phosphors.

In order to determine the presence of energy transfer from Sm^{3+} to Eu^{3+}, a series of integral spectral intensity for $Na_3(Y_{0.84-y}Eu_{0.16}Sm_y)Si_2O_7$ (y = 0.01, 0.03, 0.05, 0.07, 0.09) are carried out in Fig. 4 (left). It is obvious that the PL intensity of the Eu^{3+} activator (or energy acceptor) firstly increases and then decreases due to concentration quenching with the Sm^{3+} sensitizer (energy donor) contents continuously increase. Consequently, it demonstrates that the energy transfer from Sm^{3+} to Eu^{3+} is effective, as is reported [3,6]. To further illustrate energy transfer process, the corresponding energy level scheme of $Na_3YSi_2O_7$: Eu^{3+},Sm^{3+} with optical transitions is depicted in Fig. 4 (right). Under ultraviolet light excitation, electrons are excited from the ground state ($^6H_{5/2}$) to the excited state ($^4K_{11/2}$) of Sm^{3+}, and non-radiatively relax to the $^4G_{5/2}$ level. Subsequently, some decay to $^6H_{5/2}$, $^6H_{7/2}$ and $^6H_{9/2}$ levels via radiative process, emitting photons and others transfer the excitation energy to the $^5D_0$ level of Eu^{3+} which decay radiatively to various lower levels of ^7F_J (J = 1, 2 and 3). On the other hand, Eu^{3+} absorbs excitation energy directly and radiates to $^5D_0$ excited state, then emitting photons.

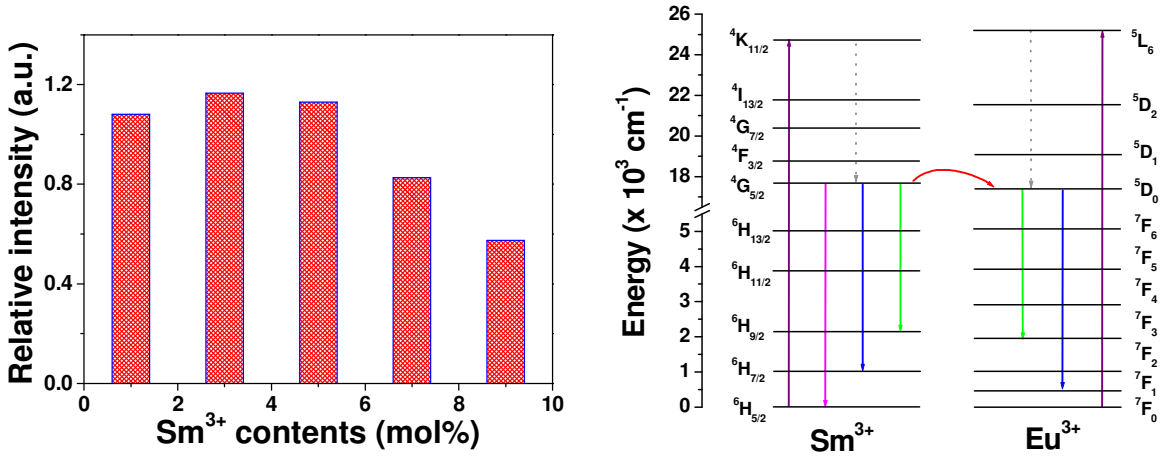


Fig. 4 Integral spectral intensity (left) of $Na_3(Y_{0.84-y}Eu_{0.16}Sm_y)Si_2O_7$ (y = 0.01, 0.03, 0.05, 0.07, 0.09) phosphors and the schematic diagram (right) of energy transfer in $Na_3YSi_2O_7$: Eu^{3+},Sm^{3+} system.

Summary

A series of $Na_3YSi_2O_7$: Eu^{3+},Sm^{3+} samples have been synthesized via solid-state reaction. The obtained phosphors exhibit typical transitions of Sm^{3+} and Eu^{3+} and Eu^{3+}/Sm^{3+}-codoped $Na_3YSi_2O_7$ shows more intense red light compared to that of Eu^{3+}-doped $Na_3YSi_2O_7$. The energy transfer from the sensitizer Sm^{3+} to the activator Eu^{3+} is effective. This system is a potential candidate for application in the solid state lighting.

Acknowledgements

This work was financially supported by the National Natural Science Foundation of China (No. 20976002), the Beijing Natural Science Foundation (No. 2122012), Key Projects for Science and Technology of Beijing Education Commission (KZ201310011013), Projects of Transformation and Industrialization of College Scientific & Technological Achievements.

References

[1] T. Sakamoto, S. Kousaka, K. Uematsu, T. Ishigaki, K. Toda, M. Sato, Synthesis and properties of $Na_3YSi_2O_7$:Eu^{3+} phosphor for fluorescent lamp, Phys. Status Solidi C 8 (2011) 2731-2734.

[2] S.Q. Yan, Synthesis and luminescence properties of Eu^{3+} and Sm^{3+} doped and co-doped $BiPO_4$ powders by a hydrothermal route. J. Mater. Sci: Mater. Electron. 25 (2014) 1868-1872.

[3] H.Y. Lin, S.Y. Chu, Concentration Dependence of Multipolar Mechanisms Responsible for Sm^{3+}→Eu^{3+} Energy Transfer in $(Ca_{0.97-3x/5.64}Sr_{0.03})_{2.82}(VO_4)_2$:$0.12Eu^{3+}$,$xSm^{3+}$ Phosphors. ECS J. Solid State Sci. Technol. 2 (2013) 121-125.

[4] H.Y. Lin, Y.C. Fang, Energy Transfer Sm^{3+}→Eu^{3+} in Potential Red Phosphor $(Ca, Ba)_3(VO_4)_2$: Sm^{3+},Eu^{3+} for Use in Organic Solar Cells and White Light-Emitting Diodes. J. Am. Ceram. Soc. 93 (2010) 3850-3856.

[5] S. Abtmeyer, R. Pazik, R.J. Wiglusz, M. Małecka, G.A. Seisenbaeva, V.G. Kessler, Lanthanum Molybdate Nanoparticles from the Bradley Reaction: Factors Influencing Their Composition, Structure, and Functional Characteristics as Potential Matrixes for Luminescent Phosphors, Inorg. Chem. 53 (2014) 943-951.

[6] X.J. Geng, Y.W. Tian, Y.J. Chen, L.J. Xiao, Y. Xie, Luminescence properties and energy transfer process of Sm^{3+}-Eu^{3+} co-doped molybdate red-emitting phosphors by hydrothermal method, Appl. Phys. B 107 (2012) 177-181.

Applied Mechanics and Materials Vol. 597 (2014) pp 121-126
© (2014) Trans Tech Publications, Switzerland
doi:10.4028/www.scientific.net/AMM.597.121

Compressive properties of Corevo® foam under uni-axial loading based on experimental and numerical analysis

MA Sulong[1, 3, a]*, V Mathier[2], T Fiedler[1], IV Belova[1], GE Murch[1]

[1]Centre for Mass and Thermal Transport in Engineering Materials, School of engineering, The University of Newcastle, Callaghan 2308, Australia.
[2]Constellium Innovation Cells, EPFL Quartier de l'Innovation E, CH-1015, Lausanne, Switzerland
[3]Universiti Teknologi Malaysia, Faculty of Mechanical Engineering, Skudai 81310 Johore, Malaysia.
[a]mohdayub.sulong@newcastle.edu.au

Keywords: Cellular material, Finite element analysis, μCT, Experimental analysis, Mechanical properties

Abstract: This paper reports on an investigation of the compressive properties of Corevo® foam. Corevo® foam is a cellular metal manufactured by the infiltration casting of salt dough with aluminium. Corevo® foam samples with different porosities are tested by using quasi-static compression loading. Their mechanical properties (i.e.: effective Young's modulus, Poisson's ratio, initial yield stress and material yield stress) are then compared to reveal the importance of the density difference. In addition, three-dimensional finite element analysis is performed on models generated from micro-computed tomography (μCT). The results of two different pore sizes are obtained and compared in the scope of this work. These numerical results are verified by comparison with the experimental analysis. Sound agreement is found. Numerical analysis in this work also includes the investigation of the mechanical material anisotropy and plastic deformation.

1) Introduction

Cellular metals are a relatively new category of material known for its multi-functionality. One feature of this material is the ability to absorb large amounts of energy at a relatively low stress level due to its high porosity structure [1]. Other general properties of cellular metals are versatile thermal properties, vibration damping and acoustic absorption [2-4]. A wide range of potential applications is offered by cellular metals when these physical properties are combined. Corevo® foam is an open-celled cellular metal with an aluminium metallic base. By using a replication casting process, Corevo® foam has a broad range of porosities (65-85%). The replication process is adopted in the manufacturing industry to produce an open-pore cellular structure due to the high accuracy of the end product in replicating the internal shape of the mould [5]. Characterisation of mechanical properties (i.e. Young's modulus, Poisson's ratio and yield strength) for Corevo® foam with a single average pore size (d=1.9 mm) is available in [6]. The study in [6] incorporates the experimental testing of cylindrical-shaped samples and the result is compared to the numerical simulations. In the present work, Corevo® foam samples with the larger pore sizes d=5.6 mm are characterised by means of experimental and numerical testing. Two samples of Corevo® foam with the larger pore size are tested with quasi-static compression loading. All the procedures involved in this experiment (unless stated otherwise) are performed according to the International Standard (ISO 13314:2011(E)) [7]. Prior to testing, the two samples were scanned by micro-computed tomography (μCT) imaging for further numerical analysis.

2) Experimental testing

Two samples obtained from Constellium, were tested in this investigation. The base material in Corevo® foam is AS7G06 (Al, 7%Si, 0.6% Mg) aluminium alloy. The physical properties of the samples are summarized in Table 1. The length of the sample was measured by using a digital calliper. Mass was determined using an A&D GX6100 precision scale with an accuracy of 0.01 g.

The average pore size in Table 1 was calculated by averaging 10 pore sizes found on a slice of a random μCT image. This image was imported into the Materialise Mimics software and a single pore size was measured by using the embedded pixel ruler tool. Fig. 1 shows the spatial distribution of the pores in the samples. The ratio of the sample diameter, D_0 to the average pore size, d is in the appropriate range ($D_0 \geq 10d$) according to the International Standard (ISO 13314:2011(E)). The porosity of the samples was calculated by subtracting the volume of the metallic phase in the sample from the cylinder of the total sample volume. The metallic phase volume can be calculated by dividing the mass of the samples by the density of the aluminium alloy ($\rho_{AS7GO6} = 2.675$ g/cm^3).

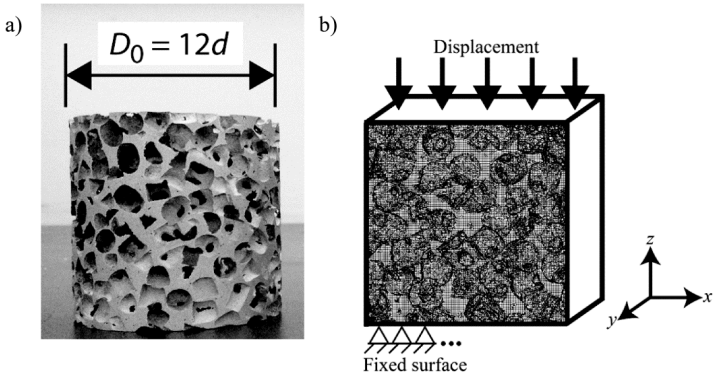


Fig. 1: (a) Sample S#2 (b) Boundary conditions imposed on Corevo® foam numerical samples.

Table 1: Physical and geometrical properties of samples

Sample	Sample Mass [g]	Length, L [mm]	Diameter, D_0 [mm]	Average pore size, d [mm]	Porosity (%)
S#1	65.82	50.03	49.9	5.60	74.6
S#2	67.95	50.03	50.0	5.55	74.1

The uni-axial testing machine used for compressive testing was a Shimadzu Autograph with a 50 kN load cell. A constant crosshead speed of 0.0002 m/s was used in both tests. The compressive stroke or the movement of the crosshead during compression test was recorded directly from the testing machine cross-head. The time in second (s), stroke or displacement (in mm) and force (in kN) from each test was recorded. The compressive test of Corevo® foam samples in this report was done at an ambient temperature of 27 ºC.

3) Modeling approach

The use of micro computed tomography (μCT) imaging is an increasingly accepted approach to model structures with complex geometry. This method accurately captures the complex internal structure of cellular metals. To date, cellular structures such as metallic hollow sphere structures (MHSS) [8], aluminium foams [9], sintered metallic fibre structures (MHSS) [10], advanced pore morphology (APM) foam elements [11], and lotus-type porous copper [12] are materials that have been characterised using this innovative imaging approach. The Corevo® foam samples in this work were scanned with a voxel length (smallest resolution) of 51.92 microns. From the μCT scan images, 3D models of the specimens were constructed.

The data from the μCT imaging was processed by using the so-called grey value thresholding. The most crucial part in this step is to differentiate the metallic phase (i.e.: AS7G06 aluminium alloy) from air. Now, a white voxel in the the micrograph is grouped into the metallic phase while a black voxel represents the air. The mass of the sample which is measured prior to the scanning process is done by using a precision scale. By using the mass of the sample, the metal volume is calculated by

dividing it by the AS7GO6 material density ρ=2675 kg.m^{-3} (i.e.: $v=m/\rho$) [13]. The segmentation threshold was adjusted in a systematic repetition until the segmented voxel volume matched with the calculated volume. The study showed that the gradient of compression force and displacement in the loading direction, dF/dy converges by using 750,000 or more elements. A hex-dominant mesh was used in the model that includes linear hexahedral-, linear pentahedral- and tethedral-elements. This type of mixed-mesh has shown superior performance in the numerical analysis of complex geometries [14, 15]. Due to calculation time limitations, the cylindrical shape of the original sample was subdivided to have a smaller cubic numerical model. The side length of the cube for numerical calculation was 35 mm.

Material properties For numerical analysis, the aluminium alloy properties for the Corevo® foam of average pore size of 5.6 mm 3D models were taken from the literature [13]: - (i) Young's modulus, E = 72.4 GPa, (ii) Poisson's ratio, v = 0.35 and initial yield stress, σ_0 = 241 MPa. The plastic hardening effect is modelled using a tangent modulus, T = 2.3 GPa to match the ultimate yield stress, σ_u = 310 MPa at the corresponding strain, ε_u = 0.03.

Boundary conditions To simulate uni-axial compressive testing, appropriate boundary conditions need to be defined on the numerical 3D model. The boundary conditions applied in this work are shown in Fig. 1b. The bottom surface of the numerical model is fixed, i.e. the normal displacement is set to zero. The displacement input is set to compress the numerical 3D model up to 0.1 macroscopic strain. This is achieved by defining a time-dependent displacement in the negative z-direction at the upper surface. The other four remaining surfaces are set to be free boundaries. The force value caused by this displacement input is called the reaction force. The sum of the reaction force for all nodes on the top surface is retrieved by a user-defined subroutine. Then, the engineering stress is calculated by normalising the accumulated reaction force by the initial surface area. The engineering strain in this work was calculated as the change of length over the initial length of the sample (i.e.: $\varepsilon_G = \Delta l/l_0$).

Prior to numerical simulations, a convergence study was conducted on S#1 to determine the required number of elements to be used in the actual calculation.

4) Results and discussions

Experimental analysis The raw data (i.e.: force and stroke) from the experiment is used to calculate the engineering stress-strain diagram (see Fig. 2). Using this stress-strain data, the quasi-elastic gradient was determined by taking the first linear deformation region of the compressive stress-strain slope. The quasi-elastic gradients are 3.60 GPa for sample S#1 and 3.50 GPa for sample S#2. The compressive offset stress was calculated as the value of the compressive stress at the plastic compressive strain of 0.2%. The 0.2% offset yield stress ($\sigma_{0.2}$) for S#1 and S#2 is 3.49 MPa and 2.62 MPa respectively. By referring to the international standard [7], the plateau stress, σ_{pl} is calculated as the arithmetic mean of stresses between the strain intervals of 0.2 and 0.4 (denoted by the light grey region in Fig. 2). The values for plateau stress for sample S#1 and S#2 are 7.5 MPa and 8.2 MPa, respectively. The plateau end stress σ_{ple} for the samples is taken from a point in the stress-strain curve at which the stress is 1.3 times the plateau stress. The corresponding values are $\sigma_{ple,S\#1}$ = 9.75 MPa and $\sigma_{ple,S\#2}$ = 10.66 MPa.

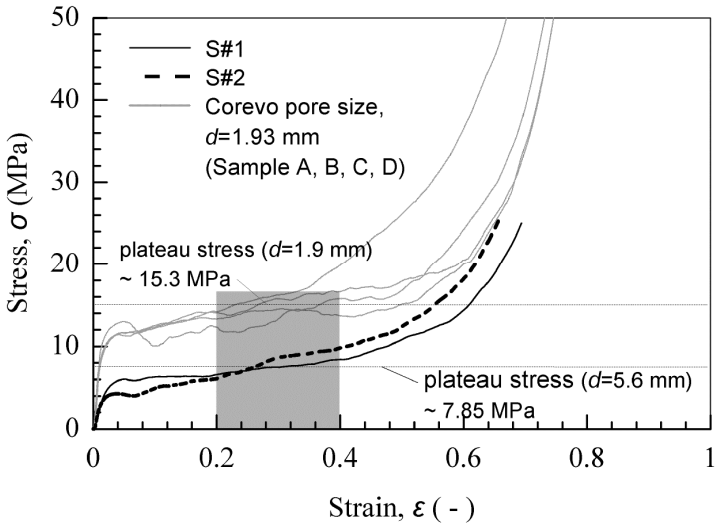


Fig. 2: Experimental quasi-static compressive test comparison of stress-strain diagram for Corevo® foam samples of both pore sizes.

Fig. 2 shows a comparison of the experimental test results between the average pore size, d=5.6 mm and d=1.9 mm Corevo® foam samples. The stress-strain diagram for all small Corevo® foam samples are plotted with light grey lines. A significant difference can be found from the comparison of the stress-strain curves. The plateau stress of the average pore size (d=5.6 mm) samples exhibit a lower value of plateau stress compared to the average pore size (d=1.9 mm) Corevo® foam. The plateau stress of smaller pore size Corevo® foam is higher by a factor of 1.95. A likely explanation to this behaviour is related to the lower volume of metallic cell walls in higher porosity Corevo® foam (5.6 mm pore size samples are 75% porous while 1.9 mm pore size samples are 72% porous). This behaviour also can be attributed to cooling rate effects. There was no heat treatment performed on the samples. Due to the fact that casting conditions can sometimes vary, this will lead to the metal in the thin struts experiencing variable cooling rates during casting. A strong effect on the mechanical properties can be expected from this variation.

Numerical Analysis The generated 3D models elaborated in section 3 are used to simulate the uni-axial compression loading test. With the availability of an extremely accurate numerical model, additional calculations are conducted with different loading directions to investigate the anisotropy of the material. The corresponding loading direction of the experimental tests in the numerical simulation is in the z-direction. This direction is also the casting direction during manufacturing. The experimental results are shown (dashed bar) together with the numerical results in Fig. 3. The experimental samples in the chart are denoted by the letter G with subscript 1 and 2 to represent the sample S#1 and S#2. The maximum value of the offset yield stress is found in the y- direction for sample S#1 and in the casting direction (i.e.: the z- direction) for S#2. However, the difference between the maximum and the minimum values of the offset yield stress is relatively small. The results for the 0.2% offset yield stress show a good agreement between the experimental and numerical simulations. It can be deduced from Fig. 3 that a mild effect of anisotropy is found for the average pore size (d=5.6 mm) Corevo® foam compared to the stronger anisotropy result investigated for the smaller pore size Corevo® foam (i.e.: d=1.9 mm).

Fig. 4a shows the equivalent plastic strain contours in the average pore size (d=5.6 mm) Corevo® foam. It can be seen that plasticity is more likely to occur in thin struts in a parallel direction to the loading direction. The mode of collapse found for average pore size of 5.6 mm samples is layer-wise in the numerical analysis (see Fig. 4) and experimental analysis (see Fig. 5). The connected arrows in Fig. 5 indicate the chain of broken cell walls during the compression test. A localized yield occurs primarily at thin cell walls and struts and propagates to the neighbouring regions. A

similar behaviour of plastic deformation is found in the smaller pore size Corevo® foam (i.e.: *d*=1.9 mm) as shown in Fig. 4b.

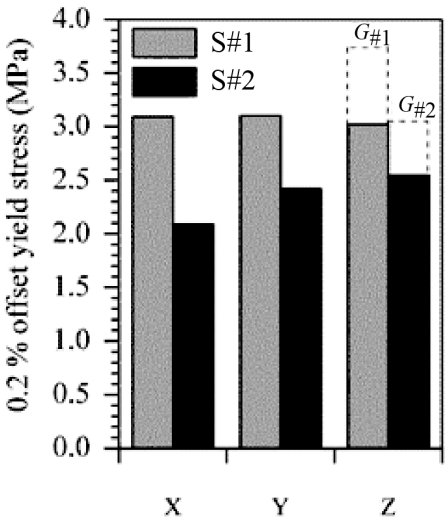


Fig. 3: 0.2% offset yield stress result of sample S#1 and S#2.

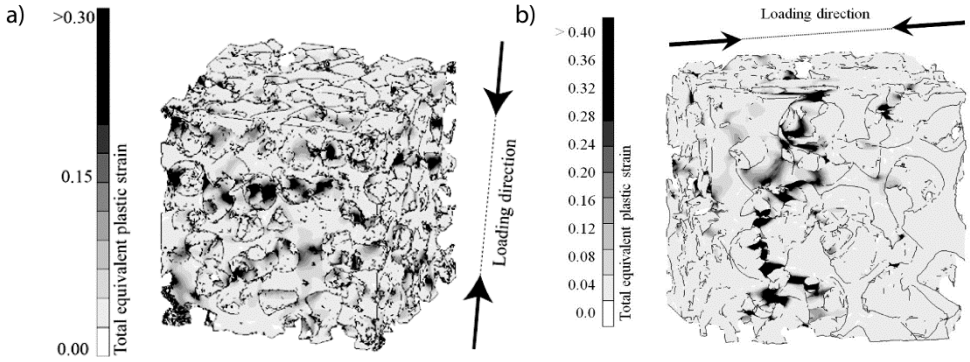


Fig. 4: Equivalent plastic strain distribution for (a) Corevo® foam samples with average pore size (*d*=5.6 mm) , sample S#2 (b) Corevo® foam samples with an average pore size (*d*=1.9 mm), sample A [6].

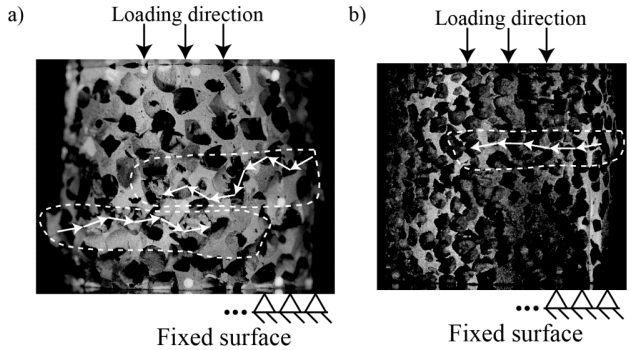


Fig. 5: Snapshots from experimental compression test for (a) Corevo® foam samples with an average pore size (*d*=5.6 mm) , sample S#2 (b) Corevo® foam samples with an average pore size (*d*=1.9 mm), sample B.

5) Conclusions

The mechanical properties of Corevo® foam with two different pore sizes were addressed in this paper. The difference in the pore size and the variation of the porosity was shown to change the general mechanical properties of this metallic cellular material. The most significant result from this investigation was that the plateau stress of higher porosity Corevo® foam possessed a lower value compared to the lower porosity foam. The value of the plateau stress for average pore size (d=5.6 mm) Corevo® foam was lowered by a factor of 1.95 compared to the average pore size (d=1.9 mm) foam of the same material. Good agreement of 0.2% offset yield stress result was found between experimental test and numerical simulation. A mild effect of elastic anisotropy was found for the average pore size (d=5.6 mm) Corevo® foam compared to the stronger elastic anisotropy result investigated for the smaller pore size Corevo® foam (i.e.: d=1.9 mm). A further numerical analysis for the plastification of Corevo® foam of average pore size (d=5.6 mm) Corevo® foam showed that a localized plastic yield concentrated at the thin cell walls in a layer-wise mode. This behaviour of plastic deformation has been reported before for Corevo® foam with an average pore size (d=1.9 mm) in [6]. The plasticity then advanced to the neighbouring area parallel to the weak thin struts of the payload direction.

6) References:

[1] Ashby, M.F., et al., *Metal Foams: A Design Guide*. 2000: Butterworth-Heinemann.

[2] Fiedler, T., et al., *Numerical analyses of the thermal conductivity of random hollow sphere structures.* Materials Letters, 2009. **63**(13): p. 1125-1127.

[3] Öechsner, A. and C. Augustin, *Multifunctional Metallic Hollow Sphere Structures.* Multifunctional Metallic Hollow Sphere Structures: Manufacturing, Properties and Application, Engineering Materials, 2009. **1**.

[4] Pannert, W., R. Winkler, and M. Merkel, *On the acoustical properties of metallic hollow sphere structures (MHSS).* Materials Letters, 2009. **63**(13-14): p. 1121-1124.

[5] Conde, Y., et al., *Replication processing of highly porous materials.* Advanced Engineering Materials, 2006. **8**(9): p. 795-803.

[6] Fiedler, T., et al., *Mechanical properties of aluminium foam derived from infiltration casting of salt dough.* Computational Materials Science, 2014. **81**: p. 246-248.

[7] *ISO 13314:2011(E) Mechanical testing of metals — Ductility testing — Compression test for porous and cellular metals*. 2011.

[8] Veyhl, C., et al., *Thermal analysis of aluminium foam based on micro-computed tomography.* Materialwissenschaft und Werkstofftechnik, 2011. **42**(5): p. 350-355.

[9] Sulong, M.A., et al., *Compressive properties of Advanced Pore Morphology (APM) foam elements.* Materials Science and Engineering: A, (0).

[10] Veyhl, C., et al., *On the thermal conductivity of sintered metallic fibre structures.* International Journal of Heat and Mass Transfer, 2012. **55**(9-10): p. 2440-2448.

[11] Vesenjak, M., et al., *Structural Characterisation of Advanced Pore Morphology (APM) Foam Elements.* Materials Letters, 2013.

[12] Fiedler, T., et al., *On the Anisotropy of Lotus-Type Porous Copper.* Advanced Engineering Materials, 2011. **14**(3): p. 144-152.

[13] Holt, J.M., H. Mindlin, and C.Y. Ho, *Structural alloys handbook*. 1995: CINDAS/Purdue University.

[14] Veyhl, C., et al., *On the mesh dependence of non-linear mechanical finite element analysis.* Finite Elements in Analysis and Design, 2010. **46**(5): p. 371-378.

[15] Sulong, M. and A. Öchsner, *Finite element simulation of the macroscopic heat conductivity of syntactic perforated hollow sphere structures.* Materialwissenschaft und Werkstofftechnik, 2012. **43**(5): p. 461-467.

Applied Mechanics and Materials Vol. 597 (2014) pp 127-130
© (2014) Trans Tech Publications, Switzerland
doi:10.4028/www.scientific.net/AMM.597.127

Fine spin filtering effect in Co-phthalocyanine molecule induced by the spin polarization of Co atom

Y. H. Zhou[1, a] , X. H. Qiu[1, a], L.L. Zhou[1, c], and Y.L. Peng[1, d]

[1]Department of Information Engineering, Gannan Medical University, Ganzhou, Jiangxi, China

[a]yhzhou80@gmu.cn, [b]xiaohui85@163.com, [c]lilizhou369@gmail.com, [c]ylpeng6124@gmail.com

Keywords: spin filter, phthalocyanine molecule, density functional theory.

Abstract. Spintronic devices will play a very important role in future information technology. In this study, By spin-polarized density-functional theory calculations combined with the Keldysh nonequilibrium Green's method, the effect of the spin direction of Co atom in Co- phthalocyanine molecule in modulating spin filtering effects under external biases are investigated. Here, an individual single molecule Co-phthalocyanine is sandwiched between two infinite 8-zigzag-graphene nanoribbon electrodes. we find that the spin direction of the Co atom relative to the magnetic polarization of the left and right electrodes can improve the spin filtering effect greatly. when the polarization direction of the two electrodes is antiparallel and the polarization of Co atom in the Co-phthalocyanine molecule upward, the configuration posesses almost perfectly spin-filter effect. The underlying mechanism of the perfect spin filtering action is applied.

Introduction

Just two decades ago, the electron spin appeared for the first time in the device world[1]. However, the spin state of a moving electron can be detected now due to the continual improvement in our understanding on how spins can be injected, manipulated and detected in the solid state[2]. The spin electronics have led to new generations of read heads in hard disk drives and random access memory, but further progress in downsizing spintronic devices is challenging because reducing the device size will lead to high resistances and shot noise. So a promising approach to extremely downsizing is to design electronic single-molecule spintronic devices as done with molecular rectifiers, switchers and transistors[3]. Most of the development in spintronics, is currently based on inorganic materials. Organic molecules have also been introduced into spin-valves, and spin dependent tunneling through organic molecules adsorbed on magnetic substrates has been demonstrated[4].

Among the many potential organic molecular candidates, hydrogen-phthalocyanine and TM-phthalocyanine form a promising and important family of compounds. Lots of experimental and theoretical investigations have been done to its electronic properties and electro-magnetic properties[5]. However, just a few researches on the electronic transport properties of phthalocyanine in electrode-molecule-electrode system have been reported, especially for it coupled to low-dimensional electrodes.Iacovita et al. investigated the spin transport across single cobalt-phthalocyanine molecues adsorbed on cobalt nanoislands and demonstrated that there was a spin-polarized electronic resonance over the center of the molecule. In the year 2011, giant magnetoresistance was gained by Schmaus in single hydrogen-phthalocyanine molecules coupled to two ferromagnetic Co electrodes. However, systematic work is still needed to study the spin transport properties of these special molecules. Graphene, which was obtained experimentally in the year 2004, has been considered as a good candidate for spin-based quantum computing and spintronics for its long spin decoherence, relaxation time, and high electronic mobility[6]. The zigzag-edged graphene nanoribbons are magnetic that the ZGNR-based device can be designed as parallel [1,1] or antiparallel [1,-1] magnetic configurations. And dual spin filter effect was shown in a 8-zigzag graphene nanoribbon, but not in a 7-zigzag graphene nanoribbon.26 Therefore, in the work, we study the

transport properties of the phthalocyanine based molecules coupled to two 8-zigzag-edged graphene nanoribbons electrodes. Giant magnetoresistance exists in all phthalocyanine two-probe configurations and chromium-phthalocyanine configurations own the best spin filter efficiency.

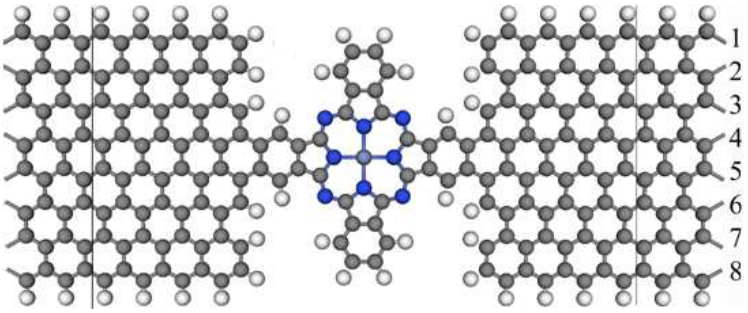


Fig. 1. (Color online) Schematic view of the twoprobe systems: zigzag-graphene nanoribbon/ Co-phthalocyanine/zigzag-graphene nanoribbon device junction

Simulation Model and Calculation Method

The model structure for our theoretical study is illustrated in Fig. 1. An individual single molecule Co-phthalocyanine is sandwiched between two infinite 8-zigzag-graphene nanoribbon electrodes as shown in Fig. 1. The number 8 is the width of the zigzag-graphene nanoribbon as was defined by Fujita previously[7]. We have chosen a supercell with a large enough vacuum layer in the x and y directions so that the device has no interaction with its mirror images. The semi-infinite electrodes are described by a supercell with two repeated carbon unitcells due to their periodicity along the transport direction. The single molecule Co-phthalocyanine together with four unit cells both in the left electrode and in the right electrode is chosen as the cental region, as indicated by two vertical lines. As the magnetic fields at two electrodes can point in the same or opposite direction, the zigzag-graphene nanoribbon electrodes can show the parallel (P) or antiparalllel (AP) spin configuration. The geometric optimization and spin-resolved electron transport properties are calculated by a developed first-principles software package Atomistix ToolKit, which is based on the spin-polarized density-functional theory combined with non-equilibrium Greens functions[8]. In our calculations, the core electrons are described by norm-conserving pseudopotentials, and the local spin density approximation (LSDA) with the Perdew-Zunger exchange-correlation potential is employed. Moreover, a cutoff energy of 150 *Ry* and a Monkhorst-Pack k-mesh of (1, 1, 100) are chosen to achieve the balance between calculation efficiency and accuracy. The structures of single Co-phthalocyanine molecules are optimized firstly, and then are optimized in the environment of two-probes, respectively. All the structures are fully relaxed using quasi-Newton method until the force tolerance of 0.01 eV/Angstrom is reached.

Results and Discussions

The spin polarized *I-V* curves of the twoprobe molecular systems are shown in Fig. 2. The spin up current owns values when the *Co* atom in the system is nonmagetism(NM) as be seen in Fig. 2(a) and (b), especially in the antiparallel configuration(AP). So the bias depedent spin filtering efficiency is low and thus not good. when taking the magnetism of the Co atom into account, the difference between the spin up and spin down current is increased, especially for AP case(see Fig. 2(c) and (d)). Therefore, the set of magnetism of Co atom can manipunate the spin filtering effect which can also be known directly from the bias-dependent spin filter efficiency(BDSFE) as a function of bias voltage in Fig. 3. The BDSFE at the finite bias voltage is defined in terms of the spin-resolved currents: $BDSFE=(I_{up}-I_{down})/(I_{up}+I_{down})$, where I_{up} and I_{down} are the spin up current and the spin down current, respectively. the BDSFE reaches nearly 100% in a wider region from 0.05 to 1.0Vwhen the Co atom is spin up in the AP case(red line), and in the P case(blue and green lines), the BDSFE is greatly increased both in width and value.

For an efficient spin filter, it is generally accepted that the transmission spectrum should show distinctive feature in the spin up and spin down channels over a range of energy close to the Fermi energy. To explain the spin filter actions, we show representative finite bias (0.6V) transmission spectra for the six cases of cobalt-phthalocyanine twoprobe systems, respectively, in Fig. 4. For the P configurations, the spin up transmission is forbidden and the spin down transmission has vales in the bias window(see Fig. 4(c)) when the Co atom set as spin up, while the Co atom is NM(see Fig. 4(c)), the spin down transmission has small values which decreases the BDSFE. So the set of Co atom' magnetism can improve the BDSFE of Co- phthalocyanine system. For AP configuration, although the spin up transmission is forbidden for the '10-1' and '1-1-1' cases(see Fig, 4(c) and (f)), the set of magnetism of Co atom increases the spin down transmission in the bias window. So the BDSFE are also inproved.

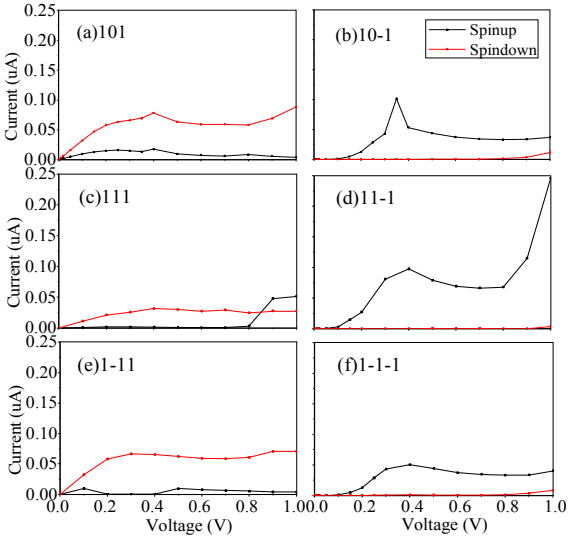


Fig. 2. (Color online) The spin-up (black) and spin-down (red) I-V curves: (a)-(e) are for the P configurations of cobalt-phthalocyanine twoprobe systems with the Co atom NM, spin up, spin down states, respectively; (d)-(f)The same as (a)-(e) but for the AP configurations. we label spin up is as "1", spin down as "-1" and NM as "0".

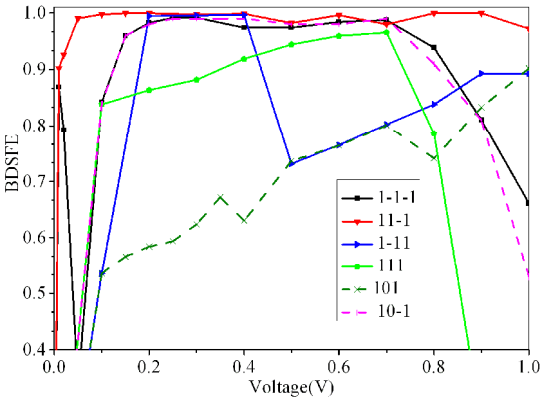


Fig. 3. (Color online) Bias-dependent spin filter efficiency as a function of bias voltage for the six cases as Fig. 2 . we label spin up is as "1", spin down as "-1" and NM as "0" .

Summary

In this study, the effect of the spin direction of Co atom in Co- phthalocyanine molecule in manipunating spin filtering effects were investigated by spin-polarized density-functional theory calculations combined with the Keldysh nonequilibrium Green's method. We found that the spin

direction of the Co atom relative to the magnetic polarization of the left and right electrodes could improve the spin filtering effect greatly. for example, when the polarization direction of the two electrodes was antiparallel and the polarization of Co atom was upward, the configuration posesses almost perfectly spin-filter effect. The reason of the perfect spin filtering action was analyzed.

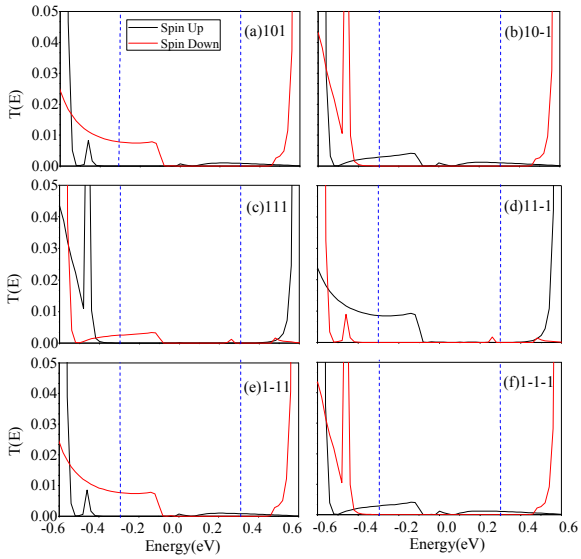


Fig. 4. (Color online) Spin-up (black) and spin-down (red) transmission spectra at the bias of 0.6V: (a)-(e) are for the P configurations of cobalt-phthalocyanine twoprobe systems with the Co atom NM, spin up, spin down states, respectively; (d)-(f)The same as (a)-(e) but for the AP configurations. The two dotted lines indicate the bias window.

Acknowledgment

This work was supported by the National Natural Science Foundation of China, (No. 61361001), by Natural Science Foundation of Jiangxi Province(No. 20132BAB211033) and by Natural Science Foundation of Jiangxi Province(No. 20122BAB212007), China.

References

[1] M. N. Baibich, J. M. Broto, A. Fert, Van Dau, F. Nguyen; F. Petroff, P. Etienne, G. Creuzet, A. Friederich, and J. Chazelas, Giant magnetoresistance of (001)Fe/(001)Cr magnetic superlattices, Phys. Rev. Lett. 61(1988) 2472-2475.

[2] S. Sanvito, Organic spintronics: Filtering spins with molecules, Nature materials 10(2011) 484-5.

[3] S. S. P. Parkin, C. Kaiser, A. Panchula, P. M. Rice, B. Hughes,; M. Samant, S. H. Yang, Giant tunneling magnetoresistance at room temperature with MgO (100) tunnel barriers, Nature materials, 3(2004) 862-7.

[4] H. Hao, X. H. Zheng, L. L. Song, R. L. Wang, Z. Zeng, Electrostatic spin crossover in a molecular junction of a single-molecule magnet, Phys. Rev. Lett. 108(2012) 2-6.

[5] C. Iacovita, M. V.Rastei, B. W. Heinrich, T. Brumme, J. Kortus, L. Limot, J. P. Bucher, Visualizing the Spin of Individual Cobalt-Phthalocyanine MoleculesPhys, Rev. Lett. 101(2008) 116602.

[6] M. G. Zeng, L. Shen,; M. Zhou, C. Zhang, Y. P. Feng, Graphene-based bipolar spin diode and spin transistor: Rectification and amplification of spin-polarized current, Phys.Rev. B, 83(2011) 115427.

[7] R. M. Metzger, Monolayer rectifiers, J. Solid State Chem. 168(2002) 696.

Applied Mechanics and Materials Vol. 597 (2014) pp 131-134
© (2014) Trans Tech Publications, Switzerland
doi:10.4028/www.scientific.net/AMM.597.131

Recent Developments in Molecularly Imprinted Solid Phase Extraction Technology

Guijun Shen[1,a*], Hongying Pei[1,b]

[1.]College of Environmental and Chemical Engineering, Dalian University, Liaoning, Dalian 116622, P.R. China

[a.]shgjdl@Gmail.com, [b.]peihongying8911@163.com

Key words: molecularly imprinting technology, solid phase extraction , separation technology

Abstract: Describes the preparation of molecularly imprinted solid phase extraction technology, extraction methods, selectivity and application status.

Introduction

Molecular imprinting technology for template synthesis of antibodies to antigens originated in immunology is the template molecule with specific functional monomer in under the action of crosslinking agent, by non covalent or covalent function in solution polymerization monomer polymerization, solid polymer is obtained. And then use organic solvent to remove the template molecules, and thus get the molecularly imprinted polymer with specific structure. The molecularly imprinted polymers with recognition specificity, can accurately identify one or a class of compounds. German Wulff and others synthesized molecularly imprinted polymer publicly in 1972 [1], from this molecularly imprinted received extensive attention of scholars.[2]

Solid-phase extraction is appeared in the mid - 1970 - s technology, it is using the solid adsorbent adsorption of the target compounds of liquid samples. Molecularly imprinted technique and solid-phase extraction technology, the combination of the molecularly imprinted solid phase extraction, it absorbs the advantages of both, as a result, the effect of separation and enrichment of the previous two better. [3]

The preparation of molecularly imprinted extraction stationary phase

As template molecule, and polymer monomer form multiple point contact, this effect will be the memory down through polymerization process, when after removal of template molecules. Polymer is formed with the template molecules in space configuration matching with the point of multiple holes, the hole will be to choose a template molecule and its analogues have identification.[4]

Depending on the interaction between the template molecule and the functional monomer, MIPs preparation methods can be divided into the following four categories:

Pre-assembly method. Pre-assembly method, also known as covalent blotting. In this method, functional monomer and the template molecules was bonded by covalent. After polymerization, removing the template molecules from the polymer to obtain a molecular imprinted polymer by decomposition reaction. When encountered the template molecule again, the polymer can form the same covalent bonding. This covalent interaction includes the role of Schiff bases, esters and boric acid esters.

self-assembly method. Self-assembly method, also known as non-covalent imprinting method. Different from covalent imprinting method, functional monomer and the template molecule linked

by non-covalent interactions in non-covalent imprinting method. The non-covalent bonds include hydrogen bonds, van der Waals forces, hydrophobic interactions and charge-transfer. After the polymerization reaction, remove the template molecule by an appropriate solvent. Then the molecularly imprinted polymers was obtained.

Covalent and non-covalent interactions hybrid. The method is a new approach that combined the pre-assembly and self-assembly. First, the functional monomer and the template molecules was combined by covalent. Then the MIPs with three-dimensional hole was obtained after polymerization and the template molecule removed. However the functional groups on the template molecule and the functional monomer is not a covalent bond, when MIPs met template molecule again, but a non-covalent binding, as molecular self-assembly.

Metal chelation. The chelation between metal ion and drugs and biological molecules is highly stereo selective and relatively mild. it can be used in molecular imprinting. MIPs prepared using metal chelating can be achieved with high selectivity for adsorption of metal ions.

Embodiment of MISPE

Dispersive solid phase extraction. Dispersed extraction is the easiest way of molecularly imprinted SPE extraction. A certain amount of the molecular imprinted polymer was put into a solution containing the target substance. And then stirred or shocked for a period of time, measured the change of concentration and calculated equilibrium adsorption amount. Wang Shengli[5] prepared Chrysophanol molecular imprinted polymers, characterized by dispersion extraction methods. Wang Yanhong[6] put the Allah Jin molecular imprinted polymers in a stoppered flask. And then added the Allah chun methanol solution and shocked 16 h in shaker.

Solid phase extraction column. There are two methods about preparation of solid phase extraction column. One is loading the template molecule, functional monomer , crosslinker and initiator into column. Initiate the polymerization by heated. And then removed the template to optioned the molecularly imprinted solid phase extraction column. Zhou jie[8] prepared molecularly imprinted solid phase extraction column of R-1-(1 - naphthyl) ethylamine using methacrylate as function monomers. The extraction column selectivity factor of 1.67. Another method is to prepare a molecularly imprinted polymer , and then grinding, sifting , and finally loaded into the solid phase extraction column.

Solid phase micro extraction. Micro extraction is an extraction technique that enriched the micro volume of polymer, and set sampling, extraction, concentration, sample in one. Compared with conventional solid phase extraction technology, it is fast , easy and convenient. Molecularly imprinted micro-extraction technology set the highly selective of molecular imprinted polymer and Quick and easy of micro-extraction technology in one. It has been widely used in the complex sample processing. Koster[11] first reported the probe molecule imprinted solid phase micro-extraction techniques with clenbuterol as a template molecule, the use of polymerization reaction MIP coating on the fiber, which was used in spiked urine Poirot mother Castro analysis, and achieved satisfactory results.

Stir cake adsorption extraction. Lin Fuhua[12] prepared extraction cake based on bisphenol A whole material based on the situ synthesis of overall material, combined with the extractor processing from disposable syringes. Put the Bisphenol A and 4 - vinyl pyridine in the porogen, and then added ethylene glycol dimethacrylate and AIBN, the reaction mixture was poured into the cylinder closed at one end, placed vertically in an oven after sealing , temperature polymerization. After completion of the polymerization, the polymer was pushed out from the syringe, the obtained was extracted cake .

Selective of molecular imprinted solid phase extraction technology

Molecularly imprinted solid phase extraction techniques learned the advantages of molecularly imprinted and solid phase extraction technology, the extraction efficiency was significantly higher than the solid-phase extraction techniques. In this regard, Jia Yuxiang[13] did a related study, adding the drug in the blank feed samples, using the SPE and MISPE treated the sample respectively and did recovery experiments. The average recovery of three kinds of benzodiazepine class of drugs using MISPE is 71% -79%, and the SPE is 79% -98%. Compared with the SPE, the impurity peaks corresponding reduction or disappearance after sample preparation with MIPs as the solid phase extraction agent. The purification effect of MISPE is obvious.

Huang Yi[15]prepared ractopamine molecularly imprinted polymer using RAC as template,acrylamide (AM) as monomer，and ethylene glycol dimethacrylate (EGDMA) as cross-linker. The clean-up efficiency of MISPE w as ideal for feed samples. The method is more sensitive and reproachable than the standard analytical method for the determination of RAC in feed matrices.

Application status of molecularly imprinted solid phase extraction technology

Extraction of natural products active ingredients. Mazyar Ahmadi Golsefidi[16] developed a simple preparation approach for modified bisphenol A (BPA) molecularly imprinted polymer sorbent used in the hollow fiber solid phase micro-extraction (MIP-HF-SPME) of chlorogenic acid (CGA). The average relative recoveries of spiked analyte in the four concentration levels were between 84.8 and 97.2%. Zeng Huan[17] prepared magnetic molecularly imprinted polymers (MMIPs) which can be used for the separation and purification of rutin from Chinese medicinal plants. The performance of the MMIPs for the adsorption of rutin in the analysis of Chinese medicinal plants was assessed. The mean recoveries were 84.33%.

Detection of drugs and drug abuse. Zhu Bo[19] develop a method for the simultaneous determination of methamphetamine (MA) and-amphetamine (AMP) in urine by high performance liquid chromatography with molecularly imprinted solid phase extraction (MISPE). This developed method is simple，sensitive and accurate. It is suitable for the detection of MA and AMP residues in biological specimens for the clinical diagnosis of drug abuse patients. Xu Shoufang[20] demonstrated the construction and characteristics of photonic and magnetic dual responsive molecularly imprinted polymers (DR-MIPs) prepared by combination of stimuli-responsive polymers and a molecular imprinting technique. The novel DR-MIPs were used as a sorbent for the enrichment of caffeine from real water and beverage samples. Recoveries ranging from 89.5–117.6% were achieved.

Detection of toxic substances. Porous polymers have aroused increasing interest due to their controllable hole(s) structure in favor of mass transfer. Xu Shoufang[21] prepared three types of porous molecularly imprinted polymers (MIPs) using atrazine as template. The validated method was successfully applied to soil sample analysis, and satisfactory recoveries were attained, such as 73.5–102.0% with the precision of 1.17–4.24% for five triazines at 10 mg L^{-1}. Shi Xizhi[22] developed Group-selective molecularly imprinted polymers (MIPs) for amphenicol antibiotics, including chloramphenicol (CAP), thiamphenicol (TAP), florfenicol (FF), and florfenicol amine (FFA). Compared with conventional solid-phase extraction, significant recoveries ranging from 92.4% to 98.8% with lower relative standard deviation values in the range of 3.2–7.3% for both intraday- and interday-assays were obtained.

Prospect

Imprinted polymers has high selectivity, and its efficiency of separation and enrichment is significantly higher than traditional solid-phase extraction techniques. For this reason, I believe molecularly imprinted solid phase extraction technology will have a good application prospect.

References

[1]H.Y. Yan, G.L. Yang. The progress of molecularly imprinted solid phase extraction technique in the application of drug residues in animal origin food detection [J]. Chinese Journal of Chromatography,7,29(2011)

[2]Y.Q. Feng, R.J. Zhou, Y.B. Tang, X.X. Hu. The application of molecularly imprinted in solid phase extraction [J].PTCA(PARTB:CHEM,ANAL),1,47,(2011)

[3] Wulff G, Asarhan A. über die Anwendung von enzymanalog gebauten Polymeren zur Racemattrennung． Angewandte Chemie International Edition,1972,84(8) :364 -375．

[4]T.W.Tan.The technology and application of molecular imprinting[M].Chemical Industry Press,2010,6

[5]S.L.Wang, L.H. Shen, J.S.Wang. Synthesis and applications of Chrysophanol imprinted polymer solid-phase extraction [J]. Journal of Chinese Medicinal Materials,2010,33（12）:1946-1949.

[6] Y.H.Wang ,J.P. Huo, H.Zhang. Preparation and Application of Atrazine Molecularly Imprinted Solid Phase Extraction Pillar [J]. Chinese Journal of Analytical Chemistry,5,38(2010).

[8]J.Zhou, S.W.Wang, H.S. Guo. In situ molecular imprinted polymers prepared by continuous rod-type template legal chiral recognition [J]. Chinese Journal of Analytical Chemistry, 2000,28:296-299.

[11]E.H.M.Koster, C.Crescenzi, W.D. Hoedt, K. Ensing. Fibers Coated with Molecularly Imprinted Polymers for Solid-Phase Micro-extraction [J]. Anal. Chem., 2001, 73(13):3140-3145.

[12]F.H.Lin, X.J.Huang, D.X.Yuan. Preparation of Stir Cake Sorptive Extraction Based on Bisphenol A Imprinted Polymer and Its Extraction Performance [J]. Chinese Journal of Analytical Chemistry,2012,40（2）： 243-248.

[13]Y.X.Jia, R.H.Jia, H.M.Chen. Preparation and Application of Diazepam Molecularly Imprinted Polymers [J]. Journal of Instrumental Analysis,1,31,(2012).

[15] Y. Huang, Q.J.Zhang, M.Liu. Molecularly-imprinted solid phase extraction coupled with high performance liquid chromatography for the determination of ractopamine in feed samples [J]. Chinese Journal of Chromatography,1,30(2012).

[16]M. A. Gosefidi, Z. Es'haghi, A. Sarafraz-Yazdi . Design,synthesis and evaluation of a molecularly imprinted polymer for hollow fiber-solid phase micro-extraction of chlorogenic acid in medicinal plants[J].Journal of Chromatography A,1229(2012):24-29.

[17]H. Zeng, Y.Z.Wang, C.Nie. Preparation of magnetic molecularly imprinted polymers for separating rutin from Chinese medicinal plants[J].Analyst,137(2012):2503-2512.

[19] B.Zhu, Q.J.Chen, M.C.Jin. Simultaneous determination of methamphetamine and amphetamine in urine by high－performance liquid chromatography with molecularly imprinted solid－phase extraction [J]. Chinese Journal of Health Laboratory Technology ,6,22(2012).

[20]S.F.Xu, J.H.Li, X.L.Song. Photonic and magnetic dual responsive molecularly imprinted polymers: preparation, recognition characteristics and properties as a novel sorbent for caffeine in complicated samples [J].Analytical Methods, 16(2012):124-133.

[21]S.F.Xu, L.X. Chen ,J.H. Li .Preparation of hollow porous molecularly imprinted polymers and their applications to solid-phase extraction of triazines in soil samples[J].Journal of Materials Chemistry,21(2011):12047-12053.

[22]X.Z.Shi, S.Q.Song, A.L.Sun. Characterisation and application of molecularly imprinted polymers for group-selective recognition of antibiotics in food samples [J]. Analyst, 137 (2012), 3381-3389.

Applied Mechanics and Materials Vol. 597 (2014) pp 135-139
© (2014) Trans Tech Publications, Switzerland
doi:10.4028/www.scientific.net/AMM.597.135

Effect of Cooling Rate on the Microstructures and Mechanical Properties of Mg-Y Alloys

Goh Chwee Sim[1, a *], Khin Sandar Tun[1,b], Tan Xinghe[2,c], Chan Kwok Weng, Jimmy[2,d], Kwok Wai Onn, Richard[2,e], Manoj Gupta[3,f], Lee Teck Kheng[1,g]

[1]Technology Development Centre, Institute of Technical Education, 2 Ang Mo Kio Drive, Singapore 567720

[2]Singapore Technologies Kinetics, 249 Jalan Boon Lay, Singapore 619523

[3]Department of Mechanical Engineering, National University of Singapore, 10 Kent Ridge Crescent, Singapore 119260

[a]goh_chwee_sim@ite.edu.sg, [b]sandar_k_tun@ite.edu.sg, [c]tanxh@stengg.com, [d]chanjimmy@stengg.com, [e]kwokrichard@stengg.com, [f]mpegm@nus.edu.sg, [g]lee_teck_kheng@ite.edu.sg

Keywords: Magnesium-Yttrium Alloys, Cooling Rate, Compressive Strength, Microstructures

Abstract. Magnesium (Mg) alloys with 30 weight percentage (wt.%) of yttrium (Y) were gravity cast using copper mold and copper mold with air cooling. The results were benchmarked with Mg-30Y alloys produced using steel mold casting. It was found that the Mg-30Y alloys cast using the copper mold with air cooling exhibited the best mechanical properties, whereby the compression strength and the Vickers hardness value peak at 633 MPa and 137.6 HV respectively. Microstructural observations show that with increasing cooling rate, and hence increasing molten metal solidification rate, the dendrite structures are much finer due to enhanced nucleation rate. This is due to limited time for the dendrites to coarsen.

Introduction

Mg alloys are recognized as alternatives to steel and aluminum for weight saving applications in the aerospace and automotive industries. This class of alloys are known for their excellent properties such as high specific strength and stiffness, damping and electromagnetic shielding capacity.

Commonly used Mg alloys which include AZ91 and AZ31 have some shortcomings such as low strength and ductility as compared to other engineering alloys. Alloying Mg with rare earth elements [1, 2] are known to improve the strength of Mg through the effect of grain size refinement. Consequently, high temperature properties such as creep can also be improved. Bai et al. has studied on the effect of Y on the microstructures and the mechanical properties of Mg-Zn-Cu-Zr alloys [1]. It was found that Y can significantly reduce the grain size of Mg from 57 to 39 μm. Xu et al. found that when Y addition to Mg-Zn-Y-Zr alloy reaches 1.08 wt.%, the tensile strength is the maximum [3]. The high tensile strength is due to the presence of the Mg-Zn-Y interdendritic I phase which is strongly bonded to the Mg matrix, and can effectively retard basal slip. In another study [4], it was observed that when the Y concentration exceeds 1 wt.%, typically, 1.78 wt.%, the ultimate tensile strength and elongation increase substantially. To date, based on literature searches, most studies use Y additions of less than 10 wt.%, the beneficial effects of Y at high concentrations have not been fully explored.

Increasing cooling rate during solidification of Mg has always played an important role in reducing micro-segregation, forming metastable phases and refinement of microstructures. Yang et al. observed that the compressive yield strength of AZ91 Mg alloy increases substantially when the molten Mg melt was quenched using liquid nitrogen [5]. This can be attributed to the fine secondary

phases that are formed during rapid solidification. Copper mold cooling for Mg melt is commonly used in the fabrication of Mg bulk metallic glasses [6-8]. Amorphous Mg alloys can be formed due to the high cooling rate provided by the copper mold, large atomic size ratio mismatch exceeding 1.12 and the large negative mixing enthalpies between the different alloying elements [9]. While copper mold casting is common for amorphous alloys, the casting of Mg-Y alloys using copper molds has not been established.

Accordingly, the purpose of this work aims to study the effects of cooling rates on Mg-30Y alloys using copper mold and copper mold with air assisted cooling. The mechanical properties and microstructures of the fabricated Mg-30Y alloys using copper mold rapid solidification will be benchmarked with steel mold cast Mg-30Y alloys.

Experimental

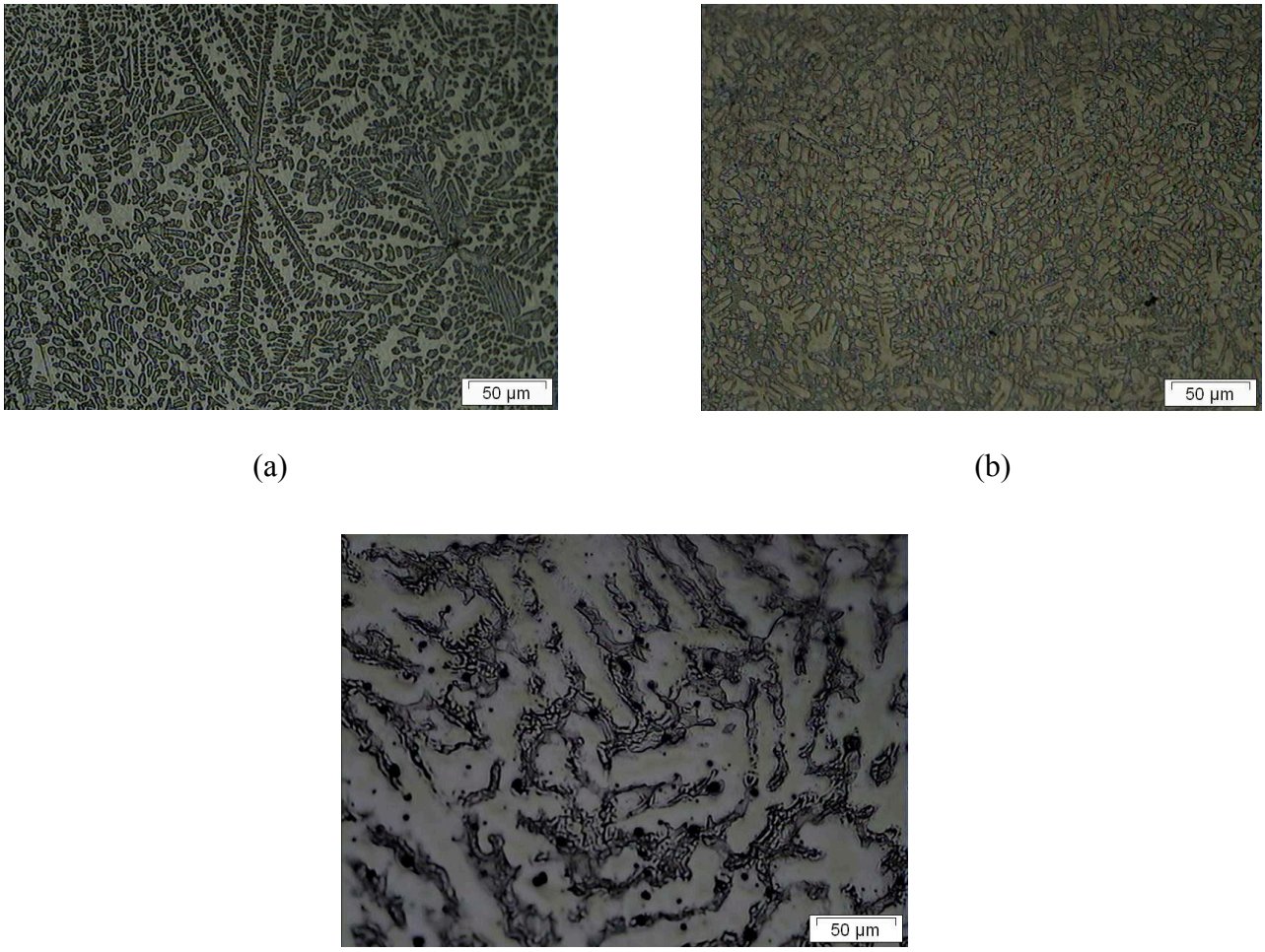
Preparation of Mg-Y Alloys. Mg ingots with >99.99% purity and Y pellets with >99.5% purity were used in this study. The Mg ingots together with the Y pellets were placed in a graphite crucible in an induction furnace. The crucible was then heated up to 950°C to melt the Mg and Y. Mixing and homogenization of the melt is carried out using the induction current. The homogenized melt is gravity cast into two different types of mold, typically, copper mold and copper mold with air cooling channels. The cavities in the copper mold are 5 mm in diameter. Solidification of the molten metal will then take place under different cooling rates. The Mg-30Y alloys gravity cast using the copper molds are then benchmarked against the Mg-30Y alloys melted under the same experimental parameters, but gravity cast into a steel mold.

Materials Characterization. Mechanical properties examined include uniaxial compressive properties and Vickers hardness. Uniaxial compressive tests were carried out with a Shimadzu AG-100kNIC testing machine at ambient temperature. The dimensions of the test specimen and testing methodology were in accordance with ASTM E9-89a. The strain rate was set at 5.0×10^{-4} s^{-1}. Microstructural examination was carried out using the Olympus STM6 optical measuring microscope and JEOL 6360A scanning electron microscope (SEM). Electron dispersive X-ray (EDX) analysis is used to identify the individual phases in the microstructure.

Results and Discussion

Microstructures. Fig. 1 shows the microstructures of the Mg-30Y alloys gravity cast using the three different types of mold. The Cu mold cooled Mg-30Y alloy shows a typical six fold symmetrical dendritic structure of the primary phase (Fig. 1a) [10]. The substantial development of the primary and secondary dendritic arms can be clearly seen. Fig. 1b shows the much finer dendritic structures of Mg-30Y alloy cast using Cu mold with air cooling. The primary and secondary dendrite phases are identified using EDX analysis as ε ($Mg_{25}Y_5$) phase, and the remaining structure as α-Mg (Fig. 2), which is in accordance to the Mg-Y phase diagram [11]. The formation of numerous and fine dendrites is a result of (1) the increase in nucleation rate due to the increase in the amount of undercooling derived from the faster cooling rate [12] and (2) limited time for dendrite growth. Multiple dendrites growth can be observed, with crystallites of different orientation growing independently, and the dendrites are observed to impinge at their tips. The numerous nuclei and the limited time available for growth prevent coarsening of individual dendrite structures.

Significantly coarser microstructures can be observed in steel mold cooled Mg-30Y alloys (Fig. 1c) as compared to Cu mold cooled alloys. According to Srivastava et al., the cooling rates that can be achieved using Cu mold range from 25 Ks^{-1} to 75 Ks^{-1} for a 5 mm diameter casting [13]. The range is due to the difference in cooling rate at the top and bottom of the mold. When the melt touches the bottom of the mold, it is cooled first. The copper mold will then be heated up, and this will affect the cooling rate for the Mg melt at the top of the mold. As the thermal conductivity of steel is 100 times lower than copper, cooling rate of Mg-30Y alloys in steel mold would be much slower. This would inevitably result in coarser dendritic microstructures in steel mold cast alloys.



(a) (b)

(c)

Fig. 1. Microstructures of (a) Cu mold cooled, (b) air cooling assisted Cu mold cooled and (c) steel mold cooled Mg-30Y alloys.

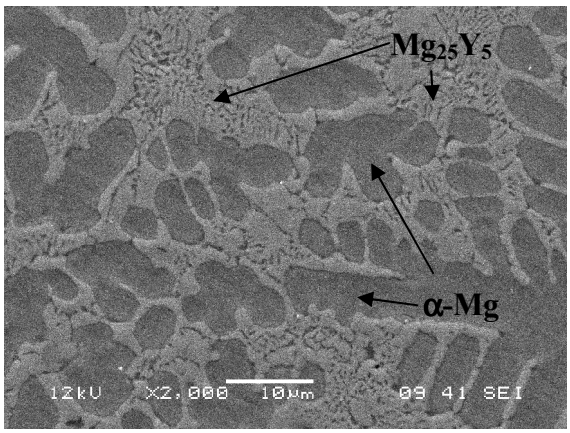


Fig. 2. Microstructure of Mg-30Y alloy cast with Cu mold with air cooling showing the respective phases

Vickers Hardness. The results from Vickers hardness testing are shown in Table 1. It can be seen that as the cooling rate increases, with the use of Cu mold and Cu mold with air cooling channels, the Vickers hardness values increase. The maximum hardness of 137.6 HV is attained with the use of Cu mold with air cooling channels. The higher hardness in Mg-30Y alloys cooled using Cu mold and Cu mold with air cooling, as compared with steel mold, is due to the finer dendritic structures in the alloy. The short spacing between the dendrite arms retards the dislocation motion, and increases the hardness of the Mg-Y alloys significantly by 48% as compared to the benchmark steel mold cast alloy.

Table 1. Mechanical Properties of Mg-30Y Alloys Gravity Cast using Different Types of Mold.

Type of Mold	Vickers Hardness (MPa)	CYS (MPa)	UCS (MPa)	Failure Strain (%)
Cu	107.1±5.4	302±23	528±12	15.4±1.8
Cu with Air Cooling	137.6±3.5	448±37	633±27	7.8±1.3
Steel	92.8±3.1	261±12	452±24	16.8±1.5

Compression Tests. The 0.2% compressive yield strength (CYS), ultimate compressive strength (UCS) and the failure strain results are shown in Table 1. Fig. 3 shows the compressive graphs of Mg-30Y gravity cast with the three different types of mold. It can be seen from Table 1 and Fig. 3 that Mg-30Y alloy cast using the Cu mold with air cooling has the highest CYS and UCS. Rapid solidification is known to refine microstructures and increase solid solution solubility [5]. The enhanced solidification rate provided by the Cu mold with air cooling has refined the microstructures to fine dendrites and increased the solid solution solubility of Y in Mg. This has resulted in the improved yield and ultimate compressive strengths of the Mg-30Y alloy.

The Mg-30Y alloy cast using Cu mold with air cooling has the lowest failure strain. This is due to the fine dendritic structures of the alloy, which inhibits dislocation motion. Plastic deformation is significantly reduced in this alloy, as compared to the steel mold cast alloy, which accounts for the relatively low failure strain.

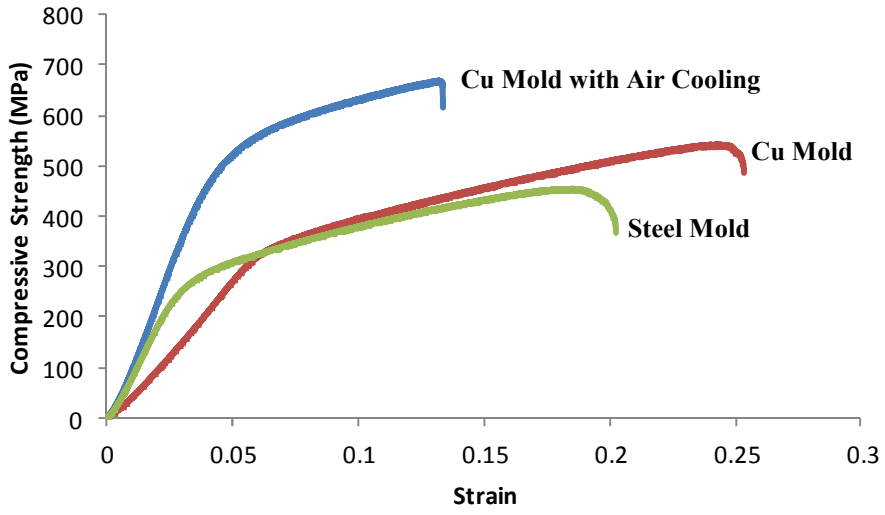


Fig. 3 Compressive graphs of Mg-30Y alloys gravity cast using three different types of mold.

Summary

The following conclusions can be drawn from this study:

1. Microstructural observations show that Mg-30Y alloys cast using Cu mold with air cooling has the most refined dendrites as compared to Cu and steel mold cast alloys. The much refined structures are due to the enhanced cooling rate and the limited time available for the dendrites to grow due to the higher solidification rate provided by the Cu mold with air cooling.
2. Mg-30Y alloys cast using copper mold with air cooling show the highest hardness of 137.6 HV. The short distance between the dendritic arms can effectively retards dislocation motion and increase the hardness of the alloy.
3. The highest CYS and UCS are observed in Mg-30Y alloys cast using Cu mold with air cooling. The refined microstructures and enhanced solid solution solubility has resulted in the improved strengths.

References

[1] Y. Bai, C. f. Fang and H. Hao, Effects of Yttrium on Microstructure and Mechanical Properties of Mg-Zn-Cu-Zr Alloys, Trans. NonFerrous Met. Soc. China. 20 (2010) s357-s360.

[2] R. H. Li, F. S. Pan, B. Jiang, H. M. Yin and T. T. Liu, Effects of Yttrium and Strontium Additions on As-cast Microstructure of Mg-14Li-1Al Alloys, Trans. NonFerrous Met. Soc. China. 21 (2011) 778-783.

[3] D. K. Xu, W. N. Tang, L. Liu, Y. B. Xu and E. H. Han, Effect of Y Concentration on the Microstructure and Mechanical Properties of As-cast Mg–Zn–Y–Zr Alloys, Journal of Alloys and Cpds. 432 (2007) 129-134.

[4] H. H. Zou, X. Q. Zeng, C. Q. Zhai and W. J. Ding, The effects of Y element on microstructure and mechanical properties of Mg-5wt.%Zn-2wt.%Al alloy, Materials Science and Engineering A. 402 (2005) 142-148.

[5] L. Yang, H. Feng, K. Q. Qiu, L. J. Chen and Z. Liu, Effect of Cooling Rate on Microstructure and Compressive Performance of AZ91 Mg Alloy, Trans. NonFerrous Met. Soc. China. 16 (2006) s1698-s1702.

[6] X. Hui, W. Dong, G. L. Chen and K. F. Yao, Formation, Microstructure and Properties of Long-Period Order Structure Reinforced Mg-Based Bulk Metallic Glass Composites, Acta Materialia. 55 (2007) 907-920.

[7] M. Kinaka, H. Kato, M. Hasegawa and A. Inoue, High Specific Strength Mg-Based Bulk Metallic Glass Matrix Composite Highly Ductilized by Ti Dispersoid, Materials Science and Engineering A. 494 (2008) 299-303.

[8] J. F. Wang, S. Huang, S. F. Guo, Y. Y. Wei and F. S. Pan, Effects of Cooling Rate on Microstructure, Mechanical and Corrosion Properties of Mg-Zn-Ca Alloy, Trans. NonFerrous Met. Soc. China. 23 (2013) 1930-1935.

[9] D. V. Louzguine-Luzgin and A. Inoue, Bulk Metallic Glasses: Formation, Structure, Properties, and Applications, in: K. H. J. Buschow (Eds.), Handbook of Magnetic Materials, Elsevier, Oxford, 2013, pp. 131-165.

[10] J. X. Zhou, J. Wang, J. Wang and Y. S. Yang, Eff. of RE and Sr add. on dendrite growth and phase pppt in AZ91D Mg alloy, Trans. NonFerrous Met. Soc. China. 20 (2010) s331 - s335.

[11] Information on http://link.springer.com/article/10.1007%2Fs11669-010-9661-4/fulltext.html

[12] Z. Y. Jian, F. E. Chang, W. H. Ma, W. Yan, G. C. Yang and Y. H. Zhou, Nucleation and undercooling of metal melt, Science in China (Series E). 43 (2000) 113-119.

[13] R. M. Srivastava, J. Eckert, W. Loser, B. K. Dhindaw and L. Schultz, Cooling Rate Evaluation for Bulk Amorphous Alloys from Eutectic Microstructures in Casting Process, Materials Transactions. 43 (2002) 1670-1675.

Applied Mechanics and Materials Vol. 597 (2014) pp 140-143
© (2014) Trans Tech Publications, Switzerland
doi:10.4028/www.scientific.net/AMM.597.140

Observation of Corrosion Resistance of 13Cr-2Ni-2Mo Stainless Steel Quenched by Induction Heating

Katsuyuki Kida [1 a], Koretomo Okamoto [2, b], Masayuki Ishida [1,c], Koshiro Mizobe[1,d] and Takuya Shibukawa [2, e]

[1] University of Toyama, 3190, Gofuku, Toyama City, Toyama Prefecture, 930-8555, Japan.
[2] YSK Co. Ltd., 3103-6, Otsu Kitanokawachi, Arita-cho, Nishimatuura-gun, Saga Prefecture, 849-4166, Japan.

[a] kida@eng.u-toyama.ac.jp, [b] k-seigi@shaft.co.jp, [c] m1471205@ems.u-toyama.ac.jp, [d] kmizobe@eng.u-toyama.ac.jp, and [e] t-shibukawa@shaft.co.jp

Keywords: 13Cr-2Ni-2Mo stainless steel, Induction heating, Corrosion resistance.

Abstract. 13%-Cr martensitic stainless steels are widely used in the production of many mechanical components that require high hardness and good corrosion resistance. In the present work, 20mm-diameter 13Cr-2Ni-2Mo steel bars were quenched by induction heating (IH) method and after that tempered in a farness. 240 hours corrosion test of the bars was carried out using a salt spray testing method (JIS Z 2371:2000). The results were compared to two stainless steels, SUS304 and SUS440C. Their inner hardness distributions were measured. It was found that the hardness of IH-quenched and farness-tempered 13Cr-2Ni-2Mo stainless steel is almost the same as that of the SUS440C. The 13Cr-2Ni-2Mo steel has the same corrosion resistance as the SUS304 steel.

Introduction

In recent years new steels have developed, and this has resulted in fewer failures in corrosion conditions. 13%-Cr martensitic stainless steels are widely used in the production of many mechanical components that require high hardness and good corrosion resistance. Many researchers reported that adding alloying elements, such as molybdenum, vanadium and nickel has a positive effect on the material's mechanical properties (Calliari et al.[1] and Takano et al.[2, 3]). The main advantages of alloy 13Cr-2Ni-2Mo stainless steel are high hardenability, cold workability and high corrosion resistance. Takano reported that the material had higher corosion resistance than SUS410 or zinc-coated carbon steel, and was applicable to `self - driling and - tapping screws.` In his research, the material was tempered at 200 ºC after quenched at 1050 ºC. In the present research, in order to make it suitable for more extensive applications in various industries, induction heating (IH) treatment was applied to the material. IH has been widely used in heat treatment of engineering steel elements (Haimbaugh [4]). In our previous studies, the microstructure of IH-hardened 13Cr-2Ni-2Mo stainless steel shafts was evaluated [7], and rolling contact fatigue life was ovserved using a single-ball RCF system [8]. Scanning laser micrographs of the IH-hardened sample in these papers indicated that the microstructure can be transformed to martensite through IH quenching.

In the present research, 20mm-diameter 13Cr-2Ni-2Mo steel bars were quenched by induction heating and after that tempered in a farness. 240 hours corrosion test of the bars was carried out using a salt spray testing method. The results were compared to two stainless steels, farness-quenched SUS304 and induction-heated SUS440C stainless steels. Changes in their surfaces before and after the tests were observed.

Experimental procedure

Specimens. The chemical composition of 13Cr-2Ni-2Mo stainless steel is shown in Table 1. The material was hot and cold drawn. In our previous paper, phase equilibrium diagram simulated by JMatPro software (UES Software Inc., USA) found transformation from ferrite to austenite begins at 775ºC. At temperatures ranging from 871ºC to 1173ºC, the ferrite content is zero. Furthermore, all $M_{23}C_6$ carbides are dissolved at temperatures higher than 992ºC. In order to produce material containing high levels of high hardness martensite after quenching, it is necessary to heat it to

temperatures ranging from 871ºC to 1173ºC, ideally from 992ºC to 1173ºC. It is noted that the standard number of Ni composition of the 13Cr-2Ni-2Mo steel ranges from 1.00 to 2.40 wt.%. The material used in the previous [7] and present researches include 1.03 wt.% and 1.04 wt.% Ni, respectively.

Shape of all bar specimens were 20 mm diameter and 50 mm length. Diameter of the coil used during the IH treatment was 30mm. Speed of the IH procedure was 12.1mm/s. After the IH, specimens were tempered at 180 ºC for 120 min and cooled in farness for 60 min. The IH heat-treated samples were cut in the radial direction. The cross sections of the specimens were polished for the hardness measurement.

The corrosion resistance of the 13Cr-2Ni-2Mo steel was compared to SUS304 and SUS440C steels. The SUS 304 samples were water-quenched at 1050 ºC for 40 minutes. The SUS440C specimens were subjected to annealing at 180 ºC for 60 minutes after IH quenching. The IH procedure speed was 26.7mm/s. The chemical compositions of the SUS304 and SUS440C steels are shown in Table 1.

Corrosion test. Samples were subjected to corrosive conditions for 240 hours. The corrosion tests were carried out using a salt spray testing method (JIS Z 2371: 2000). Test machine was SQ-800-ST (Itabashi Rikakogyo Co., Ltd., Japan). One of the samples was taken out of the machine chamber every 24 hours. In the chamber, a salted solution (5% sodium chloride) was atomized from a nozzle and temperature was kept at 35 ºC $^{+}$.2 ºC. The machine included two sampling funnels whose area was 80cm^2. Average pH values were 6.7 and 6.5 for 1.1ml/h and 1.3ml/h solutions in two cylinders connected to the funnels, respectively.

Vicker's indentation tests. The hardness distributions of the cross sections of the specimens were measured using a standard Vickers hardness tester (VMT-X7s, Matsuzawa Co., Ltd, Japan) under a load of 9.8N during 15seconds.

Table 1. Chemical compositions of the specimens (wt. %).

	C	Si	Mn	P	S	Ni	Cr	Mo	N	Fe
13Cr-2Ni-2Mo stainless steel	0.17	0.35	0.17	0.020	0.05	1.04	12.84	1.82	0.089	R.
JIS, SUS304	0.017	0.50	1.45	0.034	0.028	9.00	18.00	-	-	R.
JIS, SUS440C	1.03	0.30	0.28	0.028	0.001	0.11	16.34	0.35	-	R.

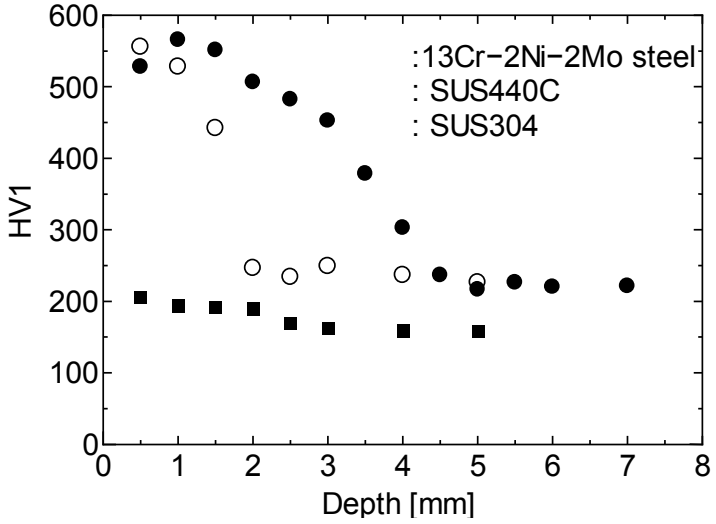


Fig. 1 Hardness distributions.

Experimental results and discussion

Vicher's hardness distribution. Figure 1 shows the hardness distributions of 13Cr-2Ni-2Mo, SUS440C and SUS304 stainless steels. The HV1 value near the surface of the 13Cr-2Ni-2Mo steel was about 530, which is almost the same as that of the SUS440C stainless steel. The depth of the hardened area where the HV1 is more than 500 is about 2 mm.

Nippon Steel & Sumikin Stainless Steel Corporation annealed and tempered the 13Cr-2Ni-2Mo specimens at 1150 ºC and at 200 ºC, and reported that its hardness was 550 HV [9]. This value is almost the same as that of the 13Cr-2Ni-2Mo steels in the present test. These results mean the present induction heating process succeeded to increase the hardness of the 20mm-diameter 13Cr-2Ni-2Mo steel bars to the level through farness-heating process.

Corrosion test. Figure 2 shows samples before the corrosion test. One of ten samples was taken out of a corrosion chamber every 24 hours. Figures 3 - 7 show the samples during the test. Each figure has three kinds of samples. Left, center and right are SUS304, SUS440C and 13Cr-2Ni-2Mo steels, respectively. Red rust is observed on SUS440C sample surface of Fig. 3. When comparing the center samples (SUS440C) in Figs. 3 - 7, it is found the rust area increases with the increase of corrosion time.

No rust is observed in SUS304 and 13Cr-2Ni-2Mo steel samples. In Ref. 9, the corrosion resistance of 13Cr-2Ni-2Mo steel was compared to those of SUS304 and SUS410 steels using the salt spray test, and reported that only SUS410 rusted during 240 hours. This result means that the induction heated 13Cr-2Ni-2Mo stainless steel has the same corrosion resistance as the SUS304 steel.



Fig. 2 Photo of specimens before corrosion test. Left, center and right are SUS304, SUS440C, and 13Cr-2Ni-2Mo stainless steels, respectively.



Fig. 3 Photo of specimens after 24 hours corrosion test.



Fig. 4 Photo of specimens after 48 hours corrosion test.



Fig. 5 Photo of specimens after 96 hours corrosion test.

Conclusions

The effect of induction heating on the corrosion resistance of 13Cr-2Ni-2Mo stainless steel was investigated. 20mm-diameter 13Cr-2Ni-2Mo steel bars were quenched using induction heating method and after that tempered at 180 ºC for 120 minutes in a farness. 240 hours corrosion test was carried out based on salt spray method. The results were compared to two stainless steels, SUS304 and SUS440C. Changes in their surfaces before and after the test were observed. Furthermore, the subsurface hardness distributions in all samples were measured. It is concluded that the hardness of IH-quenched and farness-tempered 13Cr-2Ni-2Mo stainless steel is almost the same as that of SUS440C. The 13Cr-2Ni-2Mo steel has the same corrosion resistance as SUS304 steel.



Fig. 6 Photo of specimens after 192 hours corrosion test.



Fig. 7 Photo of specimens after 240 hours corrosion test.

Acknowledgement

A part of this research was supported by the Small and Medium Enterprise Agency, No. 41120032.

References

[1] I. Calliari, M. Zanesco, M. Dabalà, K. Brunelli and E. Ramous, *Materials and Design*, Vol. 29, PP. 246-250. (2008).

[2] K. Takano, M. Sakakibara, T. Matsui and S. Takaki, *J. Iron Steel Inst. Jpn.*, Vol. 86, pp. 123-130. (2000).

[3] K. Takano, W. Murata, K. Yoshimura, M. Sakakibara and T. Matsui, *Nippon Steel Technical Report*, No. 71, pp. 53-63. (1996).

[4] R. E. Haimbaugh, *Practical Induction Heat Treating*, ASM Intl., USA. (2001).

[5] H. Koike, E. C. Santos, K. Kida, T. Honda and J. Rozwadowska, *Advanced Materials Research*, Vols. 217-218, pp.1266-1271. (2011).

[6] T. Hayashi, N. Kurosawa and K. Yamada, *JFE Technical Report*, No. 15 , pp. 4-9. (2010).

[7] T. Honda, E. C. Santos, K. Kida and T. Shibukawa, *International Journal of Materials and Product Technology*, Vol. 45, No.1/2/3/4/, pp.31-40. (2012).

[8] K. Kida, T. Honda, Y. Seto, E. C. Santos and T. Shibukawa, *Applied Mechanics and Materials*, Vols. 300-301, pp.1372-1376, (2013).

[9] http://nssc-global.com/en/pdf/product/grade/martensite/NSSC_550_en.pdf, (2013).

Applied Mechanics and Materials Vol. 597 (2014) pp 144-150
© (2014) Trans Tech Publications, Switzerland
doi:10.4028/www.scientific.net/AMM.597.144

Study on the use of fleshings-derived collagen in post tanning operations

Monica Puccini[1,a] and Domenico Castiello[2,b]

[1] Department of Civil and Industrial Engineering, University of Pisa, Largo Lucio Lazzarino 1, 56122 Pisa, Italy

[2] Po.Te.Co. Scrl – Polo Tecnologico Conciario, Via Walter Tobagi, 30, 56022 Castelfranco di Sotto Pisa, Italy

[a]m.puccini@diccism.unipi.it, [b]d.castiello@polotecnologico.com

Keywords: collagen hydrolizate, retannage, dyeing, fatliquoring

Abstract: The leather industry generates waste either in solid or liquid form. Fleshing, which is integral part of a hide, is removed during leather processing as it is an unwanted material in the final product. For every ton of leather processed, about 100–150 kg of fleshing is generated. An alternative to disposal of these wastes is to reuse them. In this study, an experimental activity research for assessing the feasibility of the reuse of the collagen hydrolizate in the retanning/dyeing/fatliquoring phase was performed. The hydrolyzed collagen, in liquid form, is obtained by alkaline hydrolysis of fleshings. The hydrolizate has been used both in a vegetable-chrome retannage/dyeing/fatliquoring and in a vegetable retannage/dyeing/fatliquoring to obtain bovine upper leather. Both in a vegetable-chrome retannage and in a vegetable retannage, the final leathers showed similar properties in terms of physical and technical properties to conventionally processed hides. The results obtained indicate that the use of the collagen hydrolizate in the retanning/dyeing/fatliquoring phase as an interesting route for recovering the fleshings.

Introduction

Leather is one of the oldest commodities in world market. Leather industry is today also synonymous with pollution, and a worldwide interest in the development of novel and cleaner tanning processes has been developed [1-3]. Every step in leather processing generates wastes either in solid or liquid form. Research interest has thus focused on the development of processes for the treatment, recycling, and reuse of these by-products, such as the separation systems for recovery of chromium and protein, and the manufacture of composites [4-7]. These studies include research activity involving the enzymatic or alkaline hydrolysis of leather wastes, generating a residue rich in liquid hydrolyzed protein [8]. The hydrolyzed protein solution could be used in several industrial sector to produce cosmetics, food, medicines, animal feeds, and fertilizers. However, the presence of traces of chromium and the low molecular weight of the obtained protein make the use of these collagene solution difficult.

Fleshing, which is integral part of a hide, is removed during leather processing as it is an unwanted material in the final leather. For every ton of leather processed, about 100–150 kg of fleshing is generated. A measure of its environmental impact is given by the wastes from fleshing of the industrial tannery district of Santa Croce sull'Arno (Italy), whose production is close to 80,000 tons/year. In Santa Croce, the fleshing of the whole district is collected and processed in a centralized plant where, through an alkaline hydrolysis, a raw collagen hydrolizate solution is obtained. The high content of salts of the raw collagen hydrolizate, whose separation is cost effecting, is the obstacle that makes difficult its reutilization.

In the present study, an experimental investigation was performed for assessing the possibility of recycling the salted collagen hydrolizate in the retanning/dyeing/fatliquoring phases of the bovine upper leather production cycle. In order to assess the feasibility of the use of the collagen hydrolizate for a wide range of final products, the retanning/dyeing/fatliquoring has been developed both after a standard chrome tannage and after a standard vegetable tannage. Besides, the collagen

hydrolizate has been inserted into the recipe either in total/partial substitution of filler/fatliquoring agents or in addition of the traditional components. The procedures, investigated and set up on pilot scale, has been validated on an industrial scale. The quality of the final leathers obtained has been assessed through their technical and mechanical properties.

Experimental procedures

The raw collagen hydrolizate solution was supplied by S.G.S. S.p.A. of Santa Croce sull'Arno (Italy), a centralized plant that treats the wastes from fleshing of all the Tuscany leather district. The hydrolizate solution is obtained through alkaline hydrolysis, degreasing and concentration.

Pilot-scale tanning studies were carried on fresh salted calfskins (weight class 12–16 kg/skin) in a semi-industrial stainless steel drum (1.2 m diameter, 0.8 m length). The hides were soaked, limed, delimed, bated, and pickled using a standard procedure. Afterward, some hides were chrome tanned and the rest was vegetable tanned (by using a mix of chestnut and tara) according to conventional procedures. After tannage, each hide, previously pressed and shaved (1.1 or 1.4 mm), was divided into two sides: one side was retanned/dyed/fatliquored according to the standard recipe, the other side by introducing the collagen hydrolizate. A chrome-vegetable retanning/dyeing/fatliquoring step followed the chrome-tannage, while a vegetable retanning/dyeing/fatliquoring step was provided for the vegetable tanned hides. The collagen hydrolizate was inserted into the chrome-vegetable retanning/dyeing/fatliquoring recipe in total/partial substitution of filler/fatliquoring agents, while in the vegetable retanning/dyeing/fatliquoring it was simply added to the standard recipe.

After retanning, the crust leathers obtained were characterized by their main physical and technical properties. The leather samples for physical testing were cut from the tanned crust leathers according to the official sampling position (IUP2 2000) from each run. The physical testing were conducted according to Italian standards (UNI 10594) for upper leather. The load at tear was determined according to the UNI EN ISO 3377-2 method using an electronic dynamometer (Pegasil, Mod. Marte) which also gives the extension at tear as a secondary output. The extension and load at grain crack were determined according to the UNI EN ISO 3379 (recently converted in UNI 11308) method using a lastometer (Pegasil, Mod. EL-51E).

The exhausted floats after retanning and after fatliquoring were sampled. Their dry matter and ash contents were determined by drying in oven at 105°C and by heating in furnace at 800°C, respectively.

Results and discussion

The composition of the collagen hydrolizate solution used in this study is reported in Table 1. The salt content appears quite elevated and it is due mainly to the presence of NaCl, used in the conservation of the hides. Besides, the protein phase is characterized by a quite low molecular weight and by the presence of a significant percentage of free amino acids. This composition is due to the high degree of hydrolysis of the polypeptides induced by the strong alkaline treatment.

Use of the collagen hydrolizate in the retannage/dyeing/fatliquoring of crome-tanned leather: semi-industrial scale runs. Three runs were performed by varying the modality of the introduction of the collagen hydrolizate in the process:

- Run 1: the collagen hydrolizate was introduced in total substitution of the anionic retanning agents (quebracho, diciandiaminic resin, and acrylic resin, global dosage 14%) and in total substitution of the fatliquoring agents (global dosage 6%);
- Run 2: the collagen hydrolizate was introduced in partial substitution of the anionic retanning agents (quebracho, diciandiaminic resin, and acrylic resin, global dosage 7%, were dosed with collagen hydrolizate 7%) and in total substitution of the fatliquoring agents (global dosage 6%);
- Run 3 the collagen hydrolizate was used in total substitution of the filler (3% dosage).

Each run was conducted by using correspondent sides of the same whole hide: one side was retanned/dyed/fatliquored according to the standard recipe (blank runs), the other according to the same recipe, modified with the total/partial substitution with the collagen hydrolizate.

Table 1. Composition and physico-chemical properties of the collagen hydrolizate solution

Properties	
Dry matter (wt %)	68
Ashes (800°C)	14
Organic nitrogen (wt%)	6.5
Organic carbon (wt %)	23.5
Free amino acids (wt %)	7.9
Total amino acids (wt %)	54
Mean molecular weight (kDa)	1.84
S (as SO_2, mg/kg)	385
P (as P_2O_5, mg/kg)	33.6
K (mg/kg)	990
Ca (as CaO, mg/kg)	853
Na (wt.%)	9.9
Cl (wt.%)	6.1
pH	7.0-7.5
Density (g/cm^3)	1.25-1.28

In order to observe the degree of exhaustion of the collagen hydrolizate, the exhausted floats after retannage and after fatliquoring were analysed by their dry and ash content. The results of the analysis are shown in Table 2. As expected, in Run 3, where the collagen hydrolizate was used only in the fatliquoring step in total substitution of the filler, no significant increase of the dry matter and of the ash content of the exhaust floats after retannage was observed. On the contrary, after fatliquoring, the exhaust float shows an increase of the dry matter and of the ash content. The higher dry matter may be related to a lower exhaustion of the collagen hydrolizate, while the higher ash content by the salt present in the hydrolizate solution. In the Runs 1 and 2, where the collagen hydrolizate was used also in the retanning phase, the dry matter and ash content increase both after re-tannage and after fatliquoring and result as higher as the collagen hydrolizate dosage increases. The exhaustion of the hydrolizate appears thus to decrease as the dosage is increased.

Results of the physical tests, conducted on the retanned, dyed and fatliquored samples, are given in Fig. 1. The physical performances of the crust leathers seem to slightly improve when the collagen hydrolizate is used. All samples show good physical properties; the extension at crack test gives a result of between 7.8 and 10 mm (well above the lower limit of 7 mm established by the norm UNI 10594). The tear load test gives a result of between 40 and 77 N, that comply with the requirements. The best performance is obtained when the hydrolizate is used in substitution of the filler.

Table 2. Dry matter content and ash content of the exhaust floats of the vegetable-chrome retannage

	Dry matter (wt%)		Ash content (wt%)	
Run	after retannage	after fatliquoring	after retannage	after fatliquoring
Run 1	3.81	1.40	1.28	0.32
Run 1- blank	3.34	1.17	1.20	0.25
Percentage increase	+ 14.1	+ 19.6	+ 6.67	+ 28.0
Run 2	2.65	1.40	1.12	0.46
Run 2 - blank	2.43	1.15	1.05	0.40
Percentage increase	+ 9.05	+ 21.7	+ 6.67	+ 15.0
Run 3	2.84	1.26	1.35	0.41
Run 3 - blank	2.80	1.13	1.32	0.33
Percentage increase	+ 1.43	+ 11.5	+ 2.27	+ 24.2

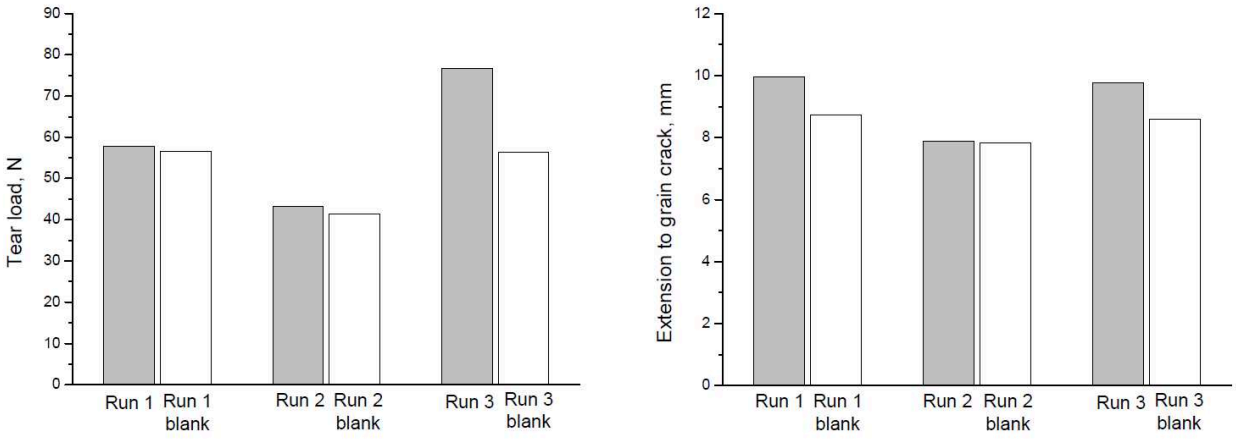


Fig. 1. Tear load and extension at crack of the vegetable-chrome retanned crust leathers

The technical performance was based on handling and tactile evaluations made upon the crust leather by the experienced technologists and expressed numerically. A rating for each property was awarded on a scale of 1 to 5. The results are reported in Table 3. It may be observed that the use of the hydrolizate improves significantly the dyeing performances: the dyeing results more intense and homogeneous. Despite the good result in terms of uniformity and yield of colour, the crust leather obtained in the Run 1 does not complies with the standards required for high-quality leathers. Also the Run 2, even if showing slightly better performances, does not reach the high quality displayed by the blank crust leather. An acceptable performance is given by the Run 3, when the hydrolizate is used in substitution of the filler.

Table 3. Technical evaluation of the vegetable-chrome crust leathers

Parameter	Blank	Run 1	Run 2	Run 3
Uniformity of colour	3	4	4	4
Intensity of colour	3	5	4.5	4.5
Roundness	3	2	3	4
Fullness	4	3	3.5	3.5
Feel	4	4	4	4.5
Lightness	5	4	5	5
Softness	4	3	3.5	4

Following the results obtained, it may be concluded that the optimal use of the collagen hydrolizate may be found in the total substitution of the filler (in the fatliquoring phase). In this case, an increase of the physical properties is achieved with respect to the standard recipe, being the technical properties practically identical. The lubricating effect of the collagen hydrolizate upon the fibrous structure, as well as the softness provided by the hydrophilic property of protein hydrolyzed may explain the resistance against mechanical stress.

Use of the collagen hydrolizate in the retannage/dyeing/fatliquoring of vegetable-tanned leather: semi-industrial scale run (Run 4). Following the same procedures reported in the previous section, in this case the retannage/dyeing/fatliquoring was conducted by simply adding the collagen hydrolizate to the retanning agents (6% dosage). In the case of a vegetable-tanned leather, the technical standard required (fullness, roundness, feel) imply the use of specific retanning and fatliquoring agents that cannot be eliminated from the recipe. Since the collagen hydrolizate has shown the capability of improving the physical and dyeing performances, it was added to the recipe to verify if this capability is displayed also in the vegetable tannage and retannage.

Results of the physical tests, conducted on the retanned, dyed and fatliquored samples, are given in Fig. 2. Also in this case, the physical performances of the crust leathers seem to slightly improve when the collagen hydrolizate is used. All samples show good physical properties; the extension to

crack test gives a result of 8.7 and 9.2 mm (well above the lower limit of 7 mm established by the norm UNI 10594). The tear load test gives a result close to 50 N, that comply with the requirements.

The technical performance results are reported in Table 4. The improvement of the dyeing performances when the hydrolizate is added to the recipe is confirmed. The other technical parameters appear comparable or, in some cases, better than the blank crust leather.

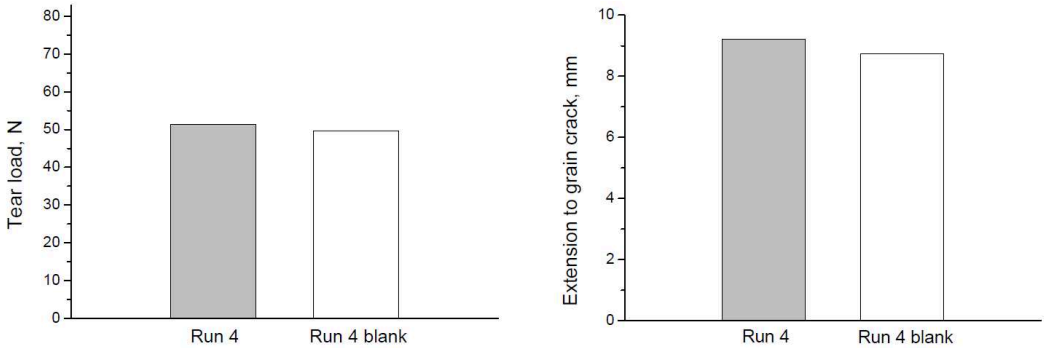


Fig. 2. Tear load and extension at crack of the vegetable retanned crust leathers

Use of the collagen hydrolizate in the retannage/dyeing/fatliquoring of chrome-tanned leather: industrial scale run (Run 5). Following the results obtained ion the pilot scale, an industrial run was performed to assess on real scale the total substitution of the filler with the collagen hydrolizate in the chrome-vegetable retannage/dyeing/fatliquoring. Due to the good results obtained in the preliminary semi-industrial scale runs, the dosage of the hydrolizate was increases from 3 to 6%.

The hides were processed using a standard formulation up to the chrome tannage according to standard procedures. After tannage the skins, previously pressed and shaved (1.4 mm), were divided into two sides, retanned and dyed. After dyeing, ten sides, extracted from the drum, were separately fatliquored in the semi-industrial drum by substituting the filler with the hydrolizate, while the other were fatliquored in the industrial drum according to the standard recipe.

Table 4. Technical evaluation of the vegetable retanned crust leathers

Parameter	Blank	Run 4
Uniformity of colour	4	4
Intensity of colour	3	4.5
Roundness	4	4
Fullness	4	4
Feel	4	4
Lightness	5	5
Softness	4	4

Table 5 reports the determination of the dry matter and ash content of the fatliquoring exhaust floats. Similarly to the semi-industrial Run 3, after fatliquoring, the exhaust float shows an increase of the dry matter and of the ash content. The higher dry matter may be explained by a lower exhaustion of the collagen hydrolizate, while the higher ash content by the salt present in the hydrolizate. The higher percentage increases are due to the higher dosage of the hydrolizate.

The physical tests (Fig. 3), and the technical evaluations (Table 6) confirm the results obtained on semi-industrial scale.

Table 5. Dry matter content and ash content of the exhaust floats of the vegetable-chrome retannage on industrial scale and ash content of the crust leathers

	Dry matter (wt%)	Ash content (wt %)	Ash content (wt%)
Run	after fatliquoring	after fatliquoring	
Run 5	1.72	0.71	6.60
Run 5- blank	1.16	0.44	7.08
Percentage increase/decrease	+ 48.3	+ 61.4	- 6.77

Table 6. Technical evaluation of the vegetable-chrome re-tanned crust leathers on industrial scale

Parameter	Blank	Run 5
Uniformity of colour	3	4
Intensity of colour	3	4.5
Roundness	4	4
Fullness	4	4
Feel	4	4.5
Lightness	5	5
Softness	4	4

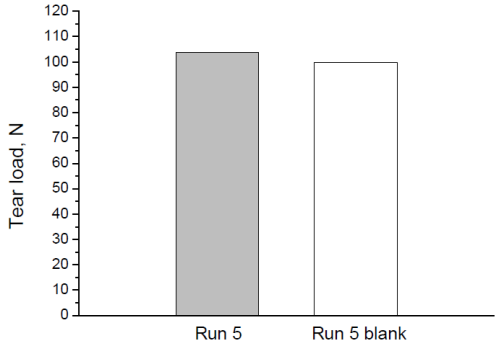


Fig. 3. Tear load and extension at crack of the vegetable retanned crust leathers on industrial scale

Conclusions

The investigation conducted assesses the feasibility of the use, in the retanning/dyeing/ fatliquoring phase, of the collagen hydrolizate obtained by alkaline hydrolysis of the fleshings, one of the most important by-product of the leather compartment. The hydrolizate has been used both in a vegetable-chrome re-tannage dyeing/fatliquoring and in a vegetable retannage dyeing/fatliquoring to obtain bovine upper leather. In the vegetable-chrome re-tannage the best results are obtained when the hydrolizate is used in total substitution of the filler in the fatliquoring step up to a dosage of 6% of solution (68% dry content) on the shaved hide weight. In the vegetable retannage/dyeing/fatliquoring the best results are obtained when the hydrolizate is used in addition to the standard components in the retanning step up to a dosage of 6% of solution on the shaved hide weight. Following a semi-industrial scale screening of the optimal operating conditions, crust leather have been obtained on industrial scale. The hydrolizate solution may be used as it is obtained by the industrial alkaline hydrolysis process currently adopted in the Santa Croce sull'Arno tanning district. Both in a vegetable-chrome retannage and in a vegetable retannage, the

final leathers show similar properties in terms of physical and technical properties. The salt content of the solution is not damaging of the physical and technical properties of the final leather, or rather the introduction of the hydrolizate in the skin structure produces better technical qualities, particularly in terms of better quality of the dyeing that results more intense and homogeneous. An elevate exhaustion of the hydrolizate was observed, so that a minimal fraction is discharged through the exhaust floats. The results obtained indicate the reutilization of the collagen hydrolizate in the retanning/dyeing/fatliquoring phase as a promising alternative for recovering the fleshings.

References

[1] M. Puccini, M. Seggiani, D. Castiello, S. Vitolo, Sustainability in process innovation: development of a green tanning process supported by LCA methodology, J. Am. Leather Chem. As. 109 (2014) 110-116.

[2] D. Castiello, M. Puccini, M. Seggiani, S. Vitolo, F. Zammori, Life Cycle Assessment (LCA) of the oxidative unhairing process by hydrogen peroxide, J. Am. Leather Chem. As. 102(11) (2009) 1-5.

[3] M. Puccini, M. Seggiani, D. Castiello, S. Vitolo, DEPOXO process: Technical and environmental study of hide oxidative unhairing, Chemical Engineering Transactions 36 (2014) 193-198.

[4] R. Murali, A. Anumary, M. Ashokkumar, P. Thanikaivelan, B. Chandrasekaran, Hybrid biodegradable films from collagenous wastes and natural polymers for biomedical applications, Waste Biomass Valor. 2(3) (2011) 323-335.

[5] M. Puccini, M. Seggiani, D. Castiello, G. Calvanese, S. Vitolo, Novel thermoplastic materials from wastes of the leather industry, Applied Mechanics and Materials 467 (2014) 41-48.

[6] D. Castiello, E. Chiellini, P. Cinelli, S. D'Antone S., M. Puccini, M. Salvadori, M. Seggiani, Polyethylene-collagen hydrolizate thermoplastic blends: thermal and mechanical properties, J. Appl. Polym. Sci. 114(6) (2009) 3827-3834.

[7] M. Puccini, D. Castiello, M. Seggiani, S. Vitolo, Properties of thermoplastic blends with polypropylene and collagen hydrolizate, Advanced Materials Research 893 (2014) 235-240.

[8] I. Bragança, A. Crispim, A. Sampaio, E. Ramalho, F. Crispim, N.S. Caetano, P.C. Silva, Adding value to tannery fleshings: Part I - Oils and protein hydrolysates - Production and application, J. Soc. Leath. Tech. Ch. 97(2) (2009) 62-67.

CHAPTER 3:

Films, Coating and Surface Engineering

Applied Mechanics and Materials Vol. 597 (2014) pp 153-156
© (2014) Trans Tech Publications, Switzerland
doi:10.4028/www.scientific.net/AMM.597.153

Ionic Distribution in Plasma for the Process of Electron-Beam Physical Vapor Deposition

Ching-Yen Ho[1,a,*] and Wen-Chieh Wu[2,b]

[1] Department of Mechanical Engineering, Hwa-Hsia Institute of Technology, Taipei 235, Taiwan

[2] Department of Electronical Engineering, Hwa-Hsia Institute of Technology, Taipei 235, Taiwan

[a]hcy2126@go.hwh.edu.tw, [b]wcw@cc.hwh.edu.tw

*Corresponding author

Keywords: Electron beam, Ionic distribution, Coating, Physical vapor deposition.

Abstract. This paper investigates ionic distribution generated by electron beam (EB) during Physical Vapor Deposition (PVD). EB-PVD has a wide range of applications in thermal barrier coatings (TBCs) due to favorable characteristics compared with other coating processes. EB-PVD is an important material coating method that utilizes electron beams as heat sources to evaporate materials, which are then deposited on a substrate. Therefore EB-induced ionic distribution dominates the quality and thickness of the final coating on the substrate. Assuming the EB-generated plasma to be only a function of radial direction, the steady-state equations of continuity and motion combined with Posson's equation were utilized to analyze the plasma distributions along the radial direction. The available experimental data are also used to validate the model. The results show that the coating efficiency can be improved by decreasing the ratio of the electron thermal energy to the initial ion energy and increasing the ratio of the initial ion density to the initial electron density. The uniformity of coating can be achieved by reducing the initial ion density.

1. Introduction

Physical Vapour Deposition (PVD) is applied to the production of material coatings, semiconductor devices, optical components and wear resistant coated mechanical parts [1]. The technique of electron-beam evaporation is a widely used physical vapour deposition method which allows high deposition rates [2]. Electron Beam Physical Vapour Deposition (EB-PVD) utilizes electron beams as heat sources to evaporate materials, which are then deposited on a substrate [3]. The physical phenomena involved during materials evaporation, transport and condensation on the substrate are of importance since these determine quality of coating, film thickness and composition [4,5].

Although the models predicting the thickness distribution profile of coating of EB-PVD had been proposed, little of papers investigating the coating uniformity due to the oscillation spatial distribution of electron beam-induced plasma have been done. Therefore this paper studies the oscillation spatial distribution of electron beam-induced ions to improve the coating quality.

2. Analysis

As shown in Fig. 1, considering a steady-state radial plasma expansion from the boundary surface of the plasma production region, the equations of continuity and motion for the ions fluid follow as

$$\nabla \bullet (n_i \quad) = 0 \tag{1}$$

$$m(\quad \bullet \nabla) \quad = -e\nabla U \tag{2}$$

and Posson's equation, which provides the self-consistent coupling between the electron motion and ion background, is used to describe the spatial distribution of the potential in the plasma expansion region.

$$-e(n_e - n_i) = \varepsilon_0 \nabla \bullet \nabla U \tag{3}$$

where *e, m,* n_i and **u** correspondingly symbolize the charge, mass, density and velocity of the ions. U is the positive potential of the plasma. n_e and ε_0 represent the electron density and the permittivity of vacuum, respectively.

It is considered that the steady-state radial plasma expands from the boundary surface of the plasma production region. To simplify the model, the following assumptions are made

(i) As shown in Fig. 1, the plasma production region is cylindrical.

(ii) The generation of charged particles is balanced by radial flow to grounded metallic walls where the zero electrostatic potential holds.

(iii) The motion of electrons and ions is collisionless.

(iv) Plasma is positively charged with maximal potential at $r = r_p$.

3. Results and discussion

Figure 1 demonstrated how the electron density varied with radial distances for the different ratios of the electron thermal energy to the initial ion energy and compared the electron density asymptotically predicted by this work with that from the measurement. The parameter **a** represents the ratio f the electron thermal energy to the initial ion energy, which is defined as $kT_e /(mv_0^2 / 2)$. The solid line and circle symbolized the calculated and measured data, respectively. From this figure it was seen that the electron density predicted by this work agrees well with that from the measurement. This validated the model developed by this study. The logarithm of electron density linearly decreases along the logarithm of radial direction distances. This result is consistent with the relation $n_e \propto 1/r^m (m \approx 1)$ [6]. The decrease of the ratio value **a** increases the electron density. This attributes to the decrease of electron temperature with the decreasing ratio value **a**.

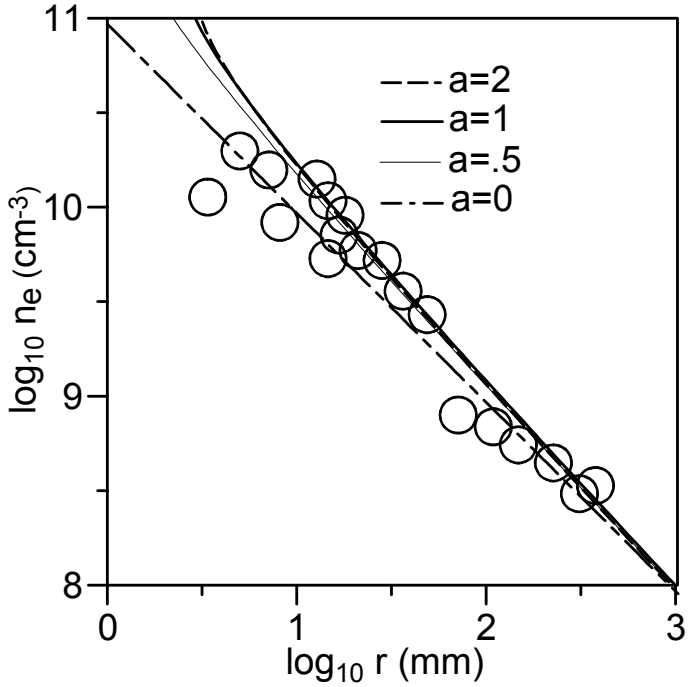


Fig. 1. Variation of the measured and asymptotically predicted electron densities (Eqs. 16 and 13) with radial distances for the different ratios of the electron thermal energy to the initial ion energy. (D=0.04, n_{ip}/n_{ep}=1)

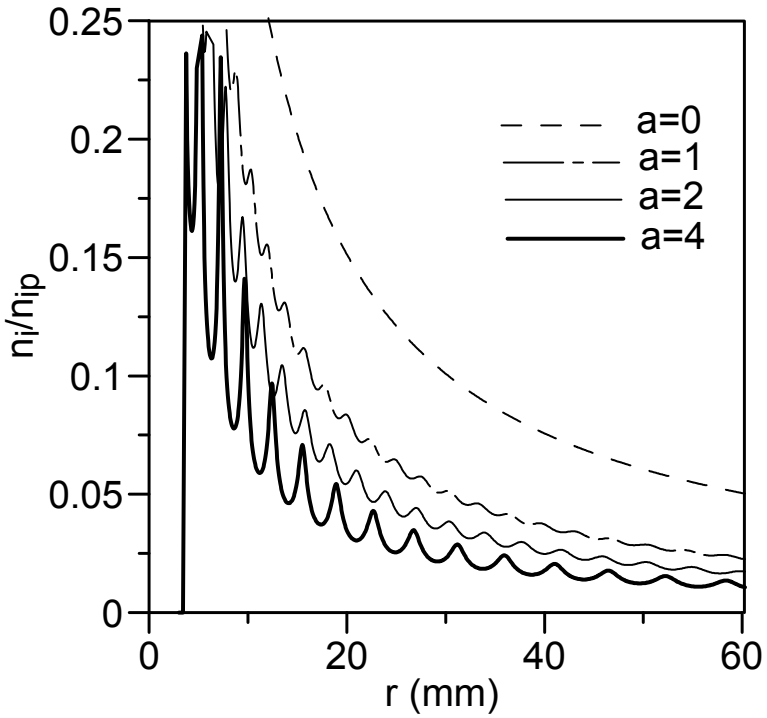


Fig. 2 Variation of ion density with radial distances for the different ratios of the electron thermal energy to the initial ion energy. (D=0.001, n_{ip}/n_{ep}=1)

The distribution of deposition is mainly determined by the ion spatial distribution. Figure 2 shows the variation of ion density with radial distances for the different ratios of the electron thermal energy to the initial ion energy. The ion density increases with the decreasing parameter **a**. However the oscillation of the ion density increases with the increase of parameter **a**, which influences uniformity of deposition. The ion density near beam region (r~3mm) is large and quickly decays with the increasing distances away from beam region. The increase of the initial ion energy (i.e. the decrease of the parameter **a)** enhances the ion density but reduces the oscillation. Therefore it is benefit for the increase of the initial ion energy to improve the efficiency of material coating.

4. Summary

This paper used the equations of continuity, momentum and Poisson to analyze the spatial distribution and oscillation of the electron beam-induced plasma along the radial direction, which dominate the uniformity and thickness of material coatings. The electron density predicted by this work agrees well with that from the measurement. As the ratio of the electron thermal energy to the initial ion energy increases, the ion density along the radial direction decreases but its oscillation increases. The decrease of the ratio of the initial ion density to the initial electron density leads to the longer period and larger amplitude of the oscillation but reduces the ion density. The coating efficiency can be improved by decreasing the ratio of the electron thermal energy to the initial ion energy and increasing the ratio of the initial ion density to the initial electron density. On the other hand, for the small enough ratio of the initial ion density to the initial electron density the uniformity of material coating can be achieved due to the wide period of the oscillation of plasma.

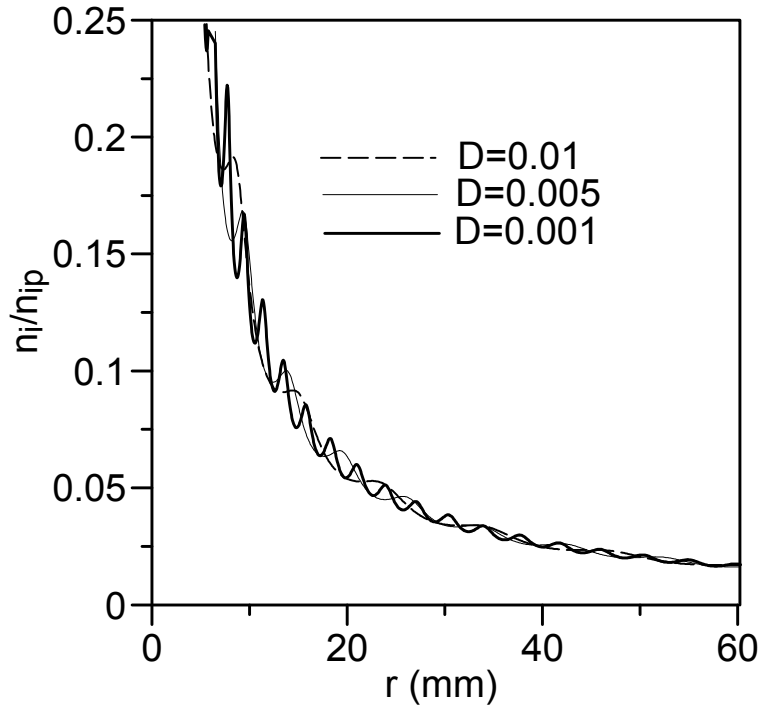


Fig. 3 Variation of ion density with radial distances for the different parameters D. (**a**=2, n_{ip}/n_{ep}=1)

Figure 3 illustrates the variation of ion density with radial distances for the different parameters *D*. The parameter *D* is defined as $\varepsilon_0 kT_e / e^2 n_{ep} r_p^2$, which changes the period of the oscillation but hardly affects the ion density as well as the amplitude of oscillation.

References

[1] B. Dikshit, M.S. Bhatia, BARC Newsletter 314 (2010) 10-19.

[2] I. Wane, Etude, réalisation et caractérisation de couches de ferrites destinées à des dispositifs intégrés micro-ondes non réciproques, Thesis, University of Limoges,2000

[3] R. F. Bunshah, Handbook of Deposition Technologies for Films and Coatings, 2nd ed. New Jersey: Noyes Publications, ed. 1994.

[4] I.M. Sobol, the Monte Carlo Method, Mir, Moscow, 1975.

[5] P. Aubreton, A. Bessaudou, C. Di Bin, Computational Materials Science 33 (2005) 400-406.

[6] I.A. Krinberg, G.M. Mladenov, Vacuum 77 (2005) 407-411.

Applied Mechanics and Materials Vol. 597 (2014) pp 157-160
© (2014) Trans Tech Publications, Switzerland
doi:10.4028/www.scientific.net/AMM.597.157

Flaking Initiation Life under Rolling Contact Fatigue of Ceramic Coated Steels Quenched after Coating Process

Hirotaka Tanabe[1,a], Keiji Ogawa[2,b], Motoyuki Nishizawa[1,c], Yui Izumi[1,d] and Tohru Takamatsu[1,e]

[1] Department of Mechanical Systems Engineering, School of Engineering, The University of Shiga Prefecture, Hassaka 2500, Hikone, Shiga 522-8533, JAPAN

[2] Department of Mechanical and Systems Engineering, Faculty of Science and Technology, Ryukoku University, Yokotani 1-5, Seta Oe, Otsu, Shiga 520-2194, JAPAN

[a] tanabe@mech.usp.ac.jp, [b] ogawa@rins.ryukoku.ac.jp, [c] jawashi.mail@gmail.com

[d] izumi.yu@mech.usp.ac.jp, [e] takamat@mech.usp.ac.jp

Keywords: Laser, Heat treatment, Thin film, Rolling contact fatigue, Adhesive strength

Abstract. In our previous studies, a new surface modification method by combination of ceramic coating and heat treatment, named "substrate quenching after coating" was developed. The thrust type rolling contact fatigue tests were carried out for TiN coated steels and CrAlN coated steels processed by substrate quenching after coating, and the effects of the type of ceramic coating (TiN or CrAlN) and the quenching methods (by furnace quenching or by laser quenching) on the flaking initiation life were investigated. For the specimens quenched by furnace, the flaking life of CrAlN coated specimen was longer than that of TiN coated specimen. This reason could be explained by the difference of the oxidization of CrAlN and TiN in their furnace quenching process. For CrAlN coated specimens, the flaking life of the specimens quenched by laser was longer than that of the specimens quenched by furnace. This reason could be explained by the difference of the process time of the furnace quenching and the laser quenching. It is considered that laser quenching after coating could be an effective way to improve the flaking initiation life under rolling contact fatigue.

Introduction

The surface modification by ceramic coating technique has been interested, and many results have already been made in the various fields. However, there still exist many problems about the adhesive strength of ceramic coating and the hardness of the steel substrate in practical use.

In our previous studies, a new surface modification method by combination of ceramic coating and heat treatment, named "substrate quenching after coating" was developed. It is possible to improve the substrate hardness[1] and the adhesive strength[1,2] of ceramic coated steels significantly by this method. Especially, by our latest method named "laser quenching after coating" [3,4], applying laser quenching technique to the process of substrate quenching after coating, the adhesive strength and substrate hardness also can be improved without any detrimental effects on the hardness and the fracture strength of ceramic coating. Moreover, by applying laser quenching, high dimensional accuracy can be achieved, and "energy saving" and "environment-friendly" process can be expected. These results suggest that "substrate quenching after coating" can be applied as an effective way to improve the performance of ceramic-coated steels.

In order to confirm the further effectiveness of the substrate quenching after coating from more practical viewpoint, the wear resistance[5,6] and fatigue strength[7] of the ceramic coated steels processed by this method have been investigated, and the improvement of wear resistance and fatigue strength were also confirmed. From these results, ball bearing is thought to be one of the good applications of this method.

The objective of this study is to reveal the effects of substrate quenching after coating on the flaking initiation life under rolling contact fatigue condition. In order to investigate the effects, the

thrust type rolling contact fatigue tests were carried out for TiN coated specimens and CrAlN coated specimens quenched after coating process, and their flaking initiation lives were investigated.

Experimental method

Specimens. The material used for the substrate was carbon tool steel JIS SK105. The substrate dimentions were: 55 mm × 55 mm × 5 mm. The surface was finished by polishing, and the surface roughness R_a was about 0.05 μm. Two kinds ceramic thin films: CrAlN and TiN were deposited onto the substrates by arc ion plating (AIP) method. The film thickness was 2.5 μm. The deposition temperature was approximately 673 K for both types of the ceramic thin films. The oxidization temperature of CrAlN and TiN is 1373K, 873K, respectively.

Rolling contact fatigue test. In this study, a thrust type rolling contact fatigue testing machine (Kashima Bearings Corporation, Japan) was used. Figure 1 shows the schematic illustration of this testing machine. In this test, the parts of the thrust ball bearing JIS 51305: a retainer, a ball-holder and 11 balls (JIS-SUJ2 steel, diameter 9.525mm) were used. The rotation speed was 1800rpm. The tests were carried out in the oil bath filled with turbine oil (MIL-PRF-23699, Showa Shell Sekiyu KK, Japan). In order to check the initiation of the flaking failure, the fatigue tests were sometimes interrupted. A digital microscope (VH8000, KEYENCE, Japan) was used for the observation of the specimen surface.

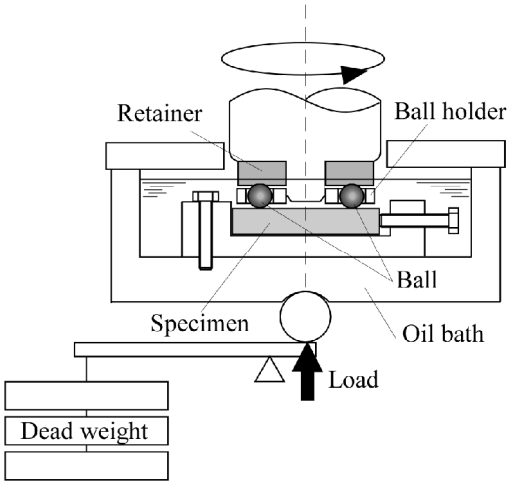


Fig.1 Schematic illustration of rolling contact fatigue testing machine

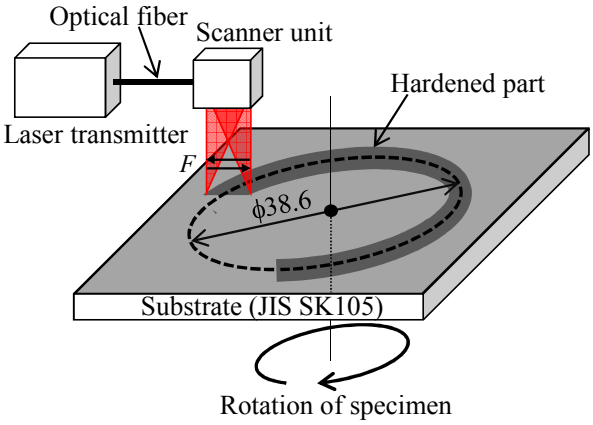


Fig.2 Schematic illustration of laser irradiation method

Table 1 Laser irradiation conditions

Scanning speed of laser spot, F (mm/s)	1000
Scanning width, W (mm)	5
Laser power, P (W)	360, 380
Spot size of laser beam, S_d (mm)	3
Rotation speed of specimen, ω (rpm)	1.96
Rotation diameter, D (mm)	38.6

Heat treatments. In this study, two types of heat treatment: furnace heat treatment and laser heat treatment were carried out. Furnace heat treatments were processed to both of TiN coated specimens and CrAlN coated specimens. Laser heat treatments were processed only to CrAlN-coated specimens.

In the furnace heat treatment process, ceramic coated specimens were heat-treated at 1333 K for 20 minutes in a nitrogen atmosphere using an atmosphere furnace (TLG-40, Thermal Co. Ltd., Japan). After this heating process, these specimens were quenched in a heat treating oil (CQV20S, Nippon Oil Corporation, Japan). The substrate hardness of the furnace quenched specimen was about *HV*800.

For the laser heat treatment, a high power diode laser (Laser line, LDM1000-40, Germany, 1 kW, F-theta lens) equipped with a galvano-scanner was used. The laser irradiation conditions were summarized in Table 1. The laser wavelength was 935 nm. The laser spot size on the specimen surface was ϕ3mm. Figure 2 shows the schematic illustration of the laser irradiation method. In order to obtain a ring-shape quenched area fit for the track of the balls of 51305 bearing (the track diameter was 38.6mm), the specimen was rotated with the laser being irradiated on the specimen surface and scanned for the radial direction. The laser scanning width was 5mm and the scanning speed *F* was 1000 mm/s. The rotation speed of the specimen was 1.96rpm.

Figure 3 shows the example of the observation results of the cross-sectional surface of CrAlN coated specimen laser irradiated under *P*= 380 W. The cross-sectional surfaces of the specimens were etched with 3% nital, and the white area of this photograph shows the quenched area. The quenched depth was about 400μm, and the quenched width was about 3.6mm. The substrate hardness of the laser quenched specimen was about *HV*850.



Fig.3 Micrograph of the cross-sectional surface of CrAlN coated specimen laser irradiated under *P*= 380 W

Experimental results and discussions

Rolling contact fatigue tests were carried out for the furnace quenched specimens and laser quenched specimens, and their flaking initiation lives were investigated. Figure 4 shows the results of the rolling contact fatigue tests. In this figure, *F* shows the load per a ball.

At first, the flaking life of the furnace quenched specimen was discussed. The flaking life of CrAlN coated specimen was longer than that of TiN coated specimen.

This reason could be explained by the difference of the oxidization temperature of CrAlN and TiN. In this study, the furnace heat treatments for these ceramic coated specimens were carried out in the nitrogen atmosphere. However, it was difficult to prevent oxidization of these films. The oxidization temperature of TiN film was lower than CrAlN film. Therefore, the oxidization of TiN progressed more easily than CrAlN, and TiN became more brittle by oxidization. As a result, the strength of TiN decreased, and it should lead the short flaking life of TiN coated specimen.

Next, the flaking lives of the furnace quenched specimen and laser quenched specimen will be compared for CrAlN coated specimens.

Next, the flaking lives of the specimens quenched “by furnace” and “by laser” are compared for CrAlN coated specimens. The flaking life of the specimens quenched by laser was longer than that of the specimens quenched by furnace. The film hardness and the residual stress in the film of the specimen quenched by furnace decreased more easily than those quenched by laser, because the process time of furnace heat treatment, in which the film was exposed to an elevated temperature, was much longer than that of laser heat treatment. This should be a cause of the difference of the flaking lives. From these results, it is considered that laser quenching after coating is effective way to improve the flaking initiation life under rolling contact fatigue.

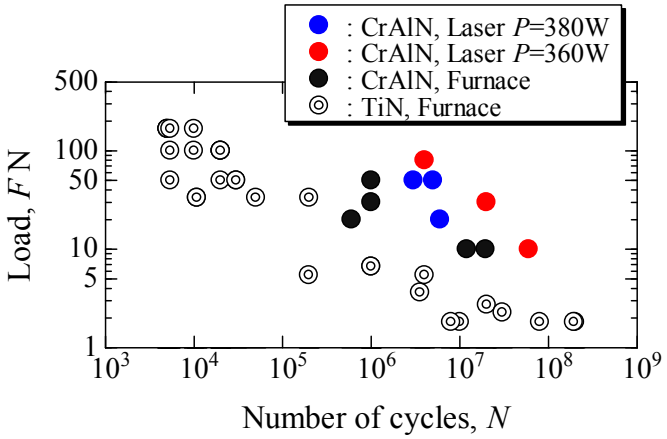


Fig.4 Flaking initiation life of ceramic coated specimens quenched after coating process.

Summary

Rolling contact fatigue tests were carried out for the TiN coated specimens and CrAlN coated specimens quenched after coating process, and the effects of the type of ceramic coating (TiN or CrAlN) and the quenching methods (by furnace quenching or by laser quenching) on the flaking initiation life were investigated. The following conclusions were obtained.

(1) For the ceramic coated specimens quenched by furnace, the flaking life of CrAlN coated specimen was longer than that of TiN coated specimen. This reason could be explained by the difference of the oxidization of CrAlN and TiN in their furnace quenching process.

(2) For CrAlN coated specimens, the flaking life of the specimens quenched by laser was longer than that of the specimens quenched by furnace. This reason could be explained by the difference of the process time of the furnace quenching and the laser quenching.

(3) It is considered that laser quenching after coating could be an effective way to improve the flaking initiation life under rolling contact fatigue.

Acknowledgements

This work was supported by JSPS Grants-in-Aid for Scientific Research (C) (No. 25420025). The authors are very grateful to Mr. Mitsuhiro Gotoh and Mr. Takehiro Takahashi for their technical supports.

References

[1] H. Tanabe, et al., Journal of Solid Mechanics and Materials Engineering, 1 (2007), pp.299-309

[2] H. Tanabe, et al., Transactions of the Japan Society of Mechanical Engineers, Part A, 72 (2006), pp. 1383-1388

[3] K. Ogawa, et al., Transactions of the Japan Society of Mechanical Engineers, Part A, 75 (2009), pp. 1172-1176

[4] H. Tanabe, et al., Applied Mechanics and Materials [978-3-03785-380-1], (2012), pp.175-180

[5] H. Tanabe, et al., Journal of Solid Mechanics and Materials Engineering, 2 (2008), pp.999-1007

[6] H. Tanabe, et al., Transactions of the Japan Society of Mechanical Engineers, Part A, 71, (2006), 568-573 (In Japanese).

[7] T. Takamatsu, et al., Transactions of the Japan Society of Mechanical Engineers, Part A, 72 (2006), pp. 1725-1730

Applied Mechanics and Materials Vol. 597 (2014) pp 161-164
© (2014) Trans Tech Publications, Switzerland
doi:10.4028/www.scientific.net/AMM.597.161

Preparation, Characterization and Dielectric Property of Novel Poly(cyanate ester) Thin Films

Xiong Yan Zhao[1,2,a *], Zhan Ying Sun[1,b] and Ming Zhu Wang[1,c]

[1]College of Material Science and Engineering, Hebei University of Science and Technology, Shijiazhuang, 050018, P. R. China

[2]Hebei Key Laboratory of Material Near-Net Forming Technology, Hebei University of Science and Technology，Shijiazhuang, 050018, P. R. China

[a]email: zhaoxy66@126.com, [b]email: dlwxtj@163.com, [c]email: wangmz@hebust.edu.cn

Keywords: Poly(cyanate ester); dielectric property; plasma polymerization; dielectric constant

Abstract. The technique of plasma polymerization was used in the preparation of the poly(cyanate ester) thin films using 4-methoxyphenol cyanate ester (MPCE), 4-Cumylphenol cyanate ester (CPCE) and 4-phenylphenol cyanate ester (PPCE) as precursors. Different from the conventional thermal polymerization of cyanate ester monomers, the plasma polymerization of three monomers proceeds mainly *via* the opening of π-bonds of the cyanate ester functional groups which are further formed into a large π-conjugated system. The dielectric properties of the resulting plasma thin films were evaluated and results show that the dielectric constant of the three polycyanurate thin films decreased with increasing frequency, while in contrast, the dielectric loss factor increased with the increasing frequency. The obtained poly(cyanate ester) thin films might be the potential new candidates to be used as intermetallic dielectrics in microelectronics.

Introduction

One of the exciting and promising developments in material science today is the design and synthesis of novel low dielectric constant polymer materials, which are found to have potential applications in the field of ultralarge-scale integration, capacitors and other electronic circuits as insulating and/or dielectric materials [1,2]. A number of studies have been conducted in this area [3,4]. The candidate materials include polynitriles, polyimides, benzocyclobutene resins, poly(binaphthylene ether), polyquinolines, and organic-inorganic hybrid polymers.

Cyanate ester resins have an attractive range of dielectric properties when considered against other candidate materials. The lower polarity associated with the cyanate ester resin's cyanurate linkage offers a way to maintain these properties associated with a thermoset while depressing the dielectric constant to the 2.5-3.0 range. With the current demand for the higher performance resulting from substitution of a lower dielectric resin, cyanate esters offer a good cost-performance ratio compared with other engineering plastics [5].

In the present work, cyanate ester monomers were chosen as precursor for plasma polymerization in an attempt to satisfy the following three aspects: (1) provide good adhesion to subtract; (2) enhance the thermal stability of the resulting films; (3) incorporation of non-polar and large space occupying groups such as methyl and phenyl can increase the free volume in the plasma thin films, which might result in the formation of a low dielectric constant material.

Experimental

Materials: The monomers, 4-methoxyphenol cyanate ester, 4-Cumylphenol cyanate ester and 4-phenylphenol cyanate ester were obtained from the Aldrich Chemical Company. The substrates used were heavily doped, *p*-type, (100) silicon wafers, quartz glass and freshly pressed infrared-grade potassium bromide. The argon used in the plasma system was highly-purified grade.

Plasma Deposition of Cyanate Ester Monomers: Plasma polymerization of MPCE, CPCE and CPCE was carried out using a radiofrequency capacitive coupled glow discharge system. The substrates were centered on the bottom electrode of the main chamber, after evacuation and purging with high purity argon three times, a cleaning/etching operation in argon plasma was performed subsequently at a discharge power of 80 W for about 2 min. After this process, a glow discharge was ignited for fixed time laps. The plasma polymerization conditions and physical properties of these plasma poly(cyanate ester) thin films are shown in Table 1.

Table 1. Plasma polymerization conditions and film thickness.

Plasma polymers	Monomers	Pressure [Pa]	Discharge power [W]	Film thickness [nm]
PPMPCE	MPCE	6.0~7.3	5	402
PPPPCE	PPCE	6.7~8.0	10	297
PPCPCE	CPCE	6.7~8.0	10	472

Characterization: The FTIR spectra were measured on a Perkin-Elmer System 2000 FTIR spectrometer. An HP 4284 A semiconductor parameter analyzer available from Hewlett-Packard Company was used to measure the capacitance and dielectric loss of the plasma polycyanurate thin films in the frequency range 100 kHz to1 MHz.

Results and discussion

Fig. 1 illustrates the FT-IR spectra of the three cyanate ester monomers. It is clear from Fig. 1 that two or three characteristic absorption bands of the cyanate ester functional group were observed between 2235 and 2280 cm^{-1} in the infrared spectrum of monomer MPCE, PPCE and CPCE. The plasma polymerization reaction of cyanate ester monomers can be followed by monitoring the corresponding changes in the absorbance bands of the functional group.

Fig. 2 shows the typical FT-IR spectra of the plasma polycyanurate thin films prepared from monomer MPCE, PPCE and CPCE, respectively. It can be seen that the intensity of absorption bands corresponding to the O–C≡N functional group has diminished significantly in three plasma polycyanurate thin films. At the same time, there appeared a broader and considerably stronger absorption band at 1677 cm^{-1} for PPMPCE, 1674cm^{-1} for PPPPCE and 1660cm^{-1} for PPCPCE, respectively, attributed to the conjugated C=N stretching vibration, which indicated that extensively conjugated C=N double bonds were formed during the plasma polymerization of three cyanate ester monomers. Since the characteristic absorption bands at 1360 and 1570 cm^{-1} corresponding to the triazine ring structure [6] were not observed in three plasma polycyanurate thin films, we can derive that the plasma polymerization of MPCE, PPCE and CPCE is quite different from the conventional thermal or catalytic polymerization reaction of cyanate ester monomers, in which the cyanate ester monomer undergoes thermal or catalytic cyclotrimerization to form polycyanurate containing triazine ring structure.

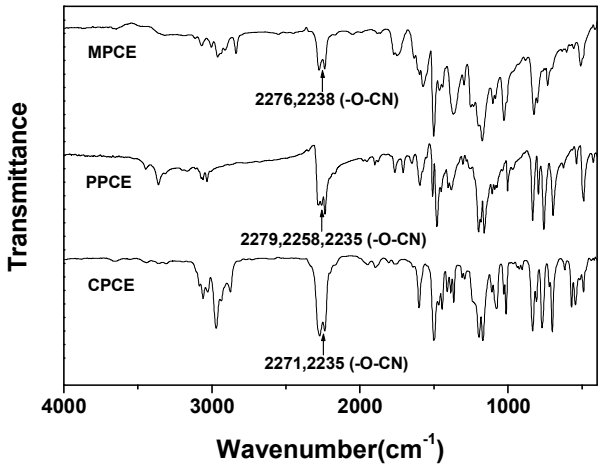


Fig.1 FT-IR spectra of the monomer MPCE, PPCE and CPCE

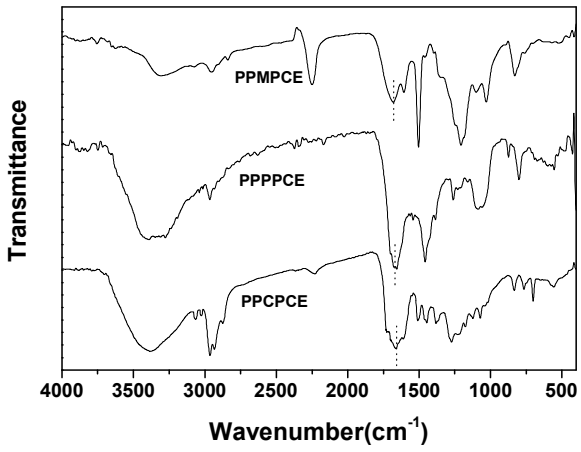


Fig. 2 FT-IR spectra of the plasma polymer PPMPCE, PPPPCE and PPCPCE

Furthermore, the corresponding characteristic absorptions of the monomers resulting from aromatic ring are evident for the plasma polycyanurates. Take the PPCPCE thin film as an example, the absorption bands at 3023 and 3059 cm^{-1} were assigned to the aromatic C–H stretching vibration. The absorption bands at 1273 and 1069 cm^{-1} are due to the in-plane bending vibration of the benzene ring C–H bonds, and those at 835, 765 and 703 cm^{-1} are due in their out-of-plane bending vibration. The absorption bands at 1608, 1505 and 1445 cm^{-1} are attributed to the benzene ring backbone stretching vibrations. Moreover, it is also clear from Fig. 2 that the characteristic absorptions at 2878 and 2963 cm^{-1} for the CH_3 stretching vibration of the monomer CPCE have also been preserved to a large extent in the PPCPCE thin film, indicating greater retention of the starting monomer structure including aromatic rings and methyl groups in the PPCPCE deposited film. Similar results were also observed in the PPMPCE and PPPPCE thin films (see Fig. 2). Thus, the FT-IR results suggest that the plasma polymerization of monomer MPCE, PPCE and CPCE proceeded mainly *via* the opening of π-bonds of the cyanate ester functional groups which are further formed into a large π-conjugated system, and not through the conventional method of forming polycyanurate through polycyclotrimerization.

The dielectric properties of three plasma polycyanurate thin films were measured by the semiconductor parameter analyzer in the frequency range 100 kHz to1 MHz. The variation of dielectric constant with frequency is shown in Fig.3. It can be seen that in the whole frequency range there is an increase in dielectric constant with a decrease in frequency. The observed frequency dependence of the dielectric constant might be attributed to the combination of two factors. First, it has been reported that there are some charges present in dielectric materials which can migrate some distance through the dielectric as an electric field is applied. When such carriers are impeded in their motion, it results in space charges and macroscopic field distortions. As the charge carriers migrate under the influence of an electric field, it is possible that they get blocked at the electrode dielectric interface, which leads to the interfacial polarization. Such distortion causes an increase in capacitance of the plasma polycyanurate thin films at low frequencies. Second, the plasma deposited polycyanurate thin films have a high concentration of radicals, and the rotation of radicals in polycyanurate thin films may result in an increase in the polarization in the low frequency region. And thus, the corresponding dielectric constant of three plasma polycyanurate thin films will increase with a decrease in frequency.

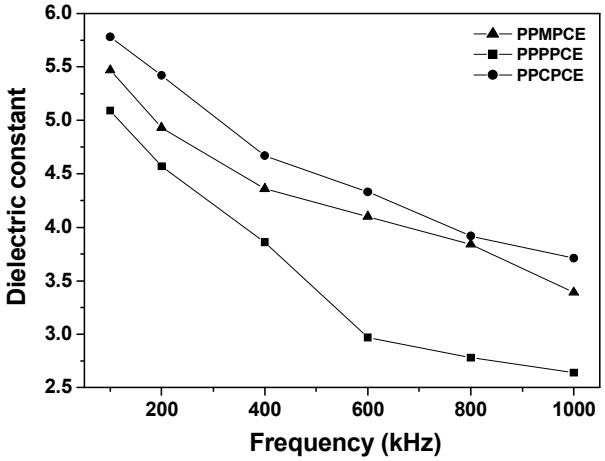


Fig.3 Variation of dielectric constant of plasma polycyanurate thin films as a function of frequency.

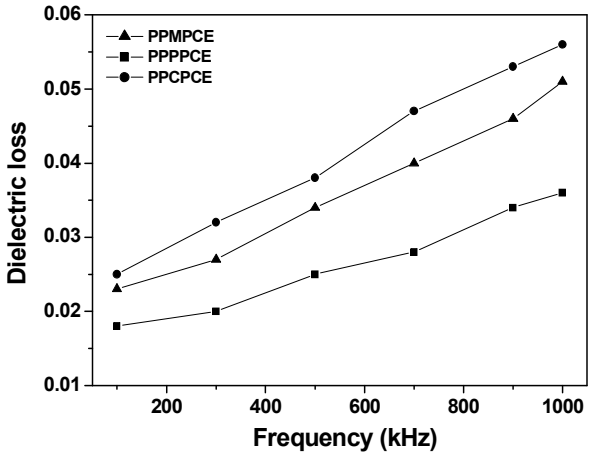


Fig. 4 Variation of dielectric loss of plasma polycyanurate thin films as a function of frequency.

Fig.4 shows the variation of the dielectric loss factor (tan δ) as a function of frequency for three polycyanurate thin films. It can be seen that the dielectric loss factor increases with increasing the frequency. There is no relaxation effect observed in the variation of tan δ in this frequency range.

Conclusions

Three kinds of poly(cyanate ester) thin films were prepared by plasma polymerization. The dielectric measurement shows that the dielectric constant of the three poly(cyanate ester) thin films decreased with increasing the frequency, and the dielectric loss factor was found to increase with increasing the frequency.

Acknowledgements

This work is financially supported by Natural Science Foundation of Hebei Province (Grant No: 2012208026). The work was also supported by Hebei Province Science and Technology Support Program, China (Grant No:14210309D)

References

[1] X.Y. Zhao, H.J. Liu, Review of polymer materials with low dielectric constant, Polym. Int. 59 (2010) 597-606.

[2] X.Y. Zhao, H.J. Liu, M.Z. Wang, Polymer Dielectric Materials, in: Recent Advances in Dielectric Materials. A. Huang Ed., Nova Science Publishers, New York, 2009.

[3] K. Tsuchiya, Y. Shibasaki, M. Aoyagi, M. Ueda, Synthesis of a novel poly(binaphthylene ether) containing trifluoromethyl groups with a low dielectric constant, Macromolecules 39 (2006) 3964–3966.

[4] X.Y. Zhao, M.Z. Wang, Z.Y. Sun, C.M. Niu, J.J. Xiao, E.J. Tang, Synthesis and dielectric property of conjugated polynitriles from cyanate ester, Plasma Process. Polym. 9 (2012) 468–472.

[5] C.P.R. Nair, D. Mathew, K.N. Ninan, Cyanate ester resins, recent developments, Adv. Polym. Sci. 155 (2001) 1-99.

[6] Y. Lin, J. Jin, M. Song, S.J. Shaw, C.A. Stone, Curing dynamics and network formation of cyanate ester resin/polyhedral oligomeric silsesquioxane nanocomposites, Polymer 52 (2011), 1716-1724.

Applied Mechanics and Materials Vol. 597 (2014) pp 165-169
© (2014) Trans Tech Publications, Switzerland
doi:10.4028/www.scientific.net/AMM.597.165

The Influencing Factors for the Thickness of Silica Sol-gel Film by the Dip Coating Process

Lei JieHong[1],[a*] Zhang Ridong [1,2,b]

[1]Physics and Electronic Information Institute, China West Normal University, Nanchong 637009, China;

[2]Research Center of Laser Fusion, CAEP, Mianyang 621900, China

[a]email: jiehonglei@126.com,[b]email: feilong19870726@163.com

Key words: dip coating process; silica film; thickness; ellipsometry method

Abstract. The porous sol-gel silica thin films were prepared on silicon substrate by the dip coating process. The surface roughness and microstructure of the film was measured by optical microscopy and AFM .Coating thickness and refractive index were measured by ellipsometry method. Influence of withdrawal speed and concentration of colloid was investigated for the thickness of silica. The relation of the thickness and withdrawal speed was fitted by the linear and power functions, and the results were analyzed and compared. It was found that the films with the same thickness prepared by different concentrations of colloid have different refractive indexes. The experimental results indicated that the thickness and refractive index of the film can be controlled by changing the withdrawal speed and colloid concentration.

Introduction

Antireflective (AR) coating plays an important role in a variety of optical technologies by reducing the reflective losses and transmission losses at the interfaces. AR coatings have been widely used in many energy-related applications such as solar thermal and photo-voltaic systems. [1]As a result of low refractive index, good durability, highly damage resistant [2,3]and environmental resistance, porous silica is considered to be one of the best antireflective coatings [4,5,6]which attracted wider interest in optical, microelectronic, and thermal applications. [7-11]

Sol-gel technique is one of the widely used techniques for the formation of porous coatings. There are two common coating methods spin coating and dip coating. Dip coating method was instead of spin coating because of its simply operation, uniform film and large area coating. The most important parameters we concerned about Silicon film, as a kind of AR coatings, are its peak value and position of transmission. The relation between film thickness and withdrawal rate has been reported before, but in the project it was not applicative.

In our work, we focused on its application in the project of dip coating and giving a greater control on position of transmission.

Experiments

Preparation of SiO_2 sol

The silica sol was prepared with tetraethylorthosilicate (TEOS) as the precursor, ethanol as the solvent, aqueous ammonia solution(25.0%~28.0%) as the catalyzer and deionized water. They were mixed up in the specific mole ratio stirred with uniform speed at room temperature. Subsequently, the reaction mixture was aged in a stable environment for 7 d to allow hydrolysis and sol formation to be completed. The silica sol, with mass fraction of was 3.0% and average particle size of about 20nm, would display a light blue color due to Rayleigh scattering.

The colloid and anhydrous ethanol were mixed according to a certain proportion. The transparent colloid with mass fraction of SiO_2 were 0.5%, 1%, 1.5%, 2%, 2.5%, respectively, was obtained. The whole preparation processed in the clean environment.

Preparation of SiO_2 thin films

In order to accurately measure the film thickness and refractive rate, selection of silicon (100).The silicon wafers substrate was firstly cleaned thoroughly. Under normal temperature and pressure, the substrates were coated using the dip coating process in clean environment.

The preparation process was in the sealed cabinet of the Antivibration table, in order to avoid the disturbance and uneven surface caused by air flow coating. Firstly the substrate smoothly dipped into the prepared sol for 20s, then pulled at a certain speed apart from the colloid, The withdrawal speeds were adjusted in 40~300 mm/min, interval of 20 mm/min, respectively, in different concentration of colloids. In order to avoid the influence of lifting height, The highest position each coating of ascension was set at the same level. Finally, all the samples dried at room temperature.

Characterization

The surface morphology of the substrate was observed using optical microscope (NikonECLIPSEE600); Surface roughness was characterized using atomic force microscopy (XE-100); The thickness and refractive index of the substrate was measured using ellipsometry (SENTECH SE850) at different positions in each coating zone to take three points averaged.

The thickness and refractive index of the films were measured by ellipsometry at a wavelength of 632.8nm and an angle of 60°.

Results and discussion

surface topography and roughness of the film

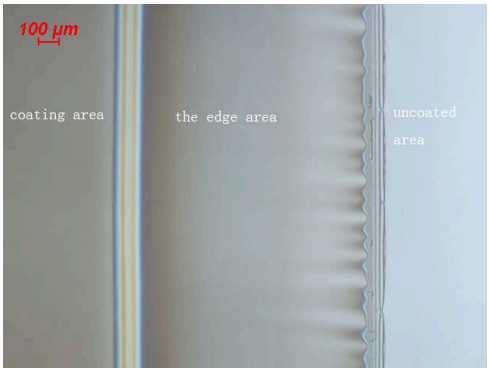


Fig.1 Microscopy image of the coating edge of the SiO_2

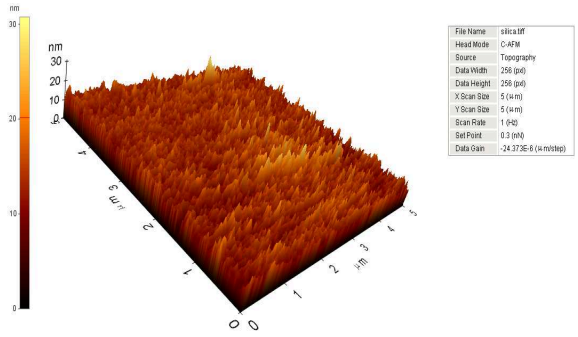


Fig.2 AFM image of the SiO_2 surface

Film uniformity affected by the liquor maturation time, the stability of the coating solution, the process conditions during the preparation. Figure1 shows the microscopy of the edge coating area of SiO_2 on the silicon substrate. It can be seen that there are three different areas. The right is uncoated area, it is the most clean and flat. The intermediate region is the edge area of coating. The left is coating area. As can be seen from the figure, the coating area was relatively uniform, the edge effect is obvious because of different surface tension of the intermediate region and the edge region.

The surface with binary structure is relatively flat as shown in the atomic force microcopy (AFM) image (Fig. 2).

The influence of the withdrawl speed on the thickness of film

Generally, the thickness of sol - gel film using the dip coating satisfies the relation Landau-Levich[16]:

$$d = 0.94(\eta V)^{2/3} / \gamma_{LV}^{1/6} (\rho g)^{1/2} \quad (1)$$

Where d is the film thickness. V is withdrawl speed. η and ρ are the density of the coating, and the solution viscosity, respectively. γ_{LV} is the surface tension of the gas-liquid interface, g is the gravitational acceleration. Relationship basically meets the polymer system, and there is a large deviation for monodisperse particles mutually exclusive[12].

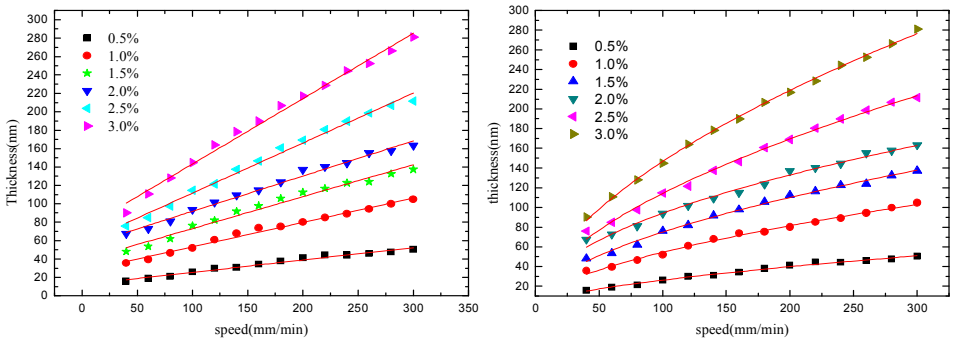


Fig.3 Coating thickness dependent with withdrawal speeds at different concentrations

Relationship between the film thickness under different concentration of colloidal and the withdrawl speed has been shown in Figure 3. It can been Seen from the figure that, in the same concentration, the film thickness increases with the withdrawl speed in a certain range of the pulling rate. The faster the speed, the bigger the viscosity, the greater the upward force of viscous, the larger exposure gravity downwardly, the more the thickness of the deposited film. Colloidal particles and the deposition time was short, the orderly arrangement of particles is poor, high porosity, the film is thicker. The solid line is the result of a least-squares fitting, the fitting of the data as shown in Table 1.

Which results in a power function fitting k was determined by the nature of the coating solution. Index was in the first larger then smaller between 0.5 and 0.6. The MSE of linear regression fit was bigger compared to the power function obtained, but the difference was not great. Description approximate linear fit was also consistent with experimental rule. With increasing concentration of colloids, k and b are increased. For the same colloid, the desired film thickness required were easy to be obtained using a linear fit parameters for the pulling speed compared to the results of the power function. Linear fitting was more convenient in the process control.

Table 1 The linear and power function fitting about the relative thickness with speeds

Concentration/%	Linear fitting	$k[10^{-6}min]$	$b[nm]$	Adj.R-Square	Power function fitting	k	b	Adj.R-Square
0.5	$d=kv+b$	0.1345	12.0425	0.9765	$d=k\bullet v^b$	1.6050	0.6058	0.9899
1.0		0.2652	26.6503	0.9886		3.7529	0.5807	0.9930
1.5		0.3465	38.4442	0.9781		5.8308	0.5546	0.9941
2.0		0.3831	53.5112	0.9893		9.4342	0.4994	0.9890
2.5		0.5433	57.3154	0.9911		8.3101	0.5691	0.9949
3.0		0.7101	72.2535	0.9919		10.2949	0.5769	0.9984

Effect of colloid concentration on film thickness

As shown in Figure 4, Within a certain concentration range, the film thickness increased with the concentration at the same speed. The higher the concentration, the more SiO2 colloidal particles contained in the colloidal solution, the less solvent was evaporated, leaving the thicker of the film.

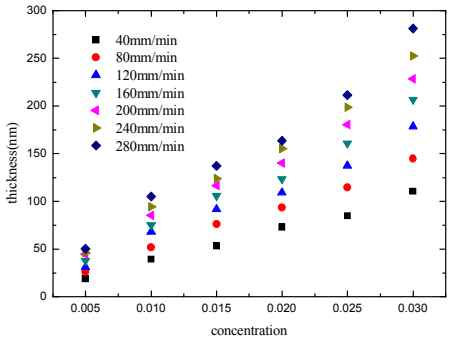


Fig.4 Coating thickness versus concentration of SiO_2 in different speeds

Impact of pulling speed and concentration on the refractive index of the film

The refractive index of the film downward trend with the withdrawl speed increased and colloid concentration increased on the whole, shown in the Figure 5.

As the withdrawl speed was increased, the deposition time on the surface becomes shorter, to reduce the degree of ordering of colloidal particles arranged on the substrate. The porosity became larger, reducing the refractive index . And the withdrawl speed is increased to a certain extent, i.e., the porosity does not increase the threshold is reached, after a refractive index substantially constant.

By the results discussed above, to obtain a film thickness at one concentration of the colloid, a corresponding withdrawl speed can selected. of the transmission peak position was decided by the thickness, the peak value was decided by the refractive index. So ideal transmissive peak would be obtained by selected the colloid concentration and speed of adjustment.

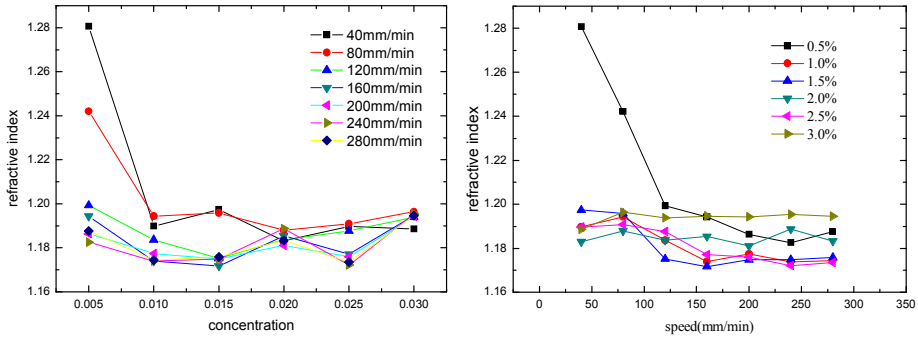


Fig.5 Refractive index versus concentration of SiO_2 and withdrawl speed

Conclusions

SiO_2 AR sol-gel coatings were prepared by the dip coating. The surface microstructure of the film was measured by optical microscopy and AFM .Coating thickness and the refractive index were measured by ellipsometry method. Influence of withdrawal speed and concentration of colloid was investigated for the thickness of silica. The relation of the thickness and withdrawal speed was fitted by the linear and power functions, and the results were analyzed and compared. It was found that the films with the same thickness prepared by different concentrations of colloid have different refractive indexes. The experimental results indicated that the thickness and refractive index of the film can be controlled by changing the withdrawal speed and colloid concentration.

References

[1] M. Cao, X. Song, J. Zhai, J. Wang and Y. Wang: J. Phys. Chem. B. Vol. 110 (2006), p. 13072
[2] S. Takada, N. Hataa, Y. Seino, N. Fujii and T. Kikkawa: J. Appl. Phys. Vol. 97(2005), p. 113504.
[3] I.M.Thomas: Appl. Opt. Vol. 25 (1986), p. 1481.
[4] P. K. Biswas, P. S. Devi P. K Chakraborty, A. Chatterjee, D. Ganguli, M. P. Kamath, and A. S. Joshi: J.Mater. Sci. Lett. Vol. 22(2003), p. 181.
[5] L. M.Cook, W. H. Lowdermilk, D. Milam and J. E.Swain, Appl. Opt. Vol. 21(1982), p, 1482.
[6] H.G. Floch and J.J. Priotton, Ceram. Bull. Vol. 69 (1990), p. 1141.
[7] J. A.Hiller, J. D. Mendelsohn and M. F. Rubner: Nat. Mater. Vol. 1(2002), p. 59.
[8] Y. Liu, W. Ren, ; L. Zhang and X. Yao: Thin Solid Films vol. 353(1999), p. 124.
[9] I. M. Thomas: Appl. Opt. Vol. 31(1992), p. 6145.
[10] G. Wu, J. Wang, J. Shen, Q. Zhang, B. Zhou, Z. Deng, B. Fan, D. Zhou and F. Zhang: High Temp. High Pressures Vol. 32(2000), p. 687.
[11] H. S. Yang, S. Y. Choi, S. H.Hyun, H. H. Park and J. K.Hong: J. Non Cryst. Solids vol. 221(1994), p. 151.
[12] C J Brinker and G. W.Scherer: *Sol-Gel Science*. : (Academic Press, London 1990) p. 788
[13] C. B. Cao: *Spectroscopic ellipsometry and its characterization on the properties of functional thin films* (Anhui University. China 2006) p. 11
[14] Q. J. Li, D. Mo. Acta Scientiarum Naturalium UN. Vol. 37(1998), p. 35.
[15] H. T. Wang: Physics Experimentation, Vol. 21(2001), p. 8.
[16] L. D. Landau and B.G.Levich: Acta Physiochim,U.R.S.S. Vol. 17(1942), p. 42.

Applied Mechanics and Materials Vol. 597 (2014) pp 170-174
© (2014) Trans Tech Publications, Switzerland
doi:10.4028/www.scientific.net/AMM.597.170

Preparation and Properties of Pyrolytic Carbon Coating on Carbon Materials Used in Czochraski Single Crystal Silicon Furnace

Wei Zhao[1,2, a], Bo Zhu[2,b], Weiwei Cao[2,c]

[1] Zhejiang Asia-Pacific Mechmanical & Electronic Co.,Ltd., Hangzhou, 311255, China

[2] Carbon Fibre Engineering Research Center, Faculty of Materials Science, Shandong University, Jinan 250061, China

[a]hero0302@163.com, [b]zhubo@sdu.edu.cn, [c]289139546@qq.com,

Keywords: CZ furnace, C/C composites, graphite, oxidation performance

Abstract. In this paper, resin and vapor deposition (CVD) pyrolytic carbon coating on carbon materials was designed based on the oxidation erosion and silicification corrosion mechanism. Meanwhile the phase structure, microstructure, anti-oxidation and anti- silicification corrosion mechanisms of both coatings were studied. The surface of resin pyrolytic carbon coating has a lot of defec comparing with CVD pyrolytic carbon coating. After static oxidation test at 900 ℃, the resin pyrolytic carbon coating haves some antioxidant protection ability, but after 4 h of static oxidation, weight loss rate is still as high as 30%. Antioxidant effect of CVD pyrolytic carbon coating is good, 4 h oxidation weightlessness rate is about 10%. After silicification corrosion at 1600 ℃, CVD pyrolytic carbon has excellent silicification protection ability.

Introduction

With the wider application of single crystal silicon in solar photovoltaic and the semiconductor industry, carbon materials used as thermal field parts developed more quickly[1]. But because the micro oxidizing atmosphere in Czochraski single crystal silicon (CZ) furnace, carbon thermal field slow oxidation, generated carbon dioxide and carbon monoxide, these gas dissolved in silicon materials caused the silicon products carbon and oxygen sedimentation[2]. In addition, in the process of pulling crystal, silicon material melt may produce silicon steam and molten silicon splash, cause carbon thermal field material surface silicification, affecting the mechanical properties of carbon parts and service life seriously[3]. So, the antioxidant protection and corrosion protection of carbon thermal field material in monocrystalline silicon furnace is necessary, and coating technology is a necessary choice[4].

Requirements of thermal field purity in Czochraski single crystal silicon furnace is very strict, so traditional anti-oxidation coating is no longer applicable. Pyrolytic carbon and carbon substrate have good bonding strength and chemical compatibility[5], which can reduce the rate of open pores significantly, prevent oxidation and silicification corrosion of carbon materials. In this paper, based on the oxidation erosion and silicification corrosion mechanism, we designed resin and vapor deposition (CVD) pyrolytic carbon coating. Meanwhile anti-oxidation and anti-silicification corrosion mechanism of resin pyrolytic carbon coating and CVD pyrolytic carbon coatings was studied.

Experimental procedures

Preparation of pyrolytic carbon coating

In this paper, carbon reinforced carbon(C/C) composites produced by ACROSS and isostatic graphite produced by Tokai Carbon Company were used as substrate. All specimens were cut into 50mm×50mm×10mm, then round off all sharp edges ready for use. The phenolic resin and the graphite powder mixed in a weight ratio of 4:6, dissolved in ethanol solution, then brushed on the surface of the specimen. The coated specimens were placed in the oven at 170 ℃ curing 2h, then

carbonized at 1000 ℃ with N_2 atmosphere. Meanwhile the C/C and graphite specimens were placed in vapor deposition furnace, carbon coating was prepared by chemical vapor deposition method, the reaction gas was: CH_4, H_2 and N_2 mixture, the reaction temperature was 1100 ℃, deposition time was 48h.

Oxidation and Siliconization

In this paper, the judgment of the silicification corrosion performance was characterized by the infiltration depth of molten Si in carbon material. Fig1 is the schematic diagram of siliconization test. high purity silicon powder(5g) was heaped on the surface of the specimen,then placed in an oven. The oven was heated up to 1600 ℃ under the protection of argon gas, holding 2 h. Cut the speciments, then observe cross section by Scanning Electron Microscope(SEM) attached with Energy Dispersive Spectrometer(EDS). Infiltration depth of Si element in carbon materials was measured by EDS.

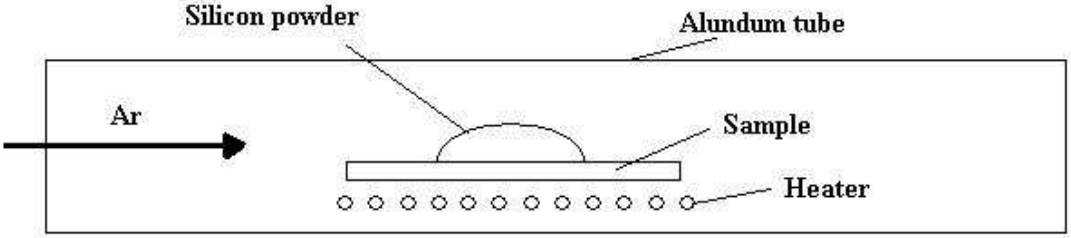


Fig 1 Schematic diagram of siliconization

In order to evaluate antioxidant performance of carbon materials, test of isothermal oxidation was used . According to the formula1 to calculate the weight loss rate ($\Delta W\%$). The $\Delta W\%$-t curves finally obtained.

$$\Delta W\% = \frac{m_0 - m_t}{m_0} \times 100\% \quad (1)$$

$\Delta W\%$, weight loss rate; m_0, weight before oxidation (g); m_t, weight after oxidation(g).

Characteristic

Morphology and crystalline structure of the sample were analyzed by scanning electron microscopy (SEM) and X-ray diffraction (XRD) with Cu Kα radiation (λ=0.154056nm).

Results and Discussion

Phase structures of pyrolytic carbon coating

Fig.2 is the XRD spectrum of different pyrolytic carbon coating. At about 26.5° has an obvious diffraction peak, which is the characteristic diffraction peak of the crystal face d_{002}, at the same time in the vicinity of 55° to 43° shows crystal face (100) and (004) characteristic diffraction peak respectively. As shown in fig.2, the resin pyrocarbon coating(RC coating) is more obvious at 55°.

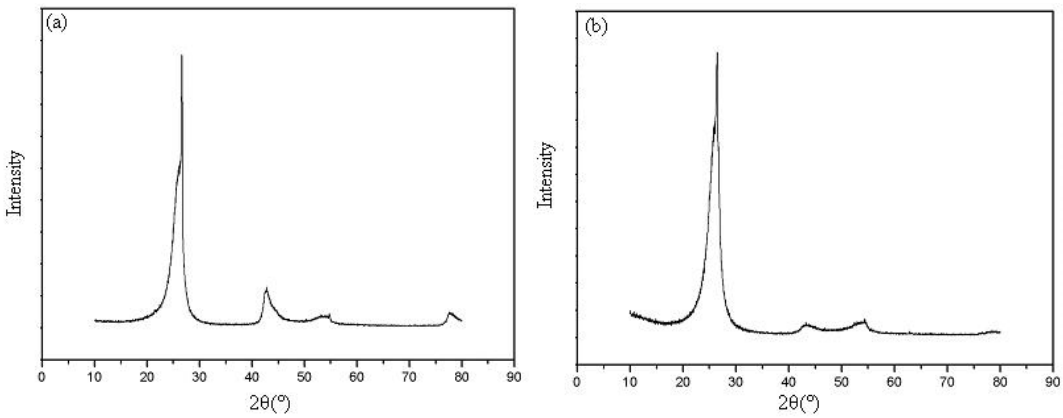


Fig 2 XRD patterns of different kind of pyrocarbon coating
(a)resin pyrocarbon (b)CVD pyrocarbon

The crystallization parameters calculated from XRD diffraction spectrum is shown in table 1. Resin pyrolytic carbon graphitization degree was 44.53%, while CVD pyrolytic carbon graphitization degree is only 16.28%. Graphite intercalating space of resin pyrolytic carbon is closer to the ideal graphite structure 0.3354 nm. The thickness of graphite layer stacking of resin pyrolytic carbon is 7.34nm, which is more thicker than CVD pyrolytic carbon.

Table 1 Crystal parameters of different kinds of pyrocarbon coating

Specimen	Graphitization degree/%	d_{002}/nm	*Lc*/nm
RC-coating	44.53	0.3402	7.34
CVD-coating	16.28	0.3426	4.63

Antioxidant properties of pyrolytic carbon coating

Fig.3 is the weight-t curve after oxidation of different pyrolytic carbon coating on C/C composites at 900 ℃. Residual weight of resin pyrolytic carbon coating after 4h oxidation is 73.6%, moreover, the residual weight of CVD pyrolytic carbon coating is 89.9%. CVD pyrolytic carbon coating and resin pyrolytic carbon coating phase structure were studied above, we found graphitization degree of CVD pyrolytic carbon coating is lower than resin pyrolytic carbon coating. But the oxidation experimental results show that CVD pyrolytic carbon coating on carbon substrate has better antioxidant property. That is because CVD pyrolytic carbon coating, although has lower graphitization degree and smaller crystallite size, is very dense. Less internal coating mismatch of carbon atoms structure, reduced the oxidation reactivity, giving it good corrosion resistance. It can be seen that effects of surface density to antioxidant property is more important than graphitization degree.

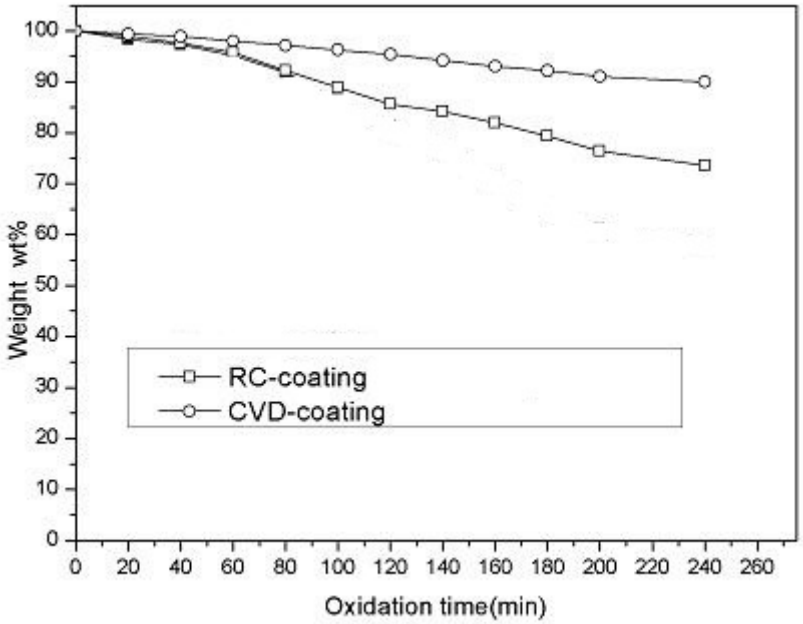


Fig 3 Weight loss rate of different pyrocarbon coating

Antisiliconization properties of pyrolytic carbon coating

Fig.4 is EDS pattern of isostatic pressing graphite coated by resin pyrocarbon coating after silicification corrosion. It can be seen from the diagram, after 2 h siliconizing processing, Si element infiltration depth from surface to inner direction is about 1 mm. Fig 5 is EDS pattern of isostatic pressing graphite coated by resin pyrocarbon coating after silicification corrosion. There exist no silicon under molten silicon and carbon substrate. CVD pyrolytic carbon coating on carbon materials have a better protection effect than resin pyrolytic carbon coating in severely silicification corrosive environment. As mentioned above, CVD pyrolytic carbon coating is very dense, there is almost no pore and penetrating crack in the coating. Meanwhile, graphite substrate is covered by coating. It makes the diffusion rate of molten Si through defect and microporous. So, densification degree of coating is the key to the silicification corrosion protective effect.

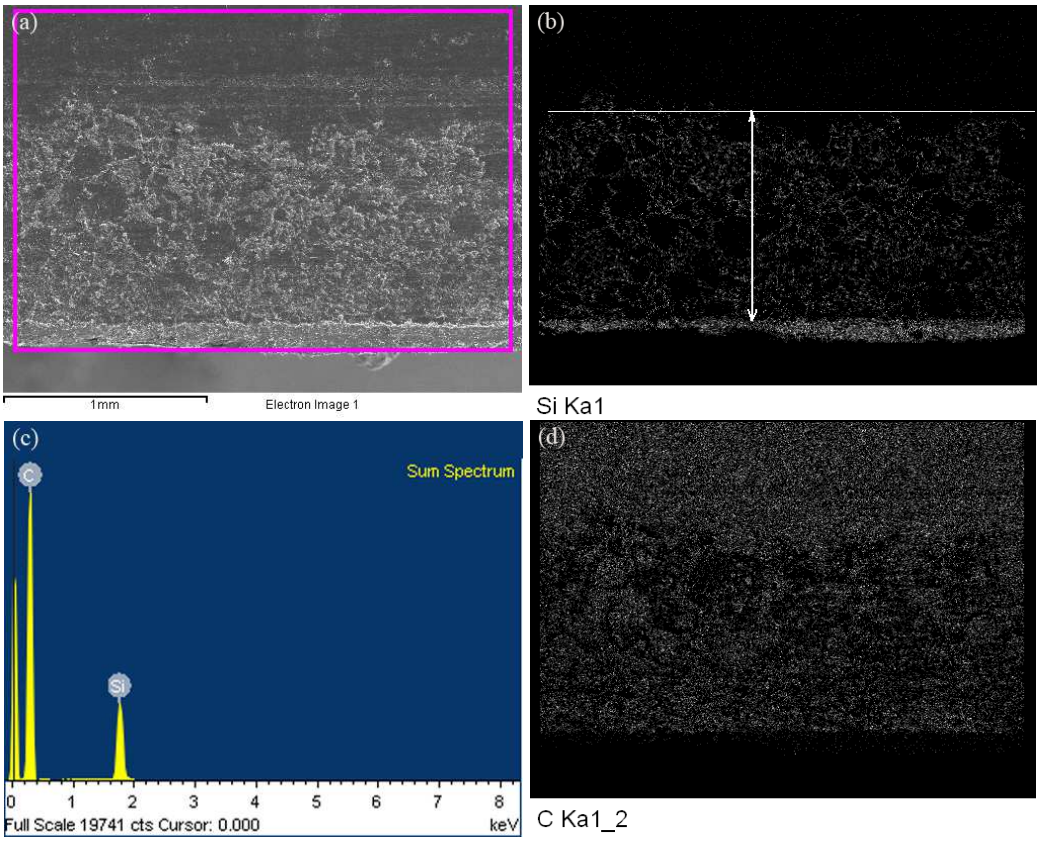


Fig 4 EDS pattern of the phenolic resin pyrocarbon coating

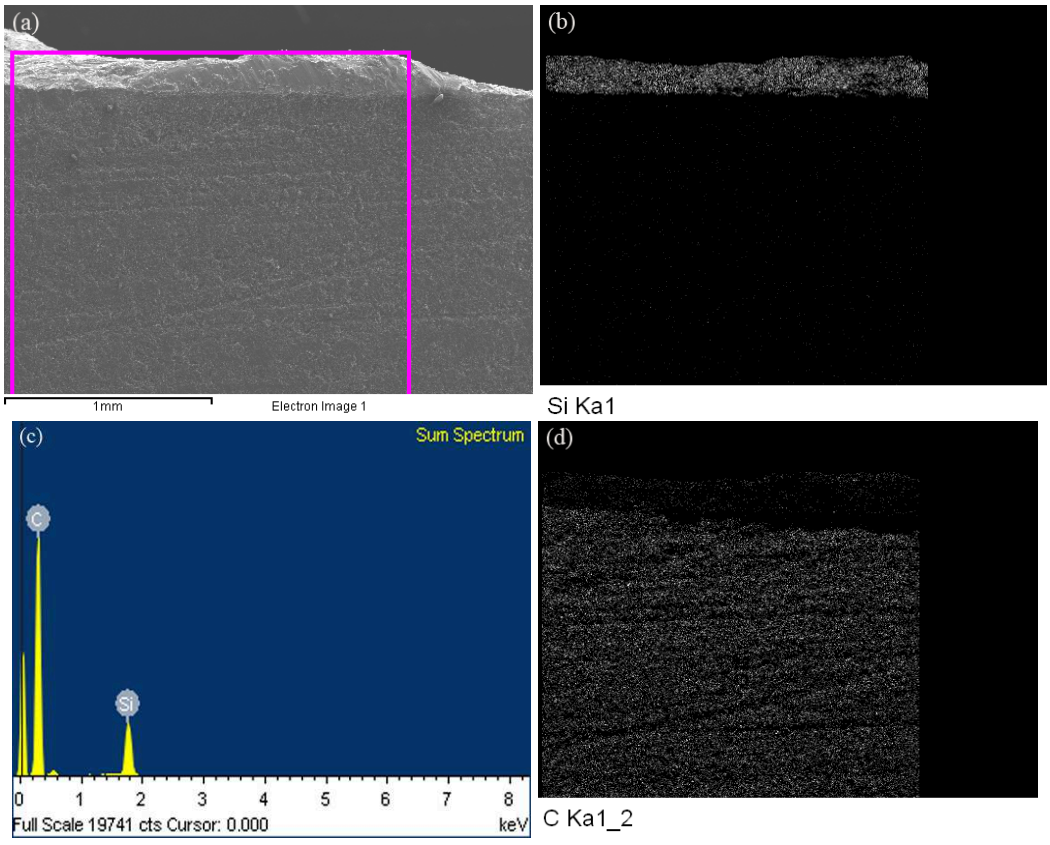


Fig 5 EDS pattern of CVD pyrocarbon coating

Conclusions

1) The surface of resin pyrolytic carbon coating has a lot of defect. After 900 ℃ static oxidation test, resin pyrolytic carbon coating on carbon materials has some antioxidant protection ability, but, weight loss rate is still as high as 30% after static oxidation for 4h.
2) Antioxidant effect of CVD pyrolytic carbon coating is good, 4 h oxidation weightlessness rate is about 10%. CVD pyrolytic carbon has excellent silicification protection ability at 1600℃.
3) Effects of surface density on antioxidant and silicification property are more important than graphitization degree.

References

[1] M.Z.Saghir, D.Labrie, A.Ginovker. Float-zone crystal growth of CdGeAs2 in microgravity: numerical simulation and experiment[J]. Journal of Crystal Growth, 2000, 208 (1-4): 370-378.

[2] Bok-Cheol Sim, In-Kyoo Lee, Kwang-hun Kim. Oxygen concentration in the Czochralski-growth crystal with cusp-magnetic field [J]. Journal of Crystal Growth. 2005, 275 (3-4): 455-459.

[3] T Sinno, E Dornberger, W von Ammon. Defect engineering of Czochralski single-crystal silicon[J]. Materials Science and Engineering: R: Reports. 2000, 28 (5-6): 149-198..

[4] L.Y.Huang, P.C.Lee, C.K.Hsieh. On the hot-zone design of Czochralski silicon growth for photovoltaic applications[J]. Journal of crystal growth . 2004, 261 (4): 433-443.

[5] Tse-Hao Ko, Wen-shyong Kuo, Shinn-Shyong Tzeng. The microstructure changes of carbon fiber pores in carbon-carbon composites during pyrosis[J]. Composites Science and Technology. 2003, 63 (13): 1965-1969.

Applied Mechanics and Materials Vol. 597 (2014) pp 175-183
© (2014) Trans Tech Publications, Switzerland
doi:10.4028/www.scientific.net/AMM.597.175

Effects of laser parameters on the formation of Al_2O_3-TiC coating by laser-assisted combustion

Caixuan Lu, Heping Li*, Peng Chen, Lihong Xue, and Youwei Yan

State Key Laboratory of Materials Processing and Die & Mould Technology, Department of Materials Science and Engineering, Huazhong University of Science and Technology,

Wuhan 430074, P. R China

E-mail:liheping@hust.edu.cn

Keywords: alumina, ceramic matrix composites, coatings, composites, titanium carbide

Abstract. Nowadays, Al_2O_3-based ceramic coatings have attracted considerable attention for their potential applications as tritium permeation barrier (TPB) in the nuclear reactor. Herein, dense composite ceramic coatings (Al_2O_3-TiC) have been successfully fabricated by a facile laser-assisted combustion method. The precursor Al-TiO_2-C powder mixture underwent combustion synthesis at high temperatures generated by an incident laser, and Al_2O_3-TiC coatings were thus obtained. Their crystal structures and morphologies were monitored by x-ray diffraction and field emission scanning electron microscopy. The laser processing parameters, including laser power and laser scanning speed, have been found to play an important role in the microstructure of the products. The optimal laser processing parameters for obtaining Al_2O_3-TiC coating were 4kW in laser power and 6mm/s in laser scanning speed. The results in this paper may be beneficial to the future study of other coatings fabricated by laser-assisted combustion.

Introduction

Ceramic materials such as Al_2O_3, ZrO_2, Y_2O_3, Cr_2O_3, TiC, SiC, TiN have found wide applications as thermal barrier coatings [1], wear resistance coatings [2], and corrosion resistance coatings [3] due to their extreme high melting point and hardness, excellent wear and oxidation resistance. Among them, Al_2O_3 is one of the most commonly used coatings in surface modification and coating technology [4]. Particularly, Al_2O_3-based ceramic coating is one of the most promising candidates as tritium permeation barrier (TPB) [5,6]. In previous studies, various methods have been developed to fabricate Al_2O_3 ceramic coatings on steel substrate such as plasma spraying [7], magnetron sputtering [8], sol-gel [9], laser cladding [10]. However, dense and multi-component coatings were still not easy to obtain because of the limitations of the methods applied previously.

Laser-assisted combustion synthesis [10,11] is a simple and convenient method for fabricating ceramic coatings on steel substrate. The high energy density produced by the laser beam can generate high temperatures, which trigger combustion synthesis in the precursor material and lead to in-situ formation of the target coatings. In this process, the energy released by the high exothermal reaction is utilized to melt the products, which can save nearly half of the laser energy. Besides, the synthesized coatings are uniform in distribution with small grain size due to the high cooling rate associated with laser processing. Masanta et al. have obtained a multi-component coating of Al_2O_3-TiC-TiB_2 by laser-assisted combustion synthesis [4]. Chatterjee et al. have investigated the effect of h-BN addition on properties of laser-assisted combustion synthesized Al_2O_3-TiB_2-TiN coatings [11]. In laser-assisted combustion synthesis, the laser processing parameters, such as laser power and laser scanning speed, play an important role in microstructure and phase composition of the coatings. However, little attention has been paid to this subject.

Herein, we have successfully developed laser-assisted combustion to fabricate Al_2O_3-TiC composite coatings, and studied the effect of laser processing parameters on the structure and micromorphology of the products.

Experimental procedure

Steel plates (AISI 1045 steel) were cut into cuboids with size of 54mm × 30mm × 5mm as substrates. The substrates were then polished with waterproof abrasive paper (200mesh) and ultrasonic cleaned in acetone to remove oxide layer and grease. Measured quantities of aluminum (AR, purity≥99.0%), titanium dioxide (AR, purity≥99.0%) and carbon (Carbon black) in the stoichiometric proportion were mixed uniformly. A small amount of polyvinyl alcohol (PVA, 3wt%) was added to the powder mixture to increase its viscosity. The slurry based powder mixture was then coated manually on the steel substrates. The thickness of pre-coated precursor powder was controlled to about 0.5mm by adjusting the weight. And then, the samples were dried in a furnace at 100 ^{o}C for 10 min to remove moisture.

Laser-assisted combustion synthesis of Al_2O_3-TiC composite coatings were conducted according to the followed reaction:

$$4Al+3TiO_2+3C=2Al_2O_3+3TiC. \quad (1)$$

A 4kW fiber laser (YLR-4000) was used to induce the reaction and clad the products on the substrate by one-way scanning as shown in Fig. 1. The focal length of the focusing lens was 250mm. The defocusing distance was adjusted to 100mm to make a Φ8mm circular beam spot. The movement of laser beam was controlled by a six-axial robot arm. Laser parameters, including laser power and laser scanning speed were presented in table 1. The whole process was undertaken with argon as the shielding gas with a flow rate of 20L/min. The samples were cut into small pieces perpendicular to laser scanning direction for further characterization of the composition and microstructure. The crystal structure of coating surfaces was investigated by X-ray diffraction (X'pert PRO, PANalytical B.V., Netherlands). The morphology and composition in the cross-section of the coatings was characterized by field emission scanning electron microscopy coupled with energy dispersive X-ray spectroscopy (Nova NanoSEM 450 microscope, FEI, Netherlands).

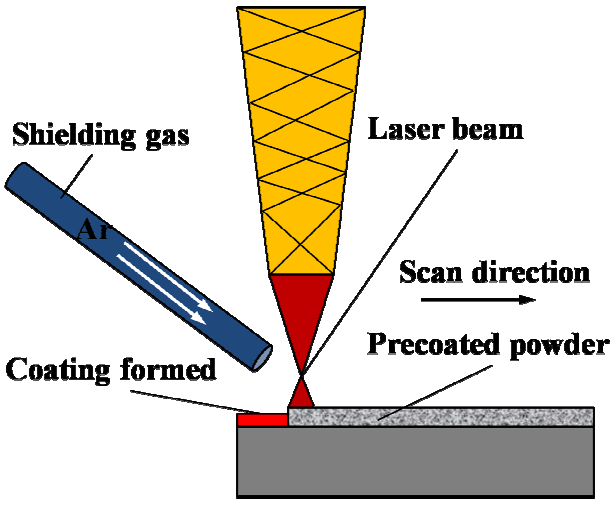


Figure 1. Schematic diagram of laser scanning on steel substrate pre-coated with precursor powder mixture.

Table 1. Laser parameters of different coatings

Sample	Laser power (kW)	Laser scan speed (mm/s)	Beam diameter (mm)
1	3	3	8
2	3	6	8
3	3	10	8
4	4	3	8
5	4	6	8
6	4	10	8

Results and discussion

Fig. 2 presents the overall morphology in the cross-section of a representative coating produced with laser power of 4kW and laser scanning speed of 3mm/s. The ceramic composite layer is well adhered to the substrate with thickness of more than 150 μm. No crack has been found in the coating.

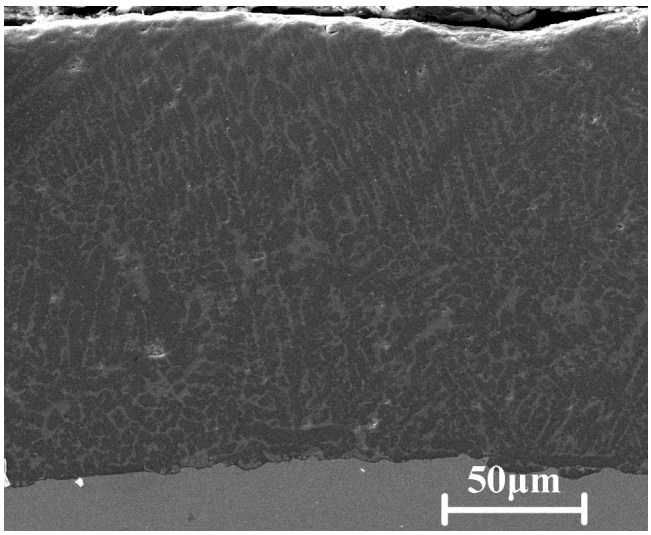


Figure 2. Cross-sectional morphology of a representative coating obtained with laser power 4kW and laser scanning speed 3mm/s.

In the back scattered electron image shown in Fig. 3, the diversity of shades in the microstructure suggests the coating was composed of two phases. Its corresponding elemental maps (Fig. 3) indicate that a dark phase is rich in aluminum and oxygen, and a grey-shaded phase as the matrix is rich in titanium and carbon. Further, the EDS results in Fig. 4 demonstrate that the dark region is mainly composed of alumina and the matrix is mainly composed of titanium carbide.

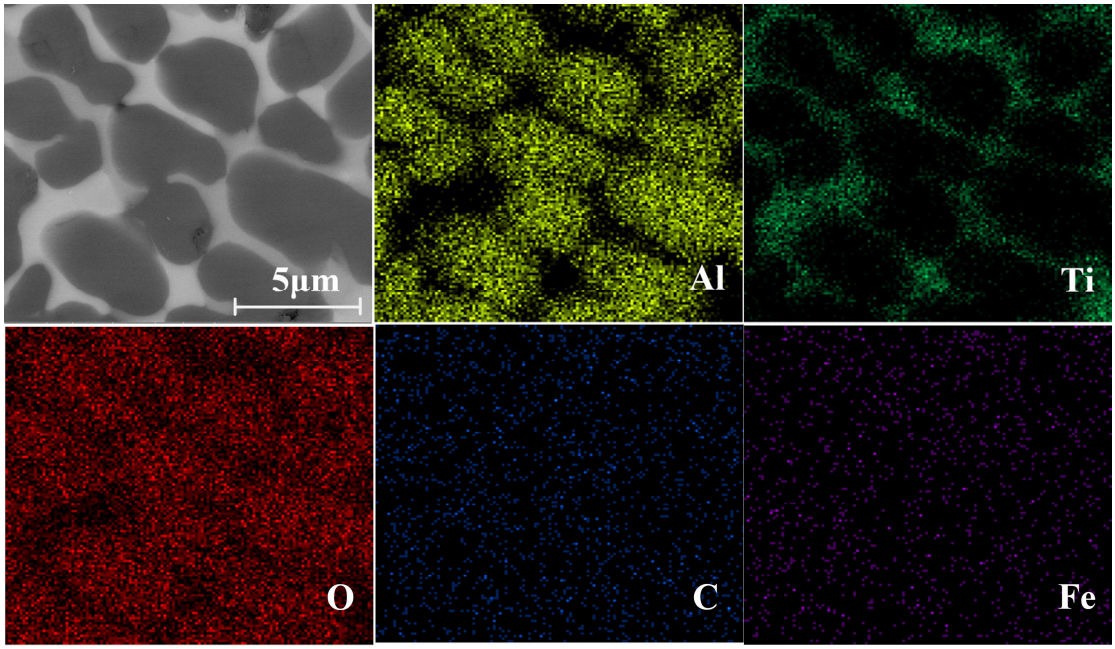


Figure 3. EDS elemental maps for Al, Ti, O, C and Fe in the cross-section of the coating obtained with laser power 4kW and laser scanning speed 3mm/s (SEM was taken in BSE mode).

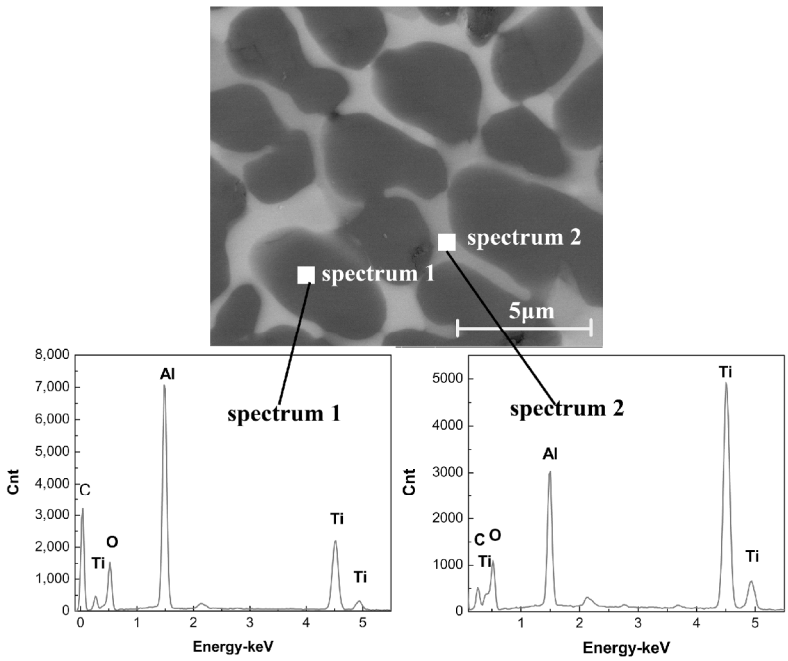


Figure 4. EDS results of the spectrums in the cross-section of the coating obtained with laser power 4kW and laser scanning speed 3mm/s.

The phase composition and structure of the as-synthesized products was examined by X-ray diffraction on the top surface of the coatings (XRD, Fig. 5). The XRD results indicate the coatings are mainly composed of alpha-Al_2O_3 and TiC. Apart from these main phases, the presence of residual titanium oxide may be due to the evaporation of aluminum when the laser scanning on the precursor materials, which made the reaction (1) not finish completely. From Fig. 5, the laser scanning speed is noticed to have distinct impact on the phase composition of the products.

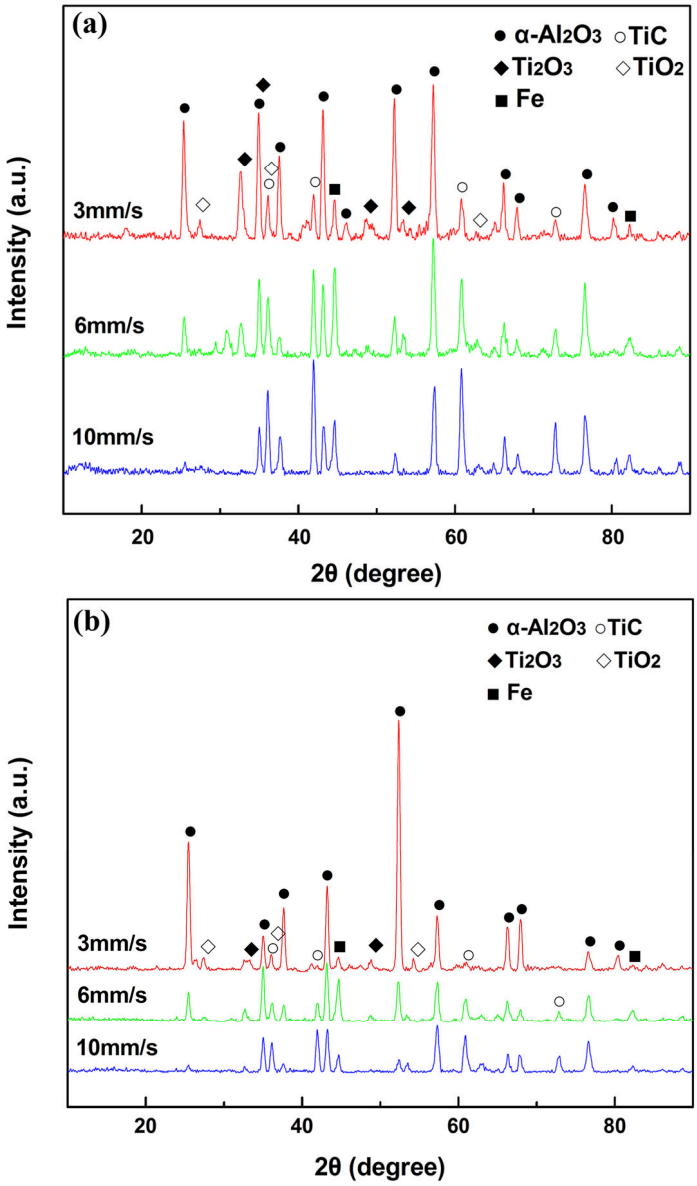


Figure 5. X-ray diffraction patterns of the coatings prepared with different laser scanning speed with laser power of (a) 3kW, (b) 4kW.

In order to figure out the effect of laser scanning speed on the structure of the coatings, the mass fractions of different phases were calculated according to the followed equation [12]:

$$W_i = \frac{I_i}{K_A^i \sum_{i=1}^{n} \frac{I_i}{K_A^i}} \tag{2}$$

Where, W_i is the mass fraction of the phase i in the coating, I_i is the intensity of the highest peak in the phase i, K_A^i is the value of RIR in standard PDF card. The calculated results are summarized in Fig. 6. In general, laser parameters have no obvious effect on the content of Al_2O_3. However, for the same laser power, the amount of TiC increases apparently when laser scanning speed goes up from 3 to 10mm/s accompanied by the decrease of titanium oxide.

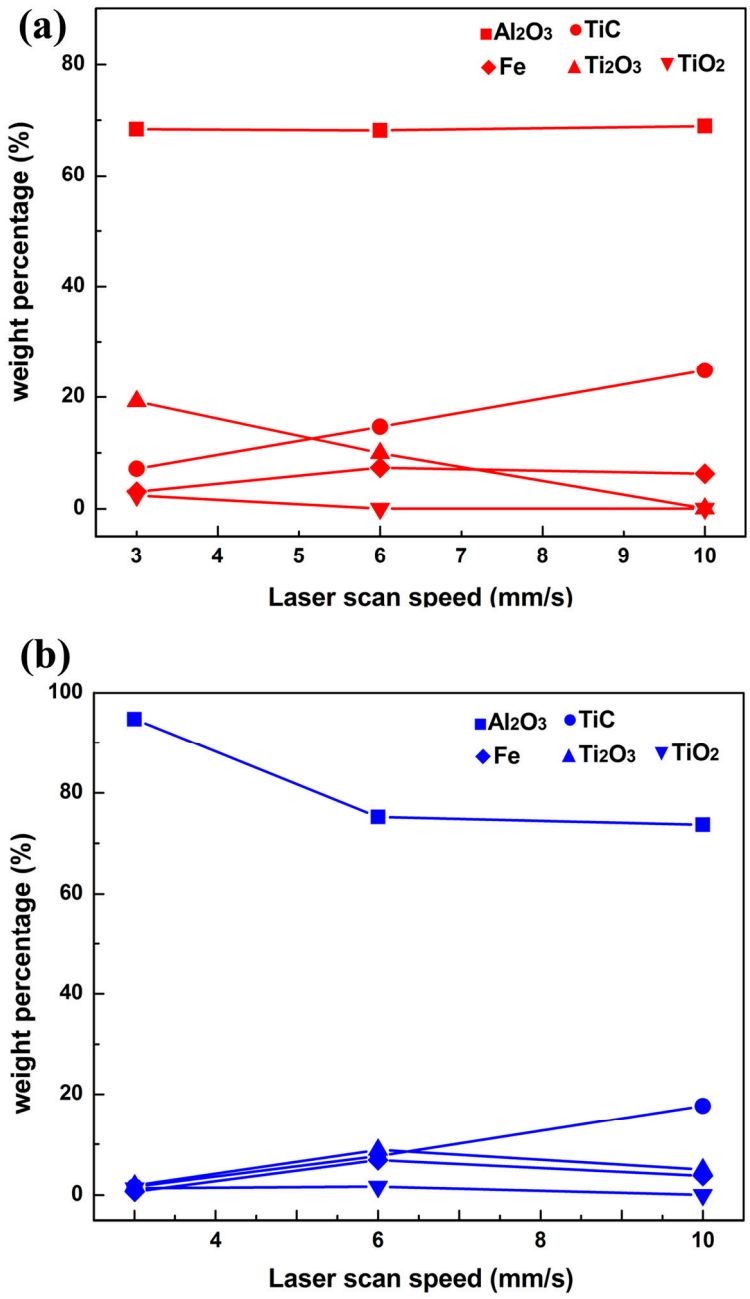


Figure 6. Effect of laser scanning speed on phase composition of the coatings with different laser power of (a) 3kW, (b) 4kW.

The microstructure in the cross-section of the coatings was observed by field emission scanning electron microscopy at high magnification (SEM, Fig. 7). Two different phases of acicular and nodular shapes distribute uniformly in the matrix (Fig. 7(a-b),(d-e)). A significant change in the microstructure is observed with the laser scanning speed increasing from 6 to 10mm/s. As shown in Fig. 7(c) and (f), gathered dispersion of globular forms are presented except for the grains of acicular forms. In general, the obtained coatings are relatively compact except some small voids that may be generated by spalling of undissolved particles during polishing process. Theoretically, the crystal size in the cross-section of the coatings decreases when laser scanning speed increases [13]. As shown in Fig. 7(d-f), when laser scanning speed increases from 3 to 6mm/s with laser power of 4kW, the crystal size diminishes slightly. However, when laser scanning speed continues to increase from 6 to 10mm/s, the crystal size increases unexpectedly. This reverse variation law also occurs with laser power of 3kW (Fig. 7(a-c)).

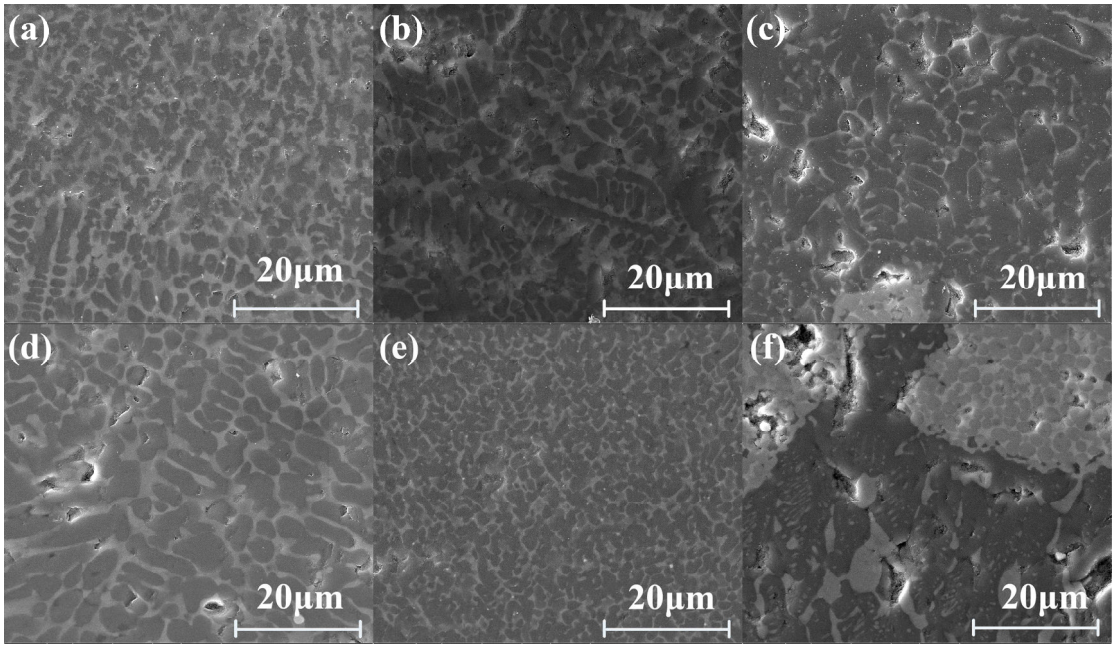


Figure 7. Cross-sectional microstructure of the coatings obtained with different laser power and laser scanning speed (a) 3kW, 3mm/s; (b) 3kW, 6mm/s; (c) 3kW, 10mm/s; (d) 4kW, 3mm/s; (e) 4kW, 6mm/s; (f) 4kW, 10mm/s.

Hence, the laser processing parameters, including laser power and laser scanning speed, have great effect on phase composition and microstructure of the obtained coatings. The exothermal reaction mentioned in section 2 would not happen at ambient temperature even though the change in Gibbs free energy of reaction (1) was negative [14]. According to the previous research [15], ignition temperature of this reaction is around 1200K. When a laser beam scanned on the steel substrate pre-coated with precursor materials, the high energy density produced by the laser beam could generate a high temperature above the ignition temperature, which triggered combustion synthesis in the precursor materials for the coating and leaded to in-situ formation of the target products. In the process of laser-assisted combustion synthesis, the actual energy density (λ_a) produced by the laser beam can be counted by the followed formula:

$$\lambda_a = \frac{P}{\upsilon D} \tag{3}$$

Where, P is the laser power, υ is the laser scanning speed, and D is the diameter of the laser beam. The calculated energy densities under different laser parameters can significantly affect the quality of the coatings. For instance, excessive energy density may cause extensive melting of the substrate and waste of energy, but insufficient energy density may not be able to trigger combustion synthesis in the precursor materials. In previous experiments, laser power below 1kW was found unable to trigger the exothermic reaction with normal laser scanning speed.

On one hand, laser scanning speed affects the actual energy density, which determines the maximum temperature in the reaction system. On the other hand, it has immediate impact on the solidification rate of melting pool. As shown in Fig. 7(d,e)，the dendritic branches and equiaxed dendrites are the typical structure appearing in solidification. And the change of laser scanning speed from 3mm/s to 6mm/s produces different solidification rates, which may be the reason of transformation from dendritic branches to equiaxed dendrites in the cross-section of the coatings according to the traditional theory of solidification [16]. When scanning speed increases to 10mm/s, the reaction products were not totally melt down, and the microstructure in the cross-section of the coating (Fig.7(f)) is very close to the structure in liquid-phase sintering [17] with stacking of

rod-shaped grains and globular-shaped grains separately. Further, more voids and cracks were found when laser scan speed is 10mm/s compared with that of 3mm/s and 6mm/s. This result may be the consequence of incompletely melt down of the reaction products and insufficient time for bubbles to rise away from the melting pool.

In general, the coating obtained with laser power of 4kW and laser scanning speed of 6mm/s showed the most satisfactory microstructure and macro appearance among all the coatings in this work.

Conclusions

Ceramic composite coating of Al_2O_3-TiC was successfully prepared by laser-assisted combustion synthesis of Al-TiO_2-C powder mixture pre-coated on steel substrate. The high energy density produced by a laser beam generated a high temperature, which triggered combustion synthesis in the precursor materials and leaded to in-situ formation of the target products. The laser processing parameters, including laser power and laser scanning speed, were found to play an important role in the microstructure of the ceramic composite coating. The coating obtained under laser power of 4kW and laser scanning speed of 3mm/s was found to be superior to other coatings with different laser processing parameters. The results in this paper may be beneficial to the future study of other coatings fabricated by laser-assisted combustion.

Acknowledgment

This study is supported by Chinese National Fusion Project For ITER (2013GB110000).

References

[1] N.P. Padture, M. Gell, E.H. Jordan, Thermal Barrier Coatings for Gas-Turbine Engine Applications, Science 296 (2002) 280-284.

[2] R. Anandkumar, A. Almeida, R. Vilar, Microstructure and sliding wear resistance of an Al-12 wt.% Si/TiC laser clad coating, Wear 282 (2012) 31-39.

[3] B. Szczygiel, M. Kolodziej, Composite Ni/Al_2O_3 coatings and their corrosion resistance, Electrochim. Acta 50 (2005) 4188-4195.

[4] M. Masanta, P. Ganesh, R. Kaul, Development of a hard nano-structured multi-component ceramic coating by laser cladding, Mater. Sci. Eng. A 508 (2009) 134-140.

[5] H.B. Liu, J. Tao, J. Xu, et al., Microstructure characterization of oxidation of aluminized coating prepared by a combined process, J. Nucl. Mater. 378 (2008) 134-138.

[6] E. Serra, P.J. Kelly, D.K. Ross, R.D. Arnell, Alumina sputtered on MANET as an effective deuterium permeation barrier, J. Nucl. Mater. 257 (1998) 194-198.

[7] G. Sivakumar, R.O. Dusane, S.V. Joshi, A novel approach to process phase pure alpha-Al_2O_3 coatings by solution precursor plasma spraying, J. Euro. Ceram. Soc. 33 (2013) 2823-2829.

[8] T. Kohara, H. Tamagaki, Y. Ikari, Deposition of alpha-Al_2O_3 hard coatings by reactive magnetron sputtering, Sur. Coat. Tech. 185 (2004) 166-171.

[9] J. Masalski, J. Gluszek, J. Zabrzeski, Improvement in corrosion resistance of the 3161 stainless steel by means of Al_2O_3 coatings deposited by the sol-gel method, Thin Solid Films 349 (1999) 186-190.

[10] Y.X. Li, J.K. Yao and Y. Liu, Synthesis and cladding of Al_2O_3 ceramic coatings on steel substrates by a laser controlled thermite reaction, Surf. Coat. Technol. 172 (2003) 57-64.

[11] S. Chatterjee, P. Ganesh, R. Palai, Effect of h-BN addition on the properties of nanostructured Al_2O_3-TiB_2-TiN based coatings developed by combined SHS and laser surface alloying, Surf. Coat. Technol. 204 (2010) 1702-1709.

[12] S.T. Li, Basis of Crystalline X-ray Diffraction, Metallurgical Industry Press, Bejing, P. R. China, 1990.

[13] M. Masanta, S.M. Shariff, A.R. Choudhury, Evaluation of modulus of elasticity, nano-hardness and fracture toughness of TiB_2-TiC-Al_2O_3 composite coating developed by SHS and laser cladding, Mater. Sci. Eng. A 528 (2011) 5327-5335.

[14] E.M. Sharifi, F. Karimzadeh, M.H. Enayati, Mechanochemically synthesized Al_2O_3-TiC nanocomposite, J. Alloys Compd. 491 (2010) 411-415.

[15] H.G. Zhu, Y.L. Jiang, Y.Q. Yao, Reaction pathways, activation energies and mechanical properties of hybrid composites synthesized in-situ from Al-TiO_2-C powder mixtures, Mater. Chem. Phys. 137 (2012) 532-542.

[16] H.Q. Hu, Metal solidification principle, second ed., China Machine Press, Bejing, P. R. China, 2000.

[17] D.S. Wang, Z.J. Tian, L.D. Shen, Influences of laser remelting on microstructure of nanostructured Al_2O_3-13wt.% TiO_2 coatings fabricated by plasma spraying, Appl. Surf. Sci. 255 (2009) 4606-4610.

Applied Mechanics and Materials Vol. 597 (2014) pp 184-187
© (2014) Trans Tech Publications, Switzerland
doi:10.4028/www.scientific.net/AMM.597.184

A study on the resistive switching of $La_{0.7}Sr_{0.3}MnO_3$ film using spectromicroscopy

Hong-Sub Lee[a], Kyung-Mun Kang[b], WooJe Han[c], Tae-Won Lee[d],

Chang-Sun Park[e], Yong-June Choi[f], and Hyung-Ho Park[g,*]

Department of Materials Science and Engineering, Yonsei University, 50 Yonsei-ro, Seodaemun-gu, Seoul, 120-749, Republic of Korea
[a]hong-sub.lee@yonsei.ac.kr, kmkang@yonsei.ac.kr[b], [c]wooje_han@yonsei.ac.kr,
[d]lvm1983@yonsei.ac.kr, [e]park_ch.s@yonsei.ac.kr, [f]yongjune_choi@yonsei.ac.kr,
hhpark@yonsei.ac.kr[g,*]

Keywords: resistive switching, ReRAM, perovskite manganite, LSMO

Abstract. Resistive random access memory (ReRAM) is a promising candidate for next generation nonvolatile memory. $La_{0.7}Sr_{0.3}MnO_3$ (LSMO) of perovskite manganite family has a great deal of attention for ReRAM material because it makes resistive switching (RS) of interface type without a "forming process". However, the full understanding of the electronic structure and RS mechanism of LSMO remains a challenging problem. Therefore, this study performed spectromicroscopic analysis to understand the relation between the change of electronic structure and RS characteristic. The results demonstrated the electron occupation by field-induced oxygen vacancies and strong correlation effects.

Introduction

Resistive random access memory (ReRAM) is a promising candidate for next generation nonvolatile memory due to its fast read/write speed and simple metal/insulator/metal (MIM) structure with possibility of the cross point array (CPA) structure [1]. The CPA structure can make the highest dense memory device. So far, various resistive switching (RS) characteristics were observed in MIM structures with transition metal oxides as dielectric, and various RS mechanisms were suggested as various RS characteristics [2]. Among the many candidate materials for ReRAM, the strongly correlated electron system $La_{0.7}Sr_{0.3}MnO_3$ (LSMO), that belongs to the perovskite manganites family of $R_{1-x}A_xMnO_3$ (R = rare-earth metal; A = divalent element), has received a great deal of attention because it shows a bipolar RS characteristic by interface type RS without the need of a "forming process" of filament type RS. And, in the interface type RS, the two states such as high resistance state (HRS) and low resistance state (LRS) are switched from redox reaction by applied electric field on the surface of RS materials. When we apply positive voltage to the LSMO surface, reduction is induced in local region and the region switch to HRS. This study performed spectromicroscopic (SPEM) analysis to understand the relation between the change of electronic structure and RS characteristic.

Experimental

The LSMO film was prepared on Pt(111)/Ti/SiO_2/Si(100) substrate by RF magnetron sputtering. The $La_{0.7}Sr_{0.3}MnO_3$ powder target was prepared by a standard solid state reaction method using La_2O_3, $SrCO_3$, and Mn_2O_3 powders as starting materials. The background pressure in the sputter chamber was lower than 1.0×10^{-7} torr, and the deposition conditions of power, substrate temperature, deposition pressure, and Ar::O_2 ratio were 100 W, 500 ^oC, 1 mtorr, and 4::1, respectively. The thickness of the LSMO film was measured as about 30 nm by using scanning electron microscope (SEM, JEOL JM-7001F). As shown in Fig. 1, the crystal structure of the films was confirmed by glancing angle x-ray diffraction (GAXRD) using a Rigaku diffractometer with Cu Kα radiation at an incident angle of 1^o.

The current voltage (I-V) behavior of the LSMO film was measured using a two-probe measurement system with an Agilent B1500A semiconductor device analyzer. And the I-V characteristic was measured by tungsten tip without top electrode for SPEM experiment. All measurements were performed at room temperature.

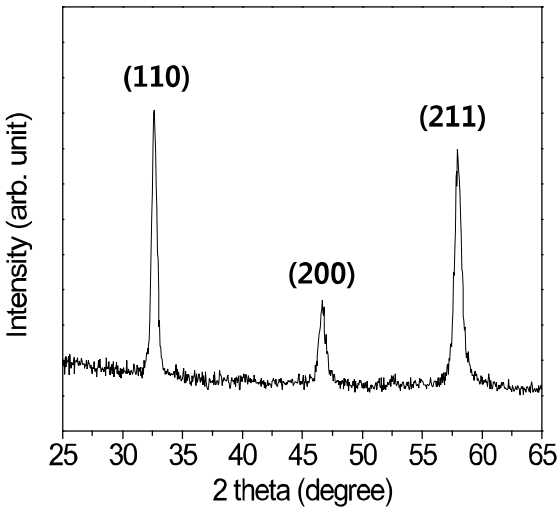


Figure 1. Glancing angle X-ray diffraction pattern of $La_{0.7}Sr_{0.3}MnO_3$ film.

The experimental setup is shown in Fig. 2. After switching the LSMO film to HRS in air (as shown in Fig 2(a)), it was investigated using SPEM as Fig 2(b) in the ultrahigh vacuum chamber of the 8A1 beam line at Pohang Accelerator Laboratory. The SPEM image was obtained by measuring the spatial distribution of O 1s absorption of the horizontally polarized beam. The energy of the incident beam in the SPEM measurement was 529 eV to detect the local HRS region. The flux of the focused X-ray was about 10^9 photons s^{-1}, and the spatial resolution of the SPEM (ie, the size of the spot) was about 500 nm x 300 nm. After the surface absorption mapping, O 1s near edge X-ray absorption fine structure was measured at both HRS and LRS positions.

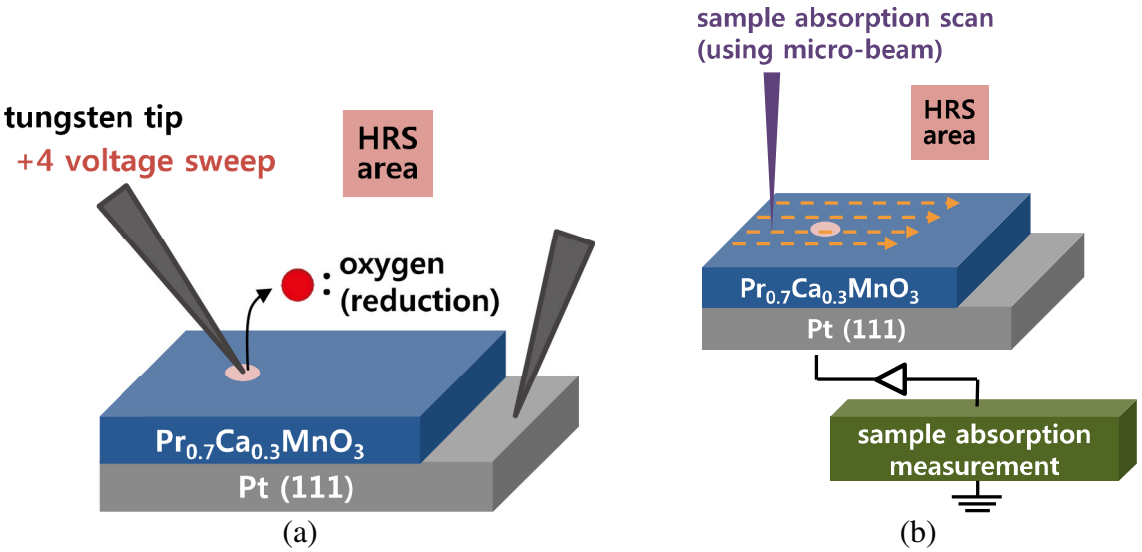


Figure 2. Schemes of (a) HRS local region preparation with I-V measurement and (b) absorption SPEM experiment.

Results and Discussion

As shown in Fig. 3, the I-V characteristic shows the typical interface type RS of with sudden set and reset resistive changes induced at the voltages of +3.5 V and -2.5 V. The voltage sweep direction was marked as black arrow with numbers. This clockwise switching in p-type LSMO was previously reported in a number of studies, and was interpreted as due to a redox reaction at the top electrode (TE) [3]. In this system, under a positive voltage, the TE takes oxygen from the LSMO surface and the LSMO surface is reduced. Under the opposite voltage, the reversal reaction is induced, and the oxidized electrode gives the oxygen ions back to the LSMO surface, leading to a clockwise effect as observed I-V curve. The spectroscopic study of the surface in both resistance states were performed to investigate the effect of the redox reaction on the electronic structure of the LSMO. An important aspect of our experimental method is to access to the intrinsic RS change in the LSMO.

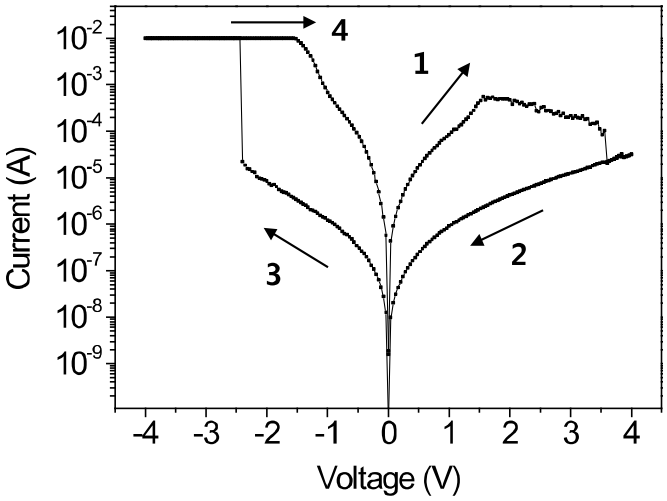
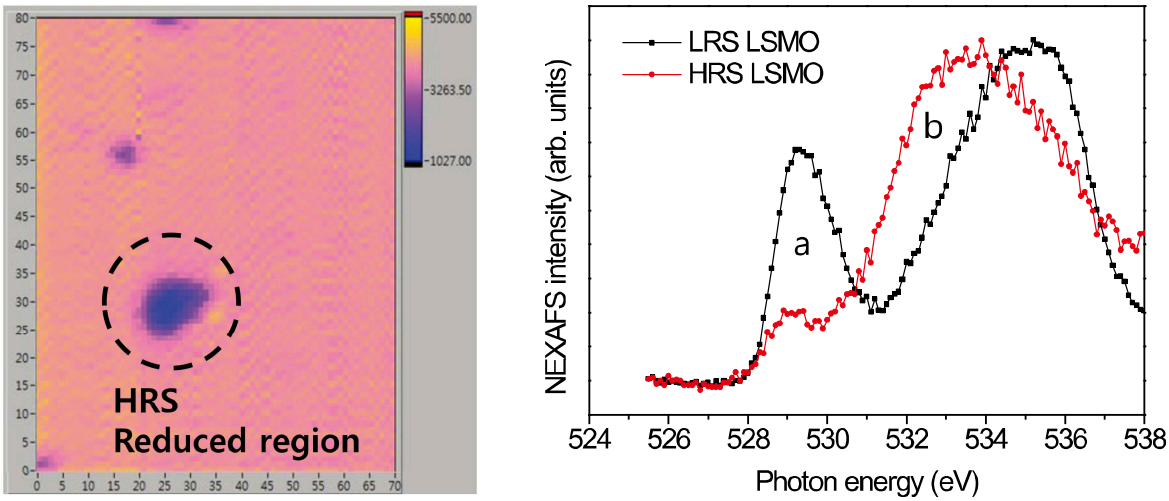


Figure 3. Resistive switching behavior of LSMO film.

After voltage sweep 1 and 2, the sample absorption was obtained at the locally induced HRS region by using incident micro-beam of 529 eV as mentioned in the experimental section. We could get a contrast image from the absorption region as blue region and it could be revealed that SPEM absorption image could identify the local HRS region as shown in Fig. 4(a). The blue and pink regions correspond to HRS and LRS regions, respectively. Based on the SPEM image, O 1s NEXAFS was measured at HRS and LRS region of LSMO, and the results were given at Fig. 4(b) which corresponds to the conduction band structure of LSMO.



(a) (b)

Figure 4. (a) Sample absorption image by 529 eV and (b) O 1s NEXAFS data of HRS LSMO and LRS LSMO.

The NEXAFS data corresponds to the absorption associated to the dipole-allowed transition where an O 1s electron is excited to unoccupied O 2p orbitals. The signal results from the hybridization of the O 2p orbitals with Mn, La and Sr. The NEXAFS spectrum within the energy range of 528 to 534 eV is dominated by Mn 3d character, while the higher-energy region, above 534 eV, is associated to the bands with A-site cations such as La^{3+} and Sr^{2+} [4]. In the initial LRS, the O 1s NEXAFS shows a prominent absorption peak '**a**', ascribed to the partially empty (hole doped) $e^1_g\uparrow$, and also to the fully empty $t_{2g}\downarrow$ and $e^2_g\uparrow$ bands (with $t_{2g}\downarrow$ states being the main contribution). In addition, there is an absorption peak of the Mn 3d $e^1_g\downarrow + e^2_g\downarrow$ band around 533 eV [4]. The spectral weight of the absorption '**a**' decreased remarkably and it corresponds to an increase in the concentration of oxygen vacancies on the HRS surface. Doping with oxygen vacancies can be effectively considered to reduce the nominal hole concentration of the system, as electrons are "released" by the missing oxygen ions. Those electrons go to fill-up the lower-energy empty states

of the hole doped Mn 3d $e^1_g\uparrow$ band, just above the Fermi energy, therefore producing a decrease of the absorption '**a**'. The second feature revealed by the HRS data is the increased absorption '**b**'. These features can be associated to the on-site Coulomb repulsion due to double occupation. In fact, we note that a decrease in the absorption '**a**' appears to be rather large to be solely due to a change in occupation of $e^1_g\uparrow$ (and also $e^2_g\uparrow$ and $t_{2g}\downarrow$) states. On the other hand, significant increase in the intensity '**b**' can be interpreted as due to Coulomb shift of the $t_{2g}\downarrow$ band with weight transferred from '**a**' which is associated to the on-site Coulomb repulsion [5].

Conclusions

The spectroscopic study on the bare surface of LSMO allowed us to demonstrate that strong correlation effects are involved in RS phenomena of this compound. The resistive switching was induced by reduction and the field-induced oxygen vacancies doped electrons to partially emptied Mn 3d $e^1_g\uparrow$ band (doped hole by Ca^{2+}). The occupation induced on-site Coulomb repulsion in perovskite manganite structure and the material resistance switched to HRS. From this study, we could understand the role of field-induced oxygen vacancies in resistive switching process of perovskite manganite material.

Acknowledgements

This work was supported by the Industrial Strategic Technology Development Program (10041926, Development of high density plasma technologies for thin film deposition of nanoscale semiconductor and flexible display processing) funded by the Ministry of Knowledge Economy (MKE, Korea). Experiments at the PLS were supported in part by MEST and POSTECH.

References

[1] M. J. Lee, C. B. Lee, D. Lee, S. R. Lee, M. Chang, J. H. Hur, Y. B. Kim, C. J. Kim, D. H. Seo, S. Seo, U. I. Chung, I. K. Yoo, K. N. Kim, A fast, high-endurance and scalable non-volatile memory device made from asymmetric Ta_2O_{5-x}/TaO_{2-x} bilayer structures, Nat. Mater. 10 (2011) 625-630.

[2] A. Sawa, Resistive switching in transition metal oxides, Mater. Today 11 (2008) 28-36.

[3] A. Sawa, T. Fujii, M. Kawasaki, Y. Tokura, Hysteretic current-voltage characteristics and resistance switching at a rectifying $Ti/Pr_{0.7}Ca_{0.3}MnO_3$ interface, Appl. Phys. Lett. 85 (2004) 4073-4075.

[4] S. Satpathy, Z. S. Popović, F. R. Vukajlović, Electronic Structure of the Perovskite Oxides: $La_{1-x}Ca_xMnO_3$, Phys. Rev. Lett. 76 (1996) 960-963.

[5] Z. Yang, Z. Huang, L. Ye, X. Xie, Influence of parameters *U* and *J* in the LSDA+*U* method on electronic structure of the perovskites La*M*O_3(M=Cr,Mn,Fe,Co,Ni), Phys. Rev. B 60 (1999) 15674-15682.

Applied Mechanics and Materials Vol. 597 (2014) pp 188-191
© (2014) Trans Tech Publications, Switzerland
doi:10.4028/www.scientific.net/AMM.597.188

The production of ITO transparent conductive materials and the development prospect in the field of biological information

Jing Jing Liu[a *]; Hong Men[b]; Qing Tian Zheng[c]; Wei Kang Jiang[d]; Hong Hui Gao[e]; Xiao Zhao[f]

School of Automation Engineering, Northeast Dianli University, Jilin, Jilin, 132012

[a]liujj1986tiger@sina.com; [b]menhong_bme@163.com; [c]1196771285@qq.com; [d]578823288@qq.com; [e]1003699192@qq.com; [f]634152524@qq.com;

Key words: ITO; Conductive film; Flexible; Biological information

Abstract: The transparent conductive film made of Indium Tin Oxide (ITO) is widely used in many fields because of its excellent electrical conductivity and optical properties. At present, the information in biological detection field has not satisfied the people's needs, which are obtained based on some kind of sensors with traditional rigid substrate preparation. The contact surface for creatures perceive and stimulation are flexible surfaces. The kinds of electrode with ITO conductive film as the base for electrode preparation have a great application prospect in biological information collection.

Indium Tin Oxide (ITO) transparent conductive film owns complex cubic structure with ferro-manganese. The electrical conductivity of ITO can reach 10^{-4} Ω•cm. And the carrier concentration and electron mobility are high. All of those make ITO transparent conductive film as all kinds of electrode substrate have good signal transmission capacity [1]. Visible light transmittance and ultraviolet absorption rate of ITO can achieve more than 85% . Good optical properties make it as a base to purchase the electrode can not only complete the original electrical signal acquisition, but also conducive to optical information fusion. ITO film ensured the service life of the preparation of electrode with hardness, wear resistance to chemical corrosion and so on.

1. The production of ITO transparent conductive film

The production of ITO transparent conductive film has a lot of manufacture kinds. Almost all the preparation of conductive film can be used for its preparation. The methods mainly include physical methods and chemical methods. Physical methods include: vacuum evaporation, magnetron sputtering method, pulse laser deposition, ion enhanced deposition and so on. Chemical methods include chemical vapor deposition method, sol-gel method, spray pyrolysis, both deposition methods and so on. ITO transparent conductive film is a kind of heavy doping n-type semiconductor material, its conductive ability mainly determined by free carrier concentration and carrier mobility [2]. Eigen indium tin oxide would lose part of the oxygen, in some cases such as heating or vacuum. Oxygen ions in the crystal lattice central plains would have two negative charges when the room temperature to provide enough energy. It is the result to make the oxygen ions unrestricted freedom of movement, formed to freedom of movement of carrier. Due to oxygen ions from the formation of oxygen vacancies, the oxygen vacancy just like with two positive charges. Because these metal oxide chemical mismatch and guide method to reduce the number of impurities and defects in material and improve the integrity of crystal [3]. The production of ITO electrode using photolithography, including surface cleaning is in conduction electron, lattice, thus

it become n type semiconductor materials [4, 5]. For increasing the carrier mobility, it is necessary to formulate exposure parameters, development conditions, and corrosion process. The magnetron sputtering, vacuum evaporation method and the chemical vapor deposition method are widely applied in industrial and laboratory.

1.1 Magnetron sputtering method

Magnetron sputtering method as the production method of ITO transparent conductive film is widely used in industrial now. Magnetron sputtering deposition contains direct current magnetron sputtering deposition and radio frequency magnetron sputtering deposition. Direct current magnetron sputtering deposition is the current development of the most mature technology. The process principle: With Ar/O_2 plasma in the mixed gas under the action of electric field and alternating magnetic field [6], the surface of target were bombarded by the high energy particles. After the energy exchange, atoms on the surface of the target material escape from the original lattice and transferred to the substrate surface and to be film. With different density of ITO materials as raw materials, the ITO transparent conductive film with resistivity $1.56\times10^{4}\Omega\cdot\mathrm{cm}$ and 87% light transmittance would be achieved using radio frequency magnetron sputtering. The results of the low density of ITO target materials preparation high quality ITO film provides a new train of thought [7].

1.2 Vacuum evaporation method

Vacuum evaporation deposition method (vacuum evaporation) is used to transparent conductive film in a vacuum chamber. The raw material within heating evaporation container was heated to make its atoms or molecules escape from the surface gasification and formed the steam flow, the incident to the substrate surface to form a transparent conductive film. According to the evaporation source heating components, evaporation coating method contained resistance evaporation, electron beam evaporation, high frequency induction evaporation, arc evaporation, laser, etc. The oxygen ion assisted electron beam evaporation technique was used to prepare high quality ITO film. The visible light transmittance was 84.8% with the resistivity of $5.4\times10^{4}\Omega\cdot\mathrm{cm}$ to reach the more advanced technology level [8].

1.3 Chemical vapor deposition method

Chemical vapor deposition is one or several of gaseous reactants (including easy evaporation of condensed matter into gaseous reactants) after evaporation in the substrate surface reaction and deposition film forming process. Chemical vapor deposition mainly includes metal oxide chemical vapor deposition, laser chemical vapor deposition and plasma enhanced chemical vapor deposition technique, etc. Because of the higher temperature in the conventional metal oxide chemical vapor deposition system, the quality of ITO transparent conductive film is usually affected. Electron cyclotron resonance plasma enhanced metal organic chemical vapor phase precipitation to implement GaN nitride thin films, such as low temperature precipitation [9].

2 The application of sensors in transparent and conductive ITO thin films.

2.1 Low temperature etching technique

We used ITO conductive films as the sensitive material, which attached to the conductive films, at the same time, using different methods in surface lines. These lines of specific electrode, on the electrode to join the voltage signal, compose of different arrangement. The laser etching technology is through the high-energy laser dot ITO layer moment gasification. It doesn't need other auxiliary material and won't cause bad influence to environment [10]. ITO thin film technology of preparing

flexible substrate current at low temperature and room temperature should be taken attention to.2 ITO conductive films in the application of the sensor.

2.2 Flexible substrate conductive membrane

Because of low temperature plating process of ITO film can not only coating on the glass substrate and a flexible substrate, it also has the good Properties such as energy saving, consumption reduction, fine features such as simplified equipment, reduce the cost at the same time . Flexible substrate conductive film has a broad prospect in the future for its flexure, light quality, non-friable, easy production and transporting conveniently large area. So magnetron sputtering deposition on the flexible substrate ITO thin film is studied in near room temperature environment. Growing in a flexible substrate ITO film will appear the problem in thin film and substrate. Chiou et al. [11] adopted the (reactive ion etching) method to increase the degree of organic materials for thin film adhesion.

Flexible ITO substrate has a light weight and the price is low, and it can be transformed arbitrarily, so it is a kind of very has the potential to conductive material, good mechanical can also be applied to the flexible electrode [12].

2.3 Detection of biological information based on the Flexible detection.

ITO conductive films can be applied as the nano-sized artificial bilayer lipid membranes in the preparation and detection sensors. ITO/BLM membrane system exhibits good stability, fast film forming rate and long service life, etc. The experiments of the photoelectric properties of ITO/BLM membrane showed that with C60 modified ITO/BLM membrane exhibits good photoelectric effect, and s has huge potential in the development of photosensitive sex electronic [13]. In recent years, the ITO microelectrode is often used in the cell membrane, and realizes the combination of fluorescence, chemiluminescence method. So the cell are researched under the electrochemical technology, at the same time, it also can be used of the microscope to look at the cell morphology[14].

3. Summary

In recent years, the production of ITO transparent conductive film technology has developed rapidly. As we gradually in-depth study of the mechanism and performance, its application is increasingly mature. ITO transparent conductive film as electrode preparation of basal preparation by all kinds of electrode has a flexible test flat and extensible information fusion. It has a great application prospect in biological information collected. Currently in preparation of a variety of experiments to study the ITO transparent conductive film interface, intrinsic properties, production preparation, etc. But ITO transparent conductive film with excellent photoelectric properties still existed indium and spread device performance attenuation problem. The amount of oxygen vacancy in a certain extent would be further controlled. Limit the indium diffusion. With those the ITO transparent conductive film has excellent photoelectric performance and can maintain long-term stability. At the same time, we need to consider the structure of the sensitive material and ITO whether to cooperate with the base. Because of it, the sensitive material of detection electrodes also was limited its application directly to a certain extent.

Acknowledgments

This work was supported by Northeast Dianli University startup funds (BSJXM – 201317).

References

[1] Akbar Eshaghi, Alireza Grae , Optical and electrical properties of indium tin oxide (ITO) nanostructured thin films deposited on polycarbonate substrates “thickness effect. Original Research[J].Article Optik - International Journal for Light and Electron Optics, 2014, 125:1478-1481.

[2] PanCA, MaTP. Hight-quality transparent conductive indium oxide prepared by thermal evaporation[J]. Applied Physics Letter, 2009, 37:163-165.

[3] Hamid Reza Fallah, Mohsen Ghasemi, Mohammad Javad Vahid, et al. Substrate temperature effect on transparent heat reflecting nanocrystalline ITO films prepared by electron beam evaporation. Renewable Energy[J]. 2010, 35: 1527-1530.

[4] Davood Raoufi, Ahmad Kiasatpour, Hamid Reza Fallah, et al. Surface characterization and microstructure of ITO thin films at different annealing temperatures[J]. Original Research Article Applied Surface Science, 2007, 253: 9085-9090.

[5] TJ Choutts, DL Young, XN Li. Characterization of transparent conducing oxides[J]. MRS Bulletin, 2000, 25-8: 58-65.

[6] A Ershov, L Pekker A Ershov, L Pekker. Model of d.c. magnetron reactive sputtering in ArO2 gas mixtures[J]. Original Research Article Thin Solid Films, 1996, 289:140-146.

[7] M. Sobri, A. Shuhaimi, V. Ganesh, et al. Effect of annealing on structural optical and electrical properties of nickel (Ni)/indium tin oxide (ITO) nanostructures prepared by RF magnetron sputtering[J]. Original Research Article Superlattices and Microstructures, 2014, 70: 82-90.

[8] R. Rakesh Kumar, K. Narasimha Rao, K. Rajanna, et al. Low temperature and self catalytic growth of ultrafine ITO nanowires by electron beam evaporation method and their optical and electrical properties[J]. Original Research Article Materials Research Bulletin. 2014, 52: 67-176.

[9] Yue Zhao, Fuwen Qin, Yizhen Bai, Zhenhe Ju, et al. Low temperature synthesis of GaN films on ITO substrates by ECR-PEMOCVD[J]. Original Research Article Vacuum, 2013, 92: 77-80.

[10] Sewook Oh, Hunsang Jung, Yo-Han Kim, et al. Characterization of ITO etching by spontaneously evaporated fume of hydrogen chloride[J]. Microelectronic Engineering. 2013, 103: 173-176.

[11] Bi-Shiou Chiou, Shu-Ta Hsieh. R.f. magnetron-sputtered indium tin oxide film on a reactively ion-etched acrylic substrate[J]. Thin Solid Films, 1993, 229: 146-155.

[12] Shimakawa K. Hosono H, Kikuchi N et al. Free carrier absorption in hightly conducting amorphous oxides[J]. Journal of Non-Crystalline Solids，1998, 230: 513-516.

[13] S.M.B. Ghorashi, A. Behjat, R. Ajeian. A study of the optical properties and adhesion of zinc sulfide anti-reflection thin film coated on a germanium substrate[J]. Solar Energy Materials and Solar Cells, 2012, 96: 50-57.

[14] Ayumi Hirano, Masaki Wakabayashi, Yuka Matsuno, et al. A single-channel sensor based on gramicidin controlled by molecular recognition at bilayer lipid membranes containing receptor[J]. Biosensors and Bioelectronics, 2003, 18(8): 973-983.

CHAPTER 4:

Machining and Forming Materials Technologies, Other Manufacturing Technologies

Applied Mechanics and Materials Vol. 597 (2014) pp 195-202
© (2014) Trans Tech Publications, Switzerland
doi:10.4028/www.scientific.net/AMM.597.195

A method to select optimal cutting force model using the measured process transfer function

Ming Zhu [1, a], Xunxing Yu [1, b], Weiwei Xiao [1, c], Kuanmin Mao [2, 3, 4, d, *]

[1, 2, 3]School of Mechanical Science and Engineering, Huazhong University of Science and Technology, Luoyu Road, Wuhan 430074, China

[4]National NC System Engineering Research Center, Huazhong University of Science and Technology, Luoyu Road, Wuhan, 430074, China

[a]mingzhu@hust.edu.cn, [b]yuxx@hust.edu.cn, [c]xiaowei619@hust.edu.cn, [d, *]maokm@hust.edu.cn

Keywords: Cutting force modelling, Cutting process dynamics, turning, chatter

Abstract. The cutting stability is determined by the dynamics of the tool-workpiece and the cutting process. Several cutting force models have been established by the former researches. Based on the analysis of the cutting process transfer function derived from the cutting force models, the characteristics of these models were analyzed in this work by ploting the function curves in the complex frequency plane. The curve shapes and centers were considered as the indicator to estimate the suitability of a cutting force model. An experimental method was proposed to select suitable cutting force model for a real cutting process.

1 Introduction

Among the methods of chatter prevention, stable cutting parameter prediction and real-time monitoring were well developed. Discrete, analytical [1] and semi-discrete [2] methods have been proposed successively for stable limits prediction. Although the calculation accuracy was gradually improved, the actual chatter prediction may sometimes be ended up in failure due to the diversity and time-varying of machining process. Even short time chatter can make irreversible trauma on workpiece, and cause a considerable economic loss. Therefore, many methods were proposed for surveillance and reduction of chatter vibration, such as vibrating cutting, control of instantaneous tool-workpiece relative position [3] and varying the spindle speed cutting.

The cutting dynamics measured in static process may not reflect the real characteristics of dynamic processes. The former researchers made much effort to establish the dynamic model of cutting process. Based on research of chip formation mechanism, the shear plane theory [4, 5] was proposed to reveal the metal-cutting dynamics. Actually, the direction of the shear plane may be influenced by such cutting parameters as cutting speed and cutting depth and so on, which may be the most fundamental resource of the difference between the static and the dynamic cutting characteristics. The cutting dynamics are represented by the relationship between the cutting parameter and the dynamic cutting force coefficients. Comparing with the former, the cutting coefficients cannot be controlled artificially and hence usually be obtained by analytical and/or experimental methods.

Cutting process models were proposed under some hypothesis conditions that facilitates cutting stability analysis. Correspondingly, different cutting conditions are considered in the models to highlight the concerned influence factors. However, it is hard to kown which model is most

suitable to reveal the actual cutting process characteristics. The cutting process transfer function represents the relationship between the cutting force and the relative tool-workpiece vibration, which can be measured and used for the selection of the most suitable cutting process model.

Oblique cutting process, i. e. Cylindrical turning on a cantilever workpiece, was analyzed in this work to explain the method of model selection for real cutting process. In section 2, characteristics of the available cutting process models were reviewed. Subsequently, the measured cutting process transfer function was used to analysis the rationality of these cutting force models in section 3. Finally, this work was concluded in section 4.

2 The cutting dynamics modeling

In the former investigations, the dynamic cutting force was modeled by taking the derivative of the force with respect to its influence factors. Tobias S. A. [6, 7] firstly proposed the method of calculating the dynamic cutting force coefficients with the static ones. Although much effort has been put into modeling the dynamic cutting process, the calculated metal-cutting characteristics may sometimes not agree well with the real case. Therefore, online measurement becomes a reliable method of cutting process model comparation.

Taking a cylindrical turning process as shown in Fig. 1 for example, several cutting force models were introduced herein below in ascending order of complexity and decreasing degree of approximation. Characteristics of these models were revealed by the cutting process transfer function.

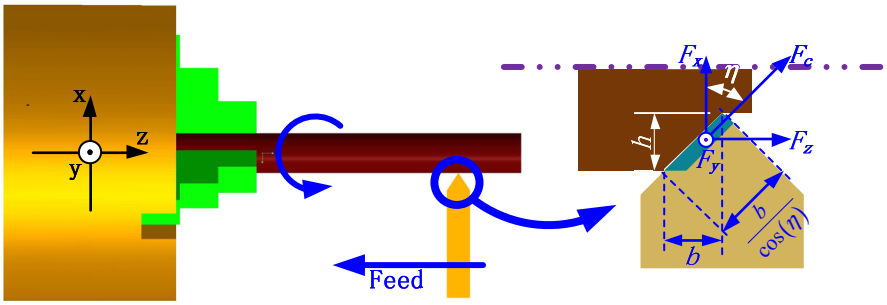


Fig. 1. The schematic of the cylindrical turning system

The dynamic cutting force modeling. Dynamic cutting force can be simply expressed as a linear function of the cutting area, as shown in Eq. (1).

$$f(t) = k_s b[-x(t) + \mu x(t-\tau)], \tag{1}$$

where $f(t)$ represents the cutting force, $x(t)$ the relative tool-workpiece displacement, k_s the cutting force coefficient, b the equivalent cutting width and τ the time delay between the inner and the outer modulations.

When obviously influenced by the cutting damping because of the cutting friction between tool edge and workpiece surface, the cutting force can be represented in the form of Eq. (2)

$$f(t) = k_s b[-x(t) + \mu x(t-\tau)] + k_e b, \tag{2}$$

where k_e denotes the edge force coefficient. The edge force is usually considered to be proportional to the tool-workpiece friction area. Therefore, Equation (2) can be reshaped as Eq. (3) for modeling the dynamic cutting process.

$$f(t) = k_s b[-x(t) + \mu x(t-T)] + \frac{bc_v \dot{x}(t)}{V} + \frac{bc_\alpha \ddot{x}(t)}{V^2}, \tag{3}$$

where V denotes the cutting speed; c_v and c_a represent influence of the length and the curvature of the vibration wave on the workpiece surface.

In order to investigate the metal-cutting characteristics with experimental method, the cutting force can be modeled in the complex frequency domain. The dynamic cutting force coefficients are expressed with complex values as shown in Eq. (4).

$$F(s) = (k_{is} + k_{id}s)bX(s) + (k_{os} + k_{od}s)\mu b e^{-s\tau} X(s) \tag{4}$$

where k_{is} and k_{id} respectively represent the real and image part of the inner modulation, and k_{os} and k_{od} of the outer modulation.

The image part of the outer modulation coefficients can be approximated to zero, while the image part of the inner modulation coefficients can not be neglected because of the influence of the displacement and/or acceleration of the relative tool-workpiece vibration. Moreover, the real parts of both the inner and outer modulations denote the influence of cutting area on cutting force and therefore can be regarded as constants, while the image parts may be significantly affected by the vibration frequency and hence usually be regarded as a linear function of vibration frequency.

Although the cutting force equations have different shapes, there are intrinsic similarities between these presentations. As the outer modulation influence only the cutting area, it is usually assumed that the outer modulation dynamic coefficient in Eq. (4) is equal to the cutting coefficient in Eq. (1). The image part of the inner modulation dynamic in Eq. (4) acts the role that the tool-workpiece friction palys in Eq. (2) and Eq. (3). Regarding the coefficients in Eq. (4) as the function of vibration frequency, it has the similar means as the edge coefficients that determined by the vibration and acceleration terms in Eq. (3).

The dynamic cutting process transfer function. Although all of the cutting force models have a similar physical interpretation, the cutting process transfer function derived from this different Equations have distinct representations. Moreover, machining process stability is determined by dynamics of both machine tool structure and cutting process [8]. Therefore, it is important to select a suitable force modeling method to establish accuracy cutting process transfer function of cutting stability analysis. The cutting process transfer functions derived from the aforementioned cutting force models were elaborated herein below. Based on the analysis of these transfer functions, the method of suitable cutting force model selection was proposed.

If cutting force is mainly determined by the cutting area, the cutting process transfer function can be express as Eq. (5), according to the cutting force model in Eq. (1).

$$\frac{F(j\omega)}{X(j\omega)} = k_s b\left(\mu e^{-j\omega\tau} - 1\right). \tag{5}$$

Equation (5) can be reshaped as:

$$\frac{F(j\omega)}{X(j\omega)} = -k_s b + k_s \mu b \cos(\omega\tau) - jk_s \mu b \sin(\omega\tau). \tag{6}$$

By plotting the transfer function in the complex frequency plane as shown in Fig. 2 (a), it can be seen that the transfer function determines a circular curve with the phase delay $\omega\tau$ changed 2π. The arc center should be located on the real axis with transverse coordinate determined by the cutting force coefficient k_s and the equivalent cutting width b. Except for the parameters k_s and b, the arc radius is also influenced by the overlap ratio μ.

When the contact edge length determined component force obviously influences the whole cutting force as shown in Eq. (2), the cutting process transfer function should represented as:

$$\frac{F(j\omega)}{X(j\omega)} = k_e b - k_s b + k_s \mu b e^{-j\omega\tau}, \tag{7}$$

Equation (7) can be reshaped as:

$$\frac{F(j\omega)}{X(j\omega)} = k_e b - k_s b + k_s \mu b \cos(\omega\tau) - jk_s \mu b \sin(\omega\tau). \tag{8}$$

The transfer function was ploted in the complex frequency plane as shown in Fig. 2 (b). It can be seen that the arc center is shifted along the real axis because of the edge cutting force influence, compararing to the Fig. 2 (a).

If the edge component of the cutting force is regarded to the function of wave length and curvature on the machined surface as shown in Eq. (3), the cutting process transfer function accordingly becomes to:

$$\frac{F(j\omega)}{X(j\omega)} = -k_s b + k_s \mu b e^{-j\omega\tau} + j\frac{bc_v\omega}{V} - \frac{bc_\alpha\omega^2}{V^2}, \tag{9}$$

and can be reshaped as:

$$\frac{F(j\omega)}{X(j\omega)} = -k_s b - \frac{bc_\alpha\omega^2}{V^2} + k_s \mu b \cos(\omega\tau) - jk_s \mu b \sin(\omega\tau) + j\frac{bc_v\omega}{V}. \tag{10}$$

The corresponding transfer function was ploted in the complex frequency plane as shown in Fig. 2 (c). As the relative change of the parameter $\omega\tau$ is small, the transfer function curve can be regarded to a circular. The arc center abscissa was moved because of the influence of the wave curvature on machined surface, while the arc center ordinate moved because of the wavelength affect.

Similarly, when the dynamics of the inner and outer modulations are analyzed separately, the cutting process transfer function can be drawn from Eq. (4) as:

$$\frac{F(j\omega)}{X(j\omega)} = -k_{is}b - jk_{id}b\omega + k_{os}\mu b e^{-j\omega\tau} + jk_{od}\mu b\omega e^{-j\omega\tau}, \tag{11}$$

Equation (11) can be reshaped to:

$$\frac{F(j\omega)}{X(j\omega)} = -k_{is}b + k_{os}\mu b\cos(\omega\tau) + k_{od}\mu b\omega\sin(\omega\tau) - jk_{id}b\omega - jk_{os}\mu b\sin(\omega\tau) + jk_{od}\mu b\omega\cos(\omega\tau) \tag{12}$$

The transfer function was plotted in Fig. 2 (d). Equation (12) and Fig. 2 (d) show that the transfer function curve can be approximately regarded to a circular. The arc radius mainly depends on the static component part of the outer modulation coefficient and is also affected by the dynamic component. Moreover, the arc center abscissa is dependent on the static component part of the inner modulation coefficient, while the arc center ordinate on the dynamic component.

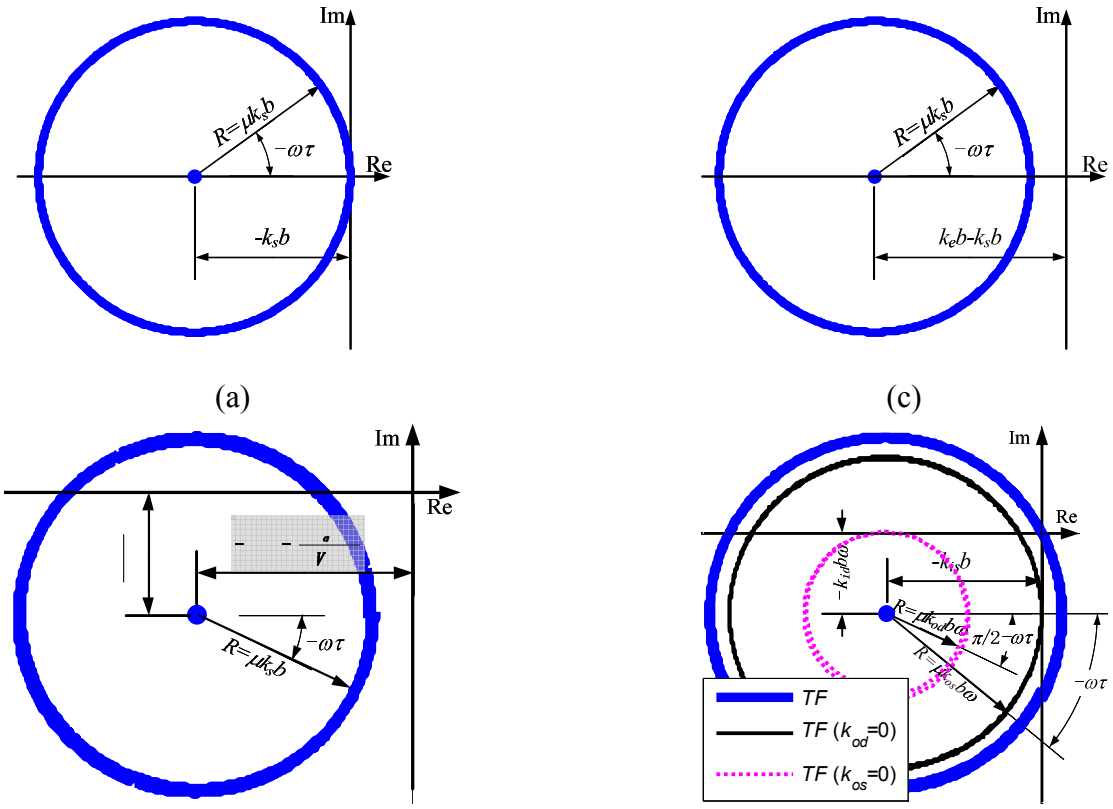


Fig. 2 Cutting process transfer function with the cutting force determined by (a) cutting area, (b) cutting area and edge length, (c) cutting area and tool-workpiece friction area, (d) relative tool-workpiece vibration frequency.

In summary, if the cutting force is mainly dependent on the chip area, the cutting dynamics in a small range of vibration frequency can be demonstrated by a circular curve in the complex frequency plane with arc center on the real axis, as shown in Fig. 2 (a). The arc center ordinate may

be moved down to the zone under the real axis because of tool-workpiece friction, as shown in Fig. 2 (b) and Fig. 2 (c). However, the relative direction angle of the transfer function to the arc center may be changed by the dynamic component of the outer modulation influence, as show in Fig. 2 (d). It can be concluded that the most suitable cutting force model can be pointed out basing on the measured transfer function.

3 Cutting force model selection using the measured process transfer function

Cylindrical turning tests have been performed on a CNC turning center, as shown in Fig. 3. The workpiece of C45E4 (SI) steel was installed to the spindle by a three-jaw chuck. The length of the workpiece is 250 mm. The workpiece diameter is 40 mm near the fixed end and it is enlarged at the free end of the workpiece for convenient of the multiple cutting tests. The workpiece was turned with a SNMG-PM tool insert, having a 0.4 mm nose diameter and a 45º cutting edge angle. The cutting speed was 126 m/min, the feed 0.1 mm/r and the cutting depth 0.2 mm.

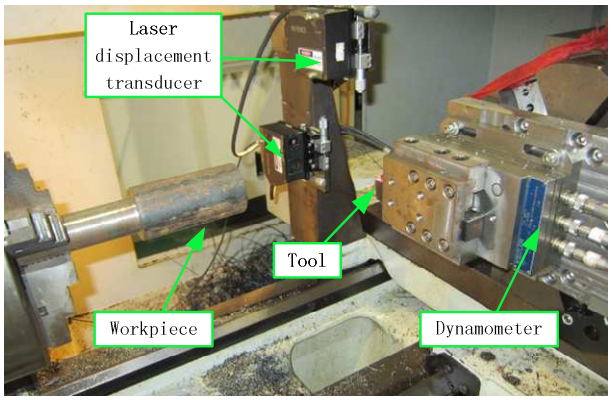


Fig. 3 Testing rigs

The self-excited chatter was regarded as the excitation of the cutting process. The chatter frequency would be changed because of the variation of the equivalent structural dynamics [9]. Figure 4 depicts the experimental data. The relative tool-workpiece displacement was measured as the input of the dynamic cutting process. In addition, the dynamic component of the cutting force was recorded as the output of the dynamic cutting process.

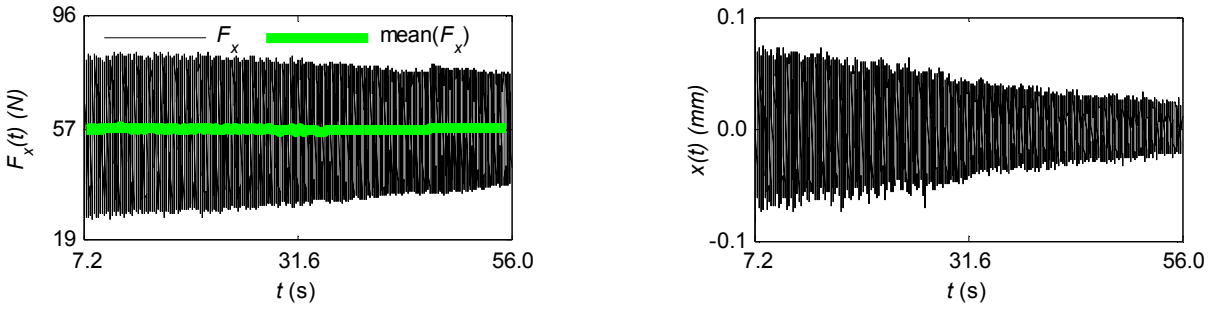


Fig. 4 Experimental data of x-axis direction:
(a) The dynamic cutting force; (b) The relative tool-workpiece vibration

The cutting process transfer function was derived from the experimental data with the Fourier Transform (FT) method, as shown in Fig. 5. A circular curve was fitted with the measured data.

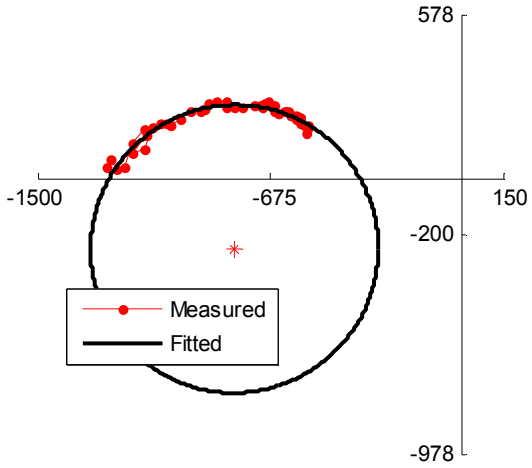


Fig. 5 The measured transfer function at x-axis direction

It is obvious that the arc center is under the real axis, which means the cutting force model shown in Eq. (3) and Eq. (4) would be more accurate than that in Eq. (1) and Eq. (2). The coordinates fitted arc center (x_0, y_0), as well as the calculated cutting dynamics according to Eq. (10) and Eq. (12) , was listed in Table 1. As the value of parameter k_s is fall between k_{is} and k_{os}, it can be considered that the cutting force coefficient reveals the influence of both the inner and the outer modulations. Moreover, the dynamic part of the outer modulation dynamics represented by k_{os} is small and can be neglected comparing to that of the inner modulation, which may mean that the outer modulation influence only the cutting area, while the inner modulation influence the cutting area and some other conditions such as the tool-workpiece friction area. The fitted cutting dynamics in Table 1 agree well with the theoretical analysis.

Table 1. The experimental results

x_o (N/mm)	y_o (N/mm)	k_{is} MPa	k_{id} MPa/(rad/s)	k_{os} MPa	k_{od} MPa/(rad/s)	k_s MPa	c_v N/mm	c_a N
-802.0	-250.2	1929	0.3373	1524	-9.919×10^{-4}	1617	-704.8	428.9

4 Conclusions

The cutting process dynamics analysis accuracy is significantly influences by the cutting force model. When the transfer function derived from different cutting force models are plotted in the complex frequency plane, the curve shapes and the centers are different with each other. Therefore, the measured cutting forces transfer function can be applied to selecting the most suitable cutting force model for cutting process analysis.

5 Acknowledgements

This work was supported by the grants from the National Key Technology R&D Program (No. 2012BAF08B01) and the National High Technology R&D Program of China (No. 2012AA040703).

6 References:

[1] Y. Altintas, E. Budak, Analytical prediction of stability lobes in milling, CIRP Annals - Manufacturing Technology 44 (1995) 357-362.

[2] T. Insperger, G. Stépán, Stability of the milling process, Mechanical Engineering 44 (2000) 47-57.

[3] K.J. Kalinski, M.A. Galewski, Chatter vibration surveillance by the optimal-linear spindle speed control, Mechanical Systems And Signal Processing 25 (2011) 383-399.

[4] M.E. Merchant, Mechanics of the metal cutting process. I. Orthogonal cutting and a type 2 chip, Journal Of Applied Physics 16 (1945) 267-275.

[5] M.E. Merchant, Mechanics of the metal cutting process. II. Plasticity conditions in orthogonal cutting, Journal Of Applied Physics 16 (1945) 318-324.

[6] M.K. Das, S.A. Tobias, The relation between the static and the dynamic cutting of metals, International Journal of Machine Tool Design and Research 7 (1967) 63-89.

[7] M.M. Nigm, M.M. Sadek, S.A. Tobias, PREDICTION OF DYNAMIC CUTTING COEFFICIENTS FROM STEADY STATE CUTTING DATA., Annals of the CIRP 21 (1972) 97-98.

[8] K.F. Ehmann, S.G. Kapoor, R.E. DeVor, I. Lazoglu, Machining process modeling: a review, Journal of Manufacturing Science and Engineering 119 (1997) 655-663.

[9] M. Zhu, K. Mao, B. Li, W. Xiao, An analytical method to select spindle speed variation parameters for chatter suppression in NC machining, Journal of Vibroengineering 16 (2014) 447-463.

Applied Mechanics and Materials Vol. 597 (2014) pp 203-207
© (2014) Trans Tech Publications, Switzerland
doi:10.4028/www.scientific.net/AMM.597.203

A Pre-processing Method of ProCAST Based on Pro/E and HyperMesh

Wei Huang[a], Huiming Shen[b,*],
Mingjun Hu[c], Shen Li[d], Xi Chen[e]
College of Mechanical Engineering, Guangxi University, Nanning 530004, China
[a]buaahw@126.com, [b]shenshenhm@163.com,
[c]457413470@qq.com, [d]ivan-lishen@qq.com, [e]395373598@qq.com

Keywords: Pro/E, HyperMesh, ProCAST, Casting simulation

Abstract. In order to improve the quality of ProCAST casting simulation, a pre-processing method is proposed based on Pro/E software and HyperMesh software. In this paper, Pro/E software parametric solid modeling and HyperMesh finite element meshing functions were used, a ProCAST pre-processing method is proposed based on Pro/E and HyperMesh software, it overcomes the meshing problems of ProCAST casting simulation and achieves the connections among Pro/E, HyperMesh and ProCAST. Compared with the basic ProCAST casting simulation meshing module, the Pro/E and HyperMesh pre-processing method improves the accuracy of modeling and meshing, the method is easy to realize with high accurancy.

Introduction

In technical economic times, the foundry industry is also striving to develop numerical simulation analysis. It not only reduces defective index through the analysis, but also make quality of casting products become higher [1,2]. ProCAST is the highest integration degree software of all the casting simulation software, it can be used in any kind of casting process for analyzing and optimizing. MeshCAST module of ProCAST is for meshing, MeshCAST can only mesh for the simplest model and the quality is poor.

In order to improve the quality of meshing in MeshCAST, Baiku Yu offered a interface mode of Pro/E and ProCAST and summarized interconnection between file output format after using Pro/E meshing and the ProCAST file format[3]; Baoshun Wang,ect made Pro/E surface modeling in ProCAST, drawing a better modeling methods connected with MeshCAST meshing[4]; Dawei Su,ect summarize a series of pre-processing[5] .

In order to improve the accuracy and speed of casting simulation, Pro/E and HyperMesh was applied into ProCAST mesh generation module in this paper, it improves the inadequate of ProCAST pre-processing module by using Pro/E solid geometry modeling software and Hypermesh meshing casting simulation software[6]. The results show that the Pro/E and HyperMesh pre-processing method improves the accuracy and speed of the simulation compared with ProCAST mesh generation modules, and verifies the feasibility and applicability of the method.

ProCAST Casting Simulation

ProCAST is a professional CAE systems for the evaluation and optimization of casting products and casting procedures developed by a French ESI company. With the help of ProCAST system, casting engineers have the capability of simulation analysis and prediction quality castings with flow field, temperature field and stress field in the formation process before completing the preparation, optimization the casting equipment parameters and process scheme[7]. ProCAST is widely used, AETC, NASA, Kelsey-Hyes, Honda Motors, etc. are ProCAST main users in the world; China First Auto Group Corporation, Shanghai Auto Foundry, Aviation Institute of Materials, etc. are the main users in our country.

ProCAST Introduction

ProCAST software set the simulation using the finite element method, it can be used for heat transfer calculation (including thermal radiation and angular coefficient calculation), calculation of the flow filling process, the calculation of thermal coupling stress field, microstructure simulation and predictive simulation of modeling Shrinkage. ProCAST can simulate the process of metal casting, accurately display inadequate filling and the position of the cold shut, gas trapping , hot spot and residual stress and deformation, it can also predict shrinkage and the changes of microstructure during the process of casting; It can be used to study the results of the design, such as the location of the gating system, vent and overflow system, the position and size of the feeder. The casting process of cavity can be accurately simulated, and the solidification process can be described accurately; Cooling or heating channel can be calculated and the use of exothermic riser effects can be displayed[8].

The basic steps to carry out casting simulations using ProCAST are as follows:

(1) Finite element mesh generation

(2) Set calculation parameters

(3) Simulation

(4) Dsplays the calculated results

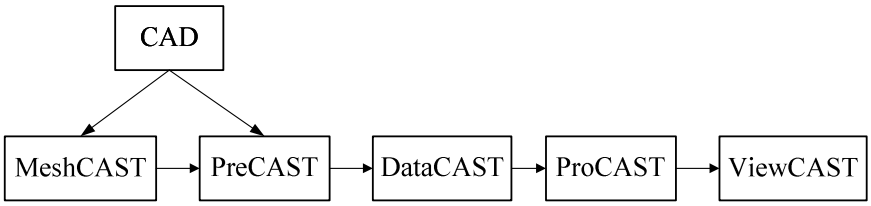


Figure 1 ProCAST simulation flow chart

ProCAST Mesh Generation Module

When using MeshCAST, if the formation of any geometric graphics software formed graphics file format (the most commonly used graphics formats such iges or stl). Then after the import of MeshCAST, it need surface meshing, body meshing and mesh optimization in pre-precessing parameters setting in ProCAST. It also need to produce body meshing and then optimization if it forms the Patran or Ideas face meshing file. Mesh optimization is set if it's the body meshing file of Patran or Ideas and the parameters can be calculated in ProCAST . As shown in the flowchart.

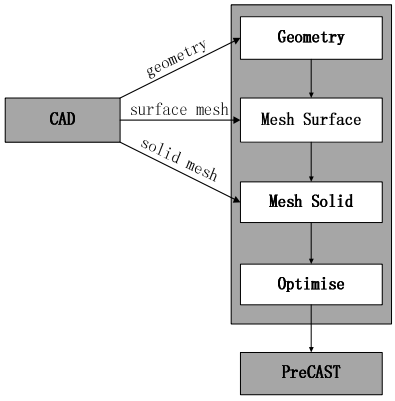


Figure 2 Graphics processing

The process of MeshCAST meshing is more complex, the grid is also easily wrong. For example, Body meshing can't be set because cross-grid often occur after the surface meshing. Although the meshing quality is improved but the model itself will change after a full detail of the automatic, manual repair, thereby it affects the accuracy of the simulation (what shows in red below is the case of the cross-grid). Furthermore MeshCAST can only be used in tetrahedral mesh, for hexahedral grid calculation accuracy, deformation characteristics, quality and other aspects of meshing has obvious advantages.

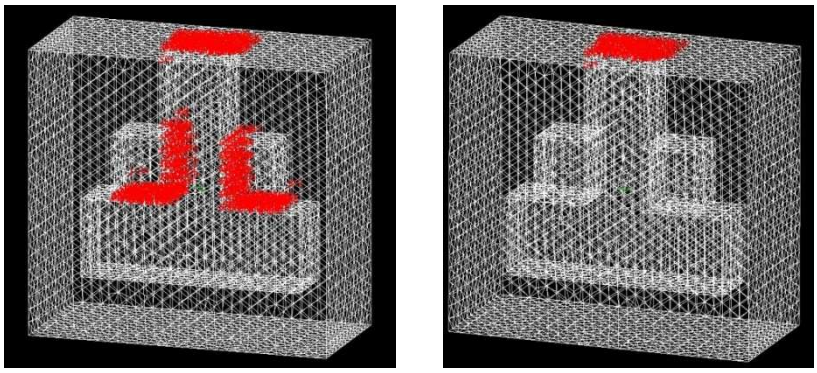


Figure 3 MeshCAST cross-grid situations

Pro / E and HyperMesh for Pre-processing Methods and Example

ProCAST does not have the solid geometry modeling function from the ProCAST simulation flowchart, it must use other software to model and then import into ProCAST for casting simulation, so we choose Pro/E for 3-D modeling. Compared with MeshCAST, HyperMesh is a high quality and efficient finite element pre-processor, which provides highly interactive visualization environment to help users build the finite element model of the product. Its open architecture provides the widest range of CAD, CAE and CFD software interfaces, and supports user-defined mode, which can be seamlessly integrated with any environment simulation.

Pro/E modeling

Pro/E design system was developed by Parametric Technology Corporation in 1989. It plays an important role in the current field of 3D modeling software and gets the recognition and promotion as the new standard in today's world of mechanical CAD / CAE / CAM field. It provides a set of complete product development plan such as design, assembly, analysis, manufacturing, simulation, product data management, secondary development, etc. Pro/E is one of today's most successful CAD / CAE / CAM software with its powerful 3D design system that has been widely used in many industries and sectors.

According to a simple example, after modeling and assembling in Pro/E, it will be saved in a format that Hypermesh can be accepted. HyperMesh supports all kinds of current universal major 3D CAD platform, the problem of data loss and geometric imperfection was solved by reading CAD model files directly without any data conversion. Supported CAD file formats as shown in Table.

Table 1 HyperMesh supported CAD file format

CATIA	UG	Pro/E	Parasolid	SolidWorks
IGES	STEP	STL	PDGS	Tribon
VDAFS	DXF	ACIS	JI	

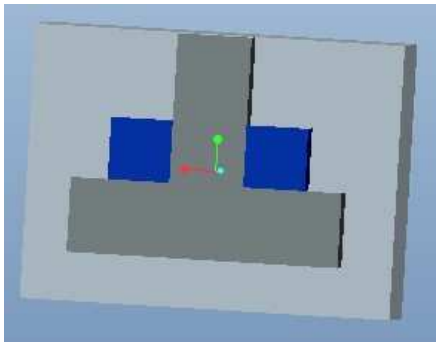


Figure 4 Pro/E solid modeling

For this example, simply stretching can be achieved through the Pro/E modeling capabilities. Of course, Pro/E is a function-defined system, a variety of different shapes can be achieved through

specific designed functions, which includes: ribs, slots, chamfers and evacuation, etc. With this tool for the body, the engineers can use design methods more naturally, more intuitively and without complex geometric. Parametric functions of Pro/E is defining body size with given symbols, So engineers can build the relationships between any form on the size and functions. When any changes in a parameter, the relevant characteristics is also automatically corrected. The function makes it easier to modify and make design optimization more perfect.

HyperMesh Mesh Generation

Pro/E model can be directly put into HyperMesh, Using HyperMesh powerful geometry cleanup function to correct errors in the geometric model, modify the geometry and enhancing the efficiency of the modeling; High quality and efficient meshing technology can not only complete the meshing of the simple model, but also complete automatic and semi-automatic meshing of the bar beam, plates and shells, tetrahedral and hexahedral meshes. It greatly simplifies the simulation of complex geometric modeling process; Advanced morphing technology allows users to change the existing grid directly to achieve new design without reconstruction of geometric model, which enhances the efficiency of the design and development of the product. The above example can be divided good hexahedral mesh use HyperMesh, hexahedral mesh as follow.

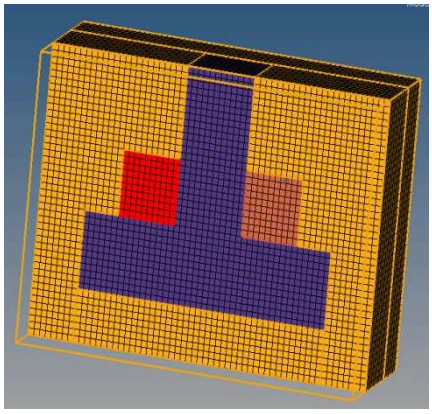


Figure 5 HyperMesh mesh

Patran format *. Out file ,Ideas format *.unv file are acceptable between HyperMesh and ProCAST after the body meshing. Partan format *. Out file is priority which is a good connection with ProCAST . Compared with former, it can import multiple body in Ideas format*.out file, but sometimes the interface will appear discontinuous, thus Patran format is widely used.

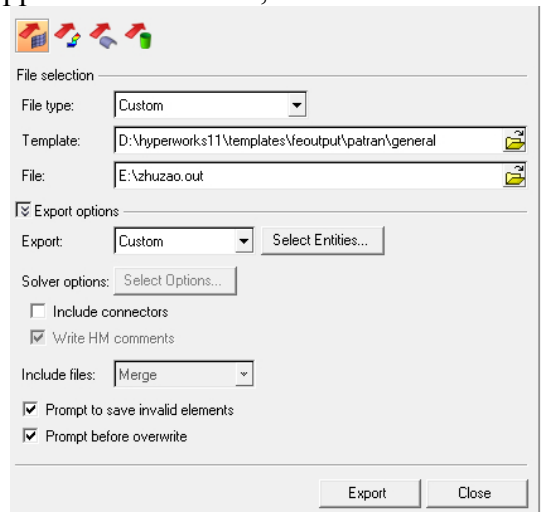


Figure 6 HyperMesh save format

Compared with MeshCAST, HyperMesh not only saves a lot of time, but also greatly improve the quality and accuracy of the grid. After meshing you can set parameters in PreCAST directly and then casting simulation can proceeded.

Summary

As a general rule, using ProCAST to complete a full analysis of casting simulation, but there are always some errors when meshing and the process is relatively complex and inefficient. According to the analysis about Pro / E and HyperMesh, A method about a combination between Pro / E and HyperMesh for pre-processing is presented in this paper.Using Pro/E and HyperMesh for solid modeling, meshing, and then import it into the ProCAST to set parameters. It not only saves time, but also improves model and meshing quality. Based on the comprehensive use of these software can learn from each other and solve practical problems. Compared with a single software processing, multi-software finite element processing is more organized, efficiency and accuracy of problem-solving has been improved.

References

[1] Xuchu Du, Zhenzhong Fan, Runzhou Hong. Technology Development of Numerical Simulation of Casting , J. Foundry Technology, 2013,34(11): 31-35.

[2] T.S. Prasanna Kumar. Casting Simulation Method, J. Comprehensive Materials Processing, 2014 (5): 235-257.

[3] Baiku Yu. The Interface Mode of Linking Pro/E to ProCAST, J. Locomotive & Rolling Stock Technology, 2001 (6): 20-24.

[4] Baoshun Wang, Jianxin Dong, Maicang Zhang. Application of Pro/E Curved Surface Modeling in ProCAST Mesh Generation, J. Foundry Technology, 2009, 30(7): 926-928.

[5] Dawei Su, Yutao Zhao, Leigang Wang. Interface Mode of Preprocess Software and ProCAST Software , J. Special Casting & Nonferrous Alloys, 2007, 27(5): 348-350.

[6] Lewis R W, Ravindran K. Finite element simulation of metal casting, J. International journal for numerical methods in engineering, 2000, 47(1-3): 29-59.

[7] Mintuan Ma, Pengbo Chen, Yinping Huang. Application of ProCAST Software in Casting Optimization, J. Hot Working Technology, 2006, 35(1): 52-53.

[8] Hongjun Hu. Function of FEM Software ProCAST and Application in Casting, J. Hot Working Technology, 2005, 1: 70-71.

Applied Mechanics and Materials Vol. 597 (2014) pp 208-212
© (2014) Trans Tech Publications, Switzerland
doi:10.4028/www.scientific.net/AMM.597.208

Assessment of the Influence of Welding Parameters on Distortion

Fábio Renck Locatelli[a *], Walter Jesus Paucar Casas[b] and Ricardo Frederico Leuck Filho[c]

Universidade Federal do Rio Grande do Sul, Departamento de Engenharia Mecânica, Rua Sarmento Leite 425, Porto Alegre, Rio Grande do Sul, CEP 90050-170, Brasil

[a]fabiorlocatelli@gmail.com, [b]walter.paucar.casas@ufrgs.br, [c]leuck.r@gmail.com

Keywords: welding distortion; temperature field; welding simulation, finite elements

Abstract. The welding involves the transfer of high localized heat flow, which results in residual stresses in the welded body. The impossibility of relieving these stresses generates welding distortions that become a problem in dimensional setting of welded structures. This study aims to evaluate the influence of some parameters in the welding process in a T-type joint. Due to the complexity of the welded joint and the deposition rate, a three-dimensional finite element model was developed for the solution of the temperature field and distortions. The transient thermal analysis used the Goldak equation for definition of the heat flux transferred to the part. The nonlinear characteristics of the phenomenon as well as the dependence of physical and mechanical properties with the temperature were considered in this work. The parameters studied were the welding speed, welding sequence and cooling time between weld beads. The results suggest that the higher welding speed, the welding sequence forward and back and with cooling interval between beads present themselves as the best parameters for welding with lower distortions.

Introduction

Knowing that the residual stresses and distortions are inevitable in welding, its effects cannot be disregarded. Distortions are defined by some authors [1,2,3,4] as the non-uniform expansion and contraction of the weld metal and the adjacent parent metal during the cycle of heating and cooling in the welding process. The distortions are summarized into six basic types: transverse shrinkage, longitudinal shrinkage, angular distortion, distortion by bending, twisting and buckling [5].

The identification of distortions in welded parts is necessary, but its identification is extremely hard. The thermal and mechanical behavior of the welding involves the knowledge of some data: the local high temperatures, the properties of materials as function of the temperature and the movel heat source. However, the welding process simulation by means of finite elements can furnish the thermomechanical behavior prediction.

The computer simulation of the welding process includes the calculation of the temperature field, residual stresses and distortions. The modeling of the welding process is complex, given the quantity of inter-related phenomena involving heat transfer, metallurgical aspects, fluid dynamics, electromagnetism and structural mechanics.

This study aims to evaluate numerically the influence of three parameters of the welding process, for which we consider the structural and thermal phenomena involved, through a numerical model developed by the finite element method.

Thermal and Structural Analysis

The welding process develops an intense and concentrated heat generation applied in the material being welded, for the purpose of fusion of materials, but involving metallurgical changes, distortions and residual stresses.

Heat Flow in Welding. The model proposed by [6] was used in this work as the reference for application of the heat flux profile in the finite element model. Among the authors who deal on heat

flow, [6] present a volumetric model of heat distribution as a function of time and position. Fig. 1 shows the double ellipsoid profile and Eq. (1) gives the heat flow distribution.

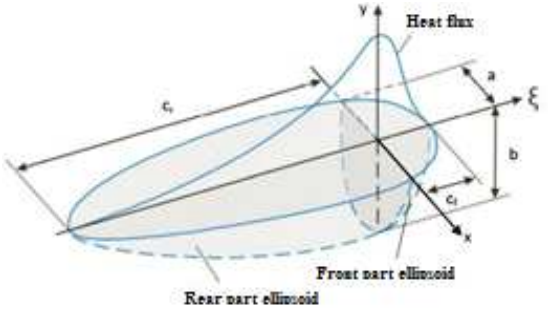


Figure 1 – Double ellipsoid profile of heat distribution [6]

$$q(x,y,\xi) = \frac{6\sqrt{3}\,fQ}{abc\pi\sqrt{\pi}} e^{-3\left(\frac{x^2}{a^2}+\frac{y^2}{b^2}+\frac{\xi^2}{c^2}\right)} \quad (1)$$

where q is the heat flux [W/mm3], (x,y,ξ) are the global reference coordinates [mm], f is the portion of heat in each ellipsoid, Q is the heat input [J/s] and (abc) are the semi-axes of the ellipsoids [mm].

The coordinate ξ is the sum of the coordinate z and the time required by the heat source to reach the next scan position. Therefore, we have $\xi=z+vt$, where v is the welding speed and t the time interval. For applications where the heat source starts from the system origin, $\xi=z$.

Respect to the geometric parameters of the source, a is the width, b is the depth and c is the length; c is divided in c_f for the front part and c_r for the rear part of the ellipsoid, respectively, thereby defining the size and shape of the ellipses, and hence the heat distribution across the source. To obtain a good approximation, c_r is considered as being the half and c_r twice the width [6].

The variable f corresponds to heat portions deposited in the front f_f and rear f_r ellipsoid, where $f_f + f_r = 2$. Experimental measurements show values of 0.6 for f_f and 1.4 for f_r, [6].

Structural Analysis of Welding. In welding there are many factors that affect the type and magnitude of distortions, among them we can: process [7], forced heat [5], welding parameters [8], value and type of constraint [9,10], mechanical and thermal properties of the material [11] and joint and plate geometry.

It is possible to reduce the distortions in the welding process, [12] gives some measures to this end: a) decreasing the speed welding, b) using symmetrical bevels and staples, c) designing the joint to receive the least amount of weld metal and holding it in order to prevent movements.

Materials and Methods

The geometry of the T joint used for modeling of the welding process is comprised by a base plate (horizontal) of 150×150×3 mm and a perpendicular one of 75×150×3 mm. The simulations were performed with the finite element program Ansys ® v. 14.5.

The numerical model assumes the same heat input, varying voltage (U), current (I) and welding speed (v_s), but fixing the welding energy. To evaluate the influence of welding speed two sets of parameters were used, defined as main (U^P=20 V, I^P=125 A, η= 0.9, ${v_s}^P$=4.5 mm/s, ${E_{liq}}^P$=500 J/mm) and alternative (U^A=23.3 V, I^A=185 A, η=0.9, ${v_s}^A$=7.5 mm/s, ${E_{liq}}^A$=517.2 J/mm).

To evaluate the influence of the welding sequence, two possibilities were used to achieve the weld beads, named as forward and back when performed in opposite direction on each side of the joint, and forward and forward when performed in the same direction, Fig. 2.



Figure 2 – Welding sequence: (a) forward and back, (b) forward and forward

The other parameter measured was the time interval between the ending instant of the first weld bead and the starting instant of the second bead on the opposite side. One situation was without time interval between welds (considering only the time necessary for moving the torch from the end of the first bead until the start of welding on the opposite side of the part, defined as 9 s for the sequence forward and back and 11.5 s for the sequence forward and forward). Another situation involved to perform the welding of the second bead just after the maximum temperature of the part to reach 100 °C (about 360 s). After combining all possibilities in Table l, we obtain eight cases.

Table 1 – Simulation cases

Case	Welding Speed		Welding Sequence		Time Interval	
	A1	A2	B1	B2	C1	C2
1	A1		B1		C1[1]	
2	A1		B1		C2	
3	A1		B2		C1[2]	
4	A1		B2		C2	
5	A2		B1		C1[1]	
6	A2		B1		C2	
7	A2		B2		C1[2]	
8	A2		B2		C2	

A1: U=20 V, I=125 A, v_s=4,5 mm/s
A2: U=23,3V, I=185A, v_s=7,5 mm/s
B1: forward and back
B2: forward and forward
C1: movement of the robot ([1]→9 s, [2]→11.5 s)
C2: cooling time 360 s

The mesh was structured for all the geometry, and divided in two parts, normal and refined. The first one is a mesh of elements with maximum size of 10 mm and applied across the assembly. The refined part is used where there are microstructural changes, such as the heat affected zone (HAZ) that comprises 10 mm from the bead, this region has a mesh with maximum size of 5 mm, Fig 3.

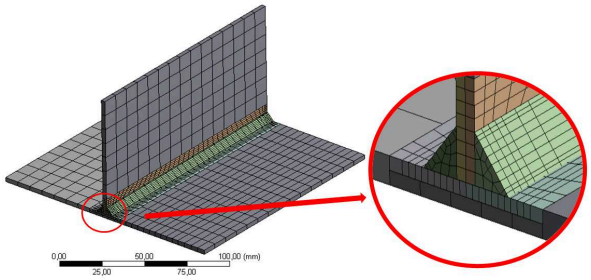


Figure 3 – Finite element mesh

The mesh set for the structural analysis was identical of the thermal analysis. used The structural element was the SOLID186. This element is used for 3D structural modeling with constant or thermal dependent properties.

The structural boundary conditions were originated from the thermal analysis, for all node and in each time step, which is called the coupling between domains. It was also necessary to clamp one corner of the horizontal plate to get convergence of the analysis. This constraint was applied based on experimental results.

Results and discussion

Regarding the welding speed. This analysis considers only variations of the speed parameter. It was found that cases using alternative speed parameters (cases 5, 6, 7 and 8) had lower distortion compared to their peers (cases 1, 2, 3 and 4), as can be seen in Table 2.

Table 2 – Variable welding speed

	Main Speed (v_s= 4,5mm/s)				Alternative Speed (v_s= 7,5mm/s)			
Case	1	2	3	4	5	6	7	8
Maximum Distortion [mm]	5.46	5.44	5.70	6.41	**4.37**	**4.31**	**4.43**	**4.89**

Regarding the welding sequence. This analysis considers only variations of the welding sequence. It was found that cases using the sequence forward and back (1, 2, 5 and 6) showed less distortion when compared to cases of the sequence forward and forward (3, 4, 7 and 8); see Table 3.

Table 3 – Variable welding sequence

	Sequence Forward and Back				Sequence Forward and Forward			
Case	1	2	5	6	3	4	7	8
Maximum Distortion [mm]	**5.46**	**5.44**	**4.37**	**4.31**	5.70	6.41	4.43	4.89

Regarding the cooling time. Table 4 considers only variations of the cooling time parameter.

Table 4 – Variable cooling time

	Cooling Time Without Interval				Cooling Time With Interval			
Case	1^1	3^2	5^1	7^2	2	4	6	8
Maximum Distortion [mm]	5.46	**5.70**	4.37	**4.43**	**5.44**	6.41	**4.31**	4,89

C1: time of movement of the robot (^{1}→9 s, ^{2}→11.5 s), C2: cooling time 360 s

In this case the results were not unanimous due to the indirect influence of the welding sequence. The sequence forward and back presents better results when performed with an interval between beads. The sequence forward and forward has less distortion when performed without time interval.

Conclusions

Regarding the welding speed. Using the alternative parameter in this work, the thermal distribution was concentrated in the welded metal, and showing a smaller heat affected zone.

Regarding the welding sequence. The sequence forward and back showed lower levels of residual stresses, therefore, their relief resulted in lower distortions.

Regarding the cooling interval. For the forward and forward welding sequence, the parameter without interval presented the best results, because of the residual stresses not fully developed help to constrain the evolution of the stresses generated during the execution of the next bead.

References

[1] T. Anderson, Distortion in aluminum welded structures, Weld. J. 82(2) (2003) 28-30.
[2] S. Kou, Welding Metallurgy, 2° ed., John Wiley & Sons, New York, 2003.
[3] D. Deng, H. Murakawa, Prediction of welding distortion and residual stress in a thin plate butt-welded joint, Comp. Mater. Sci. 43 (2008) 353-365.
[4] R. Wang, S. Rashed, H. Serizawa, H. Murakawa, J. Zhang, Numerical and experimental investigations on welding deformation, Transactions of JWRI. 37(1) (2008) 79-90.
[5] D. Radaj, Welding Residual Stress and Distortion, DVS Verlag, 2003.
[6] J. Goldak, A. Chakravarti, M. Bibby, A new finite element model for welding heat sources, Metall. Trans. 15 (1984) 299-305.

[7] P. Colegrove, C. Ikeagu, A. Thistlethwaite, S. Williams, T. Nagy, W. Suder, Welding process impact on residual stress and distortion, Sci. Technol. Weld. Joi. 14(8) (2009) 717-725.
[8] V. Vel Murtugan, V. Gunaraj, Effects of process parameters on angular distortion of gas metal arc welded structural steel plates, Weld. J. (2005) 165-171.
[9] T. L. Teng, C. P. Fung, P. H. Chang, W. C. Yang, Analysis of residual stresses and distortions in T-joint fillet welds, Int. J. Pres. Ves. Pip. 78(8) (2001) 523-538
[10] G.H. Jung, C.L. Tsai, Fundamental studies on the effect of distortion control plans on angular distortion in fillet welded T-joints, Weld. J. 83(7) (2004) 213-223.
[11] Y. Mikami, Y. Morikage, M. Mochizuki, M. Toyoda, Angular distortion of fillet welded T joint using low transformation temperature welding wire, Sci. Technol. Weld. Joi.. 14(2), (2009) 97-105.
[12] A. C. Davies, The Science and Practice of Welding: Welding Science and Technology, 10th ed., v.1, Cambridge: Cambridge University Press. (1992).

Applied Mechanics and Materials Vol. 597 (2014) pp 213-218
© (2014) Trans Tech Publications, Switzerland
doi:10.4028/www.scientific.net/AMM.597.213

Design and Optimization of Honeycomb Corrugated Chaff Forming Roller

Xiaoping Yang[1,a*],Bo Zhong[2,b],Changjie Luo[3,c]

[1] Room 207B, building D, HIT Campus of University Town of Shenzhen ,Shenzhen,China

[2] Room 207B, building D, HIT Campus of University Town of Shenzhen ,Shenzhen,China

[3] Room 412B, Shenzhen Institutes of Advanced Technology,Chinese Academy of Sciences, University Town of Shenzhen,China

[a]xpyang8@126.com, [b]729649292@qq.com, [c] 290695598@qq.com

Keywords: Corrugated chaff; forming roller; chamfer of teeth top edge ; number of teeth ; numerical simulation

Abstract. By analyzing the material properties and forming characteristics of the 0.8mm length side hexagon honeycomb corrugated chaff , we studied forming roller's design and optimization while making corrugated chaffs used forming method and focus on the influence of the chamfer of teeth top edge and number of teeth to forming quality at the corrugated chaff corner .We used finite element analysis software ANSYS / LS-DYNA to simulate the forming process of corrugated chaff , studied the stress contour and stress-time curve of typical element, found the optimal chamfer of teeth top edge and number of teeth, then we used the designed forming roller to verify the effect of chaff forming . By comparison experimental and simulation results,we found good agreement between the two, when the chamfer of teeth top edge dj = 0.08mm, number of teeth z = 40, the chaff has the best forming quality .

Introduction

The honeycomb structure is a new type of porous material which developed based on the principle of bionics, there are a variety of topologies ,such as quadrilateral , hexagonal and so on. The honeycomb has relatively low density, low stiffness , deformation controlled and many other advantages , has been widely used in anti-collision buffer , construction and other occasions [1] , in particular , the cell can be used in steam turbines and turbo engine's sealing devices for preventing leakage of steam , to ensure the safety of workers , while improving equipment efficiency [2] .

In the variety of topologies ,the 0.8mm length side hexagonal honeycombs are often used in seals ,they are produced by molding method. When making a honeycomb using molding method , the quality of the corrugated chaff determines the quality of the honeycomb , the forming roller is the key device to form corrugated chaff. According to the existing aviation standards,while forming a hexagonal honeycomb , there are standards prepared for the forming rollers only when the hexagonal side length are 3, 4, 5mm[3] ,the relevant reference standards when the hexagonal side length is 0.8mm has not been developed . The corrugated chaff forming principle is shown in Fig.1 .

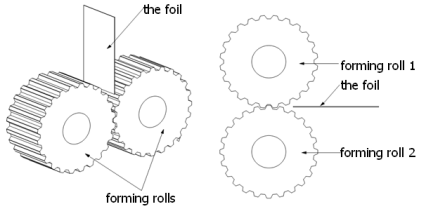


Fig.1 Corrugated chaff forming principle

There are materials aluminum , Hastelloy , etc.for honeycomb which used in seals ,the material of honeycomb foil in this paper is Hastelloy high temperature alloy ,the grade is GH536,which with a thickness of only 0.08mm . It is belonging to nickel-base superalloy solid solution strengthening

and always reliable below 900 ℃. Its main component is Ni-Cr-Fe, the chemical elements and basic physical parameters are shown in Table 1,2 respectively [4]:

Table 1 Hastelloy GH536's chemical elements

Elements	C	Cr	Ni	Co	W	Mo	Fe	Al
Percentage	0.05~0.15	20.5~23	>50	0.5~2.5	0.2~1.0	8~10	17~20	0.5
Elements	Ti	Mn	N	S	P	B	Cu	
Percentage	0.15	1	1	0.015	0.025	0.01	0.01	

Table 2 Material GH536's basic physical parameters

Solution temperature (℃)	Yield strength (MPa)	Tensile strength (MPa)	Elastic modulus (GPa)	Poisson's ratio	Elongation (%)
1177	275	690	199	0.3	30

Material of forming rollers is 45 # steel, since the thickness of the foil is very thin, the deforming of rolls is negligible in the forming process , forming rollers can be regarded as rigid in simulation.

Numerical Simulation

According to the topology of the honeycomb structure, ideal corrugated honeycomb chaff specifications is shown in Fig.2, the angle between adjacent sides θ1=θ2 =120°,side length $l_1 = l_2 = l_3 = 0.8$mm,thickness t=0.08mm.

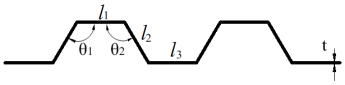


Fig.2 Ideal corrugated honeycomb chaff

Trapezoidal shaped teeth on the roller are distributed array means along the cylindrical surface , the teeth top apex angle and the teeth root apex angle is not equal, and the later will be greater than the former.Teeth parameters of forming rollers as shown in Fig.3.

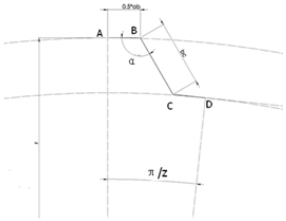


Fig.3 Trapezoidal teeth parameters of forming rollers

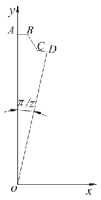


Fig.4 Coordinate of trapezoidal teeth profile

Forming roller's parameters include: the number of teeth z, addendum circle radius r, the edge length of teeth top AB, the side length of the teeth BC, teeth base length AC and vertex ∠ABC. Wherein known length of AB, BC, CD , ∠ABC and number of teeth , which can be set: AB $= a_1 / 2$, BC$= a_2$, CD$= a_3 / 2$, ∠ABC$= \alpha$, number of teeth$= z$ .The coordinate of trapezoidal teeth profile shown in Fig.4.

Then we will try to get mathematical expression of the radius r of addendum circle using the known parameters [5], let $\psi_1 = \pi/2 - \pi/z$, $\psi_2 = \pi - \pi/z$, $\psi_3 = \alpha - \pi/2$ .then:

$$(x_c, y_c) = (a_1/2 + a_2 \cdot \sin\psi_3, r - a_2 \cdot \cos\psi_3) \quad (1)$$

$$(x_d, y_d)=\left(\frac{x_c\cdot\tan\psi_2-y_c}{\tan\psi_2-\tan\psi_1}, x_d\cdot\tan\psi_1\right) \quad (2)$$

Because CD= $a_3/2$, there is:

$$\sqrt{(x_d-x_c)^2+(y_d-y_c)^2}=a_3/2 \quad (3)$$

Then we set parameters as follows:

$(a_1/2+a_2\cdot\sin\psi_3)\tan\psi_2=A$, $\tan\psi_2-\tan\psi_1=B$, $a_1/2+a_2\sin\psi_3=C$, combine equations(1),(2),(3) there is:

$$\left(\frac{A-r+a_2\cos\psi_3}{B}-C\right)^2+\left(\frac{A\tan\psi_1-r\tan\psi_1+a_2\tan\psi_1\cos\psi_3}{B}-r+a_2\cos\psi_3\right)^2=\frac{a_3^2}{4} \quad (4)$$

Set $(A+a_2\cos\psi_3-BC)/B=D$, $(A\tan\psi_1+a_2\tan\psi_1\cos\psi_3)/B+a_2\cos\psi_3=E$, $\tan\psi_1/B+1=F$, then equation(4) can be expressed as:

$$\left(\frac{1}{B^2}+F^2\right)r^2-2\left(\frac{D}{B}+EF\right)r+D^2+E^2-\frac{a_3^2}{4}=0 \quad (5)$$

Set $(1/B^2+F^2=G)$,$2(D/B+EF)=H$,$D^2+E^2-a_3^2/4=M$, then equation(5) can be expressed as:

$$Gr^2-Hr+M=0 \quad (6)$$

Solving equation(6), addendum circle radius can be obtained:

$$r=\frac{H+\sqrt{H^2-4GM}}{2G} \quad (7)$$

Coordinates of each point can be obtained:A(0,r),B($a_1/2$,r),C $\left(a_1/2+bc\cdot\sin\psi_3, r-a_2\cdot\cos\psi_3\right)$ and D $\left((x_c\cdot\tan\psi_2-y_c)/(\tan\psi_2-\tan\psi_1), x_d\tan\psi_1\right)$.So the teeth profile ABCD can be expressed mathematically in coordinate.

When teeth top side length ab = 0.8mm, length of the teeth side bc = 0.8mm, the angle α = 120 ° ,if the number of teeth z is known,then the addendum circle r can be determined , so that the forming roller can be designed.

The above mathematical relationship can be used in ANSYS/LS-DYNA software with APDL programs to simulate the parametric modeling and simulation process ,the model shown in Fig.5. This simulation model uses shell163 element for foil and solid164 element for the forming roller , the simulation set the the foil initial velocity v = 500mm / s , which equals to the line speed of the forming rollers at the engagement .



(A) finite element model (b) mating Area Enlargement

Fig.5 Finite element model

Results and Analysis

Forces work on the corrugated foil strip at a moment when the foil was forming is shown in Fig. 6 .

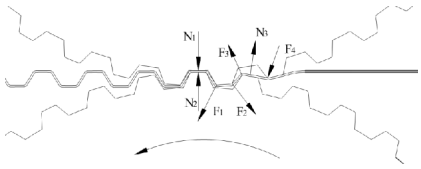
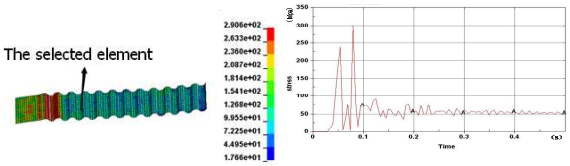


Fig.6 Forces work on the corrugated chaff at a moment during the forming process

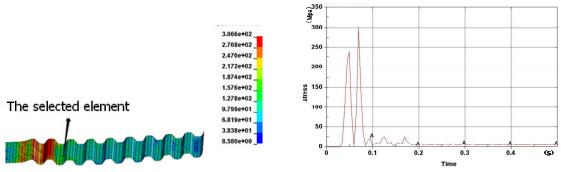
Fig.6 shows that the chamfer size of teeth top edge is closely related to the degree of bend of the corrugated extrusion. If the chamfer is too small, the corners of the chaff may be excessive compression or draw injury by the projection of the teeth top edge, causing damage to the foil, if the chamfer is too large ,then corners of formed corrugated chaff will be very large, which is not conducive to cellular manufacturing. If the number of forming rollers' teeth z is too small , teeth profile of the forming roller will be quite different from the the ideal half hexagon , which is not conducive to form the foil to precise corrugated ; the larger of z ,the more similar the trapezoidal teeth profile of forming roller to the ideal semi-regular hexagonal shape , thereby forming the better corrugated chaff . But z should not be too large , when z tends to infinity , the forming roller teeth tend to be semi-regular hexagonal mold ,in this way,there will be the phenomenon of two or more teeth meshed at the same time while forming a chaff, then supply of the material will be limited by the the adjacent meshing zone, resulting in the material be pulled , local stress will increase sharply, bending stress in some sections may be exceeds the tensile stress limit of the material ,the formed corrugated chaff may appears broken phenomenon . Therefore, we can set the chamfer of teeth top edge dj and the number of teeth z as variables ,the results of simulation analysis are as follows .

When the chamfer of teeth top edge dj is 0,0.03,0.05,0.08,0.1mm, mises stress contours of the foil while forming and stress-time curve of typical corrugated chaff element at angled corner shown in Fig.7 to Fig.11 respectively ,stress unit is MPa,time unit is second.(The bright color in Figs mises stress contours means that the portion of the material is in the engaging section just right) .



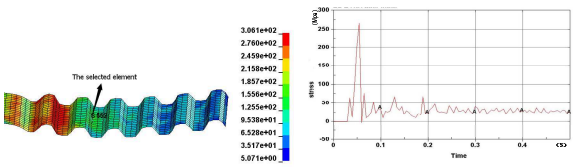
(a) mises stress contours (b)stress-time curve

Fig. 7 Force at the corner when dj = 0mm



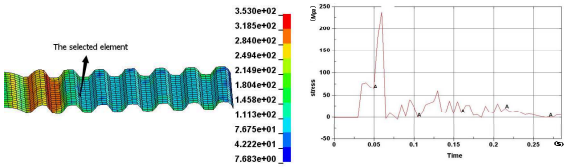
(a) mises stress contours (b) stress-time curve

Fig.8 Force at the corner when dj = 0.03mm



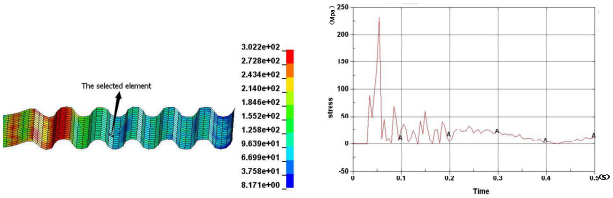
(a) mises stress contours (b)stress-time curve

Fig.9 Force at the corner when dj = 0.05mm



(a) mises stress contours (b)stress-time curve

Fig.10 Force at the corner when dj = 0.08mm

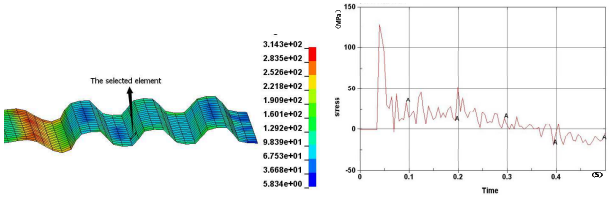


(a) mises stress contours (b)stress-time curve

Fig.11 Force at the corner when dj = 0.10mm

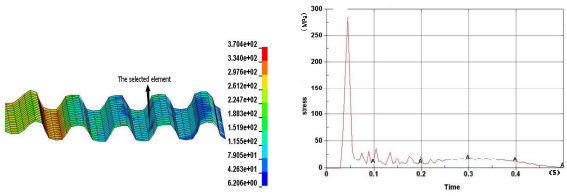
From the results above,we can find that when dj=0 or 0.03mm,the stress at the corner are over 300Mpa ,these are very large,which cause damage to the foil,the foil may be completely split when serious.when dj=0.1mm,the stress is close to the yield stress,foil can not be fully formed and the angle between the adjacent sides is not close to 120°. When dj=0.05 or 0.08mm,there is no clear distinction on the effect of formed foil,both the stress and the angle is appropriate.

Next we will take dj = 0.08mm as an optimal parameter, then study the effect of number of teeth z while forming a foil,when z is 20, 40,50 and 60,the results is below .



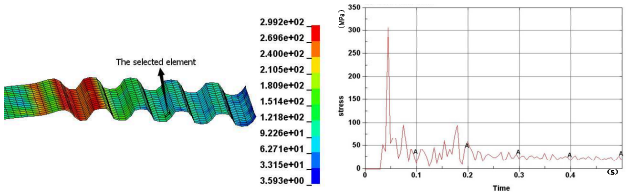
(a) mises stress contours (b)stress-time curve

Fig.12 Force at the corner when z=20



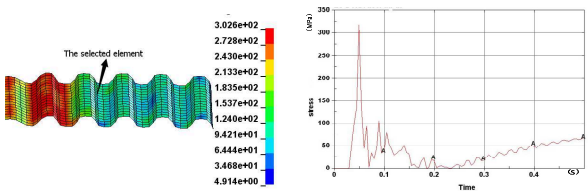
(a) mises stress contours (b)stress-time curve

Fig.13 Force at the corner when z=40



(a) mises stress contours (b)stress-time curve

Fig.14 Force at the corner when z=50



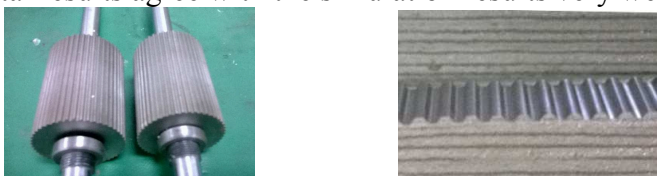
(a) mises stress contours (b)stress-time curve

Fig.15 Force at the corner when z=60

From the results above,we can find that when z=50 or 60,the stress at the corner are over 300Mpa ,these are very large,which cause damage to the foil,for there are splits at the corners .when z=20,the stress is close to the yield stress,foil can not be fully formed and the angle between the adjacent sides is not close to 120°.When z=40,both the stress and the angle are appropriate.

Experiments

Based on the above simulation results, we manufactured forming roller whose number of teeth z = 40, chamfer of teeth top edge dj = 0.08mm.we made forming experiments using self-developed cellular chaff forming prototype, observed the forming quality at corrugated chaff corners, the results are shown in Fig16. Experimental results show that there is no obvious damage cracks at the corners of the formed chaff and the angle between the adjacent sides is close to 120 °, which are expected, the experimental results agree with the simulation results very well.



(a) forming roller (b) the formed corrugated foil strip

Fig.16 Forming roller and formed corrugated foil strip

Summary

1)By analyzing the simulation results on the mises stress contour and stress-time curve at the chaff corner when chamfer of teeth top edge and number of teeth varies, we found that when chamfer of teeth top edge dj =0.08mm, the number of teeth z =40, the formed corrugated chaffs have good quality.

2) By comparing the simulation and experimental results, we find that they agree with eath other very well .

3)Further optimal design should based on the experimental values.

4)Using the forming roller that designed based on the optimized parameters,we can form corrugated chaffs that meet the requirements of honeycomb manufacture.

Acknowledgements

The authors wish to express their grateful acknowledgements to the National Natural Science Foundation of China under Grant No.51105358,Shenzhen Fundamental Research Project(No.JC201105190954A),the Shenzhen Key Laboratory of Precision Engineering (No. CXB201005250018A). The authors would like to thank the supports very much.

References

[1]Gibso LJ, Ashby MF.Cellular solids: structures and properties,2nd edition.Cambridge University press.Cam-bridge, UK, 1997

[2]Lidong He, Xiaoqiang Ye, Jinnan Liu.Investigation and Application of Honeycomb Seals[J]. Chinese Mechanical Engineering.2005,1855-1857

[3]Zufu Zhou.Composite materials science[J].Packaging Engineering. 1995,40-45

[4]Ruihong Miao.Application of metal cellular gas-tight seal in steam turbine[J].Taiyuan Science.2008,68(2) ,68-72

[5]Mei Ming.Finite element simulation and experimental research on forming honeycomb half-cell structures[D].Changsha,Chian,2013,23-24

Applied Mechanics and Materials Vol. 597 (2014) pp 219-222
© (2014) Trans Tech Publications, Switzerland
doi:10.4028/www.scientific.net/AMM.597.219

Effect of Backplate Thermal Diffusivity on Mechanical Properties of Double Sided Friction Stir Welded Aluminum for Ship Structure

Achmad Zubaydi[1,a*], Nurul Muhayat[1,2,b] , Sulistijono[3], M. Zaed Yuliadi[4], Budie Santosa[1], Dony Setyawan[1,c], Syaiful Haqi[1]

[1]Faculty of Marine Technology, Sepuluh Nopember Institute of Technology, Surabaya, Indonesia

[2]On leave from Mechanical Engineering Department, Sebelas Maret University, Solo, Indonesia

[3]Faculty of Industrial Technology, Sepuluh Nopember Institute of Technology, Surabaya, Indonesia

[4]PT PAL Indonesia, Surabaya, Indonesia

[a] zubaydi@na.its.ac.id, [b]Nurul09@mhs.na.its.ac.id, [c]dony@na.its.ac.id

Keywords: Friction stir welding. Backplate thermal diffusivity. Aluminum alloy 5083. Mechanical properties.

Abstract. The effects of backplate thermal diffusivity on mechanical properties of friction stir welded (FSW) aluminum alloy 5083 joints were studied in the present work. Three variations of backplate material, marble-block, mild steel and aluminum which represent low, medium and high diffusivity respectively, were used in the welding processes. The results showed that the increase of backplate thermal diffusivity resulted the decrease of the welding temperature. Defect free weld was obtained if backplate material was mild steel, whereas the other backplate material, marble-block and aluminum were obtained defect welds. The highest tensile strength as well as microhardness were obtained in the mild steel backplate.

Introduction

The most common welding technologies used in shipyard are gas tungsten arc welding (GTAW) and gas metal arc welding (GMAW). However this technologies have disadvantages such as high distortion and melt related defect. Therefore recently a new welding technology called friction stir welding (FSW) has been developed. FSW can reduce high welding distortion because the weld processes took place below melting temperature so that it could avoid melt related defects. However FSW thermal history affects the quality of FSWed joints.

It has been reported, the higher tool rotation rate caused the higher peak welding temperature, whereas the higher travel speed caused the lower one. The peak welding temperature decreases as well as average cooling rate due to the increasing backplate thermal diffusivity[1]. The grain size of nugget zone increase obviously due to the decrease of backplate thermal diffusivity [2]. Composite backplate made of aluminum and cooper is used to improve mechanical properties of friction stir welded aluminum alloy 2024-T3 joints. The grain size of nugget zone under composite backplate resulted in finer grain size compared to a monolithic steel backplate [3]. Different backplate thermal diffusivity could affect the weld process parameter such as weld temperature, metallurgical and mechanical properties without changing tool rotation speed or travel speed [4]. Since backplate dissipates the welding heat from welding processes, the effect of backplate thermal diffusivity is important to investigate. However no studies have evaluated on FSWed aluminum alloy 5083 which is used for ship building.

The objective of the present work is to study the effect of backplate material on joint properties of FSWed aluminum alloy 5083. There are three different backplate materials, marble-block, mild steel and aluminum which represent low, medium and high diffusivity respectively. The temperature, macrostructure, microhardness and tensile strength of joints were compared and discussed.

Experimental procedures

The base material used on this investigation was aluminum alloy 5083 with the dimension of 400 x 150 x 6 mm. The chemical composition is listed in the table 1. Oxidation film was removed from the work piece surface by grinding with abrasive paper. Double sided friction stir butt welds were made using an FSW tool material which is made from K100 bohler with shoulder diameter of 18 mm and trianguler pin with diameter and length of 4 mm and 3.8 mm respectively. The tool plunge depth of 4.0 mm, and the tool tilt angle of 2.5° were choosen to fabricate the joint. Due to high deformation resistance of 5083 aluminum alloy, the triangle pin profile was choosen that would lead to the best weldability of high deformation resistance aluminum [5].

Table 1. Chemical composition of 5083 H116 Al alloy (mass fraction, %)

Cu	Mg	Si	Fe	Mn	Zn	Cr	Ti	Al
0.09	4.74	0.13	0.24	0.73	0.02	0.15	0.01	Bal

The FSW rotation speed and welding speed were 1125 rpm and 30 mm/min, respectively. The work piece were subjected by three variation of backplate material, marble-block, mild steel and aluminum alloy which represented low, medium and high diffusivity respectively. During welding process, the welding temperatures were measured using infrared thermometer at 5 mm behind the FSW tool at advancing side and retreating side of the joint. Measured weld temperature along the joint line were averaged.

The tensile properties of each joints were evaluated using Biro Klasifikasi Indonesia tensile specimens standard [6]. The tensile specimens were cut out from the FSW joint perpendicular to the welding direction. Macrostructural examination samples were polished using multi grade emery paper and etched using Keller's reagent and then images were taken by a light optical stereozoom microscope. The hardness measurement was done across the flow arm zone at 1.5 mm of the surface of the first (top) and the second FSW (bottom) by Vicker's microhardness tester with load of 100 gr for 10 s. The points of vicker's micro-hardness test can be seen in Fig.1.

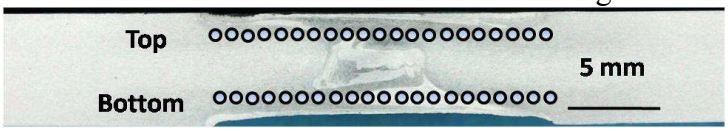


Fig.1. The points of vicker's micro hardness test

Result and Discussion

Welding Temperature. The increase of backplate thermal diffusivity resulted the decrease of the welding temperature in both first FSW and second FSW. It can be seen in Fig. 2. Using high thermal

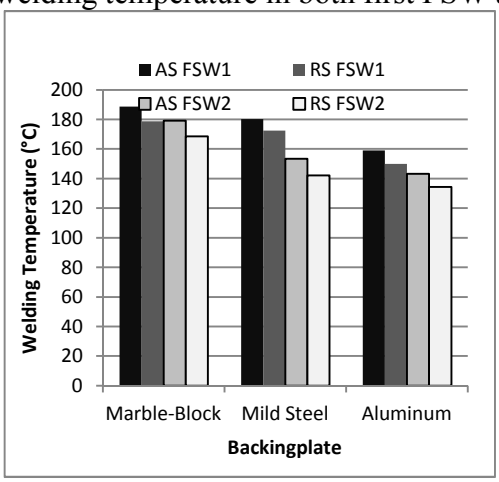


Fig. 2. Average welding temperature along joint line under different backplate material at the first FSW and second FSW (RS, retreating side and AS, advancing side).

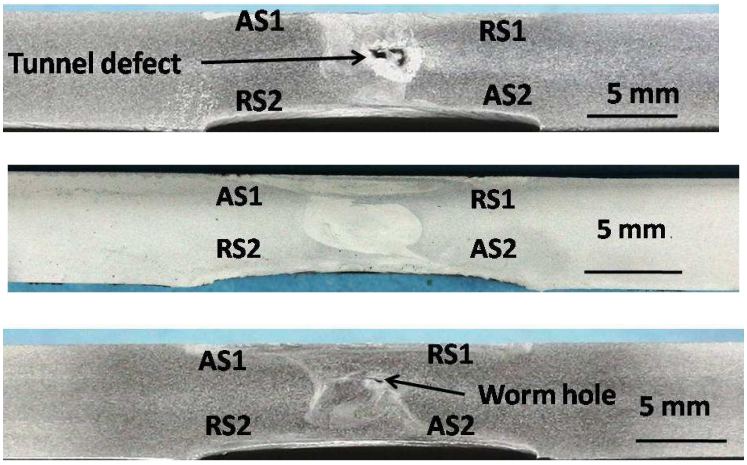


Fig. 3. Cross-sectional macrostructure of double sided friction stir welded joints of AA5083 under three different material, (a) marble-block (b) Mild steel, (d) Aluminum.

conductivity backplate caused more heat dissipated [1]. The Welding temperature at the advancing side is higher than that at the retreating side. The advancing side is the side of the weld where there is a positive combination of the tool feed rate and the peripheral tool velocity that can raise the welding temperature. On the retreating side, the vector is opposite that can lower the welding temperature. This observation is in agreement with the results of the other researcher [7]. The welding temperature of second FSW is lower than that of first FSW. It is caused by the thinning of thickness due to tool plunge depth of first FSW that influences the decrease of second FSW so that it results in lower temperature.

Macrostructure. Cross-sectional macrostructure of double sided friction stir welded joints AA 5083 under three different backplate material diffusivity are shown in Fig.3. The welded joint which is produced with Marble-block backplate makes a tunnel defect and a nugget collapse in the interference zone. There are typical of too high heat input defects. Additional heat input caused excess turbulence of the plasticized metal [8],[9]. Defect free weld can be produced with mild steel backplate because of sufficient heat input. Although the nugget shape is perfect, aluminum backplate produces a joint with a worm hole defect at the bottom of advancing side at second FSW. This is a typical insufficient heat input defect.

Hardness. Average Vicker's microhardness of friction stir welded joints at the flow arm zone of first FSW and second FSW under three different backplate are presented in Fig. 4. The lowest backplate diffusivity, marble-block produces the joint with the lowest average microhardness. It can be explained that the welding processes of which marble block as a backplate produces highest welding temperature. The highest welding temperature gives a chance for grain to grow. Coarser grain size caused lower microhardness [10]. Medium backplate diffusivity, mild steel produces the joint with the highest average microhardness. Whereas the highest backplate diffusivity, aluminum produces average microhardness which lower than that of mild steel. In addition the average microhardness of the second FSW has higher value than that of the first FSW at all backplate material. It can be explained that the second FSW takes place at the lower welding temperature than the first one and in high deformation state so that the grain size will be finer than the former. On the other side, top surface only experiences thermal cycle that results the grain growth.

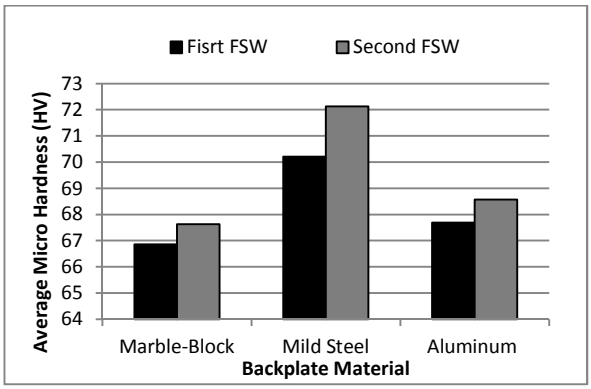


Fig. 4. (a) Average micro hardness across friction stir welded joint under different backing plate

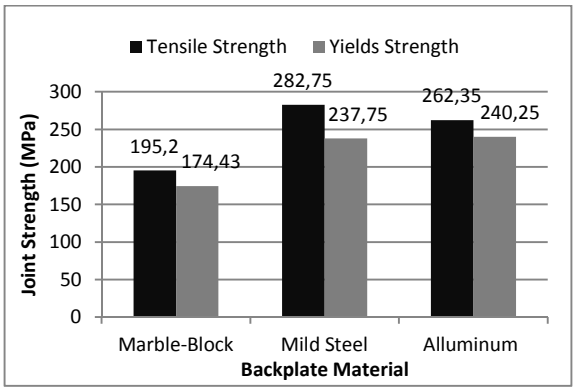


Fig. 5. Tensile properties under different backplate material.

Weld Strength. Fig. 5 represents the tensile strength of friction stir welded Aluminum Alloy 5083 under different thermal diffusivity backplate material. It can be observed that tensile strength under mild steel backplate material displays the highest tensile strength. The lowest tensile strength was obtained in the marble-block backplate material. The highest backplate thermal diffusivity, aluminum obtained the lower tensile strength than that of mild steel backplate. Marble-block has low thermal diffusivity so that it blocks the heat from workpiece to the anvil. It can increase the welding temperature at the weld joint. When the welding temperature is too high, it makes collapse nugget and tunnel defect caused by turbulence of material flow (see Fig. 3). When the backplate diffusivity increases, the weld temperature decreases to optimum point so that the sound weld was obtained. Worm hole defect which is caused by insufficient heat input found when the backplate aluminum

which has high thermal conductivity was used in the welding processes. Weld defects cause the reduce of weld strength.

Conclusion

In this study, the influences of backplate diffusivity material on the mechanical properties of the FSWed aluminum alloys AA5083-H116 were investigated. The conclusions are as follows:

1. Increasing thermal diffusivity backplate causes the reduce of welding temperature.
2. The lowest thermal diffusivity backplate causes tunnel defect at the advancing side of second FSW. Medium thermal diffusivity backplate produces sound weld, whereas the highest thermal diffusivity backplate appears worm hole defect.
3. The joint welded under medium thermal diffusivity backplate, mild steel exhibits the highest average micro hardness, whereas that under the lowest thermal diffusivity backplate shows the lowest average micro hardness.
4. Inline with the hardness that the highest tensile strength is obtained at the welded joint under medium thermal diffusivity backplate but the lowest one at the lowest thermal diffusivity backplate.

Acknowledgements

This research is funded by The Ministry of Education and Culture, Indonesia through research laboratory grant BOPTN 2014 ITS Surabaya, Contract No. 016455.50/IT2.7/PN.01.00/2014.

References

[1] Zhihan Zhang, Wenya Li, Jinglong Li, and Y.J. Chao, Numerical Analysis of Effect of Backplate Diffusivity on the Transient Temperature in Friction Stir Welding, JMEPEG (2013) 22:2446–2450

[2] Zhihan Zhang, Wenya Li, Junjun Shen, Y.J. Chao, Jinglong Li, Yu-E Ma, Effect of backplate diffusivity on microstructure and mechanical properties of friction stir welded joints, Materials and Design 50 (2013), 551-557

[3] Z.H. Zhang a, W.Y.Li a,n, Y.Feng b, J.L.Li a, Y.J.Chao, Improving mechanical properties of friction stir welded AA2024-T3 joints by using a composite backplate, Materials Science &EngineeringA598(2014)312–318

[4] P. Upadhyay n, A.P.Reynolds, Effects of forge axis force and backing plate thermal diffusivity on FSW of AA6056, Materials Science & Engineering A 558 (2012) 394–402

[5] H. Fuji, L. Cui, M. Maeda, K. Nogi, Effect of tool shape on mechanical properties and microstructure of friction stir welded aluminium alloy, Material Science and Engineering A 419 (2006) 25-31

[6] BKI, Rules For The Clasification and Construction of Seagoing Steel Ship, Volume 6 Rule For welding, Section 11, Biro Klasifikasi Indonesia, 2010.

[7] Y.M. Hwang, Z.W. Kang, Y.C. Chiou, H.H. Hsu, Experimental study on temperature distributions within the workpiece during friction stir welding of aluminum alloys, International Journal of Machine Tools & Manufacture 48 (2008) 778–787

[8] K. Elangovan, V. Balasubramanian, Influences of tool pin profile and welding speed on the formation of friction stir processing zone in AA2219 aluminium alloy, journal of materials processing technology 2 0 0 (2 0 0 8) 163–175

[9] Hua-Bin Chen, Keng Yan, Tao Lin, Shan-Ben Chen, Cheng-Yu Jiang, Yong Zhao, The investigation of typical welding defects for 5456 aluminum alloy friction stir welds, Materials Science and Engineering A 433 (2006) 64–69

[10] Y. S. Sato, M. Urata, H. Kokawa, K. Ikeda, Hall_ Petch relationship in friction stir welds of equal channel angular-pressed aluminium alloys, Materials Science and Engineering A354 (2003) 298- 305

Applied Mechanics and Materials Vol. 597 (2014) pp 223-227
© (2014) Trans Tech Publications, Switzerland
doi:10.4028/www.scientific.net/AMM.597.223

Study on External Grind-hardening Experiments and the Analysis of Hardening Effects for 40Cr Steel

Gang Yang[1,a], Zhengtong Han[2b], Changlong Du[2c]

[1] College of Applied Science and Technology, China University of Mining and Technology, Xuzhou, Jiangsu Province, China PR, 221008.

[2] College of Mechanical and Electrical Engineering, China University of Mining andTechnology, Xuzhou, Jiangsu Province, China PR, 221008.

[a]ygcast@163.com, [b]hanztcumt@163.com, [c]duclcumt@163.com

Keywords: grind-hardening, external grinding, orthogonal test, 40Cr steel

Abstract: External grind-hardening is a new technology combing grinding and quenching. Hardening tests are carried out according to 3-level and 3-factor orthogonal method for 40Cr steel, and metallographic observation and hardness measurement are put forward. Martensite is found in the surface layer structure, which hardness reaches HV647.4~719.4 and depth is about 0.22~1.1mm. The practicability of the new technology is confirmed. Orthogonal analysis is proceeded successively for the acquirements of influencing pattern and significance of factors based on the hardening results.

Introduction

The principle of grind-hardening is that grinding heat of manufacturing process and conductivity of metal workpiece are utilized to austenitizing and martensitizing respectivly for the acquirement of same or similar result of surface quenching[1-2]. The new technology is a combination of grinding and surface quenching, energe saving and environment considering, and strenghthening material performance while reducing manufacturing cost, has favorable social and economic benefits [3-4].

The studies for the technology are mainly based on plane grinding presently[1-7]. Therefore, external grinding is applied to the experiments with materials of 40Cr steel and 45 steel respectively, and various grinding parameters are employed for the verification of the grindi-hardening effectiveness and the acquirement of influencing pattern of the factors.

1 External grind-hardening Test

1.1 Test condition and grinding parameters

Tests are carried on with M1432B universal cylindrical grinder. The workpiece is the sealing ring of coal-winning machine with size of outer diameter Φ210 mm, inner diameter Φ195 mm, and thickness 24 mm. The design surface hardness is no less than HRC45.

Grinding mode for tests is single-lap dry up-grinding without longitudinal feed movement. For the research of relationship between grinding parameters and hardening effectiveness, two workpiece materials, three workpiece speed, three grinding depth, and three kind of wheel are adopted and tests is carried on with the matched parameters, as listed in Table 1. And lower workpiece speed and larger grinding depth are also adopted for the enhanced heat-intensity.

Table 1 Grinding Parameters of External Grind-hardening Experiments

Wheel Speed(m/s)	30
Workpiece Speed(m/min)	0.2, 0.5, 0.8
Grinding Depth(mm)	0.2, 0.3, 0.4
Wheel Characteristics	WA46L8V, PA46L8V, PA60L8V
Lubricating Method	Dry Grinding
Workpiece Materials	40Cr Steel

1.2 Establishment of test scheme

The test has three levels and three factors all of that are listed in Table 2.

Table 2 The Levels of the Factors

Factor	Level 1	Level 2	Level 3
A(grinding depth)	0.2	0.3	0.4
B(workpiece speed)	0.2	0.5	0.8
C(wheel Characteristics)	WA46L8V	PA46L8V	PA60L8V

It proceeds according to orthogonal table $L_9(3^4)$ [8] respectively with 40Cr steel and 45 steel. Because the factors are independent of each other, interactive effects between them are not taken into consideration. After all the tests are completed, nine hardened workpieces are obtained to each material with quenching characteristics observed obviously.

2 Verification and research of hardening results

2.1 Preparation of the samples

Each of the tested workpieces is stripped of a square sized width 10mm and depth 3mm from surface by linear cutting which is to be made sample for study by abrading, polishing, corroding and dewatering[9]. Afterwards, the metallographic observation will be conducted by S-3000N scanning electron microscope.

2.2 Metallographic observation and the analysis of results

No.6 sample is selected at random for metallographic observation, as shown in Figure 1 and Figure 2.

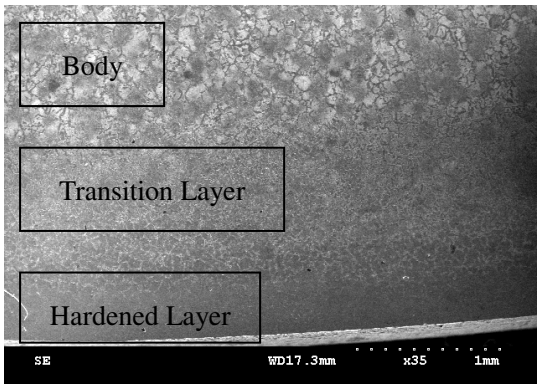


Figure 1 Surface Structure of No.6 Sample

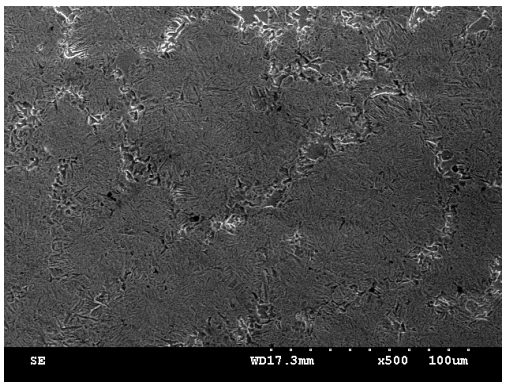


Figure 2 Structure of Hardened Layer of No.6 Sample

It's shown in Figure 1 clearly that the three parts of hardened layer, transition layer and body are divided from surface to inside. And the mixture of acicular martensite and lath martensite is the

main content of hardened layer, as shown in Figure 2; trainsition layer is the mixture of martinsite and ferrite; and body is still the mixture of ferrite and pearlite without transformation.

2.3 Measurement and result research of hardness

Surface hardness is measured by microhardness tester with load 0.4904N and loading time 20s. And the hardness values are tested every 0.2mm from surface to inside of the sample still it stabilizes at low value. As shown in Figure 3, hardness curve of No.6 sample is drawn. The dividing line is made according to the design hardness HRC45(HV446.3) of the workpiece, and the horizontal axis value of the part above it is considered as the depth of hardened surface meeting the design requirement.

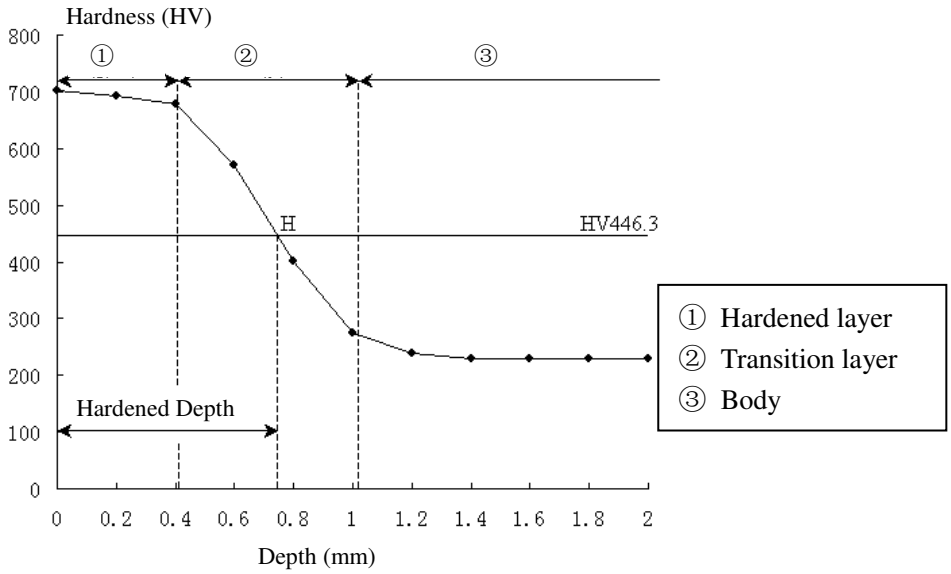


Figure 3 Hardness Distribution of No.6 Sample

The tendency of the curves is declining constantly from surface to core, and according to the decline rate, three parts can be divided approximately. At beginning, from surface to about 0.4mm below, hardness descends slowly from top value HV702.6 to HV680.3, which is corresponding to the hardened layer of metallographs and the structure of martensite. Then, hardness value dropped rapidly in the second part from HV680.3 to HV275.7 in the depth of 0.4mm to 1.0mm from surface, which makes the sharp shape of the curves and is corresponding to the transition layer of the mixture of martensite and ferrite. At last, the stern of curves is stable at HV230.2, which represents the body. The law discovered by metallographic observation is vertified and quantified.

2.4 Analysis of hardening effect of factors

The same process is repeated 9 times for all the samples, and the same rule is acquired. Every sample's depth of hardened surface satisfied with design hardness and surface hardness is obtained, which range from 0.18mm to 0.82mm and from HV711.7 to HV824.1 respectively.

According to the test data above and orthogonal table $L_9(3^4)$, the relationship between influencing factors and hardened depth and surface hardness is determined by orthogonal test and extreme difference analysis, as shown in Figure 4 and Figure 5.

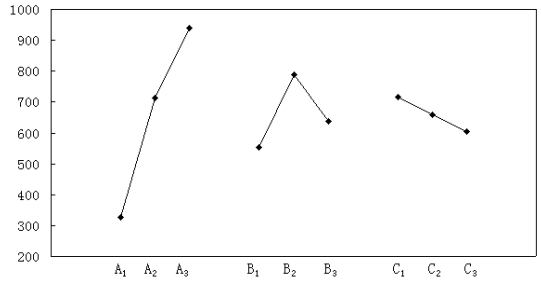


Figure 4 Relationship Between Factors and Hardened Depth

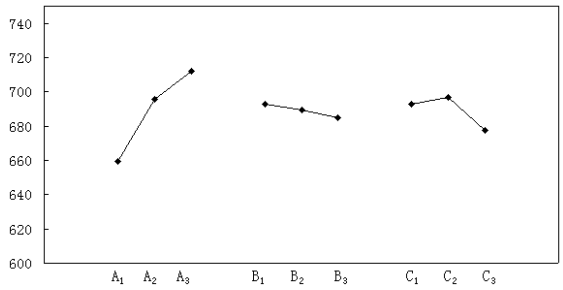


Figure 5 Relationship Between Factors and Surface Hardness

It's indicated in Figure 4 that thickness of hardened depth increases with rising of grinding depth. And it increases first and then decreases with rising of workpiece speed. The effect of wheel characteristics is that white corundum wheel is better than chromium corundum wheel and small grain wheel is better than big grain wheel. Consequently, for the most hardened depth, the best combination of factors' levels is $A_3B_2C_1$, that is grinding depth 0.4mm, workpiece speed 0.5m/s, and wheel WA46L8V.

It's illustrated in Figure 5 that surface hardness increases with rising of grinding depth. And it decreases with rising of workpiece speed. The effect of wheel characteristics is that chromium corundum wheel is better than white corundum wheel and small grain wheel is better than big grain wheel. Therefore, for the most surface hardness, the best combination of factors' levels is $A_3B_1C_2$, that is grinding depth 0.4mm, workpiece speed 0.2m/s, and wheel PA46L8V.

3 Summary

(1) External grand-hardening technology is practicable for 40Cr steel, and the surface hardness is in the range of HV647.4~719.4, and the hardened depth is between 0.22mm~1.1mm.

(2) Surface structure of hardened workpieces by external grind-hardening is divided into three parts: hardened layer, transition layer and body constituted by martensite, mixture of martensite and ferrite, and original structure respectively, which is similar to regular quenching.

(3) Thickness of hardened depth increases with rising of grinding depth. And it increases first and then decreases with rising of workpiece speed. The effect of wheel characteristics is that white corundum wheel is better than chromium corundum wheel and small grain wheel is better than big grain wheel.

(4) Surface hardness increases with rising of grinding depth. And it decreases with rising of workpiece speed. The effect of wheel characteristics is that chromium corundum wheel is better than white corundum wheel and small grain wheel is better than big grain wheel.

References

[1] Brockhoff T. : *Grind-hardening: A Comprehensive view*. Annals of CIRP Vol. 48(1999),p. 255

[2] K.M. Liu, Z. Ma, L.Y. Zhang, B. Liu : *Research Status of Grind Hardening Technology*. Material and Heat Treatment Vol. 41(2012),p. 208

[3] J.Y. Zhang, G.C. Wang, C.Y. Zhang: *A Green Surface Quenching Process – Grinding Hardening*. Machinery Design and Manufacture Vol.7(2007),p. 206

[4] Zarudi I., Zhang L.C. :*Mechanical Property Improvement of Quenchable Steel by Grinding*. Journal of Materials Science Vol. 37(2002),p. 3935

[5] Y. Zhang, P.Q. Ge, L. Zhang: *Grinding Force of Surface Grinding Hardening Thin Workpiece*. Transactions of the Chinese Society for Agricultural Machinery Vol. 43(2012),p. 231

[6] C.L. Hua, G.C. Wang, J.D. Liu: *Influence of Grinding Speed on Residual Stress Distributions at Hardening Layer Surface of the Workpiece*. Machinery Design and Manufacture Vol. 4(2012),p. 177-179

[7] K.M. Liu, B. Liu, Z. Ma: *Impact of Dry Grinding and Wet Grinding on Surface Layer Strengthening of 42CrMo Steel*. Ordnance Material Science and Engineering Vol.35(2012),p. 65

[8] K.T. Fang, C.X. Ma: *Orthogonal and Uniform Test Design*(Science Press, Beijing 2001).

[9] X.W. Xie : *Metallographic Sample Preparation Technology*(Xi'an Jiaotong University Press, Xi'An 2006).

Applied Mechanics and Materials Vol. 597 (2014) pp 228-232
© (2014) Trans Tech Publications, Switzerland
doi:10.4028/www.scientific.net/AMM.597.228

Study of spatial ellipsoid helix interpolation algorithm based on multi-axis lathe

Xiaoping Yang[1, a *], Zhimin Zhou[2,b], Yijin Gu[3,c] and Lixin Wang[4,d]

[1]Room 207B, building D, HIT Campus of University Tow of Shenzhen, Shenzhen, China

[2]Full Room 505, building 5, HIT Campus of University Tow of Shenzhen, Shenzhen, China

[3]University Town of Shenzhen, Shenzhen, China

[4]Shenzhen Institute of Advanced Technology, Chinese Academy of Sciences, Shenzhen, China

[a]xpyang8@126.com, [b]1413303695@qq.com, [c]765218518@qq.com, [d]756936302@qq.com

Keywords: Central angle division method; ellipsoid helix interpolation

Abstract. Interpolation calculation is the main performance assessment indicators in CNC system. In this paper, a self-designed multi-axis jewelry lathe is used as an experiment platform and the workpiece is a kind of silver or gold ellipsoidal ball with thin wall.According to the basic requirements of the algorithm, the structural characteristics of the machine tool and the special characteristics of the shape of the workpiece , a new interpolation algorithm named spacial ellipsoid helix interpolation is proposed and studied.

Introduction

According to the basic principles and calculation methods of interpolation algorithm, it can be divided into reference pulse interpolation and data sampling interpolation. There are methods with good function in each categories. such as the by-point comparison method and DDA method of reference pulse interpolation and straight line function method together with extended DDA data sampling method of data sampling interpolation[1]. However, most of these methods are applied to linear or circular interpolation calculations. For jewelry processing industry, there is no mature machine available to space curve interpolation needed, which led to the low degree of automation in jewelry machining industry. The lathe mentioned in this paper uses Delta multi-axis control card. Although the card provides a very rich function library, such as circular interpolation, cylindrical helical interpolation, etc., for the desired spacial ellipsoid helix interpolation, there is no ready library functions. In this paper, a spacial ellipsoid helix interpolation algorithm is proposed based on multi-axis control card, ellipse interpolation principle and central angle division method

The demands analysis of algorithm

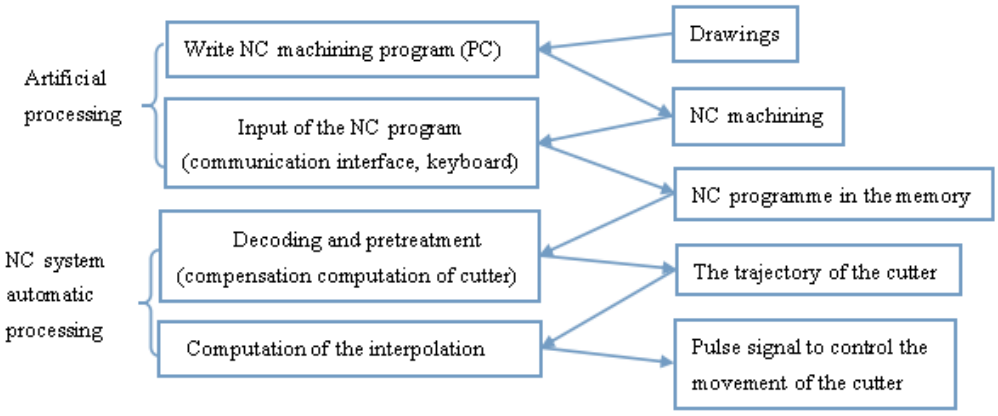


Fig. 1 Process of interpolation

The interpolation function module is a key module of the numerical control system. The number of types of algorithm is directly related to the machining range, the time and space complexity of the

algorithm directly affects the machining precision and efficiency of the CNC system[2]. Pulse equivalent is the basic movement unit of axises of CNC machine tool , and the process of interpolation is to calculates the pulse equivalent of each axis.

The unit body of the gold decorative chain is olive-like workpiece, and the subsequent pattern processing on the surface of the workpiece is programmed based on the abrasive cavity surface equation. Just as many texture patterns are parts of the helix, but the space equation expression of the curve is difficult to find. The model of movements of the cutter and the workpiece is simulated according to the pattern, which is shown left in Fig.2.

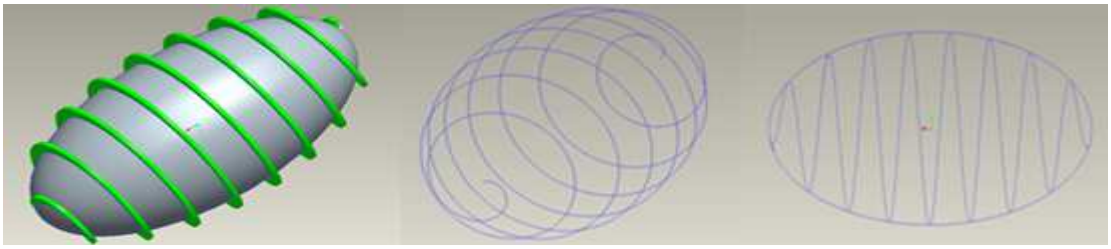


Fig. 2 Trajectory model and it's curves

Most pattens are parts of the trajectory in the figure above. So the actual trajectory of the cutter is part of the spacial helix with changeable diameter. To achieve the interpolation curve shown in Fig.2, five axises are needed together to cooperate the interpolation movement[3,4].

Take our lathe as an example,the feeding in the direction of axis X adjust the distance between the cutter and the surface of the workpiece. However the direction of axis X is changeable when axis B rotates to adjust the angle between the normal of the surface of the workpiece and the cutter. And the angle is also the angle between the axis X and the normal direction. The cutting direction changes when axis A rotates, which can adjust the cutting direction to keep consistent with tangent direction of the curve. And the movement of axis Z change the machining position on the workpiece. The rotation of axis C ensure the machining on different circumferential position. These five axis coordinate to complete the machining of the pattens on the surface of the workpiece.

Curve shown middle in Fig.2 is difficult to express in concrete equation. But the projection curve of the workpiece in ZX plane is a standard ellipse curve.We take this ellipse curve shown last in Fig.2 as research object and the trajectory of this ellipse can be interpolated through the movement of axis Z and X. Then, axis B and A should be adjusted according to the location of axis X in order to adjusted the posture of the cutter to meet the requirement of machining of the workpiece and rotary axis C is machining benchmark.

This interpolation method is based on central angle step segmentation method and the principles of data sampling is applied to divided the angle of rotation of axis C .

Derivation of calculation of the algorithm

The derivation of interpolation of the reference ellipse curve. Seen from the structure of CNC jewelry lathe, the interpolation cycle is related to computing cycles, contour feeding step and the feed speed. The relationship of contouring feed step, interpolation cycle and feed speed of axis is shown below.

$$L = FT \tag{1}$$

when the cycle is selected, the step length is proportional to feed rate according to the equation. In other words, the jewelry lathe can run smoothly with the contour step determined. On request, the contour curve is evenly divided into many feed steps within an interpolation cycle and derive the feeding amount of each axis in the next interpolation cycle according to the equation of the curve.

We take the inverse ellipse arc in the first quadrant for an example. To machine a section of spacial helix with variable diameter, we only care about the coordinate of axis Z and X and the

rotation angle. The start point and end point of the interpolation curve are marked as $A(z_a, x_a)$ and $B(z_b, x_b)$ with the rotation angle θ of the helix according to the derivation process of ellipse interpolation based on Cartesian coordinate system. The reference ellipse equation is given below.

$$\frac{z^2}{a^2}+\frac{x^2}{b^2}=1 \tag{2}$$

For data sampling interpolation algorithm of ellipse, the original central angle should be increase a constant value for each interpolation process. But the length of arc varies with respect to the fixed central angle due to the changeable eccentricity during the interpolation process, the greater the change of the eccentricity, the more obvious the change of the arc length, which lead to the result that the machine can not run smoothly. Therefore, reverse process is applied to the algorithm. Firstly, we should determine the change of the arc length followed by corresponding change of the central angle.

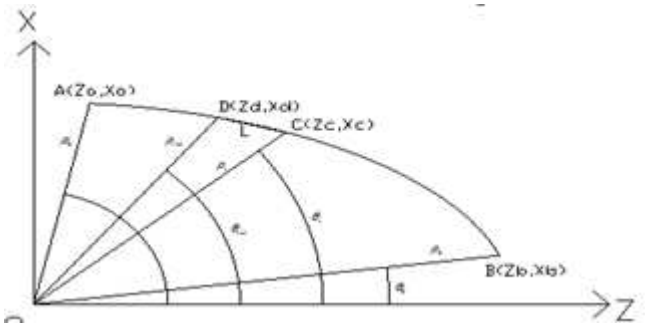


Fig. 3 Inverse arc interpolation in the first quadrant

The coordinates of the i^{th} and $i+1^{th}$ interpolation point are marked as $C(z_i, x_i)$ and $D(z_i, x_i)$。And the corresponding eccentricity angle are θ_i and θ_{i+1} with the arc length L_i. The eccentricity angle θ_0 and feed step L of the start point can be set in the process of initialization. The parameter equation of ellipse in planar Cartesian coordinates system ZOX and the eccentricity radius ρ_i of i^{th} interpolation point can be expressed as follows

$$\begin{cases} z = a\cos\theta \\ x = b\sin\theta \end{cases} \tag{3}$$

$$\rho_i = \sqrt{z_i^{\,2} + x_i^{\,2}} \tag{4}$$

Since the contour length L ranges from 0.0001mm to 0.1mm, which is far smaller than the contour curvature radius ρ of the ellipse. And the eccentric angle is very small($\Delta\theta_i << \theta$). Therefore, the corresponding increments of ellipse eccentric angle of the contour step can be approximated.

$$\Delta\theta_{i+1} = \theta_{i+1} - \theta_i \approx \frac{L}{\rho_i} = \frac{L}{\sqrt{z_i^2 + x_i^2}} \tag{5}$$

The eccentric angle θ_{i+1} of point $D(z_{i+1}, x_{i+1})$ can be calculated according to the increment of eccentric angle between point $C(z_i, x_i)$ and the next point.

$$\theta_{i+1} = \theta_i + \Delta\theta_{i+1} \tag{6}$$

The coordinate increments Δz_{i+1} and Δx_{i+1} from point $C(z_i, x_i)$ to $D(z_{i+1}, x_{i+1})$ is given below.

$$\begin{cases} \Delta z_{i+1} = a\cos\theta_{i+1} - z_i \\ \Delta x_{i+1} = b\sin\theta_{i+1} - x_i \end{cases} \tag{7}$$

So, the recursive formula of interpolation coordinate can be derived through all the functions given above.

$$\begin{cases} z_{i+1} = a\cos(\theta_i + \dfrac{L}{\sqrt{z_i^{\,2} + x_i^{\,2}}}) \\ x_{i+1} = b\sin(\theta_i + \dfrac{L}{\sqrt{z_i^{\,2} + x_i^{\,2}}}) \end{cases} \tag{8}$$

For the interpolation of clockwise arc in the first quadrant, function (5) will be modified as:

$$\Delta\theta_{i+1} = \theta_i - \theta_{i+1} \approx \frac{L}{\rho_i} = \frac{L}{\sqrt{z_i^2 + x_i^2}}$$

The start and end point of Z coordinate should be tested and stored in order to judge the location in the coordinate system of the ellipse arc segment before the start of machining. If the arc segment is in the same quadrant, the same corresponding formula is called. But the arc segment should be divided by the coordinate axis and different formulas are called correspondingly with the termination condition of interpolation given as: $z_{i+1} \le z_b$.

The calculation of rotation angle around the major axis of the workpiece. The driven axis is axis A and the drive axis is axis Z. Each time the interpolation increment Δz_{i+1} of drive axis Z is calculated, the feed step angle of axis C is computed proportionally to the axis Z. We set the proportion coefficient as k_i .The feed step angle of driven axis C is expressed as below.

$$k_i = \frac{\Delta z_{i+1}}{z_a - z_b} \tag{9}$$

$$\theta_{c_{i+1}} = k_{i+1} \times \theta \tag{10}$$

Interpolation calculation of rotation step angle of the cutter. The cutting plane should be consistent with the tangent direction of the helix in order to complete the helix patten machining on the surface of the workpiece so as to ensure both sides of the trajectory is symmetrical about the tangent of the helix, which would meet demand of beauty.

The start rotation angle should be the complementary angle of the eccentric angle of the start point. The total increment angle is the sum of the eccentric angle of the start and end point. The increment of eccentric angle and the rotation angle ΔA_{i+1} of the cutter are given below.

$$A = \arctan\frac{x_b}{z_b} - \arctan\frac{x_a}{z_a} \tag{11}$$

$$\Delta A_{i+1} = k_{i+1} \times A \tag{12}$$

So far, the derivation of the spacial ellipsoid helix interpolation algorithm comes to an end. The concrete flow chart of the interpolation process is show below.

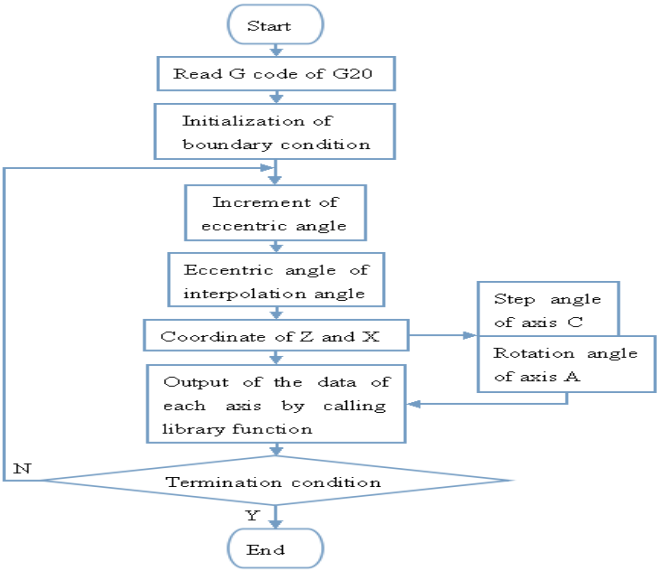


Fig. 4 Flow chart of interpolation

Verification of the interpolation algorithm through examples. In the CNC file, we enter the code G20(4, 2; (3.464, 1); (1, 1.94); 150) and set contour step as L=0.02mm. Then the coordinate of the interpolation points can be computed according to the parameters given above. The information of coordinates in the process of the interpolation has been listed in the table, which is just part of the interpolation process.

Table 1 Coordinate information of the interpolation

X/mm	Z/mm	$\Delta\theta$ /rad	C /rad	A /rad
1	3.464	0.523599	0.828445	0.003219
1.009593	3.452954	0.529146	0.845904	0.003287
1.019175	3.441675	0.534705	0.855821	0.003326
1.028748	3.430264	0.540277	0.865796	0.003364
1.03831	3.41872	0.545862	0.87583	0.003403

Summary

The time division method of equal arc length is applied to the calculation of ellipse interpolation which lead to the derivation of the interpolation recursive equations. Then, the algorithm to complete the machining of spacial ellipsoid helix is derived.

References

[1]WB Lee ,D Dao，J GLi. An NC tool path translator for virtual machining of precision optical products[J].Journal of Materials Processing Technology , 2003(140):211-216

[2]RidaT.Farouk,Jairam Manjunathaiah,Guo-fengYuan,G Codes for the Specifiction of Pythagorean-HodograPh Tool Paths and Assoeiated Feedrate FunetionsonOn Open-Arehiteeture CNC Machines[J].Intemational Journal of Maehine Tools&Manufaeture,1999,39:123-142

[3]Uddin M S, Ibaraki S, Matsubara A, et al. Prediction and compensation of machining geometric errors of five-axis machining centers with kinematic errors[J]. Precision Engineering. 2009, 33(2): 194-201

[4]Tsutsumi M, Tone S, Kato N, et al. Enhancement of geometric accuracy of five-axis machining centers based on identification and compensation of geometric deviations[J]. International Journal of Machine Tools and Manufacture. 2013, 68(0): 11-20

Applied Mechanics and Materials Vol. 597 (2014) pp 233-237
© (2014) Trans Tech Publications, Switzerland
doi:10.4028/www.scientific.net/AMM.597.233

Research on flange state during spinning of AZ31 magnesium alloy rotators

Li Linlin[1,2, a], Cai Zhongyi[1 *], Xu Hengqiu[2,b], Wang Mi[1], Zhang Rui[2], Wang Dali[2], Zhang Yuli[2], Gao Xiaofei[2]

[1]Roll Forging Research Institute, Jilin University, Changchun 130025, China

[2] Institute of Changchun Equipment Technology, Changchun 130012, China

[a]lll45773364@163.com, [b]xhqwch@sina.com

Keywords AZ31 Spinning Finite element (FE) Flange

Abstract. The stress-strain condition and flange state during spinning of magnesium alloy rotators was researched. The preliminary conclusion is obtained: There are three states during spinning of rotators, which appropriate "forward" and "straight" is conducive to forming, but the "backward" should be avoided. Based on ABAQUS/Explicit platform to analyze flange state and forming quality of these rotators under various load conditions. FE analysis shows: blank diameter, roller structure and feed ratio are key factors of formability. Most favorable process parameters are blank diameter 160mm, feed ratio 0.8r/mm, while using combination roller. Finally, the role of the main process parameters on flange state was verified by experiment method.

1 Introduction

Magnesium alloy with high strength and low weight has increasingly become an ideal material for many important industries such as automotive, aerospace and weapon [1]. Spinning as an advanced manufacturing technology can effectively improve the utilization of materials; also improve the mechanical properties of materials [2]. The related researches are very limited about spinning of magnesium alloy rotators. There are some reports about the properties and formability of magnesium alloy can contribute to research on process parameter settings and feasibility of spinning for this type of parts. According to the past research, deformation property of magnesium alloy has better ductility and formability in 250-400℃ than room temperature [3]. Some domestic researcher studied magnesium alloy spinning cylindrical parts with the FE analysis methods and made a series of achievements which optimize deformation temperature, feed ratio, roller structure, and so on[4]. Otherwise, Fan et al. researched forming feasibility of AZ31B magnesium alloy sheet which was not preheated, and then spinning the disk pieces by friction [5]. Furthermore, Professor Yang investigated the hot splitting spinning process of magnesium alloy AZ31, which provided new forming method of wheels [6]. Foreign scholars also made magnesium alloy spinning-depth research. S. Yoshihara studied the spin-magnesium alloy tube, which was demonstrated using an NC control machine at 300℃ with a main shaft rotational frequency of 300 rpm and feed per revolution of 180 mm/min [7]. Makoto Murata studied compression spinning of circular magnesium tube, analyzed the effects of the setting temperature of the roller tool on the forming properties of spinning [8]. Meanwhile, various domestic and international research of shear spinning process provided references [9]. In this study, the flange state of spin forming curvilinear rotators of magnesium alloy was investigated by experiment and FE simulation.

2 Part dimensions and spinning program

Generally, the rotators with curvilinear is decomposed into several segments conical pieces for FE analysis. Fig. 1 shows the decomposition of model, which is composed of 13 tapered section. In the 9th section, the wall angle has reached 17.35º, which the value cannot be in full accordance with ruler of the shear spinning. Meanwhile, the thinning rate of this part beyond limits when brought into

wall angle in the 13th section of 7.11º, the thinning rate reached 87.6%, and the minimum wall thickness is 1.24mm. This value doesn't meet requirements of the process. (The technological requirement is not less than 2mm for the thinnest.)

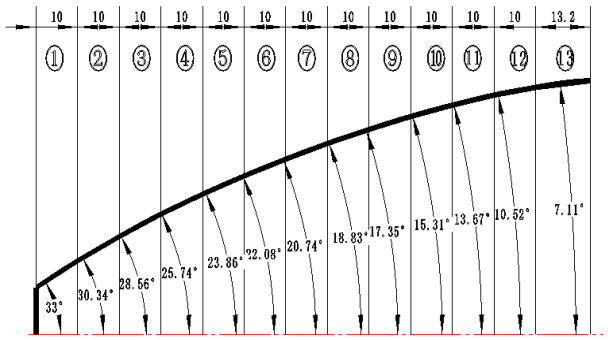


Fig. 1 Decomposition of rotators with curvilinear

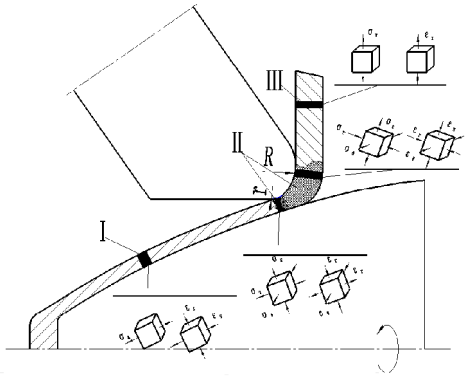
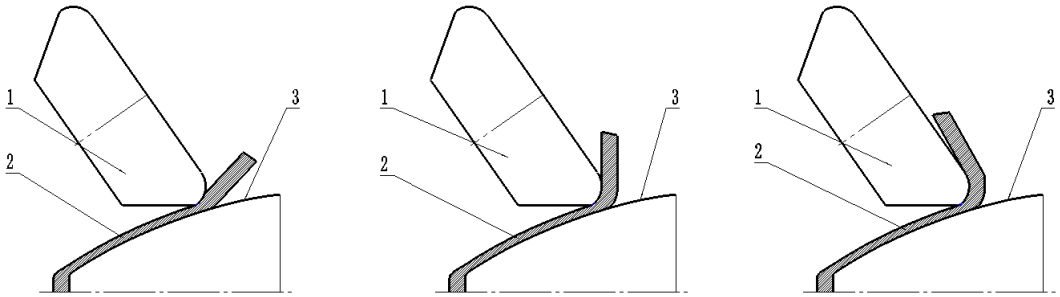


Fig. 2 Stress-strain of part spinning

What kind of technology used can obtain the part by spinning? It is important to analyze stress state of spinning process about the rotators with curvilinear. Fig. 2 is schematic diagram of one-pass spinning this part. Part is divided into three regions, Ⅰ is after-deformed region, Ⅱ is deformed region, Ⅲis un-deformed region. The roller is composed with two radius of the arc, where R is a drawing arc, r is forming arc. Region Ⅱ also be divided into two zone, which contact with R generate drawing deformation, another contact with r generate rolled and bending deformation.

Obviously, many simulations and experiments shows that the flange before roller have three states in the process of spinning, which the three states is "forward", "straight" and "backward"(Fig. 3). "Straight" state suitable for shear spinning. "Forward" state meets the basic requirements of forming, but the ovality slightly worse. "Backward" state is not conducive to forming, that various defects have occurred, such as wrinkling and cracking. So, "Forward" and "Straight" combined state is needed, and the "Backward" state should be avoided.



a) Forward b) Straight c) Backward

1-Roller; 2-Blank; 3-Mandrel

Fig. 3 Three states of the flange

3 FE simulation and experiment

3.1 Material model

The material of experimental is produced by forging. AZ31 alloy compositions and the material parameters are shown in Table 1.

Table 1 Chemical composition and parameters of material

Chemical composition of AZ31 (wt. %)								Density	Young's modulus	Poisson's ratio
Al	Zn	Mn	Si	Cu	Ni	Fe	Mg	1.77	45GPa	0.35
3	1.11	0.3	0.0143	0.0021	0.0009	0.0015	Other	g/cm^3		

Stress-strain relationship of the material is changed with temperature change rate of deformation. The stress-strain curve of the deformation rate of 0.1s-1, the temperature is 300℃shown in Fig. 4.

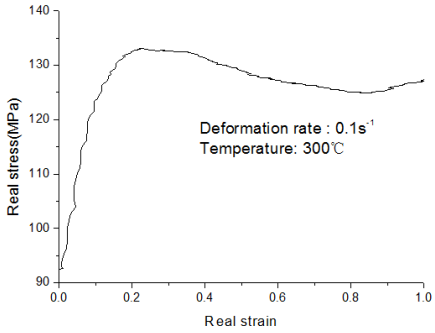


Fig. 4 Stress-strain curve of AZ31

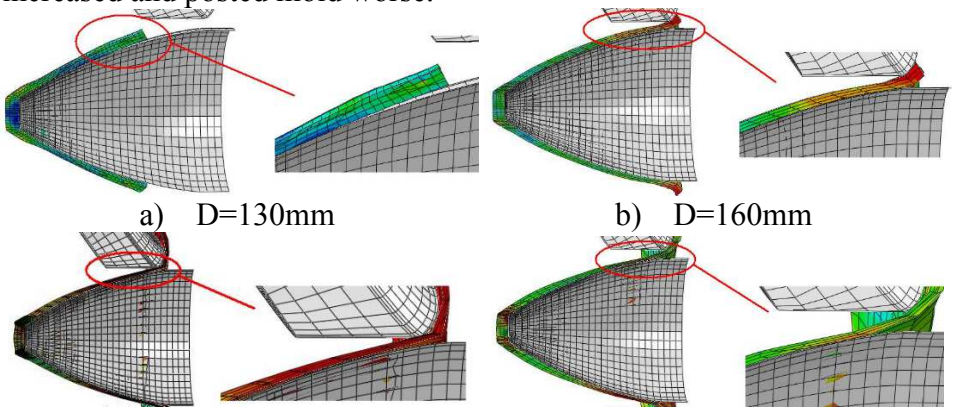
3.2 Modeling and meshing

Finite element model is built based on ABAQUS / Dynamic Explicit platform. The blank is 3D deformable solid and meshed C3D8R unit. The roller and mandrel is discrete rigid shell, meshing type is R3D4. Global mesh size 4mm, the center of local refinement is 1mm. The material properties data of Table 1, Fig. 4 are applied to software. The contact is set to the desired state without friction.

3.3 The simulation results

3.3.1 Impact of blank size

Simulation parameters are as follows: Feed ratio 0.8r/mm, spindle speed 120r/min, temperature 300℃. The results of different blank sizes spinning are shown in Fig. 5. Where 6 a) blank diameters 130 spinning, since the gap is too large, not fully formed blank pieces of the desired shape. Fig. 5 b) spinning 160mm diameter blank, due to a stable “forward” flange, posted mold well and better quality was spinning. Fig. 5 c) d) 200,240 mm diameter blank spinning, the flange state is “backward”. By the law of least resistance, the metal of formed sections has continuously thin, with roller feeding, unformed sections dumped to the direction of roller, so the forming resistance increased, while thinness rate increased and posted mold worse.



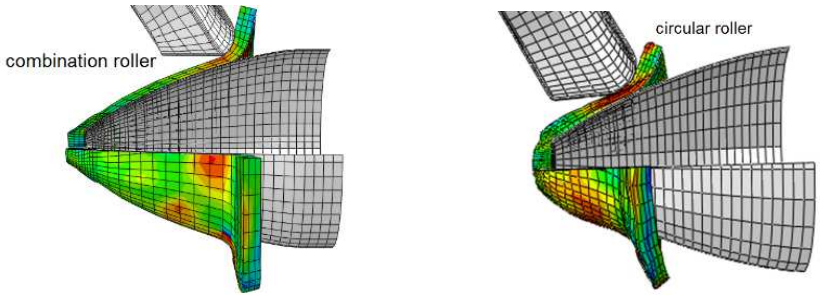
a) D=130mm b) D=160mm

c) D=200mm d) D=240mm

Fig.5 The flange states of different diameter of blank

3.3.2 Impact of roller shape

Circular roller and combination roller spinning results are shown in Fig.6. As can be seen, the circular roller spinning occur reflux phenomenon. The quality of combination roller spinning is better than circular roller; this is because the contact area between combination roller and blank is small. The blank regurgitation and resistance can be reduced.

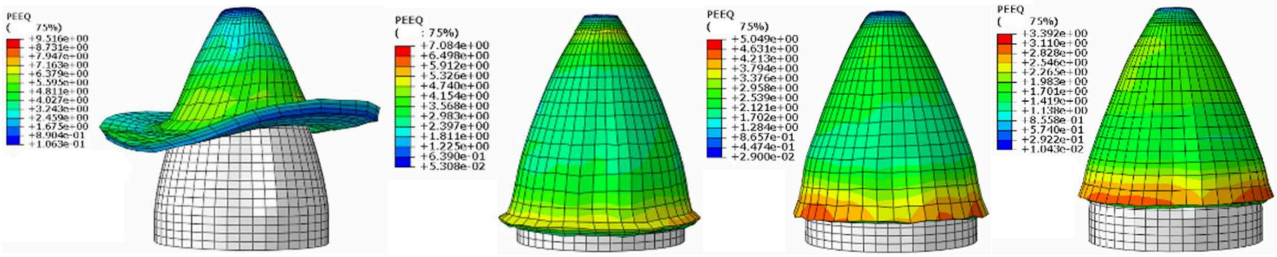


a) Combination roller b) Circular roller

Fig.6 The influence of roller structure

3.3.3 Impact of feed ratio

Simulation parameters are as follows: blank diameter 160mm, temperature 300℃. The results of different feed ratio spinning are shown in Fig.7. Spinning process of half the flange state is "backward" and appears wrinkling while the feed ratio is 0.3mm/r; when feed ratio is 0.8,1.0,1.5mm/r workpiece can be shaping well; with the increase of the feed ratio, material margin and equivalent strain are small, but the quality of the workpiece surface will be lower.



a) f= 0.3mm/r b) f= 0.8mm/r c) f=1.0mm/r d) f=1.5 mm/r

Fig.7 The influence of feed ratio

3.4 Experimental research

3.4.1 Experimental parameters

The experimental parameters are as follows: (1) roller: combination roller, diameter Dr=150mm, shaping angle R5, pressing material angle R15; (2) blank: magnesium alloy sheet (AZ31), thickness t0=10mm, diameter Db=160mm; (3) feed: rotation rate of the spindle n=75 rpm, feed ratio of the roller f=0.8 mm/r.

3.4.2 Experimental results

Blank and forming workpiece are shown in Fig.8 and forming parts size analysis chart are shown in Fig.9. As can be seen from the figure, the experimental results and the simulation results are consistent. The minimum wall thickness of the experiment is 3.42mm, so the forming workpiece after machining can meet product size requirements.



Fig.8 Blank and forming workpiece

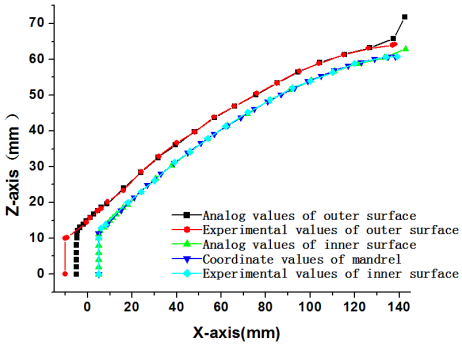


Fig.9 Forming parts size analysis chart

4. Conclusions

(1) Curve discrete into a number of straight in this paper can be applied to analyze spinning rotators with curvilinear.

(2) Workpiece forming or not and forming quality are closely related to the state of flange. Generally, “Backward” state of flange is not conducive to forming; suitable “forward” and “straight” are conducive to forming.

(3) The state of flange will change with process parameters changed. Too large blank and too small feed ratio will cause “Backward” flange, and then workpiece appear cracks, wrinkling and other defects.

(4) Process parameters were optimized by simulation, the result of experiments and simulation are basically consistent.

References

[1] F.Fereshteh-Saniee, Kh.Fallah-Nejad, A.Sh.Behestiha, H.Badnava. Investigation of tension and compression behavior of AZ80 magnesium alloy. J Materials and Design. 50 (2013)702-712.

[2] Xu HQ et al. Power spinning study of thin-walled 5A06 aluminum alloy cylinder with longitudinal and hoop inner ribs for manufacturing engineering J. Advanced Materials Research. 583(2012)301-305.

[3] Chen ZH, Deformation Magnesium Alloys, Chemical Industry Press, Beijing, 2005 (in Chinese).

[4] Li B. Research on hot spinning process and microstructure evolution of AZ81 D. Chongqing University, 2010 (in Chinese).

[5] Fan YF, Li DN, Chen WZ. Study on Spinning Process of AZ31B Magnesium Alloy Sheet J. China mechanical engineering. 23(2012)1272-1275 (in Chinese).

[6] Yang H, Huang L, Zhan M. Coupled thermo-mechanical FE simulation of the hot splitting spinning process of magnesium alloy AZ31 J. Computational Materials Science 47(2010)857-866.

[7] S. Yoshihara, B. Mac Donald, T. Hasegawa, M. Kawahara, H. Yamamoto. Design improvement of spin forming of magnesium alloy tubes using finite element J. Journal of Materials Processing Technology. 153–154(2004) 816–820.

[8] Makoto Murata, Takashi Kuboki, Tutom Murai. Compression spinning of circular magnesium tube using heated roller tool J. Journal of Materials Processing Technology. 162–163 (2005)540–545.

[9] O. Music, J.M. Allwood, K. Kawai. A review of the mechanics of metal spinning J. Journal of Materials Processing Technology. 210(2010)3–23.

Applied Mechanics and Materials Vol. 597 (2014) pp 238-241
© (2014) Trans Tech Publications, Switzerland
doi:10.4028/www.scientific.net/AMM.597.238

Numerical Simulation and Analysis for Blow-off Flow Field of a Wet Skin Pass Mill

Hai Jun Qiao[1, 2, a *], Dian Rong Gao[1, b]

[1]Coll. of Mec. Eng., Yanshan Univ., Qinhuangdao, P.R.China

[2] Coll. of Vehicles and Energy, Yanshan Univ., Qinhuangdao, P.R.China

[a]qiaohaijun@ysu.edu.cn, [b]gaodr@ysu.edu.cn

Keywords: Flow field, air nozzle, numerical simulation, blow-off, skin pass

Abstract. Blow-off air nozzles blow away the residual emulsion from roll gap and strip surface. Algorithm SIMPLY were used for the finite element numerical simulation for a representational air nozzle blow-off flow field near the roll gap in a cold-rolled skin pass mill. The working conditions of the blow-off flow field was the combination of gas pressure of 0, 2, 5 and 10bar and flip angle of 0°, 5°, 10°, 15°, 20° and 25°. The study provides a reference for control and optimization for the removal process of residual emulsion and design, manufacture, model selection and optimization for the related air nozzles.

Introduction

Blow-off ramps are generally mounted at the exit of a strip cold-rolled skin pass mill, blowing away the remaining emulsion from near roll gap and the plate surface. But because of changes in gas supplying pressure, installation angle, position and accuracy of air nozzles caused by inspection, repair, and complexity of the blow-off space and interfere of air flow of each nozzle, air flow distribution will not reasonable and practicable. Consequently, emulsion will be left over on the strip surface causing spots, black belts and other quality problems on the strip surface.

Related researches on wet skin pass mill and emulsion removal have been focused on improvement and optimization emulsion blow-off system. Guo et al. [1] introduced a small amount of industrial compressed air at high speed to anti-crimping guide plates to form an air curtain or slot nozzle, blowing off the emulsion from the work roll surface, which falls to the guide plate, and then flows into a collection trough; Gong et al. [2,3,4,5] used sluices linked to the collection trough on the top of the anti-crimping guide plates to guide emulsion splashed onto the guide plates and prevent emulsion residue on the strip surface; Zhou et al.[6] set up a row of blowing air nozzles near the crimping guides and presented ‘blow-suction’ combined air draft, taking away the emulsions nearby.

In this paper, the blow-off flow field in a tin plate cold-rolled skin pass mill was numerically studied. Some references about emulsion clearance control and optimization, related manufacturing, type selection and optimization to blow-off nozzles can be obtained.

Typical Layout Scheme for Blow-off System in a Wet Skin Pass Mill

Six air nozzles of flat type were mounted on the blow-off ramp, as shown in Fig1, blowing to the roll gap. The diameter of the work roll and the support roll is 500mm and 1100mm, respectively, respectively; and roll surface width of the work roll and the support roll is 1250 and 1200mm, respectively.

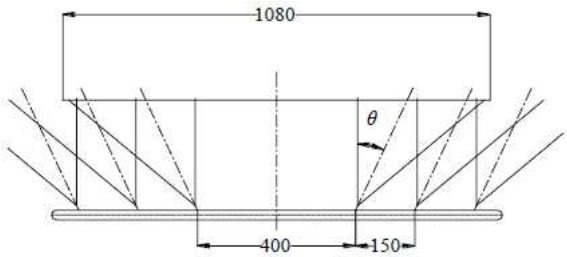
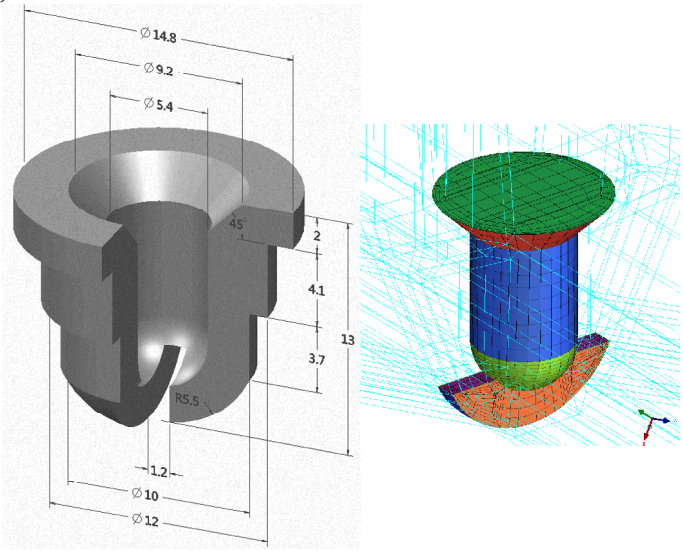


Fig. 1 Arrangement and flip angle θ of air nozzles in the blow-off ramp

Establishment of Physical Model and its Meshing

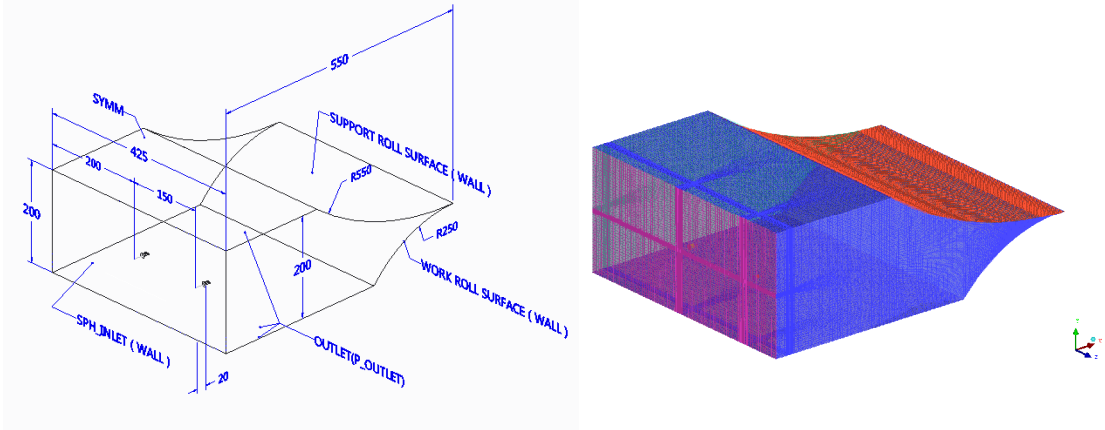
Three-dimensional modeling software Pro/Engineering was utilized for modeling the flow field, as demonstrated in Fig. 2. Flow passage inside and around area of the air nozzles were meshed with block mesh partitioning and ununiformed technique. Total number of grids is between 807053 and 1501245 in each casing, all structured hexahedral.



(a) Structure of the air nozzle (b) Its internal grids

Fig. 2 Three-dimensional structure and meshing of air nozzle

In the establishment of the model, the thickness of air nozzles wall and the length of connecting pipes were ignored to save computing resources. The origin of Cartesian rectangular coordinate was located in intersection line of geometric symmetry plane of the blow-off ramp and the horizontal center of air nozzles. Target distance was 620mm. The geometry of the blow-off flow field and its meshing are illustrated in Fig. 3.



(a) The geometry and boundary condition (b) Flow field grids

Fig. 3 Geometry, boundary condition and meshing of the blow-off flow field

Numerical Solution for the Flow Field

SIMPLY algorithms was taken for pressure-velocity coupling. Pressure item discreted by presto!. Realizable k-epsilon model and enhanced wall function model was select. Residuals of continuity equation, k, epsilon and other monitoring quantities were set to 1E-4.

Analysis and Discussion of Simulation Results

Speed Distribution of the Longitudinal Cross Section. Fig. 4 shows the velocity contour of the longitudinal cross section under 0° angle and each air supplying pressure. As can be seen from the fig. 4, with the increase of static pressure, the air velocity near the surface of the rolls and the roll gap are gradually increased, from 5m/s to 30m/s; and due to increased speed, the air disturbance effect by high-speed air convection enhanced, so, high-speed roll surface area increased significantly. Nevertheless, high speed region will no longer increase when increases to a certain extent; corresponding, vertical sweep angle is not increased. In general, the vertical angle was gradually enlarged from about 13° to 21° with incense of working pressure from 0.5bar to 5bar.

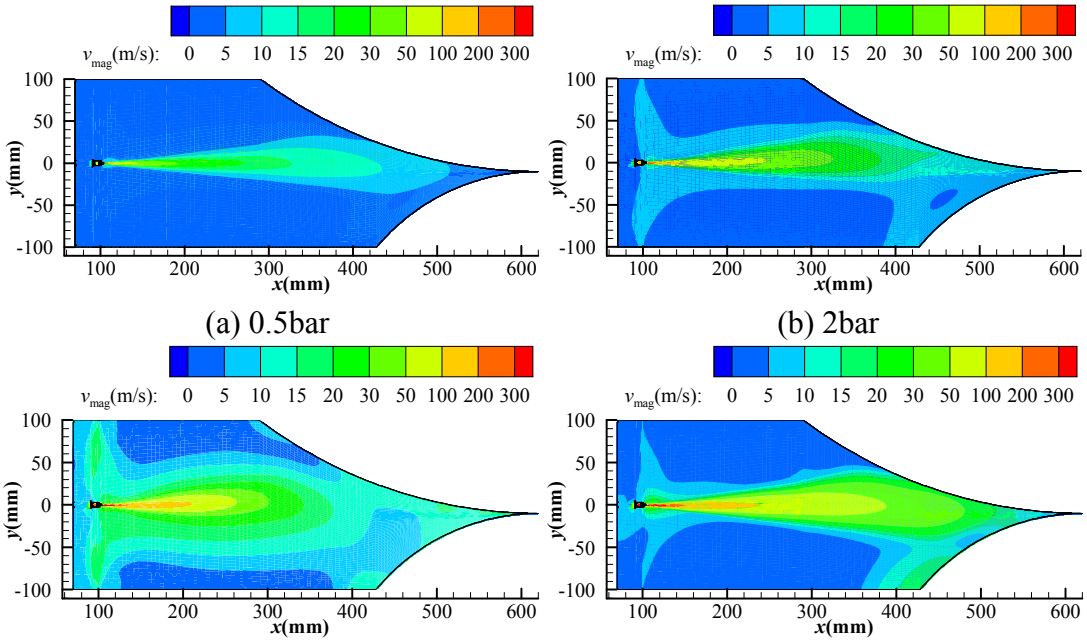


Fig. 4 Velocity contour on the longitudinal cross section under 0° flip angle

Furthermore, since velocity gradient and reflection effect near the roll surface, vortex formed in the vicinity of the work roll. It is beneficial for emulsion cleaning. However, the lower the air supply pressure was, the more deviation of vortex center from the roll gap got. As is also the case of scattering of the vortex, the active scope, the lower the intensity, and cleaning effect, and vice versa.

Forces on Support Roll Surface and Work Roll Surface. As the number of blow-off air nozzles is 6, the actual force was amplified to 3 times the numerical simulation results.

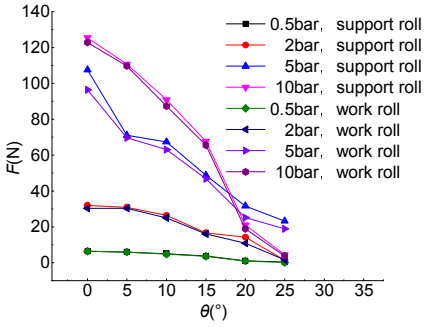


Fig. 5 Total blow-off forces on support and work roll surface

As can be seen from the graph, when air supplying pressure varies from 0.5 to 10bar, the roll surface force (F) is proportional to the change rate of air pressure, and the flip angle of the air nozzle (θ) is reversely proportional to air pressure. At same time, the greater the air supplying pressure was, the more greatly the force curve inclines; the greater the impact of the flip angle imposed on blow-off force. For instance, under air supplying pressure of 10bar, the roll surface forces of 25° flip angle is only 3.539% of that of the 0°.

The pressure distribution near the roll gap was completely symmetrical. Pressure curve is substantially a horizontal line at the central portion of the surface, and in the edge portions, two symmetrical pressure peak appears. Therefore, action mode of blow-off forces mainly is "toggling" and: near the central portion of roll gap, emulsion will be blown and "squeezed" to both sides of the roll gap and further "toggled" away from the edge of the roll gap eventually. "Squeezing" action accounted for a higher proportion while under large air supplying pressure or small flip angle.

When under air pressure of 0.5bar, the force curve was approximated to a horizontal line. That means the influence of flip angle on blow-off forces was very small. When gas pressure reached 10bar, the slope of force curve was about -2. If flip angle exceeded 10°, the blowing forces decreased rapidly. When reaching 25°, the air blow-off forces concentrated on the edges of the roll surface, so average blow-off force and emulsion cleaning effects weakened.

Conclusions

Based on the purge flow field contains a label on the beam 1.1 mouthpiece, the work roll and backup roll surfaces, including modeling, numerical solution, the following conclusions:

Action mode of blow-off forces is mainly "toggling" and "squeezing": "Squeezing" action accounted for a higher proportion while under large air supplying pressure or small flip angle.

From the law of blow-off forces on the roll surface, it can be drawn out that: under 2 ~ 10bar air supplying pressure, the force is directly proportional to the air supplying pressure, and is inversely proportional to the flip angle of nozzles. Furthermore, the greater the supply pressure is, the more inclined the force curve is, the greater the impact on force curve.

Under air supplying pressure of 0.5bar, blow-off force curves approximates to horizontal lines, and flip angle has few effect on the blow-off forces. When the air supplying pressure reaches 10bar or flip angle exceeds 15°, the rate of the force decline varies quickly. In conclusion, the best air supplying pressure is 2bar or 5bar, meanwhile flip angle of 20° and 25° should be avoided.

References

[1] J. Guo, C.Z. Gao, Application on new type emulsion purge and pumping equipment, CFHI Technology. 6 (2008) 17-18.

[2] Y.H. Geng, W. Miao, S.G. Chi, et. al., Analysis and improvement of emulsion purging equipment for 1420 mm PL-TCM, Baosteel Meishan. 006 (2010) 35-37.

[3] M.H. Gong, Improvement and optimization of blow-off system of skin pass mill, Metallurgical Equipmen. 1 (2008) 76-78.

[4] S.K. Liu, M.H. Gong, Optimization and transformation of strip blow-off system in double stand reversing rolling mill, Plant Maintenance Engineering. 4 (2008) 43-45.

[5] J.H. Wang, P. Li, Research and optimizing of temper airblow craft, Sichuan Metallurgy. 4 (2008) 43-45.

[6] S.H. Zhao, C. Ruan, Modification for Airblow System of Temper Mill, Journal of AnHui Vocational College of Metallurgy and Technology. 15 (2005) 6-7.

Applied Mechanics and Materials Vol. 597 (2014) pp 242-248
© (2014) Trans Tech Publications, Switzerland
doi:10.4028/www.scientific.net/AMM.597.242

Molecular dynamics simulation of two-phase structures of copper formed by laser grooving

Wen Peng[1, a*] , Tao Gang[1,b], Zhou Pei-jie[1,c]

[1] School of Energy and Power Engineering, Nanjing University of Science and Technology, Nanjing 210094, Jiangsu, China

[a]wenpeng231024@163.com, [b]taogang@njust.edu.cn, [c]archibrad@163.com

Keywords: molecular dynamics simulation, EAM potential function, solidification process, two-phase structures.

Abstract. It is a concerned problem that what influences of cooling rate on evolution of microstructures of the treated and untreated Cu are during solidification process after Cu's being melted by laser grooving. Based on the embedded-atom method, molecular dynamics simulations have been performed on the cooling processes of liquid metal Cu by using crystal-liquid configuration method at six different cooling rates. By the analyses of the two-phase structural features, pair correlation function, average atomic energy and mean square displacement, it is found that the cooling rate plays a critical role on the solidification process to the liquid Cu. The liquid Cu becomes its crystalline state during relatively low cooling rate, while the glass transition of the liquid Cu is performed with the relatively high cooling rate. The solidification process of the liquid Cu has effect on the solid crystal Cu and leads to form the indented interface between two-phase structures.

1. Introduction

The metal Cu is heated by high energy laser to liquid state and quenched to solid state at various cooling rates. With the crystal perfect Cu, two-phase structures emerge during laser grooving process. If the metal Cu has been grooved at the surface by laser, it can avoid the stress concentration of traditional mechanical grooving process. Thus the laser grooving technique has been widely used in the metal processing domain.

In recent years, molecular dynamics simulation has been widely used to investigate the atomic behavior in materials, so more attention are paid to simulate solidification process of liquid metal to investigate the evolution of the microstructures. The embedded atom method (EAM) potential functions have been adopted to describe the atomic interaction during the solidification process. For example, Chen et al. [1] showed that the EAM can correctly and efficiently predict the glass transition and crystallization during rapid solidification of liquid Cu; Chen et al. [2] found that the crystallization of amorphous Cu was caused by atomic diffusion; Wang et al. [3] found that the liquid Cu became the glass state at about 800K during relatively rapid cooling rate and crystallized at 1010K during relatively low cooling rate. In addition, the structural evolution of the two-dimensional metallic film and the effect of the cooling rate had been studied by Zhang et al. [4-5]. The results showed that two typical dominating structures (ring structures and parallel-string structures) intensify and diminish during the different cooling rates. According to crystal-liquid configuration method, the process of crystal growth for Cu had been observed by Wang [6].

Although many studies about the solidification process of liquid Cu at different quenching rates have been studied, the change of micro-structural features and the influence of cooling process to the untreated solid Cu are not mentioned. In this study, according to the crystal-liquid configuration method, the effects of cooling rates on the solidification behaviors of liquid Cu and untreated solid Cu are investigated through molecular dynamics simulation with the EAM potential. At the same time, the final solidified microstructures of Cu on atomic scale are studied by using a common neighbor analysis (CNA). Furthermore, the pair correlation function (PFC), average atomic energy and mean square displacement (MSD) at six cooling rates are analyzed.

2. Simulation method

We use the method of classical atomistic simulation. In this study, a face-centered cubic (fcc) metallic nanoparticle, Cu, with 2400 atoms distributes in a 20×20×1 lattice unit box. The box lattice parameter is set to be 3.615 Å. Periodic control is just exerted on x- and y- directions of the box. Free boundary condition is employed in Z-direction. Along the Y axis, the model is divided into two parts. The upper part of the model is established to simulate perfect Cu, which undergoes the process of being heated by laser grooving and being cooled. The lower part describes the untreated perfect Cu and it is connectted with the upper part. These two parts are used to simulate the two-phase structures formed by laser treatment as shown in Fig. 1.

All calculations are performed with the open-source LAMMPS code [7]. Cu atoms interact via the Zhou's EAM potential [8] with each other. The molecular dynamics time step is 1 fs. The temperature is controlled by the Nose-Hoover thermostat [9]. As an initial condition, the perfect Cu nanocrystal including the upper part and lower part is started at a constant temperature of 300K with 8×10^4 time steps to get an equilibrium state. Then the well-equilibrated initial upper part is prepared by gradually heating the perfect Cu crystal from 300K to 1800K at a low heating rate and relaxing the upper part at 1800K for 10ps. Above processes are to simulate the Cu being melted by laser grooving. Finally, the upper part is cooled from 1800K to 300K at cooling rates ranging from 10K/ps to 400K/ps. These processes are to simulate the Cu being cooled.

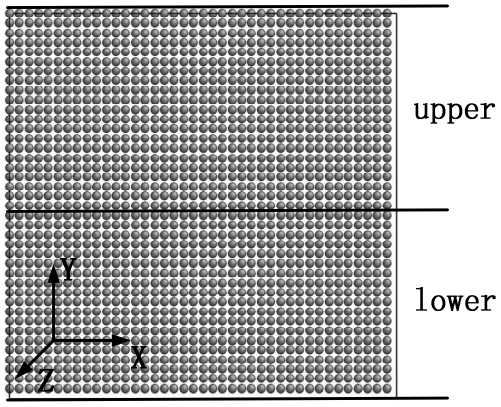


Fig. 1 The simulation sample with the upper part and lower part of Cu.

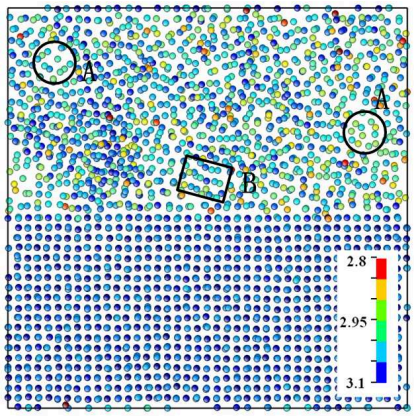


Fig. 2 The potential energy landscape of Cu with the upper part at 1800K.

3. Results And Discussion

3.1 Atomic configuration

Fig. 2 shows the potential energy landscape of the whole system when the temperature of the upper part is 1800K. The upper part at melting state has little effect on the lower part. Though some atomic transitions occur at the interface between the upper and lower parts, we can clearly distinguish the smooth interface. At high temperature of 1800K, the atoms of upper part show a disordered state in the long-range. However, in partial area，there are some ordered structures, for example, single-string structures of mark A and ring structures of mark B in Fig. 2. These two structures are not stable in the relaxation process at high temperature. Through random collisions and energy transfers between atoms, ordered clusters are dispersed into a disorder state. Meanwhile disordered atoms gather and become ordered clusters. This instable equilibrium state is broken during cooling process and then the lower part will be also influenced. Referring influences will be described in detail in the article below.

At different temperatures, the structural evolutions of the whole system at 10K/ps, 50K/ps and 200K/ps cooling rates during the solidification processes are shown in Fig. 3. During the cooling process, there is a distinct structural transition in the short-range and medium-range as the temperature decreases. To be specific, at 900K, compared with the 1600K and 1800K, the number of

the ring structures undergoes an obvious increase accompanied by the decrease of the single-string structures. A new parallel-string structure deriving from the single-string structure emerges when the temperature drops from 900K to 300K. The parallel-string structure is thought to be the crystalline precursor which can be observed with the relatively ordered arrangement. Actually, for the upper part, the growth competition between the ring structures and parallel-string structures plays a dominant role in cooling processes and finally has a significant effect on the solid state structures. At a high cooling rate of 200K/ps, the ring structure dominates and the atoms have no enough time to relax to the balance finally leading to be disordered state for the upper part. In contrast, at a low cooling rate of 10K/ps, owing to adequate relaxation of the atoms belonging to upper part, a large number of parallel-string structures emerge and the upper part perform the long-range crystalline order.

No matter what the cooling rate is, the solidification process of the upper part has certain effect on the lower part. In Fig.3, under the cooling rate of 50K/ps at 900K ring structure makes the atoms of lower part deviate steady state and destroys the smooth interface. At the same time, the ordered structure is easier to emerge and develop at the interface. This is because the atoms of upper part compared with that of the lower part have higher energy and the energy is transferred to the lower part through the interface. Owing to the energy transfer, the atoms of upper part reach the balance rapidly and form ordered structure coupling with lower part.

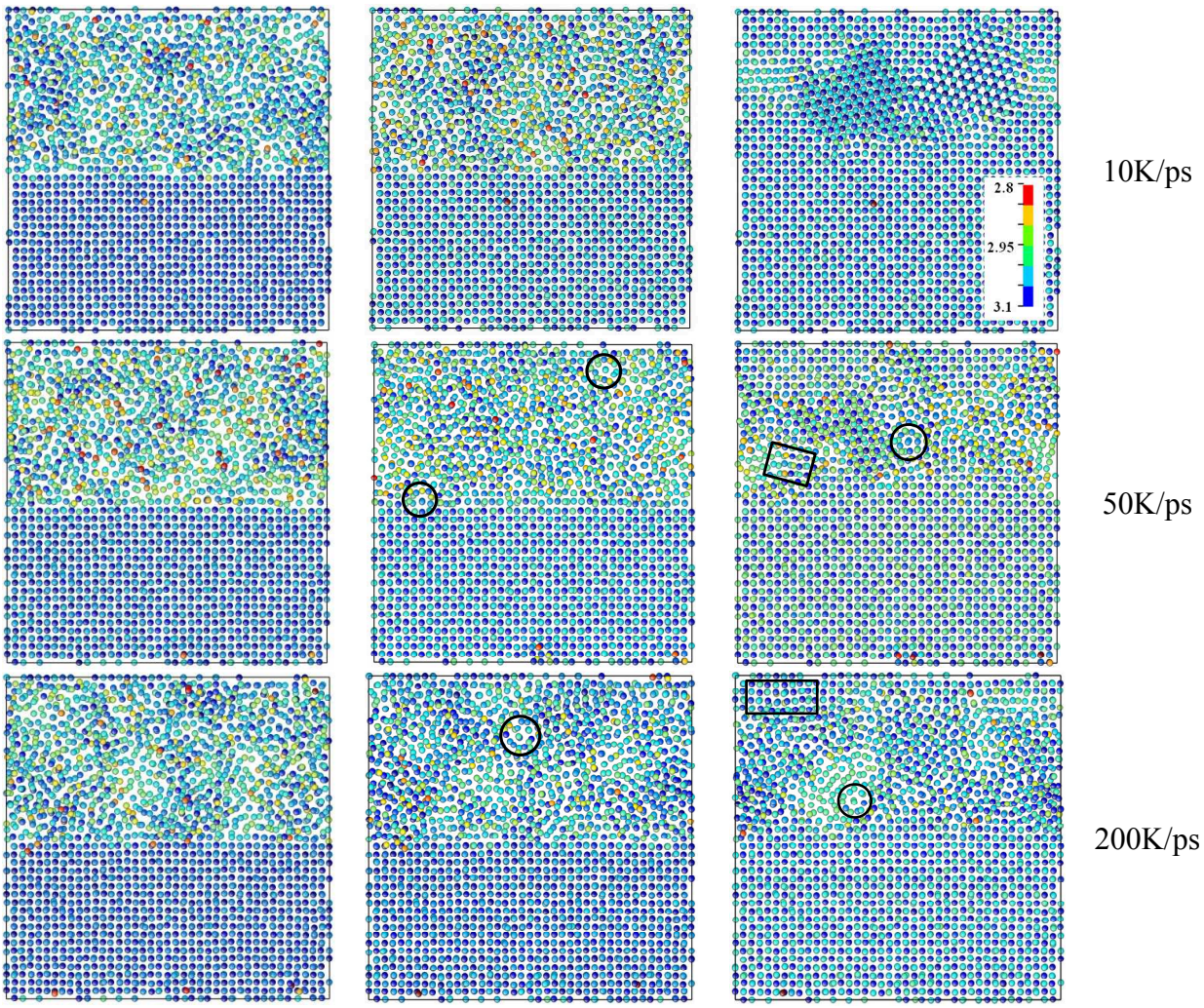
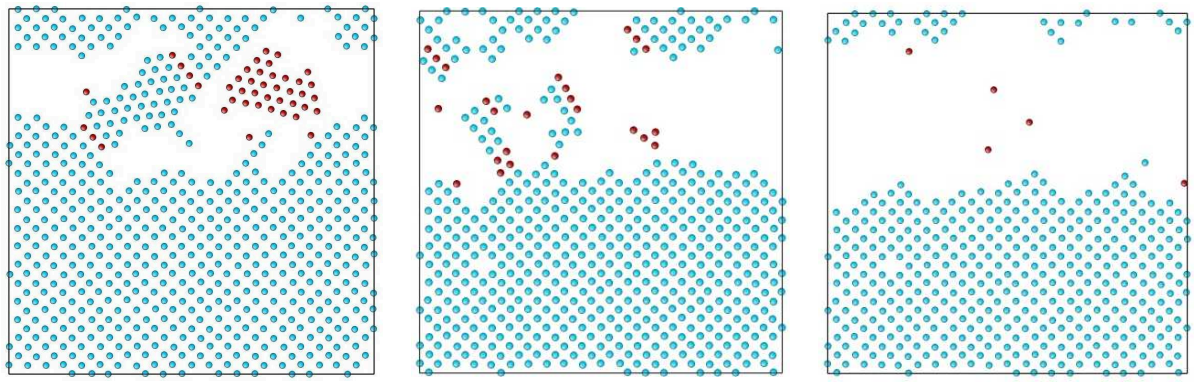


Fig. 3 The quenching processes at various temperatures with three different cooling rates.

To make clear the roles of the ordered structures during the solidification process, common neighbor analysis (CNA) [10] is used in calculation. The CNA pattern has been considered as a useful measure of the local crystal structure around an atom. Using CNA method, we present snapshots of

the final structures at 300K for some typical cooling rates of upper part in Fig. 4, where the blue and red atoms indicate the face-centered cubic (fcc) and hexagonal close packed (hcp). To clearly see the interface, we remove other atoms except fcc and hcp. Owing to nonuniformity of structures of the upper part, the ordered clusters, such as fcc and hcp crystalline clusters, and the disordered atoms emerge alternately at the interface. The interface is not smooth at all but indented. The mechanical behaviors of Cu will be influenced by the indented interface and the influence needs to be regarded and valued when the metal Cu is melted by laser grooving.



（a）10K/ps （b）50K/ps （c）200K/ps

Fig. 4 Snapshots of the crystal structures (fcc and hcp) at final 300K at various cooling rates.

As the cooling rate of upper part increases, the crystalline structures decrease obviously. At the cooling rate of 10K/ps, there are a large number of fcc structures and some hcp structures. By contrast, at a high cooling rate (200K/ps), there are a few fcc and hcp structures near the interface. When the upper part is quenched to 300K at various cooling rates, Table 1 mainly lists the percent of fcc and hcp structures of the whole system. Remaining structures are unknown structures and a rather small amount of bcc and icosahedra structures. It can be noticed that the total content of fcc and hcp crystal structures increase from 64.2% to 81.5% when the cooling rate drops from 100K/ps to 10K/ps,which indicates that the degree of crystallization in the solidified Cu nanoparticles increases with decreasing cooling rates. At cooling rates of 200K/ps and 400K/ps, the content of fcc and hcp only about 50%, which indicates that the solidified Cu nanoparticles of upper part form a noncrystal structure.

Table 1. Percent of crystal structures (fcc and hcp) analyzed by using CNA in the simulated Cu system corresponding to different cooling rates

lattice	10K/ps	30 K/ps	50 K/ps	100 K/ps	200 K/ps	400 K/ps
fcc	76.0%	80.7%	64.2%	62.2%	55.3%	49.2%
hcp	5.5%	1.7%	3.1%	2.0%	0.7%	0.5%

3.2 Pair correlation function

The pair correlation function (PFC) is often performed to describe the structure characterization of solid, liquid and amorphous states. It is defined as [11]

$$\rho g(r) = N^{-1}\left\langle \sum_{i\neq j} \delta(r + R_i - R_j) \right\rangle \quad . \tag{1}$$

which g(r) the probability of finding an atom in the range from r to r+dr, ρ is the average density of the system. R is the atoms' position, the angular bracket denotes the time average, and δ is the Dirac delta function.

First of all, we inspect the pair correlation function of liquid Cu to test whether this EAM can reasonably describe its liquid state. Fig. 5 shows that the result is consistent with the experimental

values given by Wasesa [12]. It demonstrates that the EAM function is capable of providing a good description of the solid and liquid structures of Cu.

Because of little change of PCF for lower part during solidification process, PCFs of the upper part at various cooling rates and average value of the lower part at final 300K are presented in Fig. 6. At the cooling rates of 400K/ps and 200K/ps, the second peak has an obvious split, which is regarded as a characteristic indication of disordered structures. In other words, the liquid Cu becomes the glass state and this result is in accord with the conclusion of the atomic configuration analysis. With the cooling rate decreases, the second peak splits into two sub-peaks and a small shoulder peak appears between the first and second peaks. At the cooling rates of 30K/ps and 10K/ps , although the peak heights are not so high compared with the PCF of the lower part, the sub-peaks and the shoulder peak rise to be the separate peak indicating that the ordered structures emerge and are extended to be long-range crystalline structures. Actually, the height and number of the peak of the PCF can reflect the arrangement state of the system to some degree. When peak height is higher and the numbers of the peak are more, there are more crystal structures and the orientation of the crystalline structure become more consistent [13, 14].

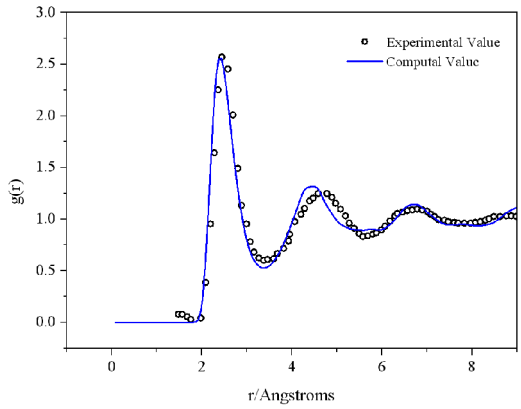


Fig. 5 Pair correlation function g(r) of liquid metal Cu at 1573K.

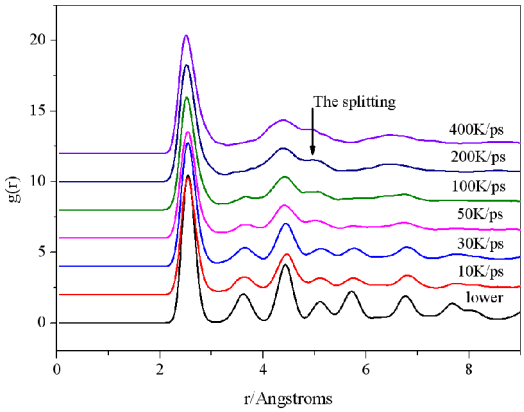
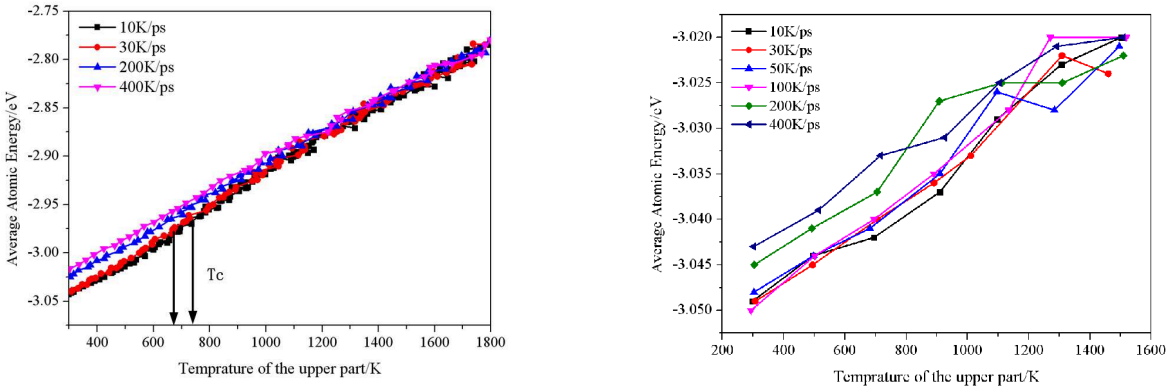


Fig. 6 Pair correlation function g(r) of the lower part and upper part in the final structure at 300K under different cooling rates

3.3 Average atomic energy

In the following part, the changes of average atomic energy at typical cooling rates are given in Fig. 7. For the cooling rates of 400K/ps and 200K/ps, a nearly continuously subtle change in the slope of energy with temperature can be observed in Fig 7 (a). Whereas, for the cooling rates of 30K/ps and 10K/ps, there are sudden drops in the average atomic energy indicating the emerge of crystal structures. The sudden changes are observed at about 670K and 730K for the cooling rates of 30K/ps and 10K/ps, which we call the crystallization point Tc. The average atomic energy also shows interesting characteristics at 300K for four cooling rates from 10K/ps to 400K/ps, and they are -3.043, -3.039, -3.025 and -3.016 eV respectively. It is widely known that low energy indicates high stability and it can be concluded the lower cooling rate leads to the more stable structure.

Fig. 7 (b) shows that the average atomic energy of lower part decreases to some degree in response to the temperature dropping of upper part. This is because the atoms of upper part have relatively high energy at high temperature and the energy transfer among atoms from the upper part to lower part at the interface. During the solidification process, the energy transfer drops with the decreasing of the energy of upper part. As can be noted, the average atomic energy of lower part decreases from -3.02 to -3.05 eV but is lower than that of upper part as a whole. It indicates that the lower part undergoes some influence by cooling process of upper part. This result is in accordance with that of the analysis of atomic configuration and PCF.



(a) (b)

Fig. 7 Simulated average atomic energy for Cu as a function of temperature during solidification process at different cooling rates (a) the upper part (b) the lower part.

3.4 Mean square displacement

Mean square displacement (MSD) is proportional to the diffusion constant of the diffusing atoms, which can be used to describe the displacements of the atoms in cooling process. The formula is given by

$$\left\langle r^2(t)\right\rangle = \frac{1}{N}\sum_{i=1}^{N}\left(\left|r_i(t)-r_i(0)\right|^2\right). \quad (1)$$

The position of an atom i at a given time t is denoted by $r_i(t)$.

The MSD for Cu of the upper part is plotted in Fig. 8 at various cooling rates. Obviously, the cooling rate has a significant influence on the MSD during the solidification process. At the cooling rate of 10K/ps, the MSD increases rapidly when the temperature of upper part decreases from 1800K to 750K and the MSD is constant 356 $Å^2$ below 750K, which indicates the atoms diffuse at a large range and arrange again for the crystallization process. In contrast, at relatively high cooling rates (200K/ps and 400K/ps), the atoms have no enough time to diffuse consisted with the analysis of PCF, the proof is that the MSD nearly has no change. The atoms oscillate near the equilibrium position and hold the amorphous state of the liquid Cu leading to glass transition.

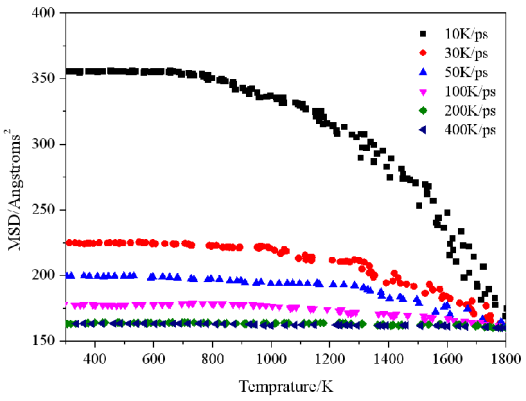


Fig.8 Mean square displacement (MSD) of upper part at various temperatures with different cooling rates

4. Conclusions

In this work, molecular dynamics simulations on the solidification of Cu nanoparticles have been performed by using crystal-liquid configuration method at six different cooling rates. The study demonstrates that the cooling rates play critical roles in the evolution of microstructures and the final two-phase microstructures.

1) The growth competition between the ring structures and parallel-string structures play a dominant role in the evolution of microstructures of liquid metal Cu during cooling processes. At the cooling rates of 400K/ps, 200K/ps and 100K/ps, the amorphous structures in the long-range form for the upper part because the ring structures dominate; at the cooling rates of 30K/ps and 10K/ps, the mixed crystal structures of fcc and hcp coming from parallel-string structures form, and their corresponding crystallization temperatures are 670K and 730K.

2) The work investigates the final atom configuration quenches at various cooling rates by using the CNA method. The total content of fcc and hcp crystal structures increases from 49.7% to 81.5% when the cooling rate drops from 400K/ps to 10 K/ps. The crystalline clusters, such as fcc and hcp, and the disordered atoms emerge alternately at the interface. The interface between two-phase structures is not smooth at all but indented.

3) The pair correlation function g(r) and mean square displacement (MSD) are studied. The peak height and the number of the peak of the PFC increase with the decreasing cooling rate. At the cooling rate of 10K/ps, the shoulder peak between the first and second peaks and the sub-peaks of the splitting second peak of the PCF develop to be separate peaks. And the MSD increases rapidly when the temperature of upper part decreases from 1800K to 750K and the MSD is constant 356 $Å^2$ below 750K, which indicates the atoms diffuse enough in the long-range and arrange again for the crystallization process.

References

[1] Chen K Y, Liu H B, Li X P, et al, Molecular dynamics simulation of local structure of aluminum and copper in super cooled liquid and solid state by using EAM, J. Phys-Condens Matter,1995, 7:2379-2394.

[2] Chen F F, Zhang H F, Qin F X, et al, Molecular dynamics study of atomic transport properties in rapidly cooling liquid copper. J. Chem Phys, 2004, 120(4): 1826-1831.

[3] Wang L, Bian X F, Li H, Molecular dynamics simulation of metal Cu during melting and crystallizing process, J. Acta Chim. Phys. Sin. 13 (2000) 544-550.

[4] K. Zhang, H Li, L. Li, X. F. Bian, Why does the second peak of pair correlation functions split in quasi-two-dimensional disordered films, J. Appl. Phys. Lett. 102, 071907 (2013).

[5] K. Zhang, P. C. Si, H. Li, Y. F. Li, H. Q. Yu, Y. Y. Jiang, Elongation behavior and local amorphization of metallic nanowire with glassy shell and crystalline, J. Europhys. Lett. 97, 26005 (2012).

[6] Wang L, Bian X F, Li H, Liquid-solid transition and crystal growth of metal Cu by molecular dynamics simulation, J. Acta Phys. Chim. Sin. 16 (2000) 825-829.

[7] Plimpton S J. Fast parallel algorithms for short-range molecular dynamics, J. Comput. Phys. 1995, 117: 1.

[8] X. W. Zhou et al, Atomic scale structure of sputtered metal multilayer, J. Acta. Mater. 2001, 49, 4005-4015.

[9] Hoover W G. Generalization of Nose's isothermal molecular dynamics: Non-Hamiltonian dynamics for the canonical ensemble, J. Phys. Rev. A 1989, 40: 2814.

[10] Honeycutt J D and Andersen H C, Molecular dynamic study of melting and freezing of small Lennard-Jones clusters, J. Phys. Chem. 1987, 91: 4950.

[11] C. H. Bennett, Serially deposited amorphous aggregates of hard spheres, J. Appl. Phys. 1972, 43, 2727.

[12] Y. Waseda, The Structure of Non-Crystalline Materials, Liquid, and Amorphous (McGraw-Hill, New York, 1980).

[13] S. P. Pan, J. Y. Qin, W. M. Wang, T. K. Gu, Origin of splitting of the second peak in the pair-distribution function for metallic glasses, J. Phys. Rev. B 2011, 84, 092201.

[14] K. Watanabe, H. Tanaka, Direct observation of medium-range crystalline order in granular liquids near the glass transition, J. Phys. Rev. Lett. 2008,100,158002.

Applied Mechanics and Materials Vol. 597 (2014) pp 249-252
© (2014) Trans Tech Publications, Switzerland
doi:10.4028/www.scientific.net/AMM.597.249

Study on optimal spacing and the residual height parameter of blade part in MASTERCAM

Shan- Hua XIAO [1, 2,a] , Wen Chao Zhou[1,b]

[1] Yibin Vocational and Technical College,Yibin 644003,CHN
[2]Chengdu University of Technology , Chengdu 610059, CHN
[a]yb_99888@163.com, [b] sk2042@163.com

Keywords: Curved surface; Spacing; Scallop height.

Abstract. Spacing is calculated by the formula in the rough machining of blade, consider the spacing as cutting parameters, research on how the length of NC program change when increase or decrease the spacing, Get the best cutting-spaced verified by physical simulation cutting; Blade finish machining parameter is set on the basis of surface roughness value,experiment and get the best scallop height blade machining.

1 Propose the Problems

Leaf processing is a major problem in today's manufacturing industry, is difficult to achieve with manual programming, the most efficient and effective way is to use CAD / CAM software. Whether blade axis machining line spacing settings are reasonable, directly related to the efficiency of processing quality and cutting parts of the product. When the spacing is small, low cutting efficiency, increase production costs; When the spacing is too large, the blade part surface roughness increases, surface quality decline, reach parts machining accuracy, and even waste. Based on this, this paper proposes the study on the best spacing and residual height parameter Settings of processing blade surface by MASTERCAM.

2 The formula of curved blade spacing

The distance of adjacent track line when Ball milling machining blade surfaces is spacing（S）, Whether spacing settings are reasonable is related to the machining efficiency and surface quality. Another parameter corresponds with spacing is residual height,which is height of residual groove（H）between the two adjacent surface normal vector direction When ball end milling cutter machining multi-axis space curved surface. In CAD / CAM processing parameter settings, line spacing is a very important parameter. The selection of spacing (S) is related to ball milling radius (r), the residual height (H), the radius of curvature of space surface (R) and so on. The spacing of ball end milling cutter machining convex surface and residual height as shown in figure 1, processing concave surface spacing and residual height is shown in figure 2. The formula for calculating spacing as Convex surface for example:

S=AB=2AD， AD=O_1E*R/(R+r), $O_1E=\sqrt{r*r-EC*EC}=\sqrt{r*r-(r-H)*(r-H)}$

Then ,$S=(2*R*\sqrt{H*(2*r-H)})/(R\pm r)$, (1)

Where r is the radius of the ball end mill tool; S is spacing; H is the height of the residual parts machined surface; R is the radius of curvature of space surfaces. In the ormula (2), when the curved surface is convex curved surface, for positive numbers; when the concave curved surface is curved, the minus sign. The radius of curvature R of the different curved surface is different, but both roughing and finish machining, cutting tool once chosen, the cutting tool radius (r) is constant, the residual height (H) can be determined based on the value of the surface roughness. For rough machining, spacing take larger value, as far as possible to improve the efficiency; For finishing, try to take a smaller value, meet the requirements of machining accuracy.

3 The formula of residual height of blade surface machining

In the CAD / CAM, you can use the residual height parameter control processing quality, which is calculated as follows:

H=OE – EC – R EC= $\sqrt{r*r-O_1E*O_1E}=\sqrt{r*r-((r+R)*(r+R)*s*s/(4*R*R))}$

OE=$((r+R)*\sqrt{R*R-S*S/4})/R$, H= $((r+R)*\sqrt{R*R-S*S/4})/R-\sqrt{r*r-((r+R)*(r+R)*s*s/(4*R*R))}-R$ （2）

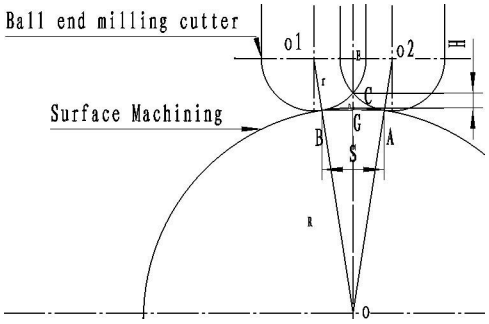


Figure1 Ball end cutter machining convex surface

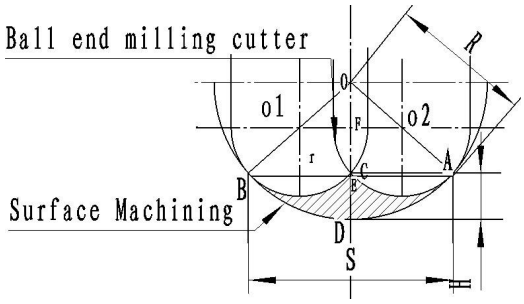


Figure2 Ball end cutter machining concave surface

Equation (2) shows that when the convex curved surface machining, the size of the residual height by the tool radius (r) and the radius of curvature of the cutting line spacing (H) and a convex curved surface machining (R) decision. Tool radius greater the smaller the residual height; cutting spaced get smaller, the smaller the residual height; greater the radius of curvature of the convex surface, the greater the residual height. For the case of processing a convex curved shape determined,curvature is fixed, when the tool is selected, ball milling radius have been identified. Similarly, we can get formula (3) of residual height of the concave surface:

$$H= R- ((R- r)* \sqrt{R * R - S * S / 4})/R - \sqrt{r * r - ((R - r) * (R - r) * s * s/(4 * R * R))} \quad (3)$$

4 The spacing and residual height parameter settings in MASTERCAM

4.1 The optimal spaced settings of blade rough machining, rough machining select carbide ball end mill Φ6mm, Blade is twisted complex surface, Selecte automatic programming software Mastercam X6, machine is axis machining center HAAS VF-3, CNC system is HAAS CNC CONTROL,Try cutting material is aluminum, cutting depth ap = 4mm, feed rate is 1200mm/min, spindle speed is 7000r/min.

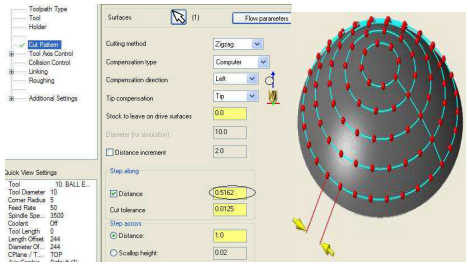


Figure 3 Set the spacing 0.5162mm

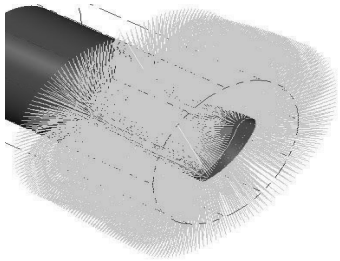
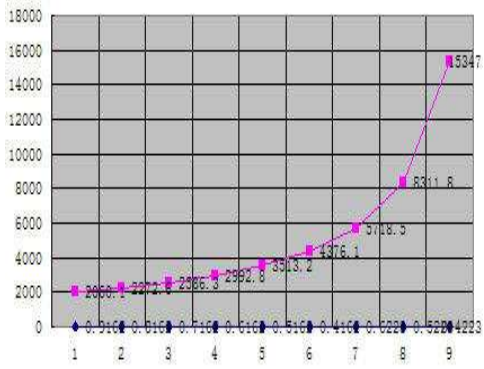


Figure 4 Toolpath

The maximum radius of curvature of the blade is R50mm, According to Ra = 12.5μm take H = 0.0125mm, leading into the above equation was calculated: S = 0 5162mm. Processing method is five axial line processing, its five-axis machining parameters spacing is shown in Figure 3, the path of the generation tool of spacing is shown in Figure 4, the generated G-code length is 987.1KB. With 0.5162 mm spacing as base, increase/decrease 0.1 mm respectively, cutting experiment was carried out, in order to study the optimal cutting space:

Table 1 Spacing increase/decrease cutting experiment table

spacing mm	lines of code (line)	length of the code KB
0. 9162	184910	2060.1
0. 8162	204000	2272.6
0. 7162	232180	2586.3
0. 6162	268690	2992.8
0. 5162	315440	3513.2
0. 4162	392950	4376.1
0. 3162	513530	5718.5
0. 2162	746470	8311.8
0. 1162	1378400	15347



We analyzed the above data, and put the generated data in the table1.From the analysis of the table 1, when the row spacing is decreased from 0.5162 to 0.1162,and the length of code increased from 3513.2KB to 15347KB, Net increase by 11815.8KB,the amplification is 77.1%, it result in a sharp increase of the processing time and low processing efficiency. When the row spacing is

increased from 0.5162 to 0.9162, and the length of code is decreased from 3513.2KB to 2060.1KB, Net decrease by 1453.1KB, the declines is 41.4%, it result in a sharp decrease of the processing time and high processing efficiency. Analysis by theoretical Calculated and repeated practice of cutting show that roughly guarantee processing efficiency, while there are certain surface quality requirements, taking the 0.6162mm Line spacing in the processing is the best value. Different Line spacing actual cutting results in Figure 5-13.

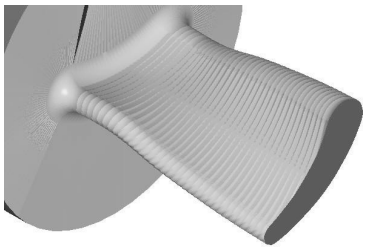


Figure5 S=0.9162mm cutting results

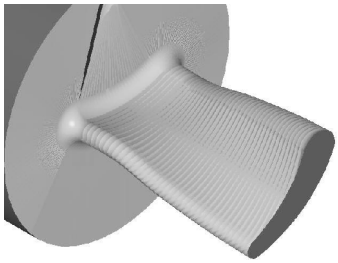
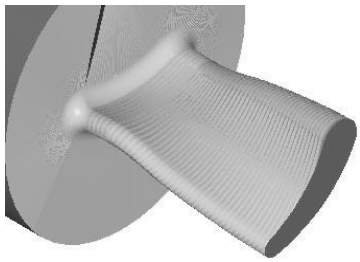


Figure6 S=0.8162mm cutting results



Figur7 S=0.7162mm cutting results

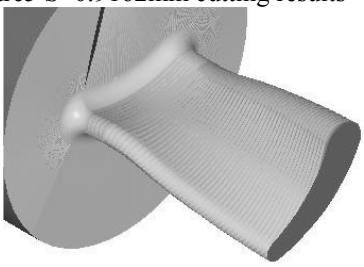


Figure8 S=0.6162mm cutting results

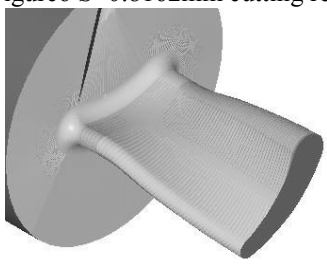


Figure 9 S=0.5162mm cutting results

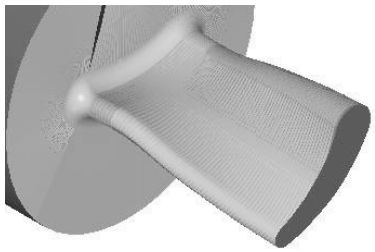


Figure10 S=0.4162mm cutting results

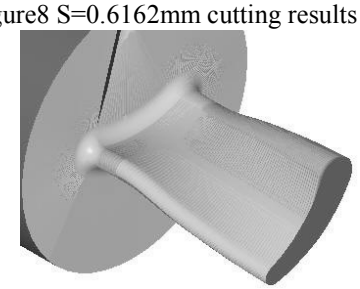


Figure11 S=0.3162mm cutting results

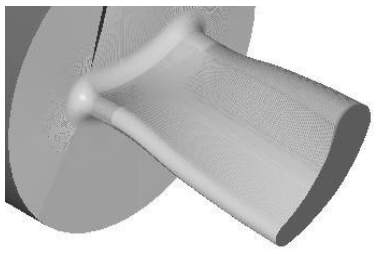


Figure12 S=0.2162mm cutting results

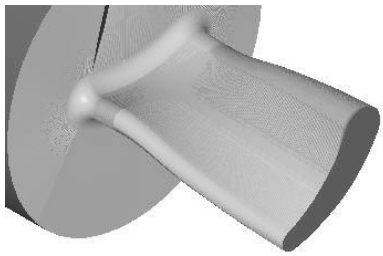


Figure13 S=0.1162mm cutting results

4.2 Blades finishing best residual height settings

In finishing the main consideration is the machining accuracy of blades and surface quality requirements, the use of scallop height parameters control the part surface quality , to ensure the machining accuracy and surface roughness values. The minimum reference value S = 0.5162mm of the above , in equation (3) calculated to give H = 0.0161 mm, the value of H for processing using the space surface processing , to achieve the accuracy required, but the roughness between the surface of the Ra6.3-12.5μm . And all the blades parts surface roughness require that the values is Ra 3.2μm, known by the residual height formula, residual height and tool radius r, the maximum radius of parts curvature R have a relationship to Line spacing S . When the parts blades shape and cutter identified, only by changing the Line spacing to obtain the desired surface roughness, cutting through several experiments, the residual height of H = 0.0032mm, the surface roughness values obtained can reach Ra3.2 μ m of requirements. Residual height parameter settings are shown in Figure 14, the best residual height trajectory are shown in Figure 15.

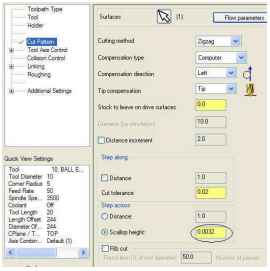


Figure14 Set residual height

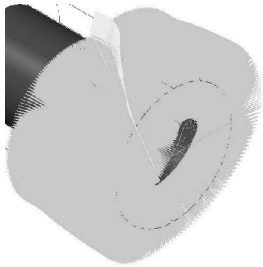


Figure15 The best residual height trajectory

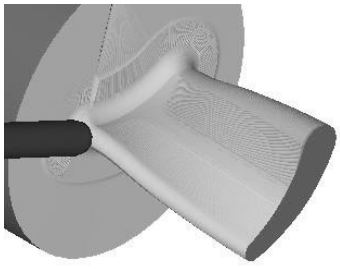


Figure16 VERICUT Simulation results

5 Mastercam X6 and Vericut simulation

5.1 Establish axis CNC machine tool simulation environment

The use of Vericut7.0 establish a geometric model of five-axis machine ,select "working directory" under the "File", set the D: \ HAAS \ VR to working directory, and then select "New Project" "mm" under the "File" to establish a project file and all files saved to the working directory.

(1) Establish assembly Coordinate :In the graphics window, select "show all axis" under the "assembly" command from the shortcut menu pop-up in system. The same method selection "model" command.

(2) Loading control system files: In the main menu, select the "configuration" under the "control", select the control file system haas.

(3) Definition of component structure tree ①Definition of component Base →X →Y →A →Spindle→cutter ②Definition of component Base →Z →Attach →Fixture→Stock→Design。Add the appropriate parts of the model to the corresponding tree, and manually tested properly after saving.

5.2 Four-axis CNC machine simulation

（1）Add tool library: Select the machining tool, select the component "Configuration Tool" window, click "Tools File" button ,in the pop-up window, select D: \ HAAS \ VR \ Haas.tls file, add the tool library.

（2）Add blank: In the component selection "blank" window, select "add model file, select" D:\ D:\HAAS\VR\Haas_Stock.tls file in the popup window, add blade blank. Similarly complete adding the work piece clamping and leaves of four axis NC program, complete the simulation results in figure 16.

6 Conclusion

(1) Calculated by formula and verified by actual cutting verification, get the optimal spacing parameters of the roughing machining of complex spatial axis blade surface to provide technical reference for efficiently axis rough machining in MASTERCAM software.

（2）In the finishing, the scallop height as the standard, cutting and obtains the best residual height parameter, ensure the part surface roughness and machining quality, set to four axis complex space curved surface parts provide reasonable parameters in MASTERCAM software, is beneficial to improve the machining efficiency of the parts, to ensure product quality.

References

[1] Xiao Shan-hua, Carbide coated inserts in the rational use of CNC turning and interference, Manufacturing Automation ,7(2012) 37-39.

[2] Xiao Shan-hua, The examples of Feature-based modeling based on manufacturing engineers of CAXA and mold Processing and application based on MasterCAM9,Mold manufacturing, 11(2007) 4-6.

[3] Song fang-zhi, NC multi axis machining technology practical course, Beijing:Tsinghua University press, 2010.

[4]Dang Xin-an, Optimizing Select Machining Parameter of Curve Surface in MasterCAM, Coal Xine Machinery, 9(2006) 127-130.

[5]Ye Zhen-hong, Reseach of Stepover for 3D Surface Machining, Coal Xine Machinery, 3(2008) 101-103.

[6] W u Fu-zhong, Constant Scallop-Height Tool Path Planning from Measured Data, Journal of Computer –Aided Design & Computer graphics，12(2007) 1618-1623.

[7]Wang Yu-ping, Research and application of MasterCAM in CNC machining, Machine Tool & Hydraulics, 2(2010) 3-8.

[8] Xiao Shan-hua, Mastercam modeling and four-axis based on blade part， Die and Mould Technology, 3(2012) 40-45.

Applied Mechanics and Materials Vol. 597 (2014) pp 253-256
© (2014) Trans Tech Publications, Switzerland
doi:10.4028/www.scientific.net/AMM.597.253

Effect of Preheat Temperature on Friction Stir Welded Aluminum Alloy 5052 Joints

Nurul Muhayat[1,a*], Triyono[1,b], Bambang Kusharjanta[1,c], Radian T Handika[1]

[1]Mechanical Engineering Department, Sebelas Maret University, Solo, Indonesia

[a*]nurulmuhayat@ymail.com, [b]triyonomesin@uns.ac.id, [c]bambang_k@uns.ac.id

Keywords: Preheat temperature. Friction Stir Welding. Aluminium alloy 5052. Mechanical Properties.

Abstract. The effects of preheat temperature on mechanical properties and the microstructure of friction stir welded (FSW) aluminum alloy 5052 joints were studied in the present work. Heated air from Heat Gun was applied in front of the FSW tool to give the preheat on friction stir welding process. Preheat temperature was set 150°C, 250°C and 300°C. Mechanical properties were correlated and analyzed according to tensile strength, macro and microstructure. Defect free welds were obtained at all preheat variations. The increasing preheat temperature produced the coarser grain size, it influenced the little decrease both the tensile strength and hardness of joints.

1. Introduction

Aluminum alloy is widely used in the vehicle to reduce the structural weight. The main problem of using aluminum alloy on the vehicle is the difficulty of joining processes. The common joining processes technology used are fusion weldings such as gas metal arc welding or gas tungsten arc welding. The disadvantages of fusion welding are high distortion and melt related defect. Friction stir welding which is the solid state welding provides joining processes that can substitute the fusion welding with less distortion and avoid melt related defect.

The source of welding heat used in FSW is generated from friction between welding tool and workpiece. Higher axial force generates higher heat input. It needs the strong clamping system to keep the work piece on the work bench that causes FSW which is not flexible. It reduces the welding productifity. Higher tool rotation speed improves heat input meanwhile higher travel speed reduces heat input. There are inter related welding parameters that cause the welding quality which is difficult to be optimized.

Recent investigation found that friction stir welded joints had both asymmetric physical and mechanical properties [1]. It was caused by the difference of welding temperature between advancing side and retreating side [2]. The advancing side had higher welding temperature caused by pheriperal velocity and travel speed which made positif combination, whereas it made the negatif combination in the retreating side. It can be minimized by application of preheat from outside of the friction system. The main function of the welding tool is only to stir and consolidate the softened material. Using preheat temperature on friction stir welding can reduce the role of tool in generating heat input.

Preheat increased the initial welding temperature on the contrary it could not accelerate in achieving peak temperature. The increase of initial welding temperature caused the decrease of yield strength that could decrease forming force for deformation during FSW process, consequently got less friction stress as well as less heat generated [3]. The increase of average grain size was caused by the increase of preheat time using high frequency induction heating due to the slow cooling rate after welding process [4]. In addition preheating temperature decreased the processes time [5]. However, the effects of preheat temperature on mechanical properties and microstructure of the friction stir welded aluminum alloy 5052 have not been well investigated.

The aim of this research is to investigate the effects of preheat temperature on mechanical properties and microstructure of friction stir welded aluminum alloy 5052. In this study, the FSW was assisted by preheat of heat gun that was applied to the welding of 5 mm thick aluminum alloy

5052 plates. After welding, the influences of the preheat on mechanical properties and microstructure of the FSWed plates were experimentally investigated.

2. Experimental Procedures.

Friction stir welded sheets were aluminum alloy 5052 with dimension of 400 x 150 x 4 mm. The base material was characterized by an ultimate tensile strength of 230 MPa. The chemical compositions were listed in the Table 1. Friction stir welding machine was modified with heat gun heater to give preheat temperature on work piece. During welding, the heat gun heater gave the preheat temperature at 5 mm in front of the FSW tool. Preheat temperatures were set 150°C, 250°C and 300°C. The sketch of preheat temperature on Friction stir welding can be seen in the Fig. 1. FSW tool was made of K100 Bohler with diameter shoulder and pin 18 mm and triangular pin with diameter and length of 4 mm and 3.8 mm, respectively.

The tool plunge depth of 3.95 mm, and the tool tilt angle of 2.5° were choosen to fabricate the joint. The FSW rotation speed and welding speed were 1125 rpm and 70 mm/min, respectively.

Table 1. Chemical composition of 5052 Al alloy (mass fraction, %)

Cu	Mg	Si	Fe	Mn	Zn	Cr	Al
0.001	2.5	0.072	0.254	0.051	0.005	0.188	Bal

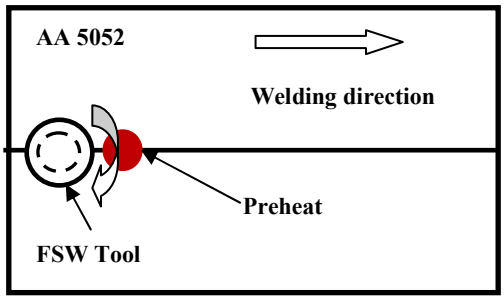


Fig. 1. Preheat position on the FSW Process

The FSW joints were sliced perpendicular to the welding direction to meet the required dimension. Transverse tensile test speciments were prepared according to the American Welding Society (AWS) D1.2 [6]. The macrostructural and microstructural specimens were polished using multi grade emery paper and etched using HF reagent, then images were taken by a light optical microscope. The hardness measurements were done at the middle of the thickness by Vicker's microhardness tester with load of 100 gr for 10 s.

3. Result and Discussion

3.1 Macrostructure.

Fig. 2 shows macrographs of the cross sections perpendicular to the tool traverse direction of the FSWed plates. Defect free joints were obtained in all preheat variation. The increase of preheat temperature soften the material so that the more material can be extruded. The result are the wider pin driven zone and the thicker shoulder driven zone. In the case of friction stir spot welded (FSSWed) joint, Sun et al. [4] obtained that due to the increase of preheat time, the penetration depth of tool was large and the more material can be extruded by the tool as well.



Fig. 2.Macrographs of FSWed joints under preheat temperature variation of (a) 150°C, (b) 250°C, and (c) 300°C

3.2 Microstructure.

Fig. 3 shows a typical microstructure of weld nugget under preheat temperature variations. It can be observed that the increase of preheat temperature lead the grain size growth. The increase of preheat temperature leads to the welding temperature around the tool more evenly which causes lower cooling rate. A coarser grain size can be obtained on the lower cooling rate. Kwon et al. [7] explained that some additional grain growth occured, due to maximum temperature of stir zone increased with the increase of tool rotation speed.

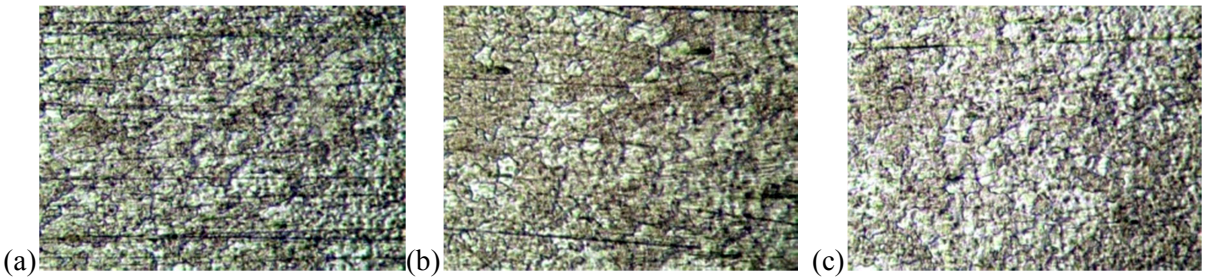


Fig.3. Microstructure at nugget zone under preheat temperature variation of (a) 150°C,(b) 250°C, (c) 300°C.

3.3 Mechanical Properties

The weld strength under variation of preheat temperature can be seen at Fig. 4. It can be observed that although the preheat temperature increase up to 300°C, there is the little decrease

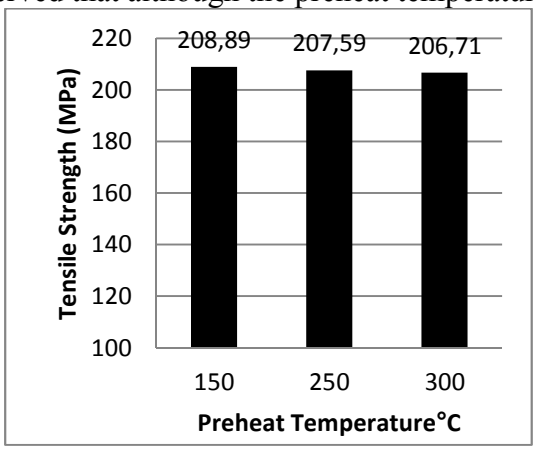


Fig.4. Tensile strength of FSWed joint under Preheat temperature variation of 150°C, 250°C dan 300°C.

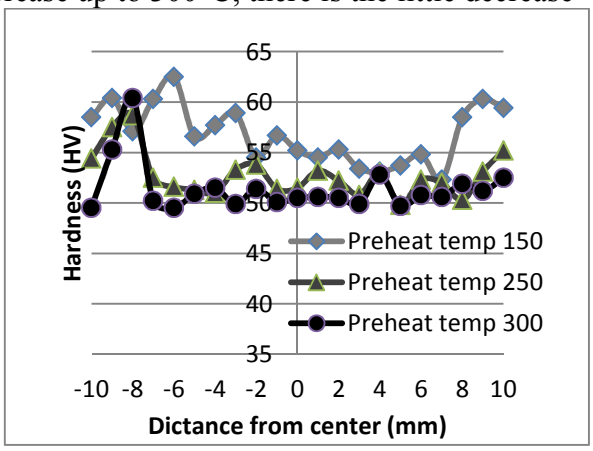


Fig. 5. Microhardness profile of FSWed Joint under preheat temperature variation of 150°C, 250°C dan 300°C.

on weld strength. Inline with weld strength that the increase of preheat temperature causes the little decrease of hardness across the joint as seen in Fig. 5. It is caused that the work piece only experiences low preheat temperature and affects on the surface of work piece. In addition, preheat temperature of 150°C shows asymmetric hardness between advancing side and retreating side. Muhayat et al. [8] explained that there was an assymetric hardness due to the difference of welding temperature between advancing side and retreating side. The increase of welding temperature makes the hardness balance.

4 Conclusion

The effects of preheat temperature on mechanical properties and microstructure of friction stir welded aluminum alloy 5052 have been investigated, the conclusion as follows:

1. Defect free joints are obtained at all preheat temperature variations.
2. The increase preheat temperature causes the wider pin driven zone and the thicker shoulder driven zone.

3. The increase preheat temperature lead to the grain growth.
4. Although the increase of preheat temperature leads to the grain growth, the tensile strength and hardness get the little decrease.

Acknowledgements

The authors gratefully acknowledge The Ministry of Education and Culture, Indonesia for funding the work reported, through research Hibah Madya grant BOPTN 2013 UNS Solo, Contract No: 165/UN27.11/PN/2013.

References

[1] D. Rao, K.Huber, J.Heerens, J.F.dosSantos, N.Huber, Asymmetric mechanical properties and tensile behaviour prediction of aluminium alloy 5083 friction stir welding joints, Materials Science & Engineering A 565 (2013) 44–50

[2] RS. Mishra, and Z.Y. Ma, Friction stir welding and processing, Materials Science and Engineering R 50 (2005) 1–78

[3] R. Keivani, B. Bagheri, F Sharifi, M Ketabchi, M Abbasi, Effects of pin angle and preheating on temperature distribution during friction stir welding operation, Trans. Nonferrous Met. Soc. China 23(2013) 2708−2713

[4] Sun, y.f., Shen, J.M., Morisada, Y., Fujii, H., Spot friction stir welding of low carbon steel plates preheated by high frequency induction, Materials and Design 54 (2014) 450–457

[5] Masoud Jabbari, Effect of the Preheating Temperature on Process Time in Friction Stir Welding of Al 6061-T6,Journal of Engineering, Volume 2013, Article ID 580805,

[6] AWS D1 Committee on Structural Welding, Sructural Welding Code-Aluminum, AWS D1.2/D1.2M: 2003,

[7] Yong-Jai Kwon, Seong-Beom Shim, Dong-Hwan Park, Friction stir welding of 5052 aluminum alloy plates, Trans. Nonferrous Met. Soc. China 19(2009) s23−s27

[8] Nurul Muhayat, Achmad Zubaydi, Sulistijono, M. Zaed Yuliadi, Effect of tool Tilt Angle and Tool Plunge Depth on Mechanical Properties of Friction Stir Welded AA 5083 Joints, Applied Mechanics and Materials Vol. 493 (2014) pp 709-714.

Applied Mechanics and Materials Vol. 597 (2014) pp 257-261
© (2014) Trans Tech Publications, Switzerland
doi:10.4028/www.scientific.net/AMM.597.257

FE modelling of Residual Stresses and Validation using Chip- mechanism and Microstructural Analysis of Ultrasonic Vibration Assisted Turning of Ti alloy Ti-6Al-4V

Sandip Patil[1,a], Digvijay Sheed[2,b], Dr. Rajkumar Singh[3,c]

[1]Sandip Patil, Kalyani Centre for Technology and Innovation; Bharat Forge Ltd. Pune, India
[2]Digvijay Sheed, Kalyani Centre for Technology and Innovation; Bharat Forge Ltd. Pune, India
[3]Dr.Rajkumar Singh, Kalyani Centre for Technology and Innovation; Bharat Forge Ltd. Pune, India
[a] sandip.patil@bharatforge.com, [b] digvijay.sheed@bharatforge.com,
[c] rajkumarsingh@bharatforge.com

Key Words: Residual stress, Elasto-plastic, Microstructure, Chips, UAT, CT, Titanium,

Abstract: Ultrasonic assisted turning (UAT) is a novel manufacturing technology, where high frequency vibrations are imposed on the movement of a cutting tool. A 2D FE transient simulation is developed in DEFORM, where ultrasonic vibrations of frequency 20 kHz and amplitude of 20 µm are provided to the cutting tool in the direction of cutting velocity. The prediction of residual stress distribution is carried out using elasto-plastic finite element simulations. Experimental analysis is carried out in measuring the strain at the cutting tool during CT and UAT along with the chip mechanism and chip microstructure study to validate the residual stress distribution. The ultrasonic vibrations yield a considerable improvement in compressive residual stresses which ultimately benefits in improving fatigue life of titanium alloys.

Introduction

Titanium and nickel alloys are difficult-to-cut materials with considerable manufacturing problems such as machining induced surface integrity and tensile residual stresses [1]. Several researchers have studied the effect of these vibration assisted techniques on machining of 'difficult-to-cut' materials such as Inconel 718. Ozel et al. [1] performed the prediction analysis of residual stresses in conventional turning of titanium and nickel based alloys with experiments and finite element simulations. Babitsky et al. [5] found that the UAT method performs better at low cutting speed using high frequency and high amplitude of vibration. Koshimizu [6] found that a reduction in cutting forces was observed during UAT of Ti-6Al-4V. Hu et al. [8] carried out the Simulation of residual Stresses in Ultrasonic Vibration Assisted Micro-milling of Al and Cu. They have predicted that residual stresses are dependent on cutting forces and cutting temperature. Abboud et al. [9] studied the Finite element-based modeling of machining-induced residual stresses in Ti-6Al-4V under finish turning conditions, but very few have used this technique effectively to study the effect of vibrations on residual stress distribution and microstructural changes in Ti6Al4V alloy during machining. The objective of this work is to analyze the effects of UAT of Ti-6Al-4V, in terms of residual stress distributions, chip morphology, chip microstructure, etc. by using experimentation technique.

Simulation Technique and Results

A 2D FE model was developed in DEFORM ™ in which cutting tool of tungsten carbide is assumed to be rigid and workpiece of Ti-6Al-4V to be elasto-plastic [1-2, 4-5, 9]. Fig. 1 shows a scheme of relative movements of the workpiece and cutting tool.

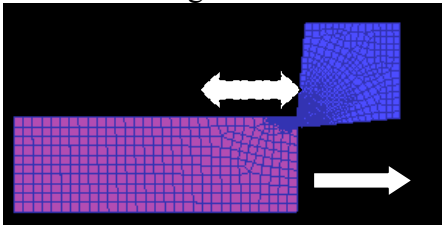


Fig.1: Experimental set up for UAT

In the current model, ultrasonic vibrations with a frequency of 20 kHz and amplitude of 20 µm were superimposed on the movement of cutting tool in the direction of cutting velocity. Dimensions of the workpiece used in the simulation were 2.5 mm in length and 0.8 mm in height with uncut chip thickness of 0.1 mm which was same as used for experimental work. The workpiece is meshed initially with approximately 5000 four noded quadrilateral elements. The number of elements increases during simulation to about 5600 due to remeshing. The size of the element in the process zone was 2 µm. The workpiece moves with a constant velocity, which correspond to cutting speed v_c and equals 333 mm/s. Kinematic boundary conditions providing this type of movement were applied to the bottom side of the workpiece whereas top surface was free. The cutting tool was rigid and it was immovable during the simulation of conventional turning process. However, it vibrates harmonically in the direction of cutting velocity during the simulation of ultrasonic assisted turning:

$$u_x = -a \cos \omega t \, , \, u_y = 0 \quad (1)$$

Where, $\omega = 2\pi f$, frequency $f = 20$ kHz, amplitude a = 20 µm.

However, the cutting tip vibration velocity is given by a ω sin ωt and a $\omega = 2513 > v_c$ (333 mm/s). This is the condition of separation of the tool from the chip within each cycle of ultrasonic vibrations. A Johnson- Cook material model accounting for the strain rate sensitivity was used for Ti-6Al-4V:

$$\sigma = (A + B\varepsilon^n)(1 + C\ln(\dot{\varepsilon} \mid \dot{\varepsilon}_o))(1 - T^*)^m \quad (2)$$

Where, $T^* = (T - T_{room}) \mid (T_{melt} - T_{room})$

$\dot{\varepsilon}$ is plastic strain rate and $\dot{\varepsilon}_o$ is reference plastic strain rate; T_{room} and T_{melt} are room and melting temperatures, respectively. For the analysis of residual stresses during UAT and CT, the workpiece was allowed to cool to room temperature by retracting the tool from workpiece and then by using point tracking the residual stresses were measured.

A substantial increment in compressive residual stresses was observed during UAT compared to that of CT. As shown in Fig.2, the residual stresses predicted on UATed surface are highly compressive in nature and it reduces and become tensile with the increase in the depth in the workpiece.

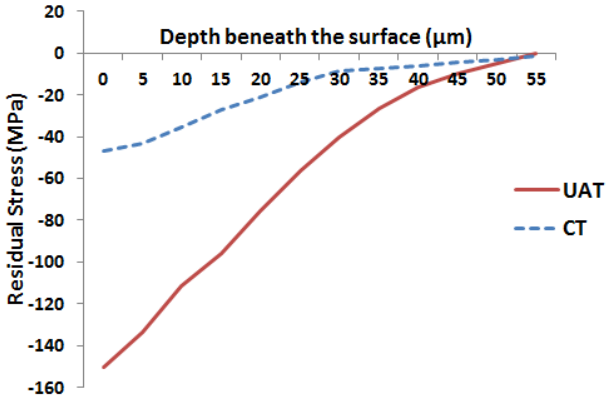


Fig.2: Modelling results of residual stresses

In machining, residual stresses are present because of plastic deformation that occurs during chip formation and contact between the tool and the machined part [8-9].

Experimentation Technique

An elaborated experimental set up was developed for the UAT of Ti-6Al-4V. The vibrations were given to the tool in the feed direction. Table 1 shows various cutting conditions used for this experimentation. The experimental results were analyzed for strain at the cutting tool, chip mechanism study and microstructural study of chip formation process during conventional turning (CT) and ultrasonic assisted turning (UAT).

Table 1: Cutting conditions

Workpiece	Ti-6Al-4V, Dia. 93mm (Hollow Pipe)
Cutting tool	KENNAMETAL (DNMG 150608)
Cutting Speed	20 m/min
Feed rate	0.1mm/rev
Depth of cut	0.1mm
Cutting	DRY

Measurement of strain at the cutting tool was carried out using strain gauges in both longitudinal and transverse directions. A digital P3 strain indicator and recorder were used to provide the output of strain. This measured strain gives an indication of cutting forces generated during machining as:

$$\sigma = \epsilon e$$

Where ϵ is modulus of elasticity, σ is stress and e is strain.

Fig 3a-b shows the position of the strain gauges mounted near to the cutting region along with P3 strain indicator.

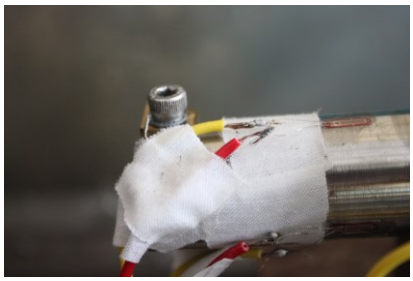


Fig.3a :Possition of strain gauges

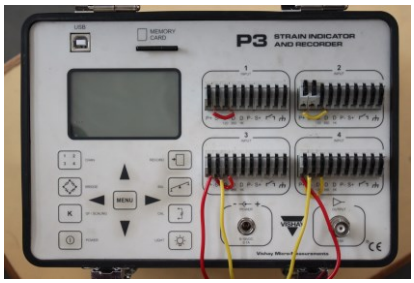


Fig.3b Strain Indicator

It was found that at a cutting speed of 20 m/min the maximum amount of strain measured in feed direction during CT was 49 μe. However, in case of UAT it was measured as 34 μe, thus 30% reduction in micro strain was measured during UAT. These reductions in strain will ultimately benefits through reduction in cutting forces during UAT.

Microstructural analysis and Discussion

In this section, quantitative data on chip morphology during UAT and CT is presented as shown in Fig 4. This data was obtained from SEM and optical images of chips generated during machining using an image analyzer software. A quantitative data on chip morphology during UAT and CT machining is tabulated as shown in Table 3.

Shear bands obtained in the chip microstructure represent localized deformation of material in small zones [11]. The surrounding area remains almost unaffected. Due to shear localization, the tool is subjected to drastic changes in cutting forces, which adversely affects the tool life and integrity of machined work surfaces. The microstructure of chips obtained with and without ultrasonic vibrations to the cutting tool at a cutting speed of 20 m/min and a feed rate of 0.1 mm/rev is as shown in Fig.5a-b It was observed that there is no shear band formation in the chips generated during UAT, whereas in CT, a shear band of width 3 μm was observed. During CT, since there is a continuous interaction between tool and chip, heat continues to generate which leads to localized thermal softening and thus formation of shear bands. However, in case of UAT, since there is an intermittent cutting, it leads to less heat concentration and hence no shear band formation is observed.

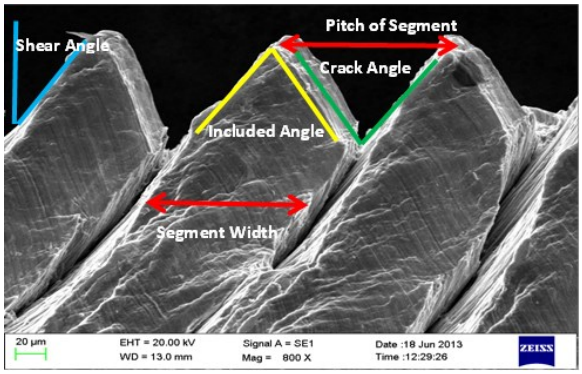


Fig.4: Terminology used to specify dimensions of chip segment

Table 3: Chip segmentation

Chip segmentation	Improvement in UAT	Significance
Chip thickness	18% reduction	Lower chip compression factor
Segment pitch	48% increase	More crack formation
Chip length / softening	45% increase	Less shear bands
Segment Width	45% increase	Delayed shear band formation
Crack angle	23% decrease	Less brittle nature of material
Included angle	23% decrease	Minimum plastic deformation
Shear angle	50% increase	Reduction in cutting forces

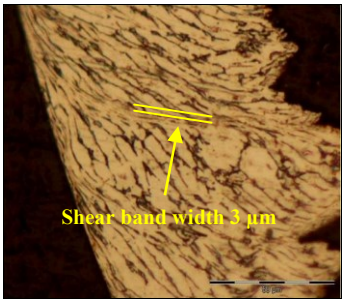


Fig.5a: CTed chip-20m/min

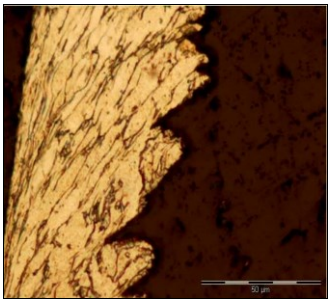


Fig.5b:UATed chip-20m/min

Conclusions

In this study 2D FE Simulations to predict machining induced residual stresses in Ti6Al4V were utilized. It was predicted that UAT process leads to higher compressive residual stresses compared to that of CT. This prediction was validated with the chip mechanism and chip microstructure study which showed reduction in cutting forces and cutting temperature during UAT than that of CT.

Acknowledgement

The authors gratefully acknowledge the extended support provided to this work by KCTI (Kalyani Centre for Technology and Innovation) for providing financial funding, laboratory and library facilities. The authors also acknowledge the support provided by Bharat Forge Ltd, Pune and DSIR (Department of Scientific and Industrial Research), Govt.of India. Finally, the authors would like to express special thanks and gratitude to review committee and top management of Bharat Forge Ltd for granting the permission to publish/present the research work.

References

[1] T.Ozel et al., " Prediction of machining induced residual stresses in turning of titanium and nickel based alloys with experiments and finite element simulation", CIRP Annals – Manufacturing Technology 2012, 61, 547-550,

[2] R. Muhammad et al., "Computational Study of Ultrasonically-Assisted Turning of Ti alloys", Int. J. Advanced Materials Research, 2011, 22, 330-336

[3] V. I. Babitsky et al., "Ultrasonically assisted turning of aviation materials: simulations and experimental study", Int. J. Ultrasonic, 2009, 42, 81-86.

[4] N. Ahmed et al., "Stresses in Ultrasonically-Assisted Turning", Int. J. Applied Mechanics and Materials, 2006, 5-6, 351-358.

[5] V. I. Babitsky et al., "Ultrasonically assisted turning of aviation materials", Int. J. Materials Processing Technology, 2003,132, 157-167.

[6] S. Koshimizu, "Ultrasonic Vibration assisted cutting of Titanium alloy", Int. J. Key Engineering Materials. 2009, 389-390, 277-282.

[7] C. Nath, M. Rahman, "Effect of machining parameters in ultrasonic vibration cutting", Int. J. Machine Tools and Manufacture, 2008,48, 965-974.

[8] Hu et.al., " Simulation of Residual Stress in Ultrasonic Vibration Assisted Micro-milling", Advanced Material Research, 2011, 188, 381-384

[9] Abboud et al., "Finite element-based modeling of machining-induced residual stresses in Ti-6Al-4V under finish turning conditions", Procedia CIRP, 2013, 63-68.

[10] Domenico Umbrello, FE simulation of conventional and high speed machining of Ti6Al4V, International Journal of Material Processing Technology, 2008, 196, 79-87

[11] J. Q. Xie, A. Bayoumi , "Some metallurgical aspect of chip formation in cutting Ti6Al4V", Int.J. Mater. Sci. Eng, 1995, 190A, 173.

Applied Mechanics and Materials Vol. 597 (2014) pp 262-265
© (2014) Trans Tech Publications, Switzerland
doi:10.4028/www.scientific.net/AMM.597.262

Research on Performance of Foundry Sand under the Effect of Chemical Binder

Qingzhou Sun [1,2,a], Jingguang Yan [1,2,b], Puqing Zhang [1,2,c]
Zhongkui Zhao[1,2,d] , Hang Du[1,2e]

[1]School of Materials Science and Engineering, Shandong Jianzhu University, Jinan 250101, China

[2] Shandong Engineering Research Center for Clean Foundry, Jinan 250101, China

[a]qingzhousun@126.com, [b]735370957@qq.com, [c]zhangpuqing777@sina.com,
[d]jorezhk@sdjzu.edu.cn, eduhang9008@163.com

Keywords: Raw sand, Chemical binder, Molding sand, Property

Abstract. This paper makes an experiental research on the performance of foundry sand under the effect of chemical binder. It discoveries the raw sand with different origin will have different properties even though they have the same particle size. The properties of their molding sand are also obviously different. For the raw sand that in the same particle size with similar acid demand value and four-screen distribution, the better grain shape will earn them a higher molding sand strength even though they have higher clay content. Under the effect of liquid binder, compared to the molding sand mixed from the sand of three-screen distribution, the molding sand mixed from those of four-screen distribution sand with other properties similar will have a higher tensile strength While under the effect of solid phenolic resin adhesive, the three-screen sand with good grain shape will have a high sand strength.

Introduction

Sand casting is not limited to the shape, size, complexity degree, alloy composition of the parts. And it is popular among foundryman for its low cost, short production cycles, and easy access to raw materials, so it has become the most popular casting way in production[1,2]. Along with the higher demand of the quality of casting products and of sand mould accordingly, chemical binder is used widely. As the chemical binder molding sand gets its tensile strength by chemical reactions and the binder is added with a small quantity, which makes proper choice of raw sand especially important[3,4,5,6]. Therefore, the experimental research on the performance of molding sand under the effect of chemical binder has been carried out to offer a theory basis for the rational choice of raw sand.

Experimental Materials

The raw sand comes from Weichang sand, Dalin sand and Zhangwu sand, of which the relevant performance indications are as shown in table 1. The solidim silicate with foundry grade is produced in Yanzhou, Shandong Province. Its modulus is 2.26, and Baume degree is 43º Be. Hardened ester is the slow ester produced in Shandong Yanzhou. The resin used in precoated sand is granular thermoplastic phenolic resin produced by Jinan Shengquan Group Co., Ltd（SQ） and with saturated aqueous solution with urotropine as curing agent, calcium stearate as lubricant. 808 Furan resin produced by SQ will be used as mixed resin for self-hardening sand, with toluenesulfonic acid as curing agent. GP201 phenolic resin and GP202 isocyanates produced by SQ will be applied as the resin for mixed cold box sand, with triethylamine as curing agent.

Instruments and Equipment

The main instruments and equipment for experiment include high efficiency rotor sand mixer, precoated sand mixer, cold box sand sampling device, DGG-9070B electro-thermostatic blast oven, SQY type of hydraulic strength tester, quick balance, platform scale, and stopwatch and so on.

Table 1 The main performance indications of raw sand

Type of raw sand	Particle size	Concentration for three screen [%]	Concentration for four screen [%]	Angular coefficient	Clay content [%]	Acid demand value [ml]
Dalin sand	50/100	87.36	94.15	1.30	0.227	6.83
Zhangwu sand	50/100	85.63	96.63	1.04	0.512	6.61
Weichang sand	50/100	97.35	98.94	1.17	0.322	6.94

Methods and procedures

Prepare some Dalin sand, Zhangwu sand and Weichang sand respectively, GP201 phenolic resin and GP202 isocyanates with the proportion of 100:1:1. Firstly, mull the sand and GP201 phenolic resin in the high efficiency rotor sand mixer for 50s; secondly, add GP202 isocyanates into them to be mulled for 50s. Finally, bring them out as cold box resin sand. Intensify the cold box sand in “8” shape of sample mold for tensile strength slightly, harden these samples through amine blowing process in cold box sand sampling device with blowing pressure of 0.25MPa, blowing time of 8s, washing pressure of 0.2MPa, and washing time of 20s. After that, take the samples out and test their instant tensile strength and 24h tensile strength. The results are as shown in table 2.

Table 2 The properties of cold box sand mixed by different raw sand

Type of sand	Instant tensile strength [Mpa]	24h Tensile strength [Mpa]
Dalin sand	2.5	2.9
Zhangwu sand	2.55	3.48
Weichang sand	2.32	2.63

Prepare some Dalin sand, Zhangwu sand and Weichang sand respectively, sodium silicate and organic ester with the proportion of 100:4:0.48. Firstly mull the sand and organic ester in the high efficiency rotor sand mixer for 15s; secondly add the sodium silicate to be mulled together for 45s; finally, bring the sand out as sodium silicate bonded sand. Put the molding sand in sealed plastic bags, take out some every 1 minute and make them as “8” shape of samples, and test their tensile strength respectively after 24h. The experimental results are as shown in table 3

Table 3 The properties of sodium silicate sand mixed by different raw sand

Sampling time [min]		1	2	3	4	5	6	7	8	9	10
24h Tensile strength [Mpa]	Dalin sand	1.11	1.01	1.00	0.98	0.82	0.72	0.70	0.46	0.23	0.00
	Zhangwu sand	1.30	1.13	1.03	0.96	0.93	0.87	0.86	0.77	0.47	0.10
	Weichang sand	0.93	0.82	0.79	0.70	0.63	0.60	0.43	0.30	0.21	0.00

Prepare some Dalin sand, Zhangwu sand and Weichang sand respectively, granular thermoplastic phenolic resin, saturated aqueous solution with urotropine, calcium stearate with the proportion of 100:3:0.36:0.3. Heat the sand to around 200℃ and then put them in coated sand mixer, which has been preheated to around 160℃. When the sand temperature drops to around 160℃, add the resin in the mixer and stir them fast; when it drops to around 110℃, add the saturated solution with urotropine in the mixer; when it drops to around 80℃, add the calcium stearate. Take them out when it drops to around 70℃ and the precoated sand comes out after being crushed and sieved when it is cooled to

room tempreture. Put precoated sand into “8” shape of sampling mould for tensile strength, keeping the temperature of 255℃ for 210s, and get the “8”shape samples for tensile strength. Test the thermal tensile strength,1h tensile strength and 24h tensile strength for each sample respectively. Their experimental results are as shown in Table 4.

Table 4 The properties of prcoated sand mixed by different raw sand

Type of sand	Thermal tensile strength [Mpa]	1h Tensile strength [Mpa]	24h Tensile strength [Mpa]
Dalian sand	0.70	1.28	1.43
Zhangwu sand	1.34	1.83	2.03
Weichang sand	1.24	1.65	1.82

Prepare some Dalian Sand, Zhangwu Sand and Weichang Sand respectively, 808 Furan resin and toluenesulfonic acid as curing agent with the proportion of 100:1.2:0.42. Mull the sand and curing agent in the high efficiency rotor mixer for 15s, and add resin to be mulled together for 45s, and then bring out them as self-hardening resin sand. Put the molding sand in sealed plastic bags, and take some sand out to make one set of “8” shape of samples for tensile strength every 1 minute waiting to be tested for their tensile strength after 24h respectively. Their experimental results are as shown in table 5.

Table 5 The properties of self-hardening resin sand mixed by different raw sand

Sampling time [min]		1	2	3	4	5	6	7	8	9	10
24h Tensile strength [Mpa]	Dalin sand	1.50	1.25	1.19	0.90	0.80	0.73	0.49	0.35	0.18	0.00
	Zhangwu sand	2.20	1.85	1.50	1.36	1.23	1.00	0.50	0.35	0.18	0.00
	Weichang sand	0.95	0.90	0.83	0.78	0.75	0.49	0.39	0.35	0.18	0.00

Analysis on the experimental results

As shown in Table1 to table5, though Dalin sand,Zhangwu sand and Weichang sand have similar acid demand value and same particle size of 50/100, their molding sand still have obviously different tensile strength due to the difference on other properties. The four kind of molding sand mixed from Zhangwu sand have the highest tensile strength. The tensile strength of its molding sand, including cold box sand, sodium silicate sand, precoated sand and self-hardening resin sand, is 24.0%,28.6%,29.5 % and 56.7% higher than the lowest one respectively. Compared to Dalin sand and Weichang sand with the same size and similar acid demand value, the Zhangwu Sand with the same size and acid demand value has the highest tensile strength due to its best grain shape with four-screen distribution even though it has a highest content of clay among the three. It shows that the grain shape rather than clay content is the key element in deciding the properties of molding sand in the condition of better size distribution.

Cold box sand, ester hardening sodium silicate sand and Furan resin self-hardening sand mixed by Dalin sand have a higher tensile strength than other molding sand from Weichang sand, while the precoated sand mixed from Weichang sand has a higher tensile strength than the molding sand from Dalin sand. It can be found by a comparison that, the grain shape of Dalin sand with the similar clay content and same particle size is not as good as Weichang sand. Dalin Sand is four-screen distribution, while Weichang sand is three screens distribution. It shows that, when the other properties are similar, the grain size distribution of the sand under the effect of liquid binder is the key element deciding the properties of molding sand. The molding sand mixed by Dalin sand with four-screen distribution has a higher tensile strength than those from Weichang sand. However, when the other properties are similar, the grain shape rather than grain size distribution of the sand under the effect of phenolic resin adhesive is the key element deciding the properties of molding sand. Precoated sand mixed by Weichang sand with the better grain shape has a higher tensile strength

Conclusion

1) The raw sand with different origin will have different properties even though they have the same particle size and similar acid demand value, and their molding sand have a big difference on tensile strength accordingly.
2) A better grain shape can also earn a high tensile strength for its molding sand of the raw sand with the same particle size of four-screen distribution and similar acid demand value, even with a high clay content.
3) Under the effect liquid binder, compared to the molding sand mixed by the raw sand of three-screen distribution with other properties similar, the molding sand from those of four-screen distribution will have a higher tensile strength.
4) Under the effect of solid phenolic resin adhesive, the molding sand of the raw sand with good grain shape will have a higher tensile strength if their other properties are similar.

Acknowledgement

This work is financially supported by Programs for Science and Technology Development of Shandong Province under Grant No.2010GSF10611.

References

[1] Y.C. Li: *Foundry Molding Materials Handbook* (Machinery Industry Press, China 2009) p.II (in Chinese)

[2] Q.D. Shi, L.H. Wang, G.L. Gao and H. Yao: *Molding Materials* (Peking University Press, China 2009) p.182 (in Chinese)

[3] Y.C. Li: *Prcoated sand and core making technology* (Machinery Industry Press, China 2008) p.31 (in Chinese)

[4] C.Z. Meng, Q.Z. Sun and P.Q. Zhang: Foundry Technology, Vol. 27(2006) No. 10, p.1048-1049(in Chinese)

[5] M.S. Xie and N.L. Jiang: *Practical technology of furan resin self hardening sand* (Machinery Industry Press, China 1994) p.12 (in Chinese)

[6] Z.T. Fan, X.P. Dong and X. Lu: *The Water Glass Sand Principle and Application* (Machinery Industry Press, China 2003) p.148 (in Chinese)

Applied Mechanics and Materials Vol. 597 (2014) pp 266-271
© (2014) Trans Tech Publications, Switzerland
doi:10.4028/www.scientific.net/AMM.597.266

The effect of the initial temperature of ring blank on conical ring rolling process

Wen Meng [a] , Guoqun Zhao*[b] and Yanjin Guan [c]

Key Laboratory for Liquid-Solid Structural Evolution and Processing of Materials (Ministry of Education), Shandong University, Jinan, Shandong 250061, PR China

[a]wenmengsdu@126.com, [b]zhaogq@sdu.edu.cn, [c]guan_yanjin@sdu.edu.cn,*Corresponding author

Keywords: Conical ring rolling; Equivalent plastic strain distribution; Temperature distribution; Average rolling force; Average rolling moment.

Abstract. A FE model of radial conical ring rolling process with a closed die structure on the top and bottom part of driven roll (RCRRCDS) process was set up based on ABAQUS/Explicit software. The effect of the initial temperature of conical ring blank on equivalent plastic strain (PEEQ) and temperature distribution of rolled ring, average rolling force and average rolling moment was investigated. The results indicated that with the increase of the initial temperature of ring blank, the PEEQ distribution of rolled ring becomes uniform at first and then less uniform; the temperature distribution gradually becomes homogeneous; and both average rolling force and average rolling moment decrease. When the initial temperature of ring blank is 925℃, the PEEQ distribution of rolled ring is most uniform; the temperature distribution of rolled ring is relatively uniform; the average rolling force and average rolling moment are relatively smaller.

Introduction

The radial conical ring rolling process with a closed die structure on the top and bottom part of driven roll (RCRRCDS) process is an important branch of ring rolling process. In RCRRCDS process, the die structure composed by the driven roll and the mandrel can effectively prevent the generation of fishtail detects of rolled ring. Thus, the size accuracy and mechanical properties of rolled ring can be ensured. The RCRRCDS process has advantages in saving materials, improving production efficiency, etc. Therefore, it has a wide use in aerospace, nuclear power and mechanical industry, etc. The most typical conical rings are nozzle supports, flanges [1], aero-engine accessory, the main part of nuclear reactor shell [2], and aluminum alloy conical ring with inner steps [3], etc.

Recently, many scholars investigated the effects of the initial temperature of ring blank on hot ring rolling processes. Wang et al. [4] simulated a hot rectangular shaped ring rolling process of Ti-6Al-4V alloy and claimed that with the increase of the initial temperature of ring, the distributions of β phase and its grain size become more uniform but the volume fraction of β phase and grain size increase. Zhu et al. [5] simulated a hot rectangular shaped ring rolling process of TA15 alloy and declared that with the increase of the initial temperature of ring, the grain size distribution of primary α phase gradually becomes uniform; the distribution of primary α phase becomes more uniform at first and then less uniform. Zhou et al. [6] simulated a steel radial-axial rectangular shaped ring rolling process and pointed out that the increase of the initial temperature of ring is helpful to improve the uniformity of the equivalent plastic strain (PEEQ) distribution of rolled ring while the decrease of the initial temperature of ring is of benefit to increase the uniformity of the temperature distribution of rolled ring. Sun et al. [7] analyzed hot rectangular shaped ring rolling process of AISI 5140 steel and draw the conclusions that the distributions of the dynamic recrystallization grain size and the volume fraction of recrystallization become less uniform with the increase of the initial temperature of ring. Gong et al. [8] simulated a conical ring rolling process with outer steps and concluded that increasing mandrel feed rate or decreasing the peripheral speed of driven roll will increase the uniformity of PEEQ distribution of rolled ring. Han [3] and Yuan [9] optimally designed the aluminum alloy and

steel conical ring blank sizes in conical ring rolling processes, respectively, by experimental and simulation method. According to the above studies, it can be concluded that the initial temperature of ring has significant effects on ring rolling processes. However, the studies about the effects of the initial temperature of ring on conical ring rolling processes were rarely reported. Therefore, in order to obtain rolled conical rings with more uniform PEEQ and temperature distributions and better mechanical properties, it is necessary to investigate the effect of the initial temperature of conical ring blank on conical ring rolling process.

Modeling of RCRRCDS process

The FE model of RCRRCDS process was established on ABAQUS/Explicit software, as shown in Fig. 1 (a). The material of conical ring is Ti-6Al-4V. Its density is 4430 kg/m^3. Its Poisson's ratio is 0.3 [10]. Its temperature-dependent physical properties such as Yong's modulus, specific heat, thermal conductivity, etc. are from reference [10]. The material constitutive model of Ti-6Al-4V within its forged temperature range (800 ℃ ~950 ℃) is from reference [11]. The coupled thermal-displacement element with eight nodes and six surfaces (C3D8RT) is adopted to discrete grid of conical ring blank. The number of mesh elements is approximately 8,000. The friction factor between rolls and conical ring is 0.5 [12]. The coefficient of thermal convection is 0.02 Ns^{-1}mm^{-1}℃. The coefficient of thermal radiation is 0.6 Ns^{-1}mm^{-1}℃^{4} [10]. The temperature of driven roll and guide rolls is 100℃. The temperature of mandrel is 200℃. The temperature of environment is 20℃.The mass scaling technology is employed. The mass scaling factor is 50.

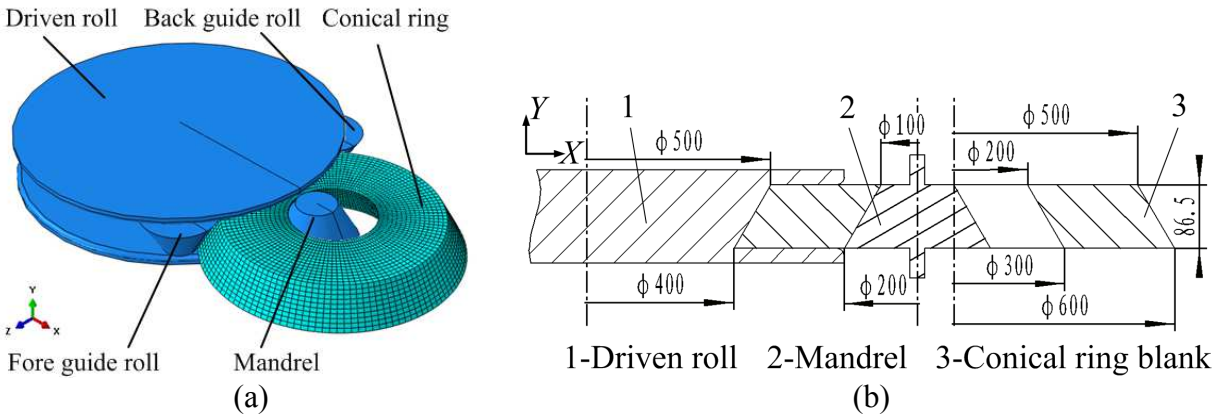


Fig.1 (a) FE model of RCRRCDS; (b) Dimensions of rolls and conical ring blank

This paper mainly investigates the conical rolling process from a conical ring blank to the desired conical ring. In order to study the effects of the initial temperature of conical ring blank on RCRRCDS process, the following numerical simulation experiment is designed. The driven roll's bottom radius is 200 mm; the mandrel's bottom radius is 100 mm; guide roll's bottom radius is 40 mm; the angular velocity of driven roll is 5 rad /s; and the total feed amount of mandrel is 70 mm. The strategy that can realize a RCRRCDS process with a constant ring's outer radius growth rate is adopted, the ring's outer radius growth rate is selected as 5 mm/s. The initial temperature of conical ring blank is selected as 825℃, 850℃, 875℃, 900℃, 925℃, and 950℃, respectively. The dimensions of the conical ring are shown in Fig. 1 (b). The following standard deviation of PEEQ (SDP) and the standard deviation of temperature (SDT) are adopted to evaluate the uniformities of the PEEQ and temperature distributions of rolled rings.

$$\mathrm{SDP}=\sqrt{\frac{\sum_{i=1}^{N}(\mathrm{PEEQ}_i-\mathrm{PEEQ}_a)^2\cdot V_i}{\sum_{i=1}^{N}V_i}} \tag{1}$$

$$\mathrm{SDT}=\sqrt{\frac{\sum_{i=1}^{N}(T_i-T_\mathrm{a})^2\cdot V_i}{\sum_{i=1}^{N}V_\mathrm{i}}} \tag{2}$$

where $\mathrm{PEEQ_a}$ is the average value of PEEQ, $\mathrm{PEEQ_a}=\sum_{i=1}^{N}(\mathrm{PEEQ}_i\cdot V_i)\big/\sum_{i=1}^{N}V_i$, PEEQ_i is the PEEQ of element i, N is the total number of elements of conical ring, V_i is the volume of element i, T_a is the average value of temperature, $T_\mathrm{a}=\sum_{i=1}^{N}(T_i\cdot V_i)\big/\sum_{i=1}^{N}V_i$, T_i is the temperature of element i. The lower the SDP is, the more uniform the PEEQ distribution is. The lower the SDT is, the more uniform the temperature distribution is.

Results and discussion

Fig. 2 shows the PEEQ distributions of rolled rings at the end of rolling process under different the initial temperature of ring blank. It can be seen from Fig. 2, that the PEEQ at outer radius surface layer (OL) and inner radius surface layer (IL) of rolled ring are bigger than that at middle layer (ML), which indicates that the deformation mainly concentrates on the IL and OL of rolled ring. The reason is that the metal at IL and OL of ring are more easily forged penetrated than that at ML.

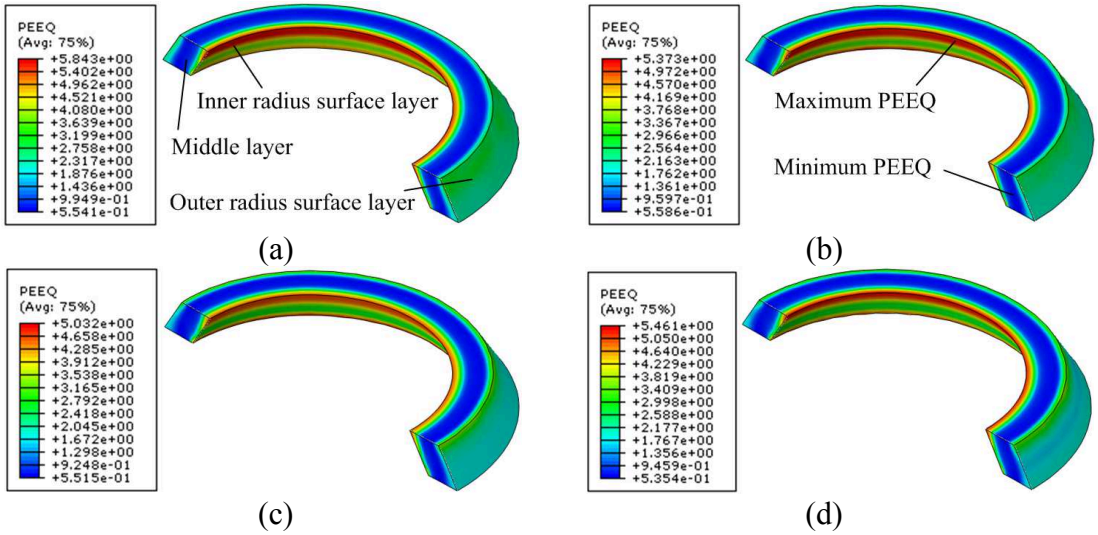


Fig. 2 The effect of initial temperature of ring blank on PEEQ distribution of rolled ring: (a) 825℃; (b) 875℃; (c) 925℃; (d) 950℃

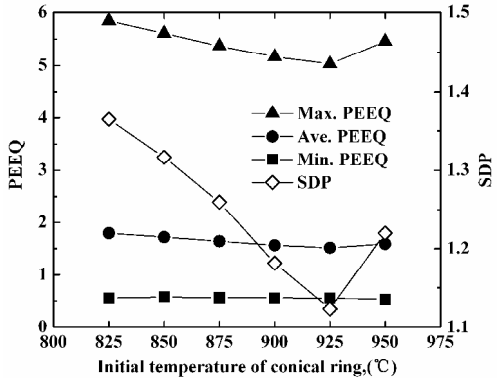


Fig. 3 The changing curves of the maximum, minimum and average PEEQ and SDP with initial temperature of ring blank

Fig. 3 shows the changing curves of the maximum, minimum and average PEEQ and SDP with the initial temperature of ring blank. It can be seen from Fig. 3 that with the increase of the initial temperature of ring blank, both the maximum PEEQ and SDP gradually decrease at first and finally increase; the average PEEQ slightly decreases; and the minimum PEEQ is basically invariable. This

indicates that with the increase of initial temperature of ring, the distribution of PEEQ becomes more uniform at first and then less uniform. The reason is that when the initial temperature of ring increases from 825℃ to 925℃, both the yield strength and deformation resistances gradually decrease and thus the ring is more easily forged penetrated, while when the initial temperature of ring further increases from 925℃ to 950℃, the temperature difference between the conical ring with the rolls and environment increases; the heat loss of conical ring increases; the deformation resistances of the metals on ring's surfaces increase; and thus the ring becomes more hardly deformed.

Fig. 4 shows the temperature distributions of rolled rings at the end of rolling process under different initial temperature of ring blank. With the increase of initial temperature of ring blank, the temperatures at the 'obtuse angle zone' of ring's cross-section are higher than those at other positions all the time; the position that the minimum temperature occurs gradually transfers from the middle part of OL of ring to the bottom of OL. The reason is that: firstly, the large deformation mainly concentrates at IL and OL of rolled ring, which leads to larger deformation heat at these positions. Secondly, suffering the restriction of the top and bottom parts of driven roll, the metals at the top and bottom parts of IL and OL can only deformed along the circumferential direction and radial direction, which leads to the deformations at the top and bottom parts of IL and OL of ring are larger than that at the middle part of IL and OL. Since the specific surface areas at the 'obtuse angle zone' of ring's cross-section are smaller than those at 'acute angle zone', heat losses at 'obtuse angle zone' are less. Thirdly, with the increase of initial temperature of ring, the temperature differences between the conical ring with the rolls and environment enlarge, and thus the heat losses at 'acute angle zone' of cross-section are larger than those at middle part of ring's surfaces. According to the analysis above, the minimum temperature gradually transfers from the middle part of ring's outer surface to the bottom of OL.

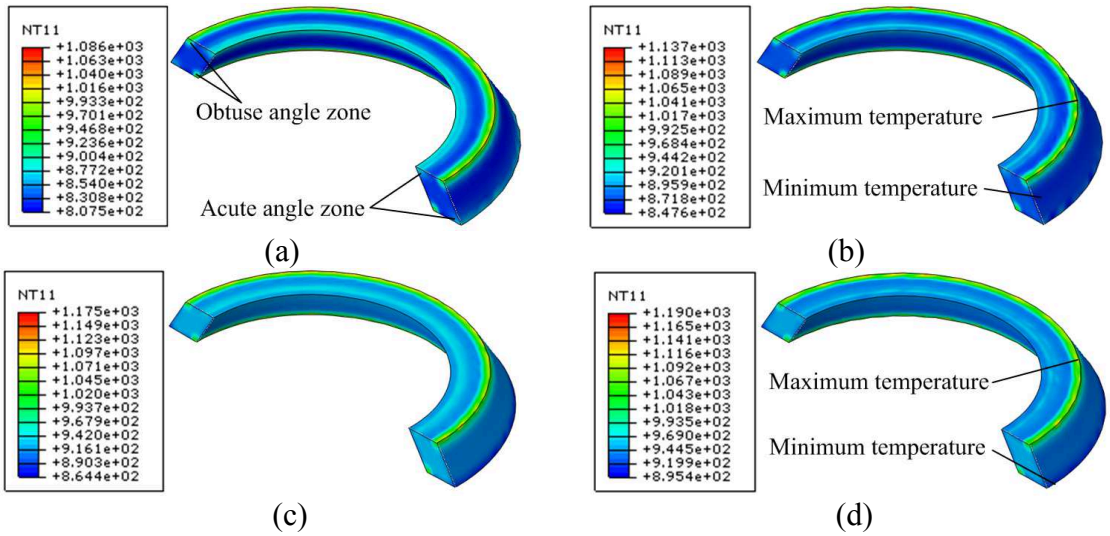


Fig. 4 The effect of initial temperature of ring blank on temperature distribution of rolled ring: (a) 825℃; (b) 875℃; (c) 925℃; (d) 950℃

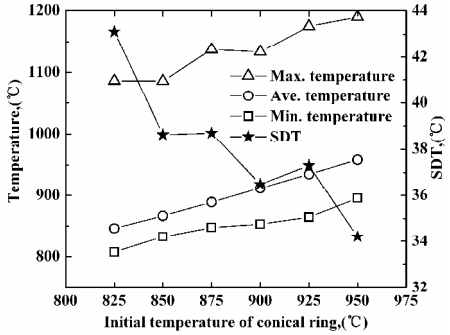


Fig. 5 The changing curves of the maximum, minimum and average temperature and SDT with initial temperature of ring blank

Fig. 5 shows the changing curves of the maximum, minimum and average temperature and SDT with the initial temperature of conical ring. With the increase of initial temperature of ring blank, the maximum, minimum and average temperatures gradually increase while SDT gradually decreases. This indicates that with the increase of initial temperature of ring blank, the distribution of temperature of rolled ring becomes more uniform. The reason is that when the initial temperature of ring is 825℃, the difference between average temperature and maximum temperature is larger than that between average temperature and minimum temperature. With the increase of initial temperature of ring blank, the difference between average temperature and maximum temperature reduces, which make the temperature distribution more uniform; the difference between average temperature and minimum temperature enlarges, which make the temperature distribution less uniform. However, the effect of the former on SDT is larger than that of the latter. Therefore, the temperature distribution of rolled ring becomes more uniform.

From Fig. 3 and Fig. 5, it can be seen that with the increase of the initial temperature of ring blank, SDP gradually decreases from 1.37 to the minimum 1.12 at first and then increases to 1.22; and SDT gradually decreases from 43 to 34. When the initial temperature of ring blank is 925℃, the PEEQ distribution of rolled ring is most uniform and the temperature distribution is relatively more uniform.

Fig. 6 shows the changing curves of average rolling force and average rolling moment with the initial temperature of ring blank. With the increase of the initial temperature of ring blank, both the average rolling force and the rolling moment gradually decreases due to the decrease of the deformation resistances of ring.

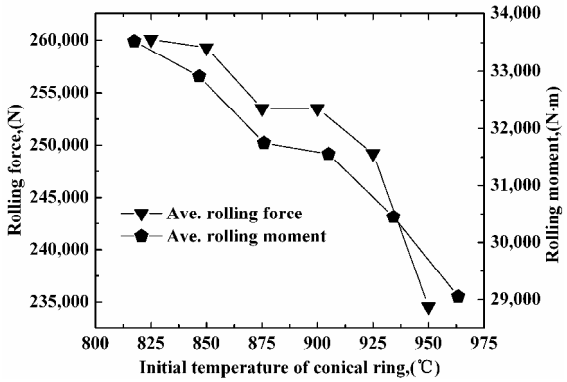


Fig. 6 The changing curves of average rolling force and average rolling moment with the initial temperature of ring blank

Summary

(1) The PEEQ at IL and OL of rolled ring are larger than that at ML. The maximum PEEQ appears at the top part of IL. The temperatures at the 'obtuse angle zone' of ring's cross-section are larger than those at other positions. As the initial temperature of ring increases from 825℃ to 950℃, the minimum temperature appears at middle part of OL of ring at first, and then the position that the minimum temperature occurs gradually transfers to bottom part of OL.

(2) With the increase of the initial temperature of ring blank, the PEEQ distribution of rolled ring becomes uniform at first and then less uniform; the temperature distribution gradually becomes uniform; and both average rolling force and average rolling moment decrease.

(3) When the initial temperature of ring blank is 925℃, the PEEQ distribution of rolled ring is most uniform; the temperature distribution is relatively uniform; and both average rolling force and average rolling moment are relatively small. Therefore, this initial temperature is the optimal temperature for the rolling processes studied in this paper.

Acknowledgements

This research work is supported by Program for Chang Jiang Scholars and Innovative Research Team in University of Ministry of Education of China (No. IRT0931).

References

[1] J. Seitz, V. Jenkouk, G. Hirt, Manufacturing dish shaped rings on radial-axial ring rolling mills, Prod. Eng. Res. Devel., 7 (2013) 611-618.

[2] Z.W. Wang, S.Q. Zeng, X.H. Yang, C. Cheng, The key technology and realization of virtual ring rolling, J. Mater. Process. Technol., 182 (2007) 374-381.

[3] X.H. Han, L. Hua, J. Lan, Z.J. Zuo, G.W. Jia, L.W. Huang, Simulation and experimental study of hot ring rolling of LD10 conical ring with inner steps, J. Wuhan Univ. Technol., 29 (2007) 7-10.

[4] M. Wang, H. Yang, C. Zhang, L.G. Guo, Microstructure evolution modeling of titanium alloy large ring in hot ring rolling, Int. J. Adv. Manuf. Technol., 66 (2013) 1427-1437.

[5] S. Zhu, H. Yang, L.G. Guo, R.J. Gu, Investigation of deformation degree and initial forming temperature dependences of microstructure in hot ring rolling of TA15 titanium alloy by multi-scale simulations, Comp. Mater. Sci., 65 (2012) 221-229.

[6] G. Zhou, L. Hua, J. Lan, D.S. Qian, FE analysis of coupled thermo-mechanical behaviors in radial–axial rolling of alloy steel large ring, Comp. Mater. Sci., 50 (2010) 65-76.

[7] Z.C. Sun, H. Yang, X.Z. Ou, Effects of process parameters on microstructural evolution during hot ring rolling of AISI 5140 steel, Comp. Mater. Sci., 49 (2010) 134-142.

[8] X. Gong, F. Yang, Research of PEEQ for Conical Ring with Outer Steps Ring Rolling, Phys. Proc., 25 (2012) 257-261.

[9] H.L. Yuan, Dorctoral Dissertation for Huazhong University of Science and Technology Wuhan, China, 2006.

[10] R.S. Lee, H.C. Lin, Process design based on the deformation mechanism for the non-isothermal forging of Ti–6Al–4V alloy, J. Mater. Process. Technol., 79 (1998) 224-235.

[11] Z.M. Hu, J.W. Brooks, T.A. Dean, Experimental and theoretical analysis of deformation and microstructural evolution in the hot-die forging of titanium alloy aerofoil sections, J. Mater. Process. Technol., 88 (1999) 251-265.

[12] M. Wang, H. Yang, Z.C. Sun, L.G. Guo, Analysis of coupled mechanical and thermal behaviors in hot rolling of large rings of titanium alloy using 3D dynamic explicit FEM, J. Mater. Process. Technol., 209 (2009) 3384-3395.

Applied Mechanics and Materials Vol. 597 (2014) pp 272-275
© (2014) Trans Tech Publications, Switzerland
doi:10.4028/www.scientific.net/AMM.597.272

Effects of External Magnetic Field on Intensity of Plasma Flow

Ching-Yen Ho[a,*], Yu-Hsiang Tsai[b] and Chuang Ma[c]

Department of Mechanical Engineering, Hwa-Hsia Institute of Technology, Taipei 235, Taiwan

[a]hcy2126@go.hwh.edu.tw, [b]tsaiys@cc.hwh.edu.tw, [c]edma@cc.hwh.edu.tw

*Corresponding author

Keywords: Intensity, plasma, magnetic field.

Abstract. This paper investigates the intensity distribution along the radial direction for plasma flow subject to external magnetic Field. The toroidal external magnetism is applied in the transverse direction of plasma flow. Considering the steady-state continuity and momentum of the plasma flow subject to external magnetic field, the intensity profile of the plasma is obtained. The results quantitatively verify the intensity enhancement of the plasma with the increasing external magnetic field.

1. Introduction

Plasma can be used in materials processing such as plasma surface improvement [1]. Intensity and distribution of plasma flow play important roles on the quality and efficiency for surface modification [2]. Intensity and distribution of plasma flow can be controlled by an applied strong magnetic field. Therefore this paper analytically studies the intensity enhancement of plasma flow subject to an applied strong magnetic field

In recent, many studies have been focused on advanced applications of plasma flow such as materials deposition processing and propulsion system in space mission. It is well known that plasma flow has attractive characteristics such as high enthalpy. Since plasma is also a typical functional fluid in the magnetic field, it is possible to control flow characteristics with E×B force. Therefore, the plasma applications could be expanded to wider fields of engineering and technology if strong magnetic field could be utilized for enhancing the functions of plasma flow. To realize the progress of the application, it is necessary to understand the fundamental aspects of plasma flow behavior under the strong magnetic field.

Experimental studies have been conducted to investigate the effects of the magnetic field on the enhancement of plasma intensity [3]. Results show that the plasma flow constricts with the increasing magnetic field and that the excitation temperature based on emission spectroscopy rises around the central portion of the plasma flow. In these studies, the effects of magnetic field on the enhancement of intensity for plasma flow are analytically examined.

2. Analysis

Considering free expansion plasma subject to a toroidal magnetic field, the equations of continuity and motion for the ions fluid follow as

$$(\frac{\partial}{\partial t}+\mathbf{u_i}\bullet\nabla)n_i=-n_i\nabla\bullet\mathbf{u_i}+\nu_i n \tag{1}$$

$$m_i n_i(\frac{\partial}{\partial t}+\mathbf{u_i}\bullet\nabla)\mathbf{u_i}=en_i(\mathbf{E}+\mathbf{u_i}\times\mathbf{B}) \tag{2}$$

For plasma subject to a toroidal magnetic field B with the curvature radius R_c, Electrons and ions drift in opposite direction, and the charge separation (polarization) induces a vertical electric field $\boldsymbol{E}$,

which eventually causes the $\boldsymbol{E} \times \boldsymbol{B}$ outward drift of plasma. The flux perpendicular to $\boldsymbol{B}$ is given as

$$n\mathbf{u} = \frac{nq}{mf(1+\Omega^2/f^2)}\mathbf{E} + \frac{kT}{mf(1+\Omega^2/f^2)}\nabla n + n\left(\frac{\mathbf{E}\times\mathbf{B}}{B^2} - \frac{kT\nabla n\times\mathbf{B}}{nqB^2}\right)/\left(1+\frac{f^2}{\Omega^2}\right) \tag{3}$$

where the symbols n, q, m, f, Ω, k, T *and* B correspondingly represent the plasma density, charge, mass, collision frequency, cyclotron frequency, Boltamann constant, temperature and scalar of magnetic field. The vectors $\boldsymbol{u}$, $\boldsymbol{E}$ and $\boldsymbol{B}$ denote velocity, electric field and magnetic field, respectively.

Considering a simple case of strong magnetic field ($\Omega >> f$) and high drift velocity ($\frac{\mathbf{E}\times\mathbf{B}}{B^2} >> \frac{kT\nabla n\times\mathbf{B}}{nqB^2}$), introducing Cartesian coordinate (x, y, z) with the magnetic field B along the z axis (toroidal direction) and the electric field E along the y axis (vertical direction), and assuming the variation of plasma density only with the x direction (major radius direction), then we obtain the x- and y-components of ion flux ($q = e$) from Eq. (3)

$$nu_x = n\left(\frac{E}{B}\right) - \frac{kT}{mf(1+\Omega^2/f^2)}\frac{dn}{dx} \tag{4}$$

$$nu_y = \frac{nq}{mf(1+\Omega^2/f^2)}E \tag{5}$$

where the weak dependence of T, B and E on the position x is neglected.

Ambipolar process generally governs the ion and electron transport. As demonstrated in the experimental observation [4], the plasrna potential is nonnegative (~$2T_e$ [eV]) against the wall potential in a toroidal magnetic field. This means that the electron loss flux (mainly along B) is faster than the ion loss flux (mainly across B). Since the slower loss process (ion diffusion across B) determines the overall diffusion.

Substituting the ion flux into the continuity equation, we obtain the plasma density n in steady state from the following differential equation.

$$\frac{kT}{mf(1+\Omega^2/f^2)}\frac{d^2n}{dx^2} - \left(\frac{E}{B}\right)\left(\frac{dn}{dx}\right) + \nu_i n = 0 \tag{6}$$

where ν_i is the ionization frequency which is the product of the gas density and the ionization rate constant. The ionization rate constant depends on the electron temperature T_e [5].

Using the boundary conditions, $n = n_0$ at $x = 0$ (the major radius position $R = R_0$) and $n = 0$ at $x = a$ (the outer wall at $R = R_0 + a$). We examine the influence of $\boldsymbol{E} \times \boldsymbol{B}$ drift on the density profile. Eq. (6) gives the following plasma density profile as a function of the normalized position $\xi = x/a$

$$\frac{n(\xi)}{n_0} = \exp\left\{\left[\frac{G}{2H}\left(1-\sqrt{1-\frac{4H}{G^2}}\right)\right]\xi\right\} - \exp\left\{\left[\frac{G}{2H}\left(1+\sqrt{1-\frac{4H}{G^2}}\right)\right]\xi - \frac{G}{H}\sqrt{1-\frac{4H}{G^2}}\right\} \tag{7}$$

where the G and H are the convection parameters ($G=E/Ba\,\nu_i$) and the diffusion parameter ($H=kT/[mf(1+\Omega^2/f^2)a^2\nu_i]$), respectively.

In typical experimental conditions where $G^2>>4H$, the density profile as

$$\frac{n(\xi)}{n_0} = \exp(\frac{\xi}{G}) - \exp[\frac{G}{H}(\xi - 1)] \tag{8}$$

where the first term on the right hand side shows an exponential increase of density along the $\boldsymbol{E} \times \boldsymbol{B}$ plasma flow, and the second term provides a diffusion loss to the wall at $\xi = 1$.

3. Results and discussion

This paper analytically investigates intensity enhancement of plasma subject to a toroidal magnetic field. Figure 1 shows the effects of magnetic field on the plasma density profile. The increase of magnetic field strength leads to the small ratio of electric field to magnetic field for fixed E, a and ν_i. From Fig.1, it is found that the small ratio of electric field to magnetic field results in the high peak value. Therefore the strong magnetic field enhances the plasma density. This result agrees with the measured data by Koike et al [6]. This also means that the plasma density is more uniform along the radial direction for plasma flow subject to the low or without magnetic field. However the strong magnetic field acting on plasma flow gives the enhancement of plasma density.

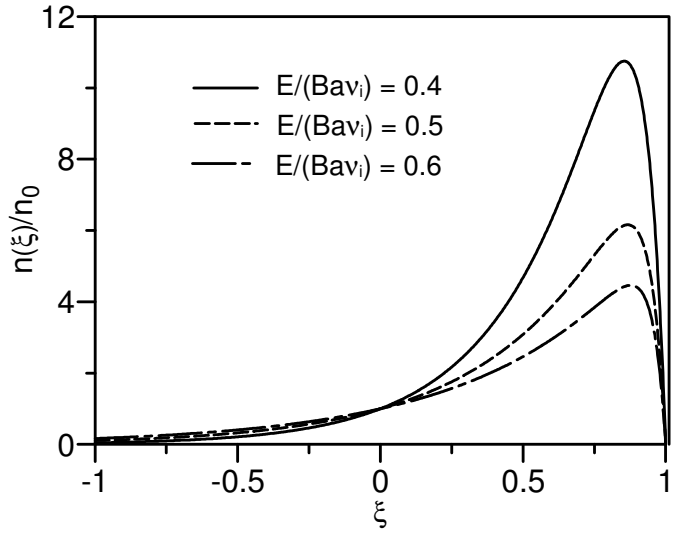


Fig. 1. Variation of plasma density with radial position for different ratios of electric field to magnetic field.

The variation of plasma density with radial position for different diffusion parameters is plotted in Fig. 2. The maximal plasma density decreases with the increasing diffusion parameters and moves toward radial centre. This also means that the increase of thermal energy or the decrease of collision frequency, cyclotron frequency and ionization frequency reduces the peak value of plasma density and makes the peak of plasma density shift to radial centre.

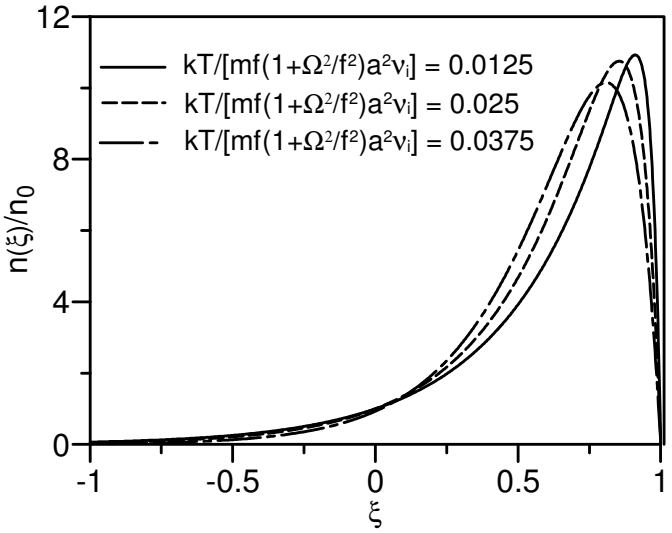


Fig. 2. Variation of plasma density with radial position for different diffusion parameters.

4. Summary

The results indicate that the intensity distribution of plasma is more uniform but the maximal intensity is lower for the smaller applied magnetic field. The peak value of intensity profile of plasma flow subject to a toroidal magnetic field decreases and shifts to the radial centre with the increasing diffusion parameters.

References

[1] M. Ueda, R.M. Oliveira, J.O. Rossi, C.B. Mello, Rita C.C. Rangel and M.S. Vieira, "Improvements of plasma immersion ion implantation (PIII) and deposition (PIII&D) processing for materials surface modification," Surface & Coatings Technology, http://dx.doi.org/10.1016/j.surfcoat.2012.06.057.

[2] V.N. Zhitomirsky, R.L. Boxman, S. Goldsmith, Surface & Coatings Technology 185 (2004) 1-11.

[3] N. Ono, K. Musha and K. Koike, JSME International J. 48B (2005) 411–416.

[4] K. Rypdal, A. Fredriksen and O.M. Olsen, Phys.Plasmas 4 (1997) 1468.

[5] M.A. Lieberman and A.K. Lichtenberg, Principles of Plasma Discharges and Materials Processing , John Wiley & Sons, p.80, 1994.

[6] K. Koike, N. Ono, Vacuum 83 (2009) 25–28.

Applied Mechanics and Materials Vol. 597 (2014) pp 276-279
© (2014) Trans Tech Publications, Switzerland
doi:10.4028/www.scientific.net/AMM.597.276

Formation and distribution mechanism of intermetallic compounds of Al/Mg joint with Zn transition metal

Qiong Gao[1, a], Kehong Wang[1, b *], Heng Ma[1, c] and Weiguo Feng[1, d]

[1]School of Materials Science and Engineering, Nanjing University of Science and Technology, Nanjing 210094, China

[a]gqiong88@163.com, [b]wkh1602@126.com, [c]maheng28923@163.com, [d]njustfwg@163.com

Keywords: Intermetallic compounds (IMCs), Mg/Al joint, Zn transition metal

Abstract. 6061 Al alloy and AZ31B Mg alloy were joined by lapping TIG welding process with Zn transition metal. Microstructrues and Micro-hardness in the fusion near the Mg substrate were examined. The formation and distribution mechanism of IMCs of Al/Mg joint, and the relationship of microstructure and mechanical property were discussed. The introduction of Zn transition metal reduces the Mg/Al IMCs effectively. The microstructure in the fusion zone near the Mg substrate composes of three regions. B zone contains of only $MgZn_2$ IMCs. That is the place of highest micro-hardness in the weld seam. A and C zones characterize with solid solution precipitated on the $MgZn_2$ basement which can enhance the ductility of Mg/Al joint. This result indicates that the distribtution of IMCs in the interfacial layer affected property of Mg/Al joint.

Introduction

Magnesium and Aluminum alloys, as the lightweight materials, are extensively employed in automotive, aircraft and electronics industries because of their energy-saving and various unique properties [1,2]. Therefore, the research on welding the dissimilar Mg-Al has been widely studied, which meant to reduce the weight of the structure [3].

However, the dissimilar welding of Mg/Al is difficult, since it always produces massive brittle intermetallic compounds and coarse crystalline in the welded joint, which will degrade the performances of welded joints seriously [4]. Hence, researchers have paid much attention in controlling the production of Mg/Al IMCs by a variety of welding methods [5,6,7]. As we known, alloying is effectively to improve the strength of material. In previous reports, zinc, as an alloying element, was added in the Mg-Al dissimilar joint to decrease the formation of Mg-Al IMCs. [8, 9]. Nevertheless, fundamental scientific understanding is still lacking, the further exploration is necessary. In this paper, we propose to join 6061 Al alloy to AZ31B Mg alloy with zinc foil by lapping TIG welding process, and attempt to present the formation and distribution of IMCs of Mg-Al joint. Furthermore, the relationship between microstructure and mechanical property is discussed in detail.

Experimental procedure

The materials used in the experiment were AZ31B magnesium and 6061 aluminum alloys with both dimensions of 4mm×50mm×110mm. The chemical compositions of base metals are respectively shown in Tables 1. The pure zinc foil was added between Mg and Al alloys with thickness of 0.4mm. Before welding, the oxide films (Al_2O_3, MgO) on the surface of base specimens and foil must be eliminated. A lap joint configuration was utilized with the Al alloy on the Mg plate shown in Fig. 1. The acute angle α is 15° between TIG torch and perpendicular line. The pre-optimized welding parameters were welding current of 180A, welding voltage of 18.9V, and the welding speed of 50 cm/min.

After welding, the welded specimen was cross-sectioned by linear cutting machine for microstructure observed. The Mg alloy side of the joints was etched in a solution of 1g oxalic acid+1mL nitric acid+1mL acetic acid+150mL distilled water. The Al alloy side was etched in 10% sodium hydroxide solution corrosion. The microstructures of joints were observed and analyzed by

SEM (FEI Quanta 250F environment scanning electronic telescope) equipped with energy dispersive X-ray spectrometer (EDS). The element distribution and phase constituents of the weld metal were measured by EDS and XRD (Bruker D8 X-ray diffractometer) respectively. The micro-hardness tests were carried out by a Vickers hardness tester (HVS-1000Z) with 0.98N load and a dwell time of 10s.

Table 1. Chemical compositions [wt. %] for AZ31B and 6061 alloys

Material	Al	Zn	Mn	Si	Fe	Cu	Ca	Cr	Mg	Other
AZ31B	2.5-3.5	0.6-1.4	0.2	0.1	0.005	0.05	0.04	—	Bal	0.3
6061	Bal	0.250	0.15	0.4-0.8	0.7	0.15-0.4	—	0.04-0.35	0.8-1.2	0.15

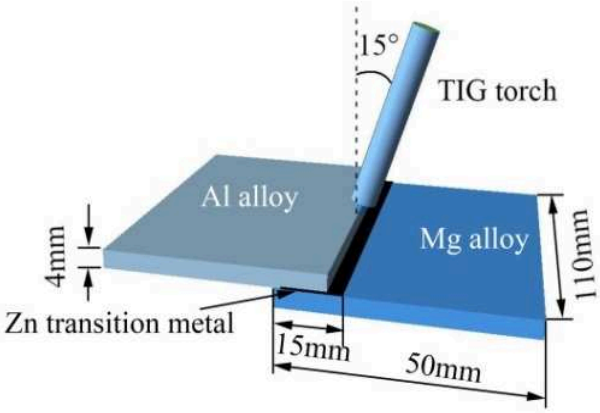


Fig. 1 The configuration and dimensions of the lapping TIG welding

Results and discussion

Microstructures in the fusion zone. The overall microstructure of the joint is shown in Fig. 2(a), in which can distinctly find out some air holes occasionally scattered over the weld metal. That is due to the low boiling temperature and melting point of zinc, resulting in zinc evaporation during welding. Moreover, it can be seen that a thin intermetallic compound layer was formed at the interface between the fusion zone and the Mg substrate, which consists of different three parts marked with *A*, *B*, and *C*. The Fig. 2(b), (c), (d) shows the high magnification of the *A*, *B*, and *C* zones. X-ray diffraction analysis was performed to determine the phase constituents of the fusion zone near Mg substrate, as illustrated in Fig. 3. In *A* zone, it mainly characterizes with equiaxed crystals instead of columnar coarse grains, which is beneficial to the property of welded joint. According to EDS analysis and X-ray diffraction analysis in Fig. 3, *A* zone consists of 44.94 wt-%Mg, 8.82 wt-%Al, 46.25 wt-%Zn, it can be concluded that it is Mg-Zn hypoeutectic structure composed of Mg-based solid, Zn-based solid solution and $MgZn_2$ IMCs. The microstructural feature of *B* zone, shown in Fig. 3(c), is cellular grains, which contains 25.72 wt-%Mg, 18.79 wt-%Al, 55.48 wt-%Zn. It's obvious that the content of Al increases with the decrease in Mg. Accordingly, the phase in *B* zone is $MgZn_2$ and a little Al-based solid solution. In Fig. 2(d), the gray dendrite crystal marked 1 and white splendid lamellar eutectic structure marked 2 are seen in *C* zone. The composition percentage of the gray dendrite crystal is 6.5 wt%-Mg, 85.25 wt%-Al, 8.24 wt%-Zn, which can be Al-based solid solution. Meanwhile, the eutectic structure' constituents are 10.43 wt%-Mg, 37.02 wt%-Al and 50.48 wt%-Zn. Based on the Al-Mg-Zn ternary phase diagram, it suggests that the splendid eutectic structure are Zn-based solid solution, Al-based solid solution and $MgZn_2$ compound.

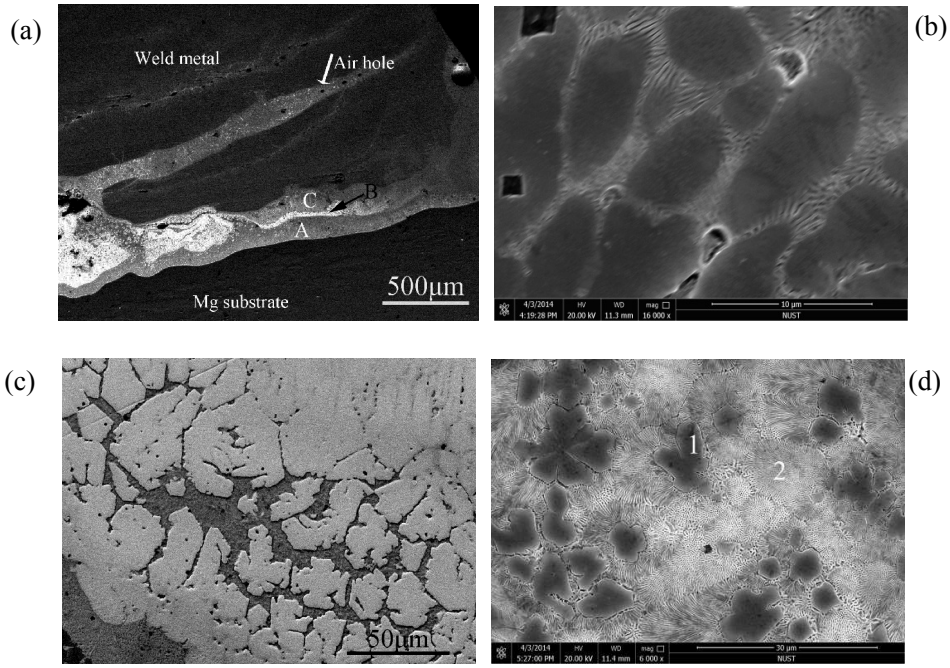


Fig. 2 (a) Overview of welded joint (b) Microstructural feature of *A* zone (c) Microstructural feature of *B* zone (d) Microstructural feature of *C* zone.

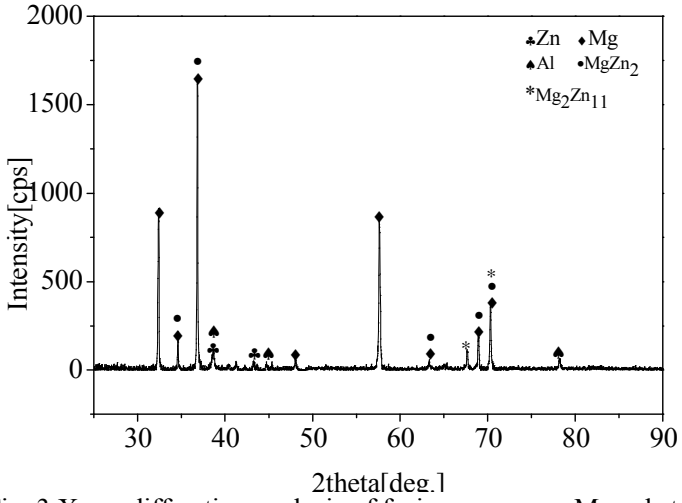


Fig. 3 X-ray diffraction analysis of fusion zone near Mg substrate

Micro-hardness analysis. The micro-hardness distribution not only can reflect the mechanical properties of the joint, but also can display the structure evolution of the fusion zone. The micro-hardness on the weld joint was measured along the path (b) in Fig. 4(a), which is shown in Fig. 4(b). The micro-hardness from Mg side to fusion zone increases sharply and the maximal values are 198 HV, which is higher than that of the Mg substrate (55HV). The results indicate the creation of hard brittle intermetallic phase in the fusion zone. It leads to the increase in the strength and the deterioration of the ductility.

As we discussed previous, the fusion zone near Mg side was divided into three parts. The corresponding micro-hardness is marked in Fib. 4(b) with A, B, and C. Obviously, Micro-hardness in B zone is the highest among the three zones. A and C zone's micro-hardness is lower than B zone's. That is because only $MgZn_2$ IMCs in B zone improve the brittleness. The B zone is preferred fracture path. However, solid solution precipitated on the $MgZn_2$ basement in A, C zones strengthening the ductility of the joint. In a conclusion, increasing the solid solution on IMCs can improve the toughness of Mg/Al joint.

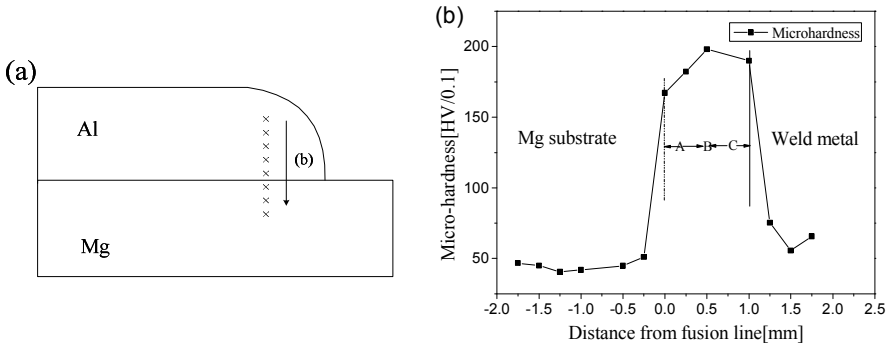


Fig. 4 (a) Micro-hardness distribution illustration diagram (b) Micro-hardness profile of the joint from weld metal to Mg substrate

Summary

(1) AZ31B Mg and 6061 Al alloys were successfully welded by lapping TIG welding process with Zn transition metal. The addition of Zn transition metal can effectively reduce the formation of Mg/Al intermetallic compounds.

(2) The microstructure of fusion zone near Mg substrate consists of three zones. *A* zone, near Mg substrate, existed Mg (Zn) solid solution and $MgZn_2$ intermetallic. *B* zone composed of $MgZn_2$ cellular grains. *C* zone contained Al (Zn) solid solution and $MgZn_2$ intermetallic.

(3) The distribution of IMCs in the interfacial layer affected the micro-hardness. The micro-hardness was lower when the region composed of solid solution precipitated on the $MgZn_2$ basement. This result indicates that increasing the solid solution on IMCs can improve the toughness of Mg/Al joint.

References

[1] Y.J. Kwon, I. Shigematsu, N. Saito, Dissimilar friction stir welding between magnesium and aluminium alloys. Mater.Lett. 62 (2008) 3827-3829.

[2] P. Liu, Y. Li, H. Geng, J. Wang, Microstructure characteristics in TIG welded joint of Mg/Al dissimilar materials, Mate.Lett. 61 (2007) 1288-1291.

[3] J. Shang, K. Wang, Q. Zhou, D. Zhang, J. Huang, G. Li, Microstructure characteristics and mechanical properties of cold metal transfer welding Mg/Al dissimilar metals, Mater. Des. 34 (2012) 559-565.

[4] Y.S. Sato, S.H.C. Park, M. Michiuchi, H. Kokawa, Constitutional liquation during dissimilar friction stir welding of Al and Mg alloys, Scripta Mater. 50 (2004) 1233-1236.

[5] A. Kostka, R.S. Coelho, J. dos Santos, A.R. Pyzalla, Microstructure of friction stir welding of aluminium alloy to magnesium alloy, Scripta Mater. 60 (2009) 953-956.

[6] J. Wang, J.C. Feng, Y.X. Wang, Microstructure of Al–Mg dissimilar weld made by cold metal transfer MIG welding, Mater. Sci.Technol. 24 (2008) 827-831.

[7] U. Suhuddin, V. Fischer, F. Kroeff, J.F. dos Santos, Microstructure and mechanical properties of friction spot welds of dissimilar AA5754 Al and AZ31 Mg alloys, Mater. Sci. Eng.: A. 590 (2014) 384-389.

[8] F. Liu, Z. Zhang, L. Liu, Microstructure evolution of Al/Mg butt joints welded by gas tungsten arc with Zn filler metal, Mater. Charact. 69 (2012) 84-89.

[9] H.T. Zhang, J.Q. Song, Microstructural evolution of aluminum/magnesium lap joints welded using MIG process with zinc foil as an interlayer, Mater. Lett. 65 (2011) 3292-3294.

CHAPTER 5:

Applied Mechanics and Construction Engineering

Applied Mechanics and Materials Vol. 597 (2014) pp 283-290
© (2014) Trans Tech Publications, Switzerland
doi:10.4028/www.scientific.net/AMM.597.283

Concrete Strength Variability in Italian RC Buildings: Analysis of a Large DataBase of Core Tests

Angelo Masi[1,a], Andrea Digrisolo[1,b] and Giuseppe Santarsiero[1,c]

[1]University of Basilicata, via dell'Ateneo Lucano, 10, 85100 Potenza (Italy)

[a]angelo.masi@unibas.it, [b]digrisolo.a@hotmail.it, [c]giuseppe.santarsiero@unibas.it

Keywords: Existing RC buildings, in-situ concrete strength, concrete cores.

Abstract. The knowledge of the materials' mechanical properties is a preliminary and important step in the seismic vulnerability assessment of existing buildings. In RC structures, the compressive strength of concrete can have a crucial role on the seismic performance and is usually difficult to estimate. Major seismic codes prescribe that concrete strength has to be determined essentially from in-situ and laboratory tests. In some cases such estimation can be complemented by default values in accordance to standards at the time of construction, therefore analysing the actual concrete properties typically found in RC existing buildings realized in different periods can make available useful data. To this end, in this paper attention has been addressed to public buildings, namely schools and hospitals. A large database made up of about 1500 test results on concrete cores extracted from about 300 RC public buildings located in Basilicata region (Italy), has been prepared and analysed. The relationships between the actual strength values (mean and dispersion) and the construction period of buildings have been studied. Theoretical distributions to approximate the discrete distributions of strength values in different construction periods have been determined, thus providing relevant data for the structural assessment of individual buildings and, especially, for large scale vulnerability evaluations.

Introduction

In earthquake-prone countries like Italy, where seismic events often cause heavy damage to residential and public buildings [1, 2], risk mitigations actions are more and more important in order to limit human and economic loss. To this end, vulnerability assessment of buildings plays an important role both to define suitable timescales for the strengthening interventions (dealing with large scale programs) and to choose effective retrofit strategies. The first step in assessing vulnerability is the knowledge of the mechanical properties of the constituent materials. The current European and Italian seismic codes [3, 4] foresee different knowledge levels (KLs) to which different confidence factors (CFs) are related. International codes like FEMA 356 [5] consider not only the mean value on the concrete strength but also the coefficient of variation (C.V.) that accounts for dispersion of data. While, contrarily to the Italian code, FEMA 356 does not consider the minimum number of tests to be performed as a function of the floor area of the building at hand.

As a rule, the main codes base the safety verifications on the mean value of concrete strength, therefore it appears interesting to analyse the variability of the mechanical properties of concrete found in a great deal of public buildings located in Basilicata region. Data available is analyzed in terms of mean values and related dispersion, with the main aim of providing reference values (mean and range) as a function of the building age.

The role played by concrete strength is not so influencing performance of RC structural members affected by ductile mechanisms, such as the flexural one. Conversely, fragile mechanisms as shear failure of members or joints can be strongly influenced by concrete strength, especially for buildings not provided with anti-seismic details, as most of the existing buildings designed only to gravity loads. Therefore, the knowledge of the expected values of concrete strength can be important in the structural assessment of individual buildings, as well as when dealing with studies aimed at defining timescales for seismic intervention in public buildings at large scale (local or national). Besides, performing vulnerability assessments based on an accurate knowledge of material properties contributes to give useful indications on insurance issues related to seismic risk.

In this context valuable studies [6] highlighted the spatial distribution of seismic risk at national scale providing risk maps based on the hazard maps developed in [7], as also reported in [8]. Structural vulnerability was evaluated on the basis of the material properties proposed in [9, 10] where mean and standard deviation values of the concrete strength of RC buildings realized before 1970 are provided. These mechanical properties were derived from compression tests on concrete cubes at the Laboratory of Testing Materials of the University of Naples performed in the framework of the routine controls prescribed during the construction of new buildings. Strength values evaluated in this way cannot account for the likely difference between actual in-situ strength and laboratory test results.

The availability of a database (DB) of strength values directly obtained from cores extracted from real structures can provide, instead, a more reliable and up to date knowledge of the strength in as-built buildings accounting for also possible variations due to time and degradation effects. In this framework, some authors [11] dealt with the data obtained from a wide survey campaign on public buildings of the Toscana region, Italy. This DB, relevant to about 400 buildings from which about 1500 concrete cores were extracted, represents a remarkable reference in estimating concrete properties at local level. Its analysis [12] provides a picture of the current state of buildings related to their period of construction. Analysis of main results shows that about 65% of the buildings constructed before 1960 have mean concrete strength less than 12MPa, while for buildings constructed from 1960 to 1972 this percentage goes down to 34% and, finally, this percentage drops to 15% for buildings constructed after 1972.

In other works aimed at the evaluation of concrete compression strength [13], data relevant to concrete cores extracted from RC structures located in Basilicata region, Italy, whose construction period ranges between 1940 and 1990, were examined. From this DB, mean values and variability of concrete strength in each period were determined. Besides, for each period the expected strength ranges were hypothesized selecting the more probable values to assign to each period by referring to the structural codes in force, the structural handbooks and the commonly adopted design and construction practices at the time.

In the present study the work started in [13] is upgraded firstly enlarging the buildings' portfolio from which concrete data is obtained, thus allowing the construction of a DB that represents a valuable set of information on the current strength of concrete in Italian structures. Besides the evaluation of the strength values in different periods, the Lognormal and Normal probability distributions well fitting the experimental data have been obtained. In order to check the goodness of these curves, some statistical tests have been carried out, such as the Kolmogorov-Smirnov test.

It is worth noting that the strength distributions obtained in the present study can be effectively used to perform large scale risk analyses, such as the study in [6], but based on more reliable assumptions concerning expected concrete strength, in terms of mean values and variability, at different periods. Further, when performing structural assessment on individual buildings, these distributions can complement the knowledge process in estimating concrete properties. In fact, as reported in EC8 – Part 3, in order to reach a knowledge level KL1, it is possible to associate data obtained from limited in-situ testing with default values in accordance with the standards of the time of construction.

Analysis of the database

The DB analyzed in the present study has been collected during the large campaign of seismic vulnerability assessments of public buildings located in Basilicata region that was carried out by the local government in execution of the national law OPCM 3274/2003 [14]. The campaign initially involved strategic buildings, such as hospitals, and buildings with considerable risk in case of collapse, such as schools. Data under study is made up of the compression test results on concrete cores extracted from the buildings under assessment. Therefore, note that the structural members (beam, column or wall) and the location from which core specimens were extracted were chosen from the professionals in charge for the assessment activities. The results of the compression tests in

terms of concrete strength are reported in the test certificates also including basic information on the core specimens (location in each structure, height, diameter, specific weight, etc.).

The DB contains results of compression tests on 1557 concrete cores extracted from 333 buildings, 275 of which are schools and 58 are hospitals, thus providing a wide data source on the actual concrete properties of as-built RC public buildings. Unclear or unreliable data were discarded. The main data obtained from the compression test on core specimens is the ultimate strength. As well known [15], this strength value can be different from the in situ strength as a consequence of some factors influencing core strength such as the h/D (height/diameter) ratio, the possible presence of rebars, the damage occurred during the extraction, etc. Therefore, in the first step of the study, strength values representative of the in situ concrete quality have been determined. After, based on these values, the influence of the construction period on concrete properties has been investigated.

Conversion of core strength to in situ strength. In order to correct strength values directly achieved on core specimens, possibly different from in situ strength, and thus obtaining comparable results, the core strength values f_{core} have been converted in the corresponding in situ strength f_c through the following relationship [15]:

$$f_c = (C_{h/D} \cdot C_{dia} \cdot C_a \cdot C_d) \cdot f_{core} \quad (1)$$

where:

- $C_{h/D}$ is the correction coefficient for h/D ratios different from 2 and equal to $C_{h/D} = 2/(1.5 + D/h)$;
- C_{dia} is the diameter correction coefficient, to be assumed equal to 1.06, 1.00 e 0.98 for D equal, respectively, to 50, 100 and 150 mm;
- C_a is the correction coefficient accounting for presence of rebars in the core, ranging from 1.03 for small diameter bars (ø 10) to 1.13 for large diameter bars (ø 20).
- C_d is the correction coefficient to account for the damage occurred during the extraction operations. FEMA 274 [16] suggest of assuming a constant value equal to 1.06, while literature often proposes to assume 1.10, in both cases only if the extraction is carefully carried out by experienced operators. However, taking into account that the lower the as-built concrete quality the larger the drilling damage, it appears more accurate to put C_d = 1.20 if $f_{car} < 20$ MPa, and $C_d = 1.10$ per $f_{car} > 20$ MPa.

The correction deriving from Eq. (1) has been made on the entire set of concrete strength values and the resulting values have been used in the following analyses.

Variability due to construction period. The analysis here made aims at putting in relationship the strength values and the construction period of the buildings from which the cores are extracted. To this end, the whole range of construction periods at hand has been subdivided into some sub-periods (hereafter periods) coincident with the main changes in the building regulation in force in Italy. As a result, the following periods have been defined: <1961; 1961–1971; 1972–1981; >1981.

The diagrams in Fig. 1 displays the main statistical values for the in situ concrete strength with respect to each of the selected construction periods. The same data is summarized in Tab. 1. Most of the cores and, then, of the buildings have been built between 1961 and 1981, specifically 77% of the cores and the 72% of the buildings fall in this range.

The results displayed in Fig. 1 and reported in Tab. 1 show that concrete strength (both mean and median values) averagely increases in more recent construction periods, while the same regular trend cannot be found for dispersion values such as standard deviation and coefficient of variation. Mean concrete strength (Fig. 1c) increases from 16.23 MPa in RC structures built before 1961 to 24.96 in structures built after 1981, with a percentage increment larger than 50%. The coefficient of variation relative to the same periods (Fig. 1f) decrease from 0.39 to 0.32 thus showing a remarkable improvement of the concrete quality over time.

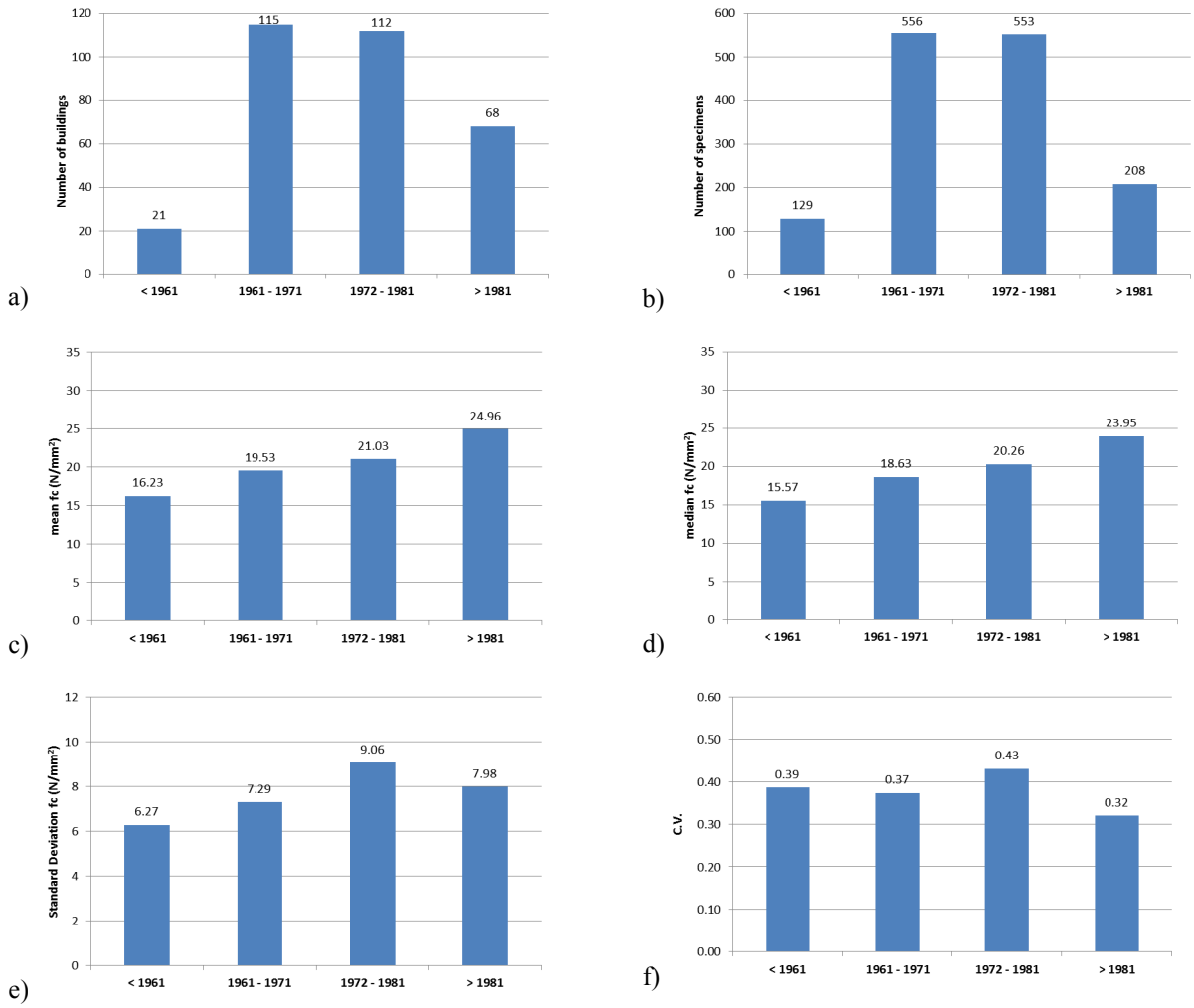


Fig. 1: Main statistical values for the concrete strength in the four identified periods: a) Number of buildings, b) Number of specimens, c) Mean values, d) Median values, e) Standard Deviations, f) Coefficients of Variation (C.V.).

Table 1: Main statistical values of concrete strength in different construction periods.

Statistical values	Construction period			
	<1961	**1961 – 1971**	**1972 – 1981**	**>1981**
Number of buildings	21	115	112	68
Number of specimens	129	556	553	208
Mean number of specimens per building	5.9	4.9	4.9	3.1
Mean value (N/mm^2)	16.23	19.53	21.03	24.96
Median value (N/mm^2)	15.57	18.63	20.26	23.95
Standard Deviation	6.27	7.29	9.06	7.98
C.V.	0.39	0.37	0.43	0.32

Taking into account the changes in the Italian building code, the suggestions provided in the most used design handbooks and the usual design practice, some tentative default values of concrete strength can be identified for each of the considered periods [13]. Before 1972 the structural code in force was the R.D. 2229 released in 1939 [17]. This code prescribed mean cube strength values R_{cm} starting from a minimum of 120 kg/cm^2 (about 12 MPa). Higher strength concretes were also covered as, for example, having cube strength equal to 160 kg/cm^2. When the D.M. 30 May 1972 [18] came into force in 1972 the reference strength values were represented by characteristic cube

values R_{ck} measured after 28 days of curing. The most common concrete class was $R_{ck}25$ (25 MPa). In the years after 1981, due to the larger presence of zones seismically classified as a consequence of the 1980 Irpinia earthquake, greater attention was devoted to materials' quality and higher strength values were averagely required.

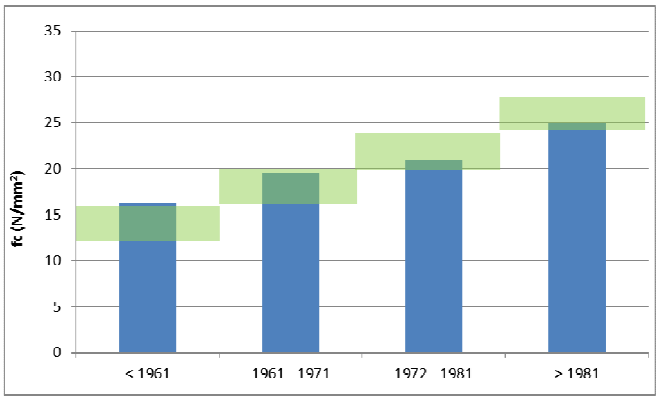


Fig. 2: Comparison between experimental mean values and expected default ranges of values (green).

Summarizing, expected maximum and minimum values of the cylinder concrete strength for each construction period can be defined. In Fig. 2 these default ranges have been compared with the mean values obtained from the DB under study. As can be seen, the mean experimental values substantially agree with the proposed default ranges generally providing larger values, except for the period < 1961 where the expected values are slightly lower than those obtained from the DB.

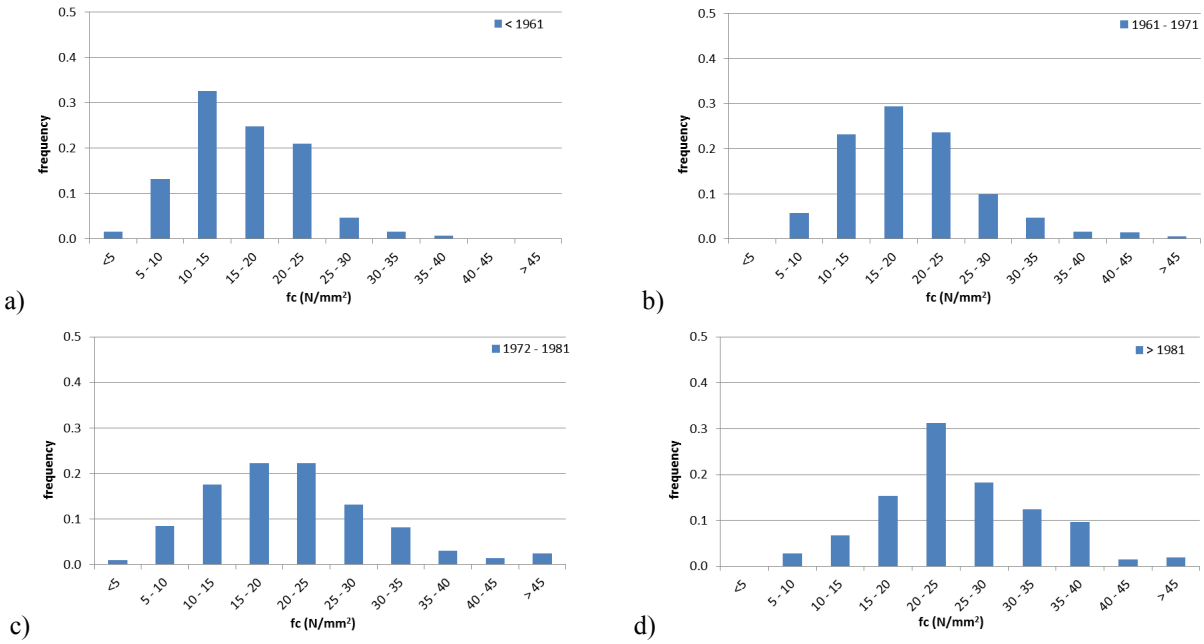


Fig. 3: Frequency distributions of concrete strength for each construction period: a) <1961, b) 1961-1971, c) 1972-1981, d) >1981.

To better analyse the variation of strength values within each construction period, the strength values displayed in Fig. 1 have been disaggregated splitting them into strength intervals for each construction period. Considering strength intervals with an amplitude of 5 MPa, Fig. 3 shows the frequency distributions (histograms) relevant to each construction period. As expected, histograms in Fig. 3 confirm the increment of concrete strength over time.

It is worth noting that the distributions appear rather regular and, thus, suitable to be approximated with theoretical continuous frequency distributions. To this end, some probability distributions widely used in engineering practice have been considered, namely the Normal and the

Lognormal distribution. Fig. 4 displays the comparison between experimental histograms and theoretical distributions (Normal and Lognormal) whose parameters are reported in Tab. 2.

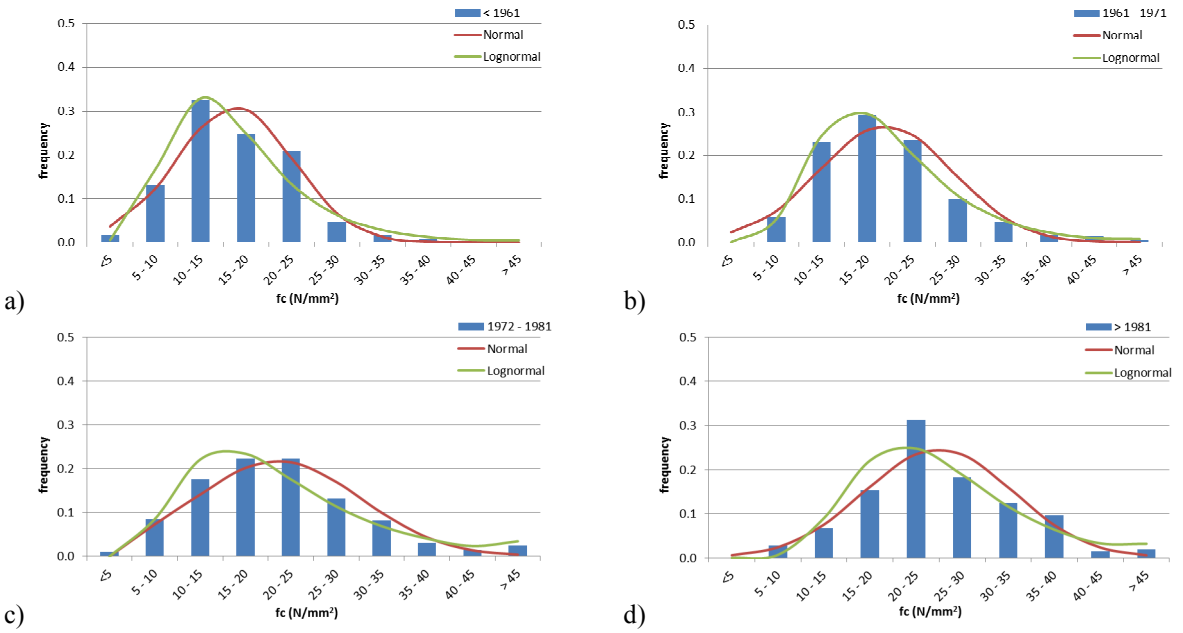


Fig. 4: Comparison between experimental histograms and theoretical distributions (Normal and Lognormal): a) <1961, b) 1961-1971, c) 1972-1981, d) >1981.

Table 2: Parameters of the Normal and Lognormal distribution

Distributions		Periods			
	Parameter	<1961	1961-1971	1972-1981	>1981
Normal	μ	16.23	19.53	21.03	24.96
	σ	6.27	7.29	9.06	7.98
Lognormal	μ	2.70	2.90	2.94	3.16
	σ	0.43	0.37	0.47	0.35

Establishing if and how well a theoretical distribution fits experimental data cannot be appropriately made through a visual inspection. For this reason, in order to evaluate the degree of agreement between the theoretical (continuous) and experimental (histogram) distribution, statistical tests on the goodness of fitting (goodness-of-fit tests) are needed. Literature (e.g. [19]) offers several types of tests although the more reliable one for this kind of problems is the Kolmogorov-Smirnov test (K-S test). It allows comparisons between datasets and relevant theoretical distributions in order to check if the population from which the experimental data derives can be considered the same described by the distribution.

The assumptions on which the K-S test is based are as follows:

H_0: there are not significant differences between the theoretical and the experimental distribution;

H_1: there are significant differences between the theoretical and the experimental distribution.

K-S test requires that the maximum absolute scatter δ, between theoretical and empirical cumulative functions, is evaluated and after compared to the critical associated value, δ_{max}. For a two-tailed test and a significance level $\alpha = 0.05$ (which defines the probability of rejecting H_0 when it is true), the results of the K-S test, in case of Normal distribution, are reported in Table 3. In all periods $\delta \leq \delta_{max}$, therefore the H_0 assumption cannot be rejected. As a consequence, there are not significant differences between the theoretical and experimental distribution, thus the experimental dataset can be considered as a random sample extracted from the theoretical distribution. The K-S test has been applied also to the Lognormal distribution. The results reported in Table 4 show that

also in this case the H_0 assumption cannot be rejected and, then, there are not significant differences between the theoretical and the experimental distribution.

Table 3: Results of the K-S test for the Normal distribution assuming α = 0.05.

	Construction periods			
	< 1961	**1961 - 1971**	**1972 - 1981**	**> 1981**
δ	0.05	0.06	0.05	0.06
δ_{max}	0.12	0.06	0.06	0.09
	OK	**OK**	**OK**	**OK**

Table 4: Results of the K-S test for the Lognormal distribution assuming α = 0.05.

	Construction periods			
	< 1961	**1961 - 1971**	**1972 - 1981**	**> 1981**
δ	0.04	0.02	0.05	0.07
δ_{max}	0.12	0.06	0.06	0.09
	OK	**OK**	**OK**	**OK**

Seeing that K-S test provides positive results for both distributions, it seems interesting examining which of them better fits the experimental data, that is the distribution having the lower scatter (α value being equal). Comparing δ values in Tables 3 and 4 it comes to light that the better distribution for the first two periods is the Lognormal one. In the third period they are equally suitable, while in the last period the Normal one is better.

Concluding remarks

Seismic risk in Italy as well as in other earthquake-prone countries represents a serious threat to human safety as demonstrated by the heavy human and economic losses suffered in the last years. As a rule, this mainly derives from the vulnerability of the building stock due to absent or inadequate seismic design further exacerbated by deterioration from ageing and lack of maintenance. Therefore, in order to mitigate seismic risk the most important action should be the reduction of the vulnerability through more or less invasive structural interventions. The knowledge of the material properties is a preliminary and fundamental step in the vulnerability evaluation and design of consequent, if any, retrofit intervention: the more accurate is the knowledge phase, the more safety- and cost-effective can be the interventions. The Italian and European codes prescribe that design strength to be used in safety verifications is obtained through tests on in situ materials, without reference to the nominal values used in the design of new buildings.

In this study, based on a huge DB of concrete tests, the changes over time of concrete strength in public buildings located in Basilicata region have been outlined. Analysing the DB as a function of different periods of construction, some Normal and Lognormal distributions able to carefully describe the related experimental data have been provided.

Results from the present study can provide useful suggestions in the vulnerability evaluation of individual buildings, as well as they can be assumed as valid estimations of the expected mean strength in the building stock when performing large scale risk analyses. To this end, theoretical distributions obtained for the concrete strength related to different construction periods can be really helpful when data directly obtained from the buildings at hand are not available and hard to obtain.

Acknowledgements

This study has been partly supported by 2014 DPC-ReLUIS Project, Research Line "Reinforced Concrete, WP1 "Seismic capacity of RC existing structural members".

References

[1] P. Ricci, F. De Luca, GM. Verderame: 6th April 2009 L'Aquila earthquake, Italy: Reinforced concrete building performance. Bull Earthquake Eng (2011), 9(1):285–305.

[2] A. Masi, G. Santarsiero, M.R. Gallipoli, M. Mucciarelli, V. Manfredi, A. Dusi, T. A. Stabile: Performance of the health facilities during the 2012 Emilia (Italy) earthquake and analysis of the Mirandola hospital case study. Bull. Earthquake Eng (in press). DOI: 10.1007/s10518-013-9518-4.

[3] Ministerial Decree 14 January 2008: Technical Norms for Constructions, 2008, (in Italian).

[4] CEN: Eurocode 8: Design of structures for earthquake resistance, Part 3: Assessment and retrofitting of buildings. June 2004, Doc. CEN/TC250/SC8/N388B. Comité Européen de Normalisation, Bruxelles (2004).

[5] FEMA 356: Prestandard and commentary for the seismic rehabilitation of buildings. Federal Emergency Management Agency, Washington D.C., November 2000.

[6] H. Crowley, M. Colombi, B. Borzi, M. Faravelli, M. Onida, M. Lopez, D. Polli, F. Meroni, R. Pinho: A comparison of seismic risk maps for Italy. Bull Earthquake Eng. (2009) 7:149-180 DOI 10.1007/s10518-008-9100-7.

[7] INGV-DPC S1: Continued assistance to the DPC for the completion and management of seismic hazard maps foreseen in the Ordinance PCM 3274 and planning of future developments. http://esse1.mi.ingv.it (in Italian) (2007)

[8] M. Stucchi, C. Meletti, V. Mondaldo, H. Crowley, G.M. Calvi, E. Boschi: Seismic Hazard Assessment (2003-2009) for the Italian Building Code. Bull. Seismol. Soc. Am. (2011) 101(4), 1885-1911.

[9] G.M. Verderame, G. Manfredi, G. Frunzio: Le proprietà meccaniche dei calcestruzzi impiegati nelle strutture in c.a. realizzate negli anni '60. In: Proceedings of the 10th Conference on "Earthquake Engineering in Italy", Potenza-Matera, 9-13 September 2001, (in Italian).

[10] G.M. Verderame, A. Stella, E. Cosenza: Le proprietà meccaniche degli acciai impiegati nelle strutture in cemento armato realizzate negli anni '60. In: Proc. of the 10th Conference on "Earthquake Engineering in Italy", Potenza-Matera, 9-13 September 2001, (in Italian).

[11] M. Ferrini, N. Signorini, P. Pelliccia, F. Pistola, V. Prestifilippo, G. Sabia: La metodologia della Regione Toscana per la valutazione della resistenza del calcestruzzo di edifici esistenti in cemento armato. In: Proc. of the Conference "Valutazione e riduzione della vulnerabilità sismica di edifici in cemento armato", Roma, 2008, (in Italian).

[12] M. Ferrini, N. Signorini, P. Pelliccia, F. Pistola, V. Prestifilippo, G. Sabia: Risultati delle campagne d'indagine svolte dalla Regione Toscana per la valutazione della resistenza del calcestruzzo di edifici esistenti in cemento armato. In: Proc. of the conference "Valutazione e riduzione della vulnerabilità sismica di edifici in cemento armato", Roma, 2008, (in Italian).

[13] A. Masi, M. Vona: Estimation of the in-situ concrete strength: provisions of the European and Italian seismic codes and possible improvements. In: Proc. of the Workshop "Eurocode 8 Perspectives from the Italian Standpoint", (E. Cosenza Ed.), 67-77, 2009, Naples, Italy.

[14] OPCM 3431 3 May 2005: Further modifications and integrations of the OPCM 3274 of the 20 March 2003, 2005, (in Italian).

[15] A. Masi, L. Chiauzzi: An experimental study on the within-member variability of in situ concrete strength in RC building structures. Construction and Building Materials. 47:951-961. 2013.

[16] FEMA 274: NEHRP commentary on the guidelines for the seismic rehabilitation of buildings. Federal Emergency Management Agency, 1997. Washington, D.C.

[17] Royal Decree n. 2229: Design code of reinforced concrete structures, 1939, (in Italian).

[18] Ministerial Decree 30 May 1972: Design code of reinforced concrete, prestressed concrete and steel structures, 1972, (in Italian).

[19] Ang A.H.S., Tang W.H.: Probability Concepts in Engineering (2nd Edition), John Wiley & Sons, 2007.

Applied Mechanics and Materials Vol. 597 (2014) pp 291-295
© (2014) Trans Tech Publications, Switzerland
doi:10.4028/www.scientific.net/AMM.597.291

Buckling Behavior of Catheter Reinforced with Braids under Axial Compression after Torsion: Effect of Deformation Speed on Buckling Region

Yasuyuki Kato [1, a *]

[1] Department of Mechanical Engineering, College of Science & Technology Nihon University, 1-8-14 Kanda-Surugadai Chiyoda-Ku, Tokyo, 101-8308, Japan

[a*] kato@mech.cst.nihon-u.ac.jp

Keywords: Catheter, Buckling Region, Displacement Speed, Initial Torsion, Viscoelastic Property

Abstract. The purpose of this research is to investigate the relation between the deformation speed and the buckling phenomenon of the catheters, which is made of soft nylon resin and is reinforced with thin stainless wires called braid. In general, the buckling phenomenon of the catheter is complicated because the different types of several loads such as torsion and bending are applied simultaneously to the catheter. In this study, as the initial step to reveal the buckling behavior under combined loading state, the buckling behaviors under combined loading of compression and torsion are examined. Especially, in this study, the buckling tests under various initial torsion are conducted by changing the axial displacement speed. And then, the effect of the stress relaxation on the occurrence region of buckling under combined loading state is revealed in this paper.

Introduction

As for the material of catheter, not only a soft characteristic but also the responsiveness and enough rigidity are required so as to satisfy the excellent operation. Therefore, the catheter, which is made of soft nylon resin and is reinforced with thin stainless wires called braid, is taken up as the subject of this research. In a series of previous study [1, 2 and 3], the stress relaxation tests under single-stage step strain have been done with the different ratio of combined load of tension and torsion or bending and torsion. As a consequence, the reducing effect of braid on the stress relaxation behavior was revealed by performing the experiments with the different relative angle between the braid angle and the principal axis of stress. Then, it became clear that the visco-elastic response under combined load is different from the response under uniaxial state.

Meanwhile, there is a possibility that the unstable phenomenon such as buckling occurs when using the relatively long catheter. Hence, it's necessary to investigate the buckling behavior along with viscoelastic behavior. In our previous study, the buckling tests have been carried out by changing the speed of axial displacement variously. As a result, it became clear that since the buckling load is reduced with decreasing the axial displacement speed, the deformation speed is closely related to the buckling behaviors of catheter. However, in the actual usage, the different types of several loads act simultaneously on the catheter, and the buckling behavior in the catheter becomes more complicated. Therefore, it is necessary to examine the buckling behavior under combined loading.

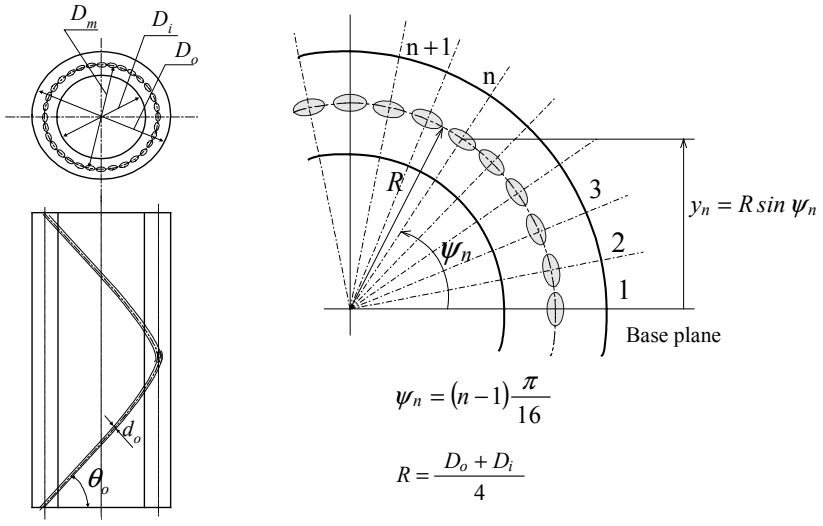
As the initial step to reveal the buckling behavior under combined loading state, the buckling tests under combined compression and torsion are carried out as the most fundamental case. Especially, the deformation path of axial compression after initial torsion is examined in this paper. Then, the influence of the stress relaxation phenomenon on the buckling behavior is revealed by examining the buckling region, which is obtained under two types of different axial displacement speeds.

Shape of Cross-section and Size of Catheter Reinforced with Braids.

Shape of Cross-section. The catheter treated in this paper is composed of matrix made from soft nylon resin and braids made from thin stainless wires. Fig.1 (a) shows the shape of the catheter per

one pitch. Here, D_o and D_i are outside and inside diameter, and D_m is mean diameter, d_o and θ_o are diameter and angle for braid. The braids in catheter consist of 32 wires in all, and 16 wires within them are woven in clockwise direction. Fig.1 (b) shows an enlarged view of the cross-section. Here, y_n and Ψ_n indicate the distance and the angle of the *n*-th braid from the neutral axis of the cross-section, and *R* shows the mean radius that these braids are disposed circularly.

Size of Test Pieces. As shown in Table 1, three types of different test pieces are used. Moreover, the gauge length L_o and the braid angle θ_o of all test pieces are the same size, i.e., 45 [mm] and 45 [deg.].



(a) Shape of the catheter per one pitch (b) Cross-section

Fig.1. Shape of Catheter Reinforced with Braids

Table 1. Size of Catheter Reinforced with Braids and Ratio of Matrix Area to Total Area

Types of test pieces	Outsides diameter D_o [mm]	Inside diameter D_i [mm]	Diameter of braid d_o [mm]	Ratio of matrix-area [-]
Contain braid No.1	1.37	1.07	0.0508	0.842
Contain braid No.2	1.67	1.14	0.0635	0.876
Contain braid No.3	2.01	1.40	0.0635	0.924

Experimental Method

In the experiments, the torsion testing machine is connected to the tensile testing machine (SHIMAZU AUTOGRAPH AGSJ) in order to apply the axial compression and torsional moment simultaneously. After attaching the test pieces to the testing machine, the experiments for determining the buckling loads were conducted in the following condition.

Buckling Tests under Compression after Initial Torsion. In order to determine the buckling region under combined loading state of compression and torsion, the compression tests after giving initial torsion are conducted by changing the axial displacement speed, see Fig.2. Here, the buckling loads are determined by performing experiments under two types of different axial displacement speeds, i.e., high-axial displacement speed and low-axial displacement speed as indicated in Table 2.

Experimental Results

Results of Flexural Rigidity and Estimation of Critical Buckling Load. The values of flexural rigidity, which was measured by conducting the four-point bending tests, and the critical buckling loads of a column with built-in ends are shown in the Table 3.

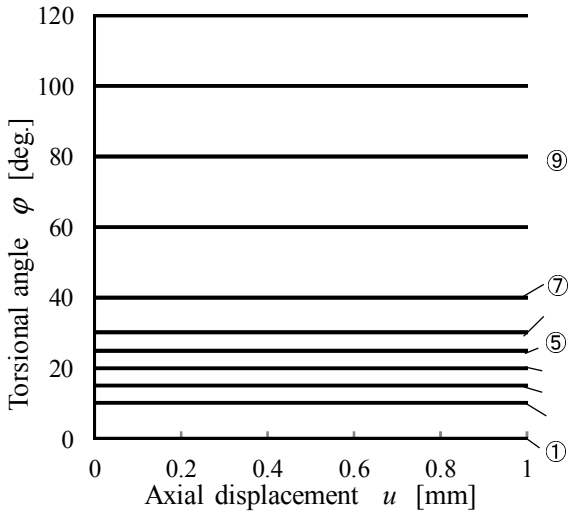


Fig.2. Experimental Conditions of Axial Compression after Torsion

Table 2. Experimental Conditions of Axial Compression after Torsion

(a) Case of High-axial displacement speed

	Torsional angle [deg.]	Torsional speed [rpm]	Axial displacement speed [mm/min]
	0	1.0	134.19
	10	1.0	134.19
	15	1.0	134.19
	20	1.0	134.19
	25	1.0	134.19
	30	1.0	134.19
	40	1.0	134.19
	60	1.0	134.19
	80	1.0	134.19
	100	1.0	134.19
	120	1.0	134.19

(b) Case of Low- axial displacement speed

	Torsional angle [deg.]	Torsional speed [rpm]	Axial displacement speed [mm/min]
	0	1.0	50.0
	10	1.0	50.0
	15	1.0	50.0
	20	1.0	50.0
	25	1.0	50.0
	30	1.0	50.0
	40	1.0	50.0
	60	1.0	50.0
	80	1.0	50.0
	100	1.0	50.0
	120	1.0	50.0

Table 3. Relation of Flexural Rigidity and Critical Buckling Load

Types of test pieces	Flexural rigidity $E_c I_c$ [N・mm^2]	Critical load P_{cr} [N]
Contain brade No.1	249.2	4.86
Contain brade No.2	465.3	9.07
Contain brade N0.3	704.0	13.7

Buckling Load under Uniaxial Compression. Focusing on result of test piece No.1 among three types of test pieces, the results of the buckling test under uniaxial compression, i.e., the result of ① in Fig.2, are described in Fig.3 (a). In this figure, the relation of the compressive load and the axial displacement, which are obtained under two types of different deformation speeds are compared. As is obviously from this figure, the buckling loads occurring under high displacement speed of 134.19 [mm/min], namely, plots in this figure, is higher values compared to the result of low displacement speed of 50.0 [mm/min]. Moreover, it can be confirmed that the buckling loads under high displacement speed are approximately equal to the critical buckling load.

Buckling Load under Compression after Initial Torsion. Next, the results of buckling test under combined load of axial compression and torsion are described. As the example of experimental results, Fig.3 (b),(c),(d),(e) show the relation between the compressive load and the axial displacement, which is obtained by the deformation path of ③, ⑤ , ⑧ and ⑪ in Fig.2. It can be seen from these figures that the buckling loads occurring under high displacement speed, plots , are higher values in

comparison with the results of low displacement speed, plots ●. Moreover, similar tendency was also seen to other experiments. In addition, the buckling load has a decreasing tendency as the torsional angle increase in the order of ③, ⑤, ⑧, ⑪. Fig.3 (f) shows the relation between the torsional moment and the torsional angle for the case of ⑪. In this figure, the torsional buckling occurs during the process of adding the initial torsion. Moreover, torsional moment is decreased during the process of the axial compression by the effect of stress relaxation.

On the basis of these results, the occurrence region of buckling can be estimated as shown in Fig.4. In this figure, the compressive load and the torsional moment are depicted together in the diagram concerning the axial displacement and the twisting angle by dividing each axial compressive force and the torsional moment by the extensional rigidity (AE_c / L_o) and the torsional rigidity ($G_c I_{pc} / L_o$). Here, hollow plots indicate the deformations, i.e., axial displacements and torsional angles, and solid plots indicate the internal forces, i.e., axial compressive forces and torsional moments. Then, the

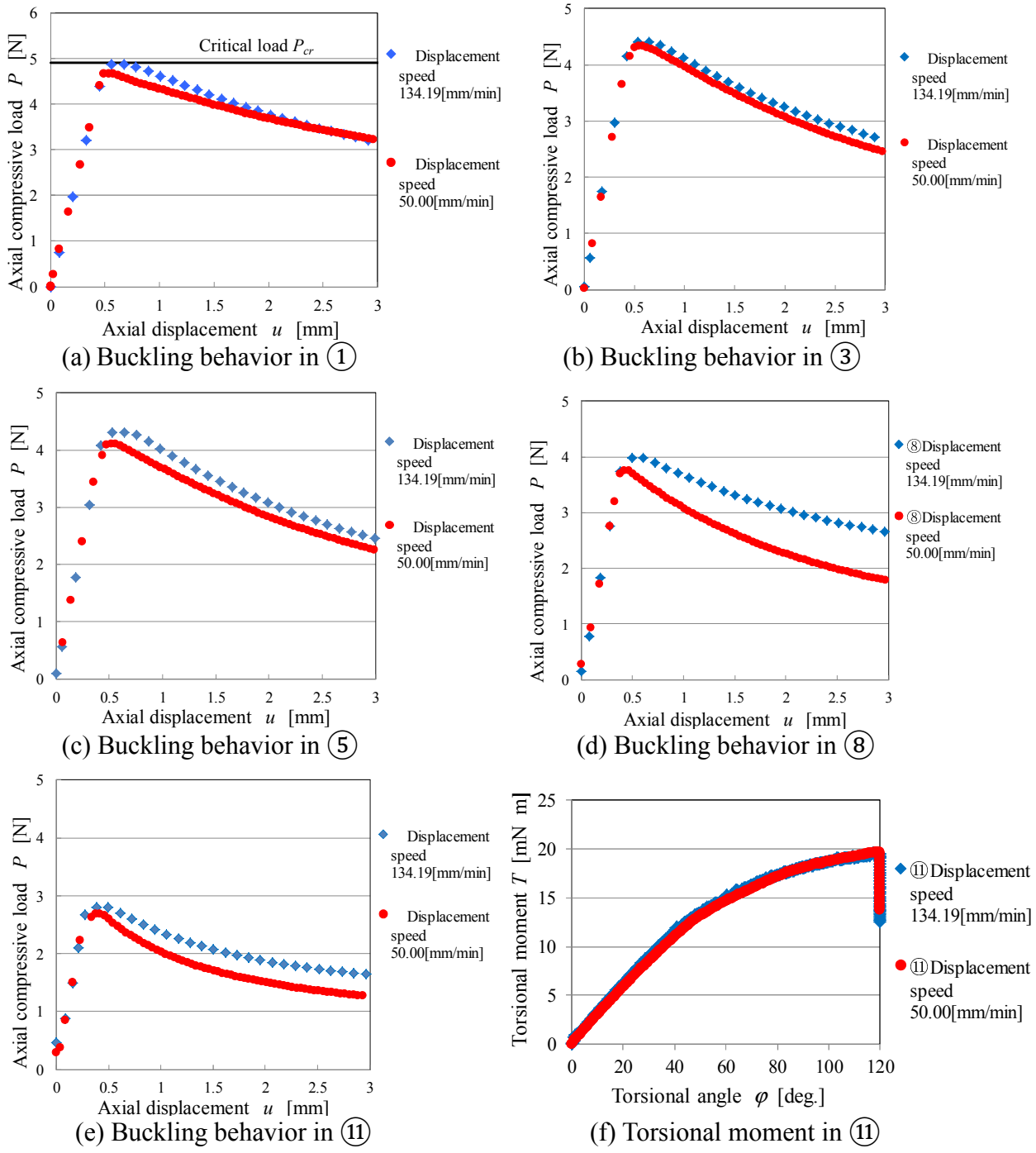


Fig.3 Buckling Behavior for Two Types of Different Deformation Speeds

points where these plots begin to bifurcate during the process of the progression of deformation and internal forces in each direction is the occurrence position of the buckling, and a curve representing the occurrence region of buckling can be estimated by connecting these points. And, the outside of this curve is unstable region that the buckling occurs. The blue short dashed line in this figure indicates the occurrence region of buckling for the high deformation speeds and the red dashed-dotted line is the occurrence region of the low deformation speeds. It can be seen from this figure that the occurrence region measured under low deformation speeds is slightly smaller than the region of high deformation speeds, and both boundary lines gradually decrease with an increase of torsion.

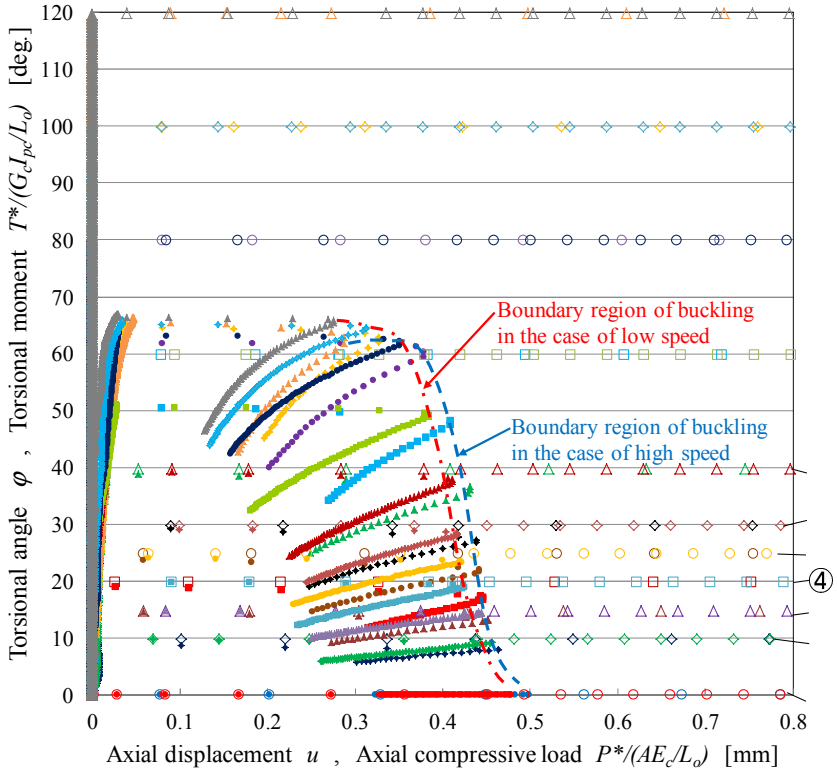


Fig.4 Buckling Region generated under Loading Tests for Compression after Initial Torsion

Summary

The buckling behaviors obtained under compression after initial torsion were examined by conducting the experiment under two types of different axial displacement speeds. Consequently, it could be confirmed that since the occurrence region of buckling measured under low displacement speeds is slightly smaller than the region of the high displacement speeds, the unstable phenomenon occurs with slightly small axial load in the case of low speed. Moreover, it became clear that these buckling loads gradually decrease with an increase in the value of initial torsion, and the torsional moments decrease during the process of axial compression and this tendency appears prominently with an increase of torsional angle.

References

[1] Y. Kato, S. Krosawa and M. Ueda: Advanced Materials Research, Vols.622-623 (2013), p. 1330.

[2] Y. Kato, M. Ueda: Applied Mechanics and Materials, Vol. 372 (2013), p. 261.

[3] Y. Kato: Advanced Materials Research, Vol. 856 (2014), p. 384.

Applied Mechanics and Materials Vol. 597 (2014) pp 296-299
© (2014) Trans Tech Publications, Switzerland
doi:10.4028/www.scientific.net/AMM.597.296

Effect of Fiber Volume Fraction on Compressive and Flexural Properties of High-Strength Steel Fiber Reinforced Concrete

Kyung Lim, Ahn[1, a], Seok Joon, Jang [1, b], Yeon Jun, Yun [1, c], Dea Geun, Yu [1, d] and Hyun Do, Yun[1, e *]

[1]Department of Architectural Engineering, Chungnam National University, Deajeon, 305-764, Republic of Korea

[a]ahn_08@nate.com, [b]suk-joon@nate.com, [c]yunjuny@cnu.ac.kr,

[d]e_orms@naver.com, [e]wiseroad@cnu.ac.kr (corresponding author)

Keywords: Steel fiber reinforced concrete (SFRC), Compressive behavior, Flexural behavior, Fiber volume fraction

Abstract. The purpose of this study is to investigate the compressive and flexural properties of high-strength steel fiber reinforced concrete (SFRC). For this purpose, a total of 5 mixture whose variable is fiber volume fraction, were made and tested in a range of high strength with 70MPa. In case of normal and ultra-high strength, experimental results were collected from existing literatures on the tests conducted in South Korea. Flexural behavior of SFRC is enhanced according to the fiber volume fraction and compressive strength. Experimental and collected data were applied to existing equations, so it was found that the distinctions occurred between experimental or collected data and calculated values. Thus, more efforts are required to predict the flexural behavior of SFRC manufactured in South Korea with respect to the fiber volume fraction.

Introduction

Concrete is a widely used material in civil infrastructure. It has excellent mechanical properties, high compressive strength, economical, durability and rigidity. However, it has disadvantages that tensile, flexural and impact resistance are low and the energy absorption capacity is small, so the brittle fracture occurs. In the development of concrete technology, the demand for high-strength concrete has been increasing, but the properties of these appear remarkably on high-strength [3]. Many studies have been conducted to complement the properties of the brittle concrete. One of them is a method of incorporating steel fiber in concrete. The incorporation of steel fiber brings an increase of tensile strength and the improvement of toughness. According to previous studies, the compressive strength of SFRC have no particular correlation with steel fiber reinforcement, but splitting tensile and flexural strength of the SFRC are known to be proportional to the volume fraction of steel fiber. Many studies are suggested that the strength characteristics were changed in accordance with variable factor; aspect ratio and shape of steel fiber as well as the volume fraction of steel fiber. This study aimed to evaluate the effect of the volume fraction and the compressive strength on mechanical

Table 1. Mix proportion of high-strength SFRC

Mixture	Fiber volume fraction [%]	Compressive strength [MPa]	Unit weight [kg/m^3]			
			Water	Cement	Fine aggregate	Coarse aggregate
SFRC 70-0.0	0.0	70	200	666	900	540
SFRC 70-0.5	0.5					
SFRC 70-1.0	1.0					
SFRC 70-1.5	1.5					
SFRC 70-2.0	2.0					

properties of SFRC. In this paper, experimental study was conducted to evaluate the flexural behavior of SFRC. The characteristics of the flexural behavior according to volume fraction was analyzed by adding the experimental data from existing literatures. Also, the suitability of equations proposed by existing researchers was considered for flexural strength.

Experimental Study

Mixture proportion. The mixture proportion of concrete and SFRC mixed in this study was presented in Table 1. Hooked end type steel fiber had a length of 30 mm, 0.5 mm diameter and 1,100 MPa tensile strength was used for SFRC materials. A fan-type mixer was utilized to manufacture concrete and SFRC materials. To prevent the phenomenon of fiber ball and improve the fiber dispersibility, the steel fiber is added at two times. The main objective of experimental program is to evaluate the effects of fiber volume fraction (0 to 2 %) on compressive and flexural responses of SFRC. To determine the actual properties of SFRC, three cylinders (Φ100x200 mm) with ASTM C 39 [1] and prisms (100x100x400 mm) as per ASTM C 1609 [2] was casted from each mixture. All specimens were cured under water (20˚C) and tested after 28 days from casting.

Test methods. To evaluate compressive behavior, three cylinders were tested using universal testing machine (UTM) of 2,000 kN maximum load carrying capacity on each test day. During the test, the strains were obtained from two linear variable displacement transducers (LVDTs) that were disposed around the cylinders. The controlled load rate was 10 μm/sec. Flexural testing was conducted under four points bending on the span length of 300 mm using UTM of 200 kN capacity. Yoke with two LVDTs was used to measure the whole vertical deflection at the mid-span and the controlled displacement rate was 0.05 mm/min.

Compressive properties. The typical vertical shear failure cracks observed of specimens tested under uniaxial compressive. The influence curing age on the compressive strength is shown in Fig. 1.

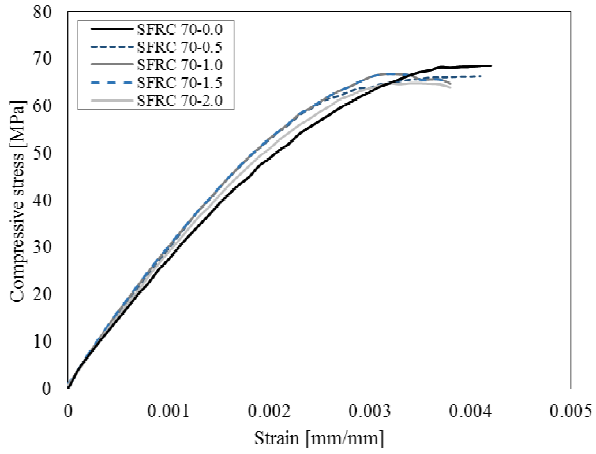


Fig. 1 Compressive response

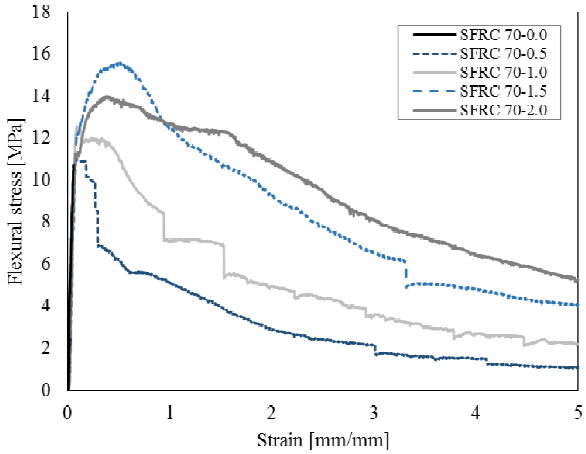


Fig. 2 Flexural response

Table 2. Summaries of test results

Mixtures	Fiber volume fraction [%]	Compressive strength [MPa]	Strain at peak strength [mm]	Flexural strength [MPa]	Deflection at peak strength [mm]
SFRC 70-0.0	0.0	66.9±2.8	0.0035±0.0005	10.9±0.6	0.073±0.010
SFRC 70-0.5	0.5	66.6±1.7	0.0032±0.0002	11.2±1.2	0.079±0.005
SFRC 70-1.0	1.0	67.1±0.5	0.0032±0.0001	12.8±0.7	0.118±0.042
SFRC 70-1.5	1.5	67.6±1.4	0.0033±0.0002	15.8±0.4	0.464±0.098
SFRC 70-2.0	2.0	65.5±1.2	0.0033±0.0003	14.4±1.2	0.892±0.495

Change of compressive strength in material shown high increase by the early 7 days regardless of the fiber volume fraction, and increased slowly by the 91 day. The effects of fiber volume fraction on compressive strength of SFRC are not significant. Table 2 provides the compressive flexural properties of concrete and SFRC.

Flexural properties. Fig. 2 shows that flexural responses of prime from average value three specimens. As expected, addition of steel fiber is improved flexural behavior of concrete. The concrete brittle failure after first cracking and SFRC specimens with 0.5, 1 % volume fraction appeared strain-softening behaviors. Especially SFRC specimens with 1.5, 2 % appeared strain-hardening phase due to the fiber bridge action. First-crack and flexural strength increased with increase the fiber volume fraction, but volume fraction 2 % appear low performance than 1.5 % specimen with fiber ball. It is remarkable that 1.5 % value is effective volume fraction of steel fiber in concrete.

Existing proposed equation evaluation

In order to investigate the relationship between compressive strength and flexural strength with different fiber volume fraction, experimental data that included a range of normal strength and ultra-high strength was collected from literatures. Table 3 summarizes the general information of those available one. Most of tests in the literature were taken at 28 days and hooked end type fiber (HSF) were popularly used in the investigations. The data collected through literature were represented in Fig. 3 and Fig. 4. The main factors for flexural behavior of SFRC were the compressive strength, fiber volume fraction. Many proposed equations have been suggested for prediction of flexural strength using the compressive strength. The equations considering only fiber volume fraction were selected to estimate the suitability of the equations for test results tested in Korea. The equations used in this study were proposed by Wafa & Ashour [4] and Song & Hwang [11].

Fig. 3 shows the results about an equation of Wafa & Ashour, Fig. 4 shows the result about an equation of Song & Hwang. As a result of applying data tested in Korea to the equations, there is a different between experimental data and calculated values. As shown in Fig. 3, flexural strength equation proposed by Wafa Ashour represents that the ratio of predictive value for experimental value is 0.78 at 0%, 0.92 at 0.5%, 0.91 at 1%, 0.91 at 1.5% and 0.9 at 2%, which were relatively correct. The

Table 3. Experimental data of SFRC

Authors	W/B	Fiber Type	Volume Fraction	Aspect ratio
Y.I. Kim et al [5]	30, 35, 50	HSF	0, 0.5, 1, 1.5, 2	60
H.H. Lee et al [6]	57	HSF, SSF	0, 1, 1.5, 2	67, 75, 80
B.H. Oh et al [7]	40	SSF	0, 1, 2	57
B.K. Koo et al [8]	30	HSF	0, 0.5, 1, 1.5	60, 75, 100
E.S. Yun et al [9]	30	HSF, ISF, CSF	0, 0.5, 1, 1.5, 2	56, 60, 80
S.J. Jang et al [10]	30	HSF	0, 1, 2	60

Note: HSF is Hooked Steel Fiber, SSF is Strait Steel Fiber, ISF is Indeted Steel Fiber, CSF is Crimped Steel Fiber

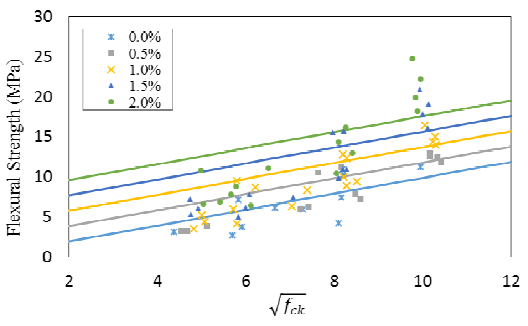


Fig. 3 Comparision between test results and prediction value of Wafa & Ashour

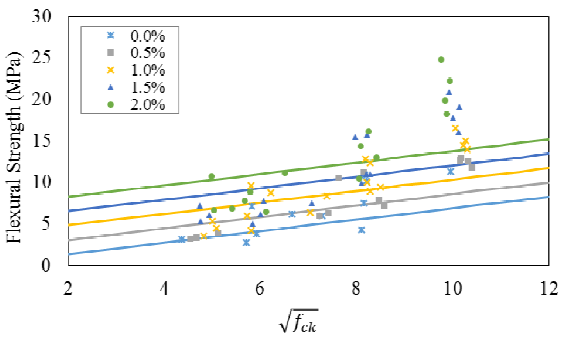


Fig. 4 Comparision between test results and prediction value of Song & Hwang

proposed equation of Song and Hwang in Fig. 4 represents that the ratio of predictive value for experimental value is 0.6 at 0%, 0.85 at 0.5%, 0.84 at 1%, 0.83 at 1.5% and 0.81 at 2%. This showed that the flexural strength is overestimated. However, It is difficult to estimate the flexural strength of SFRC with only steel fiber volume fraction because these two proposed equations have the error rate of average 25% or more. So, the predictive equation considering not only steel fiber volume fraction but also the aspect ratio of steel fiber and shape is needed to estimate the flexural behavior of SFRC.

Conclusion

In this study, to investigate the relation between compressive strength and flexural behavior, the test and statistical analysis were conducted. Based on the test results and data at literatures, the conclusions are as following:

1) As the test results on high strength concrete of 70 MPa, influence of fiber volume fraction was less effective in compressive strength of concrete. In case of flexural strength, addition of steel fiber is improved flexural behavior of concrete. But volume fraction 2 % appear low performance than 1.5 % specimen with fiber ball. It is remarkable that 5 % value is effective volume fraction of steel fiber in SFRC.
2) The test results and collected data were substituted in predictive equation proposed by Wafa & Ashour and Song & Hwang. The predictive equation proposed by Wafa & Ashour had relatively correct value, but error rate of average 25 % or more. So, the predictive equation considering the aspect ratio of steel fiber and shape is needed to estimate the flexural behavior of SFRC.
3) As a result of applying experimental and collected data to predictive equations proposed by existing researchers, the flexural behavior of SFRC was not described with the equation in consideration of only steel fiber volume fraction and the compressive strength. Thus, the influence on shape and aspect ratio of steel fiber should be estimated to predict the flexural behavior of SFRC used in South Korea.

Acknowledgements

This research was financially supported by the Ministry of Education, Science Technology (MEST) and National Research Foundation of Korea (NRF) through Research on Adventure NRF-2013R1A1A2066034) NRF-2013R1A1A2066034) and BK21 plus.

References

[1] ASTM C 39-12 Standard, ASTM, 2012

[2] ASRM C 1609-10 Standard, ASTM, 2010

[3] Abid A. Shah and Y. Ribakov, The journal of Material and Design, 2011

[4] P.S. Song and S. Hwang, Construction and Building Materials, 2004

[5] Y.I. Kim et al, Journal of the Korea Institute of Building Construction, 2008

[6] H.H. Lee et al, Journal of the Korea Concrete Institute, 2004

[7] B.H. Oh et al, Journal of the Korea Concrete Institute, 1993

[8] B.K. Koo et al, Journal of the Korea Concrete Institute, 1992

[9] E.S. Yun et al, Journal of the Architectural Institute of Korea, 2006

[10] S.J. Jang et al, Applied Mechanics and Materials, 2013

[11] Wafa, F.F and Ashour, S.A, ACI Materials Journal, 1992

Applied Mechanics and Materials Vol. 597 (2014) pp 300-303
© (2014) Trans Tech Publications, Switzerland
doi:10.4028/www.scientific.net/AMM.597.300

Analysis of Guyed transmission tower dynamic characteristic

GAN Feng-Lin, JIA Xu-Bo

Architecture Engineering College, Northeast Dianli University, Jilin 132012, China
*E-mail: jxb870920@126.com

Keywords: Guyed Transmission Tower ; inite element; numerical analysis; Dynamic Properties

ABSTRACT: In the paper aiming at lots of 87(LM21) towers in Dongchang Hasong Transmission Line held under Changchun Extra-high voltage Bureau jurisdiction, by using ANSYS software, the nonlinear finite element model for towers is built. And numerical analysis methods is adopted. It is considered that the combined effect of stay wire and transmission tower, geometric non-linear effect and the influence of stay wire initial stress. The Dynamic Properties research about Guyed Transmission is conducted. It concluded that stay wire and tower's mode of vibrationare are relatively independent ,coordinated and the interaction of each other. Natural frequency of vibration and mode of vibration appears regularly and alternately changes with the increase of the formation order .Stay wire initial stress is main factor affecting the natural frequency of the structure and the frequency increases with the increase of stay wire initial stress.

Introduction

Guyed transmission tower by cable and tower is composed of two parts, which is the main bearing part of tower, cable is mainly used to ensure the stability of the tower. To make the design of Guyed transmission tower according to the actual working state, the main problem is to establish a reaction structure stress and deformation characteristics of he calculation model .This paper by using finite element model of cable and tower, its dynamic characteristics were studied by finite element program ANSYS. Analysis of cable and tower, considering the interaction, the geometric nonlinear effect and the cable effect of initial stress on the tower's dynamic characteristics. The results show that, the whole model can reflect the coordination between the cable and tower,interdependent relationship,features outstanding guyed transmission tower structure dynamic characteristics[1].

The finite element model established

The tower portion of the structure composed of angle steels, the tower for the 33m, as the inner door type tower, the tower that material is isotropic, to satisfy the yield condition and the associated flow rule of initial V.Mises; structure for large displacement and small deformation;using the finite element analysis software ANSYS model, excluding the structure processing, installation error and initial defects in material, node as the ideal space hinged or steel node; tower body by considering the shear deformation without considering Beam188 warping of the cross-section element, cable use only tension Link10 element [2].

Multi node cable element structure dynamic characteristics

Due to the computational model directly affects the correctness of the calculation results, this paper adopts two kinds of integral study on the dynamic characteristic calculation model: 1) cable divide the overall model of multi node cable element; 2)cable divide a cable element model. Firstly, the former, 50MPa imposed in the cable initial stress, researching the structure of the 100 frequencies and mode shapes.For convenience of analysis of dynamic characteristics of variation,

according to the main parts of shapes occur they are divided into 11 intervals, listed in Table 1,part of the formation is shown in figure 2.

Table 1 Vibration mode and frequency position

Modal order	Frequency range	Vibration occurs	Modal order	Frequency range	Vibration occurs
1-8	0.868-0.871	Cable	30-36	3.486-3.487	Cable
9-11	1.42-1.73	Cable and tower	37-39	3.547-3.831	Cable and tower
12-17	1.74-1.747	Cable	40-63	4.360-6.114	Cable
18-19	1.868-1.952	Cable and tower	64-65	6.151-6.254	Cable and tower
20-27	2.614-2.617	Cable	66-100	6.992-10.53	Cable
28-29	3.228-3.485	Cable and tower			

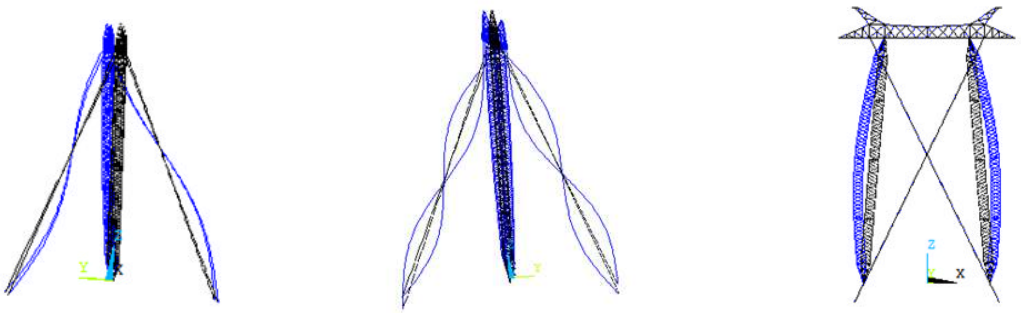


Figure 2 Part modes

From table 1 and Figure 2 makes conclusions as follows:

Coupling vibration type cable and tower in ninth modes, eighteenth modes,twenty-eighth modes, thirty-seventh modes, sixty-fourth modes, performance for the complex forms of cable and tower interaction, and with increasing order vibration mode, the modal shape becomes more and more complex. This coupling will play an important role in the dynamic response of the.We can be seen from table 1, in Guyed transmission tower 100 modes, cable is the main vibration type accounted for 89%, the tower is mainly accounted for only 11%. The characteristic depends on the cable and tower stiffness ratio, stiffness is more likely, two modes are also more big, also shows the importance of cable on the dynamic characteristics of the Guyed transmission tower.

Single node cable element dynamic property structure

For the comparison of cable is divided into a plurality of cable element and dynamic characteristics, Single node cable element vibration frequencies and modes are listed in Table 2 and figure 3. From table 2 and figure 3 visible:



Figure 3

(1) the guy is only one cable element, while considering the influence of the cable structure, It did not consider the cable vibration, therefore the guyed transmission tower mode is only in the tower body.

(2)Table 1 compared with table 2, table 2 first order frequency equivalent to table 1 ninth frequencies ; second order frequency equivalent to table 1 eighteenth frequencies ; fourth order frequency equivalent to twenty-eighth frequency table 1; table 2 fifth frequencies equivalent to the table 1 of order thirty-seventh frequency ; table 2 eighth order frequency equivalent to table 2 sixty-fourth frequencies. Indicates ,when the cable initial stress is small, Single node cable element mainly affect is the cable frequencies and mode shapes, It has little effect on dynamic characteristic of the tower, but it can not reflect the coupling between the cable and the tower.

Table 2 Single node cable element structure frequency

Modal order	Frequency	Modal order	Frequency
1	1.4192	6	3.73867
2	1.8349	7	3.8168
3	1.9366	8	6.1597
4	3.2284	9	6.2525
5	3.5341	10	11.124

the effect of Cable initial stress on Guyed transmission tower structure dynamic characteristics

The cable is the main component of Guyed transmission tower .It ensure the tower upright and stable. As flexible cable, It must exert some initial stress to make the tower body with enough rigidity in order to control the structure under external loads. If the stress is too large, although the increase in the overall stiffness of the structure, but increases the axial pressure of the tower body, unfavorable to the stability of the overall structure of the tower; if too small, It has large displacement, The tower structure is easy to shake and instability, so initial stress of cable will be directly affect the rationality of the structure stiffness. According to the References[2,3] , the cable initial stress effects on the dynamic characteristics of the structure in the 50-400MPa. When the cable with different initial stress, frequency range listed in table 3. Table 3 makes conclusions as follows:

Table 3 Cable in different initial stress effects on dynamic characteristics of structure

Initial stress/MPa	Mode number	Frequency/Hz	The coupled mode number	The first coupled modes occur order
50	1-100	0.86862-10.537	12	9
100	1-100	1.2169-13.645	14	9
150	1-100	1.3852-16.713	20	1
200	1-100	1.4057-19.300	21	1
250	1-100	1.4099-20.578	26	1
300	1-100	1.4113-21.473	26	1
350	1-100	1.4119-23.194	26	1
400	1-100	1.4120-24.798	27	1

When the cable initial stress increases, the structure frequency along with variation of modes is basically the same, with the increase of initial stress of the cable, the frequency increases.When the cable initial stress increases, coupled vibration type of tower and pull ahead of time, quantity, complicated modes. The initial stress changes between 50 from 400MPa, the first coupled modes occurs from the ninth order to first order; coupled mode number increased from 12 to 14, 20, 21, 26, 27, this phenomenon will have a direct impact on the dynamic characteristics of structure.

Summary

The whole structure of cable and tower as the research, and the cable is divided into Multi node cable element, Considering the interaction and geometric nonlinear effect of cable and tower body, It can better real reflect the dynamic characteristics of the structure. In the study on Guyed transmission tower of the first 100 modes of vibration , cable accounted for mainly is the vast majority, the shape of both modes to cable as relatively independentand the coupling vibration type cable and tower complex, It fully reflects the dynamic characteristics of rigid flexible combination of mast structure.

References

[1] Li Hai-wang, Liu Guo-liang, Chen Ying-tang, Qin Dong-Qi. Analysis of [J]. Steel structure dynamic characteristic of the chimney mast, 2009,24 (116)

[2] Wang De-He, Yang Xiao-Jun, Li Xiao-Lei. Study on effect of the cable prestress changes in wind conditions Guyed Portal tower [J]. Harbin. Heilongjiang electric power, 2011, 33 (6), 438-439.

[3] Gan Feng-Lin, Li Xiao-Lei, Gao Qian. The cable initial stress distribution affected by the force on the cable tower of GuangDong [J]. electric power, 2010,23 (9), 7-10.

Applied Mechanics and Materials Vol. 597 (2014) pp 304-307
© (2014) Trans Tech Publications, Switzerland
doi:10.4028/www.scientific.net/AMM.597.304

Analysis of the Forms of Attachment Frame and Stress Characteristics

Bin Li[1, a], Jie Liu[1,b,*], Kai-Wei Wang[1,c]

[1]Traffic and Mechanical Engineering College, Shenyang jianzhu University, Shenyang, Liaoning, 110168, China

[a]binli2010@sina.com, [b]742821657@qq.com,[c]297784418@qq.com

Keywords: Tower crane, Attachment frame, ANSYS, Scope of application

Abstract. The attachment frame forms of the attachment frame were diversified. Different forms had their own characteristics. The models of attachment frame model were set up by using finite element analysis software ANSYS which could create the model to analyze the supporting structure. The article applied load on the attachment frame and calculate the internal force of the pole and the normal force of the wall in four working conditions. The final results were displayed in graphics and list form. Finally, according to the graph and data, the article compared various attachment frame forms and presented a rational analysis.

Introduction

Attachment frame was an essential part of tower crane in the high-rise construction. There were many forms of attachment frame on the market and each form has its characteristic. In order to make the attachment frame more economic and applicable, the article stressed analysis on it and drew its mechanical characteristics. However, the structure of the tower was the statically indeterminate problems and the consideration was complex and calculation was inaccurate. Therefore, this paper stressed analysis on the attachment frame through using the ANSYS finite element method and calculated the internal force of the pole and the normal force of the wall.

The four forms of the attachment frame

The attachment frame was Influenced by the horizontal force and torque delivered by the tower crane. Structural bars of the attachment frame played a supporting role in the protection of the tower. Different forms of attachment frame which withstood tensile or pressure were different. This paper described the four forms of attachment frame, as shown in simplified form.

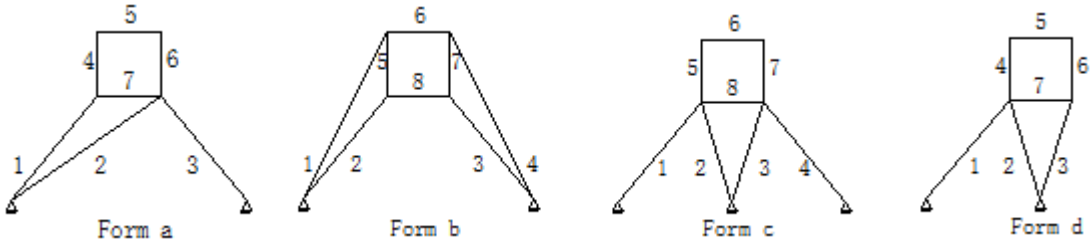


Fig.1 Four forms of attachment frame

Mechanics model of attachment frame

Attachment frame load. The attachment frame was influenced by the horizontal force and torque delivered by tower crane Lifting weight. The pole was subject to different degrees of tension and compression, the wall was subject to normal force.

Working conditions of attachment frame. When the tower crane was in the working state, the lifting arm which rotated to different positions will cause attachment frame internal force of attachment frame changing, so we should analyze the stress on different conditions. This paper mainly discusses the following four conditions: the first condition, the lifting arm was in the diagonal direction of the tower and the wind blow from back to front lifting arm. The lifting weight which was the maximum rated load was at the maximum amplitude; the second condition, the lifting arm was in the diagonal direction of the tower and the wind was perpendicular to lifting arm. The lifting weight which was the maximum rated load was at the maximum amplitude; the third condition, the lifting arm was in the axial direction of the tower and the wind blow from back to front lifting arm. The lifting weight which was the maximum rated load was at the maximum amplitude; the fourth condition, the lifting arm was in the axial direction of the tower and the wind was perpendicular to lifting arm. The lifting weight which was the maximum rated load was at the maximum amplitude.

The simplified mechanical model of the attachment frame. The attachment frame was Influenced by the horizontal force F1 and torque Mn delivered by the tower crane .Then put the torque into the force F2, force diagram as shown below.(In the case of form a)

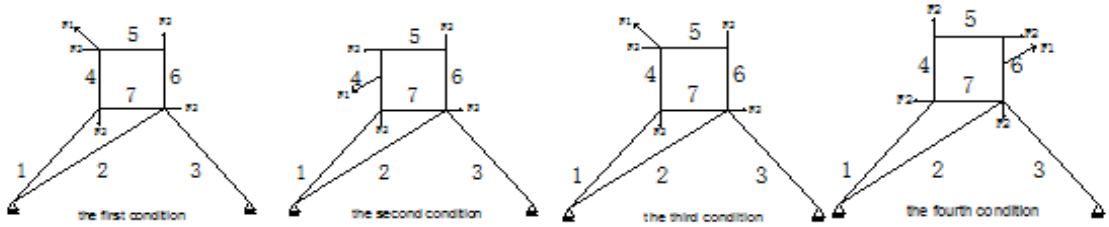


Fig.2 Force diagrams of attachment frame

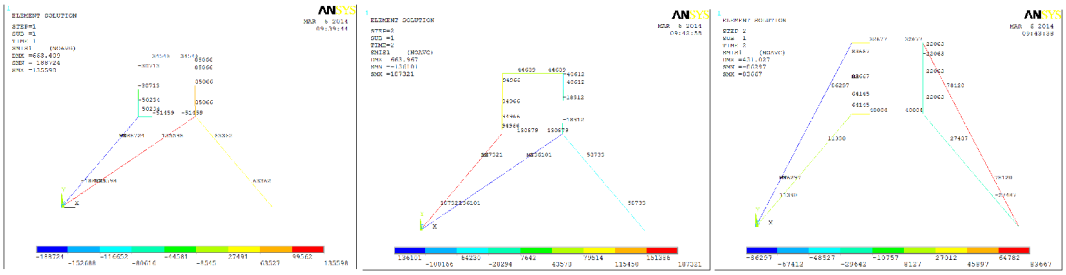
The finite element analysis

The PTT80 (6010) tower crane as an example, the maximum lifting weight was 8t.The first attachment frame height from the ground was 33 meters.

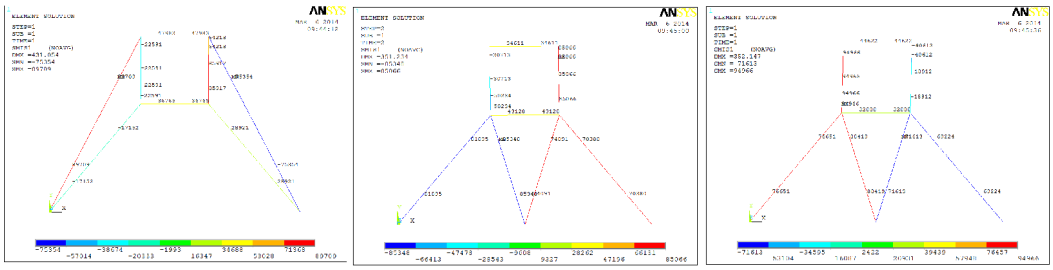
Establish the model of attachment frame by using ansys. The model of attachment frame was simple, enter the coordinates of each node in the Cartesian coordinate system, then each point could be connected into a straight line. When the model was completed, the element type must be defined. Because the pole subjects to tension and pressure, we use the beam 188 unit. The attachment frame should also be defined material properties. Finally, mesh on it.

Constraining and loading. Attachment frame was hinged together with the tower and the pole was hinged together with the wall. They could rotate around the Z axis. Therefore, the key points were constrained by 5 degrees of freedom. The force F1, F2 should be applied to the corresponding position.

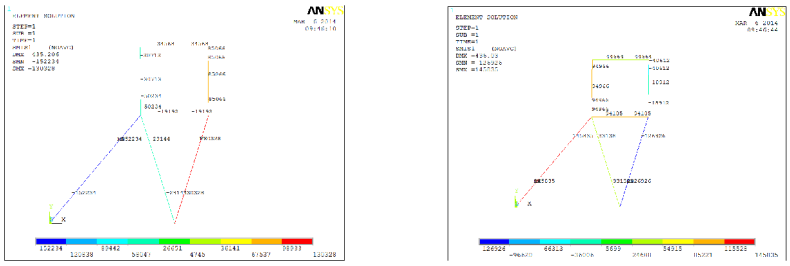
Analysis of the results. When the solution was completed, we needed to check the internal force of the pole and the normal force of the wall. The results were recorded by tables. The results are shown as below. From the data we can obtain that the force is large in second condition and fourth condition, it mainly introduces the following two conditions.



（Form a The second condition）（Form a The fourth condition）（Form b The second condition）



（Form b The fourth condition）（Form c The second condition）（Form c The second condition）



（Form d The second condition） （Form d The fourth condition）

Fig.3 The finite element stress results of attachment frame

Table 1 The force of form a, b, c, d in two kinds of conditions (unit: N)

Form a	Pole 1	Pole 2	Pole 3	Pole 4	Pole 5	Pole 6	Pole 7	$WallF_X$	$WallF_Y$
Conditin2	-188724	135598	63362	-50234	34546	85066	-51459	43984	48303
Conditin4	18732	136101	-58733	94966	44689	-40612	130879	38011	44775

Form b	Pole 1	Pole 2	Pole 3	Pole 4	Pole 5	Pole6	Pole 7	Pole8	$WallF_X$	$WallF_Y$
Conditin2	-86297	11390	-27487	78120	83667	32677	-22063	40004	32544	68913
Conditin4	89709	-17152	28921	-75354	-22591	47983	85917	36765	30393	66460

Form c	Pole 1	Pole 2	Pole 3	Pole 4	Pole 5	Pole 6	Pole 7	Pole 8	$WallF_X$	$WallF_Y$
Conditin2	-81895	-85348	74091	70380	-50234	34611	85066	43128	53000	62432
Conditin4	76651	88419	-71613	-69224	94966	44622	-40612	32888	49607	58434

Form d	Pole 1	Pole 2	Pole 3	Pole 4	Pole 5	Pole 6	Pole 7	Wall F_X	Wall F_Y
Conditin2	-152234	-29144	130328	-50234	34568	85066	-19192	96877	116054
Conditin4	145835	33138	-126926	94966	44664	-40612	94185	94318	111176

Through the above image and form, we can draw some conclusions. (1)The force of the pole 1and the pole 7 in form a are large and their values are 188724N and 130879N. The pole materials stiffness and strength requirements will be high. The values of the stress what the wall subjected to are 48303N and 44775N. They are relatively small, so form a is suitable for the occasions in which the requirement of wall strength is low. (2) The force of the pole 1and the pole 7 in form b are 89709N and 85917N. The pole materials stiffness and strength requirements are not high. The values of the stress what the wall subjected to are 32544N and 68913N. They are relatively large, so form a is suitable for the occasions in which the requirement of wall strength is high. (3) The force of the pole 1and the pole 7 in form c are 89709N and 85917N. The pole materials stiffness and strength requirements are not high. The values of the stress what the wall subjected to are 32544N and 68913N. They are relatively large, so form a is suitable for the occasions in which the requirement of wall strength is high. (4) The force in form d is the largest. The force of the pole 2 and the pole 4 in form c are 152234N and 94966N. At the same time, the values of the stress what the wall subjected to are 116054N and 111176N.The material strength and stiffness requirements are the highest, which is also the most uneconomical. However, the special structure can be used for special occasions. The attachment frame is narrow and it can be applicable to the building wall, which is narrow and small. (5)Form a and d both have 7 pole, the force is almost the same. The normal force on wall in form d is much larger than in form a. But form d can be applied to some special cases. (6) Form b and c both have 8 poles. The force is almost the same. The pole of form b is long and form c needs to add extra embedded parts on the wall, which both raise the cost. (7) Form a and form d are the static structure, form b and form c are hyperstatic structure. The pole force of form a and form d is about two times as large as form b and form c. The wall stress of form d is about two times as large as form b and form c. The wall force of form a is the minimum.

Summary

This chapter applies the ANSYS computational method to analyze the attachment frame .According to the graph and data, the chapter compares four forms of attachment frame and presents a rational analysis. The chapter provides a good decision for the choice of attachment frame, at the same time, it also provides an effective computational methods.

Acknowledgements

This research project was financially supported by Science and Technology Department of Liaoning Provincial Engineering Center Project Foundation (2010402010).

References

[1] Jiang Yong, Zhang Bo. ANSYS 7 example [M]. Tsinghua University, 2003

[2] Tower crane Design Standard, GB/13752-92, 1993, 8

[3] Shan zuhui. Mechanics of materials (1) [M]. Beijing. Higher education press, 2004

[4] Gu dimin. Construction crane [M].Beijing. China Architecture Industry Press, 1988

[5]Zhang guorui. Tower crane [M].Beijing. Mechanical Industry Press, 1991

[6]Liu peiheng. Tower crane use manual [M].Beijing. Mechanical Industry Press, 2002

Applied Mechanics and Materials Vol. 597 (2014) pp 308-311
© (2014) Trans Tech Publications, Switzerland
doi:10.4028/www.scientific.net/AMM.597.308

Damping Analysis of Laminated Plates Using Complex Stiffness Method

Qingqing Wu[1, a *], Mingqing Wang[1, b]

[1]School of Marine Science and Technology, Northwestern Polytechnical University,

Xi'an, 710072, China

[a]email: wq7203365@126.com, [b]email: mqwang@nwpu.edu.cn

Keywords: Damping; Laminated; Complex Stiffness Method

Abstract. Damping property analysis of laminated composite structures have been done based on the complex stiffness method (CSM). In view of laminated plates with viscoelastic material cores, investigation is conducted using CSM and numerical methods of finite element method and spectral finite element method. Simulation results show that analytical solutions by CSM are in good agreement with the two kinds of numerical solutions. The proposed analytical method is well suited to calculate and optimize the damping property of laminated structures especially composites with constrained layer damping treatment.

Introduction

Damping plays an important role in structures' dynamic property which contributes to damp down structures' vibration response. The excellent damping characteristics of composites have interested many researchers to carry on analysis of composite structure's dynamic property.

Oberst and Frankenfeld [1] firstly showed that when the two-layered configuration vibrates harmonically, its flexural stiffness could be regarded as being complex and its normalized imaginary part being the flexural loss factor. Ross, Ungar and Kerwin [2,3] provided an early analysis of the constrained damped configuration and had found its effective complex flexural stiffness. Ungar and Kerwin [4] then derived loss factors of viscoelastic systems in terms of energy concept which is also regarded as strain energy method nowadays. J.N. Reddy [5,6] had done a great deal of research on mechanics of laminated composite plates and shells using different analytical method and finite element method (FEM). Shorter [7] developed the spectral finite element method (SFEM) to calculate the dispersion properties of linear linear viscoelastic laminates and estimated damping loss factor of each wave type from the cross-sectional strain energy distribution. M.C. Ray and J.N. Reddy [8] developed a three-dimensional finite element model to investigate the performance of the active constrained layer damping treatment for active control of thin laminated cylindrical shells conveying fluid. A.L. Araujo e.t.a. [9] used the direct multisearch method to conduct optimal design of active damping in sandwich structures.

In this paper damping analysis of laminated plates with viscoelastic cores is done based on CSM and is demonstrated by simulations using FEM and SFEM. This research provides a better understanding of damping property in laminated structures and also contributes to damping optimization design.

Theory

Fig. 1 shows the cross section of the model used for laminated composite structure analysis. The composite model consists of laminated elastic layers with viscoelastic damping material being the cores. Elastic layers contribute to the composite's stiffness and strength while viscoelastic cores produce damping ability. When bending waves propagate in composite structures, the deformations of damping cores are constrained by elastic layers to undergo shear strain which dissipates much more energy than extensional strain.

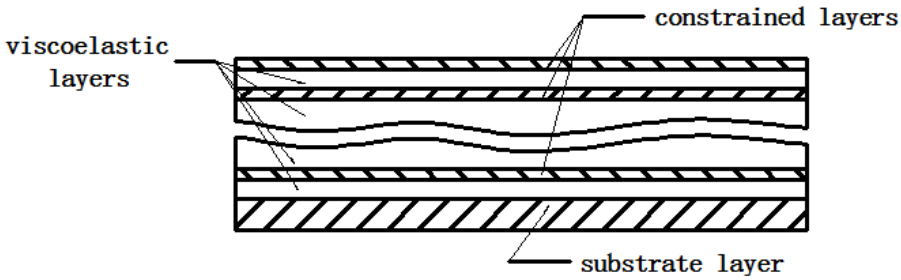


Fig. 1. Cross section of laminated composite structures

Assume that the laminated beam or plate is simply supported and all elastic layers vibrate with the same curvature $\partial\varphi/\partial x$. $(EI)_\infty$ and $(EI)_0$ represent structure's coupled and uncoupled flexural rigidity respectively. According to the theory of CSM, the complex flexural stiffness of the multi-layer structure can be written as

$$(EI)^* = (EI)_0(1+i\eta) \tag{1}$$

where η is the composite structure's loss factor.

The geometrical parameter is introduced as

$$Y = \frac{(EI)_\infty - (EI)_0}{(EI)_0} = \frac{(EI)_T}{(EI)_0} \tag{2}$$

where $(EI)_T$ represents the transfer flexural rigidity.

The total bending moment can be obtained by

$$M = (EI)^* \frac{\partial\varphi}{\partial x} = \sum M_{ii} + \sum F_i h_i = (EI)_0 \frac{\partial\varphi}{\partial x} + \sum F_i h_i \tag{3}$$

where M_{ii} is the moment exerted by the forces on the i th layer about its own neutral plane; F_i is the net extensional force on the i th layer and h_i is the distance from the neutral plane of the i th layer to the neutral plane of the composite structure at which the extensional strain is zero.

$$\sum F_i h_i = (\sum K_i l_i^2) Z^* \frac{\partial\varphi}{\partial x} = (EI)_T Z^* \frac{\partial\varphi}{\partial x} \tag{4}$$

where $K_i = E_i A_i$ = extensional stiffness of the i th layer;

l_i = distance from the i th layer to the composite neutral plane where there is no shearing;

Z^* = complex coupling parameter, defined by Eq. 5.

$$Z^* = 1 - \frac{H_v}{(EI)_T} \sum_{i=2}^{n} \left\{ K_i d_i \left[\sum_{j=2}^{n} R_j - \frac{1}{K_T} \sum_{j=2}^{n} \left(R_j \sum_{k=j}^{n} K_k \right) \right] \right\} \tag{5}$$

where $R_i = \frac{\varphi_i}{\alpha_i}$, $\alpha = \frac{\partial\theta}{\partial x}$, $\varphi = \frac{\partial\gamma}{\partial x}$; θ and γ represent flexural and shear angle respectively. d_i represents the distance from the i th layer to the center of the first elastic layer.

From Eq. 2, Eq. 3 and Eq. 4 we can obtain

$$(EI)^* = (EI)_0(1+Z^*Y) \tag{6}$$

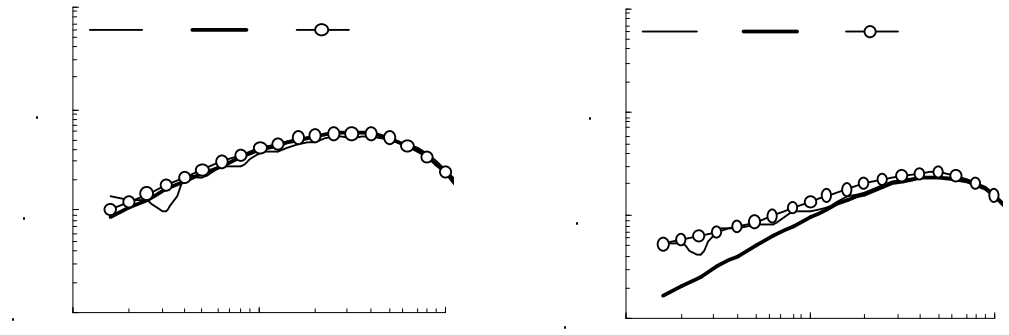
$$\eta = \frac{\mathrm{Im}(EI)^*}{\mathrm{Re}(EI)^*} = \frac{\mathrm{Im}(Z^*)Y}{1+\mathrm{Re}(Z^*)Y} \tag{7}$$

Set complex shear parameter $X_1^* = \dfrac{bG^*}{k^2 H_v K_T}$, where k is the flexural wave number and complex shear modulus $G^* = G(1+i\eta_v)$. For a laminated structure of N layers, the factor R_i of the i th viscoelastic layer can be achieved by the Eq. 8, as follows

$$\left(\frac{1}{K_T{}^2}\sum_{j=i}^{N}K_j\right)\left\{\sum_{e=2}^{N}\left(\sum_{m=e}^{N}K_m\right)R_e\right\}-\frac{1}{K_T}\left\{\left(\sum_{j=i}^{N}K_j\right)\sum_{j=2}^{i}R_j+\sum_{j=i+1}^{N}\left(\sum_{e=j}^{N}K_eR_j\right)\right\}-X_1R_i$$
$$=\frac{1}{K_T{}^2H_v}\left(\sum_{j=i}^{N}K_j\right)\left(\sum_{i=2}^{N}K_id_i\right)-\frac{1}{K_TH_v}\left(\sum_{j=i}^{N}K_jd_j\right) \tag{8}$$

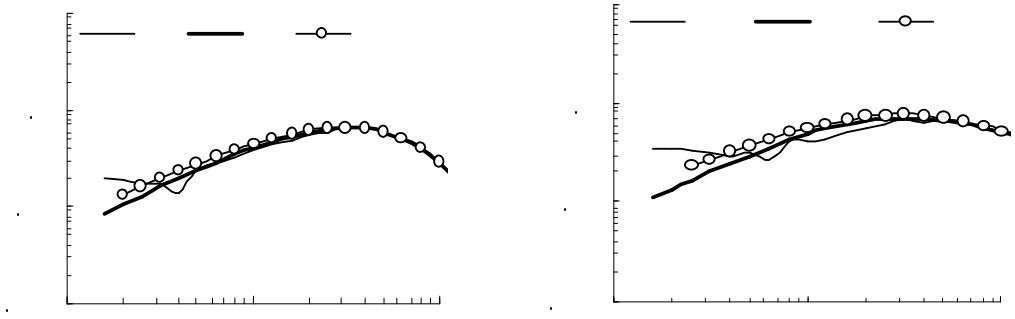
Simulation Results

Take two sandwich plates, a five-layer plate and a seven-layer plate for example. Loss factors are obtained by CSM as well as finite element method (FEM) by ANSYS and spectral finite element method (SFEM) by Autosea2. All plates consist of the same 6mm-thick steel substrate plates and the same viscoelastic material cores with $E_v = 1\times10^8$ MPa and $\eta_v = 0.2$. Both of the two sandwich plates have a 10mm-thick damping layer and a 0.5mm-thick constrained layer. The loss factor results of sandwiches constrained by aluminum layer and GFRP layer respectively are shown in Fig. 2a and Fig. 2b accordingly. Both of the five-layer plate and the seven-layer plate have 0.25mm-thick aluminum constrained layers with the thickness of damping layer being 4mm and 5mm respectively. Their loss factor solutions are shown in Fig. 3a and Fig. 3b accordingly.



(a) (b)

Fig. 2. Loss factor results of sandwich plates by different methods



(a) (b)

Fig. 3. Loss factor results of multi-layer plates by different methods

The agreement is shown to be significant between the values deduced from CSM and those numerical results of FEM and SFEM. While for frequencies below 100Hz, the agreement is not as good as that in high frequency range, the difference is quite allowable in practice. Although the substrate steel plate is as thick as 6mm, the composite structures' loss factor could be achieved up to 0.01~0.1 which can damp the substrate plate's vibration significantly. Another characteristics can be noticed is that multi-layer structures' loss factors change as freqency changes even if the core material's loss factor is set as a constant. This suggest that structural design is very important for laminate structures for the reason that geometical parameters affect structure's stiffness and damping as well.

Conclusion

Analysis research is done on damping property of laminated composite structures based on complex stiffness method. Aiming at sandwich plates and multi-layer plates, simulations are conducted by soft wares of ANSYS and Autosea2 using finite element method and spectral finite element method respectively. Loss factor solutions by CSM are in good agreement with those by FEM and SFEM. The investigation shows that laminated plates with constrained elastic layers can perform excellent damping property. This analytical research could be carried forward to conduct damping optimization design on laminated composite structures.

References

[1] H.Oberst, K.Frankenfeld. Über die Dämpfung der Biegeschwingunge dünner Bleche durch festhaftende Beläger [J]. Akustische Beihefte, 1952, 2(4): 181-194.

[2] E.M.Kerwin. Damping of flexural waves by a constrained visco-elastic layer [J]. Journal of the Acoustical Society of America, 1959, 31: 952-962.

[3] D.Ross, E.E.Ungar, E.M.Kerwin. Damping of plate flexural vibrations by means of visco-elastic laminae structural damping [J]. American Society of Mechanical Engineers, 1959: 49-87.

[4] E.E.Ungar, E.M.Kervwin. Loss factors of viscoelastic systems in terms of energy concept [J]. Journal of the Acoustical Society of Amenrica, 1962, 34(7): 954-958.

[5] J.N. Reddy. A Generalization of two-dimensional theories of laminated composite plates [J]. Communications in Applied Numerical Mehtods, 1987, 3: 173-180.

[6] J.N. Reddy. Mechanics of laminated composite plates and shells [M]. Boca Raton: CRC Press LLC, 2004.

[7] Shorter, P.J. Wave propagation and damping in linear viscoelastic laminates [J]. Journal of Acoustical Society of America, 2004, 115(5) : 1917-1925.

[8] M.C. Ray, J.N. Reddy. Active damping of laminatd cylindrical shells conveying fluid using 1-3 piezoelectric composites [J]. Composite Structures, 2013, 98: 261-271.

[9] A.L. Araujo, J.F.A. Madeira, C.M. Soares, ET al. Optimal design for active damping in sandwich structures using the direct multisearch method [J]. Composite Structures, 2013, 105: 29-34.

Applied Mechanics and Materials Vol. 597 (2014) pp 312-315
© (2014) Trans Tech Publications, Switzerland
doi:10.4028/www.scientific.net/AMM.597.312

Influence of axial compression ratio on seismic behavior of reactive powder concrete(RPC) beam-column joints

Yanzhong Ju[1, a] , Chunyu Li [2,b*]and Dehong Wang[3,c]

[1,2,3]College of Architecture Engineering，Northeast Dianli University，132012 Jilin，China

[a]juyanzhong@126.com, [b]lcyby925@126.com, [c]511048501@qq.com

Keywords: reactive powder; beam-column joints; axial compression ratio; seismic performance

Abstract. To explore the influence of axial compressive ratio on seismic behavior of reactive powder concrete(RPC) beam-column joints,this paper carry out RPC beam-column joints nonlinear finite element analysis,using software ABAQUS.The effect of different axial compression ratio on the ductility,energy dissipation capacity and bearing capacity are studied,based on hysteretic curves and skeleton curves of the components.The results show that,with the increase of axial compression ratio,skeleton curves of the components tend to be steep when the vertical load of beam ends exceed the peak point.The ultimate bearing capacity of the components are improved with the increasing of axial compression ratio which is less then 0.6,while the ultimate bearing capacity show a opposite trend when the axial compressive ratio exceed 0.6.

Introduction

Reactive powder concrete(referred to as RPC)[1],which is first successfully developed by the France company BOUYGUES in 1993,consist of quartz sand,cement, silicon powder,super plasticizer and steel fiber.Since the material increasing the fineness and activity,it is called reactive powder concrete.The compressive strength of the material is 170~230MPa,the flexure strength reach 6~10MPa,and the fracture energy is up to 30~40kJ/m^2 [2].Its excellent mechanical properties can effectively improve the seismic performance of the structure, and play an effective role in reducing the structure damage caused by the earthquake,especially suitable for the major aseismic components of the building structures such as column and beam-column joint.At present, the study of the mechanical properties of RPC has already been mature.[3]Domestic and foreign scholars have carried out extensive research on the mechanical properties of RPC components:Warnock R, Hani M, Zheng Wenzhong carried out an experimental research on the flexural and shear performance of RPC beams[4-6];MALIK A, Ju Yanzhong carried out research on axial compression, eccentric compression and seismic performance of RPC columns [7-8].At present,study on the seismic performance of reactive powder concrete beam-column joints has not been reported.In order to study the influence of different axial compression ratio on the ductility, energy dissipation capacity and bearing capacity of RPC beam-column joint,finite element model of each component is established in this paper.

Design of RPC Beam-Column Joints

The specific parameters and dimensions are shown in Table 1. The size of beam and column section are 150×250(b×h) and 200×200(b×h).The length of beam and column are 900mm and 650mm.

Table 1 The parameters of components

Joint number	Stirrup ratio of core joint[%]	Longitudinal reinforcement ratio of beam [%]	Longitudinal reinforcement ratio of column [%]	Axial compression ratio
J-1	2.83	1.76	2.54	0.3
J-2	2.83	1.76	2.54	0.4
J-3	2.83	1.76	2.54	0.5
J-4	2.83	1.76	2.54	0.6
J-5	2.83	1.76	2.54	0.7

Finite Element Model of RPC Beam-Column Joints

Finite Element Model. In the software abaqus,the plastic damage model can better simulate the mechanical behavior of concrete under monotonic, cyclic or dynamic load,and it also can control stiffness recovery of concrete when the cyclic loading reversed acting.Therefore,this paper adopts the plastic damage model to build the RPC constitutive relation.And tensile damage factor and compression damage factor are introduced to simulate the degeneration caused by the damage of the elastic stiffness of the concrete.This paper uses RPC uniaxial tension stress-strain curve and uniaxial compression stress-strain curve obtained by Yang Zhihui and Ma Yafeng[9-10]. RPC material parameters are listed in Table 2.C3D8R is selected as concrete unit in software abaqus.

Bilinear isotropic hardening model is selected as constitutive model of the steel which is in the elastic stage before yielding and after yielding steel stress - strain curve is simplified an oblique line.Steel material parameters are in Table3. T3D2 is selected as steel unit in the software abaqus.

Table 2 The material parameters of RPC

Elastic modulus[Mpa]	Poisson ratio	Peak compressive stress[Mpa]	Peak compressive strain	Peak tensile stress[Mpa]	Peak tensile strain
42050	0.25	138	0.0038	13.46	0.0003

Table 3 The material parameters of reinforcement

Type	Diameter [mm]	Use	Yield strength [Mpa]	Ultimate strength [Mpa]	Elastic modulus [Mpa]	Poisson ratio
HRB335	8	Stirrup	315.1	426.3	20000	0.3
HRB400	12	Longitudinal reinforcement	411.7	520.4	20000	0.3
HRB400	16	Longitudinal reinforcement	460.2	560.7	20000	0.3

Loading Rule of RPC Beam-Column Joints. Both the top and bottom of the column are hinged and the beam ends are set to free.Vertical concentrated load is applied on top of the column.Displacement control is adopted as the loading method at both ends of the beam.Apply the displacement hierarchically to the ends of the beam, and make it circle once per level. And increase the displacement according to 2.5mm within 10mm and 5mm more than 10mm. The displacement amplitude curves of the beam ends could be created by the “Amplitude” option of ABAQUS.

The Results of Finite Element Analysis

Hysteresis curves. The hysteresis curves of RPC beam-column joints could be obtained by finite element analysis. At the beginning of loading, the components are still in the elastic stage, through which making it produce no residual deformation after unloading. So the cycle of hysteresis curves are substantially linear and the area of the hysteresis curves increase gradually with the increasing of displacement of the load. When the axial compression ratio is small (J-1, J-2), the hysteresis curves of components are relatively full, and the ability of absorbing seismic energy and plastic deformation is fairly strong. With the axial compression ratio increasing, in one hand, the bearing capacity of component is improved; but in the other hand, the hysteresis curves become less fuller and energy dissipation capacity is poorer.In addition, when the vertical load of beam ends exceed the peak point, the strength and stiffness of components degenerate significantly.

Energy dissipation capacity. The fuller the hysteresis curve of component is, the better the energy dissipation capacity. Usually, equivalent viscous damping coefficient(h_e) which is the bigger the better is used to measure the energy dissipation capacity of components.

The equivalent viscous damping coefficients of the components under the maximum load are shown in Table 4. Table 4 shows that the equivalent viscous damping coefficients of the components decrease, namely energy dissipation capacity shows a downward trend, with the axial compressive ratio increasing.But overall, the equivalent viscous damping coefficients of RPC beam-column joints are more than 0.4, which makes RPC beam-column joints have good hysteretic energy dissipation capacity under the seismic load.

Table4 Energy dissipation of components

Joint number	J-1	J-2	J-3	J-4	J-5
h_e	0.470	0.467	0.458	0.452	0.440

Skeleton curves and ductility. The skeleton curve of each component could be obtained by connecting the peak points of the hysteresis curves.The skeleton curves could reflect the features of each component, such as the yield load P_y, the yield displacement Δ_y, the ultimate load P_u, the limit displacement Δ_u and the ductility coefficient μ.This paper adopts yield bending moment method to determine Δ_y, and the corresponding load is P_y.As the ends of the beam horizontal load drops to 85% of peak load, this paper adopts the corresponding displacement as Δ_u and the corresponding load as P_u. Ductility coefficient is defined as $\mu=\Delta_u/\Delta_y$.The results of analysis are shown in the Table 5.

As is shown in the Fig.1 and Fig.2,the ultimate bearing capacity of RPC beam-column joints increase with axial compression ratio which is less then 0.6 increases,but the higher axial compression ratio has little effect on the bearing capacity of the components.However,when the axial compression ratio is more then 0.6 ,the ultimate load of the components become decrease and the ductility coefficient significant decline.Therefore, this paper suggests that the axial compression ratio should not be higher then 0.6 when the seismic designing of RPC beam-column joints.

Table 5 Load, displacement and ductility of components

Joint number	Δ_y/mm	P_y/kN	Δ_u/mm	P_u/kN	μ
J-1	10.33	97.44	59.37	108.05	5.75
J-2	10.14	101.73	55.2	113.00	5.44
J-3	10.01	104.40	54.02	117.08	5.40
J-4	9.61	106.12	50.8	118.53	5.29
J-5	9.58	104.91	49.9	116.61	5.21

Conclusion

With the increase of axial compression ratio,the energy dissipation capacity and ductility of RPC beam-column joints show a downward trend and plastic deformation ability becomes poor at the same time.When the axial compression ratio is less than 0.6,the ultimate bearing capacity of RPC beam-column joints increase with axial compression ratio increases,and when axial compression ratio is higher than 0.6,the ultimate bearing capacity of the components decrease with axial compression ratio increases. Therefore, this paper suggests that the axial compression ratio should not be higher then 0.6 when the seismic designing of RPC beam-column joints.

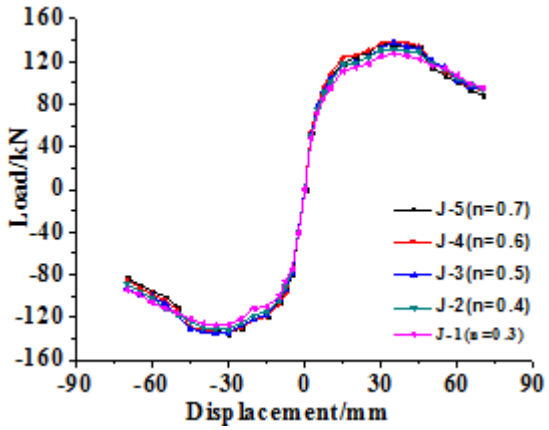


Fig.1 The skeleton curves of components

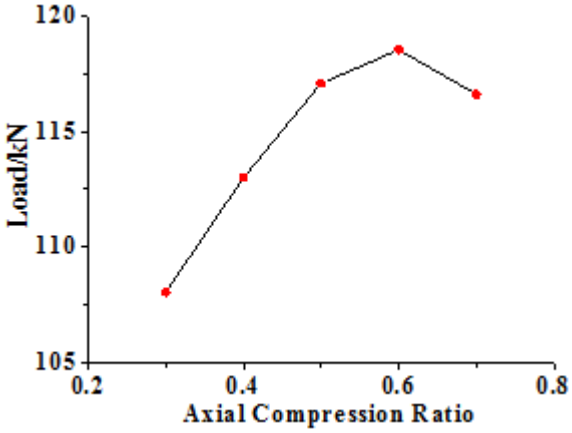


Fig.2 Ultimate bearing capacity of components

References

[1] Pierre Richard,Marcel Cheyrezy. Composition of Reactive Powder[J]. Cement and Concrete Research, 1995, 25(7):1501-1511.

[2] Bai Hong,Gao Ri.The Application of Reactive Powder Concrete in Engineering Construction [J].Building Science, Aug.2003, 19(4):51-55.

[4] Warnock R, Short-Term and Time-Dependent Flexural Behavior of Steel Fiber Reinforced Reactive Powder Concrete Beams[D], University of New South Wales, 2005.

[5] Hani M. Fahmi, Ihsan A.S AlShaarbaf, Abdullah Sinan Ahmed. Behavior of Reactive Powder Concrete Deep Beams[J]. AL-Mansour Journal, 2013, 12(20):22-44

[6] ZHENG Wenzhong,LI Li,LU Shanshan.Experimental research on mechanical performance of normal section of reinforced reactive powder concrete beam[J].Journal of Building Structures, 2011, 32(6):125-134.

[7] MALIK A R, FOSTER S J. Behaviour of reactive powder concrete columns without steel ties[J]. Journal of Advanced Concrete Technology, 2008, 6(2):377-386.

[8] JU Yanzhong,WANG Dehong,BAI Junfeng.Seismic performance of reactive powder concrete columns[J].Journal of Harbin Institute of Technology, AUG.2013, 45(8):111-116.

[9] Yang Zhihui.Study on Tension Mechanical Performance of Reactive Powder Concrete in Different Steel Fiber Volume Fractions[D].Beijing Jiaotong University, 2006.

[10] Ma Yafeng.Study on Constitutive Relationship of 200MPa Reactive Powder Concrete under Uni-axial Compression[D].Beijing Jiaotong University, 2006.

Applied Mechanics and Materials Vol. 597 (2014) pp 316-319
© (2014) Trans Tech Publications, Switzerland
doi:10.4028/www.scientific.net/AMM.597.316

Influence of curing temperature on the compressive strength of high performance concrete

Kim, Sun-Woong[1,a], Park, Wan-Shin[1,b], Eom, Nam-Yong[1,c]

Jang, Yong-Il[1,d], Yun, Hyun-Do[2,e], and Kim, Do-Gyum[3,f]

[1]Department of Construction Engineering Education, Chungnam National University, 99 Daehak-ro, Yuseong-gu, Daejeon, Republic of Korea

[2]Department of Architectural Engineering, Chungnam National University, 99 Daehak-ro, Yuseong-gu, Daejeon, Republic of Korea

[3]Korea Institute of Construction Technology, 283 Go-yangdae-ro, Ilsanseo-gu,Goyang, Republic of Korea

[a]kswoong1@naver.com, [b]salshin@cnu.ac.kr (Corresponding author), [c]eomny@nate.com, [d]jang1001@cnu.ac.kr, [e]wiseroad@cnu.ac.kr, [f]dgkim@kict.re.kr

Keywords: High performance concrete (HPC), Silica fume, Compressive strength, Cold weather, Curing days, Mixing temperature.

Abstract. The supposition that curing at cold weather conditions leads to the loss of compressive strength of the high performance concrete was investigated. This paper addresses the results of an extensive experimental study on the compressive strength under cold weather conditions. The specimen was prepared as it's inside 100-mm diameter and 200-mm heights cylindrical were used. In this work, high performance concrete was designed a water-binder ratio of 0.40. These tests were carried out to investigate the mechanical properties of HPC for 7 and 28 days. The results properties of HPC with silica fume were effective for compressive strength improvement between 7 to 28 curing days at 5℃, -5℃ and -15℃.

Introduction

The manufacture of concrete with Portland cement in adverse weather conditions involving high and low temperatures directly influences the performance of the concrete during mixing, transport and curing and its physical and mechanical properties [1]. The main problems associated with cold weather are frost damage to immature concrete and slow gain in strength leading to later stripping times and the possibility of increased damage when the shutters are removed. As part of the measures, the high performance concrete is designed to have better mechanical properties and higher workability and resistance to aggressive chemicals than traditional concrete [2]. In addition use of High performance concrete as cement replacement in concrete is a common practice due to technological, economic, and environmental benefits. High performance concrete is a relatively new material. Although it has been well recognized that the use of pozzolanic materials such as silica fume (SF) is necessary high performance concrete, can improve either or both the strength and durability properties of the concrete. Mineral admixtures such as fly ash silica fume (SF) are normally included in the production of high performance concrete because of the better engineering and performance

Table 1. The details of mix proportions (Unit : kg/m^3)

Specimen name	Cement	Coarse Aggregate	Fine aggregate	Silica fume	AD	AE
SF5 (5, -5 and -15)	368	1057	772	19	0.9	0.02

Water-binder ratio:0.40, Water : 155 kg/m^3

Table 2. Physical properties of aggregate

	Density	water absorption	Max size D_{max}	Unit weight
	(g/cm^3)	(%)	(mm)	(kg/m^3)
Coarse aggregate	2.78	1.33	20	1,702
Fine aggregate	2.68	2.80	5	1,662

properties. The presence of mineral admixtures in concrete is known to impart significant improvements in work-ability and durability[3]. This paper addresses an extensive experimental study on the compressive strength of high performance concrete in cold weather curing at 7 and 28days.

Experimental program

Table 1 shows the detail of mix proportions. The specimen investigate the effect of admixture on high performance concrete, cement was replaced by silica fume at constant water-binder ratio of 0.4, like quality of component, keeping other mix variables, mix correspondence, and mixing procedures. Detailed information about specimen used and their characteristics are presented in mixtures 5% silica fume as cement replacement, respectively. The primary objective of the research project was to investigate the supposition that compressive strength of SF5 cured during cold weather adversely affected to a larger extent than conventionally perceived. The specimen correspondence was set up to achieve target compressive strength of 41.37MPa (6000psi) in this study.

Materials. Normal Portland Cement, and silica fume (SF) were used for various high performance concrete. The physical and mechanical properties of the rounded coarse and fine aggregates are summarized in Table 2. Fine aggregate and coarse aggregate with maximum size of 5mm and 20mm and a density of 2.78 and 2.68, respectively, were used.



(a) Putting sand (b) Adding aggregate (c) Adding cement (d) Mixing

Fig. 1 Mixing procedure



(a) Slump test (b) Air content

Fig. 2 Slump test and air content

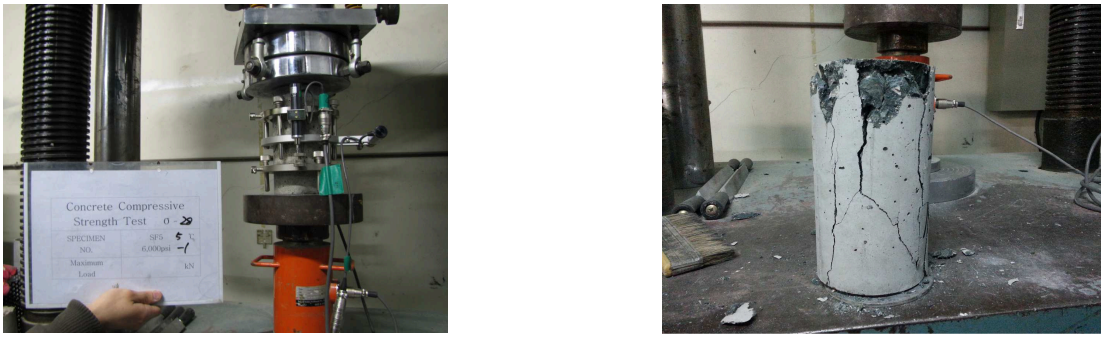


Fig. 3 Compressive strength test

Experimental procedure. Fig. 1 shows the mixing procedure. The specimens were prepared as its inside 100-mm diameter and 200-mm height cylindrical were used. All tests were conducted at the ages of 7 and 28 days curing. Fig. 3 shows the compressive test. Compressive strength was carried out in accordance to ASTM C 39[4]. Before compressive strength testing, samples were kept in room temperature for 24 h and then the cylinders were capped with an appropriate material such as sulfur prior to compressive strength test to prevent inaccurate strength results. In this work, specimens were curing plastic wrap in the refrigerator before compressive test.

Test results and discussion

Slump and air content. Fig. 2 (a) and (b) shows the slump and air content test respectively. The slump flow tests were performed according to ASTM C 143. The consistency and workability of all the concrete mixtures was determined through slump tests to achieve target slump of about 180±50mm. The air content tests were performed to achieve target air content of 4.5± 1.5%.using gravimetric methods according to ASTM231.

Table 4. Summary of strength properties

Concrete type	Compressive strength			
	Curing temperature	7 days	28days	28 days/7 days
SF5	5	16.79	27.15	1.62
	-5	15.81	25.41	1.61
	-15	2.82	4.08	1.45

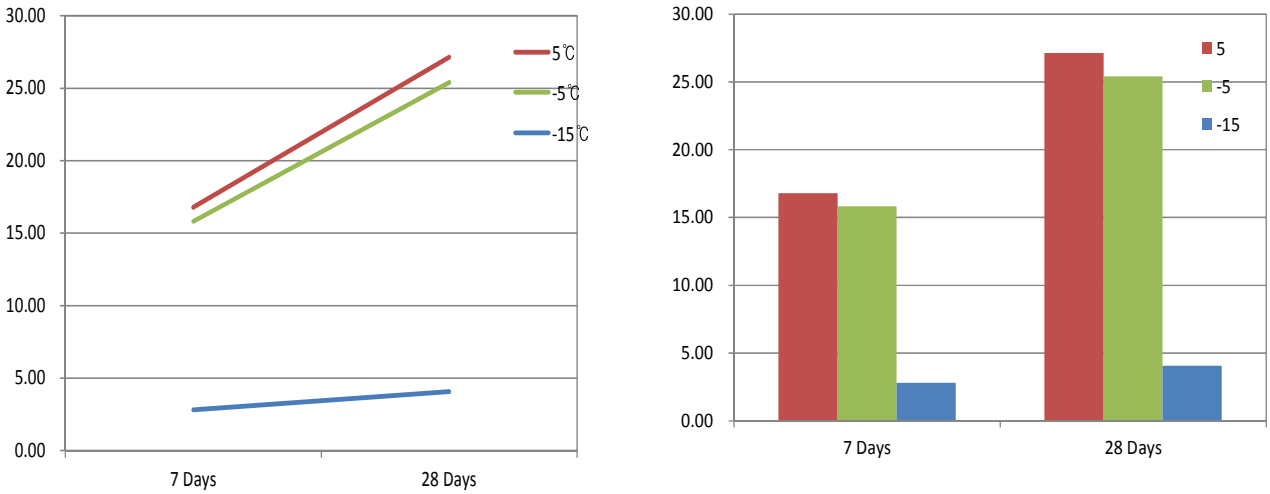


Fig. 4 Compressive strength

Compressive strength. Measured compressive strength property of specimens SF5 at 7 and 28 days (5℃, -5℃, -15℃) used in the test are summarized in Table 4. In addition, Fig. 4 indicate the variation of compressive strength of SF 5. At 7 days curing, specimens SF5 5℃, -5℃ and -15℃ could be subjected compressive strength of 16.79 MPa, 15.81 MPa and 2.81 MPa respectively. 7 days compressive strength of 5℃ is 1.07 and 5.95 times higher than those of specimens -5℃ and -15℃. 28 days curing, specimens SF5 5℃, -5℃ and -15℃ could be subjected compressive strength of 27.15 MPa, 25.41 MPa and 4.08 MPa respectively. 28 days compressive strength of 5℃ is 1.07 and 6.65 times higher than those of specimens -5℃ and -15℃. In addition, the specimens SF5 5℃, -5℃ and -15℃ 28 days compressive strength were 1.62, 1.61 and 1.45 times higher than those obtained from 7days testing, respectively. The most damaging -15℃ is for freezing compressive strength of SF 5 5℃, -5℃ and -15℃ to occur when concrete has set but has not irreparable loss of strength. The reason -15℃ curing was that void structure increased due to the decrease in the temperature to which the concrete was exposed.

Summary

This study is influence of on the high performance concrete compressive strength under cold weather conditions. In specimens were mixtures 5% silica fume as cement replacement. After mixture one group of samples was cured in the different deepfreezes at 5℃, -5℃ and -15℃ for 7 and 28 days. The test results, 7 days compressive strength of 5℃ is higher than those of specimens -5℃ and -15℃, although 28 days compressive strength of 5℃ is higher than those of specimens -5℃ and -15℃. In addition, the specimens SF5 5℃, -5℃ and -15℃ 28 days compressive strength were higher than those obtained from 7days testing, respectively.

Acknowledgements

This work was supported by Nuclear Research & Development of the Korea Institute of Energy Technology Evaluation and Planning (2011T00200161) grant funded by the Korea government Ministry of Knowledge Economy.

References

[1] J. Ortiz, A. Agudado, L. Agulló, T. Garcia In fluence of environmental temperatures on the concrete compressive strength; simulation of hot and cold weather conditions, Cement and concrete Research. 35(2005) 1970-1979.

[2] Tsung-Yueh Tu, Yuen-Yuen Chen, Chao-Lung Hwang, Properties of HPC with recycled aggregates, Cement and concrete Research. 36 (2006) 943-950.

[3] Construction and Building Materials, Performance of self-compacting concrete containing different mineral admixtures. 25(2011) 4113-4120.

[4] ASTM C 39-02, Standard test method for compressive strength of cylindrical concrete specimens, Annual Book ASTM Standards, 4(04.02), 2002.

Applied Mechanics and Materials Vol. 597 (2014) pp 320-323
© (2014) Trans Tech Publications, Switzerland
doi:10.4028/www.scientific.net/AMM.597.320

Mechanical properties of reactive powder concrete containing fly ash under different curing regimes

Dehong Wang[1,2, a *], Yanzhong Ju[1,b] and Wenzhong Zheng[2,c]

[1]School of Architecture Engineering, Northeast Dianli University, Jilin, 132012, China

[2]School of Civil Engineering, Harbin Institute of Technology, Harbin 150090, China

[a]hitwdh@126.com, [b]juyanzhong@126.com, [c]214030828@qq.com

Key words：Reactive powder concrete; Fly ash; Mechanical properties; Curing regimes

Abstract

Mechanical properties of reactive powder concrete (RPC) containing fly ash were investigated under different curing regimes (standard and steam curing) in this study. The experimental results indicate that, flexural strength of RPC increased considerably after steam curing, compared to the standard curing. Steam curing had no significant effect on compressive strength of RPC. Increasing the fly ash content improved the flexural strength of RPC under all curing regimes considerably. The compressive strength reached a maximum (103.8MPa) when the fly to ash and cement ratio is 0.3.

Introduction

Reactive powder concrete (RPC) is a new generation concrete with ultra-high strengths and outstanding durability, and it was developed through microstructure enhancement techniques for cementitious materials [1, 2]. Dense micro-structure, superior durability and mechanical properties define the RPC as an ultra-high performance concrete [3]. Nowadays to be a promising material for special concrete members, it can be used for civil engineering, mining, oceaneering and military projects.

In order to obtain ultra-high strength under very low water to cement ratios, the dosage of cement is larger; a high amount of cement not only affects the production costs, but also has negative effects on the heat of hydration and shrinkage deformation. Using fly ash to replace partial binder material (cement and silica fume) may be overcome the above problem to a certain extent [4]. The main objective of this research is to determine the influent of fly ash content and curing regimes on mechanical properties of RPC containing fly ash. The research will be providing basis for engineering application of RPC.

Experimental

The RPC considered here was prepared by the following materials: PIIO42.5R Ordinary Portland cement, silica fume, fly ash, quartz sand and superplasticizer. Fly ash is provided by jilin songhua river thermal power plant, and the density of fly ash is 2.25 g/cm^2, loss on ignition is 4.30%, fineness is around 45μm, fineness screen at a rate of 3%. Water reducing ratio of superplasticizer is around 29%.

The main objective of this research is to determine the effects of content of fly ash and curing methods on the mechanical properties of the RPC. Three mixtures were designed, the ratio of fly

ash to cement is 0.2, 0.3 and 0.4. Table 1 summarizes the mixture designs of RPC in this study. As can be seen from Table 1, abbreviations were used for mixtures according to content of fly ash. Fly ash were denoted by F, fly ash ratios by cement weight were also given in the abbreviations. For instance, F20 means quality percentage of fly ash in cement is 20%.

Table 1 Mixture proportions of RPC

Group number	cement [kg]	Silica fume [kg]	Coarse sand [kg]	Medium sand [kg]	Fine sand [kg]	Fly ash [kg]	Superplasticizer [kg]	Water [kg]
F20	688.38	206.51	774.53	389.55	178.26	137.68	61.95	163.15
F30	645.64	193.69	774.87	389.72	178.34	193.69	58.11	165.93
F40	607.90	182.37	775.18	389.87	178.41	243.16	54.71	168.39

Weight various components according to the laboratory mixtures, three kinds of quartz powders were first mixed for 2~3 min at low and high speed in mixer. Then the binding materials (i.e. cement, silica fume and fly ash) were added and re-mixed for about 3 min. Half of the water and all the superplasticizer were added and re-mixed for about 6 min at high speed. Subsequently, the left water were added and re-mixed for about 3 min at high speed. The mixture were dumped into molds, then specimens with mold were vibrated on vibrating table. Subsequently, the specimens were kept in the moulds for 24 h at room temperature of about 20℃. After that RPC specimens were removed from molds. One-half of the RPC specimens were cured in water at 25±5℃ for 27 days. The other one-half of specimens were exposed to steam curing at 80±5℃ for 3 days, then cured in water at 25±5℃ for 24days [5].

In view of the reactive powder concrete does not contain coarse aggregate, the small size effect, Cube specimens (100mm×100mm×100mm) were used to determine the compressive strength of RPC. Prismatic specimens (100mm×100mm×400mm) were used to determine the flexural strength of RPC. Test method in conformity with the standard for test method of mechanical properties on ordinary concrete [6].

Results and discussion

Figure 3 shows the compressive strength of RPC under different curing conditions. The compressive strength of F20 is closer to F30's under both curing conditions. The compressive strength of F30 with steam curing increased by 11% than cured in water, the influence of curing conditions on compressive strength of RPC is not obvious. Under room temperature curing, the compressive strength of RPC decreases as the content of fly ash increases. The measure to properly increase the content of fly ash can improve the fluidity of RPC improved significantly. Under room temperature curing condition, average compressive strength of the three groups specimens were more than 82 MPa, and the fluidity is good, so it is feasible to use RPC cast-in-place component.

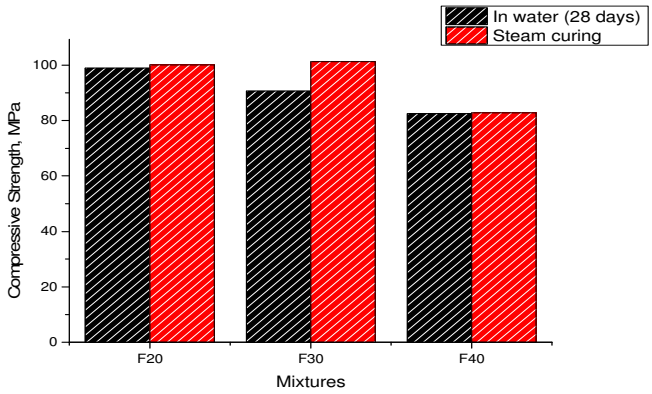


Fig.1 The Influence of fly ash content and curing conditions on compressive strength of RPC

Steam curing can accelerate pozzolanic effect and improve the microstructure of hydration products. Hydration products keep non-crystalline state after steam curing. Rise curing temperature can accelerate the hydration process of cement and increase the early strength of concrete. Under the high temperature condition, hydration calcium silicate lose part of the water, translate into xonotlite-type calcium silicate which has a higher strength [7].

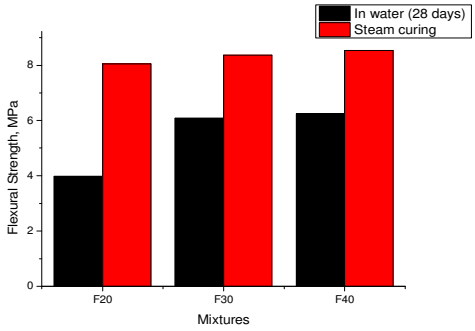


Fig.2 The Influence of fly ash content and curing conditions on flexural strength strength of RPC

Figure 2 shows flexural strength of RPC containing fly ash under different curing regimes. Flexural strength of RPC increases with the increase of fly ash content. According to the content of fly ash, improvement in flexural strength is between 53% and 57% for steam curing, the increment is between 4% and 6% for 28-day water curing. Steam curing improved the flexural strength of RPC considerably. For F20, the improvement in flexural strength is almost double for steam curing compared to the 28-day water curing. For F30 and F40, the increment is around 37% after steam curing.

Steam curing is helpful to improve the flexural strength of RPC. and the addition of fly ash can improve the grain size distribution of binder systems, when the content of fly ash is optimum, density of mixture can be improved greatly[6]. Cement particle size in the 30μm or so, the particle size distribution is not reasonable in the process of cement production, interspace of cement particles is bigger, and particles cannot reach the best dense packing. fly ash is between concrete with silica fume in particle size, particle size distribution is relatively reasonable, use of fly ash can fill the space between cement particles, make the free water discharged, increase the density and strength. Beside, the liquidity of RPC containing fly ash is better, though water to binder ratio is low.

Conclusion

The compressive strength of RPC is less affected by curing regimes, under room temperature curing compressive strength of all groups were more than 82 MPa, and the addition of fly ash can improve the grain size distribution of binder systems, to a certain extent, improve the workability of the RPC, so it's feasible to use RPC containing fly ash for cast-in-place reinforced concrete member.

Flexural strength of RPC increases with the increase of fly ash content. Under the room temperature curing condition, the compressive strength of RPC decreases with the increase of fly ash content, for groups under steam curing, the maximum compressive strength (103.8MPa) was observed in F30. Synthesizes the workability and mechanical properties of RPC, 0.3 can be chosen as fly ash to cement ratio.

Acknowledgements

The work described in this paper was fully supported by National Natural Science Foundation of China (Project No. 51378095).

Reference

[1] Richard P, Cheyrezy Marcel. Composition of reactive powder concrete. Cement and Concrete Research, 1995, 25(7): 1501-1511.

[2] Richard P, Cheyrezy MH. Reactive powder concretes with high ductility and 200–800 MPa compressive strength. ACI SP144-24 1994; 144: 507–518.

[3] JU Yanzhong, WANG Dehong, ZHANG Chao. Advance of research and application on Reactive Powder Concrete. Journal of Northeast Dianli University, 2011, 31(5/6): 9-15.

[4] Halit Yazıcı, Huseyin Yiğiter, Anıl Ş. Karabulut, et al. Utilization of fly ash and ground granulated blast furnace slag as an alternative silica source in reactive powder concrete. Fuel, 2008, 87(12): 2401-2407.

[5] JU Yanzhong, WANG Dehong, SHAN Ming. On the mechanical properties and freezing-thawing resistance of reactive powder concrete. Journal of experimental mechanics, 2012, 27(2): 214-220.

[6] GB/T 50081-2002. The standard for test method of mechanical properties on ordinary concrete.

[7] LI Li. Mechanical behavior and design method for reactive powder concrete beams. Haerbin: Harbin Institute of Technology, 2010.

Applied Mechanics and Materials Vol. 597 (2014) pp 324-327
© (2014) Trans Tech Publications, Switzerland
doi:10.4028/www.scientific.net/AMM.597.324

Static stress changes and triggering imposed by Wenchuan earthquake on Lushan M7 earthquake

Dongning Lei[1,a], Yongjian Cai[1,2], and Heng Li[1]

[1] Key Laboratory of Earthquake Geodesy, Institute of Seismology, CEA, Wuhan, 430071, China
[2] Faculty of Earth Science, China University of Geosciences, Wuhan, 430074, China
[a] 357521555@qq.com

Keywords: Lushan M7.0 earthquake; Coulomb stress; stress triggering; seismogenic structure

Introduction

Some faults rupture the surface followed by coseismic dislocation, which causes space stress changes and transmits or imposes static stress on or to neighboring faults.The static stress triggering leads to the adjacent fault ruptured in advance, which means a Coulomb stress increase and triggers a new earthquake event. In recent two decades, some studies on stress triggering became important field of seismotectonics. The occurrence of both Wenchuan M8.0 earthquake and Japan M9.0 eathquake have arisen interest of many researchers, and obtained much new result and understanding.

In 20th April 2013, a strong shock struck Lushan city and tectonically located southwestern Longmenshan fault segment, in which is the one of the biggest earthquake occurring since Wenchuan M8.0 earthquake. Both earthquake events are extremely near in the aspect of time and at a distance of 80km in spatial. After the Lushan earthquake, some debates and disagreement arise about whether the event is dependent of Wenchuan earthquake or not. Many researchers makes a large number of attempts in Lushan earthquake cause coefficients. From the view of static stress triggering, we calculate the Coulomb stress changes which the Wenchuan earthquake imposes on Lushan event for seismogenic fault plane, and preliminarily discuss the triggering relationship probably existing between the two earthquake events.

Calculation method and model

Coulomb stress calculation. When strong shock occurs, the static stress field of seismogenic fault and its adjacent area can change and is named by stress transfer. On the basis of the elastic half-space theory proposed by Okada and Coulomb stress change formula deduced by King, Shinji Toda developed the software of Coulomb 3.3. We use this software calculate the Coulomb stress change($\Delta\sigma_f$).

$$\Delta\sigma_f = \Delta\tau_s + \mu\ (\Delta\sigma_n - \Delta p) \qquad (1)$$

Where $\Delta\tau_s$ is the shear stress change in fault plane(along the slip direction is positive); $\Delta\sigma_n$ is the normal stress change(tension stress is positive); Δp is pore pressure change of rock stratum; μ is friction coefficient. The effective normal stress will change with pore pressure in rock, meanwhile, rock stress changes faster than that of pore pressure. Therefore, the effect which the pore pressure impose on effective normal stress usually replaced by effective friction coefficient μ'.

$$\mu' = \mu\ (1 - B_k) \qquad (2)$$

Here B_k is Skempton coefficient, and the value ranges from 0 to 1. According to formula (1) and (2), Coulomb fracture criterion may express as follow:

$$\Delta\sigma_f = \Delta\tau_s + \mu'\Delta\sigma_n \qquad (3)$$

In practical calculation, the Poisson's ratio is generally valued by 0.4. As to the value of μ', King thinks that it has little affect on stress results. There are some researchers who has made much work to analyze the practical influence on calculation result and made parameter sensitive analysis. The study suggests that Coulomb stress chang image vary with different value of μ'. Thence, this paper deals with this Coulomb stress change in three different values of effective friction coefficient μ', which is given to 0, 0.4 and 0.8, respectively.

The model building and parameter selecting. In calculating Coulomb stress, we need such geometry parameters as dip, strike, dip angle, rake and dislocations of the fault, which is named seismogenic fault or source fault. For seismogenic fault of great earthquake, if in calculating stress change,using unique and consistent fault plane parameters, it is not precise. These kinds of parameters don't reflect tiny difference of sliping variation in fault plane and lead to much uncertainty of Coulomb stress change image. At an aim of standing for reliable sliping and attitude of greatly seismogenic fault plane, we select the finite element model of Chen ji for numerical calculation. The model is separated into 168 net slip grids, each which is given to corresponding parameters, having a specific sliping amount ranging from 0 to 9m. We give finite element model of Wenchuan M8.0 earthquake as figure 1.

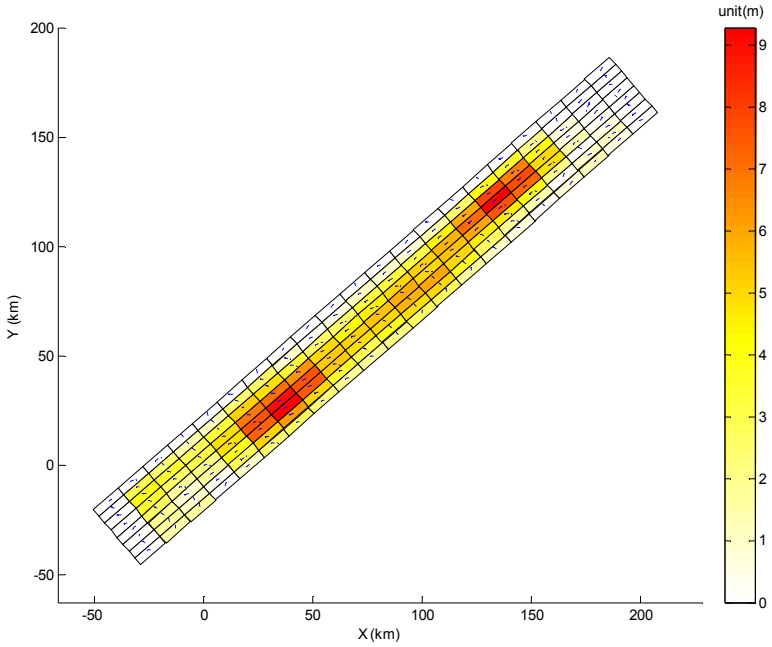


Figure 1 The finite element model of seismogenic fault of Wenchuan M8.0 earthquake

The Coulomb 3.3 software need some mechanic parameters to complete the Coulomb stress change calculation, which includes shear modus, Poisson's ratio, effective friction coefficient and calculation depth and so forth. The parameters selecting is very important because it has great affection on stress result. Usually, these parameters are given some typical values which are proved to proper and concise. In the calculation, the shear modus, Poisson' ratio and calculation depth are valued by 8×10^5bar, 0.25 and 14km, respectively. As for calculation depth, it is considered that the focal depth of Lushan M7.0 earthquake and indicates Coulomb stress changes of fault rupture in this depth.

Another important parameter is the attitude of receiver faults, which is imposed stress change and. In calculating, we select typical three set of focal mechanism solutions of Lushan earthquake and are numbered to 1, 2 and 3, respectively (Table 1). Considering that the seismogenic fault plane can't be determined , we make much calculation for nodal plane Ⅰ and nodal plane Ⅱ to obtain the normal stress, shear stress and Coulomb stress change, respectively.

Table 1 The focal mechanism solutions of Lushan M7.0 earthquake

No.	Magnitude	Nodal plane			Nodal plane			After
		Strike °	Dip °	Rake °	Strike °	Dip °	Rake °	
1	Ms7.0	214	38	102	29	53	81	Xie et al.,2013
2	Ms7.0	209	46	94	23	44	86	Lv et al.,2013
3	Mw6.6	216	47	93	32	43	87	USGS

Calculation results and discussion

According to the fault finite element numerical model of Chen ji, we calculate the Coulomb stress change in three different focal mechanism solution, meanwhile, we give three various effective friction coefficients. The calculating results suggest the Lushan earthquake epicenter is located at the increasing stress area, which is likely to show stress triggering. The maximum value of Coulomb stress change is up to 0.258 bar and minimum is 0.028 bar, both which have reached to static stress triggering threshold value.

As effective friction coefficient is concerned, the Coulomb stress change is gradually decreasing with the effective friction coefficient increasing. Furthermore, the amount of stress weakness can is up to 50%. However, as for nodal plane of seismogenic fault, the variation of both nodal planes seems to be very consistent and has no difference. We use three focal mechanism solutions to join in stress calculation, which in some extent makes good explanation about the Coulomb stress change in seismogenic fault plane.

The stress triggering between the strong earthquakes obviously behaves. The Lushan earthquake happened in southwestern segment of Longmenshan fault belt after five years, when strong Wenchuan earthquake occurred. Both shocks have very coincidence in temporal and in spatial, revealing likely static stress triggering and stress release of fault belt in advance. Some attempt conculsions can be drawn from this study that Wenchuan earthquake triggered the Lushan earthquake and is a typical stress triggering event. Much previous try and understanding on this topic keep coincident with this attempt.

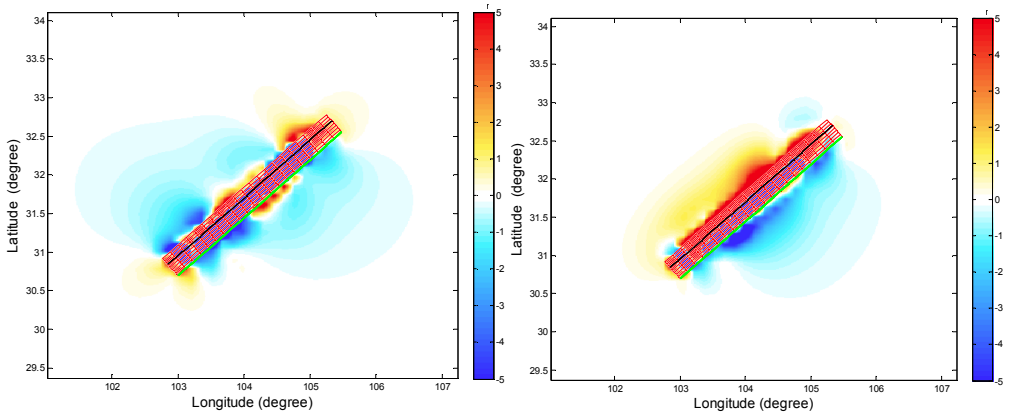


Figure 2 The Coulomb stress change of Lushan M7.0 earthquake fault plane imposed by Wenchuan M8.0 earthquake

Note: Here we only give two Coulomb stress change images, and other images are omitted. Left image indicates the Coulomb stress change image only when μ' is 0.4 and imposed on the nodal Ⅰ (214°/38°/102°)of Xie's focal mechanism solution. Right image indicates the Coulomb stress change image when μ' is 0.8 and imposed on the nodal Ⅱ(32°/43°/87°)of USGS's focal mechanism solution.

Table 2 The coulomb stress change on Lushan earthquake at 14km depth produced by Wenchuan 8.0 earthquake(unit: bar)

μ'	No.	Nodal plane			Nodal plane		
		$\Delta\sigma_f$	$\Delta\tau_s$	$\Delta\sigma_n$	$\Delta\sigma_f$	$\Delta\tau_s$	$\Delta\sigma_n$
μ'=0	1	0.251	0.251	-0.198	0.237	0.237	-0.306
	2	0.258	0.258	-0.275	0.258	0.258	-0.232
	3	0.246	0.246	-0.272	0.246	0.246	-0.213
μ'=0.4	1	0.115	0.237	-0.306	0.172	0.251	-0.198
	2	0.148	0.258	-0.275	0.165	0.258	-0.232
	3	0.137	0.254	-0.272	0.161	0.246	-0.213
μ'=0.8	1	0.093	0.251	-0.198	0.068	0.237	-0.306
	2	0.038	0.258	-0.275	0.072	0.258	-0.232
	3	0.028	0.246	-0.272	0.028	0.246	-0.213

Conclusions

Based on the finite element fault model, we use Coulomb 3.3 software calculate the Coulomb stress change of fault plane, which the Wenchuan M8.0 earthquake imposes on Lushan M7.0 earthquake in 14 km depth. According the numerical calculation, Lushan earthquake is located at the stress triggering area which is produced by Wenchuan M8.0 earthquake. The results indicate that the Coulomb stress change ranges from 0.028 bar to 0.258 bar, and maximum value is up to stress triggering critical value. The preliminary study suggests that the Wenchuan earthquake has a strong triggering on Lushan earthquake, which is extremely consistent with previous studies made by other researchers.

Acknowledgements

This study is supported by the project of Director Foundation of Institute of Seismology, China Earthquake Administration (No.IS200856069).

References

[1] Scholz,C. H.,1990. The mechanics of earthquakes and faulting, Cambridge University Press, Cambridge, UK, 439.

[2] King, G. C. P., Stein, R. S., Lin, J., 1994. Static stress changes and the triggering of earthquakes. Bull. Seismo. Soc. Amer., 84(3): 935-953.

[3]Stein,R. S.,1999. The role of stress transfer in earthquake occurrence. Nature,402(6762):605-609.doi: 10. 1038/45144.

[4] Yong-ge Wang,Zheng-kang Shen. 2010. Static Coulomb stress changes on faults caused by the 2008 Mw 7.9 Wenchuan, China earthquake[J]. Tectonophysics. 491,1-4,105-118.

[5] Okada Y.1992.Internal deformation due to shear and tensile faults in a half space[J]. Bulletin of the Seismological Society of America,82(2):1018-1040.

[6] Yun-Tai Chen, Zhixian Yang,Yong Zhang, Chao Liu.2013.A brief talk on the 20 April 2013 Lushan Mw6.7 earthquake. Aca Seismologica Sinica,35(3):285-295.

[7]Zu-jun Xie, Bi-kai Jin, Yong Zhen et al..The focal parameter inversion of 2013 Lushan earthquake using far and near seismic waveforms [J].China Science:Earth Sciences, 2013, 43: 1010–1019.

[8]Jian Lv, Xiao-shan Wang, Jin-rong Su et al. The feature of focal location and mechanism solutions of Lushan M7.0 earthquake sequence [J]. Chinese Journal of Geophysics, 2013, 56(5):1753-1763.

Applied Mechanics and Materials Vol. 597 (2014) pp 328-331
© (2014) Trans Tech Publications, Switzerland
doi:10.4028/www.scientific.net/AMM.597.328

Structural Behaviors of Non-Ductile Reinforced Concrete Frames with Engineered Cement Composite (ECC) Wing Wall Elements

Dae Hyun Kang[1,a], Won Guen Lim[1,b] Hye Ran Kim[1,c] Mi Hwa Lee[1,d] and Hyun Do Yun[1,e]

[1]Department of Architectural Engineering, Chungnam National University, Daejeon,305-764, Republic of Korea

[a]davidkkang88@gmail.com [b]kjdack@cnu.ac.kr [c]cherry2864@naver.com [d]chlgmdwk21@cnu.ac.kr [e]wiseroad@cnu.ac.kr(corresponding author)

Keywords: Wing Wall, Engineered Cement Composite (ECC), Non-Ductile Frame

Abstract In this paper, an experimental investigation was carried out to evaluate the application of engineered cement composite (ECC) wing wall elements for seismic strengthening of reinforced concrete (RC) buildings with non-ductile reinforcement details. The ECC is mixed with cement, silica fume, fly ash and polyvinyl alcohol (PVA) fiber. The ECC wing wall elements were fitted on three side of RC frame; upper beam, lower beam and column. Two specimens, non-ductile RC bare frame and RC frame strengthened with ECC wing wall, were made for this study. These specimens were made as a third scale for this study. The specimens were loaded through 1,000 kN actuator that consists of two cycles at a displacement level. The test results showed that the seismic strengthening method of ECC wing wall elements had a significant effect to improve seismic performance of non-ductile RC bare frame. As a result, the application of ECC wing wall elements in non-ductile RC bare frame may be effective alternative to seismic retrofit of non-ductile buildings.

Introduction

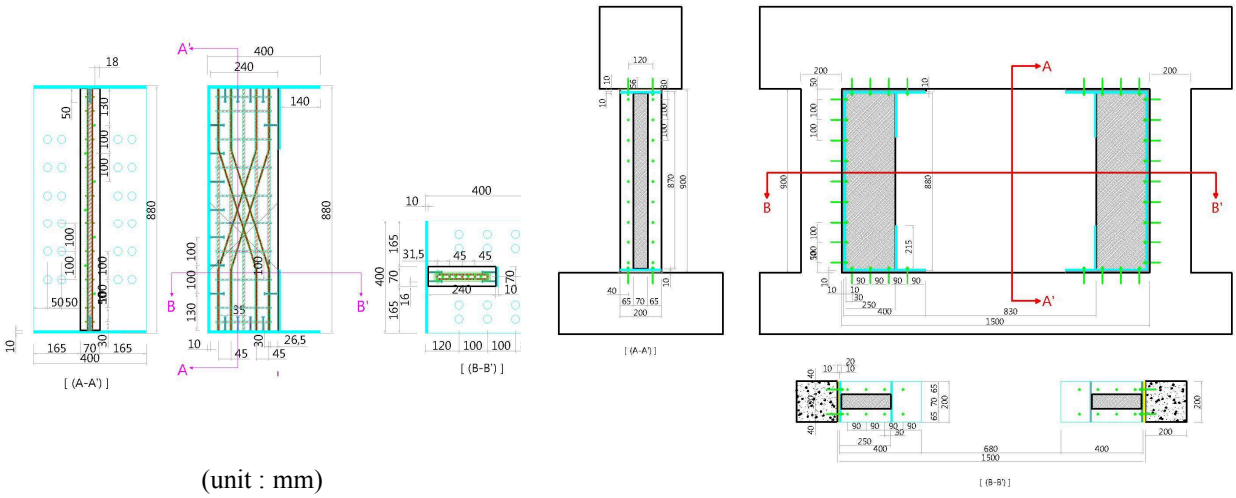
In Korea, earthquake over the 6.0 magnitude have frequently occurred. The effects of earthquake make enormous damage environmentally and economically. Among this damage, the main issue of earthquake is enormous damage of human life. Therefore, the influences of earthquake damage have enhanced seismic strengthening and design. The study for seismic performance such as infill wall system and wing wall system show increase of seismic performance. Among numerous studies, the wing wall has outstanding effect on lateral stiffness and resisting force increase. The wing wall system is being investigated for the seismic reinforcement and retrofit of RC frame structures. The wing wall system also intend for application to critical facilities such as school needed efficient space and had non-ductile building. In this study, the ECC wing wall made connection plate with ECC. The ECC have outstanding tensile strength. The concrete have brittle failure. But, the outstanding tensile strength of ECC complements concrete from brittle failure. The specimens consist of non-ductile RC frame and RC frame strengthened ECC wing wall. This experimental investigation indicates influence of non-ductile RC frame and RC frame strengthened ECC wing wall for seismic performance evaluation.

Experimental Program

Description of Specimen. The mixture properties of ECC are summarized in Table 1. The scale of specimens is 1/3 and made connection plate for strengthening in RC frame. The ECC is consisted of ordinary Portland cement, silica fume, fly ash, water and fiber. The fiber volume fraction also has 2.1 %. The tensile strength of PVA is 1,600 MPa. The PVA fiber has outstanding tensile strength. The ECC with PVA and cement composite has outstanding ductility. The specific compressive strength of RC frame is 21 MPa because numerous building built by 21 MPa ready-mixed concrete in 1980's Korea. Each specimen has been labeled as RC frame and W240-3-RCF according to the width and connection method. The ECC wing wall connected in side of column, beam and slab of RC frame as using anchor bolt and epoxy for application.

Table 1. Mixture proportion of ECC

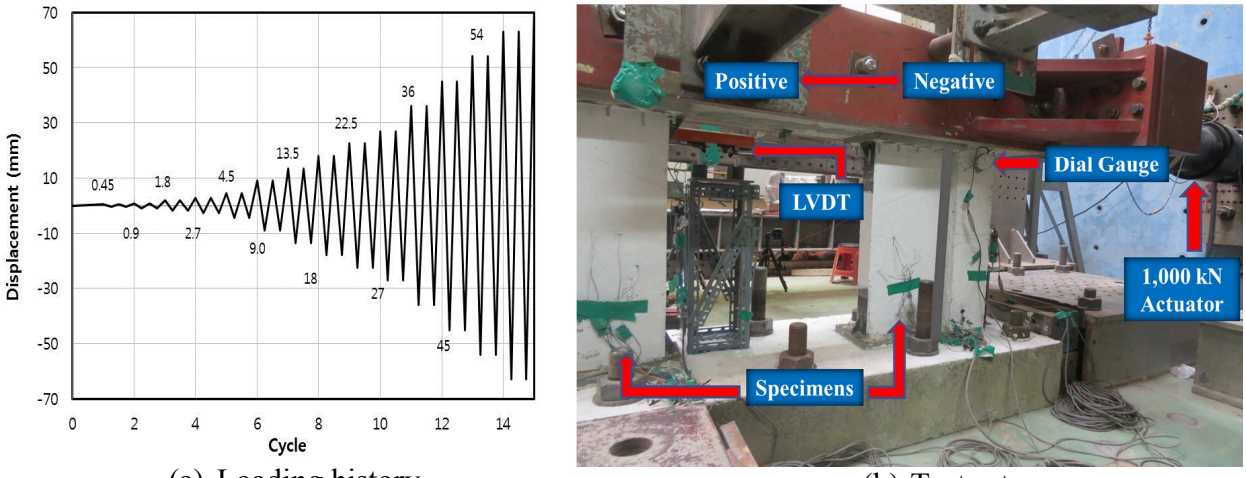
Matrix	W/B (%)	f_{ck} (MPa)	Fiber volume fraction (%)	Unit weight(kg/m^3)					
				Water	Cement	Silica fume	Fly ash	Filler	Super-plasticize
ECC	49.1	55	2.1	447.5	489	32.6	374.9	684.6	3.3



(unit : mm)

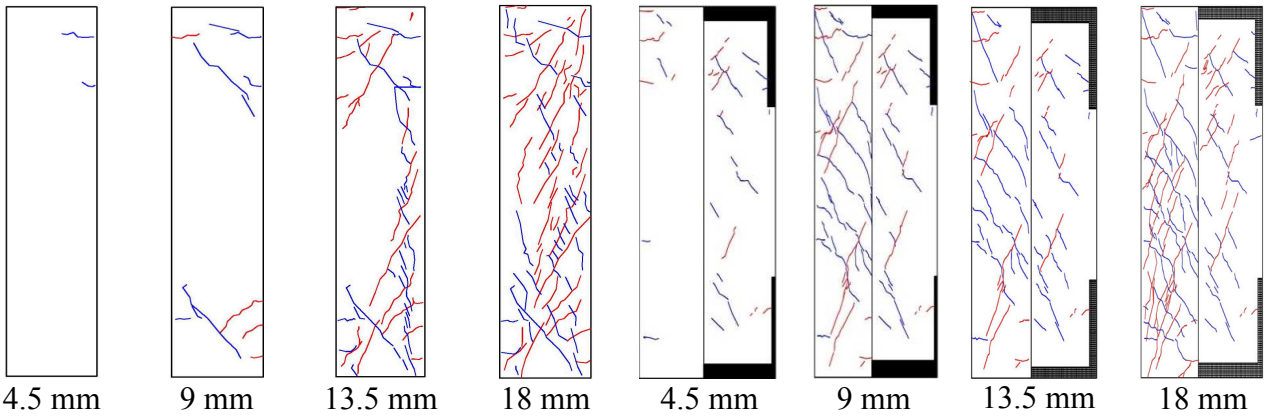
Fig. 1 Detail of wing wall and RC frame

Testing Procedure. The detail of ECC wing wall made like Fig. 1. The wing wall made connection steel plate and ECC for application with non-ductile RC frame. Test setup and instrumentation for seismic performance evaluation are shown in Fig. 2. As shown in Fig. 2, the ECC wing wall is strengthened in RC frame. The strengthened specimens were placed between 2 stopper block. The guide frame installed beam of RC frame for loading. The actuator was supported by the strong reaction wall in the laboratory. The 6 displacement transducers (DT) and 4 dial gauges (DF) were installed on the non-ductile RC frame and ECC wing wall to measure the drift and shear deformation of the ECC wing wall and RC frame. The RC frame and strengthened RC as ECC wing wall are tested by 1,000 kN actuator. These specimens are tested 2 times cyclic lateral load as displacement load method.



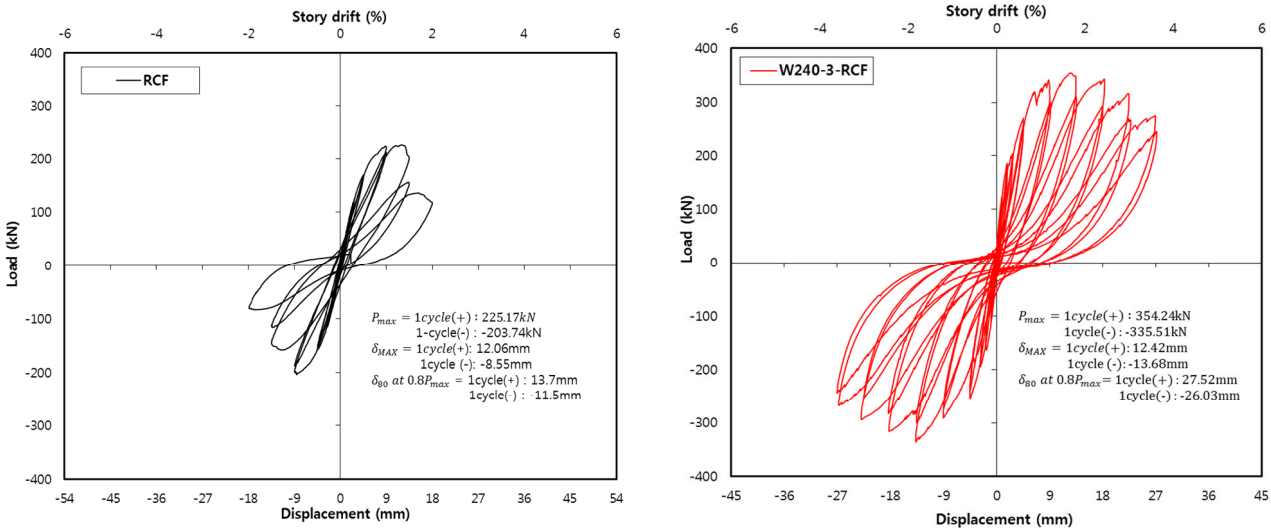
(a) Loading history (b) Test setup

Fig. 2 Load-history and Setup of specimen



(a) Right column of RCF (b) Right column and wing wall

Fig. 3 Cracking procedure of specimens



(a) RCF W240-3-RCF

Fig. 4 Load-displacement curve of RC frame

Experimental Results

Cracking procedure. Fig. 3 shows the cracking procedure of RCF and W240-3-RCF specimens. For RCF specimen, tension crack formed along the top of column during the drift ratio (DR) of 0.5 %. As lateral displacement increased up to DR of 1 %, several tension cracks propagated on the top and bottom of column. Then, few diagonal shear cracks formed newly and the width of tension cracks propagated. Until DR of 2 %, diagonal shear cracks and tension cracks formed newly. And, 0.5 % of all diagonal shear cracks and tension cracks propagated. RCF specimen damaged as shown in Fig. 3, In W240-3-RCF specimen, cracking procedure of column in RC frame occurred similarly DR of 0.5, 1, 2 and 3 %. In the ECC wing wall, tension crack and diagonal shear crack formed generally in all wing wall's section. As DR increased to 2 %, all crack formed newly. Diagonal shear crack and tension crack propagated.

Hysteretic Curves. Fig. 4 shows hysteretic behavior of RCF and W240-3-RCF. In Fig. 4, the displacement was recorded horizontal deflection by DT. Drift ratio is calculated by dividing measured horizontal width of wing wall by wall height. In the Fig. 4, the behavior of RCF specimen is characterized by low stiffness and ductility. The capacity of RCF attained in the positive (pushing) and negative (pulling) directions were 225.17 kN and 203.74 kN respectively. The behavior of W240-3-RCF shows increase of stiffness than the RCF. And, the behavior of W240-3-RCF shows significant stiffness and ductility capacity in Fig. 4. The maximum strength of RCF is 348.86 kN in the positive direction and 335.51 kN in the negative direction. As comparison with RCF and W240-3-RCF, increase of maximum strength in positive increased 35.46 %.

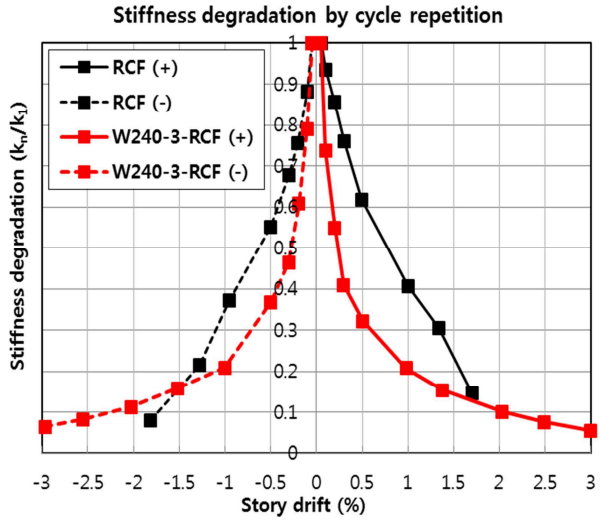


Fig. 5 Normalized stiffness

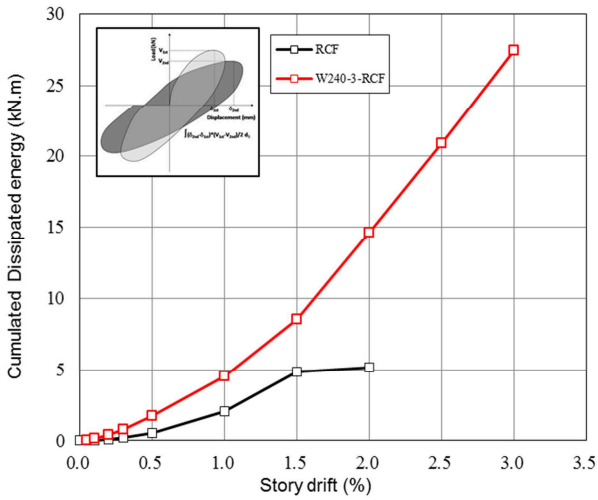


Fig. 6 Cumulative dissipated energy

Normalized Stiffness. Fig. 5 shows the normalized stiffness of RCF and W240-3-RCF. The stiffness is value measured from peak-to-peak displacement in direction respectively. As shown Fig. 5, the stiffness was normalized in order to account for the variations in parameters of each specimen. The RCF is higher in Fig. 5. The reason why W240-3-RCF is higher than RCF is because of higher initial stiffness of W240-3-RCF than RCF.

Cumulative Dissipated Energy. The cumulative dissipated energy was calculated by summing up the energy dissipated in consecutive cycles throughout the test. Using the cumulative dissipated energy based on the load and displacement hysteresis loops. As shown in Fig. 6, dissipated energy of specimens RCF and W240-3-RCF during the test to DR of 2% was 5.14 kN·m and 45.83 kN·m respectively. The energy dissipated energy of W240-3-RCF is 88.78 % higher than RCF. The application of ECC wing wall in RC frame had a significant effect on the cumulative energy.

Conclusion

In this study, based on the test result of ECC wing wall strengthening were evaluated seismic performance and concluded. And in the following conclusion, purpose of this study was summarized.

1. In case of RCF, loading dropped suddenly after maximum drift. The W240-3-RCF shows ductility capacity after maximum drift. As influence of ECC material, the strengthening of ECC wing wall in RC frame improves significantly the ductility of non-ductile RC frame.
2. The maximum strength and cumulative dissipated energy of W240-3-RCF specimen increased than RCF. As results, the strengthening of ECC wing wall in RC frame will be effective alternative to seismic retrofit of non-ductile building.

Acknowledgements

This research was financially supported by the Ministry of Education, Science Technology (MEST) and National Research Foundation of Korea (NRF) through Research on Adventure NRF-2013R1A1A2066034) NRF-2013R1A1A2066034) and BK21 plus

References

[1] Akifiro Nakamura, Masaomi Teshigawara, Yoshio Inoue, Tsutomu Ohta J. Struct. Constr. Eng., AIJ, Mar., 2011, Vol. 76, No. 661, pp. 619~617.

[2] Toshimi Kabeyasawa, Yousok Kim, Mitsuharu Sato, Hwang Hyunseong, Yoji Hosokawa. Auckland, New Zealang, April, 2011 pp.14~16

Applied Mechanics and Materials Vol. 597 (2014) pp 332-335
© (2014) Trans Tech Publications, Switzerland
doi:10.4028/www.scientific.net/AMM.597.332

The Influence of Base Pre-tilting on the Dynamic Properties of Angle Towers

Yongping Li[1, a], Long Li[2, b] *, Xiaoyu Yang[3, c]

[1]College of Architectural Engineering, Northeast Dianli University, Jilin Prov., China

[2]College of Architectural Engineering, Northeast Dianli University, Jilin Prov., China

[3]College of Architectural Engineering, Northeast Dianli University, Jilin Prov., China

[a]1956LYP@163.com, [b] lilong2014@163.com, [c]douding_yang@163.com

Key words: base pre-tilting; angle tower; dynamic property

Abstract. As a significant bearing tower that is widely adopted in the electric transmission line, the angle tower is frequently found over-tilting in the inspection and maintenance of transmission lines [1]. On the basis of the massive universal finite element software ANSYS, this study establishes a three-dimensional rigid frame for the commonly used 500kV angle tower in the Inner Mongolian area, and analyzes the dynamic properties of angle towers while setting the base pre-tilting [2,3]. It also conducts model analyses for the towers with or without base pre-tilting respectively, compares the frequency and mode of vibration, and paves way for further study of the setting of base pre-tilting and vibration response analysis [4].

Introduction

China has a vast area and complex topography, which makes the line corridor hard to be straight. Therefore the angle towers are widely adopted. The external force that angle towers bear originate from the back pull of stringing of the ground wires on two sides as well as the wind load [5] and glaciations. The resultant force direction of the two external forces is the internal angle direction of the angle tower. The tower bends under the resultant force in the internal angle direction, thus making the external principal material bear the tensile stress and the internal principal material bear the compressive stress. The complexity of the stresses makes the tower under the risk of collapsing and breakage of the electrical lines. Apart from the assemblage and the manufacturing of the towers, the factors that lead to the quality defects also include the neglecting of base pre-tilting or improper setting of the pre-tilting [6,7]. This paper establishes the finite element model on this basis and studies the influence of base pre-tilting on the dynamic properties of angle towers.

Establishment of the finite element model of the power transmission tower

Currently there are three methods of building ANSYS model: space truss method, space rigid frame method, and girder-joist method. The simulation value of space truss method is closer to the experimental value compared with the other two. Therefore this study takes the space truss method to establish the finite element model of the tower. Firstly the three-dimensional model is drawn on the CAD software. Then the CAD model is transferred to ANSYS model through APDL language compiling program. Beam188 unit is applied to simulate the rod piece of the power transmission tower. The Beam188 unit can custom the shape of the interface and better simulate the angle iron of the tower. Beam188 unit, as a quadric 3-D unit, includes shear strain, each node bearing 6-7 degrees

of freedom. This unit can well simulate the girder structure ranging from thin and long ones to thick and short ones. The Beam188 unit has a powerful analyzing function. Apart from calculating the elastic-plastic features of the materials, it can also be applied in the non-linear large strain and large rotation, as well as simulating the influence of shear deformation on the structure.

This paper takes a 500kV transmission angle tower for example, which is across Baotou to Hohehot Municipality .The details: Tower height and nominal height is 46.5m, 33m. Rotation degree is 40°. Basic root is 12.03m. Vertical, Horizontal, Ruling span is 1000m, 1000m, 600m in turn. Table 1 is the base pre-tilting experience value of Inner Mongolia electric power survey and design institute.

Table1 The base pre-tilting experience value of design institute

rotation degree	the base pre-tilting experience value
0°- 20°	5‰ of the basic root
20°- 40°	7‰ of the basic root
40°- 60°	7‰ of the basic root
60°- 90°	7‰ of the basic root

Dynamic properties of angle towers

1. The frequency of the angle tower without base pre-tilting

The modal analysis is conducted by adopting Block Lanczos method, and the calculated frequency and cycle are as Table 2. The formation of 1-5 stage modal analysis is as Fig. 2 .

Table 2 The frequency and cycle of the angle tower without base pre-tilting

stage	frequency /Hz	cycle/s
1	2.5020	0.3997
2	2.6137	0.3826
3	3.9436	0.2536
4	4.3753	0.2286
5	5.3420	0.1872
6	5.7660	0.1734
7	6.0374	0.1656
8	6.4051	0.1561
9	6.6430	0.1505
10	8.4913	0.1178

The results of Table 2 are compared with the results of current vibration cycle formula, which includes Load Code for the Design of Building Structures $T_1 = (0.007 \sim 0.013)H$ and the natural vibration period approximation formula of China's electricity sector $T_1 = 0.034\frac{H}{\sqrt{b+B}}$.

The natural vibration frequency according to Load Code for the Design of Building Structures is 2.1505 Hz, with the cycle being 0.465s. The ones gained from China's electricity sector are 2.2952 Hz and 0.4357s respectively.

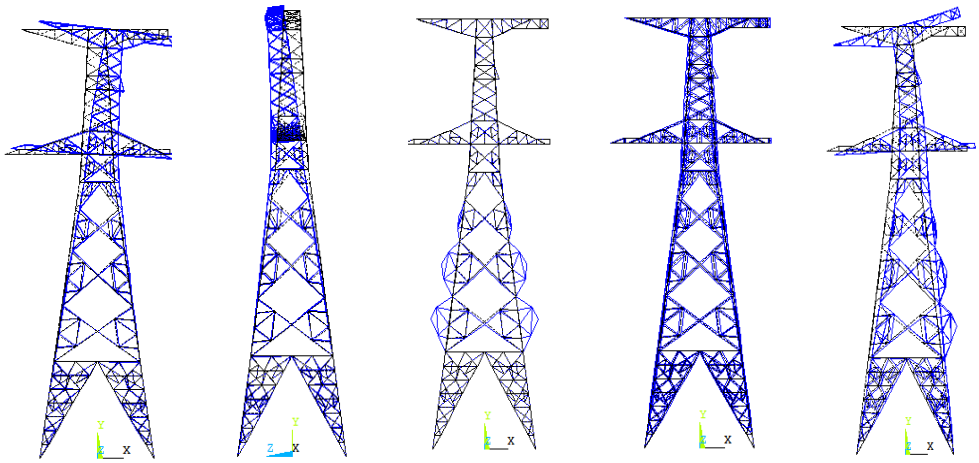


Fig.2 The formation of 1-5 stage modal analysis

From the frequency and cycle of ANSYS modal analysis and the comparison with the results of calculation one can see that the results of modal analysis are closer to the ones of China's electricity sector while having distance, the reason of which is that the formula of the electricity sector ignored many of the influence factors, while the structure of the angle tower is very complex. The large gap between the results originates from the fact that the shape and mass of the high-rise structure considered in the Load Code for the Design of Building Structures adopt linear transformation according to the height, while the power transmission tower has two cross arms with large masses, which makes the code improper for the tower.

2.The frequency of the angle tower with base pre-tilting

The setting of base pre-tilting of tower is realized through overall rotation of the finite element model. The pre-tilting value adopts the empirical value of Inner Mongolia Electric Power Survey and Designing Institute, i.e. with 7/1000 of base foot distance. The results of modal analysis are presented in Table 3.

The results of Table 2 and Table 3 show that after setting pre-tilting, the frequencies of angle tower decreased. The smaller degree of decline in the first three stages indicate that setting pre-tilting has less influence on the main frequency of bending moment in the first three stages and did not change the transverse mechanical property of tower significantly. But from the fourth stage, the influence becomes larger, with stages 5, 6 and 9 most notable, which should be noted in the future kinetic analysis.

Table 3 The frequency and cycle of the angle tower with base pre-tilting

stage	frequency /Hz	cycle/s
1	2.5018	0.3997
2	2.6134	0.3826
3	3.9436	0.2536
4	4.3759	0.2285
5	5.3407	0.1872
6	5.7648	0.1735
7	6.0374	0.1656
8	6.4048	0.1561
9	6.6413	0.1506
10	8.4914	0.1178

Summary

(1)Through modal analysis of finite element model of angle towers, the frequency is obtained and compared with the current frequency formula. The two share similarities while reserving disparities. The reason lies in the fact that the current empirical formula does not take various factors into consideration, especially the asymmetry of the angle tower that lead to the difficulty in the evaluation of the width of the tower head.

(2)From the modal analysis on the models of towers with and without base pre-tilting we can find that after setting the pre-tilting, the frequency of tower declined. The influence on the first three stages is relatively small, but the influence becomes more obvious from the fourth stage, with stages 5,6 and 9 the most significant, which should be paid more attention in the future kinetic analysis.

References

[1] Jianjun Li, NaixinLi Li, Tongwei He, The displacement calculation of angle tower, East China Electric Power. 1 (2009) 174-176.

[2] Hongnan Li, Xue Li, Gang Li, The wind-induced dynamic response analysis of iced transmission tower - line system, Disaster Prevention and Mitigation Engineering. 28 (2008) 127-133.

[3] Huaping Xie, Mingjuan He, The wind vibration response analysis of transmission tower-line system, Vibration and shock.30(2011) 45-51.

[4] Hai Hua, The pre-tilting control of angle tower, Guangdong science and technology. 3(2012)66-68.

[5] Zilong Wang, Jin Shu, The wind load calculation of angle tower, Power construction .32(2011) 51-53.

[6] Qinglin Li, The regression analysis of 500KV angle tower, Guangxi Electric Power Technology.3(2000)24-27.

[7] Jiaochen Zhang, The geometric correction method of pre-tilting data, Water Resources and Power.31(2013)177-179.

Applied Mechanics and Materials Vol. 597 (2014) pp 336-340
© (2014) Trans Tech Publications, Switzerland
doi:10.4028/www.scientific.net/AMM.597.336

Stress Analysis and Structure Improvement on Arm of Ladle Turret

Xin Yu Zhang [1,a *], Li Kun Guan [2,b]

[1]School of Mechanical Engineering, Inner Mongolia University of Science and Technology, China

[2]School of Mechanical Engineering, Inner Mongolia University of Science and Technology, China

[a]email:zxy_lhb@163.com

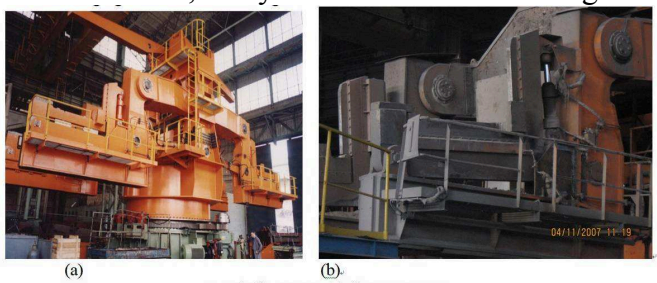
[b]email:glk@imust.cn

Keywords: ladle turret, arm, strength analysis, fatigue, finite element

Abstract. Static stress analysis on arm of ladle turret is based on finite element (FE) theory and shell theory by finite element software ANSYS. In this paper, an arm subjected to a multi-axial state of stress is examined both numerically and experimentally. The hot spot strains and stresses in the connection are determined through a detailed finite element analysis (FEA) of the joint. The arm geometry is accurately modeled using FE. Check the dangerous position on the side of the arm by different safety factor. For the experimental study, a test rig is designed and used to validate the FE model. Gain the impact factor of the arm. According to finite element calculations, assesses the fatigue strength by stress ratio method and stress amplitude method on the weld.Structural improvement is performed with increasing thickness and changing the location of the force.

Introduction

Ladle turret consists: arm, load-bearing bridge, bar, base and slewing ring bearing. Slewing bearing and base connect by a large slewing ring bearing, and can rotate. Bolts connect each component [1]. The side plate of the arm under the hydraulic cylinder cracks, as Fig.1. In order to find the reason, analyze stress of the arm using commercial FE package, ANSYS.



(a) (b)

Fig.1 ladle turret with four rotary arm

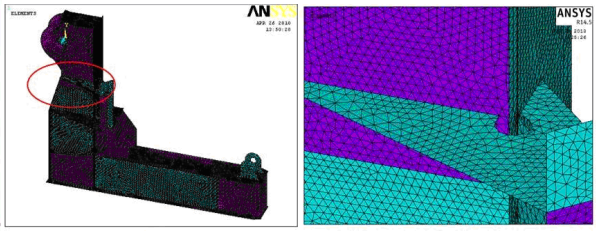


Fig.2 Finite element model of the arm

Many researchers have studied the behavior of ladle turret and arm with different types of methods.Hai Long Yue, Jia Xiang Zou and Qin Lu have focused on a slab caster ladle turret mechanical behavior, and analyzed of the problems on the model which encountered in the design process and put forward some measure to simplify the model constructively[2]. Zhen Rui Zhang, Li Li Xue studied the mechanical properties of continuous casting machine ladle turret slewing arm by 3D linear elastic FE method, and improved the structure reasonably[3]. Yi Wu Xie analyzed the mechanical properties of the ladle turret designed by DEMAG and the value of the force factors when ladle is standing on the tank on the view of the energy conversion in references [4]. Qi Xiao and Zuo Jun Jing studied the loading and the structure of a ladle turret, and analyzed that the limit of static stress. They established the FE model for stress analysis, and reported the fatigue failure with S-N curve and Miner linear cumulative damage theory, the analysis and provided a basis for design and manufacture of a ladle turret[5]. Fu Suai Li analyzed several ladle turrets and proposed the method for assess of FEA. He illustrated the difference between general method of mechanics and FEA through examining the fork arm in references[6] .

In the current paper, the behaviour of an arm of a ladle turret subjected to a multi-axial state of stress. A detailed FE analysis of the arm 3D solid elements and shell elements is performed. The hot

spot stresses and strains are determined using FE. One of the contributions of this research work is the experimental verification of the FE model developed for analysis of an arm of a ladle turret subjected to a comprehensive state of stress. A test rig has been designed and used in the experiments. Several strain gauges have been installed around the side plate of the arm in order to verify the validity of the FE model. To reduce the stress concentrations, changing the location of loading and external reinforcements for the arm are also considered.

Numerical modeling of an arm

The FE modeling of the arm of a ladle turret is a very challenging as well as delicate task owing to the complicated 3D profile of the arm.. 3D solid elements and shell elements are all adopted for modeling of the arm.The FE model established is based on the assumption of linear elasticity and small strains. One ladle turret is composed of 4 arms which take and carry ladle and steel, shown on Fig. 1. The arm is boxes welded with different thickness steel boards. The arm is 4710mm in length, 4110mm in height, 630mm in width. The material is Q235.The arm including two curve edges, was modeled by SHELL63. It has three translational and three moving degrees of freedom. The shell element looks like a plate without thickness[7].

The arm is Complex and the plates can not be directly meshed freely. Before separating the arm will be carved up blocks along the contact, then glue, so that the model is contacted by common line with common nodes. Mesh freely, the largest grid (ESIZE) set to 30mm. The model of the arm is divided into 65836 units with 33378 node, shown on Fig.2 .

Arm and base contact by links. Hinged arm support hole only released the freedom of rotation in vertical plane RotZ. Bottom arm hole release the freedom of rotation and displacement in vertical plane RotZ and dof UY. It is presented in Fig.3.

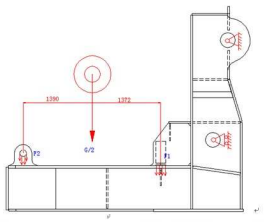
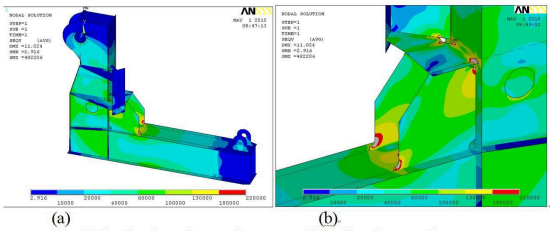


Fig.3 Forces on an arm of the ladle turret



(a) (b)

Fig.4 Distribution of stress for an arm full of molten steel

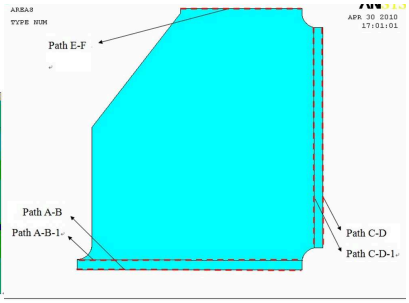


Fig.5 Path **A-B, A-B-1, C-D, C-D-1**

The conditions: receiving the bag full of molten steel, withstanding the ladle full of molten steel, releasing molten steel out of the bag, empty ladle arm, lifting an empty ladle. When the arm receives a bag full of molten steel, the force is max.

Though field-test, get the impact factor as 1.1, look at the measurement for strain in site. The rated load of the equipment is 310T, but it often operates overloaded in working. The arm is welded with structural steel with a yield tensile strength of 225MPa[8]. The following analysis of finite element static of the arm overloads by 10%, the impact loading, stress analysis as Fig. 4. The concentrated force is 918995N approximately. Inner arm surface withstand the pressure applied to the surface at the location where the range of all 196 nodes averagely. Concentrated force cantilever pin bore through the lower side of the arc lines is applied to the 42 nodes approximately. The arm suffered by density and gravity.

In the complex stress state, material failure are brittle fracture and plastic yield, the following were connected with the fourth yield criterion and the strength of the arm of the ladle turret to check[9]. The principle is a general mechanical method using the results obtained, that is, the average stress assessment section. In general, because complex geometry, its result of the local stress which calculated by finite element method, concentration factors taken into account the geometric stress concentration than the use of general mechanical calculation of the average stress obtained value, the choice of 1.1 as a factor criteria[6]. Allowable stress is 204MPa.

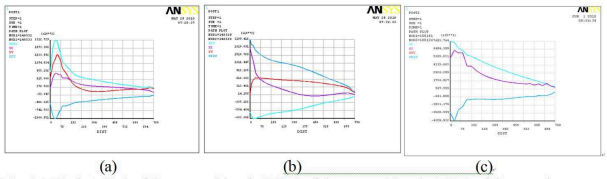
Observing the stress contour, as Fig. 4, the stress is uniform in a wide range and under the allowable stress, can not deform for permanent. But max Von Mises (effective stress) of many

points reach 482MPa, 396MPa, 346MPa, 314MPa, 300MPa on the side and the bottom fillet in the side. Yield stress occurs within this region, will not cause deform for permanent on the arm, but will decrease the fatigue life. Define the path as Fig.4. Pick up path A-B, A-B-1, C-D, C-D-1(show in Fig.5) of the Von Mises, find point A and C are the local stress concentration, the Von Mises reach 109MPa, 230MPa, 139MPa, 215MPa. Although it yields, the overall is security by allowable stress of 204MPa. There is no stress concentration with factor of 1.5 used for checking the safety to the middle of the path. The allowable stress is 150MPa.The stress of the path A-B and C-D fit the strength requirement, the path A-B-1 and C-D-1 are greater than them. Some points on the path A-B-1, C-D-1 does not meet the strength requirement. The Von Mises of the side for the first whole and filmy stress almost yield.

Check the connection strength. It is comparable because of the stress of the direction X, Y and the shear stress of the XY plane on the path from Fig. 6. .In order to obtain the stress , pick up the distance that path starting from each point on the path, the tensile stress of the points X, Y, the shear stress of the XY plane. Calculate based on the strength of connections and find that there are many points of the shell element does not meet the intensity of surface stress conditions. But the stress combined through the first whole filmy stress on path A-B-1 meet the strength requirement.

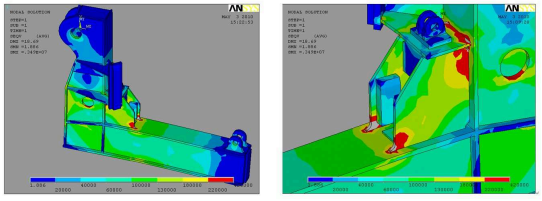
Though the node of shell has six degrees of freedom, the model is simplified to the actual condition. Shell elements represent mid-surfaces of the structure. They assume a linear stress distribution through the thickness of the plates.

In order to obtain the stress distribution of the arm, accurate physical model is established by solid elements. Perform finite element calculations with load impact factor by 1.1, the constraint is applied to the inner surface of the bearing seat, the upper bearing supports limit X, Y, Z displacement; the lower side bearing supports limit X, Z displacement. Such loads can be applied to the surface, and then acts to the node. SOLID92 element is a linear 3D 10-node tetrahedral element and each node has X, Y, Z moving degrees of freedom.



(a) (b) (c)

Fig.6 (a) Path A-B-1 of the stress (b)path C-D-1 of the stress (c)path A-B-1 of the membrane stres



(a) (b)

Fig.7 Distribution of Von Mises for an arm full of molten steel using solid element

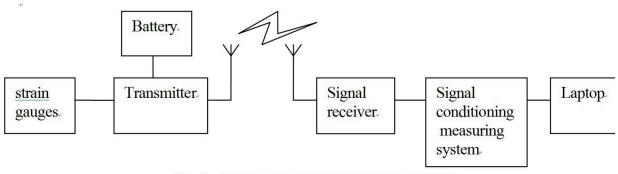
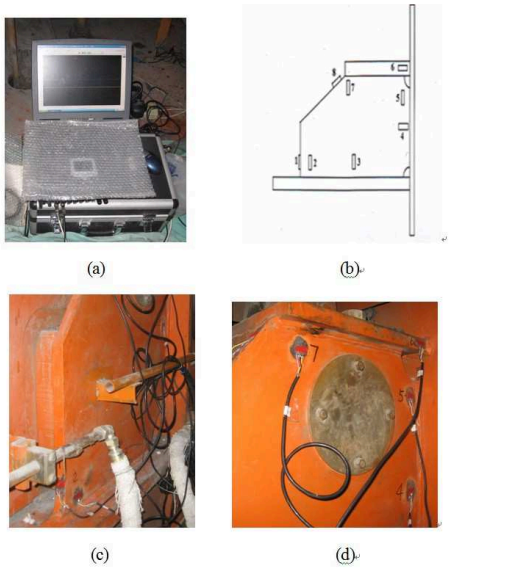


Fig.8 Strain measurement system schematic



(a) (b) (c) (d)

Fig. 9 Locations 1 to 8 of strain gauges installed: (a) test rig for signal receiver and the laptop; (b) corresponding FE model with locations 1 to 8 of strain gauges installed; (c) and (d) close-up view of the strain gauges installed.

It revealed that basic shape of the stress distribution using solid element is same to the one. But it is more than 150 MPa in a greater range for the stress of side plate. The stress using solid element is slightly larger than the stress using shell element, as shown in Fig.7. It illustrates further that the support arm established using shell elements to the FEA can basically meet the needs of strength analysis. No matter what kind of element modeling it is a simplification of the actual situation. But the real problem can be analyzed according to special situation for load and constraint.

Experimental text

In order to verify the validity and accuracy of the developed FE model for the prediction of the stresses and strains of the arm, an experimental test rig has been designed for the testing. It is a telemeter [10]. The schematic is shown in Fig. 8 and Fig. 9.

According to the results of finite element analysis and cracks on equipment, select eight test points, as Fig. 9(b). After data processing get the strain of each test point, as Table 1. Calculation by dropping empty bag (Dropping empty bag in the actual working conditions is rare) and dropping full bag package, obtain impact factor for the test strain point is from 1.0222 to 2.75, in references [7]. The impact factor is as Table 2. To avoid increasing the hardest hit for the arm in static finite element structural analysis overall, the impact coefficient is smaller, is taken as 1.1, the stress analysis of the actual need according to specific circumstances.

Experimental and numerical results

To assess the effectiveness and accuracy of the modeling, the numerical and experimental results were compared to verify the reliability of the FE model. In the application of loads of 279t, shell element, it obtains the distribution of strain about the arm.

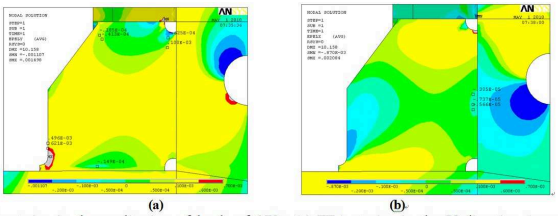
In Fig.10(a),the strain values obtained around location 1 in the Y direction are from 300 to 580(μ-strain).The maximum hot spot is in the corner at the lower of the side plate. It is a crossover for the strain at location 2.The values from 50 to 100 are all should been measured if change the location of the strain gauges slightly. It is in agreement with the experimental strain value, 60 mostly. It is in the compressive strain felid at location 3.the strain value is from 0 to -50, even lower, but no more lower than -150.It consistent with result in the site,60.It is near the stress concentration zone at location 5. Here is the boundary to tensile strain and compressive strain. Owing to ignore the role of hydraulic cylinder, the result is tensile strain at location 7. But it is compressive strain with value -105 which is been measure. From Fig. 10(b), it observed that for constraint simplified, it is not agreement between experimental and numerical strains in the X direction at location 4. If make side stand tighter more, it will be a compressive strain.Pick up path E-F, show in Fig. 10(b). It can be seen that point F is near location 6 where calculate strain is more than 700 caused by geometry mutation. The strain measured at location 6 is the value of mid –plate. The strain distribution over the plate thickness is usually non-linear in the vicinity of a notch. The membrane strain is 500 by numerical calculate, which agrees with the result measured generally. Show the results of finite element software ANSYS is accurate as Fig10.

Table 1 Location1 to 8 of Strain (μ-strain)

Test point	no-load(zero)	empty bag	Before full bag(zero)	after full bag	Max strain
1	-40	70	-40	540	580
2	-140	-135	-140	-80	60
3	-220	-240	-210	-260	-50
4	175	110	180	-45	-225
5	-245	-250	-245	-280	-35
6	280	400	280	700	420
7	-375	-400	-375	-480	-105
8	-30	0	-30	70	100

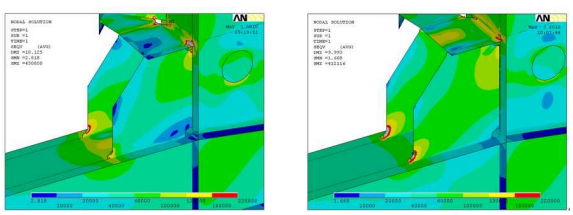
Table 2 The impact coefficient (μ-strain)

test point	strain attack	strain empty bag	impact empty bag	strain attack	strain full bag	impact full bag
1	130	110	1.1818	620	580	1.0690
2	10	5	2	65	60	1.0833
3	-55	-20	2.75	-60	-50	1.2
4	-85	-65	1.3077	-230	-225	1.0222
5	10	5	2	-45	-35	1.2857
6	170	120	1.4	460	420	1.0952
7	-35	-25	1.4	—	-105	—
8	33	30	1.1	—	100	—



(a) (b)

Fig.10 FEA strains in the application of loads of 279t: (a) FEA strains in the Y direction (compare with locations 1,2,3,5,7) ;(b) FEA strains in the X direction (compare with the point 4)



(a) (b)

Fig..11 Distribution of Von Mises on the side plate(a)case one;(b)case two.

Reinforcement

The side is the components supporting force mainly, and the level of stress of the box-shaped beams is small. There are many ways to improve the structure. We can change the thickness of the side broad or loading position of the arm[11].

Case One: make the following adjustment of the structure, increasing the thickness of side plate, changed 32mm to 50mm. Then get Von Mises contour as Fig.11(a), and compare it with Fig 4, we can see that the maximum stress of the concentration zone dropped from 482MPa to 450MPa, and the distribution of stress is essentially the same to the uniformity zone, but the values decreased generally. The stress on side was reduced to under 130MPa basically. Case Two: load move to the top of the hydraulic cylinder, and modify the thickness of the cover, changed 32mm to 50mm, based on static equilibrium, got pressure 18.191MPa,gets the stress contour as Fig.11(b). Maximum stress from the stress concentration area dropped from 482MPa to 412MPa. The distribution of stress has been changed and the stress on side reduced to under 100MPa basically.

Conclusion

Have done finite element static analysis, field measurement of strain, fatigue strength and improvements of structure to the arm for ladle turret in this paper. The results showed that the high stress of the side on arm caused yield to the material during the complex and changing environment. The fatigue strength of arm have impact, lead to cracks on weld early. Verified with field strain measurement accuracy of the finite element method, but has been more scientific and realistic on-site impact factor. Then improve the distribution of stress of the arm and obtain good results.

Acknowledgements

Inner Mongolia University of Science and Technology Innovation Fund (2011NCL069)and Inner Mongolia natural Science Fund(2012MS0711)

References

[1]Zhong Bing Wang. Advanced EAF-thin Slab Casting and Rolling Metallurgical Industry Press,2004,1:14

[2]Hai Long Yue, Jia Xiang Zou, Qin Lu.Mechanical Properties Slab caster ladle turret Metallurgical Equipment .1993 (01)1-7

[3]Zhen Rui Zhang, Li Li Xie.Finite Element Analysis for Rotary Arm of Steel Ladle Turret Hebei Metallurgy.1995 (05) 55-59

[4]Yi Wu Xie.Theoretical Calculation Analysis for Impact Coefficient of Revering Pot on ladle turret[J]. Metallurgical Equipment .1998 (01) 24-25

[5] Qi Xiao , Zuo Jun Jing.Analysis on fatigue of ladle turret's arm. Machinery,2005 (04)32-34

[6]Fu Shuai Li.Determination of Safety Factor in Strength Calculation of Ladle Turret. Casting.2007 (03)18-20

[7]You Zhi Gao. Advenced equipment and technology of casting and rolling. Northeast Institute of University Press, 1992.

[8]National Standard of China - Carbon structural steels GB50017-2003, China, 2003(12)68-69

[9]Qiang Han, Xiao Qing Huang, Guo Ning Jian.Advence Theory of Shell,January,2002.

[10]Jing Yu Chen.Fault Diagnosis and analysis of Ladle turret. Liaoning University of Technology.2008(3)10-16

[11]Wei Gao Han.Strength Analysis and Research on Structure of Arm Frame Hose Crane.China. Harbin Engineering University.2007(7)44

Applied Mechanics and Materials Vol. 597 (2014) pp 341-344
© (2014) Trans Tech Publications, Switzerland
doi:10.4028/www.scientific.net/AMM.597.341

Cathodic Prevention and Cathodic Protection of Concrete Slab with Zinc Sacrificial Anode

Jin-A Jeong[1, a *]

[1]727 TaeJongRo, Busan, Department of Ship Operation, Korea Maritime University, South Korea

[a]jina@kmou.ac.kr

Keywords: Cathodic prevention, Cathodic protection, Depolarization potential, Current

Abstract. This study is to acquire the confirmation data regarding the cathodic protection and cathodic prevention characteristics for concrete slab specimens in marine environments. It was possible to confirm the performance of cathodic protection system by the measurement of potentials and current density for the concrete slab specimens applied with zinc mesh sacrificial anode in mortar topside of the concrete specimens. The current density for the cathodic protection (CProt) that CP started after a repair of corrosion was higher than that for the cathodic prevention (CPrev) that CP commenced from the beginning of experiment, and 4 hour depolarization potentials were higher in the CPrev system than in the CProt one, and it was confirmed that the CPrev has more protection effect with less protection current, comparing to the CProt. It was also confirmed that the CP of both CPrev and CProt by means of zinc mesh sacrificial anode for reinforced concrete structures were very effective corrosion protection technology in marine environments.

Introduction

Most of the reinforced concrete as like buildings and bridge structures is a versatile, economical, and successful material [1,2]. Normally, the pH of concrete is 12–13, and these alkaline conditions of the structure lead to very slow rates of corrosion [3]. However, chloride or carbon dioxide can reduce the pH of the reinforced concrete either locally or over the entire structure, which leads to corrosion [4]. When corrosion of reinforced concrete has already occurred, it is difficult to solve the corrosion problem, because corrosion damage happens repeatedly in spite of maintenance work. Therefore, it is necessary to deal with this corrosion problem before the corrosion is initiated. To manage this problem, a lot of techniques like adding the cover thickness, coating, usage of inhibitors, cathodic protection which are introduced. The cathodic protection in these techniques has been intensively studied during the last four decades in the concrete field, and presently become a proven technology to protect the corrosion of steel in concrete [2]-[4]. In addition, The cathodic protection can be a candidate of these positive solutions to control the corrosion in marine structures. In order to overcome these drawbacks, the zinc mesh anode system has been adopted in this study as a cathodic protection technique. In addition the FRP jacket has been attached to the outside of concrete specimen to improve the current supply by restraining the evaporation of moisture from concrete. Since the effect of corrosion protection can be varied by numerous elements, i.e. temperature, dissolved oxygen, chlorides, concrete quality, etc., a number of experimental data regarding these have been attempted to develop the optimum CP design [5]-[9]. Cathodic protection has been applied extensively as a meaning of protecting corrosion of marine concrete structures, however, cathodic prevention aimed at delaying the onset of corrosion, it is applied when chlorides have not reached the reinforcement and the steel is still passive. In this study, to quantifying the possible benefits of cathodic prevention compared to cathodic protection, both systems with zinc-mesh sacrificial anode were manufactured at reinforced concrete pile specimens. The cathodic protection experiments have been carried out in the electrochemical point of view in order to reveal the effectiveness of CPrev and Cprot.

Experimental Procedure

The slab type specimen (40cm×30cm×18cm) was adopted to simulate the upper decks in marine bridges or port pier structures. Two technical terms, i.e. CPrev and CProt, have been used to distinguish the application state of CP [10],[11]. The former was the specimen initiated CP from the beginning of test, and the latter was started CP after the repair of corroded parts formed during the free-corroding period. The number of specimens was five in CPrev and five in CProt, respectively. The mixed design and the physical properties of concrete specimens were as follows. Maximum aggregate size, slump was 10mm, 100mm, and 50% of water cement ratio, 53% of absolute fine aggregate ratio was adopt to the specimens, and the concrete was cured in the laboratory at a room temperature of 20 ℃ for 28 days after pouring it in the mold. All the rebar exposed to the top of the specimen were welded for an electric connection. As shown in Fig. 1, the slab specimen had two rebar in upper layer of rectangular shape and four in lower layer, and each upper rebar was located to be a pair of two lower ones. The both ends of rebar at the mortar/air interface have been sealed by heat shrinkage tube to prevent any measurement errors resulting from the corrosion possibly occurred by the attack of corrosive materials from outside. The mid-part of rebar in mortar specimen was only exposed for an electrochemical measurement. For CP specimens, fiberglass panels with zinc mesh sacrificial anode have been used to protect rebar by means of galvanic effect of zinc. Plastic water bath was installed at the top of the specimen, and 15wt% salt water was supplied manually. The solution was made by adding salt in fresh water. The experiments have been conducted at high temperature of 40℃ with wet-dry repetition of test solution to accelerate corrosion in a short period of time. A wet-dry cycle was 7 days, which were 4 days of wet and 3 days of dry. Test parameters were corrosion potential, CP potential, protection current density, and 4 hour depolarization potential. Those were measured periodically for rebar in specimens. The reference electrode for potential measurement was silver/silver chloride electrode (SSCE, Ag/AgCl) [12], and the Fluke multimeter and the CMS300 system by Gamry Instruments Co. have been used for the other measurements [13].

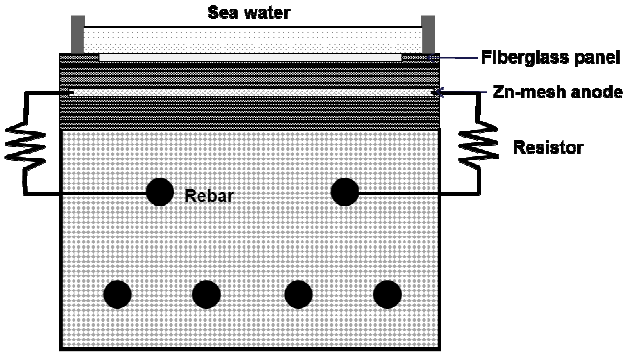


Fig. 1 Schematic drawing of slab specimen

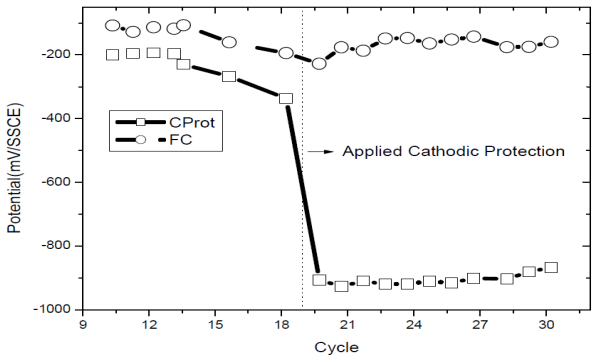


Fig. 2 Potential variations of CProt & FC specimens

Experimental Results

The corrosion potential for FC specimens was maintained relatively constant in the range of -100 ~ -200mV/SSCE. When CP was applied, however, the potential for CProt specimens after appling the cathodic protection was sharply decreased to around -900mV/SSCE, and after that the protection potential was maintained nearly constant in Fig. 2. The potential of FC specimen was -108mV/SSCE at 15 cycles and decreased to -200mV/SSCE after 30 cycles. It was assumed that water and chlorides have been reached to the surface of rebar during 15-30 cycles of wet-dry repetition. On the other hand, the rebar potential of CProt was -204mV/SSCE at 15 cycles of corrosion, however, it was significantly dropped up to -907mV/SSCE through the application of CP by zinc mesh sacrificial anode. The average current densities were 40.7mA/m2 for CPrev and 89.0mA/m2 for CProt, respectively, and the latter was over twice than the former, as shown in Fig. 3. Consequently, it is understood that the much less protection current density for CPrev is due to the maintenance of passive state on the rebar surface before attacking by detrimental factor(s) like chlorides. This is the

same results of Bertolini's experiments that were carried out on reinforced concrete columns with steel embedded both in chloride free concrete and chloride contaminated concrete in order to compare the effects of sacrificial anodes on passive steel and on corroding steel [14]-[16].

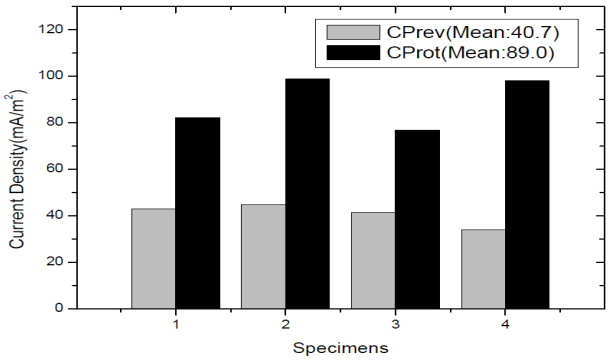


Fig. 3 Current density of CPrev & CProt

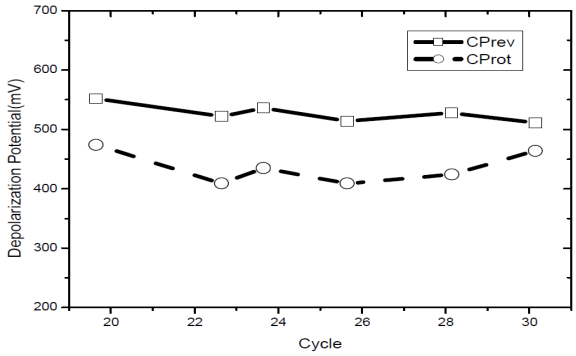


Fig. 4 Depolarization potential of CPrev & CProt

Fig. 4 is the variation of 4 hour depolarization potential for both CPrev and CProt specimens. The depolarization potentials were indicated relatively constant with time (wet-dry cycles) in the potential range of 500~560mV for CPrev and 400~480mV for CProt in every cycles. In case of concrete specimen, 100mV depolarization potential was often used to verify the effect of CP system according to the NACE SP 0290 standard [17]. From the comparison of depolarization potentials for CPrev and CProt specimens, that for CPrev was lower than CProt. It was assumed that the cathodic polarization of CPrev was readily occurred since the surface of rebar for CPrev was relatively passive and not contaminated by any corrosion element like chlorides. However, the depolarization potential for CProt was relatively low because the cathodic polarization was restrained by the corrosion products formed by chloride penetration into concrete. As the same as that more protection current density was needed for cathodic prevention than for cathodic protection, it was confirmed that the depolarization potential for CProt was far less than that for CPrev, which means the protection efficiency is relatively low in CProt condition.



Fig. 5 Surface condition of (left) CPrev, (right) CProt specimens after experiment

Fig. 5 is the pictures of Cprev and CProt specimens testing in the seawater bath after 30 cycles. There was no corrosion phenomenon in the CPrev (upper side) specimen protected by zinc mesh sacrificial anode with FRP cover from the beginning of test, however, in the CProt specimen (lower side) showed a strong trace of rust leaking from inside of the concrete. These two pictures demonstrate the effectiveness of the present cathodic protection system. In case of the CPrev specimen, no rust has been found on the surface of concrete, and no corrosion trace has been found on the rebar surface as well. On the other hand, the CProt specimen before appling the CP showed overall corrosion trace on the both concrete and rebar surfaces. It was understood that the corrosion products have been formed and leaked out of concrete during the 230 cycles in free corroding condition. This is well agreed with the test results of corrosion and protection potential, protection

current density, and 4 hour depolarization potential measurements. Therefore, it was concluded that both the CProt and CPrev specimens with zinc mesh sacrificial anode embedded in concrete was effective to protect the corrosion in marine environment.

Summary

It was confirmed that the cathodic prevention system and cathodic protection systems with zinc-mesh sacrificial anodes were very effective at preventing rebar corrosion in concrete slabs in marine environments and the better protection effects were confirmed in the specimen that was applied to the cathodic prevention than the cathodic protection. CP current density of CPrev specimen applied CP from beginning of the test decrease to the 0.45 times of CProt one applied CP after corrosion test period. The result of 4 hour depolarization potential measurement for CPrev specimen (500~560mV) was higher than that for CProt specimen (400~480mV). Visual inspection results agree well with the results of the electrochemical measurements in terms of the effectiveness of the CP systems.

References

[1] J.P.Broomfield, “Corrosion of Steel in Concrete”, 2nd ed. edited by T&F, 2007, pp. 10–64.

[2] K. Ishii, H. Seki, T. Fukute, K. Ikawa, Construction and Building Materials, vol. 12, 1997.

[3] Bennet, J.E. and Broomfield, J.P, Metal Performance, vol. 36, 1997.

[4] D. G. Enos, A. J. Williams, Jr., G. G. Clemena, and J. R. Scully, Corrosion, vol. 54, 1998.

[5] P. Pedeferri, Construction and Building Materials, vol. 10, 1996, pp. 391-402.

[6] J.A. Jeong, C.K. Jin, The effect of temperature and relative humidity on concrete slab specimens with impressed current cathodic protection system, vol. 37, Korean Society of Marine Engineers, 2013, pp. 260-265.

[7] Y.B. Ko, G.B, Kim, K.C. Park, Soundness evaluation of friction stir welded A2024 alloy by non-destructive test, vol.37, Korean Society of Marine Engineers, 2013, pp. 135-143.

[8] J.H. Jeong, Y.H. Kim, K.M. Moon, M.H. Lee, J.K Kim, Evaluation of the corrosion property on the welded zone of seawater pipe by A.C shielded metal arc welding, vol. 37, Korean Society of Marine Engineers, 2013, pp. 877-885.

[9] S.J. Kim, S.J. Lee, S.O. Chong, Effect of cavitation for electrochemical characteristics in seawater for austenitic 304 stainless steel, vol. 37, Korean Society of Marine Engineers, 2013, pp. 484-492.

[10] M. Saleem, M. Shameem, S.E. Hussain, M. M. Maslehuddin, Construction and Building Materials, vol. 10 ,1996, pp. 209-210.

[11] F. J. Presuel-Moreno, S. C. Kranc, and A. A. Sagues, Corrosion, vol. 61. 2005.

[12] ASTM C876-91, Annual Book of ASTM Standards, vol. 03.02, 1994.

[13] "CMS100 Framework Software Operator's Manual", Gamry Instruments, Inc, 1994.

[14] L. Bertolini, E. Redaelli, Corrosion Science, Vol. 51, 2009, pp. 2218-2230.

[15] A.M. Hassanein, G.K. Glass, N.R. Buenfeld, Concrete Composites, vol. 24, 2002, 159-167.

[16] T, Pastore, P. Pedeferri, L. Bertolini, F. Bolzoni, Rehabilitation of Concrete Structures, vol. 4, 1992, pp. 189~200.

[17] NACE Standard SP 0290, 2007.

Applied Mechanics and Materials Vol. 597 (2014) pp 345-348
© (2014) Trans Tech Publications, Switzerland
doi:10.4028/www.scientific.net/AMM.597.345

Engineering properties of controlled low-strength material made with residual soil and Class F fly ash

Yeong-Nain Sheen[a], Li-Jeng Huang[b] and Duc-Hien Le[c]*
Department of Civil Engineering, National Kaohsiung University of Applied Sciences, Kaohsiung 807, Taiwan, ROC
[a]sheen@kuas.edu.tw, [b]ljhuang@kuas.edu.tw, [c]hienle@kuas.edu.tw

Keywords: Controlled low-strength material; flowability; setting time; compressive strength

Abstract. This paper aims to employ combination of residual soil and Class F fly ash in developing a controlled low-strength material (CLSM), primarily used as backfilling material. In the mixture, surplus soil and concrete sand was blended well together with a given proportion of 6:4 by volume. Three levels of binder content (i.e. 80-, 100- and 130 kg/m^3) and different percentages fly ash (i.e., 0%, 15%, 30%, and 45%) substituting to Portland cement were previously chosen for mix design. Several major engineering properties of the CLSM such as fresh density, flowability, setting time, water bleeding, unconfined compressive strength, and elastic modulus were investigated via a laboratory study. Testing results indicate that most of the proposed CLSM mixtures satisfy the requirements of excavatability as the 28-days compressive strength ranges from 0.3 to 1.4 MPa. In addition, increase in FA substituting to OPC resulted in workability improvement, setting time extension as well as compressive strength and elastic modulus reduction.

Introduction

Controlled low-strength material (CLSM) is commonly used as granulated compacting soil, subgrades or trench fills. CLSM typically consists of small amount Portland cement, supplementary, fine aggregates, and a large amount of mixing water. Self-compacting/-leveling, significantly low strength, as well as almost no measured settlement after hardening are remarkable characteristics of CLSM [1]. It was reported that maximum CLSM strength of approximately up to 1.4 MPa is suitable for most of backfilling applications when re-excavation is required [2, 3]. It is also recommended that depending upon the availability and project requirements, any recycle materials would be acceptable in production of CLSM with prior tests its feasibility before uses [1]. The construction of infrastructures or high rise buildings usually generates a huge amount of waste soil needing to be removed. The moving work and creation of new landfills for surplus soil inevitably result in raising project cost and cause a negative effect for environment. On the other hand, fly ash (FA), a byproduct waste generated during the combustion of powdered coal, is frequently used as replacement material for cement and/or aggregate in concrete due to its pozzolanic and/or cementitious characteristic. The compressive strength of FA concrete has been reported to vary in wide ranges, depending on the amount, chemical composition and water-binder ratio (*w/b*). With a higher level of *w/b*, the more strength reduction may occur [4, 5]. Due to high flowability in nature, CLSM mixtures usually need a large amount of mixing water comparing to conventional concrete. Consequently, the CLSM strength−developing behavior would be different from concrete; and there has currently been a lack of studies on this issue. In this paper, a laboratory work was conducted on the soil-based CLSM, in which FA partially substituted for Portland cement in mixtures.

Experimental study

Materials used and mixture proportions. Materials for the studied CLSM mixture consist of fine aggregate, cement, FA, and water. Fine aggregate was formed by well blending between river sand and residual soil collected from a jobsite with a given proportion of 6:4, by volume. The soil was obtained from a construction site where the proposed CLSM will be used as a backfilled material, whereas the river sand with the fine modulus of 2.51 satisfy well for concrete making. The

essential properties of the collected sand and soil were expressed in Table 1. Moreover, ordinary Type I Portland cement (OPC) was used in the experiment. The Class F FA with the fineness, Blaine, of 3480 cm^2/g was employed as a partial substitution for OPC.

Table 1 Physical properties of collected sand and soil used in this study

Surplus soil	Value	River sand	Value
- Specific Gravity	2.74	- Specific Gravity	2.66
- Optimum moisture content (%)	14.8	- Water absorption (%)	3.50
- Liquid Limit (LL)	16.0	- Fineness modulus	2.51
- Plastic Index (PI)	3.50		
- Fineness Modulus (FM)	1.27		
- Soil classification	SM		

Three binder content levels, i.e. 80, 100 and 130 kg/m^3 were prepared for the experimental study. Subsequently, the corresponding water-binder ratios were selected via few trial mixes until the acceptable flowability for CLSM were achieved (200−300 mm) [1]. In addition, Class F FA substituted for OPC with various ratios, such as 0% (reference), 15%, 30%, and 45%, by weight of binder. As regards mixing procedure, the sand and soil were first mixed together with a mechanical mixer for two min. The weighted OPC and FA were then added to the dried sand-soil mix. During next one min, the materials were continuously blended before water was added to the mix. The mixing water was thereafter gradually poured into the mixer and blended for additional three min. Finally, all the ingredients were continued to blend for two min to have totally five min of mixing [2]. Table 2 presents material compositions providing for the experimental program.

Table 2 Mixture proportion and the testing results for the soil-based CLSM

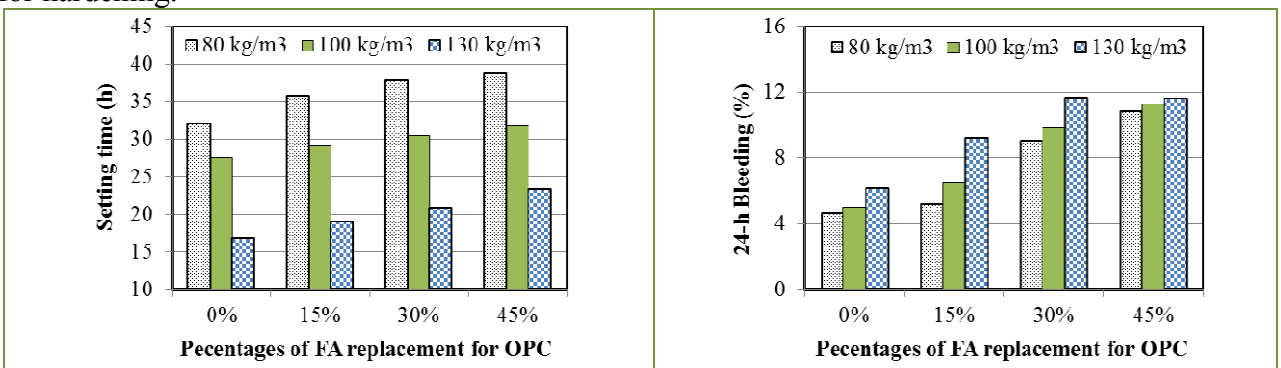
Mix ID.	Mixing proportion			Tube slump (mm)	Setting time (h)	24h-bleeding (%)	Compressive strength		
	FA	w/b	Soil				1 days	28 days	91 days
a. Binder (OPC+FA) = 80 kg/m³									
Mix-1	0%	5.0	895	210	32.0	4.64	0.15	0.47	0.50
Mix-2	15%	5.0	892	217	35.7	5.20	0.14	0.36	0.39
Mix-3	30%	5.0	890	239	37.7	9.03	0.14	0.27	0.33
Mix-4	45%	5.0	887	273	38.8	10.81	0.13	0.21	0.31
b. Binder (OPC+FA) = 100 kg/m³									
Mix-5	0%	3.2	1033	210	27.5	5.02	0.18	0.69	0.89
Mix-6	15%	3.2	1030	251	29.2	6.57	0.13	0.39	0.64
Mix-7	30%	3.2	1027	310	30.5	9.84	0.11	0.33	0.58
Mix-8	45%	3.2	1024	289	31.8	11.26	0.10	0.21	0.30
c. Binder (OPC+FA) = 130 kg/m³									
Mix-9	0%	3.2	843	215	16.8	6.13	0.43	1.2	1.31
Mix-10	15%	3.2	839	262	19.0	9.18	0.33	0.87	1.17
Mix-11	30%	3.2	835	275	20.8	11.64	0.25	0.78	0.98
Mix-12	45%	3.2	830	283	23.3	11.61	0.23	0.74	0.91

Testing procedures. The ASTM testing procedures were adopted to examine the properties of the soil-based CLSM, including fresh density, flowability, setting time, water bleeding, unconfined compressive strength (UCS), and elastic modulus. The CLSM fresh densities measuring on all mixtures as per ASTM D6023 were ranged from 1935−2113 kg/m^3. Flowability, setting time, and bleeding were measured based on ASTM D6103, ASTM C403, and ASTM C232, respectively. UCS test were conducted on 100 × 200-mm cylindrical specimens complying with ASTM D4832 at various testing ages (e.g., 1-, 28-, and 91 days). The elastic modulus of all mixtures was determined at the curing age of 28 days.

Results and discussion

Flowability. Table 2 reports the measured flow consistency for 12 mixtures, falling in ranges of 210–273 mm, 210–310 mm, and 215–283 mm for mixtures made with 80, 100, and 130 kg/m^3 binder, respectively. These values achieved well requirement of flowability for CLSM. Also, it was observed that an increase in percentage of FA resulted in a gradually flowability improvement (excepted Mix-7 only). This phenomenon would be caused by latent attribute of FA, retarding the forming process of ettringite at early hydration.

Setting time and water bleeding. In Table 2, the measured setting time was in ranges of 32.0–38.8 h (Mix.1–4), 27.5–31.8 h (Mix.5–8), and 16.8–23.3 h (Mix.9–12). Setting time is important parameter of a CLSM in the viewpoint of practical applications, deciding the suitability of this material for a specific project. In Fig. 1(a), it was obviously seen that setting time was considerably reduced with higher binder (also higher OPC) content. With an increase in binder from 80 to 130 kg/m^3, the setting time was measured to shorten up to 48% for mixtures without FA. On contrary, mixture made with more FA substituting for OPC could take a significantly longer time for hardening.



(a) Setting time (b) 24h-Bleeding

Figure 1. Variation of setting time and bleeding with various FA replacement ratios.

Bleeding is another high concern for cementitious mixture containing more mixing water like CLSM. Free water after hydration has a tendency of release to the surface (called as bleeding water) would cause the subsidence phenomenon. The measurement of final bleeding water after 24 h was reported in Table 2, ranging from about 5–12% weight of total water in mixtures. The plot in Fig. 1(b) demonstrates that water bleeding increased gradually with an increase of FA replacement ratio for OPC. Latent characteristic of the mineral admixtures would be responsible for high water in the surface. Also, higher binder content apparently resulted in more bleeding. This tendency was abnormal phenomenon comparing with normal concrete, from which mixture with high OPC content is expected to decrease water bleeding. Amount of mixing water and aggregate properties commonly have a prominent contribution on the bleeding of freshly mixed CLSM [6].

Unconfined compressive strength. Table 2 summarizes the averaged UCS results at 1-, 28-, and 91 days. It is seen in Fig. 2(a) that the 28-day UCS of CLSM ranged from 0.21–0.47 MPa, 0.21–0.69 MPa, 0.74–1.2 MPa corresponding to binder content of 80, 100, and 130 kg/m^3, respectively. For backfill application, minimum strength of 0.3 MPa is required [1]; hence, the 80-, and 100 kg/m^3 binder mixtures containing lesser 30% FA are acceptable for backfill, whereas mixture with 130 kg/m^3 binder could have FA substituting for OPC up to 45%. It is revealed that mixture prepared with more binder content is certainly accompanied with a higher strength. Moreover, the higher FA content, the lower compressive strength would be at each testing age. Such behavior was logical because FA is generally known to be not as good as OPC in strength formation, especially at high water-binder ratio [4].

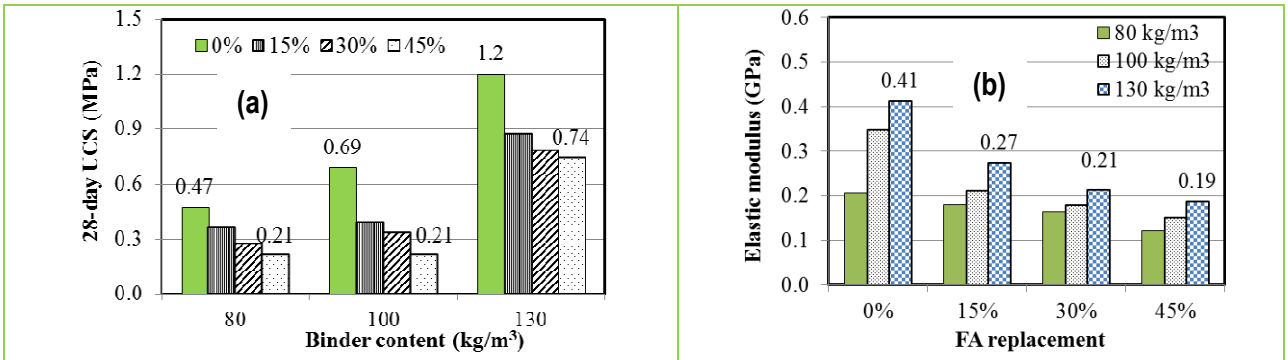


Figure 2. The 28-day compressive strength and elastic modulus.

Modulus of elasticity. The 28-day 100×200-mm cylindrical specimens were offered to investigate the modulus of elasticity (*E*). An axial load from a low-capacity hydraulic machine (100 kN) was slowly and uniformly applied to the capping specimens until failure at a constant displacement rate of 0.51 mm/min. The strain after each loading increment was measured by reading on two dial gages, graduated in 0.01 mm. The *E*-modulus was calculated as the slope of secant line, drawn from the origin to a point on the stress-strain curve at 40% peak stress. The averaged *E*-values from three samples were calculated and presented in Fig. 2(b). *E*-modulus has a reduction as higher percentage of cement replacing by FA. The 45% FA mixtures caused a drastic drop in *E*-modulus by approximately 57%–54%. Moreover, it is exhibited that modulus of elasticity increases as the binder content increases, being similar behavior to UCS.

Conclusion

- Flowability of the CLSM in this study was mostly conformed the requirement of flowable fill materials and was effectively improved as the percentage of FA substitution for OPC increases. Also, the higher FA content, the longer setting time and the more water bleeding would be.
- Mixtures with less than 30% FA substitution for OPC as the mixtures made with 80 or 100 kg/m^3 binder would be acceptable for making CLSM using as backfilled materials. Higher replacement percentage of OPC with FA is likely to decline the compressive strength.
- Elastic modulus at 28 days was ranged from 0.12–0.41 GPa, being higher than that of well granular compacted soil. Moreover, the higher FA content, the lower *E*-modulus was obtained.

Acknowledgement

The authors would like to thanks the National Science Council of the Republic of China (Taiwan) for the financially supporting this research under Contract No. NSC 101-2221-E-151-064.

References

[1] ACI-229R. Controlled-low strength materials (reproved 2005). Farmington Hills (MI)2005.
[2] Lachemi M, Şahmaran M, Hossain KMA, Lotfy A, Shehata M. Properties of controlled low-strength materials incorporating cement kiln dust and slag. Cement and Concrete Composites. 2010;32(8):623-9.
[3] Taha RA, Alnuaimi AS, Al-Jabri KS, Al-Harthy AS. Evaluation of controlled low strength materials containing industrial by-products. Building and Environment. 2007;42(9):3366-72.
[4] Poon CS, Lam L, Wong YL. A study on high strength concrete prepared with large volumes of low calcium fly ash. Cement and Concrete Research. 2000;30(3):447-55.
[5] Berryman C, Zhu J, Jensen W, Tadros M. High-percentage replacement of cement with fly ash for reinforced concrete pipe. Cement and Concrete Research. 2005;35(6):1088-91.
[6] Wu JY, Lee MZ. Benifical Reuse of Construction Surplus Clay in CLSM. International Journal of Pavement Research and Technology. 2011;4(5):293-300.

Applied Mechanics and Materials Vol. 597 (2014) pp 349-352
© (2014) Trans Tech Publications, Switzerland
doi:10.4028/www.scientific.net/AMM.597.349

On the multiple linear regression and artificial neural networks for strength prediction of soil-based controlled low-strength material

Li-Jeng Huang[a], Yeong-Nain Sheen[b] and Duc-Hien Le[c*]

Department of Civil Engineering, National Kaohsiung University of Applied Sciences, Kaohsiung 807, Taiwan, ROC

[a]ljhuang@kuas.edu.tw, [b]sheen@kuas.edu.tw, [c]hienle@kuas.edu.tw

Keywords: Controlled low-strength material (CLSM); regression; artificial neural network.

Abstract. This paper presents two approaches, multiple linear regression (MLR) and artificial neural network (ANN), to develop predictive models for unconfined compressive strength of soil-based controlled low-strength material (CLSM). Our obtained laboratory data conducting on the soil-based CLSM were employed for analysis. Two strength prediction models were proposed: (1) strength is assumed to be a function of mix proportion and curing period; and (2) it is estimated from measured ultrasonic pulse velocity combined with effect of mixture parameters and curing ages. In each model, three predicted formulas were developed; one from MLR and two from ANN. It was showed that all the proposed equations have a well-predicted capacity.

Introduction

Controlled low-strength material (CLSM) is commonly used as backfilled materials. It would be a friendly environment-cheap material and typically consists of small amount cement, fine aggregates, and a large amount of mixing water. Self-compacting/-leveling, low strength, as well as almost no measured settlement after hardening are remarkable characteristics of CLSM [1]. Recent studies have reported that maximum CLSM strength of approximately up to 1.4 MPa is suitable for most of backfilling applications when re-excavation is required [2, 3]. It is also recommended that depending upon availability and project requirements, any recycle materials would be acceptable in production of CLSM with prior tests its feasibility before uses [1]. Literature reviews showed that on-site residual soil after pipeline excavation may be an alternative source for fine constituent in production of soil-based CLSM, effectively used as backfill around buried pipelines [4]. On the other hand, fly ash (FA) is commonly used as replacement material for cement and/or aggregate in concrete or similar products. For FA concrete, the compressive strength has been reported to vary in wide ranges, depending on the amount, types of fly ash and water-binder ratio. Due to high flowability in nature, CLSM mixtures usually need a large amount of mixing water comparing to conventional concrete. Consequently, the strength–developing behavior of CLSM with high flowability made with FA would be different from concrete; and there has currently been a lack of studies on this issue. In this paper, a laboratory work was conducted on the soil-based CLSM, in which Class F FA partially substituted for Portland cement in mixtures. As a result, a set data of unconfined compressive strength (UCS) and ultrasonic pulse velocity (UPV) of all mixtures were obtained at various testing ages. Based on the testing data, predictive models were proposed to estimate compressive strength development. For this purpose, two mathematical approaches are considered for analyzing i.e. multiple linear regression (MLR) and artifitial neural network (ANN).

Laboratory studies

Materials used and mixture proportions. Materials used for the study included fine aggregate, cement, FA, and water. Fine aggregate was formed by well blending river sand and residual soil collected from a jobsite with proportion of 4:6, by volume. The collected soil is a silty-sand soil, classifying as SM in ASTM D2487 [5] with the fine modulus (FM) of 1.27; and the sand (FM=2.51) was suitable for concrete production. Type I ordinary Portland cement (OPC) was used in mixtures.

Class F FA with fineness, Blaine, of 3480 cm^2/g was employed as a partial substitution for OPC. In regard to mixing proportion, three mixing groups corresponding to three binder contents (e.g. 80, 100, and 130 kg/m^3) were produced for investigation along with associated water-binder ratios, after few trial mixes achieving the CLSM requirement of flowability (200–300 mm). In addition, four levels of OPC replacement with FA were launched (i.e., 0%, 15%, 30%, and 45%) while the binder (OPC+FA) content was kept constant at each levels. Totally, a series of 20 mixtures were produced for the experimental program, as shown in Table 1.

Table 1 CLSM Mixture proportion for this study

Mix proportion	Value				
- Binder (kg/m^3)	80	100			130
- FA substitution (%)	0; 15; 30; 45				
- Water-binder ratio	5.0	3.0	3.2	3.4	3.2
- Water-solid ratio	0.27	0.17	0.19	0.21	0.30

UCS and UPV testing results. *UCS* and *UPV* tests were conducted on the same group of three 100 × 200-mm cylinders as per ASTM D4832 [6] and ASTM C 597 [7], respectively. It is observed that the 28-day *UCS* of CLSM ranged from 0.21–1.2 MPa. For backfill application, minimum strength of 0.3 MPa is required [1]. Mixture with more binder content is certainly accompanied with a higher strength. Moreover, the higher FA content, the lower *UCS* would be. Fig. 1 illustrates typically strength development of mixtures made with 130 kg/m^3 binder; and a logarithmic relationship between compressive strength and ages is reasonable. As seen in Fig. 2, the *UPV–UCS* relationship could be performed in a best-fit exponential curve. In general, the ultrasonic waves propagating in concrete medium are highly irregular due to its viscoelasticity and inhomogeneous characteristics [8]. Thus, using only *UPV* for interpretation of compressive strength may be inefficient in term of accuracy, evidenced by the low R^2 value (0.659).

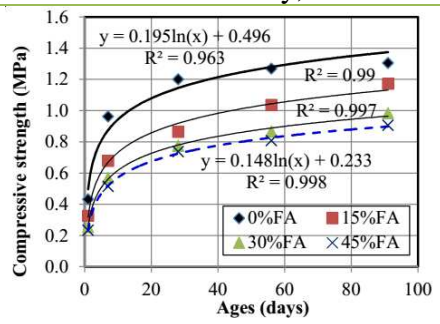


Fig. 1 A typical *UCS* vs age of CLSM.

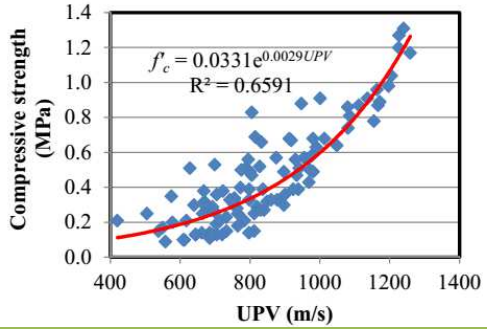


Fig. 2 The *UPV* vs *UPV* for the obtained data.

Proposed predicted models via multiple linear regression and artificial neural network

Identification of the strength models. Two considerations for establishment of the strength formulation were utilized. First, the *UCS* of CLSM is assumed a function of its mixture proportion and the testing age (Model-A1). Hence, there are totally five input variables, representing the material contents and the age of specimens in days and one output variable (*UCS*). Second, known as non-destructive examination approach, the *UCS* can be determined from measured *UPV*, in which the effects of mixture contents and ages are taken into account (Model-A2).

Multiple linear regression (MLR). For MLR implementation, *UCS* is likely performed in a linear combination of the independent variables. Eqs. 1–2 are the developed equations deriving from the MLR analysis on the testing data for strength prediction following Model-A1 (MLR-I) and Model-A2 (MLR-II), respectively. As mentioned before, highly linear correlation between *UCS* and ln(*AGE*) makes the *AGE*-variable to be reasonably transformed in a natural logarithmic quantity.

$$UCS = -12.26 + 0.10\ln(AGE) + 0.10B - 0.70FA - 24.30W_s + 2.16W_b, \quad \text{(MLR-I, } R^2 = 0.885\text{)} \quad (1)$$

$$UCS = -0.872 + 0.070\ln(AGE) + 0.007B - 0.412FA + 0.624UPV\,, \qquad \text{(MLP-II, } R^2 = 0.898\text{)} \quad (2)$$

where, *UCS*, *AGE, B, FA, W_s, W_b, UPV* denote the compressive strength (MPa), curing period (days), binder content (kg/m^3), percentage of fly ash substitution for cement, water-solid ratio, water-binder ratio, and ultrasonic pulse velocity (m/s), respestively.

The coefficients of correlation obtained from the MLR are fairly high (R^2= 0.885 and 0.898), indicating a good fitting. In summary, to predict CLSM compressive strength from its mix-proportion (Model-A1), the MLR-I model is applicable; and estimation of strength based on *UPV* (Model-A2), the MLR-II would be satisfactory. However, estimation of one-day strength was much error or even negative, because the *AGE*-variable was deviated significantly from Eqs. 1–2.

Artificial neural networks (ANN)–MLP and RBF network. It is well-known that multi-layered perceptron (MLP) and radial basis function (RBF) neural networks are popularly employed for regression [9]. Here MLP uses the sigmoid function while RBF employs the Gaussian function as activating function for hidden neurons. Two ANN topologies were simultaneously proposed to predict strength, corresponding to the Model-A1 and Model-A2, as illustrated in Figs. 3(a)–(b). The input and output variables for the ANN layouts are also those for the MLR formulas.

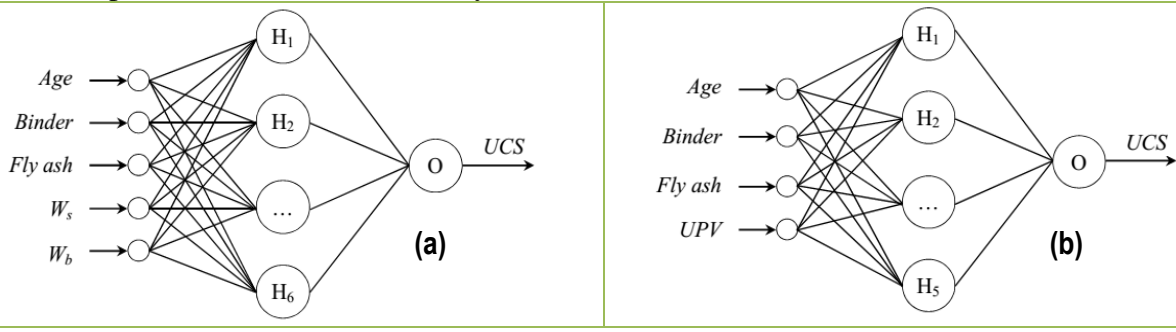


Fig. 3 ANN architecture for (a) Model-A1 and (b) Model-A2.

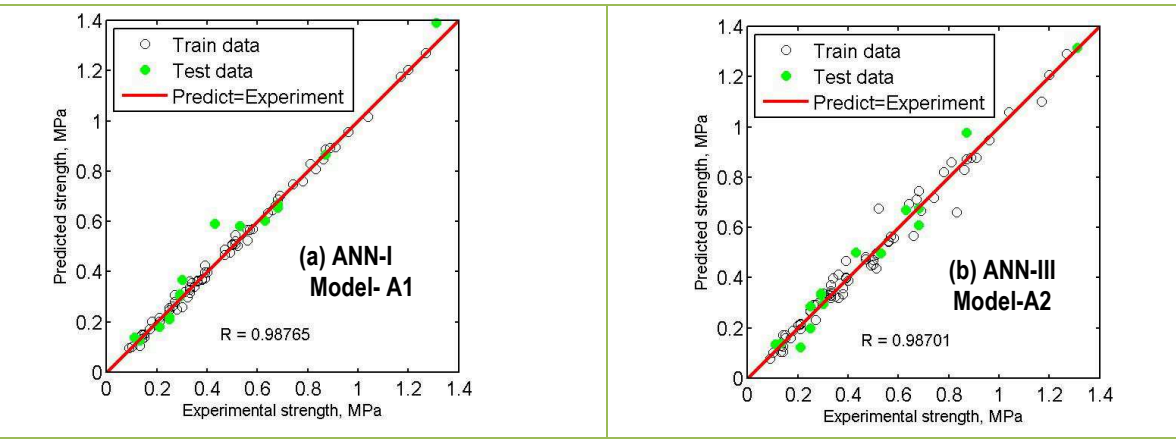


Fig. 4 Comparison of observed and predicted strength by MLP for Model-A1 and Model-A2.

The Neural Network Toolbox in MATLAB was employed for analysis. Totally, 100 experimental datapoints were randomly divided into three subsets with the proportion of 0.7, 0.15, and 0.15 providing for training, validating, and testing, respectively. The Levenberg–Marquardt algorithm was employed for training MLP networks. After few trials of training and the parameter studies, the well-trained MLP and RBF networks were provided for Model-A1 (namely as ANN-I and II) and Model-A2 (namely as ANN-III and IV), accordingly. The predictive capacity of a predicted model were monitored via quantitative evaluation of some indices, which are mean absolute percentage error (*MAPE*), root mean square error (*RMSE*), and coefficient of determination (R^2). Table 2 shows the result of correlation analysis for the obtained models. All the models exhibit a strong correlation between predicted and measured strength ($R^2 \geq 0.86$ for MLR and $R^2 \geq 0.94$ for ANN). Also, the ANN approach would be more potential than MLR in prediction because of higher

R^2 and lower *MAPE* and *RMSE* assessing on the training and testing set, indicating an excellent capacity of generalization. This is logical because MLR is a linear-based approach, whereas ANN employing nonlinear functions is more flexible in providing an input-output mapping. In comparison with the RBF, the trained MLP seems to be slightly better for strength interpolation in both the two models (Model-A1 and A2) as a result of being highest R^2 (0.969 and 0.973), and lowest *MAPE* (11.088% and 12.731%), *RMSE* (0.055 and 0.052 MPa) measured on the testing set. Figs. 4(a)–(b) plot the cross-correlation of measured and calculated strength from the MLP for Model-A1 and Model-A2, respectively.

Table 2. Statistical comparison of the proposed models

Model	Prediction approach	Training data set			Testing data set		
		MAPE (%)	RMSE (MPa)	R^2	MAPE (%)	RMSE (MPa)	R^2
A1	MLR-I (Eq. 1)	28.317	0.108	0.855	20.451	0.093	0.912
	ANN-I (MLP)	**3.585**	**0.015**	**0.997**	**11.088**	**0.055**	**0.969**
	ANN-II (RBF)	4.879	0.018	0.996	13.112	0.079	0.937
A2	MLR-II (Eq. 2)	23.414	0.090	0.898	25.318	0.110	0.878
	ANN-III (MLP)	**7.366**	**0.042**	**0.978**	**12.731**	**0.052**	**0.973**
	ANN-IV (RBF)	6.402	0.039	0.981	18.971	0.067	0.955

Conclusion

Two models for prediction of compressive strength for CLSM are proposed: (1) Model-A1 interpolates *UCS* from the mixture proportion and curing period; (2) Model-A2 evaluates *UCS* from *UPV*, curing age, and binder parameters. Two approaches were employed for constructing input-output relationship: (1) MLR: two best empirical linear regression formulas; (2) two types of ANN (MLP and RBF network). Results show that MLP networks give the best performance for strength interpolation because it possesses the lowest *RMSE* and *MAPE*, and the highest R^2.

Acknowledgement

The authors would like to thanks the financial support from National Science Council of the Republic of China (Taiwan) under Contract No. NSC 101-2221-E-151-046.

References

[1] ACI-229R. Controlled-low strength materials (reproved 2005). Farmington Hills (MI)2005.
[2] Lachemi M, Şahmaran M, Hossain KMA, Lotfy A, Shehata M. Properties of controlled low-strength materials incorporating cement kiln dust and slag. Cement and Concrete Composites. 2010;32(8):623-9.
[3] Finney AJ, Shorey EF, Anderson J. Use of native soil in place of aggregate in controlled low strength material (CLSM). International Pipelines Conference 2008. Atlanta, Georgia, United States2008. p. 1-13.
[4] Howard A, Gaughan M, Hattan S, Wilkerson M. Lean, Green, and Mean: The IPL Project. ICSDEC 2012: American Society of Civil Engineers; 2012. p. 359-66.
[5] ASTM:D2487. Standard Practice for Classification of Soils for Engineering Purposes (Unified Soil Classification System). 2006.
[6] ASTM:D4832. Standard Test Method for Preparation and Testing of Controlled Low Strength Material (CLSM) Test Cylinders. 2002.
[7] ASTM:C597. Test for Pulse Velocity Through Concrete. 2009.
[8] Trtnik G, Kavčič F, Turk G. Prediction of concrete strength using ultrasonic pulse velocity and artificial neural networks. Ultrasonics. 2009;49(1):53-60.
[9] Yilmaz I, Kaynar O. Multiple regression, ANN (RBF, MLP) and ANFIS models for prediction of swell potential of clayey soils. Expert Systems with Applications. 2011;38(5):5958-66.

Applied Mechanics and Materials Vol. 597 (2014) pp 353-357
© (2014) Trans Tech Publications, Switzerland
doi:10.4028/www.scientific.net/AMM.597.353

Measurement of sliding wear of shot-peened Partially Stabilized Zirconia plate

Hitonobu KOIKE[1 a*], Kae IWANAKA[1 b], Koji TAKAHASHI[1 c]

[1] Yokohama National University 79-5 Tokiwadai Hodogaya Yokohama, 240-8501,Japan
[a] koikeh@ynu.ac.jp, [b] iwanaka-kae-kt@ynu.jp, [c] ktaka@ynu.ac.jp

Keywords: sliding wear, PSZ, shot-peening, Si_3N_4, raman spectroscopy

Abstract. In this paper the wear performance between Partially Stabilized Zirconia (PSZ) plate and silicon nitride ball under dry conditions was investigaed. The wear durability of PSZ with shot peening was higher than that of PSZ without shot peening in the sliding wear test under low Hertzian contact pressure. By shot peening, the transformation from tetragonal to monocryclinic phase with compressive residual stress occurred locally on the PSZ surface. Due to this transformation, the wear durability on the surface of the PSZ plate was improved.

Introduction

Partially Stabilized Zirconia (PSZ) has good friction properties and wear durability comparable to that of other fine ceramic materials, and better toughness than alumina, silicon nitride and so on. Due to these characteristices, PSZ has potential for use in situations where moving parts are in physical contact in mechanical assemblies in various fields. For a frictional ceramic part application in an mechanical assembly of a bearing, a slider or an artificatial joint etc., the wear durability is one of the significant properties. Because severe wear influences mechanical performances such as positioning, contact strength and stable movement over long term operation. Recently the tribological behavior between Si_3N_4 and ZrO_2 were studied by many researchers in order to evaluate the quality problems such as failure of ceramic's part [1-3]. Kato et al. state that the adhesion wear occurred in pin-on-disk test of ZrO_2 or Si_3N_4 etc. In the mild wear region, powder formation or film appeared in the interface and plowings appeared on the worn surface [4-6]. Hokkirigawa stated there were three wear modes with regard to ceramic mechanical wear; flake, powder and plowing formation. These wear modes were decided by the effective stress intensity factor K_{eff} , contact pressure P and crack length. This means that the ceramics' sliding wear was related to K_{eff} and P [7].

Regarding the tetragonal to monoclinic phase transformation toughening, it is known that stress as mechanical stimulation induces the martensitic transformation in PSZ [8]. When the PSZ microstructure transforms from the tetragonal to the monoclinic phase, the crystalline volume increases by approximately 4 %. At that time the compressive residual stress occurs in the structure due to this volume expansion [9]. The martensitic transformation prevents the propagation of the crack tip because of the crack close effect under the compressive residual stress [9-12]. Preiffer et al. found that compressive residual stress can be introduced into the near-surface of Si_3N_4 by using a novel shot peening method[13]. Shot peening is a common procedure to improve the near-surface strength of metals. In the shot-peening process, a stream of small, hard spheres are shot at a treated surface [13]. Compressive residual stress is generated by the localized plastic deformation of the surface layer. As a result of the shot peening/blasting effect, the compressive residual stress prevents fatigue crack initiation and propagation [13,14]. Takahashi et al. stated that the tetragonal to monoclinic phase transformation occurs and the compressive residual stress is generated under the surface of the shot-peened PSZ bar and Si_3N_4 ceramic plate [15-17]. When shot peening is too strong, cracks occur on a ceramic surface because ceramic is a brittle material. Hence, the wear durability of PSZ with compressive residual stress by shot peening is not clear.

In this work, the wear of PSZ plate with compressive residual stress by shot peening was investigated. It found that under 750-950 MPa Hertzian contact pressure (Maximum Hertzian contact pressure: 1.13-1.42 GPa) in dry conditions, PSZ wear durability changed due to the crystalline transformation caused by shot peening.

Experimentals

Material. The ball-on-plate wear test specimens were produced of partially stabilized zirconia containing 5 wt% Yttrium oxide (TZ-3YSB-E from Tosoh co., Japan). The density of this material was 6.074 g/cm^3. The dimensions of the plate specimen were 25 × 25 × 4 mm. PSZ plate specimens with shot peening (SP PSZ) and without shot peening (Non-SP PSZ) were prepared. The shot peening process was applied to introduce the compressive residual stress under the surface of the PSZ plate. As the shot media, ZrO_2 beads with a 180 μm diameter were used. The peening air pressure was 0.2 MPa, and the peening time was 60 sec. The whole area of the plate was shot-peened, which was approximately 200 % coverage. After shot peening, the specimen surfaces were final-polished with the 0.1 μm diameter diamond solution. The average roughness of SP PSZ plate after polishing was 0.15 μm (R_z= 1.4 μm), and that of Non-SP plate was 0.01 μm (R_z = 0.1 μm). Si_3N_4 balls (grade 3) with 4.7625 mm diameter were used. The hardness of both PSZ plates and Si_3N_4 ball were approximately 1300 Hv and 800 Hv, respectively.

Setup . Figure 1 shows the schematic illustration of the sliding wear test. The two types of ball-on-plate wear tests were carried out with the friction player (FPR-2100, Rhesca co.,Ltd.). One was the rolling direction mode and another one was the oscillation mode. The oscillation length was 10 mm. The vertical load was 2.45-4.90 N and this load range corresponded to 750-950 MPa Hertzian contact pressure. The Hertzian contact pressure was calculated by using Equations 1 and 2 from Hertzian contact theory.

$$a = \sqrt[3]{\frac{3RQ}{4}\left\{\frac{(1-\nu_1{}^2)}{E_1} + \frac{(1-\nu_1{}^2)}{E_1}\right\}} \quad (1)$$

$$P_{mean} = \frac{Q}{\pi a^2} \quad (2)$$

where P_{mean} is Hertzian contact pressure. v_1, E_1 and v_2, E_2 are Poisson's ratios, Young's moduli of Si_3N_4 (Ball's material) and PSZ (Plate's material), respectively. Q [N] is load, a is contact radius.The frictional speed was 0.033 m/s and this speed corresponds to 100 oscillation cycles per minute. In order to calculate the wear volume of the PSZ plate after the test, the wear depth and width measured as shown in Fig. 1b by using a surf coder (SE1200, Kosaka lab. Ltd.). The ball and plate specimens prior to and after the tests were observed by an optical microscope (BX-51M, Olympus). The crystalline structure on the worn surface of the PSZ plate was investigated by a raman microscope (inVia Reflex, Renishaw). The Ar^+ excitation laser with 532 nm wavelengrh and a grating with 1800 grooves/mm were used.

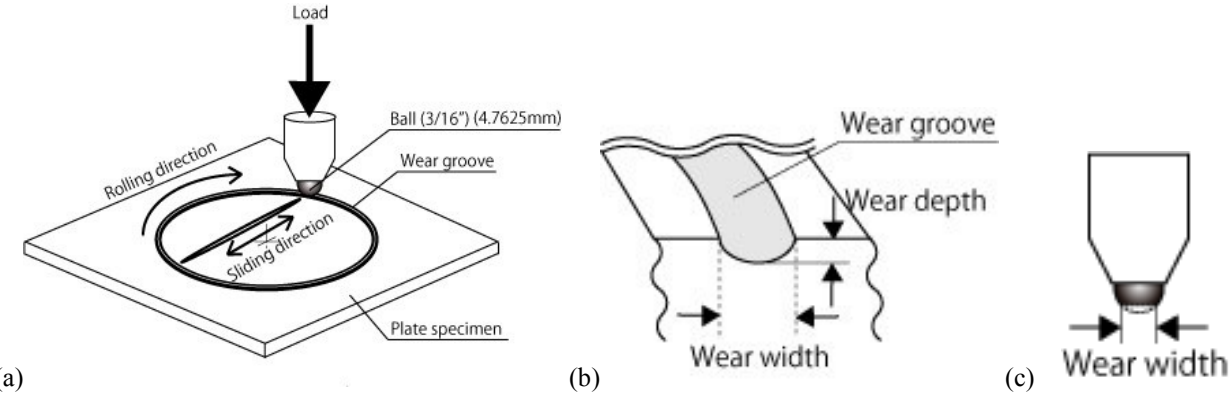


Fig. 1 Schematic illustration of the sliding wear test; (a) plate and ball, (b) wear groove of PSZ plate, (c) ball wear width.

Experimental Results and Discussion

Wear Test. Figure 2 shows the wear volume of the PSZ plates after 8×10^4 cycles under 750-950 MPa Hertzian contact pressure. When the Hertzian contact pressure was lower than 820 MPa, the wear volume of the SP PSZ plate was less than that of Non-SP. Figure 3 shows the Si_3N_4 ball's wear width.

Under 800 MPa Hertzian contact pressure, the wear width of the ball against the SP PSZ plate was narrower than that of Non-SP. This means that the wear durability of the combination of Si_3N_4 ball and SP PSZ plate was superior to the Non-SP combination under 820 MPa. Figure 4 shows the frictional coefficients of the SP and Non-SP PSZ plates during the wear test under 800 MPa. The SP and Non-SP frictional coefficients were 0.48 and 0.54, respectively. The frictional coefficient of SP PSZ was on a level with Non-SP. Figures 5 show the microscope images of wear surfaces on the raceway of the PSZ plates prior to and after testing under 800 MPa. Figs. 5a and 5b show the PSZ plates with SP and Non-SP prior to the test, respectively. Many plowing and worn particles were observed on the friction surface on both the SP and Non-SP PSZ plates (Figs. 5c and 5d). The wear width of SP PSZ plate was narrower than that of Non-SP PSZ. The wear width of SP PSZ was 0.64 mm while Non-SP PSZ was 0.90 mm. These results showed that the tribological performance was improved by SP under 800 MPa.

Raman Spectroscopy. Figures 6a and 6b show the raman spectra of the Non-SP and SP PSZ plates prior to the test. Due to SP process, the monoclinic doublet at 178 and 189 cm^{-1} corresponding to a raman shift peak changed [8,18,19]. This means that the monoclinic phase on the raceway surface of PSZ plates was increased by SP. The volume ratio (V_m) of the monoclinic phase in the SP PSZ was estimated from the Equation 3 [8,20].

$$V_m = \frac{I_m^{178} + I_m^{189}}{0.33(I_t^{145} + I_t^{256})\, I_m^{178} + I_m^{189}} \tag{3}$$

where *Im* and *It* are the intensities of peaks of the monoclinic and tetragonal phases. It found that the volume ratio of the monoclinic phase in the SP PSZ was 0.51 while the ratio in the Non-SP was 0.44. The stress-induced transformation from the tetragonal to the monoclinic phase was caused by shot peening. Therefore this transformation influenced the wear durability in the early stages of the operation time. Figures 6c and 6d show the raman shift on the raceway surface of SP PSZ plate after the wear test. At 8×10^4 cycles under 800 MPa, the peak of monoclinic phase was very clearly visible. The initial monoclinic phase remained on the raceway surface after testing under 800 MPa. However, the monoclinic phase disappeared on the raceway surface after testing under 950 MPa, and a lot of particles and film occurred on the raceway. From the tests results, it found that the shot peening influenced the wear condition of PSZ surface under low Hertzian contact pressure during the early stage in the sliding wear test.

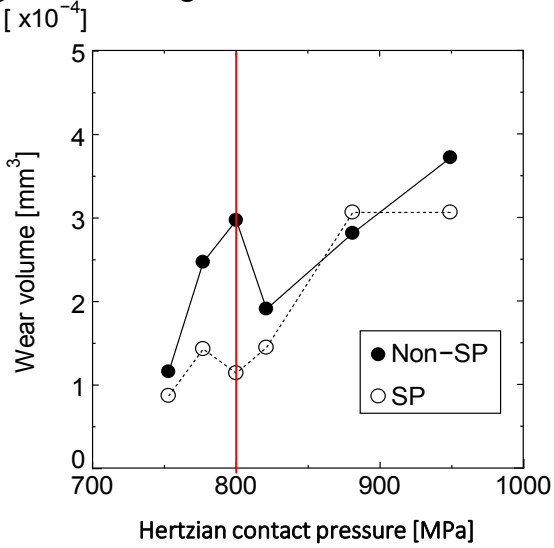


Fig. 2 Wear volume of PSZ plate after 8×10^4 cycles under 750-950 MPa.

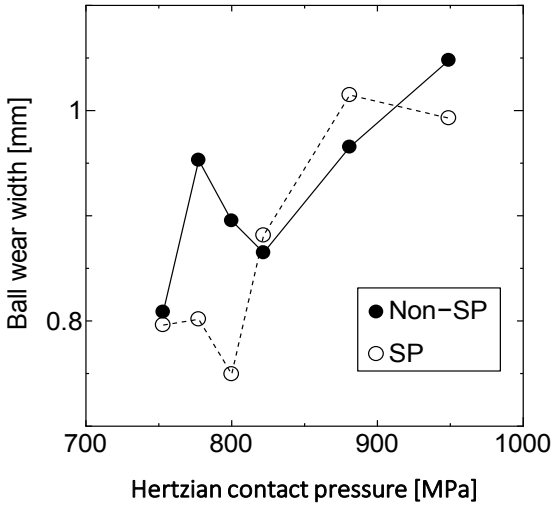


Fig. 3 Wear width of Si_3N_4 ball after 8×10^4 cycles.

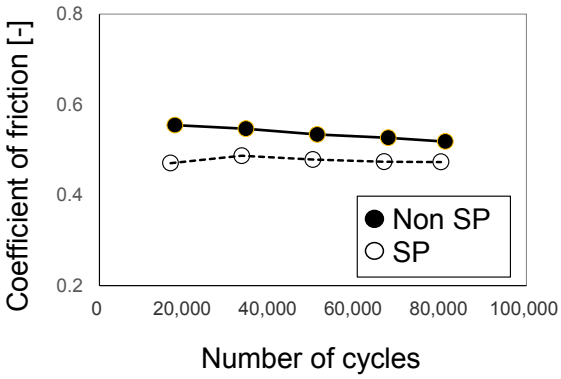


Fig. 4 Coefficients of friction for Non-SP and SP PSZ specimens.

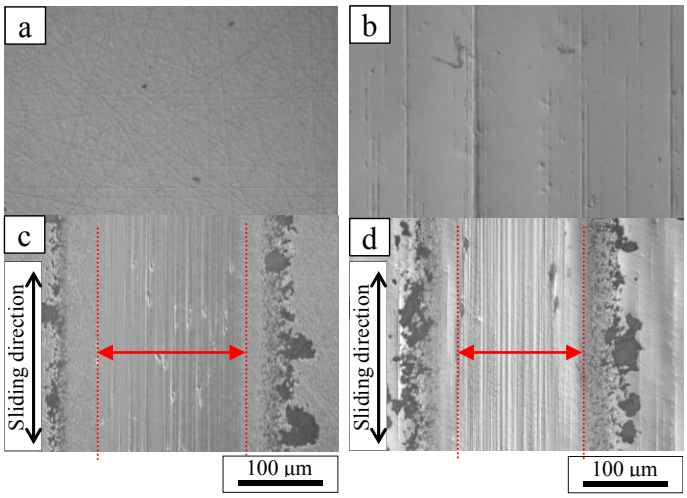


Fig. 5 Microscope image of wear sueface on the raceway of PSZ plate, (a) Non-SP and (b) SP prior to the test, (c) Non-SP and (d) SP after the test. Note that the arrows and dot lines indicate the wear widths.

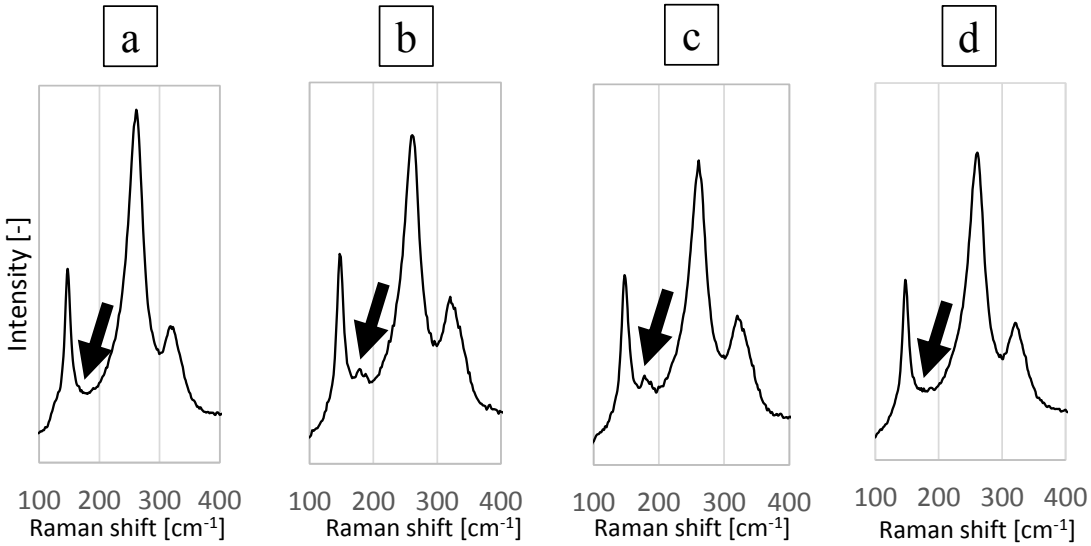


Fig. 6 Raman shift of the raceway of PSZ plates; (a) Non-SP and (b) SP prior to the wear test, (c) SP under 800 MPa and (d) SP under 950 MPa after 8×10^4 cycles testing. Note that the arrows indicate the peaks of monoclinic phase.

Conclusions

From the obtained experimental results, the following conclusions were drawn:

1) When the Hertzian contact pressure range was from 720 to 820 MPa, the wear durability of the Partially Stabilized Zirconia (PSZ) with shot peening against Si_3N_4 ball was better than without shot peening.
2) Due to shot peening, the monoclinic phase formed locally on the PSZ plate surface. After the wear test under 800 MPa, the monoclinic phase remained on the friction surface.
3) After the wear test under 950 MPa, however, the monoclinic phase disappeared on the friction surface. The wear volumes of PSZ with shot peening were comparable to that of PSZ without shot peening.

Acknowledgment Author want to special thank Mr. Takanashi at Instrument Analysis Center at Yokohama national university for Raman microscope measurement support. This work was supported by JSPS KAKENHI Grant Number 25289003.

References

[1] Walter Harrer, Marco Deluca, Roger Morrell, Failure analysis of a ceramic ball race bearing made of Y-TZP zirconia, Engineering Failure Analysis 36 (2014) 262–268.
[2] Verena Preis, Michael Behr, Gerhard Handel, Sibylle Schneider-Feyrer, Sebastian Hahnel, Martin Rosentritt, Wear performance of dental ceramics after grinding and polishing treatments, Journal of the mechanical behavior of biomedical materials, 10, (2012), 13-22.
[3] M. N. Aboushelib, Long term fatigue behavior of Zirconia based dental ceramics, Materials 2010, 3, 2975-2985.
[4] K. Kato, Wear in relation to friction- a review, Wear, 241, (2000), 151-157.
[5] Adachi, K. Kato,K. and Chen, N., Wear map of ceramics, Wear, 203-204, (1997), pp.291-301.
[6] K. Kato, K. Adachi, Wear of advance ceramics, Wear, 253, (2002),1097-1104.
[7] K. Hokkirigawa, Wear map of ceramics, Wear, 151, (1991), 219-228.
[8] Claudine Wulfman, Nadia Djaker, Michael Sadoun and Marc Lamy de la Chapelle, 3Y-TZP In-Depth Phase Transformation by Raman Spectroscopy: A Comparison of Three Methods, J. Am. Ceram. Soc., 1–8 (2014).
[9] Guazzato M, Albakry M, Ringer SP, Swain MV., Strength, fracture toughness and microstructure of a selection of all-ceramic materials. Part II. Zirconia-based dental ceramics, Dent Mater. 2004 Jun;20(5):449-56.
[10] N. SOGA, T. SHIONO, Crack growth and phase transformation in partially stabilized zirconia, SMSJ, vol.35-388,(1985), pp.59-65, (in Japanease).
[11] R. M. McMeeking and A. G. Evans, Mechanics of Transformation-Toughening in Brittle Materials, J. Am. Ceram. Soc.,65, 242 (1982).
[12] N. Miyata, Zairyo, 37-415(1988).361, (in Japanese).
[13] W. Pfeiffer and T. Frey, Journal of the European Ceramic Society, 26, 2639-2645(2006).
[14] W. J. Moon, T. Ito, S. Uchimura and H. Saka, Mater. Sci. Eng. A, 387-389, 837-839(2004).
[15] K. Iwanaka, K. Takahashi, Prevention of crack initiation and propagate by shot-peening in Partially Stabilized Zirconia, proc. M&M confercence 2013, JSME, (2013).
[16] Koji Takahashi, Yoshitada Nishio, Yoshiki Kimura, Kotoji Ando, Improvement of strength and reliability of ceramics by shot peening and crack healing, Journal of the European Ceramic Society, 30, (2010), 3047–3052.
[17] Koji Takahashi, Yoshitada Nishio, Improvement of the contact strength of Si_3N_4/SiC by a comparison of shot peening and crack-healing, Journal of solid mechanics and materials Enginnering, 6, 2, (2012), 144-153.
[18] Munoz Tabares JA, Anglada MJ. Quantive analysis of monoclinic phase in 3Y-TZP by Raman spectroscopy, J. Am. Ceram. Soc., 93, 6, (2010), 1790–1795.
[19] J. Ikeda, G. Pezzotti, T. Shimozono, M. Kondo, Residual stress evaluation in ceramic materials for artificial joints by raman spectroscopy, JSME, (2006), 193-194.
[20] C. S. Lim, T.R. Finlayson, F.Ninio and J. R. Griffiths, In-Situ Measurement of the Stress-Induced Phase Transformations in Magnesia-Partially-Stabilized Zirconia Using Raman Spectroscopy, J. Am. Ceram. Soc., 75, (1992), 1570-1573.

CHAPTER 6:

Robotics, Control System and Measurement Technologies

Applied Mechanics and Materials Vol. 597 (2014) pp 361-364
© (2014) Trans Tech Publications, Switzerland
doi:10.4028/www.scientific.net/AMM.597.361

Application of Fuzzy Control Theory in Obstacle Avoidance Simulation of Intelligent Wheelchair

Fang Li *

No.794,Huanghe road,Shahekou District,Dalian,Liaoning province,China

lifang@djtu.edu.cn

Keywords: Intelligent wheelchair, Obstacle avoidance simulation, Fuzzy control, Matlab

Abstract: This paper introduces application of the fuzzy control theory in obstacle avoidance simulation of intelligent wheelchair. Aiming at the path planning problem of intelligent wheelchair, with fuzzy theory, based on the information acquired from ultrasonic sensors that installed in the intelligent wheelchair, processed by fuzzy logic algorithm, then the fuzzy controller of fuzzy control theory was constructed in Matlab, so intelligent wheelchair obstacle avoidance simulation was conducted. The results show that this method can effectively avoid the obstacles, realize the continuous movement of intelligent wheelchair.

Introduction

Along with the increasing of the elderly and disabled, for some relatively poor self-care ability of elderly people and the disabled, they cannot operate general wheelchair, so a more convenient operation, the use of new intelligent wheelchair is more security are paid more attention to and research. For the intelligent wheelchair, wheelchair must take independent obstacle avoiding function. This paper bases on the intelligent wheelchair for obstacle avoidance simulation of fuzzy logic algorithm. Fuzzy logic algorithm is the biggest characteristic of the control rule that summed up by people's experience. The planning problem under the unknown environment has great superiority. The use of fuzzy logic algorithm for local path planning, is the real time measurement of environmental information from the robot itself based on sensor equipment, through the look-up table control strategy, this algorithm is less, can meet the real-time requirement. This obstacle avoidance simulation was conducted in Matlab.

System composition:

The intelligent wheelchair system using ultrasonic sensors to detect obstacles, which detection range is 0.15m ~ 7m . Considering the turning radius of the wheelchair, safe distance of wheelchair to obstacle was set 0.5 m. The system of 5 ultrasonic sensors were installed in the sensor angle respectively, which angle is $-90^\circ, -45^\circ, 0^\circ, 45^\circ, 90^\circ$ .Then sensor of $-90^\circ, 0^\circ, 90^\circ$ is left, front, right, is the right direction ,the remaining two groups of sensors are not in the positive direction on the assumption. So this paper will be five aspects obtain obstacle information fusion for the distance, left, three party information, but this is no longer a specific length, but in all directions of fuzzy information obstacle distance .Using the maximum minimum synthesis method, in order to reduce mutual interference between sensor information and uncertainty; the obstacle avoidance decision was decided by fuzzy controller for intelligent wheelchair.

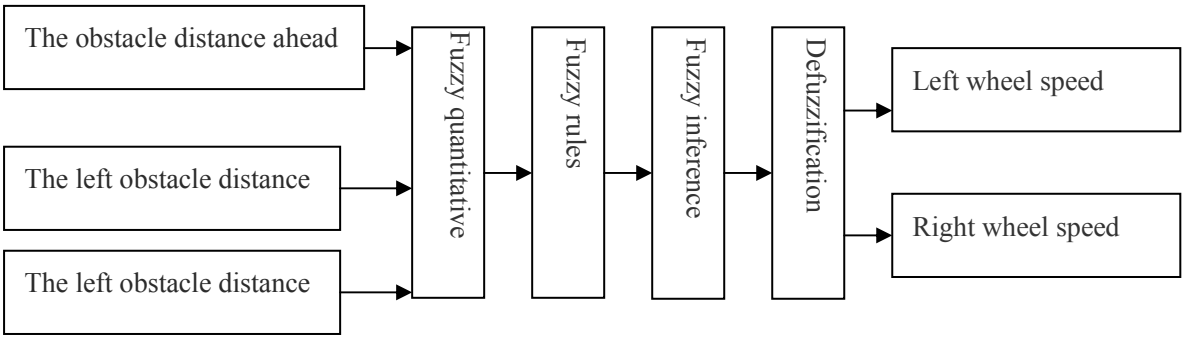
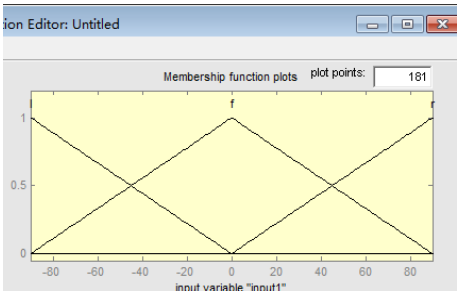


Fig.1 Fuzzy logic control scheme

Implementation of matlab obstacle avoidance simulation: [3-5]

Firstly fuzzy language of the direction that obstacles around the robot was set { left, front, right },fuzzy language of distance that obstacles to robot was set {far, in the distance, near}, membership function was respectively:



.Fig.2 Direction of membership function

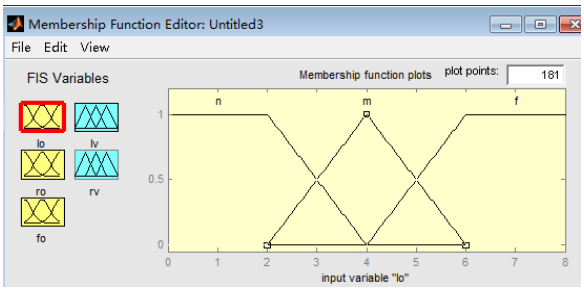


Fig.3 Distance membership function

Membership of each sensor in three directions :

Tab.1 Direction Membership

Sensor number	left	ahead	right
1	1	0	0
2	0.5	0.5	0
3	0	1	0
4	0	0.5	0.5
5	0	0	1

Direction membership and obstacles distance membership of sensor was obtained, then fuzzy relation between obstacle distance and the left, front , right direction could be gained. The sonar sensor membership matrix of position is W, the five sensor obstacle distance

Information fuzzy matrix can be used as L, so can we get the obstacle distance and direction of the fuzzy relation S, the following formula : S =L*W, said the two fuzzy set synthesis, using the maximum minimum synthesis method. Available matrix, each column represents a direction of obstacles are far from near the fuzzy membership.

In defuzzification , the output variables were LV, RV respectively for the wheelchair left, right wheel speed, the fuzzy language collection for {slow, medium, fast}. The membership functions are as follows:

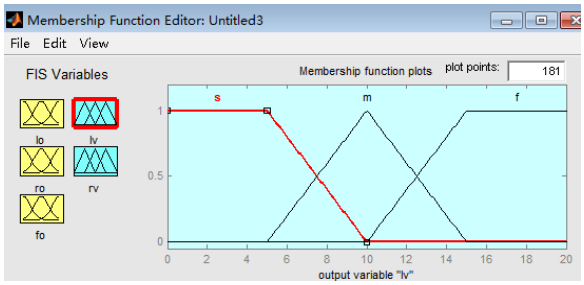


Fig.4 The speed of membership function

The fuzzy control rule is the key part of fuzzy controller, reflects the relationship between inputs and outputs, factors affecting the wheelchair advance is mainly fuzzy information wheelchair left, right, before the three directions of the obstacle distance and direction, when the wheelchair obstacle avoidance strategy, take corresponding to avoid obstacles, in the absence of the obstacle, the wheelchair to move. In this system, the following and obstacle avoidance principle：

(1) priority principle: such as distance information of front, left and right sides sensor was far, According to the original velocity direction to move the wheelchair;

(2) left priority principle: when wheelchair to turn, first turn left, if left distance information was near, andthen determine the right distance information, if the right to was near, wheelchair enter fallback mode.

(3) the motion continuity principle: at present, about the distance information is near, at this time should be back into the wheelchair obstacle avoidance model.

When the sensor of wheelchair detect obstacle information in motion, query relevant fuzzy control rules, can get around the wheel speed. The fuzzy control rules of a total of 27, as shown in fig.5：

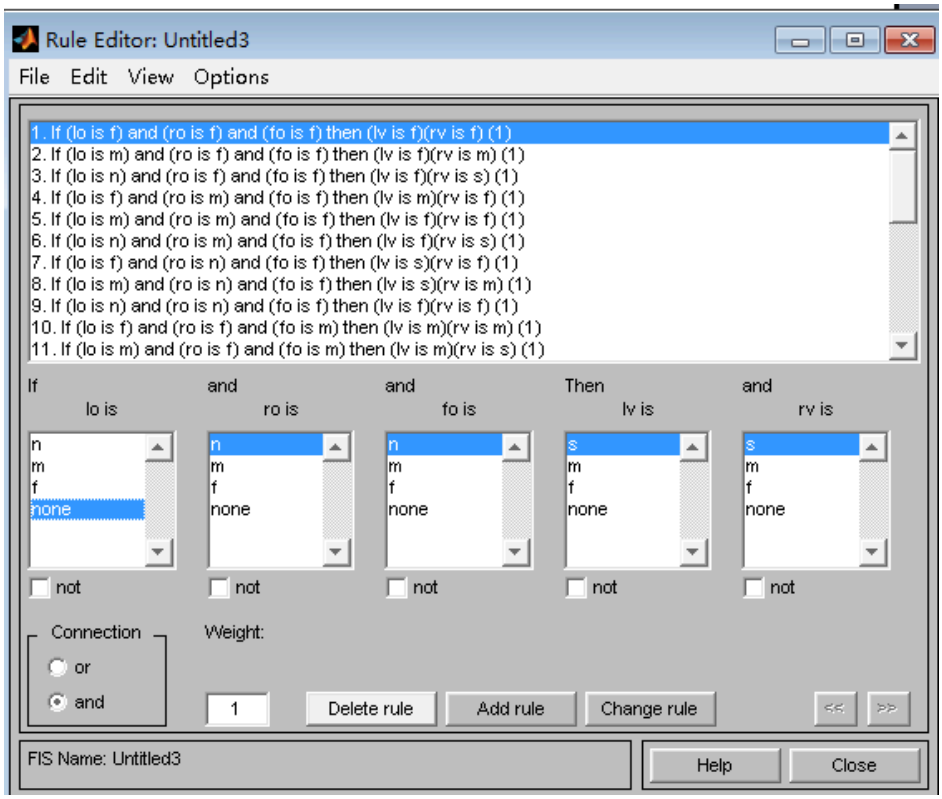


Fig.5 Obstacle avoidance simulation results:

Intelligent wheelchair Rule observation window interface show as fig 6 , three input variables lo, ro, fo, two output variables LV and RV; there are 27 fuzzy control rules; red tourism marking the location of that the current input lo=3.82, ro=4, fo=4; the output variable frame the two column shows the conclusion of each rule the above shows, LV=10.7 and RV-v=10,it is right small frame corner in the red pole position. If the red tour line, drag it to change its position, value of output LV and RV will be changed. The observable inputs affect the outputs.

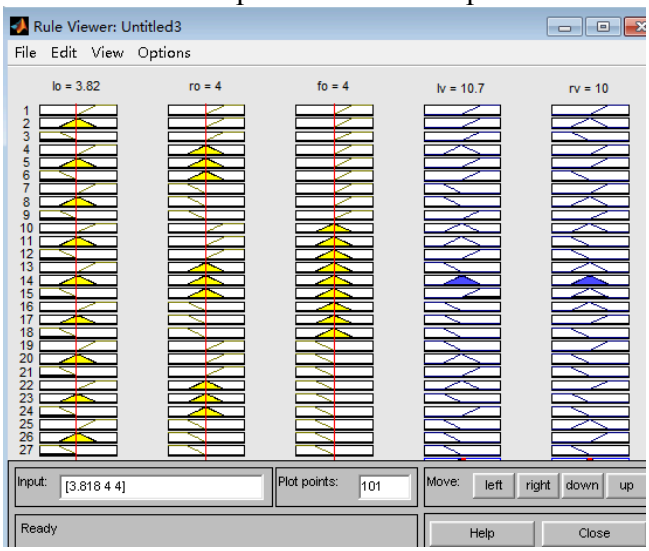


Fig.6 Results the observation window

The kinematics model is established for wheelchair in Matlab, added to the model, the information of the obstacles, the intelligent wheelchair starting point, end point coordinate, and the fuzzy controller "s Function" module, simulation model. The output of fuzzy controller to the work space, namely "to workspace",could be simulatied.

Conclusion

The simulation results show that, the intelligent wheelchair can effectively accomplish the indoor obstacle avoidance, arrived at the destination, obtain good effect of obstacle avoidance and navigation. The scheme is applied to the intelligent wheelchair, will improve the level of intelligent wheelchair, expend the other application space.

References

[1] Zhang Jian guo, Li Jun, Wang Fang. Intelligent wheelchair indoor navigation and obstacle avoidance simulation and computer simulation of [J]2011, (3):203-206

[2] Zhang Jianren, Wang Li. Fuzzy MATLAB control system (J) based onsimulation. Automation and instrumentation, 2003, (1): 6 - 8

[3] Tomohiro Takagi,Michio Sugeno.Fuzzy identification of systems and its application to modeling and control[J].IEEE Trans on System,Man,and Cybemetics,1985,15(1):116-132.

[4] Ketal W. Multiple sensor fusion for navigation systems[C]. Proc. IEEE-IEEE Vehicle Navigationand Information Systems Conference. Seattle,2002.575-578.

[5] Mahajan A, Wang K. Multisensor Integration and Fusion Model That Uses a Fuzzy Inference System[J].IEEE/ASME Transactions on Mechatronics.2001,(6)2:188-196.

Applied Mechanics and Materials Vol. 597 (2014) pp 365-371
© (2014) Trans Tech Publications, Switzerland
doi:10.4028/www.scientific.net/AMM.597.365

Research on Flexible Centroid Measurement Method for Segments of Large-thrust Carrier Rocket

Zhang Xiaolin[1,a*], Zhang Lieshan[1,b], Tang Wenyan[1,c], Wang Chao[1,d], Liu Wancun[1,e]

[1]School of Electrical Engineering and Automation, Harbin Institute of Technology, Harbin, Heilongjiang 150001, China

[a] zhangxiaolin@hit.edu.cn, [b] zhanglieshan@163.com, [c] tangwy@hit.edu.cn

Keywords: Centroid Measurement, Flexibility, Coordinate Transformation

Abstract: A new flexible centroid measurement method is provided in order to meet actual demands for centroid measurement of large-thrust carrier rocket segments. The method has the benefit of utilizing a laser tracker to accurately measure positions of support points of a weighing sensor and geometrical parameters associated with an attitude status of each segment to be measured, thereby solving the problem of a traditional three-point method that measuring accuracy in centroid measurement depends on both mechanical equipment machining accuracy and positioning accuracy. The analysis result shows that the method provided herein has an engineering application value and can realize measurement to high accuracy, automation and universality for large-thrust carrier rocket segments.

1. Introduction

The centroid for a flight vehicle is an important quality characteristic parameter to influence flight attitudes, the centroid control is a main means to realize high-accuracy guidance for the flight vehicle, and an engineering flight vehicle control system uses quality characteristic apriori information obtained by ground measurement, so that flight performances[1,2] of the flight vehicle are influenced directly by the factor whether the centroid is measured accurately. A large-thrust carrier rocket typically consist of a fairing, the first stage, an inter-stage segment, the second stage, and boosters, of which centroid parameters are fundamental inherent characteristic parameters[3] to describe large-thrust carrier rocket mechanical characteristics, and meanwhile a need for researching and manufacturing ground test equipment which determine centroid positions of the segments exists.

The main measurement techniques to measure the centroids of large-sized objects include a three-point method and a four-point method[4~7] which are used to calculate the centroid positions of the products to be measured based on the principle of moment balance. However, the traditional three-point or four-point method has limitations in measuring the centroids of large-thrust carrier rocket segments, including (1) large-sized measuring apparatuses are designed respectively and various sets of measuring equipment are researched and manufactured to meet different requirements in dimension, quality and shape of the large-thrust carrier rocket segments; (2) parameters required for calculating centroid coordinates of the products are preset and mechanical equipment are used to position the products, and thus the accuracy for measuring the centroids will be influenced by the mechanical equipment machining accuracy; and (3) a mathematical model teaches that the measuring equipment must be level-adjusted strictly prior to measurement. Angular deflection happens to a measuring table due to increased measurement times, and thus errors to measure the products will be also increased. Furthermore, the process of adjusting to the level status reduces the efficiency of measuring the products.

A flexible centroid measurement method is described herein, including the steps of measuring support forces of support points of the products by using a weighing sensor; cooperatively using a portable coordinate measuring instrument (for example, a laser tracker) to accurately measure positions of the support points and geometrical parameters associated with attitude statuses of the

segments to be measured; and changing the attitudes of the products, substituting the measured data into the mathematical model to obtain the large-thrust carrier rocket centroid positions.

2. Structure of Measuring Equipment

The measuring equipment researched and manufactured based on the flexible centroid measurement method mainly consists of a measuring frame assembly, a bottom support device assembly, a rolling drive assembly, a moving frame assembly, a console, and dedicated measuring and control software, as shown in Figure 1.

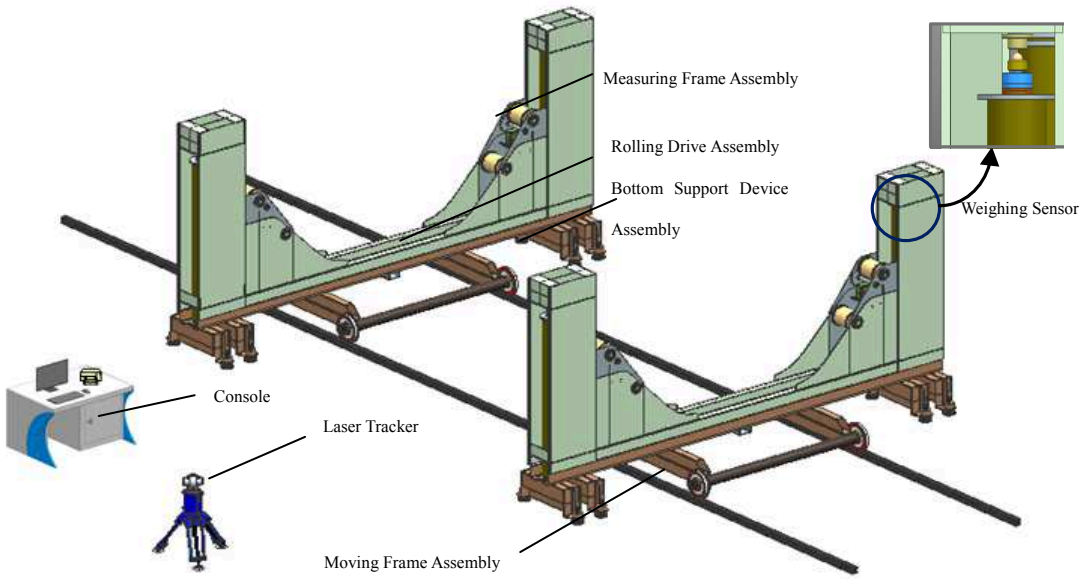


Figure 1 Structure of Flexible Centroid Measuring Equipment

The detailed description of the structure of the measuring equipment is summarized as follows:

(1) The measuring frame assembly comprising support arm assemblies at two ends, reinforcing plates and beams can be adapted to support products with diameters being 5000mm, 3350mm, 2250mm in cooperation and coordination with the rolling drive assembly.
(2) The bottom support device assembly comprises a lifting drive device assembly, a lifting device assembly, a walking device assembly, an auxiliary support truss, a sensor bracket assembly, an elevator sliding rail assembly, a sensor total operation positioning device and a spoke type weighing sensor, and is mainly used for supporting the bottom, lifting and positioning the sensor and measuring the mass and centroid.
(3) The rolling drive assembly mainly comprises a frame assembly, an auxiliary rolling device assembly, a drive device assembly and a drive roller assembly and is used for realizing the attitude transformation of the products and the electrically-driven rolling.
(4) The moving frame assembly is suitable for different lengths of products to be measured and can measure mutual spacing by using optical equipment.
(5) The console comprises a hardware circuit, an electric control box, a main control computer, a printer, a data acquisition card, a weighing instrument and the like and has the advantages such as removability, portability, split structure and the like.
(6) The dedicated measuring and control software can automatically calculate the mass, and the horizontal and longitudinal coordinates of the centroid based on data acquired from the sensor. In measurement a portable coordinate measuring instrument is applied, and the laser tracker is a laser interferometer measurement system tracked under servo control, and provides space coordinates of

a center position of a spherical reflector in real time by tracking an optical reflector, thereby accurately measuring the positions of the support points and all of the required geometrical parameters.

3. Measurement Method and Mathematical Model

Taking measurement of inter-stage segment for an example, the following description for measurement process and basic mathematical principles is provided as follows:

(1) Performing no-load measurement of the unwheeling weigher
Four weighing sensors read F_1'~F_4' in no-load measurement.
(2) Placing a product to be measured and acquiring spatially geometric positions of the weighing sensors

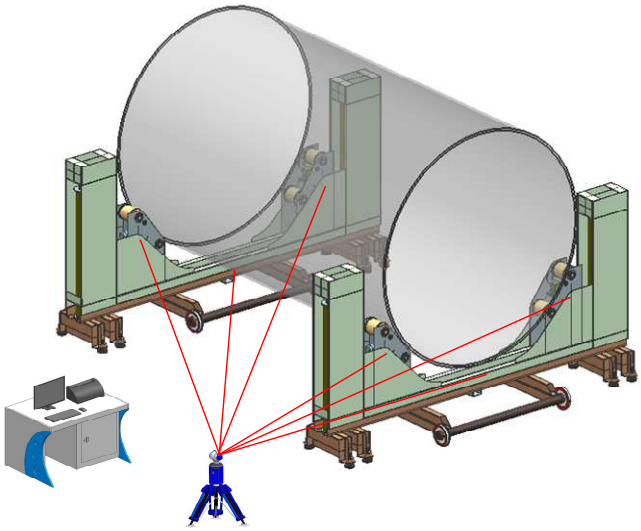


Figure 2 Schematic Representation for Acquiring Spatially Geometric Positions

After installation of the product, the laser tracker is applied to measure N positions of the optical reflector on the unwheeling weigher. Positional change will not happen to the optical reflector with respect to the sensors, so the positions of the four sensors are calculated by measuring positions of key points on the fixture, i.e. (x_i, y_i, z_i), i =1~4.
(3) Measuring a first attitude status of the product
Angles such as α, β, γ are formed hypothetically by the x-axis, the y-axis and the z-axis of a measuring coordinate system with respect with a vertical upward direction, respectively. The product is placed on the measuring fixture and pressures of the four sensors are measured again as well as values read from the four sensors are recorded, i.e. support forces F_1~F_4 provided for the fixture and the product by the four sensors.
At this time, the balance between the fixture and the product is created, and the force applied to each of the fixture and the product is zero with respect to moment of each coordinate axis of the measuring coordinate system. A moment equilibrium equation is given to obtain the following equation sets:

$$F\begin{bmatrix} 0 & \cos\gamma & -\cos\beta \\ -\cos\gamma & 0 & \cos\alpha \\ \cos\beta & -\cos\alpha & 0 \end{bmatrix}\begin{bmatrix} x \\ y \\ z \end{bmatrix} = \begin{bmatrix} 0 & \cos\gamma & -\cos\beta \\ -\cos\gamma & 0 & \cos\alpha \\ \cos\beta & -\cos\alpha & 0 \end{bmatrix}\begin{bmatrix} \sum_{i=1}^{4}(F_i - F_i')x_i \\ \sum_{i=1}^{4}(F_i - F_i')y_i \\ \sum_{i=1}^{4}(F_i - F_i')z_i \end{bmatrix} \quad (1)$$

wherein $F_o = (F + F + F + F_4) - (F'+F'+F'+F_4')$

x_i, y_i, z_i representing positions of the four sensors and values F_1'~F_4' read from the four sensors are substituted into the equation (1) to solve a straight-line equation L_1, wherein the straight line is within the measuring coordinate system and passes through the centroid of the product.

$$L_1:\begin{cases} x = f(t) \\ y = f(t) \\ z = f(t) \end{cases} \quad (2)$$

(4) Transforming the straight-line equation L_1 into a product coordinate system from the measuring coordinate system

A product coordinate system is established firstly and then a transformation matrix T between the measuring coordinate system and the product coordinate system is utilized to transform the straight-line equation L_1 into the product coordinate system from the measuring coordinate system. Rules for establishing the product coordinate system are formulated according to the actual situations. One common method to establish the product coordinate system is described, as shown in Figure 3.

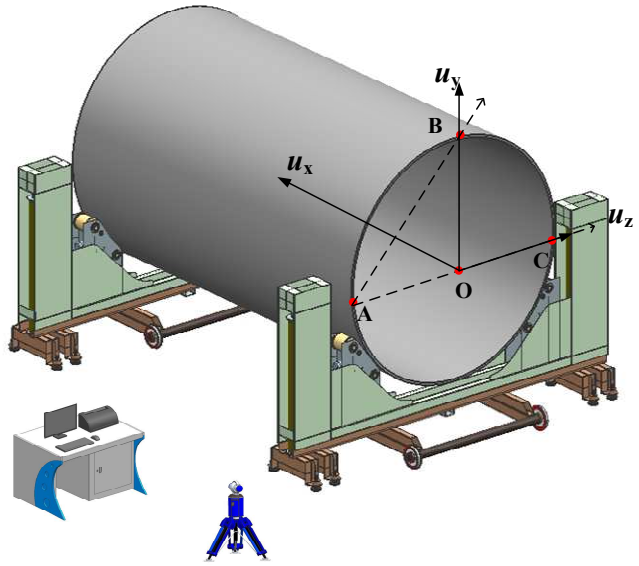


Figure 3 Method to Establish a Product Coordinate System

Several measuring points are marked on the inter-stage segment at the end face, hypothetically measuring points A, B and C. Coordinates of the three measuring points are measured in the coordinate measuring system and then fitted into a circle as well as a coordinate of the center of a circle (O) is solved as an origin of the product coordinate system.

Vectors $\overrightarrow{AC}$ and $\overrightarrow{AB}$ are solved and such configured that the vector $\overrightarrow{AC}$ is applied as a direction vector e_z of the z-axis of the product coordinate system, and $\overrightarrow{AB}\times\overrightarrow{AC}$ is used as a direction vector e_x of the x-axis of the product coordinate system, so that a direction vector e_y of the y-axis of the product coordinate system is illustrated as $\overrightarrow{AC}\times\left(\overrightarrow{AB}\times\overrightarrow{AC}\right)$, and unit direction vectors of the three vectors u_x, u_y and u_z are solved, respectively, thereby establishing the product coordinate system. The transformation matrix between the measuring coordinate system and the product coordinate system is illustrated as

$$T=\begin{bmatrix}1&0&0&0\\0&1&0&0\\0&0&1&0\\-x_0&-y_0&-z_0&1\end{bmatrix}\begin{bmatrix}u_{x1}&u_{y1}&u_{z1}&0\\u_{x2}&u_{y2}&u_{z2}&0\\u_{x3}&u_{y3}&u_{z3}&0\\0&0&0&1\end{bmatrix}$$

wherein u_{x1}, u_{x2} and u_{x3} represent the unit direction vector $u_x=(u_{x1},u_{x2},u_{x3})$ of the x-axis of the product coordinate system; u_{y1}, u_{y2} and u_{y3} represent the unit direction vector $u_y=(u_{y1},u_{y2},u_{y3})$ of the y-axis of the product coordinate system; and u_{z1}, u_{z2} and u_{z3} represent the unit direction vector $u_z=(u_{z1},u_{z2},u_{z3})$ of the z-axis of the product coordinate system.

After the transformation matrix T is obtained, the straight-line equation L_1 is transformed into the product coordinate system to obtain L_1' based on a transformation formula of the coordinate systems, i.e.（x,y,z,1）=(x',y',z',1)T, as shown in Figure 4.

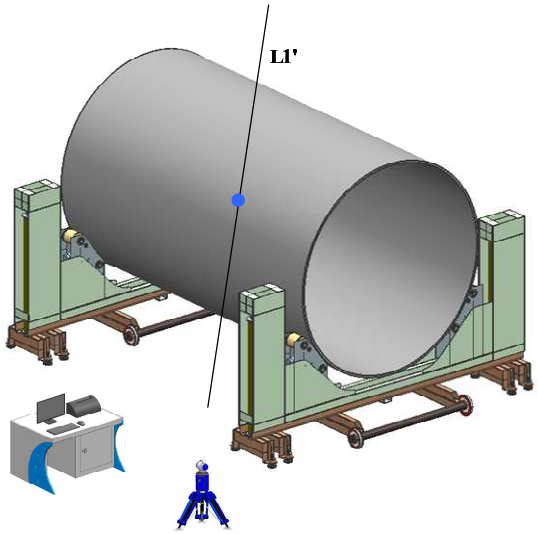


Figure 4 Measurement Result on a First Attitude Status

$$L_1' \quad \begin{cases} x' = f'(t) \\ y' = f'(t) \\ z' = f'(t) \end{cases}$$

Accordingly, the measurement of the product in the first status is done.

(5) Measuring a second attitude status of the product

The product rotates at an angle to measure it in the second status using measurement and calculation methods similar to those of the product in the first status, and finally another straight line L_2' passing through the centroid of the product is obtained in the product coordinate system.

$$L_2' \quad \begin{cases} x' = g'(t) \\ y' = g'(t) \\ z' = g'(t) \end{cases}$$

In Figure 5, the two straight lines are in the product coordinate system and pass through the centroid of the product, so the equations of the two straight lines are simultaneous to solve a point of intersection thereof, namely, a coordinate of the centroid of the product in the product coordinate system. In actual measurement, two un-coplanar straight lines in 3-dimensional space would be obtained, and a midpoint of a perpendicular bisector there-between is calculated, which is considered to be the optimal estimation of the centroid.

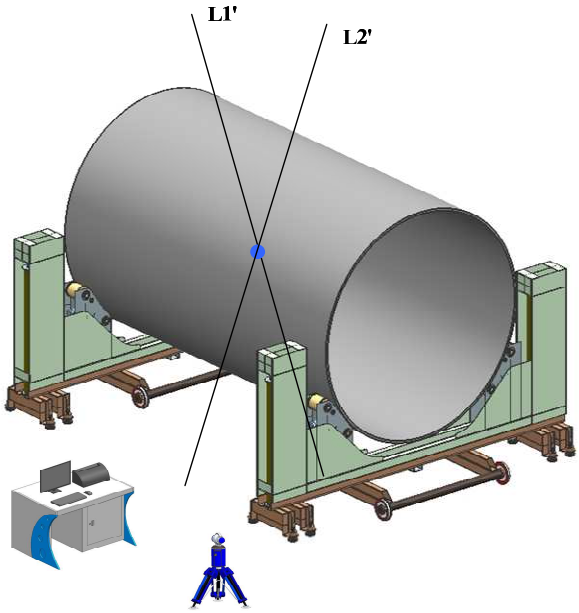


Figure 5 Measurement Result for a Second Attitude Status

4. Conclusion

The flexible centroid measurmenet method descirbed herein overcomes defects of the traditional three-point or four-point method and has the following advantages: firstly, a set of equipment is researched and manufactgured merely to measure the centroid of a given large-thrust carrier rocket segment without designing multiple sets of centroid measuring equipment, with the characteristics of economy, universality, portablity and expansibility; secondly, the parameters requird for

calculating the centroid cooridnate are measured by the precise messuring instrument (for example, the laser tracker) so that the measurement results would not be influenced by the installation of the mechanical fixture and the positioning accuracy and further the measuring accuracy is improved; and finally, in the centroid measurement the strict level adjustment is not required for the mesuring equipment and there is no restriction for the position relationship between the product and the measuring equipment. The product coordinate system can be established by measuring coordinates of some key points on the surface or bottom of the product due to addition of the measuring coordinate system, the product has flexible attitude statuses and any transformation of the two different attitudes can meet the measuring requirement. This to some extent solves the problems such as difficulty to reverse the large-sized conponents, inaccurate product positioning, and poor universality of the measuring fiture, etc. The method described above has an application value and provides new measuring thinking and ways for measuring the centroids of the large-sized flight vehicles.

References

[1] Lu Ying, Zhang An, Cao Xiaobin, et al., Control System of Missile Design and Simulation [J], Journal of Projectiles, Rockets, Missiles and Guidance, 2006, (3): 38-45.
[2] Liao He, Zhao Yanbin, Sun Kexin, et al., Applications of Mass Trim Mechanism in Spacecraft [J], Spacecraft Environment Engineering, 2009, (2): 168-171.
[3] Wang Hongxin, Xu Zaifeng, Zhao Ke, et al., Recent Advances of Mass Property Measuring Technology for Spacecraft [J], Spacecraft Environment Engineering, 2011, (2): 171-174.
[4] Richard Boynton,How to Calculate Mass Properties[C], Proceedings of the 60th Annual Conference of Society of Allied Weight Engineers, Arlington, Texas, No. 3163, 2001.
[5] Richard Boynton, Kurt Wiener. Mass Properties Measurement Handbook[C], Proceedings of the 57th Annual Conference of Society of Allied Weight Engineers, Wichita, Kansas, No. 2444, 1998.
[6] Wu Bin, Wang Haifeng and Ma Guijian, Measurement Method of Centroid for the Vehicle with Large Mass [J], Journal of Astronautic Metrology and Measurement, 2007, (6): 28-33.
[7] Lu Zhihui, Sun Zhiyang, Li Xiangyun, et al., Research on High Precision Measurement of Centroid [J], Acta Armamentarii, 2009, (12): 1748-1752.

Applied Mechanics and Materials Vol. 597 (2014) pp 372-375
© (2014) Trans Tech Publications, Switzerland
doi:10.4028/www.scientific.net/AMM.597.372

Simulation research on the compound control system of internal model add feed-forward compensator

Shengbo Zhang

Jiujiang University Jiujiang, Jiangxi, 332005, China
E-mail: B761127@tom.com

Keywords: Internal model control; Feed-forward compensator;Online identification; Internal model

Abstract: According to the characteristics of the internal model control and feed-forward control and Combining the both advantages, the compound control system of the internal model add feed-forward compensator was designed. In order to improve the dynamic performance of the control system, online identification method is adopted to establish the internal model. The designs of the internal model controller and feed-forward compensator were detailed instructions. The simulation shows that the compound control system have not only good dynamic performance, high tracking precision and strong anti-jamming capability, but also have the change of system parameters with strong robustness.

1 Introduction

The thoughts of Internal Model Control (Internal Model Control, IMC) can be traced back to the 1950's when Smith put forward the time delay estimate compensation controller. This kind of controller had solved the pure delay object control problem in theory [1]. But Smith estimates was poor robustness, when have the modeling error, the performance of the system is difficult to guarantee and get practical application. The thoughts of Internal Model Control is taking the model of the controlled object in parallel with the actual controlled object, the inverse model controller approximation model of dynamic inversion. For the single variable systems, the inverse model controller takes the inverse of minimum phase part .And through additional low-pass filter to enhance the robustness[2]. The main features are simple structure, conveniently design, strong robustness and can eliminate the interference of unpredictable. The feed-forward control is an open-loop control, which can improve the tracking performance of system, reduce the phase difference between the input and output and improve the dynamic performance of system。 Combining the advantages of both and establish the compound control system of internal model plus feed-forward compensator as shown in Fig.1

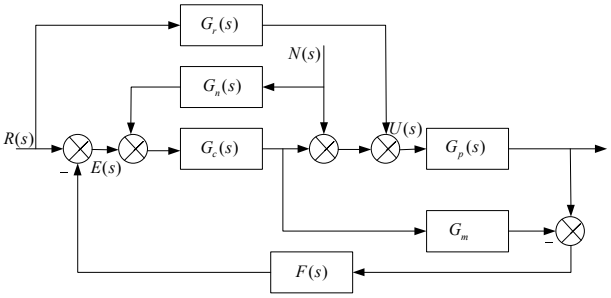


Fig.1 Composite control system block diagram

$G_c(s)$ was the internal model controller, $G_n(s)$ was the feed-forward compensator of disturbance, $G_p(s)$ was control object, $G_m(s)$ was internal model, $G_r(s)$ was the input feed-forward compensator, $F(s)$ was feedback filter.

2 Online identification of the internal model $G_m(s)$

It is difficult to obtain accurate mathematical model of controlled object because of time delay and interference in the general process control which make the control effect be not very good. But online identification can get more accurate mathematical model. Considering the object CARMA model [3].

$$y(k)=\boldsymbol{\varphi}^T(k)\boldsymbol{\theta}+\xi(k) \tag{1}$$

Using RLS similar derivation method[4], obtained the recursive least squares parameter estimation formula.

$$\begin{cases}\hat{\boldsymbol{\theta}}(k)=\hat{\boldsymbol{\theta}}(k-1)+\mathbf{K}(k)[y(k)-\boldsymbol{\varphi}^T(k)\hat{\boldsymbol{\theta}}(k-1)] \\ \mathbf{K}(k)=\dfrac{\mathbf{P}(k-1)\hat{\boldsymbol{\varphi}}(k)}{1+\hat{\boldsymbol{\varphi}}^T(k)\mathbf{P}(k-1)\hat{\boldsymbol{\varphi}}(k)} \\ \mathbf{P}(k)=[\mathbf{I}-\mathbf{K}(k)\hat{\boldsymbol{\varphi}}^T(k)]\mathbf{P}(k-1)\end{cases} \tag{2}$$

In the general case the continuous model is

$$G(s)=\frac{b_n s^n+\cdots+b_1 s+b_0}{s^n+a_{n-1}s^{n-1}+\cdots a_1 s+a_0}e^{-\tau s} \tag{3}$$

In the practical engineering application, it is often approximation for the first order inertia and second-order oscillation system. This article takes the identify model as the internal model $G_m(s)$ and simplified first-order inertia link with pure time delay.

$$G_m(s)=\frac{K_m}{T_m s+1}e^{-\tau s} \tag{4}$$

Pure time delay adopts the first-order Pade approximation [5]

$$G_m(s)=\frac{K_m(1-\tau s/2)}{(T_m s+1)(1+\tau s/2)} \tag{5}$$

According to the principle of internal model control, $G_m(s)$ was broken down into two parts

$$G_m(s)=G_m^+(s)G_m^-(s) \tag{6}$$

$G_m^+(s)$ is the model of minimum phase, $G_m^-(s)$ is the pure time delay in model and the zero parts outside the unit circle which located in the S plane. By Fig 1,the characteristic equation is

$$\frac{1}{G_c(s)}+F(s)[G_p(s)-G_m(s)]=0 \tag{7}$$

For a given model, selecting the feedback filter $F(s)$ and making all of the root on the Eq.7inside the unit circle.

$$F(s)=\frac{1}{(1+\lambda s)^2} \tag{8}$$

λ is the filter constant ,the internal model controller is:

$$G_c(s)=\frac{1}{G_m^+(s)}F(s)=\frac{(T_m s+1)(1+\tau s/2)}{K_m(1+\lambda s)^2} \tag{9}$$

In order to obtain the optimal solution, using ITAE criterion [6], namely

$$J_{ITAE} = \int_0^t t\left|R(t) - Y(t)\right|dt \tag{10}$$

From Fig.1

$$\frac{Y(s)}{R(s)} = G_c(s)G_m(s) = \frac{1-0.5\tau s}{(1+\lambda s)^2} \tag{11}$$

Assuming $R(s) = \frac{1}{s}$

$$Y(s) = \frac{1-0.5\tau s}{s(1+\lambda s)^2} \tag{12}$$

Using the inverse transformation of Laplace to Eq.12

$$y(t) = 1 - e^{-t/\lambda} - \frac{te^{-t/\lambda}}{\lambda} - 0.5\frac{te^{-t/\lambda}}{\lambda^2\tau} \tag{13}$$

Taking into the Eq.10

$$J = \int_0^\infty e^{-t/\lambda}(1 + \frac{t}{\lambda} + 0.5\frac{t}{\lambda^2\tau})tdt = \lambda + \frac{2}{\lambda} + \frac{1}{\lambda^2\tau} \tag{14}$$

On the differential equation can be concluded the λ when the J was minimum

3 Design of feed-forward compensator

After the disturbance feed-forward compensation was introduced into control system, there is no change in the closed-loop characteristic equation of system. So it does not affect the system stability. At the same time reduce the influence of disturbance and improve the anti-interference ability of the system. According to compensate the conditions of the error disturbance can be obtained Eq.16

$$G_n(s) = \frac{1 + G_c(s)G_m(s)}{G_c(s)} \tag{15}$$

According to the principle of feed-forward control, When closed-loop system is continuous, make the product between the feed-forward part $G_r(s)$ and transfer function $G_p(s)$ is 1, namely

$$G_r(s) = \frac{1}{G_p(s)} \tag{16}$$

4 Simulation

The object of simulating system

$$y(k) - 1.5y(k-1) + 0.7y(k-2) = u(k-3) + 0.5u(k-4) + \xi(k)$$

Assuming $\mathbf{P}(0) = 10^6\mathbf{I}$, $\hat{\boldsymbol{\theta}}(0) = 0$. Choose the white noise with 1 variance as the input signal and adopt RLS algorithm for parameter estimation. The simulation results as shown Fig.2 When $k = 400$, the estimation for Parameter is $a_1 = -1.5068$, $a_2 = 0.7049$, $b_0 = 1.0071$, $b_1 = 0.4820$

The typical input signal respectively is unite step. Tracking results are shown in Fig.3. At 500 second applying step disturbance whose amplitude is 0.2. At 1000 second applying step disturbance whose amplitude is -0.2 .Typical input signal is $0.5\,\mathrm{sign}(\sin(0.002\pi t)) + 0.5$, Tracking results are shown in Fig.4 When there is disturbance, the controller can quickly offset the impact and restore the corresponding output settings of the system. Showing that the compound system have good dynamic performance, high tracking precision and strong anti-jamming capability.

Supposing when t > 1300 s, the system parameters are changed as follow

$$y(k)+2.4y(k-1)-1.7y(k-2)=u(k-3)+4.2u(k-4)+\xi(k)$$

When the input signals is $0.5\sin(0.002\pi t)+0.5$ respectively. The signal tracking results is shown in Fig.5 .When the system parameters have changed, the compound control system of internal model control add feed-forward compensator has strong robustness.

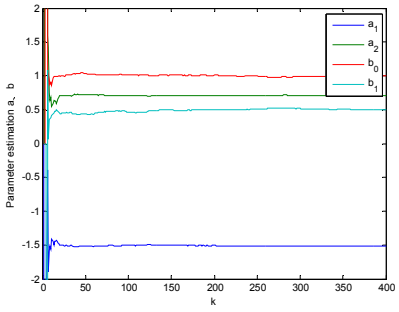


Fig. 2 The parameter estimation results

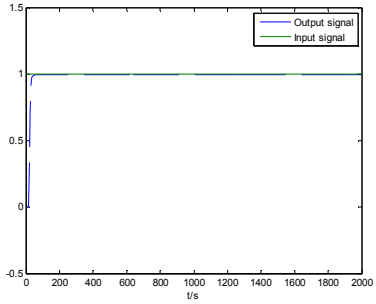


Fig.3 The step signal tracking effect

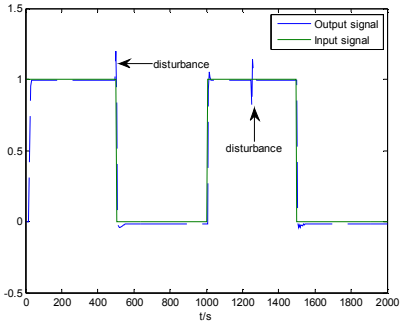


Fig.4 The square wave signal tracking effect with disturbance

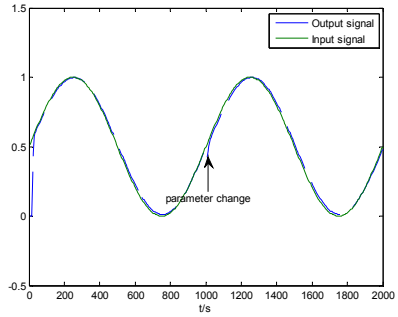


Fig.5 The sine signal tracking effect when system parameter change

5 Conclusion

As can be seen from the simulation results, the compound control system of internal model control plus feed-forward compensator is able to effectively to track with each kind of a given input signal, obtain satisfactory tracking performance and have stronger anti-interference ability and robust performance.

References

[1] Guo Ruiqing, Cheng Qiming, du Xu Feng.The control process of large time-delay [J]. Journal of Shanghai electric power college, 2008, 24 (3): 248-253

[2]Ibrahim K.IMC based automatic tuning method for PID controller[J]. Computers & Chemical Engineering,2004,2(8):281—290.

[3]Liu Hongjun, Pu han. The PID controller based on internal model control design [J]. Computer simulation, 2004, 22 (3): 207-210.

[4]Wang Mintao, Xie Keming. Parameter setting based on internal model control theory [J]. Journal of petrochemical industry automation, Vol 49, No. 2, 65—68

[5] Liu Gongbin,Hu Dejin.Self-tuning internal model PID control in the application of non-circular cut hole processing [J]. Journal of Shanghai Jiaotong university, Vol 40, No.12, 2021-2021

[6] Min rui. Smith Online Identification Prediction Control and Its Application in STM [C]Proceedings of the 4th World Congress ,Intelligent Control and Automation.2002:2254—2257.

Applied Mechanics and Materials Vol. 597 (2014) pp 376-379
© (2014) Trans Tech Publications, Switzerland
doi:10.4028/www.scientific.net/AMM.597.376

Wind-induced Vibration Control for Transmission System Using Steel-Lead Viscoelastic Damper

Gan Feng Lin[1], Jiang Hailong[2*]

[1]Architecture Engineering College, Northeast Dianli University, Jilin 132012, China;

email: gflkw@163.com

[2]Architecture Engineering College, Northeast Dianli University, Jilin 132012, China;

email: jayjianghailong@163.com

Keywords: steel-lead viscoelastic damper; wind-induced vibration; control; transmission tower; finite element method

Abstract: For wind-induced vibration of transmission tower-line system, the vibration reduction effects are studied based on a new type steel-lead viscoelastic damper. Firstly, Calculate damped coefficient basing on the test of the new type steel-lead viscoelastic damper under slow reversed cyclic horizontal loads. Then, a finite element model of transmission tower was built by using ANSYS. And the time history samples of random fluctuating wind load is obtained with the linear auto-regressive filter law principle. Next, three installation plans of dampers on tower were proposed based on analyzing the working principle damper and the structure of tower. Finally, a wind-induced vibration transient response simulation was performed respectively for the different plans. The influences of SLVD dampers on the displacement and on the acceleration of the controlled nodes were compared. SLVD damper can reduce the top node displacement by about 37.89%. The results indicated that the SLVD damper can suppress the wind-induced vibration. And through comparison, the optimal installation scheme of SLVD dampers is obtained.

Introduction

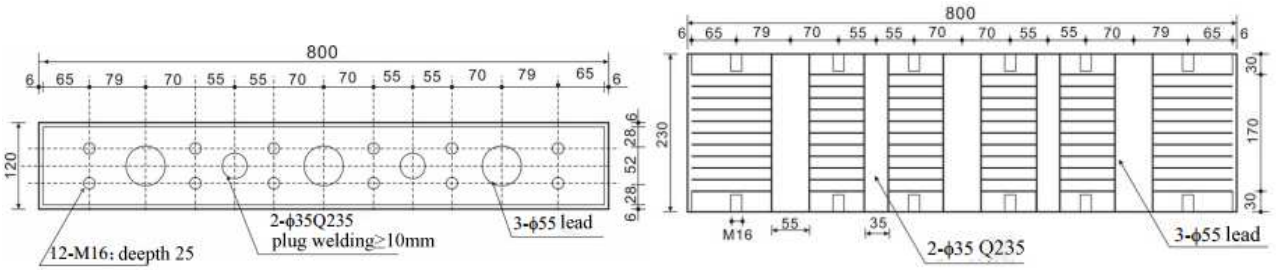
Energy dissipation technology has many features such as explicit damping mechanism, significant damping effect, simple structure, wide application, easy maintenance[1,2]. Attracting the attention of many researchers at home and abroad, a variety of different types and structures of energy Dissipation devices have been developed by domestic and foreign scholars[3].

To solve the problem that using a single energy dissipation mechanism is lack of energy dissipation capacity for the majority of energy dissipation devices, comprehensive utilization of different energy principle or mechanism is proposed to design energy damping device .And a lead viscoelastic dampers is developed[4]. This kind of damper dissipate of energy by using lead shear or extruded plastic deformation and viscoelastic material shear deformation hysteretic after yielding. For transmission tower in the angle section width limited and a small section of the damper difficult to meet the level of stiffness and energy dissipation capacity performance requirements, steel-lead viscoelastic damper is developed. It combines with the characteristics of the hysteretic behavior of steel and lead viscoelastic damper.In this paper, finite element simulation of steel-lead viscoelastic dampers on steel transmission towers is used to study the effects of wind-induced vibration control.The result can provide a theoretical reference for the practical application of SLVD damper on transmission tower wind vibration control in the future.

Steel-lead viscoelastic damper Structure, Principles and Characteristics

Steel-lead viscoelastic damper dissipate energy in this way that when the webs of the damper occurs relative displacement,both steel-lead core and the viscoelastic material can dissipate energy with shear plastic deformation at the same time. SLVD damper improve its ability of dissipation of

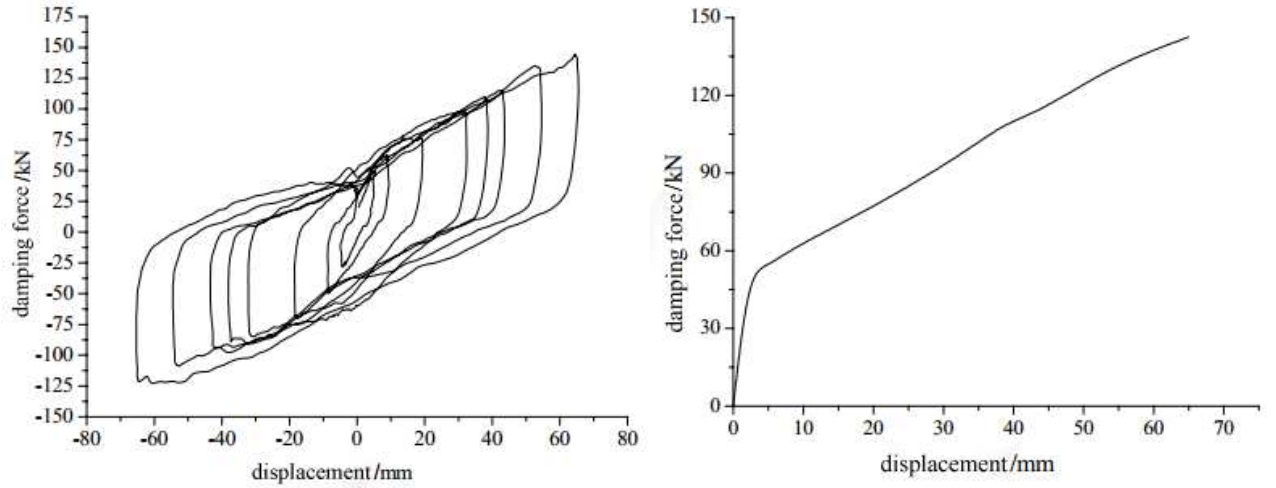
energy in the way that three parts of the SLVD damper can dissipate energy at the same time. Steel-lead viscoelastic damper is 800mm long, 120mm wide, 230mm high. Viscoelastic material layer of it is G4 rubber and mild steel bars is Q235. Its structure is shown in Figure 1.



(a) Plan (b) Section

Fig. 1 Steel-lead viscoelastic damper

Steel-lead viscoelastic damper hysteresis curve is shown in Figure 2. As can be seen from Figure 2, hysteretic curve of the steel-lead viscoelastic damper is slippery, and has good seismic energy dissipation capabilities. The lead core, steel core and viscoelsatic material plays an important part in energy dissipation of shear deformation, which can obviously increase the horizontal shear force, initial-stiffness and energy dissipation ability of the SLVD. The SLVD has no tear and creak phenomenon of the viscoelastic material in a large displacement case, and can recovery the initial position. It has good self-recovery function and large deformantion performance.



(a) Hysteretic curve of the damper (b) Skeleton curve of the damper

Fig. 2 Hysteretic and Skeleton curve of the damper

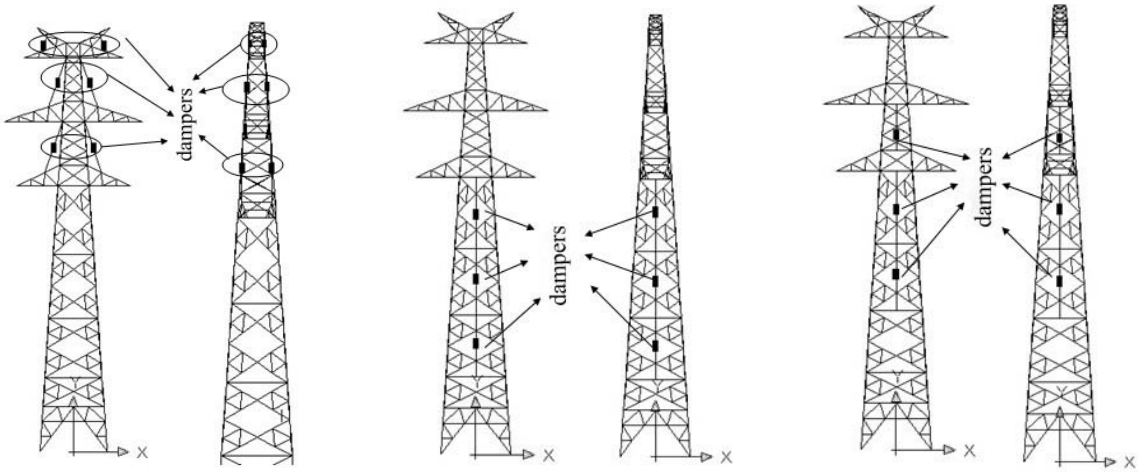
Wind-induced vibration control with SLVD

A finite element model of transmission tower was built by using ANSYS. Steel parts are simulated by BEAM188 element, and the quality of gusset plate auxiliary and connections is considered by adjusting the density of the material. In order to make sure that the prototype is consistent with model, elastic modulus and Poisson's ratio were taken 206GPa and 0.3[5,6].

The total amount of dampers is related with the energy wind load inputting structure and energy dissipation capacity of the dampers[7,8]. In the case of the damper model determination, the number of dampers required can be calculated by energy method. The formula of calculating the number of the dampers is $n = E_n / \psi m E_d$. The required number of the SLVD is calculated to be 12.

According to the displacement-type damper works, the larger structural displacement position where the dampers put on, the better Energy consumption function dampers play. Also we can get the more effect of vibrate control. Combined with the structural characteristics of the transmission tower, I

designed the following three kinds of installation plans. Installation plan 0 is transmission tower without dampers. Installation plan 1 is transmission tower with dampers installed on the crossarms. Installation plan 2 is transmission tower with dampers installed between layers. Installation plan 3 is transmission tower and tower head with dampers. As is shown in Figure 3.



(a) Installation plan 1 (b) Installation plan 2 (c) Installation plan 3

Fig. 3 Installation plans for steel-lead viscoelastic dampers

And the time history samples of random fluctuating wind load is obtained with the linear auto-regressive filter law principle. Then, a wind-induced vibration transient response simulation was performed respectively for the different plans. The displacement-time curve of node A at the top of transmission tower is shown in Figure 4.

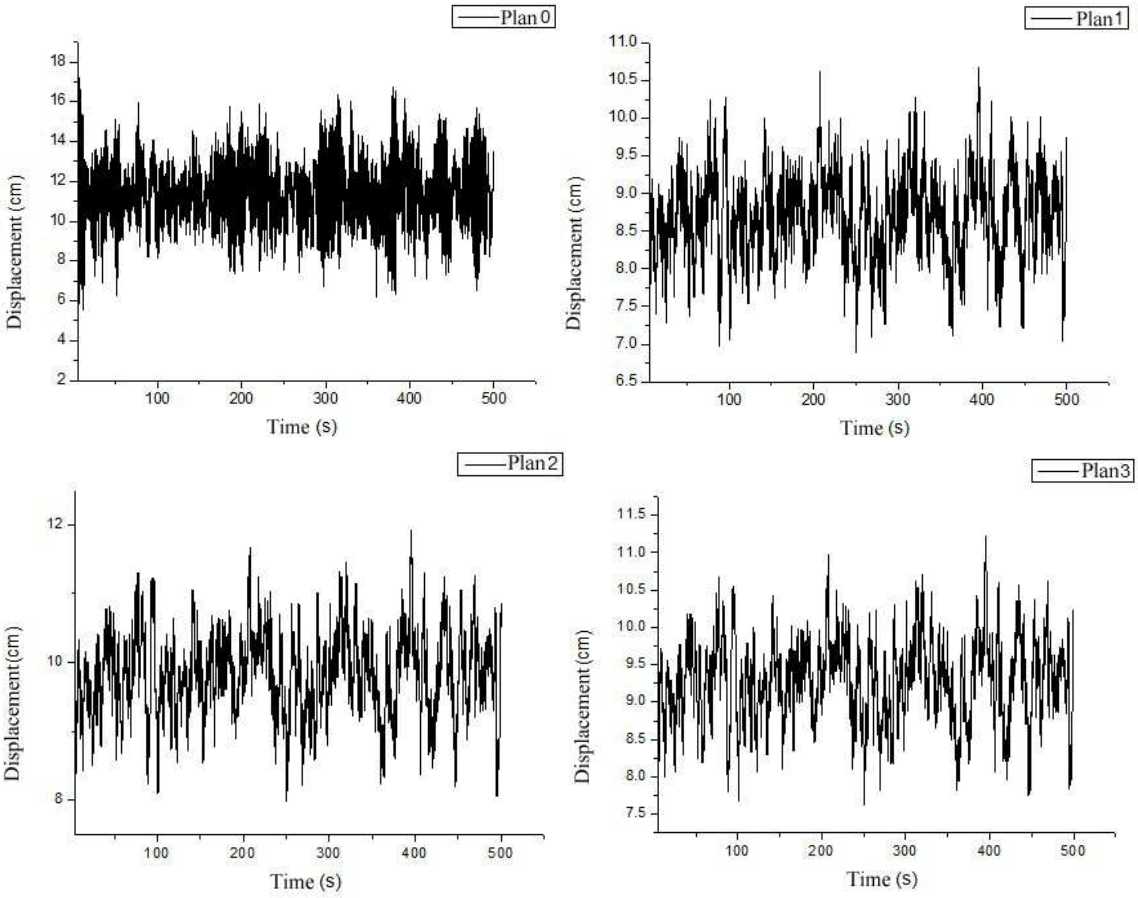


Fig. 4 Displacement of the A node on tower top

As is seen from the displacement-time curve, the SLVD damper can suppress the wind-induced vibration. The displacement-time curve comparison chart of the plan 0 and plan 1 which has the remarkable control effect is shown in Figure 5.And as can be seen from the bar chart, the control effect of plan1 is 37.8%.It is the best. Plan 3 follows by plan 1. The control effect of it can reach 33.5%.And the control effect of all plans is more than 30%. It can be indicated from the result that the SLVD damper can suppress the wind-induced vibration.

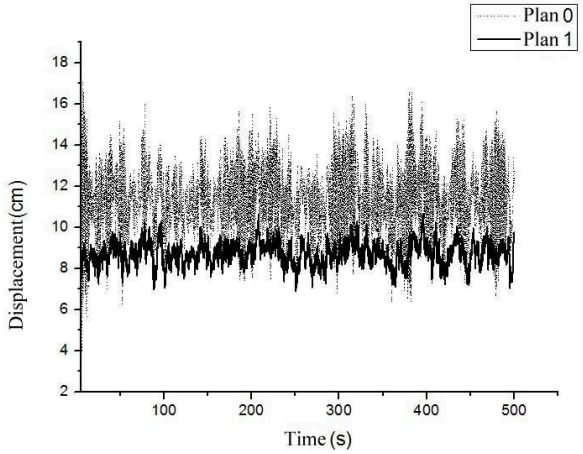


Fig. 5 The comparison of displacement

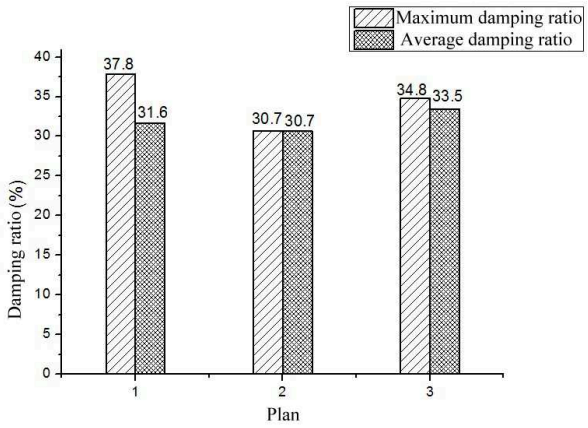


Fig. 6 Damping ratio of the controlled nodes

Summary

(a) Hysteretic curve of the steel-lead viscoelastic damper is slippery, and has good seismic energy dissipation capabilities. The simulating hysteretic curves with bilinear model are identical to the test results, it is feasible to adopt the bilinear model to simulate the damper element in the analysis of a structure with the steel-lead viscoelastic damper.

(b) The results indicate that the steel-lead viscoelastic damper can suppress the wind-induced vibration and can reduce the node displacement by more than 30%. Through comparison, installing dampers at the top of the transmission tower is the best optimal installation plan of steel-lead viscoelastic damper.

References

[1] Soong T T, Dargush G F. Passive energy dissipation on systems in structure engineering [M]. New York: John Wiley & Sons. Inc., 1997.

[2] Pall A S, Marsh C. Friction-damped concrete shear walls [J]. ACI, 1981, 78(3): 187—193.

[3] Cherry S, Filiatrault A.Seismic response control of buildings using friction dampers [J]. Earthquake Spectra, 1993, 9(3): 447—466.

[4] Zhou Yun, Deng Xuesong, Xu Zhaodong. Experimental study on properties of lead-viscoelastic dampers [J]. Earthquake Engineering and Engineering Vibration, 2001, 21(1): 139—144.

[5] Zhong Wanli, Wu Yi, Wang Wei. Analysis on fluctuating wind induced vibration for high-voltage transmission line[J].Electric Power, 2012,45(7): 1-3.

[6] Liu Ming, Li Yonggao, Zhang Houqi. Safety analysis of typical transmission tower in geologic disaster zone[J]. Electric Power, 2012, 45(5):39-43.

[7] Zhong Yin-hai, Li Li, Jiang Yi-cheng. Application of viscoelastic damper to control vibration response of transmission tower under wind[J].Journal of Huazhong University of Science and Technology:Urban Science Edition,2003,20(2):69-71.

[8] Kirekawa A, Ito Y, Asano K. Study of structural control using viscoelastic material[C]. Madrid, Spain: Proceedings of the Tenth World Conference on Earthquake Engineering,1992.

Applied Mechanics and Materials Vol. 597 (2014) pp 380-383
© (2014) Trans Tech Publications, Switzerland
doi:10.4028/www.scientific.net/AMM.597.380

Fuzzy PID Control of ABS Based on Real-time Road Surface Identification

Bo Wang [a], Pingping Lu [b *], Hsin Guan [c] and Jie Jing [d]

(State Key Laboratory of Automotive Simulation and Control, Jilin University, Changchun 130022, China)

[a] Wang.bo@ascl.jlu.edu.cn,[b] Lupingping@jlu.edu.cn,[c] Hguan@jlu.edu.cn,[d] 594393439@qq.com

Keywords: Road surface identification, Optimal slip ratio, ABS, Fuzzy-PID

Abstract. Road surface identification is of great significance in vehicle active safety electronic control systems. This paper proposes a real-time road surface identification algorithm on the basis of the estimated instantaneous road adhesive coefficient. Based on Fuzzy-PID controller and automatic road surface identification, the actual slip ratio can be controlled at the optimal slip ratio precisely, which can promote the ABS and braking performance largely. The braking simulation tests are conducted on pre-set varying road surface conditions. And the results show that the identified results are in good agreement with the pre-set road surface, the proposed algorithm can be conveniently used for various active safety electronic control systems of vehicles.

Introduction

The electronic braking systems such as Anti-lock braking Systems (ABS) aims to control the actual slip ratio at the optimal slip ratio of roads. However, it is difficult to control the braking process precisely without considering the influence of varying road surface, because different roads correspond to different optimal slip ratio. In order to make full use of the maximum road adhesive coefficient provided by different roads considering the changes of the roads and the slip ratio, it is needed to identify the varying road surface in real time. Once the road type is identified, the optimal slip ratio can be determined and the target slip ratio can be modified. The existing researches on road surface identification mainly focus on the identification of uniform road surface[1-3], rarely on varying road surface. And the robustness for a road surface identification algorithm is the key research issue among the current researches and future work[4]. This paper tries to propose a robust road surface identification algorithm for varying road conditions.

The ABS controller

Proportional, Integral and Derivative (PID) controller is one of the widely used controllers in the field of automatic control. It can be expressed as below:

$$u = K_p \cdot e(t) + K_i \cdot \int e(t)dt + K_d \cdot \frac{de(t)}{dt} \tag{1}$$

Where， u is the output， $e(t)$ is the real-time deviation between actual slip ratio and optimal slip ratio; K_p , K_i , K_d are proportional coefficient, integral coefficient and differential coefficient respectively.

PID controller has many advantages such as small calculation, easy implementation and high precision control etc, but it is inconvenient to modify the three coefficients (K_p, K_i, K_d) online with the variation of external conditions. Nowadays, fuzzy control logic has gained great acknowledgement as a methodology to design robust controllers for non-linear and time-variant systems[5]. Using fuzzy logic to modify the three coefficients (K_p, K_i, K_d) of PID controller online

according to varying conditions can improve the control precision and performance significantly on varying road surface. In this paper, the ABS fuzzy self-tuning PID parameters controller based on slip ratio control is built, and the controller structure diagram is shown in Fig.1. The optimal slip ratio comes from the result of road surface identification, which will be illustrated in the following section. The selection of membership function, control rules of fuzzy control see [6].

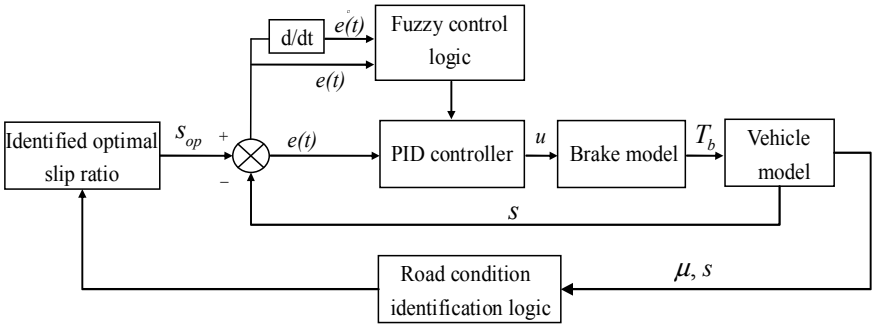


Fig.1 ABS controller diagram

The brake model is built by a simplified one-order integrator. With consideration of the delay of the hydraulic system, a proper one-order inertia element is added, as shown in Fig.2. Kf is a proportional element between brake pressure and brake torque. The input *u* of the brake model is the output of PID controller, and the output of the brake model is brake torque.

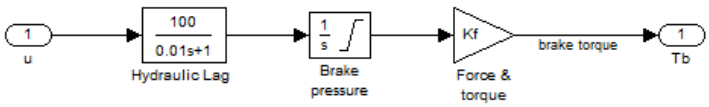


Fig. 2 Brake model

The automatic road surface identification approach

If the road surface is identified only according to single point of instantaneous road adhesive coefficient[5], the identification robustness is unsatisfactory, because there are noise and measurement errors in the required vehicle signals. In order to improve the road surface identification robustness, in this paper, the road characterization index μ is proposed as below.

$$\mu^* = \frac{1}{T}\int_{t-T}^{t} \mu \, dt \tag{2}$$

Where, μ is the instantaneous road adhesive coefficient, t is the current time, T is a constant time interval. During braking process, the dynamics equation of each wheel in rotation direction is shown in Eq. (3).

$$J\dot{\omega} = \mu F R - T - T \tag{3}$$

Where, R —radius of wheels; J —rotational inertia of wheels; T_f —rolling resistance of wheels; T_b — braking force, which can be estimated by sensors; $\dot{\omega}$ —wheel angular velocity;

—wheel normal force, which can be estimated by theoretical model.

Therefore, the instantaneous road adhesive coefficient μ can be estimated from Eq.(3) conveniently. And the road characterization index can be calculated. Burckhardt model is widely used in the vehicle system dynamics. It can be used as the theoretical road adhesive coefficient data

base[7]. The relationship between road adhesive coefficient μ and slip ratio s in Burckhardt model is as below.

$$\mu = c(1 - \exp(-c\,s)) - c\,s \tag{4}$$

Where, , c and $_3$ are parameters in the model. Different roads own a set of values of , c and $_3$. Fig.3 shows the different typical road $\mu - s$ curves.

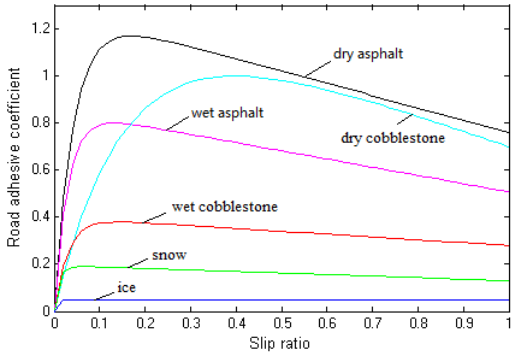


Fig.3 $\mu - s$ curves of typical road surface

Based on Burckhardt model, the theoretical road adhesive coefficient characteristic intervals of six typical roads can be obtained, as shown in Table 1. By judging the road surface in which real-time μ falling into, the current road surface can be identified. And the optimal slip ratio can be determined by look-up in Table 1.

Table 1 The Characteristic intervals of typcial roads

Typical road	Road number	Characteristic interval	Optimal slip ratio
icy	1	[0.05,0.031)	0.031
snow	2	[0.031,0.194)	0.06
wet cobblestone	3	[0.194,0.397)	0.14
wet asphalt	4	[0.397,0.81)	0.13
dry asphalt	5	[0.81,1.05)	0.17
dry cobblestone	6	[1.05,1.265]	0.4

Simulation and analysis

The 8 DOF vehicle simulation model is built in MATLAB/Simulink, see [4]. Figures 4 to 6 are the results of simulation tests during a straight line braking. The pre-set road surface is dry asphalt road, after a certain distance, the vehicle brakes on the snow road and finally brakes on wet asphalt. The identification results of left front-wheel are shown in Fig.4. It can be seen that the road surface identification algorithm can quickly and effectively identify the pre-set road surface and the identified road is in good agreement with the pre-set road. When roads change, identification algorithm can track the varied road surface effectively. Once the current road surface is identified, the optimal slip ratio for the ABS controller can be determined simultaneously by look-up from Table 1. Fig.5 shows the actual slip ratio. It can be seen from the figure that the actual slip well tracks the optimal slip ratio according to the identification algorithm previously mentioned in this paper, and the braking control is improved. Fig. 6 shows the road adhesive coefficient during entire braking time. It can be seen from the figure that the road adhesive coefficient is within the range of maximum adhesive coefficient so that the maximum adhesion conditions can be used fully on different roads. After the changes of roads, the controller can adjust the control objectives based on the identified optimal slip ratio. Benefited from the real-time road surface identification, the braking time can be shortened, and braking performance is improved.

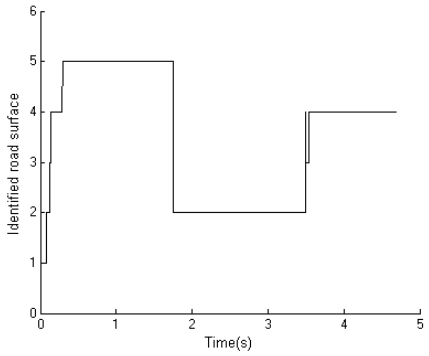


Fig.4 Road identification results

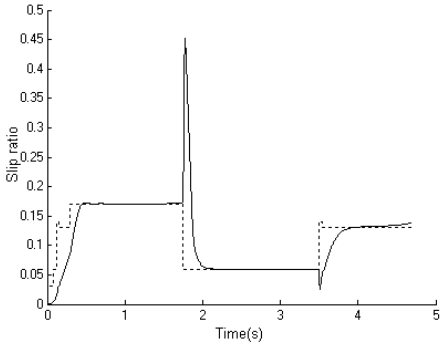


Fig.5 Slip ratio-time curve of left front wheel

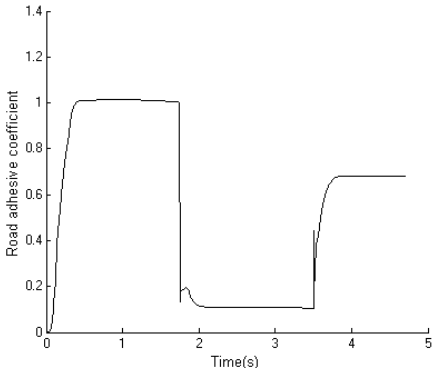


Fig.6 Road adhesive coefficient of left front wheel

Conclusions

(1) By real-time calculation of road characterization index in small time interval, the mean typical road surface can be characterized. The identification process can eliminate the influences of road roughness on road surface identification and enhance the identification robustness.
(2) The roads are divided into six types, and the road surface is identified by look-up table, which is a real-time process. Once the road surface is identified, the road characteristics (such as peak adhesion coefficient, optimum slip ratio) can be determined.
(3) The braking performance on varying roads can be greatly promoted based the real-time identification of road surface and Fuzzy-PID control of slip ratio.

References

[1] Liu Chia-shang, Peng Huei: submitted to *Vehicle System Dynamics*, 1997, p.413-425.

[2] Ricardo de Castro, Rui Esteves Araujo, Jaime S. Cardoso: submitted to *IEEE Vehicle Power and Propulsion Conference*, 2010.

[3] Steffen Muller,Michael Uchanski, Karl Hedrick: submitted to *Journal of Dynamic Systems, Measurement, and Control,* Vol.125(2003) , p.607-617.

[4] Wang Bo, Sun Renyun: submitted to *Automotive Engineering*, Vol.34 (2002), p.506-510.

[5] Juan A. Cabrera, Antonio Ortiz, Juan J. Castillo: submitted to *IEEE Transactions on vehicular technology*, Vol. 54(2005) , p.1937-1949.

[6] Zhu Weixing, Chen Yinchang: submitted to *Journal of Jiangsu University(Natural Science Edition)*, Vol. 25(2004) , p. 310-314.

[7] Burckhardt M. in: *Wrzburg,Vogel Verlag*, 1993.

Applied Mechanics and Materials Vol. 597 (2014) pp 384-387
© (2014) Trans Tech Publications, Switzerland
doi:10.4028/www.scientific.net/AMM.597.384

The Application research of Non-nuclear density gauge electromagnetic technology in the road engineering

Chai Jin-ling[1, a] , Wang Yong[1, b]

[1] Henan Vocational and Technical College of communications, China, Henan, Zhengzhou, 45000

[a] hnwy1979@126.com, [b] 673498111@qq.com,

Keywords: Road engineering; Non-nuclear density gauge; Electromagnetic; Water weight method; Calibration

Abstract. In order to ensure the control degree of compaction and meet the design requirements in the process of asphalt pavement construction, reduce the core detection for the damage in the late. It using non-nuclear density gauge to test density, and carries on the comparative analysis with the density of core test data or conversion degree of compaction data, then study the variation regularity of after the calibration for field dynamic control compaction with the roller compaction times, Conclusion non-nuclear density gauge control accuracy and error causes in the asphalt layer compaction testing. Experiment results show that non-nuclear density gauge must be proper calibration, which according to different structure layer, gradation type and different materials and core calibration method test values. At the same time suggest appropriate to increase the number of calibration for 10~15 points, which reduce error and test error for choosing, make its accuracy of control within 2%. The conversion relationship between detecting the density and the water method to testing compaction were emphatically studied, this provides a basis for non-nuclear density gauge effective application in the field compaction test grade road asphalt layer.

Introduction

In the process of asphalt pavement construction, asphalt concrete pavement compaction specification and meet the design requirements is an effective measure to ensure pavement structure layer has good road performance. So, quickly and accurately detect real-time compaction to ensure construction quality and construction progress is particularly important in construction process. The current measurement of asphalt pavement compaction method mainly include core, nuclear density meter and non-nuclear density gauge method, etc[1-3]. Core method is a traditional compaction test, and it's suitable for airport pavement detection, which is currently the most accurate and widely used method, but the shortcomings are also approved by construction workers. Relative to the more, nucleon density method is quick, without damage and can realize the real-time monitoring of the construction, the not-so-great thing is that excessive amounts of radioactive harmful to human body. At home, have more than one test found that imports of nuclear density meter radioactive prescribed [4, 5].

Non-nuclear density gauge is the human body without radiation detection equipment with the development of the nuclear density apparatus for its shortcomings, which mainly used to detect the density of compacted asphalt mixture. Optimizing the construction technology, building construction process of medium voltage degree change with rolling pass model, and its plays important roles on the construction quality control. But the test is relative density, and calibration should be carried out using the core values. Based on this point, research non-nuclear density gauge calibration procedure, which Will test the density value compared with the water method to testing density, analysis of measurement precision and bias, and using non-nuclear density gauge to compaction real-time detection with the engineering entity, which ensure the reliability of the asphalt pavement compaction[6]。

1 Non-nuclear density gauge calibration

Non-nuclear density gauge must be calibrated before using to asphalt pavement structure layer of density test[7,8]. Its principle is to relationship between the density of asphalt mixture and dielectric constant, using electromagnetic wave energy absorption or loss in the materials and to detect the density of material. For different types of asphalt mixture\ratio of asphalt mixture, the measuring values characteristics of non-nuclear density gauge are also different. Therefore, in order to get accurate determination of density value, Non-nuclear density gauge must carry on the calibration of type asphalt mixture, once the specified asphalt mixture after calibration, only on the ratio of mixture structure layer application [9].

1.1 Calibration

According to some engineering SMA-13 layer construction test section, in accordance with the equipment operating instructions, select about 5~10 points calibration instruments within the scope of the test section, Finally, the test drilling core sample density. This article selects two different production ratio (group A and group B) of the asphalt road surface layer to the calibration of instruments, the group A asphalt mixture theoretical maximum density of 2.541 g/cm^3, group B is 2.529g/cm^3, test data shown in table 1.

Table 1 Non-nuclear density gauge calibration test density

number		1	2	3	4	5	6	7	8	9	10
A	non-nuclear density gauge g/cm^3	2.467	2.548	2.470	2.427	2.487	2.452	2.478	2.474	2.439	2.489
	core sampling density g/cm^3	2.437	2.487	2.432	2.398	2.444	2.449	2.477	2.462	2.421	2.474
	difference value g/cm^3	0.03	0.061	0.038	0.029	0.043	0.003	0.001	0.012	0.018	0.015
	calibration value g/cm^3	0.25									
B	non-nuclear density gauge g/cm^3	2.415	2.509	2.512	2.446	2.528	2.415	2.509	2.512	2.446	2.528
	core sampling density g/cm^3	2.432	2.487	2.482	2.467	2.484	2.445	2.524	2.492	2.436	2.518
	difference value g/cm^3	-0.017	0.022	0.03	-0.021	0.044	-0.03	-0.015	0.02	0.01	0.01
	calibration value g/cm^3	0.053									

The table 1 shows that A, B group of deviation from the mean value 0.25 and 0.053, respectively. Therefore, the calibration value of 0.25 g/cm^3 and 0.25 g/cm^3.Among them, if test values abnormal in the calibration process, whether need to factor analysis to remove the test values. For example, group A number 2 difference value is bigger, it may be due to uneven surface or excessive pore on the affected the non-nuclear density gauge test accuracy. Thus, caused by non-nuclear density gauge measured density is smaller than measuring density; Therefore, when calculating the deviation, it would to be outliers.

1.2 Field test and indoor test results analysis

For analysis of non-nuclear density gauge accuracy used in asphalt pavement, comparing with the core density value, the method\reliability and the applicability for the asphalt road surface was studied. In this paper, to reduce the test quantity, targeted select the production ratio of group A test section, specific plan is as follows: first of all, using A set of calibration value of 0.25 g/cm^3 density compensation to non-nuclear density gauge; Randomly selected 10 points test density on the surface of the asphalt road; Then, testing the drilling core sample from the test location, the water weight method is used to test the density and conversion degree of compaction. Through analyzing two methods of test data, the accuracy and deviation of the evaluation of non-nuclear density gauge method. The maximum theoretical density and compaction degree is calculated, contrast relations as shown in figure 1/2.

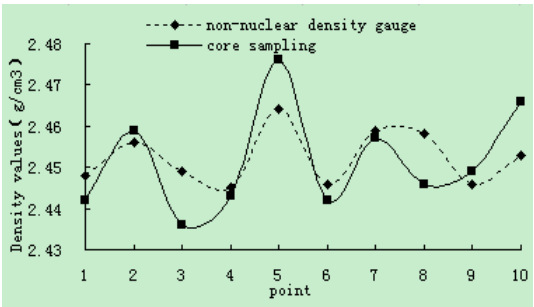


Figure 1 The relationship between non-nuclear gauge and core sampling method

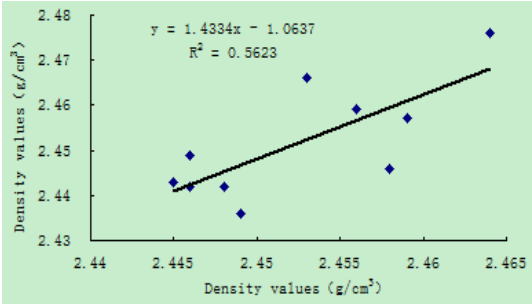


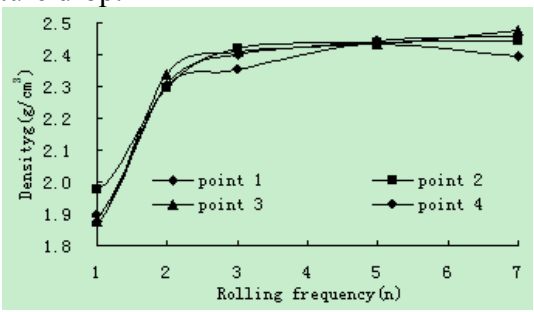
Figure 2 The correlation between non-nuclear density gauge and core sampling method

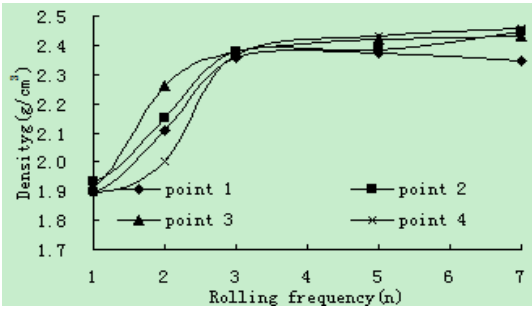
(1) After the calibration, non-nuclear density gauge testing density close to the core values, the degree of compaction of both maximum errors is 0.51% and average error is only 0.03%, Deviation in the allowed range, according to the specification recommended the compaction degree of deviation is not more than 2%.Visible, non-nuclear density gauge to test field compaction and control under suitable conditions. But some test error density value is bigger; conversion degree of compaction is slightly big. Aiming at the phenomenon, comprehensive analysis found that density value by influenced surface roughness and detecting the thickness of the test. When the surface is rough, uneven or surface layer thickness is not enough (more than structure layer thickness detection range), testing density value floating is bigger.

(2) the non-nuclear density gauge testing density and the actual core test has good correlation, figure 2 shows the correlation coefficient is 0.788, and the absolute average error is 0.275%.The results of two methods of regularity is obvious, overall, relative to the core sampling method, non-nuclear density gauge is fast, nondestructive, high precision, etc, which could be successfully applied in the compaction degree of asphalt pavement construction quality control.

2 Non-nuclear density gauge used in the field compaction test

On the asphalt road surface construction process, combined with the site construction machinery combination, non-nuclear density gauge was used to study asphalt mixture compaction condition with different rolling pass Random testing section for group A mixture ratio test section, Using non-nuclear density gauge measuring density to test degree of compaction, and to evaluate the changing rule of the degree of compaction with the increase of rolling variables or construction temperature drop.





（a）cross section 1 （b）cross section 2

Figure 3 The relationship between density and rolling frequency

By contrast, can be seen in figure 3, using non-nuclear density gauge testing density value in the construction site, Compaction degree and pavement structure layer density value increases with the increase of compaction times. In the early stages, with the increase of pavement compaction times, the change of degree of compaction is bigger for different cross section under the same compaction times. When the compaction degree of compaction degree is more and more close to design, each section of compaction degree value tends to be stable, and the difference is smaller. For SMA-13 mixture, rolling temperature and rolling effective time is very important to the degree of compaction .In

keeping the rolling temperature and on the premise of not appear on the implementation of rolling as much as possible, initial pressure process is given priority to with stability; After pressing process is given priority to with formation compaction; It is advisable to 5~7 times of rolling, its avoid formation overpressure, and reduce the impact on its road performance, and ensure the compactness\ smoothness; For the eliminate purpose of the wheel track on the final pressure, ensure the pavement roughness.

Summary

（1）the non-nuclear density gauge and core density value with the same change rule, the correlation is better, but the pavement roughness, structure layer thickness may effect the precision of non-nuclear density gauge, the instrument calibration sample size increase in order to improve the test precision, and different materials of asphalt mixture should be calibrated separately.

（2）After the non-nuclear density gauge calibration, conversion of compaction degree has higher accuracy, measurement error can be controlled within 2%, it can be better used for asphalt pavement construction in real-time, fast and nondestructive testing, which has the important meaning, has a good application prospect to ensure the quality of construction and guide the construction process and ensure the construction progress.

（3）Using non-nuclear density gauge to test engineering compaction in the process of asphalt pavement surface construction. It is reasonable to determine the mechanical combination and rolling variables, that to ensure the pavement compaction.

References

[1] JTG E60-2008, Field Test Methods of Subgrade and Pavement for Highway Engineering[S]. Beijing :China Communications press,2008.

[2] DAI Wen-bin. Asphalt mix design and compaction standards[J]. HIGHWAY, 2001, 46(10):52-56.

[3] CHEN Shao-xing, ZHANG Xiao-ning. Research on the Use of PQI in Evaluation of Segregation of Hot-mix Asphalt Pavement[J]. Journal of highway and transportation research and development, 2006,23(5):11-15.

[4] Smith BC, Diefenderfer BK. Comparison of Nuclear and Non-nuclear Pavement Density Testing Devices[R].Transportation Research Board of the National Academies, Washington, DC, 2008, pp. 121-129.

[5] Vacca PC, Whitten JE, Pelchat JM. Consolidated Guidance about Materials Licenses: Program-Specific Guidance about Portable Gauge Licenses [J]. NUREG-1556, Vol.1. U.S.Nuclear Regulatory Commission, Washington, DC, 1997.

[6] Virginia Department of Transportation. Road and Bridge Specifications. Richmond, 2008. Virginia Department of Transportation, Materials Division. Virginia Testethods. Richmond. Accessed February25,2011.

[7] Chang CM, Ballade GY. Woff TF1 Using Pavement Distress Data to Assess Impact of Const ruction on Pavement Performance [J]. Transportation Research Record 1761, Washington, DC,15-25.

[8] Romero, Pedro. Quantifying Segregation in Hot-Mix Asphalt Pavements, Proposal[R]. University of Utah, Department of Civil and Environmental Engineering, 2004.

[9] ZHOU Zhi-gang, Liu zhen-xing. Non-nuclear density gauge hot at the scene the application of the recycled asphalt pavement compaction quality control [J].Journal of China & Foreign Highway ,2009,29(5):78-83.

Applied Mechanics and Materials Vol. 597 (2014) pp 388-392
© (2014) Trans Tech Publications, Switzerland
doi:10.4028/www.scientific.net/AMM.597.388

Lie algebraic structure and Poisson conservation law for one class of multi-dimensional coupled oscillators

Yi Sun [1,a*], Ben Yong Chen [1,b] and Jing Li Fu[2,c*]

[1] Faculty of Mechanical-Engineering and Automation, Zhejiang Sci-Tech University, Hangzhou 310018, China

[2] Institute of Mathematical Physics, Zhejiang Sci-Tech University, Hangzhou 310018, China

[a]15757157607@163.com, [b]chenby@zstu.edu.cn, [c]sqfujingli@163.com

Keywords: Lie algebraic structure, Poisson conservation law, normal coordinate

Abstract. This paper researches Lie algebraic structure and Poisson conservation law for one class of multi-dimensional coupled oscillators. The equations of motion are established, and the coupled terms in the equations of motion are eliminated by introducing normal transformations. The Lie algebraic structure and Poisson conservation law are given. Finally, an example is given to illustrate the results.

Introduction

In recent years, the research on the algebraic structure and conservation law of dynamical systems has achieved a series of important results [1-4]. The results demonstrate that the Lagrange equations and Hamilton equations all have compatible algebraic structure and Lie algebraic structure, and the corresponding Poisson conservation law is also obtained. Therefore, searching for the conservation law of dynamical system [5-8] has always been playing a significant role.

For the multi-dimensional system [9-11], we find the conservation law is very difficult because of the complexity of the system. However, for one classical of multi-dimensional coupled oscillators systems, its Lagrangian and equations of motion are linearly coupled, it can be reduced to one-dimensional system by using the normal transformations. For the one-dimensional system, the Lie algebraic structure is easy to study, and the Poisson conservation law can be obtained.

Equations of motion and normal transformations

The multi-dimensional coupled oscillators system considered in this paper is shown in Fig. 1.

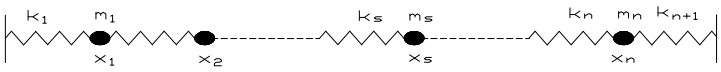


Fig. 1 The multi-dimensional coupled oscillators

The Lagrangian and the Hamiltonian of the system can be expressed as

$$L=\sum_{s=1}^{n} m_s \dot{x}_s^2/2-\left[k_1 x_1^2/2+\sum_{s=2}^{n} k_s\left(x_s-x_{s-1}\right)^2/2+k_{n+1}x_n^2/2\right],$$
$$H=\sum_{s=1}^{n} p_s^2/2m_s+\left[k_1 x_1^2/2+\sum_{s=2}^{n} k_s\left(x_s-x_{s-1}\right)^2/2+k_{n+1}x_n^2/2\right]. \tag{1}$$

Substituting the Lagrangian into Lagrange equation, we obtain the equation of motion

$$\ddot{x}_1=-\left(k_1+k_2\right)x_1/m_1+k_2x_2/m_1,\ddot{x}_2=k_2x_1/m_2-\left(k_2+k_3\right)x_2/m_2+k_3/m_2,\cdots$$
$$\ddot{x}_s=k_sx_{s-1}/m_s-\left(k_s+k_{s+1}\right)x_s/m_s+k_{s+1}/m_s,\cdots,\ddot{x}_n=-\left(k_n+k_{n+1}\right)x_n/m_n+k_nx_{n-1}/m_n. \tag{2}$$

If q is a normal coordinate of the system, according to reference [12], it should satisfy

$$\ddot{q}=\left[\left[q,H\right],H\right]=-\lambda q. \tag{3}$$

We have the following Poisson brackets

$$\left[x_1,H\right]=p_1/m_1,\left[x_2,H\right]=p_2/m_2,\cdots,\left[x_n,H\right]=p_n/m_n,$$
$$\left[p_1,H\right]=-k_1x_1+k_2\left(x_2-x_1\right),\left[p_2,H\right]=-k_2\left(x_2-x_1\right)+k_3\left(x_3-x_2\right),\cdots, \tag{4}$$
$$\left[p_{n-1},H\right]=-k_{n-1}\left(x_{n-1}-x_{n-2}\right)+k_n\left(x_n-x_{n-1}\right),\left[p_n,H\right]=-k_n\left(x_n-x_{n-1}\right)-k_{n+1}x_n,$$

where p_s are momentum. If $q_s=c_1x_1+c_2x_2+\ldots c_nx_n$ are normal coordinates of the system, we have

$$\ddot{q}_s=\left[\left[q_s,H\right],H\right]=-c_1\left(k_1x_1-k_2x_2+k_2x_1\right)/m_1-c_2\left(k_2x_2-k_2x_1-k_3x_3+k_3x_2\right)/m_2$$
$$-\cdots-c_{n-1}\left(k_{n-1}x_{n-1}-k_{n-1}x_{n-2}-k_nx_n+k_nx_{n-1}\right)/m_{n-1}-c_n\left(k_nx_n-k_nx_{n-1}+k_{n+1}x_n\right)/m_n. \tag{5}$$

Making use of Eqs. (3), (4) and (5), we have

$$\begin{vmatrix} \left(k_1+k_2\right)/m_1-\lambda & -k_2/m_2 & & & \\ -k_2/m_1 & \left(k_2+k_3\right)/m_2-\lambda & -k_3/m_3 & & \\ & \ddots & \ddots & \ddots & \\ & & -k_{n-1}/m_{n-2} & \left(k_{n-1}+k_n\right)/m_{n-1}-\lambda & -k_n/m_n \\ & & & -k_n/m_{n-1} & \left(k_n+k_{n+1}\right)/m_n-\lambda \end{vmatrix}=0. \tag{6}$$

We can obtain λ_s from Eq. (6), then c_s and q_s can be obtained.

Lie algebraic structure and the Poisson conservation law

Under the normal modes, the equations of motion are

$$\ddot{q}_s+\omega_s^2q_s=0,\left(\omega_s=\lambda_s,s=1,2,\ldots,n\right). \tag{7}$$

We discuss the algebraic structures of normal modes, introducing $2n$ contravariant vectors

$$a^{\mu}=\begin{cases} q_{\mu} & \left(\mu=1,\cdots,n\right), \\ p_{\mu-n}^{*} & \left(\mu=n+1,\cdots,2n\right). \end{cases} \tag{8}$$

Therefore, the Hamilton equations have inverter algebraic form

$$\dot{a}^{\mu} - \omega^{\mu\nu}\partial H / \partial a^{\nu} = 0, (\mu, \nu = 1, 2, \ldots, 2n), \tag{9}$$

where $\omega^{\mu\nu}$ is contravariant tensor. The function $A(a^{\mu})$ is defined as an algebraic product

$$\dot{A} = \partial A / \partial a^{\mu} \cdot \omega^{\mu\nu} \cdot \partial H / \partial a^{\nu} \overset{def}{=} A \circ H . \tag{10}$$

Eq. (10) satisfies distributive laws, scaling law, skew-symmetry and Jacobi's identity

$$\begin{aligned} &A \circ (B + C) = A \circ B + A \circ C, (A + B) \circ C = A \circ C + B \circ C, (\alpha A) \circ B = A \circ (\alpha B) = \alpha (A \circ B), \\ &A \circ B + B \circ A = 0, A \circ (B \circ C) + B \circ (C \circ A) + C \circ (A \circ B) = 0. \end{aligned} \tag{11}$$

Therefore, the Hamilton equations have the Lie algebraic structure, the Poisson integral theory can be applied to the system. The Hamiltonian H is a first integral of the system, that is

$$H = \dot{q}_s^2 / 2 + \omega_s^2 q_s^2 / 2 = p^{*2}_s / 2 + \omega_s^2 q_s^2 / 2 = \text{const} . \tag{12}$$

Making use of the sufficient and necessary condition of first integral, we have

$$\begin{aligned} &I_{s1} = \omega_s q_s \cos(\omega_s t) - \dot{q}_s \sin(\omega_s t) = \omega_s q_s \cos(\omega_s t) - p_s^* \sin(\omega_s t) = \text{const}, \\ &I_{s2} = \omega_s q_s \sin(\omega_s t) + \dot{q}_s \cos(\omega_s t) = \omega_s q_s \sin(\omega_s t) + p_s^* \cos(\omega_s t) = \text{const}, \\ &I_{s3} = \arctan(\dot{q}_s / \omega_s q_s) + \omega_s t = \arctan(p_s^* / \omega_s q_s) + \omega_s t = \text{const}. \end{aligned} \tag{13}$$

Using Eq. (13), we can obtain

$$q_s = I_{s1} / \omega_s \cdot \cos(\omega_s t) + I_{s2} / \omega_s \cdot \sin(\omega_s t) . \tag{14}$$

If the initial conditions are given, we have

$$I_{s1} = \omega_s q_{s0}, I_{s2} = \dot{q}_{s0}, I_{s3} = \arctan(\dot{q}_{s0} / \omega_s q_{s0}) = \theta_s . \tag{15}$$

From Eq. (15), we see that I_{s1} and I_{s2} are related to the initial position and initial velocity, respectively, and I_{s3} is related to the initial phase of the system.

An example

As an example, a three-dimensional coupled oscillators system is considered.

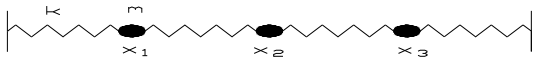


Fig. 2 The three-dimensional coupled oscillators

The equations of motion are

$$\ddot{x}_1 = -2kx_1/m + kx_2/m,\ \ddot{x}_2 = kx_1/m - 2kx_2/m + kx_3/m,\ \ddot{x}_3 = kx_2/m - 2kx_3/m. \tag{16}$$

According to the above study, the following parameters are obtained

$$\begin{aligned} &\omega_1 = \sqrt{2k/m}, \omega_2 = \sqrt{\left(2-\sqrt{2}\right)k/m}, \omega_3 = \sqrt{\left(2+\sqrt{2}\right)k/m}, \\ &c_{11} = c_{22} = -c_{13} = -c_{32} = 1/\sqrt{2}, c_{12} = 0, c_{21} = c_{23} = c_{31} = c_{33} = 1/2. \end{aligned} \tag{17}$$

Therefore, we can obtain the normal coordinates and the normal modes

$$\begin{aligned} &q_1 = x_1/\sqrt{2} - x_3/\sqrt{2}, q_2 = x_1/2 + x_2/\sqrt{2} + x_3/2, q_3 = x_1/2 - x_2/\sqrt{2} + x_3/2, \\ &\ddot{q}_1 = -2kq_1/m, \ddot{q}_2 = -\left(2-\sqrt{2}\right)kq_2/m, \ddot{q}_3 = -\left(2+\sqrt{2}\right)kq_3/m. \end{aligned} \tag{18}$$

For the normal modes, we obtain the first integrals

$$\begin{aligned} &H_1 = p_1^{*2}/2 + kq_1^2/m = \text{const}, I_{11} = \omega_1 q_1 \cos(\omega_1 t) - p_1^* \sin(\omega_1 t) = \text{const}, \\ &I_{12} = \omega_1 q_1 \sin(\omega_1 t) + p_1^* \cos(\omega_1 t) = \text{const}, I_{13} = \arctan\left(p_1^*/\omega_1 q_1\right) + \omega_1 t = \text{const}, \end{aligned} \tag{19}$$

Using the inverse transformation of coordinates, we have

$$\begin{aligned} &H_1 = \left(p_1 - p_3\right)^2/4m^2 + k\left(x_1 - x_3\right)^2/2m = \text{const}, \\ &I_{11} = \sqrt{2}/2 \cdot \omega_1 \left(x_1 - x_3\right)\cos(\omega_1 t) - \sqrt{2}/2m \cdot \left(p_1 - p_3\right)\sin(\omega_1 t) = \text{const}, \\ &I_{12} = \sqrt{2}/2 \cdot \omega_1 \left(x_1 - x_3\right)\sin(\omega_1 t) + \sqrt{2}/2m \cdot \left(p_1 - p_3\right)\cos(\omega_1 t) = \text{const}, \\ &I_{13} = \arctan\left(\left(p_1 - p_3\right)/\omega_1 m\left(x_1 - x_3\right)\right) + \omega_1 t = \text{const}. \end{aligned} \tag{20}$$

Similarly, we can also get the following first integrals

$$\begin{aligned} &H_2 = \left(p_1 + \sqrt{2}p_2 + p_3\right)^2/8m^2 + \left(1-\sqrt{2}/2\right)k\left(x_1 + \sqrt{2}x_2 + x_3\right)^2/4m = \text{const}, \\ &I_{21} = \omega_2/2 \cdot \left(x_1 + \sqrt{2}x_2 + x_3\right)\cos(\omega_2 t) - 1/2m \cdot \left(p_1 + \sqrt{2}p_2 + p_3\right)\sin(\omega_2 t) = \text{const}, \\ &I_{22} = \omega_2/2 \cdot \left(x_1 + \sqrt{2}x_2 + x_3\right)\sin(\omega_2 t) + 1/2m \cdot \left(p_1 + \sqrt{2}p_2 + p_3\right)\cos(\omega_2 t) = \text{const}, \end{aligned}$$

$$
\begin{aligned}
&I_{23} = \arctan\left(\left(p_1 + \sqrt{2}p_2 + p_3\right) / \omega_2 m\left(x_1 + \sqrt{2}x_2 + x_3\right)\right) + \omega_2 t = \text{const},\\
&H_3 = \left(p_1 - \sqrt{2}p_2 + p_3\right)^2 / 8m^2 + \left(1 + \sqrt{2}/2\right)k\left(x_1 - \sqrt{2}x_2 + x_3\right)^2 / 4m = \text{const},\\
&I_{31} = \omega_3 / 2 \cdot \left(x_1 - \sqrt{2}x_2 + x_3\right)\cos(\omega_3 t) - 1/2m \cdot \left(p_1 - \sqrt{2}p_2 + p_3\right)\sin(\omega_3 t) = \text{const},\\
&I_{32} = \omega_3 2 \cdot \left(x_1 - \sqrt{2}x_2 + x_3\right)\sin(\omega_3 t) + 1/2m \cdot \left(p_1 - \sqrt{2}p_2 + p_3\right)\cos(\omega_3 t) = \text{const},\\
&I_{33} = \arctan\left(\left(p_1 - \sqrt{2}p_2 + p_3\right) / \omega_3 m\left(x_1 - \sqrt{2}x_2 + x_3\right)\right) + \omega_2 t = \text{const}.
\end{aligned}
\tag{21}
$$

Acknowledgements

This work is supported by National Natural Science Foundation of China under Grant No. 11272287. The authors would like to thank ICAMDM2014 for acceptance of this paper, and editors for carefully reading the manuscript.

References

[1] A. Ballesteros, O. Ragnisco, A systematic construction of completely integrable Hamiltonians from coalgebras, J. Phys. A: Math. Gen. 31 (1998) 3791-3813.

[2] P. Chartier, E. Faou, A. Murua, An algebraic approach to invariant preserving integators: the case of quadratic and Hamiltonian invariants, Nume. Math. 103 (2006) 575-590.

[3] J.L. Fu, F.P Xie, Y.X. Guo, Algebraic Structure and Poisson's Integral Theory of *f*(*R*) Cosmology, Int. J. Theor. Phys. 51 (2012) 35-48.

[4] R. Hiranwal, S.C. Mishra, V. Mishra, Classical and quantum integrability for a class of potentials in two dimensions, Ann. Phys. 309 (2004) 390-420.

[5] F. Chand, S.C. Mishra, Construction of exact complex dynamical invariant of a two-dimensional classical system. Pramana-J. Phys. 67 (2006) 999-1009.

[6] R.S. Kaushal, S. Singh, Construction of complex invariants for classical dynamical systems, Ann. Physi. 288 (2001) 253-276.

[7] R.M. Angelo, E.I. Duzzioni, A.D. Ribeiro, Integrability in time-dependent systems with one degree of freedom. J. Phys. A: Math. Theor. 45 (2012) 055101.

[8] J.L. Fu J L, X.W. Li, C.R. Li, Symmetries and exact solutions of discrete nonconservative systems, Sci.Chin. Phys. Mech. Astron. 53 (2010) 1699-1706.

[9] A.A. Nassr, A.G. Razaqpur, M.J. Tait, Single and multi degree of freedom analysis of steel beams under blast loading, Nucl. Eng. Des. 242(2012) 63-77.

[10] S. Bellizzi, P. Guillemain, R. Kronland-Martinet, Identification of coupled non-linear modes from free vibration using time-frequency representations, J. Sound.Vib. 243 (2001) 191-213.

[11] M. Peeters, R. Viguié, G. Sérandour, Nonlinear normal modes, Part II: Toward a practical computation using numerical continuation techniques. Mech. Syst. Signal. Pr. 23 (2009) 195-216.

[12] H.Y. Fan, C. Li, Invariant 'eigen-operator'of the square of Schrödinger operator for deriving energy-level gap. Phys. Lett. A. 321 (2004) 75-78.

Applied Mechanics and Materials Vol. 597 (2014) pp 393-396
© (2014) Trans Tech Publications, Switzerland
doi:10.4028/www.scientific.net/AMM.597.393

Three-Level SVPWM Inverter with Li-ion Battery Driven for Robot Motor

Sheng Chen[1], Chih-Chen Chen[2]

[1]Department of Electrical Engineering Hwa-Hsia Institute of Technology, New Taipei City, Taiwan

[2]Department of Management Information Systems Hwa-Hsia Institute of Technology, New Taipei City, Taiwan

[1]senchen@cc.hwh.edu.tw

Keywords: SVPWM, Inverter, Battery

Abstract. Space vector Pulse Width Modulation (PWM) method is an advanced; computation intensive PWM method and possibly the best techniques for variable frequency drive application. Because of the constraint that the input lines must never be shorted and the output current must always be continuous, a voltage source inverter can assume only eight distinct topologies. Six out of these eight topologies produce a non-zero output voltage and are known as non-zero switching states and the remaining two topologies produce a zero output voltage and are known as zero switching states. the fluctuation in speed and torque are less when the Space Vector Modulation strategy is implemented in the vector controlled motor. Thus it can be concluded that the overall performance of a motor drive system is improved when Space Vector Modulation technique is used in robot power with the battery operated for industry application.

Introduction

With the advent of the robot age and its ever increasing requirements for its motor driving efficiency and power management with batteries, the problems associated with those essentials have received much attention. As a result, many sophisticated control technologies of the motor driver and batteries applications have been investigated in recent years in attempts to obtain more efficient use of these parts for robot applications.

The performance of a robot mostly depends on the proper selection of the motors inverter and its energy source. Several modulation techniques and control strategies for the motor inverters have been proposed and developed. The most popular modulation technique adopted in industry robot applications is the multi-carrier sinusoidal pulse-width modulation (SPWM), which is based on the classical SPWM with triangular carriers. Another alternative modulation technique applied in the inverter circuits is space-vector modulation (SVM) [1]. The waveforms of the motor inverter output can be regulated by controlling the modulation index and phase angle with a proportional plus integral (PI) controller. However, this control method has some stability problems for the case of large-signal injection into consideration, and the inverter performance will refract from the expected waveform when the inverter is addressed to a disturbance.

Three level inverters can synthesize double the voltage levels using the switching components of the same rating, then the power handling capacity can be doubled. For a provided switching frequency, three level voltage have double the bandwidth compared to two level inverters. For these features, three level inverters are many applications in medium voltage high-power drives such as for industry robot [2].

The principles of achieving synchronization and symmetries in terms of space vectors for three level inverters (SVPWM) are presented to improve the output waveform of the three level inverters when the switching frequency is low, which is achieved by maintaining the synchronization, half-wave symmetry, quarter-wave symmetry, and three-phase symmetry in the PWM waveforms. The dynamic performances of this inverters with nonlinear motor loads can achieve a good response with large-signal disturbance.

System Description

The brushless motor (BLDC) is applied for industry robot in mechanical unit as the Fig.1 shown, the space vector pulse width modulation (SVPWM) motor inverter can generate the gate signals to drive motor via IGBT/MOS switching parts; the power management unit control the battery system,which is contained the components of the LiFePO4 battery bank, super-capacitor bank and DC/DC converter for the energy supply.

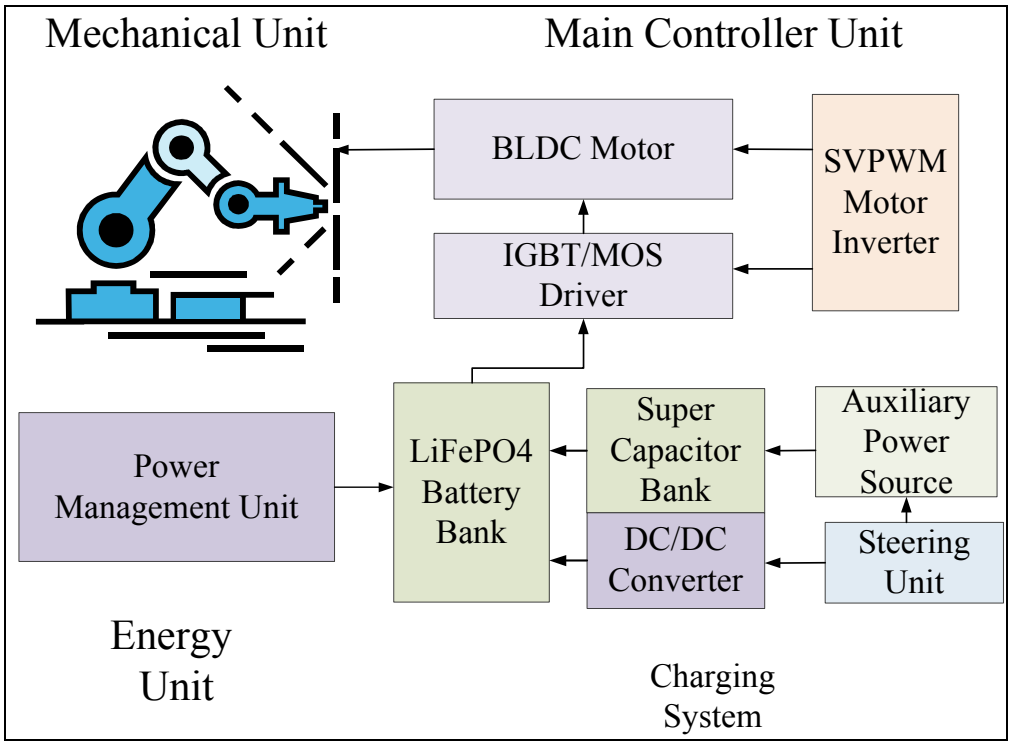


Fig.1 The block diagram of battery power and inverter applied for industry robot

Working Principle of Space Vector Pulse Width Modulation Inverter

The basic idea of the space vector pulse width modulation inverter is illustrated on the circuit diagram of a three level diode clamp inverter by the Fig. 2. and the corresponding state are defined in Table I.

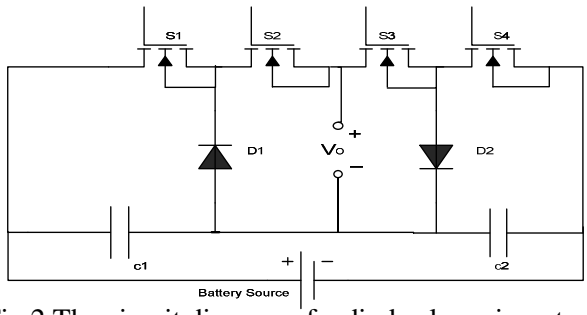
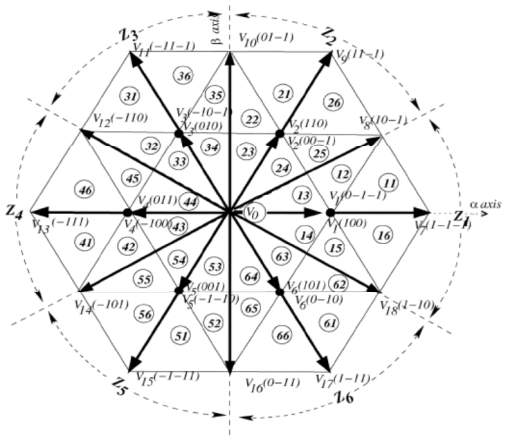


Fig.2 The circuit diagram of a diode clamp inverter

Table I

S1	S2	S3	S4	Vo	State
1	1	0	0	½*VB	1
0	1	1	0	0	0
0	0	1	1	-½*VB	-1

The space vectors associated with the three level inverters are formed the vector plane which is divided in six sectors, each sector has 60° as shown in Fig. 3. Each sector Z1 to Z6 , is associated with one pivot vector Vz and six other vectors. Only one switch is switched during state transition [3][4]. The switching time and state can be described as Eq.(1)~Eq(3) .



$$v_s(t) = v_d(q_a e^{j0} + q_b e^{j2\pi/3} + q_c e^{j4\pi/3}) \tag{1}$$

$$v_{1s}(t) = (xT_s v_1 + yT_s v_3 + zT_s v_z)/T_s \tag{2}$$

$$\begin{cases} v_{1s}(t) = xv_1 + yv_3 \\ x + y + z = 1 \\ v_{1s}e^{j\theta_s} = xv_d e^{j0} + yv_d e^{j\pi/3} \end{cases} \tag{3}$$

Fig.3 The state of SVPWM inverter

$v_s(t)$ is the voltage vector on 3 phase synchronized frame, v_d is the bus voltage, $q_{a,b,c} = +1, 0, -1$ presents the switching state , T_s is switching period, and x, y, z is the parts of switching period of the state v_1, v_3 and zero state v_z, which is bounded by v_1 and v_3 for the first region as Fig. 3 shown; The switching time and state can be solved by the Eq.(3) and similar solution for all the other five regions.

This type inverter has several favorable features, such as of blocking the dc link voltage to half, thus reduce the half voltage stress on switching devices, lower the common mode voltage steps, low output voltage harmonic and current ripple for the same switching frequency, in addition to the capability of handling higher voltages, which is easy from photo type implement to practical application.

The practical example as shown in Fig.4, it can be applied for industry robot motor driven by the Li-ion battery with S_a S_b added for extenting function to boost the battery voltage and to charge energy from motor side.

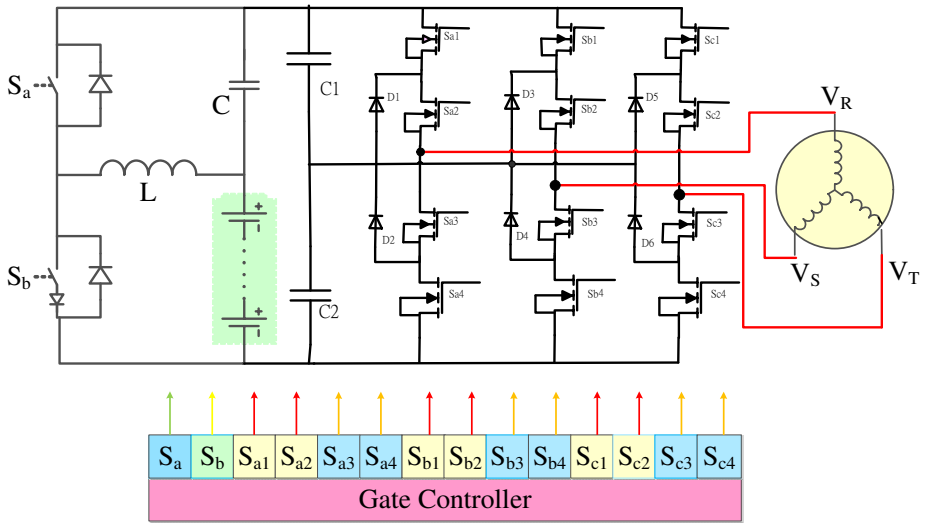


Fig.4 The circuit diagram of SVPWM Inverter with Li-ion Battery Driven

The Practical Three-Level IGBT Module

The module shown in Figure 5 is an IGBT module which means that for a potential use of this module in motor drive for industry application, the package contains a 1200V- class IGBT and free wheeling

diode (FwDi) for braking purposes. The circuitry of the module for IGBT switches indices 1 and 4 are equipped with an real time current controller (RTC) which is utilizing a fraction of the collector current flowing through the shunt resistor and creates a voltage drop accordingly, to detect an over current situation and to force the IGBT into a current controlled desaturation [5]. The following comparator pulls down the Gate Emitter voltage (Vge) when the reference voltage level (Vref) is exceeded by shunt voltage drop. As a result the comparatively low current level reduces the stress on the IGBT during a short circuit situation. This is the compact design of 3-level SVPWM inverter IGBT module, especially for the industry robot motor in application.

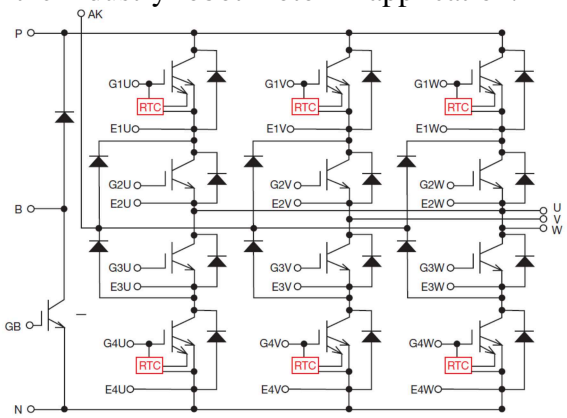


Fig. 5 IGBT module topology including circuit (Mitsubishi Electric)

Conclusion

This paper introduces SVPWM Inverter, which is applied for industry robot to the flexible speed control,This type inverter has several favorable features, such as to reduce the half voltage stress on switching devices, lower common mode voltage steps, low output voltage harmonic and current ripple for the same switching frequency, in addition to the capability of handling higher voltages, which is easy from photo type implement to practical application. A suitable pulse width modulation technique is employed to obtain the required output voltage at the line side of the inverter,SVPWM utilizes dc bus voltage more effectively, generates less THD and improved input capacitor balance. the IGBT module topology including circuit and protection is introduced for this application.

References

[1] Abdul Rahiman Beig, G. Narayanan, and V. T. Ranganathan, “Modified SVPWM Algorithm for Three Level VSI With Synchronized and Symmetrical Waveforms,” IEEE Transactions on Industrial Electronics, Vol. 54, No. 1, February 2007, pp. 486–494, Aug. 2007.

[2] Lydia Anu Jose1, K. B.Karthikeyan, “A Comparative Study of Sinusoidal PWM and Space Vector PWM of a Vector Controlled BLDC Motor,” International Journal of Advanced Research in Electrical, Electronics and Instrumentation Engineering Vol. 2, Issue 6, pp. 2662–2668,June 2013.

[3] Paul K.W. Chan, Henry S.H. Chung, and S.Y.R. Hui, “Generalized Theory of Boundary Control for Single-phase Multilevel Inverter using Second-order Switching Surface,” in Record, IEEE PESC, pp. 1733 -1739, 2007.

[4] B. Urmila and D. Subba Rayudu, “Optimum space vector pwm algorithm for Three-level inverter,” ARPN Journal of Engineering and Applied Sciences , Vol. 6, No. 9, pp.24-36, September 2011.

[5] Yamada, M.Nakamura et al.: the latest high performance and high reliability IGBT technology in new packages with conventional pin layout, PCIM 2003, pp. 329 -334.

Applied Mechanics and Materials Vol. 597 (2014) pp 397-400
© (2014) Trans Tech Publications, Switzerland
doi:10.4028/www.scientific.net/AMM.597.397

Development of Practical Wrist Rehabilitation Robot by Mirror Effect

Ikuo Yamamoto[1, a *], Miki Matsui [1], Naohiro Inagawa [2] and Takunori Tsuji [3]
Kenji Hachisuka[4], Futoshi Wada[4] and Akiko Hachisuka[4]

[1]Dept. of Mechanical Science, Nagasaki Univ., Graduate School, 1-14 Bunkyomachi, Nagasaki-shi, Nagasaki 852-8521, Japan

[2]Dept. of Media Technology, Nippon Bunri Univ., 1727 Ichigi, Oita-shi, Oita 870-0397, Japan

[3]Logical Product Corporation, 2-25-5 Matoba, Minami-ku, Fukuoka-shi, Fukuoka 811-1314, Japan

[4]Dept. of Rehabilitation Medicine, Univ. of Occupational and Environmental Health, 1-1 Iseigaoka, Yahatanishi-ku, Kitakyushu-shi, Fukuoka 807-8555, Japan

[a]iyamamoto@nagasaki-u.ac.jp

Keywords: Rehabilitation robot, Mirror effect, Wrist training

Abstract. The authors have developed wrist rehabilitation robot for hemiplegic patients. The robot is much effective for repetitive rehabilitation, and useful for patients. Mirror effect control system is developed based on the experience that a patient can easily move a limb while moving a limb on the other side. The effectiveness is successfully confirmed by the practical test in the hospital.

Introduction

The effective wrist rehabilitation robot shown in Fig.1 has been developed at practical level for hemiplegic patients, who need repetitive rehabilitation training to improve the function of upper and lower extremities and to increase the range of motion. The effectiveness of repetitive rehabilitation training is shown in medical researches [1-8]. The mild physically disabled patients can undergo self-training with such rehabilitation tools as blocks. In contrast to it, the massive physically disabled patients generally undergo forced training with training support devices. However, forced training fails to be higher effective because patients cannot exercise on their own active mind. Therefore, the effect of the treatment is unable to surpass the critical limit. Although occupational therapists can give the patients undivided attention, the number of occupational therapists is limited and there is a compelling need to reduce their work load. Many research results for rehabilitative training robot have been reported [9-14], however, it is often the case that the robot system is large and the process is complicated. Therefore, it is difficult for patients to feel unrestrained to use the robot system. Then, the research is aimed at developing a rehabilitative robot that enables the effective training of patient. The training robot conducts several modes of training. Specially, the paretic hand can undergo the rehabilitative training by the other non-paretic hand based on mirror effect control system.

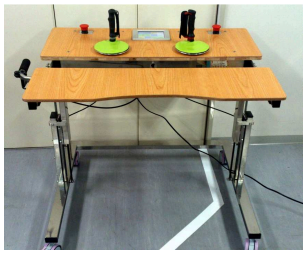


Fig.1 The effective wrist rehabilitation robot

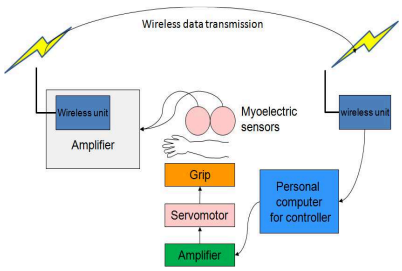


Fig.2 The rehabilitative training robot using myoelectric sensors

System configuration

The developed rehabilitative robot consists of passive, constant torque and autonomous training modes. In addition to that, the authors have developed the training robot that has a function to detect the myoelectric potential by myoelectric sensors on patient's muscle, and analyze the patient's intention to flex their wrist shown in Fig.2, Fig3 and Fig4. The training robot can provoke training through the function, so that patients can undergo effective training shown in Fig.5 [15-17]. The rehabilitative training robot consists of grip, actuator, biological signal detector, biological signal processor, training controller and both-wrist system. Grip is held by patient during training. The training movement is generated by servomotor as the actuator.

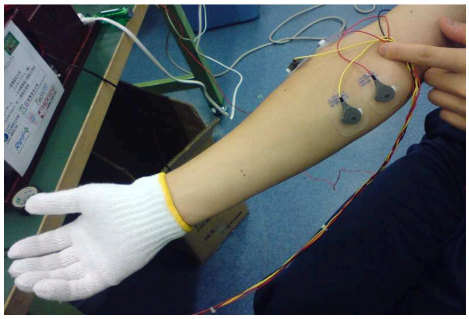


Fig.3 The myoelectric sensors

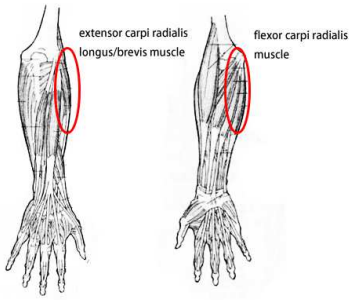


Fig.4 The extensor carpi radialis longus/brevis muscle and flexor carpi radialis muscle



Fig.5 The developed rehabilitation robot in an excited condition



Fig.6 The CAD design of the new rehabilitative training robot for hospital use

System development

The system is firstly designed by CAD shown in Fig.6. Through adjustments of manufacturing for safety use, the wrist rehabilitation robot has been developed shown in Fig.1. The picture of grip and computer display is shown in Fig.7. The robot is *small desk* size and is easy to carry. Therefore, the training can be performed in a small space in the hospital and at home. The passive mode is the mode of palmar and dorsal flexion motions started by the start button shown in Fig.7. The constant torque mode is the mode that patients operate the grip under the constant torque. The autonomous training mode has two main functions. One function is that the patients operate an arbitrary grip A of one hand in Fig.8. The palmar and dorsal flexion motions of the other hand's grip B and grip A itself are started autonomously. The other function is that the patients operate an arbitrary grip to palmar flexion direction A the palmar flexion motion B is started in Fig.9, and that the dorsal flexion motion is started when they operate it to dorsal flexion direction.



Fig.7 The grip and computer display



Fig.8 The autonomous training mode 1

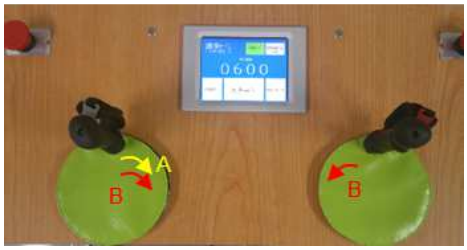


Fig.9 The autonomous training mode 2

System test

The rehabilitation robot system has been tested in the hospital. The user-friendly screen for patients with easily recognizable touch panels, therefore, it can avoid operational error when used by patients on their own. The training data can be stock for each patient, and re-start training is possible when patient stopped training. Also, the height of desk can be adjusted smoothly manually according to the height of patients. The limit switch of maximum flexion angle of patients and emergent switch to stop the servomotors are equipped with the system for safety. The most effective function is *mirror effect training*. It is found that mirror effect motion is effective in rehabilitation of patients. The control system is equipped under each circular grip of hands and mirror effect control motion adjustable to patient's state is conducted, therefore, the paretic hand can learn how to move by the real time teaching data of non-paretic hand. The same time interval of flexion training of both wrists at the different speed of rotation can be realized by the control system.

Conclusion

The practical wrist rehabilitation robot has been developed and is used in the hospital. The robots are introduced and applied to several hospitals, and the authors get clinical data to complete the research. Also, the authors improve more functions according to the requirement from medical doctor, therapists and patients.

Acknowledgement

A part of study was supported by Grant-in-Aid for Scientific Research (B) and FAIS research. The authors would like to express their sincere gratitude to Arizono Co., Etou Co., and related personnel in the hospital and university for the research and development.

References

[1] S. Saeki, Y. Matsushima, K. Hachisuka, “Cortical activation during robotic therapy for a severely affected arm in a chronic stroke patient: a case report,” J. UOEH, vol. 30, no. 2, pp. 159–165, 2008.

[2] G.B. Prange, M.J.A. Jannink, C.G.M. Groothuis-Oudshoon, H.J. Hermens, M.J. IJzerman, “Systematic review of the effect of robot-aided therapy on recovery of the hemiparetic arm after stroke,” J. Rehabil Res Dev, vol. 43, pp. 171–184, 2006.

[3] H.I. Krebs, N. Hogan, B.T. Volpe, M.L. Aisen, L. Edelstein, C. Diels, “Overview of clinical trials with MIT-MANUS: A robot-aided neuro-rehabilitation facility,” Technol. Health Care, vol. 7, pp. 419–423, 1999.

[4] C.G. Burgur, P.S. Lum, P.C. Shor, H.F. Machiel Van der Loos, “Development of robots for rehabilitation therapy: The Palo Alto VA/Standard experience,” J. Rehabil. Res. Dev., vol. 37, pp. 376–388, 2000.

[5] S. Masiero, A. Celia, G. Rosati, M. Armani, “Robotic-assisted rehabilitation of the upper limb after acute stroke,” Arch. Phys. Med. Rehabil., vol. 88, pp. 142–149, 2007.

[6] S. Hesse, G. Schulte-Tiggers, M. Konrad, M.A. Bardeleben, C. Werner, “Robot-assisted arm trainer for the passive and active practice of bilateral forearm and wrist movements in hemiparetic subjects,” Arch. Phys. Med. Rehabil., vol. 84, pp. 915-920, 2003.

[7] S. Hesse, C. Werner, M. Pohl, S. Rueckriem, J. Mehrholz, M.L. Lingnau, “Computerized arm training improves the motor control of the severely affected arm after stroke: a single-blinded randomized trial in two centers,” Stroke, vol. 36, pp. 1960-1966, 2005.

[8] M. Ferraro, J.J. Palazzolo, J. Krol, H.I. Krebs, N. Hogan, B.T. Volpe, “Robot-aided sensorimotor arm training improves outcome in patients with chronic stroke,” Neurology, vol. 61, pp. 1604-1607, 2003.

[9] Guan De Lee, Wei-Wen Wang, Kai-Wen Lee, Sheng-Yen Lin, Li-Chen Fu, Jin-Shin S. Lai, Wen-Shiang Chen, Jer-Junn J. Luh, "Arm exoskeleton rehabilitation robot with assistive system for patient after stroke," Proc. of ICCAS, pp. 1943-1948, 2012.

[10] Hong-Bo B. Wang, Ning Du, Huina Hou, Jiangshun Zhao, Hongnain N. Yu, "An upper limb rehabilitation robot based on 3-RRC parallel mechanism," Proc. of ICAMechS, pp. 668-673, 2012.

[11] Xikai Tu, Jian Huang, Liguo Yu, Qi Xu, Jiping He, "Design of a wearable rehabilitation robot integrated with functional electrical stimulation," Proc. of IEEE RAS & EMBS BioRob, pp. 1555-1560, 2012.

[12] Lei Shi, Kun Jiang, Qiang Wang, Zhen Liu, "A New Method of Quantitative Rehabilitation Rating in Robot-Assisted Recovery System," Proc. of ICINIS, pp. 278-281, 2012.

[13] Yongsuk Kang, Doyoung Jeon, "Rehabilitation robot control using the VSD method," Proc. of SII, pp. 192-197, 2012.

[14] Chao Lv, Le Xie, Wei Shao, Hai-long Yu, Yuan Wang, Jin-wu Wang, Ning Nan, "Development of a Rehabilitation Robot for Upper-Limb Movements," Intelligent Robotics and Applications, Lecture Notes in Computer Science, Vol.7507, pp. 96-102, 2012.

[15] I.Yamamoto, N.Inagawa, K.Hachisuka, et al., “Development of compact rehabilitation robot for a wrist using biological signal”, Proc.of IEEE CME, pp.557-560, 2012.

[16] I.Yamamoto, N.Inagawa, K.Hachisuka, F.Wada, A.Hachisuka, “Development of a Rehabilitative Training Robot for Both Wrists”, Proc.of 2013 ICME, pp.280-284, 2013.

[17] I.Yamamoto, N.Inagawa, M.Matsui, K.Hachisuka, F.Wada, A.Hachisuka, “Research and Development of Compact Wrist Rehabilitation Robot System”, Bio-Medical Materials and Engineering 24, pp.123-128, 2014.

Applied Mechanics and Materials Vol. 597 (2014) pp 401-406
© (2014) Trans Tech Publications, Switzerland
doi:10.4028/www.scientific.net/AMM.597.401

K-MORE: Design of a Kinect Motion Oriented iRobotics Environment

Hao-Hsiang Ku[1, a*], Tsai-Sheng Kao[2,b] and Ching-Ho Chi[3,c]

[1,2] Hwa Hsia Institute of Technology, No.111, Gongzhuan Rd., Zhonghe Dist., New Taipei City 235, Taiwan (R.O.C.)

[3] Ming Chuan University, 5 De Ming Rd., Gui Shan District, Taoyuan County 333, Taiwan (R.O.C.)

[a]kuhh@cc.hwh.edu.tw, [b]tskao@cc.hwh.edu.tw, [c]01050072@me.mcu.edu.tw

Keywords: Intelligent Robot, Kinect, Ontology, Case-based Reasoning and Wireless Sensor Networks.

Abstract. Internet and cloud-based robot services have been attractive and developed. Nowadays, how to enhance the controllability of intelligent robots is an important issue for researchers. This study designs a Kinect Motion Oriented Intelligent-Robot Environment, which is called K-MORE. K-MORE is designed for easily controlling intelligent robots, which is composed of Sensing-based Interactive Robot (SIR) service platform and Cloud Environment. K-MORE is based on open service platforms, including Arduinos, Google Android, and Google App Engine (GAE). Robots not only can be controlled by a smartphone but also can be triggered by events via GAE or Ontology Case-based Reasoning (OCBR). Furthermore, users can use a smartphone to control robots. K-MORE is well-integrated with users, intelligent robots, sensors and the cloud environment. Finally, K-MORE can be an inference model for researchers when developing a robotics-based open service platform in the future.

Introduction

New functions of an intelligent robot (iRobot) have been an important issue in the field of robotics for researchers [8, 10]. Nowadays, cloud computing and cloud-based services are on rise because they offer a high scalability and efficiency service platform. In tradition, robots do specific actions depend on pre-set programs. When robots bump into pre-schedule events, robots will do related actions and response these events. However, these kinds of robots can not well-handle exceptions, lacking of flexibilities. Hence, the current robot environments still can be improved. A well-designed iRobotics Environment should consider the following issues, which are flexibility, scalability, multi-triggers and transparency.

(1) Flexibility. iRobots are with the specific action flows depending on pre-set programs. It is lack of high complexity algorithms to handle exceptions. To tackle this problem, cloud computing and cloud based service can increase the flexibilities, because some intensive tasks can not easily be computed and handled by robotic brain.
(2) Scalability. Most commercial robots are not easily to increase some specific functions, including adding hardware equipment or software programs. To tackle this problem, open service platforms are developed for overcome this problem.
(3) Multi-triggers. A robot should observe and handle multi-events in the same time. Hence, many kinds of thresholds should be designed and defined for these events. To tackle this problem, it is an important impact factor to define multi-triggers and signals, which can trigger the iRobot from different control domains, e.g. environment sensors, Kinect sensors, cloud, smartphones, etc.
(4) Transparency. Different devices are with specific develop tools and protocols. It is different to communicate with each other. To tackle this problem, Extensible Markup Language (XML) is a markup language that can define a set of rules for encoding documents in a format. The design goals of XML emphasize simplicity, generality, and usability over heterogeneous networks.

For the aforementioned four technical issues, this study designs and proposes a Kinect Motion Oriented Intelligent-Robot Environment, which is called K-MORE. K-MORE is based on open

service platforms. iRobots not only can be controlled by a smartphone but also can be triggered by events via GAE or Ontology Case-based Reasoning (OCBR). K-MORE is well-integrated with users, intelligent robots, sensors and the cloud environment.

The rest of this paper is organized as follows. Section 2 describes related works. Section 3 describes the infrastructure and components of K-MORE. Section 4 describes the implementation of K-MORE. Finally, Section 5 gives conclusion remarks.

Related Works

In past years, many researchers have focused on designing and developing industrial robotics for increasing efficient and throughput of production processes. Current researchers seek the improvement of robotic systems by increasing the efficiency of scheduling multiple tasks and compatibility. This section introduces related studies as follows.

1. Cloud Robots

L. Turnbull and B. Samanta designed a Cloud Robotics [9]. Authors discussed the formation control of multi-robot system utilizing cloud infrastructure. The proposed cloud computing process was developed on Virtual Machine using Linux. Although Linux is an open service platform, it can real implement in other public cloud environments. Z. Dogmus *et al.* proposed ERHABROBO-ONTO, which is rehabilitation robotics ontology on the Cloud, to presents information about rehabilitation robots and their properties [4]. Although this study considers the robotics ontology, it can add other open service platform to accommodate with other services. M. Narta *et al.* adopted Robot Service Network Protocol (RSNP) and proposed the reliable cloud-based robot services [6]. RSNP is based on HTTP, SOAP, WebScoket and so on. Results indicated that the combination system of RSNP and Sanderha2 can send a large file. Although this RSNP can accommodate with many web-based protocol, it can increase the communications among services.

2. Robots with Kinect Sensors

E. Ruiz *et al.* designed a control platform for the mobile robot Roomba using robot operating system [7]. Three modules, control of the IRobot Create® (ICR), Kinect integration and Exporting information, are proposed. D.S.O. Correa *et al.* used Kinect sensor to mobile robot navigation [3]. Authors used an Artificial Neural Network (ANN) to recognize different configuration of environments. The ANN is trained using data captured by Kinect sensor in indoor environments. C.A. Arango *et al.* designed the master-slave system using Kinect and industrial robot for teleoperations [2]. Authors presented the integration of a Kinect sensor device with a robotic arm Kuka KR6 as a master-slave communication for applications of teleoperation and bioengineering. The Kinect device captures the position of the user's right hand, filters its resulting data and detects its movement using Haar wavelets.

Most cloud robots provide cloud computing and cloud services. Although these studies consider the functions of flexibility and transparency, it can increase abilities of scalability and set multiple triggers for events. Furthermore, robots with Kinect sensors usually focus on the ability of interactions. Hence, this study is to use the cloud service platform to overcome the problems of flexibility, to use Arduinos and ontology case-based reasoning (OCBR) to overcome the problems of scalability, to set triggers by environment sensors, Kinect sensors, cloud and smartphones, and to use XML overcomes the problem of transparency.

K-MORE Architecture

The system architecture of Kinect Motion Oriented Intelligent-Robot Environment (K-MORE) is illustrated as Fig. 1. K-MORE is designed for controlling mobile robot easily, which is composed of Sensing-based Interactive Robots (SIR) service platform and Cloud Environment. K-MORE is based on open service platforms, including Arduinos, Google Android, and Google App Engine (GAE). The related functions and components are described as follows.

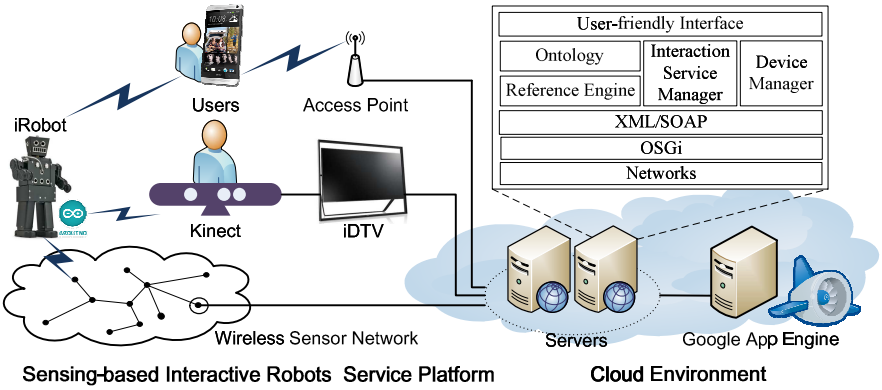


Fig. 1 The K-MORE Architecture.

1. Sensing-based Interactive Robots Service Platform

Sensing-based Interactive Robots (SIR) Service Platform is designed to make interactions among users, iRobot and sensor environments. iRobot works in multiple networks environments, e.g. IEEE802.11b/g, Zigbee, Bluetooth, etc. Hence, SIR service platform uses Arduinos to connect different networks with iRobot, shown as Fig.2. Three ways can control and communicate with iRobot. (1) Users can use a smartphone to control iRobot via a user-friendly interface. (2) Users can interact with iRobot by Kinect sensors. When a user does specific behaviors behind Kinect, the event trigger will be triggered. The triggered signals will be delivered by iDTV to cloud and to iRobot. (3) Wireless sensor networks detect and control iRobot. Related control messages can come from smartphone or cloud environment.

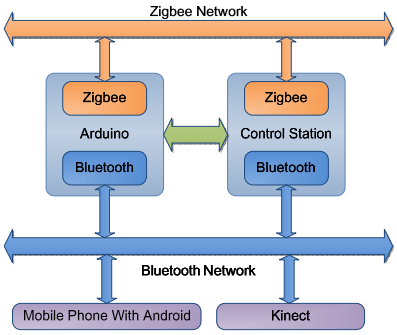


Fig 2. Integrated Multi-Networks.

2. Cloud Environment

Cloud Environment is designed for increasing computing capabilities of iRobot. Hence, the cloud environment is composed of a reference engine and Cloud-based service.

(1) Reference Engine

Figure 3 illustrates the flow chart of Ontology Case-based Reasoning (OCBR) inference engine. OCBR uses the explicit and experienced cases to address and reasons the new solutions of un-deterministic problems based on heuristic rules and theoretical models. Ontology Case-based approaches enable the core of reasoning engine to learn from the experienced and historical data. After reaching a search-based solution for a specific problem, the OCBR mechanism saves solutions and related information to reasons in next time. The control steps are described as follows [1, 5].

(i) Retrieve appropriate cases from the experienced database by sequence searching to find the most similar case. The searching scheme is based on the Euclidean Distance (ED) method. The formula of ED is as follows.

$$ED_i = \sqrt{({}_iC_1^{old} - {}_iC^{new})^2 + ({}_iC_2^{old} - {}_iC^{new})^2 + ({}_iC_3^{old} - {}_iC^{new})^2 + \cdots} \quad \forall i \in case\ \{1..i\} \tag{1}$$

EDi: The Euclidean Distance between new case and old Case i.

Casei: The i^{th} case.

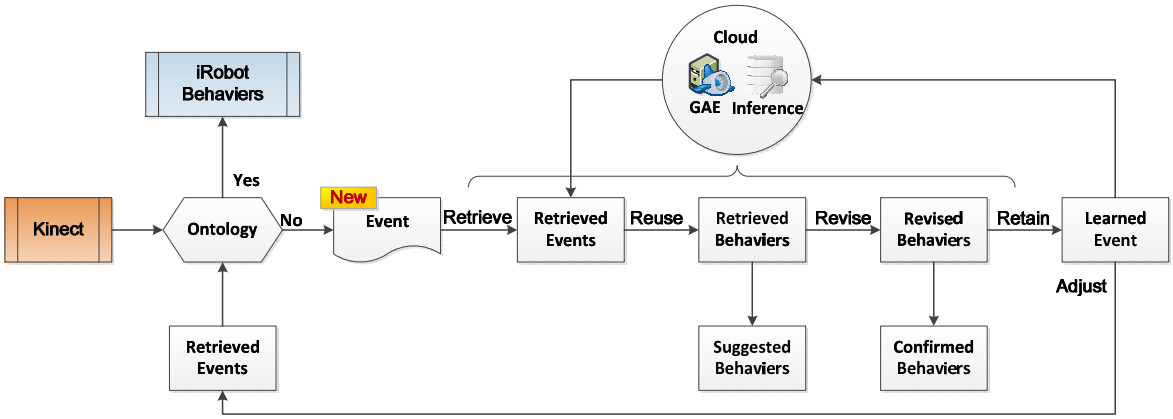


Fig. 3 Flow chart of Ontology Case-based Reasoning.

${}_iC^{new}$: The attributes of the new case.
${}_iC_k^{old}$: The attributes of the experienced (old) case, for k = 1..n.

The formula (2) illustrates the normalization process for the values of the attributes

$$Attribute_{i.new} = \frac{Attribute_{i.old}}{Attribute_{MAX}} \quad \forall i \in case\ \{1..i\} \tag{2}$$

The OCBR mechanism searches a new case and compares it with experienced cases in the database. Every experienced case generates an ED value. The case has the smallest value of the ED is the most similar case and then OCBR mechanism uses the most similar case as the modification reference of the next reasoning step.

(ii) When OCBR mechanism finishes the Retrieve phase and Reuse phase, the OCBR mechanism applied the transformed case to the new problem. Based on the reasoning results, the OCBR mechanism would determine the conclusion and give the suggestion for users.

(iii) The OCBR mechanism stores the final reasoning case need into the experienced database. As the volume of the experienced cases increases, the OCBR mechanism is capable of having more accurate reasoning determination. The reasoned ontology illustrates as Fig. 4.

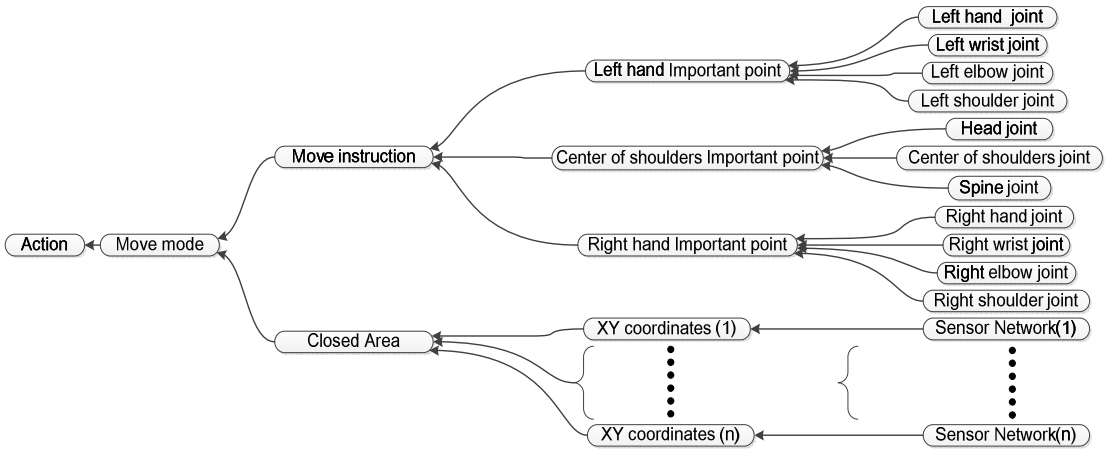


Fig. 4 The reasoned ontology.

(2) Cloud-based Service

Due to the incremental contents and services in cloud environment, K-MORE is composed of Google App Engine (GAE) to connect with cloud. GAE is a cloud-based service platform, which provides specific cloud services with Google environments. Nowadays, Google provides multiple Google cloud based open Application Programming Interfaces (APIs), Software Development Kits (SDKs), services and platforms for Internet of Thing (IoT). In this study, K-MORE will set triggers in

GAE by crontab, which is a cloud-based time schedule, to make connection iRobot with Cloud, shown as Fig. 5.

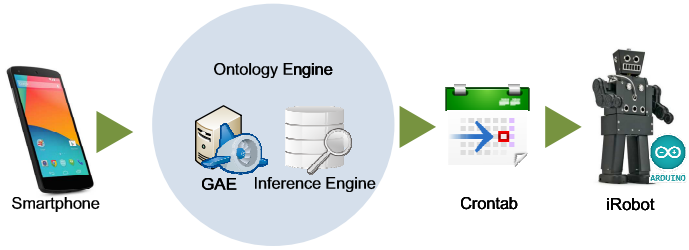


Fig. 5 The reasoned ontology for iRobot.

Implantation of Kinect Motion Oriented Intelligent-Robot Environment

This Section presents the implementation of K-MORE. Figure 6 shows the K-MORE implementation results. Figure 7 and 8 show screenshots when a user requests services of K-MORE that have rendered on a PC and on a handheld device, respectively. Furethemore, the analysis and test are execution time and error rate between OCBR and ontology. Figure 9 illustrates that OCBR is with efficient execution time than Ontology scenario. When old cases increase, the new case can easily find a similar old case and apply this scenario into new one. Hence, OCBR can efficiently reduce the execution time. Figure 10 illustrates that OCBR with lower error rate by feedback mechanism, cans provide a stable working environment for iRobot.

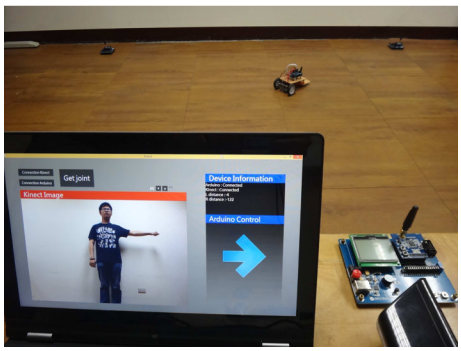


Fig. 6 A scenario of K-MORE.

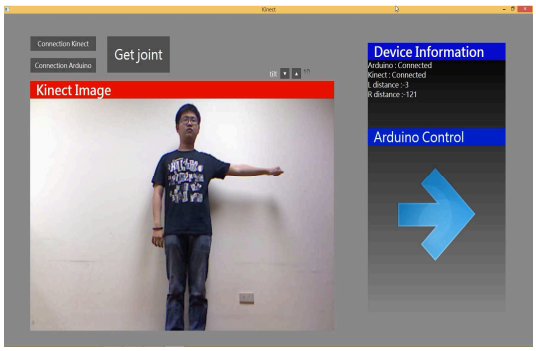


Fig. 7 A screenshot of Kinect on iDTV.

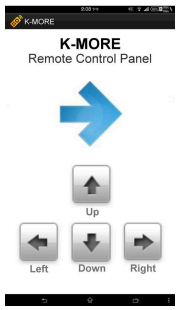
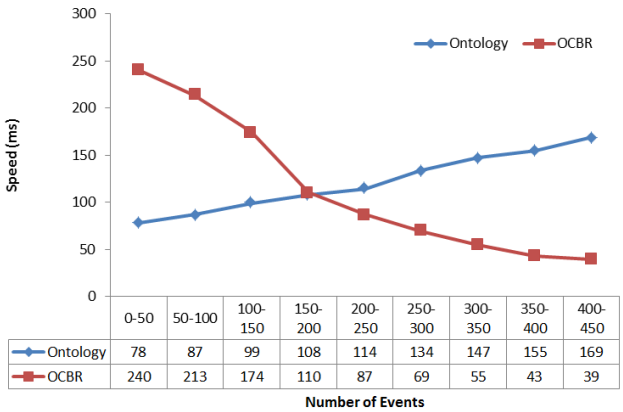
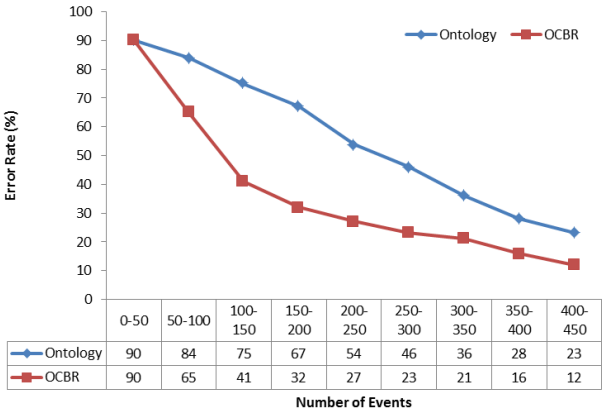


Fig. 8 A screenshot of a smartphone.



	0-50	50-100	100-150	150-200	200-250	250-300	300-350	350-400	400-450
Ontology	78	87	99	108	114	134	147	155	169
OCBR	240	213	174	110	87	69	55	43	39

Fig. 9 The execution time of OCBR.



	0-50	50-100	100-150	150-200	200-250	250-300	300-350	350-400	400-450
Ontology	90	84	75	67	54	46	36	28	23
OCBR	90	65	41	32	27	23	21	16	12

Fig. 10 The error rate of OCBR.

Conclusion

This study designs a Kinect Motion Oriented Intelligent-Robot Environment (K-MORE), which is composed of Sensing-based Interactive Robots (SIR) service platform and Cloud Environment. K-MORE is based on open service platforms, including Arduinos, Google Android, and Google App

Engine (GAE). Robots not only can be controlled by a smartphone but also can be triggered by events via GAE or Ontology Case-based Reasoning (OCBR). The proposed K-MORE can efficiently resolve mentioned four issues, flexibility, scalability, multi-triggers and transparency in this study.

(1) To tackle the problem of flexibility, K-MORE uses Ontology Case-based Reasoning and Google App Engine to increase flexibilities for iRobots.
(2) To tackle the problem of scalability, K-MORE combines Arduino, Android and Google open service platforms to increase scalability for iRobots.
(3) To tackle the problem of multi-triggers, K-MORE sets multi-control signals to trigger the iRobot from different control domains.
(4) To tackle the problem of transparency, K-MORE uses XML and SOAP to accommodate with heterogeneous applications and systems.

Furthermore, system stacks and flows are presented. The proposed K-MORE can be a reference model for developing a controlling system for robotics-based open service platform in the future.

Acknowledgment

The National Science Council of the R.O.C. under the grant NSC102-2221-E-146-005 supports this research.

References

[1] A. Aamodt and E. Plaza, “Case-Based Reasoning: Foundational Issues, Methodological Variations, and System Approaches,” AI Communications, Vol. 7, No. 1, pp39-59, 1991.
[2] C.A. Arango, J.R. Martínez, V.Z. Pérez, “Master-slave System using Kinect and an Industrial Robot for Teleoperation,” Proceedings of 2013 Pan American Health Care Exchanges (PAHCE), pp.1-6, 2013.
[3] D.S.O. Correa, D.F. Sciotti, M.G. Prado, D.O. Sales, D.F. Wolf, F.S. Osorio, “Mobile Robots Navigation in Indoor Environments Using Kinect Sensor,” Proceedings of 2012 Second Brazilian Conference on Critical Embedded Systems, pp. 36-41, 2012.
[4] Z. Dogmus, A. Papantoniou, M. Kilinc, S.A. Yildirim, E. Erdem, V. Patoglu, “Rehabilitation Robotics Ontology on the Cloud,” Proceedings of 2013 IEEE International Conference on Rehabilitation Robotics, pp. 1-6, 2013.
[5] H.H. Ku and S.Y. Huang, “Design of an Web 2.0 QoS-based Digital Convergence Service Platform,” Proceedings of 9th International Conference on Computing Technology and Information Management, Vol. 4, pp. 255-260, 2013.
[6] M. Narita, S. Okabe, Y. Kato, Y. Murakwa, K. Okabayashi, S. Kanda, “Reliable Cloud-based Robot Services,” Proceedings of 39th Annual Conference of the IEEE Industrial Electronics Society, pp. 8317-8322, 2013
[7] E. Ruiz, R. Acuna, N. Certad, A. Terrones, M.E. Cabrera, “Development of a Control Platform for the Mobile Robot Roomba using ROS and a Kinect Sensor,” Proceedings of 2013 Latin American Robotics Symposium and Competition, pp. 55-60, 2013.
[8] M. Tenorth, A.C. Perzylo, R. Lafrenz, M. Beetz, “Representation and Exchange of knowledge about Actions, Objects, and Environments in the RoboEARTH Framework,” IEEE Transactions on Automation Science and Engineering, Vol. 10, No. 3, pp. 643-651, 2013.
[9] L. Turnbull and B. Samanta, “Cloud Robotics: Formation Control of a Multi Robot System Utilizing Cloud Infrastructure,” Proceedings of 2013 IEEE Region 3 Technical, Professional, and Student Conference, pp. 1-4, 2013.
[10] G. Xing, S. Tian, H. Sun, W. Liu, H. Liu, “People-following System Design for Mobile Robots Using Kinect Sensor,” Proceedings of 2013 25th Chinese Control and Decision Conference, pp. 3190-3194, 2013.

Applied Mechanics and Materials Vol. 597 (2014) pp 407-410
© (2014) Trans Tech Publications, Switzerland
doi:10.4028/www.scientific.net/AMM.597.407

Dynamic Control of Gait and Posture Training on Robot

Chih-Chen Chen[1], Shih-Hsiang Ciou[2],Yuh-Shyan Hwang[2],Yu-Luen Chen[3], Sheng Chen[4,*]

[1] Department of Management Information Systems, Hwa-Hsia Institute of Technology, New Taipei City, Taiwan

[2] Graduate Institute of Computer and Communication Engineering,National Taipei University of Technology,Taipei,Taiwan

[3] Department of Digital Technology Design, National Taipei University of Education, Taipei, Taiwan

[4] Department of Electrical Engineering, Hwa-Hsia Institute of Technology, New Taipei City, Taiwan

*corresponding author: senchen@cc.hwh.edu.tw

Keywords: gait training, balance, fall prevention

Abstract. In the research, a robot with gait and posture training functions is developed as an interactive balance rehabilitation training system for balance control impaired people to use. The system uses an action control tool with braking and monitoring functions to obtain the dynamic posture and gravity position of the body of the trainee, followed by subsequent process with software which is developed and designed completely to generate related feedback instructions for the trainee. Moreover, the instructions are presented in image, audio and tactile feedback manners, such that the trainee is provided with multiple message instructions to perform training activities according to the action request actually. Clinically, the research may provide training contents oriented according to task need. Compared to the decomposed action approach emphasized in conventional rehabilitation, it does allow the trainee to focus on the activity and obtains more significant effect. Furthermore, the goal of falling prevention function is also achievable after trained by the robot with gait and posture training functions developed in the research.

Introduction

Patients with insufficient balance control ability exist over different ages. For children and youngsters, common minimal brain dysfunction[1], developmental dyspraxia[2], disorder of attention and motor performance[3], and general medical maladies (for example, infantile paralysis, cerebral palsy, muscular dystrophy) result in sufficient balance control ability. For the aged, aging affects body nerves, feelings, posture control, skeleton and muscle, recognition system, such that the functions of those sense organs and systems degrade significantly, especially for muscle strength, balance and walking ability[4]. After the action ability becomes worse due to above causes, falling is the most apparent phenomenon seen externally. Thus, the aging due to degradation of body function impacts actually on the degradation of balance control ability. There are more external factors (such as stroke, ipsilateral pushing derived from stroke[5], Parkinson's disease, osteoporosis[6], osteoarthritis[7] etc.) that will degrade the balance control ability of order people. As for youngsters and matures, slipping-clutch phenomena because of dysfunction due to brain trauma[8], neuropathy are all factors that affect balance control ability[9]. Moreover, there is significant relationship between balance ability and walking speed. Therefore, with respect to the appraisal and training for posture control[10], for ones whose action ability is lower than normal people, balance, walking ability and various functional activities are all very important. Hence, the research develops a set of gait and posture training robotic in combination with an interactive balance training system for people whose balance control function is damaged to perform interactive balance rehabilitation training.

Czerwosz, L. et al.(2009) introduces VR (virtual reality) into rehabilitation training of dynamic and static posture control, obviates the environmental impact and error between the system and the trainee that might occur when standing on the platform, to develop a posture retrieval platform capable of adapting various body function difference, and performs clinical test[11]. Deutsch, JE et al.(2009) indicates that the introduction of Nintendo Wii and Wii Fit platforms generates significant effect of gait speed, walking endurance, balance and self confidence for patients. It reveals that the

introduction of VR game for rehabilitation training has a considerable effect on various recoveries for patients. However, it cannot retrieve body posture specifically as input parameters of the game[12]. Sen Zhangr et al.(2011) proposes a visual image extraction approach to build a walking and dynamic balance system for tracking body motion, which, in combination with VR game, forms a new training system, which is introduced to the rehabilitation training for disordered people[13]. Cikajlo, I. et al.(2009) combines VR and interactive games to perform balance training for patients and wins enthusiastic participation and high learning effect from patients[14]. Cikajlo, I. et al.(2009) utilizes DC motor and force plate to build a set of balance training platform with tactile feedback. The trainee accepts posture control training through the reality with collision in VR, the functional balance and posture control ability of the trainee is improved[15].

Materials and Methods

The entire schematic view is as shown in Fig.1. It shows an "active dynamic gait and posture training robot" with tool control, gravity distribution sensing, posture correction and safety mechanism. It can detect postures of various actions of the trainee, including dynamic walking, lower limb lift and stretch, stairs climbing etc. Also, it can combine VR game and command the trainee for subsequent posture actions. As for the plan of hardware, there are three major parts, including action mechanism, power device and master end. Wherein, PC is the master end, which governs the operations of the action mechanism and the power device in the system, and records and analyzes returned data, in addition to provide visual and auditory feedback stimulus for the trainee. Further, in the training process of 3D VR game, the master end retrieves the lower limb posture data of the action mechanism, the dynamic force output data of the dynamic device, and the plantar pressure distribution data of the plantar pressure sensing device from the trainee for control the objects in the VR game. After calculation under game rule, feedback messages are output to the trainee, including visual stimulus on a 2D screen, auditory stimulus in an audio output device, and tactile stimulus of the power device.

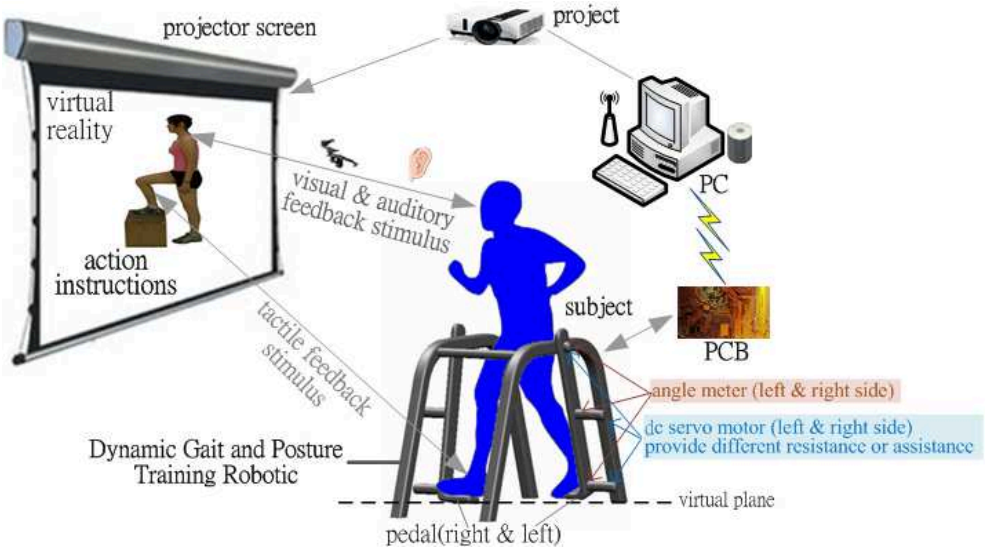


Fig.1 The entire schematic view

Fig.1 shows the action mechanism of the gait training robot. The two "∩" shaped skeletons located on left and right sides are main backbones. A lateral scaffold between the two backbones is used for connection and fixation. Two swingably arms sagging downwards are setted at the central vertex on the upper edge of each backbone. An inward pedal is provided on the bottom of the swingably arm for the trainee to tread. Three joints are provided on each swingably arm, which are located on the connection between the top of swingably arm and the main backbone (for the entire arm to be cable of swinging back and forth), on the middle of the swingably arm (for the lower half segment of the arm to swing back and forth), and on the bottom of the swingably arm (for the pedal to rotate in compliance with the ankle joint of the trainee), respectively. Several goniometers are placed on each of the six joints on the left and right swingably arms for recording the rotation situation of each joint

as the reference for estimate the lower limb posture of the trainee. The trainee may tread on the pedals of the action mechanism, and emulates lower limb actions like such as stepping back and forth, running, knee bend, single leg standing, leg lifting and stair climbing.

Fig.2 shows the status of the feet and the pedals on an action moment. Wherein, Fig. 2(a) shows the status of the feet and the pedals without contacting any virtual plane. At this time, the pedals are in a completely release status and the movement of feet is unconstrained any way. As the feet move, a motor still resistance is encountered. At this time, the motor will detect and transmit a weak current to the controller, which orders the motor to output an equivalent forward output force after the forward output is calculated from the current amount, such that the pedals move in a condition without any resistance. Fig. 2(b) shows the situation in which the feet and pedals are trodden down to the below virtual plane. At this time, if the feet keep on outputting forces downwards, the motor will output an inverse force to resist, such that the pedals keep at a height equivalent to the virtual plane, so that the trainee will feel as treading on ground. Fig. 5(c) shows the scenario in which the contact with an obstacle is emulated. As an obstacle occurs in the front, if the feet drive the pedals to keep on moving forwards, the motor will output an equivalent and backward force such that the trainee will feel as kicking the obstacle.

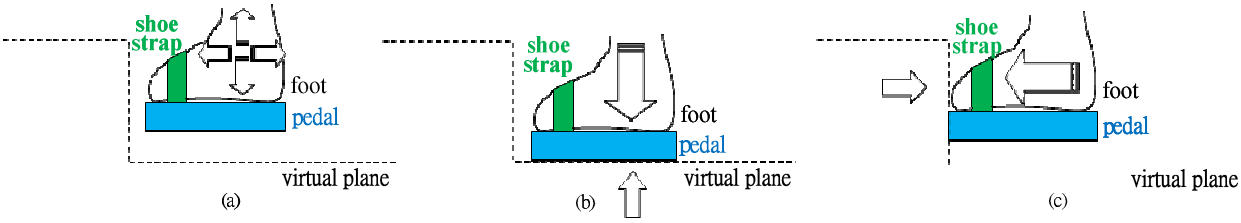


Fig.2 The status of the feet and the pedals on an action moment

Fig.3 shows a system block diagram of "Dynamic Gait and Posture Training Robotic". The common tracking targets for motor control include: location, speed, acceleration, torque etc. In Fig.1, there is one DC servo motor at each of the six joints of the left, right swingably arms on the action mechanism as the source providing torque feedback for the trainee. Fig.4 is a block diagram showing the driver of the DC servo motor. Each servo motor has a photoelectric encoder harvesting the rotation speed of the motor for the rotation speed information to be compared with current pulse signal, current signal mutually to obtain the external torque borne by the motor currently as the source of reference for posture control. The goniometer is arranged on the action mechanism to record information for analysis of the current posture of lower limbs. The action trajectories of lower limbs can be calculated if the information of the goniometer is recorded regularly and continuously.

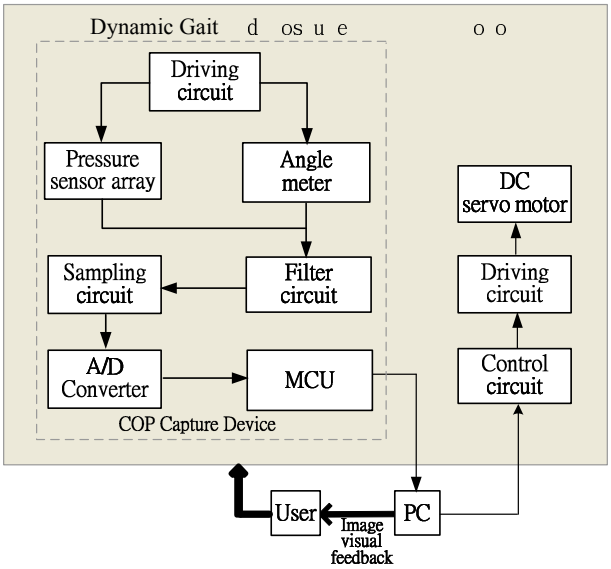


Fig.3 System block diagram

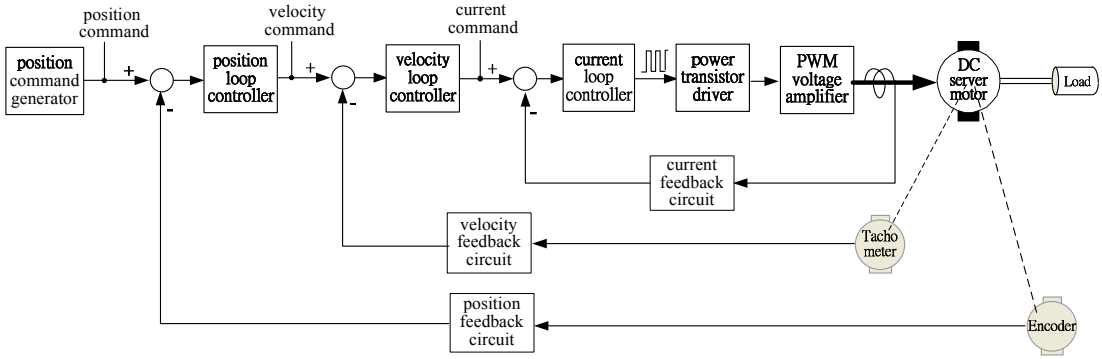


Fig.4 The driver of the DC servo motor block diagram

Results and Conclusion

The dynamic gait and posture training robot planned and designed in the research is beneficial to the enhancement of balance ability and prevention of falling. Different environments, including uphill, downhill, tilt ground, wet ground, ladder, rough road etc., are emulated for the trainee to feel the tactile feedback in VR as in a real environment. In addition, basic ability(FSST,FRT) is assessed to prove that the approach of VR and game motion proposed in the research facilitates to enhance balance ability and prevent falling. Subsequently, it proves that the game developed in the research has the effect of sensory function enhancement and stabilization by means of statistical test.

Acknowledgements

The authors wish to thank the National Science Council (NSC) in Taiwan (Grant Number: NSC 102-2627 -E-002 -005 - ，NSC 102-2221-E-152-001-) for support this research.

References

[1] GIllberg , 1985 ; Gillberg & Gillberg , 1989 , GIllberg et al , 1988.
[2] Ayres,Mailloux & Wendler, 1987;Goodgole - Edwards & Cermak , 1990.
[3] Gillberg, DAMP, 1992 :Hellgren et al, 1994.
[4] King MB, Tinetti ME, 1995, Falls in community-dwelling older persons: J Am Geriatr Soc;43: 1146-54.
[5] Pedersen PM, Wandel A, Jorgensen HS, et al, 1996, Ipsilateral pushing in stroke: incidence, relation to neuropsychological symptoms, and impact on rehabilitation—the Copenhagen stroke study. Arch Phys Med Rehabil, 77: 25-8.
[6] Geusens P, Autier P, Boonen S, Vanhoof J, Declerck K, Raus J, 2002: The relationship among history of falls, osteoporosis, and fractures in postmenopausal women. Arch Phys Med Rehabil; 83: 903-6.
[7] Arden NK, Nevitt MC, Lane NE, GoreLR, Hochberg MC, Scott JC, et al, 1999: Osteoarthritis and risk of falls, rates of bone loss, and osteoporotic fractures. Arthritis Rheum;42: 1378-85.
[8] Chih-Ming Huang, The effect of Seating and Positioning Support on Muscle Tone of the Severe Snastic Cerebral Palsy, National Cheng Kung University Tainan, Taiwan, R.O.C.
[9] Wei-Chun Hsu, Tung-Wu Lu,Hao-Ling Chen, Anticipatory Postural Adjustments in Gait Initiation from Different Initial Stance Width, Institute of Biomedical Engineering, National Taiwan University, Taiwan, R.O.C
[10] Bohannon RW. Gait performance of hemiparetic stroke patients: selected variables. Arch Phys Med Rehabil 1987;68:777-81.
[11] Czerwosz, L. ; Mraz, M. ; Curzytek, M. ; Biaszczyk, J. “Application of virtual reality in postural stability rehabilitation.” Virtual Rehabilitation International Conference, pp.214, 2009.
[12] Deutsch, J.E. ; Robbins, D. ; Morrison, J. ; Bowlby, P.G.“Wii-based compared to standard of care balance and mobility rehabilitation for two individuals post-stroke” Virtual Rehabilitation International Conference, pp.117-120, 2009.
[13] Sen Zhang ; Kee Hao Leo ; Boon Yuen Tan ; Tham, R.Q.F. “A hybrid human motion tracking system for virtual rehabilitation” Industrial Electronics and Applications, 6th, pp.1993 – 1998, 2011.
[14] Cikajlo, I. ; Rudolf, M. ; Goljar, N. ; Matjacic, Z. “Virtual reality task for telerehabilitation dynamic balance training in stroke subjects” Virtual Rehabilitation International Conference, pp.121 – 125, 2009.
[15] Cikajlo, I. ; Oblak, J. ; Matjacic, Z. “Haptic floor for virtual balance training” World Haptics Conference (WHC), pp.179 – 184, 2011.

Applied Mechanics and Materials Vol. 597 (2014) pp 411-414
© (2014) Trans Tech Publications, Switzerland
doi:10.4028/www.scientific.net/AMM.597.411

Novel Strengthened Structure of Stair-climbing Robots on Campus

Ching-Kuo Wang [1, a *], Yi-Hsiu Wu [1,b] and Yu-Shiu Cheng [1,c]

[1]Hwa Hsia Institute of Technology, New Taipei City, Taiwan

[a*] ckw@cc.hwh.edu.tw , [b] wueshal7620@gmail.com , [c] ta0320@hotmail.com

Keywords: Stair-climbing robots, Anti-lock braking system (ABS), and Fuzzy-logic controller.

Abstract. The riding comfort and the maneuverability play increasingly important roles in the development of the moving platform of manned robots. The escaping dynamics and the sensor-based automation have been topics in the issues of the automobile industry since 1995's. It occurs when the vehicle slips away from its prescribed trajectory during braking or cornering. This paper is to construct an intelligent controller to avoid escaping phenomenon for the wheeled and the caterpillar robot platforms. The proposed algorithm is focused on modeling, analysis, and control of nonholonomically vehicle dynamics on the geometric point of view. The stratagem of the anti-lock braking system (ABS) is to navigate the cornering dynamics using the intelligent controller, which successfully integrate a fuzzy-logic controller and multi-stage electronic sensors. Finally, dynamic simulations and experiments of a sensor-based prototype are made to justify the performance of the proposed algorithm.

Introduction

Physical modeling of the wheeled vehicle with nonholonomic constraints has been significant issues because few of them can be classified under the existing theories. Bloch, MaCclamroch et al. [1,3] have derived constrained equations by reducing degrees of freedom from constraints and simulated the dynamics by prescribing additional constraints. Such an algebraic approach successfully formulates nonholonomic systems in the state space. However, the pointwisely coordinate transformation is so tedious that the real-time controller can hardly be realized. Kolmanovsky and MaCclamroch [1,4] devoted to the derivation of the normal form for acatastatic nonholonomic mechanical systems. Huang and Wang [3,4] proposed the concept of complementary distribution using the geometric formulation under the assumption of the complementary Frobenius theorem (CFT). Infinitesimal displacements of constrained systems are piecewisely mapped on the constraint manifold and allowed to move only in the tangent subspace. These "hard" constraints can be softened in the real would, such as anti-lock braking system (ABS) [2,3]. Theoretically, modern vehicle dynamics include steering, escaping, tire dynamics, actuator dynamics and structural dynamics. Many articles related to ABS were developed in terms of the sensor-based models [2,4]. The pseudo violation of the nonholonomic constraint is in the normal subspace and the tangent subspace of the constraint manifold. The proposed hybrid fuzzy controller (HFC) constructs a significant innovation with "soft" constraints for constrained dynamics, on which the mechanical system with quasi-nonholonomic constraints are modeled in the geometric viewpoint instead of the algebraic viewpoint.

Geometric Formulation of Nonholonomic Constraints

The architecture structures of the caterpillar robot platform is illustrated in Figure 1, which include the mechatronic structure of geometric modules, and architecture structures of the caterpillar robot. The nonholonomic dynamics is a significant branch of analytical mechanics, and plays a significant role in the development of caterpillar robot. Nonholonomic constraints of caterpillar tires experience fast, however, infinitesimal displacement existed in the normal subspace of the constraint manifold.

Consider an n-dimensional vehicle system subjected to $m < n$ independent velocity-level or Pfaffian one-form constraints $\varpi_i(q),\ i=1,\cdots,m$ in $\mathrm{M} \subset R^m$. The constraints can be denoted as

$$\varpi_i(q) = N_i(q)\dot{q}(t) + N_{0i}(q,t) = \sum_{j=1}^{n} N_{ij}(q)dq_j + N_{0i}(q,t), \qquad i=1,\cdots,m, \tag{1}$$

where $\mathrm{M} \subset R^m$ is the constraint manifold and $q(t) \in R^n$ is the generalized coordinetes. $N(q) = [N_1^T \cdots N_m^T]^T \in R^{m\times n}$ is called the constraint matrix or the normal matrix and $N_{ij}(q),\ i=1,\cdots,m,\ j=1,\cdots,n$ is the element of the constraint matrix. $N_i(q) \in R^n,\ i=1,\cdots,m$ is the normal vector of the constraint matrix and $N_{0i}(q,t),\ i=1,\cdots,m$ implies the acatastatic term of the nonholonomic constraint. Let $\Delta(q) \subset R^{n-m}$ be the distribution of the constraint manifold and $g_i(q) \subset \Delta(q),\ i=m+1,\cdots,n$ is the tangent vector of the constraint manifold $\mathrm{M} \subset R^m$, then

$$g_i(q) = \sum_{j=1}^{n} \tilde{T}_{ij}(q) \frac{\partial}{\partial q_j}, \tag{2}$$

where $\tilde{T}_{ij}(q)$ is the coefficient. The dual relation exists in the inner product of $N_i(q)$ and $g_j(q)$, i.e.,

$$N_i(q) \cdot g_j(q) = \sum_{k=1}^{n} N_{ik}(q)\tilde{T}_{kj}(q) = \delta_{ij}, \tag{3}$$

where $\delta_{ij}, i=1,\cdots,m,\ j=m+1,\cdots,n$ is the Kronecker symbol. The so-called "hard" constraints can be softened if the equality $N_i(q)\cdot g_j(q) = \delta_{ij}$ no longer holds. Namely, the infinitesimal displacement dq_j escaped from the constraints does not move orthogonally to the normal subspace.

Coulomb's Friction of the Stair-climbing Caterpillar Robots

Theoretically, the so-called quasi-nonholonomic dynamics [2,3] is extended from the velocity-level constrained dynamics. Let $T_q\mathrm{M}$ and $N_q\mathrm{M}$ be defined as the tangent subspace and the normal subspace of the constraint manifold, respectively.

Definition 1: Physical constraints in the geometric space.

Consider an n-dimensional system lying on an m-dimensional constraint manifold $\mathrm{M} \equiv \{q(t) \in \mathrm{M}_T | \varpi_i(q) = 0,\ i=1,\cdots,m\}$ in the topological space $\mathrm{M}_T \subset R^n$. Let $\varpi_i(q),\ i=1,\cdots,m$ be a real smooth function vanishing on its minimum space $\mathrm{M} \subset \mathrm{M}_T$. Geometric models of the constraints are defined as $\varpi_i(q) = 0$ for points in the neighborhood of $q(t) \in \mathrm{M}$. On the other hand, the unconstrained variables are defined as $\varpi_i(q) > 0$ for points $q(t) \notin \mathrm{M}$ in $\mathrm{M}_T \subset R^n$. □



Fig. 1. Architecture structures of the caterpillar robot platform. (a) mechatronic structure of the caterpillar robot, (b) novel scenary of the caterpillar robot on campus.

A typical example of quasi-nonholonomic dynamics can be illustrated as the vector field $\hat{g}(q) = g(q) \oplus g^c(q)$, where $g(q)=[g_1(q)\cdots g_{n-m}(q)] \subset T_q\mathrm{M}$ and $g^c(q)=[g^c_{n-m+1}(q)\cdots g^c_n(q)]. \subset N_q\mathrm{M}$ The notation "$\oplus$" is the direct sum operator. Ideally, the quasi-constrained motion can be described as

$$\dot{q}(t) = \sum_{i=1}^{n-m} g_i(q)\hat{u}_i(t) \oplus \sum_{i=n-m+1}^{n} g_i^c(q)\hat{u}_i(t) \equiv \sum_{i=1}^{n-m} g_i(q)\hat{u}_i(t) \oplus \dot{q}^e(t), \tag{4}$$

if there is no pseudo violation. Note that $g_i(q),\ i=1,\cdots,n-m$ and $g_i^c(q),\ i=n-m+1,\cdots,n$, are complementary. $\dot{q}^e(t)=\sum g_i^c(q)\hat{u}_i(t)$ is high-frequency quasi-nonholonomic velocity in the normal subspace. $\hat{u}_i(q)\in C^1$ is an n-dimensional velocity component both in $T_q\mathrm{M}$ and $N_q\mathrm{M}$.

Definition 2: Quasi-nonholonomic velocity of the constraint manifold

Consider an m-dimensional constraint manifold $\mathrm{M} \subset \mathrm{M}_T$, where $\mathrm{M}_T \subset R^n$ is an n-dimensional state space and $g_i(q)\in T_q\mathrm{M}$, $g_i^c(q)\in N_q\mathrm{M}$ are in the tangent subspace and complementary subspace of the constraint manifold, respectively. The so-called quasi-nonholonomic velocity or the escaping velocity is defined as $\dot{q}(t)=\sum g_i(q)\hat{u}_i(t)\oplus\dot{q}^e(t)$. The term "escaping" implies that the constrained system moves in the tangent and the normal subspaces simultaneously. □

Physical Modeling of the autonomous Controller

Topological navigation of the caterpillar vehicle is steered using a sliding controller. While, the escaping dynamics of caterpillar tires in the lateral and the transverse direction are modeled as the ABS environment and controlled using a fuzzy controller. This paper is organized as follows. In the next section, integrability of the Pfaffian forms is discussed in the geometric point of view. Conventional Frobenius theorem [4] gave sufficient and necessary conditions to the existence of constraint manifolds for holonomic systems. However, nonholonomic constraints are not integrable on the tangent subspace of the constraint manifold, respectively.

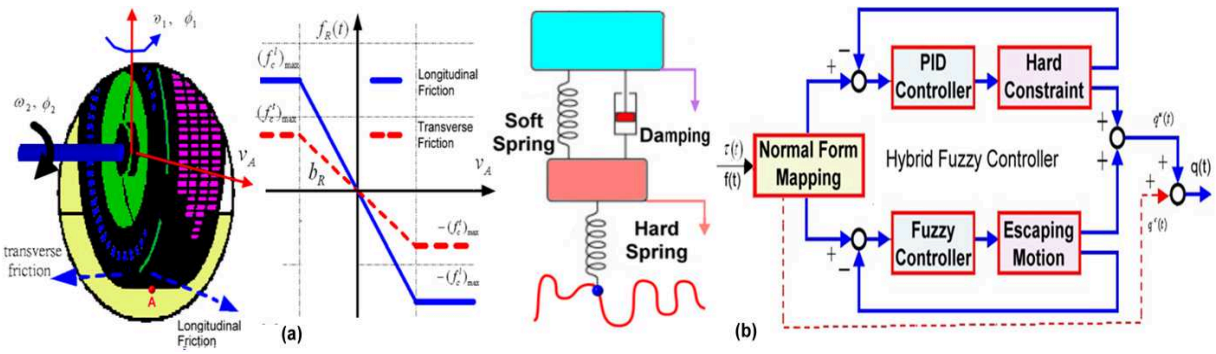


Fig. 2. Block diagram of the normal-form mapping controller. (a) physical modeling and dynamic modeling of the Stair-climbing vehicle, (b) nonholonomic plant with a hybrid fuzzy controller (HFC).

Computer Simulations

The caterpillar robot with prescribed nonholonomic controller is computer simulated as follows. This class of controller is designed to integrate cornering effects from tracking control system (TCS) and escaping effect from anti-lock braking system (ABS). However, the caterpillar robot is modeled as a lumped structure in this paper so that the complexity of the suspension system is ignored. Applying the structural dynamics, the caterpillar robot can be modeled as a flexible structure instead of a lumped structure. The specifications of the stair-climbing vehicle can be simplified as follows:

The Gross weight, payload, and physical size are 45kg with 65kg are 75cmx45cmx35cm, respectively. Motor speed and power requirement are3400rpm with 1/55 gear reduction, 150W with 24DCV voltage and 6 DCA electric current, respectively. The simulation results of the stair-climbing vehicle are successfully illustrated in Fig. 3.

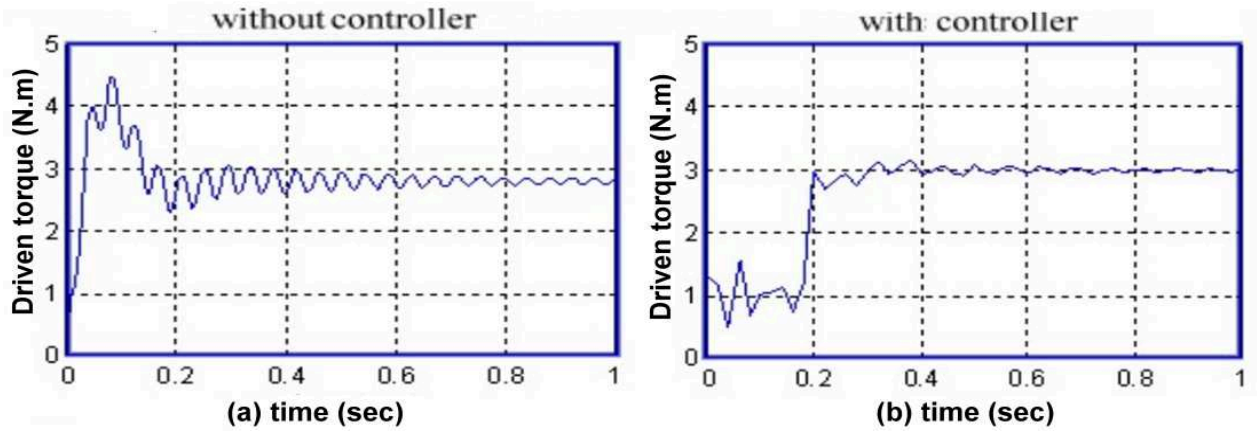


Fig. 3. Computer simulation of the caterpillar vehicle and the viscous frictions for ABS command pedal. (a) without controller, (b) with controller

The nonholonomic controller with an anti-lock braking system (ABS) is applied and the PID tuning parameters are modulated according to the given loading effects. The self-fabricated caterpillar robot is successfully achieved to be driven upstairs with the speed 3 km/hr. turning to the left direction. It also improve the riding comfort and the maneuverability for high-quality moving platform of the caterpillar robot.

Conclusions

This paper has successfully demonstrated the navigation of the caterpillar robot with ABS under the assumption of the Coulomb's viscous friction. Significant contributions of this paper include less computer time, more effective controllers, significant sense of physics on the constraint manifold and the unified nonlinear formulation for the navigation problem. However, the caterpillar robot is modeled as a lumped structure in this paper so that the complexity of the suspension system is ignored. Applying the structural dynamics, the caterpillar robot can be modeled as a flexible structure instead of a lumped structure. The future trend in the development of modern caterpillar robot is to improve the riding comfort and the maneuverability for high-quality moving platform. Those topics will be considered as challenging tasks to research in the near future.

Acknowledgment

This research was financially supported by the National Science Council, Taiwan, R.O.C., under the contract ：NSC 100-2632-E-146 -001-MY3 and NSC 102-2221-E-146 -002 -

References

[1] A. M. Bloch, M. Reyhanoglu and N. H. McClamroch, "Control and Stabilization of Nonholonomic Dynamic Systems," IEEE Transaction on Automatic Control, Vol. 37, No.11 (1992), 1746-1757.

[2] A. M. Bloch and P. E. Crouch, "Newton Law and Integral of Nonholonomic Systems," SIAM Journal on Control and Optimization, Vol.36, Iss.6 (1998), 2020-2039.

[3] H. P. Huang and C. K. Wang, "Intelligent Control of Wheeled Vehicles with Anti-lock Braking Systems," International Journal of Vehicle Design, Vol. 26, No.2/3(2001), 218-238.

[4] C. K. Wang and H. P. Huang, "The SLQG/LTR Controller of the Escaping Dynamics for Nonholonomic Systems," Journal of the Chinese Society of Mechanical Engineers, Vol. 23, No.4 (2002), 383-388.

CHAPTER 7:

Electrical Devices and Embedded Systems, Machine Elements, Systems and Mechanisms

Applied Mechanics and Materials Vol. 597 (2014) pp 417-420
© (2014) Trans Tech Publications, Switzerland
doi:10.4028/www.scientific.net/AMM.597.417

Computer Aided Design of a New Universal Clamping Mechanism

Jeremy (Zheng) Li, Ph.D., Associate Professor[1,a]

[1]University of Bridgeport, 221 University Ave., Bridgeport, CT 06604, USA

[a] zhengli@bridgeport.edu

Keywords: Computer-aided design, automated production, 3D modeling, cost-effective, high speed manufacturing, engineering analysis, optimization, efficient;

Abstract

The tooling and fixture play important roles in manufacturing and production. It affects both product quality and quantity. Better tooling and fixture can also promote cost-effective manufacturing process. This paper introduces a new type of universal clamping mechanism based on computer-aided 3D modeling, engineering structural analysis, and prototype testing. It can be applied to easily and reliably clamp different geometrical shape of work pieces per user requirements. This new clamping mechanism, with less moving components, can assist manufacturing industry for high speed production, easy part handling, precise clamping, and lower tooling cost.

1. Introduction

Proper tooling and fixture design can well support industrial production. When the work pieces are positioned, it must be fixed and pressed against the machine locating surfaces in order to withstand the external assembly or cutting forces acting upon it [1]. The tool design engineers consider this action as clamping and the mechanism utilized for this clamping action is known as clamping mechanism [2]. Many different clamping mechanisms were developed in the past but sometimes it was difficult to choose the tooling and fixture for certain products with irregular geometrical shape [3, 4]. In general, the selection of clamping mechanism is mainly depending on the work pieces and types of manufacturing operation. Usually the simple work pieces with uniform geometry only require simple clamping mechanism but work pieces from casting and forging with irregular or section-variable contours need specially designed clamping mechanism [5, 6]. The design of clamping mechanisms, including simple and complicated, must meet the following spec: (1) the work pieces must be firmly clamped while being manufactured (2) the loading and unloading should be easy and fast (3) the clamping device is capable of handling vibration or shock (4) the work pieces will not be damaged by clamping device [7]. The Clamping forces are required to directly apply to the locating surfaces and the cutting tools should be safely away from the clamping device. The clamping device is critical to maintain final and precise geometry and dimensions of the products.

2. New universal clamping mechanism

A new universal clamping mechanism is studied, designed, and developed via 3D modeling, structural analysis, and prototype testing. This new clamping mechanism, shown in Fig. 1, can easily and accurately clamp work pieces with irregular geometry. This is a cost-effective mechanism due to its simplified design.

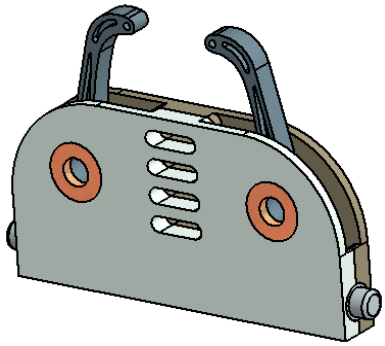


Fig. 1 New universal clamping mechanism

The operation of this clamping mechanism can be described as follows:

In this clamping mechanism, the main body is made up by top and bottom covers. Two arms with teeth at its lower section and one worm gear shaft with opposite directional threads at both ends are mounted in the main body. Two arms, supported by roller bearings inside bearing housing, can be open or closed to release or hold work piece when worm gear shaft is rotated at one end. This clamping mechanism design is simple due to few simplified components.

3. Computer aided modeling and simulation

The computer aided 3D modeling and simulation results are shown in Figs. 2 – 5.

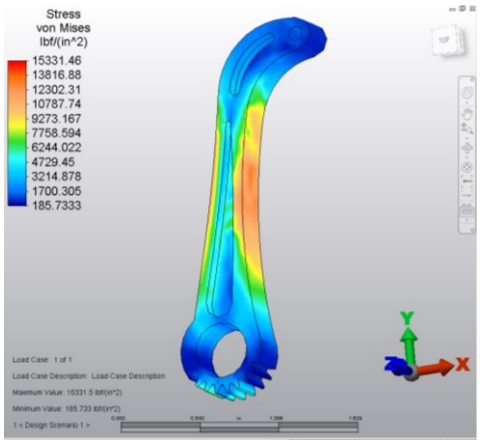


Fig. 2 Stress profile of clamper arm

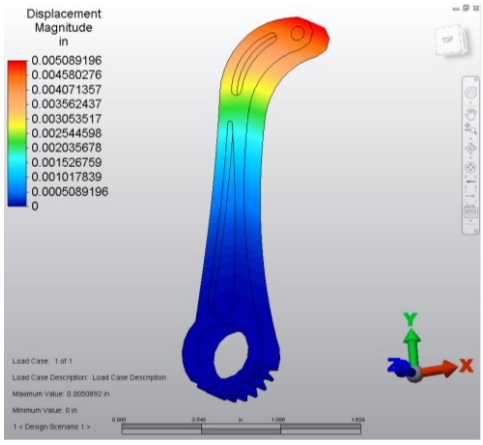


Fig. 3 Deflection profile of clamper arm

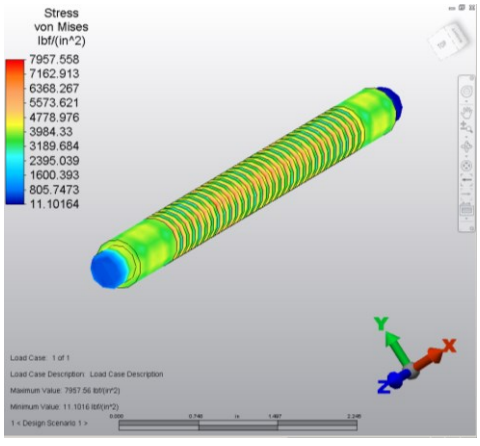


Fig. 4 Stress profile of worm gear shaft

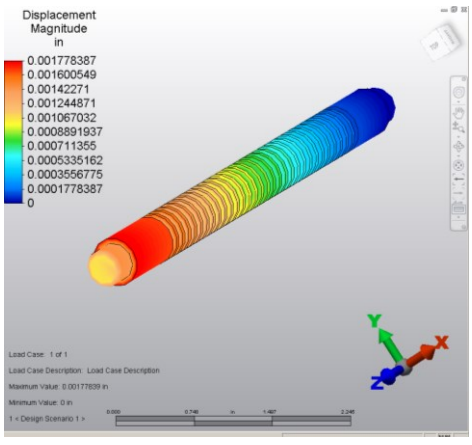


Fig. 5 Deflection profile of worm gear shaft

The above simulations show that the maximum stress of 15331.46 psi and 7967.56 psi are produced in clamping arm and worm gear shaft respectively. Since these maximum stresses are all below the yield stress of 36000 psi in mild steel and the maximum deformations are within material allowable limit, these major components can function properly.

4. Prototype testing

The prototype has been built and tested to verify the results from computer aided modeling and simulation. Table 1 presents the experimental result for clamping arm and worm gear shaft in this new universal clamping mechanism.

Table 1 Prototype testing on clamping arm and worm gear shaft

Number of Test	Clamping arm		Worm gear shaft	
	Stress (psi)	Deformation (inch)	Stress (psi)	Deformation (inch)
1	15331.38	0.00518	7957.54	0.00188
2	15331.24	0.00524	7957.88	0.00175
3	15331.48	0.00538	7957.75	0.00198
4	15331.08	0.00518	7957.88	0.00195
5	15331.12	0.00529	7957.76	0.00175
6	15331.09	0.00538	7957.98	0.00199
7	15331.11	0.00519	7957.95	0.00185
8	15331.48	0.00522	7957.78	0.00198
9	15331.18	0.00524	7957.89	0.00196
10	15331.22	0.00518	7957.85	0.00191
Average	15331.24	0.00525	7957.83	0.00190

Table 1 indicates that the maximum stress and deformation in clamping arm are 15331.24 psi and 0.00525 inches which are very close to 15331.46 psi and 0.00507 inches from computer aided simulation. Table 1 also shows that the maximum stress and deformation in worm gear shaft are 7957.83 psi and 0.00190 inches which are closely equal to 7967.56 psi and 0.00178 inches from computer aided simulation. It verifies the credibility of analytic methodology utilized in this research.

5. Conclusion

This new clamping device can be applied in many different manufacturing operations including drilling, milling, shaping, planning, and boring. This new design can make loading and unloading processes more easily and fast. It also include that the holding force on variable work pieces is safely pre-engaged, worm gear shaft can be self-locked after grabbing work pieces, high tolerance control in this clamping mechanism is not required, and it can be flexibly applied to the work pieces with irregular geometry. The future improvement will focus on further increase of clamping force, optimize the geometrical feature of clamping arm via computer aided engineering analysis, and modify the worm gear shaft for cost-effective production.

References

[1]. ZhiSong Chen, KangMin Zhong, Analysis and application of hinge-rod and lever series connected combination mechanism, J. Machine Design. 27 (2010), 57-58.

[2]. Yang Liu, KangMin Zhong, Hydraulic bi-directional clamping fixture composed of hydraulic cylinder and toggle-lever reinforcement mechanism, J. Machinery Design & Manufacture. 3 (2009), 245-246.

[3]. Jeremy (Zheng) Li, Computer-Aided Analysis of Gas Turbine with Hot Spinning, J. Mechanical Engineering (i-manager's research Network). 2 (2012), 1-5.

[4]. Bo Wang, KangMin Zhong, Hydraulic bi-directional clamping fixture composed of non-toggle hydraulic cylinder and toggle-lever reinforcement mechanism, J. Machinery. 42 (2004), 69-70.

[5]. Yunxia Dou, Mingdi Wang, Dongning Su, KangMin Zhong, Reconfigurable pneumatic clamping device of industry manipulator based on toggle-lever force amplifier in series, ASME International Mechanical Engineering Congress and Exposition. 4 (2010), 183-186.

[6]. Jeremy (Zheng) Li, Study and Development of an Energy-Saving Mechanical System, Intl J. Recent Trends in Engineering. 1 (2009), 51-54.

[7]. Wen Lu, Kangmin Zhong, Parallel and Synchronal Double-Acting-Path Toggle Force Amplifier and Its Application to Hydraulic Drive, J. Construction Machinery and Equipment. 1 (2005), 45-46.

Applied Mechanics and Materials Vol. 597 (2014) pp 421-424
© (2014) Trans Tech Publications, Switzerland
doi:10.4028/www.scientific.net/AMM.597.421

Experimental Study of Corrosion Sensors for the Design Technology of Bridge Longevity

Jin-A Jeong[1, a *]

[1]727 TaeJongRo, Busan, Department of Ship Operation, Korea Maritime University, South Korea

[a]jina@kmou.ac.kr

Keywords: Concrete, Corrosion sensor, Electrochemical, Potential

Abstract. Corrosion of steel reinforcement is a major factor in the deterioration of harbor and bridge structure. Steel corrosion in concrete must be checked for investigating the condition of a reinforced concrete structure. The several way how to measuring corrosion condition of reinforced concrete, but the corrosion potential measurement is a very simple, rapid, cost-effective and non- destructive technique to evaluate the severity of corrosion in reinforced concrete structure. However some particular situations may not relate to the reinforcement corrosion probability and a simple comparison of the corrosion potential data with the ASTM Standard on steel reinforcement corrosion probability could prove meaningless because of environment factors as oxygen concentration, chloride content, the concrete resistance. Therefore this paper proposed compact designed corrosion sensors to monitor several corrosion factors, and the electrochemical measurement and evaluation have been carried out to investigate rebar corrosion, and a reasonable prediction of corrosion has been obtained in terms of nondestructive electrochemical point of view.

Introduction

Various detrimental factors in harsh environments have influences on the deterioration of concrete structures. Especially, in marine environment, chlorides have significant effect on the corrosion of marine structures such as marine bridges, underwater tunnels, pier structures, etc. Once the corrosion of reinforcement reaches to a certain level, the damage becomes accelerated and followed by cracking, delamination, and/or spalling. The reinforced concrete as like buildings and bridge structures is a versatile, economical, and successful material [1]-[2]. Normally, the pH of concrete is 12–13, and these alkaline conditions of the structure lead to very slow rates of corrosion [3]. Recently, the design life of concrete structures tends to be extended from 50 years to 75 years or even 100 years, however, a number of cases have been reported premature failures before the design life [4]. However, chloride or carbon dioxide can reduce the pH of the reinforced concrete either locally or over the entire structure, which leads to corrosion [5]-[7]. When corrosion of reinforced concrete has already occurred, it is difficult to solve the corrosion problem, because corrosion damage happens repeatedly in spite of maintenance work. Therefore, it is necessary to deal with this corrosion problem before the corrosion is initiated. To manage this problem, the corrosion monitoring of concrete structures, therefore, becomes very important for the appropriate management of those structures before losing the right time for maintenance. This is the primary reason that the condition monitoring of concrete structures are needed for their longevity. Various non-destructive techniques to monitor the corrosion of rebar in concrete have been introduced so far, and a number of attempts to develop more efficient sensors are still going on world-widely [8]. In corrosion sensors, potential is the most popular criteria to evaluate the corrosion of steel in concrete. In case of embedded sensor, various functions including current density, corrosion rate, concrete resistivity, moisture content, temperature, and chloride content are also utilized [9]-[13]. In this study, therefore, corrosion sensors, which have several functions, i.e. corrosion potential, corrosion rate, concrete resistivity, temperature, and current density (in case of cathodic protection), has been proposed, and among those functions, some electrochemical characteristics, i.e., corrosion potential, corrosion rate, and temperature effect, have been investigated.

Experimental Procedure

Fig. 1 is the schematic drawing of the proposed sensors in this study for corrosion monitoring in concrete. In an overall view, the working and counter electrodes (WE & CE) of flat round sensor were installed at the Teflon material body. The working electrode of flat round sensor with 1 cm diameter was machined and installed at the center of a sensor. The counter electrode made of stainless steel (STS) 316L was a flat donut type. Two electrodes have a galvanic couple, however, working and counter electrodes (WE & CE) of rod sensor were installed at the center of the sensor with mortar, and two probes were located at upper and lower caps, respectively. An ordinary deformed rebar (D10), acting as a working electrode, was 1 cm diameter and 8 cm long, which was vertically installed at the center of a sensor. The counter electrode made of stainless steel (STS) 316L was a cylindrical type, surrounded by the working electrode for a uniform current distribution between the two electrodes. A mesh-shape counter electrode was used to make corrosion factors such as chlorides and water penetrate easily through the counter and reach to the working electrode, rebar. These two electrodes were fixed by the upper and lower caps made of Teflon material to give electric insulation and anti-alkaline property to endure the high-alkalinity in concrete. The space between two caps around the rebar and STS 316L mesh was grouted by mortar to make a similar concrete environment when the sensor is embedded in real structures. The water/cement (w/c) ratio of mortar was 0.7 in order to give the less density of concrete and an easy arrival of corrosion elements to rebar to improve sensitivity. The mortar of rod sensor was cured for 7 days in air.

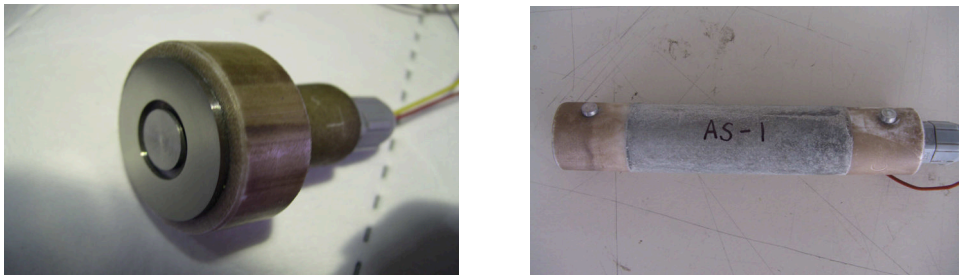


Fig. 1 Flat round type (left) and rod type (right) of corrosion sensors

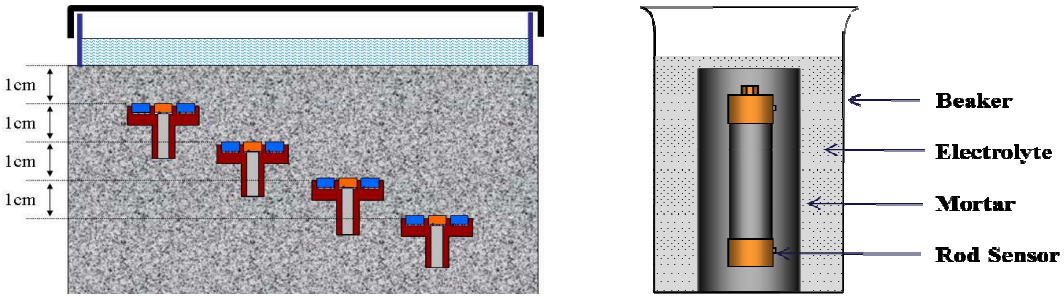


Fig. 2 Two types of specimen for testing the corrosion sensors

The upper probe was also employed as a pseudo-reference electrode during electrochemical polarization measurements including corrosion rate test. Probes were made of 99.7% titanium (Ti) considering reliability for a long period of time and machined by 3.1mm in diameter and 6.4mm in length. All inside space of the sensor was filled with epoxy to prevent concrete specimens from any detrimental material like seawater. In order to test the performance of the corrosion sensor at various environmental conditions, the concrete mortar specimens with individual embedded sensor have been manufactured. To mix mortar, washed sand for a general building construction, ordinary Portland cement, and fresh tap water have been used, and the mixing ratio of sand : cement : water was 2 : 1 : 0.5 (water/cement = 0.5).Two types of corrosion sensors embedded in cement mortar specimens as shown in Fig. 2 illustrated the sensor embedded in the cube slab and cylindrical mortar specimen. In case of cube slab specimen, flat round sensors were located every different cover thickness at intervals of 1 cm. In case of rod sensor specimen, corrosion tests were carried out in several kinds of

electrolytes. Test environments were four kinds, i.e. air(Air), tap water(TW), natural seawater(SW), and 15% seawater(15%SW) that was added more salt to natural seawater up to 15%(15% SW-WD). The test temperature was 25°C. The wet and dry cycle tests in 15% seawater condition (15WD) have been carried out with a week period of cycle, i.e. 4 days of wet and 3 days of dry.
The test parameters were corrosion potential, temperature, corrosion rate, and galvanic corrosion test, and in order to characterize the performance of sensors, those parameters have been investigated both qualitatively and quantitatively. Corrosion rate has been measured by the potentiostat with Gamry Instruments CMS300 system designed to measure a linear polarization resistance (Rp) and to convert to the corrosion current density (Icorr) [14]. The reference electrode for potential measurement was silver/silver chloride electrode (SSCE, Ag/AgCl), and the Fluke multimeter and the CMS300 system by Gamry Instruments Co. have been used for the other measurements [15].

Experimental Results

Fig. 3 shows the variation of galvanic current between the working electrode and counter electrode with cover thickness. The initial galvanic currents were nealy the zero ampere, but the value of the galvanic current from the sensors were increased with times.

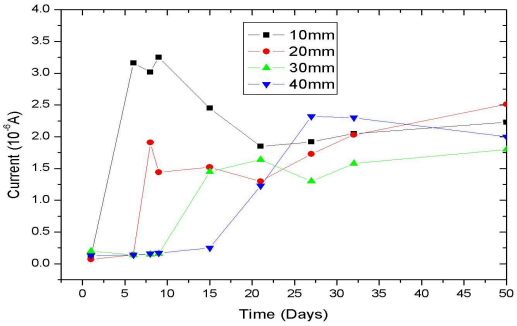


Fig. 3 Galvanic current of flat round sensor

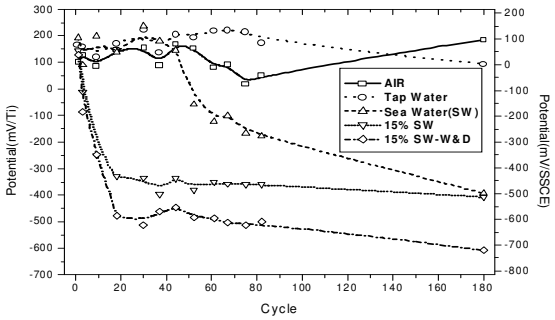


Fig.4 Corrosion potential of rod sensor

Especially the sensor 10mm of cover thickness drastically increased to the 3 μA in early stages. The sensor 20mm of cover thickness increased to the 2 μA in 7 days, the sensor 30mm of cover thickness was 14 days, and the sensor 40mm of cover thickness was 21 days and the change was mitigated after about 25 days. It was assumed that the sensor respond to the penetrated corrosive facts of different depth from the surface of the specimen. Consequently, it was confirmed that the function of galvanic current measurement with the proposed flat round sensor has well reacted with environmental severity. Fig. 4 shows the variation of corrosion potentials of rebar in rod sensor. The right side of scale in the graph is the calibrated potentials to Ag/AgCl electrode (SSCE) values using the average potential of Ti pseudo-reference electrode, 115mV/SSCE, which was obtained from the preliminary tests. At the beginning of the test, potentials for all specimens showed nearly the same values in the range of 10~100mV/SSCE, however, those were varied with time, and it was influence by environmental conditions. In the two specimens (15% SW & 15% SW-WD), exposed to the most harsh conditions of 15% seawater, potentials went down from the beginning of the test and reached to -450mV/SSCE after experiments of 15 cycles. The potential of specimens exposed to natural seawater was no change in the beginning stage of the test, however, it was remarkably decreased to -200mV/SSCE after about 40 cycles, and the change was mitigated after about 60 cycles. The potentials in atmosphere and tap water that did not contain chloride have maintained nearly the original values during the 180 cycles of the test. It is known that the corrosion potential is decreased with increasing chloride contents in concrete [16]. The present potential variation with chloride is agreed with the Gonzalez results, which reported the potential without chloride maintained around -100mV/SCE (Saturated Calomel Electrode), however, that with chloride was reduced to about -400mV/SCE [17].

Summary

From the results regarding the electrochemical performance of the proposed corrosion sensors to monitor the corrosion of reinforced concrete structures related to the design technology of bridge longevity, the followings have been obtained. It was confirmed that the function of galvanic current measurement with the proposed sensor has well reacted with environmental severity. Through the corrosion potential measurements in various corrosion environments, it was confirmed that the proposed sensor was reasonable to obtain the corrosion state of structures. The most severe corrosive condition of 15% seawater in wet-dry cycle exhibited the lowest.

Through the electrochemical measurement tests in various environment conditions, it was found that the corrosion and the associated information have been accurately monitored by proposed sensor.

References

[1] Ahmad, S., Cement and Concrete Composites, vol. 25, 2003, pp. 459-471.

[2] Baessler, and Ralph, NACE, Corrosion Conference, Paper No. 07377, 2007, pp. 1-13.

[3] Bjegovic, D., Jackson, J., Mikulic, D., and Sekulic, D., "Corrosion measurement in concrete utilizing different sensor technologies", NACE, Corrosion Conference, Paper No. 03435, 2003, 1-9.

[4] Broomfield, J. P., "Corrosion of steel in concrete", E&FN Spon., 1997.

[5] Broomfield, J. P., "Corrosion of steel in concrete", 2nd ed. Taylor & Francis, 2007.

[6] F. J. Presuel-Moreno, S. C. Kranc, and A. A. Sagues, vol. 61. 2005.

[7] Qian, S. Y., Cusson, D., and Chagnon, N., Corrosion, vol. 59(5), 2003, pp. 457-468.

[8] Sagues, A. A., and Powers, R.G., Corrosion, vol. 52(7), 1996. pp. 508-522.

[9] J.A. Jeong, C.K. Jin, Y.H. Kim, W.S. Chung, JACT, vol. 11, 2013, pp.1-6

[10] J.A. Jeong, C.K. Jin, The effect of temperature and relative humidity on concrete slab specimens with impressed current cathodic protection system, vol. 37, Korean Society of Marine Engineers, 2013, pp. 260-265.

[11] Y.B. Ko, G.B, Kim, K.C. Park, Soundness evaluation of friction stir welded A2024 alloy by non-destructive test, vol.37, Korean Society of Marine Engineers, 2013, pp. 135-143.

[12] J.H. Jeong, Y.H. Kim, K.M. Moon, M.H. Lee, J.K Kim, Evaluation of the corrosion property on the welded zone of seawater pipe by A.C shielded metal arc welding, vol. 37, Korean Society of Marine Engineers, 2013, pp. 877-885.

[13] S.J. Kim, S.J. Lee, S.O. Chong, Effect of cavitation for electrochemical characteristics in seawater for austenitic 304 stainless steel, vol. 37, Korean Society of Marine Engineers, 2013, pp. 484-492.

[14] ASTM Standard G 59-91, Annual Book of ASTM Standards, vol. 3(2), pp. 230-233. 1994.

[15] ASTM C876-91, Annual Book of ASTM Standards, vol. 3(2), 1994.

[16] M. Saleem, M. Shameem, S.E. Hussain, M. Maslehuddin, Construction and Building Materials, vol. 10 ,1996, pp. 209-210.

[17] Gonzalez, J. A., Miranda, J. M., Feliu, S., Corrosion Science, vol. 46, 2004.J.P.Broomfield, “Corrosion of Steel in Concrete”, 2nd ed. edited by T&F, 2007, pp. 10–64.

Applied Mechanics and Materials Vol. 597 (2014) pp 425-430
© (2014) Trans Tech Publications, Switzerland
doi:10.4028/www.scientific.net/AMM.597.425

A Theoretical Study of the Phase Angle for the β type Pulse-Steam Stirling Expander

Guang-Jer Lai[1, a], Chen-Kuang Lin[1, b], Yoshiyuki Kobayashi[2], Masahiro Matsuo[3], Min-Chie Chiu[4, c*]

[1] Department of Mechanical Engineering, Tatung University, No.40, Sec. 3,Zhongshan N. Rd., Taipei City 104,Taiwan, ROC.

[2] Ibaraki Chuo High School, Japan

[3] Saitama University, Japan

[4] Department of Mechanical and Automation Engineering, Chung Chou University of Science and Technology, No. 6, Lane 2, Sec.3, Shanchiao Rd., Yuanlin, Changhua 51003, Taiwan, ROC.

[a]gjlai@ttu.edu.tw, [b]tenlater@hotmail.com, [c]minchie.chiu@msa.hinet.net

Keywords: pulse steam expander, Stirling engine, phase angle.

Abstract. This paper introduces a small steam expander linked to a moderate/small industrial steam boiler to form a small scale cogeneration system for the purpose of energy conservation and carbon-emission reduction. Here, a traditional regulator will be replaced by the steam expander. In order to effectively extract the high pressure steam's unused energy (flow energy) from the boiler, the steam will be induced into an expanding process. Here, a Pulse-Steam Stirling Expander (PSSE), which is different from a normal steam expander, is proposed in the study. In order to decrease the steam condensation and increase the overall output power, the PSSE expander adopts an isothermal process instead of the traditional isentropic process. The PSSE cycle, which is composed of an isothermal process and an isovolumetric process, is similar to the Stirling cycle. Therefore, considering the influence of the valve's opening/closing within the PSSE cycle and adopting the Stirling engine's Schmidt theory, the mathematical model of the PSSE cycle has been established. The characteristic analysis of the PSSE expander has been assessed based on the mathematical model. Moreover, a prototype of the PSSE expander has been constructed and tested. According to theoretical analysis and experimental data, the output power for the PSSE expander is closely related to the phase angle between the displacer and the piston. Consequently, the mathematical model of the PSSE expander proposed in this study can be applied to design the practical PSSE expander in industry.

Introduction

Because of the recent interest in energy conservation and carbon-emission reduction, creating a high efficiency co-generation system is crucial. A high scale co-generation system has currently been developed. In order to fully promote the availability for all industrial stream supplying systems, establishing a small scale co-generation system is compulsory. Furthermore, the small steam expander will be the key technique to enhance the efficiency of the small scale co-generation system. In this study, the construction of the PSSE expander is based on the CO_2 powered engine shown in Fig. 1. Moreover, the isentropic expansion process of the traditional steam expander is replaced by the Stirling cycle's isothermal expansion process. This design will reduce the steam condensation during the expansion process and largely increase the efficiency of the output work [1].

Mathematical Model of the PSSE Expander

Design Principle of PSSE The β Type PSSE Expander. In a steam supplying system, a regulator can be replaced by a traditional steam expander to obtain useful output work. However, the steam quality will decrease during the expansion process. Especially in a small steam supplying system, steam condensation will easily occur. To overcome this drawback, the PSSE expander proposed in

this study will use an isothermal process to replace the isentropic expansion. Moreover, in order to fulfill the rear

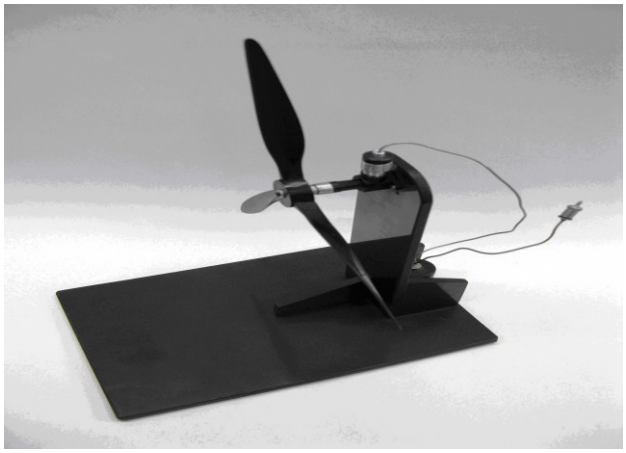


Fig. 1 CO_2 powered engine.

manufacturing process, the quality of the exhaust steam will be appropriately adjusted by controlling the inlet heat. The thermal cycle of the PSSE expander combines the isentropic-isovolumetric cycle and the Stirling cycle [2, 3]. The mechanism of the PSSE expander is the same as the CO_2 powered engine. The upward and downward movement of the piston will control the timing of valve's opening and closing. A phase angle between the displacer and the piston can be set. The phase angle is tightly related to the efficiency of the output work for the PSSE expander. Therefore, deciding the best phase angle for the PSSE engine to produce the greatest mechanical work is the main issue in this study. The cycle of the PSSE expander having two isothermal processes and two isovolumetric processes can be set the same as that of the Stirling cycle; therefore, the P-V diagram between the PSSE cycle and the Stirling cycle is similar. Hence, the Schmidt theory used for the Stirling engine is adopted to predict the best phase angle for the PSSE.

Schmidt Theory for Stirling Engine. In the study of Stirling engines, the Schmidt theory has been widely used to analyze the P-V diagram. The temperature and volume between the hot end and the cool end are the important factors. The internal transient pressure and transient volume and phase angle will be calculated using the ideal gas equation (PV = mRT). The P-V diagram is then plotted via the temperature and volume between the hot end and the cool end. Moreover, the P-V diagram will be plotted via the data of the transient pressure and transient volume.

Traditionally, the mechanical work of the β type Stirling engine is less than that of the α type Stirling engine. However, the β type Stirling engine has the advantage of being very efficient, having fewer mechanical parts, and costing less. Therefore, the β type Stirling engine is often adopted in industry. Fig.2 is the mechnism of the β type Stirling engine. The transient pressure and transient volume of the β type Stirling engine have been predicted using the Schmidt theory [4].

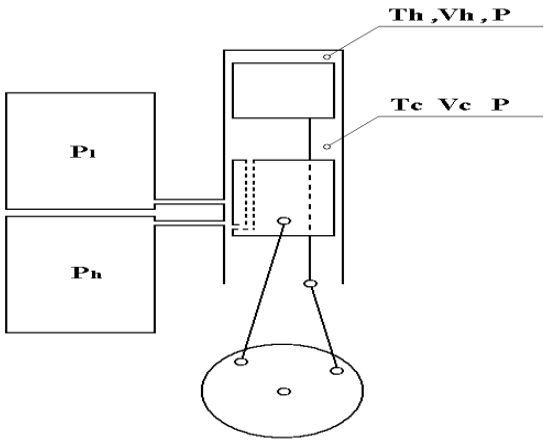


Fig. 2 PSSE expander.

The Schmidt calculation is listed below:
The relationship between the transient volume and the phase angle (θ) of the output axes at hot end space is

$$V_h = \frac{v_{sd}}{2}(1-\cos\theta) \quad (1)$$

Similarly, the transient volume at a cold end space is the summation of the cool end space and the piston's transient volume.

$$V_c = \frac{v_{sd}}{2}(1+\cos\theta) + \frac{v_{sp}}{2}(1-\cos(\theta-\alpha)) \quad (2)$$

The internal transient volume for the engine is the summation of the mentioned volumes and the internal dead space of the displacer.

$$V = V_h + V_c + V_{dh} + V_{dc} + V_r \quad (3)$$

The relationship of the internal working fluid's mass, pressure, temperature, and volume is expressed in an ideal gas equation.

$$m = \frac{PV}{RT} \quad (4)$$

The relationship of the volume and temperature can be classified into three parts (the hot end, the cool end, and the displacer)

$$m = \frac{PV_h}{RT_h} + \frac{P(V_{dh}+V_r+V_{dc})}{RT_r} + \frac{PV_c}{RT_c}; P = \frac{mR}{\frac{V_h}{T_h}+\frac{V_c}{T_c}+\frac{V_d}{T_d}} \quad (5)$$

The temperature ratio of the cool end and the hot end, volume ration, and the dead space ration are expressed as

$$\tau = \frac{V_c}{V_h}; \kappa = \frac{V_{sp}}{V_{sd}}; X = \frac{V_{dh}+V_r+V_{dc}}{V_h} \quad (6)$$

The overlapped volume ratio of the displacer and the piston is

$$X_B = \frac{V_b}{V_{sd}} \quad (7)$$

Plugging Eqs.(6) and (7) into Eq.(5) yields

$$m = \frac{P}{RT_c}\left(\tau V_h + \frac{2\tau(V_{dh}+V_r+V_{dc})}{1+\tau} + V_c\right) \quad (8)$$

Assuming that

$$\phi = \tan^{-1}\frac{\kappa \sin\alpha}{\tau + \kappa\cos\alpha + 1}; S = \tau + \frac{4\tau X}{1+\tau} + \tau + 1 - 2X_B$$

$$B = \sqrt{\tau^2 + 2\kappa(\tau+1)\cos\alpha + \kappa^2 + 2\tau + 1}; \delta = \frac{B}{S} \quad (9)$$

Plugging Eq.(9) into Eq.(8) yields

$$P = \frac{2mRT_c}{V_{mh}(S - B\cos(\theta-\phi))} \quad (10)$$

Eq.(10) is rearranged and written as

$$P = \frac{P_{mean}\sqrt{1-\delta^2}}{1 - \delta \cdot \cos(\theta-\phi)} \quad (11)$$

Analysis of the β type PSSE Expander by Schmidt Theory. To simplify the analysis, the prototype PSSE is designed with no overlapped space between the displacer and the piston. It means that V_b and X_B are zero.

$$X_B = \frac{V_b}{V_{sd}} = 0$$

$$P = \frac{P_{mean}\sqrt{1-\delta^2}}{1-\delta\cdot\cos(\theta-\phi)} \quad (12)$$

The internal transient pressure (P) will be the same as the pressure source (P_h) when the intake valve opens. Plugging the θ_{hvc} and P_h ($P=P_h$ at $\theta_{hvo} > \theta > \theta_{hvc}$) into the equation, the average effective P_{mean-e} for the isothermal expansion process can be obtained. The transient pressure will be the same as the pressure source when the intake valve opens. Therefore, it is

$$P_e = \frac{P_{mean-e}\sqrt{1-\delta^2}}{1-\delta\cdot\cos(\theta-\phi)} \quad \text{at } \theta_{hvc} > (\theta-\alpha) > \theta_{lvo} \quad (13)$$

$$P_h = \frac{P_{mean-e}\sqrt{1-\delta^2}}{1-\delta\cdot\cos(\theta_{hvc}-\phi)} \quad (14)$$

$$P_{mean-e} = \frac{P_h(1-\delta\cdot\cos(\theta_{hvc}-\phi))}{\sqrt{1-\delta^2}} \quad (15)$$

$$P_e = \frac{P_h(1-\delta\cdot\cos(\theta_{hvc}-\phi))}{1-\delta\cdot\cos(\theta-\phi)} \quad \text{at } \theta_{hvc} > (\theta-\alpha) > \theta_{lvo}) \quad (16)$$

Similarly, the internal transient pressure will be the same as the exhaust pressure (P_h) when the exhaust valve opens. Plugging the θ_{lvc} and P_c into equation, the average effective P_{mean-c} for the isothermal compression process can be obtained. It is

$$P_c = \frac{P_{mean-c}\sqrt{1-\delta^2}}{1-\delta\cdot\cos(\theta-\phi)} \text{ (where } \theta_{lvc} > (\theta-\alpha) > \theta_{hvo}) \quad (17)$$

$$P_l = \frac{P_{mean-c}\sqrt{1-\delta^2}}{1-\delta\cdot\cos(\theta_{lvc}-\phi)} \quad (18)$$

$$P_{mean-c} = \frac{P_l(1-\delta\cdot\cos(\theta_{lvc}-\phi))}{\sqrt{1-\delta^2}} \quad (19)$$

$$P_c = \frac{P_l(1-\delta\cdot\cos(\theta_{lvc}-\phi))}{1-\delta\cdot\cos(\theta-\phi)} \text{ (where } \theta_{lvc} > (\theta-\alpha) > \theta_{hvo}) \quad (20)$$

The relationship of P-θ and V-θ for the PSSE cycle can be obtained as

$$P = P_e = \frac{P_h(1-\delta\cdot\cos(\theta_{hvc}-\phi))}{1-\delta\cdot\cos(\theta-\phi)} \quad \text{at } \theta_{lvc} > (\theta-\alpha) > \theta_{lvo} \quad (21)$$

$$P = P_c = \frac{P_l(1-\delta\cdot\cos(\theta_{lvc}-\phi))}{1-\delta\cdot\cos(\theta-\phi)} \quad \text{at } \theta_{lvc} > (\theta-\alpha) > \theta_{hvo} \quad (22)$$

$$P = P_h \text{ at } \theta_{hvo} > (\theta-\alpha) > \theta_{hvc} \quad (23)$$

$$P = P_l \text{ at } \theta_{lvo} > (\theta-\alpha) > \theta_{lvc} \quad (24)$$

$$V_h = \frac{V_{sd}}{2}(1-\cos\theta) \quad (25)$$

$$V_c = \frac{V_{sd}}{2}(1+\cos\theta) + \frac{V_{sp}}{2}(1-\cos(\theta-\alpha)) \quad (26)$$

$$V = V_h + V_c + V_{dh} + V_{dc} + V_r \quad (27)$$

According to the above Eqs.(21)~(27), the theoretical P-V diagram of the PSSE cycle is plotted in Fig. 3. As indicated in Fig. 3, the first process is one part of the high pressure Stirling cycle. The second one is the isovolumetric exhaust process. The third is one part of the low pressure Stirling cycle. The fourth is the isovolumetric intake process. So, the PSSE's isothermal expansion process is in agreement with the upper part of the Stirling cycle A ($\theta_{lvc} > (\theta-\alpha) > \theta_{lvo}$). The PSSE's isothermal compression process is in agreement with the lower part of the Stirling cycle B ($\theta_{hvc} > (\theta-\alpha) > \theta_{hvo}$). Theoretically, the internal pressure will suddenly rise and remain the same when the intake valve opens. Therefore, the pressure will remain the same as the P_h (the high pressure source) when the

intake valve opens ($\theta_{hvo} > (\theta-\alpha) > \theta_{hvc}$). Moreover, the pressure will remain the same as the P_l (the low pressure source) when the exhaust valve opens ($\theta_{lvo} > (\theta-\alpha) > \theta_{lvc}$).

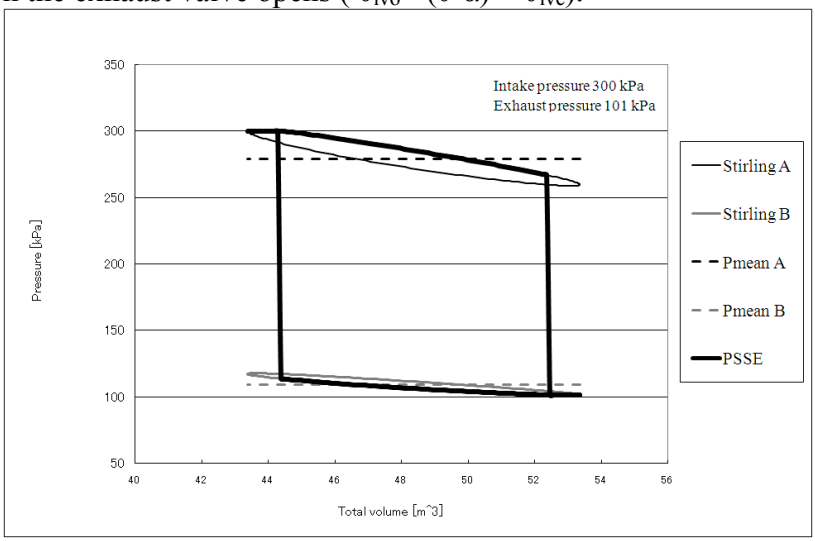


Fig. 3 Ideal PSSE cycle.

Results and Discussion

The purpose of this paper is to establish a prediction method for the PSSE cycle's output work. The related essential design parameters, such as the phase angle, can be decided by using a theoretical prediction. Based on the prototype of the β type PSSE expander, the best phase angles of the PSSE a will be fully assessed. By plugging the related dimensions of the prototype PSSE and the operating condition into the theoretical formula, the related PSSE's P-V diagrams with respect to various operating conditions can be plotted. The area of the P-V diagrams represents the outputted mechanical work. Here, the phase angle will be varied by 1° per each time by fixing the other parameters. The related mechanical work with respect to the phase angle is plotted in Fig. 4. As indicated in Fig. 4, the mechanical work reaches the maximum when the phase angle is 19°.

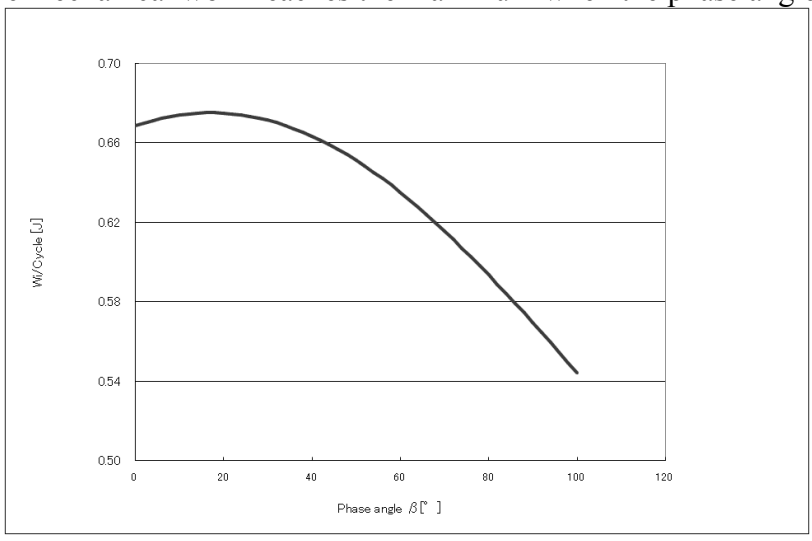


Fig. 4 Outputted mechanical work with respect to the phase angle for the PSSE cycle.

The primary difference between the PSSE cycle and the Stirling cycle is the intake and exhaust of the high pressure working fluid. The cylinder space will connect with the pressure source or the atmosphere, and the internal pressure will be kept at the high pressure or the low pressure when the valves opens. Based on the mechanism character of the PSSE, the internal pressure will rise due to the heat transfer of the displacer and the working fluid when the valve closes. The time interval for the displacer's movement at the maximal speed and the valve opening will be overlapped when the phase angle is set at 90°; therefore, the working fluid 's heat absorbed from the displacer and the hot end will not increase the pressure much. On the other hand, the displacer will move at the maximal speed when

the valve closes if the phase angle is set at 19°; therefore, the working fluid ‘s heat absorbed from the displacer and the hot end will greatly increase the pressure and produce maximal mechanical work. By plugging the design parameters of the PSSE and related operating conditions into the theoretical formula, the resulting P-V diagram with respect to various cycles is plotted in Fig. 5. As indicated in Fig. 5, the dark profile represents the PSSE cycle at phase angle (α) of 19°. In addition, the deep gray profile represents the PSSE cycle at phase angle (α) of 90°. Moreover, the shallow gray profile is the isentropic-isovolumetric cycle.For the three kinds of cycles in Fig. 5, the valve opening/closing timing are set the same; therefore, the three cycles are fully overlapped at the isovolumetric process. The mechanical output works of the three cycles will be different due to different expansion processes. Fig. 5 indicates that the P-V area of the PSSE cycle with α=90° is larger than that of the isentropic-isovolumetric cycle. Moreover, the P-V area of the PSSE cycle with α=19° is larger than that of the PSSE cycle with α=90°. The increment percentage of the P-V area is 12.59% around.

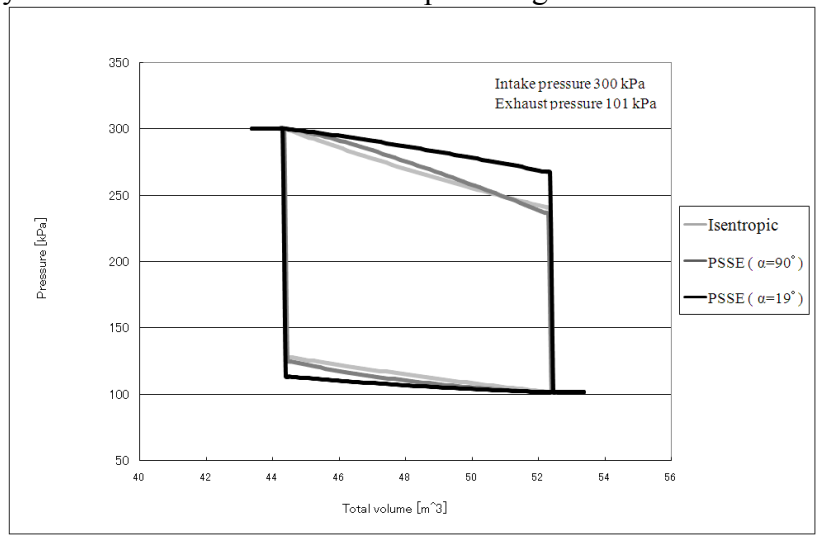


Fig. 5 P-V diagram for PSSE cycle at α=19° and α=90°.

Conclusion

Based on the Schmidt theory, to obtain the best design parameters for the β type PSSE expander, a theoretical mathematical model is established. Considering the valve’s opening/closing effect, the best design parameter was approached by using the theoretical mathematical model. Results reveal that the phase angle (α) influences the outputted mechanical work. Therefore, the investigation of the best phase angle (α) to generate a maximal mechanical work has been assessed in this study. Some conclusions are made and listed below:

A. The theoretical model of the PSSE cycle was established by adding the high pressure steam intake process and exhaust process to the Schmidt’s Stirling model. The simulated results reveal that the outputted mechanical work will be the maximal if the phase angle (α) between the piston and the displacer is set at 19°. In developing the PSSE expanders with various specification in future, the best phase angle (α) to produce the maximal mechanical work can be assessed by using the proposed theoretical model.

B. Results reveal that under the same running condition, the mechanical outputed work of a PSSE cycle with α=19°is larger than that of an isentropic-isovolumetric cycle by 30%.

References

[1] T. Brookes, CO2 Powered Model Aircraft, Nexus Special Interests, 2002.

[2] Kobayashi Yoshiyuki, Model steam rankine Stirling engine for educational use, The Symposium on Stirlling Cycle 12 (2009) 83-84.

[3] G. Walker, Stirling Engines, Oxford Univ. Press, 1980.

[4] D.G. Thombare, S.K. Verma, Technological development in the Stirling cycle engines, Renewable & Sustainable Energy Reviews 12(1) (2008) 1-38.

Applied Mechanics and Materials Vol. 597 (2014) pp 431-434
© (2014) Trans Tech Publications, Switzerland
doi:10.4028/www.scientific.net/AMM.597.431

Damage Identification of the Blade based on Distributed Fiber Bragg Grating Sensors

Yan Hui Zhang[1,a], Wen Yu Yang[1,b*]

[1] State Key Lab of Digital Manufacturing Equipment and Technology, Huazhong University of Science and Technology, Wuhan, Hubei, 430074, China

[a]yanhuizhang86@gmail.com, [b]mewyang@mail.hust.edu.cn

Keywords: Blade, damage identification, fiber Bragg grating, structural health monitoring

Abstract. As the foundation work of the damage identification for the blade, the purpose of this paper is to determine which parts of the blade are more sensitive to the damage and how serious damage could affect the dynamic response of the blade structure. Several damage states are simulated using the magnets, and then the distributed fiber Bragg grating sensor system is used to measure the dynamic strain response of the blade under the random excitation. The dynamic strain time domain signal is first analyzed, and then the different damage states are identified. In order to eliminate the adverse affect of the environmental and operational variations, the Hilbert-Huang Transform method is used to extract the damage-induced signal component. Lastly the damage index based on the autoregressive model and Mahalanobis distance method is constructed to detect damage. Some conclusions are obtained from the experimental results.

Introduction

The blade failure usually leads to the major accident of the steam turbine, which could cause lots of the losses due to the long-term shutdown of the steam turbine. The damage often appears in the blade due to the fatigue, corrosion, and other factors. The blade damage may cause the accident of steam turbine. So the damage identification is an important foundation work to guarantee good performance of the blade.

Using fiber Bragg grating (FBG) [1-4] as the distributed sensor network to measure the dynamic strain response of the blade under the random excitation, this paper here strives to answer two basic questions: which parts of the blade are more sensitive to the damage and how serious damage could affect the dynamic response of the blade structure. In order to eliminate the adverse effects of the environmental and operational variations, this paper tries to extract the damage-induced signal component that is sensitive to the damage but insensitive to the environmental and operational variations using Hilbert-Huang transform (HHT). Then based on the autoregressive (AR) model and the Mahalanobis distance method, the damage-induced signal component is used to construct the damage index for the damage identification of the blade.

Experimental apparatus and procedure

One type of the nuclear power blade, as shown in Fig. 1, was used in the experiment. The length of the blade is 1146 mm. In order to reduce the gas corrosion, the welding hardening process was applied on one side of the blade edge. Also, in order to facilitate the analysis, the blade along the cross-section direction could be divided into three regions: root region, middle region, and edge region.

According to the symmetry of the blade structure, twenty-two FBGs were bonded on the surface of the blade to measure the dynamic strain response of the blade. These FBGs were assigned to three individual fibers to facilitate wiring and then connected to the three channels of the optical demodulator produced by Micron Optics Inc®. The sampling rate of the FBGs was set to 2 kHz. Fig. 1 is the arrangement of the FBG sensor network, in which the letter "C" is the abbreviation of "Channel" and "C1" to "C22" denote the twenty-two Channels of FBGs.

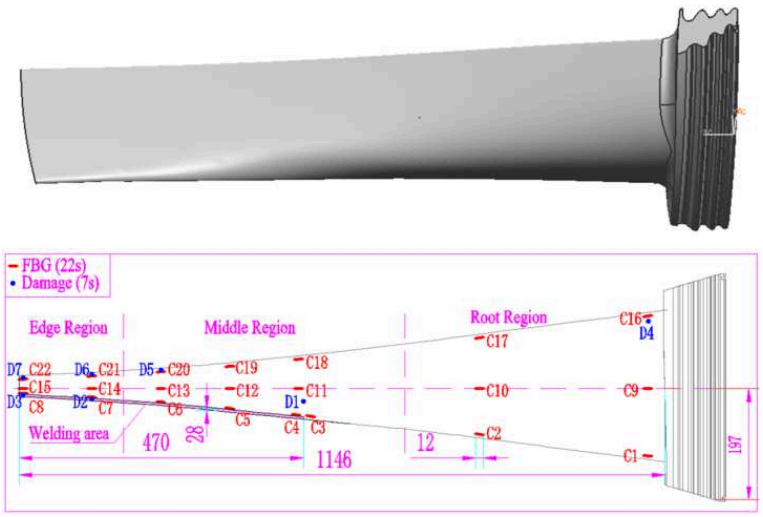


Fig. 1 Layout of the FBG sensors

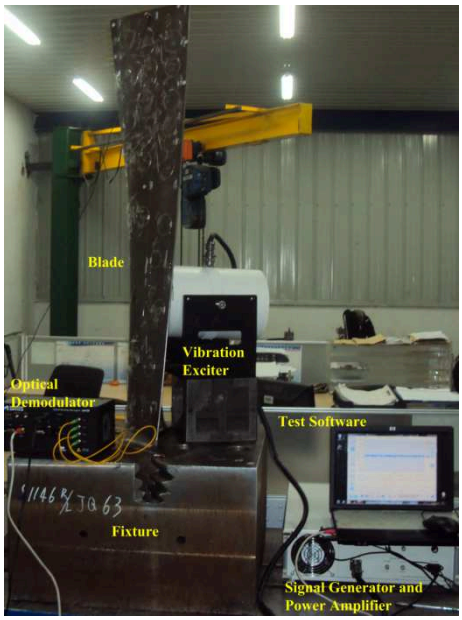


Fig. 2 Picture of the experiment

Due to the limitation of the experimental conditions, the fixture was used to cantilevered fix the blade, and then the excitation device provided the 0~5 kHz broadband random excitation to the blade. The picture of the experimental real objects can be seen in Fig. 2.

In order to simulate the different damage states of the blade, several different specifications of the magnets were used as the mass blocks, and then were placed on the different regions of the blade. According to the weight of the added magnets, the eleven different damage states were designed, which are summarized in Table 1. According to the shape of the blade, seven specific regions are selected to place the mass blocks, as shown in Fig. 1, in which "D1" to "D7" denote the seven simulated damages at the seven different regions.

Table 1 Details of different health states

State	Added weight at each position (g)	Description
State 1	0	Baseline state, no magnet
State 2	1.42	One small magnet
State 3	2.54	One middle magnet
State 4	7	One large magnet
State 5	9.54	One middle magnet and one large magnet

The strain spectra of the dynamic strain responses from channels 1 to 15 in the undamaged state are shown in Fig. 3.

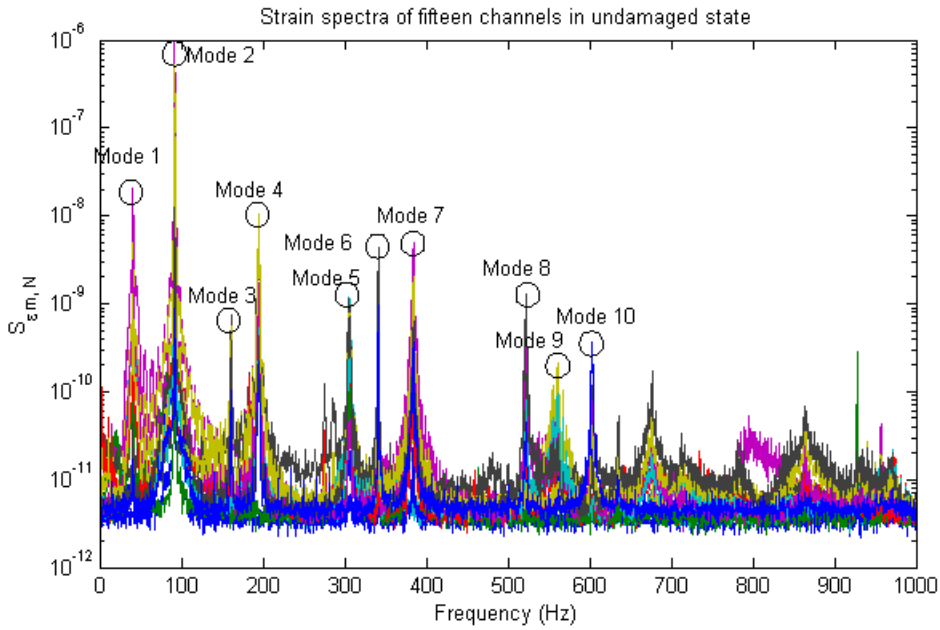


Fig. 3 Strain spectra of fifteen channels in undamaged state

Table 2 summaries the modal frequency respectively estimated from the hand tapping test and the vibration exciter test. In order to examine the identification accuracy of the modal frequency, the frequency requirement of the blade machining process card is also shown in Table 2.

Table 2 Frequency identification results of the blade

Mode	Process card (Hz)	Vibration exciter (Hz)	Hand tapping (Hz)	Error(%)
Mode 1	39~41	40.3226	39.8720	-1.1175
Mode 2	90~96	93.3180	95.4270	2.2600
Mode 3	155~165	160.1382	161.3681	0.7680
Mode 4	185~198	197.0046	195.6210	-0.7023
Mode 5	296~310	307.6037	298.3108	-3.0211
Mode 6	330~354	342.1659	335.0456	-2.0809

When the blade frequencies are located in this interval, the blade is qualified. As can be seen from Table 2 above, the identified modal frequencies from the vibration exciter test are close to that from the hand tapping test, which are all located in the required range of the process card.

Modeling Process for Damage Identification

The purpose of the damage identification here is to determine: which parts of the blade are more sensitive to the damage; how serious damage would cause the change of the dynamic strain response of the blade. However, only the time domain analysis of the dynamic strain signal cannot quantitatively determine the change of the signal. Therefore, in order to identify the change of the signal from the different damage states and to quantify the severity of the damage causing the change of the signal response, the statistical pattern recognition method is used to model the dynamic strain response.

In the actual case, not only the damage causes the change of the strain response of the structure, but also the environmental and operational variations, such as the different excitation load and environmental temperature, could lead to the change of the signal response. HHT-based signal

decomposition method is used to eliminate the adverse effects of the environmental and operational variations [5,6]. Then the AR-based method is used to extract the damage features, and the Mahalanobis distance-based method is used to identify the damage [7].

Conclusions

From the strain time domain signal analysis, the strain response at the blade middle region is the most obvious, alternatively, the strain responses at the blade root and edge regions are relatively smaller. By discussing the effect of the weld hardening on the strain response, we can find that the amplitude of the strain response at the welding area is smaller than that of the non-welding area.

From the damage identification results, the following conclusions can be got:

The blade root region is insensitive to the damage. For example, the damage, D4, is placed near Channel 16. But with the increase of the damage serious, the damage has little effect on the dynamic strain response of this region, which does not indicate the existence of the damage. For the blade middle region, the two side parts are more sensitive to the damage than the central part. For example, although Channel 18 is far from the damage, D1, Channel 18 also indicates the existence of the damage, which is similar to the identification result of Channel 3. Alternatively, Channel 11 does not indicate the existence of the damage. The blade edge region is sensitive to the damage. For example, Channel 7, 8, 15, and 22 all indicate the presence of the damage.

Acknowledgments

This work was supported by the Major State Basic Research Development Program of China (973 Program) (No. 2014CB046704).

References

[1] J.R. Lee, C.Y. Ryu, B.Y. Koo, S.G. Kang, C.S. Hong, C.G. Kim, In-flight health monitoring of a subscale wing using a fiber Bragg grating sensor system, Smart materials and structures, 12(2003) 147.

[2] D.H. Kang, C.U. Kim, C.G. Kim, The embedment of fiber Bragg grating sensors into filament wound pressure tanks considering multiplexing, NDT & E International, 39(2006) 109-116.

[3] M. Amano, I. Takahashi, Y. Okabe, N. Takeda, H. Takeya, T. Ozaki. Identification of Damage Location in Advanced Grid Structures Using Fiber Bragg Grating Sensor--T. Masayoshi, ed.: SPIE, (2005) 644-655.

[4] A. Panopoulou, T. Loutas, D. Roulias, S. Fransen, V. Kostopoulos. Dynamic Fiber Bragg Gratings Based Health Monitoring System of Composite Aerospace Structures. Acta Astronautica. 2011.

[5] P.F. Pai, L. Huang, Hilbert-Huang decomposition of time signals for structural damage detection, SPIE2006, p. 61770.

[6] J.A. Oliver, J.B. Kosmatka, Evaluation of the Hilbert-Huang transform for modal-based structural health monitoring applications, in: P.J. Shull, A.L. Gyekenyesi, A.A. Mufti (Eds.), Nondestructive Evaluation and Health Monitoring of Aerospace Materials, Composites, and Civil Infrastructure IV2005, pp. 274-285.

[7] H. Sohn, C. Farrar, N. Hunter, K. Worden. Applying the Lanl Statistical Pattern Recognition Paradigm for Structural Health Monitoring to Data from a Surface-Effect Fast Patrol Boat: Los Alamos National Lab., NM (US), 2001

Applied Mechanics and Materials Vol. 597 (2014) pp 435-438
© (2014) Trans Tech Publications, Switzerland
doi:10.4028/www.scientific.net/AMM.597.435

Design of Electrochemical Biosensor on Naphthalene Content Detection in Water Based on SCM

Liu Yuan[1,a], Yu Yaping[1,b*], Wu Haiyun[1,c], Chang Ruokui[1,d]

[1]College of Engineering and Technology, Tianjin Agricultural University, Tianjin 300384, China

[a]lywlywzwzly@126.com,[b]yaping261@163.com,

[c]haiyunwu2013@163.com,[d]529007475@qq.com

Keywords: SCM; Naphthalene content; Three-electrode electrochemical system;Biosensor

Abstract: In order to achieve rapid detection of naphthalene content in water, the electrochemical biosensor has been developed based on microcontroller by the cyclic voltammetry (CV). The system is consisted of a three-electrode electrochemical system, converting circuit, IAP15F2K61S2 microcontroller and display unit. The voltammetric oxidation-reduction response of a bare gold electrode has been gained in a potential window from −0.3 V to +0.6V. After data acquisition and processing, according to the change of peak current of voltammograms, the naphthalene content is detected and displayed.the sensor can finish the detection of naphthalene content in 15 minutes.

Introduction

With environmental pollution increasing, carcinogenic PAHs increasing, it has become one of the main substances harmful to people's health[1]. There are many kinds of PAHs, including naphthalene content of the component is maximum, which is usually found in water and soil. The design of the electrochemical biological immune sensor is used to detect naphthalene concentration in water.

Working Principle of the Sensor

The sensor is consisted of three-electrode electrochemical configuration, I/V converter and display unit (shown in Fig.1) [2]. When the three-electrode is laid into the test solution by the SCM to provide continuously a variable voltage signal from -0.3 to 0.6V. Excitation signal is accurately applied to the three-electrode electrochemical sensors through an external circuit constant potential to drive the sample solution and generate electrochemical reaction, the response signals are processed (ie, I/V signal conversion, amplification, filtering, A/D converter, and so on.) and then which are sent to the microcontroller. The peak currents are calculated by voltammetry curves. According to changes in cyclic voltammetry cathodic peak current, the content of naphthalene can be determined in the solution [3].

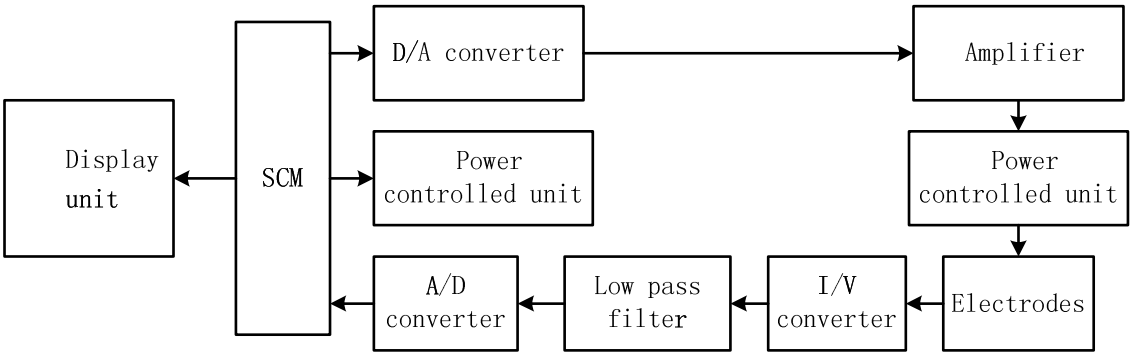


Fig.1 Three-electrode electrochemistry biosensor system

System Design

Design of Hardware System.

Three-electrode Electrochemical System. Electrochemical experiments were performed in a three electrode cell configuration using a reference electrode (SCE) and a platinum counter electrode. All potentials in the text are referred to the SCE. The working electrodes were gold in laid disk electrodes (d=2mm) which were mechanically polished with alumina polishing pads. Cyclic voltammetry (CV) were used for electrochemical characterization.

The electrolyte is consisted of potassium ferricyanide / potassium ferrocyanide + KCL + PBS. Electrode as a sensitive element, naphthalene antigen is fixed on the electrode surface, after the antigen antibody reacted with each other on the electrode to form an antigen - antibody complex, cyclic voltammogram cathodic peak current changes. According to changes in the cathodic peak current, the content of naphthalene in the solution can be determined.

Design of Signal Processing Circuit. Signal processing circuit is consisted of the micro-controller, A/D converters, voltage inverter, control amplifier, two voltage followers, I / V converter and low-pass filtering unit, as shown in Fig 2.

Potentiostat circuit is used to keep a constant potential between the working electrode and the reference electrode. The reference electrode is connected to the inverting terminal of the amplifier, the non-inverting input terminal of the amplifier connected the reference ground as reference potential, and the negative feedback closed loop system is formed by the auxiliary electrode connecting to output terminal of amplifier. When the current in the electrode is changed with respect to the reference potential, any minor changes in electrode potential will be corrected by the negative feedback circuit, so as to achieve the purpose of automatic constant potential[4,5].

Potentiostat circuit keeps the constant voltage between the working electrode and the reference electrode. Current signal is collected by the auxiliary electrode through the I/V conversion circuit, the low-pass filter circuit, then by IAP15F2K61S2 micro-controller computing, and shows the results.

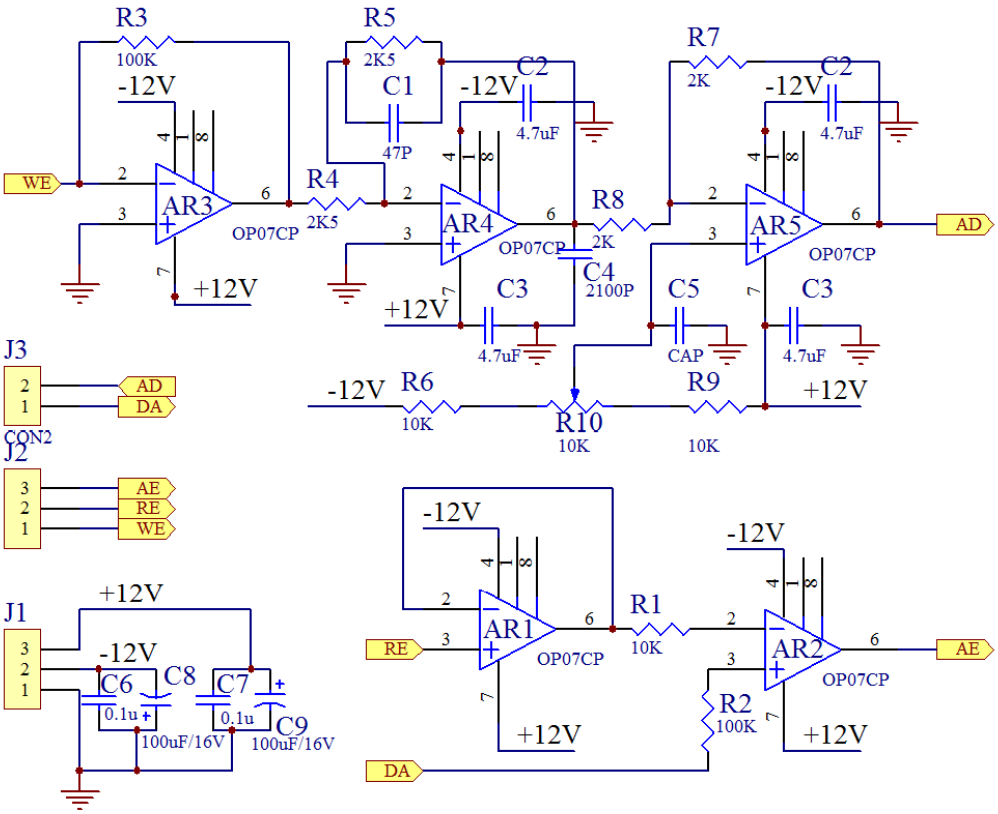


Fig.2 Potentiostat circuit

Generation of Excitation Signal. The part of the hardware circuit in Fig.3. Excitation signal, cyclic voltammetry, is given by the microcontroller to provide continuous voltage signal from -0.3

to 0.6V by D / A converter, optoelectronic isolator, amplification circuit, which is sent to the potentiostat circuit. In the excitation signal, chemical oxidation / reduction reactions on electrodes produces a current through the cyclic voltammograms measured to find the peak current.

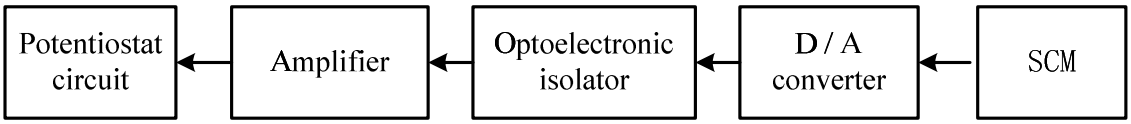


Fig.3 Generation of cyclic voltammetry signal

Design of Display Unit. Display module is adopted 12864 LCD. 12864 LCD is a kind of 4/8 bit parallel, two-wire or three-wire serial interface ways, which contains an GB one level, two level simplified Chinese character dot-matrix graphic LCD module; its display resolution is 128 × 64, it has 8192 16 * 16 characters, and 128 16 * 8 ASCII character set. Because of flexible interface module and convenient operation instructions, the Chinese human-machine interactive graphical interface can be constituted. In LCD connection circuit, the resistor, R_{25} , can adjust the display brightness.

Design of Software.

Design of Main Program . The main program is consisted of subprogram of data acquisition, data process, excitation signal generation and display unit.

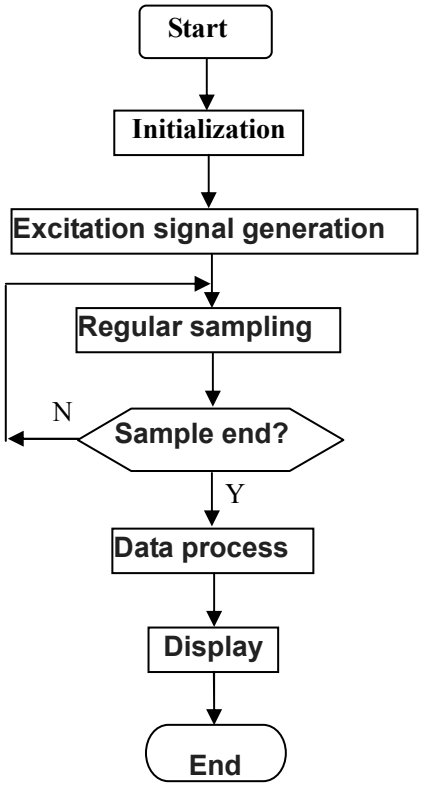


Fig.4 Block diagram of main program

Design of Excitation Signal Program. Scan signal, which is formed by the SCM, voltage range is from -0.3 to 0.6V.

Design of Display Program. 12864 LCD has the characteristic of flexible interface mode and simple, easy operation instructions, which we can get accurate and efficient detection data.

Tests and Analysis

Experiment Instrument and Methods. Before the test, peak value of current of the blank solution, that is to say, the sample did not contain the naphthalene, is for standardized value.then different concentrations of naphthalene content are tested by the sensors. First, the water which contained a certain amount of naphthalene was added to the sample cell and connected the circuit,

after the film modified electrode was laid in the solution 12 minutes, DPV signal excitation between -0.3V to 0.6V was adopted. 12864 LCD displayed the concentration of naphthalene .

After every sample was measured, the electrodes were laid in PBS buffer solution to renew the surfaces of those and to be repeated well.all tests have been done in room temperature.

Experiment Parameter Set. In order to gain test parameters, tests were done to get reference value by Electrochemical workstation CHI66D. The scan rate and sample time were determined. For the samples of different concentration,Multiple sample data are recorded from 3 min to 28 min. The experiment shows oxidation -reduction response of different concentration samples is changed obviously between 12min and 15 min.

Test. The concentration of samples is set individually 1.5PPb, 2.5 PPb, 3.5PPb , 5.5 PPb and 7.5 PPb，the number of certain concentration sample is 6. Current data were collected between 12 min and 15 min and peak value of current were gained. According to the relation between the peak value of current and concentration of samples, the test curve was gained.

Conclusions

The main factor of influence accuracy has the following aspect: The technology of film modified electrodes; Good Reproducibility of electrodes; The laid time of samples; Methods determined of standardize curves.

Electrochemical biosensor combines immunoassay, electrochemical with sensor technology, which has high selectivity, easy structure and easy use. The sensor can quickly finish the detection of naphthalene content in 15 minutes, which can provide the reference for studying portable instruments.

Acknowledge

The design is supported by Development Foundation of Tianjin Agricultural University (Project no. 2011N04; Project no. 2013N02).

References

[1] Xiao Fei. Study on Novel Electrochemical Immunosensors Based on Nanomaterials and Their Application in Food Safety Detection [D]. East China Normal University.(2012)

[2] WANG Zhao-yu, WU Xiao-ming, LIU Zhong-ming. Design of Three -electrode Electrochemical Detection System Based on C8051F020 Microcontroller[J].Chinese Journal of Medical Physics.30 (2013)3909-3912

[3] Chen Kun. Supervised by Associate ProStudy on On-chip Electrochemical Sensing System [D]. Chongqing University.(2011).

[4] Zhong Haijun, Deng Shaoping.Current state of research on potentiostat and applications of electrochemical detetion systems based on potentiostat[J]. Analytical instruments. 2(2009)2-5.

[5]YAO Yu-sheng, XIE Yong-ping, WEN Tao. Design of Potentiostat for Three-electrode Electrochemical Sensor [J]. Instrument Technique and Sensor.9(2009)23-25.

Applied Mechanics and Materials Vol. 597 (2014) pp 439-443
© (2014) Trans Tech Publications, Switzerland
doi:10.4028/www.scientific.net/AMM.597.439

Design of Reflective/Diffractive Objective Optical System for Handed Low-light Night Vision Google

Ning Li[1,a], Ruilan ZHANG[1,b]

[1]Beihua Univercity 3999 Binjiang Road, Jilin, Jilin, China 132013

[a]bhdxln@163.com, [b]bhdxzrl@163.com

Keywords: reflective/diffractive hybrid optical system, low-light night vision goole, Optical system design.

Abstract: For the design direction of low-light night vision goggle become more and more miniaturization and high image quality[1], this artical design a reflective/diffractive objective optical system with optical software ZEMAX. It combines diffractive elements with reflective elements to design a reflective / diffractive objective with a 14.5° field of view and a 1.0 / 1.2 relative aperture and a 95mm focal length , and it introduces an improved method based on primary aberration theory in reflective/diffractive hybrid optical system. Etching diffractive optical element on the mirror can be usful for correcting aberration and improving the image quality.

Intorduction

Low-light night vision google images the weak natural light at the photocathode of image intensifier, transforms the weak optical image into an enhanced electronic image for several times , and finally converts electronic image into optical image which is visible as light to human eyes[2]. With rapid development of technology, it has poised a higher demand for the volume and imaging quality. As a result, designing more suitable optical system has becoming increasingly attractive, it is significant for application [3].

Although the traditional objective optical system satisfies some demands, but it can't satisfy with large field of view, large relative aperture , good image, wide wave range and more smaller at the same time.In order to satisfy all above, this paper depends on the particular performance advantage of diffractive optical elements in optical design, such as beneficial to correct optical aberration, has less secondary spectroscopic and increase the field of view. Applying diffractive optical elements on the Cassegrain form, a modification of reflection/ diffraction primary aberration theory has been used and diffraction facial parameter has been derived. According to this we design a reflective/diffractive objective optical system with optical software ZEMAX.

Rationale of objective optical system

Low-light night vision google is to be met to enjoy the use condition of day and night, so the spectral range not only includes visible, but aslo includes near-infrared[4]. This paper chooses the spectral range for 400nm～900nm and uses the secondary inverting image intensifie, focal distance of objective is 95mm with a 14.5° field of view and a 1.0/1.2 relative aperture. This design demands the modulation transfer function is no less than 0.6 at 20c/mm frequency and at least 0.35 at 40c/mm frequency in 0.7 field of view.

As this design chooses a width spectral range, there will be large secondary spectroscopic and chromatic aberration in pure refraction system. We consider using diffractive optical elements instead of original method, it can enlarge the field of view and avoid using high aspheric in the

optical system at the same time. As advantage of diffractive optical elements for unique dispersion, good thermal performance, wide choice of material and facial feature, it has found a wide variety of practical applications in reflective/diffractive hybrid optical system..

The paper has determined the initiating structure of refractive and reflective objective optical system at first , then inserted diffractive optical elements on the primary mirror and secondary mirror. It can be assumed the diffraction coefficient depending on the phase function equation of diffractive optical elements and optimized again.

Depending on the outline dimensional parameters and Gaussian formulae[5], we can conclude:

Shading ratio, that is the secondary mirror distance from the focus of the primary mirror:

$$\alpha = \frac{l_1}{f_1^{'}} \tag{1}$$

l_1 is the distance of object to the secondary mirror, $f_1^{'}$ is the focus of the primary mirror;

Magnification of the secondary mirror: $\beta = \frac{l_1^{'}}{l_1}$ (2)

$l_1^{'}$ is the distance of the secondary mirror to image;

Curvature radius of the primary mirror: $r_1 = \frac{2D}{D/f^{'}} = 2f^{'}$ (3)

D is the masking aperture of the primary mirror;

Curvature radius of the secondary mirror: $r_2 = r_1 \cdot \frac{\alpha\beta}{1+\beta}$ (4)

Optimal design of objecive optical system

1)Ascertainment to the initiating structure of reflective/diffractive hybrid Cassegrain objective optical system.

Figure 1 is the structure drawing of conventional Cassegrain objective optical system. According to the requirement of this design, the focus of system is 95mm , relative aperture is1/1.2, it uses Cassegrain system to make the structure more compact and fulfill a miniaturization requirement.

We substitute above requirements into(3), it can be obtained primary mirror radius is 190mm. Then depending on(1) (2)(4)three expression which can ascertain secondary mirror curvature radius is 1800mm. And adding three lens behind secondary mirror to consist of correction lens, these are BAK7,BAK7,Q1 glasses.

2)After obtaining initiating structure for curvature radius , interval of primary mirror and secondary mirror ,then do optimal design.

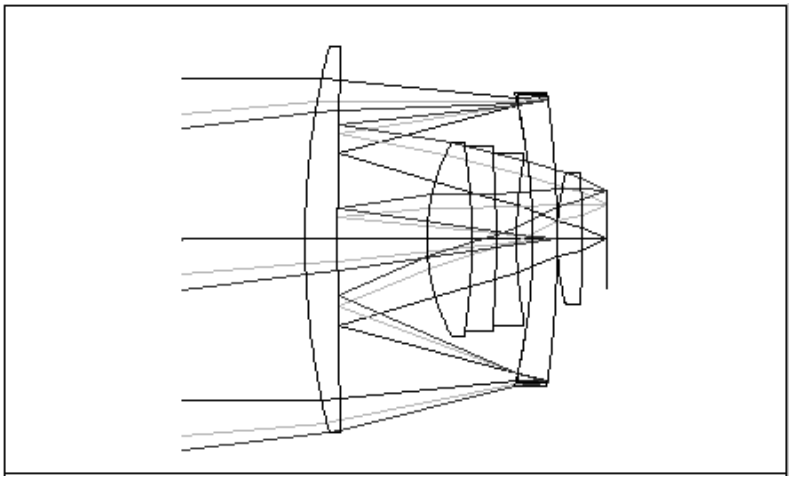


Figure 1 Initiating structure of objective optical system

Optimization is usually chosen curvature radius and interval of primary mirror and secondary mirror as variables, so as structure and material of subsequent lens group[6].In this design, chooses primary and secondary mirror as quadrics, subsequent lens as spherical. It is optimized by changing structural parameter such as curvature radius of primary and secondary mirror and quadrics,etc. The system structure is received by using optical software ZEMAX as in fig. 2 and fig. 3 shows transfer function for different fields of view. As you can see from figure 2-3, the imaging quality in large field is far deviation from diffraction limit and fail to meet using requirements.

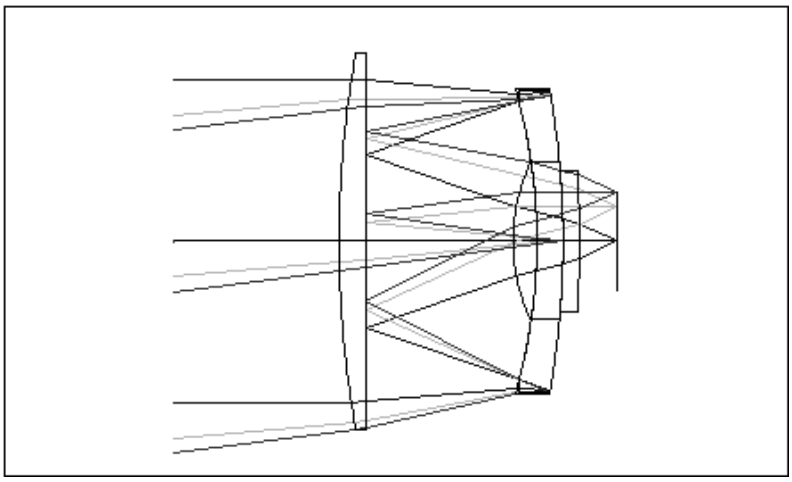


Figure 2 Postoptimality structure of objective optical system

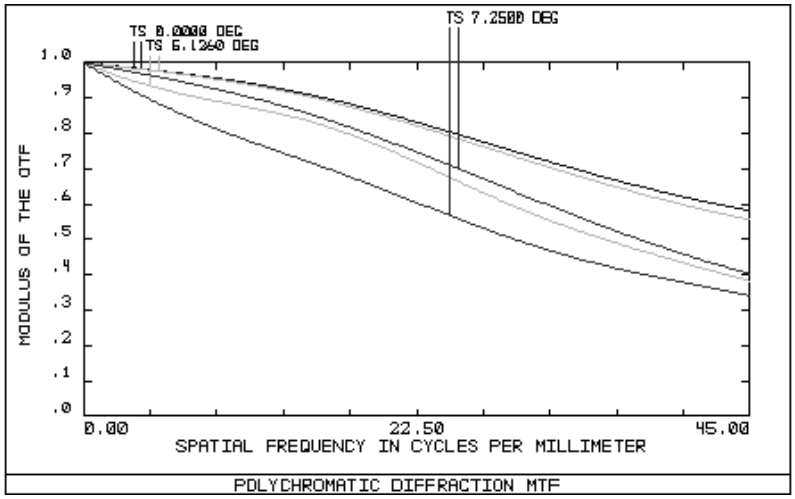


Figure 3 Postoptimality transfer function of objective optical system

3) add diffractive optical elements

In general, people put diffractive elements on the subsequent eyepiece lens when designing such optical system. Yet this design considering etch diffractive optical elements at the mirror's surface, so it can enlarge the field of view while at the same time optimize performance criteria.

Phase function of axis symmetric structure of diffractive optical elements is:

$$\varphi(r) = C_2 r^2 + C_4 r^4 + C_6 r^6 + \ldots$$

C_{2i}(i=1,2,3…) is phase coefficient, r represents radial coordinates of diffractive optical elements. We first work out the coefficient of diffractive optical path difference C_2, $C_2$is often used for eliminating chromatic aberration, C_4 can eliminate spherical aberration, C_6 is the higher-order terms which can be used improvement imaging quality. During design, we find it can bring more spherochromatic aberration if optimize C_6 again after optimizing C_2, C_4. So we usually optimize C_2 and C_4 only to avoid more spherochromatic aberration for system. Structure parameter of primary and secondary mirror is shown in Table 1.

Table1 Diffraction structural parameter of primary and secondary mirror

		Max term#	Norm Radius	Coeff.on p^2	Coeff.on p^4
1	Standard				
STO	Binary 2	2	1.000000	0.005687	-1.445428E-008
3	Binary 2	2	1.000000	-0.035645	3.0867098E-007

Fig. 4 is the postoptimality structure of reflective/diffractive hybrid Cassegrain objective optical system. Fig.5 is the optical transfer function in different fields of view and all fields of view are reached at diffraction limit, MTF at 40lp/mm is above 0.4.

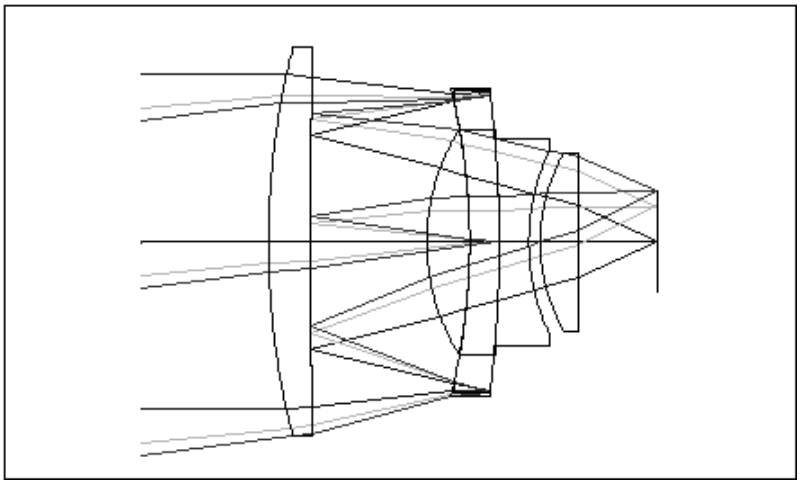


Figure 4 Reflective/diffractive hybrid objective optical system

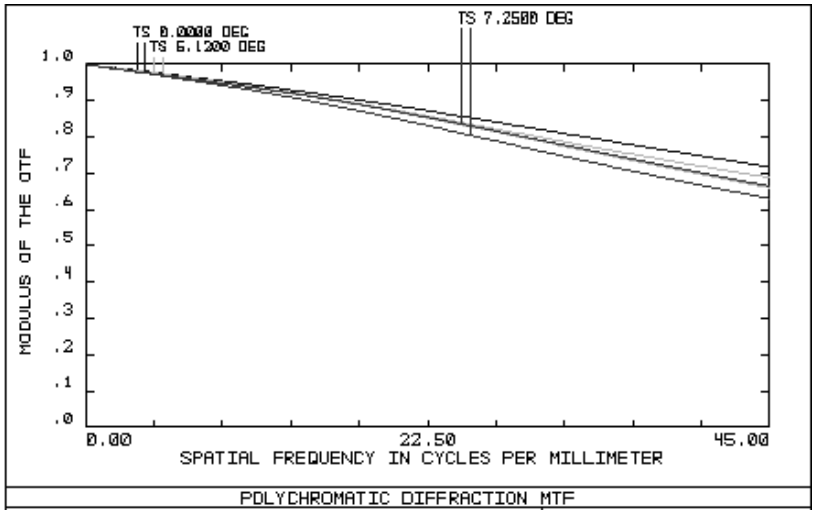


Figure 5 Transfer function of reflective/diffractive hybrid objective optical system

Conclusion

In this paper, using optical software ZEMAX, we design objective optical system of low-light night vision goggle through choosing etching diffractive optical elements on the mirror. And ultimately we received good image quality. Using diffraction can not only facilitate correct imaging quality of system, but aslo not add complexity of system structure. As development of imaging performance and processing technology, more and more reflective/diffractive hybrid system can be used in all fields.

References

[1]Rouke Jennifer L,Crawford Mary Kate, Fischer David J.et at. Design of three-elementnight-vision goggle objectives[J].Appl. Opt. , 1998, 37: 622-626.

[2] WANG Xi-jun, ZHOU Hai-xian. Design of reractive-diffractive hybrid objective lens in airborne night vision goggle[J].2002,Vol.9 No.3

[3] LIU Jun, LIU Xin. Miniaturization Design of Objective Lens Optical Systems Used in Low-Level-Light Night Vision[J].2009,29(6)

[4] WANG Yong-zhong. Modern military optical technology[M].Beijing:Science Press, 2003.

[5] LIN Yin-sen. The primary aberration characteristics analysis of the mangin mirror[J]. Optical Instruments,1981(2):53-61

[6]TANG Yong, LI Yuyao. ZEMAX's Application in Dimension Calculation of Optical Design[J].Journal of changchun university of science and technology, 2009,32(2).

Applied Mechanics and Materials Vol. 597 (2014) pp 444-449
© (2014) Trans Tech Publications, Switzerland
doi:10.4028/www.scientific.net/AMM.597.444

Fault Diagnosis of Mechanized Bridge's Electrical System Based on I2C-bus and Virtual Instrument Technology

Sun Yongsheng, Yang Xiaoqiang[a,*], Li Pei and Sun Yan

[1]PLA University of Science and Technology, Nanjing 210007, China

[*]Corresponding author, [b]yanglab@126.com

Keywords: Dedicated Interface Adapter, I2C bus, Fault Diagnosis, Embedded equipment, Mechanized bridge.

Abstract. The electrical system fault testing and diagnosis system based on I^2C-bus and embedded equipment is proposed. This system is accomplished with the integration of PXI-based computer, field fault testing platform, dedicated interface adapter unit and accessories with software program of virtual instrument and database management and fault guidance system. It can obtain various state parameters of the heavy mechanized bridge by interface adapter unit and corresponding sensors. The dedicated interface adapter unit, that is the core of the hardware platform is composed of chassis, embedded microcomputer controller, I^2C-bus data acquisition modules, VPC connection package and military aviation sockets. Because of its flexibility and modular design, it can support different data conversion, for example, analog, digital, and serial, while functioning as an intelligent conversion bridge between field fault testing platform or PXI computer and electrical system of heavy mechanized bridge electrical system. The fault diagnosis software is of hierarchical modular structure with integration of system management control, fault detection and circuit hardware driver modules together with fault repair and diagnosis database. Therefore it provides functions of human-machine interaction, equipment fault detection, fault diagnosis and analysis, as well as repair and maintenance guidance The fault testing and diagnosis system in this work is also featured with handy structure, lightweight, low consumption, large storage capacity, excellent expandability and intelligent inference capability. The system can be used in the online fault testing and diagnosis of similar engineering equipments. So it has important engineering and military application value to the rapid fault testing and fault diagnosis of engineering equipments.

Introduction

Because the heavy mechanized bridge is usually used in open field of river and lake, it will face various technical problems and difficulties in operation to perform field fault diagnosis using intelligent fault testing system based on microcomputer platform. Thus many current fault diagnosis systems cannot be applied in its failure troubleshooting. How to develop novel fault diagnosis system and maintenance system for the mechanized bridge comes to be an important task. In this work, the data acquisition, signal processing, expert system as well as embedded technology are comprehensively applied to develop portable fault testing device of heavy mechanized bridge. Accordingly it can locate the fault position and fault mode, detect the fault parts/components as well as provide fault maintenance solutions by monitoring of equipment operation state, fault data processing and diagnosis. Consequently it can accomplish the rapid testing and maintenance to fault equipment, for example electronic system etc. [1].

Fault Analysis of Electrical System

The faults of electrical system are frequently short circuit of grounded of coil, not entirely open or closed of switch and contact as well as low operating voltage of controlled solenoid valve and others. With detailed analysis of the electrical schematic diagram and technical knowledge, these faults result from two causes of short circuit and open circuit. The fault state presents as two states of opening and

closing. Further analysis demonstrates that the faults of electrical system focus on operating system and its related circuits. The faults of electrical operating system are very challenging task since the faults of electrical operating system other than display system and lighting system have great influence on the performance of the heavy mechanized bridge. The engaged failures of electrical operating system is presented as follows.

Resistance Change. The contact resistance of electrical component connector or wiring of hydraulic system becomes bigger due to external environmental erosion. It results in poor contact, causing low voltage or total failure.

Power Leakage. The faults are present as power leakage of electrical components. Obviously, different components require different applied driving voltage in the electrical system of the mechanized bridge. Specifically, the working status of solenoid valve plays key role in controlling the cylinder of total hydraulic control system. When the supply voltage of solenoid valve is insufficient, valve port opening of solenoid valve is interfered. It would cause the flow variation of hydraulic system. These could result in many faults, for example, cylinder behaves improperly, and actuator runs slowly as well as working attachment operates abnormally.

Low Resistance of Insulator. Most of the electrical components are separated from the chassis by external insulator. In environmental vibration and corrosion the insulating resistance gradually degrades. The circuit current crossing would result in uncontrollable state.

Physical Damage. Major physical damage of the wire could result in failure. Although the wires of electrical system are widely distributed through the entire chassis and the cables are bound with harness, they still could be lacerated or damaged. Then the control circuit and connection wire are damaged due to the loss of external protection. This would result in break in control circuit and the mechanized bridge couldn't operate properly.

General Design and Working Principle

General Design of Fault Diagnosis System. In order to quantitatively detect the operating parameters of a mechanized bridge, an intelligent fault testing system is designed. It can perform data acquisition of the electrical system parameters through sensors and other accessories. The general technical scenario of the fault diagnosis system is presented as integration of fault testing platform, dedicated interface adapter unit together with hardware and software. The general architecture of fault diagnosis system is described in Fig 1.

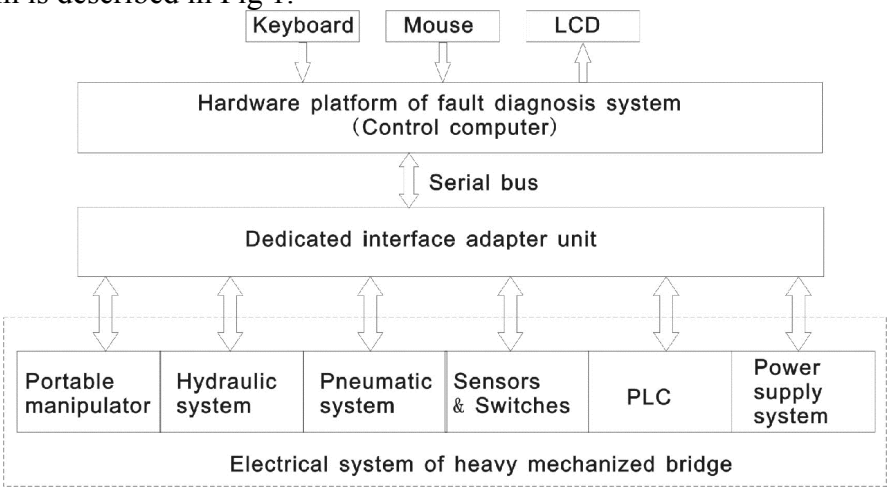


Fig.1 General Architecture of Fault Diagnosis System

The fault diagnosis system is designed not only to test the analog and digital output signal of various components as well as the communication signal between every subsystem of the hydraulic excavator, but also provide virtual excitation signals for the system under test of hydraulic system and electrical system. It therefore employs the work excitation function of electrical control system and fault diagnosis of the hydraulic and electrical system. Accordingly, it may carry out the performance test and fault diagnosis for the electrical system and hydraulic system of heavy mechanized bridge

chassis and bridge launching system, for example, the portable manipulator, hydraulic components, pneumatic parts, sensors & switches, PLC as well as power supply system. It could locate the fault to the replaceable unit of control board, block as well as corresponding hydraulic parts and subsystem.

Working Principle. According to working principle and signal features of input and output of electrical system of mechanized bridge, the field fault diagnosis hardware platform (computer) and fault diagnosis program of fault diagnosis system sends corresponding commands and data to the dedicated interface adapter unit. When interface adapter unit receives commands from upper computer, it translates the commands according to communication protocol and accomplishes further processing steps. The adapter engages excitation signal on output port and detects the response from input port of mechanized bridge's electrical components, then it transmits the related status data to the computer. The computer performs technical status detection and fault diagnosis to the bridge components under test as well as storage of the testing process data and diagnosis results by characteristics of excitation and response signals of components under test. These signal characteristics involve the absence and presence, error and phase relationship as well as time sequence of excitation and response signal. In addition, the fault diagnosis system could provide repair guidance for faulty components

Hardware Design

Field Fault Diagnosis Platform. The field fault detection and diagnosis platform is composed of PXI-bus chassis, microcomputer controller, I2C-bus controller and other PXI-bus signal conditioning modules that are all based on virtual instrumentation technology.

According to the need of general technical scheme, the fault test and diagnosis platform can accomplish its function with host computer- PC. The virtual instrument platform is the central unit. It uses hardware structure of PXI chassis, VPC Interconnect adapters, master controller and PXI modular instruments ensuring the system requirements of opening and expansibility. It is actually equal to a dedicated computer installed special data acquisition and signal conditioning modules. Windows operating system is also running on it. In addition, it use PXI-8420 serial module to communicate with the adapter unit. The software of the platform is developed based on its operating system.

Interface Adapter Unit. The function of interface adapter unit is to establish the electrical connection channel between test resource and equipment under test. The isolation, amplification, transformation of signal is accomplished through it. Thus the input and output signals are standardized to accommodate not only the requirements of fault detection system universality, but also the special requirements of interface signal for equipment under test. Dedicated interface adapter unit consists of chassis, connection panel, signal conditioning circuit and receivers.

Specially, two parallel sets of signal conditioning circuit are engaged in the interface adapter unit for the different applications: portable fault detection or platform testing. These circuits share the same power supply and conditioning circuit. There are two data acquisition card of EM-32DI28DO and EM-V8AI8AO respectively in dedicated interface adapter unit. Data acquisition boards are stacked to lower circuit boards via PC 104 interface connection bus.

Conventionally, when interface adapter unit is connected to PXI-based platform of computer, all the test signals are connect to the channels of PXI cards through front panel receivers, internal signal conditioning circuits and VPC 90 series modules. Two conditioning circuit modules are stacked inside the interface adapter unit. The bottom layer board includes power control module, signal conditioning circuit of PLC chassis as well as signal conditioning circuit of control box. Top layer board includes signal conditioning circuit of portable manipulator, hydraulic system, pneumatic system, sensors & switches, power supply system and data communication units.

When the interface adapter unit is connected to portable computer, the portable computer as a host one accomplishes data communication with corresponding module of interface adapter unit. The data communication module implements function of detected data communication. It exchanges data with

host computer via serial interface and control the dedicated processing module through internal I2C-bus. Consequently, it implements the processing of tested data.

Hierarchical Design of Interface Adapter Unit. The interface adapter unit is composed of control board and expansion modules as indicated in Figure 2. The control board receives the control command from control computer and allocates the transformed data to expansion modules. It acquires the data of expansion module and translated them to control computer for processing and display. The expansion modules serve as the interface between adapter and equipment under test. It performs the data acquisition of digital and analog signal as well as provides the analog and digital excitation signal needed by test. The interface adapter unit's modular object-oriented design enables its flexible and powerful function of fault detection and diagnosis.

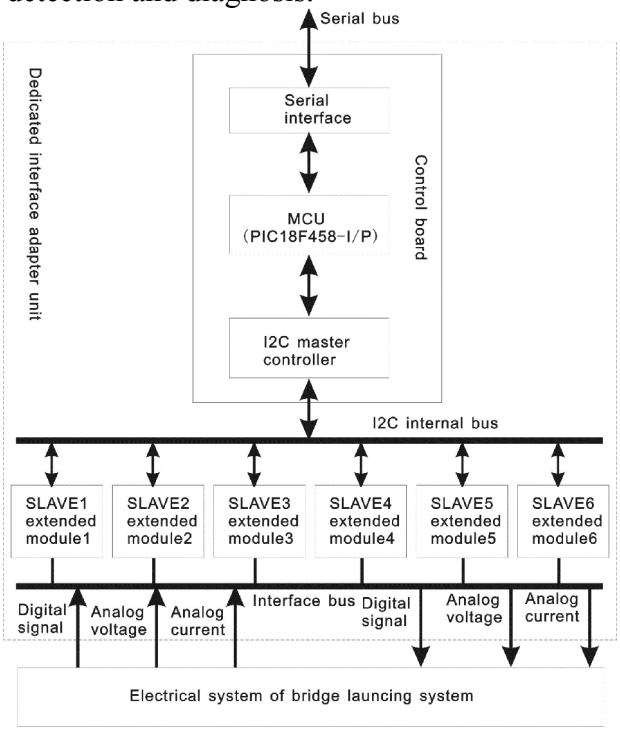


Fig. 2 Hardware Block Diagram of Interface Adapter Unit

Test Circuit of Proximity Switch. The test circuit is used to carry out the state test and signal simulation of proximity switches in bridge launching system. It is composed of 8 precisely the same circuits. Each circuit includes two switch input testing channel, one current testing and one switch output converting channels. The output signal of proximity switch and portable manipulator is connected to next 74LS 244 data latch through the resistor divider of R08/R09 (10/R11). Then it is read by microcomputer unit (MCU). In order to determine power supply status of proximity switch, its current across R01 is sampled, amplified by U01A and routed to A/D converter. The simulation output signal of proximity switch can be accomplished by electronic switch composed of Q01, Q02 and other components. Thus the operating status of proximity switch could be ascertained online under the control of MCU. Furthermore, if the proximity switch of bridge launching system failed, the MCU and its peripheral circuits could generate correct simulation switch signals.

Measurement Principle of Portable Manipulator Power Supply System. The power supply detection of portable manipulator is mainly used to test the supply current and voltage from operation controller to portable manipulator so as to get the power consumption status and working condition of various control switch of the manipulator. Thus the working condition of portable manipulator could be detected by this circuit. The test circuit uses same current to voltage converting circuit (I/V converter) and a voltage divider with the current supply test circuit of proximity switch

Test Circuit of Analog Sensor. The test circuit of analog sensor is used to test the current supply and output signal of the sensor. The current test circuit is identical to the above I/V converting one. It could determine the working status of the sensor. However, the output voltage signal of sensor is

tested by an emitter follower in order to reduce the influence on the senor circuit. In addition, it can also be used to check whether the A/D converter of operating controller is in normal state.

The test circuit of sensor power supply consists of two identical ones that are used to detect the power supply condition of two channels from virtual instrument to chassis sensors. The power supply system includes current and voltage supply. The output 12 voltages' current of virtual instrument is sampled by I/V converter which is composed of R101 and U3A. The sampling of output voltage is carried out by emitter follower composed of U3B and other peripheral components. The sampling data of current and voltage are transmitted simultaneously to 10 bits A/D converter of MCU. Then the working status of chassis sensor is checked.

I2C-bus Communication Within Modules of Interface Adapter Unit. The communication of I2C-bus modules in interface adapter unit is implemented by binary code. The data transfer rate is 100 kbits/s with 7-bit address. Frame format of message is shown in Fig. 8. After the START condition (S), a slave address is sent. This address is 7 bits long followed by an eighth bit which is a data direction bit (R/W)- a '0' indicates transmission (WRITE) , a '1' indicates a request for data (READ). After it the transferred message is present immediately. The data transfer is terminated by a STOP condition (P) generated by the master.

In this work 7-bit address is used. The 6 extended modules consist of 6 slave receivers with address range from 0001001x to 0001101x. In this case the last bit (x) is the R/W bit that determines the direction of the message. When the active master is powered, it delays to transmit a request message to slave. The address slave acknowledges usable slave address.

Master parses the configuration of host computer and sends the information to extended module accordingly. Furthermore, it polls the logic status or AD status alternately and sends them to host computer. Master implements the data synthesis from the slave device and transmitted them to host computer via serial interface. Then the master poll the next slave, send 0xa and 0xd. Thus the poll is over.

Software Platform

The fault detection and diagnosis software is composed of two parts: test software module and remote display software module. The test software carries out the parameter test, data record and analysis. The remote display software is linked to fault detection and diagnosis software through TCP/IP protocol. It receives test information and displays the test process timely. The fault detection and diagnosis software includes 14 internal modules, and load 2 ACCESS database file: Rec.mdb and Repair.mdb. The general software architecture is shown in Fig. 3.

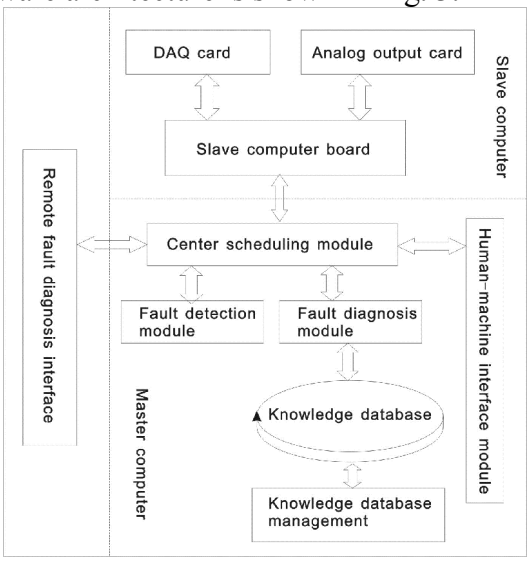


Fig. 3 Block Diagram of Software Platform

Summary

In this work, the fault diagnosis system including field test platform, PXI-based computer and fault diagnosis program of heavy mechanized bridge is developed. The main contribution of this paper could be briefly summarized as follows.

1) This system can accomplish online testing in case of normal manipulation of entire bridge launching electrical system. Then it carries out complete online detection in normal operation and driving mode. Similarly it can locate the fault to standalone equipment and replaceable unit of circuit board, thus it accommodates the need of fault test and diagnosis of military troops.

2) Its hardware platform adopts modular structure of PXI-based virtual instrument platform integrated with dedicated interface adapter unit and connection accessories. The software program is developed based on modular hierarchy, intelligent fault diagnosis technique and database. This program has high intelligence, repeatable performance as well as precise location of electrical system fault.

3) Dedicated interface adapter unit is designed with standardization and modularization as well as function of preventing error insertion. Specifically, it can be connected to military universal testing platform or portable computer so as to construct special testing system of advanced performance and strong universality, and achieve high precise testing.

4) The design of modular structure and application of embedded technology is valuable to the development of online and field testing device for various engineering equipment. The work can effectively enhance the field fault detection capability.

Acknowledgement

The research is financed by the Jiangsu Provincial Youth Science Research Foundation of China (BK 2012061).

References

[1] L.B. Jack, A.K. Nandi. Fault Detection Using Support Vector Machines and Artificial Neural Networdks Augmented by Gentic Algorithms. *Mechanical Systems and Signal Processing*, Volume 16, Issues 2-3, March 2002, 373-390

[2] L González f1, I Anderson, D Deane, C Summers, D Buxton. Detection of Immune System Cells in Paraffin Wax-embedded Ovine Tissues. *Journal of Comparative Pathology*, Volume 125, Issue 1, July 2001, 41-47

[3] Paul Kocher, Ruby Lee, Gary McGraw, Anand Raghunathan. Security as a new dimension in embedded system design. *Proceedings of the 41st annual Design Automation Conference*, ACM New York, NY, USA @2004.

[4] Rolf Isermann. Model-based fault-detection and diagnosis – status and applications, *Annual Reviews in Control*, Volume 29, Issue 1, 2005, 71-85

[5] Rolf Isermann. Supervision, fault-detection and fault-diagnosis methods — An introduction, *Control Engineering Practice*, Volume 5, Issue 5, May 1997, 639-652.

[6] Samuel R. Madden, Michael J. Franklin, Joseph M. Hellerstein, Wei Hong. an acquisitional query processing system for sensor networks. *ACM Transactions on Database Systems*, Volume 30 Issue 1, 1324-1339，March 2005

Applied Mechanics and Materials Vol. 597 (2014) pp 450-453
© (2014) Trans Tech Publications, Switzerland
doi:10.4028/www.scientific.net/AMM.597.450

Meshing Efficiency of Involute Helical Gears Based on Elastohydrodynamic Lubrication

Bin Wang[1,2,a], Xin-bo Chen[1,3,b]

[1]School of Automotive Studies, Tongji University, Shanghai 201804, China
[2]School of Mechanical Engineering, Yancheng Institute of Technology, Yancheng 204051, China
[3]Clean Energy Automotive Engineering Center, Tongji University, Shanghai 201804, China
[a]wangbin@ycit.cn, [b]austin_1@aliyun.com

Keywords: meshing efficiency, helical gear, power lose, elastohydynamic

Abstract. To analyze the dynamic efficiency of helical gear during meshing process, a meshing efficiency model based on elastohydrodynamic lubrication (EHL) was established. The meshing plane between the pinion and gear was divided into seven parts in accordance to the regularity of unit load distribution. The total meshing power lose and average meshing power lose were calculated through a double integration method. The simulation results show that the method is feasible to calculate the meshing efficiency of gear pairs.

Introduction

The power lose caused by the friction of gear pairs inevitably converted into heat, which has an important influence on the failure of transmission performance and the design of lubrication system [1]. Hence the research of meshing efficiency of gear pairs helps to descend the meshing power lose, better the working environment, and improving the life and security of the gear pairs.

Literature [2-4] analyzed the meshing efficiency of spur gear pairs and established a meshing model under the environment of elastohydrodynamic lubrication. Helical gears are widely used on account of the large contact ratio and stable transmission of the gears, therefore the research on the dynamic efficiency of helical gears is more important. Different from spur gears, the length of contact line and the load distribution along the contact line of the helical gears changes with the variation of meshing position. Even at different point of the contact line, the sliding velocity, rolling velocity, radius of curvature, sliding friction coefficient, and contact pressure are different. For gear pairs of large axial contact ratio, there exist the possibility of more than two pair gear teeth engaging at the same time. Therefore the meshing efficiency analysis of helical gears is more complex than that of spur gears.

On the basis of transient meshing analysis, the gear with large axial contact ratio is divided into several parts. And the total power lose among different parts is easy to be calculated by integration, thus the power lose and meshing efficiency of whole meshing area can be attained.

Power lose analysis of helical gears with large contact ratio

Because each helical gear can be similarly treated as a combination of thin spur gears, which are arranged in phase angle, each helical gear slice can be treated as spur gear. Thus the mathematic calculation method of spur gear can be used on helical gear slice. Fig. 1 shows the schematic diagram of helical gear slices. $\overline{N_1N_2}$ is theoretical length of line of action; K is meshing point; P is

pitch point; *C,D* delegates the start point of single-tooth contact and end of single-tooth contact, respectively; B_1,B_2: actual start of mesh cycle and end of mesh cycle, respectively; *b* is tooth width of spur gear, mm. The whole meshing power loses of a helical gear can expressed as:

$$P = \sum_{I=1}^{n} \Delta P \tag{1}$$

Where n is the total number of helical gear slices.

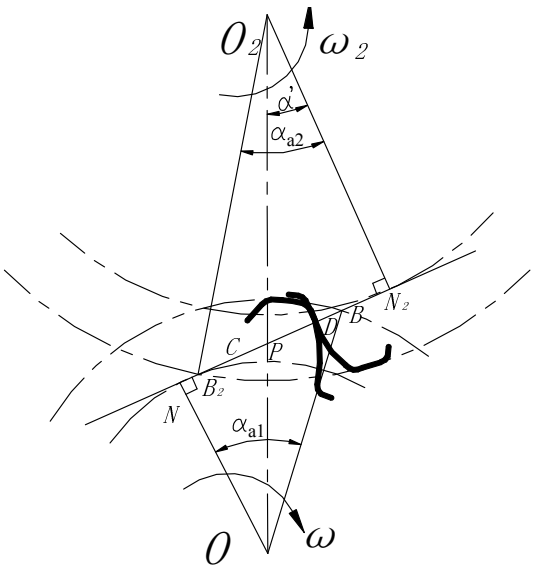


Fig. 1 The schematic diagram of helical gear slices

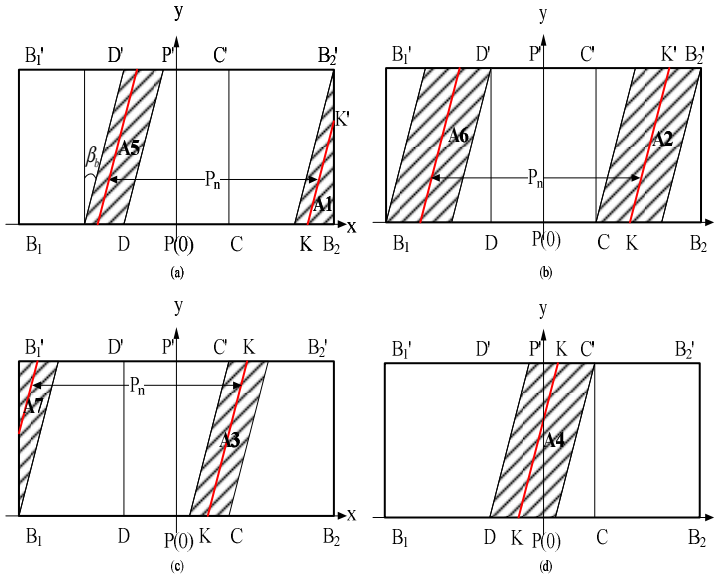


Fig. 2 The division of plane of action (only for gears of small axial contact ratio)

$r_1^{'}$, $r_2^{'}$: radius of pinion and gear pitch circle, respectively, mm; r_{b1}, r_{b2}: radius of pinion and gear base circle, respectively, mm; r_1, r_2: radius of pinion and gear reference circle, mm; F_n: overall normal load, $F_n = 2T_1 / (d_1 \cos\alpha')$, N; $F_n^{'}$: instantaneous normal load, N/mm; i: transmission ratio; n_1: rotational speed of pinion, rpm; x: length of $\overline{KP}$, mm; $V_s(x), V_r(x)$: instantaneous sliding and rolling velocity of meshing point, respectively, m/s; α_{a1}, α_{a2}: addendum circle pressure angle of pinion and gear, respectively, deg; α, α': reference circle and pitch circle pressure angle, respectively, deg.

For a helical gear with small axial contact ratio, all lines of action of each helical gear slice have formed a rectangle plane of action (as shown in Fig. 2). To analyze the power lose of helical gear, the rectangle plane of action are divided into 7 areas (A1~A7). A1~A3, A5~A7 are double teeth meshing areas, and A4 is single tooth meshing area. A coordinate system is established where pitch point P is regarded as original point, the line of action of front face is regarded as x axis, and the line perpendicular to the all lines of action on the plane is regarded as the y axis. For the contact mode of gears is line contact, the position of each point on the line of contact is expressed as (x, y).Let $e_1 = PB_1$, $e_2 = PB_2$, we have $e_1 = r_{b1}(tg\alpha_{a1} - tg\alpha')$ and $e_2 = r_{b2}(tg\alpha_{a2} - tg\alpha')$. According to the geometry calculation, the boundary coordinates of A1~A7 is expressed as in Table 1.

Length of line of action. When double gear teeth mesh, the contact line of two teeth locate on A1A5,A2A6,A3A7 two different meshing area. When a single gear tooth meshes, the contact line locates in A1A5, A2A6, and A3A7. The lengthes of contact line in A2 to A6 are fixed values; however, the contact line in A1 and A7 varies dynamically. The lengthes of contact lines in different area are expressed by following formulas.

Table 1 Boundary coordinates of Area A1~A7 of helical gears

Plane of action	Lower limit of contact line x_{Ai}^{a}	Upper limit of contact line x_{Ai}^{b}
A1	$e_2-(b-y)tg\beta$	e_2
A2	$-e_1+p_n+ytg\beta$	$e_2-(b-y)tg\beta$
A3	$-e_1+p_n+ytg\beta-btg\beta$	$-e_1+p_n+ytg\beta$
A4	$e_2-(b-y)tg\beta-p_n+btg\beta$	$-e_1+p_n+ytg\beta-btg\beta$
A5	$e_2-(b-y)tg\beta-p_n$	$e_2-(b-y)tg\beta-p_n+btg\beta$
A6	$-e_1+ytg\beta$	$e_2-(b-y)tg\beta-p_n$
A7	$-e_1$	$-e_1+ytg\beta$
Coordinates of the lower and upper limits of contact line [0,b]		

$$\begin{cases} L_{A1}=[(e_2-x)ctg\beta+y]/\cos\beta \\ L_{A7}=[b-y+(e_1+x)ctg\beta]/\cos\beta \\ L_{Ai}=b/\cos\beta \qquad (i=2,3,4,5,6) \end{cases} \tag{2}$$

$$F_n=F_t/(\cos\beta\cos\alpha_n)=2T_1/(d_1\cos\beta\cos\alpha_n) \tag{3}$$

Where F_n is the normal load of the helical gear, N; L_{total} is the total length of contact line, mm; a_n is the normal angle of pressure，deg. The unit load of the contact line of gear is expressed by the formula $F_n'=Fn/L_{total}$. Bringing Formula (4) into above formula, then we have:

$$F_n'(x,y)=\begin{cases} 2T_1/\{d_1\cos\alpha_n[(r_{b2}(tg\alpha_{a2}-tg\alpha')-x)ctg\beta+y+b]\} & (A1A5) \\ T_1/(d_1b\cos\alpha_n) & (A2A6) \\ 2T_1/\{d_1\cos\alpha_n[2b-y+(r_{b1}(tg\alpha_{a1}-tg\alpha')+x)ctg\beta]\} & (A3A7) \\ 2T_1/(d_1b\cos\alpha_n) & (A4) \end{cases} \tag{4}$$

The instantaneous sliding velocity $V_S(x)$ and rolling velocity $V_R(x)$:

$$\begin{cases} V_S(x,y)=R_1\omega_1-R_2\omega_2=\dfrac{\pi}{30}n_1(1+1/i)|x|\times10^{-3} \\ V_R(x,y)=R_1\omega_1+R_2\omega_2=\dfrac{\pi}{30}n_1[d_1\sin\alpha'+(1-1/i)|x|]\times10^{-3} \end{cases} \tag{5}$$

Where $V_S(x,y)$ is the instantaneous sliding velocity of meshing point, m/s; $V_R(x,y)$ is the instantaneous rolling velocity of meshing point, m/s; n_1 is rotational velocity of pinion, r/min; x is radius of curvature of pinion and gear, respectively, mm.

Friction factor. Literature [5] gives an empirical formula, which has been proved accurate and widely used. Through unit conversion, the empirical formula is written as:

$$f_e(x,y)=0.0127[50/(50-39.37\delta)]\lg[29.66F_n'/(\rho V_S(x,y)V_R^2(x,y))] \tag{6}$$

Where $f_e(x,y)$ is instantaneous friction factor; δ is surface roughness, μm; ρ is the viscosity of lubricating oil.

Instantaneous friction power lose. According to the knowledge of dynamics, the instantaneous friction power lose can be expressed by the following formula.

$$P_S(x,y)=f(x,y)F_n'(x,y)V_S(x,y) \tag{7}$$

In different area of action A_i, the formula of relative sliding and rolling power lose of each meshing point can be written as:

$$\begin{cases} \iint_{Ai} P_S(x,y)dxdy = \int_0^b \int_{x_{Ai}^a}^{x_{Ai}^b} f(x,y)F_{\mathrm{n}}'(x,y)V_{\mathrm{S}}(x,y)dxdy \\ \iint_{Ai} P_R(x,y)dxdy = \int_0^b \int_{x_{Ai}^a}^{x_{Ai}^b} f(x,y)F_{\mathrm{n}}'(x,y)V_{\mathrm{R}}(x,y)dxdy \end{cases} \tag{8}$$

The total friction power loses of gears with small axial contact ratio can be expressed as:

$$P = P_S + P_R = \sum_{i=1}^{7} \iint_{Ai} P_S(x,y)dxdy + \sum_{i=1}^{7} \iint_{Ai} P_S(x,y)dxdy \tag{9}$$

Taking the influence of contact ratio β on power lose into account, the formula of average power lose of gears can be written as:

$$\overline{P} = (Ps + Pr)(\alpha_{B1} - \alpha_{B2})Z_1 / [2\pi(e_1 + e_2)] \tag{10}$$

Where Z_1 is the tooth number of pinion. The transmission efficiency of helical gears can be expressed as:

$$\eta = (P_e - \overline{P}) / P_e \tag{11}$$

Conclusions

Through the structure analysis of helical gear, the instantaneous friction power lose model was established. The meshing surface between the pinion and gear was divided into seven parts in accordance to the regularity of unit load distribution. The total meshing power lose and average meshing power lose were calculated through a double integration method. The way was proved to be convenient and accurate.

Acknowledgments

The authors gratefully acknowledge the financial support of the Major State Basic Research Development Program of China (973 Program) under grant No. 2011CB711202, the National High Technology Research and Development Program of China (863 Program) under grant No. 2012AA110701, National Natural Science Foundation of China under grant No.51375344, and Jiangsu Provincial Research Foundation for Basic Research (Jiangsu Provincial Natural Science Foundation) under Grant No. BK20131221.

References

[1] XU H, KAHRAMAN A. Prediction of mechanical efficiency of parallel axis gear pairs. *Journal of Mechanical Design*; 129(1): 58-68. (2007)

[2] CHEN Xin-bo, LU Zhi-jian. Modeling of Dynamic Efficiency of Spur Gear Pairs Based on Elastohydrodynamic Lubrication and Its Validation. *Journal of TONGJI University (Natural Science)*; 41(5): 773-778. (2013)

[3] YAO Jian-chu, CHEN Yi-bao, ZHOU Ji. Study on a method for calculating gearing meshing efficiency. *Chinese Journal of Mechanical Engineering*; 371(11): 18-21. (2001)

[4] ZHOU Zhe-bo. Study on gear meshing efficiency under condition of elasto-hydrodynamic lubrication. *Journal of Machine Design*; 21(12): 40- 42. (2004)

[5] Martin K. F. A review of friction predictions in gear teeth. *Wear*; 49: 201-238. (1978)

Applied Mechanics and Materials Vol. 597 (2014) pp 454-457
© (2014) Trans Tech Publications, Switzerland
doi:10.4028/www.scientific.net/AMM.597.454

Research about deformations identification for globoidal cam machine based on multi-body system theory

Liping Zhao[1, a *], Hongren Chen[1,b], Yiyong Yao[2,c], Hu Zhao[3,d] and Peng Yan[1,e]

[1]State Key Laboratory for Manufacturing Systems Engineering, Xi'an Jiaotong University, China

[2]School of Mechanical Engineering, Xi'an Jiaotong University, China

[3]Guangzhou MinJia Manufacturing Technology CO., LTD, China

[a]lipingzh@mail.xjtu.edu.cn*, [b]chrjixie@stu.xjtu.edu.cn, [c]yyyao@mail.xjtu.edu.cn, [d]zhaoduohu@163.com, [e]swordyp@163.com

Keywords: Sensitive deformation, error sensitivity direction, multi-body system theory, globoidal cam.

Abstract. Deformation error caused by cutting heart and external force is one of the key factors influencing machining precision in machining process. Aiming to identify the machine deformation which has the most important influence on machining precision, an identification method for sensitive error and deformation based on multi-body system theory has been proposed, which lay the basis of stiffness distribution of a machine tool and structure optimization of parts. At the end of this paper, the effective of this method is verified by using the machine tool for globoidal cam.

Introduction

The deformation error caused by cutting heart and external force is one of the important error sources of NC machine tools. The external forces include the gravity of moving parts and workpiece, cutting force, driving force, inertia force and friction. The forces make the parts and joint surfaces deformed, such as displacement, bending deformation, torsional deformation. The deformation will cause relative displacement between tools and workpieces, and affected the precision of a machine tool [1]. Huang [2] proposed the control strategy of machine tool precision for sensitive error. Cheng [3] proposed a method to recognize the key parameters of geometric error sources. Li [4] presented a method to build the topology of machines and the transform matrix. Ye [5] established the error model between the manufacturing error and space error of a machine tool. This paper uses the multi-body system theory to establish the theoretical model of sensitive error. The sensitive analysis is carried out on the deformation. The machine tool stiffness could be distributed reasonably.

The modeling of motion transmission for globoidal cam based on multi-body system theory

The processing principal for globoidal cam and motion principal is shown in Fig.1 (a) and Fig.1 (b). The motion of a machine tool includes the main motion and feed motion. The motion transmission model is determined by the size and shape of workpieces. The transmission model includes motion style, degree of freedom, the arrangement and order. The motion transmission relationship between tool and workpiece is expressed by using the coordinate transmission matrix of multi-body system theory. The motion transmission chain can be written as W/A'X'B'Z'·Y/T. • is the base of a machine tool. W is the workpiece, and T is the tool. The motion units of a machine tool include rectilinear motion in X, Y, Z directions and the rotational motion of X, Y, Z directions. The number of degree of freedom and the motion style can be determined. The globoidal cam, driven plate mesh and the rotation angle of driven plate is θ. The contact angle β is the angle between Y_3-axis and Y_1-axis. R_1 is the vector equation of conjugate contact point c between the tool and workpiece in the coordinate system $O_1X_1Y_1Z_1$ [6]. R_0 is the vector equation of contact point c in coordinate system OXYZ. R_2 is the vector equation of contact point c in coordinate system $O_2X_2Y_2Z_2$. The homogeneous coordinate transformations are written as Eq. (1)-(3).

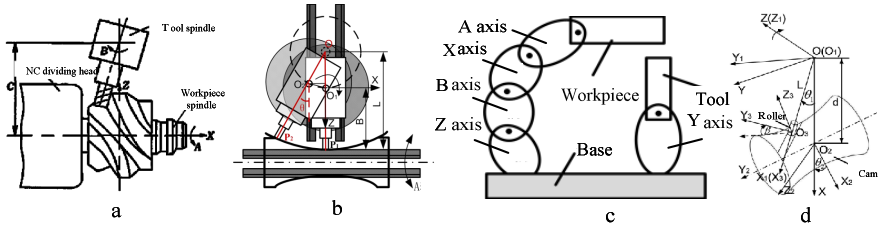


Fig.1 Processing principal for globoidal cam

$$R_0 = \left[L\cos\theta_1 - r\cos\beta\sin\theta_1 \quad L\sin\theta_1 + r\cos\beta\cos\theta_1 \quad r\sin\beta\right]^T \tag{1}$$

$$R_1 = \left[L \quad r\cos\beta \quad r\sin\beta\right]^T \tag{2}$$

$$R_2 = \begin{bmatrix} L\cos\theta_1\cos\theta_2 - r\cos\beta\sin\theta_1\cos\theta_2 - d\cos\theta_2 - r\sin\beta\sin\theta_2 \\ L\sin\theta_1 + r\cos\beta\cos\theta_1 \\ L\cos\theta_1\sin\theta_2 - r\cos\beta\sin\theta_1\sin\theta_2 - d\sin\theta_2 + r\sin\beta\cos\theta_2 \end{bmatrix} \tag{3}$$

where L is the distance between the swing center of tools and the meshing point. r is the radius of the roller.

The identification of sensitive deformation based on multi-body system theory

Error Sensitivity Direction of Processing for Globoidal Cam. The sensitive analysis of globoidal cam can be conducted based on the sensitive equation. n is unit vector of error in the error sensitive direction on the coordinate system $O_3X_3Y_3Z_3$. n_0, n_1, n_2 are the vectors in the coordinate system $O_1X_1Y_1Z_1$, OXYZ and $O_2X_2Y_2Z_2$ respectively. The homogeneous coordinate system can be written as:

$$\vec{n}_0 = (L\cos\theta_1 - \cos\beta\sin\theta_1, L\sin\theta_1 + \cos\beta\cos\theta_1, \sin\beta) \tag{4}$$

$$\vec{n} = (0,1,0), \vec{n}_1 = (L, \cos\beta, \sin\beta) \tag{5}$$

$$\tan\beta = \pm\frac{L}{(d - L\cos\theta_1)i} \tag{6}$$

$$\begin{aligned}\vec{n}_2 = (&L\cos\theta_1\cos\theta_2 - \cos\beta\sin\theta_1\cos\theta_2 - d\cos\theta_2 - \sin\beta\sin\theta_2, L\sin\theta_1 + \cos\beta\cos\theta_1, \\ &L\cos\theta_1\sin\theta_2 - \cos\beta\sin\theta_1\sin\theta_2 - d\sin\theta_2 + \sin\beta\cos\theta_2)\end{aligned} \tag{7}$$

where β is contact angle. $i = Z_1/Z_2$ is the transmission ratio. Z_1 is the number of rollers. Z_2 is the number of globoidal cam head. d is the center distance of globoidal cam.

Therefore, the homogeneous coordinate transformation T_{23} between the coordinate system $O_3X_3Y_3Z_3$ of sensitive error and the coordinate system $O_2X_2Y_2Z_2$ of workpiece is following.

$$\begin{aligned}[T_{23}] = [T_{20}]\bullet[T_{01}]\bullet[T_{13}] &= \begin{bmatrix} \cos\theta_2 & 0 & -\sin\theta_2 & -d\cos\theta_2 \\ 0 & 1 & 0 & 0 \\ \sin\theta_2 & 0 & \cos\theta_2 & -d\sin\theta_2 \\ 0 & 0 & 0 & 1 \end{bmatrix} \bullet \begin{bmatrix} \cos\theta_1 & -\sin\theta_1 & 0 & 0 \\ \sin\theta_1 & \cos\theta_1 & 0 & 0 \\ 0 & 0 & 1 & 0 \\ 0 & 0 & 0 & 1 \end{bmatrix} \bullet \begin{bmatrix} 1 & 0 & 0 & L \\ 0 & \cos\beta & -\sin\beta & 0 \\ 0 & \sin\beta & \cos\beta & 0 \\ 0 & 0 & 0 & 1 \end{bmatrix} \\ &= \begin{bmatrix} \cos\theta_1\cos\theta_2 & -\cos\theta_2\sin\theta_1\cos\beta - \sin\theta_2\sin\beta & \sin\theta_1\sin\beta\cos\theta_2 - \cos\beta\sin\theta_2 & L\cos\theta_1\cos\theta_2 - d\cos\theta_2 \\ \sin\theta_1 & \cos\theta_1\cos\beta & -\cos\theta_1\sin\beta & L\sin\theta_1 \\ \cos\theta_1\sin\theta_2 & -\sin\theta_1\sin\theta_2\cos\beta + \cos\theta_2\sin\beta & \sin\theta_1\sin\theta_2\sin\beta + \cos\theta_2\cos\beta & L\cos\theta_1\sin\theta_2 - d\sin\theta_2 \\ 0 & 0 & 0 & 1 \end{bmatrix}\end{aligned} \tag{8}$$

The sensitive direction of error changes with the change of the tool swing angle θ_1 and the workpiece turning angle θ_2.

Motion Sensitivity Analysis for Globoidal Cam Machine. Machine tool is assembled by multiple components through the joint interfaces. This exist joint interfaces would result in a decline of the whole structural stiffness. As the slide is the weakest link for sensitive error. The slide would produce oriented deviation under external force, which is shown in Fig.2.

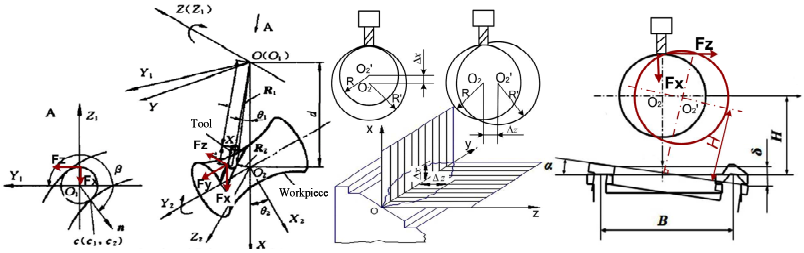


Fig.2 Orientation error of slide

To explore the machine tool which has a great effect on the machining accuracy, the sensitive deformation is controlled and compensated. The sensitivity error analysis for machine tool is divided into four parts: Firstly, the relative position error between tool and workpiece. Secondly, the component generates six kinds of sensitive deformation, which are the displacement deformation and torsional deformation. Thirdly, the sensitive error of the machine tool includes the component error and joint interfaces error. Finally, the sensitive deformation of machine tool would result in a relative displacement between tool and workpiece.

The grinding force in the globoidal cam process is $\vec{F} = (F\sin\theta_1, -F\cos\theta_1\cos\beta, -F\cos\theta_1\sin\beta)$, which is shown in Fig.2 (a). The component force along the z and x direction would lead to the slide generate straightness errors Δz and Δx in the horizontal and vertical plane shown in Fig. 2(b). It also generates displacement in the axis of the workpiece as well as error $\Delta R = \Delta x$ and $\Delta R = \Delta z^2/2R$ in radial direction. In Fig.2(c), the workpiece spindle would generate translational and torsional deformation, workpiece error in the radial direction is $\Delta R \approx \sqrt{(\delta H/B)^2 + R^2} - R$, the parallelism error of the front and rear guide rail can be donated as the torsional error around the Y axis.

Modeling for Machine Sensitive Error based on Multi-body System Theory. The modeling for machine sensitive error can be divided into four parts shown in Fig.3.

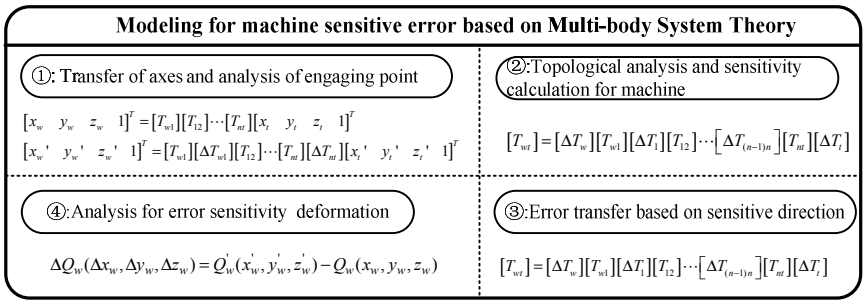


Fig.3 Construction of sensitive error model based on multi-body system theory

The building process can be described as follows. Firstly, the topological structure of machine is analyzed and the homogeneous coordinate transformation is sued. Then the amount of engagement point deviation from tool coordinate system to workpiece coordinate system is calculated. Finally, the machine sensitive error model in units of machine parts and joint interfaces is constructed.

Case study

According to sensitive deformation of the machine tool, the contact point of the tool is regarded as the analysis point, and the position of globoidal cam is taken as an example. Supposes that the deformation error of linear displacement is 0.01mm, and the torsional deformation error is 0.01. So the deviation result in the error sensitive direction is shown as Table 1.

Table 1 The deviation in the error sensitive direction

Displacement error	Deviation	Torsional error	Deviation
Δx_1	0.0093	$\Delta\alpha_1$	-0.0169
Δy_1	0.0034	$\Delta\beta_1$	0.0428
Δz_1	-0.0003	$\Delta\gamma_1$	-0.0407
…	…	…	…
Δx_4	-0.00919	$\Delta\alpha_4$	0.13972
Δy_4	-0.00193	$\Delta\beta_4$	-0.20454
Δz_4	0.00343	$\Delta\gamma_4$	0.25910
…	…	…	…
Δx_8	0.0039	$\Delta\alpha_8$	0.0056
Δy_8	0.0000	$\Delta\beta_8$	-0.0396

In Table 1, the linear displacement error of the parts is reflected on the error sensitive direction. The deviation of error sensitive direction brought by Δx_1 and Δz_8 is large, so the workpiece-axis in X direction and the tool-axis in Z direction are the main sensitive deformation. Therefore, the radial stiffness in the direction of the tool-axis and workpiece-axis should be improved. In addition, the deviation caused by torsional deformation has the obvious difference. The deviation caused by $\Delta\beta_4$, $\Delta\gamma_4$ is large. So the torsion of the machine bed and machine column around Y-axis is sensitive deformation, and the torsion of the machine bed around Z-axis is also sensitive deformation. Therefore, the torsional stiffness of the machine bed and machine column around Y-axis and the machine bed around Z-axis should be improved. The joint surface between the machine bed and the slide and the joint surface between the machine bed and ground should be designed reasonably.

Summary

In machining process, the deformations of each part and interface are caused under the function of cutting heat and multi external force, which will result in the relative displacement between tool and workpiece. With this issue, this paper proposes a sensitivity error model based on multi-body system theory. The deformation sensitivity of parts and interfaces are explored to identify the sensitive deformations. Some measures are made to control the sensitive deformations of machine to allocate the machine rigidity, which provide theory support for optimizing the layout of parts and interfaces.

Acknowledgments

This work is supported by National Scientific & Technological Major Projects (2012ZX04002071)

References

[1] B. Y. Liao. Modern mechanical dynamics and Its Engineering Application. Beijing, 2004.

[2] Q. Huang, G. B. Zhang, X. Y. Zhang. Sensitivity analysis of the pose error of machine tool. Journal of Mechanical Engineering. 45(2009) 141-146.

[3] Q. Cheng, G. B. Liu, Z. F. Zhang. An identification approach for key geometric error sources of machine tool based on sensitivity analysis. Journal of Mechanical Engineering. 48(2012)171-179.

[4] H. L. Li, Q. H. Miao, H. T. Wu. Modeling of positioning error for five-axis NC machining center based on multi-body system theory. China Manufacturing Industry Informatization. 36(2007)16-19.

[5] P. Q. Ye, D. Zhai, T. Zhao. Sensitivity analysis of volumetric errors to manufacturing tolerances for a horizontal machining center. Journal of Tsinghua University. 51(2011) 587-591.

[6] Z. H. Hu, P. Zhang, R. Qi. A study on multi-axis NC machining processes for continuous indexing globoidal cams. China Mechanical Engineering.16(2005) 2184-2187.

Applied Mechanics and Materials Vol. 597 (2014) pp 458-463
© (2014) Trans Tech Publications, Switzerland
doi:10.4028/www.scientific.net/AMM.597.458

Selective tension apparatus development of vibration membrane for stereo speaker production

Kim UkSu[1, a], Jung YoonJun[1, b], Jeong BaWi[1, c], Kim MinSu[2, d], Yang GilSurp[3, e], and Park JeongWoo[4, f*]

[1]Department of advanced parts and materials engineering, Chosun University, 309, Pilmun-daero, Dong-gu, Gwangju South Korea

[2]Department of mechanical design engineering, Chosun University, 309, Pilmun-daero, Dong-gu, Gwangju South Korea

[3]The most beautiful tree corp., 309, Pilmun-daero, Dong-gu, Gwangju South Korea

[4]Department of mechanical system engineering, Chosun University, 309, Pilmun-daero, Dong-gu, Gwangju South Korea

[a]uksunano@gmail.com, [f]jwoopark@chosun.ac.kr

* Please mark the corresponding author with an asterisk

Keywords: Stereo speaker, Vibration membrane, Tension apparatus, Tension point, Al profile

Abstract. In recent years, interest is growing about stereoscopic to the dissemination and development of 3D-TV. However, according to the development of image is also very important to the development of real sound. So recently interest is growing about the stereo sound. It is limited to typical speakers for implementing to stereo speakers. So, recently, has improved sound using flat panel sound. In this study, analyzed apparatus and selected optimum points through the design and CAE (Computer aided engineering) for production of selective tension apparatus of vibration membrane for the flat panel type speaker production. Many tension points offer variety sound environments but it action adverse element in mass production. In this study analyzed through the CAE by designing in tension point location and tension frame for stereo speaker production. CAE was analyzed the optimized conditions using ansys program. The results variously changed parts of affected tension by tension point location or according to the quantity clamped. We selected to optimized tension point and tension frame based on the simulation results. This study is intended to suitable for mass production in the stereo speaker production.

Introduction

In recent years, the 3D TV comes into wide use in the worldwide appliances market. The application of a 3D image spreads from films to TVs. Advancements of the image technique provide viewers with visual pleasure. The sound of them is important as much as the 3D image. It is one of difficult techniques that the realistic sound to reduce a distortion as much as possible is provided for listeners. These days the stereophonic sound is developed to make use of the flat panel type speaker. These skills caused difficulties in mass production. All portions of the vibration membrane keep tension in case of the flat panel type speaker. It is similar to the tension control equipment that the vibration membrane is given tension. Percussion always expresses a vibration differently depending on condition of tension. In this study, the vibration membrane is given selective tension similarly to percussion. But if there are many points of tension is not suitable for mass production, which provides the operator tiredness. This will cause deration of product quality.

In order to give tension of the vibration membrane, the frame is necessary. Aluminum profiles (Al profile) were selected as the frame commonly used in general fabrication. Aluminum profiles are suitable to give subtle tension of square vibration membrane.

The aim of this study is to design an apparatus which uses selective tension of vibration membrane to produce flat panel type speakers suitable for mass production and select optimum tension points through the CAE and analyze this apparatus [1, 2].

Analysis of tension position for vibration membrane

In this study, we have to seek idealized condition for tensile force of flat speaker film. The number of tension point has a decisive effect on the sound. In an attempt to apply tensile force to the thin vibration-membrane, tension points are condignly selected. Prior to making a tension machine, reliability measurement for suitable tension point is conducted by Ansys. First, A strain is analyzed when tension points on the vibration membrane is ten part. Vibration membrane size is as follows: width 1410mm, length 750mm, thickness 0.115mm. Tensile force is applied to the clamping with 50N. A clamp is manufactured with widely used structural steel. Figure 1 is three dimensional modeling of assembly drawing before analysis. In the figure 1(a), clamp is located in membrane with 3×2(width × length), clamp's width is 160mm. In the case of (b), clamp is located in membrane with 5×3 and clamp's width is 100mm. The distance of each clamp is constant. The shape of the clamp used in the experiments was expressed simply. All the specified size is equal with the actual production's size.

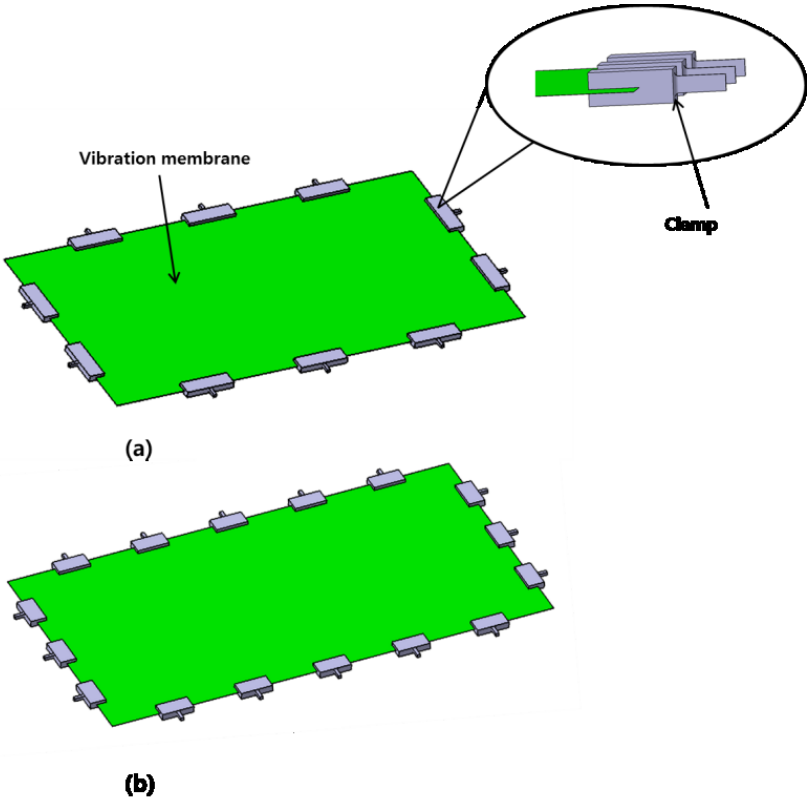


Fig. 1, 3D modeling for tension point analysis of vibration membrane (a) 3 x 2 (b) 5 x 3

Figure 2 is analysis result of stretched vibration membrane by clamp(3×2) using Ansys's total deformation mode. (a) and (b) are in the process of stretching film by clamp. It is considerably deformed in clamping area and deformation become low toward center. Although deformation is constantly generated, in the direction of the horizontal axis, flexure occurs between clamp and clamp.

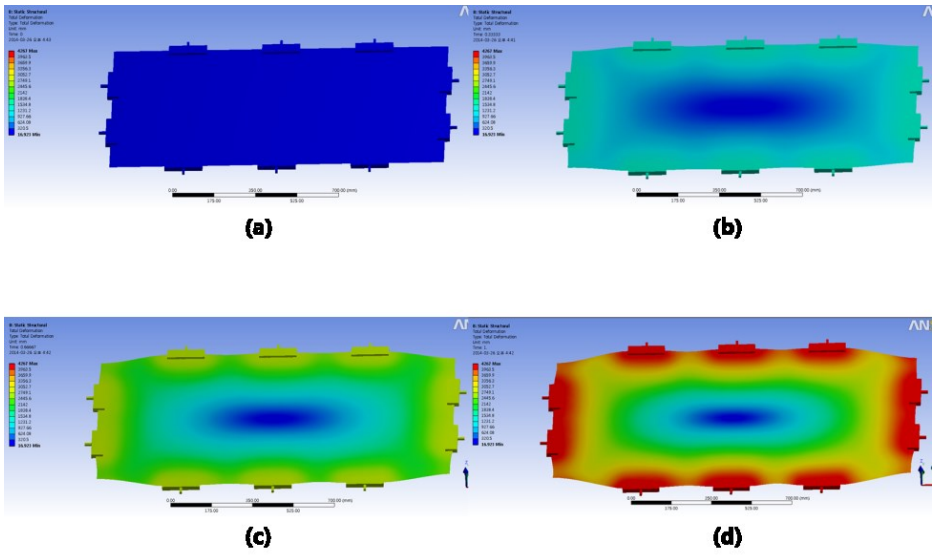


Fig. 2, Analysis of total deformation 3 x 2 clamp

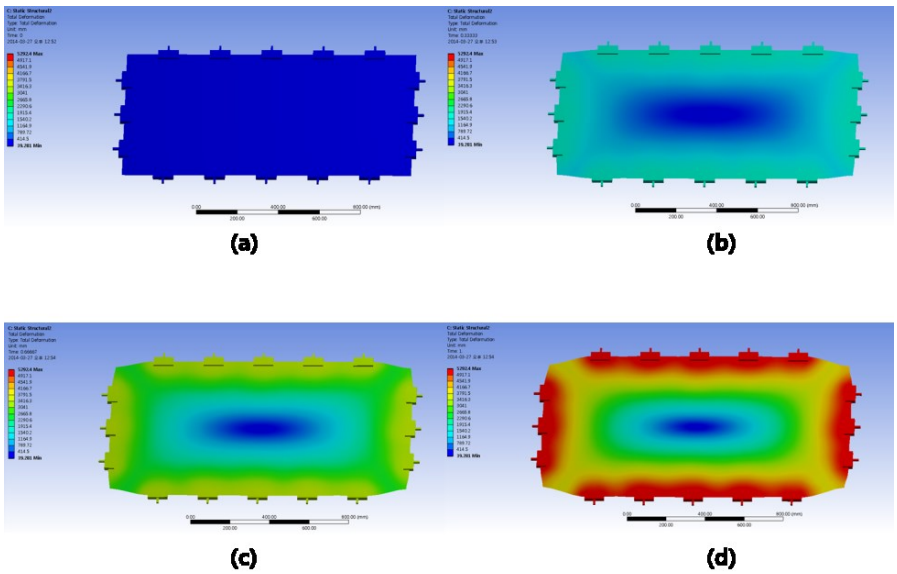


Fig. 3, Analysis of total deformation 5 x 3 clamp

Figure 3 is analysis result of stretched vibration membrane by clamp(5×3) using Ansys's total deformation mode. (a) and (b) are in the process of stretching film by clamp. In the clamping area, deformation is considerably generated like figure 2. The center of the vibration membrane has low deformation. Overall, deformation is constantly generated. Figure 3 is better than figure 2 in the way that deformation is constant in the area of clamp.

Frame design and analysis

Frame had progressed design and manufacturing on the basis of tensile position analysis results on vibration membrane. Tensile strength in the 10 directions should be able to hold out in order to give optional tension of vibration membrane. In this study, frame material is al profile on A6N01S-T5 [3, 4]. Al profile is an advantage which is the easy availability because of the disseminated frame in market Al profiles is advantage that it is easy availability. Al profiles can be composed to large second

moment because it is possible assemble the complicated shape. In other words, 1.2 times more strength than a typical iron angle, have a weight of 1/3. Detailed information about the al profiles are shown in Table 1.Al profiles can be control minutely to tension of vibration membrane by the T-slots. Figure 1 shows the frame structure and the approximate size of the selected image. Considering the size of the vibration membrane was selected (area 2000mm, width 1300mm, height 850mm). Figure 4 shows the image of the approximately selected size.

Table, 1 Al profile technical data

Size	30(height) x 90(width)mm
Material	A6N01S-T5
Surface processing	Anodizing
Weight	2.54 kg/m
Section area	938.2mm^2
Second section moment	Ix=9.5 x 10cm^4 Iy=76.2 x 10cm^4

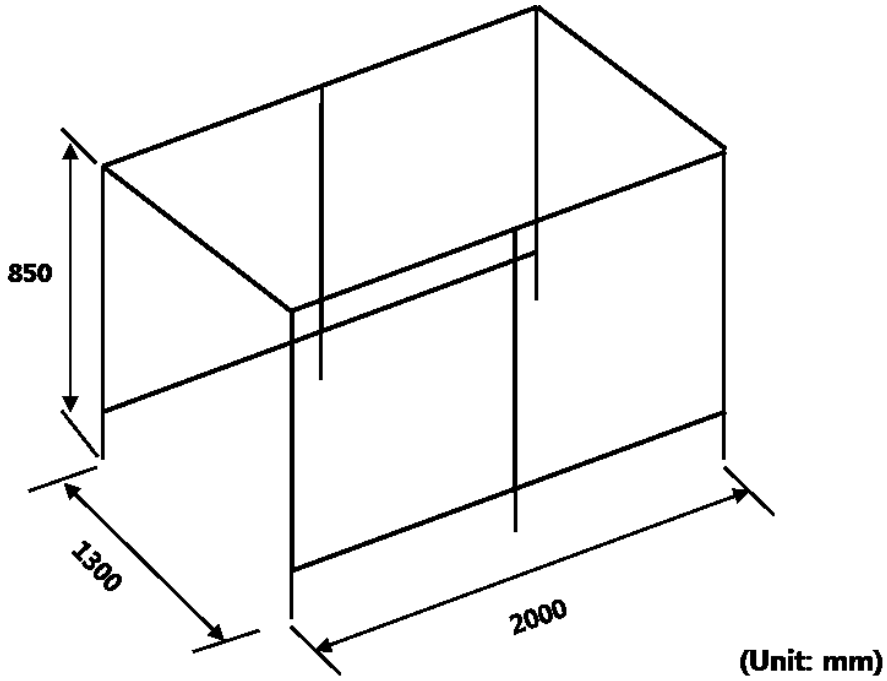


Fig. 4, Selection of vibration membrane tension frame size

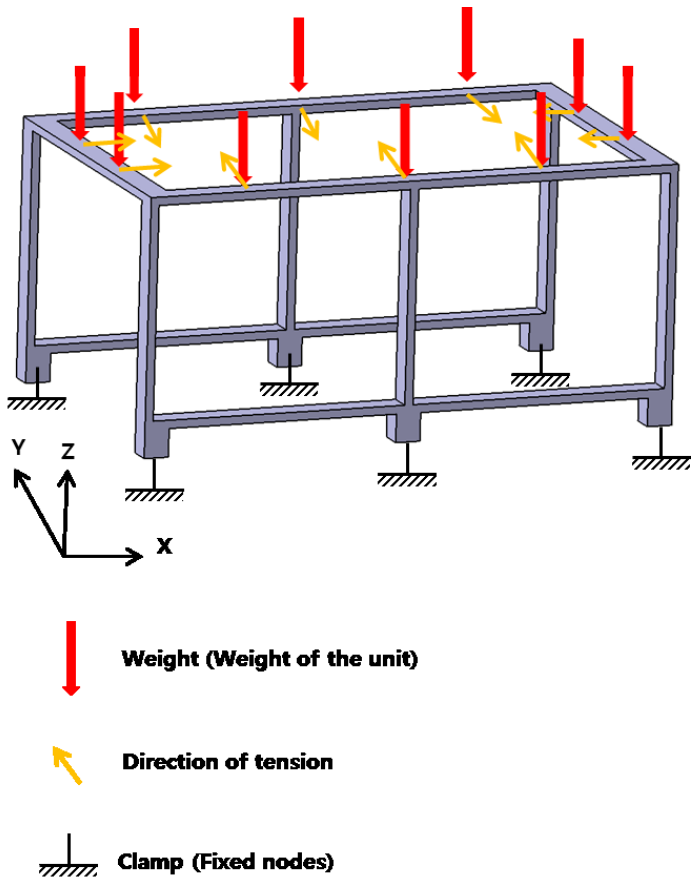
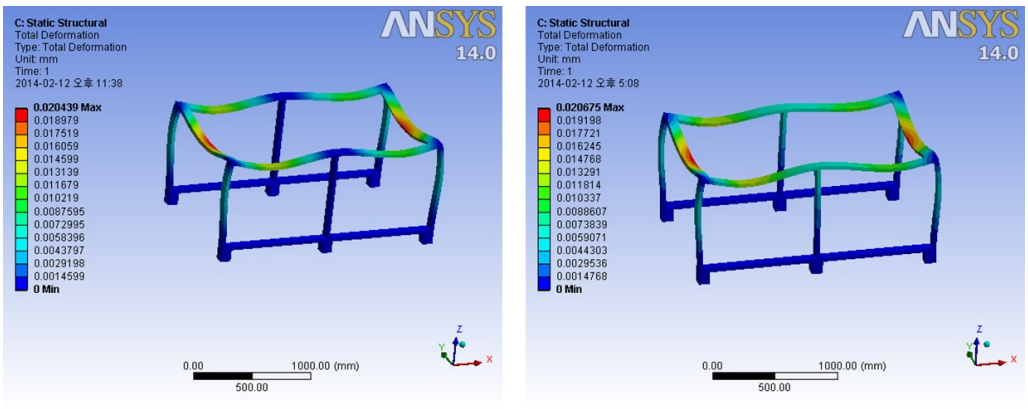


Fig. 5, 3D modeling for analysis of vibration membrane tension frame



(a) (b)

Fig. 6, Structural analysis resuly of the vibration membrane tension frame (a) Z-Weight (b) Z, Tension force

Figure 5 show the degree of effectiveness force while vibration membrane tensile force. I put a condition to frame the force that will pull from each clamp and weight of tension unit. In addition, I was a fixed part of the bottom. The simulation result of the conditions, there was shown in Figure 6.

Figure 6 (a) is an analysis of the deformation of no tension on the quite. Maximum deflection is about 0.02mm and the lowest about of deflection is approximately 0.001mm. The Figure 6 (b), is the result of simulation by generation tension. Maximum deflection is about 0.02mm, the smallest about of deflection is about 0.001mm, if you look at the simulation results of both, there is no difference in the amount of deformation.

Conclusion

Simulation results show, Figure3 is maintain good quality by produced vibration membrane than figure2. But this study, figure2 is fit to determine because must have fitted of goal to mass production. Especially, the volume increases, the clamp because the work process increase, the production period is lengthened. Show transform part, figure 2 suitable because it is not but range effect but decrease to combine part of drum than figure3. When the frame is the maximum tensile, strain is not noticeable enough to write down. So speaker deems suitable to produce.

Good speaker should be production to the stereo speaker to environment with little dust free in order to give a better effect of speaker. it expects good efficiency using stainless steel frame than al profile. In particular, peak and valley of stainless steel surface is reduced if using electrochemical polishing (ECP). If the frame is pollution, cleaning is easier [5].

Acknowledgement

This work (Grants No. C0118695) was supported by Business for Cooperative R&D between Industry, Academy, and Research Institute funded Korea Small and Medium Business Administration in 2013.

References

[1] T. G. Myers, THIN FILMS WITH HIGH SURFACE TENSION, Society for Industrial and Applied Mathematics, 40 (1998) 441-462

[2] Z. Z. Chen, Z. L. Lou, X. Y. Ruan, Finite volume simulation and mould optimization of aluminum profile extrusion, Journal of Materials Processing Technology, 190 (2007) 382-386

[3] L. Peng, X. Shuisheng, C. Lei, Die structure optimization for a large, multi-cavity aluminum profile using numerical simulation and experiments, 36 (2012) 152-160

[4] G. Gou, N. Huang, H. Chen, H. Liu, Z. Guo, Research on corrosion behavior of A6N01S-T5 aluminum alloy welded joint for high-speed trains, Journal of Mechanical Science and Technology, 26 (2012) 1471-1476

[5] J. W. Park, D. W. Lee, Pulse electrochemical polishing for microrecesses based on a coulostatic analysis, Int. J. Adv. Manuf. Technol., 40 (2009) 742-748

Applied Mechanics and Materials Vol. 597 (2014) pp 464-467
© (2014) Trans Tech Publications, Switzerland
doi:10.4028/www.scientific.net/AMM.597.464

The establishment and weight calculation method of evaluation indexes for the float board propulsion system

Yao-quan Cai[1,a*], Fan-ming Zeng[1,b*],Jin-lin Liu[1,c*]

[1]College of Power Engineering, Naval University of Engineering, Wuhan, China
[a]caiyaoquan.ccool@163.com, [b]Zeng_fm@sina.com, [c]20094105@qq.com

Keywords: Propulsion System; Quality Function Deployment; Rough Analytic Hierarchy Process; Evaluation Indexes Calculation.

Abstract: This article aims at solving the problem of evaluation indexes establishment in the process of complexity and the evaluation indexes weight calculation in the process of ambiguity and uncertainty for the float board propulsion system, study and establish evaluation system of the float board propulsion system, make an intensive analysis of calculation method for indexes weight based on rough analytic hierarchy process and calculate the weight of evaluation indexes for the float board propulsion system. This will provide scientific guidance for design and evaluation of the project and lays the certain theory foundation for quality of the design for the float board propulsion system.

Introduction

As the fundamental equipment of human's development and utilization of sea resources, the float board can greatly expand marine living space and activity space for humans, it is also significant to vindicate marine rights and interests and extend marine space. Therefore, the design for the float board is an important topic for ship building and ocean engineering in present. The using of scientific and reasonable design methods is significant to advance the design quality of the propulsion system, even the float board. As the evaluation criterion of the design for the propulsion system, it is an important link of the design in the float board for the establishment and weight calculation of the evaluation indexes system.

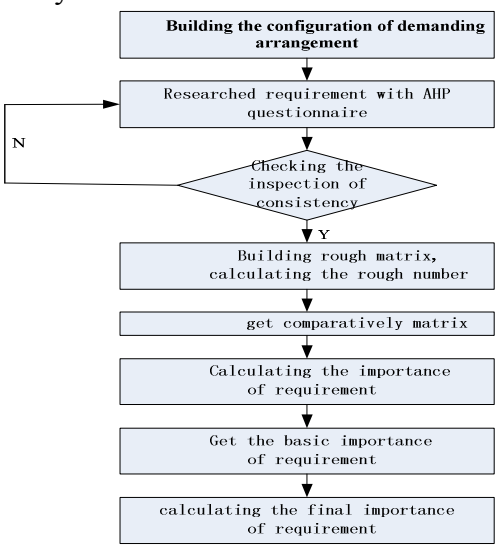


Fig.1 Application step of RAHP

The result always can't reflect the requirement indexes weight exactly because the rough and uncertainty of the float board propulsion system design's requirement. By studying and establishing the evaluation indexes system of the float board marine power plant and then using the Rough

Analytic Hierarchy Process to calculate the requirement indexes weight, checking up the essentiality matrix and colligating all regular matrix would decrease the uncertainty's error mostly. The process is carried out s as shown in Fig.1.

The Establishment of Evaluation Indexes System

According to the design requirement, the maximum speed of the float board is 10kn, under various conditions the float board can have heading regulatory function and zero mph turning a circle. There are two kinds propulsion mode that is azimuth thruster and popded propeller to satisfy the conditions in the preliminary analysis process of total design requirement. It needs to establish the evaluation system of propulsion plant for comprehensive demonstration which is used for two propulsion programs in the process of program demonstration. According to characteristic of the propulsion plant, the evaluation indexes are divided into four hierarchies. The first evaluation indexes: (1) total power; (2) economy; (3) impact-resistance; (4) reliability and service life; (5) survivability; (6) maneuverability; (7) operability and maintainability; (8) life cycle cost. The second evaluation indexes: (1) propeller performance; (2) propeller distributing; (3) emergency ability; (4) control mode; (5) power distributing; (6) safety backup. The third evaluation indexes: (1) seal performance; (2) steering module; (3) sewage system; (4) cooling device; (5) insulating performance; (6) bearing arrangement; (7) shape design. The fourth evaluation indexes aims at ever part in ever assembly, for example, geometrical configuration intensity requirement of the bearing etc. After establishing the evaluation indexes system, it needs to calculate indexes weight, and reasonable establishing the weight is significance for program design and evaluation work and can have an effect upon program design and evaluation result. The calculation method based on the Rough Analytic Hierarchy Process for requirement indexes weight is used in former three-ply, which can lay a foundation for next design process in propulsion system program.

The Apply Method of RAHP

Considering each hierarchy requirement, 6 experts gave the judgements and 6 AHP-questionnaires were obtained in each hierarchy. The first hierarchy is A_i, The second hierarchy is A_j , The third hierarchy is A_k.

$$A_i = \begin{bmatrix} 1 & X_{12}^i & \cdots & X_{18}^i \\ X_{21}^i & 1 & \cdots & \\ \vdots & \vdots & & \vdots \\ X_{81}^i & X_{82}^i & \cdots & 1 \end{bmatrix} \quad A_j = \begin{bmatrix} 1 & X_{12}^j & \cdots & X_{16}^j \\ X_{21}^j & 1 & \cdots & \\ \vdots & \vdots & & \vdots \\ X_{61}^j & X_{62}^j & \cdots & 1 \end{bmatrix} \quad A_k = \begin{bmatrix} 1 & X_{12}^k & \cdots & X_{17}^k \\ X_{21}^k & 1 & \cdots & \\ \vdots & \vdots & & \vdots \\ X_{71}^k & X_{72}^k & \cdots & 1 \end{bmatrix}$$

In formula $i \in [1,6]$, $j \in [7,12]$, $k \in [13,18]$. We must check the coherence up after obtained the pairwise comparison matrix .From the equation CI=(λmax-n)/(n-1) we could working-out the coherence number (CI). λmax is the biggest eigenvalue of matrix A of which n is the dimension of the matrix .The coherence rate (CR) is generally used to evaluate the coherence of pairwise comparison matrix. CR=CI/RI.RI is random index, depending on the dimension n of matrix.

If the matrix passed the checking of coherence, to dispose the rough number, the rough group decision matrix A_i is designed A_1^*, A_j is designed A_2^*, A_k is designed A_3^*, as follows. A_2^* and A_3^* are not listed because of length limit.

$$A_1^* = \begin{bmatrix} 111111 & 657643 & 546665 & 435533 & 445444 & 544356 & 332334 & 767678 \\ 1\frac{1}{6}\frac{1}{5}\frac{1}{7}\frac{1}{6}\frac{1}{4}\frac{1}{3} & 111111 & 1\frac{1}{2}\frac{1}{2}\frac{1}{2}133 & 1\frac{1}{3}\frac{1}{3}\frac{1}{3}\frac{1}{2}\frac{1}{2}1 & 1\frac{1}{3}\frac{1}{2}\frac{1}{3}\frac{1}{3}12 & 1\frac{1}{2}\frac{1}{2}\frac{1}{4}\frac{1}{4}24 & 1\frac{1}{4}\frac{1}{3}\frac{1}{6}\frac{1}{4}\frac{1}{2}2 & 221146 \\ 1\frac{1}{5}\frac{1}{4}\frac{1}{6}\frac{1}{6}\frac{1}{6}\frac{1}{5} & 2221\frac{1}{3}\frac{1}{3} & 111111 & 1\frac{1}{2}\frac{1}{2}\frac{1}{2}\frac{1}{2}\frac{1}{4}\frac{1}{3} & \frac{1}{2}1\frac{1}{2}\frac{1}{3}\frac{1}{3}\frac{1}{3} & 11\frac{1}{3}\frac{1}{4}\frac{1}{2}2 & 1\frac{1}{3}\frac{1}{2}\frac{1}{5}\frac{1}{5}\frac{1}{4}\frac{1}{2} & 332124 \\ 1\frac{1}{4}\frac{1}{3}\frac{1}{5}\frac{1}{5}\frac{1}{3}\frac{1}{3} & 333221 & 222243 & 111111 & 121\frac{1}{2}22 & 22\frac{1}{2}\frac{1}{3}34 & \frac{1}{2}1\frac{1}{4}\frac{1}{3}12 & 443256 \\ 1\frac{1}{4}\frac{1}{4}\frac{1}{5}\frac{1}{4}\frac{1}{4}\frac{1}{4} & 32331\frac{1}{2} & 212332 & 1\frac{1}{2}12\frac{1}{2}\frac{1}{2} & 111111 & 21\frac{1}{2}\frac{1}{2}23 & 1\frac{1}{2}\frac{1}{2}\frac{1}{4}\frac{1}{2}\frac{1}{2}1 & 433345 \\ 1\frac{1}{5}\frac{1}{4}\frac{1}{4}\frac{1}{3}\frac{1}{5}\frac{1}{6} & 2244\frac{1}{2}\frac{1}{4} & 11342\frac{1}{2} & \frac{1}{2}\frac{1}{2}23\frac{1}{3}\frac{1}{4} & \frac{1}{2}122\frac{1}{2}\frac{1}{3} & 111111 & 1\frac{1}{2}\frac{1}{2}\frac{1}{3}1\frac{1}{4}\frac{1}{3} & 434423 \\ 1\frac{1}{3}\frac{1}{3}\frac{1}{2}\frac{1}{3}\frac{1}{4} & 43642\frac{1}{2} & 325542 & 21431\frac{1}{2} & 224221 & 223143 & 111111 & 545455 \\ 1\frac{1}{7}\frac{1}{6}\frac{1}{7}\frac{1}{6}\frac{1}{7}\frac{1}{8} & \frac{1}{2}\frac{1}{2}11\frac{1}{4}\frac{1}{6} & \frac{1}{3}\frac{1}{3}\frac{1}{2}1\frac{1}{2}\frac{1}{4} & 1\frac{1}{4}\frac{1}{4}\frac{1}{3}\frac{1}{2}\frac{1}{5}\frac{1}{6} & 1\frac{1}{4}\frac{1}{3}\frac{1}{3}\frac{1}{4}\frac{1}{5} & 1\frac{1}{4}\frac{1}{3}\frac{1}{4}\frac{1}{4}\frac{1}{2}\frac{1}{3} & 1\frac{1}{5}\frac{1}{4}\frac{1}{5}\frac{1}{4}\frac{1}{5}\frac{1}{5} & 111111 \end{bmatrix}$$

$$X_{12}^* = \{X_{12}^1, X_{12}^2, \cdots, X_{12}^6\}$$

To educe all elements rough numbers and rough intervals of rough group decision matrix after designing the rough pairwise comparison matrix.

$$X = \begin{bmatrix} [1,1] & [X_{12}^-, X_{12}^+] & \cdots & [X_{18}^-, X_{18}^+] \\ [X_{21}^-, X_{12}^{i+}] & [1,1] & \cdots & [X_{28}^-, X_{28}^+] \\ \vdots & \vdots & & \vdots \\ [X_{81}^-, X_{81}^+] & [X_{82}^-, X_{82}^+] & \cdots & [1,1] \end{bmatrix}$$

$[X_{ij}^-, X_{ij}^+]$ is a rough number, X_{ij}^-, X_{ij}^+ is the lower and upper limiting values. The rough pairwise comparison matrix of A_1^*, A_2^*, A_3^* is X_1, X_2, X_3. X_2 and X_3 are not listed because of length limit

$$X_1 = \begin{bmatrix} [1,1] & [4.211,6.072] & [4.889,5.756] & [3.319,4.361] & [4.028,4.306] & [3.872,5.128] & [2.700,3.300] & [6.439,7.236] \\ [0.171,0.257] & [1,1] & [0.826,2.097] & [0.383,0.639] & [0.437,1.153] & [0.533,2.167] & [0.291,1.019] & [1.611,3.889] \\ [0.175,0.209] & [0.843,1.718] & [1,1] & [0.377,0.483] & [0.383,0.639] & [0.497,1.268] & [0.254,0.417] & [1.872,3.128] \\ [0.240,0.310] & [1.889,2.756] & [2.117,2.917] & [1,1] & [1.069,1.769] & [1.118,2.879] & [0.497,1.268] & [3.100,4.900] \\ [0.235,0.249] & [1.444,2.706] & [1.764,2.561] & [0.636,1.236] & [1,1] & [0.928,2.111] & [0.432,0.657] & [3.244,4.111] \\ [0.201,0.269] & [1.208,3.104] & [1.118,2.803] & [0.525,1.811] & [0.653,1.520] & [1,1] & [0.352,0.648] & [2.889,3.756] \\ [0.311,0.386] & [2.039,4.439] & [2.681,4.319] & [1.118,2.803] & [1.728,2.628] & [1.872,3.128] & [1,1] & [4.444,4.889] \\ [0.139,0.156] & [0.370,0.787] & [0.352,0.648] & [0.218,0.362] & [0.253,0.314] & [0.273,0.373] & [0.206,0.228] & [1,1] \end{bmatrix}$$

Calculating each hierarchy requirement weight of expert .Disassembled the matrix X into rough lower boundary matrix X- and rough upper boundary matrix X+, figured out the eigenvalue and eigenvector. ForX_1, we can acquire requirement weight as follows.

$$W^- = [w_1^-, w_2^-, \cdots, w_8^-]^T = [-0.830, -0.125, -0.124, -0.255, -0.219, -0.178, -0.360, -0.073]$$

$$W^+ = [w_1^+, w_2^+, \cdots, w_8^+]^T = [0.728,0.210,0.145,0.309,0.246,0.256,0.423,0.071]$$

Acquire requirement weight of the first hierarchy requirement Ni through normalization .

$$f(N) = \frac{1}{2}(|f^-| + |f^+|) = [0.093,0.112,0.011,0.085,0.501,0.170,0.325]$$

（supposing the danger coefficient is 0.5）

And in the same way, the requirement weight of the second and the third hierarchy can be acquired as follows.

$$[f_1, f_2, f_3, f_4, f_5, f_6] = [0.253,0.167,0.089,0.110,0.172,0.013]$$

$$[f_1, f_2, f_3, f_4, f_5, f_6, f_7] = [0.093,0.112,0.011,0.085,0.501,0.170,0.325]$$

The application of Rough Analytic Hierarchy Process which is used for the requirement weight of expert in Quality Function Deployment can eliminate its un-coherence .In the same time it made the process more nicety because of having idiographic data. Because there is no hypothesis and it was calculated with the date root in actual inquisitional result. The calculated result with Rough Analytic Hierarchy Process objectivity of data was ensured. Based on the analysis above, the sort of the first hierarchy indexes are total power, operability and maintainability, reliability and service

life, survivability, maneuverability, economy, impact-resistance, life cycle cost; the second evaluation indexes are propeller performance, power distributing, propeller distributing, control mode, emergency ability, safety backup; the third evaluation indexes are shape design, bearing arrangement, steering module, seal performance, cooling device, insulating performance, sewage system.

Summarization

This article study and establishes the method of evaluation indexes weight calculation and then calculates the evaluation indexes weight of the float board propulsion system, which aims at solving the evaluation indexes weight calculation in the process of ambiguity and uncertainty for the float board propulsion system establish. This evaluation indexes that are divided into four hierarchies are good for design and evaluation of the float board propulsion system. The study of this article will provide scientific guidance for design and evaluation of the project and lays the certain theory foundation for quality of the design for the float board propulsion system

Reference

[1] Xiong Wei. Quality Function Deployment, Bei Jing, Science Press, 2009.
[2] Wu Xiao-ping and Wang Yu, Theory and method of integration evaluating the warship equipment system, Beijing, Science Press, 2007.
[3] Zhang Qing-wen, Application of podded electric propulsor and research on the propeller, Da Lian, dalian university of technology,2005.
[4] Zhang Wei, Numerical simulation and analysis on hydrodynamic performance of the podded propulsor. Shang Hai, shang hai jiao tong university, 2008.
[5] Wang Xiao-dun and Xiong Wei, “Rough AHP approach for determining the importance ratings of customer requirements in QFD,” Computer Integrated Manufacturing Systems, vol.16 No.4, pp. 763-771, April 2010 .
[6] Yang De-ling and Chen Yao-gang, “The use and improvement of analytical approaches to QFD,” Science Research Management, vol.24 No 5, pp. 121-127, September 2003.
[7] Zeng Fan-ming, Wu Jia-ming Elements of Marine Power Plant, Beijing, National Defence Industry Publishing Company, 2009.
[8] O. M. Faltinsen, Loken A. E. Slow drift oseillations of a ship in irregular waves. A.0.R. 1979,1(1),31-50.

Applied Mechanics and Materials Vol. 597 (2014) pp 468-471
© (2014) Trans Tech Publications, Switzerland
doi:10.4028/www.scientific.net/AMM.597.468

The Simulation Studies of PWM Voltage Source Rectifier under Unbalanced Grid Voltage

ZHANG Junli[1,a *] LI Yuren[2,b]

[1] Northwestern Polytechnical University, Xi'an, 710007, China

Baoji University of Arts and Sciences, Baoji, 721013, China

[2] Northwestern Polytechnical University, Xi'an, 710007, China

[a]E-mail: zjl259@163.com, [b]E-mail:liyuren@nwpu.edu.cn

Keywords: wind power generation system, simulation, PWM rectifier, response speed, mathematical model, controller

Abstract: Under the balanced or unbalanced grid voltage, the PWM voltage source rectifiers should have many advantages such as sinusoidal input current, unity power factor, four-quadrant operation, the DC voltage stability, etc., so it can be employed in very broad application field. When there is only fundamental positive sequence current component in AC current, the voltage in DC side will remain constant, the rectifier will achieve efficient transformation of power quality. It is necessary to start from control strategies to eliminate harmful components such as the negative sequence current, to improve power quality in rectifier transformation. The mathematical model of PWM rectifier under unbalanced grid voltage was established in the synchronous rotating coordinate system in this paper. The simulation studies of rectifier under unbalanced grid voltage were conducted

Ⅰ. Introduction

The problems of traditional power energy are environmental pollution and the less and less quality, so the development and utilization of renewable energy sources such as wind power energy and solar power energy are attracting more and more attention. Harmonic problems in power system are mainly caused by the application of power electronics equipments like diode or thyristor rectifiers, which absorb non-sinusoidal currents from the Common Connected Point (CCP) of the grid. High power factor rectifiers subsequently occur and have been used in many occasions. Pulse Width Modulation (PWM) rectifiers, which can sent to or absorb from almost sinusoidal AC current and realize unity power factor, have been widely investigated, and some of them based on Voltage Source Converter (VSC) have already been put into practice [1,2,3]. For PWM rectifiers based on VSC, there are a variety of the trigger pulse generation methods. These methods are applied to improve the quality of the voltages and currents of the rectifiers from different perspectives. References [4, 5, 6] demonstrated the realization process of SPWM pulse generator based on CPLD. Although it is relatively simple and easy, SPWM generator technology has many disadvantages such as high harmonic content and low voltage utilization rate. References [7, 8] analyzed Selective Harmonic Elimination (SHE-PWM) technology used in the VSC pulse generator system. SHE-PWM technology can eliminate the low-order harmonics of the AC output voltages and currents, but it eliminates lower order harmonics at the expense of pulsing high voltage harmonics. For Selective Harmonic Elimination (SHE-PWM) technology, the frequencies of voltage harmonics concentrate near the switching frequency.

The asymmetric grid fault will bring many problems: the negative sequence current in grid side converter ac side resulting in the three phase current asymmetry; 2 times fundamental frequency fluctuations in grid side converter dc side. The dc side voltage fluctuations will cause the 3rd harmonic in ac input current which will pollute the grid and damage other electricity equipments. The dc side voltage fluctuations will cause frequently capacitor charging and/or discharging and reduce its life. Large fluctuations of dc side voltage in the grid side converter will cause system instability [9, 10, 11].The traditional methods used mainly restrained negative sequence current and counterpoised three phase current, but they do not eliminate the dc side voltage ripple.

Ⅱ. The mathematical model of PWM rectifier

The three-phase PWM rectifier is consisted of three legs, each of which has two switches with anti-paralleled diodes as shown in Fig.1.

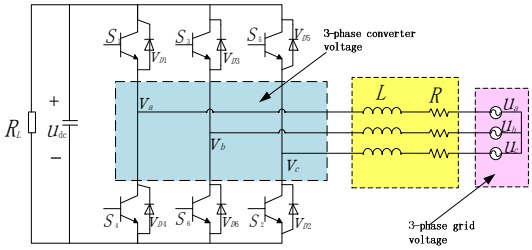


Fig. 1 Schematic of Grid-Connected PWM converter

The schematic diagram of the voltage source PWM converter is shown figure 1. In figure 1, u_a, u_b and u_c is the instantaneous voltage value of a-phase, b-phase, c-phase of the grid respectively, v_a, v_b and v_c is the instantaneous voltage value of a-phase, b-phase, c-phase of the converter ac side respectively, i_a, i_b and i_c is the instantaneous current value of a-phase, b-phase, c-phase of the grid respectively, L is the inductance value of line reactor, R is the line resistance, C is the capacitance of the dc side and u_{dc} is its both ends voltage, R_L is the load resistance.

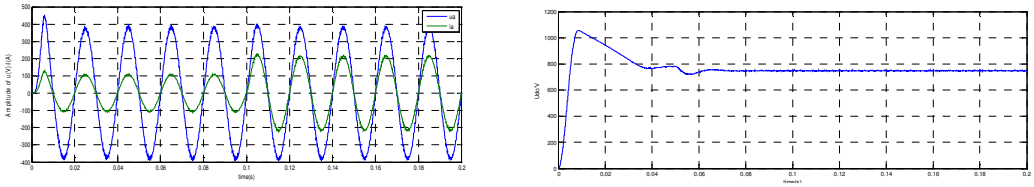
$$\begin{cases} u_{gd2}^{p} = R_g i_{gd2}^{p} + L_g \dfrac{di_{gd2}^{p}}{dt} + u_{cd2} - \omega L_g i_{gd2}^{p} \\ u_{gq2}^{p} = R_g i_{gq2}^{p} + L_g \dfrac{di_{gq2}^{p}}{dt} + u_{cq2} - \omega L_g i_{gq2}^{p} \end{cases} \tag{1}$$

$$\begin{cases} P_{g2}^{p} = \dfrac{3}{2}(i_{gdp}^{p} u_{gdn}^{p} + i_{gqp}^{p} u_{gqn}^{p} + u_{gdp}^{p} i_{gdn}^{p} + u_{gqp}^{p} i_{gqn}^{p}) \\ Q_{g2}^{p} = \dfrac{3}{2}(i_{gdp}^{p} u_{gqn}^{p} - i_{gqp}^{p} u_{gdn}^{p} + u_{gqp}^{p} i_{gdn}^{p} - u_{gdp}^{p} i_{gqn}^{p}) \end{cases} \tag{2}$$

In synchronous rotating coordinate system, voltage and power components of 2nd frequency were shown in (1) (2) respectively, wherein, u, P, Q was voltage, active power and reactive power, respectively, superscript p represented the forward rotation coordinate system, the subscript g indicated the grid, d, q denoted d-axis and q-axis components of the rotating coordinate system, 2 represented 2nd frequency components [12].

III. Simulation Analysis

In dynamic state, when voltage source PWM converter operated in unit power factor, active power stepped change, voltage and current waveforms of phase a, voltage waveform of the dc side were shown in figure1.



(a) Voltage and current of phase a (b) Voltage of dc side

Fig. 1 Step responses of active power in unit power factor operation

As PWM converter running at unity power factor, when active power stepped change, its dynamic response process could be completed in a half grid cycle and response speed was fast. The dc side voltage decreased in different degrees, which was mainly due to the increase of dc side capacitor not following the increase of the load. But the small voltage decrease in dc side capacitor was entirely within the acceptable range.

IV. Conclusions

To avoid the positive and negative sequence decomposition process in control unit, the mathematical model of PWM rectifier under unbalanced grid voltage was established in the synchronous rotating coordinate system in this paper. The simulation studies of rectifier under unbalanced grid voltage were conducted and the results indicated that this method improved the system response speed, reduced the computation amount of control system, and it had the advantages such as the elimination or suppression of all harmonics, only requirement of real-time values of voltage and current, without detection and treatment of all the positive and negative sequence component harmonics, with strong robustness and easy implementation, et al..

Acknowledgment

Project Supported by Shaanxi Provincial Department of Education (2013JK1022). Project Supported by Baoji City Science and Technology Bureau (2013R1-2). Project Supported by National Natural Science Foundation of China (51207002).

References

[1] Beig, A.R.. Constant v/f induction motor drive with synchronised space vector pulse width modulation [J]. IET Power Electronics, 2012, 5(8), pp:1446-1455.

[2] Jie, Li, yujie, Zhang. Technology of grid-connected wind power generation [C]. Advanced Materials Research, 2012, 542-543, pp:47-51.

[3] Liu, Chao, Huo, Y., Wang, Q. Research on SR wind power system [C]. Proceedings of the 2013 International Conference on Advanced Mechatronic Systems, 2013, pp:268-273.

[4] Brando, G., Dannier, A., Del Pizzo, A. Generalized direct power control for multilevel VSR converters [C].IEEE EuroCon 2013, pp:1086-1093.

[5] Zheng, Xiancheng, Huang, Shen, Zhang, Xiaobin. Exploring output impedance of PWM rectifier in an aircraft's variable frequency power system [J]. Journal of Northwestern Polytechnical University, 2013, 31(4), pp:647-652.

[6] Fan, Shengfang, Zhang, Kai, Xiong, Jian, et al. An improved control system for modular multilevel converters featuring new modulation strategy and voltage balancing control [C].2013 IEEE Energy Conversion Congress and Exposition,pp:4000-4007.

[7] Cai, Xinhong, Zhao, Chengyong, Pang, Hui, et al. A novel DC voltage control of MMC-HVDC power transmission system based on discrete mathematical model of MMC [J].Power System Technology, 2013,37(9), pp:2403-2409.

[8] Lepanov, Mikhail, Rozanov, Yuriy. Multifunctional regulator based on SMES and power electronic converter for increase of power quality and power supply reliability [C]. Proceedings of 2013 4th International Conference on Power Engineering, Energy and Electrical Drives, 2013, pp:1387-1391.

[9] Tian, Yusheng, Jiang, Qirong. A dual-current-loop control method based on system current detection for LCL-filter-based Active Power Filters [C]. 2013 - 39th Annual Conference of the IEEE Industrial Electronics Society 2013, pp:8498-8503.

[10] Rojas, C.A., Perez, M.A., Wilson, A., et al. Reactive power control using a carrier-based modulation for Cascaded Matrix Converter [C]. 2013 - 39th Annual Conference of the IEEE Industrial Electronics Society, 2013, pp:4913-4918.

[11] Wolf, Christopher M., Degner, Michael W., Briz, Fernando. Analysis of current sampling errors in PWM, VSI drives [C]. 2013 IEEE Energy Conversion Congress and Exposition, 2013, pp:1770-1777.

[12] WANG Meng, XIA Changliang, SONG Zhanfeng, et al.. A Power Resonance Compensation Control Strategy for PWM Rectifiers Under Unbalanced Grid Voltage Conditions [J]. Proceedings of the CSEE, 2012, 32(21):46-53.

Applied Mechanics and Materials Vol. 597 (2014) pp 472-475
© (2014) Trans Tech Publications, Switzerland
doi:10.4028/www.scientific.net/AMM.597.472

The Skimmer Selection Based on Fuzzy Decision in Response to Oil Spill

ZHANG Yindong[1,a], LIU Yang[2,b]

[1]College of Marine Engineering, Dalian Maritime University, Dalian, 116026, china

[2]College of Economics and Management, Dalian University, Dalian, 116622, china

[a]dong-zyd@163.com, [b]l_y_apple@163.com

Keywords: Oil spill response, Fuzzy Synthetic Evaluation, Skimmer

Abstract. The decision method based on Fuzzy Synthetic Evaluation is presented to achieve skimmer selection in oil spill response. Firstly, the evaluation index system of skimmer is determined. Secondly, the fuzzy set theory is introduced to achieve quantification of skimmer qualitative indexes and the evaluation matrix of skimmer is established by expert investigation. Then the alternative skimmers are evaluated by the method of Fuzzy Synthetic Evaluation, and the optimal selection of skimmer can be obtained.

Introduction

Oil spill has become a major issue in the protection of ocean environment over the past decades and oil spill response is to minimize the overall impacts on natural and economic resources with all possible technical means. Mechanical recovery is the most commonly used oil spill response technology which can recover floating oil from the water surface with mechanized equipment known as skimmers which are specialized devices to recover oil (including oil–water mixtures) from the sea surface, without changing either the physical or the chemical properties of the oil. There are numerous types or categories of skimmers, including weir, brush, rope, drum and DIP(Dynamic Inclined Plane), and each skimmer has different performance under various operating conditions [1,2]. So the skimmer selection based on fuzzy decision in the oil spill response is presented in the paper to choose the most appropriate device to recover floating oil efficiently under various operating conditions.

The Evaluation Index System of Skimmer

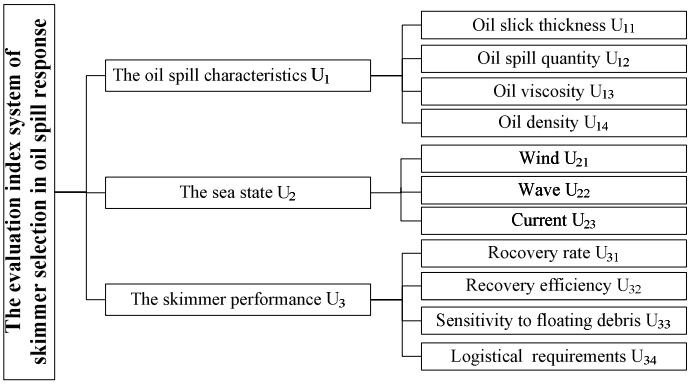


Fig.1 The evaluation index system of skimmer

The oil spill response is normally a complex, multi-disciplinary affair, few people can be expected to possess all of the specific knowledge about skimmer required to arrange an effective response operation[3,4]. Moreover, each oil spill accident is different from the other in many respects such as occurrence location, sea state, oil characteristics and quantity, which make various requirements about chosen skimmer performance. The evaluation of skimmer performance involves many fuzziness factors and through a comprehensive analysis, a new evaluation index system is built.

The Fuzzy Synthetic Evaluation Process

The Establishment of Skimmer Evaluation Index Set. Using a modified Delphi method, by information collection and expert consultation, the skimmer evaluation index set U is determined. The set U is divided into *n* subsets and the following conditions are met.

$$\bigcup_{1}^{n} U_i = U, U_i \cap U_j = \varnothing, i \neq j \tag{1}$$

For skimmers selection decision problem, evaluation index system shown in Fig. 1 is established.

$U=\{U_1, U_2, U_3\}, U_1=\{U_{11}, U_{12}, U_{13}, U_{14}\}, U_2=\{U_{21}, U_{22}, U_{23}\}, U_3=\{U_{31}, U_{32}, U_{33}, U_{34}\}$.

The Establishment of Index Weigh Set. The experts in the field of oil spill mechanical recovery are invited to determine relative importance of each factor in the evaluation system, which is applied to construct judgment matrix W.

$$W=\begin{bmatrix} w_{11} & w_{12} & \cdots & w_{1n} \\ w_{21} & w_{22} & \cdots & w_{2n} \\ \vdots & \vdots & \vdots & \vdots \\ w_{n1} & w_{n2} & \cdots & w_{nn} \end{bmatrix} \quad \text{And } w_{ij}=1/w_{ji}, w_{ii}=1$$

According to method of Analytic Hierarchy Process, the weight value is obtained as follows[5]:

$$a_i = \left(\prod_{i=1}^{n} w_{ij}\right)^{1/n} \Big/ \sum_{i=1}^{n} \left(\prod_{j=1}^{n} w_{ij}\right)^{1/n} \tag{2}$$

The Establishment of Comment and Score Set. The comment set V is determined according to the actual situation and its division should not be too coarse or too tiny, generally divided into 5-7 levels. In the skimmer selection decision-making problem, the comment set with five levels is built, that is $V=(v_1, v_2, v_3, v_4, v_5)$ = (good, better, common, poorer, poor). And the corresponding score set is expressed as $F=(1, 0.8, 0.6, 0.4, 0.2)$.

The Second Level Fuzzy Synthetic Evaluation of U_{ij}. Because of the ambiguity, the index U_{ij} can't be represented by specific values. Through expert investigation method, the subjection degree of U_{ij} for comment V_j is obtained. According to the principle that the higher evaluation score of skimmer can be achieved when skimmer working characteristics is more suitable for the working conditions. So the judgment matrix is constructed on the basis of the principle above. Through evaluating each single factor of U_i, The fuzzy evaluation matrix R_i is described as follows:

$$R_i = \begin{bmatrix} r_{i11} & r_{i12} & \cdots & r_{i1k} \\ r_{i21} & r_{i22} & \cdots & r_{i2k} \\ \vdots & \vdots & \vdots & \vdots \\ r_{im1} & r_{im2} & \cdots & r_{imk} \end{bmatrix}.$$

Here, K represents level number of comment set and r_{imj} represents the subjection degree of U_{im} for comment V_j.

The comprehensive evaluation of U_i is carried out and the result B_i is shown by the following.

$$B_i = W_i R_i = W_i \begin{bmatrix} r_{i11} & r_{i12} & \cdots & r_{i1k} \\ r_{i21} & r_{i22} & \cdots & r_{i2k} \\ \vdots & \vdots & \vdots & \vdots \\ r_{im1} & r_{im2} & \cdots & r_{imk} \end{bmatrix} = (b_{i1}, b_{i2}, \cdots, b_{ik})$$

Here, the b_{ij} is determined by $M(\cdot, \oplus)$ operator and $t = 1, 2, \cdots, k$ .Through the normalized processing of B_i, the B_i' is obtained. Similarly, after the synthetically evaluating sub-factors of U, the overall evaluation matrix B is achieved [6].

$$B=(B_1', B_2', \cdots, B_n')^T$$

The Fuzzy Synthetic Evaluation of U. If the level 1 fuzzy synthetic evaluation results of U is represented as Z, the Z can be obtained by the following formula.

$$Z = W \bullet B = W \bullet (B_1', B_2', \cdots, B_n')^T = (z_1, z_2, \cdots, z_m)$$

Here, the $z_i(i=1,2,\cdots,m)$ is calculated by $M(\bullet, \oplus)$ operator. And then the synthetic evaluation results of the skimmer named C can be achieved by the following formula [7, 8].

$$C = Z \bullet F^T$$

Therefore, according to the above step, the fuzzy synthetic evaluation results of every candidate skimmer can be obtained and the skimmer with the highest evaluation score is selected optimal device which would recover oil spill efficiently.

The Case of Skimmer Selection in Oil Spill Response

If an oil spill had occurred in the harbor because of ship collision and 200 tons of fuel oil with low viscosity (100cSt) and density (900kg/m3) is leak into the water. The floating oil had been contained by boom and the thickness of oil slick is 20mm. At present, the sea state is level 2 and the intensity of wind, wave and current is moderate. There are five kinds of skimmers available in the oil spill repository of harbor, which include the skimmer of weir, brush, disc, vacuum suction and DIP.

The evaluation index set of skimmer selection has been accomplished as shown in Fig.1. The comment set V and score set F are the same as above. In the case of weir skimmer, by application of Analytic Hierarchy Process, the judgment matrix W of rule layer is built as follows.

$$W = \begin{bmatrix} 1 & 1 & 3/2 \\ 1 & 1 & 3/2 \\ 2/3 & 2/3 & 1 \end{bmatrix}$$

According to the formula (2), the weight of level 1 evaluation index is in line with the consistency test and described as follows.

$$W = (0.2857, 0.2857, 0.4286)$$

Using the same method as above, the weight of level 2 evaluation index about weir skimmer is obtained as follows.

$$W_1 = (0.3, 0.2, 0.3, 0.2),\ W_2 = (0.25, 0.5, 0.25),\ W_3 = (0.3, 0.3, 0.2, 0.2)$$

Through expert investigation, single factor fuzzy evaluation matrixes of the weir skimmer in this oil spill accident are obtained and shown as follows.

$$R_1 = \begin{bmatrix} 0.2 & 0.5 & 0.3 & 0 & 0 \\ 0.3 & 0.4 & 0.2 & 0.1 & 0 \\ 0.2 & 0.4 & 0.4 & 0 & 0 \\ 0.2 & 0.3 & 0.3 & 0.2 & 0 \end{bmatrix},\ R_2 = \begin{bmatrix} 0.2 & 0.3 & 0.3 & 0.1 & 0.1 \\ 0 & 0.2 & 0.3 & 0.4 & 0.1 \\ 0.1 & 0.2 & 0.3 & 0.3 & 0.1 \end{bmatrix},\ R_3 = \begin{bmatrix} 0.5 & 0.3 & 0.2 & 0 & 0 \\ 0 & 0.1 & 0.2 & 0.5 & 0.2 \\ 0.1 & 0.2 & 0.3 & 0.4 & 0 \\ 0.1 & 0.2 & 0.3 & 0.3 & 0.1 \end{bmatrix}$$

The comprehensive evaluation of weir skimmer is carried out and the result $B^{(1)}$ is shown by the following.

$$B^{(1)} = \begin{bmatrix} B_1' \\ B_2' \\ B_3' \end{bmatrix} = \begin{bmatrix} W_1 \bullet R_1 \\ W_2 \bullet R_2 \\ W_3 \bullet R_3 \end{bmatrix} = \begin{bmatrix} 0.22 & 0.41 & 0.31 & 0.06 & 0 \\ 0.075 & 0.225 & 0.3 & 0.3 & 0.1 \\ 0.19 & 0.2 & 0.24 & 0.29 & 0.08 \end{bmatrix}$$

The level 1 fuzzy synthetic evaluation results of weir skimmer named $Z^{(1)}$ can be represented as follows.

$$Z^{(1)} = W \bullet B^{(1)} = (0.1654, 0.2682, 0.2777, 0.2262, 0.0626)$$

So the overall evaluation value of weir skimmer named $C^{(1)}$ is obtained and shown as follows.

$$C^{(1)} = Z^{(1)} \bullet F = 0.6495$$

Similarly, the overall evaluation values of other four skimmers are achieved and expressed as follows.

$$C^{(2)} = 0.4865, C^{(3)} = 0.3573, C^{(4)} = 0.2837, C^{(5)} = 0.7362.$$

According to the overall evaluation values of five skimmers, for oil spill response decision maker, the DIP skimmer is the optimal selection to deal with this oil spill accident and the weir skimmer is another alternative selection.

Conclusion

As the important step in oil spill response, the skimmer selection in mechanical recovery directly determines final effect of pollution control. According to the performance characteristics of skimmers, the evaluation index system is presented in the paper and the fuzzy set theory is introduced to achieve quantification of skimmer qualitative index. Then the alternative skimmers are evaluated by the method of Fuzzy Synthetic Evaluation, with the excessive subjectivity in skimmer evaluation being reduced, and the decision results can be better suited to the actual situation.

Acknowledgements

This work was financially supported by the Fundamental Research Funds for the Central Universities(No.3132013028), National Natural Science Foundation Item (No. 51109021) and Ministry of Transportation Basic Research Project (No.2014329225040).

References

[1] N. P. Ventikos, E. Vergetis, H. N. Psaraftis, Journal of Hazardous Materials, 107(2004), 51-58.

[2] A. B.Nordvik, Pure Appl. Chem., 1 (1999), 5-16.

[3] Ornitz, Barbara E., Esq. Champ, Michael A., Elsevier, Amsterdam, 2002.

[4] M.Fingas, J. Charles, Lewis Publishers, New York 2000.

[5] Z.S. Xu, Fuzzy Optimization Decision Making., 2 (2007), 109-121.

[6] Y.D. Zhang, H.P. Zhang, Y.L. Ji, W.H. Li, Fourth International Seminar on Modern Cutting and Measurement Engineering. 11 (2011), 1–3,.

[7] M. Hua, Q. Z. Zhang, and H. S. Hong, Chemical Industry Times, vol.19(10) , (2005), 34-36.

[8] M. Jianjun, Journal of Textile Research, 12(2008), 100-102.

Applied Mechanics and Materials Vol. 597 (2014) pp 476-479
© (2014) Trans Tech Publications, Switzerland
doi:10.4028/www.scientific.net/AMM.597.476

Research on Manufacturing of Blade Screw in Solid-liquid Separator

Wang Jianjun[1,a], Wang Ke[1,b], Wu Qiong[2,c]

[1]Shenyang University of Technology, Shenyang 110023, China
[2]Zhejiang University of Water Resources and Electric Power, Hangzhou 310018, China
E-Mail: [a]wangjjyf@qq.com, [b]sunxingw@ 126.com, [c]385191263@qq.com

Keywords: Blade Screw, Solid-liquid separator, Expansion plan, Polar radius equation

Abstract: Blade screw propeller is used as the pushing and squeezing machine which is often used in the liquid separator for software materials. The core part of blade screw is stainless steel material with wide tooth, thin wall and other characteristics, and its processing method is different from the cylindrical surface spiral groove processing. Usually, its machining process is based on a certain forming technology to produce spiral leaf firstly, then welding leaves on the shaft. The cylindrical blade screw in test equipment adopts triangle method to calculate the blank dimensions. Variable cross section of the outer ring graph is realized by using the polar radius equation drawing in the drawing software.

1. Introduction

Solid-liquid separator is a widely used general machinery. With the development of engineering technology, it is widely applied in the chemical, pharmaceutical, textile, mining, energy, metallurgy, food, beverage, water treatment and other fields. The technological level of its development will directly affect the advancement of modern industrial production. The equipment which utilizing the principle of screw extrusion to do the solid-liquid separation is a type of solid liquid separator, whose characteristic is continuously-feed, continuous-discharge, high dehydration rate, compact structure, small footprint, easy installation, low maintenance cost and it can also be equipped with washing accessories[1]. Therefore, many solid-liquid separators adopt screw propeller as forward-pushing extrusion mechanism. The screw propeller blades, which is a key component of solid liquid separator, shows good performance and satisfactory effect in the material extraction of fiber and wool. The blade screw mentioned in this paper is one of the key parts in the equipment of the extraction of qualitative materials lotion and solid-liquid separation test.

2. Working Principle of the Screw Propeller Blade

The working principle of the screw propeller is: solid-liquid mixed materials get into inner cavity through the inlet and then flow to the left side with the rotating driving force of the screw blade. In the process of material flowing, the liquid is discharged through a cavity hole. With the cavity pressure gradually increasing and finally reaching the maximum point in the cone part 4[2], then the solid material will discharge at the discharging port and go to the next processing.

Analyzing of dewatering principle of screw propeller blades, the rotary extrusion process can be regarded as a black box system, in which the input parameters interact with each other but relationship between them is unknown. The input object is solid-liquid mixed material, with the initial moisture content and viscosity, the screw rotation speed, blade screw size and inlet pressure as parameters, the output becomes material or solid containing a small amount of water. In the manufacturing process of new product, by adjusting the inlet pressure, the screw rotation speed of blade, we can achieve the requirement of the extraction. Propeller adopts enclosed structure which can guarantee the working environment clean while olid materials handling, but it has higher requirements for the blade of the cylindrical machining. According to different occasions, the structure of the screw blade is slightly different. Some by joining together of cylinder and cone surface, some inner diameter changes while external diameter maintain the same, others take inner and external diameter gradual change at the same time, but all these share the common characteristics of having tooth width, thin wall and large volume between the spiral blades and they are suitable for the software delivery and extrusion of the flocculent material.

3. Blade Screw Manufacturing

3.1 Spiral Blade Forming Technique

The spiral groove processing of cylindrical surface usually use the technique of the forming cutter milling, turning, ordinary flat cutter milling[3], whirlwind milling, or with no instantaneous center envelope. The spiral blade of the blade screw often choose the material such as stainless steel and the processing method is different from the cylindrical surface of spiral groove processing—that is, using some forming technology to manufacture spiral blade and then, welding the spiral blades on the surface of a cylinder in turn or as a whole. There are various methods of spiral blade forming, which in general can be divided into two categories: one is single chip forming technology, including single chip shape method, manual copying method and mold pressing method, etc., this process need to divide blade screw into pitch for unit production; The other kind is continuous forming technology, including combination method, winding forming, extrusion forming and roll forming method, etc. Different forming technology has its own characteristics and application scope, the single chip shape method, manual copying method and extrusion forming method is suitable for single small batch production, the rest of the forming method is suitable for batch mass production situation [4].

3.2 Basic Size and Material of Screw

The spiral blade used in the equipment of extraction of qualitative materials lotion and solid-liquid separator test equipment is shown, the external diameter of blade screw D, the inside diameter d, the pitch of screw P and the angle parameter of the cone β is informed. There are requirements for spiral outer surface finish and spiral blade should be made of SUS304 stainless steel. This equipment is designed for some special kind of wool qualitative material extraction. With a small batch production, we should choose single chip shape method under the category of single chip forming technology.

4. Manufacturing Process of Blade Screw

The technological process of manufacturing blade screw by single chip shape method is: Firstly, prepare a single unit material for stretch forming and make unit pitch spiral blade; then by means of argon arc welding put multiple spiral blades together and nest in the shaft. Then again adopts argon arc welding between the inner ring of the helical blade and the joint surface of the cylinder; for there is a strict requirement for the space between the outer revolution surface and the inner cavity of solid-liquid separator. During the process of unit screw blade manufacturing, we need to leave some allowance in outer diameter for cylindrical finish machining; the last procedure is the blade helical surface polishing.

4.1 The Calculation of the Preparatory Material Size of Cylindrical Spiral Blade

There are two ways of calculation of the preparatory material size of cylindrical spiral blade: one with notch and the other not. There are small distinction between different methods. Considering that the test equipment is in small batch production, we adopt the calculation method of notch-bearing for convenience.

As shown in Fig. 1, triangle method is in common use in the calculation of notch-bearing blades. The spiral line is seen as the hypotenuse winding on a cylinder, whose diameter is d (or D). Based on the relationship of three sides of a right triangle, the length of the inner spiral line is derived as $s = \sqrt{(\pi d)^2 + P^2}$, the outer spiral line is $S = \sqrt{(\pi D)^2 + P^2}$, P in the equation is the pitch.

According to the relation between arc length, radius and the included angle, we can deduce the material preparatory formula of cylindrical spiral blades, as shown in Fig. 2:

$$t = (D-d)/2 \quad , \quad d_1 = 2ts/(S-s) \quad , \quad D_1 = 2tS/(S-s) \quad , \quad \alpha = (\pi D_1 - S)\times 360^\circ / \pi D_1$$

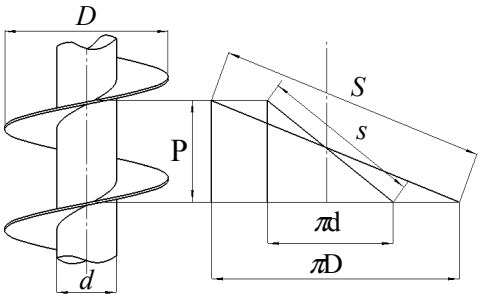


Fig.1 Calculation of Spiral Length by triangle method

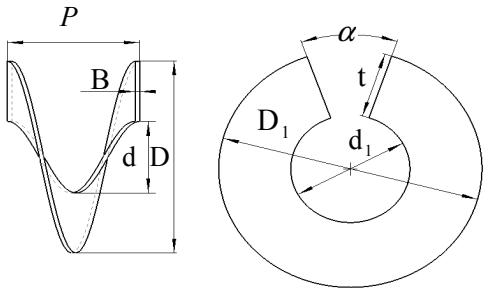


Fig.2 Developed Drawing of the Spiral Blade of the Cylindrical Part

Considering the assembling and welding of the spiral blades and the axes, there should be a welding joint δ in the inner diameter of the blades. In addition, there are accurate requirements for the external diameter, so finish machining allowance ε is needed. When facing practical calculation, we should rectify the inner diameter *d* and the external diameter *D*, namely $d^{'} = d + \delta$, $\mathrm{D}^{'} = \mathrm{D} + \varepsilon$. The external diameter in this test equipment $D = 293mm$, the spindle diameter $\mathrm{d} = 107mm$, the pitch $\mathrm{P} = 170mm$, the thickness of the blade $B = 3mm$, the weld joint $\delta = 1mm$, excircle finish machining allowance $\varepsilon = 3mm$, so we can figure out that $d^{'} = 108mm$, $\mathrm{D}^{'} = 296\,mm$, put them into the formula as the substitution of *d* and *D,* we can work out that $t = 94mm$, $d_1 \approx 126\,mm$, $D_1 \approx 314mm$, $\alpha = 15.11^{\circ}$.

4.2 Calculation of Material Preparation of Conical Spiral Blades

The calculation of the expanding sizes of conical spiral blade is one of the key technologies in the conical spiral blade production. From the perspective of mathematical model, there are double variables, namely as the angle changes, radius and arc length are changing at the same time. In the practical, it is difficult to calculate by using higher function method.

Some research have mentioned adopting "360 - degree calculation method" and "arbitrary angle processing method" [6], but these methods can only calculate the length of the spiral line approximately, which cannot visually describe the shape of the preparatory material, and it is not convenient to make the spiral blade cutting.

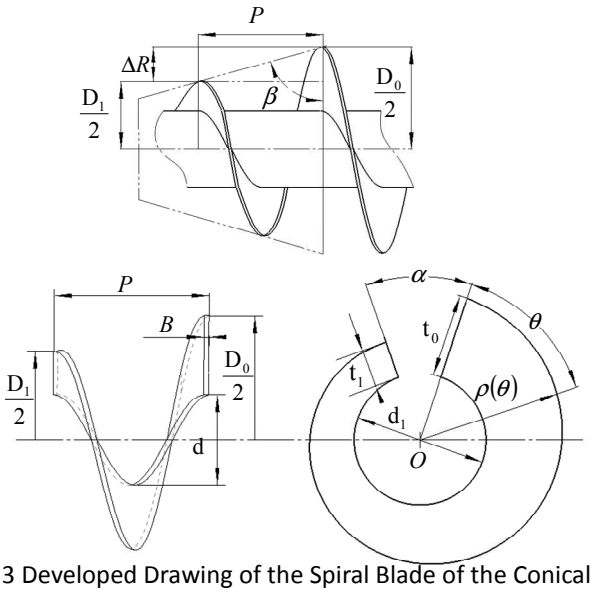


Fig.3 Developed Drawing of the Spiral Blade of the Conical Par

By comparing the conical spiral blade and cylindrical helical blade, it's easy to find the difference of outer ring. The outer diameter of cylindrical spiral blade is a constant value, while the outer radius of conical spiral blade changes along with the change of angle (see figure 3). So by calculating the width difference of inner and outer ring notch $\Delta\mathrm{R}$, we can know the law of curvature radius and the

transformation of the angle, therefore, deducing the polar diameter equation of conical spiral blade so as to draw the pictures of preparatory material, the derivational process is as follows:

The width difference of inner and outer ring notch:

$\Delta R = P / tg\beta$, $t_0 = (D_0 - d)/2$, $t_1 = t_0 - \Delta R$

Polar diameter change rate: $\xi = \Delta R / (2\pi - \alpha)$

Polar diameter equation: $\rho(\theta) = D_0/2 - \theta \times \xi$

Informed: $D_0 = D' = 296\ mm$, $d = d' = 108\ mm$, $\beta = 74^\circ$, in the calculation of unit conicalspiral blade we get $\alpha = 15.11^\circ$, put all these figures into formula, we can get: $t_0 = 94\ mm$, $\Delta R = 48.7467\ mm$, $t_1 = 45.25\ mm$, $\xi = 8.0982$, polar diameter equation is $\rho(\theta) = 148 - 8.0982\,\theta$.

According to the equation, we need to choose the function “formulas and curves” under drawing menu in CAXA electronic board. After selecting the polar coordinates, we could get an expanding picture of the cylindrical spiral blade if we input the angle end value and the parametric equation. The rest of the spiral blade of conical part figure is similar to the first paragraph, the difference is the initial outer diameter of the spiral blade.

4.3 Blade Screw Excircle Finish Machining

After welding the screw blades to the screw shaft individually, when doing the excircle finish turning, due to the thin blade wall, it is difficult to do the direct machining, and hard to guarantee the size accuracy and surface finish. Therefore we need to weld some pillar spot between adjacent blades before finishing. After the excircle finish turning, we need to remove those pillars, and then do the blade surface polishing. In practical application, due to the different working environment of blade screw, some other processing method, such as coating on blade surface is also needed.

5. Summary

As a key part of the screw propeller in solid-liquid separation machine, the manufacturing of blade will directly affects the work efficiency of the equipment. As the representatives, the blade screw in the extraction of qualitative materials lotion and solid-liquid separation test equipment provides a significant reference to other types of blade screw machining. When drawing the conical spiral blade by means of the computer drawing, it is convenient to solve the problem of size-calculation and can achieve the effect of convenient production of spiral blade.

References

[1] Lin Xiaojun, Shan Chenwei, NC Machining Technique about Screw Grooves on Cylinder [J]. Manufacturing Automation, 2010(8): 10-12.

[2] Li Xin, Mechanism Study of Screw Squeezer Based on Extrude Theory [D]. Beijing: Beijing University of Chemical Technology, 2011.

[3] Wu Jun, Fan Deshun, Interrupted Screw Filter [J]. Filtration and Separation. 2008(18): 36-37.

[4] Fan Xiaobo, Research on Thesis of Paper—Rolling Process of Endless Spirals and FEA Simulation [D]. Jiangsu: Jiangsu University, 2006.

[5] Jin Guangfa, Several Calculating Methods for the Evolving Dimension of the Helical Foil [J]. Mechanical Engineer, 2003(2): 64-65.

Applied Mechanics and Materials Vol. 597 (2014) pp 480-483
© (2014) Trans Tech Publications, Switzerland
doi:10.4028/www.scientific.net/AMM.597.480

VLC-LED Receiver Condenser with Optimized CPC

Wu Zhoxiao [*], Nie Youjin, Jin Wei, Zhang Zhixu, Qiao Qian, Gu Erdan

College of Control Engineering, Northeastern University at Qinhuangdao, 066004, China
ysuwzx@126.com

Keywords: VLC-LED (visible light communication based on LED); receiver; ray-tracing; CPC; concentration ratio

Abstract. In order to enhance the signal intensity of VLC-LED receiver, this paper describes a receiver condenser which is designed based on optimized CPC (compound parabolic concentrator) by using a truncated method, for achieving the aim of boosting receiver's ability of gathering light and enhancing signal intensity. The Monte Carlo-ray tracing simulation results shows that in the VLC-LED system, the optimized CPC condenser has those advantages, such as higher concentration ratio, larger concentrate light deviation angle.

1. Introduction

VLC-LED is a communication system that modulates the signal to the LED in order to transfer information. It could be widely used in those occasions electromagnetic interference strictly limited [1]. The receiver of the VLC-LED is responsible for detecting, recovering and processing signals. The SNR of the VLC-LED which is one of the key elements of the VLC-LED decides the communication performance of the whole system [2, 3]. But it is difficult to collect the lights as it is dispersive. When lights arrive at detector, they are extremely weak. So adding a condenser in front of receiver is quite necessary to reinforce signal.

In recent years, on the choice of the condenser of the receiver of the VLC-LED, hemispherical lens and Fresnel lens were adopted. Researches showed that hemispherical has a disadvantage in concentration ratio and Fresnel lens has a tendency to form light spot in the central point [4]. With the development of optical communication technique, using CPC as the optical antenna of the receiver was proposed [5]. Comparing with hemispherical lens and Fresnel lens, CPC is thinner, and has a larger angle of view, etc. But normal CPC is voluminous and its Condenser offset angle is small.

In this paper, truncated method is used to optimize CPC. Research showed that although the optimized CPC has a slight reduce in Condenser capacity, but the height reduce 50%, volume reduce 45%, maximum acceptance angle add from 29°to 43°, comparing with normal CPC.

2. Optimized CPC model

2.1 CPC structure

Intercept a section of the parabolic and revolve a circle around the axis of the condenser, the CPC (compound parabolic concentrator) comes out, the structure shown in Figure 1. Parabolic A round its focal point F_1 spines $\theta_{\max}$ in counterclockwise direction, similarly parabolic B round its focal point F_2 spines $\theta_{\max}$ in clockwise direction, so that F_1 (the focal point of parabolic A) falls on the bottom end of the parabolic B, F_2 (the focal point of parabolic B) falls on the bottom end of the parabolic A. By this analysis, *CD* is the diameter of the CPC entrance port, F_1 F_2 is the diameter of the focal plane, $\theta_{\max}$ is the maximum concentration angle of CPC.The included angle between

incident light and Y-axis is defined as incident angle θ_i . When $\theta_i > \theta_{\max}$ the incident light emitted from the entrance port after reflected by the CPC, otherwise the incident light concentrated on the focal plane after a reflection. When $\theta_i < \theta_{\max}$, in order to achieve the purpose of focusing the light energy collected on the focal plane.

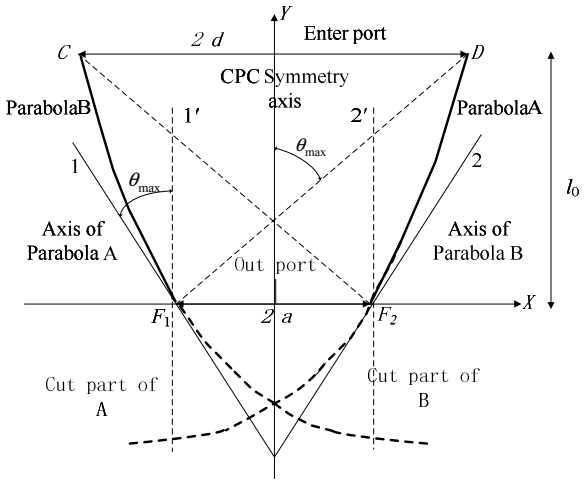


Figure 1 Compound parabolic concentrator

If *d* (radius of the entrance port) and *a* (radius of the exit port) meet:

$$\frac{d}{a} = \frac{1}{\sin\theta_{\max}} \tag{1}$$

The maximum theoretical concentration ratio will be reached:

$$C_{\max} = \frac{1}{\sin^2\theta_{\max}} \tag{2}$$

2.2 The structure of Optimized CPC

The upside of CPC almost parallel to the axis of symmetry, and the light-gathering efficiency at the upper end of the entrance port is not high, compared with the same concentration ratio of CPC, the length of the CPC which use the method of truncated is much shorter, so the truncated method is very important to improver the economy of the CPC. The structure of the CPC after truncated shown in Figure 2.

The truncated rate γ is defined as the proportion of the length of the cut off part in a specification CPC:

$$\gamma = \frac{l - l_T}{l} = \frac{l'}{l} \tag{3}$$

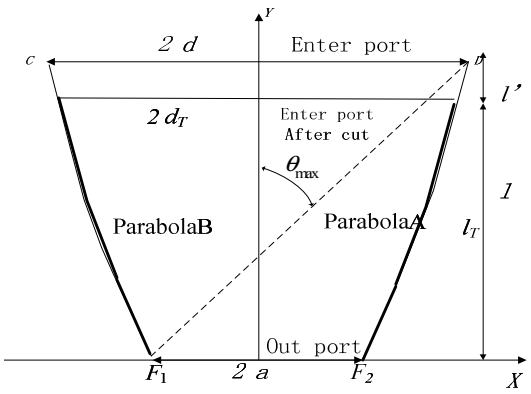


Figure 2 Schematic diagram of two-dimensional truncated CPC

3. Comparison between optimized CPC and standard CPC

Use Monte Carlo-ray tracing method to calculate the ray tracing of the optimized CPC.Parallel light incident CPC, and gradually increase the parallel light incident angle, observing optimized CPC whether there is light to reach the observation plane. Finally found, there are two incident lights when incident angle is 45.6°, but no light at 45.7°incidence. Be possible to determine that the optimal CPC after truncated has the maximum acceptance angle (accurate to 0.1°) experimental value 45.6 °.

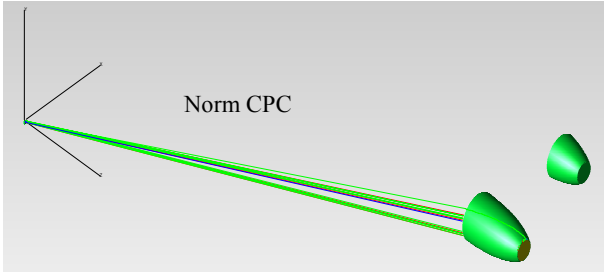
The data above suggest that, the deviation between the theoretical value and the experiment value is 3.27°.This is because in the Trace Pro simulation system, the nature of the parallel light is "Grid source", the light distribution within a rectangle 30 × 30mm, the density of the light is average, and there may be have no incident light when test on the edge; in order to closer to the actual situation, the thickness of the CPC baffle-board is 0.5mm, this can shield and reflect part of the light and reduce the amount of light to enter the CPC. But the influence of the thickness of the panel is ignored when the theoretical model is two-dimensional.

When testing the condenser performance, the communication distance D=500mm, the observation distance H=2mm, the deviation angle α=0, and the parameters of the condenser performance are shown in Table 1.

Table 1 Condenser parameters before and after optimized

parameters / type	Single-rays Minimum Lumens	Single-rays Maxim- um Lumens	Single-rays Mean Lumens	The number of lines incident
Norm CPC	8.3075×10^{-12}	2.3444	0.33865	1377
Opti CPC	22.6×10^{-12}	3.0052	0.28351	1125

This paper we also test the field angle of the optimized CPC. The maximum angle of deviation of CPC before and after optimization is shown in Figure 3.



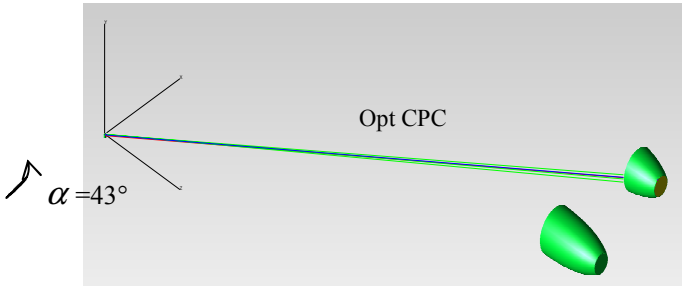


Figure 3 Maximum offset angle before and after truncated

The simulation results show, after 1/2 truncated although the total luminous flux and number the concentrated light decreased, but the falling range is only 16% to 18%; as for the dimensions of the device, the height of the optimized CPC reduced 50%, the volume reduced 45%. Therefore, light-gathering efficiency of the optimized CPC is improved; moreover after optimized, the field angle increased from 29° to 43° , all of these made mobility of the receiver improved significantly.

4.Conclusions

This article designed a new condenser of VLC-LED system based on the theory of specification CPC and truncated optimized CPC, the rear radius of the CPC is 11mm, the original acceptance angle is 25° ,and the truncated rate is 1/2. The Simulation results show that the number of converging light lines of the optimized CPC reduced by 16% to 18%, but the optimized CPC has a much more suitable size, the height of the optimized CPC reduced 50% and the volume reduced nearly 45%, so that the condensing efficiency improved. The FOV increased after the CPC optimized, and the original offset angle increase from $\alpha = 29°$ to $\alpha = 43°$, the mobility of the receiver can be improved significantly. Finally, compared the optimized CPC with hemispherical lens and the Fresnel lens in the same volume as condenser of receiver, the result shows that the optimized CPC has a maximum light intensity, the value is 60.1% higher than hemispherical lens and 31.78% higher than Fresnel lens, and the optimized CPC is easy to install, concentrating more uniform, so this new condenser construe is much more suitable to the VLC-LED system.

5. Acknowledgement

This work is supported by The National Nature Science Fund of China（61172044）and Research Funds of the northeastern university at Qinhuangdao (XNK201308).

References

[1]Vučić J, Kottke C, Nerreter S, et al. 513 Mbit/s visible light communications link based on DMT-modulation of a white LED[J]. Journal of Lightwave Technology, 2010, 28(24): 3512-3518.

[2]Li G, Su Y,Pei G, et al. Preliminary Experimental Comparison of the Performance of a Novel Lens-Walled Compound Parabolic Concentrator (CPC) with the Conventional Mirror and Solid CPCs [J]. International Journal of Green Energy, 2013, 10(8): 848-859.

[3]Kessentini, Hamdi; Bouden, Chiheb. Numerical and experimental study of an integrated solar collector with CPC reflectors [J]. Renewable Energy, 2013, 57: 577-586.

[4]Fang J, Zhang H, Jia H, et al. Compound parabolic concentrator applied as receiving antenna in scattering optical communication[J]. Chinese Optics Letters, 2010, 8(5): 478-481.

[5]NIU L,LIAO H, ZHANG J, et al. Optimization design of compound parabolic concentrator in the weak light detector [J]. Acta Photonica Sinica, 2009, 38(12): 3079-3083.

Applied Mechanics and Materials Vol. 597 (2014) pp 484-487
© (2014) Trans Tech Publications, Switzerland
doi:10.4028/www.scientific.net/AMM.597.484

300 MW Coal Tangential Boiler Furnace Numerical Simulation

Hongxian Liu [1, a*], Binxia Li [2,b]

Energy and Power Engineering College, Northeast Dianli University, Jilin 132012, China,

[a]Email: 603818108@qq.com

[b]Email: 981553201@qq.com

Keywords: tangential firing boiler; Numerical simulation; The residual rotation; The temperature deviation

Abstract. By using the computational fluid dynamics software Fluent and the choice of the reasonable mathematical model, the flow, heat transfer and combustion are simulated in a 300 MW tangential firing boiler furnace. In the process of numerical simulation in the furnace, the gas phase turbulent flow usesRealizable model for both sides and solves the governing equations using SIMPLEC algorithm. Calculation results show that the highest temperature in the furnace is in the burner area,the whole furnace space rotates flow field, residual rotation still exists in the exit of the furnace, and the smoke temperature deviation causes in the residual rotation of furnace exit.

Introduction

For wide adaptation of coal and high combustion efficiency, tangential firing way has been widely used in coal-fired power plants in China. In large tangential firing boiler, with the rotation of the airflow rise, rotation weakenes gradually, but residual rotation in furnace exit still exists, so that in furnace outlet smoke temperature and smoke velocity are distribution, triggering overtemperature tube-burst accident, and with the increase of the capacity of the boiler, the smoke temperature deviation has a tendency to increase, which has a serious influence on the safety and economy of boiler operation. The flow and heat transfer in a tangential firing boiler furnace and the combustion characteristic, has the important value of engineering application. With the development of the computer, the numerical simulation method in boiler design and operation and reform plays a more and more important role. Numerical simulation can serve as a good auxiliary method, both reducing the number of laboratory experiments and saving a lot of manpower material resources, and can be calculated on a computer screen image reproduction[1].

Based on Fluent computational fluid dynamics software as a platform, for 300 MW boiler furnace of a certain power plant, to simulate the flow, heat transfer and combustion process of the velocity field, temperature field distribution in the hearth, to understand and grasp the four tangential firing pulverized coal fired boiler furnace process and its regularity, and provide the beneficial reference for design and operation of large power plant boiler

the research object is introduced

Research object is a 300 MW boiler furnace which is a subcritical parameter, a reheat and natural circulation drum boiler, using balanced ventilation, once-through burner, the four tangential firing mode, the gasification of lignite. Boiler regards maximum continuous load (namely BMCR condition) as design parameters, the biggest continuous evaporation capacity of 1165 t/h boiler; For 350 MW unit electrical load (TRL working condition), rated capacity of boiler is 1109.0 t/h.

Burner boiler is single furnace, using the oscillating, four layout, and tangential combustion mode, with 5 MPS212HP - II medium-speed coal mill, which are the positive pressure direct blowing pulverizing system, every Angle of the burner for five layer wind vents that can be bobbing up and down, for plus or minus 30 ° of maximum pendulum Angle. When namely BMCR condition, four coal mill run, 1 second. Using four tangential arrangement swinging burner, in hot state run, a bobbing, secondary air nozzle, swing Angle should be able to meet the design value, maximum pendulum Angle for plus or minus 30 °

Main fountainhead for lignite huolinhe opencast coal mine is in Inner Mongolia, and ash in coal quality analysis, data analysis results are as follows:

Design and verify of coal coal and ash component analysis see the table below:

Order number	Name	Symbol	Unit	The design of coal	Check the coal
1	received carbon	Car	%	38.73	38.28
2	received hydrogen	Har	%	2.57	2.46
3	received oxygen	Oar	%	12.30	9.49
4	received n	Nar	%	0.79	0.66
5	arb sulfur	St，ar	%	0.34	0.44
6	received ash	Aar	%	14.38	17.17
7	as-received moisture	Mt	%	30.89	31.5
8	Airdry basis moisture	Mad	%	13.0	13.0
9	Arb volatile	Var	%	27.49	24.74
10	Received lowcalorific value Qnet	Qnet，ar	kJ/kg	13090	13840
11	For grinding coefficien	HGI		60	55.3
12	Ash deformation temperature	DT	℃	1080	1245
13	The ash softening temperature	ST	℃	1290	1390
14	grey hemisphere	HT	℃	1340	1390
15	Ashfusion temperature	FT	℃	1450	1430

Coal quality data sheet

Mesh geometry

Grid is the foundation of numerical calculation. Grid quality directly affect the precision of the numerical solution, and the influence in many cases even is decisive. High quality of the solution of the grid to the flow field can be realized with high quality, the research achievements of CFD can be used in the industrial design.

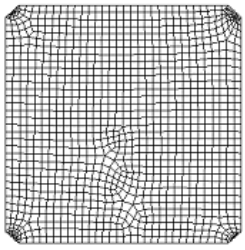


FIG. 1 The grid structure of burner area

Boiler approximation for cuboid, appearance is simple, into the furnace cross-section grid, and then along the height direction outspread, grid generation furnace body. Chamber of a stove or furnace cross-section with Paving[2-3] method to generate unstructured quadrilateral grids, Paving method is put forward in the 1880 s Blacker and Stephenson. Its principle is to first along the border (for even more domain including outer boundary and boundary) in accordance with the sequence arrangement of quadrilateral element, and has been developing to the inside area, until the grid to cover the entire space. Paving method to generate unstructured quadrilateral mesh can be well fitting boundary shape, the boundary mesh quality is higher, the irregular grid node number. Grid is generated by Paving method as shown. Generated after the furnace cross-section grid, the grid along the height direction outspread, adopting a method of generating hexahedral grid Cooper method one by one, to generate hexahedral grid. Chamber of a stove or furnace grid diagram as shown in figure , the grid number about 500000.

The flowing figure shows the burner area on a cross section of the grid.

The calculation results and discussion

The temperature field

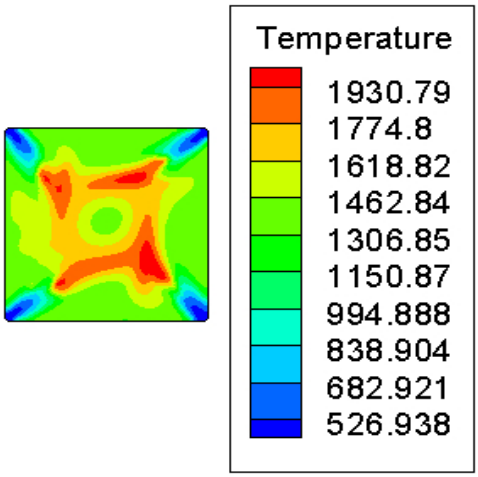


FIG. 2 The temperature distribution of underlying secondary air section

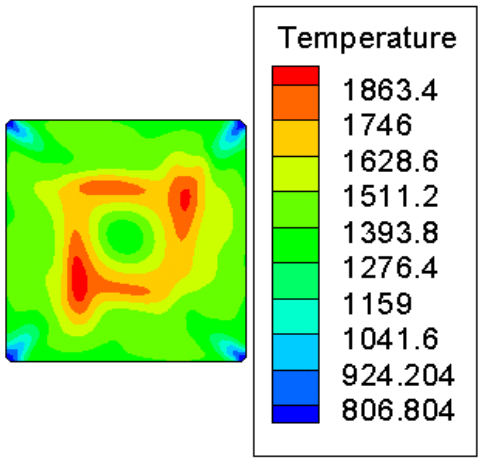


FIG. 3The temperature distribution of wind section

Figure 2 for the next set of burner area the temperature of the first layer of a wind section equipotential graph, figure 3 illustrates the: for a layer of the burner, the low temperature around the furnace center and the water wall, between the regional higher temperature; In each layer of burner, primary air vents with pulverized coal into the furnace by rapid heating, rapid volatile precipitation and burning, the local high temperature. Simulation results basically accord with the four tangential boiler combustion rule.

Figure 3 is for the underlying level of secondary air temperature distribution in the cross-section. By figure 4 can be seen that near the burner nozzle, pulverizer coal with primary air is into the furnace by rapid heating, rapid precipitation and volatile combustion, so the local high temperature is near the burner nozzle. Furnace flame shape of reverse tangential combustion and the combustion condition in the corners is of the rule of tangential firing.

The velocity field

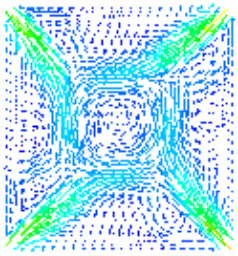


FIG. 4 The Velocity distribution of underlying wind section

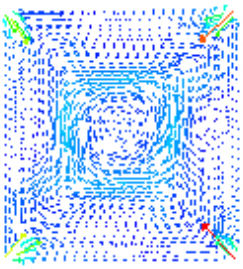


FIG. 5 The Velocity distribution of secondary air section

As you can see from figure 4 and figure 5, that primary air and secondary air by a blast, in sharp contrast to the rotating airflow inside the furnace, four corners is sprayed into the air in the center of the chamber of a stove or furnace formed a counterclockwise circle, tangential air velocity of the center of the chamber of a stove or furnace and obviously on the high side near the wall, form a low speed area in the center of the furnace.

Summary

The numerical simulation of the flow of the furnace, the heat transfer, and combustion characteristic forecast more accurately the distribution of flow field and temperature field in the furnace, which provides the beneficial reference for boiler design and operation. The calculation and experiment show that the residual rotation is the main cause of the smoke temperature deviation, which will cause the superheater and reheater tube.

References

[1] FangHaixin, ZengLingke,WangHui. The application of FLUENT software and pollutant generation model analysis[J]. Industrial furnace, 2004, 26(3) : 31-34.

[2] Blacker T D,Stephenson M B .Paving: a new approach to automated mesh generation[J]. Int. J. for Numer. Meth. In Eng,1991,32: 811-847.

[3] Kyu Yeul Lee, Doo Yeoun Cho, Tac Wan Kim. An algorithm for automatic 2D quadrilateral mesh generation with line constraints[J].Computer-Aided Design, 2003, 35: 1055-1068.

[4] SojiYamakawa, KenjiShimade. Quad-Layer.Ayered quadrilateral meshing of narrow two-dimensional domain by bubble packing and chordal axis transformation[C]. Proceedings of 2001 Design Automation Conference: 1-12.

Applied Mechanics and Materials Vol. 597 (2014) pp 488-491
© (2014) Trans Tech Publications, Switzerland
doi:10.4028/www.scientific.net/AMM.597.488

Optimization design analysis on electrical performance of ITER axial composite insulation break

Chang Chun Yang

College of Electric Engineering, Jiujiang University, China 332005

395254993@qq.com

Keywords: Optimization design analysis, Electrical performance, ITER, Insulation Break (IB)

Abstract. The electrical design analysis was conducted using the finite element method. An electrical properties design model was optimized and analyzed. The optimal parameters Li=100mm, L=300mm, Do=48mm, R=2mm, ε_r =3 have been achieved. The analysis results showed that the value of the maximal electric field in GFRP section is 3.396kV/mm. This position locates on the arc top of the interface between SS electrode and GFRP section. The field strength is respectively less than allowable 4kV/mm and 2kV/mm in GFRP and in air to meet the technical requirements of ITER axial insulation breaks.

Introduction

Low-temperature high-pressure Helium tightness axial composite insulation breaks are key components of ITER (International Thermal nuclear fusion Experimental Reactor) magnet systems [1]. The outer surface has a metal screen which is integrated into the ground screen of the high voltage cryogenic line, and there is metal reinforcing of both the insulating part, particularly where it overlaps the steel tubes to form a bond [2]. There length must be sufficient to prevent electrical breakdown between the two steel tubes through the fluid or gas. During the assembly and operation of the apparatus the cold shrink generated thermal stress, due to the large superconducting magnet and the return temperature of the cooling process, and the electromagnetic interaction generated tensile stress during charging and discharging, then causing damage hermetic insulation, which led to the cryogenic liquid into the vacuum system, prone to PASCHEN discharge, the entire apparatus will have a devastating damage [3]. Fig.1 shows a sketch of a preliminary design for the ITER insulating break component before assembly.

Electric design requirements

The insulation breaks for all cryo-lines will be similar, in spite of the fact voltage levels and working conditions are not the same for the different coil circuits. This means the insulation break shall be designed and tested with reference to the highest voltage level and in the worst environmental conditions considered during the operation of the ITER cryo-lines[4].

The IBs are assembled in air or helium circumstances. Because the breakdown strength of in GFRP and in air is generally 20~30kV/mm and 10kV/mm respectively, the allowable electric field in GFRP and in air should be less than 4kV/mm and 2kV/mm respectively if the safety factor is 5.

This length ensures a dielectric strength along the inner pipe interface between high voltage and low voltage parts. Ideally these components shall be designed to withstand testing at least 2 times the maximum voltage level plus 1 kV, i.e. 56 kV according to the rule recommended by ITER organization. Considering the impact of a possible failure of such components on ITER operation [5], we set nevertheless the design voltage level of these components as follows: design breakdown voltage in the bulk between outside and inside of the axial insulation break higher than 2 times the maximum voltage level in fault conditions i.e. > 56 kV. Design breakdown voltage side-to-side in dry air or pressurised helium in order to get equivalent dielectric strength as air, sufficiently high to

possibly allow the execution of dielectric tests of the assembled ITER coils, i.e. same criterion as above > 56 kV [6].

Optimization design

In the electrical design analysis, the simplified assumptions are made as follows: (1) Inner diameter and Outer diameter of geometric parameters for stainless steel pipes are respectively 17.3mm and 21.3mm. (2) Relative permittivity of GFRP can be designed as 3. This is based on volume content of epoxy-resin adhesive and fiberglass. In this analysis. (3) Relative permittivity of GFRP is 3, and Relative permittivity of air circumstance as well as vacuum is 1.0. Optimized parameters L=300mm, Lo=140mm, Li=100mm, R=2mm, θ=131°, Do=48mm.

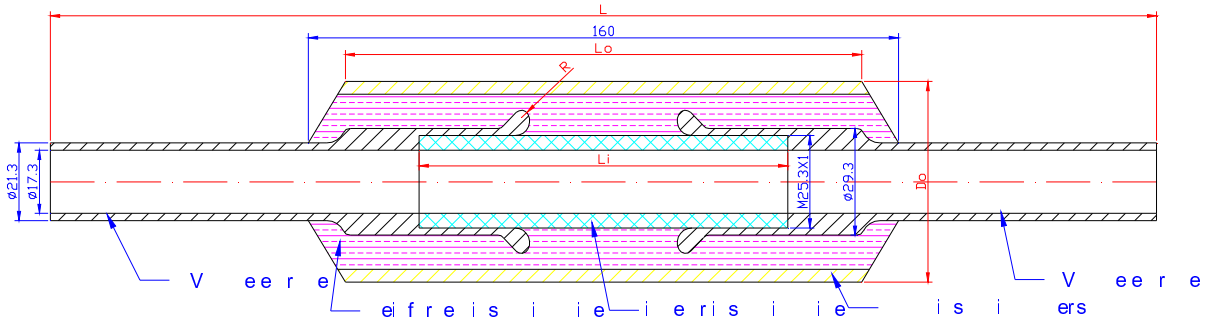


Fig.1.Cross section parameters of ITER axial IB design

The pipe's ends were shaped to reduce the electric field strength in the material and on the boundary surfaces for avoiding slide discharges. The electrical and mechanical properties were analyzed using ANSYS [6]. Preliminary design parameters are listed in Table 1.

Table 1.Optimizing design parameters [7,8]

No.	R(mm)	Do(mm)	Li(mm)	Lo(mm)	L(mm)	ε_r
1	1	48	90	140	300	**3**
2	2	55	100	140	300	**3**
3	1.5	55	100	140	300	**3**
4	2.5	55	100	140	300	**3**
5	**2**	**50**	**120**	**160**	**320**	**3**

Optimized design parameters model results were as follows: (1) According to the electrical design analysis due to different R, it shows that the peak electrical field is lower when the value of R is 2mm. (2) According to the electrical design analysis due to different Do, it shows that the peak electrical field along outer contour is falling down with lower Do, but considering mechanical strength, the value of Do is recommended as 55mm. (3) According to the electrical design analysis due to different Li, it shows that the peak electrical field is increasing with decreasing Li. By the electric field design criterion, the length of inner insulation pipe is recommended as 100mm. (4) According to the electrical design analysis due to different L, it shows that the change of peak electrical field is small, but considering the welding and torsion, so the value of L is recommended as 300mm.

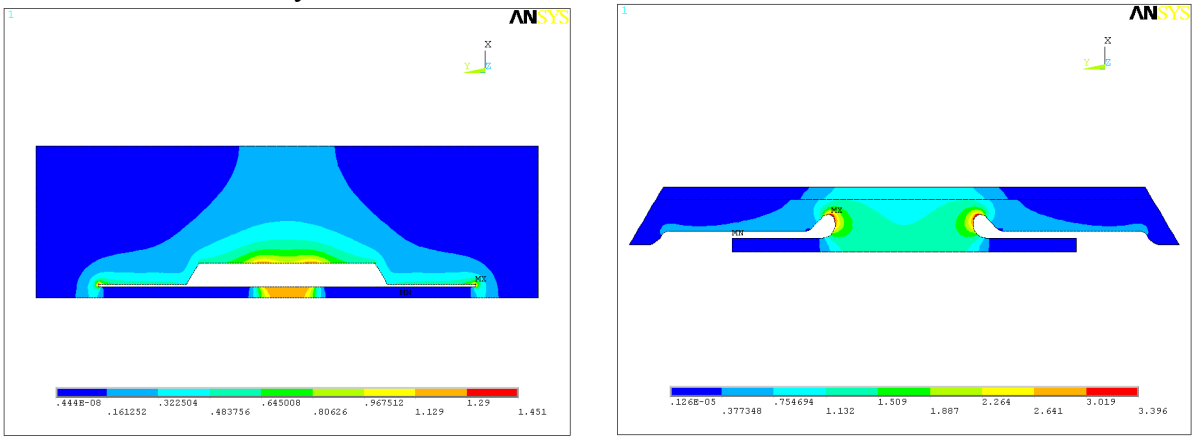
Electrical design analysis

1) Model and mesh

The electrical analysis of the ITER IBs was conducted using the finite element software ANSYS12.0. In this analysis, a 2-D 8-Node Electrostatic Solid axi-symmetric plane element PLANE121 was used to model the GFRP section.The boundary conditions and leads for the electrical design analysis were as follows: (1) Recommended optimized parameters L=300mm, Lo=300mm, Li=100mm, R=2mm, Do=55mm. (2) In this analysis, Relative permittivity of GFRP is 3, Relative permittivity of GKG layers is 3.5, and Relative permittivity of air circumstance as well as vacuum is

1.0. (3) Boundary conditions on outer surface of air medium is in infinity. (4) High voltage lead at the one terminal SS pipe electrode is 56kV, low voltage lead at the other terminal SS pipe electrode is 0.

2) Von electric field analysis



(a) Electric field of air section (b) Electric field of GFRP section

Fig.2.Electric field strength contour of air section and GFRP section under 56kV

In Fig.2, it is clear that the value of the maximal electric field in GFRP section is 3.396kV/mm. This position locates on the arc top of the interface between SS electrode and GFRP section. The value of the maximal electric field in air section is 1.451kV/mm. This position locates on top end of the outer interface between air medium and SS electrode. It is safe electrical field value for ITER electric design.

3) Interface electric field analysis

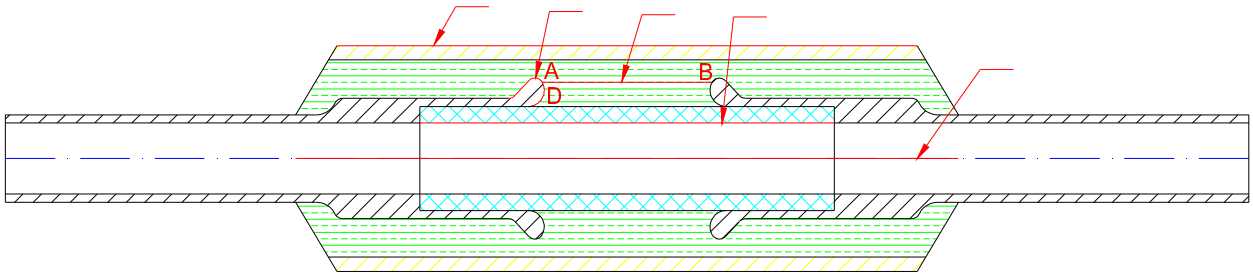


Fig.3.The sketch of interface profile distribution

The different electric field strength distribution paths are shown in Fig.3. The electric field strength distribution along S, L1, L2, and L3 path are shown in from Fig.4 to Fig.7. It is evident that the maximal value of electric field strength for insulation break is 3.396kV/mm in Fig.4 and Fig.5, the maximal value of electric field strength along the outer interface between air medium and GFRP section is 1.231kV/mm from Fig.6, and the maximal value of electric field strength along the surface of inner insulation pipe is 1.271kV/mm from Fig.7, but the maximal value of electric field strength along the axial line of inner insulation pipe in air is only 1.203kV/mm.

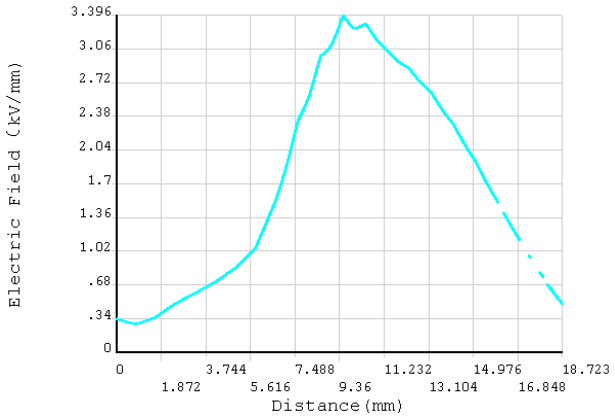


Fig.4.Electric field along S arc line from C, A to D

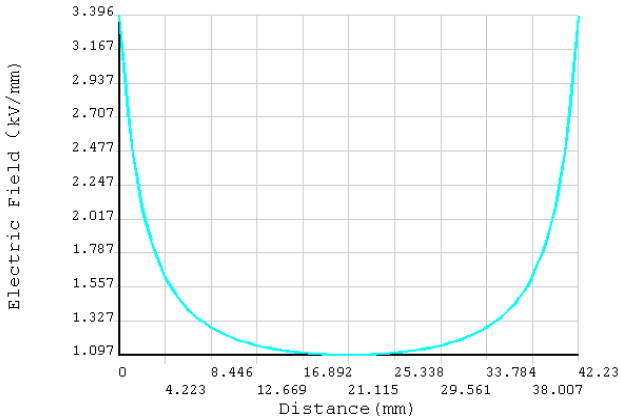


Fig.5.Electric field along L1 line from A to B

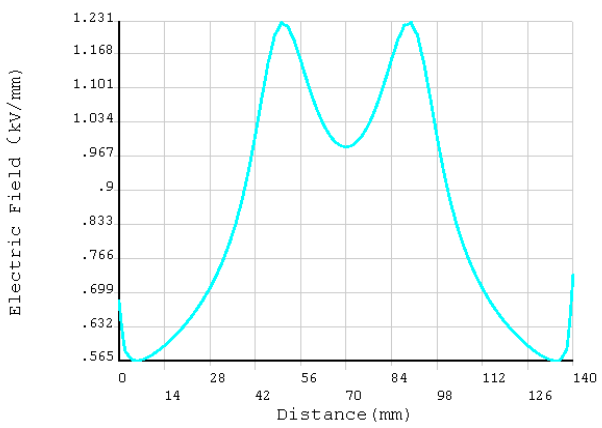


Fig.6.Electric field along L2 line from E to F

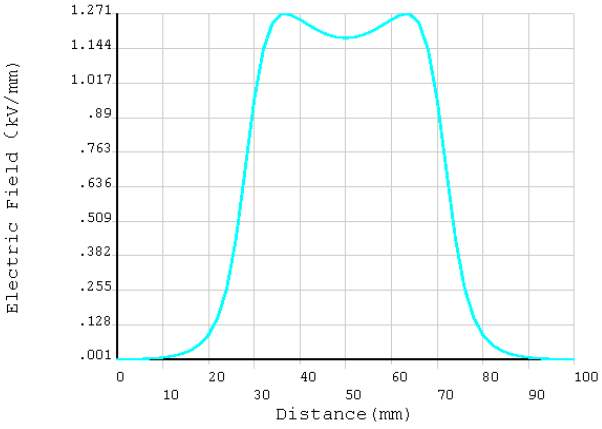


Fig.7 Electric field along L3 line from G to H

Conclusion

The electrical design analysis was conducted using the finite element method. An electrical properties design parameters model was optimized and analyzed. The optimal parameters Li=100mm, L=300mm, Do=48mm, R=2mm, ε_r =3 have been achieved. The results as follows: (1) design model parameters for ITER IBs prototype: Li=100mm, L=300mm, Do=48mm, R=2mm, ε_r =3. (2) The field strength of the axial break along the interface inner pipe is 1.23kV/mm. (3) The maximal field strength of the IBs locates on the top end of SS316L electrodes, the value of the maximum field strength is equal to 2.8kV/mm.

Acknowledgements

The research work was supported by National Natural Science Foundation of China under Grant No. 51107138.

References

[1] Yang Changchun. Experiment research on low-temperature mechanic fatigue performance of ITER axial insulation breaks. Cryogenic & Superconductivity, 39(11), pp.7-10, 2011.

[2] Yang Changchun Pan Wanjiang. Design and analysis on ITER axial insulation breaks. Nuclear Fusion and Plasma Physics, 30(3), pp.272-276, 2010.

[3] Wu Cheng, Pan Wanjiang, Yang Changchun. Research on performance test of ITER composite axial insulation breaks. Cryogenic & Superconductivity, 39(10), pp.12-16. 2011.

[4] Zhang Yuanbin, Pan Wanjiang, Xi Weibin, Study of the property of EAST composite insulators with finite element analysis[J]. Nuclear Fusion and Plasma Physics, 27(2), pp.137-140, 2007

[5] Yu X., Wu, W. Pan, W., Han S., Wang L., Wei, J. Liu L.; Du S., Zhou Z. Foussat, A.; Libeyre, P., Development of Insulation Technology with Vacuum-Pressure-Impregnation (VPI) for ITER Correction Coil. IEEE Transactions on Applied Superconductivity, 22 (3), pp. 212-206, 2012.

[6] Zhang Yuanbin, Pan Wanjiang. Theoretical and experimental analysis of cryogenic mechanics property for EAST Tokamak composite insulators [J]. Atomic Energy Science and Technology, 41(6), pp.752-755, 2007.

[7] BAUER K, FINK S.The electrical insulation system of a forced flow cooled superconducting (SC) magnet[J]. Cryogenics, 38 pp.1 123-1 134, 1998

[8]Yang Changchun Pan Wanjiang Wu Songtao. Test research on the performance of EAST composite axial insulation breaks. Cryogenics, (4), pp.23-27, 2009.

Applied Mechanics and Materials Vol. 597 (2014) pp 492-497
© (2014) Trans Tech Publications, Switzerland
doi:10.4028/www.scientific.net/AMM.597.492

Research on Overloading Protection of Permanent Magnetic Coupler in Coal Mine

Wenqi Yuan[1, a *], Yue Liu[1,b], Dong Li[1,c], Guoying Meng[1,d]

[1]School of Mechanical Electronic & Information Engineering, China University of Mining & Technology(Beijing), Beijing 100083, China

[a]magicyuan2011@126.com, [b]ly86@foxmail.com, [c]530864495@qq.com, [d]mgy@cumtb.edu.cn

Keywords: magnetic coupler; overloading protection; the curves of mechanical characteristics

Abstract. In this paper, with simulations and experiments analysed by the software of Ansoft Maxwell, research on overloading protection of permanent magnetic coupler in coal mine is carried out and the conclusive curves of mechanical characteristics are plotted through experimental data. The conclusion can be gained from mechanical characteristic curves: when the output value of torque reaches the maximum torque of magnetic coupler, the output torque and speed will drop along with increases of the slip, and the input power value of motor is less than the power value at the time when the motor torque value is at the maximum. It explains that the magnetic coupler has the function for overloading protection.

1. Introduction

Permanent magnetic coupler is a torque transmission device from the motor to the load. The energy transfer and speed adjustment is achieved by the air gap between the conductor and the permanent magnet at the principle of electromagnetic conversion. This device has many advantages such as no mechanical connection, soft starting and needless from precise alignment techniques. The fundamental difference between magnetic coupler and mechanical type coupler is that not any mechanical or hydraulic joins the driving shaft and the driven shaft which can realize the rotation of power transmission. The unique advantages of the permanent magnet coupler has great advantages in underground coal mine [1].

Many transport equipments used in coal mine like belt conveyors and scraper conveyers often overload or stall suddenly because of coal drop too much or mass materials block accidents, and then damage the motor and transmission mechanism. Meanwhile, the scraper conveyors start not less than 6 times every hour frequently. Starting is often full loaded or overloaded, which not only makes the chain gets very heavy impact, but also results in motor overheating.

The mian contribution of this paper is the analysis and discussion on the function of overloading protection of motor against stuck or overload at the load side of permanent magnetic coupler due to special reasons.

2. The simulation analysis of overloading protection

The three-dimensional structure of permanent magnetic coupler shown in Fig.1 is mainly composed of two copper plates and two aluminum plate embedded permanent magnets and other parts. Shown as Fig.2, the copper plates fix together with the frame of outer steel plates respectively and connect with the driving shaft of motor. The aluminum plate embedded permanent magnets fix together with the frame of inner steel plates and join the load shaft [2]. The structure and parameters of permanent magnetic coupler in this experiment summarize in Table 1. According to the above information, the prototype is designed for the experiment of overloading protection.

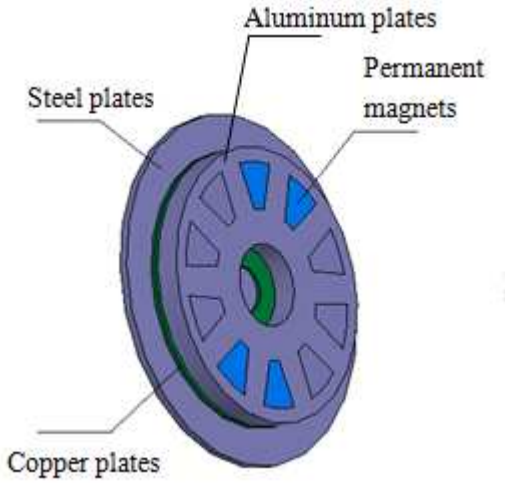


Fig.1 The three-dimensional structure of permanent magnetic coupler

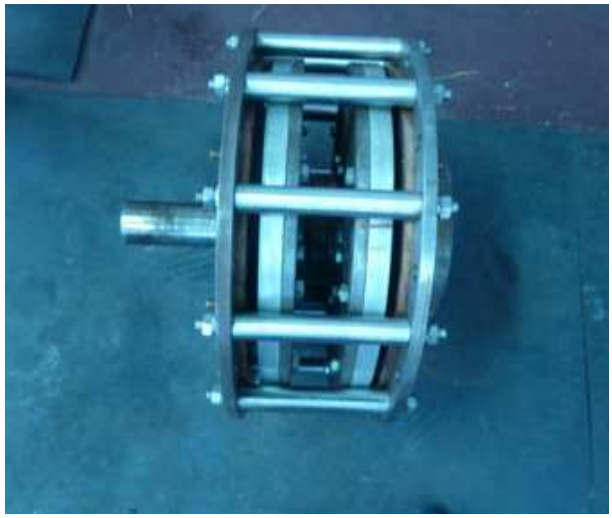


Fig.2 A picture of the actual permanent magnetic coupler

Table 1 The design parameters of permanent magnetic coupler

Part	Parameter	Value(mm)	Material property
Copper plates	Outer diameter	400	Copper
	Inside diameter	68	
	Thickness	6	
Steel plates	Outer diameter	440	45#Steel
	Inside diameter	80	
	Thickness	12	
Permanent magnets	Upper width	66	NdFeB N45SH
	Bottom width	21	
	Radial length	75	
	Thickness	15	
	Number of pole	2	
Aluminum plates	Outer diameter	400	ZL101
	Inside diameter	120	
	Thickness	20	
Air gap	Air gap	12	

Under the circumstance of different slips, the relationship of output torque and speed is simulated by the finite element software Maxwell. Mechanical characteristics of permanent magnet coupler is carried out as shown in Fig.3. Seen from the simulation figure, with the speed reducing, as well as the slip increasing, output torque also increases gradually. This is the stable operating region of the permanent magnetic coupler when the output torque reaches a maximum value, the torque will no longer change, namely its mechanical characteristic curve likes “rectangle” [3]. According to the simulation results, the maximum value of torque can be transferred is about $85N \cdot m$. When the overload occurs during the operation, the speed declines sharply, the torque is unchanged. Known from the power expression $P = T \cdot \Omega$, when the load torque exceeds the maximum torque of coupler, the output power of motor does not increase but it decreases [4]. Thus overloading protection performance of permanent magnetic coupler is verified.

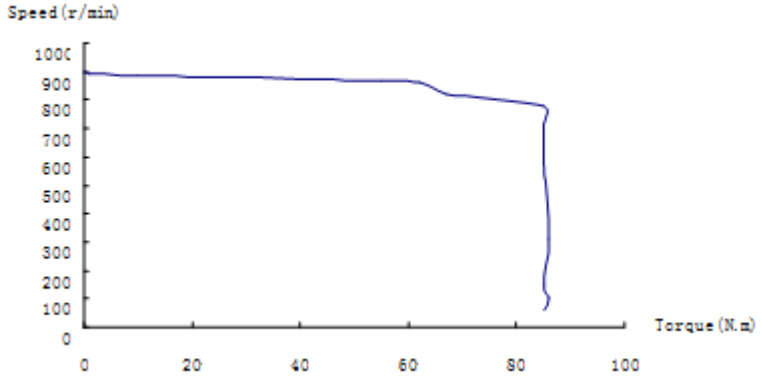


Fig.3 the simulation curve of mechanical characteristics

3. Experiments in overloading protection performance

For the further study on the overloading protection performance of permanent magnetic coupler, the actual experiment research is carried out. In the course of the experiment, the motor rated speed is set for $900r/\min$, the experimental results is shown as Table 2. Observe these data, when the output speed is reducing, namely the slip increases, the transmission torque of the magnetic coupler is increasing. Until the value of torque is larger than the maximum value, then the output torque has a decreasing trend, which shows that the output power of electric motor will be smaller under the circumstances of blocking [5]. Also that is to say, the magnetic coupler has ability to protect the motor from the problems caused by overloading.

Table 2 Experimental data on the condition that input speed is set for $900r/\min$

Output torque of coupler N.m）	Output speed of coupler r/min）	Input power of motor (kW)	Output torque of coupler N.m）	Output speed of coupler r/min）	Input power of motor (kW)
0	599.8	0.003	50.9	111.2	3.372
0.92	597.9	0.0061	49.9	82.3	3.320
2.84	593.7	0.184	49.4	64.7	3.329
5.48	589	0.354	48.9	56.7	3.268
9.31	581.2	0.598	48.5	40.4	3.250
14.33	569.5	0.925	48.2	34.4	3.246
20.26	555.3	1.295	48.1	27.6	3.241
26.78	540.4	1.724	47.6	22.59	3.225
35.12	513.9	2.299	47.6	16.4	3.219
44.4	480.3	2.857	47.2	13.83	3.21
52.1	433.1	3.365	47	16.16	3.22
57.4	300.8	3.728	47.5	19.4	3.22
53.3	172.9	3.529			

The experimental platform is set up at the laboratory as shown as Fig.4. The rated power of motor is $37kW$. The experimental process is that: firstly, it is necessary to select the frequency; secondly, the motor starts with no-load in order to has the stable speed; then the loading is becoming heavier artificially. Recording instrument is used for measuring the input & output speed and torque, the power and the efficiency.

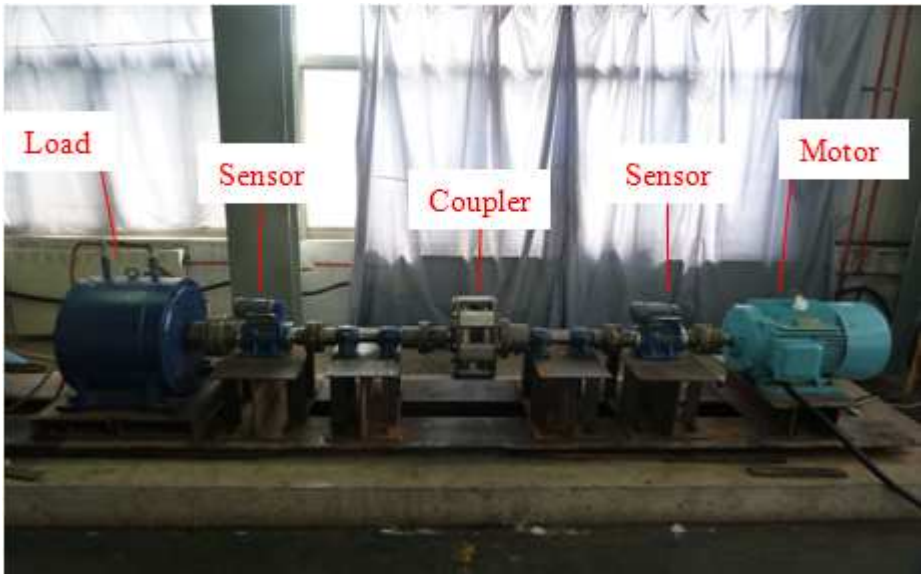


Fig.4 The experimental platform of permanent magnetic coupler

4. The curves of mechanical characteristic

In this study, the three-phase permanent magnetic synchronous motor(model:TYCX225S-4) is set to operate in $20Hz$, $30Hz$, $40Hz$ and $50Hz$ respectively, namely the input speed for experiment is $600r/\min$, $900r/\min$, $1200r/\min$, $1500r/\min$. The data is recorded in the process of testing in company with the curves of mechanical characteristic as shown as Fig.5, Fig.6, Fig.7 and Fig.8.

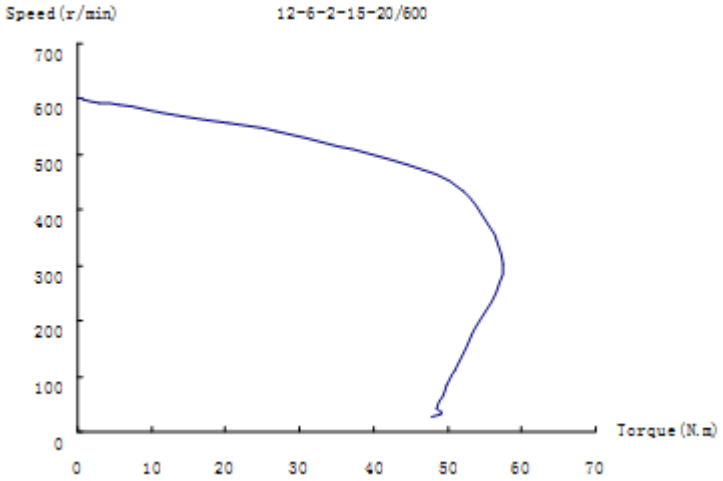


Fig.5 The curve of mechanical characteristic: air gap is $12mm$, copper thickness is $6mm$, the number of magnetic pole is 2, magnetic thickness is $15mm$, speed is $600r/\min$

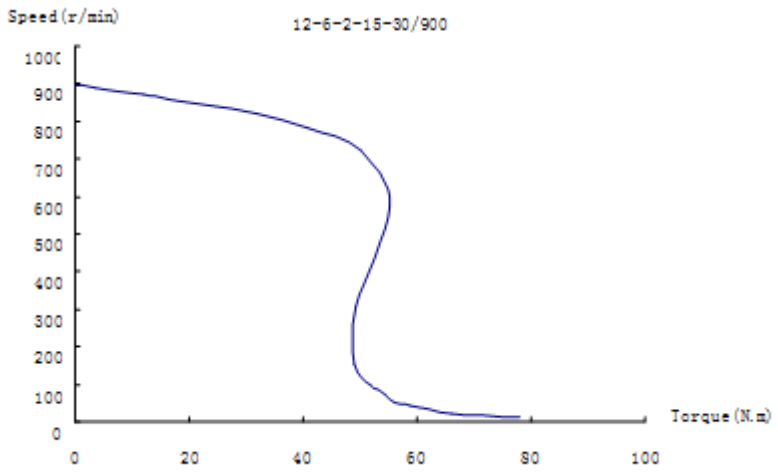


Fig.6 The curve of mechanical characteristic: air gap is $12mm$, copper thickness is $6mm$, the number of magnetic pole is 2 , magnetic thickness is $15mm$, speed is $900r$ / min

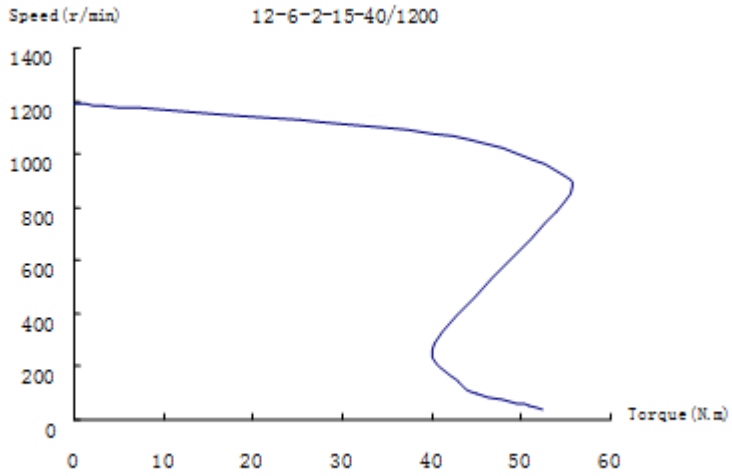


Fig.7 The curve of mechanical characteristic: air gap is $12mm$, copper thickness is $6mm$, the number of magnetic pole is 2 , magnetic thickness is $15mm$, speed is $1200r$ / min

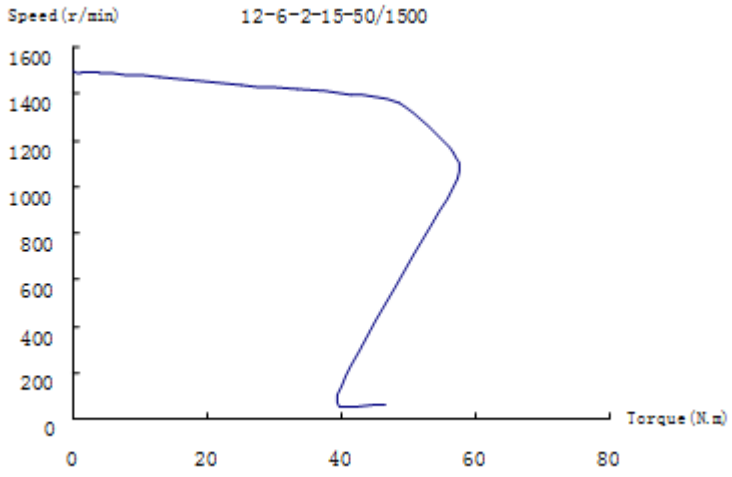


Fig.8 The curve of mechanical characteristic: air gap is $12mm$, copper thickness is $6mm$, the number of magnetic pole is 2 , magnetic thickness is $15mm$, speed is $1500r$ / min

Seen from the four kinds of mechanical characteristic curves, the output torque increases with the increasement of the slip from $0r/\min$ to $200r/\min$, which belongs to the normal work region of the magnetic coupler. In this interval, the maximum value of output torque is $40 \sim 50N/m$. But when the slip is greater than $200r/\min$, the value of output torque become dropping after achieving the maximum value. With the increasement of the load, the output speed will reduce; as the slip increases, the input power of the motor is less than the power at the time when the vaule of torque get the maximum. All of these characteristic reflects the performance of overloading protection.

5. Conclusion

1. When the load blocks heavily, permanent magnetic coupler can protect the motor. It makes the protection of overloading come true. So the research on overloading in coal mine has a practical significance.
2. There is no rigid connection between parts of the permanent magnetic coupler, thus it can eliminate the impact and vibration. Because the working principle determines the output speed is lower than the input speed, the gap of speed will increase with the increasement of the load. Significantly, the input shaft can rotate normally even though the load is too heavy to stop. It is important to protect the motor effectively.

References

[1] Shengjiang Liu. Research on Mine Permanent Magnetic Driving Device[J]. Coal Mine Machinery. 2013,34(9):184-185.

[2] Honggang Zhang. Calculation and Analysis of Permanent Magnetic Coupling Losses[D]. Jilin University, 2008.

[3] Kerong Peng. Research on the Structure and Characteristics of Permanent Magnetic Coupling[D]. Harbin Institute of Technology, 2008.

[4] Yong Wang. Magnetic mechanical analysis and design method[M]. Hefei: Hefei University of Technology Press, 2007.

[5] Qi Zhang. Magnetic coupling characteristic test platform design[D]. Dalian Maritime University, 2013.

Applied Mechanics and Materials Vol. 597 (2014) pp 498-501
© (2014) Trans Tech Publications, Switzerland
doi:10.4028/www.scientific.net/AMM.597.498

The Research of Drive Roll's Dynamics Characteristics

Li Shao-Hai[1,a]

[1]XIJING University, Xi'an,710123, China
[a]qinsongboy@126.com

Keywords Drive roll; Modal analysis; Natural frequency; Finite element; Vibration;

Abstract. In order to research the dynamic characteristics of drive roll, finite element model of the drive roll was set up by ANSYS/Workbench. The drive roll's natural frequency and vibration mode concerned in reality were acquired based on modal analysis, deformation trend and size of each mode shape were analysed, then deformation of the weak positions about each mode was cleared, and some measures about improving its dynamic characteristics were proposed, all of these offered a support to strengthen drive roll's damping property.

Introduction

Drive roll is one of important parts for belt conveyor, and the dynamic characteristics of it would directly affect the belt conveyor's operation[1]. Presently, because of some new design methods such as CAD/CAE are applied to the field of coal mine machinery, the operating speed of the belt conveyor is higher more and more, and then some further design for the drive roll is put forward at the same time, and it is important to keep favourable dynamic characteristics while it is rotating with high speed. In this paper, finite element model of the drive roll is set up by ANSYS/Workbench, and some important natural frequencies and vibration modes of it are calculated based on modal analysis, then some ways and means are put forward for improving the drive roll's dynamic characteristics, and these results offers a reference to structure design of the drive roll.

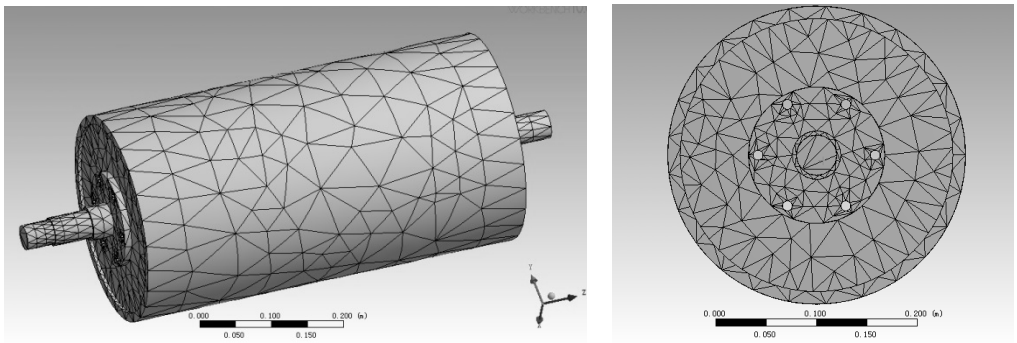


Fig.1 Finite element model

Finite element modeling

Workbench is a new generation collaborative simulation environment which developed by ANSYS corporation, the preprocessing and postprocessing of it are different from classical ANSYS, it not only has many powerful functions such as modeling and analysis, but also establishes data exchange interface program with lots of other CAD systems, thus some great conveniences is provided to engineering design[2]. In this paper, a minitype belt conveyor's drive roll is used to as reference, and the finite element of it is set up by ANSYS/Workbench, the material attribute of the

model is shown by table1. The drive roll is meshed by tetrahedral entities grid, as shown in fig.1[3], the finite element model of it includes 7631 elements and 14068 nodes.

Table1 Material attribute

Material type	elastic modulus/GPa	Poisson's ratio	Mass density/ Kg•m^{-3}
Q235	206	0.3	7800
45Cr	193	0.28	7850

Modal analysis

Vibration equation. Modal analysis is an effective measure to predict and judge dynamic characteristics of structure, based on that, and some improving references would be provided for mechanical system. Ignore influence of the damp, calculated and analysis free modal of the drive roll, according to structural dynamics, free vibration equation with non-damping for the structure as shown in formula (1) [4]. Among the formula, [M]-mass matrix, [K]-stiffness matrix, {X}-displacement vector. The equation of natural frequency for the drive roll is formula (2), and the parameter ω is defined as natural frequency.

$$[M]\{\ddot{X}\}+[K]\{X\}=0 \qquad (1)$$

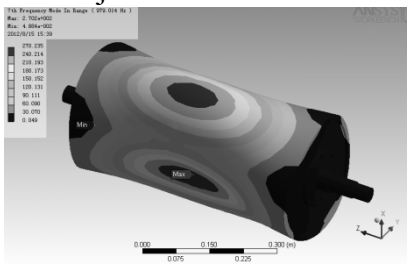
$$\left|[K]-\omega^2[M]\right|=0 \qquad (2)$$

Natural frequency and vibration mode. Solve the finite element model by ANSYS/Workbench, 42204 natural frequencies and vibration modes of the drive roll are calculated. Because lower-order modal is more important than others in practical engineering, the first to the forth modal results are shown in this paper, as shown in fig.2. By the table 1 known, the deformation for each vibration mode are different, besides, the front natural frequencies of the drive roll are relative larger, its fundamental frequency is 797.01Hz, and the resonance speed equal to it is 47820.3r/min, the speed is higher far and away than present belt conveyor's operation speed. So we can know that, the drive roll's structure is reasonable, and the dynamic characteristics is favourable.

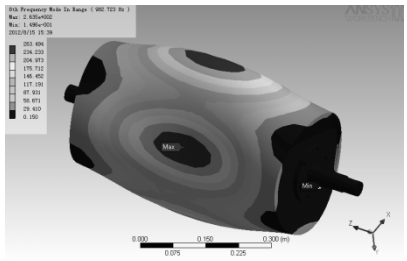
Table 2 Natural frequency and deformation of top 4

Modal Oder	1	2	3	4
Natural frequency/Hz	797.014	982.723	1637.880	1640.330
Maximum deformation/mm	270.235	263.494	300.864	193.056
Minimum deformation/mm	0.049	0.150	0.104	0.648

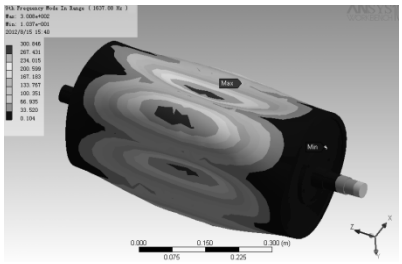
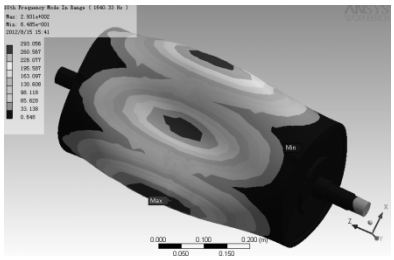
By the fig.2 known, the first and the second vibration mode are mainly barrel's deformation, the barrel is deformed form cylinder to concave, and the maximum deformation appears on the center of it, and the deformation quantity is decreased progressively with oval from inside to outside. Thus we can know that, the center position is the easiest breaker place when the drive roll is vibrating with the top 2 natural frequency. The fifth and the sixth vibration mode are exactly similar to the top 2, and the difference of its just is deformation.



a First modal



b Second modal

c Third modal d Forth modal

Fig.2 Modal shapes of top 4

Improving dynamic characteristics

According to vibration mechanical, fundamental frequency is more sensitive to resonance, fundamental frequency is more higher, vibration resistance of the structure is more strength. Thus, in order to adapt high speed design requirement of the belt conveyor, the fundamental frequency should be enhanced as much as possible during the course of structure design of the drive roll[5]. According to the formula of natural frequency for single degree-of-freedom system, as shown in formula (3). The parameter m and k in formula (3) respectively are mass and stiffness of the system[4]. Based on formula (2) and (3), we can know that, the modal parameters of a vibration system are relative to its mass and structure stiffness, thus some methods and thinking are put forward to improve dynamic characteristics of the drive roll.

$$\omega = \sqrt{k/m} \qquad (3)$$

Material is confirmed. The dynamic characteristics of the drive roll can be enhanced by improving its structure style, for example, the stiffness can be enhanced effectively through increasing radials and reinforcing rib's thickness, therefore, the fundamental frequency of the drive roll is enlarged and the vibration resistance of it is also strengthened.

Structure is confirmed. Some material with strong vibration resistance could be used to improve the drive roll's dynamic characteristics, such as cast iron, carbon structural steel and composite of carbon fibre etc.

Material and structure are all confirmed. The device of vibration absorbing should be installed on the drive roll or belt conveyor so as to decrease vibration of the machine, it is also an effective method to improve the dynamic characteristics of the drive roll.

Conclution

The drive roll is a representative rotational part, the influence of its dynamic characteristics must be thought over during the course of practical design. Based on finite element modeling and modal analysis for the drive roll on ANSYS/Workbench, the important natural frequencies and vibration modes of it are acquired, then the deformation trend and size is cleared, at the same time, some measures are put forward to improving its dynamic characteristics. In result, some valuable references are offered to dynamic design of the drive roll, and the foundation for belt conveyor's high speed design is also established.

Acknowledgement

This work is financially supported by the items in XIJING University, which named "Deep hole processing and chip removal research based on vibration principle", No. XJ130236

References

[1] Chen Qing-Hua, Pan Di-Lin. Finite Element Analysis of Driving Drum Of Belt Conveyor And Its Optimized Design[J]. Coal Mine Machinery, 2004, 01:12-15.

[2] Li Fan-Chun. Design, Model And Virtual Simulation Based On ANSYS Workbench[M]. Electronic Industry Press, 2011.

[3] Li Feng, Cui Zhi-Yuan, Han Gang. Finite Element Analysis For Belt Conveyor's Pulley Based On ANSYS[J].Journal Of Taiyuan University Of Science And Technology, 2007, 28(04):307-310.

[4] Zhu Bo-Fang. Principle And Application Of Finite Element Method (3rd Edition) [M]. China Waterpower Press: Intellectual Property Right Press,2009.

[5] Liu Kai, Zhang An-Ning, Ye Guo-Hui. Finite Element Alysis Of Driving Pulley Of Belt Conveyor Based On ANSYS[J]. Coal Mine Machinery, 2011, 01:101-102.

Applied Mechanics and Materials Vol. 597 (2014) pp 502-506
© (2014) Trans Tech Publications, Switzerland
doi:10.4028/www.scientific.net/AMM.597.502

Analysis and Research on the Picking Roller of the Half-feed Peanut Combine Harvester

Xiaolian LÜ[1,2,a], Zhichao HU[*3,b], Baoliang PENG[3,c]

[1]Key Laboratory of Modern Agricultural Equipment, Ministry of Agriculture, Nanjing, Jiangshu, 210014, China

[2]College of Machinery and Electronic Engineering, Chuzhou University, Chuzhou, Anhui, 239000, China

[3]Nanjing Research Institute for Agricultural Mechanization, Ministry of Agriculture, Nanjing, Jiangshu, 210014, China

[a]lxl500@163.com, [b]nfzhongzi@163.com, [c]734392925@qq.com

Keywords: Peanut, Picking roller, Mechanism, Structure parameter, Picking blade

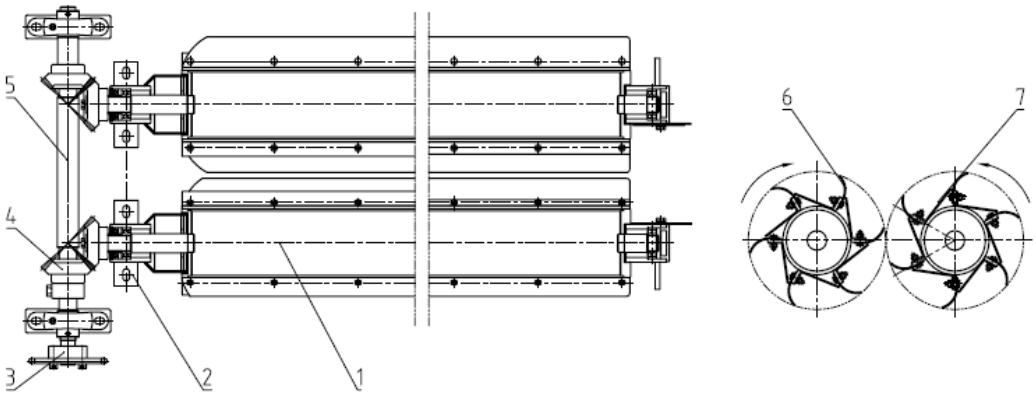
Abstract: Picking peanuts is the key operational link and the core technology of peanut combine harvester. On the basis the theoretical analysis of picking mechanism and structural parameters of the half-feed picking roller, and combined with the picking performance experimental, the structural parameters of the picking blades and blades quantity of picking roller were studied. The results show that: when the straight-shaped blade is picking, the picking force is strong, the broken branch and seedling phenomenon is serious, peanut broken rate and peanut with handle rate are higher; the arc-shaped blade reduced peanut damage, and effectively reduced the rate of the peanut with handle. The picking blade radian has a large impact to the peanut broken and loss rate. When the blade radian is 70° and the blade radius is 35mm, total loss rate is the lowest on the picking segment of the blade. The blade quantity has significant influence to the peanut broken and loss rate. The peanut broken rate of the 8 blades is 2 to 3 times of the 4 and 6 blades; the picking net rate of the 4 blades is much lower than 6 and 8 blades. The self-design the picking roller is 6 arc-shaped blades, the blade radius is 35mm, and the blade radian is 70°. The study provides the design basis for the research and development of the half-feed peanut picking device.

Introduction

Peanut combine harvester can be divided into whole-feed type and half-feed type by the different feeding methods [1-3]. Whole-feed peanut picking machine is mainly used for picking dry peanut. It has a lager feeding volume, high productivity, high power consumption, poor picking quality. Half-feed peanut picking machine can be used for picking fresh and dry peanut. Compared with whole-feed peanut picking machine, it has smaller feeding volume, low productivity, low power consumption, good picking quality, and can better meet the requirements of the picking fresh peanut, but the structure and transmission system of the half-feed peanut picking device are more complex, higher technical requirements. At present, it has some problem of the unstable operating performance and low productivity. Picking peanuts is the key operational link and the core technology of peanut combine harvester. The structural and parameter of the picking roller determines the performance of the peanut combine harvester. Through the theoretical and experimental method, the picking mechanism and structural parameters of the half-feed picking roller were studied. On the basis, the half-feed picking roller is designed and optimized.

Composition and working principle of the picking roller

Based on a systematic study on peanut picking technique in domestic and abroad [3-9], the designed picking roller is as shown in Figure 1. The picking roller is mainly composed of the roller body, transmission sprocket, bevel gear, transmission axis, and picking blades. Picking device uses two roller, and two rollers adopts the differential phase combination way. The picking roller and the clamping conveying chain are upper and lower configure. The bevel gears of the installed on transmission axis are match the bevel gears of the fixed on picking roller. Transmission sprocket drive transmission axis rotation and transmission axis drive the two picking rollers relative rotation by the bevel gears. When the machine operating, peanut vine is forward conveyed by the clamping conveying chain, and the two picking roller is relative rotation by the sprocket driven; the clamping conveying chain is located above the intersection of the two picking roller, when peanut vine passed the picking roller, the high-speed rotation picking blades on the roller hit and comb brush the peanut vine, peanut is separated from the vine by continuous action in groups of picking blades, the picking peanut operating is finished.



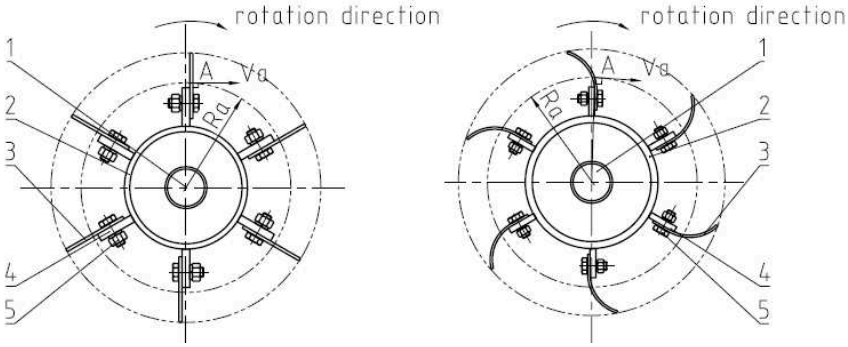
(a) (b)

1. Roller body 2. Mounts 3. Transmission sprocket 4. Bevel gear 5. Transmission axis 6. Blade 7. Rubber sheet

Fig.1 Structural schematic of peanut picking roller

Studies on the picking mechanism

Due to external forces action, peanut is separated from the stalk and stem at the connected place. In the picking operating process, the picking roller is the high speed rotation, peanut is separated from the vine by hit and comb brush action of the picking blades on the roller. The picking operation mechanism and performance is determined by the structure and shape of picking blades, the picking blades is usually straight-shaped and arc- shaped, as shown in Figure 2.



(a) Straight-shaped blade (b) Arc-shaped blade

1. Axis 2. Picking roller 3. Blade 4. Blade mounts 5. Fixing bolts

Fig.2 The different shape and motion analysis of picking roller blade

They are a different shape in the radial direction, the straight-shaped blade does not bending, the arc-shaped blade are arc-shaped in addition to mount parts. According to the study of picking mechanism of different shape blades can be known (as shown in Figure 2): when straight-shaped blade is high speed rotation, the direction of movement speed and hitting force is consistent to various points on the same blade, but the values are different. Though the analysis of the motion, the velocity of the each point of the picking blade is shown as follows by formula (1).

$$Va = \omega \cdot Ra \quad (1)$$

In formula: Va- the movement speed of a point on picking blade; ω- rotation speed of picking roller; Ra- the distance of a point to the roller axis center.

So that the farther the distance of the point to the roller axis center is, the greater the velocity of the point on picking blade is, and the greater the hitting force of the point on picking blade is. Usually, the outer and end of the picking blade is first action on peanut vine, picking force is stronger and picking net rate is higher, but peanut broken rate and peanut with handle rate are higher, and the broken branch and seedling phenomenon is serious. When arc-shaped blade is high-speed rotation, the points of the radial direction on the same blade turn into hitting zone. Compared with straight-shaped blades, its hitting force is relatively weak, and comb brush effect is enhanced. On the same rotation speed, compared with straight-shaped blades, peanut broken rate and impurity rate of the arc-shaped blade were decreased, but picking net rate is too decreased.

The structure and parameters of the picking roller

The shade of the picking blade: Though the picking test on the testing bench, the influence of the straight-shaped blade and arc-shaped blade to picking quality is tested [10,11]. Test conditions: the blade length of picking roller is 1000mm, the blade quantity of single roller is 6, the maximum diameter of the roller is 230mm, the center distance between the two picking roller is 220mm, the rotation speeds of the picking roller were 300r/min and 400r/min, the peanut varieties is taihua 4, the average height of the plant is 400mm, the peanut range of single plant is φ150mm. Test method: the peanut broken rate(P%), picking net rate (D%), impurity rate (Z%) are testing indicators, per peanut plant is as testing unit; The test is done by the manual harvested and feed peanut seedlings; the picking test of different shape picking blades is repeated three times, per picking test is continuous feed seedling 20, and testing broken peanut weight G_1, intact peanut weight G_2, not picking peanut weight G_3, and roots, stems, leaves and other debris G_4, the results were calculated the average. The calculating methods of the detection index are: $P\% = 100\% \times G_1 / (G_1 + G_2 + G_3)$, $D\% = 100\% \times (G_1 + G_2) / (G_1 + G_2 + G_3)$, $Z\% = 100\% \times G_4 / (G_1 + G_2 + G_3 + G_4)$.

The testing results showed that: when using straight-shaped blade, the broken branch and seedling phenomenon is serious snags, broken seedling serious, peanut broken rate and peanut with handle rate are higher; the arc-shaped blade effectively reduced peanut damage, prevented tearing vine and roots, especially reduced the rate of the peanut with handle. In test, the picking net rate is slightly lower, but still at a higher level. In comprehensive consideration, the picking blade is determined arc-shaped.

The structure parameters of the picking blade： The structural parameters of the picking blade is mainly composed of the blade radius R_y, blade radian γ, the circle radius of the arc starting point of the blade R_0, the circle radius of hitting starting point of the blade R_j, the radius of picking roller R_g, as shown in Figure 3. When the R_0 and R_g are determined, R_y determines the blade radian; the smaller R_y is, the greater the blade radian is. In order to determine a reasonable radius of picking blade, picking testing of different structural parameters blades are done on the picking testing bench, as shown in Table 1. The testing results showed that: the blade radian has a large impact to the peanut broken and loss rate; the smaller the blade radian is, the longer the blade radius is, and the higher

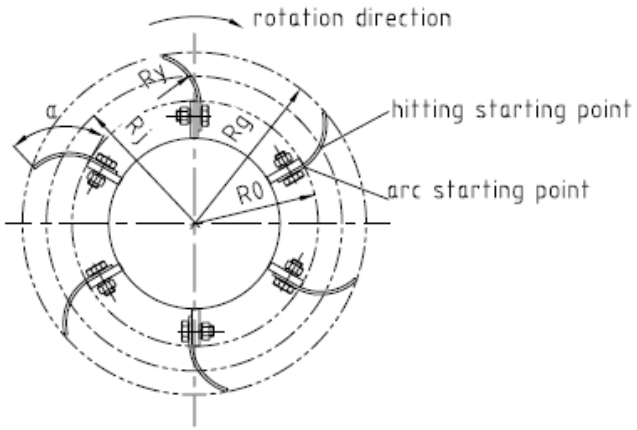


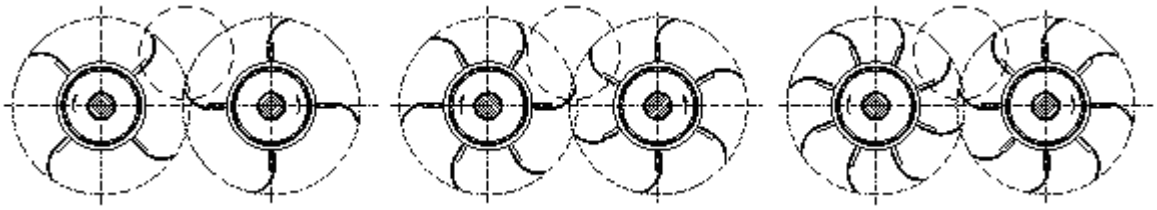
Fig.3 Structural parameters of picking roller

picking broken rate is, the lower picking loss rate; when the blade radian is 30° and the blade radius is 60mm, the rotation speeds of the picking roller were 300r/min or 400r/min, peanut broken rates were respectively 1.6 % or 2.4%; when the blade radian is 70°, and the blade radius is 35mm, total loss rate is the lowest on the picking segment of the blade. Though the analysis of the motion of the picking blade, it can be known: from the inside to outside of the blade hit the peanut plant, action force gradually becomes strong; when the R_0 and R_g are determined, the smaller the blade radian is, the longer the blade radius is, and the closer the hitting starting point is to outside of the blade, the stronger the picking action is; the bigger the blade radian is, the smaller the blade radius is, and the closer the hitting starting point is to inside of the blade, the longer the effective picking segment is, the softer the picking action is. In comprehensive consideration the two effects, the blade radius is 35mm, and the blade radian is 70°.

Tab.1 Picking blades with different structural parameters

Blade No.	Blade radius / mm	Blade radian / °
1	30	90
2	35	70
3	40	50
4	50	40
5	60	30

The blade quantity of the picking roller： The quantity of the picking blades are the key factors of the picking effect. Through analysis of movement balanced of the picking roller, we can know that the quantity of the blades should be selected even. The more quantity of the blade is helpful to improve the efficiency and effect of the picking roller, but the more quantity of the blade reduced the space between two picking roller, which caused the higher peanut broken rate and impurity rate, increased energy consumption and manufacturing costs. Reference to relevant research [7~10], the blade quantity of single roller initially selected 4, 6, 8. Configuration status of picking rollers differed in the blade quantity is as shown in Figure 4.



(a) 4 blades (b) 6 blades (c) 8 blades

Fig.4 Configuration status of picking rollers differed in the blade quantity

Though the picking experiment, the peanut broken rate, picking net rate, impurity rate and peanut with handle rate are respectively tested in the condition of different quantity blades. The testing results showed that: when the quantity of picking blades is different, the peanut broken rate and picking net rate have large differences; when the rotation speeds of the picking roller were 300r/min or 400r/min, peanut broken rates of the 8 blade were respectively 1.6 % or 2.4%, and were 2 to 3 times of the 4 blades, 6 blades; the picking net rate of the 4 blade were respectively 96.4%, 98.4%, and much lower than of the 6 blades and 8 blades; the impurity rate and peanut with handle rate of the 8 blades are significantly higher than of the 6 blades, the rate of the 6 blades is also slightly higher than of the 4 blades. Though analysis shows that: the more the blades quantity is, the smaller the distance between the adjacent picking blades, the greater the peanut broken rate is; the higher the picking frequency is, the higher the picking net rate is; the picking frequency of the 6 blades is 1.5 times of the 4 blades, the picking frequency of the 8 blades is 2 times of the 4 blades. In comprehensive analysis, the 6 blades can get the ideal picking quality.

Conclusion

When the straight-shaped blade is height-speed rotation, the outer and end of the picking blade is first action with peanut vine, picking force is strong and picking net rate is higher, but peanut broken rate and peanut with handle rate are increase, the broken branch and seedling phenomenon are serious. When arc-shaped blade is high-speed rotation, the points of the radial direction on the same blade turn into hitting zone. Compared with straight-shaped blades, its hitting force is relatively weak, comb brush effect is enhanced. On the same rotation speed, compared with straight-shaped blades, peanut broken rate and impurity rate of the arc-shaped blade were decreased,but picking net rate is decreased. The testing results showed that: The blade radian has a large impact to the peanut broken and loss rate; the smaller the blade radian is, the longer the blade radius is, and the higher picking broken rate is, the lower picking loss rate; when the blade radian is 70°, and the blade radius is 35mm, total loss rate is the lowest on the picking segment of the blade; the peanut broken rate and picking net rate have large differences at different quantity picking blades, peanut broken rates of the 8 blade were 2 to 3 times of the 4 blades, 6 blades, the picking net rate of the 4 blade were much lower than of the 6 blades and 8 blades. Through theoretical analysis and experimental research, the design of the picking roller is as follows: The picking roller and the clamping conveying chain are upper and lower configure, two rollers adopts the differential phase combination way, the design the picking roller adopts 6 backward slopping arc-shaped blades,the blade radius is 35mm, and the blade radian is 70°.

Acknowledgements

The study was supported by the Key Laboratory of Modern Agricultural Equipment, Ministry of Agriculture, P.R.China (201303002), the National Natural Science Foundation of China (51375247) and the Natural Science Foundation of Anhui province of china (1408085ME103).

References

[1] Zhimeng Zhang, Wenguang Hu, Tingting Xu. Journal of Peanut Science, Vol. 34, No. 3(2005), pp. 6-10. In Chinese
[2] Xiaolian Lü, Haiou Wang, Huijuan Zhang, Zhichao Hu. Journal of Agricultural Mechanization Research, No. 6(2012), pp. 245-248. In Chinese
[3] Baofa Li, Agriculture Mechanics. Beijing: China Agriculture Press. (2008), In Chinese
[4] Xiaolian Lü, Haiou Wang, Huijuan Zhang, Zhichao Hu. Hubei Agricultural Sciences, Vol. 51, No. 18(2012), pp. 4116-4118. In Chinese
[5] Timothy A Meeks, Archie Flanders. Journal of Agricultural and Applied Economics, Vol. 37, No. 1(2005), pp. 249-261.
[6] Kiniry J R. Field Crops Research, Vol. 91, No. 2(2005), pp. 297~ 306.
[7] Shufa Chen, Yaoming Li, Xingzhao Sun. Chinese Agriculture Mechanization, No. 1(2005), pp. 47-49. In Chinese
[8] Hongjun Wang, Lingqiang Min, Baoshen Huang. Farm Machinery, No. 6(2005), pp.71. In Chinese
[9] Shuqi Shang, Guoying Li, Ranbing Yang. Transactions of the Chinese Society of Agricultural Engineering, Vol. 25, No. 6(2009), pp. 125-129. In Chinese
[10] Xizhen Li, Ranbing Yang, Jiandong Li. Journal of Agricultural Mechanization Research, No. 4(2008), pp. 155- 157, 170. In Chinese
[11] Zhichao Hu, Haiou Wang, Jiannan Wang. Transactions o f the Chinese Society for Agricultural Machinery, Vol. 41, No. 4(2010), pp. 79-84. In Chinese

Applied Mechanics and Materials Vol. 597 (2014) pp 507-514
© (2014) Trans Tech Publications, Switzerland
doi:10.4028/www.scientific.net/AMM.597.507

Statics and Grasp Stiffness Analysis of an Underactuated Cable-truss Mechanism

Nan Wu[1, a *], Rongqiang Liu[1,b] and Hongwei Guo[1,c]

[1] State Key Laboratory of Robotics and System, Harbin Institute of Technology, Harbin, Heilongjiang, 150001, China

[a]wunan573646@163.com, [b]liurq@hit.edu.cn, [c]guohw@hit.edu.cn

Keywords: underactuated mechanism, statics, grasp stiffness, simulation

Abstract. Although much literature is available on the statics and grasp stiffness analysis of underactuated mechanisms, little research has been done on them of the underactuated cable-truss mechanism. The underactuated cable-truss mechanism grasps the target in the form of envelopment. Considering the grasping characteristics of the mechanism, the research on the relationship between the grasping force and the driving force is extremely important, as well as the study of the grasp stiffness. The statics analysis of an underactuated cable-truss mechanism, constituted by five cable-truss units, was given by means of combining with the vector method and the principle of virtual work in this paper. To prove the correctness of the analysis, the simulation was presented. The stiffness of the cable-truss unit was defined and the curve, showing the influence of the proportion relationship between the essential parameters to the stiffness, was obtained. Then, the stiffness of the mechanism was discussed.

Introduction

The grasping force that underactuated mechanism can provide and the mechanism stiffness are important factors used to evaluate the grasping characteristics of the mechanism. Much attention has been paid to the statics and grasp stiffness analysis of underactuated mechanism in recent years. The static equations of one underactuated hand with four identical fingers, named SRI, is obtained by Aukes D [1]. The relationship between the grasping force and the spring preloads of an adaptive hand is studied by Aukes D and Heyneman B [2]. Aaron M. Dollar and Robert D. Howe demonstrate that the SDM Hand can reliably grasp objects while keeping acquisition contact forces low [3]. Gert A. Kragten and Aris C. Kool develope a static grasp model to calculate the effect of design parameters of one underactuated hand [4]. Grasp force optimization in the design of an underactuated robotic hand has been done by Schuurmans J [5]. Shengqi Tan and Wenzeng Zhang provide a method for the statics analysis of an underactuated humanoid robotic hand [6]. An underactuated humanoid robot hand with changeable grasping force is designed by Wengzeng Zhao [7,8].

As a new type of underactuated mechanism, the underactuated cable-truss mechanism has many advantages like light weight, simple structure, and wide adaptability. It can be extended to large-scale spatial gripper and capture the target effectively without its precise position and shape. By using the vector method and the principle of virtual work, the matrix used to express the relationship between the grasping force and the driving force is established. The result of an example by programming is presented, as well as that of the statics simulation. The correctness of the statics analysis is proved as these results agree much well. The stiffness of the cable-truss unit is defined by the ratio of the external disturbance force and the change of the angle. Base on the statics analysis and the stiffness analysis of the cable-truss unit, the grasp stiffness of the mechanism is obtained. In mechanism field, the larger principal eigenvalue of the stiffness matrix usually represents better mechanism stiffness. Considering this principle, the influence of the proportion relationship of the essential parameters to the stiffness is discussed and the best proportion is collected.

Mechanism and Parameters

Fig. 1 shows the 3D model of the underactuated cable-truss mechanism that grasps the target in the form of envelopment. The mechanism consists of five cable-truss units. The units will deform if the length of cable 1 and that of cable 2 change by driving the motors for rotation. Reverse deformation is prevented with the limits even the external force is bigger than what is designed and the mechanism can be controlled to deform orderly by configuring the friction torque in the joints.

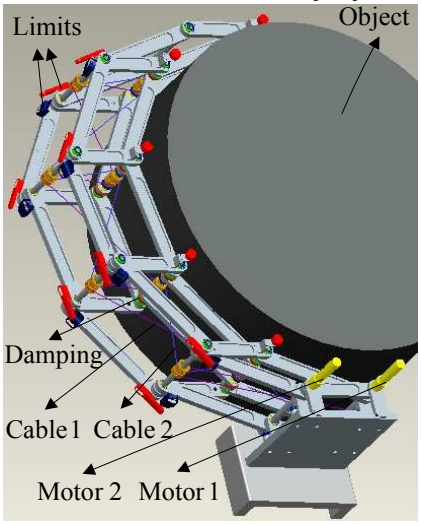


Fig. 1 3D model of the mechanism with the object

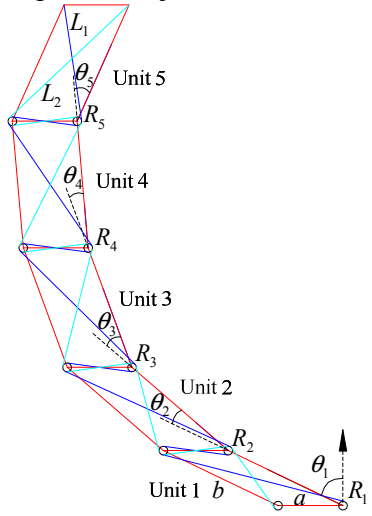


Fig. 2 Essential parameters

Fig. 2 gives the essential parameters of the mechanism. Let L_1 and L_2 be the length of cable 1 and that of cable 2. The length of the cross-bars and that of the vertical-bars of the units are respectively recorded as a and b. $\theta_1, \theta_2, \theta_3, \theta_4$ and θ_5 are the generalized coordinates of the units. With the help of the geometric knowledge, the total differential expression of the length of the cables, L_k(k=1,2) , is given in the form:

$$dL_k = \frac{\partial L_k}{\partial \theta_1}\cdot d\theta_1 + \frac{\partial L_k}{\partial \theta_2}\cdot d\theta_2 + \frac{\partial L_k}{\partial \theta_3}\cdot d\theta_3 + \frac{\partial L_k}{\partial \theta_4}\cdot d\theta_4 + \frac{\partial L_k}{\partial \theta_5}\cdot d\theta_5 \tag{1}$$

with

$$\begin{aligned}
\frac{\partial L_k}{\partial \theta_1} &= \sum_{i=1}^{5} \frac{(-1)^k ab\cos\left(\sum_{j=1}^{i}\theta_j\right)}{\sqrt{a^2+b^2-(R_i+R_{i+1})^2+(-1)^k\cdot 2ab\sin\left(\sum_{j=1}^{i}\theta_j\right)}} \\
&+ \sum_{i=1}^{2} R_i\left((-1)^{i+k}-(-1)^{i+k}\cdot\left(a^2+(-1)^{i+k}ab\sin(\theta_1)\right)\Big/\left(a^2+b^2+(-1)^{i+k}\cdot 2ab\sin(\theta_1)\right)\right) \\
&+ \sum_{i=1}^{2} \frac{(-1)^{i+k-1}\cdot R_i(R_1+R_2)ab\cos(\theta_1)}{\left(a^2+b^2+(-1)^{i+k}\cdot 2ab\sin(\theta_1)\right)\sqrt{a^2+b^2-(R_1+R_2)^2+(-1)^{i+k}\cdot 2ab\sin(\theta_1)}} \\
&+ \sum_{i=2}^{5}(R_i+R_{i+1})\frac{(-1)^k-(-1)^k\left(a^2+(-1)^k\cdot ab\sin\left(\sum_{j=1}^{i}\theta_j\right)\right)}{a^2+b^2+(-1)^k\cdot 2ab\sin\left(\sum_{j=1}^{i}\theta_j\right)} \\
&+ \sum_{i=2}^{5} \frac{\left((-1)^{k+1}\cdot(R_i+R_{i+1})^2 ab\cos\left(\sum_{j=1}^{i}\theta_j\right)\right)\Big/\left(a^2+b^2+(-1)^k\cdot 2ab\sin\left(\sum_{j=1}^{i}\theta_j\right)\right)}{\sqrt{a^2+b^2-(R_i+R_{i+1})^2+(-1)^k\cdot 2ab\sin\left(\sum_{j=1}^{i}\theta_j\right)}}
\end{aligned} \tag{2}$$

$$\frac{\partial L_k}{\partial \theta_q}=\sum_{i=q}^{5}\frac{(-1)^k ab\cos\left(\sum_{j=1}^{i}\theta_j\right)}{\sqrt{a^2+b^2-(R_i+R_{i+1})^2+(-1)^k\cdot 2ab\sin\left(\sum_{j=1}^{i}\theta_j\right)}}$$
$$+\sum_{i=q}^{5}(R_i+R_{i+1})\frac{(-1)^k-(-1)^k\left(a^2+(-1)^k\cdot ab\sin\left(\sum_{j=1}^{i}\theta_j\right)\right)}{a^2+b^2+(-1)^k\cdot 2ab\sin\left(\sum_{j=1}^{i}\theta_j\right)} \tag{3}$$
$$+\sum_{i=q}^{5}\frac{\left((-1)^{k+1}\cdot(R_i+R_{i+1})^2 ab\cos\left(\sum_{j=1}^{i}\theta_j\right)\right)\Big/\left(a^2+b^2+(-1)^k\cdot 2ab\sin\left(\sum_{j=1}^{i}\theta_j\right)\right)}{\sqrt{a^2+b^2-(R_i+R_{i+1})^2+(-1)^k\cdot 2ab\sin\left(\sum_{j=1}^{i}\theta_j\right)}}$$

with q=2,3,4,5.

Statics Analysis

The relationship between the grasping force that the mechanism can provide and the external force is the same as that between action and reaction, so the transformation matrix between the driving forces and the external forces is expressed. Fig. 3 shows the schematic of the external forces.

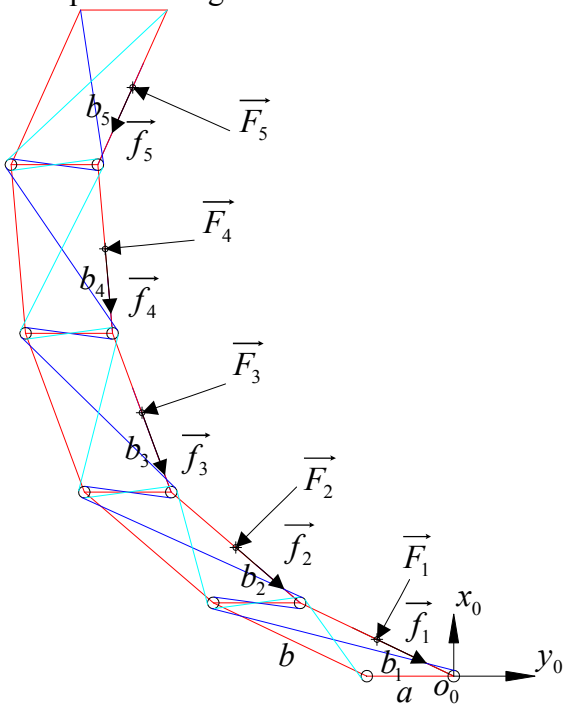


Fig. 3 Schematic of the external forces

Let $F_i(i=1,2,3,4,5)$ be the amplitude of the force vector $\vec{F}_i$. The coordinate system is established as in Fig. 3 and k_i represents the friction coefficient, then Eq. 4 and Eq. 5 can be obtained.

$$\vec{F}_i=F_i\left(\sin\left(\sum_{j=1}^{i}\theta_j\right),-\cos\left(\sum_{j=1}^{i}\theta_j\right)\right) \tag{4}$$

$$\vec{f}_i=k_iF_i\left(-\cos\left(\sum_{j=1}^{i}\theta_j\right),-\sin\left(\sum_{j=1}^{i}\theta_j\right)\right) \tag{5}$$

The radius vectors corresponding to the positions of the points of forces application can be expressed as:

$$\vec{r_1} = (b_1 \cos(\theta_1), b_1 \sin(\theta_1)) \tag{6}$$

$$\vec{r_q} = \left(\sum_{i=1}^{q-1} b \cos\left(\sum_{j=1}^{i} \theta_j \right) + b_q \cos\left(\sum_{i=1}^{q} \theta_i \right), \sum_{i=1}^{q-1} b \sin\left(\sum_{j=1}^{i} \theta_j \right) + b_q \sin\left(\sum_{i=1}^{q} \theta_i \right) \right) \tag{7}$$

with q=2,3,4,5.

Suppose that $\vec{F_i}(i = 1,2,3,4,5)$ remain the same in the progress that the generalized coordinate θ_1 produces the virtual displacement $\delta\theta_1$, the changes of $\vec{r_1}$ can be given.

$$\delta\vec{r_1} = b_1 \delta\theta_1 (-\sin(\theta_1), \cos(\theta_1)) \tag{8}$$

And $\vec{\delta r_q}(q = 2,3,4,5)$ can be expressed in the form:

$$\delta\theta_1 \left(-\sum_{i=1}^{q-1} b \sin\left(\sum_{j=1}^{i} \theta_j \right) - b_q \sin\left(\sum_{i=1}^{q} \theta_i \right), \sum_{i=1}^{q-1} b \cos\left(\sum_{j=1}^{i} \theta_j \right) + b_q \cos\left(\sum_{i=1}^{q} \theta_i \right) \right) \tag{9}$$

The virtual work made by the external forces can be obtained.

$$\delta W_{Fi} = \vec{F_i} \cdot \delta\vec{r_i} \tag{10}$$

$$\delta W_{fi} = \vec{f_i} \cdot \delta\vec{r_i} \tag{11}$$

According to Eq. 1, the changes of the cables can be given as:

$$\delta L_1 = \frac{\partial L_1}{\partial \theta_1} \delta\theta_1 \tag{12}$$

$$\delta L_2 = \frac{\partial L_2}{\partial \theta_2} \delta\theta_1 \tag{13}$$

Considering the positive work and negative work, the virtual work generated by the tensions of the cables can be presented.

$$\delta W_{T1} = -T_1 \cdot \delta L_1 = -T_1 \frac{\partial L_1}{\partial \theta_1} \delta\theta_1 \tag{14}$$

$$\delta W_{T2} = -T_2 \cdot \delta L_2 = -T_2 \frac{\partial L_2}{\partial \theta_1} \delta\theta_1 \tag{15}$$

If the friction torque produced by the damping of the first unit is indicated as M_1, Eq. 16 can be obtained.

$$\delta W_{M1} = M_1 \cdot \delta\theta_1 \tag{16}$$

Taking the principle of virtual work into account, Eq. 17 is given.

$$\delta W_{T1} + \delta W_{T2} + \delta W_{M1} + \sum_{i=1}^{5} (\delta W_{Fi} + \delta W_{fi}) = 0 \tag{17}$$

Substituting Eq. 4-Eq. 16 into Eq. 17, Eq. 18 is obtained.

$$\begin{aligned} &\left(-\frac{\partial L_1}{\partial \theta_1} \right) T_1 + \left(-\frac{\partial L_2}{\partial \theta_1} \right) T_2 + M_1 \\ &= (b_1) F_1 + \sum_{q=2}^{5} \left(\left(b \left(\sum_{i=2}^{q} \cos\left(\sum_{j=i}^{q} \theta_j \right) + k_p \sum_{i=2}^{q} \sin\left(\sum_{j=i}^{q} \theta_j \right) \right) + b_q \right) F_q \right) \end{aligned} \tag{18}$$

The other four equations can be worked out referring to the progress that Eq. 18 is obtained. Let M_i be the friction torque produced by the damping of the unit i(i=2,3,4,5). Then, Eq. 19 can be given.

$$A_F [F_1 \quad F_2 \quad F_3 \quad F_4 \quad F_5]^T = A_{TM} [T_1 \quad T_2 \quad M_1 \quad M_2 \quad M_3 \quad M_4 \quad M_5]^T \tag{19}$$

with

$$A_{TM}=\begin{bmatrix} -\frac{\partial L_1}{\partial \theta_1} & -\frac{\partial L_2}{\partial \theta_1} & 1 & 0 & 0 & 0 & 0 \\ -\frac{\partial L_1}{\partial \theta_2} & -\frac{\partial L_2}{\partial \theta_2} & 0 & 1 & 0 & 0 & 0 \\ -\frac{\partial L_1}{\partial \theta_3} & -\frac{\partial L_2}{\partial \theta_3} & 0 & 0 & 1 & 0 & 0 \\ -\frac{\partial L_1}{\partial \theta_4} & -\frac{\partial L_2}{\partial \theta_4} & 0 & 0 & 0 & 1 & 0 \\ -\frac{\partial L_1}{\partial \theta_5} & -\frac{\partial L_2}{\partial \theta_5} & 0 & 0 & 0 & 0 & 1 \end{bmatrix} \tag{20}$$

$$A_F=\begin{bmatrix} b_1 & a_{12} & a_{13} & a_{14} & a_{15} \\ 0 & b_2 & a_{23} & a_{24} & a_{25} \\ 0 & 0 & b_3 & a_{34} & a_{35} \\ 0 & 0 & 0 & b_4 & a_{45} \\ 0 & 0 & 0 & 0 & b_5 \end{bmatrix} \tag{21}$$

with

$$a_{1q}=b\left(\sum_{i=2}^{q}\cos\left(\sum_{j=i}^{q}\theta_j\right)+k_p\sum_{i=2}^{q}\sin\left(\sum_{j=i}^{q}\theta_j\right)\right)+b_q \qquad (q=2,3,4,5) \tag{22}$$

$$a_{2q}=b\left(\sum_{i=3}^{q}\cos\left(\sum_{j=i}^{q}\theta_j\right)+k_p\sum_{i=3}^{q}\sin\left(\sum_{j=i}^{q}\theta_j\right)\right)+b_q \qquad (q=3,4,5) \tag{23}$$

$$a_{3q}=b\left(\sum_{i=4}^{q}\cos\left(\sum_{j=i}^{q}\theta_j\right)+k_p\sum_{i=4}^{q}\sin\left(\sum_{j=i}^{q}\theta_j\right)\right)+b_q \qquad (q=4,5) \tag{24}$$

$$a_{45}=b(\cos(\theta_5)+k_5\sin(\theta_5))+b_5 \tag{25}$$

Example and Simulation

Based on the statics model, the statics result of an example is given by programming. The imaginary lines shown in Fig. 4 display the calculation results.

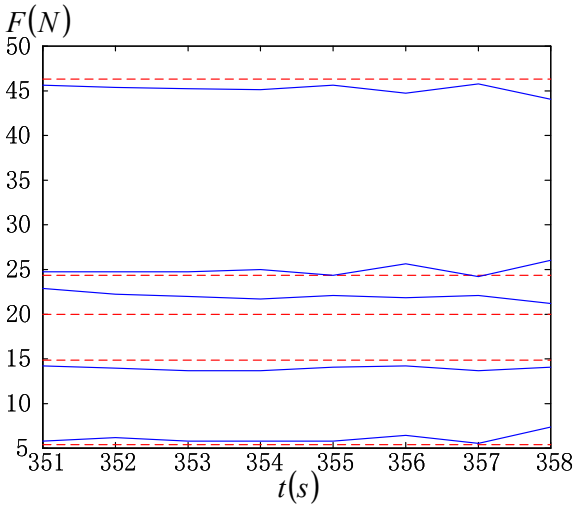


Fig. 4 Calculation and simulation results

Fig. 5 presents the simulation model that has been simplified and the measurement results are illustrated as the solid curves given in Fig. 4. The simulation results are all highly consistent with the calculation results, which proves the correctness of the statics analysis.

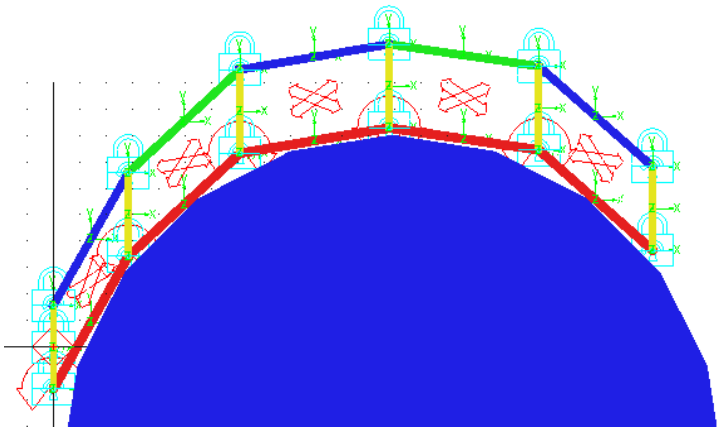


Fig. 5 Simulation model

Grasp stiffness

Stiffness of one Cable-truss Unit. Firstly, the problem of the stiffness of one cable-truss unit is solved. Fi. 6 provides the parameters of the cable-truss unit and the cables are in state of original length. With the aid of the geometric knowledge, Eq. 26 and Eq. 27 are obtained.

$$dL_1 = \left(-ab\cos(\theta)/\sqrt{a^2+b^2-2ab\sin(\theta)}\right)d\theta \tag{26}$$

$$dL_2 = \left(ab\cos(\theta)/\sqrt{a^2+b^2+2ab\sin(\theta)}\right)d\theta \tag{27}$$

with $\theta \in \left(-\frac{\pi}{2},\frac{\pi}{2}\right)$

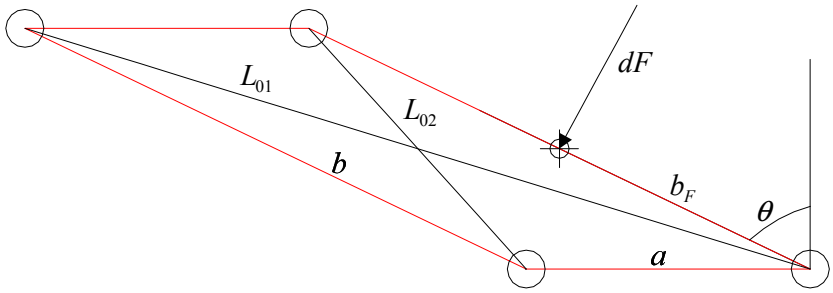


Fig. 6 Schematic of the parameters of the cable-truss unit

Let dF be the change of the external force that is perpendicular to the bar and suppose that dF>0. The position of dF is illustrated in Fig. 6. Considering that the cable can just provide tension and ignoring the radius of the joints, Eq. 28 is obtained.

$$dFb_F d\theta = \mathrm{T}_1 dL_1 \tag{28}$$

Let k_T be the tensile stiffness of the cable, Eq. 29 is given.

$$\mathrm{T}_1 = k_T dL_1 \tag{29}$$

Substituting Eq. 29 into Eq. 28, the stiffness of the unit can be expressed in the form:

$$k_F = \frac{dF}{d\theta} = \frac{abk_T\cos^2(\theta)}{b_F\left(a^2+b^2-2ab\sin(\theta)\right)} \tag{30}$$

If c=a/b, referring to the Eq. 30, the influence of θ and c to k_F can be illustrated as the curves shown in Fig. 7.

As presented in Fig. 7, the maximum of the stiffness remain unchanged and the value of θ corresponding to the maximum decreases as the value of c increases if c>1. On the other hand, the maximum of the stiffness and the value of θ corresponding to it increase as the value of c increases if c<1.

If dF<0, the results also can be obtained by the method above. According to the results, the best value of c can be collected base on the actual work requirements.

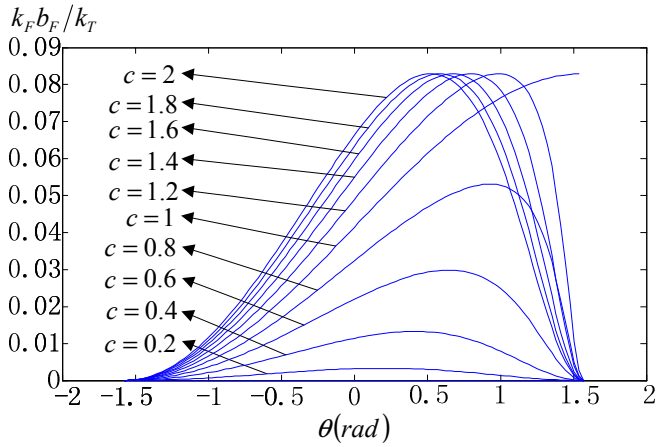


Fig. 7 The curves which illustrate the influence of θ and c to k_F

Stiffness of Mechanism. Ignoring the deformation of the bars and hinges, the grasp stiffness of the mechanism, denoted by K_F, can be expressed base on the statics and stiffness of one unit analysis.

$$K_F = \begin{bmatrix} k_{F11} & k_{F12} & k_{F13} & k_{F14} & k_{F15} \\ k_{F21} & k_{F22} & k_{F32} & k_{F42} & k_{F52} \\ k_{F31} & k_{F32} & k_{F33} & k_{F34} & k_{F35} \\ k_{F41} & k_{F42} & k_{F43} & k_{F44} & k_{F45} \\ k_{F51} & k_{F52} & k_{F53} & k_{F54} & k_{F55} \end{bmatrix} \tag{31}$$

with

$$k_{F5p} = \frac{k_T}{b_5}\left(\frac{\partial L_1}{\partial \theta_5}\right)\left(\frac{\partial L_1}{\partial \theta_p}\right) \tag{32}$$

$$k_{F4p} = \frac{k_T}{b_4}\left(\frac{\partial L_1}{\partial \theta_4}\right)\left(\frac{\partial L_1}{\partial \theta_p}\right) - \left(b\left(\cos(\theta_5) + k_5 \sin(\theta_5)\right) + b_5\right)\left(k_{F5p}/b_4\right) \tag{33}$$

$$\begin{aligned} k_{F3p} &= \frac{k_T}{b_3}\left(\frac{\partial L_1}{\partial \theta_3}\right)\left(\frac{\partial L_1}{\partial \theta_p}\right) \\ &\quad - \sum_{q=4}^{5}\left(\left(b\left(\sum_{i=4}^{q}\cos\left(\sum_{j=i}^{q}\theta_j\right) + k_q\sum_{i=4}^{q}\sin\left(\sum_{j=i}^{q}\theta_j\right)\right) + b_q\right)\frac{k_{Fqp}}{b_3}\right) \end{aligned} \tag{34}$$

$$\begin{aligned} k_{F2p} &= \frac{k_T}{b_2}\left(\frac{\partial L_1}{\partial \theta_2}\right)\left(\frac{\partial L_1}{\partial \theta_p}\right) \\ &\quad - \sum_{q=3}^{5}\left(\left(b\left(\sum_{i=3}^{q}\cos\left(\sum_{j=i}^{q}\theta_j\right) + k_q\sum_{i=3}^{q}\sin\left(\sum_{j=i}^{q}\theta_j\right)\right) + b_q\right)\frac{k_{Fqp}}{b_2}\right) \end{aligned} \tag{35}$$

$$\begin{aligned} k_{F1p} &= \frac{k_T}{b_1}\left(\frac{\partial L_1}{\partial \theta_1}\right)\left(\frac{\partial L_1}{\partial \theta_p}\right) \\ &\quad - \sum_{q=2}^{5}\left(\left(b\left(\sum_{i=2}^{q}\cos\left(\sum_{j=i}^{q}\theta_j\right) + k_q\sum_{i=2}^{q}\sin\left(\sum_{j=i}^{q}\theta_j\right)\right) + b_q\right)\frac{k_{Fqp}}{b_1}\right) \end{aligned} \tag{36}$$

with p=1,2,3,4,5.

The larger principal eigenvalue of the stiffness matrix usually means better mechanism stiffness in mechanism field. Fig. 8 reveals the relationship between the principal eigenvalue of K_F and c. As shown in Fig. 8, the maximum of the principal eigenvalue is obtained when c=1.6.

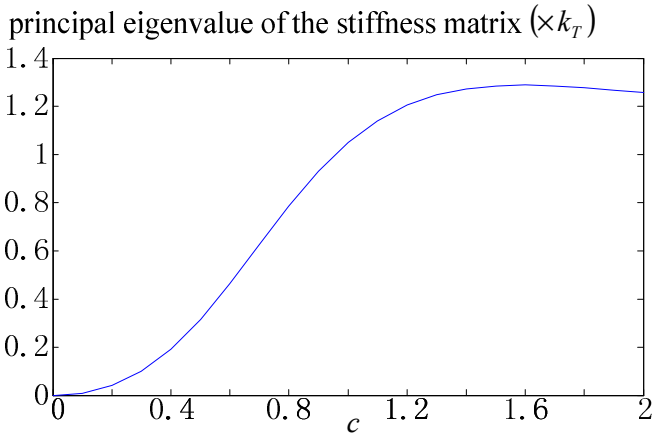


Fig. 8 The change of the principal eigenvalue of K_F

Conclusion

By means of combining with the vector method and the principle of virtual work, this paper presents the statics analysis of an underactuated cable-truss mechanism made up by five cable-truss units. The matrix representing the relationship between the grasping forces and driving forces is obtained and the statics simulation is given by simplifying the 3D model. The calculation results and the simulation results agree quite well, which proves the correctness of the statics analysis. Base on the progress that the stiffness of the unit is worked out and the statics analysis, the stiffness of the mechanism is established and the influence of the proportion relationship between the essential parameters to the stiffness is discussed.

Acknowledgements

Funding for this work is provided by the National Natural Science Foundation of China (Project NO. 51275107) and “111 Project”(Grand NO. B07018).

References

[1] Aukes D, Kim S, Carcis P. Selectively Compliant Underactuated Hand for Mobile Manipulation[C]//IEEE ICRA. Saint Paul, Minnesota, USA: IEEE, 2012: 2824-2829.

[2] Aukes D, Heyneman B. Varying spring preloads to select grasp strategies in an adaptive hand [C]//IEEE/RSJ IROS. San Francisco, CA, USA: IEEE, 2011: 1373-1379.

[3] Aaron M. Dollar, Robert D. Howe. The SDM Hand: A Highly Adaptive Compliant Grasper for Unstructured Environments [J]. International Journal of Robotics Research, 2010(in press): 1-11.

[4] Gert A. Kragten, Aris C. Kool, Just L. Grasp force optimization in the design of an underactuated robotic hand[C]//IEEE 10th ICORR. Kobe, Japan: IEEE, 2009: 2493-2498.

[5] Schuurmans J, Linde R Q. Ability to hold grasped objects by underactuated hands: performance prediction and experiments[C]//IEEE ICRA. Noordwijk, The Netherlands: IEEE, 2007: 776-782.

[6] Shengqi Tan, Wenzeng Zhang. Design and Analysis of Underactuated Humanoid Robotic Hand Based on Slip Block-Cam Mechanism [C]//IEEE ROBIO. Biomimetics. Guilin, China: IEEE, 2009: 2356-2361.

[7] Wengzeng Zhao, Xiande Ma. Underactuated humanoid robot hand with end power grasping [N]. J Tsinghua Univ (Sci & Tech), 2009, Vo l. 49, No. 2: 194-197.

[8] Wengzeng Zhao, Qiang Chen. Underactuated humanoid robot hand with changeable grasping force[N]. J Tsinghua Univ (Sci & Tech), 2003, Vo l. 43, No. 8: 1143-1147.

Applied Mechanics and Materials Vol. 597 (2014) pp 515-518
© (2014) Trans Tech Publications, Switzerland
doi:10.4028/www.scientific.net/AMM.597.515

An All-digital, Cyclic and Synthesizable TDC in the ADPLL-based Clocking Digital Systems for Multidomain Power Management

Shao-Hua Chen[1,2a], and Ming-Bo Lin[1]

[1]Department of Electronic Engineering, National Taiwan University of Science and Technology, Taipei, Taiwan

[2]Department of Electrical Engineering, Hwa Hsia Institute of Technology, New Taipei City, Taiwan

[a]ritachen@cc.hwh.edu.tw

Keywords: all-digital phase-locked loop (ADPLL), dynamic voltage and frequency scaling (DVFS), system-on-chip (SoC) and time-to-digital converter (TDC).

Abstract. In this paper, we propose an all-digital, cyclic and synthesizable TDC architecture, which may be used as a core block in ADPLLs to replace the analog block as a phase/frequency detector and a charge pump. Traditional designs of the DVFS scheme for multidomain power management are based on a conventional analog PLL to generate the dynamic voltage and frequency in which the use of a digital TDC eliminates the need for current sources in conventional analog PLLs.

Introduction

With the rapid growth of the digital systems, such as the integration of various complex signal processing modules and graphical units for portable electronics applications, the need for the reduction of cost and power consumption in such systems becomes a primary design constraint for portable operation [1]. To lower the power consumption, many power management approaches for digital systems have been developed in the literature during the past decade. Among these, DVFS is a commonly used technique for saving the power consumption of a CMOS integrated circuit (IC).

To achieve continuous control of the clock frequency and the supply voltage, traditional designs of the DVFS schemes [3] are based on a charge-pump PLL (the conventional analog PLL) to find the clock frequency level and the supply voltage level on the minimum energy point (MEP) for power management. With the move towards nanometer technologies, digital approaches become dominant because current modern process scaling has been offering several benefits to digital circuits. The digital PLL has recently emerged as an appealing alternative to the more conventional analog PLL to benefit from the features of advanced digital processes, thereby resulting in a simple, area-effective and low-power solution [4]. In this paper, we propose an all-digital, cyclic, synthesizable TDC, which can be used as a digital building block for an ADPLL.

Design Overview

The restriction on power consumption is severe for portable, battery-powered electronics applications (i.e., smart phones, gaming consoles and mobile computers) since it is desirable to optimize the speed while still meeting the minimum requirements on size, battery lifetime, and the weight of batteries. Therefore, low-power design is the most important factor to be taken into consideration while designing SoC for mobile devices. Furthermore, because of the steady increase of the functional complexity and the integration level of SoC, the chip is separated into multiple independent power domains which have various performance requirements. Each domain has its own clock frequency and supply voltage, where dynamic frequency and voltage scaling can be applied to each domain to efficiently manage the power consumption according to the independent runtime workload information.

As mentioned, an ADPLL is used in the DVFS scheme to generate the dynamically varying values of frequency and benefits from the advanced digital processes, where the operating frequency is dynamically decreased to match the reduction in the supply voltage. Therefore, a significantly reduction in the energy required for digital systems can be achieved, as described by

$$P_{avg} = C_{load} \times V_{DD}^2 \times f_{CLK}, \tag{1}$$

where P_{avg} is the average (dynamic) power consumption, C_{load} is the load capacitance under consideration, f_{CLK} is the operating frequency and V_{DD} is the supply voltage.

In the ADPLL (Fig. 1), the TDC compares the phase error between the reference clock, f_{ref}, and the divided clock, f_{div}. Then, the digitized phase error is filtered by a digital loop filter (DLF), and applied to control the frequency of a digitally controlled oscillator (DCO). Here, the TDC replaces analog blocks such as a phase/frequency detector and a charge pump of the conventional analog PLL, the DLF replaces the analog RC loop filter, and the voltage-controlled oscillator (VCO) is replaced by the DCO, reducing the power dissipation and area of the ADPLL. As shown in Fig. 2, one of the key advantages of digital PLLs over their analog counterparts is that they eliminate the need for large capacitors within the loop filter by using digital circuits to obtain the desired filtering function. The resulting area savings is critical for achieving a low-cost solution, and the general PLL implementation is more easily scaled down in size as new technology processes are utilized.

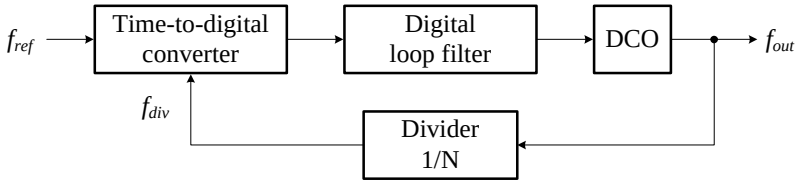


Fig. 1: Block diagram of all digital PLL.

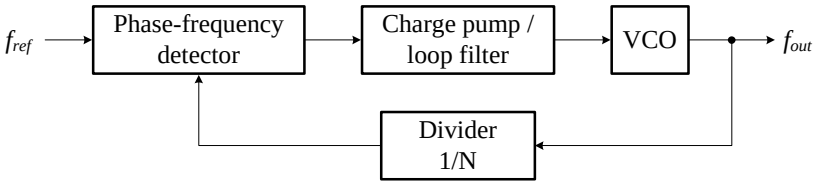


Fig. 2: Block diagram of the conventional analog PLL.

This topology decreases the area cost of the power management unit and enables the highly reconfigurable design for simplicity.

The Proposed Cyclic TDC Architecture

The key idea of the proposed cyclic TDC architecture is to leverage the cyclic-delaying clock technique to simplify the control circuit. As such, the proposed cyclic TDC is able to measure a time interval with a large dynamic range and also facilitates a potentially simpler implementation than the traditional delay-chain based architecture [2]. As depicted in Fig 3, the key concept of the proposed delay-chain based TDC is all digital, scalable and cyclic, where the delay chain is created as a train of buffers. The pulse-shaping block, controlled with a control logic circuit, schedules the flow of the START signal to the CK inputs of flip-flops of the delay chain.

To illustrate the operation of the proposed TDC, let us first consider the situation of a short time interval to be measured. The time interval of interest is the time difference between the rising edge

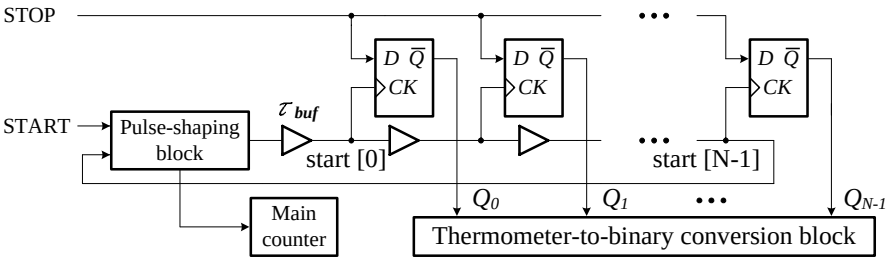


Fig. 3: The proposed scalable, cyclic delay-chain TDC loop.

of the START signal at the CK input and the rising edge of the STOP signal at the D input of flip-flops. To quantify this, let each buffer in the delay chain have an average propagation delay of τ_{buf}. Thus, the rising edge of the START signal propagating through each of the successive buffers will experience a propagation delay of τ_{buf}. Note that the delay chain operates like a multiphase clock generator that samples the state of the STOP input signal at each phase with a time interval of τ_{buf}. As a result, the STOP signal is sampled by an array of flip-flops on the rising edge of the delayed clock vector start[0:N-1]. Hence, the time-measurement result is determined by the rightmost position of the flip-flop that stores a logic-1 state. The thermometer-coded output is then converted to its binary equivalent using a simple decoder.

As the time interval of interest is large, the START signal can loop the same delay chain several times, as depicted in Fig. 3. The number of looping through the delay chain by the START signal is accumulated by the main counter. Let the count of the main counter be CNT before the rising edge of the STOP signal. In principle, the measured estimate, T_m, for the time interval, T, to be measured between the START signal and the STOP signal is composed of the count CNT of the main counter and the interpolated result n that is the rightmost flip-flop that stores a logic-1 state, as illustrated in Fig. 4. Consequently, the time interval of measurement, T_m, can be expressed as follows:

$$T_m = [N \times CNT + n] \times \tau_{buf} \tag{2}$$

where N is the number of delay stages within the delay chain. An illustration is given in Fig. 4 with N = 12, $n = 8$, and $CNT = 2$.

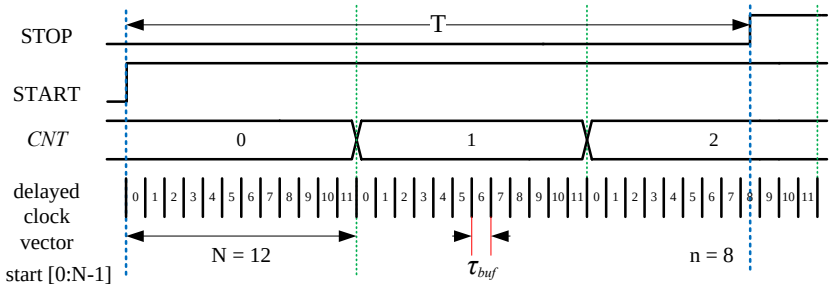


Fig. 4: Timing of TDC core signals.

TDC Performance

In order to acquire the entire TDC transfer characteristics associated with the measured time interval, we verified the functionality of the proposed TDC by using Verilog HDL behavioral simulation based on the timing delays obtained from HSPICE simulation results. The resulting characteristics is presented in Fig. 5, where the measured time interval is plotted on the x-axis and the corresponding interpolated value, n, is represented by the y-axis.

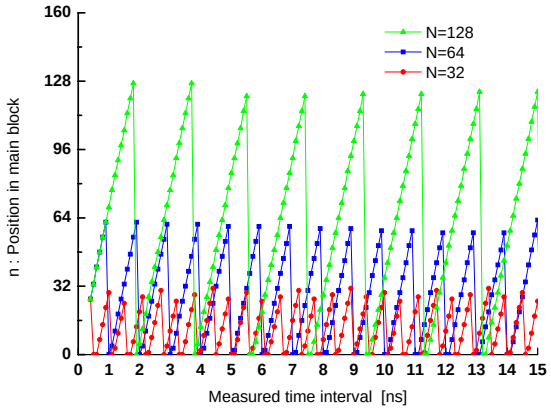


Fig. 5: Transfer characteristic with certain position n in the main block.

The full-range transfer curve obtained exhibits a sawtooth waveform with a repetition period equal to one complete loop cycle along with the propagation delay of the pulse-shaping block, i.e., T_{LB}, as illustrated in Fig. 5. It makes sense to this periodicity for the proposed scalable, cyclic TDC architecture, which efficiently achieves high linearity and a high dynamic range, where the range of the main counter can be easily adjusted on demand.

Conclusion

In this paper, we presented a wide dynamic range, low-power, area-efficient, cyclic TDC architecture that can easily achieve the flexibility as well as the scalability and portability to different process technologies.

The proposed cyclic TDC architecture has the following features. First, it reveals superior periodicity and a high dynamic range. Second, it consists of all digital circuits that can be synthesized from a standard logic library or can manually be built from digital gates; thereby, its resolution and area are scaled in accordance with the scaling factors inherently associated with VLSI technologies. In addition, digital architectures are well-known for their noise and variation robustness and furthermore well-established digital design methodologies can shorten design cycles and verification time significantly. On the other hand, the TDC directly affects the performance of the ADPLL. Third, from the synthesis results for the realization of the read-out scheme, the reduction of the number of the delay cells not only yields better linearity but also reduces area. Fourth, there is no custom circuit design or custom layout that requires comprehensive characterization, making the TDC a portable and scalable block. Fifth, the digital interface between the blocks improves testability and programmability of the ADPLL.

References

[1] Vadim Gutnik, and Anantha P. Chandrakasan, ``Embedded power supply for low-power DSP," *IEEE Trans. on Very Large Scale Integration (VLSI) Systems,* vol. 5, no. 4, pp. 425--435, Dec. 1997.

[2] Jussi-Pekka Jansson, Antti Mäntyniemi, and Juha Kostamovaara, ``A CMOS time-to-digital converter with better than 10 ps single-shot precision," *IEEE J. of Solid-State Circuits,* vol. 41, no. 6, pp. 1286--1296, Jun. 2006.

[3] Jeabin Lee et al., ``A power management unit with continuous co-locking of clock frequency and supply voltage for dynamic voltage and frequency scaling," *IEEE International Symposium on Circuits and Systems ,* pp. 2112--2115, May. 2007.

[4] Thomas Olsson, and Peter Nilsson, ``A digitally controlled PLL for SoC applications," *IEEE J. of Solid-State Circuits,* vol. 39, no. 5, pp. 751--760, May. 2004.

CHAPTER 8:

Vehicles, Transport and Navigation Development

Applied Mechanics and Materials Vol. 597 (2014) pp 521-524
© (2014) Trans Tech Publications, Switzerland
doi:10.4028/www.scientific.net/AMM.597.521

A Novel Adaptive UKF and Its Application in the SINS/GPS Integrated Navigation

Yong Li*, She-Sheng Gao, Yi Yang

School of Automation, Northwester Polytechnical University, Xi`an 710072, China

*liyongshuxue1989@163.com

Keywords: Integrated navigation, UKF, EM algorithm, SINS/GPS.

Abstract. This paper reports the solution of the state estimation problem of nonlinear systems without knowing prior noise statistical characteristics. An adaptive UKF algorithm is proposed. This novel UKF algorithm is constructed by traditional UKF and EM algorithm, also it improve accuracy through Taylor series approximation. By applying the proposed algorithm into SINS/GPS integrated navigation system and comparing with the unscented Kalman filtering (UKF) algorithm, the adaptive UKF algorithm we proposed can effectively improve the filtering performance , also it outperforms UKF in terms of accuracy.

1. Introduction

UKF approximates the posterior probability density function of the nonlinear system state throughing the unscented transformation [1].Compared with EKF, There is no need for UKF to calculate the nonlinear state function and measuring the Jacobi matrix. Simultaneously , UKF calculate simply with a high filtering precision and good convergence. Therefore UKF has received extensive attention of scholars [2]. But, When the prior noise statistical characteristics is unknown. the traditional UKF filerting will be bad. what`s more, Prior statistical characteristic of noise in actual application are difficult to obtain accurately and easy to change,which obviously limits the application of the UKF [3-5].

2. Description of UKF algorithm

General form of UKF under discrete nonlinear conditions can be described as follow

$$\begin{cases} x_k = f(x_{k-1}) + w_{k-1} \\ z_k = h(x_k) + \mathrm{v}_k \end{cases} \tag{1}$$

where $k \geq 0$ represents discrete-time variable, $x \in R^n$ represents state variable, $z \in R^m$ represents output vector. f and h are nonlinear vector function and $f \in R^n \to R^n, h \in R^m \to R^m$, $w_k \in R^n$ denotes system noise, $\mathrm{v}_k \in R^m$ denotes the measurement noise. Assume w_k , v_k as a zero mean white noise processes with Gaussian distribution. Q denotes the non-negative definite matrix, R denotes positive definite symmetric matrix.

Step 1: Initialization $\hat{X}_0 = E[X_0]$ and $P_0 = E\left[\left(X_0 - \hat{X}_0\right)\left(X_0 - \hat{X}_0\right)^T\right]$

Step 2: Sigma points calculation and time update

$$\begin{cases} \boldsymbol{\xi}_{0,k-1} = \hat{\boldsymbol{X}}_{k-1} \\ \boldsymbol{\xi}_{i,k-1} = \hat{\boldsymbol{X}}_{k-1} + \left(\sqrt{(n+\lambda)P_{k-1}}\right)_i, \quad i = 1,2,\cdots,n \\ \boldsymbol{\xi}_{i,k-1} = \hat{\boldsymbol{X}}_{k-1} - \left(\sqrt{(n+\lambda)P_{k-1}}\right)_i, \quad i = n+1, n+2,\cdots,2n \end{cases} \tag{2}$$

where $\sqrt{(n+\lambda)P_{k-1}}$ is the *ith* column of lower triangular decomposition square root of the matrix $(n+\lambda)P_{k-1}$.

$$\boldsymbol{\xi}_{i,k/k-1} = f(\boldsymbol{\xi}_{i,k-1}) + \boldsymbol{q}_{k-1}, \quad i = 0,1,\cdots,2n \tag{3}$$

$$\hat{\boldsymbol{X}}_{k/k-1} = \sum_{i=0}^{2n} \omega_i^m \boldsymbol{\xi}_{i,k/k-1} = \sum_{i=0}^{2n} \omega_i^m f(\boldsymbol{\xi}_{i,k-1}) \tag{4}$$

$$P_{k/k-1}=\sum_{i=0}^{2n}\omega_i^c(\boldsymbol{\xi}_{i,k/k-1}-\hat{\boldsymbol{X}}_{k/k-1})(\boldsymbol{\xi}_{i,k/k-1}-\hat{\boldsymbol{X}}_{k/k-1})^T+Q \tag{5}$$

$$\boldsymbol{\gamma}_{i,k/k-1}=h(\boldsymbol{\xi}_{i,k/k-1}),\ i=0,1,\cdots,2n \tag{6}$$

$$\hat{\boldsymbol{Z}}_{k/k-1}=\sum_{i=0}^{2n}\omega_i^m\boldsymbol{\gamma}_{i,k/k-1}=\sum_{i=0}^{2n}\omega_i^m h(\boldsymbol{\xi}_{i,k/k-1}) \tag{7}$$

where $\omega_0^m=\lambda/(n+\lambda)$, $\omega_0^c=\lambda/(n+\lambda)+(1-\alpha^2+\beta)$, $\omega_i^m=\omega_i^c=1/2(n+\lambda)\quad i=1,...,2n$, $\lambda=\alpha^2(n+\kappa)-n$,and $10^{-4}\le\alpha\le1$, $\kappa=3-n$,the value of β has relationship with x. in this paper let $\alpha=1,\beta=0,\kappa=2$

Step 3: Measurement update

$$P_{\hat{\boldsymbol{Z}}_{k/k-1}}=\sum_{i=0}^{2n}\omega_i^c\left(\boldsymbol{\gamma}_{i,k/k-1}-\hat{\boldsymbol{Z}}_{k/k-1}\right)\left(\boldsymbol{\gamma}_{i,k/k-1}-\hat{\boldsymbol{Z}}_{k/k-1}\right)^T+R \tag{8}$$

$$P_{\hat{\boldsymbol{X}}_{k/k-1}\hat{\boldsymbol{Z}}_{k/k-1}}=\sum_{i=0}^{2n}\omega_i^c\left(\boldsymbol{\xi}_{i,k/k-1}-\hat{\boldsymbol{X}}_{k/k-1}\right)\left(\boldsymbol{\gamma}_{i,k/k-1}-\hat{\boldsymbol{Z}}_{k/k-1}\right)^T \tag{9}$$

$$K_k=P_{\hat{\boldsymbol{X}}_{k/k-1}\hat{\boldsymbol{Z}}_{k/k-1}}P_{\hat{\boldsymbol{Z}}_{k/k-1}}^{-1} \tag{10}$$

$$\hat{\boldsymbol{X}}_k=\hat{\boldsymbol{X}}_{k/k-1}+K_k(\boldsymbol{Z}_k-\hat{\boldsymbol{Z}}_{k/k-1}) \tag{11}$$

$$P_k=P_{k,k-1}-K_kP_{\hat{\boldsymbol{Z}}_{k/k-1}}K_k^T \tag{12}$$

3. An adaptive UKF algorithm based on EM algorithm

The EM algorithm can estimate noise covariance matrix by iteration[6-7] and increase the precision of traditional UKF filtering under the condition of prior noise statistical characteristics unknown. Suppose $\Theta=\{R,Q\}$ denotes noise covariance of Eq.1, and Θ can be estimated through EM algorithm and maximum likelihood estimation

$$\hat{\Theta}_{EM}=\arg\max_{\Theta}E\{\ln[L(\Theta\mid z_{1:k},x_{1:k})]\} \tag{13}$$

where $\ln[L(\Theta\mid z_{1:k},x_{1:k})]$ is the log-likelihood function of Θ, and the system function is a Markov process thus

$$p(z_{1:k},x_{1:k}\mid\Theta)=\frac{1}{(2\pi)|P_0|^{1/2}}\exp[-\frac{(x_0-\hat{x}_0)^TP_0^{-1}(x_0-\hat{x}_0)}{2}]\times\prod_{i=1}^{k}\frac{1}{(2\pi)^{n/2}|Q|^{1/2}}\exp[-\frac{w_{i-1}^TQ^{-1}w_{i-1}}{2}]\times\prod_{i=0}^{k}\frac{1}{(2\pi)^{m/2}|R|^{1/2}}\times\exp[-\frac{v_i^TR^{-1}v_i}{2}] \tag{14}$$

where $w_{i-1}=x_i-f(x_{i-1})$, $v_i=y_i-h(x_i)$ .Eq.15 can be get through(17)and Eq. $tr\{xx^T\}=tr\{x^Tx\}$

$$\begin{aligned}E(-\log L(\Theta\mid z_{1:k},x_{1:k}))=&\log(|P_0|)+N\log(|Q|)+N\log(|R|)+E[tr\{P_0^{-1}(x_0-\hat{x}_0)(x_0-\hat{x}_0)^T\}\mid x_{1:k}z_{1:k}]+\\&E\{\sum_{i=1}^{k}[tr\{Q^{-1}(w_{i-1}w_{i-1}{}^T)\}\mid x_{1:k}z_{1:k}]\}+E\{\sum_{i=0}^{k}[tr\{R^{-1}(v_iv^T{}_i)\}\mid x_{1:k}z_{1:k}]\}\end{aligned} \tag{15}$$

To calculate the expect of $\log L(\Theta\mid z_{1:k},x_{1:k})$, $\{w_{i-1}w^T{}_{i-1}\}$ and $\{v_iv^T{}_i\}$ should be known. We use Taylor series approximation linearizes the nonlinear functions $f(\cdot)$ and $h(\cdot)$

$$x_i-f(x_{i-1})\approx x_i-f(\hat{x}_{i-1})-[\frac{\partial f}{\partial x}]_{x=\hat{x}_{i-1}}(x_{i-1}-\hat{x}_{i-1}) \tag{16}$$

$$x_i-f(x_{i-1})\approx x_i-f(\hat{x}_{i-1})-[\frac{\partial f}{\partial x}]_{x=\hat{x}_{i-1}}(x_{i-1}-\hat{x}_{i-1}) \tag{17}$$

put Eq.16 and Eq.187 to Eq.15, ignore constant term and get the following equation

$$\begin{aligned}E(-\log L(\Theta\mid z_{1:k},x_{1:k}))=&\log(|P_0|)+N\log(|Q|)+N\log(|R|)+tr\{P_0^{-1}(P_0^{(j-1)})(x_0-\hat{x}_0)(x_0-\hat{x}_0)^T)\}+\\&tr\{Q^{-1}(B_1^{(j-1)}-B_2^{(j-1)}-(B_2^{(j-1)})^T+B_3^{(j-1)})\}+tr\{R^{-1}(B_4^{(j-1)}-B_5^{(j-1)}-(B_5^{(j-1)})^T+B_6^{(j-1)})\}\end{aligned} \tag{18}$$

where $C_i=[\frac{\partial h}{\partial x}]_{x=\hat{x}_i}$, $B_1=\sum_{i=1}^{k}[P_i+\hat{x}_i\hat{x}_i^{\mathrm{T}}]$, $B_2=\sum_{i=1}^{k}[P_{i/i-1}\Phi_{i-1}^T+\hat{x}_{i-1}f^T(\hat{x}_{i-1})]$, $B_3=\sum_{i=0}^{k}f(\hat{x}_{i-1})f^T(\hat{x}_{i-1})+\Phi_{i-1}P_{i-1}\Phi^T{}_{i-1}$,

$B_4=\sum_{i=1}^{k}[z_iz_i^T]$, $B_5=\sum_{i=1}^{k}[z_ih^T(\hat{x}_i)]$, $B_6=\sum_{i=1}^{k}C_i[P_i+\hat{x}_i\hat{x}_i^T]C^T{}_i+h(\hat{x}_i)h^T(\hat{x}_i)$, $\Phi_{i-1}=[\frac{\partial f}{\partial x}]_{x=\hat{x}_{i-1}}$,

Taking the partial derivative of $E(-\log L(\Theta\mid z_{1:k},x_{1:k}))$ with respect to Q and R and setting it to zero iterate j times yields the optimal noise estimation system

$$\mathrm{Q}^{(j)}=\frac{1}{N}[B_1^{(j-1)}-B_2^{(j-1)}-(B_2^{(j-1)})^T+B_3^{(j-1)}] \tag{19}$$

$$R^{(j)} = \frac{1}{N}[B_4^{(j-1)} - B_5^{(j-1)} - (B_5^{(j-1)})^T + B_6^{(j-1)}] \tag{20}$$

4. Experiments and Analysis

Practical experiments were conducted to observe the flight of an ASN 206 reconnaissance UAV in the City of Xi'an, Shaanxi, China. The UAV uses a SINS/GPS integrated navigation system for spatial navigation and positioning. The GPS clock offset is 0.5m, clock bias 0.01m/s (the related time 1h), pseudorange observation noise 10m, pseudorange rate observation noise 0.5m/s.The gyro constant drift is 0.01°/h, and the white noise 0.001°/h. The accelerometer's zero bias is $10^{-4}g$, the random drift $10^{-5}g\sqrt{s}$. The UAV's average flight speed is about 270km/h, the average flight height is about 2km. The flight time is about 80min. The kinematic model of the UAV's navigation system can be described similarly as Eq.1 where the system state vector $\mathbf{X}$ is defined as

$$\mathbf{X} = [\varphi_E, \varphi_N, \varphi_U, \delta V_E, \delta V_N, \delta V_U, \delta L, \delta\lambda, \delta h]^{\mathrm{T}} \tag{21}$$

Where $(\varphi_E, \varphi_N, \varphi_U)$ is the attitude error, $(\delta V_E, \delta V_N, \delta V_U)$ is the velocity error, and $(\delta L, \delta\lambda, \delta h)$ is the position error with components in latitude, longitude and altitude. The kinematic model's error vector $\mathbf{W}$ is defined as

$$\mathbf{W} = [\varepsilon_E, \varepsilon_N, \varepsilon_U, \nabla_E, \nabla_N, \nabla_U]^{\mathrm{T}} \tag{22}$$

where $(\varepsilon_E, \varepsilon_N, \varepsilon_U)$ is the gyro constant drift, and $(\nabla_E, \nabla_N, \nabla_U)$ is the accelerometer zero-bias. The observation vector $\mathbf{Z}$ is defined as the difference between SINS and GPS data, i.e.,

$$\mathbf{Z} = [\delta L, \delta\lambda, \delta h, \delta V_E, \delta V_N]^{\mathrm{T}} = [L_I - L_G, \lambda_I - \lambda_G, h_I - h_G, V_{EI} - V_{EG}, V_{NI} - V_{NG}]^{\mathrm{T}} \tag{23}$$

where (L_I, λ_I, h_I) is the latitude, longitude and altitude of SINS, (V_{EI}, V_{NI}) the latitudinal and longitudinal velocities of SINS, (L_G, λ_G, h_G) the latitude, longitude and altitude of GPS, and (V_{EG}, V_{NG}) the latitudinal and longitudinal velocities of GPS. In order to analyse the disturbance due to systematic errors of kinematic and observation models, the experimental data were selected from the flight data of the UAV within a continuous time period of 2000s. The window width is 15. Trials were conducted to estimate the positioning error of the UAV by using UKF and adaptive UKF proposed in this paper, respectively. The obtained experimental results demonstrate the similar trend as the case of the moving vehicle. Fig. 1 shows that the traditional UKF method has the large magnitude of oscillations, and the resultant error is within (-10m, +10m). It can be seen from Fig. 2 that the magnitude of oscillations is reduced by adaptive UKF method we proposed, and the position error is within (-7m, +7m). This demonstrates the proposed adaptive UKF can effectively resist the disturbances of the systematic errors,and improve the filtering performance.

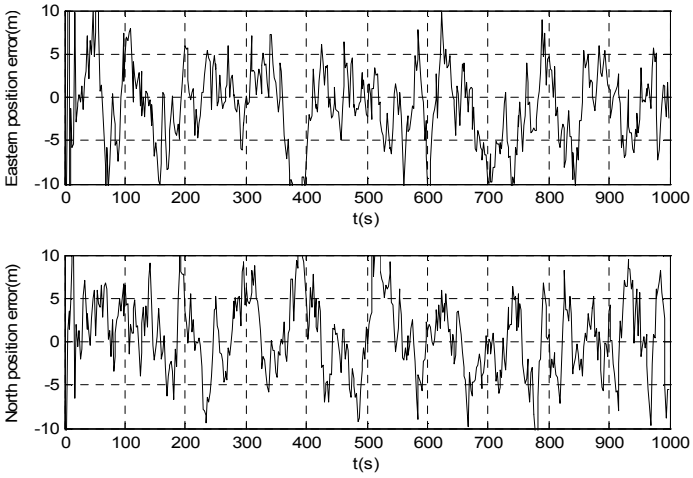


Fig.1 Position error estimation of UKF

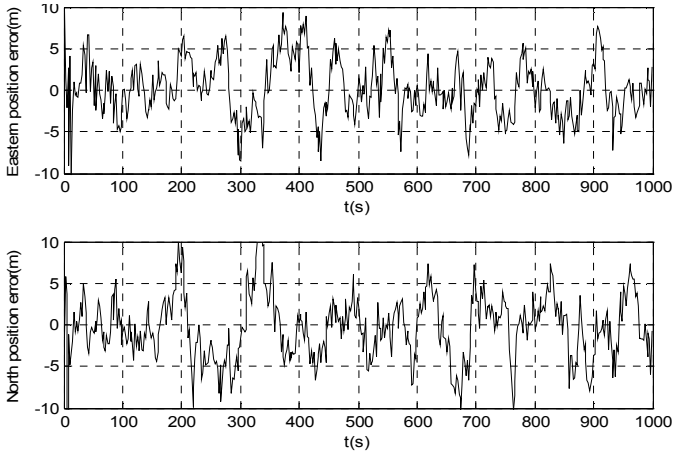


Fig.2 Position error estimation of adaptive UKF

5. Conclusions

In order to solve the state estimation problem of nonlinear systems , when prior noise statistical characteristics is unknown. A novel adaptive UKF method is proposed. By using the adaptive UKF to SINS/GPS integrated navigation system and the experiments result we can clearly see that the adaptive UKF proposed outperforms traditional UKF in terms of accuracy and the time.

6. References

[1] Zhao Lin, Wang Xiao-Xu, Sun Ming, Ding Ji-Cheng, YanChao. Adaptive UKF filtering algorithm based on maximum a posterior estimation and exponential weighting. Acta Au-tomatica Sinica, 2010, 36(7): 1007-1019

[2]J. Valappil, C. Georgakis, Systematic estimation of state noise statistics for extended Kalman filters, AIChE J. 46 (2) (2000) 292-308.

[3] Den¾ux T. Maximum likelihood estimation from fuzzy data using the EM algorithm. Fuzzy Sets and Systems, 2011,183(1): 72-91。

[4] Xue Li, Gao shesheng, Zhao Yan. Unscented particle filtering with adaptive adjusted weight and its application in integrated navigation[J]. Journal of Chinese Inertial Technology.2012, 20(4):459-463.

[5] G.C. Goodwin, J.C. Aguero, Approximate EM algorithms for parameter and state estimation in nonlinear stochastic models,44th IEEE Conference on Decision and Control, 2005, pp. 368–373.

[6]M.S. Arulampalam, S. Maskell, T. Clapp, A tutorial on particle filters for online nonlinear/non-Gaussian Bayesian tracking, IEEE Trans. Signal Process. 50 (2) (2002) 174–188.

[7] D.M. Himmelblau, Process Analysis by Statistical Methods, John Wiley & Sons Inc., New York, 1970

[8] Bavdekar V A, Deshpande A P, Patwardhan S C. Identification of process and measurement noise covariance for state and parameter estimation using extended Kalman filter. Journal of Process Control, 2011, 21(4): 585-601

Applied Mechanics and Materials Vol. 597 (2014) pp 525-530
© (2014) Trans Tech Publications, Switzerland
doi:10.4028/www.scientific.net/AMM.597.525

A Variable Proportional Valve Braking Force Distribution Strategy including SOC constraints of Electric Vehicles

Yu Hongxia[1,a], Lin Zhenyang[1,b*]

[1]School of Information Technology and Engineering Shenyang University of Technology Shenyang110870, China

[a]Email: hongxia7512@163.com, [b]691236745@qq.com

Keywords: electric vehicle , braking force distribution, regenerative braking, SOC

Abstract. Braking force distribution plays an important role in energy recovery of electric vehicles. A new braking force distribution based on the variable proportional valve is proposed to solve the traditional proportional valve braking force distribution problem. By considering the safety brake force distribution area, the variable proportional valve friction braking force distribution line is optimized, the regenerative braking force equations are deduced using the optimized friction braking force distribution line at different braking intensity, then the regenerative braking force is corrected by considering mechanical characteristics of motor and SOC of battery constraints. Simulation results show that the proposed regenerative braking energy recovery has been significantly improved.

I. Introduction

With the development of automobile industry, people pay more and more great attention to the problem like increasingly deteriorating air and scarce petroleum exacerbated by the traditional internal combustion engines. Almost half of the energy is dissipated in the braking process for the traditional internal combustion engines [1].Compared with the traditional car, electric vehicle(EV) and hybrid electric vehicle(HEV) show great potentials to solve such problems. Regenerative braking energy recovery can effectively recover part of the energy loss due to the vehicle brake[2-4]. So that it can improve energy efficiency and increase driving range of electric vehicle.

The regenerative braking force is restricted by the mechanical characteristics of motor, braking safety, driving comfort and so on. Therefore it is necessary to accomplish traditional friction braking and regenerative braking commonly. According to the ECE braking regulation, many approaches are proposed to solve the problem of the braking force distribution, such as fixed coefficient distribution method with low energy recovery and large brake switch fluctuations[5], optimal energy recovery distribution method with poor braking effectiveness[6], the strategy based on fuzzy control of braking force[7], and distribution method based on ideal braking force distribution curve I. However, the methods above are not ideal to meet the constraint conditions .

In this work, a new variable proportional valve braking force distribution strategy considering the constraint conditions for EVs is proposed. This paper is organized as follows: first, safety range of braking force distribution, second, braking force distribution based on the variable proportional valve, third, considering the motor mechanical characteristics and SOC constraints, forth, simulation results, the last conclusion.

II. Safety Range of Braking Force Distribution

For general cars, according to the factors like distribution of braking force of front and rear axles, road adhesion coefficient and so on, the following three conditions may occur during braking:

1. The front wheels lock first, and then the rear wheels lock；2. The rear wheels lock first, and then the front wheels lock; 3. The front and rear wheels lock at the same time. Compared to the previous two situations, it makes full use of the conditions attached.

Therefore, the brake force distribution will affect the direction stability of the vehicle when braking. Ideal front and rear braking force distribution curve I line is shown in Figure 1. The braking forces on the curve meet:

$$F_{u2} = \frac{1}{2}\left[\frac{G}{h_g}\sqrt{b^2 + \frac{4h_gL}{G}F_{u1}} - \left(\frac{Gb}{h_g} + 2F_{u1}\right)\right] \tag{1}$$

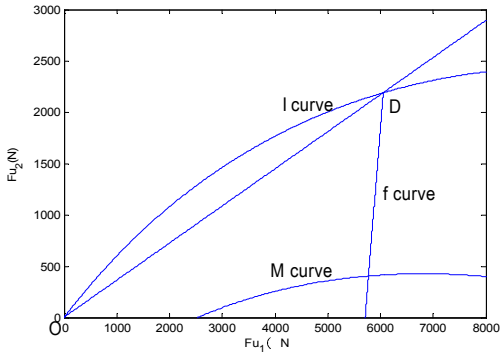


Figure 1.Safe range of braking force distribution and traditional proportional valve curve

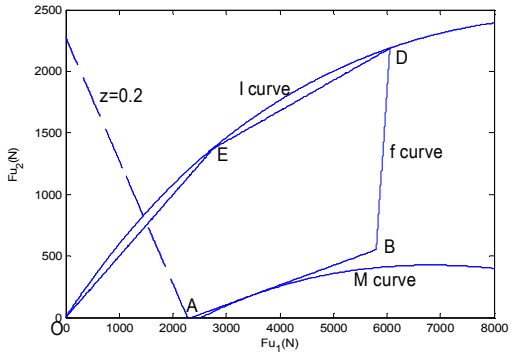


Figure 2. Variable proportional valve optimization curve and braking force distribution with new strategy

The straight line f in Figure 1 shows the brake force distribution when a car locks front wheel braking force without locking rear wheel in a condition attached to the ground. The braking forces meet:

$$F_{u2} = \frac{(l - \phi_0)F_{u1}}{\phi_0 h_g} - \frac{Gb}{h_g} \tag{2}$$

M curve is the smallest rear wheel braking force distribution curve according to ECE regulations (United Nations Economic Commission for Europe car regulations). The braking forces on M curve meet:

$$\frac{h_g}{lG}(F_{u1} + F_{u2})^2 + \frac{b + 0.07h_g}{l}(F_{u1} + F_{u2}) - 0.85F_{u1} + 0.07\frac{Gb}{l} = 0 \tag{3}$$

I line, M line, f line, and the horizontal line is the region surrounded safe braking force distribution range. The distribution of the braking force should be in this area .

III. Braking Force Distribution Based on the Proportional-adjustable Valve

A. Optimization Of Mechanical Braking Force Distribution Line

To facilitate practical application, people often use the fixed percentage of brake force distribution line instead of the ideal brake force distribution line, as shown in the Fig.1 OD line.

However, if braking force ratio is fixed，The actual braking force distribution curve has a big difference with ideal braking force distribution curve. And it has low adhesion efficiency. So that we should optimal the braking force distribution curve again.

Optimized braking force distribution line consists of OE line and ED line in Fig.2. To make the curve more approached to I curve, it is necessary to optimal the E point. Synchronization friction coefficient is 0.7, so the D point is fixed. The target is to make the area OED minimum. The objective function is:

$$\min \int_0^{X_D} \frac{1}{2}\left[\frac{G}{h_g}\sqrt{b^2 + \frac{4h_g}{G}x} - \left(\frac{Gb}{h_g} + 2x\right)\right]dx - \int_0^{X_E}\frac{Y_E}{X_E}x\,dx - \int_{X_E}^{X_D}\left(\frac{Y_D - Y_E}{X_D - X_E}(x - X_D) + Y_D\right)dx \tag{4}$$

D point is fixed, so that The first term is fixed. The problem is transformed into seeking the maximum of the last two terms.

$$\max \int_0^{X_E} \frac{Y_E}{X_E} x dx - \int_{X_E}^{X_D} \left(\frac{Y_D - Y_E}{X_D - X_E}(x - X_D) + Y_D \right) dx = \frac{1}{2} X_E Y_E + \frac{1}{2}(Y_E + Y_D)(X_D - X_E) \tag{5}$$

E point is obtained by optimizing calculated, and then the Linear equations of OE and ED are obtained:

$$\text{OE}: \quad Fu2 = 0.4985 Fu1 \tag{6}$$

$$\text{ED}: \quad Fu2 = 0.2469 Fu1 + 692 \tag{7}$$

In the safe braking range, in order to increase front-wheel force as much as possible, the rear wheel braking force should be changed according to the M curve.

Front and rear wheel braking force distribution. The braking force includes friction force on front and rear wheels and regenerative force on driving wheel. Based on meeting the ECE regulations, this paper uses the tangent of M curve instead of M curve, form the composite braking force distribution curve. Front and rear wheel friction braking force in accordance with the OED.

According to M curve and A (the intersection of z=0.2 and x axis), the equation of CD line can be calculated:

$$Fxb2 = 0.16(Fxb1 - 2354) \tag{8}$$

Fxb2 is the rear axle braking force, Fxb1 is the front axle braking force.

B. Regenerative Braking Force Distribution Equation

In the case of different braking intensity, the corresponding relationship between the regenerative braking force and braking intensity is like the following (Fxb1 and Fxb2 is the front and rear axle braking force, Fu1 and Fu2 is the friction braking force of front and rear axle , Fre is regenerative force.):

a. When $0 \le z \le 0.2$,the front wheel provides all the braking force, Fxb1=Gz. The regenerative force on the front wheel Fre = Gz, Fu1 and Fu2 is 0.

b. When $0.2 \le z \le 0.54$， The relationship of front and rear wheel braking force is:

$$Fxb2 + Fxb1 = Gz \tag{9}$$

According to the equation (8) and (9), we can get Fu2:

$$Fu2 = 0.138Gz - 325 \tag{10}$$

According to the OE line equation and (10), Fu1 and Fre are calculated:

$$Fu1 = 0.277Gz - 652 \tag{11}$$

$$Fre = Fxb1 - Fu1 = 0.585Gz + 977 \tag{12}$$

c. When $0.54 \le z \le 0.62$, the DB segment of f curve is:

$$Fxb2 = 6.42Fxb1 - 3.11G \tag{13}$$

By equation of (9) and (13), Fu2 is obtained:

$$Fu2 = 0.865Gz - 0.42G \tag{14}$$

Combined with OE equation and equation (13), Fu1 and Fre is calculated:

$$Fu1 = 1.735Gz - 0.843G \tag{15}$$

$$Fre = Fxb1 - Fu1 = -1.6Gz + 1.263G \tag{16}$$

d. When $0.62 \le z \le 0.7$, According to equation (2),(5) and ED line equation,

$$Fu1 = 3.5Gz - 1.697G - 2803 \tag{17}$$

$$Fu2 = 0.865Gz - 0.419G \tag{18}$$

$$Fre = -3.37Gz + 2.12G + 2803 \tag{19}$$

e. When $0.7 \le z \le 1$,

$$Fu1 = 0.8Gz - 555 \tag{20}$$

$$Fu2 = 0.2Gz + 555 \tag{21}$$

$$Fre = 0 \tag{22}$$

According to the distribution relationship of braking strength, each braking force ratio in the total braking force kre (regenerative braking force ratio), ku1(friction force on front wheel ratio), ku2 (friction force on rear wheel ratio) can be calculated.

IV. Considering the Motor Mechanical Characteristics and SOC Constraints

In practical applications, the characteristics of the motor and battery SOC constraints should be considered.

When a car running in a high speed, motor speed is greater than the base speed, the motor is in constant power region. It reduces the maximum regenerative braking force with the motor's rotational speed increasing. The motor speed decreases with the car braking. When the motor speed is lower than the base speed, the motor get into the constant torque region. The regenerative force is fixed. Based on the above analysis, the motor regenerative braking torque limit should be considered. If the available regenerative braking force is less than the required regenerative braking force, the available regenerative braking force will be adopted. When the available regenerative braking force is greater, the motor will follow the system requirement to provide the required regenerative braking force.

In the process of braking, vehicle safety includes not only front and rear wheel braking force safety, but also the battery safety. As the main power unit of electric vehicle, the overcharging seriously affects its cycle life and safety. So that when the SOC is more than 0.8, it is necessary to improve the distribution strategy above. By introducing a weight factor c so the vehicle braking recover energy can be limited. The relationship between c and SOC is as the following:

$$c = f(SOC) = \begin{cases} 0 & (SOC \geq 0.9) \\ -10 * SOC + 9 & (0.8 \leq SOC < 0.9) \\ 1 & (SOC < 0.8) \end{cases}$$

Then the new regenerative braking force Fre_n is obtained as follow:

$$Fre_n = c * Fre \tag{23}$$

The weighting factor c is multiplied by Fre which is calculated by the braking force strategy above, then the new regenerative Fre1 is obtained. Fre1 is the regenerative force which is the considering the battery overcharging problem. So the strategy considering battery overcharging is proposed.

V. Simulation Results

Based on the braking force distribution strategy proposed above, validity of the algorithms proposed is verified in ADVISOR2002. In simulation, UDDS, WVUSUB, CSHVR and HDDSHDV operation conditions are selected to verified the energy utilization rate. The simulation results are shown in table1, as can be seen from table 1，in each operation conditions, the ability to recycle energy is improved obviously after the new strategy is adopted.

Table 1 Energy utilization rate under different conditions

Strategy	UDDS	WVUSUB	CSHVR	HDDSHDV
Advisor 2002	33.8%	30.6%	22.6%	40.6%
New strategy	35.6 %	32.1%	26.1%	42.3%

This work first selects 4 kinds of simulation conditions. As can be seen from table 1，in each simulation conditions, the ability to recycle energy is improved obviously after the new strategy is adopted.

To observe the effectiveness of the algorithm further, UDDS is selected as the typical simulation condition in this work. The trend of speed and time in UDDS is shown in Fig.6. Cycle time is 1367s; distance traveled is 11.99km; maximum speed is 91.25km/h; average speed is 31.51km/h; maximum acceleration is 1.48m/s^2; maximum deceleration is -1.48m/s^2. Choose the cycle of UDDS is 3.

The battery SOC is shown in Fig.3 when the car finishes 3 cycles of UDDS condition, as shown in Fig.3, the battery SOC decreased 0.695 using the proposed strategy, but the SOC decreased more and faster if using the strategy in advisor. Table 2 shows electric car recycling energy and the energy utilization rate in different case of control strategy.

Table 2 Braking energy recovery results under the condition CYC_UDDS

	Control strategy	
	Advisor2002	New strategy
Energy Consumption(kJ)	20913	20866
Total braking energy (kJ)	5368	5369
Energy recovery (kJ)	1429	2587
Energy recovery efficiency (%)	26.6	48.2
Effective energy recovery rate (%)	6.1	12.4
Energy utilization rate (%)	33.8	35.6

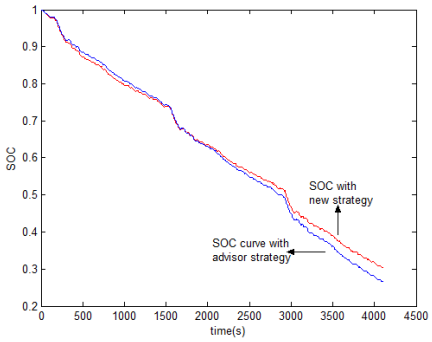


Figure 3.Trend diagram of SOC and time in UDDS

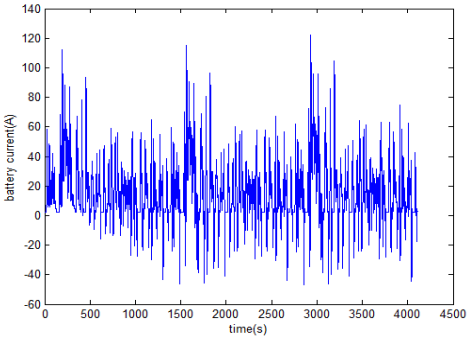


Figure 4. Trend diagram of battery current and time in UDDS

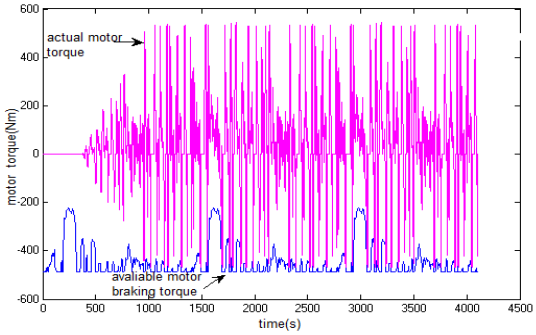


Figure 5. Available regenerative motor and actual output motor torque

Fig.4 gives the battery SOC curve, as seen from Fig.4, at the beginning of simulation, the battery current is 0. Battery current appears when SOC is less than 0.86 after 450s. When it is less than 0, the battery current is charging current and the battery is charging. Obviously, the charging current only appears when the SOC is not higher than 0.86. It proves that the new strategy restrains the overcharging effectively and can protect the battery in electric vehicle.

Fig.5 shows the available regenerative torque that the motor can provide and the output torque. When the vehicle is braking, the actual motor torque is less than 0. The actual motor torque less than 0 is the regenerative torque. Obviously, the available motor braking torque is greater than the regenerative torque constantly when the car is braking. Therefore, the strategy considering the motor characteristics successfully assure that the regenerative force meets the motor characteristics constraints.

VI. Conclusions

The energy-saving, energy utilization rate, the energy recovery performance of electric vehicles depends to a large extent on their regenerative braking strategy. The article analyzed the method of braking force distribution and proposed an algorithm to get the optimized mechanical braking force distribution line and the regenerative braking force distribution equation based on the variable proportional valve strategy, considering in the actual application some constraints like battery overcharging occurring. In simulation, Four driving conditions (UDDS, WVUSUB, CSHVR and HDDSHDV) are selected to test the vehicle energy efficiency and CYC_UDDS is selected to test the car's performance about the constraints in ADVISOR2002.

Experimental results show that it can realize more recovery vehicle braking energy while meeting safety requirements. The performances like energy utilization rate, the energy recovery and so on are evidently improved compared with the strategy in ADVISOR2002. At the same time it meets the mechanical properties and prevents battery overcharging effectively. The strategy is easy and practicability.

Acknowledgment

This work is supported by the Key Laboratory Program of Liaoning Provincial Department of Education (L201211602).

References

[1] FALCONE P, KHOSHFETRAT PAKAZAD D, SOLYOM S. Predictive approaches to rear axle regenerative braking control in hybrid vehicles//Joint 48th IEEE Conference on Decision and control and 28th Chinese Control Conference,2009:7627-7632.

[2] GAO Yi-min, CHU Liang, EHSANI M. Design and control principles of hybrid braking system for EV,HEV and FCV// Vehicle Power and Propulsion Conference ,Arlington, 2007:384-391.

[3] Binggang Cao, Zhifeng Bai, Wei Zhang. Research on Control for Regenerative Braking of Electric Vehicle. 0-7803-9435-6,IEEE,2005:92-97.

[4] APTER R, PRATHALER M. Regeneration of power in Hybrid vehicles// Vehicular Technology Conference, Birminghan.2002:2063-2069.

[5] CHU Liang, SHANG Ming-li, FANG Yong, GAO jian-hua, ZHOU Fei-kun. Braking force distribution strategy for HEV based on braking strength// 2010 International Conference on Measuring Technology and Mechatronics Automation, Changsha, 2010:759-764.

[6] LI Yu-fang, LIN Yi, HE Hong-wen, CHEN Lu-hua. A study on control algorithm of regenerative braking for EV/HEV. Automotive Engineering.2007,29(12):1059-1063.(in Chinese)

[7]Paterson, J.; Ramsay, M. Electric Vehicle Braking by Fuzzy Logic Control. In Proceedings of the IEEE Industry Applications Society Annual Meeting Toronto,Canada,2-8 October 1993; Volume 3, pp.2200-2204.

[8] MUTOH N, YAHAGI H. Control methods suitable for electric vehicles with independently driven front and rear wheel structure. IEEE transaction on Industrial Electronics, 2007,54(2):665-672.

Applied Mechanics and Materials Vol. 597 (2014) pp 531-534
© (2014) Trans Tech Publications, Switzerland
doi:10.4028/www.scientific.net/AMM.597.531

Finite Element Analysis of Key Component on Two Wheels Scooter

Zhidong Huang[1, a *], Yunpu Du[1,b], Baoquan Liu[1,c], Guang Yang[1,d], Yufeng Liu[1,e] and Xinguang Zhao[1,f]

[1]Dept. of Mechanical Engineering, Liaoning Institute of Science and Technology, Benxi, Liaoning, 117004, China

[a]hzdstarcraft@126.com, [b]duyunpu@163.com, [c]928330622@qq.com, [d]yangguang_723@126.com, [e]liuyufeng0511@vip.qq.com, [f]zxguang_0512@163.com

Keywords: scooter, finite element analysis, stress analysis, driving system

Abstract. Based on Solidworks software, the three-dimensional model of two wheels scooter is set up. The finite element model of two wheels scooter is generated. Finite element analysis of driving system on two wheels scooter is investigated. The stress and strain of driving system is investigated. The stress diagram and the strain diagram are obtained. The method and the result can be used as a reference of innovative design of two wheels scooter.

Introduction

Nowadays, the scooters are rich in species numbers on the market such as two wheels scooter, three wheels scooter and four wheels scooter. Some scholars have devoted themselves to the research on scooter. Introducing scooter into floor cleaning is presented by Ref [1] and it can significantly shorten the housework time and reduce the work pressure. Adopting Fatigue/ANSYS, a software module is developed by Ref [2]. On the platform, visual analysis of fatigue life and design optimization can be carried out for the scooter. The 3D solid model and assembly of the scooter stepping on both feet is obtained with Pro/E software by Ref [3]. The simulation analysis on motion machanism of scooter is investigated and the displacement variation curve of scooter is given out. In a word, the two wheels scooter is the foundation of scooter. Therefore, this paper intends to set up the three-dimensional model of two wheels scooter. Finite element analysis of driving system on two wheels scooter is obtained by Solidwoks software, which is significant for the innovative design two wheels scooter.

Theory of Finite Element Analysis

The linear equation of system can be expressed as:

$$[K]\times\{u\}=\{F\} \tag{1}$$

$$[K]\times\{u\}=\{F_a\}+\{F_r\} \tag{2}$$

Here [K] is stiffness matrix and $[K]=\sum_{m=1}^{n}[K_e]$. $\{u\}$ is vector of diaplacement. n is the number of element. [K_e] is element stiffness matrix. [F_r] is vector of loading. $\{F_a\}$ is total loading.

Based on Eq.(1) and Eq.(2), $\{u\}$ can be obtained:

$$\{\varepsilon^{el}\}=[B]\times\{u\}-\{\varepsilon^{th}\} \tag{3}$$

$$\{\sigma\}=[D]\times\{\varepsilon^{el}\} \tag{4}$$

Here $\{\varepsilon^{el}\}$ is the strain. $[B]$ is strain-displacement matrix of node. $\{u\}$ is displacement vector of node. $\{\varepsilon^{th}\}$ is vector of thermal strain. $\{\sigma\}$ is vector of stress. $[D]$ is coefficient of elastic matrix.

Based on Eq.(3) and Eq.(4), the stress of node can be obtained.

Three-Dimensional Model of Two Wheels Scooter

Based on the configuration of certain scooter, the three-dimensional model of the scooter is set up. The driving system is shown in Fig.1 and the structure of two wheels scooter is shown in Fig.2.

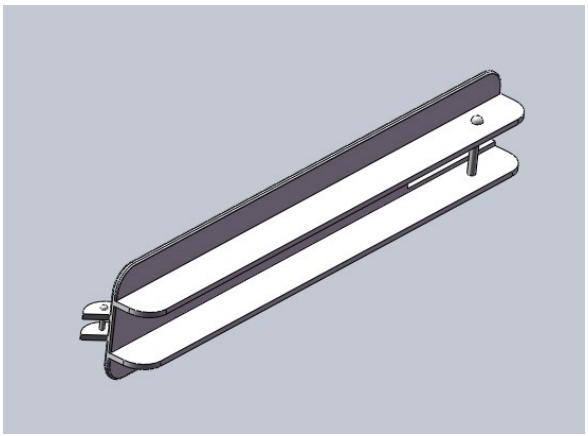


Fig.1 The driving system.



Fig.2 The structure of two wheels scooter.

Finite element Analysis of Two Wheels Scooter

Based on the three-dimensional model of two wheels scooter, the finite element model of two wheels scooter is generated. And finite element analysis of driving system on two wheels scooter is investigated.

Material Properties. The material of two wheels scooter is alloy steel and the material properties are listed in Table.1.

Table 1 The material properties.

Material	Alloy steel	Poisson ratio	0.33
Yield strength	2.75742e+007 N/m^2	Mass density	2700 kg/m^3
Tensile strength	6.89356e+007 N/m^2	Modulus of rigidity	2.7e+010 N/m^2
Modulus of elasticity	6.9e+010 N/m^2	Thermal expansion coefficient	2.4e-005 /Kelvin

Mesh Generation. The meshing size is 5mm. The total number of nodes is 141747 and the total number of element is 83569. The mesh generation diagram of driving system is shown in Fig.3.
Constraint and Load. The constraint and load are applied and the diagrams are shown in Fig.4 and Fig.5.

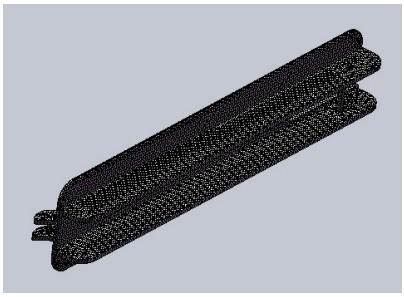


Fig.3 The mesh generation diagram.

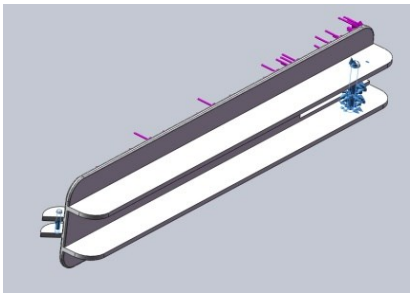


Fig.4 The constraint diagram.

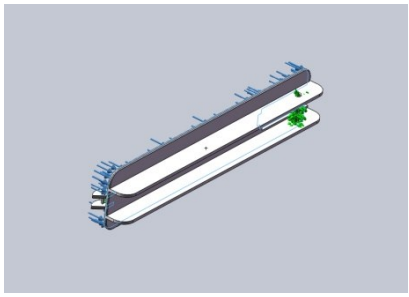


Fig.5 The load diagram.

Modal Analysis of Driving System. After solving, the stress, displacement and strain diagrams are shown in Fig.6-8.

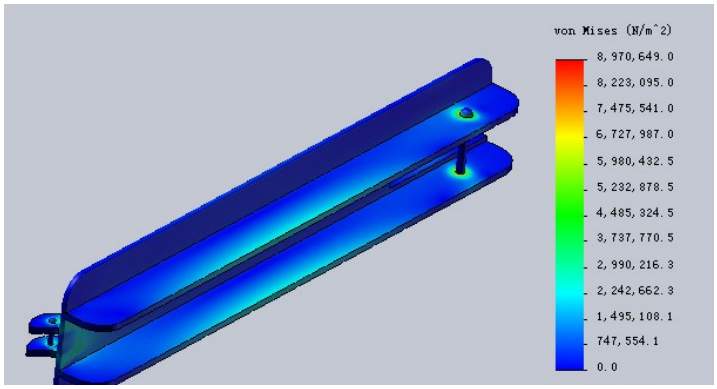


Fig.6 The stress diagram.

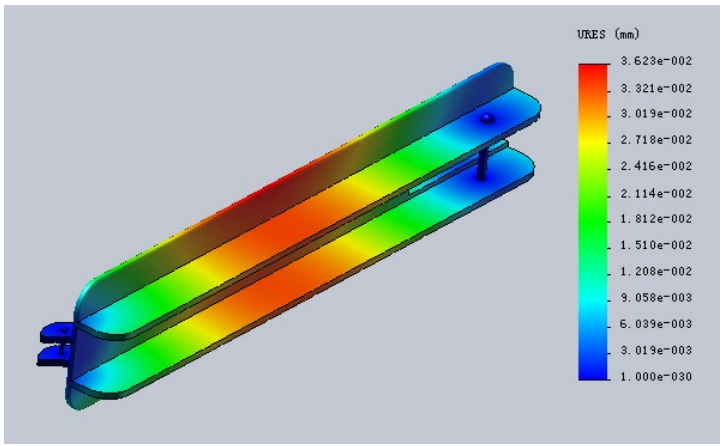


Fig.7 The displacement diagram.

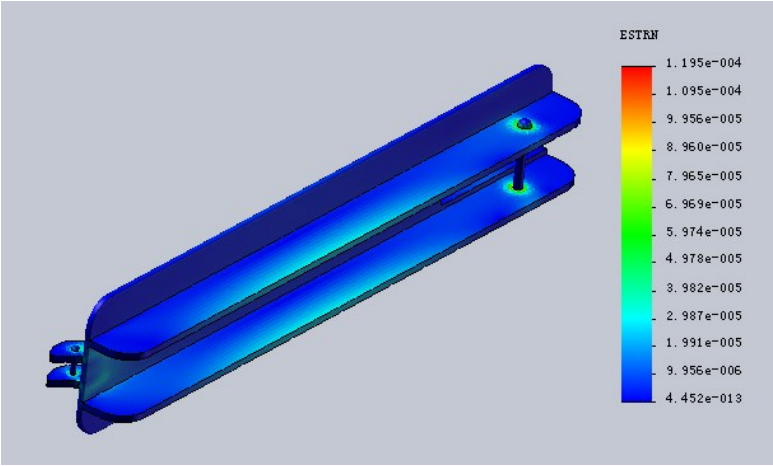


Fig.8 The strain diagram.

Analysis. It is concluded in Fig6-8 that the maximum value of stress is 8.97065e+006 N/m^2 and it is far less than the yield strength. Therefore, the mechanism is safe. The maximum value of displacement is 0.0362335mm and the maximum value of strain is 0.000119473. The result is ideal.

Conclusions

This paper focuses on finite element analysis of two wheels scooter. The three-dimensional model of two wheels scooter is set up. The finite element model of two wheels scooter is generated. Finite element analysis of driving system on two wheels scooter is investigated. The stress and strain of driving system is investigated. The stress, displacement and strain diagrams are clarified. The method and the result can be used as a reference of innovative design of two wheels scooter.

Acknowledgements

This work was financially supported by Students' Innovation and Entrepreneurship Training Program of Liaoning Province (201311430003) and Key Undergraduate Specialty of Liaoning Province Ordinary College (ZD201245).

References

[1] F. Zhang, X.Z. Yang and T. Li: Journal of Hubei Polytechnic University Vol. 29 (2013), p. 13-16 (In Chinese)

[2] T.X. Tian, Y.G. Hu and H.J. Shen: Mechanical Engineer No. 9 (2005), p. 59-60 (In Chinese)

[3] P.P. Liu, D.D. Zhang: Development & Innovation of Machinery & Electrical Products Vol. 22 (2009), p. 67-68 (In Chinese)

[4] Y.M. Zhang: *Mechanical Vibration Dynamics* (Jilin Scienc and Technology Press, China 2000).

Applied Mechanics and Materials Vol. 597 (2014) pp 535-539
© (2014) Trans Tech Publications, Switzerland
doi:10.4028/www.scientific.net/AMM.597.535

Multi-objective Optimization for the Section Structure of Sandwich Plate Applied in the High-speed Train Compartments

Yiqing Wang[1a], Xu Chen [1], Bin Wang[1], Xinbin Kuang[1], Xiaogeng Tian[2]

[1] School of Mechanical Engineering, Xi'an Jiaotong University, Xi`an, 710049, P. R. China
[2] School of Aerospace, Xian Jiaotong University, Xi`an, 710049, P. R. China
[a] Yiqingw@mail.xjtu.edu.cn

Key Words: Sandwich plate; Surrogate model; NSGA-α algorithm; Multi-objective optimization; Pareto optimal solution set.

Abstract: In order to obtain the side walls section structures of high speed train applicable to different running speeds and conditions, a multi-objective optimization design is made based on the structure of topology optimization. In this optimization formulation, the weight of sandwich plate, static compliance and maximum deformation are used as the objective functions; the thickness of face panels and cores in five parts of the side wall are variables; and the air pressure gradient in compartments is the constraint function. Surrogate model techniques are adopted for constructing the response surfaces based on the optimization. Finally, a multi-objective optimization is performed using the NSGA-II algorithm and the optimization generates a Pareto solution set. The structure performance in Pareto set is greatly improved by 8.21% -33.58% than that of topology structure. In addition, the Pareto solution set provides engineers with many alternative Pareto-optimal solutions for optimization design of the sandwich plate section applied in the high-speed train.

Introduction

The territory in China is vast, which acrosses a number of different climates and has a variety of geographical features. So the running environment of high speed train in China is of great difference from other countries [1]. For example, in the line of Wuhan – Guangzhou with an operation mileage of 1068.6 km, there are 684 bridges and 226 tunnels. When a high speed train travels through a tunnel, if its running speed was 350 km/h above, the railway carriages would bear a huge pneumatic impact load. The huge pneumatic impact load on the high speed train would cause many problems, such as the vibration of the structure of the compartments which searously influences passengers' seating comfort [2]. Therefore, it is necessary to carry out optimization design for the structures of high speed train side walls according to the operation environment of domestic high speed trains.

High speed train compartments side wall structure design research generally concentrates on two aspects. First, size optimization design is always carried out on side wall structure of the compartments basisd on strength and stiffness[3]. Second, with the maximum deformation as constraint condition, single objective optimization design research under static load is always carried out for the purpose of reducing compartments weight[4].

High speed train loads consist of dynamic load and static load, which should be taken into account during optimization. In addition, high speed train compartments side wall structure has many performance indices, such as weight and stiffness and deformation, so it should be a multi-objective optimization design under different running speeds and environments. In order to achieve a balance among targets, multi-objective optimization design technology is applied successfully [6-5], but rarely in the high speed train compartments side wall. Structural topology optimization can improves the material distribution and force transmission path of a structure in the stress condition. Compared with the size and shape optimization, structural topology can drastically improve the performance of the structure. And topology optimization as a conceptual design is widely used in industrial field[6].
Latin hypercube sampling is one of the most effective test scheme design methods to determine the

sample points in optimization design [7]. It uses equal probability distribution of random orthogonal principle, which can get a high precision response surface equation in rare test sample points. At the same time, the Latin hypercube sampling has a strong adaptability, and the number of sample points can be determined according to the actual situation. And Uniform Latin hypercube sampling introduces entropy judgment on the basis of Latin hypercube sampling. It adopts a maxmin approach making the minimum distance between two sample points the largest and thereby makes sample points distributed more uniformly in the sample space.

There are many algorithms to solve multi-objective optimization problems, and the non-dominant genetic algorithm NSGA-II is by far one of the most outstanding multi-objective optimization algorithms [8, 9]. It uses a hierarchical non-dominated sorting method and introduces elite reservation policy and crowding distance, reducing the algorithm computational complexity and making the solution set spread evenly as far as possible on the front of the whole Pareto solution set.

In this paper, Multi-objective optimization design research is carried out on sandwich plate section structure of high speed train compartment side wall. During the optimization process, the Uniform Latin hypercube sampling technique, the surrogate model technique and the multi-objective genetic algorithm NSGA-II are Integrated. Adopt the weight, compliance, and maximum deformation as the goals, the air pressure changing gradient as the constration to obtain the Pareto optimization solution set and the coordination solution among targets.

1. Multi-objective optimization of high speed train car side wall sandwich plate section

1.1 The multi-objective optimization problem of compartment side wall section structure

when the train is running in a tunnel, air pressure will be produced in the compartment surface, which is the biggest pressure load[10]. On the compartment surface, the alternating aerodynamic load leads to the air pressure gradient change inside the compartment, which seriously influences seating comfort[12]. Therefore, take the load of the train running in the tunnel as the static load, and take the aerodynamic load when the train intersecting in a tunnel as the dynamic load, take the compartment section with 30 mm long as optimization design object.

The figure 1 is high speed train compartment side wall structure from the topology optimization. The multi-objective optimization design is based on the topology optimization structure of high speed train compartment side wall section. Considering the width of the aluminum extrusions is 600 ~ 800 mm[1], the side wall structure is divided into five sections, and thickness of each section of panel and sandwich xi (I = 1 ~ 10) is acted as the design variable, as shown in figure 1.

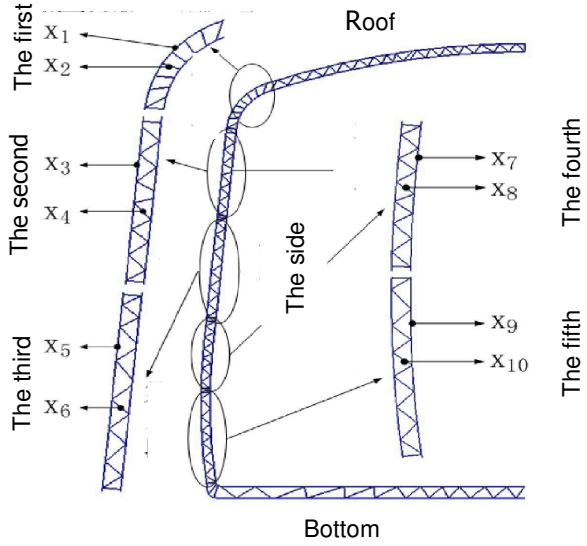


Figure 1 The topology optimization results of high speed train carriage side wall section

Optimization design objective functions have many indicators, such as side wall section structure weight and side wall compliance and side wall maximum deformation static performance indicator. According to the current compartment structure's size, determining that the scope of design variables is 1.5 ~ 4.5 mm. Constraint function is a dynamic performance index –pressure variation gradient value, whose value should not exceed 300 pa/s.

The expression of Multi-objective optimization problems is:

$$\left.\begin{array}{l} \min m(x)、D(x)、F(x) \\ s.t \quad p(x) \le 300 pa/s \\ x=(x_1, x_2, \cdots x_{10}) \\ 1.5mm \le x_i \le 4.5mm, \quad i=1,2,\cdots 10 \end{array}\right\} \tag{1}$$

In the formula, P is the normal temperature atmospheric pressure. $w(h)$ is the initial width of side wall. $w(t, h)$ is the width of compartment in different times.

According to the equation of gas state, air pressure gradient is:

$$\frac{dp(t)}{dt}=\frac{p\sum_{i=1}^{N} w(h_i)}{(\sum_{i=1}^{N}(w(h_i)-w(t,h_i)))^2}\sum_{i=1}^{N}\frac{dw(t,h_i)}{dt} \tag{2}$$

In the formula, $m(x)$ and $D(x)$ respectively are the weight of compartment side wall structure and the maximum deformation function. The compliance function expresses the energy that is absorbed by the side wall structure in the process of deformation.

1.2 Finite element analysis of sample points

Using MATLAB operate Ansys to complete static and dynamic finite element analysis of sample points, and the weight, compliance and the maximum deformation of the side wall are extracted from static finite element analysis. Transient dynamics analysis finite element model is used to calculate the air pressure variation gradient value.

1.3 Solving surrogate model

After getting each sample response value through the finite element analysis, the surrogate model of objectives and constraints is established. Because of the simple and small calculation cost, the basis function of polynomial regression model can be easily used to analyze the variance of test model, the polynomial regression model is used to fit the corresponding values of sample points in the paper.

The polynomial regression model of the relationship between design variable x and actual response value y is:

$$y(x)=y(x)+\varepsilon=\sum_{j-1}^{N} a_j \varphi_j(x)+\varepsilon \tag{3}$$

In the formula, y(x) is an approximate function. ε is the error of the regression model. N is the number of basis functions, α_j is a coefficient of base functions, which is solved out in the Least squares coefficient method.

2. The solution of multi-objective optimization and the result analysis

Using the non-dominant genetic algorithm NSGA-II, introducing the constraint non-control concept, in the hypothesis that the crossover probability is 0.9, which the mutation probability is 0.1, that cross distribution index and variation distribution index is twenty, thirty, and that genetic iterations are 1000 times, we solve the above surrogate model. The influence law of structure variable x1~ x10 for the performances of the compartment structure is shown in table 1.

Table 1 The structure of high speed train side wall and the property Pareto solution set

Number	x1 /mm	x2 /mm	x3 /mm	x4 /mm	x5 /mm	x6 /mm	x7 /mm	x8 /mm	x9 /mm	x10 /mm	Weight/kg	Strain energy/J	Maximum deformation /mm
1	4.500	1.804	4.500	2.770	4.500	4.500	4.500	3.464	4.500	1.922	2.662	152.170	0.969
2	1.969	4.245	4.500	2.732	4.500	1.500	4.500	4.500	4.500	4.500	2.633	219.793	0.898
3	2.671	3.520	2.049	1.501	2.159	1.500	1.748	1.500	1.500	1.501	1.299	608.810	2.945
4	2.636	3.371	1.590	1.546	2.837	1.509	1.714	1.500	1.726	1.522	1.342	760.591	2.800
5	2.765	3.630	2.240	1.500	2.069	1.506	1.537	1.551	1.527	1.528	1.309	562.467	2.960
6	4.500	2.507	4.500	2.711	4.500	4.500	4.500	3.842	4.453	2.253	2.727	157.442	0.953
◦													
◦													
◦													
27	2.683	3.563	2.031	1.523	2.201	1.500	1.765	1.500	1.500	1.513	1.307	609.289	2.917
28	2.165	1.959	2.744	2.816	4.497	1.577	3.085	1.962	3.420	3.533	2.010	315.710	1.223
29	2.406	3.215	2.640	2.121	2.418	1.700	1.500	1.500	1.684	1.500	1.403	451.548	2.531
30	4.291	2.070	3.890	2.634	3.922	3.020	3.070	2.019	3.228	1.945	2.139	209.511	1.247

Figure 2 shows the topological optimization solution of the maximum deformation of high speed train side wall section and the multi-objective optimization Pareto solution set. It can be seen that, in the condition that the unit weight of compartment sandwich plate section is consistent, size variables of the structure distribute more reasonably and the result of multi-objective optimization for structure side wall maximum deformation is smaller. In the hypothesis that having the same structure weigh for the carriage side wall section, in Pareto solution set, the biggest deformation performance of the carriage structure increases by 8.21% ~ 33.58% than topological structure's.

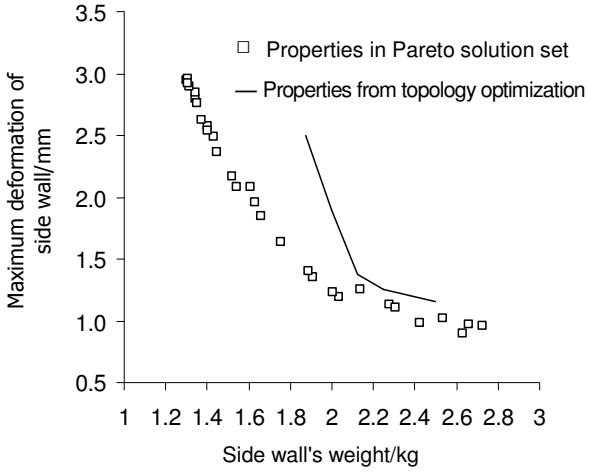


Figure 2 Performance of side wall from topology optimization and multi-objective optimization

The solution sets not only meet the design requirements of high speed train at a high speed, but also can meet design structure requirements in other speeds. These Pareto optimization solution sets offer designers a variety of alternatives. According to specific application situation, and combining with designers experience, the designer can choose several groups of schemes in the Pareto optimization solution set and then determine the final scheme. Considering different running speeds, weight of high speed train compartment side wall, stiffness and pressure change gradient performance, table 2 is to provide alternatives for high speed train compartment design. For example, when a high speed train is in low speed (160 km/h ~ 200 km/h) operation, the smaller compartment weight can effectively save energy. So we can choose group 3, 5 and 27 schemes whose weights are light in table 1 as priority alternatives.

When a high-speed train is in high speed (300 km/h ~ 350 km/h) operation, in the purpose of pursuing the higher compartment side wall stiffness and smaller pressure variation gradient value, we can choose group 1, 6, 8 schemes and so on as alternatives. When a high-speed train is in medium speed (200 km/h ~ 300 km/h) operation, we need a comprehensive consideration of various performance indicators and can choose group 13, 25, 29 schemes etc. in the Pareto solution set as alternatives.

Table2 High speed train side wall performances in Pareto solution set

Pareto solution set	Quality/Kg	Strain energy /J	Maximum deformation /mm	Air pressure gradent/Pa·s^{-1}
3	1.2992	214.0471	1.0873	88.7093
5	1.309	177.0476	0.9414	88.5803
27	1.3075	216.1409	1.0886	88.11
1	2.6624	152.1697	0.9689	122.5864
6	2.7266	157.4424	0.9528	119.7758
8	2.5401	173.2634	1.0144	122.2743
13	1.4015	139.523	0.8127	211.6501
25	1.4308	131.2881	0.7889	194.581
29	1.4028	127.4623	0.7858	226.0678

3 Conclusion

This paper presents a multi-objective optimization method for designing high speed train compartment side wall section structure. Based on the side wall structure from topology optimization technology, combined with uniform Latin hypercube sampling technique, surrogate model technology and multi-objective genetic algorithm NSGA-II, a multi-objective optimization problem was formulated in pursuit of weight, compliance, maximum deformation of high speed train compartment side wall sandwich plate by defining the compartment side wall structure parameters as variables and using air pressure change gradient, which influences the high-speed train compartment comfort as a constraint function. The relevant optimization design is carried out on the high speed train compartment side wall sandwich plate section to obtain a multi-objective optimization solution set. The structure performance in the set is greatly improved by 8.21% to 33.58% than that of a topology structure.

References

[1] Li Tie, Luan Pingjing. Comparison research on overall design standards for passenger cars in China and abroad [J]. Foreign Rolling Stock. 2006(5):36-39 (Chinese).

[2] RAGHUNATHAN R. S., KIM H. D., SETOGUCHI T. Aerodynamics of high-speed railway train [J]. PROGRESS IN AEROSPACE SCIENCES, 2002, 38(6/7):469-514.

[3] KIM N., PARK T. A study on the dynamic performance of the 200km/h Korean tilting train by means of roller rig test[J]. Journal of Mechanical Science and Technology, 2009(4):25-30.

[4] LI Hongxia, YANG Hong, LI decai. Analysis of optimized values of the cross section of the carbodies of high speed trains [J]. Rolling Stock, 2007(2):8-10 (Chinese).

[5] LIAO X., LI Q., YANG X., et al. Multiobjective optimization for crash safety design of vehicles using stepwise regression model [J]. Struct Multidisc Optim, 2008(35):561-569.

[6] Bendsoe M. P., Sigmund O. Topology Optimization: Theory, Methods and Applications [M]. Heidelberg: Springer verlag berlin heidelberg new york, 2004: 370.

[7] BUTLER N. A. Optimal and orthogonal Latin hypercube design for computer experiments[J]. Biometrika,2001,88(3):847-857.

[8] DEB K., Member A. A fast and elitist multiobjective genetic algorithm NSGA-II[J]. IEEE TRANSACTIONS ON EVolutionary Computation,2002,6(2):182-197.

[9] GONG MaoGuo, JIAO Licheng, YANG Dongdong, et al. Evolutionary Multi-Objective Optimization Algorithms [J]. Journal of Software, 2009, 20(2): 271-289 (Chinese).

[10] LI Renxian, ZHAO Jing LIU Jie, et al.Influence of Air Pressure Pulse on Side Windows of high-speed Trains passing each Other [J]. Journal of Mechanical Engineering, 2010(4): 87-92 (Chinese).

Applied Mechanics and Materials Vol. 597 (2014) pp 540-543
© (2014) Trans Tech Publications, Switzerland
doi:10.4028/www.scientific.net/AMM.597.540

Secondary Developments of ANSYS for Temperature and Stress Field Simulation of Brake Disc based on VB

Mengling Wu[1, a], Xiaoyu Zhu[1,b], Jianyong Zuo[1,c *]

[1] Institute of Railway and Urban Mass Transit, Tongji University, Shanghai, 201804, China

[a]872429592@qq.com, [b]tjzxy1988@gmail.com, [c]zuojy@tongji.edu.cn

Keywords: brake disc; ANSYS; secondary development; temperature field; stress field

Abstract. In the ANSYS finite element analysis with large-sized computer there is always a need for repeatedly modeling some similar questions. By using both the ANSYS for a secondary development platform and visual basic 6.0 for a visual operation interface, an APDL language is generated, so that a parametric modeling can be realized. With the help of the created software, the temperature and stress field contours of brake disc can be calculated and the efficiency of the calculation is enhanced.

Introduction

Brake disc is one of the most important parts of metro train braking system. During train emergency braking a large amount of kinetic energy is converted to frictional heat, causing temperature rise of friction pair. Then the heat transfers to inside of brake disc and outside by brake pad. Brake disc cooling capacity is confined by the material structure and other factors. During brake some heat build-up occurs in brake disc, which leads to temperature rise and thermal stress [1]. As a large universal finite element analysis software, ANSYS provides not only a powerful finite element analysis program, but also has good openness. In this paper, secondary developments of ANSYS are conducted by using Visual Basic 6.0 and the brake disc thermal analysis system is established.

Software introduction

Parametric design language of ANSYS (APDL). APDL is an interpretive language which is very similar to the FORTRAN to provide general programming languages, such as parameters, macros, abbreviations, vector and matrix operations, functions, process control (loop and branch), repeating orders, the user program and accessing to the ANSYS database. In addition, it also provides a simple interface customization, realizing the interactive input of parameters, message mechanism, interface driver and application running and so on. The application of ANSYS finite element analysis which is organized and managed by the programming language of APDL and macro technology can help to achieve the following goals: parametric modeling, parametric grid partition and control, material definition of parameterization, definition of parametric load and boundary conditions, parametric analysis of the control and the solving as well as the display of parametric post-processing results. Finally, the whole process of parametric finite element analysis can be realized. Meanwhile, it is the highest technical of ANSYS analysis. In the process of parametric analysis, you can simply modify parameters to achieve repeated analysis of various sizes, multiple design plans and series of products with different load, greatly improving the analytic efficiency but reducing the analytic cost.

Secondary development of ANSYS by VB. Taking advantage of VB to encapsulate ANSYS, namely means making use of VB on ANSYS secondary development. Users only need to choose parameters and the system will automatically call the calculation program of ANSYS to proceed meshing, loading and solving. With the help of friendly, convenient and easy-to-use interactive interface of VB front development, users can encapsulate the ANSYS command flow background which is complex, difficult to understand and master, and users simply need to input the required dimensions, material properties and load parameters under the guidance of the front interface. The analysis and results will be returned to the user for post-processing after the background calculation of the system. The system has a higher ability to deal with real problems, so one engineering staff who even if never seriously studied ANSYS software, can operate the finite element analysis with it.

The method calling the ANSYS program, developed by Visual Basic integrated development environment, will be encapsulated in the click event of the Command1 control and generate the APDL language macro file, then submit the ANSYS software program for batch processing. The so-called encapsulation is to use VB to call ANSYS software as a subroutine, and then results of ANSYS will be returned to the VB output interface. The specific practical operation needs to use the Function shell. The code added in Command1 is shown as follow [2]

Result=Shell("C:\Program Files\ANSYS Inc\v110\ANSYS\bin\intel\ANSYS110.exe-b-p ansysul-i file_in-o file_out,1")

Where ansysul is the product feature code of ANSYS, file_in and file_out respectively stand for the file name and storage location of the input command stream file and output result file.

By using text control in Visual Basic integrated development environment the parameters will be transferred to macro command file of ANSYS. Programming adds code to the code segment Private Sub Command1_Click( ){...}. The code is shown as follow [3]

l = Text1.Text Transferring the inner diameter of the brake disc friction surface to Variable l,
h= Text2.Text Transferring the outer diameter of the brake disc friction surface to Variable h,
E = Text3.Text Transferring the elastic modulus of the brake disc to Variable E,
C = Text3.Text Transferring the specific heat capacity of the brake disc to Variable C,
D = Text3.Text Transferring the thermal conductivity of the brake disc to Variable D,
R = Text3.Text Transferring the thermal expansion coefficient of the brake disc to Variable R,
...

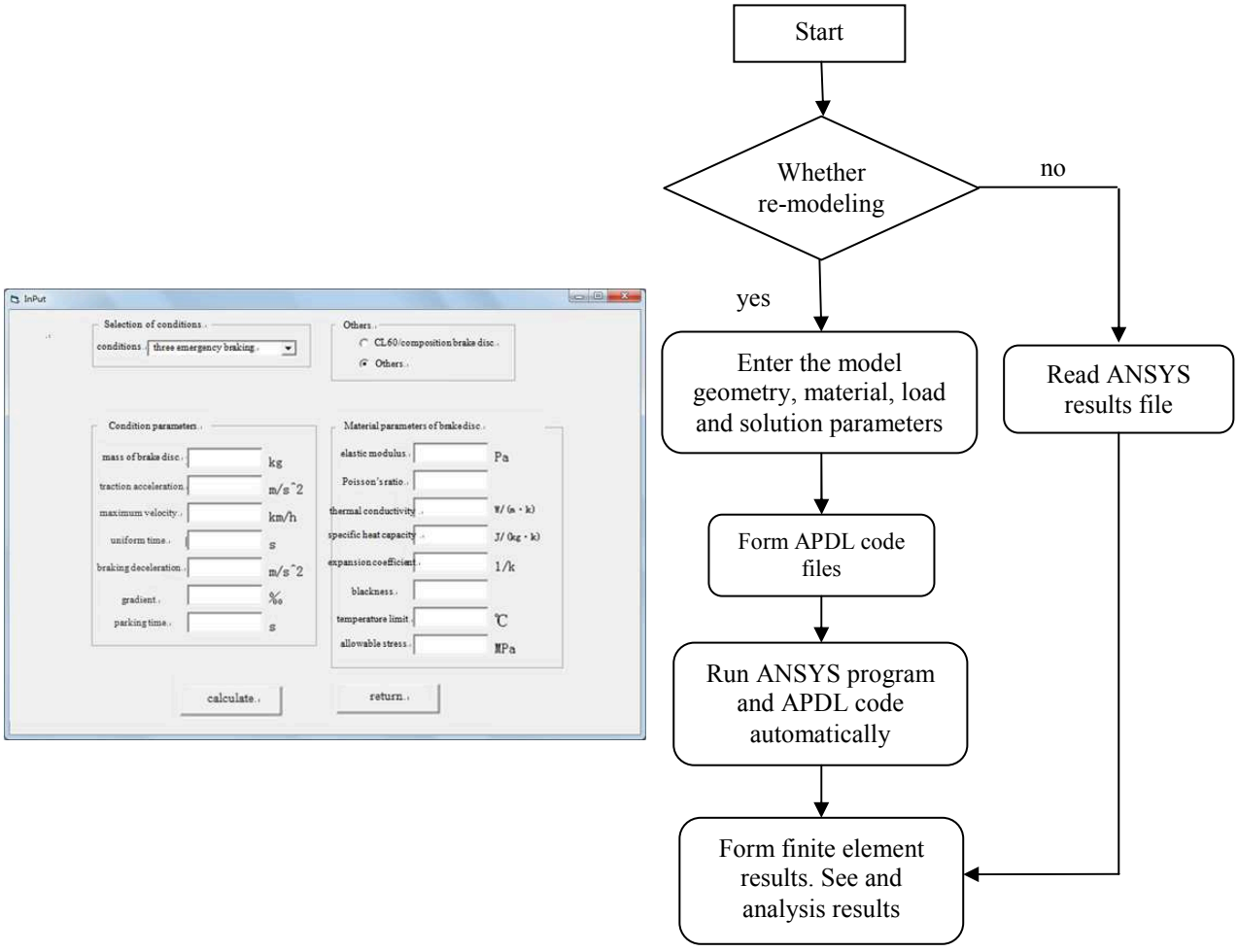


Fig. 1 Software process and interface

The ANSYS calculation results will be post-processed by APDL language with the help of VB. The needed result files will be saved to the working path as ".txt" file and images will be saved directly. The analysis results can be displayed in the foreground by using VB string handling and picture processing function. The software process and interface are shown in Fig. 1.

Temperature and stress field simulation of brake disc

Simulation conditions. This paper takes the axis disc under three successive emergency braking as example. The material of the brake disc is gray cast iron. The material parameter is shown in Table 1. Considering the symmetry feature of the brake disc's structure and the force the brake disc and brake pad suffering, only one twelfth of brake disc is selected to mesh. The finite element model of the brake disc is shown as Fig. 2.



Fig. 2 The finite element model of the brake disc

Table 1 The material parameter of gray cast iron

Temperature ($°C$)	Elastic modulus (MPa)	Specific heat capacity (J/(g·K))	Density (kg/m^3)	Thermal expansion coefficient (10^{-6}/K)	Thermal conductivity (W/(m·K))
20	112500	0.4187	7350	8.7	46.49
200	106300	0.461		11.6	45.23
300	98860	0.494		12.1	40.21
400	91400	0.507		12.7	36.86

The axle load of the train is 14t. Emergency deceleration is 1.3 m/s^2. Initial velocity of the emergency brake is 80km/h. Traction acceleration is 0.97m/s^2. An emergency braking cycle includes 4 phases: emergency brake period (0-17s); parking period (17-82s); acceleration period (82-105s); uniform running period (105-128s). Three emergency braking totally lasts 384s. As the load of each period is different, load step file is adopted in input and solving process.

Heat load input of train brake disc. The brake disc thermal load input is applied to the contact surface of the brake disc and brake pad in the form of heat flux. In actual braking process, because of the existence of mechanical resistance and air resistance, only a part of the kinetic energy of the train is converted into heat and brake pad also absorbs some of the heat. Therefore, brake disc absorbs 90% of the total kinetic energy based on past experience [4]. The heat generated by the friction of brake pad and brake disc can be expressed as

$$Q_{(t)} = \eta E = \frac{1}{2}\eta M(v_0^2 - v_t^2) \tag{1}$$

Where E is kinetic energy, M is the train mass, v_0, v_1 is the initial and final speed of the train during brake, η is the efficiency of the train kinetic energy converted into foundation brake friction heat, which is 0.9.

According to the definition of heat flux, heat flux $q_{(t)}$ can be expressed as

$$q_{(t)} = \frac{dQ_{(t)}}{dt} / S = -0.9\frac{Ma^2 t + Mv_0 a}{n\pi(R^2 - r^2)} \tag{2}$$

Where S is friction area of brake disc, that is, the annular area the brake pad sweeps on the brake disc, $S=\pi(R^2-r^2)$, R , r is outside and inside diameter of the annular area, a is braking deceleration.

Because braking deceleration is not a constant value, the heat flux is written into piecewise functions and loaded in ANSYS to calculate.

Simulation results. Fig. 3 is the temperature field contour of the brake disc when maximum temperature occurs during three successive emergency braking. From this picture we can see that the maximum temperature appears at friction area of the brake disc. The maximum temperature in process of entire three consecutive emergency braking is 293.272 $°C$, which is not over the prescribed temperature 300 $°C$ (When more than 300 $°C$, brake pad wear intensifies and pungent fume may emerge) and satisfies the requirement.

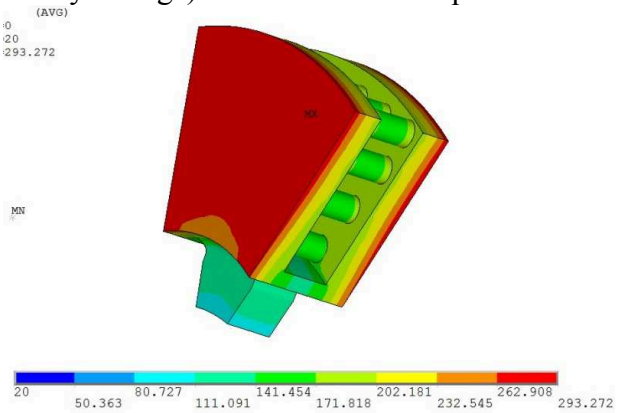


Fig. 3 Temperature field contours of brake disc

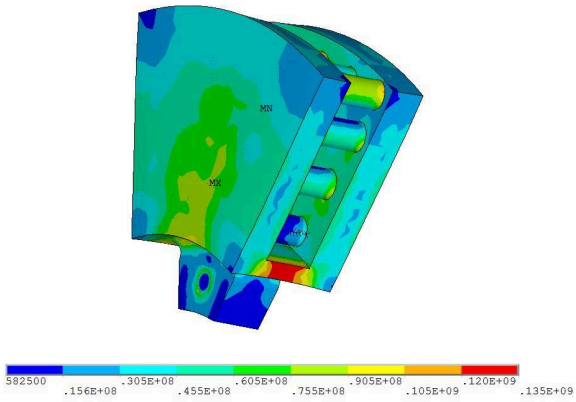


Fig. 4 Stress field contours of brake disc

Fig. 4 is the stress field contours when maximum stress occurs during three successive emergency braking. Greater stress occurs in cooling ribs, disc body junctions and structural mutations. This is caused by uneven heat transfer and convection. Thermal stress depends not only on the distribution of the temperature field, but also spatial structure [5]. Fig. 4 shows the maximum Von Mises equivalent stress is 135MPa, which is less than the selected gray iron yield limit. According to the forth strength criterion, the brake disc meets the requirement of the brake condition.

Summary

During secondary development by VB ANSYS is called to calculate the temperature and stress field of train brake disc under three successive emergency braking. Easily used interface is developed through VB, which makes those who are not familiar with ANSYS software can also conduct temperature and stress field simulation by using the software. Research is simplified and the efficiency of the calculation is enhanced. By analyzing the simulation results, a conclusion can be drawn that the brake disc can meet the requirements.

References

[1] M.L. Wu: submitted to Rolling Stock (1995)

[2] C.H. Zhang, S.K. Li, Finite Element Analysis Theory and Engineering Application, Electronic Industry Press, Beijing, 2007

[3] H.T. Sheng, ANSYS Finite Element Theory and Engineering Application Examples, Tsinghua University Press, Beijing, 2006

[4] Y. Yang, G. Wang: submitted to Computer Simulation (2005)

[5] Q. Ding, J.L. Xie: submitted to Journal of The China Railway Society (2002)

Applied Mechanics and Materials Vol. 597 (2014) pp 544-550
© (2014) Trans Tech Publications, Switzerland
doi:10.4028/www.scientific.net/AMM.597.544

Simplified Dynamics Modeling of Seat-Passenger in Vehicle Frontal Crash

Yaoyuan Wang[1,a], Zhuoyang Lyu[2,b] and Liangliang Wang[1,c] ,Zhenhua Yan[1,d,*]

[1]College of Mechanical Science and Engineering, Jilin University, Changchun 130025, China

[2]College of Automotive Engineering, Jilin University, Changchun 130025, China

[a]wangyy1411@163.com, [b]zhuoyanglyu@163.com, [c]wangll41101321@gmail.com, [d]Yanzhenhua@jlu.edu.cn,

Keywords: seat; coupled; dynamics; vehicle frontal crash; Madymo.

Abstract. To quickly predict the performance of the seat in frontal crash during the initial stage of the seat development, in this paper a simplified coupled dynamic model of seat-passenger interaction is established according to the dynamics analysis method of Lagrange, and the fourth order Runge-Kutta method is used to resolve differential equation. Moreover, the simulation of Madymo testifies the simplified coupled dynamic model of seat-passenger interaction in frontal crash. Therefore, this model will be effective and feasible in predicting the performance of the seat in frontal crash during the initial stage of the seat development, for example, the performance of anti-submarining protection.

Introduction

Since vehicle seats are critically important components for security protection, the performance of the vehicle seats should meet the national standards [1-3], like strength test regulations for vehicle frontal crash, rear crash and fixed-point strength test regulations for safety belt. To develop a new vehicle seat, all of the accurate three-dimensional data of seat need to be obtained according to certain seat and the specific structure of the new car. Furthermore, the dynamic performance of the seat could be predicted by simulation of car crash with FEM or the method of Multi-body System Dynamics based on the three-dimensional data of seat. According to the simulated results, the seat structure will be optimized and again simulated. But there exist the following problems: long design cycle, large amount of repetition work, high cost. Auto companies always focus on shortening the development cycle of seat, which will reduce delays in getting products to market. To improve the precision of the prediction of the simulation of car crash with FEM or the multi-rigid-body dynamics model and shorten the design period, a feasible method should be explored to predict the performance of the seat without the three-dimensional data of seat. In this paper, we establish a simplified coupled dynamic model of seat-passenger interaction for predicting the performance of the seat during the initial stage of the seat development, for example, the prediction for the performance of anti-submarining protection.

Dynamics modeling of seat-passenger interaction has become a hot topic recently in academia. In vehicle passive safety research, computer model of human body is usually used to replace dummy used in crash test, which proved to be economical and effective [4], especially in the initial stage of the seat development [5]. In this respect, researchers generally use the multi-rigid-body model to analyze the seat-passenger interaction. By simplifying the human body as a multi-rigid-body system and

establishing the environment around the passenger, we can study the kinematics response and the damage of the passenger, which will give us instructions for optimizing the design of the seat.[6-8] With regard to the finite element model, we can use it to simulate large deflections of these parts, such as the deflections of human thorax, head, leg etc.[9-11] after a collision. On the basis of the finite element analysis results, we can learn about how the materials and structures exert an influence on the passive safety of passenger after a collision. And researchers generally use the R-W method, Kane's method etc. of multi-body system dynamics to establish the coupled dynamic model of seat and passenger, which can be further used for the kinematical analysis of human body. [12-14] Moreover, programs for kinematics simulation are designed for study of crash. Based on those programs [15], the solving and assessment programs for vehicle occupant restraint system are developed, which achieves the rapid optimization by computer model.

Since the coupled dynamic model of seat-passenger has the obvious advantages of simple, high usability, effective, high accuracy, low cost and short research period, in this paper we establish a simplified coupled dynamic model of seat-passenger interaction is established according to the dynamics analysis method of Lagrange. Moreover, dynamic response of passenger during the collision has been studied by simulation with Madymo software. Based on the simulation results and simplified coupled dynamic model, we analyze the effect the angle between the front part of the seat and horizontal plane will have on the performance of anti-submarining protection of the seat. The model proposed in this paper acts as an effective tool for preliminary study of the structure design of safety facilities, materials characteristics and the effect they have on the passenger safety.

Establishment of Coupled Dynamic Model of Seat and Passenger

Establishment of Simplified Model. In this model, the seat frame, chassis can be viewed as a rigid body; foam skin of seat, safety belts, human feet can be simplified as spring-damper system, where spring and damping are regarded as linear elements. The human body can be simplified as 4 parts. They are head, torso, thighs and crura. Each two parts are connected by revolute joints.

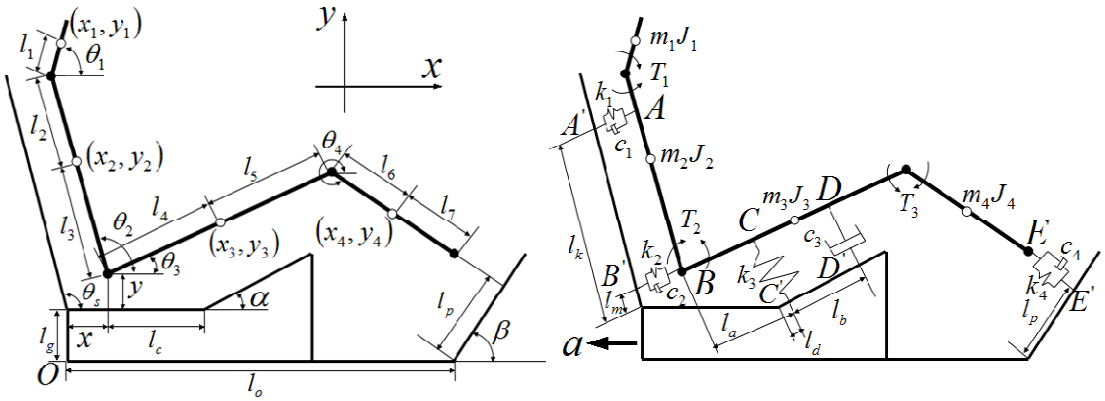


Fig. 1 Illustrations of coupled model of seat and passenger.

We view the forces of head and torso, torso and thighs, thighs and crura as a torque, which makes the model conforming more to the actual situation [16-18], Where T_i satisfies the following formulas:

$$T_i = T_{\max,i} \tanh\left(2\frac{\omega_i}{\omega_{i,0}}\right), \tag{1}$$

$$\omega_i = \dot{\theta}_i - \dot{\theta}_{i+1}. \tag{2}$$

Referring to the experiment of real vehicle frontal crash, we apply an acceleration a to the seat in the direction of the negative x-axis to establish a coupled dynamics model of seat and passenger, and simulate the response of the human body in a vehicle frontal crash.

The meanings of parameters in the model are as follows:

k_i——stiffness coefficient, c_i——damping coefficient, m_i ——quality of certain mass center of each part, J_i——moment of inertia, Θ_1——angle between head and horizontal plane, Θ_2——angle between torso and horizontal plane, Θ_3——angle between thighs and horizontal plane, Θ_4——angle between crura and horizontal plane, Θ_s——angle between seat back and horizontal plane, α——angle between the front part of the seat and horizontal plane, β—— angle between car dashboards and chassis, x——Abscissa of Hinge point between torso and thighs, y——Ordinate of Hinge point between torso and thighs, a—— horizontal acceleration loaded in the car seat.

Establishment of Kinetic Equation. In the paper, we use Lagrange-equation to establish kinetic equation. The general form of Lagrange-equation is

$$\frac{d}{dt}\left(\frac{\partial T}{\partial \dot{q}_r}\right)-\frac{\partial T}{\partial q_r}+\frac{\partial U}{\partial q_r}+\frac{\partial D}{\partial \dot{q}_r}=Q_r, \tag{3}$$

where T is kinetic energy of system,U is potential energy of system,D is dissipated energy caused by damping in the system,q_r:generalized coordinates, Q_r is generalized forces in generalized coordinates.

The expressions of parameters are as follows:

$$T=\frac{1}{2}\left(\sum_{i=1}^{4}m_i\dot{x}_i^2+\sum_{i=1}^{4}m_i\dot{y}_i^2+\sum_{i=1}^{4}J_i\dot{\theta}_i^2\right), \tag{4}$$

$$U=\frac{1}{2}\left(\sum_{i=1}^{4}k_i\delta_i^2+k_4\delta_{4k}^2\right), \tag{5}$$

$$D=\frac{1}{2}\left(\sum_{i=1}^{4}c_i\dot{\delta}_i^2+k_4\dot{\delta}_{4c}^2\right), \tag{6}$$

where δ_i: is deformation of the spring or damping, δ_{4k}: is deformation of the spring 4, δ_{4c} is deformation of damping 4.

Dynamic equations based on Lagrange-equation are as follows:

$$\sum_{i=1}^{4}m_i\ddot{x}_i+\sum_{i=1}^{3}\left[\frac{k_i\delta_iM_i}{\sqrt{f_i}}+\frac{M_ic_i}{f_i}\left(M_i\cdot\dot{M}_i+N_i\cdot\dot{N}_i\right)\right]+\frac{k_4\delta_{4k}M_{4k}}{\sqrt{f_{4k}}}+\frac{M_{4c}c_4}{f_{4c}}\left(M_{4c}\cdot\dot{M}_{4c}+N_{4c}\cdot\dot{N}_{4c}\right)=0 \tag{7}$$

$$\sum_{i=1}^{4}m_i\ddot{y}_i+\sum_{i=1}^{3}\left[\frac{k_i\delta_iN_i}{\sqrt{f_i}}+\frac{N_ic_i}{f_i}\left(M_i\cdot\dot{M}_i+N_i\cdot\dot{N}_i\right)\right]+\frac{k_4\delta_{4k}N_{4k}}{\sqrt{f_{4k}}}+\frac{N_{4c}c_4}{f_{4c}}\left(M_{4c}\cdot\dot{M}_{4c}+N_{4c}\cdot\dot{N}_{4c}\right)=0 \tag{8}$$

$$m_1l_1\left(\ddot{x}_1\sin\theta_1-\ddot{y}_1\cos\theta_1\right)-J_1\ddot{\theta}_1=T_1 \tag{9}$$

$$-m_1\left(l_2+l_3\right)\left(\ddot{x}_1\sin\theta_2-\ddot{y}_1\cos\theta_2\right)-m_3l_3\left(\ddot{x}_2\sin\theta_2-\ddot{y}_2\cos\theta_2\right)+J_2\ddot{\theta}_2+\left(l_k-l_m\right)\left(N_1\cos\theta_2-M_1\sin\theta_2\right)$$
$$\cdot\left[\frac{k_1\delta_1}{\sqrt{f_1}}+\frac{c_1}{f_1}\left(M_1\cdot\dot{M}_1+N_1\cdot\dot{N}_1\right)\right]=T_1-T_2 \tag{10}$$

$$-m_3l_4\left(\ddot{x}_3\sin\theta_3-\ddot{y}_3\cos\theta_3\right)-m_4\left(l_4+l_5\right)\left(\ddot{x}_4\sin\theta_3-\ddot{y}_4\cos\theta_3\right)+J_3\ddot{\theta}_3+\left(l_4+l_5\right)\left(N_3\cos\theta_3-M_3\sin\theta_3\right)\cdot$$
$$\cdot\left[\frac{k_3\delta_3}{\sqrt{f_3}}+\frac{c_3}{f_3}\left(M_3\cdot\dot{M}_3+N_3\cdot\dot{N}_3\right)\right]+\frac{k_4\delta_{4k}}{\sqrt{f_{4k}}}l_a\left(N_{4k}\cos\theta_3-M_{4k}\sin\theta_3\right)+\frac{c_4}{f_{4c}}\left(l_a+l_b\right)\left(M_3\cdot\dot{M}_3+N_3\cdot\dot{N}_3\right)\cdot$$
$$\cdot\left(N_{4c}\cos\theta_3-M_{4c}\sin\theta_3\right)=T_2-T_3 \tag{11}$$

$$-m_4 l_6\left(\ddot{x}_4\sin\theta_4-\ddot{y}_4\cos\theta_4\right)+J_4\ddot{\theta}_4+\left(l_6+l_7\right)\left(N_3\cos\theta_4-M_3\sin\theta_4\right)\cdot\left[\frac{k_3\delta_3}{\sqrt{f_3}}+\frac{c_3}{f_3}\left(M_3\cdot\dot{M}_3+N_3\cdot\dot{N}_3\right)\right]=T_3 \quad (12)$$

We constructed a simultaneous equation with (7), (8), (9), (10), (11) and (12). In the simultaneous equation,

$$\ddot{x}_1=\ddot{x}-\left(l_2+l_3\right)\left(\sin\theta_2\cdot\ddot{\theta}_2+\cos\theta_2\cdot\dot{\theta}_2^2\right)-l_1\left(\sin\theta_1\cdot\ddot{\theta}_1+\cos\theta_1\cdot\dot{\theta}_1^2\right),\ \ddot{x}_2=\ddot{x}-l_3\sin\theta_2\cdot\ddot{\theta}_2-l_3\cos\theta_2\cdot\dot{\theta}_2^2,$$

$$\ddot{x}_3=\ddot{x}-l_4\left(\sin\theta_3\cdot\ddot{\theta}_3+\cos\theta_3\cdot\dot{\theta}_3^2\right),\ddot{x}_4=\ddot{x}-\left(l_4+l_5\right)\left(\sin\theta_3\cdot\ddot{\theta}_3+\cos\theta_3\cdot\dot{\theta}_3^2\right)-l_6\left(\sin\theta_4\cdot\ddot{\theta}_4+\cos\theta_4\cdot\dot{\theta}_4^2\right),$$

$$\ddot{y}_1=\ddot{y}+\left(l_2+l_3\right)\left(\cos\theta_2\cdot\ddot{\theta}_2-\sin\theta_2\cdot\dot{\theta}_2^2\right)+l_1\left(\cos\theta_1\cdot\ddot{\theta}_1-\sin\theta_1\cdot\dot{\theta}_1^2\right),\ddot{y}_2=\ddot{y}+l_3\left(\cos\theta_2\cdot\ddot{\theta}_2-\sin\theta_2\cdot\dot{\theta}_2^2\right),$$

$$\ddot{y}_3=\ddot{y}+l_4\left(\cos\theta_3\cdot\ddot{\theta}_3-\sin\theta_3\cdot\dot{\theta}_3^2\right),\ddot{y}_4=\ddot{y}+\left(l_4+l_5\right)\left(\cos\theta_3\cdot\ddot{\theta}_3-\sin\theta_3\cdot\dot{\theta}_3^2\right)+l_6\left(\cos\theta_4\cdot\ddot{\theta}_4-\sin\theta_4\cdot\dot{\theta}_4^2\right),$$

$$M_1=x+\left(l_k-l_m\right)\cos\theta_2+\frac{40}{\pi}t-\frac{8}{\pi^2}\sin\left(5\pi t\right)-l_k\cos\theta_s,M_2=x+\frac{40}{\pi}t-\frac{8}{\pi^2}\sin\left(5\pi t\right)-l_m\cos\theta_s,$$

$$M_3=x+\left(l_4+l_5\right)\cos\theta_3+\left(l_6+l_7\right)\cos\theta_4+\frac{40}{\pi}t-\frac{8}{\pi^2}\sin\left(5\pi t\right)-l_o-l_p\cos\beta,$$

$$M_{4k}=x+l_a\cos\theta_3+\frac{40}{\pi}t-\frac{8}{\pi^2}\sin\left(5\pi t\right)-x_0-l_c-l_d\cos\alpha,$$

$$M_{4c}=x+\left(l_a+l_b\right)\cos\theta_3+\frac{40}{\pi}t-\frac{8}{\pi^2}\sin\left(5\pi t\right)-x_o-l_c-\left(l_d+l_b\right)\cos\alpha,$$

$$N_1=y+\left(l_k-l_m\right)\sin\theta_2-l_k\sin\theta_s,N_2=y-l_m\sin\theta_s,N_3=y+\left(l_4+l_5\right)\sin\theta_3+\left(l_6+l_7\right)\sin\theta_4+l_q-l_p\sin\beta,$$

$$N_{4k}=y+l_a\sin\theta_3-l_d\sin\alpha,N_{4c}=y+\left(l_a+l_b\right)\sin\theta_3-\left(l_d+l_b\right)\sin\alpha,\dot{M}_1=\dot{x}-\left(l_k-l_m\right)\sin\theta_2\cdot\dot{\theta}_2+\frac{40}{\pi}-\frac{40}{\pi}\cos\left(5\pi t\right),$$

$$\dot{M}_2=\dot{x}+\frac{40}{\pi}-\frac{40}{\pi}\cos\left(5\pi t\right),\dot{M}_3=\dot{x}-\left(l_4+l_5\right)\sin\theta_3\cdot\dot{\theta}_3-\left(l_6+l_7\right)\sin\theta_4\cdot\dot{\theta}_4+\frac{40}{\pi}-\frac{40}{\pi}\cos\left(5\pi t\right),$$

$$\dot{M}_{4c}=\dot{x}-\left(l_a+l_b\right)\sin\theta_3\cdot\dot{\theta}_3+\frac{40}{\pi}-\frac{40}{\pi}\cos\left(5\pi t\right),\dot{N}_1=\dot{y}+\left(l_k-l_m\right)\cos\theta_2\cdot\dot{\theta}_2,\dot{N}_2=\dot{y},$$

$$\dot{N}_3=\dot{y}+\left(l_4+l_5\right)\cos\theta_3\cdot\dot{\theta}_3+\left(l_6+l_7\right)\cos\theta_4\cdot\dot{\theta}_4,\dot{N}_{4c}=\dot{y}+\left(l_a+l_b\right)\cos\theta_3\cdot\dot{\theta}_3,$$

$$f_1=\overline{AA'}^2,f_2=\overline{BB'}^2,f_3=\overline{EE'}^2,f_{4k}=\overline{CC'}^2,f_{4c}=\overline{DD'}^2$$

Then putting simulation data into equations and solving with MATLAB, we get the dynamic response of human body.

Simulation of Vehicle Frontal Crash Based on Madymo

Establishment of Simulation Model of Occupant Restraint System in Vehicle Frontal Crash.

In the paper we establish Coupled Model of seat and passenger with Madymo. We use Hybrid III50th Male Dummy, model of mixed safety belt to simulate. The mixed safety belt model is the mixture of multi-body safety belt model and finite element safety belt model. It can simulate the situation of slide of safety belt in different direction and submarining exactly, making the model closer to real condition.

Model of occupant restraint system in vehicle frontal crash can be shown in Fig. 2.

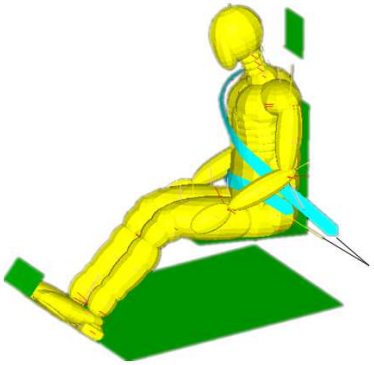


Fig. 2 Simulation model of Occupant Restraint System.

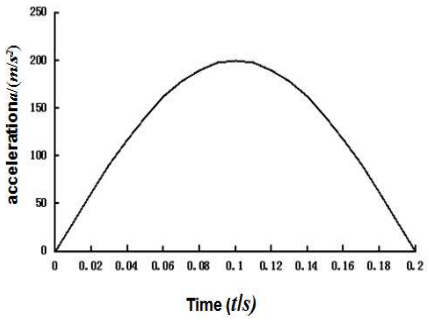


Fig. 3 Acceleration curve.

Definition of acceleration. Define the acceleration as that in Fig. 3 and load the acceleration separately on Madymo model and simplified model to perform simulation research.

Resolution and Verification of Coupled Dynamic Model of Seat and Passenger

Parameters of Simulation. According to the actual parameters and experimental analysis of the seat and dummy[13], Comparing the solution results of this model with those of Madymo, and performing model parameter optimization, we obtain the table of simulation parameters of the simplified model, which is shown in Table 1.

Table 1 Parameters of Simulation.

Parameter	Value	Parameter	Value	Parameter	Value	Parameter	Value
m_1[kg]	*3.988*	J_1[kg•m^2]	*0.02159*	l_1[m]	*0.1207*	Θ_{10}[°]	*100*
m_2[kg]	*34.134*	J_2[kg•m^2]	*1.39277*	l_2+l_3[m]	*0.6223*	Θ_{20}[°]	*110*
m_3[kg]	*17.844*	J_3[kg•m^2]	*0.33520*	l_4+l_5[m]	*0.5334*	Θ_{30}[°]	*14*
m_4[kg]	*7.984*	J_4[kg•m^2]	*0.19732*	l_6+l_7[m]	*0.4572*	Θ_{40}[°]	*320*
β[°]	*50*	L_p[m]	*0.1397*	y_0[m]	*0.1100*	k_3[N/m]	*64648*
α[°]	*30*	l_q[m]	*0.1630*	x_0[m]	*0.1650*	k_4[N/m]	*15279*
Θ_{s0}[°]	*110*	l_k[m]	*0.5780*	k_1[N/m]	*23059*	c_1[N•s/m]	*70.48*
l_0[m]	*0.9378*	l_m[m]	*0.0760*	k_2[N/m]	*23059*	c_2[N•s/m]	*70.48*
c_3[N•s/m]	*157.16*	c_4[N•s/m]	*5638.40*	l_a[m]	*0.174*	l_b[m]	*0.2729*
$T_{max,1}$ [Nm•s /rad]	*3.920*	$T_{max,2}$ [Nm•s /rad]	*38.280*	$T_{max,3}$ [Nm•s /rad]	*14.112*	w_0[rad/s]	*0.349*
l_c[m]	*0.335*	l_d[m]	*0.0635*				

Units of parameter values in the table are: mass / kg, moment of inertia / (kg.m^2), length / m, the angle / °, stiffness coefficient/ (N / m), the damping coefficient / (N•s/m), torque / (N•ms / rad), angular velocity / (rad / s).

Simulation Results. Combining the setting of generalized coordinates in simplified model, we extract the Fig. 4 which can reflect relationship between articulated point of torso and thigh and time from simplified model and Madymo model. As is shown to us, although there are calculation errors between the results of the simplified model and the Madymo simulation results, but the trend and peaks of the two curves are almost the same, which indicates that the model is valid.

We use this model to solve the influence of tip angle α on submarining, as is shown in Fig. 5. It can be seen that when α increases, submarining decreases, and anti-submarining properties is improved.

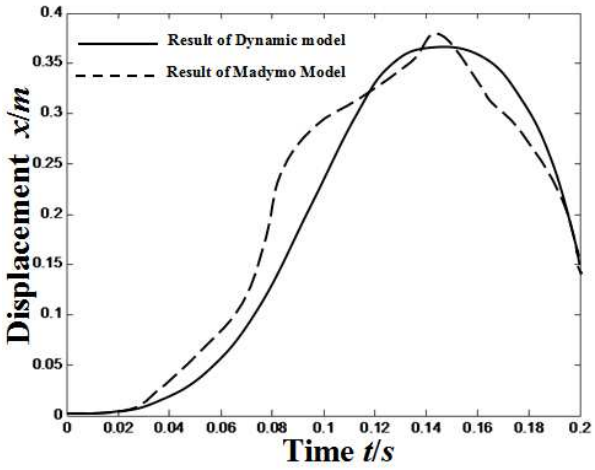


Fig.4 Displacement of Hinge Point of the Human Torso and Thigh.

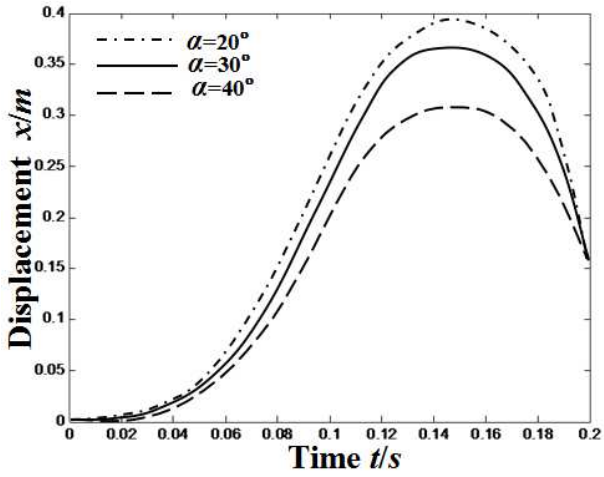


Fig. 5 Displacement of Hinge Point of the Human Torso and Thigh.

Conclusions

(1) From the perspective of multi-rigid-body dynamics, we established a simplified coupled dynamic model of seat-passenger interaction according to the Lagrange-equation, and the fourth order Runge-Kutta method was used to resolve differential equation.

(2) By using MATLAB, we obtained the dynamic response during the vehicle frontal crash. By the comparison between simulation results and calculations , the dynamic model is proved to be feasible and effective.

(3) By utilizing the dynamic model we developed, we analyzed the effect the angle between the front part of the seat and horizontal plane have on the performance of anti-submarining protection of the seat. We get the conclusion that the performance of anti-submarining protection of the seat will be better with the angle α increasing.

References

[1] GB 11551-2003, The protection of the occupants in the event of a frontal collision for passenger car[S](in Chinese)

[2] GB 15083-2006, Strength requirement and test of automobile seats, their anchorages and any head restraints[S](in Chinese)

[3] GB 11550-2009, Strength requirement and test of automobile seats head restraints[S](in Chinese)

[4] KIng A I. Suggestion for making rapid advances in automotive safety in China[J]. Journal of Automotive Safety and Energy, 2010, 1(1): 1-5.

[5] Zhan Zhang-song, Xiong Shu-sheng. Study on occupant dynamics computer simulation in automotive collision[J]. Journal of Zhejiang University(Engineering Science), 2002, 1: 019.

[6] Vadiraj B, Omkar S N, Kandagal S B, et al. Human Response Characteristics to Impact Conditions During Spacecraft Takeoff and Impact Landing[J]. International Journal of Aerospace Innovations, 2012, 4(3): 95-102.

[7] Himmetoglu S, Acar M, Bouazza-Marouf K, et al. A multi-body human model for rear-impact simulation[J]. Proceedings of the Institution of Mechanical Engineers, Part D: Journal of Automobile Engineering, 2009, 223(5): 623-638.

[8] Himmetoglu S, Acar M, Bouazza-Marouf K, et al. Car seat design to improve rear-impact protection[J]. Proceedings of the Institution of Mechanical Engineers, Part D: Journal of Automobile Engineering, 2011, 225(4): 441-459.

[9] Iwamoto M, Kisanuki Y, Watanabe I, et al. Development of a finite element model of the total human model for safety (THUMS) and application to injury reconstruction[C]//Proceedings of the International IRCOBI Conference. 2002.

[10] T.L. Teng, T.M. Shih, C.C. Wu, A finite element model for a frontal impact dummy, Journal of Technology 19 (1) (2004) 31–38.

[11] Nagasaka K, Mizuno K, Tanaka E, et al. Finite element analysis of knee injury risks in car-to-pedestrian impacts[J]. Traffic injury prevention, 2003, 4(4): 345-354.

[12] Ippili R K, Davies P, Bajaj A K, et al. Nonlinear multi-body dynamic modeling of seat–occupant system with polyurethane seat and H-point prediction[J]. International Journal of Industrial Ergonomics, 2008, 38(5): 368-383.

[13] Kim S K, White S W, Bajaj A K, et al. Simplified models of the vibration of mannequins in car seats[J]. Journal of sound and vibration, 2003, 264(1): 49-90.

[14] Zhang Yan, Wang Shu-xin, Lai Xin-min, Zhu Ping. Dynamic Responses of Human Body with Belt Constraints During Vehicle Crash[J]. Mechanical Science and Technology, 2004, 23(8): 944-946(in Chinese)

[15] Yeh I, YAN F U, Kachnowski B, et al. Optimization of a vehicle restraint system using a genetic algorithm[J]. SAE transactions, 2005, 114(6): 1504-1511.

[16] S. Nishiyama, Development of simulation system on vehicle-occupant dynamic interaction (1st Report,Theoretical analysis and system verification),Transactions of the Japan Society of Mechanical Engineers C 59(568) (1993) 3613–3621.

[17] S. Nishiyama, Development of simulation system on vehicle-occupant dynamic interaction (2nd Report, Influenceof sitting posture on human comfort),Transactions of the Japan Society of Mechanical Engineers C 59 (568)(1993) 3622–3629.

[18] S. Nishiyama, Development of simulation system on vehicle-occupant dynamic interaction (3rd Report, Influence of parameters of occupant-seat system on human comfort), Transactions of the Japan Society of Mechanical Engineers C 60 (573) (1994) 1509–1516.

Applied Mechanics and Materials Vol. 597 (2014) pp 551-556
© (2014) Trans Tech Publications, Switzerland
doi:10.4028/www.scientific.net/AMM.597.551

Study on the Stress Variation Mechanism for the Rails under the Wheels Repeated Rolling Effects

SONG Hua[1,a*],SONG Lin Bang[1,b],YAO Jin Kai[1c],LIAN Fa Bo[2],LI Wei[3]

[1]University of Science and Technology Liaoning, Anshan, Liaoning 114051

[2]Anshan Iron & Steel Co., Ltd., Anshan, Liaoning 114021

[3]China Academy of Railway Sciences，Beijing 100081

[a]songhua88@126.com, [b]943477303@qq.com,[c]576384622@qq.com

Keywords: Heavy rail, Wheel/rail contact, Dynamic simulation, Circulating rolling

Abstract：Based on the real geometry and boundary conditions of the wheels and rails, the models of 60kg/m U75V heavy rail and the wear regions of LM are built using ANSYS/LS-DYNA software. The internal stress value and variation of the heavy rails that were repeatedly crushed by the rolling wheels are analyzed using the ANSYS/LS-DYNA3D software. The relationship of the internal stress and variation of heavy rails with the repeated rolling of the wheels are obtained. It provides an important theoretical proof and reference significance to prevent the different failure behaviors of the rails.

Introduction

As known, the rails' internal stress value and distribution are closely related to their failure behaviors. With increasing the trains' axle load, speed and freight, the using conditions for the heavy rails are becoming worse. So the precise study on the rails' internal stress is very necessary.

The Hertz contact theory, traditional finite element model and modified finite element model were comparatively studied in reference 1. The results indicated that the Hertz theory is not suitable to carry out the accurate calculation for the current wheel-rail contact problem. The finite element method are much closer to the real situation than the Hertz contact theory.

The wheel-rail rolling contact dynamic stress and strain were systematically analyzed in reference 2. The wheel-rail two-dimensional finite element model was established and the internal stress variation of the rails under the wheels' rolling effect was considered, however, the model for the wheels' repeated rolling did not implement the real rolling effect. Meanwhile, it did not conclude the influences of the rail bottom supporting environment on the rail's internal stress and distribution.

The influence of sleeper and axle load on wheel-rail contact stress was investigated for the elastic plastic static analysis in reference 3. The method of finite element parameters quadratic programming was used for the elastic and elastic-plastic analysis to obtain the effects of different wheel diameters, axle load, traction and friction coefficient on the rail stress in reference 4.

The wheel-rail contact stress on the different axle load and lateral forces was calculated by using the subway curve segment wheel-rail contact finite element model through ANSYS software in reference 5.

The influences of the wheel-rail elastic-plastic strain was considered in reference 6. The distribution of maximum equivalent plastic strain and shearing strain and the relationship between wheel-rail yield strength and the material cumulative plastic deformation was obtained.

The relationship between the wheel-rail rolling contact stress and the surface tangential force were studied to establish a three-dimensional finite element model using ANSYS software in reference 7. The rolling contact fatigue cracks on the wheel-rail contact surface were analyzed based on the influences of the rail surface contact stress for the ten wheels repeated-rolling effects in reference 8.

From the above references, a lot of works have been done to research the rail stress, however, there are still existing some defects as follows:

(1) The real geometry of wheel-rail has not been considered and the effect of the wheel axle load was simplified as a concentrated stress load. So the as-calculated rail stress is quite different from the actual situation.

(2) When applying constraint parameters on the rail's three dimensional model, the rail bottom is usually restrained completely, the supporting effects of the sleepers on the rail's internal stress distribution have not been taken into account.

(3) The dynamic interaction process of the repeated rolling of wheels on the rails has not been considered.

In this paper, the real geometry of wheel-rail, boundary condition and the support of sleeper are taken into account to establish an three-dimensional dynamic contact finite model by ANSYS/LS-DYNA software. The internal stress of the rails under the wheel' repeated rolling effects is simulated and analyzed. This analysis for the wheel-rail contact stress is more reasonable.

The establishment of wheel-rail contact model

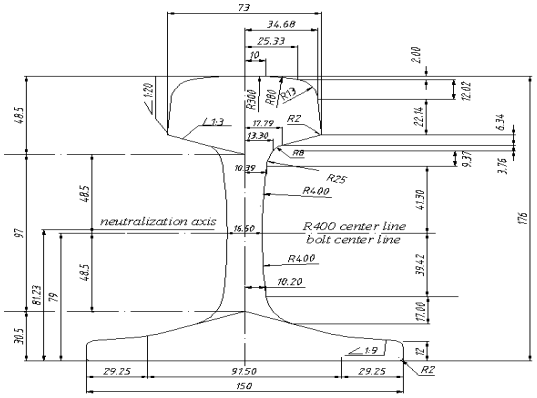


Fig. 1 The section of 60kg/m U75V rail

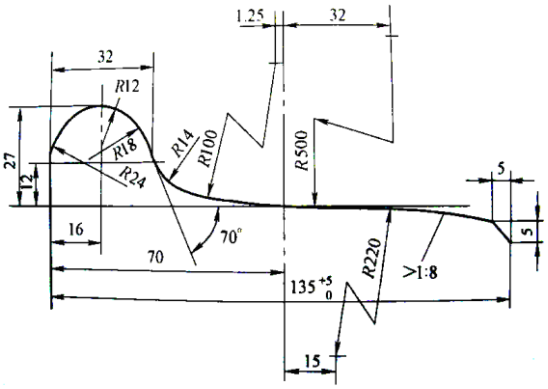
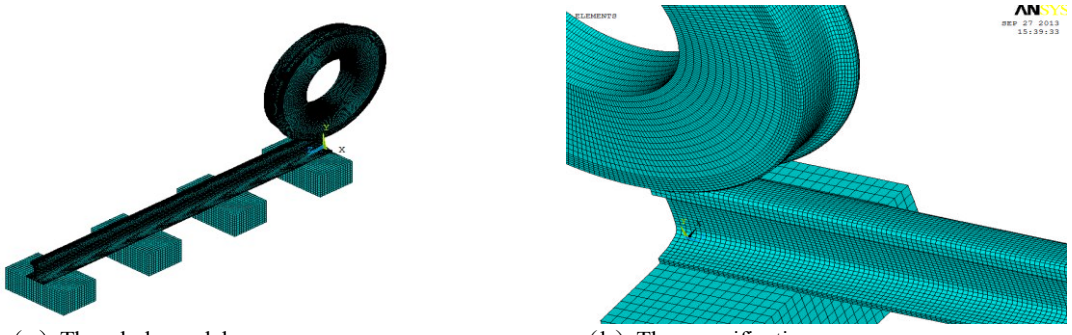


Fig. 2 The wear regions of LM



（a）The whole model （b）The magnification

Fig. 3 The finite element models of the wheels and rail

The wheel-rail model unit is solid 164 and the rail material is U75V. The bilinear kinematic hardening model is BKIN and the basic parameters are:μ=0.3,ρ=7.83g/cm^3; E=2.1×10^{5}Mpa ; σ_s=525Mpa; Eτ=1.18×10^{4}Mpa.The μ is Poisson's ratio, ρ is density, E is elastic modulus, σ_s is yield limit and Eτ is tangent modulus.

The rail's internal stress situation will be mainly simulated and analyzed. After considering the calculation accuracy of rail-wheel contact and required computer hardware, the length of U75V heavy rail is set to 2500mm. The wheels and sleepers are set to be the rigid substance. The basic dimensions of the rail's cross section are shown in Fig 1.

The LM worn tread is used for the wheel's profile. The wheel diameter is 915 mm and the contour shape is shown in Fig 2. The profile dimensions for the sleeper are 500, 277, 200 mm. The interval distance within the sleepers is 464 mm. The wheel-rail finite element model is divided to 212418 units and 238167 nodes. Among of them, the rail occupies 44000 units and 57479 nodes.

After meshing, the whole model is shown as Fig 3a. The Fig 3b is the enlarged picture for the wheel-rail contact part. The velocity of the train is 120 Km/h. The angular velocity of the wheel is 72.86 rad/s. The friction coefficient of the wheel-rail is 0.3 and the axle load of the wheel is 15 ton.

Stress analysis of rail under the wheels repeated rolling

In order to obtain the impact of the rail stress by the repeated rolling wheels, the vertical stress (y-stress), the longitudinal stress (z-stress) and the equivalent stress are studied. The two cross sections on the sleeper (z=1620mm) and in between sleepers (z=1250mm) are selected for the study as shown in Fig 4. The 25 nodes of the heavy rail in the symmetrical center line are analyzed as shown in Fig 5. For simulating the continuous rolling status for the wheels, the initial interval time for the adjacent wheels is set as 0.05 s. The three stresses variation curves of the 25 nodes after 10 times rolling of the wheels are shown in Fig 6 and 7.

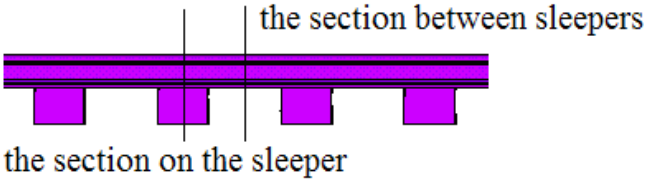


Fig. 4 The section of the rail

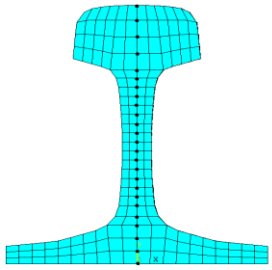
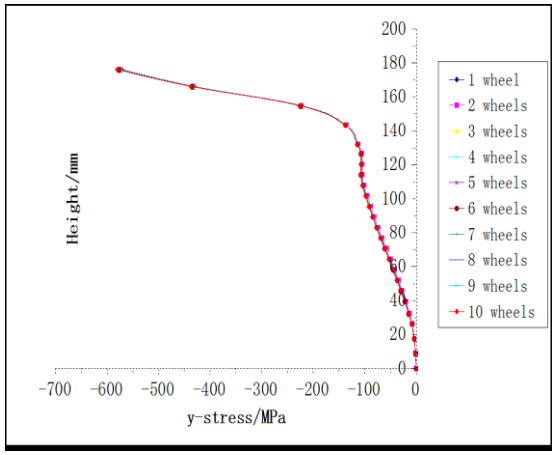
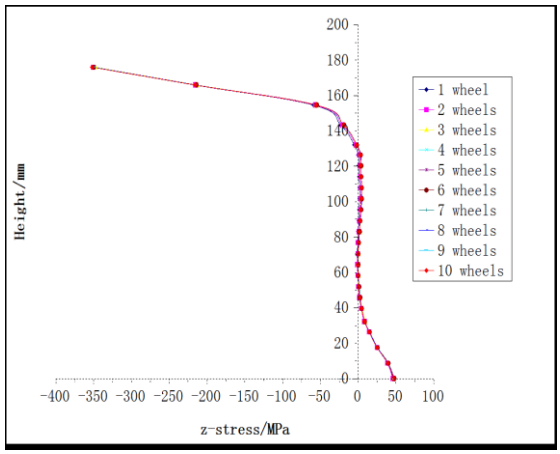


Fig. 5 The 25 nodes of heavy rail placement on the center line

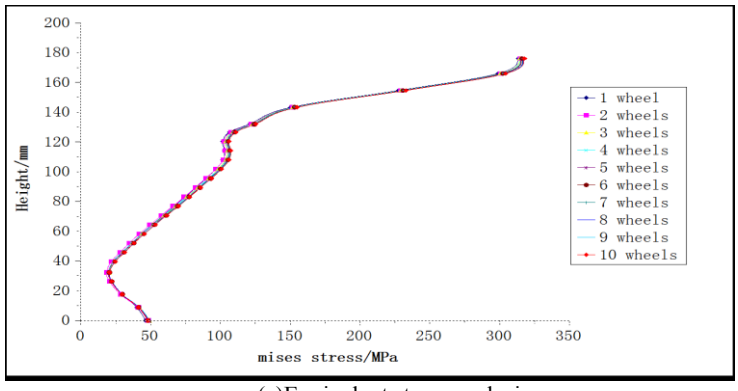
The stress analysis of the section between the sleepers



(a)Vertical stress analysis



(b)Longitudinal stress analysis



(c)Equivalent stress analysis

Fig. 6 The figure of three kinds of stresses at the section between the sleepers

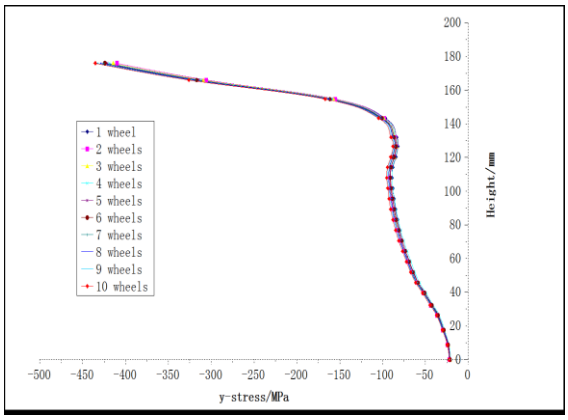
Vertical stress analysis. As can be seen from Fig 6a, the vertical stress variation for each node of the rail is very small when the rolling time is from 1 to 10. The ten stress curves are basically overlapped each other. The vertical stress on the central line of the sleeper's cross section are all pressure stress. The maximum vertical stress appears at the head part of the rail with a value of 600 MPa. The minimum vertical stress appears at the rail's bottom and is 0 MPa. The stress distribution

gradually decreases from the head surface to the bottom surface. But the vertical stress in the head part of the rail decreases very quickly, from -600 MPa to 150 MPa.

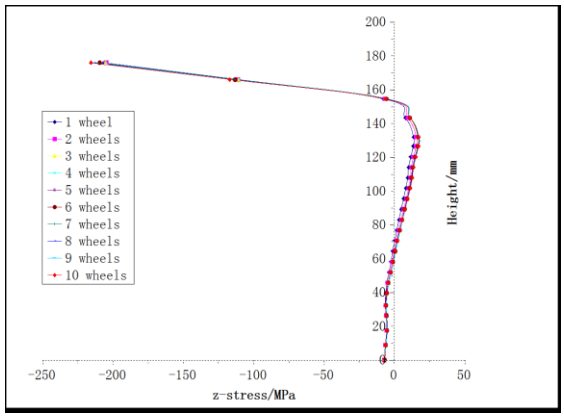
Longitudinal stress analysis. As shown in Fig 6, the ten stress curves are almost overlapped for the rolling times from 1 to 10. This indicates that the number of wheels has not evident influence on rail's longitudinal stress. The longitudinal stress on the whole nodes of rail head and rail bottom are pressure stress and tensile stress, respectively. The maximum longitudinal stress is about -350 Mpa and the maximum tensile stress appears at the rail bottom with a value of ~50 MPa.

Equivalent stress analysis. As shown in Fig 6c, with increasing the number of wheel, ten equivalent stress curves gradually shift to right side. This indicates that the equivalent stress value in the center line increases gradually. The increasing trend in the rail bottom part is smaller than those in the rail head and rail web parts. It means that the wheels' repeated rolling has an evident influence on the equivalent stress in the rail's head part. The equivalent stress values decrease gradually from the rail head to rail bottom. The maximum value appears at the rail's head with a value of 317 MPa. The minimum value is 35 MPa appearing at the point ~30 mm far from the rail's bottom.

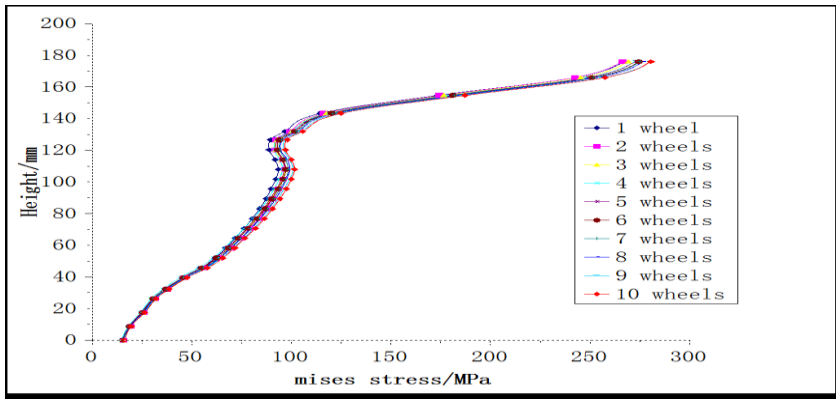
The stress analysis of the cross section between the sleepers



(a)Vertical stress analysis



(b)Longitudinal stress analysis



(c)Equivalent stress analysis

Fig. 7 The figure of three kinds of stresses at the section on the sleeper

Vertical stress analysis. As shown in Fig 7a, the vertical stress distribution of the sleeper's cross section is quite similar to the vertical stress distribution at the section between the sleepers. They are all pressure stresses and decreases gradually from the rail head surface to the rail bottom surface. But the stress value at the rail head is about -450 MPa, which is smaller than the vertical stress between the sleepers section. The vertical stress in rail bottom is -20MPa, which is bigger than the vertical stress between the sleepers section. With increasing the number of wheels, the ten vertical stress curves show a left shifting trend, which indicates that the vertical stresses of each node shows different increases with increasing rolling times.

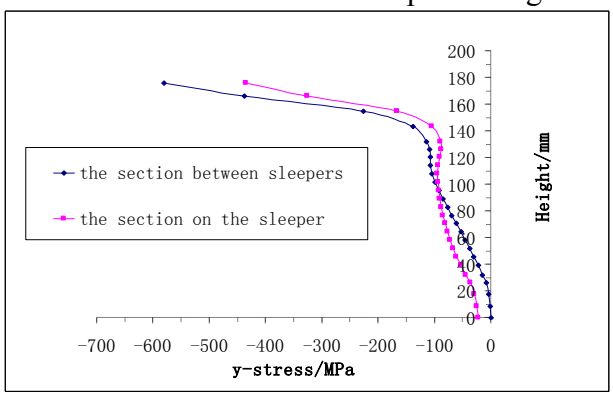
Longitudinal stress analysis. The rail's upside is showing with a pressure stress. The bottom of rail head and the upside of the rail web are showing with tensile stress as can be seen from Fig 7b. So the stress distribution in the whole cross section is showing a pressure-tensile-pressure variation.

With increasing the number of the wheels, the longitudinal stress curves on the whole nodes of the center line show a right shifting trend. That is the pressure stress in the rail head decreases gradually, the tensile stress of the rail web increases gradually , but the pressure stress of the rail bottom changes very small.

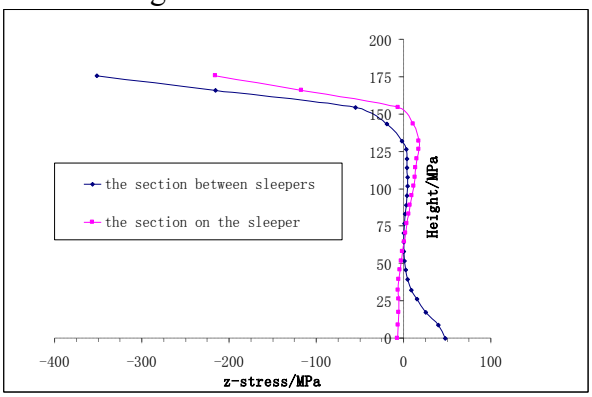
Equivalent stress analysis. With increasing the number of the rolling times, the equivalent stress curves of each node in the rail's center line show a right shifting trend as shown in Fig 7c. In another word, the equivalent stress increases with increasing the wheels' rolling times. Especially, the upper part of rail head and the middle part of rail web show a bigger stress change. The equivalent stress values decrease gradually from the rail head to the rail bottom. After experiencing ten times rolling, the equivalent stress on the rail head surface is the biggest with a value of ~280 MPa. The equivalent stress on the rail bottom is the smallest with a value of ~20 MPa.

Stress contrast

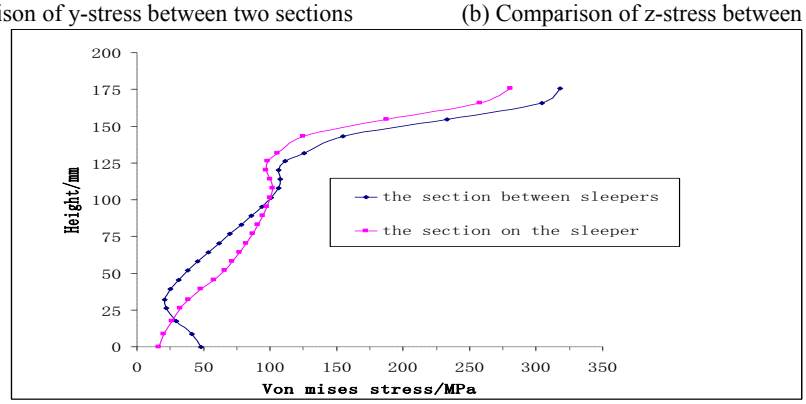
Fig 8 is showing the comparison of y-stress, z-stress and Von equivalent stress between the two cross sectional center lines after experiencing ten wheels rolling.



(a) Comparison of y-stress between two sections



(b) Comparison of z-stress between two sections



（c）Comparison of Von mises stress between two sections

Fig. 8 Comparison of stress between two sections

The maximum y-stress, z-stress and Von equivalent stress are all occurred at the rail head surface. The cross sectional stresses on the sleepers and within the sleepers are different. The maximum stresses with the sleepers are all bigger than the stresses on the sleepers. The maximum difference for y-stress is 145 MPa, for z-stress is 136 MPa, for Von equivalent stress is 37 MPa. These prove that the supporting effect from the sleepers is helpful to alleviate the rail's stress. So it is helpful to pave more sleepers for reducing the rail fatigue and increasing the rail's life time.

Conclusions

(1) Based on considering the real geometry of wheel-rail, boundary conditions and the sleepers' supporting effects, the three dimensional dynamic contact finite model is established by ANSYS/LS-DYNA software. The internal stresses that were repeatedly crushed by the rolling wheels are simulated and analyzed. The analysis for the wheel-rail contact stress is much closer to the real situation.

(2) Under the effects of the wheels, the equivalent stress in the rail head is the biggest. The stress decreases gradually from the rail head to the rail bottom and the stress decrease in the rail head is very fast.
(3) With increasing the number of wheel's rolling times on the rail, the stress increases gradually. But the stress increment is very small.
(4) The stresses within the sleepers and on the sleepers are different. The stresses within the sleepers are all bigger than those on the sleepers. The maximum difference for the vertical stresses is 145 MPa, for the longitudinal stresses is 136 MPa, for the Von equivalent stress is 37 MPa.

Foundation project: Supported by National Science Foundation of China（51374127）

References

[1] Lu Ping ,Cui Da-bin, Wang Ning.Calculation and Analysis Method of Wheel/Rail Contact Stresses[J]. Lubrication Engineering,2009,Vol.34,No.7,28-32.
[2] Wen Ze-feng ,Jin Xue-song , Xiao Xin-biao.Elastic-plastic analysis for rolling contact stresses and deformations of rall under multiple-step non-steady state loading[J]. Engineering Mechanics,2007,Vol.24,No.12,158-164.
[3] Xue Cheng-feng .The Elastic- Plastic Analysis of the Wheel- rail Contact Stress[J].Science & Technology Information,2007,No.34,39,72.
[4] Zhang Jun,Wu Chang-hua. Elasto-plastic analysis of wheel-rail contact problem[J]. Journal of the China Railway Society,2000,Vol.22,No.3,16-21.
[5] Sun Chuan-xi, Zhang Jun,Wang Chun-yan,Lu Zhong-ji. Finite element method analysis of the underground wheel/Rail contact problem in Curvilinear Sections[J].Journal of Dalian Jiaotong University,2008,Vol.29,No.4,22-26.
[6] Guo Jun, Wen Ze-feng,Jin Xue-song, Liu Qi-yue .Three-dimensional elastic-plastic rolling contact stresses in rail[J].Journal of Southwest Jiaotong University,2007,Vol.42,No.3,262-268.
[7] Guo Jun,Wen Ze-feng,Li Wei,Jin Xue-song.Effect of tangential force on elastic-plastic rolling contact stress of rail[J]. Lubrication Engineering, 2010,Vol.35,No.7,6-9.
[8] Makoto Akama.Development of Finite Element Model for Analysis of Rolling Contact Fatigue Crack in Wheel/Rail Systems[J].QR of RTRI, 2007,Vol.48,No.1,8-14.
[9] Wen Ze-feng.Study on rail corrugation[D].Cheng Du: Chengdu:Southwest Jiao Tong University,2006.
[10] Hu Jia-jie.Research on growth of fatigue crack of rail steel under moment of flexure condition[D].Chengdu:Southwest Jiao Tong University,2008.
[11] Wang Cai-yun,Shen Peng,Liu Qi-yue.Numerical and experiment analysis of the effect of speed on rail wear[J]. Lubrication Engineering , 2011,Vol.36, No.11,19-24.
[12] Wang Wen-jian,Zhang Hong-fei,Liu Qi-yue. Research progress of adhesion mechanism of high-speed wheel/rail and simulation experiments[J].Lubrication Engineering, 2011, Vol.36, No.11, 105-108.
[13] Mo Bei,Yan Qing-zhi,Wang Hua.Development of high-speed wheel and rail steel and the damage of wheel and rail under high speed[J]. Railway Locomotive & CAR,2012, Vol.32,No.3,66-70.
[14] Filippov.K.S. Improvement in Quality of Rail Means of Degass[J]. STAL, 1999(12):35-42.
[15] Fujie Xia,Colin Cole,Peter Wolfs.The dynamic wheel-rail contact stresses for wagon on various tracks[J]. Wear,2008,265:1549-1555.

Applied Mechanics and Materials Vol. 597 (2014) pp 557-561
© (2014) Trans Tech Publications, Switzerland
doi:10.4028/www.scientific.net/AMM.597.557

SINS Transfer Alignment Based on Robust SDRE Filter

Dayong Wang , Ping Sun, Peng Jianyi [1], Xing Huo Gang XU[2, b]

Wuhan Mechanical Technology College,Wuhan Hubei , 430075, China

[1]email: pjyxp@163.com

Keywords: SINS; alignment; SDRE filte

Abstract. In order to improve the rapid response ability of the inertial navigation system mounted on the aircrafts which are onboard a ship, a novel rapid transfer alignment method of the strapdown inertial navigation system(SINS) on a rocking base is put forward. Interfering motions such as rolling, pitching, and yawing motions caused by sea waves are effectively used. Meanwhile, to remedy the effects of modeling uncertainty and adapt the nonlinear character in the error models, a robust SDRE (state-dependent Riccati equation) filter design is developed based on the infinity-norm minimization criterion. The filter presented can solve the problem that the standard Kalman filter cannot give the optimal solution when the system model and stochastic information are unknown accurately. Simulation results show that the misalignment angle error estimation can be upgraded dramatically and the new algorithm is less sensitive to uncertainty noise.

Introduction

Due to its small size, high precision, good concealment, the strapdown inertial navigation system (SINS) has developed rapidly in military and civilian fields in recent years [1]. Initial alignment is a fatal technology for SINS, and it affects the navigation performance of the system directly. Transfer alignment is a kind of initial techniques which makes use of the main INS with high accuracy to calibrate the slave INS. Actually this is a data matching process between the main INS and the slave INS [2]. In the precise alignment stage, the small misalignment angles between reference frame and true frame are computed accurately through processing the information of various sensors, and the accurate initial transformation matrix is formulated. Different filtering algorithms are often used in this stage. The state-dependent Riccati equation (SDRE) techniques are rapidly emerging as general design and synthesis methods of nonlinear feedback estimators for a broad class of nonlinear problems [3]. When the system model is inaccurate and noise characteristics don't meet the Gaussian conditions, it is an adequate filter to solve these uncertainties. A filtering algorithm is presented as a kind of robust SDRE filtering for the SINS alignment problem.

The structure of the paper is as follows. Section 2 introduces the SINS error model for the alignment. Section 3 presents the robust SDRE filter. Computer simulation of testing algorithm is presented in Section 4. Finally, Section 5 summarizes and concludes the work.

Models of transfer alignment

1 Coordinate frames

Coordinate frames used below are described as follows [4].

Inertial frame (i frame): Its origin is at the Earth center; z_i axis is normal to the equatorial plane; x_i axis lies in equatorial plane, its direction can be specified arbitrarily; y_i axis complements the right handed system.

Navigation frame (n frame): It is a local geographic coordinate frame; x_n axis points towards east, and y_n axis points towards north; z_n axis is parallel to the upward vertical at the local Earth surface referenced position location.

Body frame (b frame): Its origin is at the centroid of body; x_b axis is along transverse axis; y_b axis is along longitudinal axis; z_b axis is perpendicular to longitudinal plan of symmetry.

Earth fixed frame (e frame): It is a frame fixed to Earth and the origin is at its center. Its z_e axis is coincident with the Earth's polar axis while the other two axes are fixed to the Earth within the equatorial plane.

2 State equations

The misalignment angle equation and the velocity error equation model [5] for the SINS of the carrier craft are described as follows：

$$\dot{X} = AX + Gw \tag{1}$$

where

$$X = [\delta V_E, \delta V_N, \delta V_U, \phi_E, \phi_N, \phi_U, \nabla_x, \nabla_y, \nabla_z, \varepsilon_x, \varepsilon_y, \varepsilon_z]^T$$

$$w = [w_{ax}, w_{ay}, w_{az}, w_{gx}, w_{gy}, w_{gz}]^T$$

$$A = \begin{bmatrix} A_1 & A_2 & C_b^n & 0 \\ 0 & A_3 & 0 & -C_b^n \\ 0 & 0 & 0 & 0 \\ 0 & 0 & 0 & 0 \end{bmatrix}$$

$$A_1 = \begin{bmatrix} 0 & 2\omega_{ie}\sin L & -2\omega_{ie}\cos L \\ -2\omega_{ie}\sin L & 0 & 0 \\ 2\omega_{ie}\cos L & 0 & 0 \end{bmatrix}$$

$$A_2 = \begin{bmatrix} 0 & -g & 0 \\ g & 0 & 0 \\ 0 & 0 & 0 \end{bmatrix}$$

$$A_3 = \begin{bmatrix} 0 & \omega_{ie}\sin L & -\omega_{ie}\cos L \\ -\omega_{ie}\sin L & 0 & 0 \\ \omega_{ie}\cos L & 0 & 0 \end{bmatrix}$$

and ω_{ie} is the Earth's rotation rate, g the local acceleration of gravity, L the local latitude; ∇_x, ∇_y and ∇_z are the biases of three accelerometers respectively, ε_x, ε_y, ε_z the drifts of three gyros respectively, δV_E, δV_N and δV_U east, north and vertical velocity errors respectively, ϕ_E, ϕ_N and ϕ_U east, north and azimuth misalignment angles respectively; C_b^n is the transformation matrix between the body frame and the navigation frame, and w the system noise vector.

3 Measurement equations

Assuming that the ground-speed of the ship is V_{em}^n, the ground-speed of the aircraft is V_{es}^n, the measurement of velocity is [2] :

$$Z_v = V_{es}^n - \left(V_{em}^n + V_{LA}^n\right) \tag{2}$$

and the velocity error is described as δV_{es}^n, δV_{em}^n, δV_{LA}^n.

Robust SDRE filter

Consider a smooth nonlinear uncertain system described by continuous-time equations of the following form [6] :

$$\dot{x}(t) = f(x) + \Delta f(x) + G(t)\omega_0(t) \tag{3}$$

$$y(t)=h(x)+\Delta h(x)+D(t)v_0(t) \tag{4}$$

where $x(t)\in R^n$ is the state, $y(t)\in R^m$ is the measured output, and $\omega_0(t)\in R^p$, $v_0(t)\in R^q$ are process and measurement noises with unknown statistical properties, which stand for exogenous disturbance inputs. Let $\Delta f(x)$ and $\Delta h(x)$ represent the system model uncertainties, we have:

$$\begin{bmatrix}\Delta f(x)\\ \Delta h(x)\end{bmatrix}=\begin{bmatrix}E_1(t)\Delta_1(t)\\ E_2(t)\Delta_2(t)\end{bmatrix}N(x) \tag{5}$$

in which $N(x)\in C^1$, $E_1(t)$ and $E_2(t)$ are known matrix functions with appropriate dimensions that characterize the structure of the uncertainties. Let $C_b^n=\begin{bmatrix}t_{11} & t_{12} & t_{13}\\ t_{21} & t_{22} & t_{23}\\ t_{31} & t_{32} & t_{33}\end{bmatrix}$, and the pitch, roll, and yaw angles determined by the attitude matrix be as follows:

$$\begin{aligned}\psi_s&=\psi+\delta\psi\\ \theta_s&=\theta+\delta\theta\\ \gamma_s&=\gamma+\delta\gamma\end{aligned}, \tag{6}$$

take the pitch angle for example, we can get

$$\tan(\psi+\delta\psi)=\frac{T_{12}+T_{22}\phi_u-T_{32}\phi_N}{T_{22}-T_{12}\phi_u+T_{32}\phi_E}. \tag{7}$$

The nonlinear dynamics (1) and (2) can be put into the following uncertain state-dependent coefficient (SDC) form:

$$\dot{X}=A(x)X+Gw \tag{8}$$

$$Z=C(x)x+D(x)v_0(t) \tag{9}$$

where,

$$A(x)=\begin{bmatrix}A_1-\frac{A_2}{\phi_u} & A_2 & C_b^n+\frac{A_2}{\phi_u} & 0\\ 0 & A_3 & 0 & -C_b^n\\ 0 & 0 & 0 & 0\\ 0 & 0 & 0 & 0\end{bmatrix}.$$

The proposed filter has an SDRE-like structure and is prescribed to be:

$$\dot{\hat{X}}=A(\hat{X})\hat{X}+K(t)\left[Z-C(\hat{X})\hat{X}\right]$$

$$+\mu^{-2}P(t)\nabla_x$$

where, $\mu>0$ is a free design parameter and the filter gain matrix, $K(t)\in R^{n\times m}$, is defined as:

$$K(t)=P(t)C^T(\hat{X})R^{-1}.$$

The positive definite matrix P(t) is updated through the following state-dependent differential Riccati equation (SDDRE) [7] :

$$\dot{P}(t)=A(\hat{X})P(t)+P(t)A^T(\hat{X})+\Gamma(t)Q\Gamma^T(t)$$

$$-P(t)[C^T(\hat{X})R^{-1}C(\hat{X})-\mu^{-2}\nabla_x]P(t)$$

Simulation results

Define the simulation conditions as follows: for a moderate accuracy SINS, the constant and random drifts of each gyro are both chosen as 0.02 (°)/h; and the constant and random biases of each accelerometer are both chosen as $1\times10^{-4}g$; the true attitude angles of the system are 0°, 0° and 0°; the local latitude of SINS place is 19.75°. After the coarse alignment, the horizontal accuracy is 0.15°, and the azimuth accuracy is 0.35°. The initial state vector $\boldsymbol{X}(0)$ is assumed to be $\boldsymbol{0}$. The initial state covariance matrix is defined as

$$P_0 = diag\{(0.1m/s)^2,(0.1m/s)^2,(0.1m/s)^2,$$
$$(1^\circ)^2,(1^\circ)^2,(1^\circ)^2,(0.02(^\circ)/h)^2,(0.02(^\circ)/h)^2,$$
$$(0.02(^\circ)/h)^2,(1\times10^{-4}g)^2,$$
$$(1\times10^{-4}g)^2,(1\times10^{-4}g)^2\}$$

The simulation results are shown in Figs. 1-3.

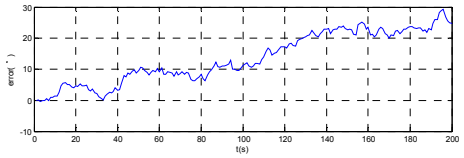


Fig.1 Estimation error of misalignment angle φ_E

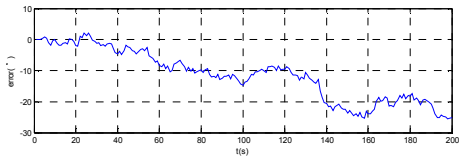


Fig.2 Estimation error of misalignment angle φN

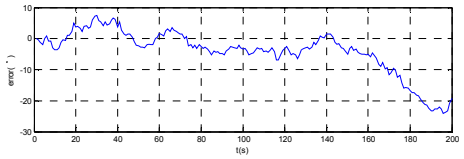


Fig.3 Estimation error of misalignment angle φU

From the figures above，it can be seen that the transfer alignment method based on SDRE filter can complete the estimation of misalignment in less than 200s．The estimation errors of the misalignment angle in all directions are less than 0.5

Conclusion

The accuracy of initial alignment suffers from the relatively high noise levels of the inertial sensors measurements. This leads to the requirements of more sufficient algorithms. This article suggests a robust SDRE filter design to remedy the effects of modeling uncertainty and adapt the nonlinear character in the error models. The results of the simulation indicate that the novel method proposed in this paper is effective for initial alignment in a non-stationary environment.

References

[1] Gao W X, Miao L J, Ni M L. Multiple Fading Factors Kalman Filter for SINS Static Alignment Application. Chinese Journal of Aeronautics 2011; 24: 476-483.

[2] Xu J H, Wang Y J, Xiao Z C. Rapid transfer alignment for SINS of carrier craft. Journal of Systems Engineering and Electronics 2013; 24(2): 303-308.

[3] Çimen T. Systematic and effective design of nonlinear feedback controllers via the state-dependent Riccati equation (SDRE) method. Annual Reviews in Control 2010; 34(1): 32-51.

[4] Qin Y Y. Inertial navigation. Beijing: Science Press, 2006.

[5] Gao W X, Miao L J, Shen J. A method of resistance to disturbance for SINS initial alignment. Transactions of Beijing Institute of Technology 2010; 30(1): 190-194.

[6] Hossein Beikzadeh, Hamid D. Taghirad. Robust SDRE filter design for nonlinear uncertain systems with an H_∞ performance criterion. ISA Transactions 2012; 51: 146-152.

[7] Pertew AM, Marquez HJ, Zhao Q. H-infinite observer design for Lipschitz nonlinear systems. IEEE Transactions on Automatic Control 2006; 51(7):1211–1216

13Cr-2Ni-2Mo Stainless Steel 140
3-Point Bending Test 89
3D Modeling 417
3D Weaving Composite 89
40Cr Steel 223

A

AA5083 Aluminum Alloy 219
ABS 380
Adhesive Strength 157
Adsorption Mechanism 72
Air Nozzle 238
Al Profile 458
Alignment 557
All-Digital Phase-Locked Loop (ADPLL) 515
Alumina 175
Aluminum 103
Aluminum Alloy 5052 253
Angle Tower 332
ANSYS 304, 540
Anti-Lock Braking System (ABS) 411
Antibacterial Activity 45
Antibacterial Mechanism 45
Application 36
Arm 336
Artificial Neural Network (ANN) 349
Attachment Frame 304
Automated Production 417
Average Rolling Force 266
Average Rolling Moment 266
Axial Compression Ratio 312
AZ31 233

B

Backplate Thermal Diffusivity 219
Balance 407
Band Gap 84
Base Pre-Tilting 332
Battery 393
Beam-Column Joint 312
Biological Information 188
Biosensor 435
Blade 431
Blade Screw 476
Blow-Off 238
Brake Disc 540
Braking Force Distribution 525
Buckling Region 291

C

C/C Composites 170
Calibration 384
Carbon Nanotube (CN) 36, 40
Case-Based Reasoning 401
Casting Simulation 203
Catheter 291
Cathodic Prevention 341
Cathodic Protection 341
Cellular Material 121
Cement Matrix 40
Central Angle Division Method 228
Centroid Measurement 365
Ceramic Matrix Composites 175
Chamfer of Teeth Top Edge 213
Chatter 195
Chemical Binder 262
Chemical Vapor Deposition 99
Chips 257
Circulating Rolling 551
Coating 153, 175
Coating Process 28
Coaxial Electrospinning 13
Cold Weather 316
Collagen Hydrolizate 144
Complex Stiffness Method 308
Composite 103, 175
Composite Material 59
Composite Particles 28
Compressive Behavior 296
Compressive Strength 135, 316, 345
Compressive Stress 17
Computer-Aided Design 417
Concentration Ratio 480
Concrete 421
Concrete Cores 283
Conductive Film 188
Conical Ring Rolling 266
Control 376

Controlled Low-Strength Material (CLSM) 345, 349
Controller 468
Cooling Rate 135
Coordinate Transformation 365
Corrosion Resistance 140
Corrosion Sensor 421
Corrugated Chaff 213
Cost-Effective 417
Cosurfactant 13
Coulomb Stress 324
Coulter Counter 7
Coupled 544
CPC 480
CT 257
$Cu_2ZnSnSe_4$ Compounds 84
Curing Days 316
Curing Regimes 320
Current 341
Curved Surface 249
Curves of Mechanical Characteristics 492
Cutting Force Modelling 195
Cutting Process Dynamics 195
CZ Furnace 170

D

Damage Identification 431
Damping 308
Data Model 59
Data Storage 59
Database 59
Dedicated Interface Adapter 444
Delamination 89
Density Functional Theory (DFT) 127
Depolarization Potential 341
Development 36
Dielectric Constant 161
Dielectric Property 161
Dip Coating Process 165
Displacement Speed 291
Dope 53
Drive Roll 498
Driving System 531
Dyeing 144
Dynamic 544
Dynamic Propertry 300, 332
Dynamic Simulation 551
Dynamic Voltage Frequency Scaling (DVFS) 515

E

EAM Potential Function 242
Efficient 417
Elasto-Plastic 257
Elastohydynamic 450
Electric Vehicle (EV) 525
Electrical Performance 488
Electrochemical 421
Electromagnetic 384
Electron Beam 153
Electron-Phonon Coupling 113
Ellipsoid Helix Interpolation 228
Ellipsometry Method 165
EM Algorithm 521
Embedded Equipment 444
Energy Transfer 117
Engineered Cement Composite (ECC) 328
Engineering Analysis 417
Epoxy 63
Equivalent Plastic Strain Distribution 266
Error Sensitivity Direction 454
Evaluation Indexes Calculation 464
Existing Rc Buildings 283
Expansion Plan 476
Experimental Analysis 121
External Grinding 223

F

Fall Prevention 407
Fatigue 336
Fatliquoring 144
Fault Diagnosis 444
Feed-Forward Compensator 372
Fiber Bragg Grating 431
Fiber-Reinforced Composite 59
Fiber Volume Fraction 296
Finite Element (FE) 208, 233, 336, 498
Finite Element Analysis (FEA) 121, 531
Finite Element Method (FEM) 376
First-Principle 113
Flange 233
Flexibility 365
Flexible 188
Flexural Behavior 296
Flow Field 238

Flowability 345
Fly Ash 320
Forming Roller 213
Friction Stir Welding 219, 253
Fuzzy Control 361
Fuzzy-Logic Controller 411
Fuzzy PID 380
Fuzzy Synthetic Evaluation 472

G

Gait Training 407
Globoidal Cam 454
Graphene 21
Graphite 170
Grasp Stiffness 507
Grind-Hardening 223
Guide Sleeve 89
Guyed Transmission Tower 300

H

H_2O_2 Oxidized Loofah Sponge 72
Hardener 63
Hardness 103
Heat Treatment 157
Heavy Rail 551
Helical Gear 450
High Performance Concrete (HPC) 316
High Speed Manufacturing 417
Homopolymerization 63
Hydrothermal Synthesis 109
HyperMesh 203

I

I2C Bus 444
In-Situ Concrete Strength 283
Induction Heating 140
Information System 59
Inite Element 300
Initial Torsion 291
Injection 103
Insulation Break (IB) 488
Integrated Navigation 521
Intelligent Robot 401
Intelligent Wheelchair 361
Intensity 272
Intermetallic Compounds (IMCs) 276
Internal Model 372
Internal Model Control 372
Inverter 393
Ionic Distribution 153
ITER 488
ITO 188

K

Kinect 401

L

Ladle Turret 336
Laminated 308
Large Scale 99
Laser 157
Lie Algebraic Structure 388
Light Emitting Diode (LED) 117
Lightweight Construction 59
Lithium Ion Battery 53
Low-Light Night Vision Goole 439
LSMO 184
Luminescence Materials 117
Lushan M7.0 Earthquake 324

M

MADYMO 544
Magnesium-Yttrium Alloys 135
Magnetic Coupler 492
Magnetic Field 272
Material Data Management 59
Material Database 59
Mathematical Model 468
MATLAB 361
Matrix Material 95
MB Adsorption Kinetics 72
μCt 121
Mechanical-Alloying 103
Mechanical Property 63, 121, 219, 253, 320
Mechanism 502
Mechanized Bridge 444
Meshing Efficiency 450
Mesoporous Materials 13
Metal Nanoparticles (MNPs) 3
Mg/Al Joint 276
Micro-Nanofabrication 7
Microstructure 95, 103, 135, 257
Mirror Effect 397
Mixing Ratio 63
Mixing Temperature 316

Modal Analysis 498
Model Fit 72
Molding Sand 262
Molecular Dynamics Simulation 242
Molecularly Imprinting Technology 131
Monte Carlo Simulation 40
Morpholoy 109
Multi-Body System Theory 454
Multi-Layer Graphene 99
Multi-Objective Optimization 535

N

Nano-$CaCO_3$ 28
Nanochannel 7
Nanocomposite 32
Nanofiber 13
Nanoindentation 17
Nanostructure 49
Naphthalene Content 435
Natural Frequency 498
Non-Ductile Frame 328
Non-Nuclear Density Gauge 384
Normal Coordinate 388
NSGA-II Algorithm 535
Number of Teeth 213
Numerical Analysis 300
Numerical Simulation 213, 238, 484

O

Obstacle Avoidance Simulation 361
Oil Spill Response 472
Online Identification 372
Ontology 401
Optical System Design 439
Optimal Slip Ratio 380
Optimization 417
Optimization Design Analysis 488
Orthogonal Test 223
OsB_2 113
Overloading Protection 492
Oxidation Performance 170

P

Pareto Optimal Solution Set 535
Partially Stabilized Zirconia 353
Peanut 502
Perovskite Manganite 184
Phase angle 425
Phononic Crystal 78
Phthalocyanine Molecule 127
Physical Vapor Deposition 153
Picking Blade 502
Picking Roller 502
Plasma 272
Plasma Polymerization 161
Poisson Conservation Law 388
Polar Radius Equation 476
Poly(butylene succinate) 32
Poly(cyanate ester) 161
Polymethylsilane (PMS) 49
Potential 421
Powder 103
Power Lose 450
Preheat Temperature 253
Preparation 45
Pro/E 203
ProCAST 203
Project Management 59
Property 95, 262
Propulsion System 464
Pulse Steam Expander 425
PWM Rectifier 468

Q

Quality Function Deployment (QFD) 464

R

Rail Contact 551
Raman Spectroscopy 353
Rare Earth 117
Raw Sand 262
Ray-Tracing 480
Reactive Powder 312
Reactive Powder Concrete 320
Receiver 480
Reflective/Diffractive Hybrid Optical System 439
Regenerative Braking 525
Regression 349
Rehabilitation Robot 397
ReRAM 184
Residual Rotation 484
Residual Stress 257
Resistive Switching 184
Response Speed 468

Retannage 144
Road Engineering 384
Road Surface Identification 380
Rolling Contact Fatigue 157
Rough Analytic Hierarchy Process 464

S

Sandwich Plate 535
Scallop Height 249
SCM 435
Scooter 531
Scope of Application 304
SDRE Filte 557
Seat 544
Secondary Development 540
Seismic Performance 312
Seismogenic Structure 324
Sensitive Deformation 454
Separation Technology 131
Setting Time 345
Short-Beam Shear Strength 89
Shot-Peening 353
Si_3N_4 353
Silica 13
Silica Film 165
Silica Fume (SF) 316
Silicon Carbide 49, 99
Silver Doping Nanozinc Oxide 45
Simulation 468, 507
SINS 557
SINS/GPS 521
Sinter 95
Skimmer 472
Skin Pass 238
Sliding Wear 353
SOC 525
Solar Cell 3
Solid-Liquid Separator 476
Solid Phase Extraction 131
Solidification Process 242
Solvo-Thermal Process 84
Solvothermal Method 49
Spacing 249
Spin Filter 127
Spinning 233
Stair-Climbing Robots 411
Statics 507
Steel Fiber Reinforced Concrete (SFRC) 296
Steel-Lead Viscoelastic Damper 376
Stereo Speaker 458
Stirling Engine 425
Strength Analysis 336
Stress Analysis 531
Stress Dependence 17
Stress Field 540
Stress-Strain Curve 17
Stress Triggering 324
Structural Health Monitoring 431
Structure Parameter 502
Superconductivity 113
Surface Plasmon Resonance (SPR) 3
Surrogate Model 535
SVPWM 393
System-on-Chip (SoC) 515

T

Tangential Firing Boiler 484
Temperature Deviation 484
Temperature Distribution 266
Temperature Field 208, 540
Tension Apparatus 458
Tension Point 458
Thermal Bubble 7
Thermal Tuning 78
Thickness 165
Thin Film 157
Thin Plate 78
Three-Electrode Electrochemical System 435
Time-To-Digital Converter (TDC) 515
TiO_2 Nanotube 53
Titanium 257
Titanium Carbide 175
Titanium Dioxide 32
Tower Crane 304
Transmission Tower 376
Turning 195
Two-Phase Structures 242

U

UAT 257
UKF 521
Ultraviolet Aging 32
Underactuated Mechanism 507
Upconversion Luminescence 109

V

Vehicle Frontal Crash 544
Vibration 498
Vibration Band Gap 78
Vibration Membrane 458
Viscoelastic Property 291
Visible Light Communication Based on LED (VLC-LED) 480

W

Water Weight Method 384
Welding Distortion 208
Welding Simulation 208
Wheel 551
Wind-Induced Vibration 376
Wind Power Generation System 468
Wing Wall 328
Wireless Sensor Network (WSN) 401
Wrist Training 397

Z

Zn Transition Metal 276
$Zn(OH)_2$/Graphene Nanocomposites 21
ZnO/Graphene Nanocomposites 21

A

Ahn, K.L. 296

B

Belova, I.V. 121

C

Cai, Y.J. 324
Cai, Y.Q. 464
Cai, Z.Y. 233
Cao, J.H. 13
Cao, W.W. 170
Casas, W.J.P. 208
Castiello, D. 144
Chai, J.L. 384
Chang, R.K. 435
Chen, B.Y. 388
Chen, C.C. 393, 407
Chen, D.D. 7
Chen, H.R. 454
Chen, M. 7
Chen, P. 175
Chen, S. 393, 407
Chen, S.H. 515
Chen, X. 203, 535
Chen, X.B. 450
Chen, Y.L. 407
Cheng, Y.S. 411
Chi, C.H. 401
Chiu, M.C. 425
Choi, Y.J. 184
Chou, C.S. 84
Chu, Z.Y. 99
Chuankrerkkul, N. 103
Ciou, S.H. 407
Cui, D.P. 117

D

Dangelmaier, W. 59
Di, Q.M. 109, 117
Digrisolo, A. 283
Dou, Y.H. 72
Du, C.L. 223
Du, H. 262
Du, Y.P. 531
Duan, X.M. 3

E

Eom, N.Y. 316

F

Feng, W.G. 276
Fiedler, T. 121
Filho, R.F.L. 208
Fu, J.L. 388

G

Gan, F.L. 300, 376
Gao, D.R. 238
Gao, H.H. 188
Gao, J. 113
Gao, Q. 276
Gao, S.S. 521
Gao, X.F. 233
Gu, E.D. 480
Gu, Y.J. 228
Guan, H. 380
Guan, L.K. 336
Guan, Y.J. 266
Guo, B.H. 32
Guo, H.W. 78, 507
Gupta, M. 135

H

Hachisuka, A. 397
Hachisuka, K. 397
Han, L. 109, 117
Han, W.J. 184
Han, Y. 40, 95
Han, Z.T. 223
Handika, R.T. 253
Haqi, S. 219
He, Y. 21
Ho, C.Y. 153, 272
Hsieh, L.Z. 3
Hu, M.J. 203
Hu, T.J. 49, 99
Hu, X.X. 53

Hu, Z.C. 502
Huang, L.J. 345, 349
Huang, W. 203
Huang, Z.D. 531
Huo, N.B. 28
Hwang, Y.S. 407

I

Ihara, I. 17
Inagawa, N. 397
Ishida, M. 140
Iwanaka, K. 353
Izumi, Y. 157

J

Jang, S.J. 296
Jang, Y.I. 316
Jeong, B.W. 458
Jeong, J.A. 341, 421
Jhang, J.W. 84
Jia, X.B. 300
Jia, X.J. 28
Jiang, D.W. 7
Jiang, H.L. 376
Jiang, K.P. 7
Jiang, W.K. 188
Jin, W. 480
Jing, J. 380
Ju, Y.Z. 312, 320
Jung, Y.J. 458

K

Kang, D.H. 328
Kang, K.M. 184
Kao, T.S. 401
Kato, Y. 291
Kida, K. 140
Kim, D.G. 316
Kim, H.R. 328
Kim, M.S. 458
Kim, S.W. 316
Kim, U.S. 458
Klahan, S. 103
Kobayashi, Y. 425
Koike, H. 353
Ku, H.H. 401
Kuang, X.B. 535
Kusharjanta, B. 253

L

Lai, G.J. 425
Le, D.H. 345, 349
Lee, H.S. 184
Lee, M.H. 328
Lee, T.K. 135
Lee, T.W. 184
Lei, D.N. 324
Lei, J.H. 165
Li, B. 304
Li, B.X. 484
Li, C.Y. 312
Li, D. 492
Li, F. 361
Li, G.Y. 49, 99
Li, H. 324
Li, H.P. 175
Li, H.X. 49
Li, J.Z. 417
Li, L. 332
Li, L.L. 233
Li, N. 439
Li, Q. 45, 72, 72
Li, S. 203
Li, S.H. 498
Li, W. 551
Li, X.D. 49, 99
Li, X.W. 45, 72
Li, Y. 521
Li, Y.H. 99
Li, Y.P. 332
Li, Y.R. 468
Lian, F.B. 551
Lim, W.G. 328
Lin, C.K. 425
Lin, M.B. 515
Lin, M.H. 3
Lin, Z.Y. 525
Liu, B.Q. 531
Liu, D. 32
Liu, F. 89
Liu, H.X. 484
Liu, J. 304
Liu, J.J. 188
Liu, J.L. 464
Liu, J.X. 53
Liu, L. 32
Liu, Q.Q. 45

Liu, R.Q. 78, 507
Liu, S. 28
Liu, W.C. 365
Liu, Y. 435, 472, 492
Liu, Y.F. 531
Locatelli, F.R. 208
Lu, C.X. 175
Lu, P.P. 380
Lu, W.H. 84
Lü, X.L. 502
Luo, C.J. 213
Lyu, Z.Y. 544

M

Ma, C. 272
Ma, H. 276
Ma, J. 99
Ma, M. 53
Mao, K.M. 195
Masi, A. 283
Mathier, V. 121
Matsui, M. 397
Matsuo, M. 425
Matsuya, I. 17
Men, H. 188
Meng, G.Y. 492
Meng, W. 266
Mizobe, K. 140
Monhof, M. 59
Muhayat, N. 219, 253
Murch, G.E. 121

N

Nie, Y.J. 480
Nishizawa, M. 157

O

Ogawa, K. 157
Ohtsuki, K. 17
Okamoto, K. 140
Onn, K.W.R. 135

P

Park, C.S. 184
Park, H.H. 184
Park, J.W. 458
Park, W.S. 316
Patcharawit, T. 103
Patil, S. 257
Pei, H.Y. 131
Pei, L. 444
Peng, B.L. 502
Peng, J.Y. 557
Peng, Y.L. 127
Puccini, M. 144

Q

Qiao, H.J. 238
Qiao, Q. 480
Qiu, X.H. 127

R

Rupkrathok, P. 103

S

Santarsiero, G. 283
Santosa, B. 219
Satheesh, B. 63
Setyawan, D. 219
Shan, Z.D. 89
Sheed, D. 257
Sheen, Y.N. 345, 349
Shen, G.J. 131
Shen, H.M. 203
Shibukawa, T. 140
Sim, G.C. 135
Singh, R. 257
Sommer-Dittrich, T. 59
Song, H. 551
Song, L.B. 551
Streichhan, J. 59
Sulistijono, 219
Sulong, M.A. 121
Sun, J.Y. 109, 117
Sun, P. 557
Sun, Q.Z. 262
Sun, Y. 388
Sun, Y.S. 444
Sun, Z.Y. 161

T

Takahashi, K. 353
Takamatsu, T. 157
Tan, X.H. 135
Tanabe, H. 157
Tang, W.Y. 365

Tao, G. 242
Tian, X.G. 535
Triyono, 253
Tsai, Y.H. 272
Tshai, K.Y. 63
Tsuji, T. 397
Tun, K.S. 135

W

Wada, F. 397
Wang, B. 380, 450, 535
Wang, B.M. 40
Wang, C. 365
Wang, C.K. 411
Wang, D.H. 312, 320
Wang, D.L. 233
Wang, D.Y. 557
Wang, G. 13
Wang, J.J. 476
Wang, K. 476
Wang, K.H. 276
Wang, K.W. 304
Wang, L.L. 544
Wang, L.P. 45
Wang, L.X. 228
Wang, M. 72, 233
Wang, M.Q. 308
Wang, M.Z. 161
Wang, S.R. 95
Wang, Y. 72, 89, 384
Wang, Y.J. 95
Wang, Y.Q. 113, 535
Wang, Y.R. 32
Wang, Y.W. 72
Wang, Y.Y. 544
Wang, Z.P. 21
Warrior, N. 63
Wen, P. 242
Weng, C.K.J. 135
Wu, D.Y. 13
Wu, G.L. 21
Wu, H.Y. 435
Wu, M.L. 540
Wu, N. 507
Wu, P. 84
Wu, Q. 476
Wu, Q.Q. 308
Wu, W.C. 153
Wu, X.C. 89
Wu, Y.H. 411
Wu, Z.X. 480
Wu, Z.Y. 53

X

Xiao, S.H. 249
Xiao, W.W. 195
Xu, H.Q. 233
Xu, Q.G. 109, 117
Xu, X.H.G. 557
Xue, B. 109
Xue, G.J. 95
Xue, L.H. 175

Y

Yamamoto, I. 397
Yan, J.G. 262
Yan, P. 454
Yan, S. 444
Yan, S.P. 113
Yan, Y.W. 175
Yan, Z.H. 544
Yang, C.C. 488
Yang, G. 223, 531
Yang, G.S. 458
Yang, W.Y. 431
Yang, X.P. 213, 228
Yang, X.Q. 444
Yang, X.Y. 332
Yang, Y. 521
Yang, Y.Q. 49
Yao, J.K. 551
Yao, Y.Y. 454
Yu, D.G. 296
Yu, H.X. 525
Yu, M.L. 40
Yu, X.X. 195
Yu, Y.P. 435
Yuan, W.Q. 492
Yuliadi, M.Z. 219
Yun, H.D. 296, 316, 328
Yun, Y.J. 296

Z

Zeng, F.M. 464
Zhang, A.Y. 36
Zhang, C. 45
Zhang, J.L. 468

Zhang, L.S. 365
Zhang, P.Q. 262
Zhang, R. 233
Zhang, R.D. 165
Zhang, R.L. 439
Zhang, S.B. 372
Zhang, W.P. 13
Zhang, X.L. 365
Zhang, X.Y. 336
Zhang, Y. 40
Zhang, Y.D. 472
Zhang, Y.H. 431
Zhang, Y.L. 233
Zhang, Y.Q. 13
Zhang, Z.X. 480
Zhao, G.Q. 266
Zhao, H. 454
Zhao, H.J. 78
Zhao, L.P. 454
Zhao, W. 170
Zhao, X. 188
Zhao, X.G. 531
Zhao, X.H. 45, 72
Zhao, X.Y. 161
Zhao, Y.F. 7
Zhao, Z.K. 262
Zheng, Q.T. 188
Zheng, W.Z. 320
Zheng, X.R. 53
Zhong, B. 213
Zhou, L.L. 127
Zhou, P.J. 242
Zhou, W.C. 249
Zhou, Y. 13
Zhou, Y.H. 127
Zhou, Z.M. 228
Zhu, B. 170
Zhu, M. 195
Zhu, X.Y. 540
Zubaydi, A. 219
Zuo, J.Y. 540
Zuo, Y.P. 32